



Geomaterials in Geotechnical Engineering

Advances in Civil Engineering

Geomaterials in Geotechnical Engineering

Lead Guest Editor: Yongfeng Deng

Guest Editors: Annan Zhou, Xinbao Yu, Yonggui Chen,
and Dingwen Zhang



Copyright © 2019 Hindawi. All rights reserved.

This is a special issue published in “Advances in Civil Engineering.” All articles are open access articles distributed under the Creative Commons Attribution License, which permits unrestricted use, distribution, and reproduction in any medium, provided the original work is properly cited.

Editorial Board

- Khalid Abdel-Rahman, Germany
José Aguiar, Portugal
Reza Akhavian, USA
Maria Cruz Alonso, Spain
Serji N. Amirkhanian, USA
P. Ch. Anastasopoulos, USA
Venu G. M. Annamdas, Singapore
Mehrdad Arashpour, Australia
Pedro Arias-Sánchez, Spain
Farhad Aslani, Australia
Daniele Baraldi, Italy
E. Bastidas-Arteaga, France
Chiara Bedon, Italy
Rafik Belarbi, France
Giovanni Biondi, Italy
Hugo C. Biscaia, Portugal
Giosuè Boscato, Italy
Melina Bosco, Italy
Jorge Branco, Portugal
Emanuele Brunesi, Italy
Alberto Campisano, Italy
Francesco Canestrari, Italy
Giulio Castori, Italy
Robert Černý, Czech Republic
Constantin Chalioris, Greece
Noel Challamel, France
Daniel W.M. Chan, Hong Kong
Edwin H W Chan, Hong Kong
Carlos Chastre, Portugal
Ghassan Chehab, Lebanon
Wensu Chen, Australia
Nicholas Chileshe, Australia
Heap-Yih (John) Chong, Australia
Francesco Colangelo, Italy
Ottavia Corbi, Italy
Marco Corradi, Italy
Mario D'Aniello, Italy
Jorge de Brito, Portugal
Gianmarco de Felice, Italy
Stefano de Miranda, Italy
Tayfun Dede, Turkey
Angelo Di Egidio, Italy
Luigi Di Sarno, Italy
Giulio Dondi, Italy
- Mohamed ElGawady, USA
Ahmed Elghazouli, UK
Behzad Esmaeili, USA
Flora Faleschini, Italy
Harry Far, Australia
Antonio Formisano, Italy
Giovanni Garcea, Italy
Emilio García-Taengua, UK
Elhem Ghorbel, France
Agathoklis Giaralis, UK
Rodrigo Gonçalves, Portugal
Arturo Gonzalez, Ireland
Belén González-Fonteboa, Spain
Salvatore Grasso, Italy
Fan Gu, UK
Kirk Hatfield, USA
Khandaker Hossain, Canada
Zahid Hossain, USA
Mohammad R. Hosseini, Australia
Bon-Gang Hwang, Singapore
Dong-Sheng Jeng, Australia
Jian Ji, China
Andreas Lampropoulos, UK
Raffaele Landolfo, Italy
Eul-Bum Lee, Republic of Korea
Chun-Qing Li, Australia
Dongsheng Li, China
Li Li, Canada
Xuemei Liu, Australia
Zaobao Liu, China
Davide Lo Presti, UK
Sui Pheng Low, Singapore
Lyan-Ywan Lu, Taiwan
Eric Lui, USA
Zhongguo John Ma, USA
Lorenzo Macorini, UK
Yann Malecot, France
John Mander, USA
Giuseppe Carlo Marano, Italy
Fabio Mazza, Italy
Claudio Mazzotti, Italy
Ahmed Mebarki, France
Shazim A. Memon, Kazakhstan
Giovanni Minafò, Italy
- Hossein Moayed, Iran
Abbas Mohajerani, Australia
Fabrizio Mollaioli, Italy
Rosario Montuori, Italy
Ayman S. Mosallam, USA
Roberto Nascimbene, Italy
Luís C. Neves, UK
Trung Ngo, Australia
Sanjay Nimbalkar, Australia
Giuseppe Oliveto, Italy
Alejandro Orfila, Spain
Togay Ozbakkaloglu, Australia
Hayri Baytan Ozmen, Turkey
Alessandro Palmeri, UK
Fabrizio Paolacci, Italy
Fulvio Parisi, Italy
Ignacio Paya-Zaforteza, Spain
Arnaud Perrot, France
Christophe Petit, France
Giuseppe Piccardo, Italy
Prodromos Psarropoulos, Greece
Giuseppe Quaranta, Italy
Carlo Rainieri, Italy
Damien Rangaard, France
Dimitris Rizos, USA
Geoffrey W. Rodgers, New Zealand
Hugo Rodrigues, Portugal
Hamid Reza Ronagh, Australia
Pier Paolo Rossi, Italy
Lukasz Sadowski, Poland
Anna Saetta, Italy
Timo Saksala, Finland
Evangelos J. Sapountzakis, Greece
Vasilis Sarhosis, UK
Halil Sezen, USA
M. Shahria Alam, Canada
Faiz U.A. Shaikh, Australia
Mostafa Sharifzadeh, Australia
Sanjay Kumar Shukla, Australia
Amir Si Larbi, France
Stefano Sorace, Italy
Flavio Stochino, Italy
Claudio Tamagnini, Italy
Yaya Tan, China



Patrick W.C. Tang, Australia
Yinshan Tang, UK
Huu-Tai Thai, Australia
Filippo Ubertini, Italy
Humberto Varum, Portugal
Castorina S. Vieira, Portugal
C. Vipulanandan, USA
Claudia Vitone, Italy
Hao Wang, USA
Lei Wang, USA

Linbing Wang, USA
Wayne Yu Wang, UK
Roman Wan-Wendner, Austria
Bo Xia, Australia
Wei-Chau Xie, Canada
Michael Yam, Hong Kong
Libo Yan, Germany
Jian Yang, China
Xu Yang, Australia
Hui Yao, China

Victor Yepes, Spain
Gürol Yildirim, Turkey
Qingliang Yu, Netherlands
Mariano Angelo Zanini, Italy
Xiong Zhang, USA
Yuqing Zhang, UK
Dong Zhao, USA
Xianbo Zhao, Australia
Annan Zhou, Australia
Abdul Aziz bin Abdul Samad, Malaysia

Contents

Geomaterials in Geotechnical Engineering

Yongfeng Deng , Annan Zhou , Xinbao Yu , Yonggui Chen , and Dingwen Zhang 
Editorial (2 pages), Article ID 8614305, Volume 2019 (2019)

A Fractal Model to Interpret Porosity-Dependent Hydraulic Properties for Unsaturated Soils

Annan Zhou , Yang Fan, Wen-Chieh Cheng , and Junran Zhang 
Research Article (13 pages), Article ID 3965803, Volume 2019 (2019)

Effect of Ca/Al Ratio on Stabilization/Solidification of Lead-Contaminated Soil by Ettringite

Lian Xiang , Huamei Zhu, and Ruoyun Zhou 
Research Article (8 pages), Article ID 3612962, Volume 2018 (2019)

Numerical Study of the Dynamic Compaction Process considering the Phenomenon of Particle Breakage

Xi Li , Jing Li, Xinyan Ma, Jidong Teng, and Sheng Zhang 
Research Article (10 pages), Article ID 1838370, Volume 2018 (2019)

Laboratory and Centrifuge Model Tests on Influence of Swelling Rock with Drying-Wetting Cycles on Stability of Canal Slope

Chen Zhang , Zheng-yin Cai , Ying-hao Huang, and Hao Chen 
Research Article (10 pages), Article ID 4785960, Volume 2018 (2019)

Formation Mechanism and Mechanical Properties of Soil-Rock Mixture Containing Macropore

Feng Zhu , Wei Qian, Huilin Le, Haotian Fan, and Wuchao Wang
Research Article (11 pages), Article ID 1594546, Volume 2018 (2019)

A Study on Ceramsite Production Using Dredging Sea Mud and Its Biofilm Formation Capacity Evaluation

Ting Xia , Yue Li, Zhixing Xiao, Shixiang Wang, Qingkai Wu, Suwen Sun, Hui Peng, Dan Chen, and Zhihua Wang 
Research Article (9 pages), Article ID 2401984, Volume 2018 (2019)

Study on Material Properties of Magnesium Oxide Carbonized Prestressed Pipe Piles

Henian Zhang, Miao Cao, Kaixiang Chen, Chen Shen , Peisheng Xi, Fang Zhang, and Shaohan Wang
Research Article (7 pages), Article ID 1202306, Volume 2018 (2019)

Study on Compaction Characteristics and Construction Control of Mixtures of Red Clay and Gravel

Biao Zeng , Lin-feng Wang , Yun Tian , Tao-rui Zeng , and Bing Li 
Research Article (8 pages), Article ID 8079379, Volume 2018 (2019)

Engineering Characteristics and Reinforcement Approaches of Organic Sandy Soil

Jun Hu , Liang Jia , Wei Wang , Hong Wei, and Juan Du
Research Article (12 pages), Article ID 7203907, Volume 2018 (2019)

Study on the Spatially Variable Saturated Hydraulic Conductivity and Deformation Behavior of Accumulation Reservoir Landslide Based on Surface Nuclear Magnetic Resonance Survey

Shu Zhang , Yunshan Xiahou, Huiming Tang , Lei Huang , Xiao Liu, and Qiong Wu
Research Article (15 pages), Article ID 7290640, Volume 2018 (2019)

Shearing Performance of Lime-Reinforced Iron Tailing Powder Based on Energy Dissipation

Ping Jiang , Lingqi Qiu, Na Li , Wei Wang , Aizhao Zhou, and Jingping Xiao
Research Article (8 pages), Article ID 4748526, Volume 2018 (2019)

Numerical Modeling of Thermal-Dependent Creep Behavior of Soft Clays under One-Dimensional Condition

Qi-Yin Zhu  and Ping Qi
Research Article (11 pages), Article ID 9827673, Volume 2018 (2019)

Effect of Colluvial Soil Slope Fracture's Anisotropy Characteristics on Rainwater Infiltration Process

Ling Zeng, Jie Liu, Jun-hui Zhang , Han-bing Bian, and Wei-hua Lu
Research Article (11 pages), Article ID 7351628, Volume 2018 (2019)

Experimental Study on the Fine-Grained Uranium Tailings Reinforced by MICP

Rong Gui , Yu-xiang Pan , De-xin Ding, Yong Liu, and Zhi-jun Zhang 
Research Article (10 pages), Article ID 2928985, Volume 2018 (2019)

Crystalline Swelling Process of Mg-Exchanged Montmorillonite: Effect of External Environmental Solicitation

Marwa Ammar and Walid Oueslati 
Research Article (18 pages), Article ID 8130932, Volume 2018 (2019)

Effect of Osmotic Pressure on Migration Behavior of nZnO in GCLs

Ping Yang, Tao Jiang , Youlong Zhang, and Zhicheng Li
Research Article (9 pages), Article ID 6703485, Volume 2018 (2019)

Consolidated Undrained Triaxial Compression Tests and Strength Criterion of Solidified Dredged Materials

Jianwen Ding , Xusong Feng, Yupeng Cao , Sen Qian , and Feng Ji
Research Article (10 pages), Article ID 9130835, Volume 2018 (2019)

Studying Shear Performance of Flax Fiber-Reinforced Clay by Triaxial Test

Qiang Ma , Yicong Yang , Henglin Xiao , and Wenwen Xing 
Research Article (8 pages), Article ID 1290572, Volume 2018 (2019)

Investigating the Factors Affecting the Properties of Coral Sand Treated with Microbially Induced Calcite Precipitation

Wenni Deng  and Yue Wang 
Research Article (6 pages), Article ID 9590653, Volume 2018 (2019)

Effect on the Resistance of Concrete Acid Corrosion in Superficial Soil Layers

Jihong Wei , Jin Liu , Yuxia Bai, Zezhuo Song, Qiao Feng, Yi Lu, and Shaorui Sun 
Research Article (9 pages), Article ID 7435719, Volume 2018 (2019)

Research on the Slurry for Long-Distance Large-Diameter Pipe Jacking in Expansive Soil

Xian Yang , Yang Liu, and Chao Yang
Research Article (9 pages), Article ID 9040471, Volume 2018 (2019)

Deformation and Damping Characteristics of Lightweight Clay-EPS Soil under Cyclic Loading

Yundong Zhou, Mingdong Li , Qibao He, and Kejun Wen 
Research Article (10 pages), Article ID 8093719, Volume 2018 (2019)

Utilization of Electroplating Sludge as Subgrade Backfill Materials: Mechanical and Environmental Risk Evaluation

Yu Zhang, Peixin Shi , Lijuan Chen, and Qiang Tang 
Research Article (9 pages), Article ID 4891418, Volume 2018 (2019)

Lab Study on the Effect of Cation Exchange Capacity on Slurry Performance in Slurry Shields

By Pinghe Sun, Binkui Zhao, Han Cao , Jingyuan Wang, Dingqiang Mo, and Shaohe Zhang
Research Article (9 pages), Article ID 2942576, Volume 2018 (2019)

Optimization of Slope Structural Parameters Based on Mathews Stability Graph Probability Model

Long Zhang , Jian-hua Hu , Xue-liang Wang, and Lei Zhao
Research Article (7 pages), Article ID 1754328, Volume 2018 (2019)

Fractal Pattern of Particle Crushing of Granular Geomaterials during One-Dimensional Compression

Jiru Zhang  and Biwen Zhang 
Research Article (14 pages), Article ID 2153971, Volume 2018 (2019)

Practical Approach to Predicting the K_0 Behavior of In Situ Sandy Gravel

Ming-Jie Jiang , Jun-Gao Zhu , En-yue Ji, Ying-qi Wei, and Zhi-zhou Geng
Research Article (9 pages), Article ID 9582918, Volume 2018 (2019)

Experimental Studies on Drying-Wetting Cycle Characteristics of Expansive Soils Improved by Industrial Wastes

Hao Ye, Chengfu Chu , Long Xu, Kunlong Guo, and Dong Li
Research Article (9 pages), Article ID 2321361, Volume 2018 (2019)

Analysis of Large-Strain Consolidation Behavior of Soil with High Water Content in Consideration of Self-Weight

Yupeng Cao , Jian Yang , Guizhong Xu , and Jianwen Xu 
Research Article (10 pages), Article ID 6240960, Volume 2018 (2019)

Investigations on Engineering Properties of Solidified/Stabilized Pb-Contaminated Soil Based on Alkaline Residue

Fusheng Zha , Dongdong Pan, Long Xu, Bo Kang, Chengbin Yang , and Chengfu Chu
Research Article (9 pages), Article ID 8595419, Volume 2018 (2019)

Quantification of the Transparency of the Transparent Soil in Geotechnical Modeling

Li-Da Yi, Hua-Bin Lv, Tian Ye, and Yi-Ping Zhang 

Research Article (8 pages), Article ID 2915924, Volume 2018 (2019)

A Systematic Method to Evaluate the Shear Properties of Soil-Rock Mixture considering the Rock Size Effect

Minghui Ren , Guangsi Zhao , Xianhao Qiu, Qinghua Xue, and Meiting Chen

Research Article (9 pages), Article ID 6509728, Volume 2018 (2019)

Thermal Conductivity of Compacted GO-GMZ Bentonite Used as Buffer Material for a High-Level Radioactive Waste Repository

Yong-Gui Chen , Xue-Min Liu, Xiang Mu, Wei-Min Ye, Yu-Jun Cui, Bao Chen, and Dong-Bei Wu

Research Article (11 pages), Article ID 9530813, Volume 2018 (2019)

Geotechnical Properties and Microstructure of Lime-Fly Ash-Phosphogypsum-Stabilized Soil

Tebogo Pilgrene Mashifana , Felix Ndubisi Okonta, and Freeman Ntuli

Research Article (9 pages), Article ID 3640868, Volume 2018 (2019)

Experimental Study on Electrical Resistivity of Cement-Stabilized Lead-Contaminated Soils

Zhiguo Cao , Lian Xiang, Erxing Peng, and Kai Li

Research Article (11 pages), Article ID 4628784, Volume 2018 (2019)

Estimation of Influence Scope of Lateral Displacement of Soft Ground under Vacuum Pressure with PVD

Jingyun Liu, Hongtao Fu, Jun Wang , Yuanqiang Cai, and Xiuqing Hu

Research Article (11 pages), Article ID 8248049, Volume 2018 (2019)

Calculation of Capillary Rise Height of Soils by SWCC Model

Yuhan Li , Chen Zhang, Chenghao Chen , and Hao Chen 

Research Article (10 pages), Article ID 5190354, Volume 2018 (2019)

Microstudy of the Anisotropy of Sandy Material

Kunyong Zhang , Zhenjun Zang , Leslie Okine, and Jose Luis Chavez Torres 

Research Article (13 pages), Article ID 3971643, Volume 2018 (2019)

Influences of Drying and Wetting Cycles and Compaction Degree on Strength of Yudong Silt for Subgrade and Its Prediction

Junran Zhang , Tong Jiang , Xingcui Wang, Chong Liu, and Zhiquan Huang

Research Article (10 pages), Article ID 1364186, Volume 2018 (2019)

Test on the Stabilization of Oil-Contaminated Wenzhou Clay by Cement

Chuang Yu, Raoping Liao, Chaopeng Zhu, Xiaoqing Cai, and Jianjun Ma 

Research Article (9 pages), Article ID 9675479, Volume 2018 (2019)

A Simplified Nonlinear Method for a Laterally Loaded Pile in Sloping Ground

Pingbao Yin , Wei He , and Zhaohui Joey Yang 

Research Article (9 pages), Article ID 5438618, Volume 2018 (2019)

Study on the Fractal Characteristics of Fracture Network Evolution Induced by Mining

Tao Liang, Xiaoli Liu , Sijing Wang, Enzhi Wang, and Quansheng Li

Research Article (13 pages), Article ID 9589364, Volume 2018 (2019)

Effects of Spatially Varying Seismic Ground Motions and Incident Angles on Behavior of Long Tunnels

Yundong Zhou, Yongxin Wu , Ziheng Shangguan, and Zhanbin Wang

Research Article (6 pages), Article ID 8195396, Volume 2018 (2019)

Experimental and Theoretical Studies on the Creep Behavior of Bayer Red Mud

Baoyun Zhao , Wei Huang, Zhile Shu, Mengmeng Han, and Yanbo Feng

Research Article (9 pages), Article ID 6327971, Volume 2018 (2019)

Editorial

Geomaterials in Geotechnical Engineering

Yongfeng Deng ¹, **Annan Zhou** ², **Xinbao Yu** ³, **Yonggui Chen** ⁴,
and Dingwen Zhang ¹

¹*Southeast University, Nanjing, China*

²*Royal Melbourne Institute of Technology (RMIT), Melbourne, Australia*

³*University of Texas at Arlington, Arlington, USA*

⁴*Tongji University, Shanghai, China*

Correspondence should be addressed to Annan Zhou; annan.zhou@rmit.edu.au

Received 26 December 2018; Accepted 26 December 2018; Published 21 January 2019

Copyright © 2019 Yongfeng Deng et al. This is an open access article distributed under the Creative Commons Attribution License, which permits unrestricted use, distribution, and reproduction in any medium, provided the original work is properly cited.

In the special issue, a total of 79 manuscripts were received, and 44 of these were accepted. This special issue aims to highlight some recent innovations on multiphase geomaterials before and after modifications. Geomaterials are materials inspired by geological systems originating from the billion years long history of the earth. However, with the industrialization, these materials are artificially processed to the outputs as construction materials or by-product wastes. The geomaterials may include rock, clay, granular materials, treated soils, and industrial waste. The cognition on the observed behaviour of geomaterials should be upgraded by newly developed multiphase/scale analysis methods. It could be of great benefit to enhance the safety and reliability of geotechnical infrastructures built on/by geomaterials if a clear understanding can be achieved. Therefore, the micro-macro behaviour, interpretation and modelling, modification, and engineering application of multiphase geomaterials should be systematically studied by the new testing technologies, new theoretical frameworks, and new analysis tools. In particular, as environmental requirement and engineering availability of by-product wastes, the efficient recycling of the waste for geotechnical infrastructures is included in this issue.

1. Natural Geomaterials

This special issue successfully attracted several interesting original articles addressing the mechanical and hydraulic behaviour of natural geomaterials.

Special attentions have been paid to the mechanical and hydraulic behaviour of natural geomaterials under complex loading conditions like drying-wetting cycles and loading

cycles. For example, C. Zhang et al. presented a series of laboratory and centrifuge model tests on influence of swelling rock with drying-wetting cycles on stability of canal slope. L. Zeng et al. studied the effect of colluvial soil slope fracture's anisotropy characteristics on the rainwater infiltration process. Y. Zhou et al. focused on the deformation and damping characteristics of lightweight clay-EPS soil under cyclic loading. Y. Li et al. presented a new method to perform a calculation of capillary rise height of soils by the SWCC model. J. Zhang et al. studied influences of drying and wetting cycles and compaction degree on strength of Yudong silt for subgrade.

One of the highlights is the engineering behaviour of mixed natural geomaterials like soil-rock mixtures. For example, F. Zhu et al. provided a study on formation mechanism and mechanical properties of soil-rock mixture containing macropores. B. Zeng et al. presented a study on compaction characteristics and construction control of mixtures of red clay and gravel. M. Ren et al. proposed a systematic method to evaluate the shear properties of soil-rock mixture considering the rock size effect.

In the scope of study on the natural geomaterials, another focus is creep behaviour. B. Zhao et al., for example, presented experimental and theoretical studies on the creep behaviour of Bayer red mud. Q.-Y. Zhu and P. Qi presented numerical modelling of thermal-dependent creep behaviour of soft clays under the one-dimensional condition.

Microstructure and its variation in the natural geomaterials such as particle breakage and anisotropy are also highlighted in this issue. For example, X. Li et al. presented a numerical study of the dynamic compaction process

considering the phenomenon of particle breakage. J. Zhang and B. Zhang investigated the fractal pattern of particle crushing of granular geomaterials during one-dimensional compression. K. Zhang et al. presented a microstudy of the anisotropy of the sandy material.

2. Treated Geomaterials

Compared with the natural geomaterials, this special issue gathered more innovative studies on the mechanical and hydraulic behaviour of treated geomaterials.

The strength and deformation behaviour of the treated geomaterials are essential for their engineering applications. Therefore, many research works in this special issue are related to the experimental study on the strength and deformation behaviour. For example, P. Jiang et al. studied the shearing performance of lime-reinforced iron tailing powder based on energy dissipation. R. Gui et al. presented an experimental study on the fine-grained uranium tailings reinforced by MICP. J. Ding et al. performed a series of consolidated undrained triaxial compression tests and proposed a strength criterion of solidified dredged materials. Q. Ma et al. employed triaxial tests to study the shear performance of flax fiber-reinforced clay.

Regarding the research related to the treated geomaterials, the environmental effects of treated geomaterials are also one of the focuses. For example, P. Yang et al. studied the effect of osmotic pressure on migration behaviour of n ZnO in GCLs. M. Ammar and W. Oueslati presented a study on the crystalline swelling process of Mg-exchanged montmorillonite. J. Wei et al. studied the effect on the resistance of concrete acid corrosion in superficial soil layers. Y. Zhang et al. presented a mechanical and environmental risk evaluation for the utilization of electroplating sludge as subgrade backfill materials. F. Zha et al. investigated engineering properties of solidified/stabilized Pb-contaminated soil based on alkaline residue. Y.-G. Chen et al. provided a study on thermal conductivity of compacted GO-GMZ bentonite used as a buffer material for a high-level radioactive waste repository. Z. Cao et al. presented an experimental study on electrical resistivity of cement-stabilized lead-contaminated soils.

Some attentions are also on reinforcement approaches. For example, J. Hu et al. presented innovative reinforcement approaches for organic sandy soil. T. Xia et al. demonstrated a study on ceramsite production using dredging sea mud and its biofilm formation capacity evaluation. C. Yu et al. discussed the stabilization of oil-contaminated Wenzhou clay by cement.

Regarding the hydraulic properties of treated materials, H. Ye et al. presented experimental studies on drying-wetting cycle characteristics of expansive soils improved by industrial wastes. Some interesting research works related to the microstructure of treated geomaterials are included. For example, T. P. Mashifana et al. studied geotechnical properties and microstructure of lime-fly ash-phosphogypsum-stabilized soil.

Therefore, in our opinion, this special issue brings new insights into the natural and treated multiphase geomaterials,

in terms of the theoretical studies from micro- to macroscale and experimental investigations in laboratory and in situ. We hope that the information delivered in this special issue will help to pave the way for the understanding and development of multiphase geomaterials and their engineering applications.

Conflicts of Interest

The editors declare that they have no conflicts of interest regarding the publication of this special issue.

*Yongfeng Deng
Annan Zhou
Xinbao Yu
Yonggui Chen
Dingwen Zhang*

Research Article

A Fractal Model to Interpret Porosity-Dependent Hydraulic Properties for Unsaturated Soils

Annan Zhou ¹, Yang Fan,² Wen-Chieh Cheng ³ and Junran Zhang ⁴

¹School of Engineering, Royal Melbourne Institute of Technology (RMIT), Melbourne, VIC 3001, Australia

²School of Transportation Science and Engineering, Beihang University, Beijing 100191, China

³School of Civil Engineering, Xi'an University of Architecture and Technology, Xi'an 710055, China

⁴Henan Province Key Laboratory of Geomechanics and Structural Engineering,
North China University of Water Resources and Electric Power, Zhengzhou, Henan 450045, China

Correspondence should be addressed to Annan Zhou; annan.zhou@rmit.edu.au

Received 14 June 2018; Accepted 12 November 2018; Published 8 January 2019

Academic Editor: Castorina S. Vieira

Copyright © 2019 Annan Zhou et al. This is an open access article distributed under the Creative Commons Attribution License, which permits unrestricted use, distribution, and reproduction in any medium, provided the original work is properly cited.

This paper presents a simple fractal model to quantify the effects of initial porosity on the soil-water retention curve and hydraulic conductivity of unsaturated soils. In the proposed conceptual model, the change of maximum pore radius, which largely determines the change of the air-entry value, is directly related to the fractal dimension of pore volume (D) and porosity change. The hydraulic properties of unsaturated soils are then governed by the maximum pore radius, the fractal dimension of pore volume (D), and the fractal dimension of drainable pore volume ($D_d \leq D$). The new fractal model removes the empirical fitting parameters that have no physical meaning from existing models for porosity-dependent water retention and hydraulic behaviour and employs parameters of fractal dimensions that are intrinsic to the nature of the fractal porous materials. The proposed model is then validated against experimental data from the literature on soil-water retention behaviour and unsaturated conductivity.

1. Introduction

Hydraulic properties usually refer to the properties that are related to the water retention behaviour and the hydraulic conductivity of soil, which have numerous applications in geotechnical engineering [1–6]. Soil-water retention behaviour is usually described by the soil-water retention curve (SWRC or the soil-water characteristic curve, SWCC), which is defined as the relationship between the effective degree of saturation, S_e , and the matric suction, s . Conversely, the hydraulic conductivity of soil is commonly described using the hydraulic conductivity function (HCF), which is defined as the relationship between the relative coefficient of conductivity, K_r (the ratio between the unsaturated and saturated values, K/K_s), and the matric suction, s , or the effective degree of saturation, S_e . It is generally recognised that the hydraulic conductivity for unsaturated soils can be effectively estimated using the soil-water retention curve, which is one of the most important applications of SWRC [7].

Numerous equations have been proposed to model SWRCs for partially saturated soils [7–11] and for HCFs [7, 11–14]. Some of these equations are based on a functional regression of the experimental data, while others are based on empirical correlations with other soil properties, such as particle or pore-size distribution, porosity, and specific surface area. However, concerns are often raised about the empirical nature of those models because they do not shed any light on the fundamental physical principles that govern the processes of unsaturated flow and drainage [15]. Several physical models for soil hydraulic properties based on the concept of fractal geometry for soil texture and pore structure have been developed [15–24]. The most important motivation to develop fractal SWRC models and fractal HCF models is that these models are able to remove the empirical fitting parameters that have no physical meaning and employ parameters of fractal dimensions that are intrinsic to the nature of the fractal porous materials [15].

One specific factor that affects the SWRC and HCF is the porosity (ϕ) or void ratio ($e = \phi/(1 - \phi)$) of the soil. A change

in soil porosity can lead to a significant change in the SWRC and HCF (experimental evidence can be found in the studies of Cronney and Coleman [25] and Laliberte et al. [26]); such a change is a common feature of natural soils [27]. However, it is difficult to justify that samples of a given soil with different porosities should be treated as entirely different soils for modelling. Nevertheless, most of the empirical and fractal SWRC and HCF models mentioned above omit the porosity dependency of soil hydraulic properties.

The issue of the effects of porosity on the hydraulic properties of soil was perhaps first raised by Cronney and Coleman [25] and then followed by Laliberte et al. [26]. Recently, the study of the porosity effects on hydraulic properties of unsaturated soils has attracted much attention because of the rapid development of unsaturated soil mechanics involving hydromechanical coupling [28–38]. In the literature, a few approaches have been proposed to model the effect of soil porosity on SWRCs and HCFs. For example, Gallipoli et al. [28] suggested including a function of specific volume (v) in the SWRC equation proposed by Van Genuchten [11]. Assouline suggested an empirical approach based on regression that could model the effects of an increasing soil bulk density on the soil-water retention curve (SWRC) and the hydraulic conductivity function (HCF) [27, 39]. Sun et al. proposed a hydraulic model where a change in the degree of saturation (S_r) can be caused by a change in the matric suction or a change in soil volume (v) [40, 41]. Masin [30] proposed a hydraulic model that can predict the dependency of the degree of saturation (S_r) on the void ratio (e) using the effective stress principle. Tarantino [42] proposed a SWRC equation for deformable soils based on an empirical power function of the water ratio (e_w). Very recently, Sheng and Zhou [43] and Zhou et al. [44] proposed an incremental relationship between the degree of saturation (S_r) and the void ratio (e) by realising that the SWRC is obtained under constant stress instead of constant volume.

However, almost all these approaches are based on phenomenological methodology. Therefore, the modelling parameters used to interpret the dependency of SWRC and HCF on the initial void ratio (e.g., parameters ϕ and ψ in Gallipoli et al. [28]; parameter λ_{se} in Sun et al. [45]; parameter λ_{p0} in Masin [30]; and parameter ζ in Zhou et al. [44]) lack any physical meaning and depend on experimental observations. In this paper, we propose a simple physical model based on fractal geometry to quantify the effects of initial porosity on the soil-water retention curve (SWRC) and the hydraulic conductivity function (HCF) of unsaturated soils. The proposed porosity-dependent SWRC and HCF models only require three parameters: the air-entry value at a specific initial void ratio (s_{ae}^*), the fractal dimension of pore volume (D), and the fractal dimension of drainable pore volume (D_d).

2. Theory and Presentation of the Model

2.1. Fractal Porous Medium. As shown in Figure 1, a porous medium (V_0) contains a broad range of pore sizes, which decrease in the mean radius from r_0 to r_u ($u \gg 1$) and in pore volume from P_0 (the volume of the maximum pore) to

P_u (the volume of the minimum pore). The pores are further divided into two categories [46, 47]: interparticle pores (including interaggregate macropores and intraaggregate micropores), which can be deformed via external loads and dewatered by the capillary process or heating, and intraparticle pores, which contain water that is strongly bounded with soil solids. Mercury intrusion porosimetry (MIP) test can be employed to determine the distribution of interparticle pores of soil [48]. During the test, mercury was compressed into pores with different radii at different intrusion pressures. The MIP technique has been widely used for geomaterials like soils. The major limitations of MIP technique include (1) it can only measure the largest available access to a pore (i.e., the size of the entrance towards a pore; for most cases, the entrance size to a pore can be substantially smaller than the inner pore size.) and (2) all the calculations are based on the assumption of cylinder pores. Intraparticle pores are nondeformable, and the intraparticle pore water cannot be dehydrated in the context of this research. In other words, strongly bounded water can be approximately considered a part of the soil solids (V_m in Figure 1) in this research. The mean radius of the interparticle pores decreases from r_0 to r_{m-1} , and the pore volume decreases from P_0 to P_{m-1} . The mean radius of the interparticle pores decreases from r_m to r_u , and the pore volume decreases from P_m to P_u .

Following Rieu and Sposito [22], a real porous medium can be assumed to be a fractal medium in which there is self-similarity of the pore radius in the entire domain from r_0 to r_u . In terms of pore space, we assume that

$$\begin{aligned} r_{i+1} &= \gamma r_i, \\ P_{i+1} &= \gamma^E P_i, \end{aligned} \quad (1)$$

where E is the Euclidean dimension, which is equal to 2 for two-dimensional objects (such as the Sierpinski triangle and the Sierpinski carpet) and 3 for three-dimensional objects (such as the Menger sponge), respectively. γ is a linear similarity ratio that is introduced to describe the scaling property of a fractal medium. For example, γ is equal to 1/3 for the Sierpinski carpet (Figure 2) and 1/2 for the Sierpinski triangle, respectively. V_i is defined as the i^{th} self-similar partial volume, which contains all pores that have a radius $\leq r_i$. V_{m-1} is the self-similar partial volume that contains the smallest interparticle pores (radius r_{m-1}) and V_m , which stands for the volume of a soil solid particle that is nondeformable and contains all of the intraparticle pores. If the i^{th} self-similar partial volume can be represented by its mean radius R_i , similar to pores in the fractal medium [22], we have

$$\begin{aligned} R_{i+1} &= \gamma R_i, \\ V_{i+1} &= \gamma^E V_i. \end{aligned} \quad (2)$$

The self-similarity property of a fractal porous medium means that the $(i + 1)^{\text{th}}$ self-similar partial volume repeats the same pore property of the i^{th} self-similar partial volume. For example, for the Sierpinski carpet (Figure 2), V_0 contains 1 P_0 and 8 ($=3^2 - 1$) V_1 , V_1 contains 1 P_1 and 8 V_2 , \dots , V_{m-1} contains 1 P_{m-1} and 8 V_m . In general, such a self-similarity can be written as

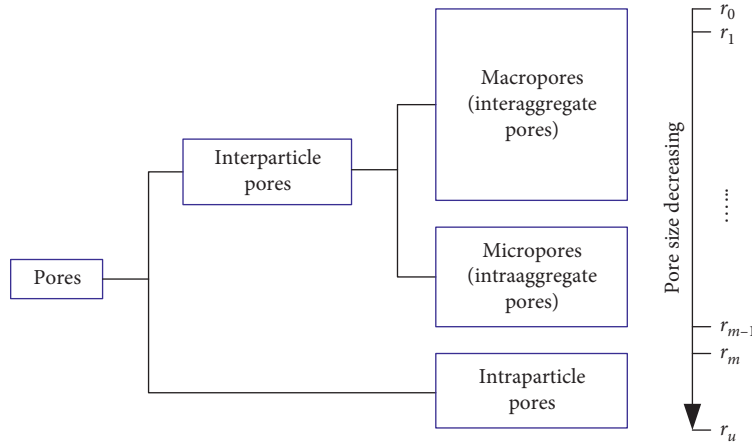
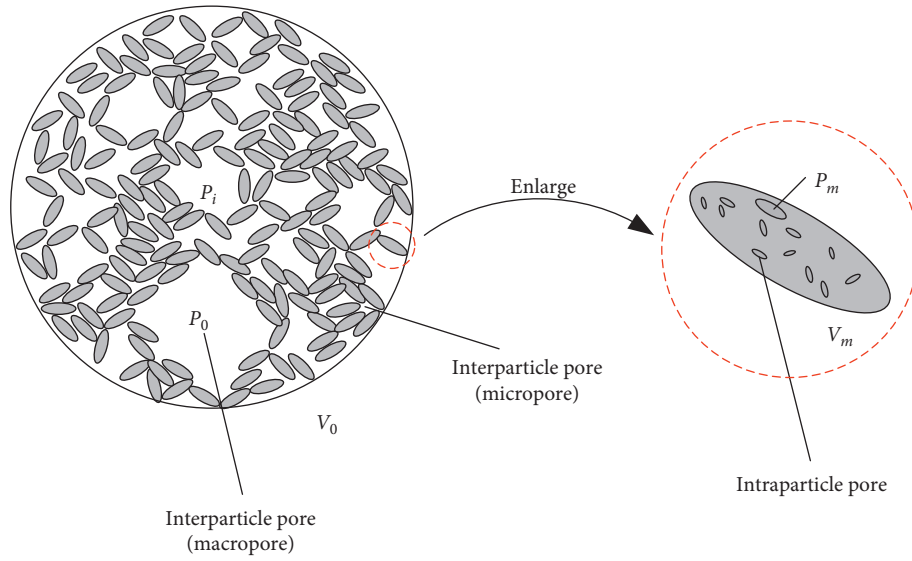


FIGURE 1: Characterization of pores.

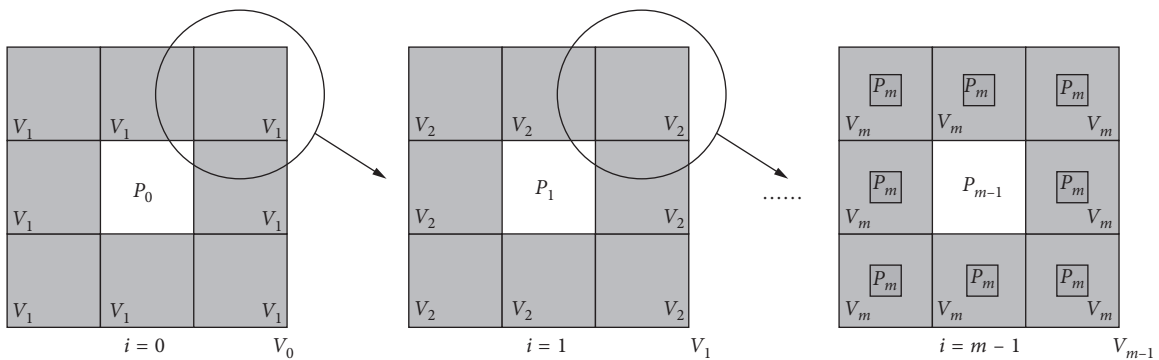


FIGURE 2: Schematic diagram of fractal porous medium (Sierpinski carpet).

$$V_i = NV_{i+1} + P_i, \quad (3)$$

where a constant number N stands for the number of the $(i + 1)^{\text{th}}$ self-similar partial volume in the i^{th} self-similar partial volume. For the Sierpinski carpet, as shown in Figure 2, $N = 8$. According to equation (3), the total volume V_0 can be written as

$$V_0 = \sum_{i=0}^{m-1} N^i P_i + N^m V_m, \quad (4)$$

where $N^m V_m$ stands for the total solid volume (V_s) in this porous medium. In addition, the pore coefficient Γ is defined as the ratio between the i^{th} pore volume and the i^{th} self-similar partial volume, i.e., $\Gamma = P_i/V_i$. $\Gamma = (1/3)^2$ for the

Sierpinski carpet. V_{i+1}/V_i can be written as a function of Γ , i.e.,

$$\frac{V_{i+1}}{V_i} = \frac{1-\Gamma}{N}. \quad (5)$$

Combining equations (4) and (5) generates

$$\frac{V_m}{V_0} = \frac{V_m}{V_{m-1}} \frac{V_{m-1}}{V_{m-2}} \dots \frac{V_2}{V_1} \frac{V_1}{V_0} = \frac{(1-\Gamma)^m}{N^m}. \quad (6)$$

According to equation (6), the porosity of the medium thus can be written as

$$\phi = \frac{V_0 - V_s}{V_0} = \frac{V_0 - N^m V_m}{V_0} = 1 - (1-\Gamma)^m. \quad (7)$$

For a fractal medium, in terms of pore volume distribution, the number of N and the linear similarity ratio γ can be related through the fractal dimension D [49] of pore space:

$$D_v \equiv \frac{\log N}{\log(1/\gamma)} \text{ or } N = \gamma^{-D}. \quad (8)$$

As mentioned in the study of Gimenez [50], the fractal dimension D of pore volume can be measured using two-dimensional images of cross sections of soils with either the box-counting technique or by the pore size count [51, 52].

Combining equations (2), (5), and (8), we have

$$\frac{V_{i+1}}{V_i} = \frac{1-\Gamma}{N} = \gamma^E \longrightarrow \Gamma = 1 - \gamma^{E-D} \text{ or } 1 - \Gamma = \gamma^{E-D}. \quad (9)$$

Therefore, the porosity of the medium can be rewritten by substituting equation (9) into equation (7):

$$\phi = 1 - (\gamma^m)^{E-D}. \quad (10)$$

According to equation (1), γ^m can be replaced by r_m/r_0 . Therefore, equation (10) can be rewritten as

$$\phi = 1 - \left(\frac{r_m}{r_0}\right)^{E-D} \quad (0 < D < E), \quad (11)$$

where r_m is the radius of maximum intraparticle pores, which is a constant because the soil particles are assumed as nondeformable. It also augured that equation (11) disagrees with the porosity equation proposed by Katz and Thompson [53] and results in zero porosity when $D=E$ and, therefore, questioned its validity. However, Hunt [54] concluded that Katz and Thompson's model and Rieu and Sposito's model (equation (11)) can be precisely compatible if Katz and Thompson's model involves solid structures and Rieu and Sposito's model involves pore spaces. As mentioned in the study of Hunt [54]; Rieu and Sposito's model is valid for the pore space and Katz and Thompson's cannot be valid if D refers to the pore space. Therefore, it is important to note that the fractal dimension (D) here refers to the pore space other than the solid space in this research. In fact, the condition $D=E$ does not happen for soils in the real world. Experimental evidence [50] shows that the

fractal dimensions for various soils are less than the Euclidean dimension. Therefore, Perrier et al. [21] added a boundary condition for equation (11), which always requires $0 < D < E$. This boundary condition is also adopted in this article.

According to Xu and Xia [55], the fractal dimension can be assumed to be independent of the soil porosity. Therefore, the porosity change only changes the value of r_0 in equation (11). The change of r_0 will lead to the change of the entire interparticle pore system. The maximum interparticle pore radius is r_0' if the porosity changes from ϕ to ϕ' , and r_0' can be written as

$$\frac{r_0'}{r_0} = \left(\frac{1-\phi}{1-\phi'}\right)^{1/(E-D)}. \quad (12)$$

2.2. Porosity-Dependent SWRC. Water in the interparticle pores can be drained by applying soil matric suction. If the fractal porous medium containing interparticle pores with radius $> r_i$ is completely dried due to the capillary flow process, the volumetric water content θ_i can be written as

$$\theta_i = \frac{\sum_{i=i}^{m-1} N^i P_i}{V_0}. \quad (13)$$

However, some interparticle pores with radius $> r_i$ may be isolated by solids and pores with a radius less than r_i . As drying occurs, not all pores of a given size drain at the appropriate suction because of incomplete pore connectivity [56, 57]. The number of drained pores, N_d , is assumed to be fractal and proportional to the power of $(1/\gamma)$, as expressed by

$$N_d = \gamma^{-D_d} \leq \gamma^{-D} = N, \quad (14)$$

where D_d ($\leq D$) is the fractal dimension for the drainable pore space defined by Perfect [57] and Cihan et al. [56]. Theoretically, D_d is equal to $D - \log(P_d)/\log(\gamma)$, where P_d is the scale-invariant drainage probability for the pore network [57]. Experimentally, D_d can be estimated from the water retention curve; for example, Crawford et al. [58] reported D_d values ranging from 2.90 to 2.97 ($E=3$) along with corresponding D values (obtained from thin section analysis) of between 2.94 and 2.98, for eight Japanese soils.

Therefore, volumetric water content θ_i can be revised as

$$\theta_i = \frac{\sum_{i=0}^{m-1} N^i P_i - \sum_{i=0}^{i-1} N_d^i P_i}{V_0}. \quad (15)$$

Equation (13) is a special case of equation (15) when $N_d = N$. The porosity ϕ , which is related to D rather than D_d , can also be expressed similarly:

$$\phi = \frac{V_0 - V_s}{V_0} = \frac{\sum_{i=0}^{m-1} N^i P_i}{V_0}. \quad (16)$$

Comparing equations (15) and (16) yields

$$\frac{\theta_i}{\phi} = \frac{P_0 [1 + \gamma^{(E-D)} + \dots + \gamma^{(m-1)(E-D)}] - P_0 [1 + \gamma^{(E-D_d)} + \dots + \gamma^{(i-1)(E-D_d)}]}{P_0 [1 + \gamma^{(E-D)} + \dots + \gamma^{(m-1)(E-D)}]}, \quad (17)$$

$$= \frac{\left(\frac{(1 - \gamma)^{m(E-D)}}{(1 - \gamma^{(E-D)})} \right) - \left(\frac{(1 - \gamma)^{i(E-D_d)}}{(1 - \gamma^{(E-D_d)})} \right)}{\left(\frac{(1 - \gamma)^{m(E-D)}}{(1 - \gamma^{(E-D)})} \right)} = 1 - \left[\frac{1 - \gamma^{(E-D)}}{1 - \gamma^{(E-D_d)}} \right] \left[\frac{1 - (\gamma)^{i(E-D_d)}}{\phi} \right].$$

Considering $\gamma^i = r_i/r_0$, equation (17) can be simplified as

$$\theta_i = \phi - \left[\frac{1 - \gamma^{(E-D)}}{1 - \gamma^{(E-D_d)}} \right] \left[1 - \left(\frac{r_i}{r_0} \right)^{(E-D_d)} \right] \quad (r_m \leq r_i \leq r_0), \quad (18)$$

when r_i is set to r_0 , which means pores with a radius larger than r_0 are drained (i.e., no pores are drained), the water content is equal to the porosity which coincides with the fully saturated condition. The residual volumetric water constant (θ_m) can be calculated when r_i is set to r_m :

$$\theta_m = \phi - \left[\frac{1 - \gamma^{(E-D)}}{1 - \gamma^{(E-D_d)}} \right] \left[1 - (1 - \phi)^{(E-D_d)/(E-D)} \right], \quad (19)$$

when r_i is set to r_m , pores with a radius larger than r_m are drained (i.e., the entire interparticle pores) except from those isolated pores. If $D = D_d$ (i.e., no isolated pores), $\theta_m = 0$, which coincides with the dried condition (i.e., only intra-particle water exists).

Therefore, the effective degree of saturation (S_e) can be written by combining equations (18) and (19):

$$S_e = \frac{\theta_i - \theta_m}{\phi - \theta_m} = \frac{(r_i/r_0)^{(E-D_d)} - (1 - \phi)^{(E-D_d)/(E-D)}}{1 - (1 - \phi)^{(E-D_d)/(E-D)}}. \quad (20)$$

Applying the Young–Laplace equation (i.e., $s = \sigma^{lg}/r$, σ^{lg} is the liquid–gas interfacial tension) to equation (18) yields

$$S_e = \begin{cases} 1, & s \leq s_{ae}, \\ \frac{(s/s_{ae})^{(D_d-E)} - (1 - \phi)^a}{1 - (1 - \phi)^a}, & s_{ae}(1 - \phi)^{1/(D-E)} > s > s_{ae}, \\ 0, & s \geq s_{ae}(1 - \phi)^{1/(D-E)}, \end{cases} \quad (21)$$

where a is equal to $(D_d - E)/(D - E)$, s is the matric suction or capillary potential, and s_{ae} is the air-entry value, which is inversely proportion to r_0 . If s_{ae} is associated with r_0 and s_{ae}^* with r_0^* , then according to (12), we have

$$s_{ae} = s_{ae}^* \left(\frac{1 - \phi^*}{1 - \phi} \right)^{1/(D-E)}. \quad (22)$$

Substituting equation (22) into equation (21) produces

$$S_e = \begin{cases} 1, & s \leq s_{ae}^* \left(\frac{1 - \phi^*}{1 - \phi} \right)^{1/(D-E)}, \\ \frac{(s/s_{ae}^*)^{(D_d-E)} - (1 - \phi^*)^a}{\left(\frac{(1 - \phi^*)}{(1 - \phi)} \right)^a - (1 - \phi^*)^a}, & s_{ae}^*(1 - \phi^*)^{1/(D-E)} > s > s_{ae}^* \left(\frac{1 - \phi^*}{1 - \phi} \right)^{1/(D-E)}, \\ 0, & s \geq s_{ae}^*(1 - \phi^*)^{1/(D-E)}, \end{cases} \quad (23)$$

if $D_d = D$ and $\phi^* = \phi$, equation (23) degenerates back to the renown fractal SWRC model proposed by Rieu and Sposito [22]:

$$S_e = \begin{cases} 1, & s \leq s_{ae}, \\ \frac{1}{\phi} \left(\frac{s}{s_{ae}} \right)^{(D-E)} - \frac{1}{\phi} + 1, & s_{ae}(1 - \phi)^{1/(D-E)} > s > s_{ae}, \\ 0, & s \geq s_{ae}(1 - \phi)^{1/(D-E)}. \end{cases} \quad (24)$$

2.3. Porosity-Dependent HCF. The hydraulic conductivity function (HCF) plays a pivotal role in the flow and transport processes under both saturated and unsaturated conditions. The HCF for unsaturated soils is usually represented by the relative hydraulic conductivity K_r , which is defined as the ratio between the unsaturated hydraulic conductivity K and the corresponding saturated hydraulic conductivity K_s . A number of methods have been proposed to quantify the relative hydraulic conductivity K_r for unsaturated soils [7, 12, 19, 59–61], and most of them express K_r as a function of the effective degree of saturation (S_e), volumetric water content (θ),

and matric suction (s). Among the proposed HCFs for unsaturated soils, the most cited HCF is that proposed by Mualem [7]:

$$K_r = \sqrt{S_e} \left(\frac{\int_0^{S_e} (1/s) dS_e}{\int_0^1 (1/s) dS_e} \right)^2. \quad (25)$$

$$K_r = \begin{cases} 1, & s \leq s_{ac}^* \left(\frac{1-\phi^*}{1-\phi} \right)^{1/(D-E)}, \\ \left[\frac{(s/s_{ac}^*)^{(D_d-E)} - (1-\phi^*)^a}{((1-\phi^*)/(1-\phi))^a - (1-\phi^*)^a} \right]^{0.5} \left[\frac{(s/s_{ac}^*)^{(D_d-E-1)} - (1-\phi^*)^b}{((1-\phi^*)/(1-\phi))^b - (1-\phi^*)^b} \right]^2, & s_{ac}^* (1-\phi^*)^{1/(D-E)} > s > s_{ac}^* \left(\frac{1-\phi^*}{1-\phi} \right)^{1/(D-E)}, \\ 0, & s \geq s_{ac}^* (1-\phi^*)^{1/(D-E)}, \end{cases} \quad (26)$$

where b is equal to $(D_d - E - 1)/(D - E)$.

3. Experimental Validations

3.1. SWRCs with Different Initial Porosities. A series of drying tests on a compacted till were reported by Vanapalli et al. [62]. The soil specimens were compacted to different initial void ratios at the optimum water content. Figures 3(a)–3(d) show the drying test results for these specimens, by different symbols for different initial void ratios (e) or initial porosities (ϕ). The test data with an initial void ratio of 0.517 ($\phi^* = 0.341$) were adopted to calibrate the parameters using the method of least squares. The values of D and D_d can be determined by maximising the value of R^2 when the air-entry value s_{ac}^* is set to 8 kPa according to the data points:

$$R^2 = 1 - \frac{\sum_1^j (S_e^{Cal} - S_e^{Exp})^2}{\sum_1^j (S_e^{Cal} - \bar{S}_e^{Cal})^2}, \quad (27)$$

where j is the number of experimental data points (in this case, $j = 11$), S_e^{Exp} is the measured (experimental) effective degree of saturation for a data point, and S_e^{Cal} is the calculated effective degree of saturation for a data point for the same data point by equation (23). \bar{S}_e^{Cal} is the mean of the calculated effective degree of saturation for all data points. For all the cases in this study, the Euclidean dimension E is set to 2. Thus, we have the range of D_d and D as $1 < D_d \leq D < 2$. The initial values of D_d and D are set to 1, and the increment for D_d and D is set to 10^{-3} (i.e., $\Delta D_d = \Delta D = 10^{-3}$). For each set of D_d and D , a value R^2 is calculated and recorded. Finally, the maximum value of R^2 can be achieved, which is equal to 0.9837, when $D_d = 1.915$ and $D = 1.972$. The other 3 data sets (corresponding to $e = 0.514$, $e = 0.474$, and $e = 0.444$) were used to validate the

proposed equation. The predicted SWRCs were calculated using equation (23) and are shown as solid curves in Figure 3. The value of R^2 for rest three data sets is computed to illustrate the validity of the model predictions. The predicted SWRCs in Figures 3(b)–3(d) match the experimental data well with R^2 varying from 0.9364 to 0.9726, indicating that the proposed fractal approach captures the effects of the initial void ratio on the SWRCs well.

A series of laboratory experiments were conducted by Huang et al. [63] to investigate the water retention behaviour of a deformable unsaturated soil. The soil tested was silty sand from the Saskatchewan Department of Highway borrow pit. This silty sand consisted of 52.5% sand, 37.5% silt, and 10% clay. The specific gravity, liquid limit, and plastic limit were 2.68, 22.2%, and 16.6%, respectively. The air-dried silty sand was mixed with distilled water to prepare slurried specimens for the experimental program. Six initially slurried specimens (grouped as PPCT2) were one-dimensionally preconsolidated under different pressures to obtain different initial void ratios for the water retention tests. The test results are replotted in the S_e - s plane together with the predictions of equation (23) in Figures 4(a)–4(f). The water retention test data for an initial void ratio of 0.525 ($\phi^* = 0.344$) were used to calibrate the parameters. The values of D ($=1.883$) and D_d ($=1.883$) were determined by maximising the value of R^2 ($=0.9966$) when the air-entry value s_{ac}^* set to 24 kPa according to the data points. As shown in Figures 4(b)–4(f), the predicted SWRCs agree very well with the experimental SWRCs ($R^2 = 0.9821 \sim 0.9968$).

Very recently, Salager et al. [64] conducted a series of tests on a clayey sand to investigate the water retention behaviour of a granular soil. The tested soil consisted of 72% sand, 18% silt, and 10% clay. The water retention behaviour of the clayey sand compacted at five different void ratios (e) is replotted in the S_e - s plane in Figures 5(a)–5(e). The variation in the initial void ratios ranges from 0.44 to 1.01.

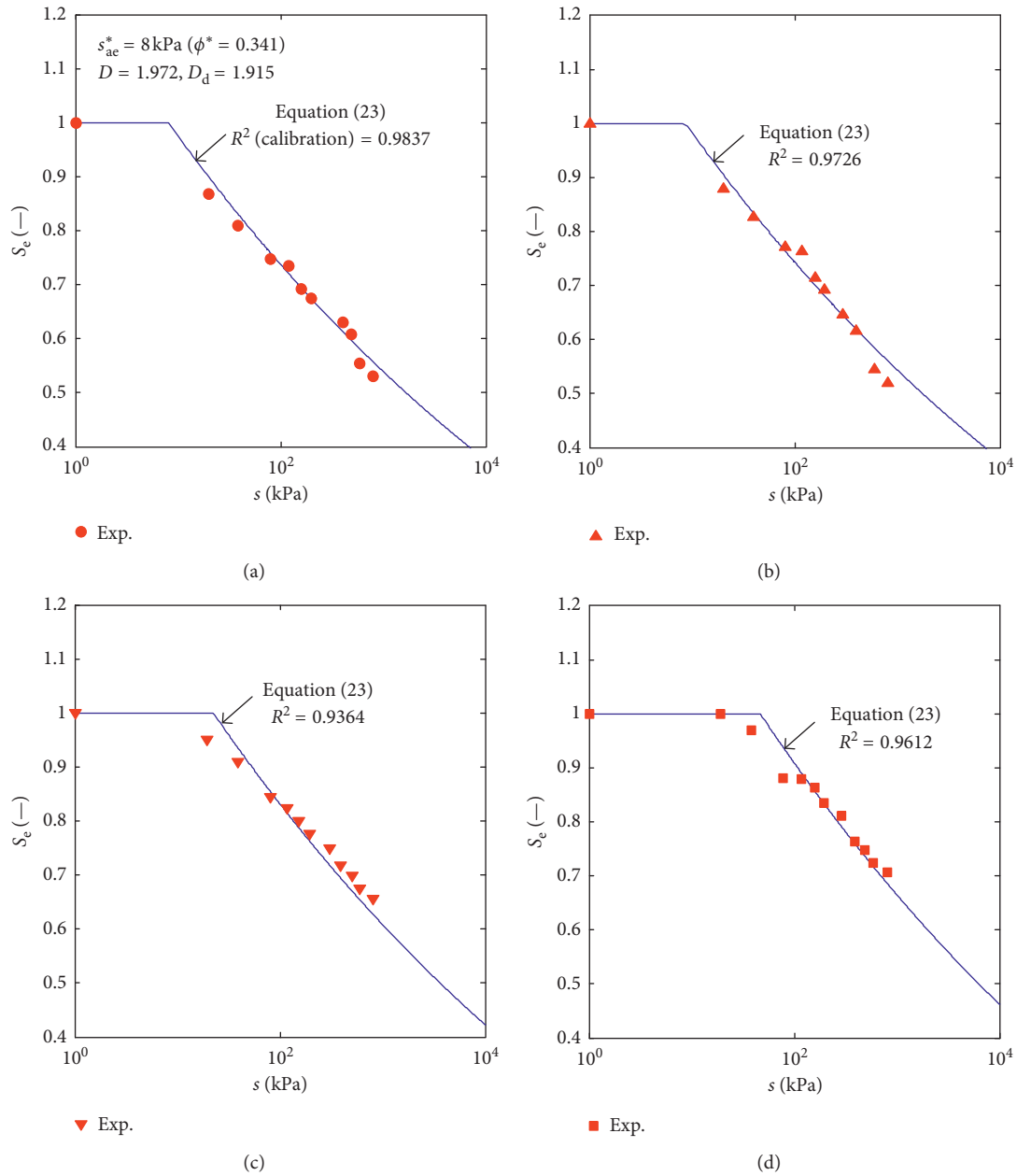


FIGURE 3: Measured and predicted SWRCs for specimens compacted at optimum water content (data after Vanapalli et al. [62]): (a) $e = 0.517$; (b) $e = 0.514$; (c) $e = 0.474$; (d) $e = 0.444$.

The water retention data for the loosest specimen ($e^* = 1.01$, i.e., $\phi^* = 0.502$) were adopted to calibrate the parameters. The values of $D (=1.951)$ and $D_d (=1.935)$ were determined by maximising the value of $R^2 (=0.9834)$ when the air-entry value s_{ac}^* is set to 0.2 kPa according to the data points. The SWRCs predicted by equation (23) are shown in Figures 5(b)–5(e). Again, the comparison between the experimental data and predictions is of acceptable accuracy with the value of R^2 between 0.8865 and 0.9794.

3.2. HCFs with Different Initial Porosities. Laliberte et al. [26] measured the SWRCs (S_e versus s) and HCFs (K_r versus s) of

a silt loam, which is referred to as the Touchet silt loam, with different initial porosities. A Touchet silt loam is coarse silt, consisting of 32% sand, 53% silt, and 15% clay, with a particle density of 2.599 g/cm³. The initial porosities for the water retention tests are 0.493 ($e^* = 0.972$), 0.463 ($e = 0.862$), and 0.430 ($e = 0.754$). The initial porosities for the hydraulic conductivity tests are 0.503 ($e = 1.012$), 0.478 ($e = 0.916$), 0.449 ($e = 0.815$), 0.423 ($e = 0.733$), and 0.395 ($e = 0.653$). The data set for the loosest specimen ($\phi^* = 0.493$) of the water retention test is used for calibration. The parameters for SWRC are set to $s_{ac}^* = 4.5$ kPa, $D = 1.7$, and $D_d = 1.05$, which result in a value of $R^2 = 0.9909$ for all data sets with three different initial porosities (Figure 6(a)). As shown in

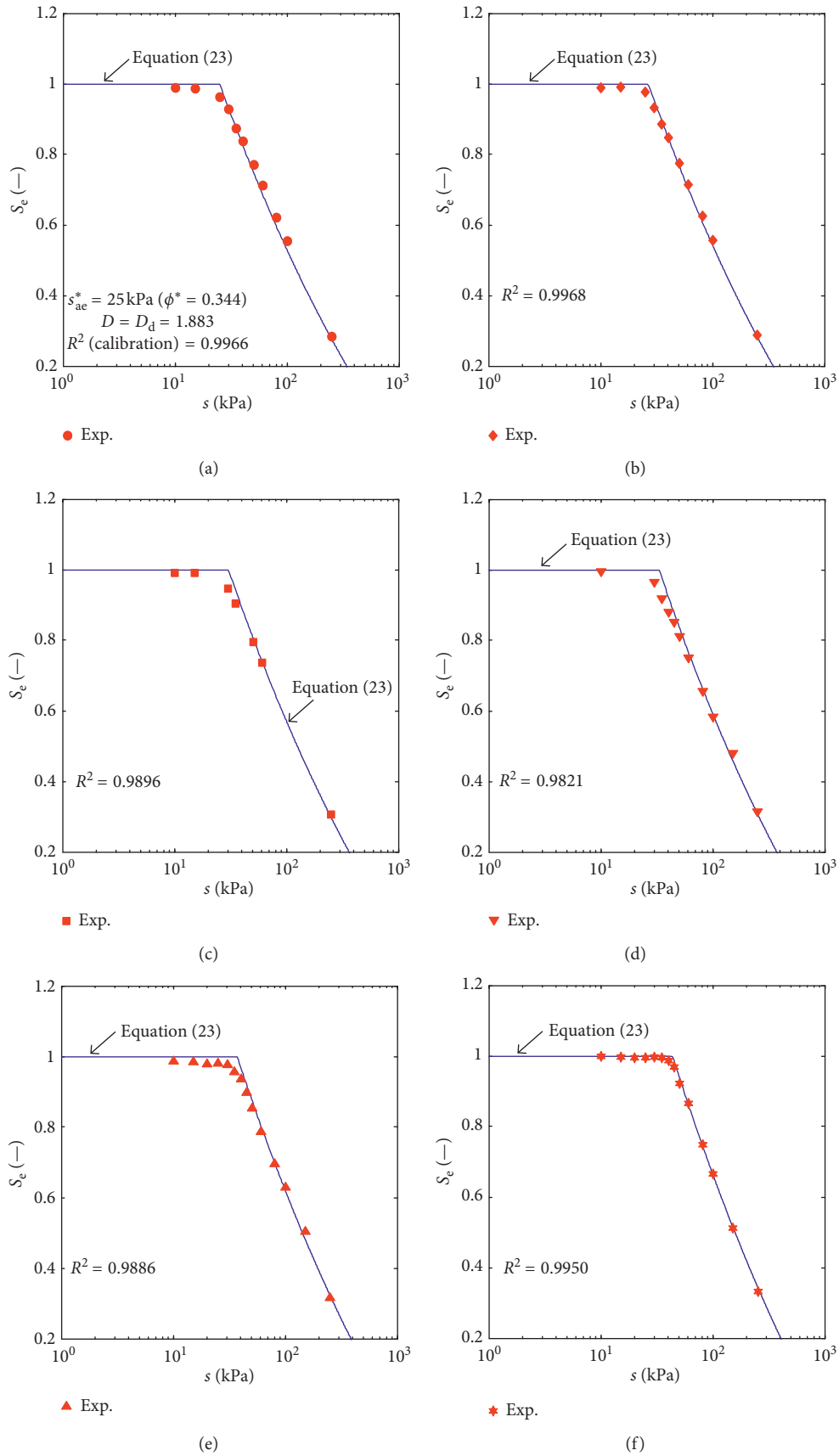


FIGURE 4: Measured and predicted SWRCs for silty sand with different initial void ratios (data after Huang et al. [63]): (a) $e = 0.525$; (b) $e = 0.513$; (c) $e = 0.490$; (d) $e = 0.474$; (e) $e = 0.454$; (f) $e = 0.426$.

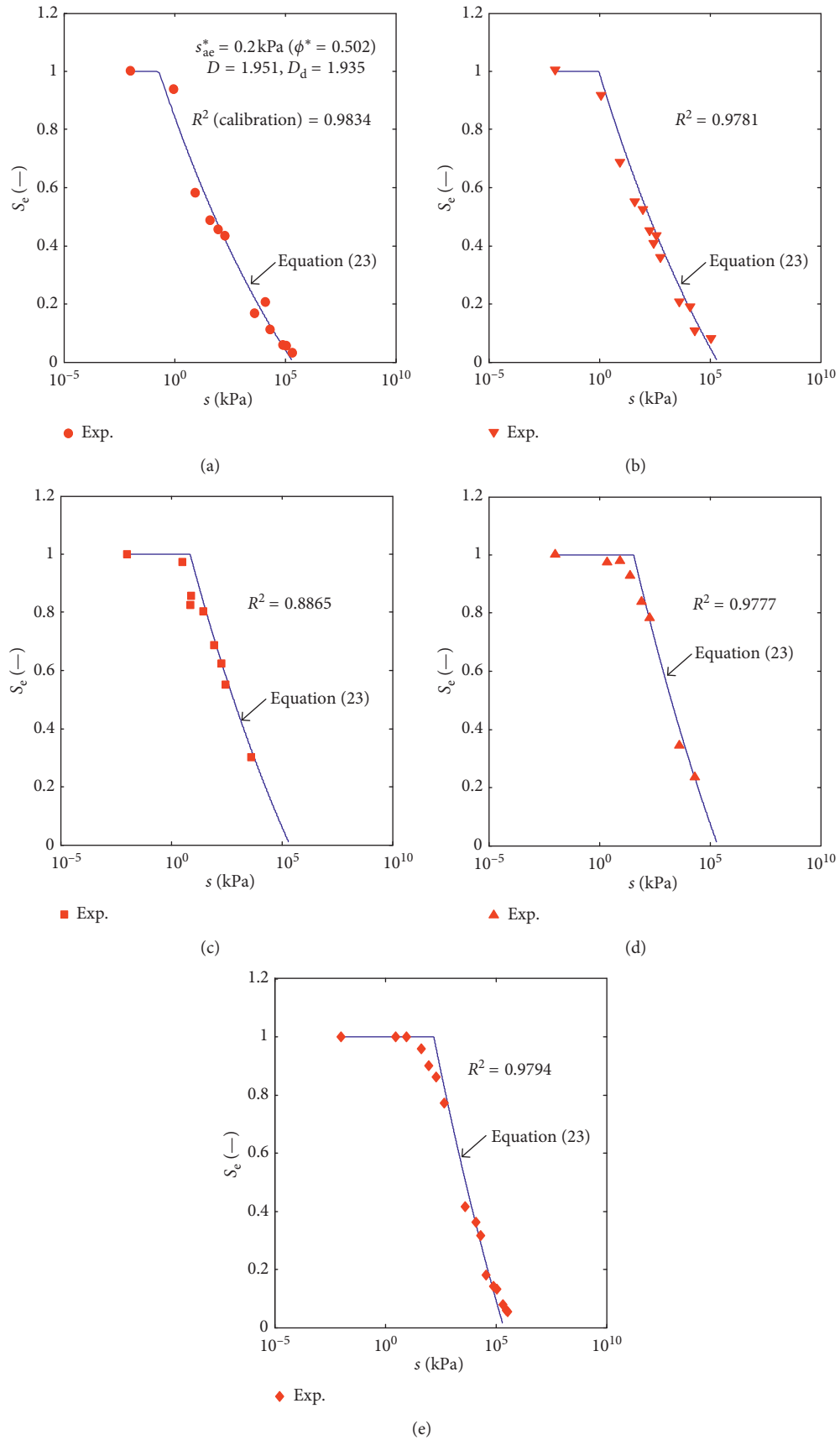


FIGURE 5: Measured and predicted family of SWRCs for a clayey sand with different initial void ratios (data after Salager et al. [64]): (a) $e = 1.01$; (b) $e = 0.86$; (c) $e = 0.68$; (d) $e = 0.55$; (e) $e = 0.44$.

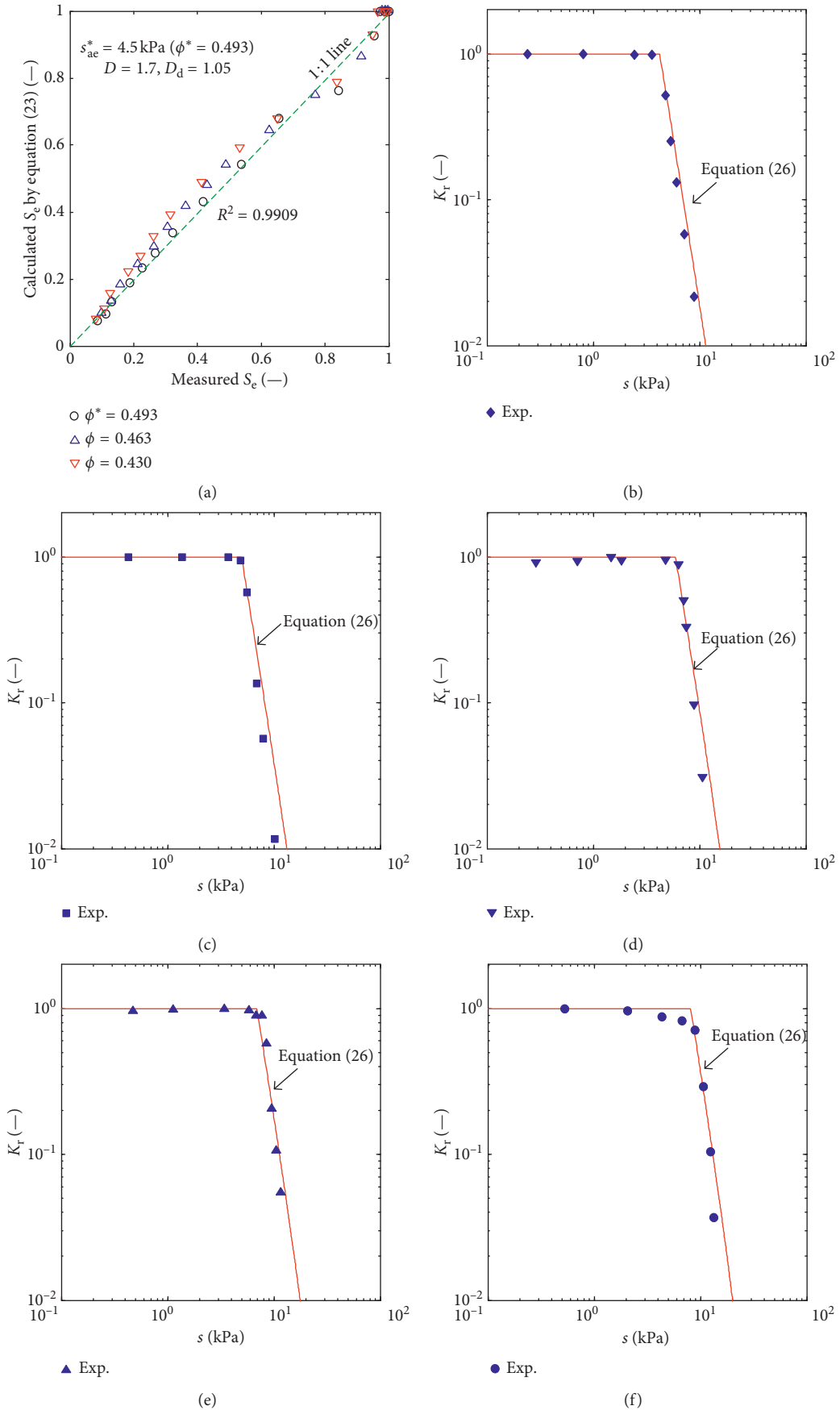


FIGURE 6: Comparison between measured and predicted SWRCs and HCFs for the Touchet silt loam: (a) SWRCs, (b) HCF ($\phi = 0.503$), (c) HCF ($\phi = 0.478$), (d) HCF ($\phi = 0.449$), (e) HCF ($\phi = 0.423$), and (f) HCF ($\phi = 0.395$).

Figures 6(b)–6(f), the measured relative hydraulic conductivities for five different initial porosities (0.503–0.395) are replotted in the K_r - s plane (double logarithmic scales), which are the predictions obtained using equation (26). The predicted K_r - s curves agree with the experimental data reasonably well, which confirms that the proposed porosity-dependent fractal HCF model (i.e., equation (26)) captures well the effects of the initial porosity on the soil's unsaturated permeability.

4. Conclusions

A simple physical model based on fractal geometry was proposed to quantify the effects of initial porosity on the soil-water retention curve (SWRC) and the hydraulic conductivity function (HCF) for unsaturated porous media. The proposed fractal model involves three parameters: (1) the air-entry value that is related to the size of the maximum pores, (2) the fractal dimension of pore volume (D), and (3) the fractal dimension of drainable pore volume (D_d). The range of D and D_d is limited to between $E - 1$ and E (i.e., Euclidean dimension). The difference between D and D_d ($D \geq D_d$) implies that incomplete pore connectivity may exist in the porous medium. The values of D and D_d can be calibrated conveniently using one data set of the water retention tests at initial porosity. A regression analysis using the method of least squares indicates that the proposed model is valid to reproduce the porosity-dependent SWRCs and HCFs for a variety of unsaturated soils.

Data Availability

The data used to support the findings of this study are included within the article.

Conflicts of Interest

The authors declare that they have no conflicts of interest.

Acknowledgments

This research was financially supported by the National Natural Science Foundation of China (51679004).

References

- [1] S.-L. Shen, Z.-F. Wang, J. Yang, and C.-E. Ho, "Generalized approach for prediction of jet grout column diameter," *Journal of Geotechnical and Geoenvironmental Engineering*, vol. 139, no. 12, pp. 2060–2069, 2013.
- [2] S.-L. Shen, J.-P. Wang, H.-N. Wu, Y.-S. Xu, G.-L. Ye, and Z.-Y. Yin, "Evaluation of hydraulic conductivity for both marine and deltaic deposits based on piezocone testing," *Ocean Engineering*, vol. 110, pp. 174–182, 2015.
- [3] S.-L. Shen, Y.-X. Wu, Y.-S. Xu, T. Hino, and H.-N. Wu, "Evaluation of hydraulic parameters from pumping tests in multi-aquifers with vertical leakage in Tianjin," *Computers and Geotechnics*, vol. 68, pp. 196–207, 2015.
- [4] S. L. Shen, Z. F. Wang, and W. C. Cheng, "Estimation of lateral displacement induced by jet grouting in clayey soils," *Géotechnique*, vol. 67, no. 7, pp. 621–630, 2017.
- [5] S.-L. Shen, Y.-X. Wu, and A. Misra, "Calculation of head difference at two sides of a cut-off barrier during excavation dewatering," *Computers and Geotechnics*, vol. 91, pp. 192–202, 2017.
- [6] Y.-S. Xu, H.-N. Wu, J. S. Shen, and N. Zhang, "Risk and impacts on the environment of free-phase biogas in quaternary deposits along the coastal region of Shanghai," *Ocean Engineering*, vol. 137, pp. 129–137, 2017.
- [7] Y. Mualem, "A new model for predicting the hydraulic conductivity of unsaturated porous media," *Water Resources Research*, vol. 12, no. 3, pp. 513–522, 2010.
- [8] R. Brooks and A. Corey, *Hydraulic Properties of Porous Media*, Colorado State University, Fort Collins, CO, USA, 1964.
- [9] D. G. Fredlund and A. Xing, "Equations for the soil-water characteristic curve," *Canadian Geotechnical Journal*, vol. 31, no. 4, pp. 521–532, 1994.
- [10] W. Gardner, "Mathematics of isothermal water conduction in unsaturated soils, highway research board special report 40," in *Proceedings of International Symposium on Physico-Chemical Phenomenon in Soils*, pp. 78–87, Washington, DC, USA, 1956.
- [11] M. T. van Genuchten, "A closed-form equation for predicting the hydraulic conductivity of unsaturated soils 1," *Soil Science Society of America Journal*, vol. 44, no. 5, pp. 892–898, 1980.
- [12] S. Assouline, "A model for soil relative hydraulic conductivity based on the water retention characteristic curve," *Water Resources Research*, vol. 37, no. 2, pp. 265–271, 2001.
- [13] N. T. Burdine, "Relative permeability calculations from pore size distribution data," *Journal of Petroleum Technology*, vol. 5, no. 3, pp. 71–78, 2013.
- [14] D. G. Fredlund, A. Xing, and S. Huang, "Equations for the soil-water characteristic curve," *Canadian Geotechnical Journal*, vol. 31, no. 4, pp. 521–532, 1994.
- [15] S. W. Tyler and S. W. Wheatcraft, "Fractal processes in soil water retention," *Water Resources Research*, vol. 26, no. 5, pp. 1047–1054, 2010.
- [16] N. R. A. Bird, E. Perrier, and M. Rieu, "The water retention function for a model of soil structure with pore and solid fractal distributions," *European Journal of Soil Science*, vol. 51, no. 1, pp. 55–63, 2008.
- [17] A. Cihan, J. S. Tyner, and E. Perfect, "Predicting relative permeability from water retention: a direct approach based on fractal geometry," *Water Resources Research*, vol. 45, no. 4, p. W04404, 2009.
- [18] C. Fuentes, M. Vauclin, J.-Y. Parlange, and R. Haverkamp, "A note on the soil-water conductivity of a fractal soil," *Transport in Porous Media*, vol. 23, no. 1, pp. 31–36, 1996.
- [19] Y. A. Pachepsky, R. A. Shcherbakov, and L. P. Korsunskaya, "Scaling of soil water retention using a fractal model," *Soil Science*, vol. 159, no. 2, pp. 99–104, 1995.
- [20] E. Perfect, N. B. McLaughlin, B. D. Kay, and G. C. Topp, "An improved fractal equation for the soil water retention curve," *Water Resources Research*, vol. 32, no. 2, pp. 281–287, 1996.
- [21] E. Perrier, M. Rieu, G. Sposito, and G. de Marsily, "Models of the water retention curve for soils with a fractal pore size distribution," *Water Resources Research*, vol. 32, no. 10, pp. 3025–3031, 1996.
- [22] M. Rieu and G. Sposito, "Fractal fragmentation, soil porosity, and soil water properties: I. Theory," *Soil Science Society of America Journal*, vol. 55, no. 5, pp. 1231–1238, 1991.
- [23] Y. Xu, "Calculation of unsaturated hydraulic conductivity using a fractal model for the pore-size distribution," *Computers and Geotechnics*, vol. 31, no. 7, pp. 549–557, 2004.

- [24] Y. F. Xu and D. A. Sun, "A fractal model for soil pores and its application to determination of water permeability," *Physica A: Statistical Mechanics and its Applications*, vol. 316, no. 1-4, pp. 56-64, 2002.
- [25] D. Croney and J. D. Coleman, "Soil structure in relation to soil suction (pF)," *Journal of Soil Science*, vol. 5, no. 1, pp. 75-84, 2006.
- [26] G. E. Laliberte, A. Corey, and R. Brooks, *Properties of Unsaturated Porous Media*, Colorado State University, Fort Collins, CO, USA, 1966.
- [27] S. Assouline, "Modeling the relationship between soil bulk density and the water retention curve," *Vadose Zone Journal*, vol. 5, no. 2, pp. 554-562, 2006.
- [28] D. Gallipoli, S. J. Wheeler, and M. Karstunen, "Modelling the variation of degree of saturation in a deformable unsaturated soil," *Géotechnique*, vol. 53, no. 1, pp. 105-112, 2003.
- [29] T. Luo, Y.-P. Yao, A.-N. Zhou, and X.-G. Tian, "A three-dimensional criterion for asymptotic states," *Computers and Geotechnics*, vol. 41, pp. 90-94, 2012.
- [30] D. Masin, "Predicting the dependency of a degree of saturation on void ratio and suction using effective stress principle for unsaturated soils," *International Journal for Numerical and Analytical Methods in Geomechanics*, vol. 34, pp. 73-90, 2010.
- [31] M. Nuth and L. Laloui, "Advances in modelling hysteretic water retention curve in deformable soils," *Computers and Geotechnics*, vol. 35, no. 6, pp. 835-844, 2008.
- [32] Y. Yao, W. Hou, and A. Zhou, "Constitutive model for overconsolidated clays," *Science in China Series E: Technological Sciences*, vol. 51, no. 2, pp. 179-191, 2008.
- [33] A. Zhou and D. Sheng, "An advanced hydro-mechanical constitutive model for unsaturated soils with different initial densities," *Computers and Geotechnics*, vol. 63, pp. 46-66, 2015.
- [34] A.-N. Zhou, D. Sheng, S. W. Sloan, and A. Gens, "Interpretation of unsaturated soil behaviour in the stress-saturation space, I: volume change and water retention behaviour," *Computers and Geotechnics*, vol. 43, pp. 178-187, 2012.
- [35] A. Zhou, D. Sheng, S. W. Sloan, and A. Gens, "Modelling volume change behaviour for unsaturated soils in the stress-saturation space," *Unsaturated Soils: Research and Applications*, vol. 43, pp. 111-118, 2012.
- [36] A.-N. Zhou, D. Sheng, and J. Li, "Modelling water retention and volume change behaviours of unsaturated soils in non-isothermal conditions," *Computers and Geotechnics*, vol. 55, pp. 1-13, 2014.
- [37] A. Zhou, S. Wu, J. Li, and D. Sheng, "Including degree of capillary saturation into constitutive modelling of unsaturated soils," *Computers and Geotechnics*, vol. 95, pp. 82-98, 2018.
- [38] A.-N. Zhou, "A contact angle-dependent hysteresis model for soil-water retention behaviour," *Computers and Geotechnics*, vol. 49, pp. 36-42, 2013.
- [39] S. Assouline, "Modeling the relationship between soil bulk density and the hydraulic conductivity function," *Vadose Zone Journal*, vol. 5, no. 2, pp. 697-705, 2006.
- [40] D. A. Sun, D. Sheng, and S. W. Sloan, "Elastoplastic modelling of hydraulic and stress-strain behaviour of unsaturated soils," *Mechanics of Materials*, vol. 39, no. 3, pp. 212-221, 2007.
- [41] D. A. Sun, D. Sheng, and Y. Xu, "Collapse behaviour of unsaturated compacted soil with different initial densities," *Canadian Geotechnical Journal*, vol. 44, no. 6, pp. 673-686, 2007.
- [42] A. Tarantino, "A water retention model for deformable soils," *Géotechnique*, vol. 59, no. 9, pp. 751-762, 2009.
- [43] D. Sheng and A.-N. Zhou, "Coupling hydraulic with mechanical models for unsaturated soils," *Canadian Geotechnical Journal*, vol. 48, no. 5, pp. 826-840, 2011.
- [44] A.-N. Zhou, D. Sheng, and J. P. Carter, "Modelling the effect of initial density on soil-water characteristic curves," *Géotechnique*, vol. 62, no. 8, pp. 669-680, 2012.
- [45] D. A. Sun, D. Sheng, L. Xiang, and S. W. Sloan, "Elastoplastic prediction of hydro-mechanical behaviour of unsaturated soils under undrained conditions," *Computers and Geotechnics*, vol. 35, no. 6, pp. 845-852, 2008.
- [46] A. Tarantino, "Unsaturated soils: compacted versus reconstituted states," in *Unsaturated Soils*, E. E. Alonso and A. Gens, Eds., pp. 113-136, CRC Press, Barcelona, Spain, 2011.
- [47] A. Zhou, R. Huang, and D. Sheng, "Capillary water retention curve and shear strength of unsaturated soils," *Canadian Geotechnical Journal*, vol. 53, no. 6, pp. 974-987, 2016.
- [48] E. Romero and P. H. Simms, "Microstructure investigation in unsaturated soils: a review with special attention to contribution of mercury intrusion porosimetry and environmental scanning electron microscopy," *Geotechnical and Geological Engineering*, vol. 26, no. 6, pp. 705-727, 2008.
- [49] B. B. Mandelbrot, *The Fractal Geometry of Nature*, WH Freeman and Co., New York, NY, USA, 1983.
- [50] D. Giménez, E. Perfect, W. J. Rawls, and Y. Pachepsky, "Fractal models for predicting soil hydraulic properties: a review," *Engineering Geology*, vol. 48, pp. 161-183, 1997.
- [51] Y. Xu, "The fractal evolution of particle fragmentation under different fracture energy," *Powder Technology*, vol. 323, pp. 337-345, 2018.
- [52] Y. Xu, "Shear strength of granular materials based on fractal fragmentation of particles," *Powder Technology*, vol. 333, pp. 1-8, 2018.
- [53] A. J. Katz and A. H. Thompson, "Fractal sandstone pores: implications for conductivity and pore formation," *Physical Review Letters*, vol. 54, no. 12, pp. 1325-1328, 1985.
- [54] A. G. Hunt, "Comments on 'fractal fragmentation, soil porosity, and soil water properties: I. Theory'," *Soil Science Society of America Journal*, vol. 71, no. 4, pp. 1418-1419, 2007.
- [55] Y. Xu and X. Xia, "Fractal model for virgin compression of pure clays," *Mechanics Research Communications*, vol. 33, no. 2, pp. 206-216, 2006.
- [56] A. Cihan, E. Perfect, and J. S. Tyner, "Water retention models for scale-variant and scale-invariant drainage of mass prefractal porous media," *Vadose Zone Journal*, vol. 6, no. 4, pp. 786-792, 2007.
- [57] E. Perfect, "Modeling the primary drainage curve of prefractal porous media," *Vadose Zone Journal*, vol. 4, no. 4, pp. 959-966, 2005.
- [58] J. W. Crawford, N. Matsui, and I. M. Young, "The relation between the moisture-release curve and the structure of soil," *European Journal of Soil Science*, vol. 46, no. 3, pp. 369-375, 1995.
- [59] G. Cai, A. Zhou, and D. Sheng, "Permeability function for unsaturated soils with different initial densities," *Canadian Geotechnical Journal*, vol. 51, no. 12, pp. 1456-1467, 2014.
- [60] G. S. Campbell, "A simple method for determining unsaturated conductivity from moisture retention data," *Soil Science*, vol. 117, no. 6, pp. 311-314, 1974.
- [61] J. Stolte, J. M. Halbertsma, G. J. Veerman et al., "Comparison of six methods to determine unsaturated soil hydraulic conductivity," *Soil Science Society of America Journal*, vol. 58, no. 6, pp. 1596-1603, 1994.
- [62] S. K. Vanapalli, D. G. Fredlund, and D. E. Pufahl, "The influence of soil structure and stress history on the soil-water characteristics of a compacted till," *Géotechnique*, vol. 49, no. 2, pp. 143-159, 1999.
- [63] S. Huang, S. L. Barbour, and D. G. Fredlund, "Development and verification of a coefficient of permeability function for a

deformable unsaturated soil," *Canadian Geotechnical Journal*, vol. 35, no. 3, pp. 411-425, 1998.

- [64] S. Salager, M. S. El Youssoufi, and C. Saix, "Definition and experimental determination of a soil-water retention surface," *Canadian Geotechnical Journal*, vol. 47, no. 6, pp. 609-622, 2010.

Research Article

Effect of Ca/Al Ratio on Stabilization/Solidification of Lead-Contaminated Soil by Ettringite

Lian Xiang , Huamei Zhu, and Ruoyun Zhou 

School of Transportation, Southeast University, Nanjing, Jiangsu 210096, China

Correspondence should be addressed to Ruoyun Zhou; 220172969@seu.edu.cn

Received 15 June 2018; Accepted 11 December 2018; Published 30 December 2018

Guest Editor: Xinbao Yu

Copyright © 2018 Lian Xiang et al. This is an open access article distributed under the Creative Commons Attribution License, which permits unrestricted use, distribution, and reproduction in any medium, provided the original work is properly cited.

Ettringite is commonly used for the stabilization/solidification for heavy metal-contaminated soils, and its treatment effect will be influenced by Ca/Al mole ratio. Lead-contaminated soil samples were solidified using ettringite with different Ca/Al mole ratios. The pH value, unconfined compressive strength of solidified samples, and leaching concentration were investigated to understand the influence of Ca/Al mole ratio on properties of ettringite-solidified contaminated soils. The microstructural characteristics of solidified contaminated soils were also explored. The results show that lead leaching concentration decreases dramatically with increasing the content of lime and curing time. Lead concentration drops from 49.89 mg/L to 0.19 mg/L when Ca/Al mole ratio increases from 4:3 to 10:3 at 28 days and from 36.57 mg/L to near 0 mg/L at 90 days. In addition, the unconfined compressive strength of samples drops at first and then increases with the increase of Ca/Al mole ratio. Besides, the pH values of solidified soil and leachate rise with the increase of content of lime. The pH values of solidified soil increase from 9.68 to 11.34, and there is little difference between 28 days and 90 days. However, the pH values of leachate increase from 5.56 to 8.59 at 28 days, and 90-day pH values increase from 5.65 to 9.44. The results of SEM, XRD, and EDS tests also indicate that Ca/Al mole ratio affects the shape of ettringite, the stabilization/solidification effectiveness of contaminated soil, and the pore of solidified soil. When Ca/Al mole ratio equals to 8:3, ettringite content has a substantial increase, and lead leaching concentration is lower than 5 mg/L.

1. Introduction

Heavy metal-contaminated soils have attracted much attention from engineers and environmentalists during the past decades for it may cause significant damages on human health and ecosystem [1]. There are many techniques that can be used to reduce the bad effect of heavy metal-contaminated soils, among which solidification/stabilization is seen as a common way [2–5] with its economic advantage and effectiveness. Solidification/stabilization is to mix contaminated soils with binders to transfer the waste to environmentally acceptable materials for construction [6]. As a type of commonly used binder, the ordinary Portland cement can facilitate the formation of insoluble hydroxide from heavy metal ions through creating an alkaline environment, and its effect of parcel, adsorption, and complexation also promote the solidification process. However, cement production consumes large amounts of nonrenewable resources and

energy. For instance, producing 1-ton cement may consume 1.5-ton lime and clay, 113 kg standard coal, and 5000 MJ energy [7]. Moreover, a great deal of pollutants is created in cement production such as CO₂, SO₂, CO, NO_x, and dust [8].

As part of the cement hydration product, ettringite (3Ca·Al₂O₃·3CaSO₄·32H₂O), named as Aft, can adsorb more external heavy metal ions by replacement and surface electronegativity [9, 10]. When ettringite is used to stabilize/solidify heavy metal ions, ion replacement is related to ion radius [9]. Ion replacement can only occur between ions with similar radius. Not only the typical heavy metal ions Pb²⁺, Cd²⁺, and Cr³⁺ can replace Ca²⁺, Al³⁺, in ettringite, but also SO₄²⁻ can be substituted by oxygen-containing heavy metal anions such as CrO₄²⁻ [11], enabling heavy metal ions to be a part of ettringite crystal, and then the stabilization/solidification of heavy metals can be achieved.

Many studies indicated that the solidification/stabilization of contaminated soils with ettringite may be

affected by the concentration of certain ions. Luz [12] and Peysson [9] prepared two types of cement paste, for which the ratio of phosphogypsum to calcium sulfoaluminate cement was 2:8 and 3:7, respectively, to conduct the stabilization/immobilization tests of heavy metals including Cr^{6+} , Cr^{3+} , Cd^{2+} , Pb^{2+} , and Zn^{2+} . The leaching test results of solidified cement pastes showed two main findings:

- (i) The retentions of Cr^{3+} , Cd^{2+} , Pb^{2+} , and Zn^{2+} reached 99%, regardless of the curing age, the dosage of phosphogypsum, or the concentration of heavy metal ions.
- (ii) The retention of Cr^{6+} is closely related to the content of phosphogypsum and the concentration of Cr^{6+} .

Wang [13, 14] used ettringite produced by the solution method to stabilize/immobilize Cu^{2+} and Cr ions of different valencies. They reported that the solidifying mechanism and stability of ettringite on Cr^{6+} , Cr^{3+} , and Cu^{2+} were different. The Cr^{6+} ion squeezed into the interlayer structure of ettringite changed the molecular symmetry and had a great influence on ettringite crystals. When ettringite was in the environment of carbonization, freezing, and thawing, the retention of Cr^{3+} and Cu^{2+} was less affected, but the retention of Cr^{6+} remarkably reduced. Through the stabilization/immobilization tests of cement mortar, Ma [15] pointed that when using sulfoaluminate cement to stabilize/immobilize heavy metal Zn^{2+} , the leaching concentration of Zn^{2+} is only 1/4 of the same amount of Portland cement.

The ettringite crystals are mainly produced by the reaction of AlO_2^- , Ca^{2+} , and SO_4^{2-} . The AlO_2^- ions not only determine whether the ettringite can be formed, but also determine its formation rate. The SO_4^{2-} ion has an important influence on stability of ettringite since the ettringite can only exist stably when the mole ratio of SO_4^{2-} and AlO_2^- is greater than 0.42 [16]. The Ca^{2+} is also a significant influencing factor because its content affects the production and stability of ettringite. When the mass ratio of CaO to Al_2O_3 exceeds 3.5, the ettringite is stable and keeps developing. When the mass ratio is less than 2.0, the ettringite formed at early stage decomposes partially and transforms into monosulfate calcium sulfoaluminate [17].

In order to clarify the effect of Ca/Al mole ratio on the stabilization and immobilization of heavy metal lead by ettringite, this study investigated the physical, mechanical, and leaching performances of solidified soil with different Ca/Al mole ratios. The binder consisted of high-alumina cement, lime, and gypsum and remained the total content of 15% through experiments, and the S/Al mole ratio kept unchanged. Changes of Ca/Al mole ratio were achieved by adjusting the content of lime. By means of scanning electron microscopy (SEM), X-ray diffraction (XRD), and mercury intrusion porosimetry (MIP), this study also investigated the microcosmic mechanism that the Ca/Al mole ratio affects the leaching and mechanical performances of solidification/immobilization of heavy metal-contaminated soil by ettringite. The results revealed that the variation of Ca/Al mole ratio in ettringite has

significant influences on its performance when solidifying/stabilizing lead-contaminated soils.

2. Materials and Methods

2.1. Test Material. The basic physical properties of test soil are given in Table 1. Based on Table 1, the soil is named as silty clay with the liquid limit of 37.2% and plastic index of 14.3%. According to the compaction test, the optimum water content of the soil sample was 15.4%. With the reference that the optimum water-cement ratio for hydration of sulfoaluminate cement is 0.6 [18], the water content of soil sample was set as 24%.

The composition of binder is shown in Table 2. The binder was made up of high-alumina cement, lime, and gypsum to study the effect Ca^{2+} and Al^{3+} ion contents on ettringite production. This series of binder was named ASC in which A, S, and C represent high-alumina cement, gypsum, and lime, respectively. To ensure that the mole ratio of SO_4^{2-} ions to Al^{3+} ions is greater than 0.42 and its effect on results is excluded, the S/Al mole ratio was kept as 2:3, and the lime content was changed. In Table 2, sample number is the mole ratio of Ca/Al.

Table 3 shows the composition of substances in binder measured by X-ray fluorescence (XRF). Based on the content of Al_2O_3 , CaO, and SiO_2 , it was found that the content of monocalcium aluminate is the largest, accounting for about 75% of the total mass. The calcium silicate and impurities accounted for 20% and 5%, respectively.

2.2. Test Method. Sample preparation. The mass ratio of binder to dry soil was set as 15%, the water content was 24%, and the concentration of lead was 5000 mg/kg. The mould with the diameter of 50 mm and the height of 100 mm was used to prepare samples, and the mass of a sample is controlled as 370 ± 10 g. After preparation, the samples were put into standard maintaining room with a temperature of $20 \pm 2^\circ\text{C}$ and relative humidity of above 95%.

The unconfined compressive strength tests were conducted for samples maintained to a predetermined age using the CBR-2 load ratio tester, referring to the specification ASTM D4219-02 [19].

According to the solid waste extraction procedure for leaching toxicity-acetic acid buffer solution method (HJ/T 300-2007) [20], this study extracted heavy metal Pb^{2+} from solidified soils, and its concentration was measured using an absorption spectrometer.

The microstructure, pore structure, and mineral composition were analyzed by SEM, XRD, and MIP tests.

3. Results and Discussion

3.1. Temperature. In the ASC series of samples, the sample temperature decreases as the lime addition increases. This shows that the hydration reaction of ASC series binder is smaller than that of cement hydration reaction.

Figure 1(a) shows the fluctuation of temperature with time in the first three days of solidified soil samples and ordinary Portland cement samples with different lime contents. The temperature of samples reached steady states

TABLE 1: Physical properties of tested soil.

Plastic limit (%)	Liquid limit (%)	Optimum water content (%)	Maximum dry density (g/cm ³)
22.9	37.2	15.4	1.938

TABLE 2: Composition of binder (unit: %).

Sample number	Al:Ca:S mole ratio	High-alumina cement	Lime	Gypsum
Ca/Al = 4:3	3:4:2	7.5	0	7.5
Ca/Al = 6:3	3:6:2	6.36	2.28	6.36
Ca/Al = 8:3	3:8:2	5.6	3.8	5.6
Ca/Al = 10:3	3:10:2	5	5	5

TABLE 3: Material composition (unit: %).

Composition	Al ₂ O ₃	SiO ₂	CaO	SO ₃	Fe ₂ O ₃	Others
High-alumina cement	44.75	8.95	32.16	/	1.86	12.28
Lime	/	/	99.99	/	/	0.01
Gypsum	/	/	36.50	52.14	/	11.36

within 24 hours. And the temperature of cement sample was higher than that of the ASC series. In the ASC series of samples, the temperature decreased as the lime content increased, which indicated that the hydration of ASC series released less heat than cement.

The temperature changes in the first 12 hours are shown in Figure 1(b). It can be seen from the partial enlarged detail that the sample temperature has reached a steady state in the first 12 hours, and the heat release was mainly concentrated in the first 4 hours. With the increase of lime content, the temperature change of the sample in the first 4 hours decreased sharply. The high temperature at that time was caused by the heat release of the reaction between lime and water, but the temperature difference was within 3°C. When the samples were mixed, the lime had released plenty of heat. Therefore, the influence of lime on the sample temperature was small and not considered in the subsequent experiments.

3.2. Water Content. The water content of solidified soil samples with different lime contents is shown in Figure 2. The water content of all ettringite-solidified soils reduced with the increase of lime content. The water content slightly decreased at 28 days while reduced from 18% to around 14% at 90 days. It can be concluded that as the lime content and curing time enhanced, the decrease of water content became larger.

The binder was composed of high-alumina cement, gypsum, and lime. The high-alumina cement mainly contained mineral components like calcium monoaluminate and calcium silicate. In the hydration of binder, it took 26 units of water (excluding the crystal water in gypsum) to generate 1 unit of ettringite crystal. Without producing ettringite, hydration of the same binder consumed only 12 units of water, indicating that the water used for producing ettringite was much larger than that used for the hydration of high-alumina cement and lime.

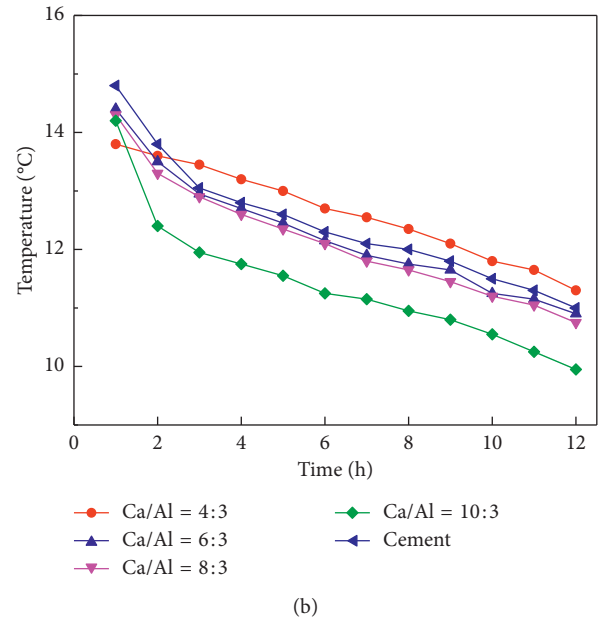
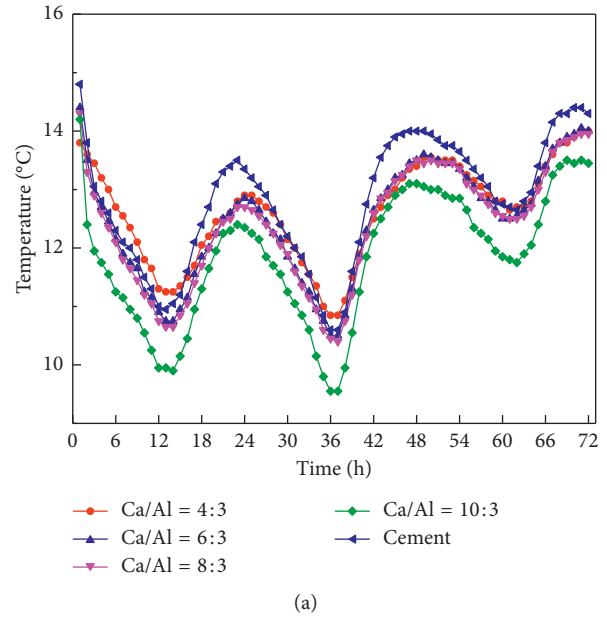


FIGURE 1: Relationships between temperature and curing time with different lime contents. (a) Within 3 d; (b) within 12 h.

As shown in Figure 2, without producing ettringite, as the lime content increased, the theoretical water content enhanced when the hydration was complete. Figure 2 also presents that the curing time became larger, and water content reduced as the lime content increased, indicating the production increase and long-term stability of ettringite.

Many studies indicated that some changes would appear with the increase of temperature: at 100°C, ettringite will lose a tiny portion of crystal water [21]; at 130°C, the thermal decomposition of gypsum will cause it to lose part of crystal water [22]; at 270°C, the thermal decomposition of hydrated calcium aluminate will cause it to lose a large amount of crystal water [23]; at 400°C, the structure of hydrated

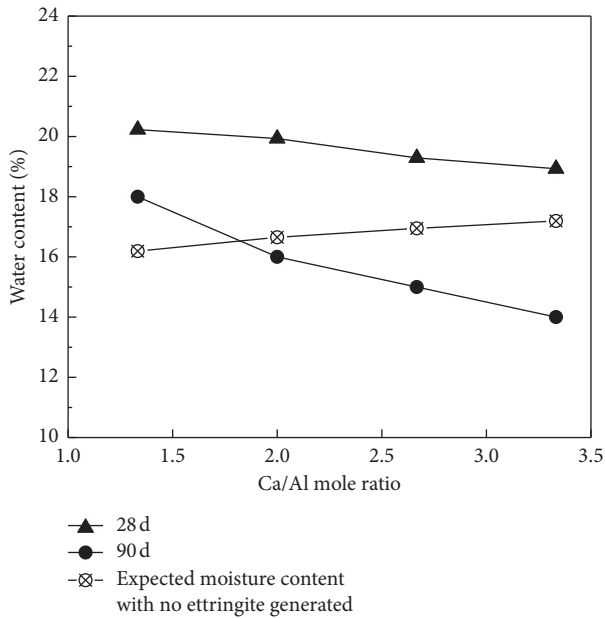


FIGURE 2: Variation of moisture content with lime content.

calcium aluminate will be still stable [24]; at 580°C, calcium hydroxide will decompose into CaO and H₂O.

3.3. Solidified Soil Leaching Toxicity. Figure 3 shows the change of the pH of the pore solution and the leachate of the solidified soil when the lime content varied. In terms of Figure 3, with the increase of lime content, the pH of the solidified soil pore solution increased substantially linearly. Apart from that, the curing time had little effect on the pH of the pore solution. As for the pH of the leachate, it also grew with the increase of lime content. When the lime content was low, the pH climbed slowly, but under the condition of high lime content, the pH surged rapidly. Moreover, the pH of the leachate at 90 d was higher than that at the 28 d.

The leaching concentration of solidified heavy metal-contaminated soils with different lime contents is presented in Figure 4. The concentration of heavy metal Pb²⁺ in solidified soil was 5000 mg/L, and the curing time was 28 d and 90 d, respectively. As shown in Figure 4, with the increase of lime content and curing time, the leaching concentration of heavy metals declined. Besides, it should be noticed that the concentration of Pb²⁺ ion leaching of Ca/Al = 10 : 3 solidified soil was much lower than 5 mg/L prescribed in the hazardous waste standard at 28d, which was 0.1911 mg/L. Furthermore, at 90 d, the concentration of the solidified soil sample with Ca/Al = 8 : 3 was 3.66 mg/L, also lower than 5 mg/L. This is because the formation of ettringite requires a certain amount of Ca²⁺. When the content of calcareous lime increases, the pH of the solidified soil increases, the Ca²⁺ concentration increases, and the amount of ettringite increases, which significantly improves the solidification effect of heavy metals. The ettringite has long-term stability. With the increase of curing time, ettringite is stably present and continuously formed, and the effect of curing/stabilizing the heavy metal is further improved.

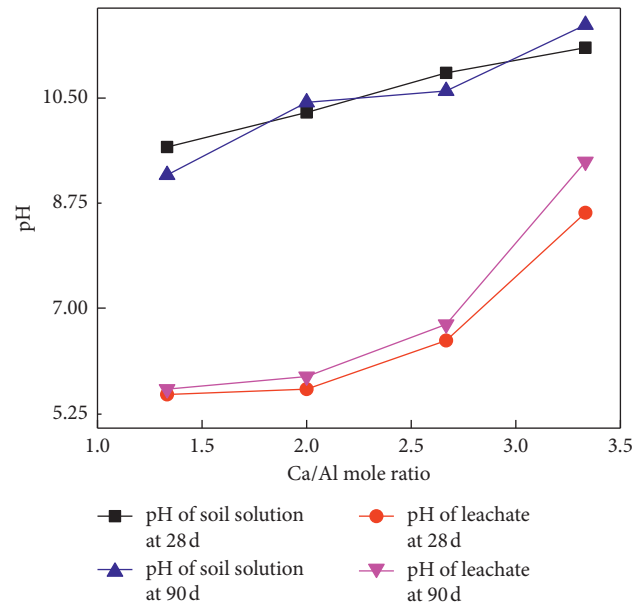


FIGURE 3: pH of soil solution and leachate.

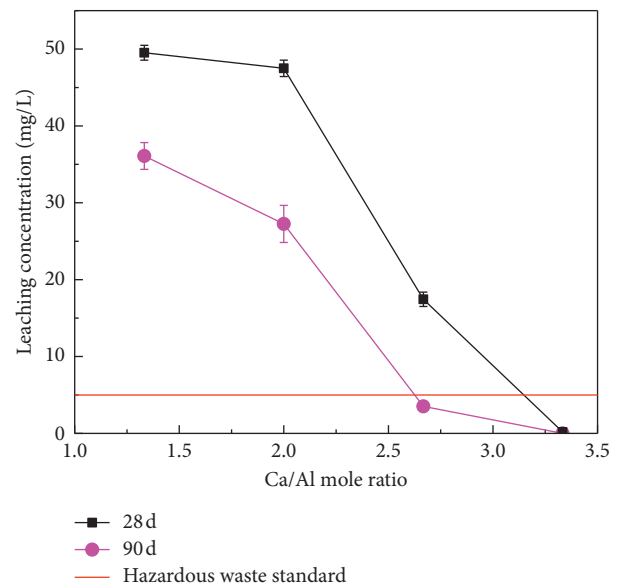


FIGURE 4: Leaching concentrations of lead (Pb²⁺).

The formation of ettringite requires a certain amount of Ca²⁺. The increase in the content of lime resulted in increase in pH of the solidified soil and the increase of Ca²⁺ concentration and eventually accelerated the production of ettringite, which significantly improved the solidification of heavy metals. To sum up, as curing time passed by, ettringite was stably and continuously generated, and the effect of stabilization/solidification on the heavy metal can be further enhanced.

3.4. Strength Properties of Solidified Soil. The change of the unconfined compressive strength of heavy metal-contaminated soils stabilized/solidified by ettringite is shown in Figure 5.

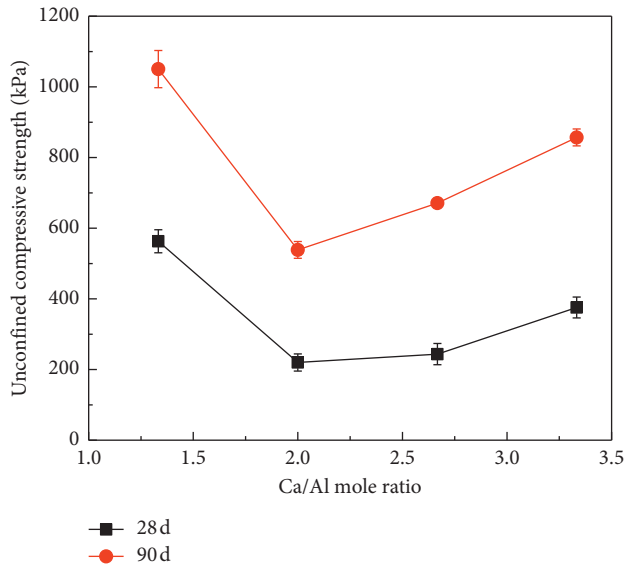


FIGURE 5: Unconfined compressive strength of solidified samples.

It presents that as the lime content increased, the unconfined compressive strength fell first and then rose. When the quantity of lime was small, the development of soil strength mainly resulted from the cementation between soil particles and calcium aluminate produced by the hydration reaction of high-aluminum cement. As the lime content increased, the content of high-aluminum cement declined, and the cementation between calcium aluminate and the soil particles was weakened, but the filling effect of ettringite on the soil pores became stronger, contributing to the growth of strength. Besides, cementation and filling cannot replace each other. When the curing reached 90 days, the unconfined compressive strength was about 2 times that of 28 d, which indicated that as the curing time passed by, the hydration reaction of the binder continued, and both the cementation and filling effect kept the trend of increase, benefiting the strength growth of soil samples.

3.5. Analysis of Microscopic Test Results

3.5.1. Analysis of Mercury Injection Test Results. The cumulative pore volume change of solidified soil samples during the 90 days of curing is shown in Figure 6, and the pore distribution density is presented in Figure 7.

As can be seen from Figure 6, with the growth of lime content, the cumulative pore volume of the sample first increased and then declined, followed by Ca/Al = 8:3, 10:3, 6:3, and 4:3 in a descending order. The cumulative pore volume curve of the samples was slightly different. For Ca/Al = 4:3 and 6:3, the curves were comparatively flat, and the cumulative pore volume rose rapidly below 1 μm. For Ca/Al = 8:3 and 10:3, the curves eased after a dramatic increase when the aperture was 10 μm. As for the aperture that was less than 0.01 μm, the curve was gentle.

Figure 7 indicates that when the amount of lime was small, the pore size of the sample was mainly distributed

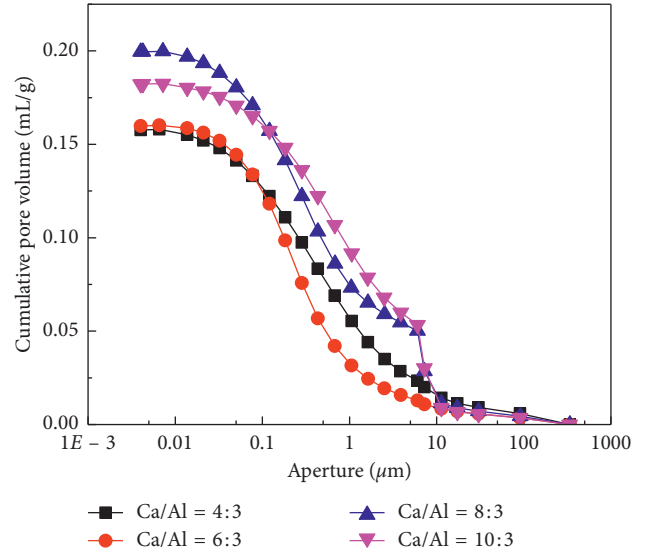


FIGURE 6: Variation of cumulative pore volume with different lime contents.

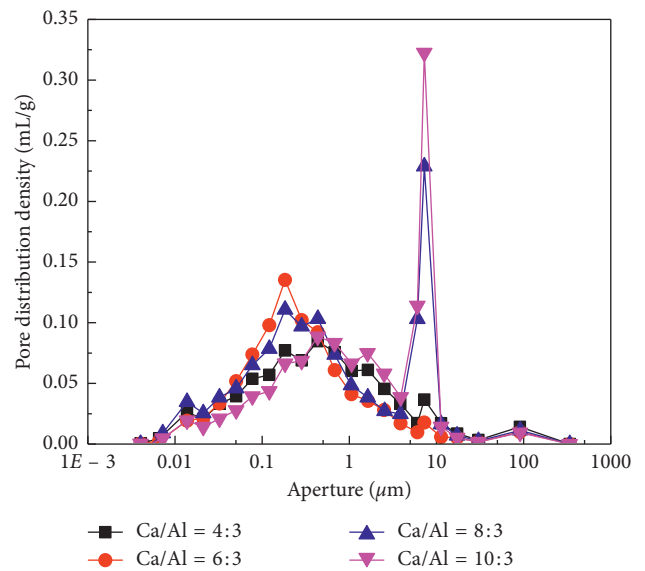


FIGURE 7: Variation of pore distribution density with different lime contents.

between 0.1 μm and 1 μm; when the amount of lime was large, that is, Ca/Al = 8:3 and 10:3, the sample pore size distribution focused on 0.1 μm–1 μm and 5 μm–10 μm, respectively. The peaks of the pore distribution density curves of the samples with Ca/Al = 6:3 and 8:3 were more to the left than the samples with Ca/Al = 4:3 and 10:3, and the peak value of the samples with Ca/Al = 6:3 and 8:3 was slightly higher.

Obviously, when Ca/Al = 6:3, the filling effect of the binder on the sample exerted the best because the pore distribution density reached a peak around the 0.1 μm, and the cumulative pore volume was the smallest. When Ca/Al = 8:3, there were two peaks of the curve: the low peak value still stayed around 0.1 μm, but marginally decreased

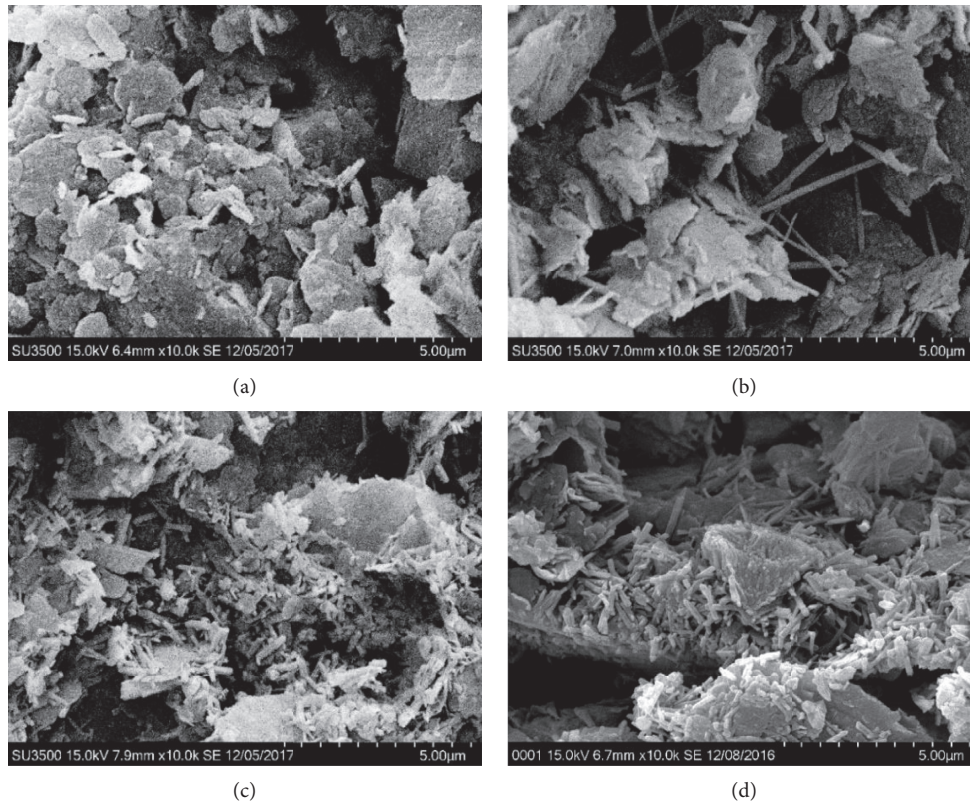


FIGURE 8: SEM pictures of solidified samples at 90 d. (a) Ca/Al = 4 : 3; (b) Ca/Al = 6 : 3; (c) Ca/Al = 8 : 3; (d) Ca/Al = 10 : 3.

compared with the one at Ca/Al = 6 : 3 and the high pore peak value appeared at $5\ \mu\text{m}$ – $10\ \mu\text{m}$ and reached $0.30\ \text{mL/g}$, manifesting that the ettringite generated by the binder expanded the soil sample and developed cracks. When Ca/Al = 10 : 3, the peak of the low-peak value fell and shifted to around $0.5\ \mu\text{m}$ and the high-peak value continued to rise to about $0.325\ \text{mL/g}$ at the range of $5\ \mu\text{m}$ to $10\ \mu\text{m}$, indicating that the expansion of ettringite became more obvious. To conclude, with the growth of lime content, the amount of ettringite increased, and the impact on the pore volume and the pore distribution density solidified soil became greater.

3.5.2. Analysis of SEM Experiment Results. From Figure 8, it can be seen that as the content of lime increased, the amount of ettringite increased gradually with the growth of lime content. In this process, the distribution of ettringite altered from suspension in space to adhere to the surface of solid particles. When Ca/Al = 4 : 3, the hydration products of the binder were mainly hydrated calcium aluminate, and there was a very small amount of ettringite, which was nearly an even dispersion; when Ca/Al = 6 : 3, the ettringite was in an elongated column shape. Meanwhile, calcium aluminate hydrate interacted with ettringite and evenly filled pores; when Ca/Al = 8 : 3, the amount of the calcium aluminate hydrate content greatly reduced, but the ettringite production increased a lot, and the ettringite began to aggregate to the surface of particles; when Ca/Al = 10 : 3, the ettringite

was the main hydration products of the binder, which grew on the surface of soil particles.

According to Figure 8 combined with the data of mercury injection experiment, after the increase of ettringite production and the shift of the generation place of the ettringite, a large number of pores with the sizes of $5\ \mu\text{m}$ to $10\ \mu\text{m}$ were produced in the solidified soil samples. The increase in porosity would decrease the strength of the soil samples; however, the increase in the content of ettringite would improve the strength of the solidified soil samples due to the filling effect of pores. Therefore, controlling the ettringite content and the generation place is of great significance for the strength of the solidified soil sample.

3.5.3. Analysis of XRD Experimental Results. XRD test was conducted on solidified soil samples with different lime contents. The test pattern is shown in Figure 9. The ordinate refers to d , which is a dimensionless quantity. The abscissa is the diffraction angle 2θ , and there is a corresponding relationship between d and 2θ .

When the characteristic peak d value of ettringite reached 5.61, it can be easily discriminated and was not disturbed by other mineral peaks [25]. When Ca/Al = 4 : 3 or 6 : 3, only a small amount of ettringite peaks could be analyzed. When Ca/Al = 8 : 3 or 10 : 3, the peak at $d = 5.61$ was obvious, and both the height and the number of other peaks increased. It shows that the content of ettringite is positively relevant to the lime content.

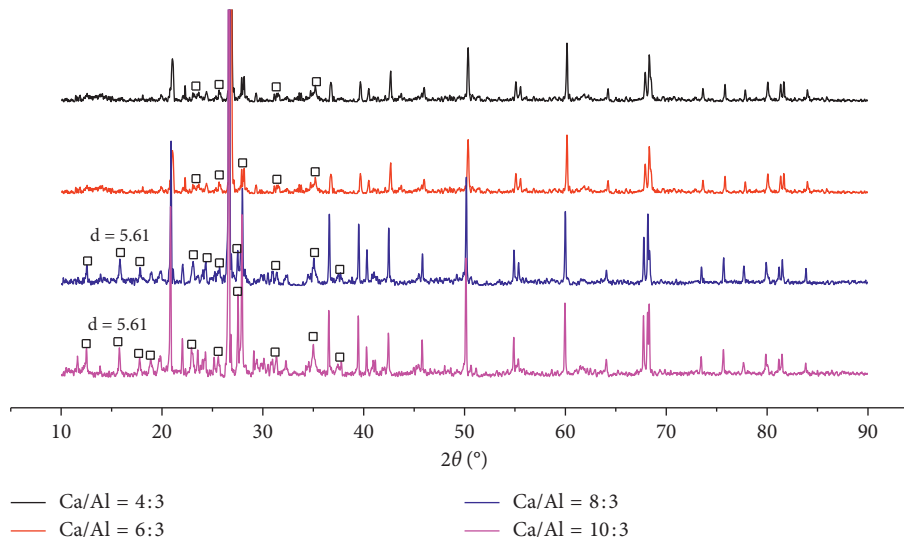


FIGURE 9: XRD spectra with different lime contents.

4. Conclusions

This study used the binders with different proportions of high-alumina cement, lime, and gypsum to immobilize lead-contaminated soils. The effect of mole ratios of Ca/Al on the physical performance and leaching characteristic of immobilized soil was investigated. The mineral composition and microstructure of immobilized soil was also studied. The following conclusions can be drawn:

- (1) With the Ca/Al mole ratio increasing from 4:3 to 10:3, the leaching concentration of lead reduced from 49.89 mg/L to 0.19 mg/L at 28 days and from 36.57 mg/L to 0 mg/L at 90 days. The pore fluid pH value in solidified soil at 28 days was not significantly different from that at 90 days, increasing from 9.68 to 11.34. The PH value of leachate increased from 5.56 to 8.59 at 28 days and increased from 5.56 to 9.44 at 90 days. When the Ca/Al mole ratio was 8:3, the leaching concentration of lead at 90 days was 3.66 mg/L, which meets the standard of 5 mg/L for hazardous waste. It is concluded that the Ca/Al mole ratio of the binder used for stabilizing/solidifying heavy metals based on ettringite should be greater than 8:3.
- (2) According to results from the microtests, with the increase of Ca/Al mole ratio, the ettringite content in solidified soil increased and crystals moved from inner space to surface of soil particles.
- (3) As the Ca/Al mole ratio increased, the unconfined compressive strength of solidified soil decreased firstly and then increased. The unconfined compressive strength at 90 days was 2 times that at 28 days. The strength of solidified soil mainly depended on the filling effect of ettringite and the cementation of hydrated calcium aluminate. Thus, the increase of lime content weakened the cementation and enhanced the filling effect.

- (4) As the curing time and Ca/Al mole ration increases, the water content reduces, indicating that the promotion of lime content is beneficial to ettringite formation and its long-term stability which will increase with time elapse.
- (5) A large amount of heat was released by the reaction between lime with water, and the exotherm was mainly concentrated in the first 4 hours. The sample temperature has reached a steady state until the first 12 hours, and the temperature difference was controlled within 3°C. Therefore, the influence of lime on sample temperature was small and not considered.

Data Availability

The data used to support the findings of this study are available from the corresponding author upon request.

Conflicts of Interest

The authors declare that they have no conflicts of interest.

Acknowledgments

This study is supported by the National Natural Science Foundation of China (Grant no. 51578148) and the Fundamental Research Funds for the Central Universities (No. 2242017K40128).

References

- [1] C. Tiberg, J. Kumpiene, J. P. Gustafsson et al., "Immobilization of Cu and As in two contaminated soils with zero-valent iron - long-term performance and mechanisms," *Applied Geochemistry*, vol. 67, pp. 144–152, 2016.
- [2] M. Yan, G. Zeng, X. Li et al., "Incentive effect of bentonite and concrete admixtures on stabilization/solidification for heavy metal-polluted sediments of xiangjiang river," *Environmental*

- Science and Pollution Research*, vol. 24, no. 1, pp. 892–901, 2016.
- [3] A. R. Goodarzi and M. Movahedrad, “Stabilization/solidification of zinc-contaminated kaolin clay using ground granulated blast-furnace slag and different types of activators,” *Applied Geochemistry*, vol. 81, pp. 155–165, 2017.
 - [4] F. Jin, F. Wang, and A. Al-Tabbaa, “Three-year performance of in-situ solidified/stabilised soil using novel MgO-bearing binders,” *Chemosphere*, vol. 144, pp. 681–688, 2016.
 - [5] A. Al-Tabbaa and D. Johnson, “State of practice report: stabilization/Solidification of contaminated materials with wet deep soil mixing,” in *Proceeding of International Conference on Deep Mixing*, pp. 697–731, Sweden, February 2005.
 - [6] B. I. El-Eswed, R. I. Yousef, M. Alshaaer, I. Hamadne, S. I. Al-Gharabli, and F. Khalili, “Stabilization/solidification of heavy metals in kaolin/zeolite based geopolymers,” *International Journal of Mineral Processing*, vol. 137, pp. 34–42, 2015.
 - [7] L. I. Tao-ping, “China Cement industry Energy efficiency status and energy-saving potential report,” *Cement Engineering*, no. 4, pp. 1–10, 2004.
 - [8] D. Higgins, “Briefing: GGBS and sustainability,” *Proceedings of the Institution of Civil Engineers-Construction Materials*, vol. 160, pp. 99–101, 2007.
 - [9] S. Peysson, J. Péra, and M. Chabannet, “Immobilization of heavy metals by calcium sulfoaluminate cement,” *Cement and Concrete Research*, vol. 35, no. 12, pp. 2261–2270, 2005.
 - [10] V. Albino, R. Cioffi, M. Marroccoli, and L. Santoro, “Potential application of ettringite generating systems for hazardous waste stabilization,” *Journal of Hazardous Materials*, vol. 51, no. 1–3, pp. 241–252, 1996.
 - [11] I. Odler, *Special Inorganic Cements*, CRC Press, London, UK, 2000.
 - [12] C. A. Luz, J. Pera, M. Cheriaf, and J. C. Rocha, “Behaviour of calcium sulfoaluminate cement in presence of high concentrations of chromium salts,” *Cement and Concrete Research*, vol. 37, no. 4, pp. 624–629, 2007.
 - [13] X. Wang, S. Cui, L. Wang et al., “Solidification and stability of ettringite doped Cr ion with different valences,” *Bulletin of the Chinese Ceramic Society*, vol. 34, no. 11, pp. 3308–3314, 2015.
 - [14] X. Wang, B. Yan, L. Wang et al., “The research on the mechanism of solidification and stability of ettringite doped Cr^{6+} and Cu^{2+} ,” *Bulletin of the Chinese Ceramic Society*, vol. 32, no. 2, pp. 186–192, 2013.
 - [15] B. Ma, B. Wu, X. Li et al., “Influence of Zn^{2+} on the hydration properties of the sulfoaluminate and ordinary Portland cement,” *Journal of Wuhan University of Technology*, vol. 7, no. 14, pp. 30–34, 2010.
 - [16] H. Chen, Q. Ye, and J. Shen, “Long-term stability of ettringite in cement paste,” *Materials Science and Engineering*, vol. 19, no. 2, pp. 69–71, 2001.
 - [17] D. Zhang, L. Xiang, and Z. Cao, “Effect of CaO on ettringite stabilization/solidification of lead-contaminated soil,” *Rock and Soil Mechanics*, vol. 39, no. 1, pp. 29–35, 2018.
 - [18] F. P. Classer and L. Zhang, “Calculation of chemical water demand for hydration of calcium sulfoaluminate cement,” *Journal of the Chinese Ceramic Society*, vol. 28, no. 4, pp. 340–347, 2000.
 - [19] American Society for Testing and Materials, *ASTM D4219-02 Standard Test Method for Unconfined Compressive Strength Index of Chemical-Grouted Soils*, American Society for Testing Materials, West Conshohocken, PA, USA, 2002.
 - [20] Institute of Solid Waste Pollution Control Technology, Chinese Research Academy of Environmental Science, *HJ/T 300-2007 Solid Waste-Extraction Procedure for Leaching Toxicity-Acetic Acid Buffer Solution Method*, China Environmental Science Press, Beijing, China, 2007.
 - [21] F. Chen, “Effect of temperature on the growth characteristics of ettringite,” *World of Building Materials*, vol. 32, no. 3, pp. 7–9, 2011.
 - [22] L. Ma, A. Yang, and Y. Liu, “Characterization and analysis of TG and DSC on the thermal dehydration of phosphogypsum and pure gypsum,” *Applied Chemical Industry*, vol. 44, no. 5, pp. 959–962, 2015.
 - [23] G. Pan, R. Mao, and J. Yuan, “Study on dehydration phase of hydrated calcium aluminate (CAH) and its hydration,” *Journal of Wuhan University of technology*, vol. 19, no. 3, pp. 25–27, 1997.
 - [24] S. Yu, *Study on Dehydration Phase and its Re-Hydration Characteristics of Hydrated Calcium Silicate*, Wuhan University of Technology, Wuhan, China, 2012.
 - [25] X. Huang, S. Xu, and J. Ning, “Experimental research on stabilized soft soils by alumina bearing modifier,” *Chinese Journal of Rock Mechanics and Engineering*, vol. 6, no. 1, pp. 156–161, 2007.

Research Article

Numerical Study of the Dynamic Compaction Process considering the Phenomenon of Particle Breakage

Xi Li ^{1,2}, Jing Li,¹ Xinyan Ma,³ Jidong Teng,^{1,4} and Sheng Zhang ^{1,4}

¹School of Civil Engineering, Central South University, Changsha, Hunan 410075, China

²School of Traffic and Transportation Engineering, Changsha University of Science and Technology, Changsha 410114, China

³China Airport Construction Group Corporation, Beijing 100101, China

⁴National Engineering Laboratory for High Speed Railway Construction, Changsha 410075, China

Correspondence should be addressed to Xi Li; csu_lixi@csu.edu.cn and Sheng Zhang; zhang-sheng@csu.edu.cn

Received 16 June 2018; Revised 12 September 2018; Accepted 24 September 2018; Published 23 December 2018

Academic Editor: Annan Zhou

Copyright © 2018 Xi Li et al. This is an open access article distributed under the Creative Commons Attribution License, which permits unrestricted use, distribution, and reproduction in any medium, provided the original work is properly cited.

Dynamic compaction (DC) is commonly used to strengthen the coarse grained soil foundation, where particle breakage of coarse soils is unavoidable under high-energy impacts. In this paper, a novel method of modeling DC progress was developed, which can realize particle breakage by impact stress. A particle failure criterion of critical stress is first employed. The “population balance” between particles before and after crushing is guaranteed by the overlapping method. The performance of the DC model is successfully validated against literature data. A series of DC tests were then carried out. The effect of particle breakage on key parameters of DC including crater depth and impact stress was discussed. Besides, it is observed that the relationship between breakage amount and tamping times can be expressed by a logarithmic curve. The present method will contribute to a better understanding of DC and benefit further research on the macro-micro mechanism of DC.

1. Introduction

Dynamic compaction (DC) refers to the ground improvement method in which a heavy weight is dropped onto the ground surface from a great height to increase the density of the underlying soils. The DC method has been found to be useful in improving the mechanical behavior of underlying soil layers, especially loose granular materials [1–4]. Recently, the DC method has been widely used in many engineering fields, such as airports, seaports, dams, and railways.

Many analytical or semianalytical studies have been carried out to predict the important parameters involved in real DC treatments, including the degree and depth of improvement [5–7], the dynamic stress distribution in depth [8–10], the crater depth [5, 11, 12], and the numerical simulation of DC [13–18].

Although the topic of DC has been widely researched in geomechanics, the performance design and the application

of dynamic compaction are still largely empirical in nature. This may be due to the complexity of the soil itself and the substantial challenges associated with a DC field test. Under the impact stress of a hammer, the soil foundation generates a series of complex responses, including the reorganization of local soil particles, the dramatic plastic deformation near the impact location, and the interior deformation under a stress wave. It is difficult to address all these responses in a deterministic model and collect sufficient data resources in a DC field test.

A numerical method simulation of DC attracts more attention in published literature. Poran and Rodriguez [13] presented one of the earliest 2D models for simulating DC in dry sand using the finite element code. Their computed results are good when the sand is relatively loose, but when densification occurs, the computed results depart substantially from experimental data. Based on the findings of Poran and Rodriguez, Lee et al. [14] and Gu et al. [15] described dry sand behavior under the DC process, utilizing

a finite element program. They discussed the effects of drop energy, the momentum of the falling tamper, and the tamper radius on the depth of improvement. In addition, they proposed a method for estimating the depth and the degree of improvement. Wang et al. [16] developed a method for estimating ground deformation with a numerical model created in LS-DYNA.

Considering numerical studies of DC, the discrete element method, which is neither limited by the large deformation nor the constitutive model of the soil, is superior [17, 18]. Ma et al. [18] pointed out that the improvement and the maximum influence depth of DC can be easily evaluated via the porosity changes of the gravel soil obtained by the particle flow discrete (PFC) element method. Jiang et al. [3] conducted a series of DC tests with PFC^{3D} to evaluate the compacting effects via the porosity and the ground settlement.

It is worth noting that particle breakage is unavoidable in the DC procedure and is more prone to occur for coarsely granular soil. Particle breakage will change the particle size distribution (PSD) and influence the soil mechanical properties. Previous literature has reported that particle breakage causes the PSD to behave as a soil variable, undermining the basic definition of soil and hence the soil mechanics principles [19–22]. However, the simulation of particle breakage is infrequently studied in the DC process. Further, little research has been carried out to study the effects of particle breakage on DC.

In this paper, a numerical study is carried out using the particle flow code in three dimensions (PFC^{3D}). Particular attention is paid to develop a numerical model of the DC process that can stimulate the phenomena of particle breakage caused by DC. The influence of particle breakage on crater depth and impact stress by DC is presented. The relationship between particle breakage amount and impact time is also discussed in detail.

2. Number Simulation of DC

2.1. Contact Model. The effect of dynamic hysteresis on the soil during DC is considered in this paper, and the hysteretic damping contact model is shown in Figure 1. The normal stiffness for loading, k_{n_load} , and unloading, k_{n_unload} , used in the hysteretic damping model is calculated by using the following equation:

$$k_{n_load} = \frac{2R_h k_m}{1 + R_h}, \quad (1)$$

$$k_{n_unload} = \frac{2k_m}{1 + R_h},$$

where the parameter R_h is the ratio of k_{n_load} to k_{n_unload} ($1.0 < R_h < 0.0$). The dynamic hysteresis of the soil is more apparent when the R_h is close to zero. The parameter k_m is the average normal stiffness of k_{n_load} and k_{n_unload} . The normal stiffness for unloading is greater than that for loading in the dynamic contact process, and a simple

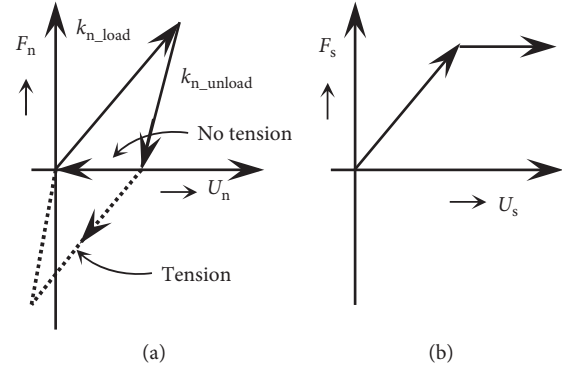


FIGURE 1: Constitutive relation of the hysteretic model: (a) normal direction; (b) shear direction.

hysteresis loop is formed by the linear contact for particle loading and unloading.

2.2. Parameters of DC Model. The scale of the DC model and the calculation time cost are in conflict in PFC^{3D}. When preparing a numerical sample, the accuracy and the computing time needed in the DC model are taken into consideration. As shown in Figure 2, a cylindrical specimen with a height of 3.5 m and a bottom diameter of 3.5 m is used in this paper. Two walls, including one platen and a cylindrical wall, are created as the sample boundary. A total of 73318 balls, all with the same radius of 0.04 m, are created to stimulate the soil foundation. The hammer is simulated by 88 particles bound together by the “clump logic” code in PFC^{3D}. The diameter of the hammer is 0.5 m, the height is 0.2 m, and the weight of the hammer is 3 kN. The diameter of the hammer is 1/7 of the sample. The sample is large enough for the limited level of tamping energy.

To specify the values of microscale parameters in this DC model, the work from Wang et al., Ma et al., Wada et al., and Huang et al. [16–18, 23] is referenced, and the microscale parameters are determined, as shown in Table 1.

2.3. Simulation of Particle Breakage. The physical process of real particle breakage occurs when a single particle breaks into two or more smaller particles as the particle reaches a critical condition. Currently, particle breakage has been modeled by DEM with two alternative approaches.

The first approach is the fragment replacement method (FRM), in which single elements break and are replaced by a new generation of smaller grains, previously nonexistent in the simulation [24–27]. The second approach is the bonded-particle model (BPM), which indicates that a certain number of subparticles bond together to stimulate a single particle. The particle breaks if the magnitude of the force equals or exceeds the contact bond strength [28–31]. The first method repeatedly demonstrates superiority in computing time and particle breakage. Therefore, the FRM method is adopted in this paper.

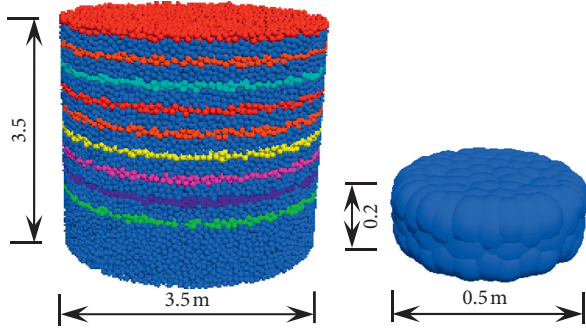


FIGURE 2: Discrete element model of dynamic compaction.

TABLE 1: Microscale parameters of PFC^{3D} model.

Parameters	Values
Particle number	73318
Particle density (kg·m ⁻³)	2600
Particle radius (m)	0.04
Mass damping	0.70
Normal stiffness of the particles (N·m ⁻²)	5 × 10 ⁶
Tangential stiffness of the particles (N·m ⁻²)	5 × 10 ⁶
Hysteretic damping	0.50
Initial ground void ratio	0.40
Interparticle frictional coefficient	0.50
Tamp density (kg·m ⁻³)	7800
Rammer gravity (N)	3000.30
Normal stiffness of the boundaries (N·m ⁻²)	1.00 × 10 ⁸
Tangential stiffness of the boundaries (N·m ⁻²)	1.00 × 10 ⁸
Poisson's ratio	0.30
m	10.00
d_0 (mm)	2.00
θ_0 (rad)	$\pi/18$
$\sigma_{lim,0}$ (Pa)	3.00 × 10 ⁹

The two most important points in the FRM method are the particle failure criterion and the particle spawning procedure. The particle failure criterion is used to decide when a particle is crushed. The particle spawning procedure establishes the relationship between the disappearing broken particle and the new generation of smaller particles (subparticles).

2.3.1. Particle Failure Criterion. The particle failure criterion is a condition to determine when the particle breakages occur. Astrom and Herrmann [32] and Marketos and Bolton [33] adopted this condition directly as the maximum contact force acting on the particle. Lobo-guerrero [34] suggests the use of a limit tensile strength, which is related to forces acting on discs, similar to a Brazilian test. Ben-Nun and Einav [35] use explicit multiplicative correction factors to account for the effects of the coordination number and the contact curvature.

A multiaxial failure criterion was presented by Russell et al. [36] with the analysis of the elastic stress distribution induced by point loads on a sphere. An analytical expression for the maximum mobilized shear strength for a diametrically

loaded sphere was obtained. The failure criterion for particle breakage can be expressed as

$$\kappa_{mob} \leq \kappa, \quad (2)$$

where κ_{mob} and κ are the mobilized and intrinsic strengths of the grain, respectively. The value of κ is given by

$$\kappa = \frac{1 + \chi}{\sqrt{3}} |\sigma_c|, \quad (3)$$

$$\chi = \frac{|\sigma_c|}{\sigma_t} - 1,$$

where χ is a parameter of the microstructure properties of the materials. For most geological materials, χ ranges from 10 to 170. σ_c and σ_t are the uniaxial compressive strength and the tensile strength, respectively.

κ_{mob} is the maximum stress at the center of the contact area (Figure 3), and an approximate expression for the maximum mobilized strength valid for small contact angles is

$$\kappa_{mob} = \frac{F}{\pi R^2 \sin^2 \theta_0} \times \frac{\sqrt{3}(1 + \chi^2)}{\chi}$$

$$\times \frac{((3/32) + (\sqrt{2}/24) + ((\sqrt{2}/12) - (1/4))\nu + ((1/2) - (\sqrt{2}/3))\nu^2)}{(2 - \sqrt{2})(1 + \nu)}$$

$$= \frac{F}{\pi R^2 \sin^2 \theta_0} f(\chi, \nu), \quad (4)$$

where ν is the Poisson's ratio, F is the load, R is the particle radius, and θ_0 is a solid angle "seen" from the center of the particle, defining the small area of stress application (Figure 3). Substituting Equation (4) into Equation (2) results in a limiting criterion for the normal contact forces as follows:

$$F_{lim} \leq \frac{\kappa}{f(\chi, \nu)} \pi R^2 \sin^2 \theta_0 = \sigma_{lim} A_F. \quad (5)$$

As indicated in Equation (5), the limiting force F_{lim} is obtained from the limit strength σ_{lim} and a contact area A_F .

In this paper, the size effect is incorporated as a dependent of the mean strength value of the particle diameter through a correction factor f_{size} , which can be calculated in a Weibull form:

$$f_{size}(d) = \left(\frac{d}{d_0} \right)^{-3/m}, \quad (6)$$

where m is a material parameter, d is the particle diameter, and d_0 is the reference diameter (chosen as 2 mm). Then, the value of σ_{lim} can be expressed as

$$\sigma_{lim} = \sigma_{lim,0} f_{size}(d), \quad (7)$$

where $\sigma_{lim,0}$ is the mean limit strength at d_0 .

To evaluate the contact area A_F in Equation (5), the Hertzian contact theory is adopted in this work. The radius of the contact area is determined by

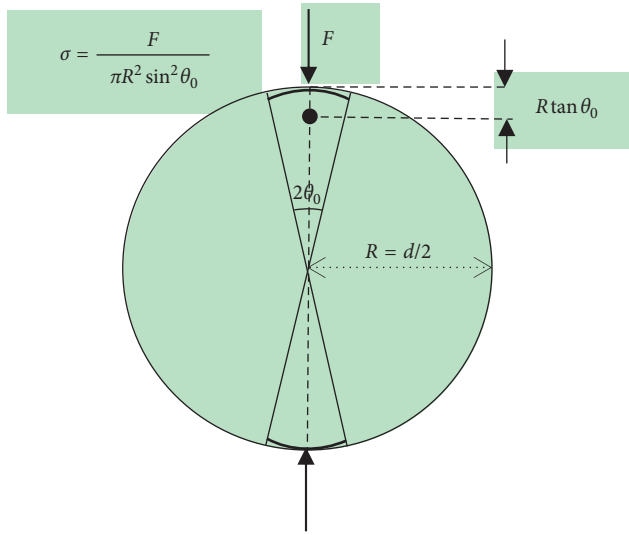


FIGURE 3: Force F acts normal to the sphere surface on an area defined by the angle θ_0 .

$$r_F = \left(\frac{3Fr'}{4E'} \right)^{1/3},$$

$$r' = \left(\frac{1}{r_1} + \frac{1}{r_2} \right)^{-1}, \quad (8)$$

$$E' = \left(\frac{1-\nu_1^2}{E_1} + \frac{1-\nu_2^2}{E_2} \right)^{-1},$$

where r_1 and r_2 are the radiuses of the contacting spheres and E_1 , ν_1 , E_2 , and ν_2 are their moduli. At this point, the criterion of particle breakage is developed.

2.3.2. Subparticle Substitution Model. For the method that replaces the broken parent particles with subparticles, we must ensure the mass conservation and reduce the local stress prominence caused by the overlap of the particles. This challenge needs to be considered because of the inevitable gaps between subparticles. The subparticle overlapping method is adopted in this paper. This method satisfies mass conservation by producing overlapping subparticles within the boundary of the original particle, and then, the subparticles are dispersed with an interaction force. McDowell and de Bono [24] pointed out that particle overlap causes the particle fragments to move as a single particle would when crushed between flat platens. To ensure sample stability and to accommodate the artificial pressure increase, in this study, particle breakages are updated immediately after the number of computational steps, equivalent to 0.003 s. This period is deemed sufficient to allow the artificially induced energy to dissipate.

As for the number of subparticles, Takei et al. [37] noted that the number of fragments after particle crushing is generally smaller than 10 for quartz particles. Research of McDowell and de Bono [24] shows that the number of subparticles has little or no effect on the one-dimensional

normal compression lines. Therefore, four subparticles were chosen in this model. As shown in Figure 4, a particle will split into four equally sized smaller subparticles once the breakage criterion is satisfied. The subparticles inherit the velocity and material parameters of the mother particle at once. Mass conservation is strictly obeyed, and the particle breakage effect on the soil foundation is vastly minimized in the model.

2.4. Process of Dynamic Compaction. The DEM model of DC consists of two main processes, i.e., sample preparation and dynamic tamping. The specific steps of DC are as follows:

- (1) A total of 73318 particles were created in the cylindrical space enclosed by the walls. The parameters of the particles are shown in Table 1. The particles were consolidated in the designated space under the influence of gravity (the acceleration of gravity was set to 9.8 m/s^2 in this study).
- (2) The heavy hammer was created immediately above the center of the soil sample and free falling under the action of gravity. To improve the calculation efficiency, the drop height of the hammer was set by the initial velocity ($\sqrt{2gH}$) in this study.
- (3) During each tamping process, key parameters such as displacement, velocity of the hammer, and contact stress between the hammer and foundation are monitored. The tamping process is complete when the hammer velocity decreases to 0 and the amount of crater depth no longer increases.
- (4) The hammer is regenerated above the soil and assigned a specific initial speed for the next tamping. In this study, tamping with the same falling distances was carried out at the same point of the soil foundation, and the drop height of the hammer was 2 m, 4 m, 6 m, 8 m, and 10 m, respectively. For each height, the sample was tamped 10 times.

3. Verification of the DC Model

The particles of the gravel soil are treated as spheres in PFC^{3D}. In this paper, the applicability of the model is verified with the results from field tests.

Figure 5 shows the time-displacement curve of the hammer when the drop height is 2 m. Although the value of the crater depth from the DC model is not in total agreement with that of the field tests, the time-displacement curve obtained from this DC model shares the same characteristics with field tests [38, 39]. For a single DC process, the displacement of the hammer increases rapidly until the lowest point is reached and finally tends to be stable. For repeated DC, the crater depth first increases with the amount of compaction and then tends to be stable, which agrees with the physical process of the increase in the soil density and the modulus after DC.

Figure 6 shows the time-stress curve of the bottom of the hammer when the drop height is 2 m. It can be seen that the dynamic stress at the bottom of the hammer has a single

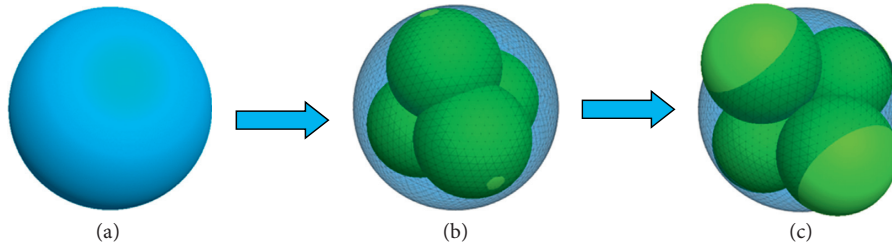


FIGURE 4: The configurations of postcrushing replacement.

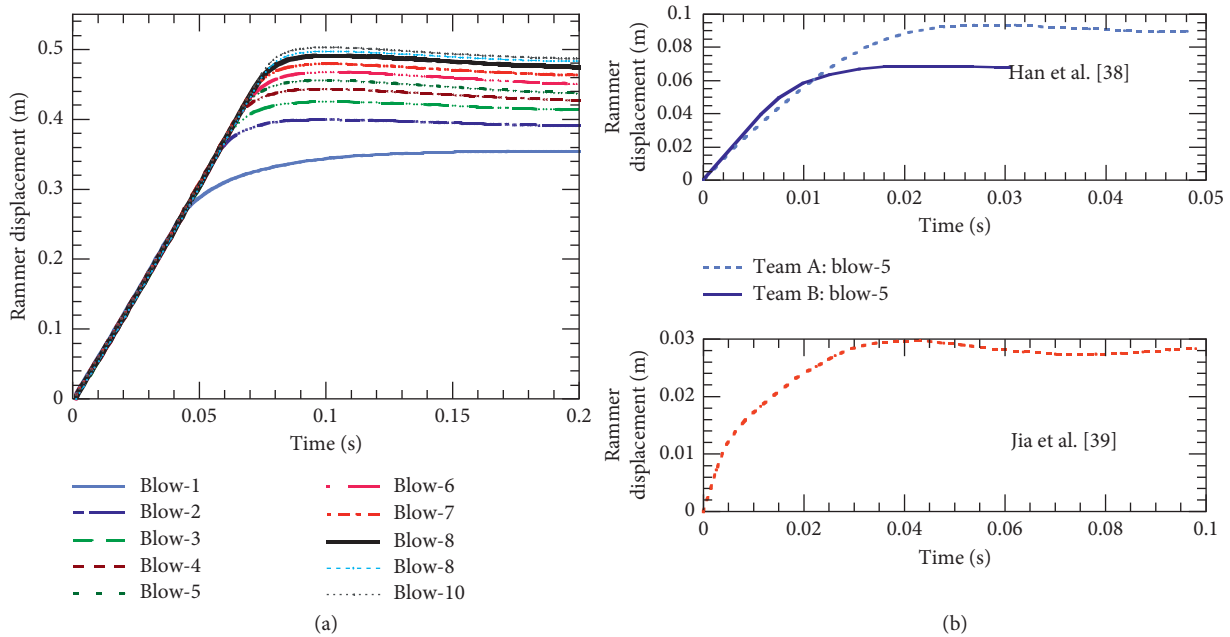


FIGURE 5: Hammer displacement over time in different studies: (a) displacement in this paper; (b) displacement in [38, 39].

peak triangle; the stress increment rate in the impact loading stage is obviously larger than the rate in the unloading stage. The results are also the same as those of Han et al. [38] and Jia et al. [39]. Therefore, it is inferred that the established DC model is sufficient to predict the whole tamping process.

4. Effect of Particle Breaking on DC

In DC practice, the crater depth of each impact is widely adopted to determine the optimal number of blows, and the impact stress is the direct indication of ground strength. The crater and the dynamic stress are two key parameters in the study of DC. Therefore, the effect of particle breakage on these two key parameters will be analyzed in this section.

4.1. Effect of Particle Breakage on Crater Depth. In the process of 10 blows, the depth of the crater per drop was analyzed with and without particle breakage. Figure 7 shows the crater depth under different drop heights. As shown in Figure 7, it is obvious that the crater depth increases with an increasing

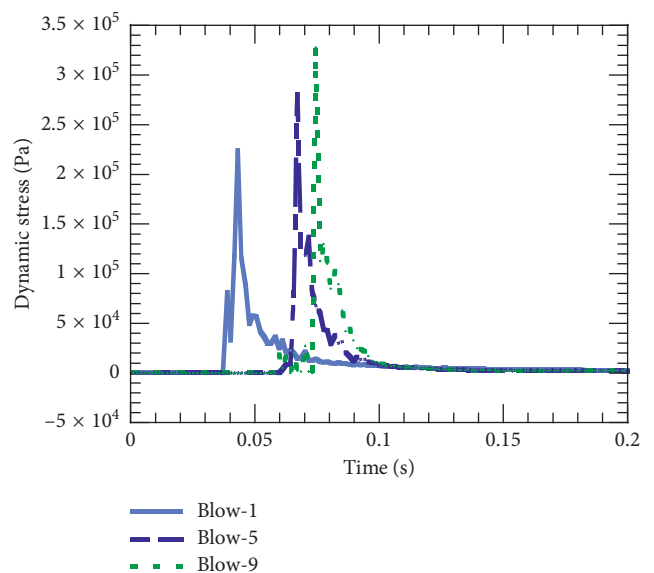


FIGURE 6: Time-stress curve of the bottom of the hammer.

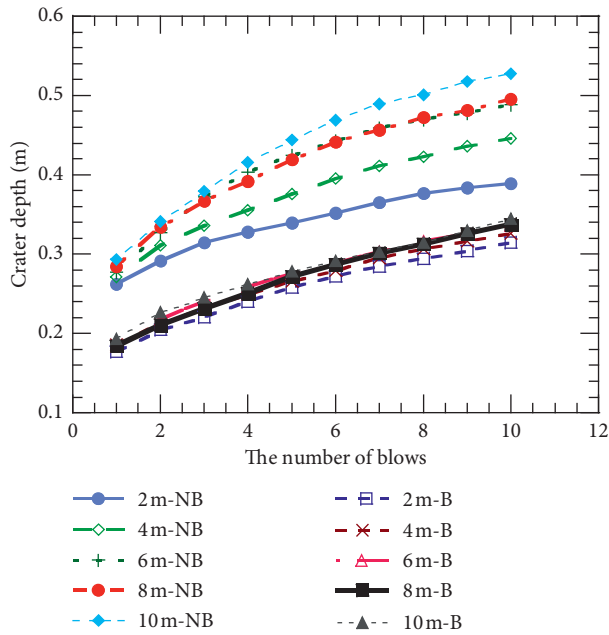


FIGURE 7: The crater depth under different dropping distances (NB means no particle breakage; B means particle breakage).

drop height for the same number of blows in both cases. Although the crater depth increases with an increasing number of blows, the amount of the increase decreases.

It is notable that the crater depth changes significantly with the occurrence of particle breakage during the DC process. Under the same DC conditions, particle breakage leads to a decrease in crater depth. For example, in the case of a 10 m drop height and 10 blows, the crater depths are 0.53 m without particle breakage and 0.34 m with particle breakage. The crater depth is reduced by 35.8%. In addition, particle breakage will decrease the crater difference caused by the drop height. The main reason for this decrease is that particle breakage consumes part of the tamping energy and the gap between the subparticles generated after particle breakage.

Particle breakage is only concentrated near the point of tamping. Hence, the effect of particle breakage on the increase in crater depth is limited. The true reason for tamping settlement is the accumulation of particle relative movement. All the microcosmic relative movements add up to a macroscopic tamping settlement. However, particle breakage requires tamping energy, and fewer particles are able to make the relative movement.

4.2. Effect of Particle Breakage on Dynamic Stress. To compare the effect of particle breakage on the dynamic stress in the DC process, 10 soil samples with same parameters were prepared. A series of DC tests were conducted with and without considering particle breakage at drop heights ranging from 2 m to 10 m. The results are shown in Figure 8.

As shown in Figure 8, particle breakage led to an increase in the peak value of impact stress, with the exception of the case of a drop height of 8 m. The dynamic stress of the bottom of the hammer without considering particle

breakage at 2 m, 4 m, 6 m, and 10 m increased by 45%, 37%, 35%, and 47%, respectively, when compared to the dynamic stress if particle breakage was considered.

5. Particle Breakage during DC Process

In this section, the evolution of particle breakage during the DC process is analyzed. Considering that particle breakage occurs mostly near the compaction point, the change in particle size distribution (PSD) is investigated within a cylindrical area of diameter 0.7 m and height 0.5 m.

Figure 9 shows the evolution of PSDs with an increasing number of blows from a constant drop height of 10 m. It can be seen that the PSD curve lifts with an increase in the number of blows, indicating that the content of fine particles increases and the particle breakage aggravates.

By using the parameter of the breakage index proposed by Einav [40], the relationship between B_r and the number of blows from different drop heights is shown in Figure 10. It can be found that the larger the input energy (drop height) is, the larger the amount of breakage is. In addition, the breakage index increases with an increasing number of blows. However, the increment decreases with the number of blows. It appears that the relationship between B_r and the number of blows can be expressed by a logarithmic function.

6. Conclusions

Numerical simulations of the dynamic compaction process for gravel soil ground were developed in this paper via a particle flow code in three dimensions. The focus of the paper was the study of the effects of particle breakage on DC which has not been addressed in previous DC literature. The following conclusions could be drawn:

- (1) The three-dimensional numerical model can simulate the phenomenon of particle breakage in the dynamic compaction process. Mass conservation during particle breakage simulation can be ensured.
- (2) Under the same tamping energy level, particle breakage reduces the crater depth and weakens the difference of crater depth between different energy levels. This can be explained by crushing energy consumption and the enlargement of the space volume of the subparticles after crushing.
- (3) Particle breakage increases the impact stress by approximately 35%–47%. However, the increased impact stress is mainly used for particle breakage instead of increasing the amount of crater depth.
- (4) Particle breakage mainly concentrates at the impact point. There is no particle breakage at other locations and the boundaries of the soil. Therefore, the broken particles cannot play a role of accelerating the consolidation of the ground soil. In addition, the extent of particle breakage and the number of tamping blows show a strong logarithmic relationship.

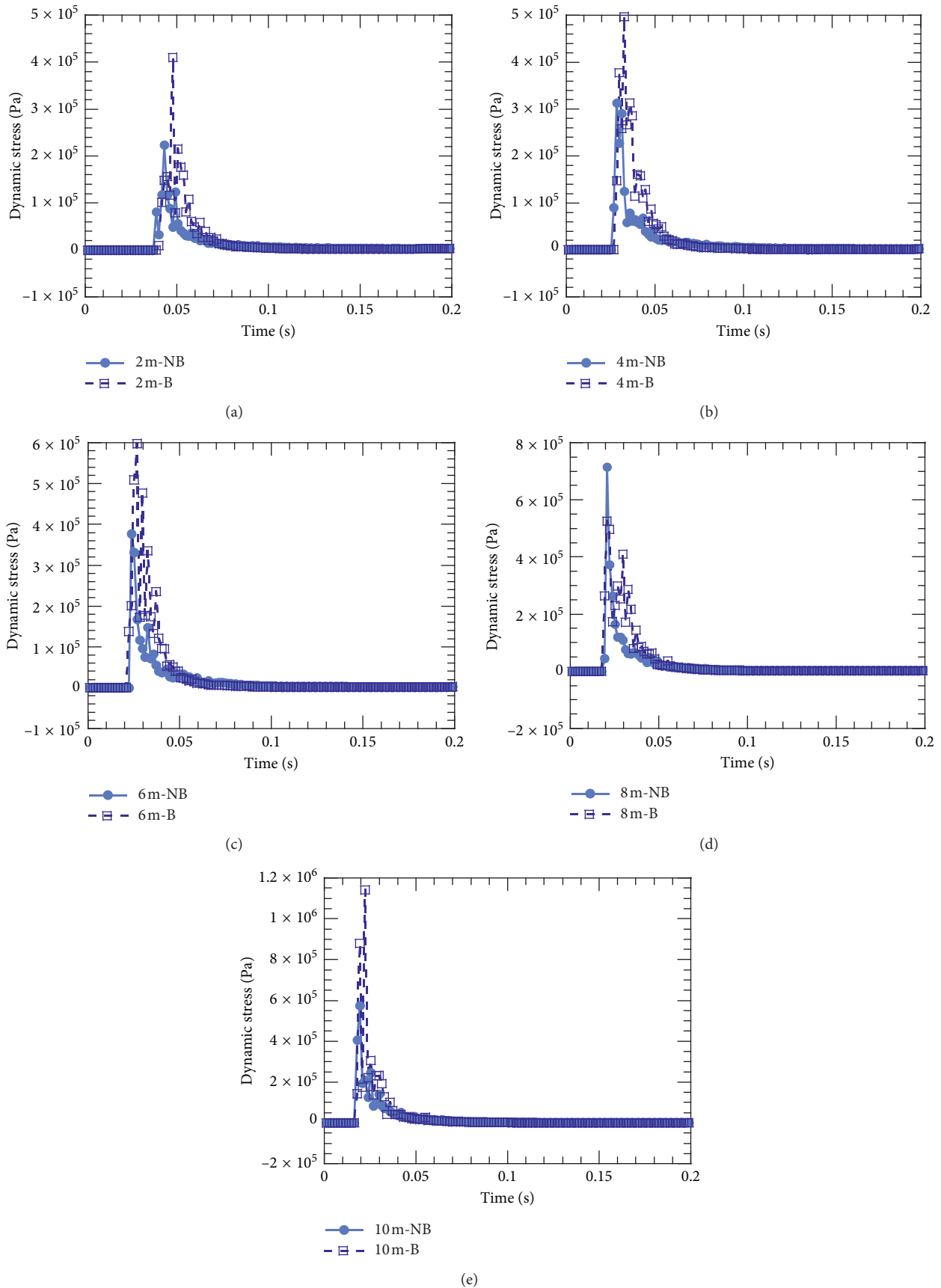


FIGURE 8: Time history of dynamic stress of tamper bottom (NB means no particle breakage; B means breakage).

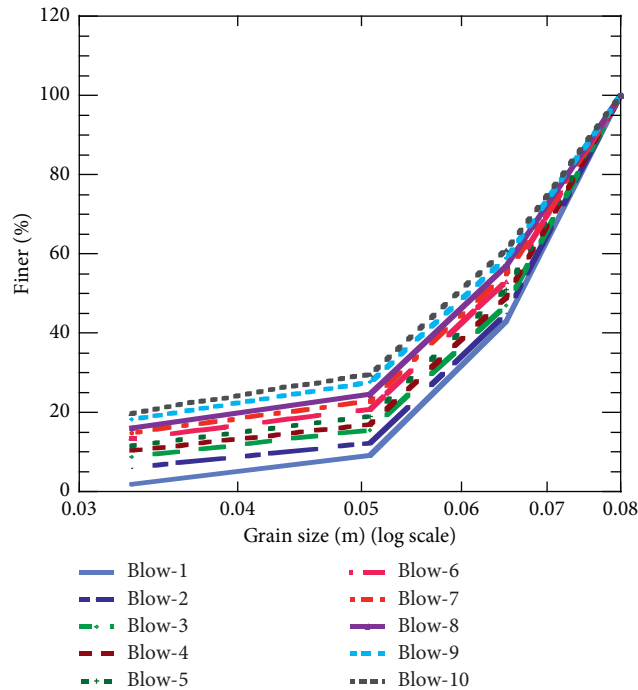
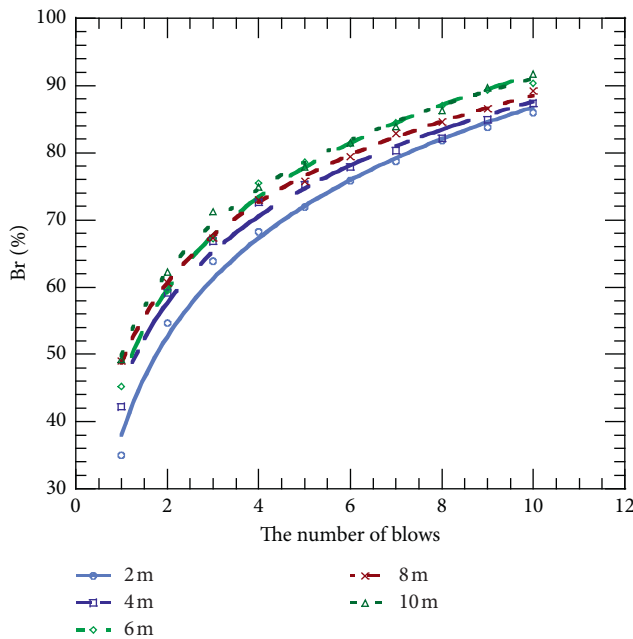


FIGURE 9: Particle gradation near the impact point under 10 blows.



Falling distance (m)	$Br = a \ln(x) + b$		
x	a	b	r^2
2	21.23	37.9	0.990
4	18.60	44.7	0.989
6	19.83	45.8	0.996
8	17.33	48.6	0.999
10	17.91	49.82	0.996

FIGURE 10: The relationship between the relative breakage and the number of tamping blows.

(5) Soil behavior under the combined action of DC and particle breakage is a complex issue. This paper mainly focuses on the stimulation of the dynamic compaction process objectively. Other aspects that require further study include, but are not limited to, the optimal DC operational parameters, effective reinforcement depth, the assessment of the

foundation strength, and the behaviors of particle breakage by dynamic compaction.

Data Availability

The data used to support the findings of this study are available from the corresponding author upon request.

Conflicts of Interest

The authors declare that they have no conflicts of interest.

Acknowledgments

This research was supported by the Natural Science Foundation of China (No. 51722812), Natural Science Foundation of Hunan Province (Grant No. 2017JJ1033), National Basic Research Program of China (No. 2014CB047001), and Central South University Autonomous Exploration Project (Grant No. 2017zzts150).

References

- [1] P. W. Mayne, J. S. Jones, and J. C. Dumas, "Ground response to dynamic compaction," *Journal of Geotechnical Engineering*, vol. 110, no. 6, pp. 757–774, 1984.
- [2] T.-W. Feng, K.-H. Chen, Y.-T. Su, and Y.-C. Shi, "Laboratory investigation of efficiency of conical-based pounders for dynamic compaction," *Géotechnique*, vol. 50, no. 6, pp. 667–674, 2000.
- [3] M. Jiang, D. Wu, and B. Xi, "DEM simulation of dynamic compaction with different tamping energy and calibrated damping parameters," in *Proceedings of 7th International Conference on Discrete Element Methods*, pp. 845–851, Springer, Singapore, December 2017.
- [4] Y. K. Chow, D. M. Yong, K. Y. Yong et al., "Dynamic compaction analysis," *Journal of Geotechnical Engineering*, vol. 118, no. 8, pp. 1141–1157, 1992.
- [5] G. Mullins, M. Gunaratne, P. Stinnette et al., "Prediction of dynamic compaction pounder penetration," *Soils and Foundations*, vol. 40, no. 5, pp. 91–97, 2000.
- [6] S. J. Feng, K. Tan, and W. H. Shui, "Dynamic compaction of ultra-high energy in combination with ground replacement in coastal reclamation areas," *Marine Georesources and Geotechnology*, vol. 33, no. 2, pp. 109–121, 2015.
- [7] S. J. Feng, F. L. Du, Z. M. Shi et al., "Field study on the reinforcement of collapsible loess using dynamic compaction," *Engineering Geology*, vol. 185, pp. 105–115, 2015.
- [8] P. W. Mayne and J. S. Jones, "Impact stresses during dynamic compaction," *Journal of Geotechnical Engineering*, vol. 109, no. 10, pp. 1342–1346, 1983.
- [9] R. W. Pearce and R. A. Scott, "Soil compaction by impact," *Géotechnique*, vol. 25, pp. 19–30, 1975.
- [10] R. L. Michalowski and S. S. Nadukuru, "Static fatigue, time effects, and delayed increase in penetration resistance after dynamic compaction of sands," *Journal of Geotechnical and Geoenvironmental Engineering*, vol. 138, no. 5, pp. 564–574, 2012.
- [11] S. J. Feng, W. H. Shui, L. Y. Gao et al., "Field studies of the effectiveness of dynamic compaction in coastal reclamation areas," *Bulletin of Engineering Geology and the Environment*, vol. 69, no. 1, pp. 129–136, 2010.
- [12] S. J. Feng, K. Tan, W. H. Shui, and Y. Zhang, "Densification of desert sands by high energy dynamic compaction," *Engineering Geology*, vol. 157, pp. 48–54, 2013.
- [13] C. J. Poran and J. A. Rodriguez, "Finite element analysis of impact behavior of sand," *Journal of the Japanese Society of Soil Mechanics and Foundation Engineering*, vol. 32, no. 4, pp. 81–92, 2008.
- [14] F. H. Lee and Q. Gu, "Method for estimating dynamic compaction effect on sand," *Journal of Geotechnical and Geoenvironmental Engineering*, vol. 130, no. 2, pp. 139–152, 2004.
- [15] Q. Gu and F. H. Lee, "Ground response to dynamic compaction of dry sand," *Géotechnique*, vol. 52, no. 7, pp. 481–493, 2002.
- [16] W. Wang, J. J. Chen, and J. H. Wang, "Estimation method for ground deformation of granular soils caused by dynamic compaction," *Soil Dynamics and Earthquake Engineering*, vol. 92, pp. 266–278, 2017.
- [17] K. Wada, H. Senshu, and T. Matsui, "Numerical simulation of impact cratering on granular material," *Icarus*, vol. 180, no. 2, pp. 528–545, 2006.
- [18] Z. Y. Ma, F. N. Dang, and H. J. Liao, "Numerical study of the dynamic compaction of gravel soil ground using the discrete element method," *Granular Matter*, vol. 16, no. 6, pp. 881–889, 2014.
- [19] S. Zhang, C. X. Tong, X. Li et al., "A new method for studying the evolution of particle breakage," *Géotechnique*, vol. 65, no. 11, pp. 911–922, 2015.
- [20] S. Zhang, X. Li, J. Teng et al., "A theoretical method for determining sample mass in a sieving test," *Computers and Geotechnics*, vol. 91, pp. 12–16, 2017.
- [21] Y. P. Yao, W. Hou, and A. N. Zhou, "UH model: three-dimensional unified hardening model for overconsolidated clays," *Geotechnique*, vol. 59, no. 5, pp. 451–469, 2009.
- [22] A. N. Zhou, D. Sheng, S. W. Sloan et al., "Interpretation of unsaturated soil behaviour in the stress – saturation space, I: volume change and water retention behaviour," *Computers and Geotechnics*, vol. 43, pp. 178–187, 2012.
- [23] J. Huang, S. Xu, and S. Hu, "The role of contact friction in the dynamic breakage behavior of granular materials," *Granular Matter*, vol. 17, no. 1, pp. 111–120, 2015.
- [24] G. R. McDowell and J. P. De Bono, "On the micro mechanics of one-dimensional normal compression," *Géotechnique*, vol. 63, no. 11, pp. 895–908, 2013.
- [25] W. Zhou, L. Yang, G. Ma et al., "DEM analysis of the size effects on the behavior of crushable granular materials," *Granular Matter*, vol. 18, no. 3, pp. 1–11, 2016.
- [26] M. B. Cil and G. Buscarnera, "DEM assessment of scaling laws capturing the grain size dependence of yielding in granular soils," *Granular Matter*, vol. 18, no. 3, pp. 1–15, 2016.
- [27] M. O. Ciantia, M. Arroyo, F. Calvetti, and A. Gens, "An approach to enhance efficiency of DEM modelling of soils with crushable grains," *Géotechnique*, vol. 65, no. 2, pp. 91–110, 2015.
- [28] M. B. Cil and K. A. Alshibli, "3D evolution of sand fracture under 1D compression," *Géotechnique*, vol. 64, no. 5, pp. 351–364, 2014.
- [29] M. D. Bolton, Y. Nakata, and Y. P. Cheng, "Micro-and macro-mechanical behavior of DEM crushable materials," *Géotechnique*, vol. 58, no. 6, pp. 471–480, 2008.
- [30] G. R. McDowell and O. Harireche, "Discrete element modelling of yielding and normal compression of sand," *Géotechnique*, vol. 52, no. 4, pp. 299–304, 2002.
- [31] K. F. Zhang, S. Zhang, and J. D. Teng, "Influences of self-organization of granular materials on particle crushing based on discrete element method," *Chinese Journal of Geotechnical Engineering*, vol. 40, pp. 743–751, 2018, (in Chinese).
- [32] J. A. Astrom and H. J. Herrmann, "Fragmentation of grains in a two-dimensional packing," *European Physical Journal B-Condensed Matter and Complex Systems*, vol. 5, no. 3, pp. 551–554, 1998.

- [33] G. Marketos and M. D. Bolton, "Compaction bands simulated in discrete element models," *Journal of Structural Geology*, vol. 31, no. 5, pp. 479–490, 2009.
- [34] S. Lobo-guerrero, "Crushing a weak granular material: experimental numerical analyses," *Géotechnique*, vol. 55, no. 3, pp. 245–249, 2005.
- [35] O. Ben-Nun and I. Einav, "A refined DEM study of grain size reduction in uniaxial compression," in *Proceedings of the 12th international conference of the international association for computer methods and advances in geomechanics (IACMAG)*, pp. 702–708, Goa, India, October 2008.
- [36] A. R. Russell, D. M. Wood, and M. Kikumoto, "Crushing of particles in idealised granular assemblies," *Journal of the Mechanics and Physics of Solids*, vol. 57, no. 8, pp. 1293–1313, 2009.
- [37] M. Takei, O. Kusakabe, and T. Hayashi, "Time-dependent behavior of crushable materials in one-dimensional compression tests," *Soils and foundations*, vol. 41, no. 1, pp. 97–121, 2001.
- [38] Y. H. Han, Y. L. Dong, and X. H. Bai, "Model test on process of hammer under dynamic compaction of loess," *Chinese Journal of Rock Mechanics and Engineering*, vol. 34, pp. 631–638, 2015, (in Chinese).
- [39] M. C. Jia, L. Wang, and J. Zhou, "Mesomechanical analysis of characteristics of dry sands in response to dynamic compaction with PFC2D," *Rock and Soil Mechanics*, vol. 30, pp. 871–878, 2009, (in Chinese).
- [40] I. Einav, "Breakage mechanics. part I. Theory," *Journal of the Mechanics and Physics of Solids*, vol. 55, no. 6, pp. 1274–1297, 2007.

Research Article

Laboratory and Centrifuge Model Tests on Influence of Swelling Rock with Drying-Wetting Cycles on Stability of Canal Slope

Chen Zhang ^{1,2}, Zheng-yin Cai ^{1,2}, Ying-hao Huang,^{1,2} and Hao Chen ¹

¹Nanjing Hydraulic Research Institute, Nanjing, China

²State Key Laboratory of Hydrology-Water Resources and Hydraulic Engineering, Nanjing, China

Correspondence should be addressed to Zheng-yin Cai; zycai@nhri.cn

Received 14 June 2018; Revised 2 September 2018; Accepted 19 September 2018; Published 20 December 2018

Guest Editor: Yongfeng Deng

Copyright © 2018 Chen Zhang et al. This is an open access article distributed under the Creative Commons Attribution License, which permits unrestricted use, distribution, and reproduction in any medium, provided the original work is properly cited.

This study focused on the swelling behavior of swelling rock from canal basement under multiple drying-wetting (D-W) cycles. A series of laboratory tests were conducted on a swelling rock, with the cracking and strength behaviors investigated. By using image-processing technique, the crack patterns were described, and then quantitatively analyzed on the basis of the fractal dimension. The experimental data indicated that swelling ability, including cracking level, fractal dimension, and strength, decrease with increasing drying and wetting cycle. On this basis, a series of centrifuge model simulations for simulating slope failure by drying-wetting cycles were performed, where the drying process was achieved by heat bulbs. The monitoring results suggested that a global slope failure has occurred after total cycle of 4th corresponding to 4 years. Due to the development of surface cracking, the infiltration in the slope was severe and nonuniform in space and time. Meanwhile, the failure mechanism of soft rock slope induced by D-W was discussed.

1. Introduction

Swelling rocks contain silicate clay minerals that have the potential for swelling and shrinkage under changing moisture contents. Progressive deformation of the swelling rock can be caused during the drying-wetting (D-W) cycle, which may affect the safety of building foundations, tunnels, water canals, and liner and cover systems in waste containment facilities. The expansibility behavior of expansive soft rock has always been one of the major problems in damage to hydraulic infrastructure. For example, a water transfer project in Xinjiang area, with a large number of swelling mudstones distributed, slope failures, and local collapses (Figure 1), often occurs along the main canal. The canal damages caused by swelling rock reached approximately two-third of the annual damages reported, and the cost for repairing canal structures damaged by swelling mudstones accounted for 60% of the total annual maintenance cost.

A large number of swelling soil slope failure cases have been investigated, which were found to show some typical

characteristics, such as shallow layer, tractive sliding, gentle motion type, and seasonal occurrence [1]. These characteristics are closely associated with the behavior of swelling soil. Therefore, many laboratory and in situ tests were conducted to study the phenomenon of swelling and shrinkage [2–5], D-W process [6–8], cracking in clay soils [9–12], and mechanical and hydraulic behaviors of expansive soils [13, 14]. However, comprehensive theory on failure mechanism and stability analysis methods of expansive soil slope are still insufficient due to the complex characteristics of swelling soil. Current engineering practices for determining the physicommechanical parameters of expansive rocks are mostly based on simplified laboratory tests or empirical equations. These practices may prone to mischaracterize the engineering characteristics, even result in a contradictory conclusion.

Commonly, the assessment of expansion potential was accomplished by one cycle of wetting in geotechnical practice. In some arid areas, the water is mainly from leakage, resulting in a long-term process under slow seepage and evaporation until slope failure, which is different from



FIGURE 1: Typical slope failure of main canal in Xinjiang, China.

humid areas that are caused by drastic climate change in a short time. Nevertheless, for canal slope, due to the inevitable leakage, evaporation, rainfall, and other extreme climate conditions, it often has a more significant D-W boundary. Moreover, due to the limits of existing theory, hazardous working conditions, and the long-time scales of failure behavior, less academic attention has been paid on the issue of development of cracks and D-W cycles on stability of canal slope in arid areas. Recently, some innovative techniques, including image analysis [12, 15, 16] and fractal dimension analysis [17], have been used in soil-cracking studies. They were conducted on swelling soil to investigate the evolution of surface cracks, inner fractures, volume change, etc. Additionally, due to the characteristics of self-weight equality, the centrifuge-modeling technique has been used for examining the instability of expansive soil slope [18–21], and these studies provide reference for the full-scale landslide.

The objective of the present study is to investigate the swelling behavior of soft rocks in canal basement under cyclic moisture changes. For this purpose, two swelling rocks were obtained from the main canal of north Xinjiang water canals. After each cycle, the surface cracks and strength characteristics of swelling rocks were measured. A quantitative method was developed to characterize the crack patterns by combining the image processing with the fractal dimension concept. Additionally, the failure of swelling rock canal slope was investigated by centrifuge modeling.

2. Laboratory D-W Tests

In order to better understand cracking behavior and strength characteristics in swelling rocks from canal basement, a series of small specimen tests were carried out with two typical swelling rocks subjected to D-W, including crack observation test and direct shear test.

2.1. Preparation of Swelling Rock Specimens. The tested materials were prepared with two swelling rocks, which were taken from the construction field of a water transfer project in Xinjiang, a typical arid area in China. Compared with the “cyan mudstone” (CM), the swell potentials of the “yellow mudstone” (YM) are lighter than “cyan mudstone” where the names are based on apparent dominating color. The

physical properties of the tested swelling rocks are listed in Table 1.

Considering the influence of density, swell potentials, and its’ influences on strength of swelling rock under multiple D-W cycles, four test groups with different dry density and swelling potential were designed. Before preparation, swelling rocks were air-dried via mortar and pestle to reduce the size of the clay clods, and stored in buckets. In order to make the moisture equilibration, the remolded samples were prepared for 24 h to the optimal water content with 18.8% by CM and 14.75% by YM. The soil behavior is significantly affected by specimen size. In general, the physical soil model should be large enough to simulate the large cracks. However, the purpose, in this research, is to study the characteristics of cracks development and strength simultaneously under the D-W cycles. Therefore, the samples in crack observation tests and direct shear tests were prepared in the same size, which are 61.8 mm in diameter and 20 mm in thickness (standard size in direct shear test in CHN code [22]). The compaction tests showed that the maximum dry density of “natural CM” is close to 1.6 g/cm^3 and 1.8 g/cm^3 of “natural YM”; however, the degree of compaction of the prototype is about 90%. Based on this, the dry density of remolded samples had been designed as 1.8 g/cm^3 , 1.6 g/cm^3 , and 1.5 g/cm^3 in CM and 1.8 g/cm^3 in YM, respectively. Among them, the specimens of 1.6 g/cm^3 and 1.5 g/cm^3 were used to investigate the influence of density.

After solid pressing by one layer, the specimen surfaces were smoothed lightly with a grafter to obtain a uniform thickness. A thin layer of Vaseline was applied on the inner walls of the containers to reduce the boundary friction. The wetting process of the prepared cylindrical specimens was presented in vacuum saturation until the vacuum degree reached 95% (accuracy 0.1 g). After the completion of vacuum saturation, the specimen was exposed to the open environment ($20^\circ\text{C} \pm 1.2^\circ\text{C}$ without direct sunlight, and relative humidity $50\% \pm 10\%$) until the water was reduced to the residual moisture content. After the drying process completed, the sample was vacuum-saturated. To complete the D-W cycles, the aforementioned process was repeated. One battery consisted of five samples, four of which were used to observe cracks, and the remaining one was used for direct shear tests.

TABLE 1: Physical properties of tested materials.

Physical property	Value	
	CM	YM
Liquid limit, L_L (%)	61.3	57.1
Plastic limit, L_p (%)	20.1	17.6
Plasticity index, P_I	41.2	39.5
Percentage of clay (%)	30.1	32.5
Swelling ratio	88	74
CHCS classification	CH	

2.2. Observation of Crack Patterns. At the end of each D-W cycle, the surface of each specimen was pictured by using digital camera to capture the crack patterns. The camera lens was fixed parallel to the sample surface with a suitable distance to ensure the sample totally within the shooting range, as shown in Figure 2. Negative sources on image quality were minimized by blacking out the lab and illuminating the specimens by LED surrounding the container without camera flashlight. Every initial RGB images in each D-W cycle are shown in Figure 3. Now, a series of typical crack patterns after different D-W cycles are observed with different dry density and swelling ingredients. The distinct phenomenon is the development of surface fractures along with the increase of wetting and drying cycles. During the first D-W cycle, obvious cracks can be visually observed on the specimen surface with dry density of 1.8 g/cm^3 and 1.6 g/cm^3 . On the one hand, ring-shaped cracks appear in specimens with dry density of 1.8 g/cm^3 . After three cycles, more crack areas for all sampling compared to previous cycles. However, in the 4th cycle, the area seems no longer grown by visual inspection.

In order to analyze the geometric characteristics of cracking quantitatively, the digital image processing is launched by using MATLAB software. The initial RGB images of four specimens at the same dry density are wholly processed. It means that the shrinkage crack present around the specimen is included. The binary image of developing cracks on surface specimens are presented in Figure 3, where a function of "Graythresh" in the software is used in the image processing. It is easy to use the converted matrix to calculate the geometric parameters of the binary images, such as the fractal dimension and the surface crack ratio [23].

The box-counting dimension, D_b [24], is used in this study for fractal analysis; the number of square boxes intersected by the image, $N(s)$, and the side length of the squares, s , are also obtained where each image is covered by a sequence of grids of descending sizes and for each of the grids. The linear regression equation of $\log(N(s))$ against $\log(s)$ that used to estimate the fractal dimension is as follows:

$$\log(N(s)) = D_b \log(s) + A, \quad (1)$$

where the A is a constant; $N(s)$ is proportional to r^{-D_b} . D-W cycles for all specimens are depicted by solid line in Figure 4. The curves also demonstrate a decreasing trend in the crack with increasing number of D-W cycles, which well corresponds to the phenomenon of swelling clayey soils. As we know, during the air-drying processes, the action of the

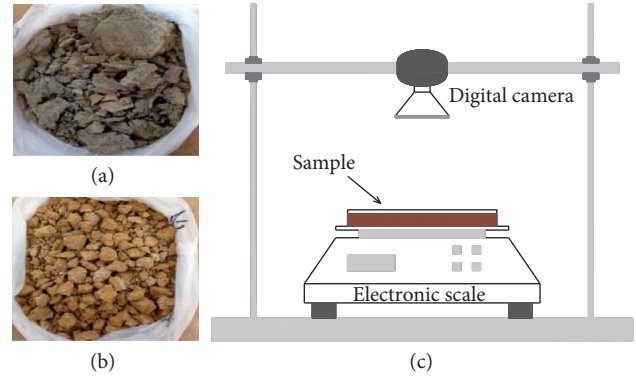


FIGURE 2: Using rocks and experimental set-up used for crack observation.

moisture gradient will lead to the stress redistribution with the tension of the upper part and the compression of the lower part. With the cracks gradually developed and finally covered on the whole sample surface, the moisture content of the surface and shallow layer of specimens gradually decrease. After rehydration, although the cracks close, the tensile strength at the position of cracks cannot be restored. This is the main reason for the expansion of cracks under repeated D-W cycles. On the contrary, the influence of dry density is not prominent; the fractal count of the sample with the density of 1.6 g/cm^3 is higher than the sample with density of 1.5 g/cm^3 . Notice that the fractal count of 1.8 g/cm^3 , before the 3rd cycle, is close to 1.6 g/cm^3 . But it drops at the last two cycles. It is observed that the irregular net cracks on surface with dry density of 1.5 and 1.6 g/cm^3 are more than that of the sample of 1.8 g/cm^3 ; however, the main crack of sample with 1.8 g/cm^3 is the shrinkage crack which occurs at the side of the ring sampler, resulting in the relatively low level of irregular and chaotic degree of cracking, which is the essence of fractal dimension.

With the same dry density condition, the total fractal count of CM is higher than that of the yellow stone (although the count is almost close to the last two cycles). This was attributed to higher clay minerals occurring closer to the surface and higher swelling potentials for higher dry density. As previously described, the fractal dimension D_b can be used to evaluate the spatial distribution of cracks, the density of cracks, and the tendency of the crack traces to fill the area in which they are embedded. At least, the abovementioned result suggested that the interconnectivity of soft rock surface cracks is susceptible to the effects of density and mineral contents.

2.3. Strength Characteristics under D-W Cycles. A series of direct shear test was conducted to investigate the relationship between the strength and the crack patterns on multiple D-W cycles. All shear tests were carried out in each sample after the wetting process, under vertical loads of 50 kPa, 100 kPa, 200 kPa, and 300 kPa. The cohesion as well as the number of D-W cycles for each sample is also depicted in Figure 5 by a hollow wire. It can be seen that the computed fractal dimensions of the three clay samples during cyclic

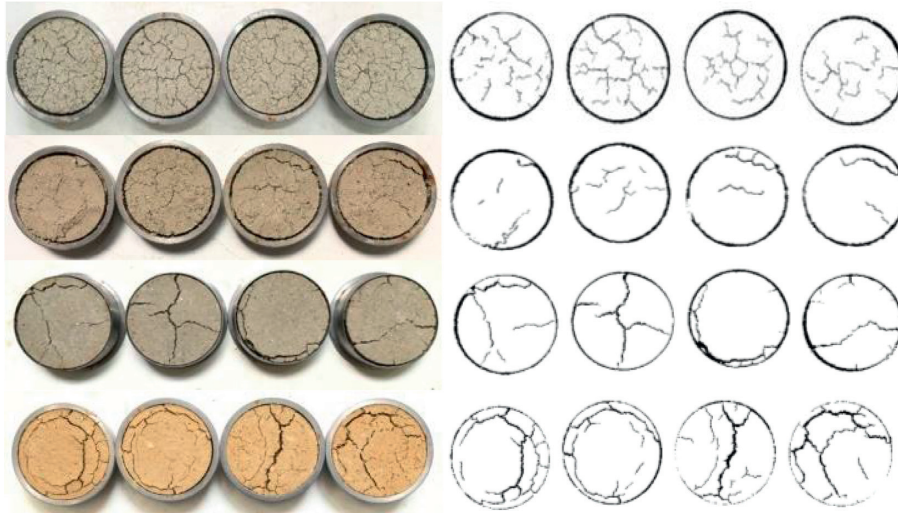


FIGURE 3: Initial and binary images of three different samples at the ending of tests (1.8 g/cm^3 , 1.6 g/cm^3 , and 1.5 g/cm^3 of cyan mudstone and 1.8 g/cm^3 of yellow mudstone from top to bottom).

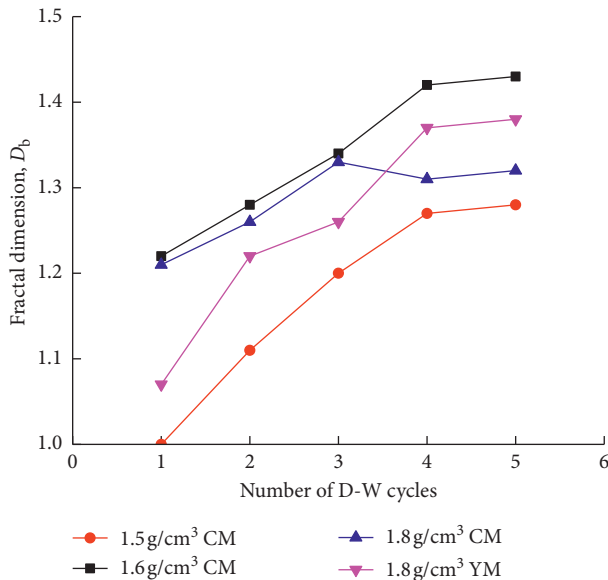


FIGURE 4: Variations of fractal dimension with the number of D-W cycles.

drying-wetting are within the theoretically allowable range of 1.0 and 1.6. The fractal dimension of each sample increased with the increasing of D-W cycles until the corresponding shear strength decreased to its residual value. The shear strength of cyan mudstone samples with the dry density of 1.8, 1.6, and 1.5 g/cm^3 of CM and 1.8 g/cm^3 of YM were decreased approximately from 103 kPa, 30 kPa, 21.5 kPa, and 91 kPa to 58 kPa, 16.1 kPa, 15.9 kPa, and 60.2 kPa, respectively. The results in Figure 5 suggested that the successive D-W do not increase the development of cracks, but reduce the rock strength. However, this change begins to converge after the 4th cycle; it may be considered that if a canal which is filled with this soft rock is not damaged in 5 D-W cycles, the probability of failure will be greatly reduced in further cycles; in other words, the

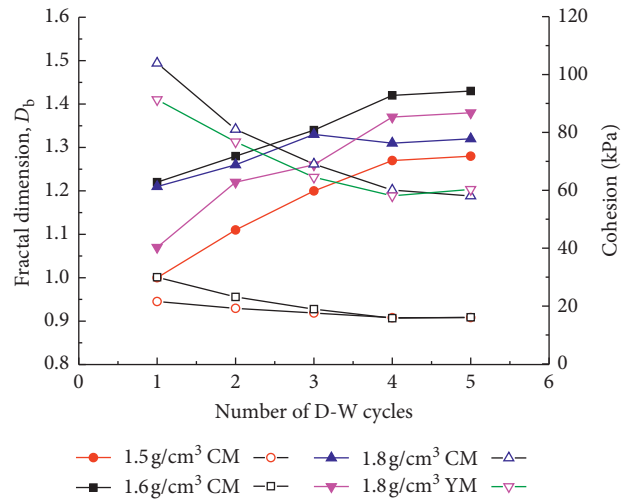


FIGURE 5: Variations of cohesion as well as fractal dimension with the number of D-W cycles.

subsequent damage is not caused by a pure reduction in strength reduce and development of cracks. Similar to previous investigation about swelling clayey soil, the angle of friction of the soft rock remained more or less constant under D-W cycles (no longer given in this paper). The fractal dimension D_b can be used to evaluate the spatial distribution of cracks, the strength of cracks, and the tendency of the crack traces to fill the area in which they are embedded.

It is noted that the cohesion of CM and YM with the density of 1.8 g/cm^3 is much larger than that of other specimens. Some test results [25, 26] showed that the strength is slightly affected by the density. On the contrary, the effect of density on strength is obvious in this study. This tendency can also be demonstrated by the observed two test phenomena: (1) the initial strength level after first D-W cycle, and (2) decreasing amplitude of strength. However, in Figure 3, it can also be seen that the soil sample with a lower

density level shows more visible cracking, especially penetrating cracks on the sample surface after the first cycle. On the other hand, the fractal dimension D_b of the CM samples with a density of 1.6 g/cm^3 was always at a higher level in every D-W cycle, as the analysis of the fractal dimension is shown in Figure 5. This structural damage may strongly affect the shear test results and related to the soil properties and sample sizes.

3. Centrifuge Modeling

3.1. Slope Models and Testing Procedures. Due to the stress confinement, the centrifuge-modeling technique was used for examining slope instability and deformations of geological problems. As aforementioned, such long-time scales of the D-W process on canal slope in arid area request too much resource while field tests have been undertaken, but in centrifugal model, a reduced-scale model of lineal dimensions N^2 times smaller is used to simulate the full-scale problem under an acceleration N times the gravity. Thus, centrifuge modeling of such problems is an attractive proposition. With this aim in view, an experimental campaign has been initiated to investigate the performance of swelling rock slope subjected to D-W cycles by centrifuge modeling. According to the results of cracking test, the model soil were conducted on CM to obtain a dry density of 1.6 g/cm^3 for Model 1 and 1.5 g/cm^3 for Model 2, corresponding to the greater level of fractal dimension and lowest level, respectively. The model was constructed in a rigid container with inner dimensions of $680 \text{ mm} \times 350 \text{ mm} \times 450 \text{ mm}$ (length \times width \times height). The model was prepared with initial water contents of 18.8%. After the hit-solid process, the slope was excavated to its final grade of 1 (V):2.5 (H) with a height of 100 mm. The finished slope was covered with plastic sheets and cured overnight before testing was conducted by introducing moisture to the slope surface. A video was placed in front of the slope in order to view the slope face during flight and the grid lines on the slope for measuring ultimate displacements. Eight miniature cylindrical pore pressure transducers (PPTs) that can measure a pressure from 0 to 350 kPa were embedded at different locations to observe the change in positive pore pressure during testing. The view of slope model and location of PPTs are depicted in Figure 6, in which P1 to P3 and P4 to P7 are placed at a parallel distance of 20 mm and 40 mm from the slope face, respectively.

Before the wetting process, the water was added to the phreatic line of 90 mm under 1 g to simulate the water in canal. A thick geo-cloth was laid on the bottom of the slope to prevent the impact of water splashing. The centrifuge took about 5 min to attain the targeted acceleration of 50 g, and then hold the acceleration under 50 g until the process terminated. The water in the canal model would be drained before the drying process. In order to provide a heat boundary, a battery of light bulbs at the top of the slope model was assembled upon 90 mm from the model surface to providing heat source for evaporation. The power of each bulb is 50 watt. The test was ended until the slope feature was observed in the video capture system. The test was

performed by wetting the model for 90 mins and then drying the model for 220 mins. The required time was calculated as water supply and stop period of the prototype in accordance with N^2 times to the model scale 50. This time was approximately split in a 4-month/8-month ratio of the lengths of the wet and dry seasons in a year.

3.2. Testing Results. The seasonal D-W cycles have been shown to produce significant irrecoverable regional deformation below a slope in swelling rock. Figure 7 presents the ultimate slope failure in the lateral and vertical view. It can be seen that a large number of spots scattered on the surface after slope failure, and the failures in two models are the same as global and lateral fail. During the test, it was found out that slope failure occurred not instantaneously, a significant progressive failure was observed for this slope. No exception the failure occurs within 5 D-W cycles that typically occurred right after the 5th cycle in Model 1 and the 4th cycle in Model 2, corresponding to 5 years and 4 years in the prototype, respectively. At least, it indicated that the degree of soft rock slope failure originates in mineralogical composition and content. The tensile crack could be observed at the top of slope in two tests, which in Model 2 is more obvious than in Model 1. In Model 2, the width of the crack is approximately 3 mm in horizontal and 5 mm in vertical direction. The displacement was in calculating for the final height which was obtained as grid lines. The location of maximum displacement of two models is presented in the vector diagram of slope feature in Figure 8. The displacement trend of two models is close. By multiplying the height by the gravity at failure, the maximum displacement of slope is up to 1.3 m and 1.4 m, respectively.

Figure 9 shows the variation of measured pore pressure within Model 1 at the onset of seepage for model slope. In the first wetting process, the PPT did not record significant change in pore pressure except P1, which is located at the upper portion of slope bottom; this was because of the fact that the precipitation did not infiltrate to a depth where they are located. However, during the next period of the wetting process, with the development of desiccation cracking in the prior drying process, water fills the cracks and fissures; in addition to increasing the hydrostatic forces, the water is slowly absorbed by the swelling rocks. In the 3rd cycle, the P1, P2, and P3 which are located at the upper portion of the slope were recorded. After 5 cycles, all PPTs were recorded except P4, which is located near the top slope under the surface of 40 mm from the vertical of slope line. Besides, it can be seen that, from 3 to 5 cycles, the pore pressure started to increase with the acceleration. It indicated that, due to the effect of fracture develops, the water directly penetrated to the location of PPT at the beginning of the wetting process. Another phenomenon is no significant increase in pore pressure has been observed. The excess pore pressure was not responded to the slope failure. Owing to the limited space in model, enough PPTs were not installed to monitor the infiltration process with model time.

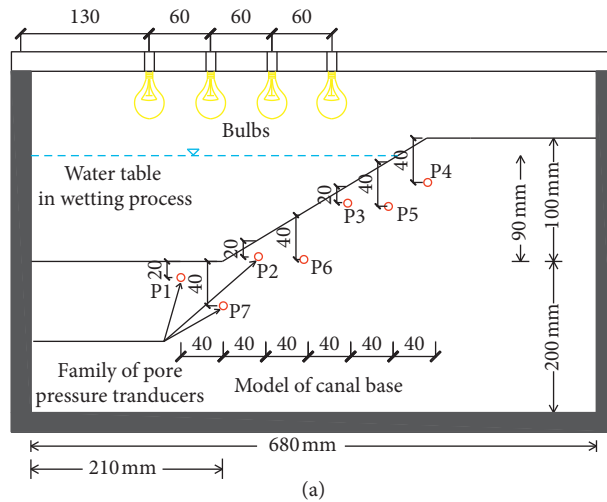


FIGURE 6: Centrifuge modeling of canal slope using bulbs (not to scale).

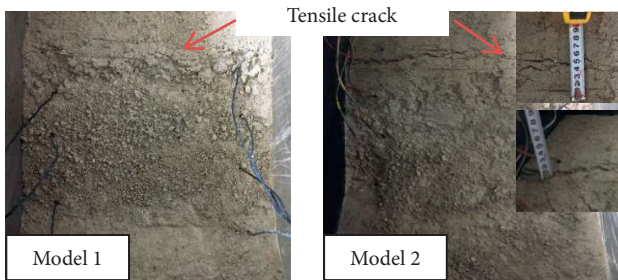


FIGURE 7: Vertical view of model surface after slope failure.

Figure 10 shows the “infiltration region” in two tests, which is an alternative strategy for the reflection of infiltration in swelling rock slope. Basing on the average value of PPTS in the stable phase (the saturation of the region is judged by comparing the reading with the hydrostatic pressure at the corresponding position), the region of 1st and 2nd cycles can be estimated. It was founded that the depth of

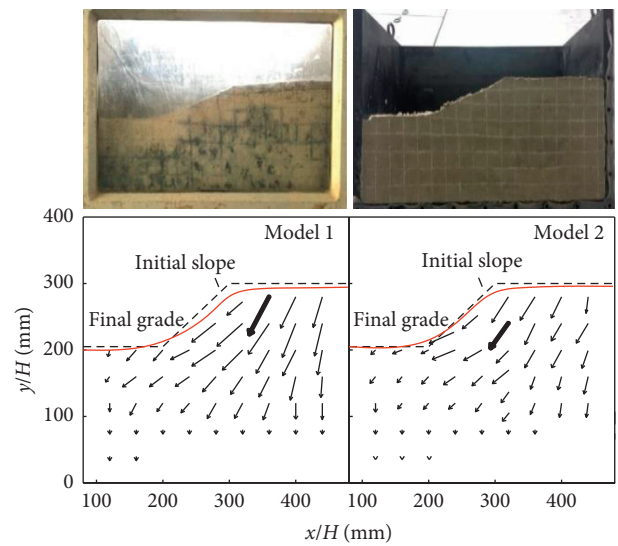


FIGURE 8: Slope failure and ultimate vector of displacements.

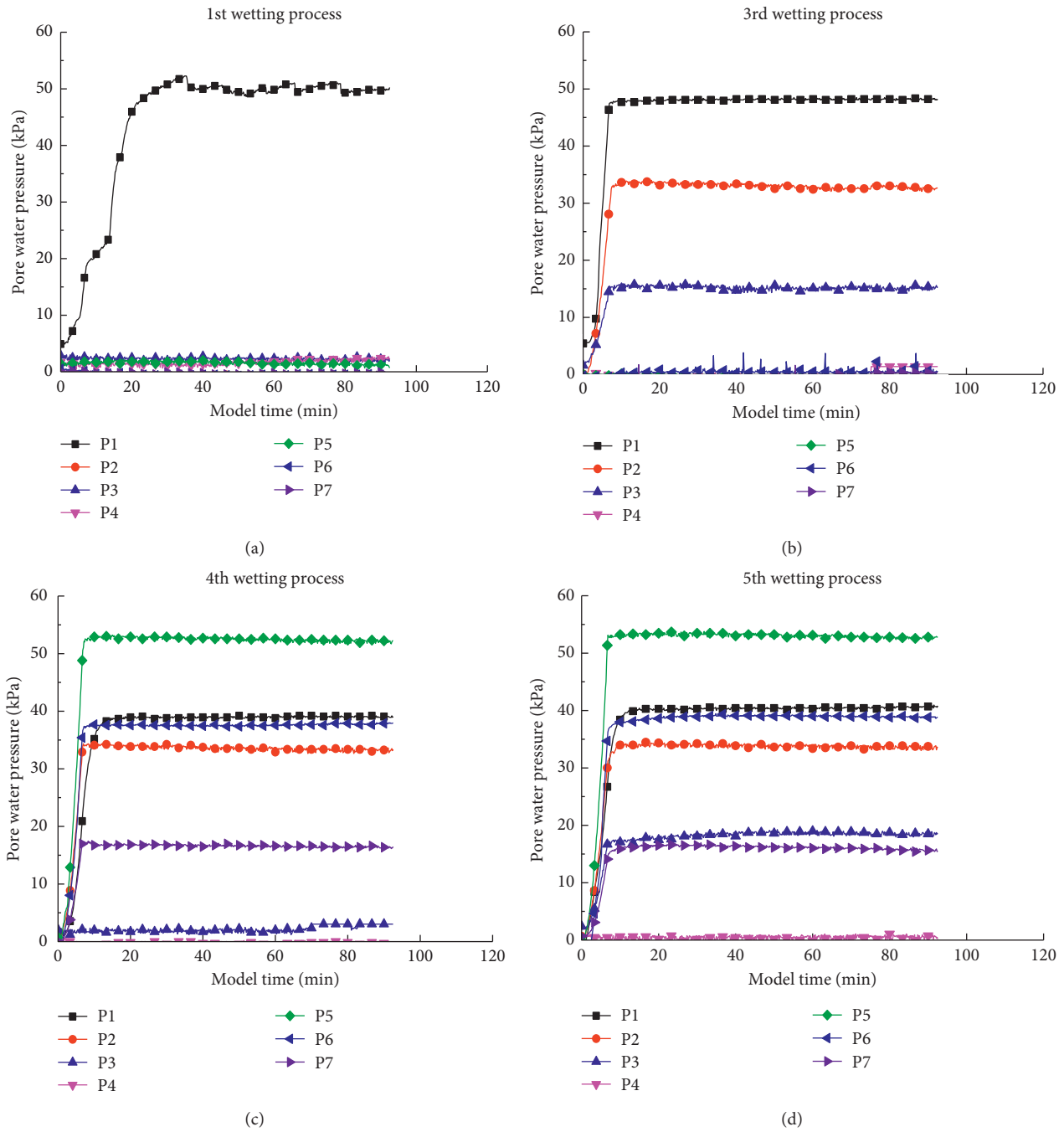


FIGURE 9: Variation of pore water pressure with model time.

the infiltrating area can reach 20 mm (with model scale) vertical below the surface for the first cycle in Model 1 without cracking, and similarly reach to 24 mm in Model 2. Due to the development of cracking, after 3 cycles, the infiltration region has reached to 40 mm below the surface in Model 1 and 50 mm in Model 2, respectively. In addition to monitoring the degree of region under infiltration, the saturation data recorded at the end of tests are presented in Figure 10. It can be seen that the regions were eventually extended to 44 mm in Model 1 and 53 mm in Model 2. The distribution of the saturate region is mainly near the surface

and larger in toe and bottom, which is related to the depth of crack, hydrostatic force, and centrifugal acceleration. This accumulation of infiltration led eventually to the onset of progressive failure from the surface to inner surface, resulting in a large region of softening.

In the interval of each cycle, the cracks were depicted by plastic film on model surface of slope, as much as possible. Limited to space, the development of cracks on model surface in test 1 is given in Figure 11, with obvious cracking after every cycle which is depicted by pen. Owing to the existence of these cracks under circumstance of D-W cycles,

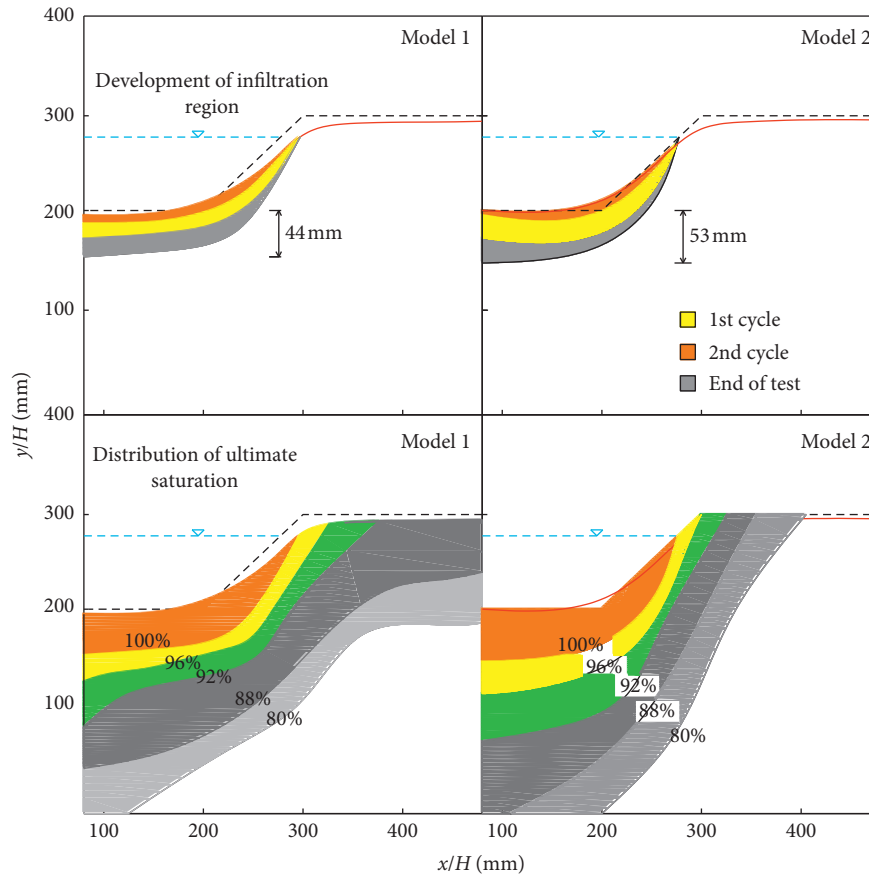


FIGURE 10: The development of “infiltration region” and ultimate distribution of saturation in models.

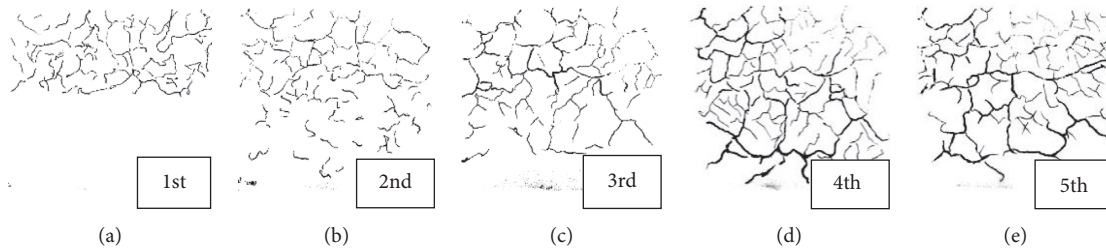


FIGURE 11: Depiction of surface cracks at the end of each D-W cycles in Model 1.

the canal suffered devastating damage after several years of coming into use. As the laboratory D-W tests showed, the seasonal shrinking and swelling behavior of the cracked clay zone results in a progressive reduction of the bulk shear strength of the swelling rock to the point where it may approach its residual strength. In centrifugal model test, the effect of the absorbed water is to increase the unit weight of clay as well as to decrease its shear strength. These mechanisms result in a simultaneous increasing in the sliding forces of slope and decrease in the resisting forces which are presented by centrifugal force. However, some previous research noted that cracking and hydraulic conductivity of swelling clay or rocks are controlled by plasticity and swelling [27]. The slope basement with highly swelling potential may enhance the effect of infiltration,

and then aggravate slope failure. Although the results of laboratory D-W tests show that residual strength can still reach a safe conclusion by limit equilibrium slope stability methods, the maximum available shear strength on the base of each of the vertical slices may not be invoked for such swelling slopes.

In fact, the method of using bulbs for heating requires control of ambient temperature and humidity and requires rigorous math-physical methods to analyze testing results. Nevertheless, compared with the previous studies, one-time scale was carried out in this test that avoids the situation of mismatching of time. As far as the wreck mode of the canal slope is concerned, the centrifuge modeling has examined the lateral global failure about soft rock slope in relation to the hydric and evaporation due to climate and situation of

seasonal water delivery, which is associated with cracking, infiltration, swelling, and strength reduction.

4. Conclusions

A series of crack observation tests and direct shear tests were conducted on the remolded soft rock subjected to dry-wetting cycles, and a centrifuge modeling is presented herein for simulating full-scale slope failure induced by D-W cycles. The conclusions are as follows:

- (1) The fractal dimension D_b was used to quantitatively analyze the degree of cracking of the specimens under cyclic D-W. The fractal analysis showed that the fractal dimension D_b is related to the dry density and swelling potentials, finally related to the swelling composition of soft rock.
- (2) The cohesion decreases with increasing D-W cycles. After 4 cycles, the variation of cohesion changed in a negligibly small manner. The strength reducing is accompanied with cracking and will almost no longer develop until cracking converges to be stable.
- (3) The centrifuge test results showed that at least four D-W cycles under the 50 g with true time of 4 years led to slope failure, which was the type of global and lateral failure without significant excess pore pressure. Both dry density level and D-W accumulation affected soft rock slope instability.

The relationship between fractal dimension and strength in laboratory tests and quantitative evaporation process in centrifuge modeling will be emphasized in subsequent studies.

Data Availability

The data used to support the findings of this study are included within the article.

Conflicts of Interest

The authors declare that they have no conflicts of interest.

Acknowledgments

This work was supported by the “National Key Research and Development Program of China” (Grant No. 2017YFC0405100), the “National Natural Science Foundation of China” (Grant Nos. 51709185 and 51879166), and the “Technical demonstration project of China Ministry of water Resource of the People’s Republic of China” (Grant. No. SF-201704). It was also a part of work in the project funded by the Fundamental Research Funds for the Central Scientific Research Institute (Grant No. Y318001).

References

- [1] D. Rosenbalm and C. E. Zapata, “Effect of wetting and drying cycles on the behavior of compacted expansive soils,” *Journal of Materials in Civil Engineering*, vol. 29, no. 1, article 04016191, 2016.
- [2] F. H. Chen, “Foundations on expansive soils,” in *Developments in Geotechnical Engineering*, vol. 54, pp. 20–40, Elsevier, Amsterdam, Netherlands, 1988.
- [3] A. A. Basha, A. S. Al-Homoud, A. I. Husein Malkawi, and M. A. Al-Bashabsheh, “Swelling-shrinkage behavior of natural expansive clays,” *Applied Clay Science*, vol. 11, no. 2–4, pp. 211–227, 1996.
- [4] H. Péron, L. Laloui, T. Hueckel, L. Hu et al., “Experimental study of desiccation of soil,” in *Proceedings of Unsaturated Soils*, vol. 189, pp. 1073–1084, Carefree, Arizona, April 2006.
- [5] A. J. Puppala, B. Katha, and L. R. Hoyos, “Volumetric shrinkage strain measurements in expansive soils using digital imaging technology,” *Geotechnical Testing Journal*, vol. 27, no. 6, article 12069, 2004.
- [6] J. M. Fleureau, J. C. Verbrugge, A. G. Correia, P. J. Huergo, and S. Kheirbek-Saoud, “Aspects of the behaviour of compacted clayey soils on drying and wetting paths,” *Canadian Geotechnical Journal*, vol. 39, no. 6, pp. 1341–1357, 2002.
- [7] F. Yazdandoust and S. S. Yasrobi, “Effect of cyclic wetting and drying on swelling behavior of polymer-stabilized expansive clays,” *Applied Clay Science*, vol. 50, no. 4, pp. 461–468, 2010.
- [8] H. Nowamooz and F. Masrouri, “Influence of suction cycles on the soil fabric of compacted swelling soil,” *Comptes Rendus Geoscience*, vol. 342, no. 12, pp. 901–910, 2010.
- [9] P. C. Knodel, A. E. Dif, and W. F. Bluemel, “Expansive soils under cyclic drying and wetting,” *Geotechnical Testing Journal*, vol. 14, no. 1, pp. 96–102, 1991.
- [10] R. Ayad, J. M. Konrad, and M. Soulié, “Desiccation of a sensitive clay: application of the model CRACK,” *Canadian Geotechnical Journal*, vol. 34, no. 6, pp. 943–951, 1997.
- [11] C. S. Tang, Y. J. Cui, A. M. Tang, and B. Shi, “Experiment evidence on the temperature dependence of desiccation cracking behavior of clayey soils,” *Engineering Geology*, vol. 114, no. 3–4, pp. 261–266, 2010.
- [12] C. S. Tang, Y. J. Cui, B. Shi, A.-M. Tang, and C. Liu, “Desiccation and cracking behaviour of clay layer from slurry state under wetting–drying cycles,” *Geoderma*, vol. 166, no. 1, pp. 111–118, 2011.
- [13] J. H. Li and L. M. Zhang, “Study of desiccation crack initiation and development at ground surface,” *Engineering Geology*, vol. 123, no. 4, pp. 347–358, 2011.
- [14] M. Fernandes, A. Denis, R. Fabre, J.-F. Lataste, and M. Chrétien, “In situ study of the shrinkage–swelling of a clay soil over several cycles of drought–rewetting,” *Engineering Geology*, vol. 192, pp. 63–75, 2015.
- [15] H. Wang, J. Siopongco, L. J. Wade, and A. Yamauchi, “Fractal analysis on root systems of rice plants in response to drought stress,” *Environmental and Experimental Botany*, vol. 65, no. 2–3, pp. 338–344, 2009.
- [16] W. Tang and Y. Wang, “Fractal characterization of impact fracture surface of steel,” *Applied Surface Science*, vol. 258, no. 10, pp. 4777–4781, 2012.
- [17] Y. Lu, S. H. Liu, L. P. Weng, Z. Li, and L. Xu, “Fractal analysis of cracking in a clayey soil under freeze–thaw cycles,” *Engineering Geology*, vol. 208, pp. 93–99, 2016.
- [18] L. Nova-Roessig and N. Sitar, “Centrifuge model studies of the seismic response of reinforced soil slopes,” *Journal of Geotechnical and Geoenvironmental Engineering*, vol. 132, no. 3, pp. 388–400, 2006.
- [19] M. Kitazume and T. Takeyama, “Centrifuge model tests on influence of slope height on stability of soft clay slope,” in *Proceedings of Geo-Congress*, pp. 2094–2097, San Diego, CA, USA, March 2013.

- [20] H. Ling and H. I. Ling, "Centrifuge model simulations of rainfall-induced slope instability," *Journal of Geotechnical and Geoenvironmental Engineering*, vol. 138, no. 9, pp. 1151–1157, 2012.
- [21] W. A. Take and M. D. Bolton, "Seasonal ratcheting and softening in clay slopes, leading to first-time failure," *Géotechnique*, vol. 61, no. 9, pp. 757–769, 2011.
- [22] Standard for Soil Test Method, GB/T 50123-1999, in Chinese.
- [23] F. K. Decarlo and N. Shokri, "Effects of substrate on cracking patterns and dynamics in desiccating clay layers," *Water Resources Research*, vol. 50, no. 4, pp. 3039–3051, 2014.
- [24] H. O. Peitgen, H. Jürgens, and D. Saupe, *Chaos and Fractals: New Frontiers of Science*, Springer, Berlin, Germany, 2004.
- [25] W. H. Liu, Q. Yang, X. W. Tang et al., "Mechanical behaviors of soils with different initial dry densities under drying-wetting cycle," *Journal of Hydraulic Engineering*, vol. 45, no. 3, pp. 261–268, 2014, in Chinese.
- [26] B. Xu, Z. Z. Yin, and S. L. Liu, "Experimental study of factors influencing expansive soil strength," *Rock and Soil Mechanics*, vol. 32, no. 1, pp. 44–50, 2011, in Chinese.
- [27] M. H. T. Rayhani, E. K. Yanful, and A. Fakher, "Physical modeling of desiccation cracking in plastic soils," *Engineering Geology*, vol. 98, no. 1-2, pp. 25–31, 2008.

Research Article

Formation Mechanism and Mechanical Properties of Soil-Rock Mixture Containing Macropore

Feng Zhu , Wei Qian, Huilin Le, Haotian Fan, and Wuchao Wang

School of Earth Science and Engineering, Hohai University, Nanjing 211100, China

Correspondence should be addressed to Feng Zhu; 578971556@qq.com

Received 15 June 2018; Revised 20 October 2018; Accepted 8 November 2018; Published 11 December 2018

Academic Editor: Annan Zhou

Copyright © 2018 Feng Zhu et al. This is an open access article distributed under the Creative Commons Attribution License, which permits unrestricted use, distribution, and reproduction in any medium, provided the original work is properly cited.

In southwestern China, soil-rock mixture containing macropore (SRMCM) is very common in large-scale accumulation slopes. The formation mechanism and mechanical parameters of SRMCM play an important role in slope stability. In this paper, we designed a new physical model test to study the formation mechanism of SRMCM. We analyzed different factors that influence the formation of SRMCM. The mechanical properties of SRMCM are obtained by direct shear test. New physical model test demonstrates the best slurry consistency (30%) and slope angle (35°~45°) to form SRMCM. The results of direct shear test show that the strength parameters of SRMCM are high and it is influenced by the angle of macropore structure. When the angle of macropore structure increases, so does the cohesion of SRMCM. In this process, the internal friction angle does not change much.

1. Introduction

SRMCM (soil-rock mixture containing macropore) is a special type of soil-rock mixture, in which, macropore structure is defined as an accumulation of gravels without clay formed in different stratum of slopes. Figure 1 shows that SRMCM always appears with local stratification in deep-thick accumulation slopes, which is different from common soil-rock mixture (Figure 2). The formation mechanism and mechanical parameters of SRMCM play an important role in slope stability. However, the study of SRMCM has not been conducted.

In southwestern China, SRMCM is very common in large-scale accumulation slopes. The slope angles vary from 35° to 45°, and there are a lot debris flow deposits. The annual precipitation is 600 mm~800 mm, and the rainfall is usually heavy. The slope angles, debris flow, and rainfall might be the cause for SRMCM. To date, no experiments have ever been conducted to determine the best slurry consistency and slope angle to form SRMCM.

Inside SRMCM, binder bonds the particles in point state. The binder is upper soil that can move down to coarse particle layer by leaching. From field investigation, many slopes in southwestern China have very steep ditch banks on

both sides of the gully. The free face is almost vertical after rainfall erosion on slope edge for many years. The steep slope of SRMCM can stay stable rather than collapse and sliding during an earthquake. It is important to study the mechanical properties of SRMCM during the evaluation of talus slide.

An inhomogeneous rock-soil system consists of high-strength stone, fine-particle soil, and pores. The strength characteristics of this system depend on rock and soil thresholds, visual grain size, and stone [1]. An unconventional in situ shear test apparatus is used to investigate the strength properties of the shale-limestone chaotic complex (SLCC) bimrock [2, 3]. A generalized conceptual empirical approach is used to predict the overall strength of unwelded bimrocks and bimsoils [4]. There is little field investigation of SRMCM. No field shear test and empirical method have ever been proposed for the mechanical properties of SRMCM.

In laboratory, CT scan and fluctuation method are used to reconstruct the 3D model of gravel to study content, feature size, and soil-gravel distribution [5, 6]. Indoor shear test is used to obtain mechanical characteristics of unsaturated soil-rock mixture [7–10]. Afifpour and Moarfvand [11, 12] used a servo-control machine to conduct



FIGURE 1: Soil-rock mixture containing macropore (SRMCM).



FIGURE 2: Soil-rock mixture (SRM).

uniaxial compression tests on model bimrocks to obtain mechanical parameters such as uniaxial compressive strength (UCS), Young's modulus, failure strain, and full-scale stress-strain curves. Ergenzinger et al. [13], Xu et al. [14–16], and Zhao et al. [17] used discrete element method (DEM) to investigate the strength and failure properties of SRMS in shear zone. Particle flow code (PFC) 3D is developed to establish a stochastic structural model and simulate pressure shear deformation damage test [9]. Ding et al. [18] and Meng et al. [19] established a numerical simulation method based on microstructures. This method is reasonable after comparison with indoor test results.

In this paper, we develop a physical model test to study the formation mechanism of SRMCM. This simulates the formation process of SRMCM, and different factors in this process are considered. Mechanical properties of SRMCM are analyzed by indoor tests. Our parameters can be used as a reference in slope stability evaluation of Mahe talus slide at Lenggu hydropower station.

2. Formation Mechanism of Macropore Structure

2.1. Field Investigation of SRMCM in Mahe Talus Slide. Mahe talus slide is located in downstream of Mahe opposite to the concealed bend of Caiyu highway. The natural slope of Mahe talus slide is gentle rubble and the width on upper surface is narrower than lower surface. The angle of the slope varies from 30° to 35°. Ephemeral gully development occurs inside.

The gravels in SRMCM come from the crushed rock layer. The bedrock surface of Mahe talus slide is antidip, and it is made of heavily crushed metamorphic sandstones. Joint fissure develops fully. Figure 3 shows the existing collapse conditions. The distribution of SRMCM layers is random, and the collapsing gravels cave along the slope from the top to accumulate in concave slope surface.

Figure 3(a) shows that there are many cementing soil-rock mixtures overlying or underlying the SRMCM. Due to the short distance between cementing soil-rock mixtures and the ground surface, the soil-rock mixtures are not cemented by gravity; rather, they are cemented as slurry-stone fragmental materials flowing along the slope and accumulating on the crushed rock layer. The fragmental materials are generated at the top part of slope on rainstorm conditions. The thickness of slurries on the crushed rock layer ranges from 50 to 100 cm. This thin layer of slurries is formed because of the relatively high velocity. Figure 3(b) shows the transitional zone of slurry-stone fragmental materials flowing on crushed rock layer. Only the leaching of mussy water can be seen on the surface of crushed rock layer. Figure 3(b) shows the multilayer SRMCM in Mahe talus slide. In dry climate, the SRMCM may be formed by endless superposition of cementation layers. These layers emerge after quick dehydration and consolidation of slurry. The drilling in the middle of Mahe talus slide reveals that SRMCM may exist on the bedrock-cover discontinuity and been buried deeply. Figure 4 shows the boundary of Mahe talus slide.

2.2. Size Distribution Test. On the complex terrain of Mahe talus slide, we collected ten groups of samples from five slide parts for size distribution test. Figure 5 shows the samples being collected from Mahe talus slide.

Figure 6 shows the grading analysis curve of ten samples. Table 1 gives particle composition of the ten samples.

To remove the super-size particles for the indoor tests, the scalping method was chosen for the grain size > 60 mm. The soil can still be in natural gradation after the scalping. However, the nonuniform coefficient C_u would change, and thus, the integral strength of soil. The content of gravel after scalping is calculated in formula (1):

$$p_i = \frac{p_{0i}}{(100 - p_{d\max})}, \quad (1)$$

where p_i denotes the content of gravel after scalping, p_{0i} denotes the content of gravel before scalping, and $p_{d\max}$ denotes the content of super-size gravel.

Table 2 shows the particle composition of soil after scalping.

2.3. Formation Test of the Macropore

2.3.1. Properties of the Test Material. Soil, gravels, and water are used as materials to prepare the slurry. The soil and gravels are taken from Mahe talus slide. Figure 7(a) shows the prepared soil with particle diameter < 5 mm. Figure 7(b) shows the gravel with different diameters, 5 mm~10 mm,

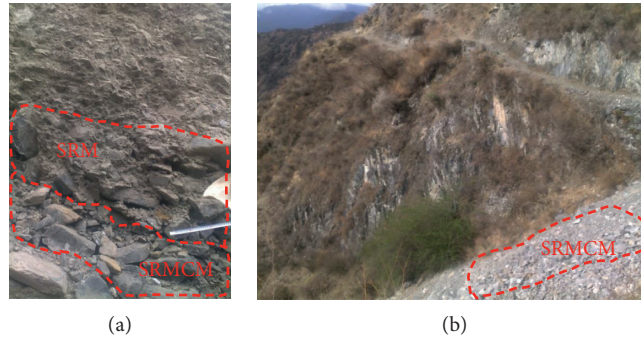


FIGURE 3: Formation mechanism of the SRMCM. (a) SRM overlying or underlying the SRMCM. (b) The multilayer SRMCM in Mahe talus slide.

10 mm~20 mm, and 20 mm~30 mm. The three groups of gravels are mixed to the mass ratio of 1 : 2 : 1.

2.3.2. *The Model Test Tank Which Can Alter Angle.* The model test tank (Figure 8) was made of four parts as follows:

- (1) *Floor.* The materials for the floor are transparent acrylic sheets with size of 120 cm × 60 cm. Grooves are set on the floor to fix the foreplate and backboard, and to change the width of SRMCM. The intervals of groove are 30 cm, 40 cm, and 50 cm.
- (2) *Foreplate and Backboard.* The foreplate and backboard of the size 120 cm × 80 cm are made of transparent organic glass with thickness of 2 cm. Four circular holes of diameters 10 mm are set in the base angles of glass to intercalate the bolts to fix the foreplate and backboard. 8 circular holes of diameters 10 mm are set in the middle of glass with radiation distribution to intercalate the bolts to fix the middle part of the steel plate. The four angles between the 8 circular holes above and the horizontal are 15°, 25°, 35°, and 45°, respectively. Intercalating the bolts into different holes would change the angles of baffle.
- (3) *Multiangle Baffle.* The baffle is made of stainless steel plate of thickness 5 mm. From the statistics of relief intensity of mountain landslide, three undulation angles are set in the middle of the baffle to simulate the mountain undulation angles. Three different widths of 30 cm, 40 cm, and 50 cm are set for every angle. Twelve stainless steel plates are made to simulate the formation process of SRMCM.
- (4) *Bolts.* The bolts are stainless steel of the diameter 8 mm. Two herringbone nuts are put in every bolt for dismounting.

2.3.3. *Test Procedure.* Sixteen independent tests are made. We performed every test twice to reduce errors.

- (1) Preparation of SRM slurry. After the soil samples of 60 kg weight and the gravel samples of 18 kg (30% weight of the soil samples) were mixed averagely, the water of 15.6 kg was put in to prepare the SRM slurry of 26% consistence. The SRM slurry prepared above

was then stirred uniformly and placed for 30 minutes after being covered with plastic film. Figure 9 shows the SRM slurry after being stirred uniformly.

- (2) The floor was put in a relatively wide field; two organic glasses with 16 fixing holes were set in the necks whose interval is 30 cm. 8 fixing holes were set in each glass, and the bolts were intercalated in these holes. The nuts were in neither too tight nor too loose to make sure the steel plate could be put in successfully. Type I steel plate was put inside the organic glasses with the inclination angle of which to be 15°, and the bolts were calated to fix the steel plate.
- (3) The mixed gravels were paved on the steel plate with the thickness of 5 cm. After that, the SRM slurry was poured onto the steel plate. Then, the process of slurry invading into macropore space was recorded by taking photos. According to the thickness of macropore space, whether the macropore structure can form in a different angle or not was known. At last, the thickness of macropore structure was recorded.
- (4) The formed SRMCM would be sunned for 15~20 d to air-dry in a drying and ventilating area.
- (5) The angle set in step (2) was changed to 25°, 35°, and 45°, and then step (3) and step (4) were repeated. Steps (2), (3), and (4) were repeated with the consistence of SRM slurry changing to 30%, 32%, and 34%. The relationship of slope angle, thickness of macropore structure, and the angle was observed under different consistence.
- (6) In step (5), four SRMCM samples with the size of 15 cm × 15 cm × 15 cm were taken out in each angle and were baked in oven for 24 hours under the 110°C constant temperature. Then all 32 samples were tested by shear test. Figure 10 shows the test procedure of macropore structure formation.

2.3.4. Test Results

(1) *Relationship between Slope Angle, Slurry Consistency, and Macropore Structure Formation.* Four slurries were prepared with different water contents of 26%, 30%, 32%, and 34%. The model test tank was set with four different angles of 15°,

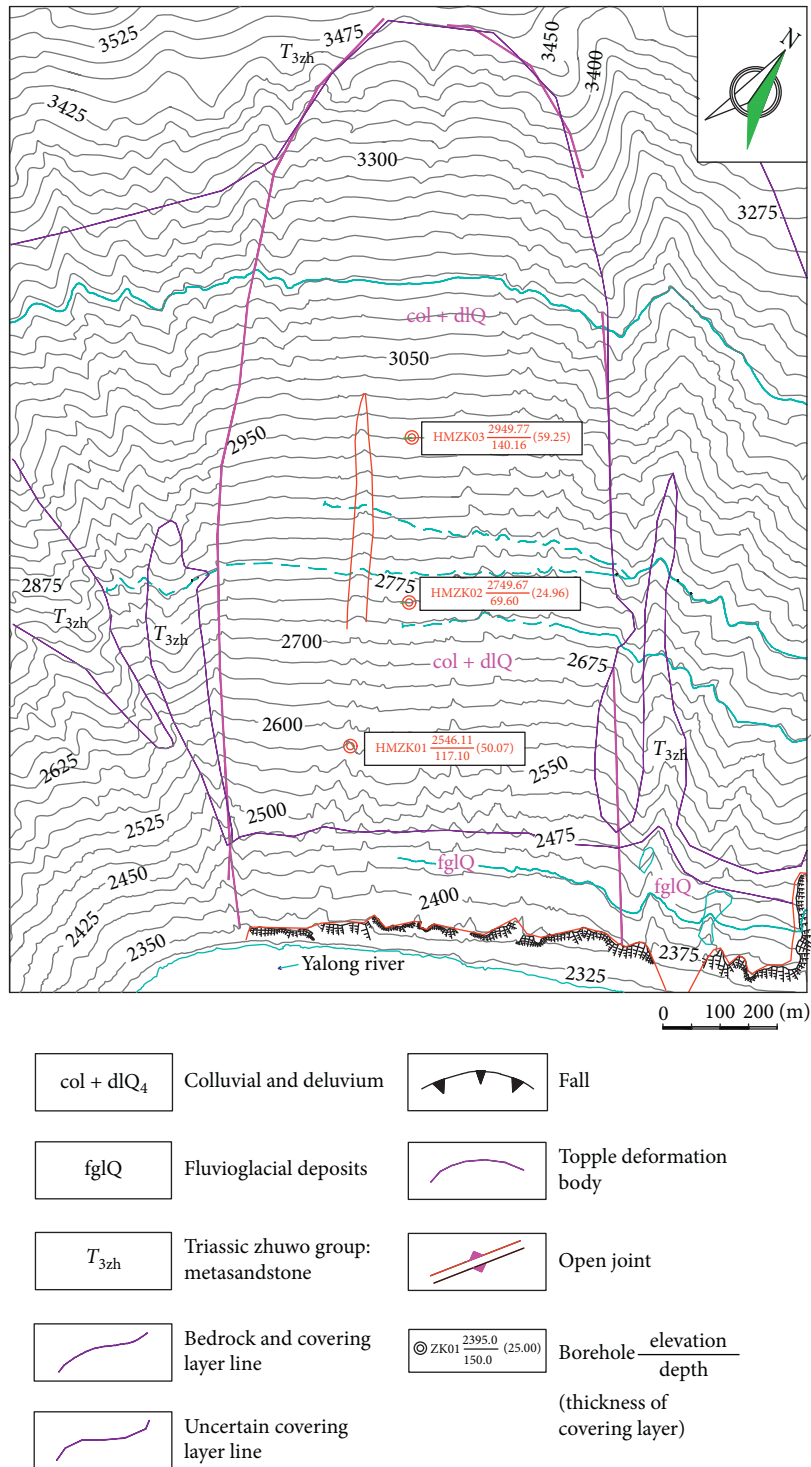


FIGURE 4: Boundary of Mahe talus slide.

25°, 35°, and 45° according to the field statistics of undulation angle of slope. After doing 16 unrepeated tests in which the model test tank with different angles and the slurries with different consistence were combined, and Table 3 shows the relationship between slope angle, slurry consistence, and macropore structure formation.

According to Table 3, in the 16 tests, the macropore structure formed in 8 tests while not formed in the other 8 tests. The test results show that macropore structure forms in

a certain slope when the SRM slurries of certain consistence invade into crushed rock layer. In gentle slope, macropore structure cannot form as the fluidity of the slurries with dense consistence is low, which makes the component force of down flow small and the slurries can hardly flow down. With the increase of water content in slurries, the consistency of slurries becomes more and more diluted and macropore structure forms as the slurries flow down slowly along the face of slope with the decreasing of downward



FIGURE 5: Samples being collected from Mahe talus slide.

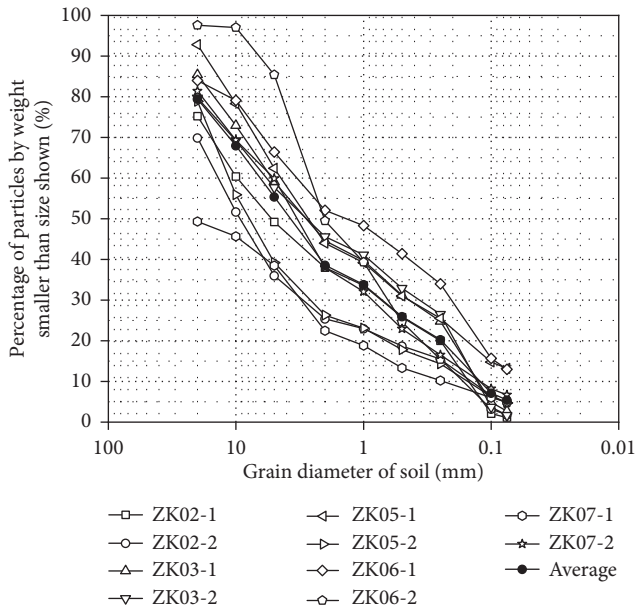


FIGURE 6: Grading analysis curve of ten samples.

TABLE 1: Particle composition of the ten samples.

Name of the particle	Range of particle size (mm)	Content of gravels (%)	Average content (%)
Gravel	>60	4.05~11.0	7.34
	>5	47.25~74.20	61.22
Silt	0.075~5	20.31~29.48	23.49
	0.005~0.075	3.7~8.6	5.59
Clay	<0.005	6.0~13.9	9.7

TABLE 2: Particle composition of samples after scalping.

Name of the particle	Range of particle size (mm)	Content of gravels (%)	Average content (%)
Gravel	>5	50.3~72.5	60.1
	0.075~5	20.52~29.72	23.8
Soil particles	0.005~0.075	4.3~10.5	6.4
	<0.005	6.0~16.3	9.7%

resistance. With the increasing of slope angle, the component force of down flow becomes bigger and bigger despite the low water content and dense consistence. After that, the slurries invade the crushed rock layer, the rear slurries push

the frontage slurries to flow down continuously, and the macropore structure forms. When the angle of slope increases to a certain degree and the slurries dilute enough, the slurries flow down along the face of slope quickly with a thin layer of slurries on the crushed rock layer. Meanwhile, only little part of slurries invade the crushed rock layer, while more slurries flow down along the face of slope under gravity action, thus makes the macropore structure forming hardly.

(2) *Relationship between Slope Angle, Slurry Consistency, and Thickness of Macropore Structure.* The thicknesses of macropore structure must be different as the consistencies of slurries and thicknesses of slurries invading the crushed rock layer are different. In the tests, the designed thickness of crushed rock layer is 5 cm. Figure 11 shows the thicknesses of macropore structure layers under different slope angles in the tests.

According to Figure 11, under same water contents of mud, the density (thickness) of macropore increases when the dip angle of macropore structure becomes larger (from 15° to 45°), because the larger dip angle makes downward resistance decrease, and the increasing fluidity makes the thickness of invading smaller. The thickness of macropore ranges from 15 mm to 40 mm. When the dip angle increases to a certain degree, most slurries flow down along the face of slope and there is no thickness of macropore structure, as the macropore structure cannot form. Under same slope angle, with the increase of the water contents of slurry, the consistency becomes smaller, the fluidity of SRM slurry increases, and the thickness of invading slurries become bigger firstly, then become smaller. Under the interaction of changing the consistence and slope angle, the density (thickness) of macropore structure changes little in one range of slope angle with the changing consistency. That is, macropore structure forms most easily with the slope angle of 35°, which is basically the same with the slope angle of Mahe talus slide (as is shown in Figure 4). It is hard to form the macropore structure when the slope is too gentle or too steep.

3. Shear Strength Parameter Tests of the SRMCM

20 samples of SRMCM were taken to carry out indoor direct shear test, and they were divided into four groups. In every



FIGURE 7: Soil and Gravel samples. (a) Soil sample. (b) Gravel samples.

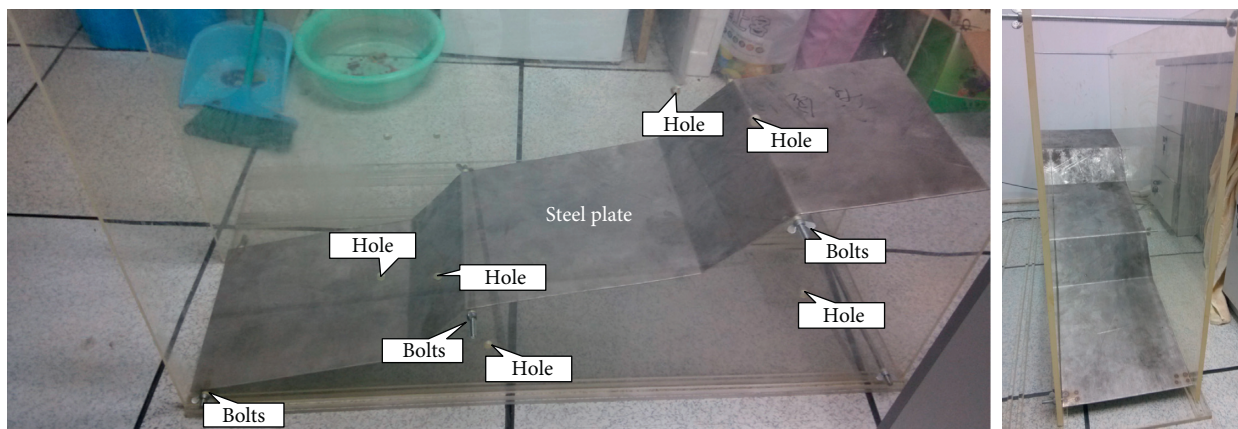


FIGURE 8: Model test tank which can alter the angle.



FIGURE 9: SRM slurry.

group, the size of samples was $15\text{ cm} \times 15\text{ cm} \times 15\text{ cm}$. The samples with different angles of macropore structure in SRMCM as 15° , 25° , 35° , and 45° were prepared based on the model test tank. The samples whose angle of macropore structure in SRMCM is 0° were prepared as the control group. All the samples were put in dry and ventilated conditions for 15–20 d to completely air-dry. Figure 12 shows the samples of SRMCM before indoor direct shear test.

3.1. Test Procedure. The tests were carried out under normal pressures of 100, 200, 300, and 400 kPa to define the shear strength parameters. In the test, the loading rate in every step was controlled in same level and not over 0.2 mm/min. Pressure sustained for a period after shear failure, and the residual strength was determinate. The loading stopped if shear displacement kept increasing or was more than 15 mm. Normal stress would be relieved before shear stress

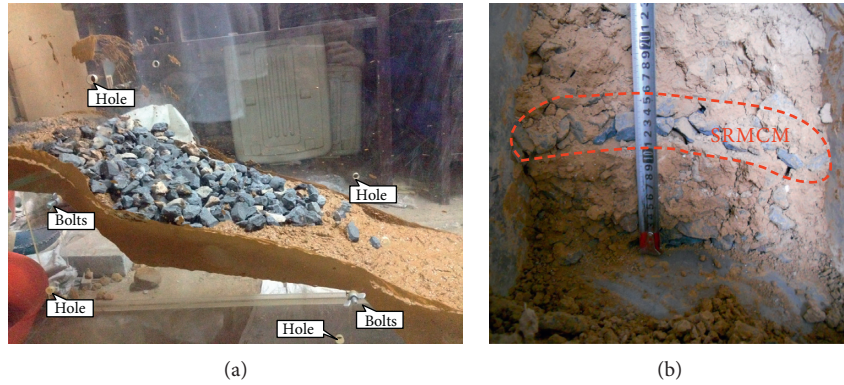


FIGURE 10: Test procedure of macropore structure formation. (a) The process of making the sample. (b) Final sample.

TABLE 3: Relationship between slope angle, slurry consistence, and macropore structure.

Undulation angles (°)	Content of water (%)			
	26	30	32	34
15°	×	×	×	√
25°	×	×	×	√
35°	×	√	√	√
45°	√	√	√	×

“√” means the macropore structure can form; “×” means the macropore structure cannot form.

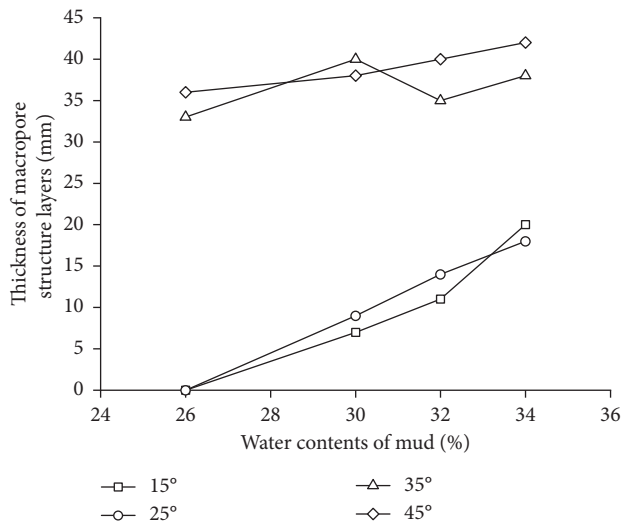


FIGURE 11: Thickness of macropore structure layers.

in pressure relief. Figure 13 shows the samples of SRMCM after indoor direct shear test.

3.2. Test Results. According to the results of indoor direct shear test, Figure 14 shows the curves of shear stress and shear displacement in different angles of macropore structure.

The results of indoor direct shear test are listed as follows:



FIGURE 12: Samples of SRMCM before the indoor direct shear test.



FIGURE 13: Samples of SRMCM after the indoor direct shear test.

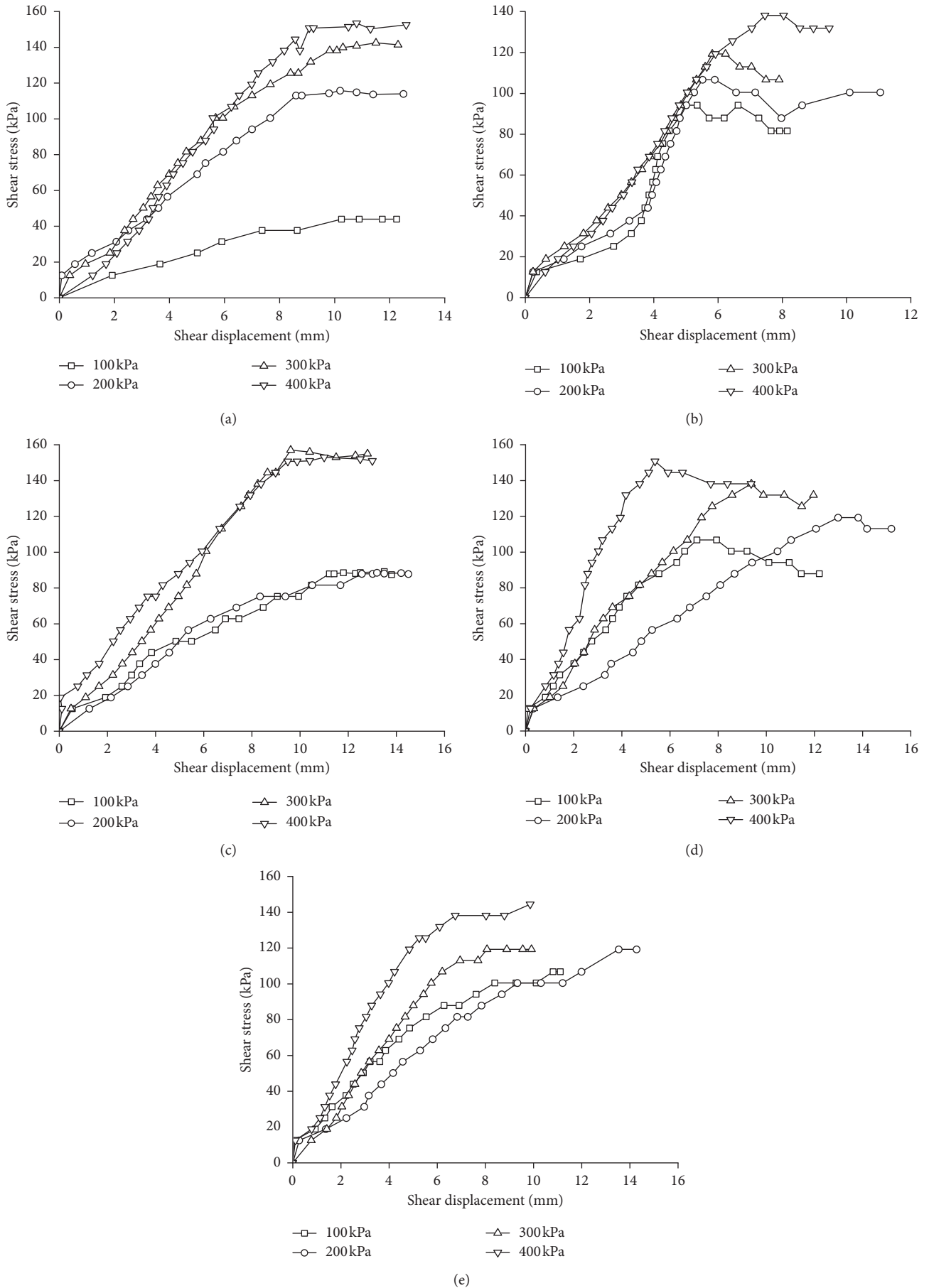


FIGURE 14: Curves of shear stress and shear displacement in different angles of macropore structure. (a) 0° , (b) 15° , (c) 25° , (d) 35° , and (e) 45° .

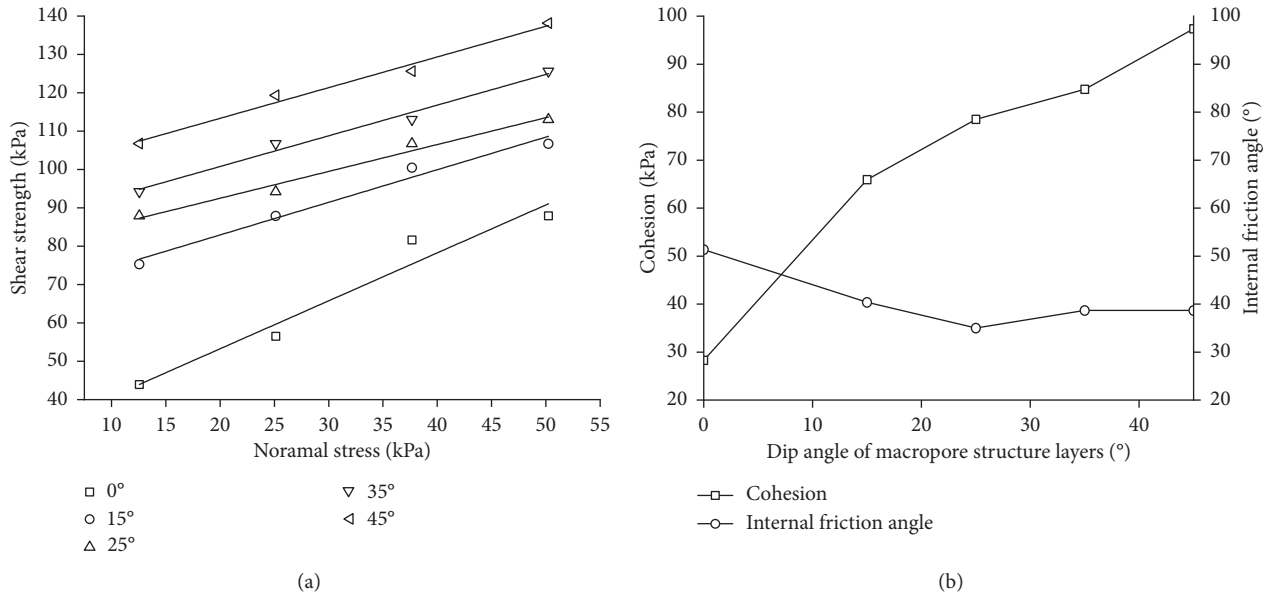


FIGURE 15: Shear strength of SRMCM in different angles of macropore structure. (a) Fitting curves of different angle. (b) Relationship between strength parameters and different dip angles.

- (1) With the increase of axial compression, the strength of SRMCM increases gradually, and the strength changes obviously in different axial compression. When the angle of macropore structure in SRMCM is 0°, the change of SRMCM strength is especially obvious in different axial compression. That is because the macropore structure is happened to be on and parallel to the shear surface. The shear strength of SRMCM is decided by the bite force between the gravels in macropore structure and has no relationship with the bond strength between fine soil. So, when in low axial compression, the gravels can throw over the gravels nearby with small bite force and low strength.
- (2) When the angle of macropore structure in SRMCM increases, the hardening degree of SRM sample increase gradually. When in same shear displacement, the larger the macropore structure angle is, the higher the strength is, especially in angle of 45°. In angle of 45°, the shear strength is beyond 130 kPa when the displacement is 4 mm. With the increase of macropore structure angle, the angle between shear zone and macropore structure becomes larger. Two SRM layers encapsulate the macropore structure, with the increase of shear strength, the inclined macropore structure will surely stagger unconnected, the gravels on shear zone will roll mutually, and one part of the gravels will inlay the SRM nearby. Under a certain axial compression, the inlaying will cost quite large energy with the external expression of shear strength increasing.
- (3) Figure 14 shows that the macropore structure is one stable structure, and the strength of macropore

structure does not have apparent peak no matter either in a big or small angle. After reaching a high level, the shear stress sustains a high state but not gets the apparent tendency of decreasing. The shear stress will not increase while the shear displacement keeps increasing when the horizontal load is applied continually, rather than the common material failure whose shear stress decreases apparently after failure.

- (4) According to the curves of shear stress and shear displacement, the shear strengths in different axial compression are obtained. Figure 15 shows the stress curve gotten by fitting the shear strengths in different axial compression with the using of Mohr-Coulomb theory.

According to Figure 15, the cohesion of macropore structure is very large except when the angle of macropore structure is 0°, and with the increase of angle, cohesion keeps enlarging while internal friction angle changes little. When the dip angle of macropores is low, the cohesion depends on the sliding friction of the fine-grained soil. When dip angle of macropores is high, the number of macropores is large and the cohesion depends on the sliding friction of fine-grained soil, the friction of soil and rock, and the contact force of rocks. When dip angle of macropores keeps increasing, the number of macropores keeps increasing, the contact force of rocks keeps increasing, and the cohesion keeps increasing. When the angle of macropore structure is 0°, the cohesion is very small while the internal friction angle is very large because of the interaction of gravels but not of soil particles. When under shearing, the angles of macropore structure are different from that of the shear plane, the upper and lower shear planes stagger unconnected, and macropore structure staggers unconnected. Due to the bite force between the gravels, the gravels must bypass the gravels nearby to produce the displacement that enlarges the shear strength.

4. Conclusion

In this paper, Mahe talus slide of the Lenggu hydropower station was used as an example. Field investigation was used to know the structural properties of SRMCM in Mahe talus slide. The formation mechanism of SRMCM was analyzed by a new physical model test. The mechanical properties of SRMCM were analyzed by indoor direct shear test. The main conclusions of the study include the following:

- (1) The SRMCM is one stable structure forming in a certain slope when the SRM slurries of certain consistence invade into the crushed rock layer.
- (2) The formation of SRMCM is closely related to the consistence of slurries. The SRMCM cannot form with the consistency too high or too low. The test shows that in water content of 30%, the slurries flow most fluently, and the SRMCM forms most easily. In the physical model test, the thickness of macropore structure forming with 35°~45° slope angle is the largest; that is, the SRMCM forms most easily with 35°~45° slope angle in real.
- (3) The shear strength of SRMCM is very high. When the angle of macropore structure keeps increasing, the cohesion keeps enlarging while internal friction angle changes little. It deepens the understanding of the slope failure mechanism when there are SRMCMs in the slope.

Data Availability

The data used to support the findings of this study are available from the corresponding author upon request.

Conflicts of Interest

The authors declare that there are no conflicts of interest regarding the publication of this paper.

Acknowledgments

This research was financially supported by the Natural Science Foundation of China (grant no. 41672258) and Postgraduate Research and Practice Innovation Program of Jiangsu Province (no. KYCX17_0501). This research was also supported by "The Fundamental Research Funds for the Central Universities" (no. 26120172017B665X1). The authors gratefully acknowledge M.S. Penglei XU in School of Earth Sciences and Engineering, Hohai University, China, for his contribution to the laboratorial experiment.

References

- [1] W. Xu and R. Hu, "Conception, classification and significations of soil-rock mixture," *Hydrogeology and Engineering Geology*, vol. 36, no. 4, pp. 50–56, 2009.
- [2] N. Coli, P. Berry, and D. Boldini, "In-situ non-conventional shear tests for the mechanical characterisation of a bimrock," *International Journal of Rock Mechanics and Mining Sciences*, vol. 48, no. 1, pp. 95–102, 2011.
- [3] Z. L. Zhang, W. J. Xu, W. Xia, and H. Y. Zhang, "Large-scale in-situ test for mechanical characterization of soil-rock mixture used in an embankment dam," *International Journal of Rock Mechanics and Mining Sciences*, vol. 86, pp. 317–322, 2016.
- [4] H. Kalender, E. Sonmez, C. Medley, K. Tunusluoglu, and E. Kasapoglu, "An approach to predicting the overall strengths of unwelded bimrocks and bimsoils," *Engineering Geology*, vol. 183, pp. 65–79, 2014.
- [5] S. Li, D. Zhang, S. S. Du, and B. Shi, "Computed tomography based numerical simulation for triaxial test of soil-rock mixture," *Computers and Geotechnics*, vol. 73, pp. 179–188, 2016.
- [6] H. Y. Zhang, W. J. Xu, and Y. Z. Yu, "Triaxial tests of soil-rock mixtures with different rock block distributions," *Soils and Foundations*, vol. 56, no. 1, pp. 44–56, 2016.
- [7] S. Sun, P. Xu, J. Wu et al., "Strength parameter identification and application of soil-rock mixture for steep-walled talus slopes in southwestern China," *Bulletin of Engineering Geology and the Environment*, vol. 73, no. 4, pp. 123–140, 2014.
- [8] H. Z. Wei, W. J. Xu, X. F. Xu, Q. S. Meng, and C. F. Wei, "Mechanical properties of strongly weathered rock-soil mixtures with different rock block contents," *International Journal of Geomechanics*, vol. 18, no. 5, article 04018026, 2018.
- [9] D. F. Cen, D. Huang, and F. Ren, "Shear deformation and strength of the interphase between the soil-rock mixture and the benched bedrock slope surface," *Acta Geotechnica*, vol. 12, no. 2, pp. 391–413, 2017.
- [10] B. Zhao, W. Huang, Z. Shu, M. Han, and Y. Feng, "Experimental and theoretical studies on the creep behavior of bayer red mud," *Advances in Civil Engineering*, vol. 2018, Article ID 6327971, 9 pages, 2018.
- [11] M. Afifipour and P. Moarefvand, "Mechanical behavior of bimrocks having high rock block proportion," *International Journal of Rock Mechanics and Mining Sciences*, vol. 65, no. 1, pp. 40–48, 2014.
- [12] M. Afifipour and P. Moarefvand, "Experimental study of post-peak behavior of bimrocks with high rock block proportions," *Journal of Central South University*, vol. 21, no. 2, pp. 761–767, 2014.
- [13] C. Ergenzinger, R. Seifried, and P. Eberhard, "A discrete element model predicting the strength of ballast stones," *Computers and Structures*, vol. 108–109, no. 4, pp. 3–13, 2012.
- [14] W. J. Xu, S. Wang, H. Y. Zhang, and Z. L. Zhang, "Discrete element modelling of a soil-rock mixture used in an embankment dam," *International Journal of Rock Mechanics and Mining Sciences*, vol. 86, pp. 141–156, 2016.
- [15] W. J. Xu, L. M. Hu, and W. Gao, "Random generation of the meso-structure of a soil-rock mixture and its application in the study of the mechanical behavior in a landslide dam," *International Journal of Rock Mechanics and Mining Sciences*, vol. 86, pp. 166–178, 2016.
- [16] W. J. Xu, C. Q. Li, and H. Y. Zhang, "DEM analyses of the mechanical behavior of soil and soil-rock mixture via the 3D direct shear test," *Geomechanics and Engineering*, vol. 9, no. 6, pp. 815–827, 2015.
- [17] Q. Zhao, N. Zhang, R. Peng, G. Li, C. Han, and Y. Guo, "Discrete element simulation of roadway stability in an efflorescent oxidation zone," *Advances in Civil Engineering*, vol. 2018, Article ID 4183748, 15 pages, 2018.
- [18] X. Ding, H. Zhang, S. Huang, B. Lu, and Q. Zhang, "Research on mechanical characteristics of unsaturated soil-rock mixture based on numerical tests of mesostructured," *Chinese*

Journal of Rock Mechanics and Engineering, vol. 31, no. 8, pp. 1554–1566, 2012.

- [19] Q. X. Meng, H. L. Wang, W. Y. Xu, and M. Cai, “A numerical homogenization study of the elastic property of a soil-rock mixture using random mesostructure generation,” *Computers and Geotechnics*, vol. 98, pp. 48–57, 2018.

Research Article

A Study on Ceramsite Production Using Dredging Sea Mud and Its Biofilm Formation Capacity Evaluation

Ting Xia ¹, Yue Li,¹ Zhixing Xiao,¹ Shixiang Wang,¹ Qingkai Wu,¹ Suwen Sun,¹ Hui Peng,¹ Dan Chen,¹ and Zihua Wang ²

¹College of Urban Construction, Nanjing Tech University, Nanjing 211816, China

²Research Center of Urban Underground Space, Nanjing Tech University, Nanjing 210009, China

Correspondence should be addressed to Ting Xia; xiating@njtech.edu.cn and Zihua Wang; wzhnjut@163.com

Received 4 June 2018; Revised 4 September 2018; Accepted 10 September 2018; Published 6 December 2018

Academic Editor: Dingwen Zhang

Copyright © 2018 Ting Xia et al. This is an open access article distributed under the Creative Commons Attribution License, which permits unrestricted use, distribution, and reproduction in any medium, provided the original work is properly cited.

Dredging sea mud produced during the coastal infrastructure construction has been gradually becoming an environmental problem in China. Making ceramsite is an attractive way to convert the waste sea mud to resources used for many industrial sectors. However, the impact of preheating and sintering conditions on the ceramsite properties and the biofilm formation capacity of the ceramsite are still poorly understood. This study aims to fill these knowledge gaps. Results suggested the optimal conditions for the preheating temperature was 350°C, the preheating time was 15 min, the sintering temperature was 1040°C, and the sintering time was 9 min. The dredging sea mud-derived ceramsite showed better biofilm formation capacity with high COD and NH₄⁺-N removal performance compared with the commercial ceramsites. The content of the chloride ion in the ceramsite granules is close to zero, and the low cost of this material, implying this dredging sea mud-derived ceramsite, could be an engineering favorable material for using it as a biocarrier in the real application.

1. Introduction

The development of the marine economy has led to a dramatic increase in infrastructure construction activities and transportation industry in coastal areas [1]. Accordingly, a large amount of dredging sea mud (DSM) has been produced. The improper disposal of these mud not only takes up a lot of space but also causes environmental pollution and other problems (odour, disease, etc.). Thus, safety treatment of these DSM has received considerable attention [2, 3].

The commonly used DSM treatment methods mainly are physicochemical methods, such as solidification; Zhu et al. [4] conducted dredging mud solidification treatment, confirming that the solidificated dredging mud could be utilized as solid filler material. In addition, DSM contains some organic matter and, therefore, could be utilized in agriculture and aquaculture. Xie et al. [5] confirmed that DSM can be used in agricultural cultivation. Besides these methods described above, an important way to treat waste DSM is to be the raw materials for sintering the ceramsite. Chi et al. [6] used seabed sludge for ceramsite production, and the results

showed that the product performance fully meets the requirements of the Chinese national technical standards for clay ceramsite. Ceramsite is a commonly used biocarrier for biofilm formation in sewage and biological contact oxidation wastewater treatment process. The rough surface and internal porous structure provide good adsorption capacity for pollutants removal, and also it is easy to grow microorganisms on its surface for biofilm formation.

Traditionally, nonrenewable natural resources, such as clay and shale, have been employed for the preparation of ceramsite by the method of high-temperature sintering [7, 8]. In recent years, the use of wastes, such as sewage sludge, coal fly ash, mine tailings, and river sediment, as the raw material for ceramsite sintering has been received increasing attention [8–11]. There is a relatively less study investigating the DSM for the production of ceramsite. DSM could be one of the best substitutes for clay because its major components are similar to those of clay. In our previous study, we have prepared ceramsite by using the mixture of DSM, sewage sludge, and the additive of calcium carbonate [12, 13]. The produced ceramsite met the Chinese standard

GB/T 17431.1-2010. Although Chi et al. [6] produced ceramsite successfully by the single raw material of sedimented sea mud in Qingdao, China, the sintering mechanism was not revealed deeply. In addition, DSM has more salinity and water than clay. In the sintering process of DSM, many researchers worry that chloride has undesirable effects including scumming [14, 15]. The content of the soluble salt in the sea mud is likely to relate to the preheating and sintering temperature [6, 15].

Thus, the aim of this study is to investigate the impact of preheating and sintering conditions on the properties of DSM-derived ceramsite. In addition, for further application as biocarrier, the capacity of water purification and the biofilm formation of DSM-derived ceramsite was also evaluated.

2. Materials and Methods

2.1. Characteristics of DSM. The DSM was collected from a coastal site which located in Lianyungang, Jiangsu province, China (N34°46'15.32", E119°19'24.74"). The color of this DSM is dark with salty smell. The DSM was sieved firstly to remove the large-sized agglomerates, followed by its property analysis according to the "Standard for Soil Test Method" (HJ 835-2017). The results are shown in Table 1:

2.2. The Feasibility of DSM from Lianyungang for Ceramsite Sintering. The DSM collected from different coastal areas may have different properties. To meet the ceramsite-forming conditions, the raw chemical composition range for the sintering ceramsite is generally on the basis of Riley and Wilson's research. Table 2 shows the main chemical composition of the raw material from Lianyungang by the EDX, and the content of major chemical composition of DSM complies with Riley's three-phase diagram and the required chemical composition range for making ceramsite. It can be seen from the table that the DSM from Lianyungang is expected to be sintered into ceramsite alone. Because LOI in the raw material is up to 8.58%, the ceramsite would be with high porosity. The feasibility of DSM from Lianyungang for ceramsite sintering was further studied by comparing the basic properties of DSM with clay materials which are conventional raw material for ceramsite sintering, and Table 3 shows the different properties. It can be seen that the DSM has a higher water content than clay, reaching 50%–60%. The composition of DSM is mainly composed of clay and powder, and the plasticity index is excellent, so it is judged that the DSM is easy for granulation. At the same time, the salt content of the DSM (mostly sodium chloride) is high, and the transformation process of chlorine should be concerned in the sintering process. The DSM from Lianyungang is used as a single raw material to form a ceramsite by molding, drying, preheating, and sintering. The ceramsite with a particle size of 3~5 mm is selected for use in the following experiment.

2.3. DSM Ceramsite Presintering Experiment. In order to determine the main process conditions that need to be controlled during the ceramsite sintering process, it is necessary to set up a presintering experiment before the

optimization process to determine the effect of the preheating conditions and the sintering conditions on ceramsite properties.

Because the moisture content of the DSM is high and the evaporation of the combined water in the raw material is about 250°C. Wang et al. [16] used TGA-FTIR technology to study the combustion and pyrolysis characteristics of sludge from different sources and pointed out that the decomposition temperature of organic matter is about 350°C. Therefore, the preheating temperature in this study can be set in the range of 250~400°C, and the preheating time can be set in the range of 5~20 min [17]. The sintering temperature in this study is mainly determined by reference to the sintering temperature of the high-temperature sintered clay ceramsite, and the sintering time ranges from 6 to 15 minutes [18]. The presintering experimental design is shown in Table 4, and the results of the presintering experiment are shown in Table 5.

According to the results of the presintering experiment, the preheating temperature can be set in the range of 200~450°C, and the preheating time is preferably in the range of 10~20 min. When the sintering temperature is varied from 1000~1100°C, it is possible to obtain ceramsite with good performance. According to the results of the presintering experiment, the sintering time can be set at 6~12 min.

2.4. Effect of Preheating Conditions on Ceramsite Properties. According to the results of the presintering experiment, three preheating time periods (10 min, 15 min, and 20 min) were selected to investigate the effect of the preheating method on ceramsite properties. The preheating temperature was controlled between 200~450°C, and the temperature increase rate was 8°C/min [19]. The properties of ceramsite, such as expansion rate, bulk density, compressive strength, and water absorption, were compared.

2.5. Effect of Sintering Conditions on Ceramsite Properties. According to the results of the presintering experiment, three sintering time periods (6 min, 9 min, and 12 min) were selected to investigate the effect of the sintering method on ceramsite properties. The sintering temperature was controlled between 1000~1080°C, and the temperature increase rate was 10°C/min; the properties of ceramsite, such as expansion rate, bulk density, compressive strength, and water absorption, were compared.

2.6. Analysis of Dissolved Salts Transformation during Ceramsite Production. The Cl⁻ content variation during ceramsite sintering was studied by measuring the Cl⁻ content under different sintering temperatures. The DSM under different temperatures were sampled and grinded, and the powder was then dissolved into the ultrapure water with mild vibration; after 1 day, the DSM powder suspension was filtered. The filtrate was then subjected to Cl⁻ analysis.

2.7. Sea Mud-Derived Ceramsite as Biofilm Carrier for COD and NH₄⁺-N Removal. A plexiglass column (Φ10 cm ×

TABLE 1: The properties of dredged sea mud.

Density (g cm ⁻³)	Water content (%)	Liquid limit (%)	Plastic limit (%)	Particle-size distribution (%)	Property
1.45	50–60	23–28	45–58	Clay (50.5) powder (49.5)	Saturated low liquid limit clayey silt

TABLE 2: Chemical composition (%) of DSM.

Item	SiO ₂	Al ₂ O ₃	Fe ₂ O ₃	CaO	MgO	K ₂ O	Na ₂ O	LOI
Sea mud	57.10	17.30	11.30	3.10	2.17	4.01	3.01	2.58
Riley's three-phase diagram	55–70	14–20	5–10	3–7 (CaO + MgO)		1.5–4 (K ₂ O + Na ₂ O)		/

TABLE 3: The properties of DSM and clay materials.

Item	DSM	Clay
Water content (%)	50–60	15–30
Particle characteristics	Mainly based on clay and powder and contains a small amount of fine sand	Thicker particles and contains sand-sized particles
Liquid/plastic limit	High	Middle
Salt content	High	Low
Chemical composition	Mainly silicon and aluminum High fused ingredients content	Mainly silicon and aluminum Low fused ingredients content

TABLE 4: Presintering experimental design.

Factor/level	1	2	3	4
A (min)	5	10	15	20
B (°C)	250	300	350	400
C (min)	6	9	12	15
D (°C)	900	1000	1100	1200

60 cm) packed with sea mud-derived ceramsite or commercial ceramsite with a particle size of 3–5 cm is used for hanging the biofilm and removing the COD and NH₄⁺-N. An air pump for column aeration was connected, and the flow rate was 20 L·min⁻¹. After ceramsite installation was completed, a synthetic wastewater (COD: 12 mg/L; NH₄⁺-N: 5 mg/L) was filled into the column, and the wastewater was intercirculated and aerated during experiment; the water samples were taken periodically for measurement.

2.8. Analysis Methods. *EDX analysis:* the chemical composition of the raw material was measured by using an inductively coupled plasma emission spectrometer. *XRD analysis:* the mineral composition of sea mud raw material and sea mud-derived ceramsite was analyzed by using an X-ray diffraction analyzer. *SEM analysis:* the internal structure of sea mud raw material and sea mud derived-ceramsite was analyzed by using a scanning electron microscope. The Cl⁻ ion solubility of sea mud samples sintering at different temperatures was analyzed by the Wantong ion chromatograph. COD was determined using potassium

permanganate titration. NH₄⁺-N was determined using Nessler's reagent method.

3. Results and Discussion

3.1. Ceramsite Sintering by DSM from Lianyungang. According to Tables 1 and 2, the plasticity index of DSM is excellent. The content of major chemical composition of dredged sea mud complies with the Riley's three-phase diagram.

Figure 1 showed the XRD patterns of the mineral composition of DSM and DSM-derived ceramsite. Compared with the raw materials, kalisilite (KAlSiO₄) was not detected in ceramsite. This may due to the minerals contained in the raw materials (mainly oxides of Fe oxides and alkaline metal oxides) transformed and produced to fenaksite [KNaFe(Si₄O₁₀)] under high temperature. In addition, anorthoclase (KAlSi₃O₈) and brinrobertsite [(Na, K, Ca)_x(Al, Fe, Mg)₄(Si, Al)₈O₂₀(OH)₄*3.54(H₂O) (x = 0.35)] recombination at high temperature may generate albite-calcium [NaCaAl (SiAl)₂O₈].

The SEM images of surfaces of DSM and the DSM-derived ceramsite are shown in Figure 2. Compared with ceramsite (Figure 2(b)), the structure of the raw materials of DSM (Figure 2(a)) is more loosely arranged. The particle size of DSM is different, and the shape is irregular. The quantity of pores in ceramsite (Figure 2(b)) is more than that in the raw materials (Figure 2(a)). The more micropores and the irregular surface may contribute higher porosity and specific surface area of sea mud-derived ceramsite.

3.2. Effect of Preheating Conditions on Ceramsite Properties.

The preheating temperature and preheating time greatly impact the properties of the ceramsite, such as the formation of pottery and the pore and strength characteristics of the ceramsite. Here, the preheating time was controlled as 10 min, 15 min, and 20 min, respectively. The preheating temperature and heating rate were described in Section 2.3. The bulk density, water absorption, compressive strength, and expansion rate were analyzed under different preheating time periods.

Figure 3(a) shows that, at the same preheating temperature, with the prolonging of the preheating time of the raw material, the bulk density of the ceramsite decreased. In

TABLE 5: Presintering results.

No.	A (X ₁) (min)	B (X ₂) (°C)	C (X ₃) (min)	D (X ₄) (°C)	Bulk density (g.cm ⁻³)	Water absorption (%)	Compressive strength (MPa)	Expansion rate (%)
1	5	250	6	900	797	46	○	1.01
2	5	300	9	1000	674	18.7	2.29	1.3
3	5	350	12	1100	617	16	3.7	1.3
4	5	400	15	1200	/	/	/	/
5	10	250	9	1100	553	19	3.3	1.3
6	10	300	6	1200	/	/	/	/
7	10	350	15	900	756	28	○	1.3
8	10	400	12	1000	623	12.7	4.1	1.7
9	15	250	12	1200	/	/	/	/
10	15	300	15	1100	455	35.3	3.5	1.2
11	15	350	6	1000	695	22	2.7	2.0
12	15	400	9	900	763	36	○	1.5
13	20	250	15	1000	665	25	2.8	1.7
14	20	300	12	900	749	20	○	1.5
15	20	350	9	1200	/	/	/	/
16	20	400	6	1100	578	14	3.8	1.4

Note: "○" means that it is not made into ceramicsite and "/" means that the ceramicsite is overfired.

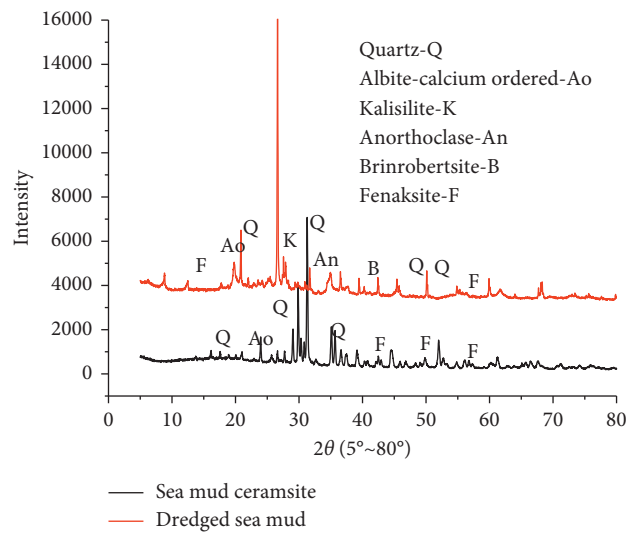


FIGURE 1: XRD analysis results on DSM and ceramicsite. Q: quartz; Ao: albite-calcium ordered; K: kalisilite; An: anorthoclase; B: brinrobertsite; F: fenaksite.

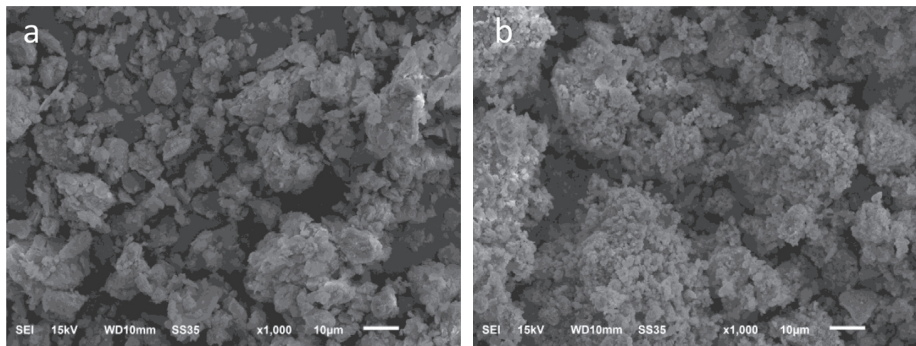


FIGURE 2: Scanning electron microscope image of (a) raw material 1000× and (b) ceramicsites 1000×.

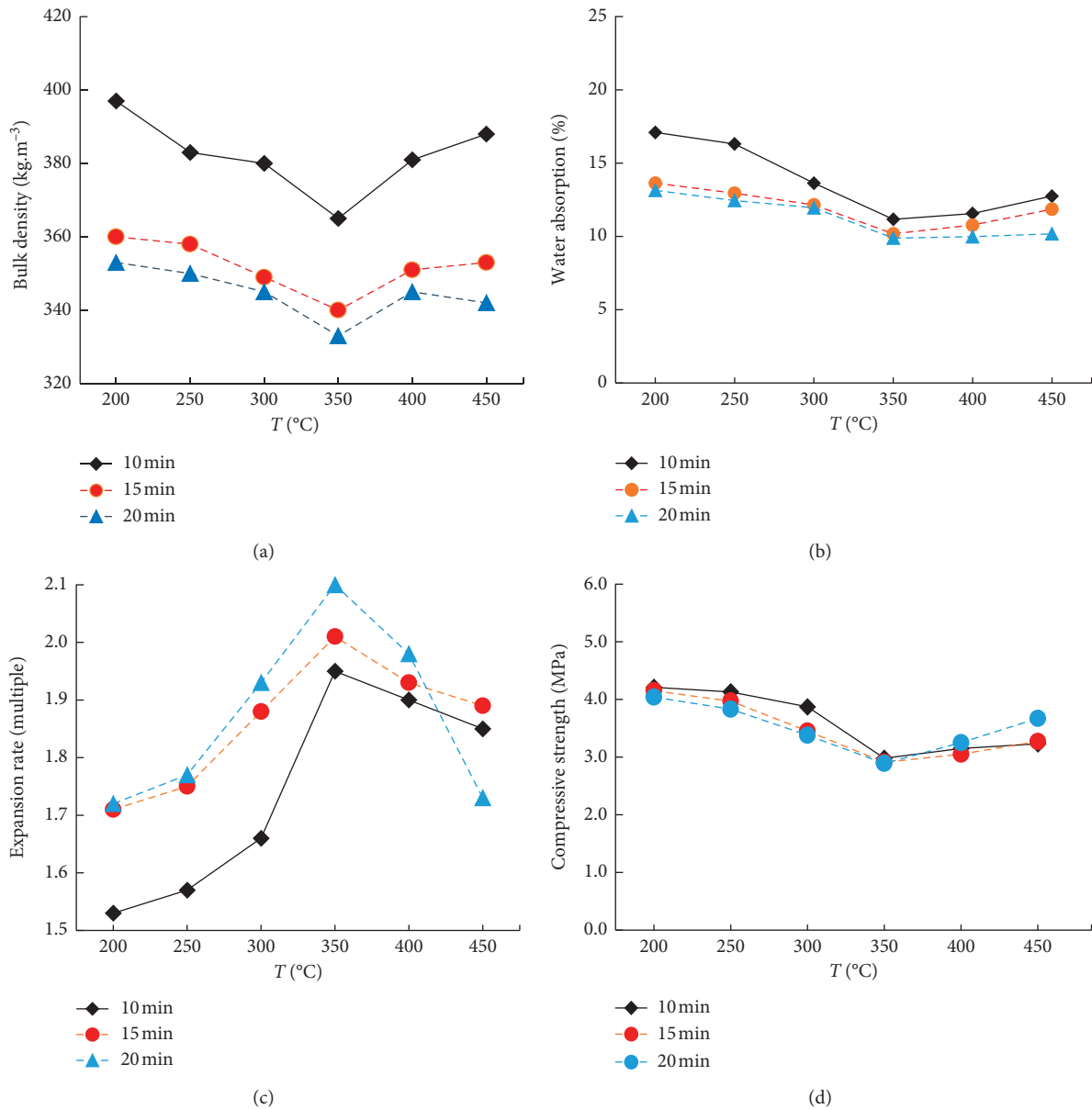


FIGURE 3: Effect of the preheating system on the performance of ceramsite. (a) Bulk density-temperature curve; (b) water absorption-temperature curve; (c) expansion rate-temperature curve; (d) compressive strength-temperature curve.

addition, 350°C seems to be an inflection point because the bulk density showed the decreasing trend when the preheating temperature was increased from 200~350°C and increasing as the temperature continued to rise.

Figure 3(b) showed that the water absorption rate of the ceramsite slightly decreased with the prolongation of the preheating time, although the water absorption rate of ceramsite under 15 min preheating was similar with that under 20 min. In the similar manner, the water absorption rate was decreased firstly and increased after the preheating temperature was above 350°C.

Figure 3(c) shows that the degree of swelling of the ceramsite is greatly influenced by the preheating temperature. The longer the preheating time, the more the swelling of ceramsite when preheating temperature was below 400°C.

It is very interesting that the variation of the expansion rate of ceramsite showed an inverse trend compared with other property index, which increased firstly and decreased when the preheating temperature was above 350°C. Different from other index, the compressive strength of ceramsite is less affected by the preheating time and temperature.

The above test results suggested that changes in the preheating temperature and preheating time of the raw material have a great influence on the bulk density and the expansion rate of the ceramsite and a slight influence on the water absorption rate.

According to the analysis, this phenomenon is mainly related to the preheating temperature. There are two main purposes for preheating in the ceramsite sintering process. The first is to pyrolyze most of the organic matter in the sea

mud into a gas to make the ceramsite lighter. The second is to remove the moisture in the sea mud so as to avoid evaporation of the water during the heating process, which may cause the body to burst and affect the strength of the ceramsite. When the preheating temperature is low, the decomposition rate of the organic matter in the sea mud is gentle, no gas is generated, and the ceramsite expansion rate is not high. At this time, when the gas escapes from the ceramsite, the pores formed on the surface are small, so the ceramsite bulk density and compressive strength are high. As the preheating temperature increases, the gas generated by the decomposition of organic matter increases, the pores inside and on the surface of the ceramsite increase, the expansion ratio increases, and the bulk density and compressive strength decrease. However, when the preheating temperature exceeds a certain value, too much gas generated by the organic matter may excessively impact the surface of the ceramsite, causing the sintered body to crack and being difficult to expand. Which in turn affects the expansion rate and compressive strength of the ceramsite. Therefore, it is important to choose a reasonable preheating temperature and preheating time.

The preheating temperature of 350°C and the preheating time of 15 min were suggested to be the good preheating conditions considering the light weighting, high strength, and water absorption capacity.

3.3. Effect of Sintering Conditions on Ceramsite Properties. The sintering time was controlled as 6 min, 9 min, and 12 min, respectively. The preheating temperature and heating rate were described in Section 2.4. The bulk density, water absorption, compressive strength, and expansion rate were analyzed under different sintering time periods.

As shown in Figure 4, except for compressive strength, the longer sintering time showed a higher value, and there were no obvious trends for other three indexes with different sintering time periods. As the temperature increased, the bulk density and water absorption index increased firstly and then decreased. In contrast, the expansion rate and compressive strength showed a reversed trend. There was obvious inflection point of temperature for each index (1020°C for bulk density, 1040°C for water absorption, 1040°C for expansion rate, and 1060°C for compressive strength).

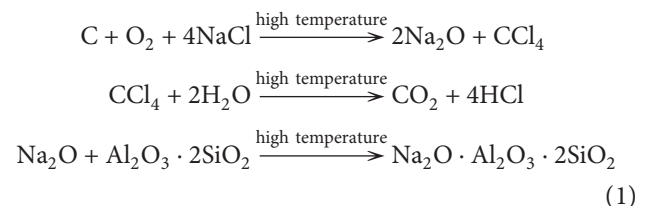
According to the analysis, this phenomenon is mainly related to the changes in the interior of the raw material at high temperatures. At a certain temperature, the inside of the raw material will melt and soften to form a certain amount of molten mineral. The sea mud contains various organic impurities, decomposed salts, and flammable minerals and can generate a certain amount of gas at a high temperature to expand and deform the ceramsite. The higher the sintering temperature, the longer the sintering time, the smaller the binding of the ceramsite to the gas expansion, the higher the expansion rate, and the smaller the bulk density. When the sintering temperature rises to a certain value, an excessive liquid phase is generated inside the material ball, which causes the liquid phase viscosity to

be too low, the pore structure is destroyed, the pores inside the ceramsite become smaller or less, the ceramsite expansion rate decreases, and the bulk density increases. According to the experimental observation, the rebound phenomenon of water absorption may be related to the excessive sintering temperature or excessive sintering time, which causes the surface of the material ball to be burned through, which makes the surface of the ceramsite more open.

Based on the above results, when the sintering temperature was controlled in the range of 1020°C to 1060°C, the ceramic granules have better properties. The optimum conditions were the sintering temperature of 1040°C and the sintering time of 9 min. The property indexes of sintered ceramsite measured under this condition were as follows: the bulk density was 410 kg/m³, the water absorption rate was 10%, the compressive strength was greater than 3 MPa, and the expansion rate was between 1.9 and 2.3.

3.4. Transformation of Dissolved Salts during Ceramsite Production. The DSM from Lianyungang has a high salt content. If the product contains high levels of chloride ions, it may cause moisture absorption, blooming, and corrosion [6, 12]. The average Cl⁻ content in the raw materials was 2.45%. As Figure 5 shows, when the sintering temperature was lower than 600°C, the Cl⁻ content in the sea mud does not significantly reduced. Above 700°C, the Cl⁻ content decreased sharply with the sintering temperature, and when it was greater than about 900°C, the Cl⁻ content was close to zero (the Cl⁻ content was about 0.07 at 1000°C), indicating that a transfer and conversion of the chlorine element occurred in the sintering process.

The low chlorine content in the produced ceramsite was probably because of the production of HCl gas during the sintering process. The DSM contained NaCl, (Al₂O₃ · SiO₂ · 2H₂O), H₂O, and carbon, which are four substances that are indispensable for the preparation of hydrochloric acid. Therefore, when the sintering temperature was above 900°C, complex chemical changes occur to produce HCl gas, and chlorine has disappeared and rarely exists in a crystalline and glassy ionic state. The main reactions during this process were suggested as follows [15]:



3.5. Biofilm Formation on DSM Derived Ceramsite for COD and NH₄⁺-N Removal. Under continuous water circulation, aeration, and natural light conditions, the biofilm on the surface of the carrier was accumulated. Higher extracellular polymeric substances (EPS) and dehydrogenase activity (DHA) production in the biofilm

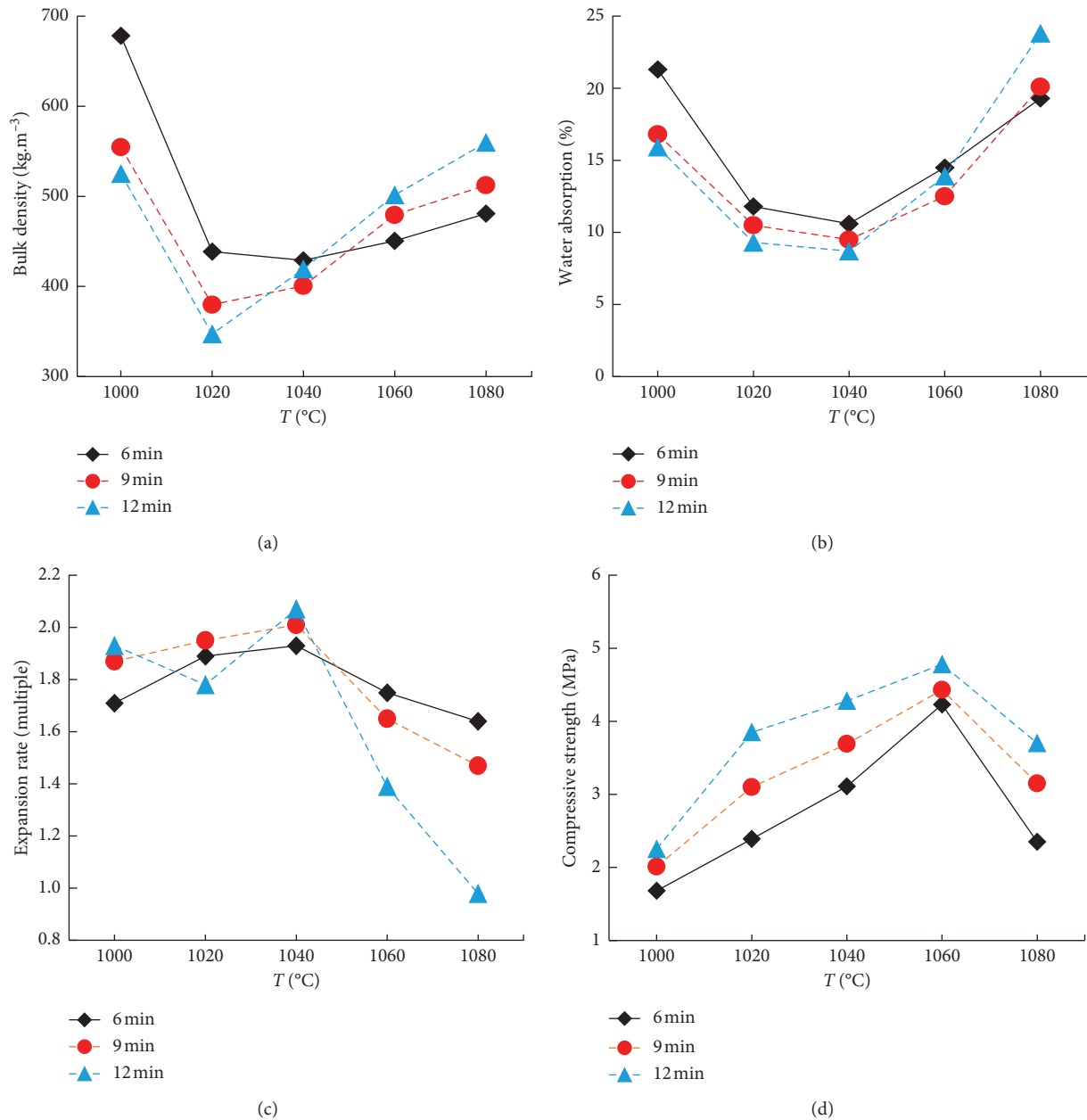


FIGURE 4: Effect of the sintering system on the performance of marine clay ceramic. (a) Bulk density-temperature curve; (b) water absorption-temperature curve; (c) expansion rate-temperature curve; (d) compressive strength-temperature curve.

formed on the surface of DSM derived ceramics compared to those produced in biofilm on the surface of commercially ceramics (clay is the main component). The results are shown in Figure 6. The reason for this is that DSM-derived ceramics has a larger surface area than commercial ceramics and is more conducive to biofilm deposition.

The removal rates of COD and $\text{NH}_4^+\text{-N}$ were also compared between these two filter medias during the test as shown in Figures 7(a) and 7(b). The removal efficiency of COD and $\text{NH}_4^+\text{-N}$ reached 80.81% and 65.344% after 18 days of operation of the column filled with DSM-derived ceramics, and the DHA value is $1.544 \mu\text{g}(\text{h}\cdot\text{cm}^2)^{-1}$. Therefore, the biofilm formation on the surface of ceramics can be

regarded as mature. In addition, compared with the control group (commercially ceramics), the removal rate of COD and $\text{NH}_4^+\text{-N}$ in the DSM-derived ceramics granules of the experimental group were higher, and this is consistent with the results of more EPS and DHA production for the biofilm on the sea mud-derived ceramics.

4. Conclusion

- (1) It is feasible to use DSM from the Lian yungang for ceramics sintering. The sintered ceramics has high porosity and surface area.
- (2) The optimal conditions for the preheating temperature was controlled at 350°C, the preheating time

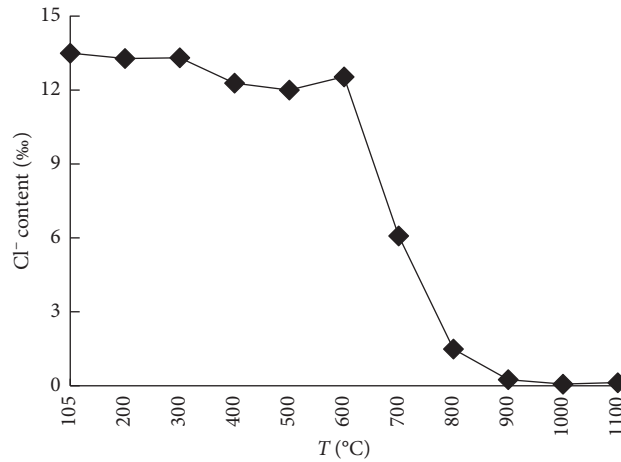


FIGURE 5: Changes of chlorine content with different sintering temperatures.

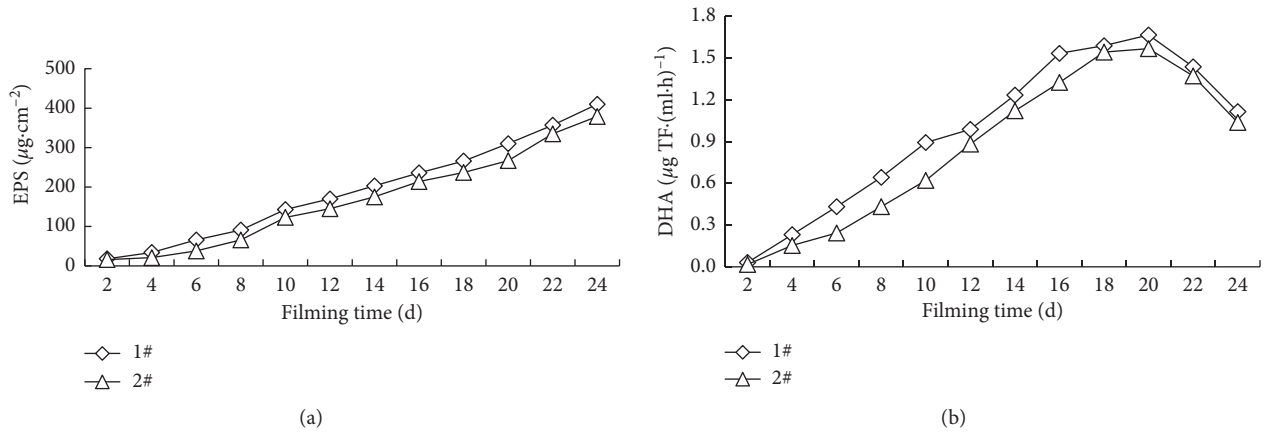


FIGURE 6: (a) EPS production in the biofilm; (b) DHA production in the biofilm. 1#: the biocarrier was the DSM-derived ceramsite; 2#: the biocarrier was the commercial ceramsite

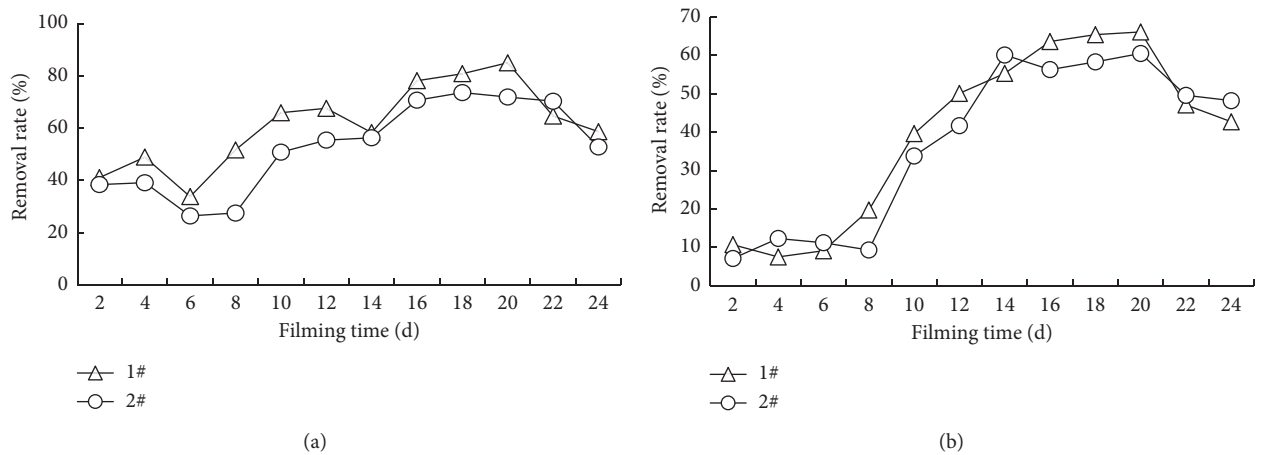


FIGURE 7: (a) Change of COD_{Mn} removal rate during filming. (b) Change of NH₄⁺-N removal rate during film hanging. 1#: the DSM-derived ceramsite condition; 2#: the commercial ceramsite condition.

was 15 min, the sintering temperature was 1040°C, and the sintering time was 9 min. Under this condition, the bulk density of produced ceramsite was

410 kg/m³, the water absorption rate was 10%, the compressive strength was above 3 MPa, and the expansion rate was around 2, which was classified

as ultralightweight ceramsite according to GB/T 17431.1–2010.

- (3) The content of the chloride ion in the ceramsite granules prepared by DSM is close to zero, and the content of soluble chloride ions is extremely low.
- (4) The sea mud-derived ceramsite showed better bio-film formation capacity with high COD and NH_4^+ -N removal capacity compared with the commercial ceramsite (clay is the main component).

Data Availability

We declare that the materials described in the manuscript, including all relevant raw data, will be freely available to any scientist wishing to use them for noncommercial purposes, without breaching participant confidentiality.

Conflicts of Interest

The authors declare that there are no conflicts of interest regarding the publication of this paper.

Acknowledgments

This work was supported by China's National Water Pollution Control and Governance of Science and Technology Major Special (2018ZX07208-004).

References

- [1] M. Li, Z. Zhang, K. Xu et al., "Pilot experimental research on sintering perforated brick from dredged sea sediments," *Journal of Computational and Theoretical Nanoscience*, vol. 13, no. 4, pp. 2616–2622, 2016.
- [2] J. Xie, X. C. Lin, P. Shi et al., "Study on using sea dredged mud to produce light weight Aggregate," *Journal of Zhanjiang Ocean University*, vol. 24, no. 6, pp. 32–36, 2004.
- [3] Z. G. Li, "Study on calcining clay brick by using silt and sea mud," *Brick and Tile World*, vol. 5, pp. 43–45, 2006.
- [4] W. Zhu, Z. C. Feng, C. L. Zhang, and J. Xie, "Study on the field test of reclamation for dredging mud," *China Harbour Engineering*, vol. 4, no. 5, pp. 23–25, 2005.
- [5] X. Xie, L. Zhang, S. Liu, T. Zhang, and H. Yang, "Aerated sea mud is beneficial for post-nursery culture of early juvenile sea cucumber *Apostichopus japonicus*, (Selenka)," *Aquaculture International*, vol. 24, no. 1, pp. 211–224, 2016.
- [6] P. Y. Chi, L. D. Zhang, Q. Qian et al., "Research on light ceramsite made by silt sea mud," *Insulation Materials and Building Energy Saving*, vol. 3, pp. 28–30, 2002.
- [7] C. Jiang, L. Jia, B. Zhang, Y. He, and G. Kirumba, "Comparison of quartz sand, anthracite, shale and biological ceramsite for adsorptive removal of phosphorus from aqueous solution," *Journal of Environmental Sciences*, vol. 26, no. 2, pp. 466–477, 2014.
- [8] T. P. Li, T. T. Sun, and D. X. Li, "Preparation, sintering behavior, and expansion performance of ceramsite filter media from dewatered sewage sludge, coal fly ash, and river sediment," *Journal of Material Cycles and Waste Management*, vol. 20, no. 1, pp. 71–79, 2018.
- [9] G. R. Xu, J. L. Zou, and G. B. Li, "Ceramsite obtained from water and wastewater sludge and its characteristics affected by $(\text{Fe}_2\text{O}_3+\text{CaO}+\text{MgO})/(\text{SiO}_2+\text{Al}_2\text{O}_3)$," *Water Research*, vol. 43, no. 11, pp. 2885–2893, 2009.
- [10] D. T. Yue, Q. Y. Yue, B. Y. Gao et al., "Preparation and bloating mechanism of porous ultra-lightweight ceramsite by Dehydrated Sewage sludge and yellow river sediments," *Journal of Wuhan University of Technology-Mater*, vol. 29, no. 6, pp. 1129–1135, 2014.
- [11] S. Wang, S. Li, Y. Zhao, and Z. Wei, "Removal of cadmium from aqueous solutions using ceramsite mainly composed of Pb-Zn tailings," *Journal of Residuals Science and Technology*, vol. 13, no. 2, pp. S1–S5, 2016.
- [12] Y. Y. Liu and T. Xia, "Study on ceramsite production with sludge and sea mud in municipal sewage plant," *Industrial Safety and Environmental Protection*, vol. 3, pp. 18–21, 2016.
- [13] M. D. Li, T. Xia, Y. Y. Liu et al., "Experimental research on sintering ceramsite of dredged saline sediment from seaport," *Journal of Chongqing Jiaotong University (natural science)*, vol. 35, no. 6, pp. 81–85, 2016.
- [14] M. Gao, A. G. Tian, M. D. Li et al., "Experimental research on key technology of dehydration desalination for sea siltbrick making," *New Building Materials*, vol. 40, no. 2, pp. 35–37, 2013.
- [15] M. Li and X. Cong, "Chemical changes and the mechanisms in the sintering process of sea silt," *Bulgarian Chemical Communications*, vol. 49, no. 1, pp. 250–255, 2017.
- [16] X. R. Wang, Y. Y. Jin, X. Du et al., "Feasibility research on sintering municipal sewage for manufacturing haydite," *China Water and Wastewater*, vol. 23, no. 7, pp. 11–15, 2007.
- [17] Y. H. Yang, Z. A. Wei, Y. L. Chen, Y. Li, and X. Li, "Utilizing phosphate mine tailings to produce ceramisite," *Construction and Building Materials*, vol. 155, no. 30, pp. 1081–1090, 2017.
- [18] Z. H. Yang, W. J. Song, J. H. Yang, L. Deng, Z. Cao, and M. L. Shi, "High-strength ceramsite made with sludge and low-quality fly ash," *Journal of Materials in Civil Engineering*, vol. 25, no. 7, pp. 851–856, 2013.
- [19] J. Qin, C. M. Yang, C. Cui, J. Huang, A. Hussain, and H. Ma, "Ca²⁺ and OH[−] release of ceramsites containing anorthite and gehlenite prepared from waste lime mud," *Journal of Environmental Sciences*, vol. 47, pp. 91–99, 2016.

Research Article

Study on Material Properties of Magnesium Oxide Carbonized Prestressed Pipe Piles

Henian Zhang,¹ Miao Cao,² Kaixiang Chen,³ Chen Shen ,⁴ Peisheng Xi,⁵ Fang Zhang,⁴ and Shaohan Wang⁴

¹Senior Engineer, Anhui Jianzhu University, Anhui Urban Construction and Underground Space Engineering Technology Research Center, Hefei 230022, China

²Undergraduate, Hohai University, College of the Environment, Nanjing 210000, China

³Doctoral Student, The Key Laboratory of Road and Traffic Engineering, Ministry of Education, Tongji University, Shanghai 230000, China

⁴Graduate Student, Anhui Jianzhu University, Anhui Urban Construction and Underground Space Engineering Technology Research Center, Hefei 230022, China

⁵Professor, Anhui Jianzhu University, Anhui Urban Construction and Underground Space Engineering Technology Research Center, Hefei 230022, China

Correspondence should be addressed to Chen Shen; ivans_shen@126.com

Received 25 June 2018; Accepted 27 August 2018; Published 28 November 2018

Academic Editor: Xinbao Yu

Copyright © 2018 Henian Zhang et al. This is an open access article distributed under the Creative Commons Attribution License, which permits unrestricted use, distribution, and reproduction in any medium, provided the original work is properly cited.

Traditional PHC pipe pile in foundation engineering consumes high energy and has insufficient durability. A magnesium oxide carbonization test block is a new type of environmental protection block which bases on activated magnesium oxide cementation technology. The use of CO₂ carbonation technology allows reactive magnesia to react to form basic magnesium carbonate to increase the compressive strength and durability of the block. Three kinds of different magnesium oxide powders were subjected to pressure test and determined the key technical parameters, such as optimal raw materials, sample preparation methods, carbonization environment and technology, and optimized design of pipe pile concrete material system.

1. Introduction

Prestressed high-strength concrete pipe piles (PHC pipe piles) are widely used in industrial and civil construction, roads and railway bridges, ports, and other engineering structures. With the continuous deepening of the theoretical research of high-strength concrete, its experimental research under the new preparation technology on various properties is more extensive. The large-scale use of traditional PHC pipe piles has seriously damaged farmland resources [1], and its main raw material Portland cement has huge environmental problems. Australian researcher Harrison (2001) [2, 3] developed a new type of cement mixed with activated magnesia and ordinary Portland cement, which is based on environmental protection to design. The hydration rate of active magnesium oxide is fast, and magnesium hydroxide can react with carbon dioxide (carbonization) to

form magnesium carbonate compound which has strong cement strength, and this is an environmentally friendly, sustainable, and efficient new material. Magnesium carbonate can regenerate magnesium oxide after calcination [4], and it means that the process is reversible and active magnesium oxide products have recyclability and recycling characteristics.

More in-depth research on active magnesium oxide cement is led by Dr. Al-Tabbaa, Ph.D., University of Cambridge, UK. Al-Tabbaa has conducted extensive research on the carbonation technology of active magnesium oxide, including hydration characteristics, microstructure, carbonization properties, and industrial production; Liska and Al-Tabbaa [5] have found that active magnesia cement has superior capability to Portland cement in resisting hydrochloric acid and sulfuric acid. Cwirzen and Cwirzen [6] study the compressive strength of different magnesium

oxide contents (0–20%); the experimental results show that, after 28 days of carbonization, the strength of the test piece with the magnesium oxide content of 0 is 32 MPa, the strength of the magnesium oxide is 10%, and the strength of the 20% test piece is 42 MPa and 40 MPa, respectively. Yi et al. [7, 8] used a modified three-axis device to carbonize and cure the sand; they found that blending 5% of active MgO can complete carbonization during 3~6 hours, and its strength can reach 2 to 3 times the strength of curing 28 d cement stabilized soil. However, this technology is still in the preliminary development stage; Formosaa et al. [9] indicated that MPC formulated with a low-cost MgO by-product could be an interesting alternative to other repair mortars; Zhang et al. [10] concluded that the carbonization blocks could have a higher strength; laboratory tests were performed to investigate the influence of the mixing amount of reactive MgO on compressive strength, microcharacteristics, and durability of the block, and they indicated that the carbonized products of reactive MgO are mainly hydromagnesite and nesquehonite/dypingite, with the higher amount of reactive MgO, the more carbonized products. Mo and Daman [11] concluded that active MgO produced a large amount of Mg-Ca carbonate, which made the microstructure of the cement paste denser. This is also the reason why MgO cement has stronger strength than ordinary Portland cement. Cai et al. [12] conducted comparative tests on different activated magnesia carbonized silt and found that, under the same conditions, the sample with high activity is stronger than the sample with lower activity and the sample with higher activity has higher density increase rate. Ye et al. [13] found that the strength of magnesium oxide cement decreased significantly with the increase of fly ash content in early stages. However, with the passage of time, the influence of fly ash content on strength becomes smaller and smaller. With the continuous progress of concrete technology, the preparation methods of high-strength concrete have been emerging. Some researchers have obtained ultrahigh-strength concrete materials through special ways. The carbonization technology based on active magnesium oxide is a new research direction which has attracted much attention in recent years; just a few scientific research institutions have conducted preliminary studies, and this technique is seriously lacking relevant experimental data. In order to reduce environmental pollution caused by Portland cement as a solidifying agent, mainly from the following three aspects to optimize the improvement (1) replacement of Portland cement as a curing agent for blocks with new materials, (2) research low emission, low energy, and recyclable recycling block preparation method, and (3) development of the best material mix ratio and preparation method were done in the previous research.

2. Materials and Methods

2.1. Experiment Materials. The cement used in this experiment is 32.5 grade ordinary Portland cement. Its various technical indicators meet the corresponding provisions of the *Ordinary Portland Cement* (GB175-2007); the chemical composition of the active magnesium oxide is shown in Table 1, and the identifier and quantity of different active

TABLE 1: Chemical composition of reactive MgO (%).

MgO	SO ₃	CaO	Fe ₂ O ₃	SiO ₂	Al ₂ O ₃	P ₂ O ₅
95.50%	1.17%	1.05%	0.18%	1.02%	0.24%	0.28%

TABLE 2: Material usage.

Magnesium oxide activity	Number	Ratio (MgO/water)	Note
High	M ₀	/	All is ordinary cement
High	M ₁	1:2	The mass of magnesium oxide and cement
High	M ₂	1:1	mixture is 300 g
High	M ₃	2:1	

magnesium oxide contents are shown in Table 2. Active magnesia content refers to the amount of MgO in active magnesia cement. According to the study by Mo and Panesar [14], after 56 days of carbonization, the strength of the 40% magnesium oxide test piece is close to that of the 20% magnesium oxide test piece so that three different proportions (mass ratio) are used; MgO in the curing agent doping are 15%, 25%, and 35%.

2.2. Sample Preparation

- (1) *Optimum Carbonized Masonry Raw Material and Forming Method.* Unlike conventional blocks, the strength of carbonized blocks is based on the chemical interaction among magnesium oxide, water, and carbon dioxide (solid, liquid, and gas phases), so we should have specific requirements for the moisture content, porosity, saturation, and initial strength of the block.
- (2) *Optimal Carbonization Environment and Carbonization Method.* Through indoor testing, based on (1), we choose the best raw materials and molding methods to make masonry in order to research carbon dioxide solubility, humidity, temperature, pressure, and other carbonization environmental parameters suitable for masonry carbonization and to research the most effective carbonization methods and processes.
- (3) *Carbonized Masonry Strength and Durability.* Through laboratory tests based on (1) and (2), test the compressive strength, wet and dry cycles, and freeze-thaw cycle of typical carbonized masonry to determine the strength and durability of carbonized masonry.

2.3. Experiment Procedure. The static pressure method is adopted for sample preparation, and the specific process is as follows:

- (1) Weigh a certain amount of raw materials, stir for five minutes in a small indoor blender, and add weighed water, and then stir for five minutes to ensure uniform mixing

- (2) Weigh a sample of the required sample quality, pour the stirred sample into a cylindrical mold (diameter of 50 mm and height of 100 mm), with a vertical pressure on the jack to make cylindrical specimen height of about 80 mm
- (3) Demold the cylindrical specimens after compaction and move them to the carbonation tank for curing
- (4) When the specimens have been cured to the 3rd, 7th, 14th, 21st, and 28th days, they are, respectively, tested for compressive strength and shear strength, crack resistance, drying shrinkage and expansibility, and diameter, weight, and height of the final sample, and then other tests were carried out

3. Analysis of Test Results

3.1. Optimal Material Mix Ratio. Figure 1 shows the compressive strength values of different magnesium oxide contents in the case of using high-activity magnesia; Figure 2 is the compressive strength of different water-cement ratios in the carbon block. A total of 7 groups of trials were present, 15 test blocks per group.

As we can see from Figure 1, regardless of the amount of active magnesia tested, the strength of the blocks is significantly higher than the compressive strength of the active magnesia block. When the blending amount is M_1 , the more the compressive strength of the block is, the more the carbonization time is; after 14 days of carbonization, the compressive strength of the block slightly decreased. When the blending amount is M_2 , the compressive strength of the test block at 3rd day of carbonization is higher than that of other groups; after 14 days of carbonization, the compressive strength of the test piece decreased, and the final strength value was slightly closer to M_1 . When the blending amount is M_3 , the strength of the test block at 3rd day of carbonization is slightly higher than M_1 , slightly lower than M_2 . After 7 days of carbonization, the strength of the test block was significantly lower than M_1 and M_2 test blocks. And after 14 days of carbonization, the compressive strength of the test block decreased significantly.

From Figure 2, it can be seen that the compressive strengths of the water-cement ratios of the H_2 and H_3 cement blocks are increasing with time. The compressive strength of the H_1 block is reduced within 3–7 days, and the compressive strength of the block increased greatly after 7 days of carbonization.

3.2. Optimal Molding Method. A total of 7 groups of trials were present, 15 test blocks per group. Figure 3 shows the compressive strength of carbonized blocks with different forming methods; Figure 4 shows the effect of different pressure parameters on the compressive strength of carbonized blocks.

As we can see from Figure 3, the compressive strength of the test block produced by the pressure forming method is the highest, and it has the fastest growth rate and the highest compressive strength within 0–7 days. During 7–14 days, the growth rate of the test block made by the pressure forming

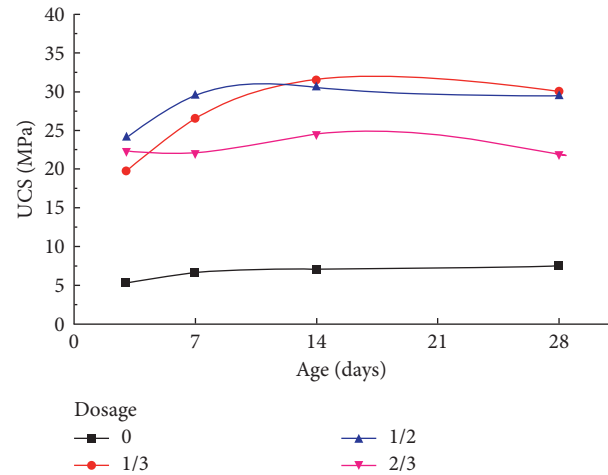


FIGURE 1: Compressive strength of different magnesium oxide contents.

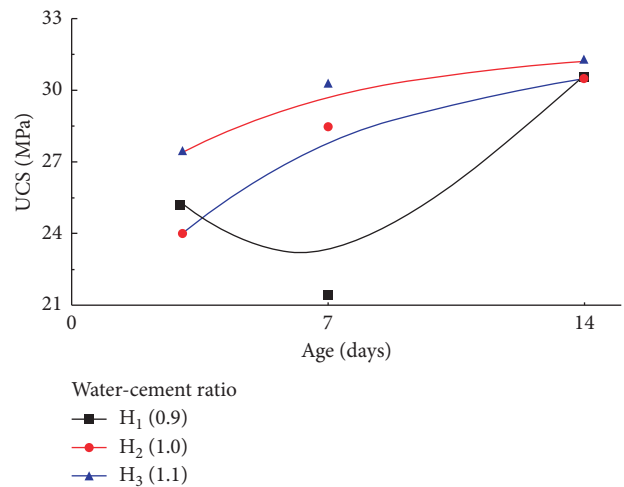


FIGURE 2: Compressive strength of different water-cement ratios.

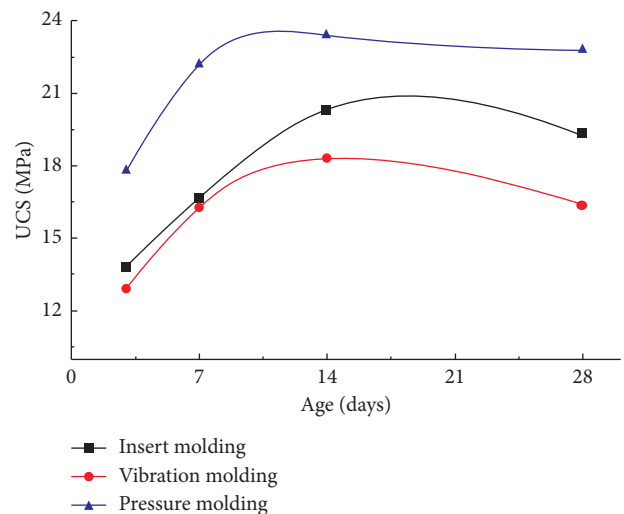


FIGURE 3: Compressive strength of different forming methods.

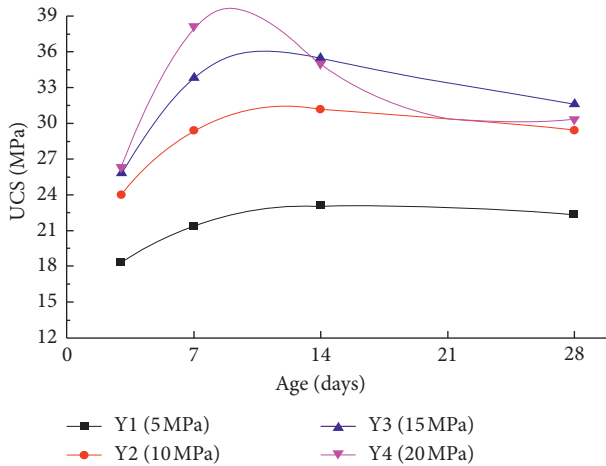


FIGURE 4: Compressive strength of different pressure parameters.

method is lower than that of the test block made by the transplant molding method and the vibration forming method.

From Figure 4, we can see that, in the early stage of carbonization (0–7 days), the Y_4 pressure parameter makes the highest increase in the strength of the test block. In the middle period of carbonization (7–14 days), the compressive strength of the Y_4 test block decreases greatly, and the compressive strengths of the Y_1 , Y_2 , and Y_3 test blocks slightly increase. In the later stage of carbonization (14–28 days), the decrease in compressive strength of the Y_4 test block is slightly smaller than that in the medium term. The decreasing order from small to large is Y_1 , Y_2 , and Y_3 .

3.3. Optimal Carbonization Environment. Liu et al. [15] and Colleparidi [16] concluded that the performance of concrete is closely related to the humidity during curing, especially the control of temperature and humidity conditions in the early curing process, which has an important influence on the hydration hardening rate, microstructure characteristics, strength development, and durability of the concrete, especially on the concrete surface. The impact of the structure is more pronounced [14]. Figures 5–7 are the effects of different humidity, CO_2 concentrations, and temperatures on the compressive strength of the test block, respectively. A total of 13 groups of trials were present, 15 test blocks per group.

It can be seen from Figures 5–7 that the humidity, CO_2 concentration, and temperature during carbonization are closely related to the compressive strength of the block. Too low or too high will reduce the compressive strength of the carbonized block, which is very important for the practical application of the project. From the experimental results, it can be seen that the best optimal carbonization environment is S_3 , C_2 , and W_2 .

3.4. Water Resistance Test. Whether the pipe piles produced under the current process conditions can meet the water resistance requirements of some severe service environments, especially in the sea, ports, and cold regions, and western regions with high concentration of corrosive media

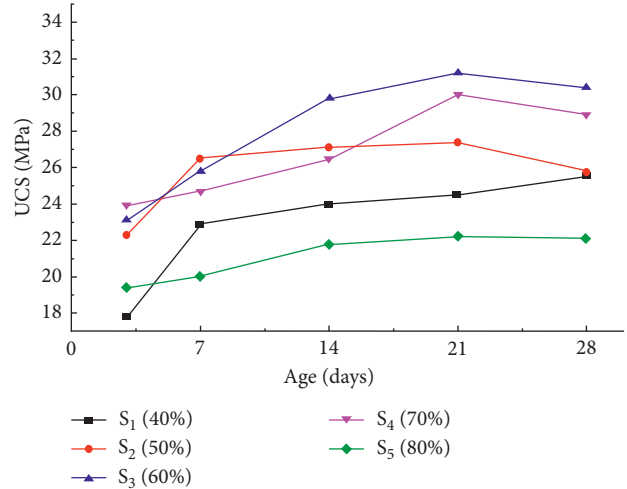


FIGURE 5: Compressive strength of different humidity.

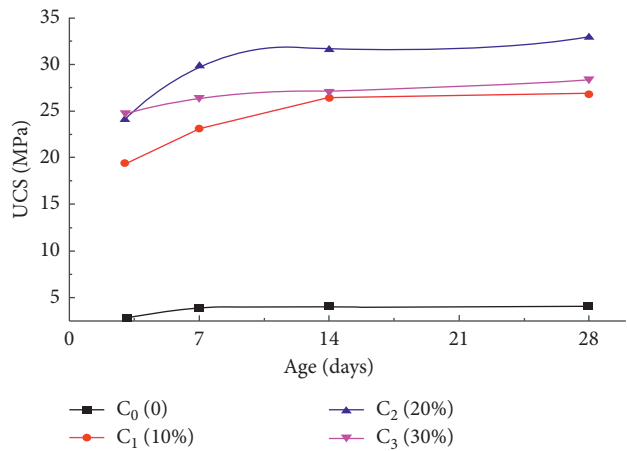


FIGURE 6: Compressive strength of different CO_2 concentrations.

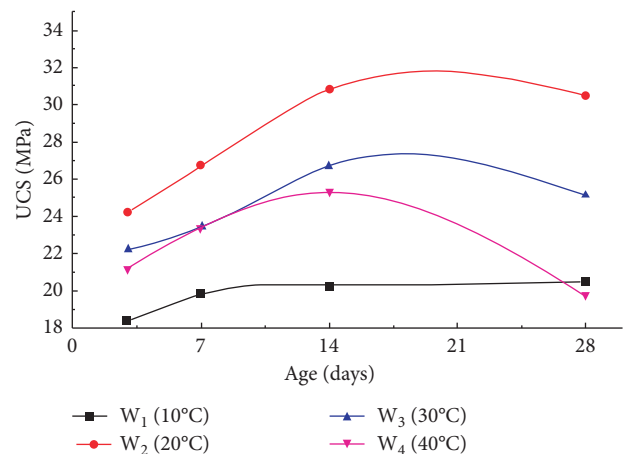


FIGURE 7: Compressive strength of different temperatures.

in the groundwater, coastal areas, and inland areas is tested. The index of water resistance is the softening coefficient; according to the softening coefficient, the water resistance of

active magnesium oxide carbonized block can be evaluated. From the carbonization to the 28th day of the test block, five test pieces were selected for the test, and the test piece was a cylinder having a height of 80 mm and a diameter of 5 mm. The five pieces were numbered as S_1 , S_2 , S_3 , S_4 , and S_5 . The selected five test pieces were immersed in water for 1–3 days; after that, the surface moisture was wiped out, and then the strength of the five test pieces was tested. According to the steps of the softening coefficient test in the test method for the performance of autoclaved aerated concrete, the specific steps of the test are carried out. Table 3 shows the water resistance test results of the carbonized blocks.

Putting the sample into the water, the shape of the sample does not change significantly from the previous. However, since the test piece was placed in water for a long time and chemically reacted with water, a small amount of magnesium carbonate trihydrate ($MgCO_3 \cdot 3H_2O$) and silicate crystals were precipitated on the surface of the test piece. When the sample is removed after 3 days, it will be found that the water will drop out of the sample, but soon drip dry, due to the presence of pores in the test piece. During the compression process of the test block, the failure mode of the test block is not significantly different from that of the test block without water immersion. However, due to the high compactness of the active magnesium oxide carbonized block, there will be a small amount of magnesium oxide not involved in the reaction (see the white part shown in Figure 8).

The test has determined that the softening coefficient of the block after putting in water is 0.9576. From the results, the compressive strength of the active magnesium oxide carbonized block is not significantly reduced. The increase in the strength of A_2 may be due to the presence of CO_2 in water. When the test block is placed in water, the strength of the test block is increased by the reaction of magnesium oxide without reaction with water and CO_2 in water. The active magnesium oxide carbon block has high water resistance.

3.5. Freezing and Thawing Cycle Test. Through measuring the damage of the magnesia carbide block during freeze-thaw cycle and measuring the compressive strength loss rate and mass loss rate of the active magnesia carbide block after the specified freeze-thaw cycle test, the frost resistance of the block is evaluated. The test block is composed of 80 mm high and 50 mm diameter cylindrical blocks in one group with 5 pieces in each group. Respectively, they were numbered D_1 , D_2 , D_3 , D_4 , and D_5 . The number of freeze-thaw cycles of freeze-thaw specimens is 25 cycles according to the specification for the number of freeze-resisting times in the hot summer freezing area. The temperature of the specimens was lowered to $-15^\circ C$ and began to count for 4 hours, and then water was released to dissolve, and they were heated up to $20^\circ C$ and began to count for 2 hours as a cycle. The test procedure was carried out in accordance with the freeze resistance test procedure in the “Test Methods for the Small Concrete Hollow Block”. The mass loss rate and compressive strength loss rate of the active magnesium oxide carbonized block after freeze-thaw are shown in Tables 4 and 5.

TABLE 3: Compressive strength after water immersion.

Numbering	Diameter (mm)	Destructive load (kN)	Compressive strength (MPa)
S_1	50	17.9	18.14
S_2	50	20.4	20.79
S_3	50	19.7	20.08
S_4	50	19.2	19.57
S_5	50	19.2	19.57
Arithmetic mean			19.63

According to the requirement of dry shrinkage value of blocks in “Test Methods for the Small Concrete Hollow Block” [17–19], the influence of the pressure-temperature coupling on the block displacement of the block is also tested in this experiment. The relevant test was carried out using the frost heaving-thawing universal testing machine. The specific parameters are as follows: displacement change rate—0.004 mm/s; displacement final change—2 mm; temperature settings—ambient temperature to $-15^\circ C$; and data acquisition—2 times/s. The results are shown in Figure 9.

There was no obvious change in the appearance of the sample during freeze-thaw cycles. After freezing resistance of the sample, it was obvious that the temperature of the sample was low, and the block did not show freeze-thaw damage. After the sample was placed at $20^\circ C$ for 2 hours, it was obvious that a few crystals appeared around the sample. It can be seen from Figure 9 that the large displacement in the AB stage is due to instrument error, the BC stage temperature has no effect on sample displacement changes due to the coupling of pressure and temperature, and the displacement of the specimen is greatly changed in the CD stage. In the DE stage, the temperature plays a dominant role, the pressure gradually decreases, and the displacement of the sample is 2 mm, and this means that the durability of the test block is well. The freeze-thaw loss rate of the sample mass is less than 5%, and the freeze-thaw loss rate of the compressive strength is less than 25%, which also shows that the sample has good frost resistance.

3.6. Pipe Pile Preparation Application Analysis. The mixing, molding, and curing of PHC pipe pile determine the workability of concrete. The good workability of pipe pile concrete is the key to ensure the quality and production efficiency of pipe pile. Sand and stone aggregate have significant influence on the workability and compressive strength of pipe pile concrete. Sand and stone aggregate with low mud content, good gradation, and sufficient strength should be used for pipe pile preparation. However, under the process, current production conditions indicate that the quality is low and the price is high. Besides, the production cost of the pipe piles is difficult to control. For large building projects and underground projects, when ordinary concrete is used, the concrete structure has a large section, large self-weight, insufficient bearing capacity, high transportation and pouring capacity, and excessive consumption of materials and energy, which really cannot meet the design and construction requirements well. The technology of Portland

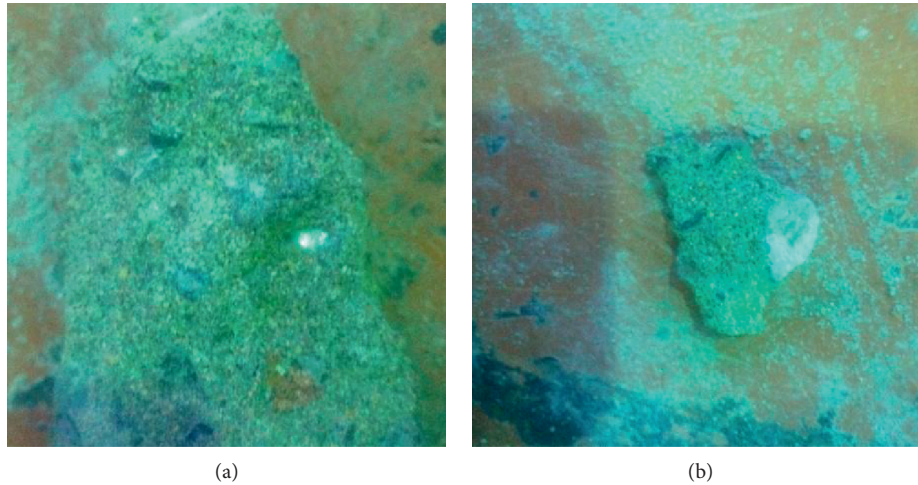


FIGURE 8: Picture inside the sample.

TABLE 4: Mass loss rate of active magnesium oxide carbonized block after freeze-thaw.

Numbering	Quality before freezing and thawing (g)	Quality after freezing and thawing (g)	Loss rate (%)
D ₁	362.1	357.3	1.33
D ₂	358.9	356.7	0.61
D ₃	375.2	371.4	1.01
D ₄	365.4	362.3	0.85
D ₅	371.6	366.1	1.48
Arithmetic mean			1.06

TABLE 5: Compressive strength loss rate after freeze-thaw.

Numbering	Compressive strength before freezing and thawing (MPa)	Compressive strength after freezing and thawing (MPa)	Compressive strength loss rate (%)
D ₁	24.5	22.1	9.80
D ₂	24.0	22.3	7.08
D ₃	26.5	23.2	12.45
D ₄	24.2	22.4	7.43
D ₅	25.5	19.4	23.92
Arithmetic mean			12.14

cement, active mineral admixture, and high-efficiency water reducer are more mature. Its main mechanism is to reduce the water-binder ratio of concrete while reducing the content of harmful pores and defects in the concrete structure, to reduce the alkalinity of hydration products, and to promote the conversion of low-strength hydration products to high-strength hydration products. The strength of concrete materials mainly depends on the ratio of water to cement. According to the classical water-cement ratio theory, the lower the ratio of water to cement ratio is, the higher the strength of concrete is. In the preparation of high-strength concrete, the water-cement ratio should be reduced as much as possible while maintaining the concrete's

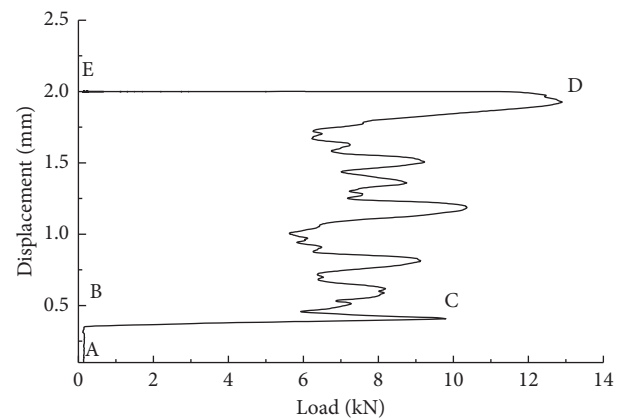


FIGURE 9: The influence of pressure-temperature coupling on block displacement.

working performance. In order to realize the bureaucratic and bureaucratic performance in coagulation, in addition to the control of the water-binder ratio, the selection of raw materials is also a key factor in the preparation of high-strength concrete. At the same time, it is also necessary to improve the compressive strength of concrete, significantly improve the durability of concrete structures, and improve the application of prefabricated concrete pipe piles in geotechnical engineering examples. The development of energy-saving preparation technology for high-strength and high-performance tubular pile concrete has achieved a new breakthrough in the concrete material system, which provides a better theoretical basis for the popularization and application of tubular pile in underground engineering and, at the same time, opens a new way to the high-performance and long-life of concrete structures in complex environments.

4. Conclusions

- (1) The optimum content of active magnesium oxide carbonized block is 35%. The optimum carbonization environment is humidity 60%, temperature

20°C, and 20% CO₂. Best forming method is 10 MPa pressure. The best optimum water-cement ratio is 1.0.

- (2) With the greater the compressive strength, the content of active magnesium oxide is the higher, and the compressive strength of the carbonized block reaches or even exceeds 80% on the 3rd day of carbonization, and the maximum compressive strength is 2–3 times of that of the ordinary cement block.
- (3) Compared with ordinary cement block, active magnesium oxide as the curing agent for masonry can reduce energy consumption and CO₂ emission; the popularization and application of this energy-saving technology are of great significance to the energy saving and emission reduction and sustainable development of pipe pile industry and has a broad application prospect.

Data Availability

The data used to support the findings of this study are included within the article.

Conflicts of Interest

The authors declare that they have no conflicts of interest.

Acknowledgments

The National Natural Science Foundation of China (51604006) is gratefully acknowledged.

References

- [1] N. Luo, *Study on Environmental Load of Chinese Sintered Brick Manufacturing Process*, Beijing Industry University, Beijing, China, 2009.
- [2] J. Harrison, "Reactive magnesium oxide cements," US. Patent WO01 55049 A1, 2001.
- [3] J. Harrison, "New cements based on the addition of reactive magnesia to Portland cement with or without added pozzolan," in *Proceedings of CIA Conference: Concrete in the Third Millennium*, Brisbane, Australia, August 2003.
- [4] H. Ge, T. Deng, Y. Yao, and Y. Guo, "Research progress of active MgO production process," *Trace Element Science in Guangdong*, vol. 12, pp. 29–34, 2010.
- [5] M. Liska and A. Al-Tabbaa, "Performance of magnesia cements in porous blocks in acid and magnesium environments," *Advances in Cement Research*, vol. 24, no. 4, pp. 221–232, 2012.
- [6] A. Cwirzen and K. H. Cwirzen, "Effects of reactive magnesia on microstructure and frost durability of Portland cement-based binders," *Journal of Civil Engineering*, vol. 25, no. 12, pp. 1941–1950, 2013.
- [7] Y. Yi, M. Liska, C. Unluer, and A. Al-Tabbaa, "Carbonating magnesia for soil stabilization," *Canadian Geotechnical Journal*, vol. 50, no. 8, pp. 899–905, 2013.
- [8] Y. Yi, *Sustainable Novel Deep Mixing Methods and Theory*, Southeast University, Nanjing, China, 2013.
- [9] J. Formosaa, A. M. Lacastab, A. Navarroc et al., "Magnesium Phosphate Cements formulated with a low-grade MgO by-product: physico-mechanical and durability aspects," *Construction and Building Materials*, vol. 91, pp. 150–157, 2015.
- [10] H. Zhang, K. Chen, and P. Xi, "Study on performance and mechanism of carbonized blocks based on active MgO content," *Journal of Building Materials*, vol. 6, 2017.
- [11] L. Mo and K. P. Daman, "Microstructure of high-concentration carbon dioxide carbonized active magnesium oxide cement paste," *Journal of the Chinese Ceramic Society*, vol. 2, pp. 142–149, 2014.
- [12] G. Cai, S. Liu, Y. Du, Z. Xu, and J. Cao, "Contrastive experiment of different activated magnesium oxide carbonized silt," *Journal of Southeast University*, vol. 5, pp. 958–963, 2015.
- [13] Q. Ye, Y. Pei, and H. Chen, "Effect of fly ash on the expansion of magnesia cement—the influence of fly ash on the structure and mechanical properties of the environment where the expansion source is located," *Material Review*, vol. S2, pp. 465–467+477, 2011.
- [14] L. W. Mo and D. Panesar, "Accelerated carbonation—a potential approach to sequester CO₂ in cement paste containing slag and reactive MgO," *Cement and Concrete Composites*, vol. 43, pp. 69–77, 2013.
- [15] J. Liu, D. Ding, and Z. Liu, "Effect of curing methods and wet curing duration on properties of plain and slag-cement concrete," *Journal of the Chinese Ceramic Society*, vol. 36, no. 5, pp. 901–911, 2008.
- [16] M. Collepardi, *The New Concrete*, Translated by S. Liu, F. Leng, and L. Li, China Building Materials Industry Press, Beijing, China, 2008.
- [17] GB/T4111-1997, *Test Methods for the Small Concrete Hollow Block*, Standards Press of China, Beijing, China, 1997.
- [18] GB11968-2006, *Autoclaved Aerated Concrete Blocks*, Standards Press of China, Beijing, China, 2006.
- [19] GB/T 11969-2008, *Test Methods of Autoclaved Aerated Concrete*, Standards Press of China, Beijing, China, 2008.

Research Article

Study on Compaction Characteristics and Construction Control of Mixtures of Red Clay and Gravel

Biao Zeng ^{1,2} Lin-feng Wang ^{1,2} Yun Tian ^{1,2} Tao-ruì Zeng ^{1,2} and Bing Li ³

¹Key Laboratory of Geological Hazards Mitigation for Mountainous Highway and Waterway of Chongqing Municipal Education Commission, Chongqing Jiaotong University, Chongqing, China

²School of River & Ocean Engineering, Chongqing Jiaotong University, Chongqing, China

³China Communication South Road and Bridge Company, Ltd., Beijing, China

Correspondence should be addressed to Lin-feng Wang; wanglinfeng@cqjtu.edu.cn

Received 15 June 2018; Revised 27 August 2018; Accepted 30 September 2018; Published 4 November 2018

Academic Editor: Dingwen Zhang

Copyright © 2018 Biao Zeng et al. This is an open access article distributed under the Creative Commons Attribution License, which permits unrestricted use, distribution, and reproduction in any medium, provided the original work is properly cited.

Red clay cannot be used as embankment filler directly due to its water-sensitive property. Gravel is usually added into red clay to enhance its performance in engineering practice. In order to investigate the influence of mixtures of red clay and gravel on the road performance, gravitational compaction experiment of red clay and vibratory compaction experiment of mixtures of red clay and gravel were conducted, respectively. The results indicate that compaction curves of red clay have double peak; the second peak is the real maximum dry density, and its corresponding moisture content is the optimal moisture content. The dry density of mixtures of red clay and gravel is influenced by the content of gravel, vibration frequency, and vibration time. The optimal content of gravel is 30%, the best vibration frequency is 45 Hz, and the optimal vibration time is 5 minutes for the mixtures of red clay and gravel in this study. The effectiveness of optimal content of gravel and optimum vibration parameters was confirmed by a CBR test. According to the compaction experiment results and actual situation in the field, a suitable construction method of subgrade using the mixtures of red clay and gravel was put forward. The feasibility of this method was also confirmed by postconstruction deformation data of the field test embankment.

1. Introduction

Red clay is widely distributed in the southwest of China, which is water-sensitive [1]. Because of its large porosity, small density, and high moisture content, it is very easy to lead to roadbed subsidence, shallow sliding collapse, and other engineering disasters if it is used as roadbed filler directly [2, 3]. However, with the development of highways in China, red clay is inevitably used in subgrade construction. There are two kinds of methods to improve its road performance in engineering, such as the chemical method and physical method. The chemical method can cause a series of chemical reactions to absorb soil moisture and create cementitious substances by adding lime, cement, or other chemical materials. It makes the red clay compaction easy and increases its strength [4–8]. But, it is difficult to mix

evenly in the construction site by the chemical method. Therefore, the actual effect is not obvious. The physical method often improves the overall strength of the soil by materials with higher strength such as gravel and industrial slag. By contrast, this kind of method has lower cost, simpler operation, and can be used widely [9–11].

In fact, gravel is often used to improve road performance of red clay in construction sites, but laboratory research focused on the effect of gravel on the performance is seldom. In this study, in order to achieve the best compacting effect, a gravitational compaction of red clay and a vibrating compaction of mixtures of red clay and gravel were conducted. According to the compaction experiment results and the actual situation in the field, a suitable construction method of subgrade for the mixtures of red clay and gravel was put forward.

2. Materials and Methods

2.1. Materials

2.1.1. Red Clay. The samples of red clay used in this experiment were taken from the Zun-Gui Highway in China. Clay depth ranges from 5 meters to 10 meters. The appearance is brownish red with white and dark green impurities. The samples are in plastic state with high natural moisture content. Their physical properties and material composition are shown in Tables 1 and 2, respectively.

According to Table 1, red clay has a high natural moisture content and the liquid limit of red clay is 103.1. The plastic limit is 30.6, and the plasticity index reaches to 72.5. Table 1 shows that the physical properties of red clay are quite particular. The reasons for these special properties are mainly related to the material composition and structural characteristics of red clay. It can be seen from Table 2 that there are many fine particles and high content of clay minerals and oxides in red clay. Mineral particles are mainly pellets with mass and fine pores. The free oxides between particles can form a cemented connection with good water stability, and the water in the soil is mainly bound water. The porous space provides a storage space for it [12, 13], so red clay has high natural moisture content and high liquid limit moisture content. In spite of this, the consistency of red clay is 0.94. Its state is plastic state, and some are even solid state. Therefore, red clay has some bad physical properties such as high moisture content, high plasticity index, and high void ratio while it has some good mechanical properties such as high strength and medium compressibility. This also provides a possibility for the application of red clay as roadbed filler.

2.1.2. Gravel. The samples of gravel were also taken from the Zun-Gui Highway in China. It is a type of dolomite with gray colour and hard texture. Its particle gradation curve is shown in Figure 1.

2.2. Experimental Scheme

2.2.1. Gravitational Compaction Experiment. This experiment was strictly referenced to the “standard method for geotechnical test” [14]. According to the method, the gravitational compaction experiment of red clay was carried out. Two methods for sample preparation were used in this experiment. One was the dry method, which dried red clay in the oven and controlled its moisture content by adding water. The other was the wet method, which dried the red clay under the sun and controlled the moisture content through sun-dry time. After sample preparation, loose red clay would be placed in a cylinder whose diameter is 10 cm and height is 12.7 cm for gravitational compaction. The dry density of samples in different moisture content would be recorded. The compaction curve was drawn to obtain the maximum dry density and the optimum moisture content [15–17], and the optimal moisture content was taken as the

TABLE 1: Physical and mechanical properties of red clay.

W_L (%)	W_P (%)	Natural moisture content (%)	Free expansion rate (%)	Plasticity index	Consistency
103.1	30.6	35.0	25.3	72.5	0.94

control index moisture content in the experiment of vibrating compaction.

2.2.2. Vibratory Compaction Experiment. Because both the nature of clay and gravel can be shown in the mixtures of red clay and gravel, the particle diameter of the gravel is larger than the maximum size standard stipulated of gravitational compaction experiment. It is not feasible to research the compaction characteristics of mixtures of red clay and gravel with the gravitational compaction method. Therefore, the experiment of vibratory compaction was conducted. Different amounts of gravel (10%, 20%, 30%, 40%, and 60%) were mixed into red clay in this experiment, and then water was added and the material was choked up for 24 hours. After sample preparation, loose mixtures of red clay and gravel would be placed in a cylinder whose diameter is 28 cm and height is 25 cm for vibratory compaction. The optimal content of gravel was obtained by analyzing the relationship between dry density and gravel content. Then, by changing vibration frequency and vibration time, the relationship between vibration parameters and dry density was analyzed. Finally, the optimal vibration parameters were obtained.

2.2.3. CBR Test. CBR, known as California bearing ratio, is a method of judging the carrying capacity of materials, which is presented by the California Highway Bureau. At present, it has been an important basis for the selection of subgrade filler and the judgement of compaction strength [8, 18, 19]. This test was to process the red clay under the optimum moisture content by gravitational compaction and process the mixtures of red clay and gravel under the optimal gravel content by vibratory compaction. The optimal vibration parameters were used in the vibratory compaction. The size of the CBR test was the same as that of compaction experiment. Then, the strength of these two methods was tested on the CBR tester to validate the effect of gravel treated red clay.

3. Results and Discussion

3.1. Double Peak in the Compaction Curve of Red Clay. In the light of the results of gravitational compaction experiment of red clay, the relationships between dry density and moisture content are shown in Figure 2.

According to the curve in Figure 2, the maximum dry density of the dry method is 1.56 g/cm^3 and the optimal moisture content is 27%. And, the maximum dry density of the wet method is 1.43 g/cm^3 , and the optimal moisture content is 28.1%. By comparing the data above, it is obvious

TABLE 2: Material composition of red clay.

Material composition	Clay mineral (65%)				Free oxide (23%)				Detrital minerals (12%)
	Kaolinite	Chlorite	Illite	Others	Silica	Alumina	Ferric oxide	Others	
Content (%)	8.71	27.75	10.92	17.62	12.02	6.06	2.71	2.14	—

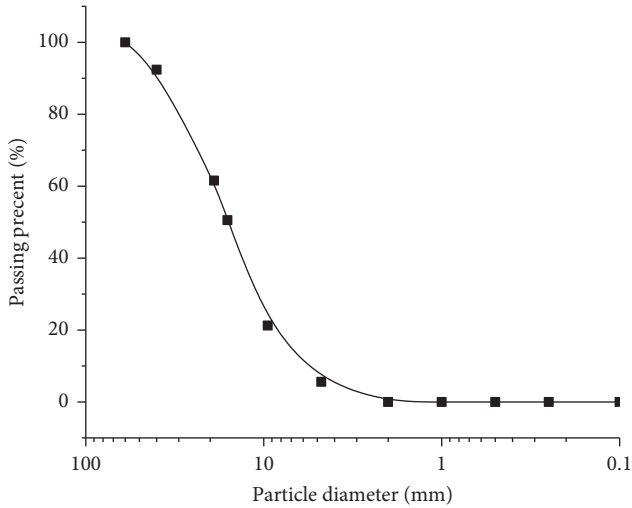


FIGURE 1: Granular grading of gravel.

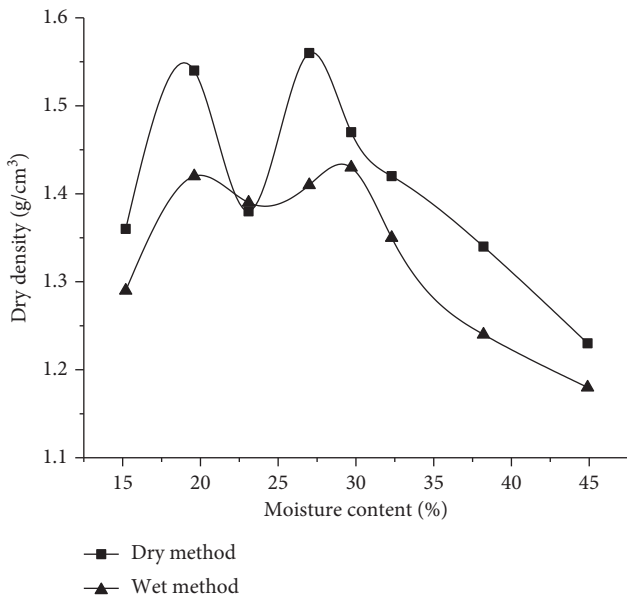


FIGURE 2: Relationship between dry density and moisture content.

that the maximum dry density of the dry method is larger than that of the wet method, while the optimal moisture content of the dry method is smaller than the wet method. After the analysis of this phenomenon, one of the important reasons discovered is that red clay is irreversible. The dry method compaction is equivalent to a dry-wet circulation [20–22]. The structure of the red clay is destroyed, and it results in the loss of bound water. But, the wet method compaction helps keep the bound water. Therefore, it is

concluded that the optimal moisture content is higher than that of the dry method.

Actually, the results of the dry method are inapplicable in the construction sites. This is because its maximum dry density is higher and optimum moisture content is lower. The moisture content of natural red clay is high; the cost of the dry method is much higher than that of the wet method. Therefore, the result of the wet method is more conducive to guide engineering practice.

According to Figure 2, it can also be found that the curve of gravitation compaction appears as a double peak. It is obvious that the first peak is lower than the second peak. When it comes to this phenomenon, reasons can be found in the following aspects. First, the soil structure of red clay is too strong to destroy by compaction energy when it is of low moisture content. Therefore, the first peak appears. Second, red clay is softening gradually while increasing the moisture content; the heavy hammer of gravitation compaction energy can destroy its structure, and then red clay is recomacted. The dry density becomes largest when the moisture content reached a critical value. So, another peak appears. Although there are two peaks of dry density in the compaction curve, it is known from Table 1 that the moisture content of the red clay in the natural state is high. It is difficult to reach the low moisture content without manual control. Therefore, it is considered that the second peak is the real maximum dry density, and its corresponding moisture content is the optimal moisture content.

3.2. Vibration Compaction Characteristics of Mixtures of Red Clay and Gravel

3.2.1. *Effect of Gravel Content on Dry Density.* Because of the difference between red clay and gravel in material density, the dry density can vary with the change of content of clay and gravel under certain conditions. The relationship between content of gravel and dry density is shown in Figure 3.

It can be seen from Figure 3 that the dry density of samples increases with the increase of gravel content in the same vibration parameters, but they are not linear. The curve can be roughly divided into three sections. Firstly, when the gravel content is less than 20%, the slope of curve is low and dry density increases slowly. Secondly, when the gravel content is between 20% and 40%, the slope rises sharply. At the same time, the value of dry density increases sharply. Finally, when gravel content is between 40% and 60%, with the increase of gravel content, dry density is still rising, but it rises slowly again.

The main reason for this phenomenon is that the red clay has larger specific surface area, larger void ratio, and smaller quality [23]. Therefore, with the increase of gravel

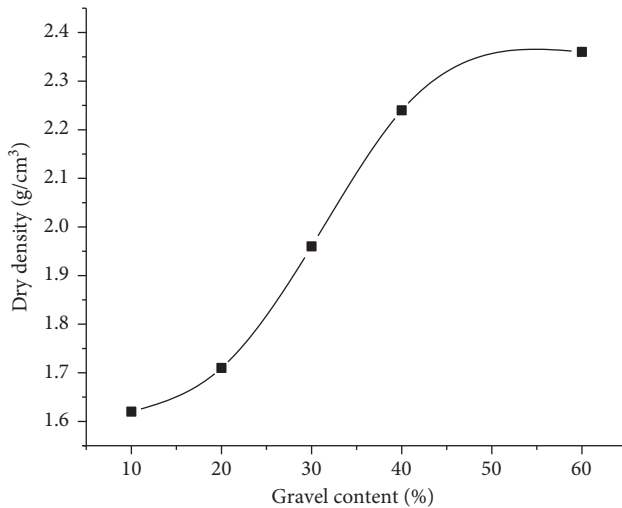


FIGURE 3: Relationship between dry density and gravel content.

content, the dry density of filler increases gradually. When the content of gravel is low (<20%), the gravel fails to form a skeleton in the red clay. The gravel is suspending in the red clay. It can be called as “suspension-compaction structure.” The dry density increases slowly because the red clay still plays a major role. With the increase of gravel content (20%–40%), gravel plays a role of skeleton in the soil gradually. The red clay can be used as fine material filling to skeleton pores, crude and fine material squeeze each other, and the degree of compaction is further enhanced. The mixtures of red clay and gravel reached a densest state. When the content of gravel is large (40%–60%), gravel continues to play a role of skeleton. However, the vibration parameters are defined, and there is not enough energy to squeeze the mixtures. Although the dry density results in an enlarged appearance, the degree of compaction is actually reduced when compared with the preceding stage (20%-40%). There are similar phenomena in the construction site; when the vibration parameters are certain, it is uneconomical and unscientific to improve the compaction quality by increasing the content of gravel simply. With the increase of gravel content, the construction cost and construction difficulty would increase step-by-step, respectively, and it would not improve the degree of subgrade compaction obviously. It is defined that the optimal gravel content is 30% based on a comprehensive consideration of experimental data and the actual situation of engineering.

3.2.2. Effect of Vibration Frequency on Dry Density.

Vibratory compaction is a resonance of the mixtures through high frequency vibration produced by the vibrating compaction instrument. When the vibratory frequency is close to its own natural frequency of the mixtures, the particles will rearrange and squeeze each other. At the same time, small particles will be embedded in the pores of large particles to increase the degree of compaction. Therefore, the frequency of vibration has a great influence on the dry density and compactness of the mixtures.

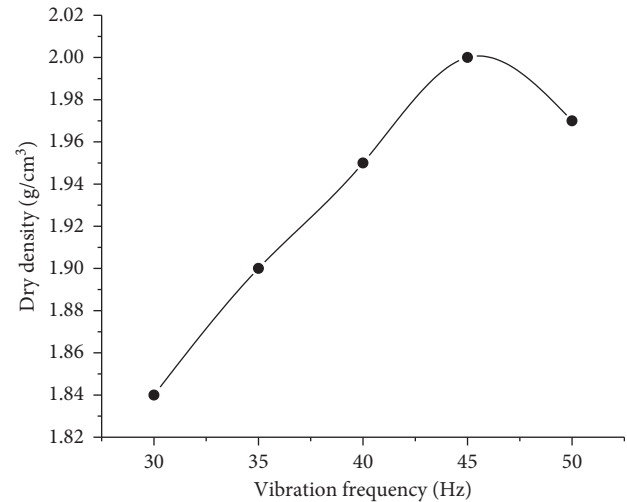


FIGURE 4: Relationship between dry density and vibration frequency.

According to the experiment scheme, the relationship between vibration frequency and dry density is shown in Figure 4.

It can be concluded from Figure 4 that, when the time of vibration and the content of gravel are certain, the dry density of the mixtures of red clay and gravel increases at first and then decreases. There is a peak on the curve. Based on the analysis, this phenomenon can be explained from the respect of energy. With the increase of frequency, the original stress of the mixtures of red clay and gravel is damaged, and then the particles are rearranged. Under the effect of vibration and pressure, the vibrating energy is absorbed by filler, and the filler is compacted gradually until the optimal frequency occurs, the absorbing energy reaches the maximum value. If the frequency continues to increase, the excess energy cannot be absorbed by filler. What's more, it can destroy the filler which has been compacted. So, there is a downward trend in dry density. Similar situation will appear on the construction site. When the intensity of the vibratory roller is too large, it not only fails to compact subgrade but also can damage the structure of subgrade filler, resulting in irregular impact or excessive compaction. According to the experimental results, the optimal vibration compaction frequency of the mixtures is 45 Hz.

3.2.3. Effect of Vibration Time on Dry Density. During the vibration compaction experiment, the dry density of mixtures of red clay and gravel not only relates to gravel content and vibration frequency but also has a close relationship with vibration time. The relationship between vibration time and dry density is shown in Figure 5.

It can be seen that when the content of gravel and vibration frequency are certain, the dry density of mixtures of red clay and gravel increases with the increasing vibration time. As shown in Figure 5, the relationship between vibration time and dry density is close to linear when the

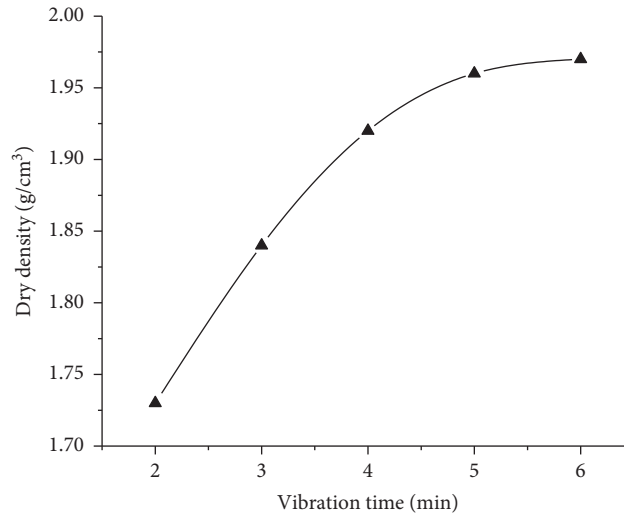


FIGURE 5: Relationship between dry density and vibration time.

TABLE 3: Minimum strength and compaction degree of highway subgrade construction.

Project classification	Subgrade part	Depth (m)	CBR (%)	Maximum particle size of packing (mm)	Compactness (%)
Fill subgrade	Upper roadbed	0–0.3	8	<100	>97
	Lower roadbed	0.3–0.8	5	<100	>97
	Upper embankment	0.8–1.5	4	<150	>95
	Lower embankment	>1.5	3	<150	>93

vibration time is less than 4 min. If the vibration time continues to increase, the slope of the curve becomes lower gradually and dry density increases slowly. With the increase of time, dry density changes little when the vibration time is more than 5 min. So, it is concluded that the compaction efficiency is best when the vibration time is 5 min.

3.3. CBR Test. The current standard “technical code for construction of highway subgrade” clearly stipulates the minimum strength and compactness of the subgrade, and the specific parameters are shown in Table 3 [24]. The results of the CBR test are shown in Table 4. It can be seen that the modified red clay is better than the pure red clay in the CBR value, water absorption, and swelling capacity. In particular, the improvement of the CBR value makes the subgrade strength increase about 3 times, which can come to the standard requirement of the CBR value of the filler in each position of the roadbed. Therefore, the compaction properties and strength properties of the compacted mixtures of red clay and gravel under the optimal gravel content and the optimal vibration parameters have been significantly improved in the CBR test.

4. Field Application

From the results of the vibration compaction experiment, the optimum vibration frequency of the mixtures of red clay and gravel is 45 Hz and the optimum vibration time is 5 min. Too high or too low vibration frequency and too long or too short vibration time is not conducive to the compaction of filler. According to the comparison and selection of the road

roller on the construction site, the rolling effect of the “YZC10J double-steel wheel vibratory roller” is similar to that of the indoor test parameters, so this road roller is adopted to compact the filler. Some field tests were conducted for ensuring the optimal compaction time of 5 min. It is found that the compacting effect is the same as 5 min indoor compaction when the speed of the roller is 4.8 km/h and the rolling times are 4. The specific working parameters are shown in Table 5.

In the filling process of subgrade, there is also a very important issue to consider, that is, the “loose paving thickness” of the mixtures of red clay and gravel [25]. In fact, there is no large type of clay and gravel mixing equipment, which is the reason why the clay and gravel mixed embankment cannot be used widely [26, 27]. Therefore, this paper proposes to use the rotary tiller to mix red clay and gravel. Red clay and gravel are used in different levels. The operation depth of the rotary tiller is 25 cm, so the depth is used to control different content of red clay and gravel, that is, first spreading about $25 * 0.7 = 17.5$ cm thickness of red clay, and then spreading about $25 * 0.3 = 7.5$ cm of gravel, afterwards, using the rotary tiller for ploughing. The mixing process can not only reduce the natural moisture content of red clay but also makes the mixtures evenly distributed and easy to compaction. Use the road roller to compact it after mixing. When a layer of filler is compacted, repeat the above operation. This method has good effect on practical use. The compaction degree is tested by using the sand replacement method. The results show that the compaction degree is above 94%, which is much higher than that of filling with red clay directly.

TABLE 4: The results of CBR test.

Filler	Gravel content (%)	Compaction method	CBR (%)	Water absorption (g)	Swelling capacity (%)
Red clay	0	Heavy compaction	3.5	110	1.58
Mixtures of red clay and gravel	30	Vibratory compaction	11	80	0.5

TABLE 5: The working parameters of YZC10J roller.

Model type	Weight (kg)	Vibration force (kN)	Vibration frequency (Hz)	Speed (km/h)			Width (mm)
YZC10J	10000	98	42	2.4	4.8	8.4	1700



FIGURE 6: The schematic diagram of the location of the settlement monitoring point.

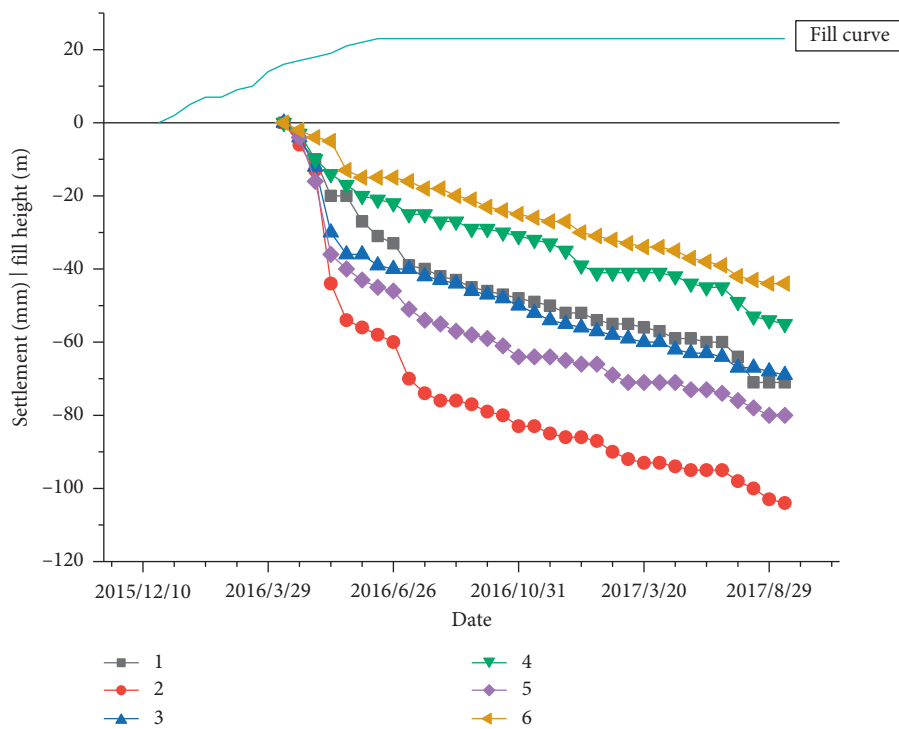


FIGURE 7: The relation curve between settlement and time in subgrade monitoring point.

In order to verify the actual improvement effect of the optimum gravel content and the optimum vibration parameters, a field test embankment was filled by using the road roller and compaction method. And, a real time monitoring of the typical section in the field test embankment was conducted. The field test embankment was filled with 23 m height. The embankment began to be filled in December 2015 and completed in June 2016. The schematic diagram of the location of the settlement monitoring point is shown in Figure 6.

As shown in Figure 7, the slope of the settlement curve is high in the first three months and then slows down. It shows that the early settlement of the roadbed is large, and then, the settlement decreases gradually. The settlement increment is approximately 20 mm in May, and settlement increment of some point is over 40 mm. The settlement increment is 8 mm in June, and it slows down gradually. The settlement increment is 7 mm in July, and the monthly settlement increment is maintained within 5 mm until May 2017. After that, the settlement increment is about 1 to 2 mm, the settlement gradually converged. Finally, the total settlement of each monitoring point is between 40 mm and 110 mm. It is much lower than the allowable settlement of expressway subgrade which is 300 mm. Therefore, with the appropriate construction parameters, the compactness and settlement of mixtures of red clay and gravel can reach the standard. It can be used as roadbed filler. It shows that the application of this method is successful.

5. Conclusions

This paper focuses on the compaction characteristics of red clay and mixtures of red clay and gravel. The effectiveness of optimal content of gravel and optimum vibration parameters is confirmed by the CBR test. A suitable construction method of subgrade for the mixtures is put forward. Some conclusions drawn from this study are as follows:

- (i) There are two peaks in the compaction curve of red clay. This phenomenon is caused by strong structural property of red clay with low moisture content. It is considered that the second peak is the real maximum dry density; its corresponding moisture content is the optimal moisture content in a comprehensive consideration of the actual situation of engineering.
- (ii) In the experiment of vibratory compaction, the dry density of mixtures increases with the increase of gravel content under the condition of the same vibration parameters. However, there is an optimum content of gravel in the mixtures of red clay and gravel. When the gravel content is 30%, it can control construction cost while ensuring compaction quality.
- (iii) The change of vibration parameters leads to the change of vibration energy in the experiment of vibratory compaction. The energy absorbed by mixtures has a threshold value. There are optimum vibration parameters in this experiment. When the vibration frequency is 45 Hz and the vibration time is 5 min, the compaction efficiency of the mixtures of red clay and gravel is the best.
- (iv) The compaction properties and strength properties of the compacted mixtures of red clay and gravel under the optimal gravel content and the optimal vibration parameters are significantly improved in the CBR test.
- (v) According to the indoor compaction experiment results and the actual situation in the field, a suitable construction method of subgrade for the mixture of red clay and gravel is put forward. The feasibility of this method is also confirmed by postconstruction deformation data of the field test embankment.

Data Availability

The data used to support the findings of this study are included within the article.

Conflicts of Interest

The authors declare that they have no conflicts of interest.

Acknowledgments

The study was supported by the National Natural Science Foundation of China (51408084).

References

- [1] Y. Tang, K. Sun, and X. Zhang, "Microstructure changes of red clay during its loss and leakage in the karst rocky desertification area," *Environmental Earth Sciences*, vol. 75, no. 6, p. 537, 2016.
- [2] C. T. Gnanendran, J. Piratheepan, J. Ramanujam et al., "Accelerated laboratory pavement model test on cemented base and clay subgrade," *Geotechnical Testing Journal*, vol. 34, no. 4, article 103311, 2011.
- [3] J. M. Ling, W. Wang, and H. B. Wu, "Residual deformation of saturated clay subgrade under vehicle load," *Journal of Tongji University*, vol. 30, no. 11, pp. 1315–1320, 2002.
- [4] D. R. Snethen, G. A. Miller, and A. B. Cerato, "Evaluation and field verification of strength and structural improvement of chemically stabilized subgrade soil," *Field Studies*, vol. 4, no. 4, pp. 206–207, 2008.
- [5] A. S. Zaimoglu, "Optimization of unconfined compressive strength of fine-grained soils modified with polypropylene fibers and additive materials," *KSCE Journal of Civil Engineering*, vol. 19, no. 3, pp. 578–582, 2015.
- [6] M. Li, C. Fang, S. Kawasaki et al., "Fly ash incorporated with biocement to improve strength of expansive soil," *Scientific Reports*, vol. 8, no. 1, pp. 1–20, 2018.
- [7] R. D. V. Flores, G. D. Emidio, and W. F. V. Impe, "Small-strain shear modulus and strength increase of cement-treated clay," *Geotechnical Testing Journal*, vol. 33, no. 1, p. 62, 2010.
- [8] F. G. Bell, "Lime stabilization of clay minerals and soils," *Engineering Geology*, vol. 42, no. 4, pp. 223–237, 1996.

- [9] K. M. H. I. Ibrahim, "Effect of percentage of low plastic fines on the unsaturated shear strength of compacted gravel soil," *Ain Shams Engineering Journal*, vol. 6, no. 2, pp. 413–419, 2015.
- [10] M. Fall, J. P. Tisot, and I. K. Cisse, "Undrained behaviour of compacted gravel lateritic soils from western Senegal under monotonic and cyclic triaxial loading," *Engineering Geology*, vol. 47, no. 1-2, pp. 71–87, 1997.
- [11] J. S. Chen, T. Z. Tang, W. Y. B. Zhao et al., "Field tests study of concrete-cored sand-gravel piles applied to strengthen embankment engineering," *Journal of Hydraulic Engineering*, vol. 29, no. 7, pp. 957–962, 2007.
- [12] A. K. Jha and P. V. Sivapullaiah, "Mechanism of improvement in the strength and volume change behavior of lime stabilized soil," *Engineering Geology*, vol. 198, no. 2, pp. 53–64, 2015.
- [13] Z. L. Ding, J. M. Sun, S. L. Yang et al., "Geochemistry of the Pliocene red clay formation in the Chinese Loess Plateau and implications for its origin, source provenance and paleoclimate change," *Geochimica Et Cosmochimica Acta*, vol. 65, no. 6, pp. 901–913, 2001.
- [14] Highway Research Institute of Ministry of Communications, *Standard method for Geotechnical Test: JTG E40-2007*, China Communications Press, Beijing, China, 2007.
- [15] G. Richard, I. Cousin, J. F. Sillon et al., "Effect of compaction on the porosity of a silty soil: influence on unsaturated hydraulic properties," *European Journal of Soil Science*, vol. 52, no. 1, pp. 49–58, 2010.
- [16] J. Yang and L. Zou, "Experiment on mechanical indexes of natural gravel improved red clay and forecasting by mathematical model," *Journal of Highway and Transportation Research and Development*, vol. 32, no. 9, pp. 41–48, 2015.
- [17] V. Sivakumar and S. J. Wheeler, "Influence of compaction procedure on the mechanical behaviour of an unsaturated compacted clay. Part 1: wetting and isotropic compression," *Géotechnique*, vol. 50, no. 4, pp. 359–368, 2000.
- [18] S. A. Naeini and R. Ziaie-Moayed, "Effect of plasticity index and reinforcement on the CBR value of soft clay," *International Journal of Civil Engineering*, vol. 7, no. 2, pp. 124–130, 2009.
- [19] E. Ene and C. Okagbue, "Some basic geotechnical properties of expansive soil modified using pyroclastic dust," *Engineering Geology*, vol. 107, no. 1, pp. 61–65, 2009.
- [20] Y. J. Cui, M. Yahia-Aissa, and P. Delage, "A model for the volume change behavior of heavily compacted swelling clays," *Engineering Geology*, vol. 64, no. 2, pp. 233–250, 2002.
- [21] N. Z. Guo, J. F. Zou, L. Li et al., "Dynamic compaction theory and experiments in high roadbed filled with red sandgravel," *Journal of Central South University: Science and Technology*, vol. 39, no. 1, pp. 185–189, 2008.
- [22] Y.-R. Zheng, X. Lu, X.-Z. Li, and Y.-X. Feng, "Research on theory and technology of improving soft clay with DCM," *Chinese Journal of Geotechnical Engineering*, vol. 22, no. 1, pp. 18–22, 2000.
- [23] M. K. Zadeh, N. H. Mondol, and J. Jahren, "Experimental mechanical compaction of sands and sand-clay mixtures: a study to investigate evolution of gravel properties with full control on mineralogy and gravel texture," *Geophysical Prospecting*, vol. 64, no. 4, pp. 915–941, 2016.
- [24] CCCC First Highway Engineering Group Co. Ltd., *Technical Code for Construction of Highway Subgrade: JTG F10-2006*, China Communications Press, Beijing, China, 2006.
- [25] J. C. D. O. S. Horta, *The Design and Construction of Low-Volume Roads in the Northwestern Sahara*, Transportation Research Record, vol. 2, no. 1, pp. 281–304, 1987.
- [26] L. I. Jian-Guo, W. Xun, E. Branch et al., "Research on the relationship among roadbed bearing capacity, embankment stability and settlement," *Journal of Railway Engineering Society*, vol. 31, no. 9, pp. 12–15, 2014.
- [27] X. Yang, Y. Zhu, and N. Guo, "Strength and deformation characteristic of soil-gravel mixture and settlement prediction in high filled projects," *Chinese Journal of Gravel Mechanics and Engineering*, vol. 36, no. 7, pp. 1789–1790, 2017.

Research Article

Engineering Characteristics and Reinforcement Approaches of Organic Sandy Soil

Jun Hu ¹, Liang Jia ², Wei Wang ³, Hong Wei,⁴ and Juan Du¹

¹Associate Professor, College of Civil Engineering and Architecture, Hainan University, Haikou, Hainan 570228, China

²Associate Professor, College of Civil Engineering, Lanzhou University of Technology, Lanzhou, Gansu 730050, China

³Professor, School of Civil Engineering, Shaoxing University, Shaoxing, Zhejiang 312000, China

⁴Professor, College of Civil Engineering and Architecture, Hainan University, Haikou, Hainan 570228, China

Correspondence should be addressed to Wei Wang; wangwells@qq.com

Received 3 April 2018; Revised 11 August 2018; Accepted 10 September 2018; Published 24 October 2018

Academic Editor: Annan Zhou

Copyright © 2018 Jun Hu et al. This is an open access article distributed under the Creative Commons Attribution License, which permits unrestricted use, distribution, and reproduction in any medium, provided the original work is properly cited.

Organic sandy soil is widely distributed throughout Hainan Island. This study aimed at addressing the distribution, composition, and formation of organic sandy soil. The engineering properties of organic sandy soil were examined. The experimental results showed that the coefficient of uniformity and coefficient of curvature were 2.07 and 1.25, respectively. The maximum dry density and optimum water content were 1.723 g/cm³ and 12.23%, respectively. The undrained shear strength of organic sandy soil was around 37.5 kPa. The effective stress parameters c and φ were around 4 kPa and 23°, respectively. The compound tangent-exponential model was adopted for capturing the stress-strain behavior of organic sandy soil. As the unconfined compressive strength of the cement-admixed organic sandy soil was much lower than that of ordinary sand, some innovative ground improvement technologies were proposed for stabilizing organic sandy soil, such as thermal pile, fiber, and steel-, bamboo-, and freezing-cemented soil columns. The main purpose of these technologies is to enhance the bearing capacity of organic sandy soil but reduce the usage of cement, as the latter is not an eco-friendly material.

1. Introduction

Hainan is a rapidly growing tourism province in China with a very long coastline and plants of bays (Figure 1). Many construction projects are well under way in Hainan Island, especially in the coastal areas, so as to make it an international tourist island. Organic sandy soil is widely spread in this island, and field investigations have revealed that 8 of the 12 selected bays in Hainan Island have organic sandy soil (Haikou, Fengjia Bay, Yingge Bay, and Sanya). Organic soil is a material not suitable for engineering because of its high compressibility and low shear strength. It causes some engineering problems, such as inadequate strength after reinforcement or even failure of composite foundation because of its special engineering properties [1].

Although some studies have been conducted on organic soils [2–4], the knowledge of organic sand remains scanty. To

deal with organic soils for construction projects such as ground improvement, one commonly adopted method is to stabilize it with some chemical admixtures [5]. Stabilization of soft ground by deep mixing [6] and jet grouting [7] is widely employed in coastal areas, such as Singapore and Hainan Island, for stability and deformation control in many ground improvement and underground construction projects such as tunneling or deep excavations. The use of cement to enhance the engineering properties of soft soils or sands has been widely used and well established [8, 9]. However, whether traditional treatment methods are available for organic sandy soil is still unclear. This study investigated the engineering properties (e.g., strength parameters) of organic sandy soil and proposed some innovative ground improvement techniques for this kind of sand. The tests in the current study are conducted according to the Chinese Standard for the soil test method (GB/T50123-1999); some other standards are also

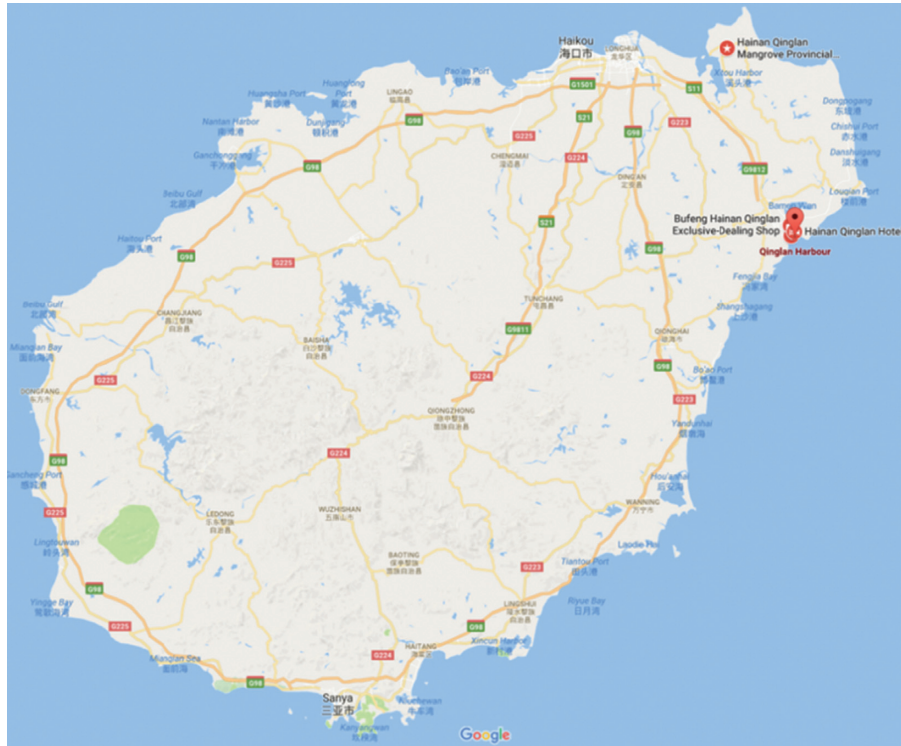


FIGURE 1: Map of key coastal bays in Hainan Province (Map data © 2018 Google).

referenced, such as ASTM and British Standard, which will be specified where they are used.

2. Formation of Organic Sandy Soil

The location for *in situ* sampling of organic sandy soil in one construction site at Qinglan Harbor in Wenchang City is shown in Figure 1 (the red point). A quantitative analysis was conducted by the ASTM D2974 [10] to check the organic content in the sand. The results showed that the soil contained between 5% and 8% of organic matter content (Table 1).

Figures 2 and 3 show the scanning electron microscopic images of organic sandy soil and ordinary sand, respectively. The arrangement of particles reflects the microstructure of *in situ* organic sandy soils, as the tested samples are directly obtained from field. The smooth surface of the organic sandy soil is covered by a layer that makes the surface smooth with a few pores (Figure 2), completely contrary to the rough and porous surface of ordinary sand (Figure 3) [11]. It should be noted that the shape of microparticles is likely to have significant influence on the macromechanical behavior [12]; this effect was not investigated extensively in the current study.

A solubility analysis was also conducted to further check how the organic matters existed in the sands. The sand specimens were put in the oven at 70° for 24 h; the temperature was not so high to burn the organic coat. Then, the sands were separated into three parts by crushing the samples, and the mass of each part was measured. The three parts were soaked in distilled water,

TABLE 1: Organic content of sand specimens from different sampling depths.

Sample	Organic content (%)	Sampling depth (m)
1	7.56	2-3
2	6.88	3-4
3	5.26	4-5

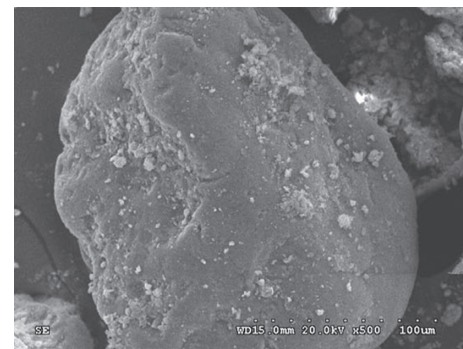


FIGURE 2: Scanning electron microscopic images of organic sandy soil.

HCl solution (pH = 5), and NaOH solution (pH = 9), respectively, for 48 h. Each specimen was then taken out from the solution, dried, and weighed under room temperature to check the loss of mass. The percentage of mass loss for the specimens in distilled water, acid, and alkali solutions was 0.436%, 0.432%, and 0.356%, respectively. The small amount of mass loss indicated that the organic matters did not exist independently as particles, but were

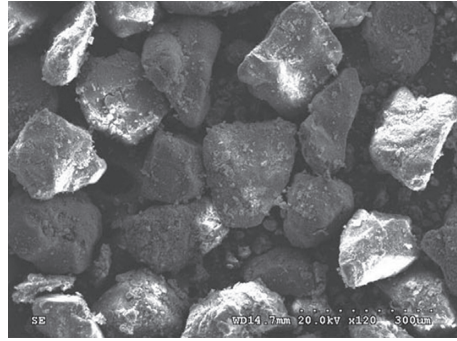


FIGURE 3: Scanning electron microscopic images of ordinary sand.

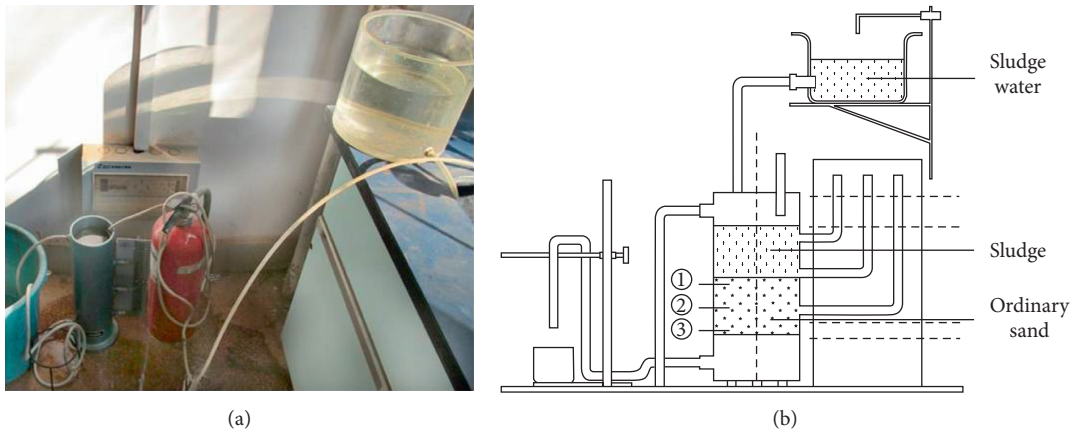


FIGURE 4: Experimental design for modeling the formation of organic sandy soil: (a) real product; (b) diagram.

combined with the sand particles closely. Organic matters may immerse in the pores or are adsorbed on the surface of the sand owing to the long-term microbial activity and physical or chemical effects. Due to the specific type of existence of organic matters, this sand is named “organic sandy soil.”

The process for forming organic sandy soil was assumed to be as follows. The organic matters from dead animals or plants penetrated into the stratum due to the effect of rainwater and groundwater. Then, they were gradually adsorbed on the surfaces of sand particles across ages. Subsequently, they immersed into the pores of sand particles. Finally, the organic sandy soils were formed through the physical, chemical, and biological reactions between organic matter and minerals of sand particles. To model the formation process of organic sandy soil, an indoor experiment was conducted based on the concept of constant head permeability test (Figure 4). The sludge water and sludge were mixed with dead leaves to increase the organic content. After around 3 months, the organic content was determined in the ordinary sand. The organic content of parts 1, 2, and 3 was 0.31, 0.03, and 0, respectively. Also, the organic content in the sand was found to decrease with the sampling depth, which was consistent with the results obtained from in situ specimens. This confirmed that the assumption about the formation of organic sandy soil was reasonable.

3. Engineering Properties of Organic Sandy Soil

According to BS 1377-2: 1990 [13], a dry sieving method was adopted to check the grain size distribution of organic sandy soil (Figure 5). It was identified that d_{60} , d_{30} , and d_{10} were 0.18, 0.14, and 0.087 mm, respectively.

The coefficient of uniformity C_u and the coefficient of curvature were 2.07 and 1.25, respectively. The compaction tests shown in Figure 6 revealed that the maximum dry density and optimum water content of organic sandy soil were 1.723 g/cm^3 and 12.23%, respectively. The minimum dry density of the sand was 1.570 g/cm^3 , whereas its natural dry density was 1.617 g/cm^3 . Therefore, the relative density of organic sandy soil in the natural state was around 0.56. The specific gravity and permeability of the sand were found to be 2.621 and $3.257 \times 10^{-3} \text{ cm/s}$, respectively.

As the sand specimen was very easy to be disturbed, it was made in the laboratory. The sand was dried in air and sieved through a 2 mm sieve. The initial water content w_0 was measured, and the mass of water to be added m_w was calculated using the following expression:

$$m_w = \frac{m_1}{1 + 0.01w_0} \times (w' - w_0), \quad (1)$$

where m_1 is the mass of sand and w' is the designed water content. Then, the mass of sand needed for one specimen m_2 was obtained using the following expression:

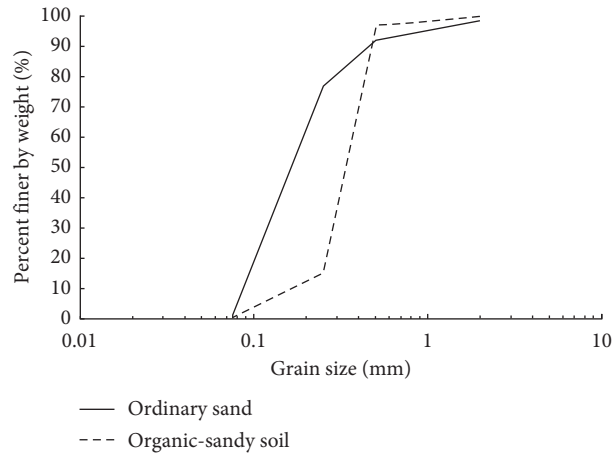


FIGURE 5: Grain size distribution curves of ordinary and organic sandy soils.

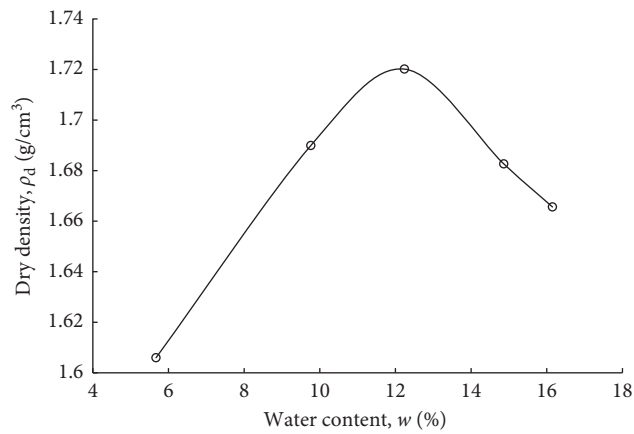


FIGURE 6: Dry density versus water content from compaction tests.

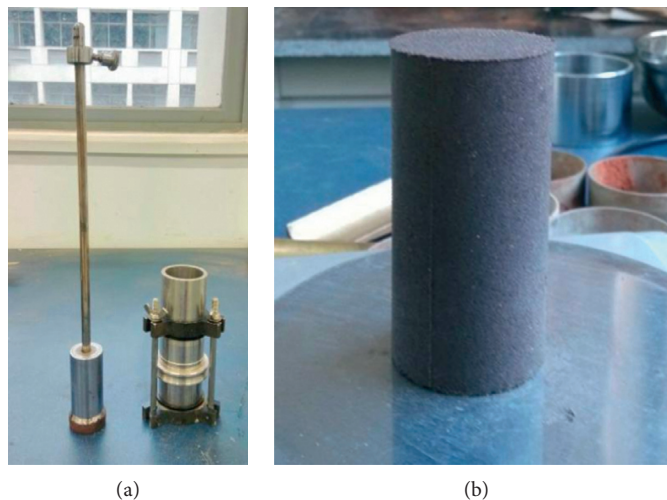


FIGURE 7: Compacted sand specimen: (a) compaction tool; (b) sand specimen.

$$m_2 = (1 + 0.01w')\rho_d V, \quad (2)$$

where ρ_d corresponds to the dry density of sand while V is the volume of specimen (with a diameter of 35 mm and

length 70 mm). The specimen of sand was compacted in a cylinder with grease inside, as shown in Figure 7. Five layers of sand were put into the cylinder, and 12 times of compaction were conducted for each layer to ensure the

compaction quality. The average density and relative density of the samples are 1.71 g/cm^3 and 0.56, respectively. These indices indicate that the samples are medium in terms of density.

Triaxial tests were conducted on the organic sandy soil with various confining pressures (i.e., 50, 150, and 200 kPa) using the Geocomp triaxial apparatus (Figure 8). The setup of the specimen and test process are illustrated in Figure 9.

Unconsolidated-undrained (UU) triaxial shear tests were used to determine the undrained shear strength of organic sandy soil (Figure 10). The stress-strain curves for various effective confining pressures are shown in Figure 10(a). The Mohr circle for the three confining pressures was similar (Figure 10(b)). Theoretically, the three circles should be exactly the same size, with horizontal envelope lines. The slight difference might be because it was difficult to saturate the specimen fully. Another reason for the difference may be due to the variation in density of soil samples, as equal compaction energy was used for each soil layer. The undrained shear strength of the specimen was around 37.5 kPa. Figure 11 shows the results from the consolidated-undrained (CIU) triaxial shear test. When the shear strain was larger than 1%, the effect of confining pressure was obvious and the specimen under higher confining pressure tended to achieve a greater shearing stress (Figure 11(a)). During the early stage of the test, positive excess pore pressure was generated (Figure 11(b)). Then, the negative excess pore pressure increased with shear strain, implying that the volume of the specimen was enlarged during shearing (i.e., stress dilatancy [14]; Figure 9(c)). The deviator stress of 15% shear strain was defined as failure stress (Figure 11(c)). With the generation of negative excess pore pressure, the effective stress Mohr circle was on the right side of the total stress Mohr circle. The total stress parameters c_u and ϕ_u were 14.6 kPa and 21.85° , respectively. The effective stress parameters c'_u and ϕ'_u were 4.3 kPa and 23.09° , respectively. Figure 12 exhibits the results from the consolidated-drained (CID) triaxial shear test. The deviator stress increased with the shearing strain, and the difference for various confining pressures within a strain of 0.05% was not much (Figure 12(a)). When the strain increased continuously, higher confining pressure led to higher deviator stress. Further, a slight stress compression was observed during the early stage of shearing (Figure 12(b)). However, the volume strain increased with the increase in shearing strain in the later stage of shearing, up to a shearing strain of 10%. It means that significant stress dilatancy was observed [15]. The Mohr circles in Figure 12(c) indicated that the effective stress parameters c_d and ϕ_d were 4.2 kPa and 22.23° , respectively, consistent with those obtained from CIU tests.

The compound tangent-exponential model [16] was adopted to model the stress-strain curves obtained from the triaxial tests:

$$q = A \tan \left[B \left(1 - e^{-C\varepsilon} \right) \right], \quad (3)$$

where q is the deviator stress (in kPa); ε is the axial strain (in %); and A , B , and C are the fitting parameters. The summary of fitting parameters for each stress-strain curve is given in Table 2. Figure 13 shows that the fitting curve agreed well



FIGURE 8: Geocomp triaxial apparatus.

with the experimental data from the triaxial test. Moreover, Figure 14 illustrates that the normalized stress-strain curves for UU and CIU tests fell into a narrow band for various applied confining pressures. The fitting formula was also obtained as follows:

$$\begin{aligned} UU : q &= \tan \left[0.78 \left(1 - e^{-3.6\varepsilon} \right) \right], \\ CIU : q &= \tan \left[0.78 \left(1 - e^{-1.6\varepsilon} \right) \right]. \end{aligned} \quad (4)$$

It showed that, for normalized stress-strain curves of UU and CIU tests, the fitting parameters A and B were set as 1 and 0.78, respectively. The difference lay in the value of C .

4. Proposed Reinforcement Methods

Figure 15 shows the results from unconfined compression tests for ordinary Portland cement-admixed sands. The three different types of sands were ordinary sand, organic sandy soil after removing its organic matters, and original organic sandy soil. The cement content was 10%. However, the unconfined compressive strength was found to be significantly lower for the cement-treated organic sandy soil than for the cemented ordinary sand. To increase the engineering performance of the cement-treated organic sandy soil, the traditional way is to increase the cement content. Besides, several innovative techniques have been proposed for the ground improvement, which may be adopted for the organic sandy soil. The results in Figure 15 also indicate that, as a relatively weak and organic component, the organic coat may detach/crush under stress or be steadily degraded under acid or alkaline conditions.

Figures 16 and 17 show the outside view and schematic diagram of the thermal pile, respectively [17]. As shown in Figures 17(a) and 17(b), the thermal pile comprises a liquid pipe, a heating pipe, a brick pile, a drying section, and a liquid suction pipe. The heating pipe with a closed bottom is inserted into the soft ground. The brick pile surrounds the outer edge of the heating pipe, while a drying section is present around the brick pile. The liquid pipe lies within the center of the heating pipe, and its upper portion is higher than the top edge of the heating pipe. The top of the heating pipe is sealed. The liquid suction pipe and liquid pipe are connected with each other. The technology of thermal pile is

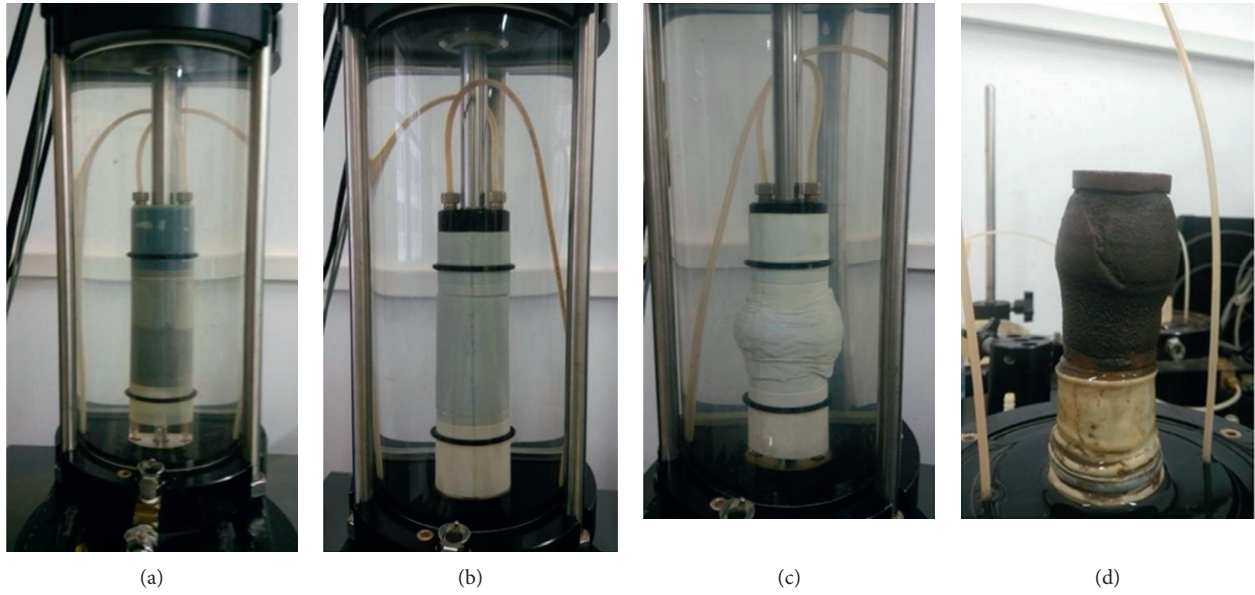


FIGURE 9: Procedure of the triaxial test: (a) setup of the specimen; (b) consolidation; (c) shearing; (d) dismantle of the specimen.

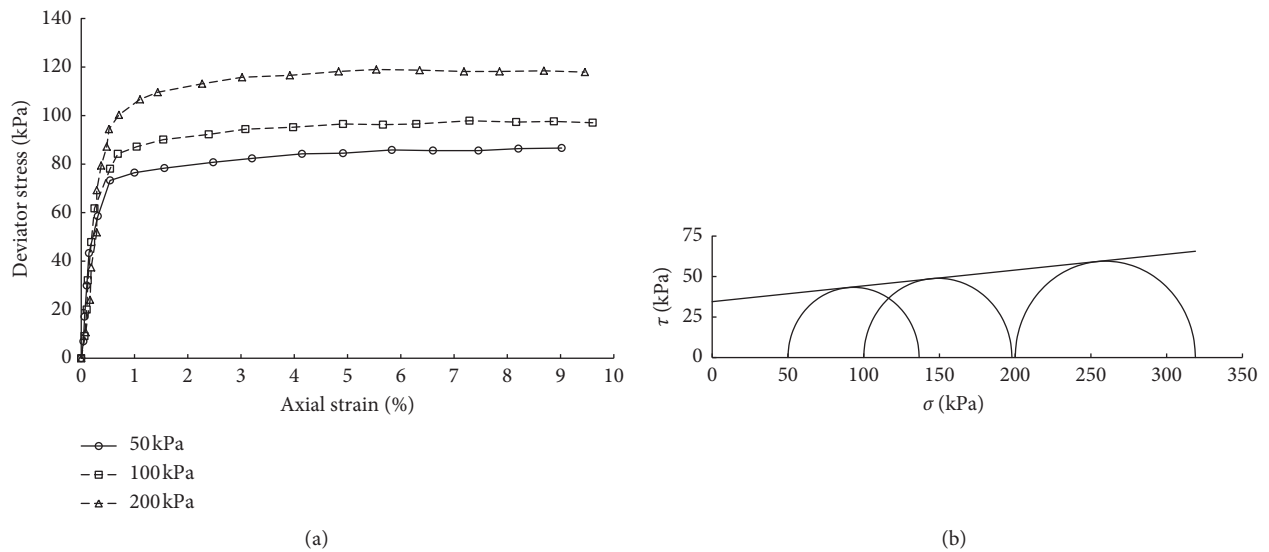


FIGURE 10: Results from the unconsolidated-undrained triaxial shear test: (a) stress-strain curves; (b) Mohr circle.

safe and environmental friendly, with easy-to-control quality. Moreover, it can be widely applied in engineering projects for a wide range of soils, such as bentonite and collapsible loess. For the treatment of organic sandy soil, the advantage of this technology is that it can remove the organic matters.

Figure 18 is the schematic diagram of the fiber- and steel-reinforced cemented soil column, which includes the fiber-reinforced cemented soil column and the steel cage [18]. The cylindrical steel cage is composed of longitudinal main bars and spiral stirrups outside of the cage. For accurate positioning, steel bars are used on the outside of the cylindrical framework. Strengthen tendons are fixed for each 2–2.5 m along the steel cage. This reinforcement method is easy to

design, operate, and control quality. Moreover, the reinforcement depth can be very deep with reasonable cost. Therefore, the technique can be used in the ground improvement projects for the organic sandy soil foundation. It can also be used as a supporting structure during excavation.

Figure 19 shows the outside view of the bamboo-reinforced cemented soil column [19]. Bamboo is a fast-growing natural resource available to mankind as a construction material; otherwise, it is burned or left to decay after its useful life [20]. One or more bamboos are inserted at the center of the column, and other bamboos are placed around them. The selected bamboos should be vertical in shape. The diameter of bamboo is usually between 50 and 100 mm, which should be designed according to the

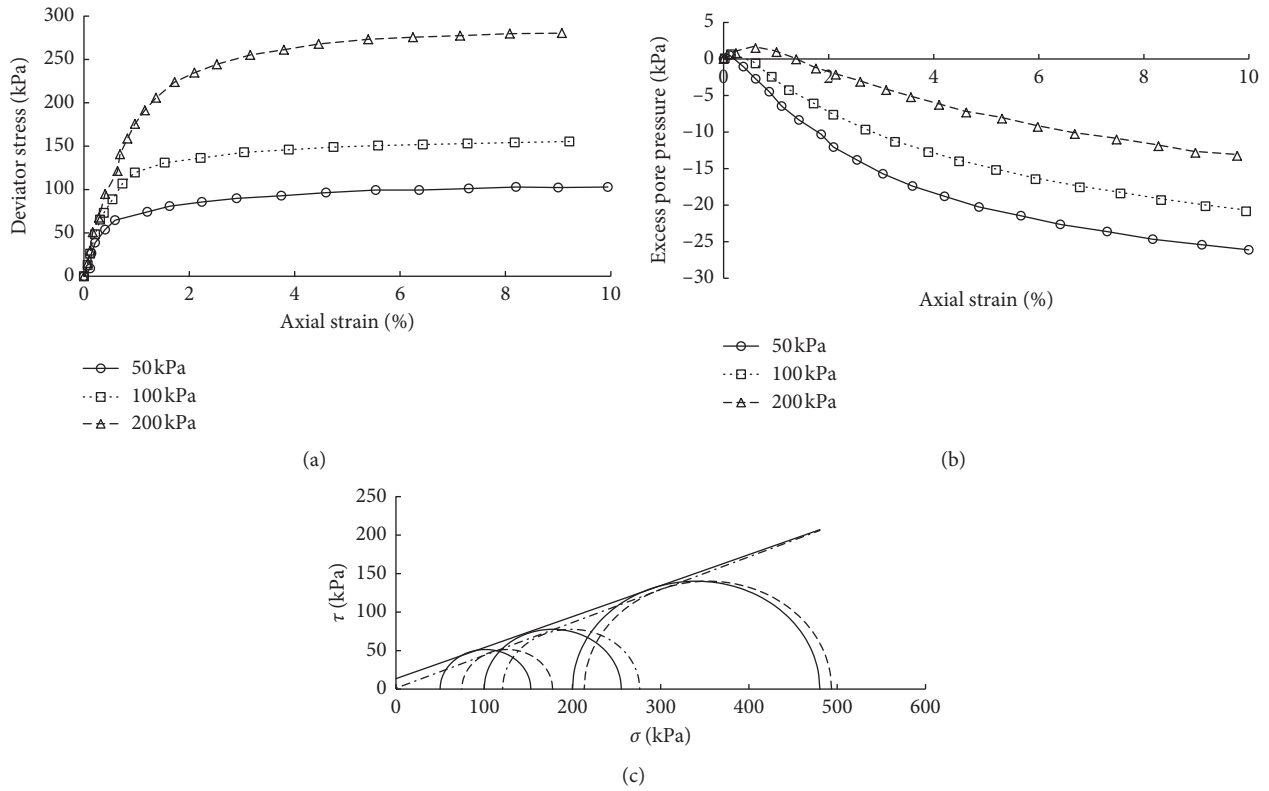


FIGURE 11: Results from consolidation-undrained triaxial shear test: (a) stress-strain curves; (b) variation in excess pore pressure with shearing strain; (c) Mohr circle.

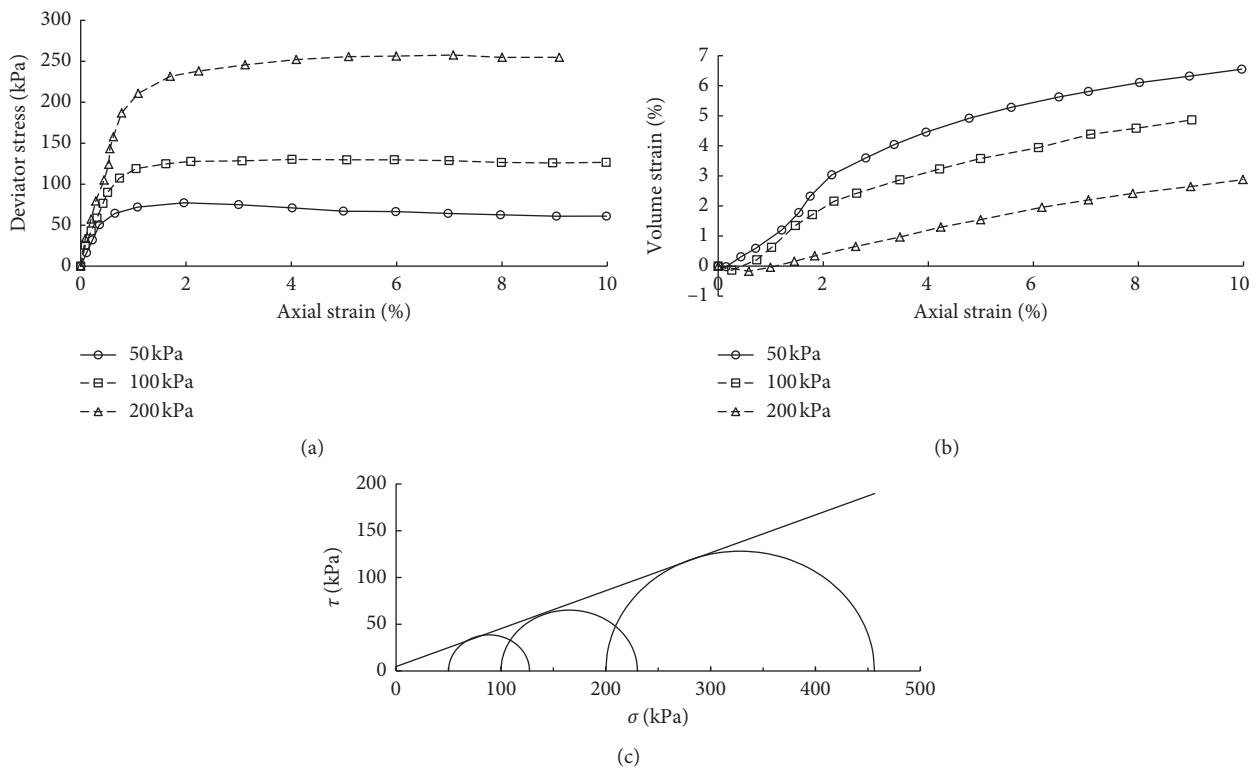


FIGURE 12: Results of the consolidation-drained triaxial shear test; (a) stress-strain curves; (b) variation in volume strain with shearing strain; (c) Mohr circle.

TABLE 2: Fitting parameters for stress-strain curves.

Test	Confining pressure (kPa)	A	B	C
UU	50	3800	0.0225	2.6
	100	3200	0.03	2.8
	200	3100	0.038	2.3
CIU	50	3900	0.026	1.5
	100	5500	0.028	1.5
	200	7300	0.038	0.9
CID	50	1550	0.05	2.5
	100	2550	0.05	2.5
	200	5800	0.044	1.6

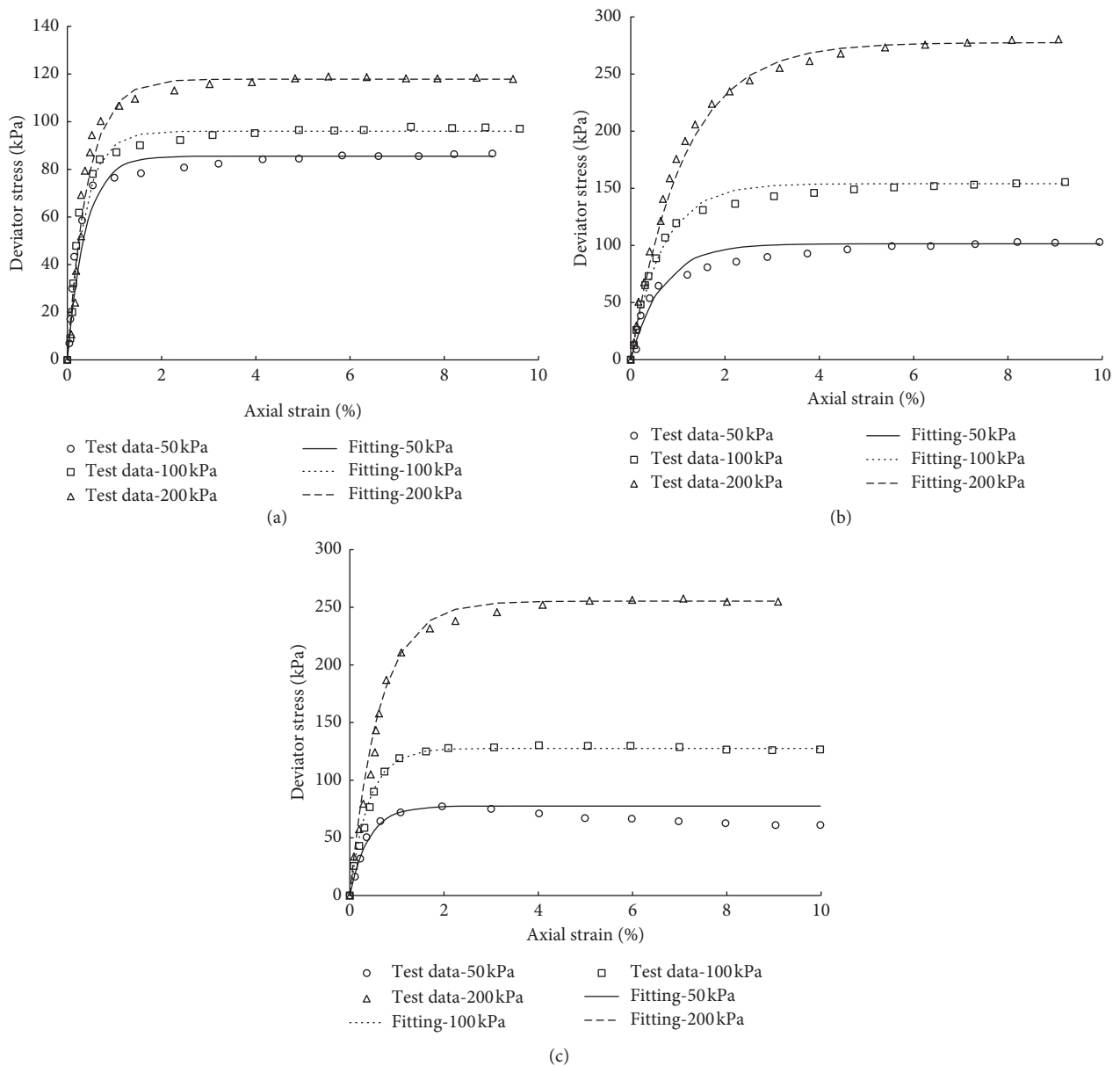


FIGURE 13: Fitting curves for data from the triaxial shear test: (a) unconsolidated-undrained triaxial shear test; (b) consolidation-undrained triaxial shear test; (c) consolidation-drained triaxial shear test.

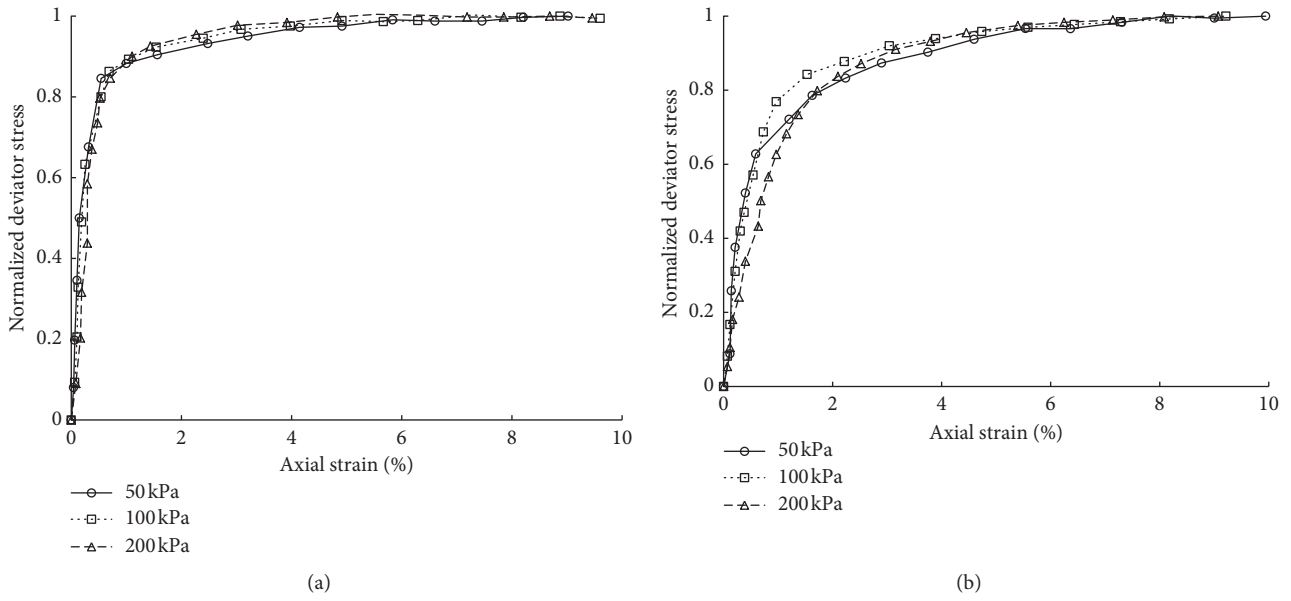


FIGURE 14: Normalized stress-strain curves: (a) unconsolidated-undrained triaxial shear test; (b) consolidation-undrained triaxial shear test.

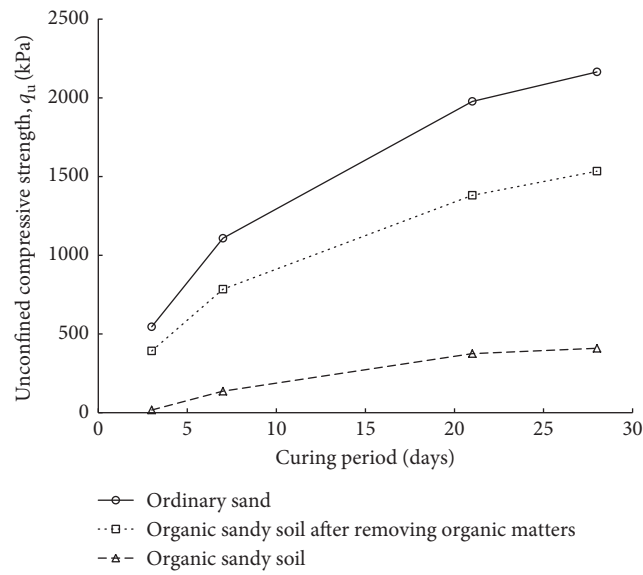


FIGURE 15: Unconfined compression test for cement-admixed sand.

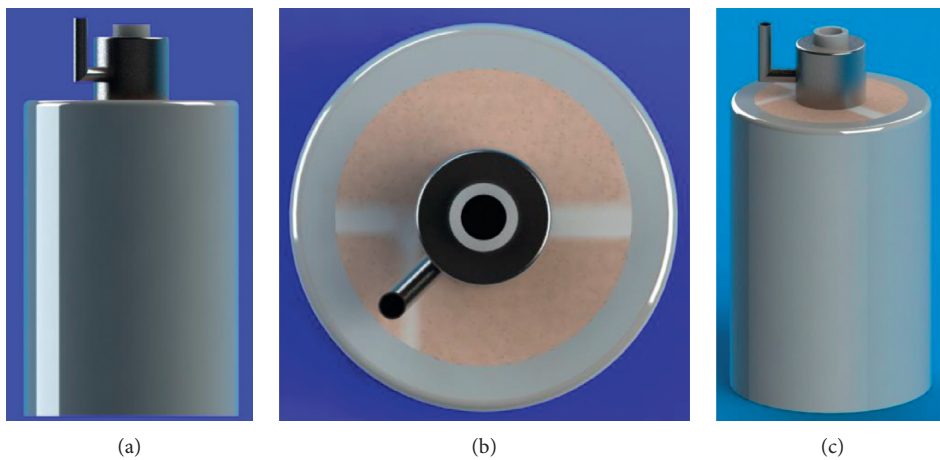


FIGURE 16: Outside view of the thermal pile: (a) front view; (b) plan view; (c) spatial pattern.

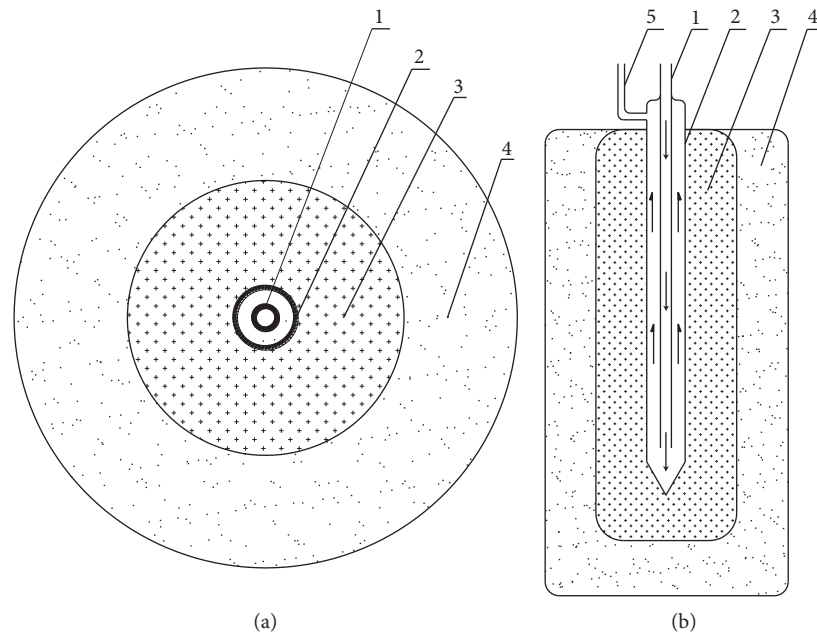


FIGURE 17: Schematic diagram of the thermal pile (1: liquid pipe; 2: heating pipe; 3: brick pile; 4: drying section; 5: liquid suction pipe); (a) plan view; (b) elevation view.

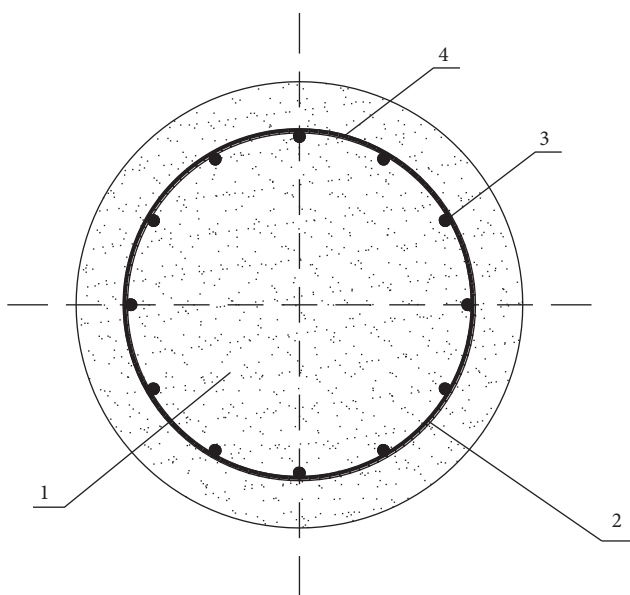


FIGURE 18: Schematic diagram of the fiber- and steel-reinforced cemented soil column (1: fiber-reinforced cemented soil column; 2: steel cage; 3: main bars; 4: spiral stirrups).

diameter of the cemented soil column. The bamboo should be inserted into the cement-admixed soil immediately after the mixing of the cement with soil to ensure that the process is finished before hardening of the cemented soil. The sharp end of the bamboo should be faced downward for easy penetration. First, the bamboo can be set up and penetrated into the slurry manually. Then, a pile driving machine can be used to insert fully the bamboo into the column. The bottom of the bamboo is around 1-2 m higher than the end of the column. The outer part of the bamboos is cut, and the

20–30 cm length of the bamboo is left above the top of the column. Then, a steel net is used to connect all the columns through the top part of the bamboo, and concrete is cast on the top of the columns to act as a raft. The adding of bamboo increases the horizontal bearing capacity of the column. Due to the eco-friendly nature, low cost, and lower strength of bamboo compared with steel, this technology can be applied for the temporary ground reinforcement before conducting tunnel boring.

Figure 20 shows the outside view of the freezing-cemented soil column, including the cement-mixed soil column and freezing pipe. The idea came from the artificial ground freezing method, which was adopted in this study to create a watertight connection between the tunnel and the shaft for conducting the tunnel boring [21, 22]. The freezing pipe is made of seamless low-carbon steel or other pipes, such as PVC, PPR, ABS, and PE pipes. The typical diameter of the freezing pipe is 89, 108, 127, 146, or 159 mm. The bottom of the freezing pipe is 0.5–1 m higher than the bottoms of the column. Using a freezing pipe in the cemented soil can protect the soil from ground motion caused by freezing and thawing cycles. Besides, it can reduce the cement content and increase the water-proof performance of the ground, which is of great importance for underground construction projects.

5. Conclusions

The organic sandy soils are widely distributed around the coastal areas of Hainan Island. The organic matters in this sand are immersed into the pores of sand particles and adsorbed on the surface of the sand. In this study, the formation process of the organic sandy soil was simulated by a laboratory test, and the tested organic content showed

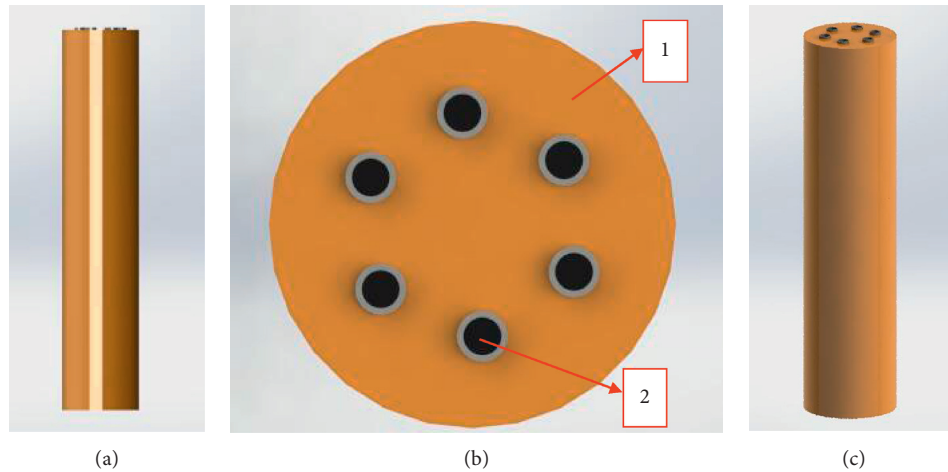


FIGURE 19: Outside view of the bamboo-reinforced cemented soil column (1: column body; 2: bamboo): (a) front view; (b) plan view; (c) spatial pattern.

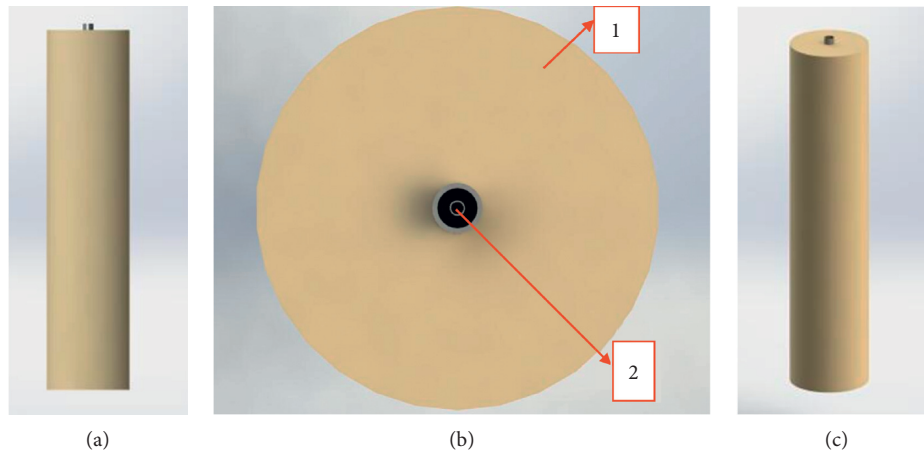


FIGURE 20: Schematic diagram of the freezing-cemented soil column (1: column body; 2: freezing pipe): (a) front view; (b) plan view; (c) spatial pattern.

a similar trend as that of the in situ specimen. The coefficient of uniformity C_u and the coefficient of curvature were 2.07 and 1.25, respectively. The maximum dry density and optimum water content were 1.723 g/cm^3 and 12.23%, respectively. The triaxial tests revealed that the undrained shear strength of organic sandy soil was around 37.5 kPa. The effective stress parameters c and ϕ were around 4 kPa and 23° , respectively. The compound tangent-exponential model could capture the stress-strain behavior of organic sandy soil well. The unconfined compressive strength of the cemented organic sandy soil was much lower than that of ordinary sand. Therefore, several advanced techniques for stabilizing the organic sandy soil were introduced in detail, including thermal pile, fiber, and steel-, bamboo-, and freezing-cemented soil columns.

It should be noted that the cement-admixed organic sandy soil possesses a high variability in its engineering mechanical indices, such as the strength and stiffness [23, 24]. To fully capture the variability, random fields may need to be employed [25]. As a limitation, this kind of

variability was not considered in this study, which forms the scope of future investigations.

Data Availability

All the data used to support the findings of this study are included within the article.

Conflicts of Interest

The authors declare no conflicts of interest.

Acknowledgments

This study was supported by the Key Research & Development Plan Sci-Tech Cooperation Program of Hainan Province in China (ZDYF2016226), the Scientific Research Project of Education Department of Hainan Province (Hnky2016ZD-7 and Hnky2015-10), the National Natural Science Foundation of China (51568044 and 41772311), and

the Zhejiang Provincial Natural Science Foundation of China (LY17E080016). The assistance in laboratory tests offered by Mr. Y. S. Hu is greatly appreciated, who was a formerly graduate student at Hainan University.

References

- [1] Q. Wand, H. Wei, J. Du, and H. Jun, "Design and research of mix ratio for infected gulf-phase organic sand based on orthogonal test," *Natural Science Journal of Hainan University*, vol. 33, no. 9, pp. 25–30, 2015, in Chinese.
- [2] M. R. Mitchell, R. E. Link, K. Venkataramana, B. Rao, and D. Singh, "A critical review of the methodologies employed for determination of tensile strength of fine-grained soils," *Journal of Testing and Evaluation*, vol. 37, no. 2, article 101989, 2009.
- [3] B. B. Huat, A. Asadi, and S. Kazemian, "Experimental investigation on geomechanical properties of tropical organic soils and peat," *American Journal of Engineering and Applied Sciences*, vol. 2, no. 1, pp. 184–188, 2009.
- [4] A. Madaschi and A. Gajo, "One-dimensional response of peaty soils subjected to a wide range of oedometric conditions," *Géotechnique*, vol. 65, no. 4, pp. 274–286, 2015.
- [5] M. Gunaratne, P. Stinnette, A. G. Mullins, C. L. Kuo, and W. F. Echelberger, "Compressibility relations for peat and organic soil," *Journal of Testing and Evaluation*, vol. 26, no. 1, pp. 1–9, 1998.
- [6] Y. Liu, F. H. Lee, S. T. Quek, E. J. Chen, and J. T. Yi, "Effect of spatial variation of strength and modulus on the lateral compression response of cement-admixed clay slab," *Géotechnique*, vol. 65, no. 10, pp. 851–865, 2015.
- [7] P. Croce, A. Flora, and G. Modoni, *Jet Grouting*, CRC Press, Taylor & Francis Group, Boca Raton, FL, USA, 2014.
- [8] S. Sugawara, S. Shigenawa, H. Gotoh, and T. Hosoi, "Large scale jet grouting for prestrutting in soft clay," in *Proceedings of 2nd International Conference on Ground Improvement Geosystems*, pp. 353–356, Tokyo, Japan, May 1996.
- [9] K. Yao, Q. Chen, J. Ho, H. Xiao, and F. H. Lee, "Strain-dependent shear stiffness of cement-treated marine clay," *Journal of Materials in Civil Engineering*, vol. 30, no. 10, article 04018255, 2018.
- [10] ASTM Standard, "Standard test methods for moisture, ash, and organic matter of peat and other organic soils," Annual Book of ASTM Standards, West Conshohocken, PA, USA, 1993.
- [11] J. Yi and H. Wei, "Existing form and causes of bay face-organic sand," *Applied Mechanics and Materials*, vol. 405–408, pp. 2730–2733, 2013.
- [12] A. Afzali-Nejad, A. Lashkari, and P. T. Shourijeh, "Influence of particle shape on the shear strength and dilation of sand-woven geotextile interfaces," *Geotextiles and Geomembranes*, vol. 45, no. 1, pp. 54–66, 2017.
- [13] British Standard, *Methods of Test for Soils for Civil Engineering Purposes*, British Standard, London, UK, 1990.
- [14] W. P. Rowe, "The stress-dilatancy relation for static equilibrium of an assembly of particles in contact," in *Proceedings of the Royal Society A: Mathematical, Physical and Engineering Sciences*, vol. A269, pp. 500–527, London, UK, October 1962.
- [15] K. Been and M. G. Jefferies, "A state parameter for sands," *Géotechnique*, vol. 35, no. 2, pp. 99–112, 1985.
- [16] W. Wang, P. Jin, and F. Zhang, "Direct shear test of short-fill-age municipal solid wastes and its shear stress-deformation model," *Rock and Soil Mechanics*, vol. 32, no. 1, pp. 166–170, 2011, in Chinese.
- [17] J. Hu, "Reinforcement pile with heat," China Patent ZL201620031077.X, 2016, in Chinese.
- [18] J. Hu, "Reinforcement fiber cement soil pile," China Patent ZL201521085879, 2015, in Chinese.
- [19] J. Hu and L. Jia, "Bamboo reinforced cement mixing pile," China Patent ZL201420614713, vol. 2, pp. 10–23, 2014, in Chinese.
- [20] R. Sudin and N. Swamy, "Bamboo and wood fibre cement composites for sustainable infrastructure regeneration," *Journal of Materials Science*, vol. 41, no. 21, pp. 6917–6924, 2006.
- [21] B. Stille, J. Brantmark, L. Wilson, and U. Hakansson, "Ground freezing design in tunnelling—two case studies from Stockholm," in *Proceedings of Tunnels and Underground Structures*, J. Zhao, J. N. Shirlaw, and R. Krishnan, Eds., pp. 185–190, Balkema, Rotterdam, Netherlands, 2000.
- [22] G. Russo, A. Corbo, F. Cavuoto, and S. Autuori, "Artificial ground freezing to excavate a tunnel in sandy soil. Measurements and back analysis," *Tunnelling and Underground Space Technology*, vol. 50, pp. 226–238, 2015.
- [23] Y. Pan, H. Xiao, F. H. Lee, and K. K. Phoon, "Modified isotropic compression relationship for cement-admixed marine clay at low confining stress," *Geotechnical Testing Journal*, vol. 39, no. 4, article 20150147, 2016.
- [24] Y. Liu, Y. Jiang, H. Xiao, and F. H. Lee, "Determination of representative strength of deep cement-mixed clay from core strength data," *Géotechnique*, vol. 67, no. 4, pp. 350–364, 2017.
- [25] Y. Liu, L. Q. He, Y. J. Jiang, M. M. Sun, E. J. Chen, and F. H. Lee, "Effect of in-situ water content variation on the spatial variation of strength of deep cement-mixed clay," *Géotechnique*, vol. 68, pp. 1–15, 2018.

Research Article

Study on the Spatially Variable Saturated Hydraulic Conductivity and Deformation Behavior of Accumulation Reservoir Landslide Based on Surface Nuclear Magnetic Resonance Survey

Shu Zhang ¹, Yunshan Xiahou,¹ Huiming Tang ^{1,2}, Lei Huang ², Xiao Liu,¹ and Qiong Wu²

¹Three Gorges Research Center for Geo-Hazard, China University of Geosciences, Wuhan, Hubei 430074, China

²Faculty of Engineering, China University of Geosciences, Wuhan, Hubei 430074, China

Correspondence should be addressed to Shu Zhang; szhang@cug.edu.cn and Huiming Tang; tanghm@cug.edu.cn

Received 15 June 2018; Accepted 24 September 2018; Published 23 October 2018

Guest Editor: Yongfeng Deng

Copyright © 2018 Shu Zhang et al. This is an open access article distributed under the Creative Commons Attribution License, which permits unrestricted use, distribution, and reproduction in any medium, provided the original work is properly cited.

Saturated hydraulic conductivity (K_s) is spatially variable in accumulation landslide sites that exert significant effort onto landslide seepage and deformation behavior. To better understand spatial variability and the effect of K_s on the slide mass of an accumulation landslide, this study introduced the surface nuclear magnetic resonance (SNMR) technology to study a representative reservoir accumulation landslide field in the Three Gorges Reservoir area (TGRA), the Baishuihe landslide, to obtain a series of relative reliable spatial measurements of K_s effectively on the basis of calibration in terms of the field tests measurements. The estimated K_s values were distributed log-normally for the overall landslide mass site with a wide range of $3.00 \times 10^{-6} \sim 7.80 \times 10^{-3}$ cm/s, which reaches about 3 orders of magnitude. Variogram analysis indicated that the K_s values have the range (A) of 295.89 m and 65.56 m for the overall site and major cross-sectional analysis, respectively. A finite-element seepage-stress analysis associated with a Kriging-interpolated spatial K_s variable calculation model based on the best-fitted theoretical variogram was subsequently performed to study the seepage and deformation behavior of the landslide. The available monitored data and simulated results of the finite-element seepage-stress analysis indicated that the Baishuihe landslide is a progressive landslide, and the main factor influencing the deformation is rainfall and reservoir water fluctuation. This study provides an unconventional framework for studying the heterogeneous geomaterial and contributes to a better understanding of the spatial variation of the hydraulic property of accumulation reservoir landslides at a field scale.

1. Introduction

Accompanied by the reservoir operation of hydropower projects, reservoir landslides have become a typical geohazard in reservoir areas in the world [1, 2]. The instability of the reservoir landslide may arouse devastating economic and social costs, even the loss of human life. Under the combined effect of reservoir water-level fluctuation and rainfall, saturated hydraulic conductivity (K_s) is a key soil hydraulic parameter, which controls the water seepage process, determines water distribution, and thus exerts

a dominant impact on landslide deformation and instability [3–6].

It is generally accepted that K_s is characterized by spatial variability at different scales due to the parent material and environmental process [7–10]. However, K_s values are usually assumed to be identical and are generally derived from experiments of a few samples. The variations of the values derived from the characteristics of discontinuity, heterogeneity, and anisotropy have not been taken into account in this assumption [11]. In this sense, the understanding of spatial variability of hydrological properties

should be taken into account when performing a landslide analysis.

Considerable research studies have been devoted to investigate the regional-scale variation, probability distribution pattern, and geostatistic-based spatial variation of measured K_s values of different geomaterials, such as loessial soil [10, 11], river sediments [12–14], alluvial floodplains [15], and costal farmlands [16]. K_s exhibits significant spatial variation and autocorrelation in the aforementioned research studies regardless of homogeneous or heterogeneous geomaterials. However, the research involving K_s field-scale spatial variation of the accumulation reservoir landslide is still insufficient.

Different techniques have been employed to evaluate K_s both in the laboratory and in the field. Laboratory permeameter tests have the challenge of introducing errors induced by soil disturbance during sampling and transportational processes. In addition, the sampled soil is deprived of other dominant hydraulic effects presented in the field [17]. By contrast, field methods (instrumental methods and hydrogeophysical methods) address the soil in the field condition; thus, the small-scale heterogeneities caused by the soil structure, composition, texture, plant growth, and other factors may contribute to the measuring results [11]. Other than the widely adopted direct/indirect instrumental methods, hydrogeophysical methods utilized the link between what can be measured with geophysical instruments and the subsurface hydrological properties using a noninvasive process, thus providing cost-effective and relatively dense spatial information about the site of research interest. Among these hydrogeophysical methods, nuclear magnetic resonance (NMR) is a promising method for characterizing groundwater systems, which measure the NMR response of water molecules excited by electromagnetic pulses [18, 19]. It is applied as surface NMR (SNMR), borehole NMR (BNMR), and laboratory NMR (lab-NMR).

SNMR technology is a noninvasive surface-based method, which can be used to derive information about the pore structure and hydraulic conductivity of the formation from the empirical relations of determined water content and the relaxation time without the need to drill boreholes [20–22]. Some studies have utilized SNMR to distinguish the underlying formations of landslide [23], but further application of SNMR to landslide studies has not been extensively investigated to date.

In this sense, the objective of this study are (1) to apply the SNMR technology to a representative accumulation reservoir landslide in TGRA and estimate spatial K_s values of the subsurface colluvial-deluvial geomaterials based on newest comprehensive geotechnical investigation; (2) to perform descriptive statistics and analyze the spatial variation of the estimated K_s values; and (3) to investigate the effect of spatially variable K_s to the deformation behavior of the landslide under the combinative effect of reservoir water fluctuation and rainfall through a 2D numerical simulation.

2. SNMR Method

2.1. Basics of SNMR. The magnetic spin is an inherent property of an atom that possesses an angular momentum, with an associated magnetic moment. Under the action of the stable earth's stable magnetic field, the hydrogen protons spin continuously in a precess motion about the magnetic field axis at the characteristic proton Larmor frequency, which is proportional to the magnetogyric ratio of the intensity of the earth's magnetic field and atomic nucleus. The orientation of the static field and the plane of precession perpendicular to it are commonly referred to as longitudinal direction and transverse direction, respectively [18]. During the process of the SNMR survey, an alternating current with the resonance of Larmor frequency is supplied to the large surface-based wire-loop transmitter, which is typically a circular or square loop of 50–100 m in diameter/edge length. A slight macroscopic spin magnetization moment is produced at the same time by the excitation pulse of the oscillating current. When the current pulse is terminated, magnetic resonance signals produced by the excitation of different pulse moments can be explored by the same surface-based transmitting coil. After an instrument delay known as “dead time” (τ_{dead}), the magnetic resonance signal can be measured and expressed as follows:

$$e(t) = E_0 \exp\left(\frac{-t}{T_2^*}\right) \cos(2\pi f_0 t + \varphi_0), \quad (1)$$

where E_0 is the initial amplitude of the signal, which can be obtained by the measured amplitude E_{0d} and the relaxation time T_2^* as $E_0 = E_{0d} \exp(\tau_{\text{dead}}/T_2^*)$, and f_0 and φ_0 denote the initial frequency and initial phase, respectively. The phase φ_{0d} correlates with the electrical conductivity of the geomaterials, but it is not currently used for SNMR data interpretation. With regard to the relaxation time, it is believed that T_2^* is susceptible to the disturbance of electromagnetic noise; therefore, T_1^* is adopted for hydrological parameter interpretation [18]. The strength of the signal and rate of decay are related to the magnitude of hydrogen protons in groundwater molecules. In other words, the amplitude of the magnetic resonance signal is proportional to the free water content of the surveyed area [24].

2.2. SNMR-Determined Hydrological Properties. The SNMR technology provides a strategy for estimating how hydrological parameters (e.g., porosity, water content, permeability, transmissivity, etc.) of the aquifer can be estimated [18, 19]. The initial signal amplitude E_{0d} is proportional to the number of protons in the measured sample, which is equivalent to the volume of water in the measured sample [25], so the SNMR-estimated effective porosity (\emptyset) can be determined from E_{0d} using an instrument-specific calibration factor.

With regard to hydraulic conductivity estimation, Schlumberger-Doll Research (SDR) models give an equation to estimate the permeability k_{SDR} [26]:

$$k_{\text{SDR}} = b \emptyset^m (T_{2(1)\text{ML}})^n, \quad (2)$$

where b , n , and m are the empirical constants and $T_{2(1)ML}$ is used to present the average surface-area-to-value ratio of the pore of the entire saturated pore space, which can be replaced by $T_{2(1)}$ or $T_{2(1)}^*$. Under the condition of the unconsolidated near-surface aquifer material as we measured, $n = 2$ and $m = 1$, b is regarded as a turning parameter to obtain the best possible match between the measurement and estimation [27–29]. Therefore, hydraulic conductivity K can be related to k by the equation $K = ((\rho g)/\mu)k$, where $g = 9.8 \text{ m/s}^2$ is the gravitational acceleration, μ is the temperature-dependent dynamic viscosity, and ρ is the temperature-dependent density, which can be determined in terms of table lookup according to the temperature.

For all of the analyses above, the physical constants can be absorbed into the constant b' in the SDR equation as follows:

$$K_{\text{SDR}} = b' \cdot \emptyset \cdot T_1^{*2}, \quad (3)$$

where b' should be calibrated based on the temperature as well as the drilling data and other forms of measurement on core samples for the requirement of accuracy [29].

3. Case Study: The Baishuihe Landslide

3.1. Background. The Baishuihe landslide is a typical accumulation reservoir landslide in TGRA. It is located on the south bank of the Yangtze River, 56 km west of the Three Gorges Dam (Figures 1(a) and 1(b)), with the main sliding direction of 20° with respect to the north. It produced remarkable deformation since the first impoundment of the Three Gorges Reservoir in 2003 and has a great influence on the shipping safety of Yangtze River. The multiyear time-displacement data of the landslide surface obtained from GPS monitoring exhibited a step-like pattern, which aroused much research attention [30–33]. However, most previous research studies aimed at predicting the deformation behavior and paid little attention to the engineering geological model and landslide mechanism.

The sophisticated engineering surveys involving 23 boreholes with a total length of 699.20 m and 14 exploratory trenches with a total volume of 101.24 m^3 (shown in Figure 1(c)) have been carried out by Sanxia University in 2012 and China university of Geosciences, Wuhan, in 2013 [34], respectively. Based on the revealed observations, the boundary of the Baishuihe landslide had been determined as the predetermined warning area of the landslide. As shown in Figure 1(b), the morphology of the landslide exhibited an irregular gentle concave shape with the elevation from 120 m to 297 m and the volume of $645 \times 10^4 \text{ m}^3$. To date, multiple monitoring devices had been arranged in this typical landslide, involving GPS, borehole clinometer, SNMR, and distributed optical fiber sensor deformation monitoring, as shown in Figure 1(c). The GPS therein was arranged in 2007 by the government, but the monitoring data after 2012 are still unpublicized till now.

3.2. Geological Setting. The Baishuihe landslide is developed in the clastic rocks of the Lower Jurassic Xiangxi Formation

(J_{1x}), with the specific lithology of dark gray thin-bedded and medium-bedded siltstone mingling with thin stratified mudstone and coalbed. The inclination direction is $15^\circ \sim 20^\circ$, coinciding with the main sliding direction. Therefore, the landslide is a monoclinic consequent bedding landslide along the weak intercalated layer initially. However, GPS monitoring data and in situ observations indicated that the deformation is mainly along the formatted sliding zone or the local area of sliding mass rather than along the weak intercalated layer.

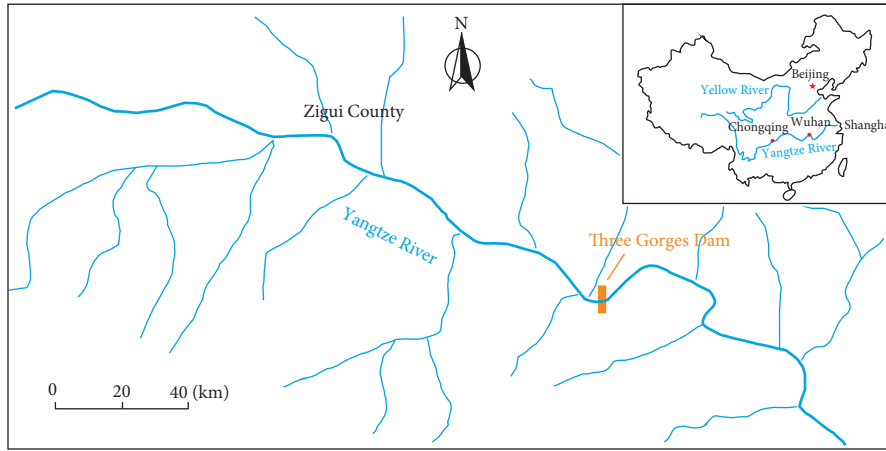
According to the drilled holes logs, the slide mass was composed of a soil-rock mixture with the thickness of 7.75~38.50 m. It comprised various dimensions of sub-angular siltstone gravels together with silty clay and clay; the gravel content was approximately 10~70% (Figure 2(a)). There was no unified and continuous layered boundary among the geomaterials. As revealed, the slide zone was composed of subrounded or subangular gravels mixed with silty clay, with an average thickness of 0.7 m. The gravel with the dimension of 1~6 cm accounted for a proportion of 20~30% in the sliding-zone soil (Figure 2(b)).

According to the drilled holes logs and engineering geological investigation, the representative engineering geological cross section can be plotted, as shown in Figure 3.

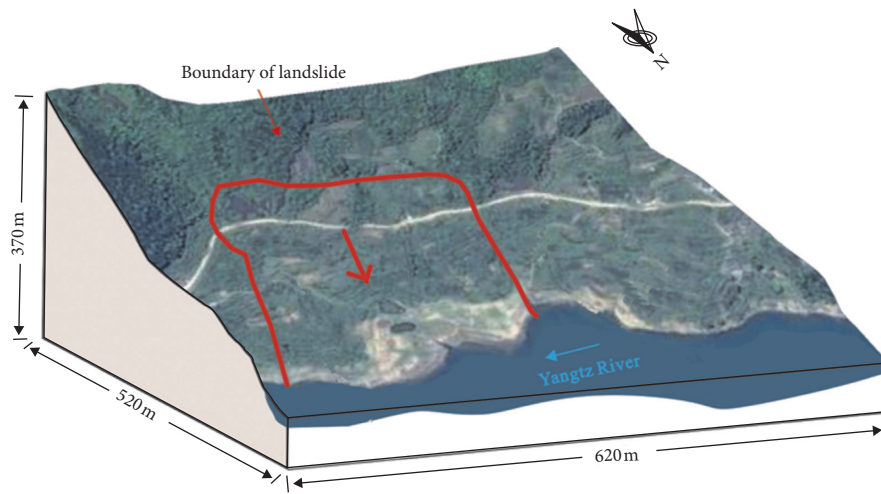
4. Field-Scale Spatial Variability of K_s

4.1. Interpretation of SNMR Data. There were 15 SNMR survey points arranged in the landslide site in total, which are distributed in 4 survey lines, as shown in Figure 1(c). The SNMR device NUMIS Poly from IRIS Instruments was adopted in this study. The data were measured and interpreted in September 2013 for the spatial variability study and landslide deformation behavior analysis. The built-in procedures of the NUMIS system were applied to address the first-hand surveyed data. After backward extension and noise filtering of the signal, the data can be interpreted using a classic inversion method of least squares based on Tikhonov regularization.

The measured and estimated data for each vertical survey line were not continuous. Therefore, the estimated data with a presupposed interval of 2 m were set for data extraction. The points of discontinuity were taken into account as well at the same time. As has been measured by the comprehensive field/laboratory tests, the double-ring infiltrometer tests indicated that the K_s values of the landslide surface were within the range of $4.2 \times 10^{-5} \sim 5.0 \times 10^{-4} \text{ cm/s}$; the borehole water injection tests indicated that the K_s values of the slide mass were within the range of $2.1 \times 10^{-6} \sim 1.4 \times 10^{-4} \text{ cm/s}$. The laboratory tests indicated that the K_s values of silty clay were within $3.05 \times 10^{-5} \sim 7.12 \times 10^{-5} \text{ cm/s}$, while for clay, the result was $5.77 \times 10^{-6} \text{ cm/s}$. According to the aforementioned field measurements, the constant b' was calibrated as 4.32 herein. Figure 4 presents the comparison of the lithology indicated by drilled cores together with the surveyed T_1^* values as well as the estimated \emptyset and K_s values. Notably, we discarded the measured data of the bedrock and slide zone based on the consideration that the research object was the slide mass of the Baishuihe landslide.



(a)



(b)

FIGURE 1: Continued.

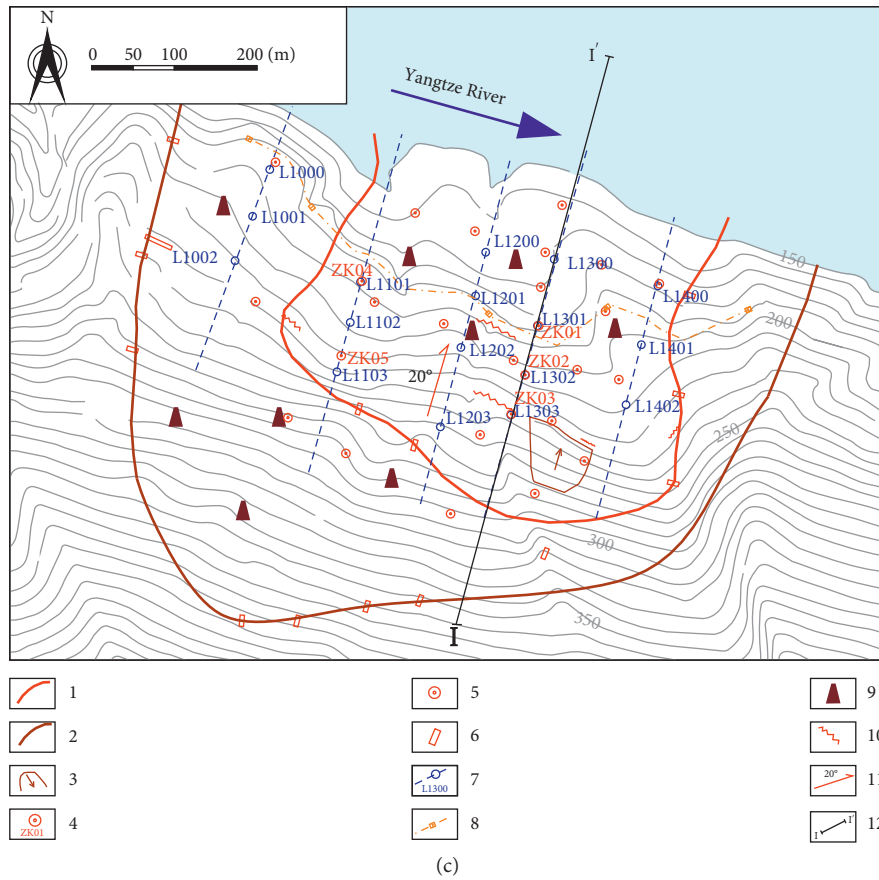


FIGURE 1: (a) Location, (b) overview, and (c) planar map of the Baishuihe landslide. (1) Boundary of the landslide based on the engineering geological exploration; (2) the predetermined boundary of the landslide; (3) small collapse; (4) borehole drilled by China University of Geosciences, Wuhan; (5) borehole drilled by Sanxia University; (6) exploratory trench; (7) SNMR survey points and survey line; (8) distributed optical fiber sensor deformation monitoring; (9) GPS monitoring points; (10) ground surface fissures; (11) sliding direction; (12) cross-sectional line.

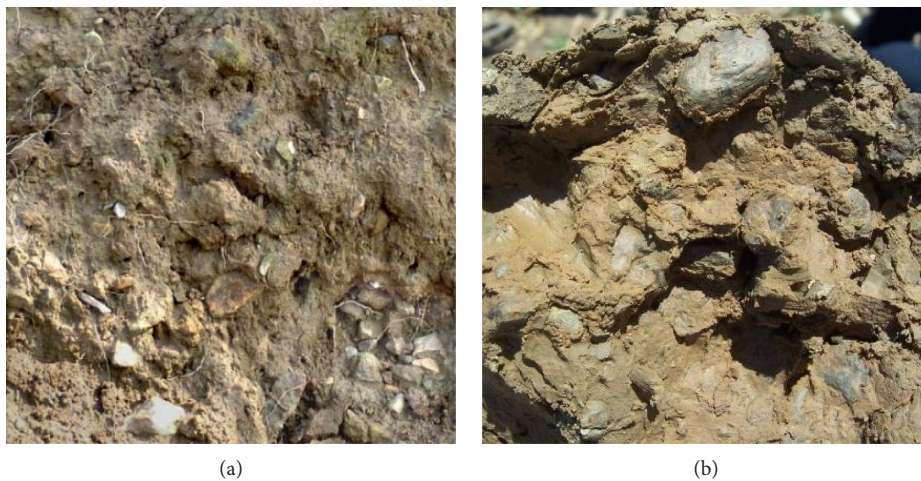


FIGURE 2: Structure of the geomaterial in the Baishuihe landslide. (a) Colluvial-deluvial deposit soil-rock mixture of the slide mass. (b) Gravel soil of the sliding zone.

4.2. Descriptive Statistics. Descriptive statistics including the overall variability and probability distributions of the estimated parameters of the overall site and major profile

(Figure 2) were discussed. Overall variability can be stated using the maximum, minimum, mean, median, standard deviation (SD), and coefficient of variation (CV) parameters

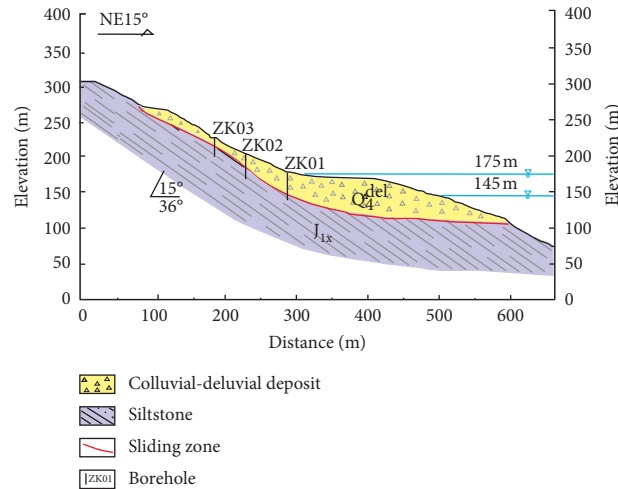


FIGURE 3: Schematic geological cross section (I-I') of the Baishuihe landslide.

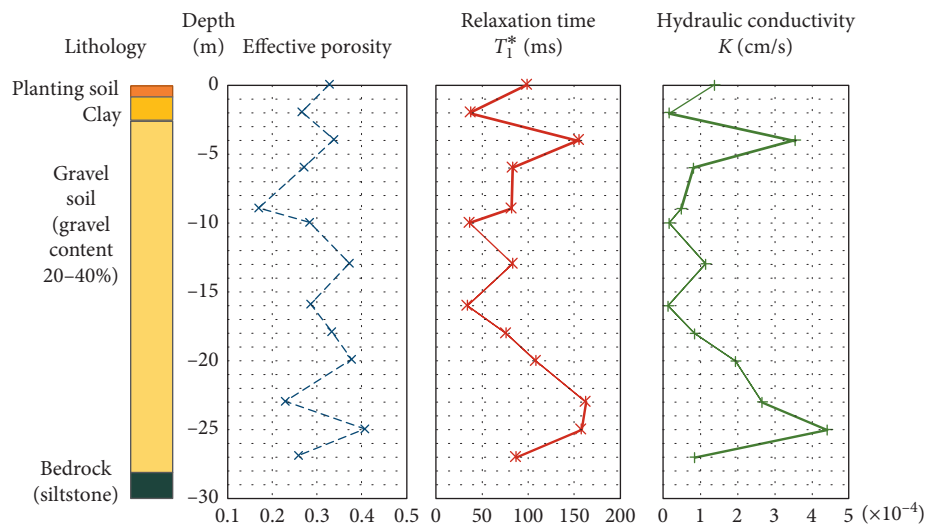


FIGURE 4: Comparison of drilled core lithology and the SNMR data.

of the estimated data, as shown in Table 1. Notably, the estimated K_s results for the overall landslide site and major cross section had the range between $3.00 \times 10^{-6} \sim 7.80 \times 10^{-3}$ cm/s and $4.70 \times 10^{-6} \sim 7.00 \times 10^{-3}$ cm/s, which reaches about 3 orders of magnitude. The magnitude of the mean and median values corresponds with the field measurements. The median values were smaller than the mean value for the two analyzed research locations, which reflected the left skewness of the analyzed data. The median value is believed to be more representative generally because it rises superior to the effect of the extreme values compared to the mean value. The CV, a dimensionless parameter of the standard deviation divided by the mean value, representing the degree of variation, was 46% and 53% for the overall site and major cross section, respectively. These results implied moderate variability for both the overall site and the major cross section.

With regard to the probability distribution, the frequency histograms of the estimated parameters are shown in Figure 5. As has been exhibited, both of the histograms for K_s

for the overall site and the major cross section presented the pattern of left skewness, indicating that the data had a nonnormal distribution. A logarithmic transformation (natural base) was performed on the estimated data for further statistical analysis. As shown in Table 1 and Figure 5, the log-transformed values were normally distributed. Lilliefors tests also indicated that the K_s values for both the overall site and major profile were distributed log normally.

4.3. Spatial Variability Analysis. Geostatistics is a useful tool for analyzing spatial variability and interpolating between point observations [35]. The variogram which describes the spatial variability of K_s is a function of the sampling distance under the intrinsic hypothesis of the variable, as shown in the following equation:

$$\gamma(h) = \frac{1}{2N(h)} \sum_{i=1}^{N(h)} [Z(u_i) - Z(u_{i+h})]^2, \quad (4)$$

TABLE 1: Descriptive statistics for the K_s value of the slide mass of the Baishuihe landslide.

Location	Number	Maximum	Minimum	Mean	Median	SD	CV
Overall site	169	7.00×10^{-3}	3.00×10^{-7}	2.99×10^{-4}	3.20×10^{-5}	8.71×10^{-4}	34
Major profile	55	7.00×10^{-3}	4.70×10^{-6}	6.09×10^{-4}	1.40×10^{-4}	1.35×10^{-3}	45

Note: K_s , saturated hydraulic conductivity (cm/s); SD, standard deviation; CV, coefficient of variation (%).

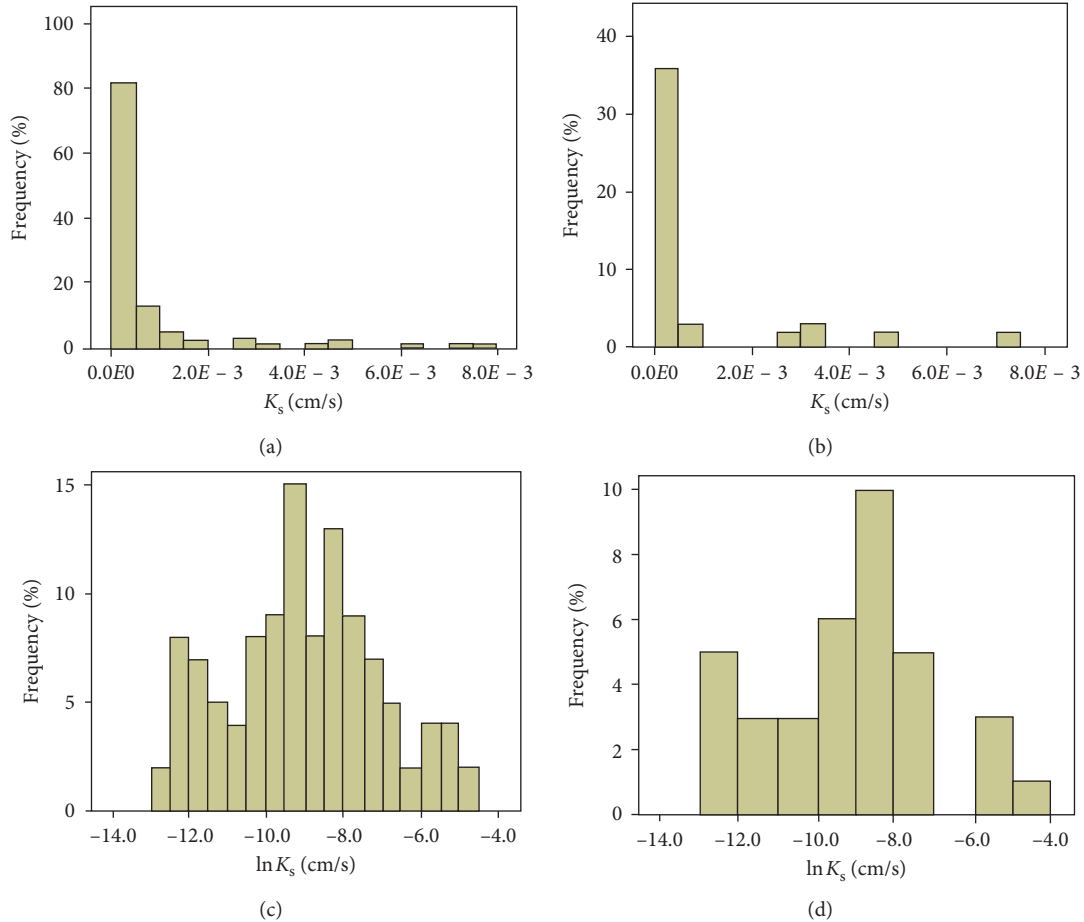


FIGURE 5: Histograms of the estimated K_s values: (a) K_s for the overall site; (b) K_s for the major cross section; (c) $\ln K_s$ for the overall site; (d) $\ln K_s$ for the major cross section.

where for each site i , $Z(u_i)$ and $Z(u_{i+h})$ are values of Z at locations u_i and u_{i+h} , respectively; h is the lag; and $N(h)$ is the number of pairs of sample points separated by h . The value of $\gamma(h_i)$ at a different separation distance h_i can be calculated in terms of Equation (4). Therefore, the calculated $[h_i, \gamma(h_i)]$ points constitute experimental variograms. The variogram describes the spatial variability in terms of 3 representative parameters. The nugget (C_0) represents the variability induced by microheterogeneity and experimental error, which occurs at distances smaller than the sampling intervals. The sill ($C_0 + C$) represents the total variance of the variable, and the range (A) represents the action range of the spatial correlation. The value of $\gamma(h)$ would not increase but fluctuates around $C_0 + C$ when the separation distance reaches A [36]. The theoretical variogram models (i.e., exponential model, spherical model, Gaussian model,

etc.) are employed to fit the calculated experimental variograms. The best-fitted theoretical models indicated by the greatest coefficient of correlation (R) and the least residual sum of squares (RSS) can be undertaken to represent the experimental variograms.

In this study, we investigated the omnidirectional spatial variable patterns for $\ln K_s$ values of the overall site and major profile because of the insufficient data pairs along some characteristic directions. The scale effect caused by the different data intervals along vertical and horizontal directions was also taken into consideration by calculating different experimental variograms, which was characterized by small-scale variograms and large-scale variograms, respectively.

The calculated experimental variograms and the modeled theoretical variograms fitted by the exponential model,

spherical model, and Gaussian model are shown in Figure 6. The corresponding fitting parameters for the 3 models are listed in Table 2. It is noticeable that a was the fitting parameter which equaled to A for the spherical model, while it equaled to $3a$ and $\sqrt{3}a$ for exponential and Gaussian models, respectively. A greater A represents a greater range of variable regular changes and greater spatial correlation [37]. The greatest R and the least RSS indicated the best fit model for $\ln K_s$, i.e., K_s . For the overall site study, the exponential model provided the best fit for the small-scale study because of the least RSS and the slight difference among the three models, while the spherical model provided the best fit for the large-scale study. For the major cross section, the spatial variation for a small-scale study was insignificant and the spherical model provided the best fit for a large-scale study. According to the fitting parameters, the (nested) variogram functions can be deduced for representing the variogram structure [34]. The variogram function for $\ln K_s$ of the overall site and major profile can be deduced as follows.

Overall site:

$$\gamma(h) = \begin{cases} 1.5, & h = 0, \\ 2.5 - e^{-(h/2.83)} + 4.9 \left(\frac{3}{2} \cdot \frac{h}{295.89} - \frac{1}{2} \cdot \frac{h^3}{295.89^3} \right), & 0 < h \leq 295.89, \\ 7.4, & h > 295.89. \end{cases} \quad (5)$$

Major profile:

$$\gamma(h) = \begin{cases} 0.58, & h = 0, \\ 0.58 + 2.96 \left(\frac{3}{2} \cdot \frac{h}{65.56} - \frac{1}{2} \cdot \frac{h^3}{65.56^3} \right), & 0 < h \leq 65.56, \\ 3.54, & h > 65.56. \end{cases} \quad (6)$$

Equations (5) and (6) indicated that the studied variables ($\ln K_s$ values) were spatially correlated within A of the large-scale study. The A values reached 295.89 m and 65.56 m, respectively, for the overall site and major cross section, which suggested that the investigated spatial variation was remarkably dependent on the research direction. The directional variogram structure can be investigated in the further studies in terms of more comprehensive measurements and estimations. Meanwhile, the effect of small-scale spatial variability contributed significantly to the nugget and sill, which represents the randomness derived from the microstructure and errors as well as the variable variation degree within the studied range.

The nugget-to-sill ratio (NSR) was employed to define the degree of spatial dependency. The greater the NSR value, the greater the variation degree caused by randomness. A low NSR value (<25%) indicates a strong spatial dependence of the variables under the strong impact of structural factors. A higher NSR value (25%~75%) indicates a moderately spatial variable dependence. If it is higher than 75%, the

variable is of weak spatial dependence, and randomness plays an important role [11, 38]. As shown in Table 2, all NSR values (except for the NSR of $\ln K_s$ for the overall site with a small scale) were lower than 25%, suggesting that the spatial variation of K_s is mainly dependent on the deposit structure. The K_s for the overall site with a small scale depended on structural factors and randomness.

5. Deformation Behavior Analysis Based on Spatial Variable K_s

5.1. Analyzing Method and Calculation Model. A 2D deformation behavior analysis of the major profile associated with the spatial variable K_s value under the combined effect of reservoir water fluctuation and rainfall has been carried out in this study. The commercial finite-element code SEEP/W (by Geoslope International Ltd.) [39], which is capable of solving finite-element equations for the steady-state flow governed by Darcy's law and for transient flow under the hypothesis of Terzaghi-Rendulic uncoupled consolidation, was used herein.

An ordinary Kriging estimation method was then applied to the orthogonal structural grids (4 m × 4 m) subjected to the geometry of the slide mass on the basis of conditional spatial data (SNMR-measured K_s) and a covariance matrix derived from the variogram structure analyzed in the aforementioned section. The method is believed to provide the best unbiased linear estimation for the unknown points [36, 37] using a system equation:

$$\begin{bmatrix} \mathbf{K} & \mathbf{I} \\ \mathbf{I}^T & 0 \end{bmatrix} \begin{bmatrix} \boldsymbol{\beta} \\ \lambda \end{bmatrix} = \begin{bmatrix} \mathbf{k} \\ 1 \end{bmatrix}, \quad (7)$$

$$\mathbf{K} = \begin{bmatrix} K_{11} & K_{12} & \cdots & K_{1p} \\ K_{21} & K_{22} & \cdots & K_{2p} \\ \vdots & \vdots & \cdots & \vdots \\ K_{p1} & K_{p2} & \cdots & K_{pp} \end{bmatrix},$$

$$\boldsymbol{\beta} = [\beta_1 \ \beta_2 \ \cdots \ \beta_p]^T,$$

$$\mathbf{k} = [K_{i1} \ K_{i2} \ \cdots \ K_{ip}]^T,$$

$$(i = [1, n_e] \text{ and } i \neq 1, 2, \dots, p),$$

where \mathbf{K} is the covariance matrix; \mathbf{I} is a column vector of all points with a length of p ; $\boldsymbol{\beta}$ is the vector of weights of the known data with $\sum_{i=1}^p \beta_i = 1$; \mathbf{k} is the vector of covariance between the estimated points and known points; and λ is a Lagrange multiplier. As shown in Figure 7, the variation range of the K_s values transformed from the interpolated $\ln K_s$ values of the research domain was $1.37 \times 10^{-6} \sim 1.11 \times 10^{-2}$ cm/s, which coincided with the laboratory and field measurements.

The calculation model was generated in SEEP/W. As shown in Figure 8, the mesh element of the slide mass had the same specification with the estimation grid. There were 1968 nodes in total and 1970 elements available in this calculation model. The K_s value of each element of the slide mass can be assigned individually by rewriting the XML file

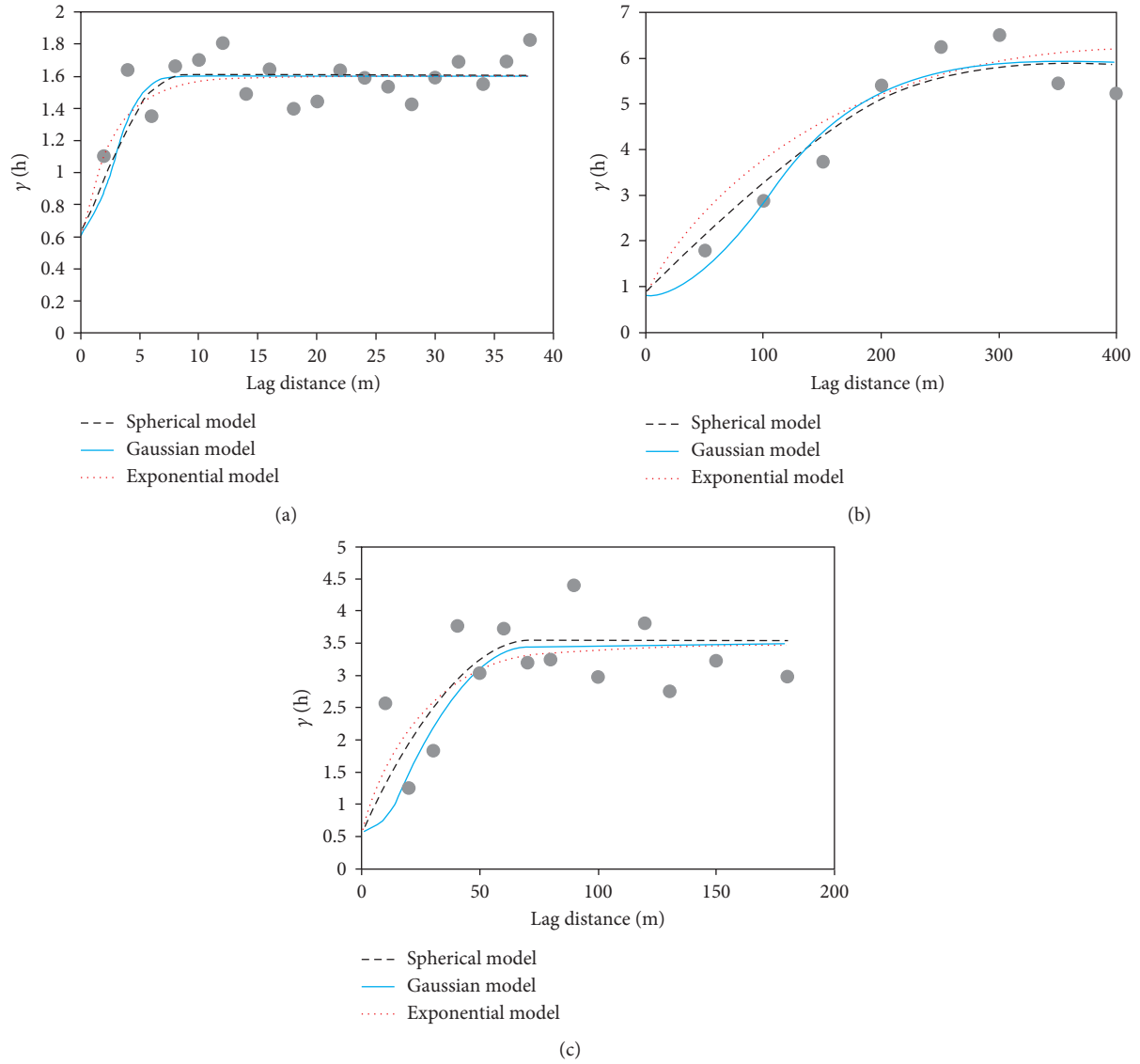


FIGURE 6: Omnidirectional variograms of the estimated $\ln K_s$ values: (a) the small-scale variogram for $\ln K_s$ for the overall site; (b) the large-scale variogram for $\ln K_s$ for the overall site; (c) the large-scale variogram for $\ln K_s$ for the major cross section.

TABLE 2: Parameters of fitting theoretical variogram models for the $\ln K_s$ value.

Study site	Study scale	Theoretical model	a (m)	A (m)	C_0	$C + C_0$	NSR (%)	R	RSS
Overall site	Small	Spherical	8.12	8.12	0.60	1.60	37.50	0.5956	0.4174
		Exponential	2.83	8.49	0.60	1.60	37.50	0.5959	0.3620
		Gaussian	3.51	6.08	0.60	1.60	37.50	0.6121	0.4307
	Large	Spherical	295.89	295.89	0.90	5.80	15.52	0.9787	1.7291
		Exponential	134.50	403.50	0.80	6.50	12.31	0.9228	4.3707
		Gaussian	138.30	239.54	0.80	5.10	15.69	0.9530	1.8442
Major profile	Large	Spherical	65.56	65.56	0.58	3.54	16.38	0.6479	5.548
		Exponential	24.83	74.49	0.55	3.56	15.45	0.5970	5.572
		Gaussian	33.98	58.85	0.56	3.58	15.64	0.6620	6.446

Note: NSR, nugget-to-sill ratio; R , coefficient of correlation; RSS, residual sum of squares; the best-fit theoretical model is marked in bold.

of SEEP/W. The front of the slope related to the reservoir water level, while the surface above the water level was assigned as a rainfall boundary with variable precipitation.

The back edge was assigned a constant water head of 240 m, while the bottom was assigned as a zero-flux boundary. The SIGMA/W code was subsequently utilized for analyzing the

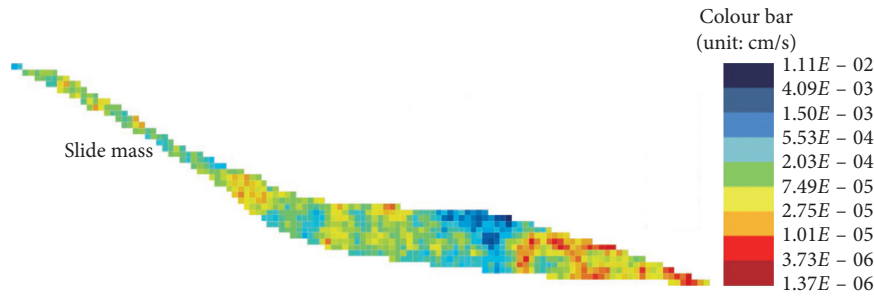


FIGURE 7: Estimated K_s value of the slide mass based on the ordinary Kriging interpolation method.

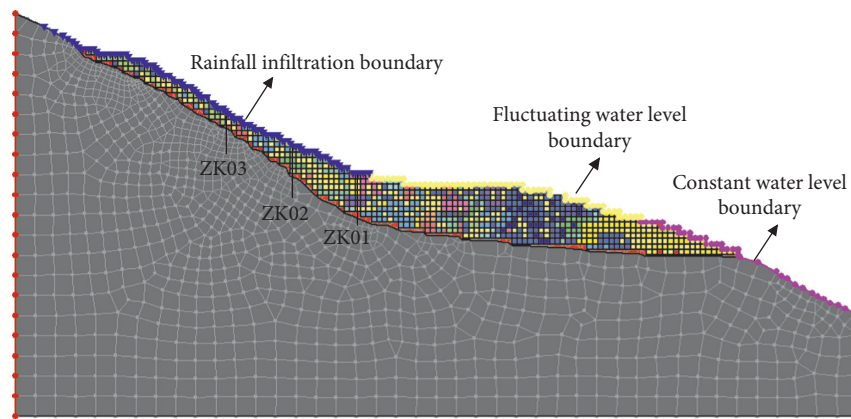


FIGURE 8: Meshed elements and presupposed boundary condition of the calculation model in SEEP/W.

deformation behavior associated with the seepage field results.

According to the laboratory experimental measurements and engineering geologic analogy method, the adopted calculation parameters are shown in Table 3. Apart from K_s values of the slide mass, the other parameters for the landslide were identified as a single variable. The volumetric water content function for the slide zone was estimated on the basis of laboratory experimental results, of which $\alpha = 0.029 \text{ kPa}^{-1}$, $n = 1.24$, $\theta_r = 0.103$, and $\theta_s = 0.315$, while the volumetric water content function for the slide mass was estimated on the basis of the grain size distribution and the estimated K_s according to the modified Kovacs method [40].

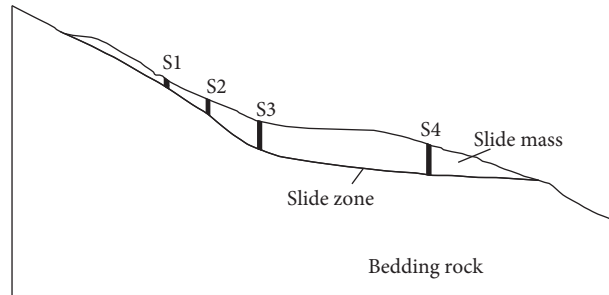
Three inclinometer holes were arranged in this major profile corresponding to ZK01, ZK02, and ZK03, as shown in Figure 8. However, two of the three inclinometer tubes had been destroyed because of undetermined reasons. Therefore, ZK01 was the remaining inclinometer hole for in-depth displacement monitoring. The actual daily rainfall precipitation and reservoir water level of the exact monitoring period, from December 28, 2013, to October 20, 2014, were selected as the calculation condition for seepage and deformation behavior analysis.

5.2. Results and Comparison. The simulated seepage and deformation behavior for 4 sections (as shown in Figure 9) were investigated in this study, including the three sections (S1, S2, and S3) corresponding to the drilled holes with

inclinometers of ZK03, ZK02, and ZK01, respectively, as well as S4 representing the unavailable bottom section beneath the water level. The horizontal cumulative displacement time history of the surfaces of the 4 studied sections are presented in Figure 10 to compare with the outer condition of rainfall and fluctuating water level. A significant deformation was detected at the bottom of the landslide (S4) at the very beginning under the condition of reduction of the reservoir water level. However, the displacement sustained at approximately 200 mm from January to July 2014 until a heavy rainstorm occurred in August 7 and facilitated the deformation under the combinational effect of reservoir water storage. The time history of S4 indicates that the deformation of the front of the landslide is sensitive to both fluctuating water level and rainfall. However, the upper sections of the landslide (S1–S3) produced negligible deformation during the entire simulation period relatively, which indicates that the deformation of the landslide is progressive. The onset of the deformation of S1–S3 was initially facilitated by an expedited drawdown of the water level and relatively intense rainfall. The step-like displacement was re-onset by the intensive rainfall in July and August of that year. The deformation for S2 and S3 increased drastically after a remarkable heavy rainfall on August 7, 2014, and lasted for two months after the remarkable rainfall was associated with the increasing water level. Miao et al. also proposed that the displacement of the Baishuihe landslide changed stepwise at the rainfall-concentrated months from May to October of every year through a multiyear displacement analysis [33].

TABLE 3: Parameters of the calculation model.

Component	γ (kN/m ³)	K_s (cm/s)	C (kPa)	ϕ (°)	E (Pa)	ν
Slide mass	20.7	—	18.62	17	7.90×10^7	0.31
Slide zone	20	3.37×10^{-6}	26.1	15.5	1.22×10^7	0.33
Bedrock	24.8	1.21×10^{-8}	228	34.2	6.81×10^9	0.26



S1 Monitoring section

FIGURE 9: Monitored sections' sketch of numerical simulation.

The multiyear displacement monitoring data also indicated that the landslide has cumulated a spectacular displacement (approximately 1~2 m) at the intermediate section by stages since the first impoundment of the Three Gorges Reservoir in 2007, but it remains stable [30–33] because of the toe resistance result from the gentle slope of the interface of the sliding mass and the bedrock.

During the simulation period, five representative points in time were selected to evaluate the seepage and deformation processes, as illustrated in Table 4. The simulated pore water pressure and displacement profile of the investigated points in time along the 4 sections were extracted from the numerical simulation, as presented in Figure 11. As indicated by Figures 11(a)–11(c), the stable depth of the zero-pore water pressure implying the embedded water table during the entire simulation period suggests that the water level and rainfall have little impact on the underlying water table at the upper and intermediate sections. However, the water table at the toe section varies remarkably in close relation to the fluctuating water level and rainfall (Figure 11(d)). The pore water pressure profiles above the bedrock for S1, S2, and S3 present a convoluted pattern with a negative value, indicating that the suction is greatly dependent on the daily rainfall at the upper section of the landslide.

As suction dissipated in the slide mass above the bedrock because of the rainfall, the kinematics of the landslide deformation changed with progressive movement in the geomaterials. The deformation of the top section (S1, as in Figure 11(e)) presents the pattern of greatest displacement at the surface dissipating along with the depth, without drastically changing at the sliding zone, which is implicative of a superficial deformation. The simulated displacement of the surface of S1 reached the peak value (58.40 mm) on October 7 2014 after a heavy storm, and the subsequent deformation was negligible. The deformation for S2 and S3 followed a translational mechanism, represented by relative

uniform displacements above the sliding zone (Figures 11(f) and 11(g)). The in-field-monitored depth-displacement profile for S3 (ZK01) is also exhibited in Figure 11(g). The monitored displacement deflected at the depth of 28 m beneath the ground surface, corresponding to the depth of the sliding zone. Such commensurate patterns with the simulated displacement curve demonstrate the reliability of the numerical results. Relatively, the displacement of the toe (S4) exhibits a distinct pattern that is tortuous with a great rotation at the depth of 8 m for the entire investigated period, which is implicative of a secondary sliding surface located in this depth at the toe. The deformation of S4 was significant from the very beginning and maintained its stability until October 2014, which is implicative of the great effect of the heavy rainfall and fluctuating water level.

According to the field investigation on October 20 2014, the Baishuihe landslide has produced remarkable crack in the middle platform (Figure 12(a)) and shallow collapse of the back edge (Figure 12(b)). The inclinometer PVC tubes located in ZK02 and ZK03 were discovered to have been destroyed at the depth of less than 1 m. The distributed optical fiber sensor arranged at the front of the landslide was discovered to be pulled apart as well. However, the exact time of occurrence of the great deformation is not verifiable. The newly outcropped large crack and collapse suggested that the deformation was not occurring for a long time, no more than 2 months. It is noticeable that the maximum simulated displacement for ZK02 and ZK03 (59.84 mm and 31.39 mm) was not large enough for the complete damage of the inclinometer pipes in general. The reason lies on the shallow deformation along the weaker zone (not sliding zone) due to the complex effects of vegetation cover, development of tension cracks, erosion, etc. The shallow deformation is also difficult to be captured during the numerical simulation.

All of the field observations and simulated results provided insights into the complex deformation behavior of the

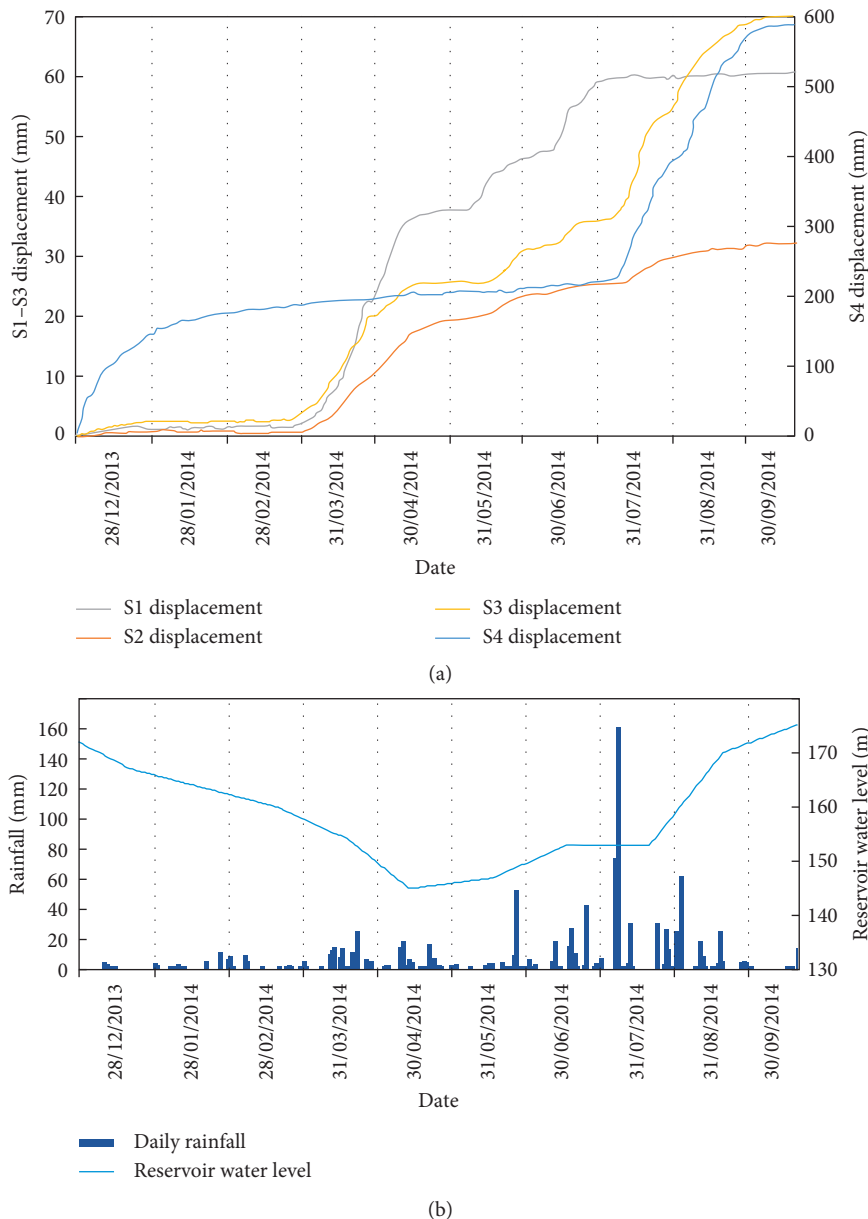


FIGURE 10: Surface displacement (a) and daily rainfall and reservoir water level (b) from December 28, 2013, to October 20, 2014.

Baishuihe landslide. The deformation behavior is progressive, occurring initially at the front of the landslide and progressing backwards. The deformation is greatly influenced by rainfall and reservoir water fluctuation. When the reservoir water level drops, a hydraulic gradient is produced due to the quick decrease of the water level compared to that of the groundwater table and it exerts an adverse effect on the landslide stability. When the reservoir stores water, the groundwater table level lifts gradually, thus increasing the weight of the geomaterial beneath the water table and softening the material. The pore water pressure in the slide mass and the sliding zone increases simultaneously; thus, the effective stress of the geomaterial beneath the water table decreases and produces deformation. In the case of heavy rain, the infiltration of the rain decreases the suction of the

slide mass and thus decreases the effective stress. Besides, the heavy rainfall produces surface runoff and causes the erosion of the landslide surface, which exacerbates the deformation of the surface. Consequently, the reservoir water impoundment and heavy rainfall are the most important factors that affect the Baishuihe landslide deformation.

6. Conclusions

The presented case study described the spatial variability of K_s values of a representative accumulation reservoir landslide in TGRA, China, estimated by the SNMR survey work arranged in the landslide field. The finite-element seepage-stress simulation results based on the spatially variable K_s values provided insights into the deformation behavior of

TABLE 4: Representative points in time and description.

Date	Days	Rainfall (mm)	Water level (m)	Inclinometer monitoring	Description
December 28, 2013	1	0	174	✓	High water level
March 27, 2014	90	0.8	158	—	Water level drawdown
June 6, 2014	161	0	146	✓	Low water level
August 7, 2014	223	160.7	153	—	Low water level with very heavy daily rainfall
October 20, 2014	297	13.2	175	✓	High water level

Note: ✓ means having inclinometer monitoring data for comparison.

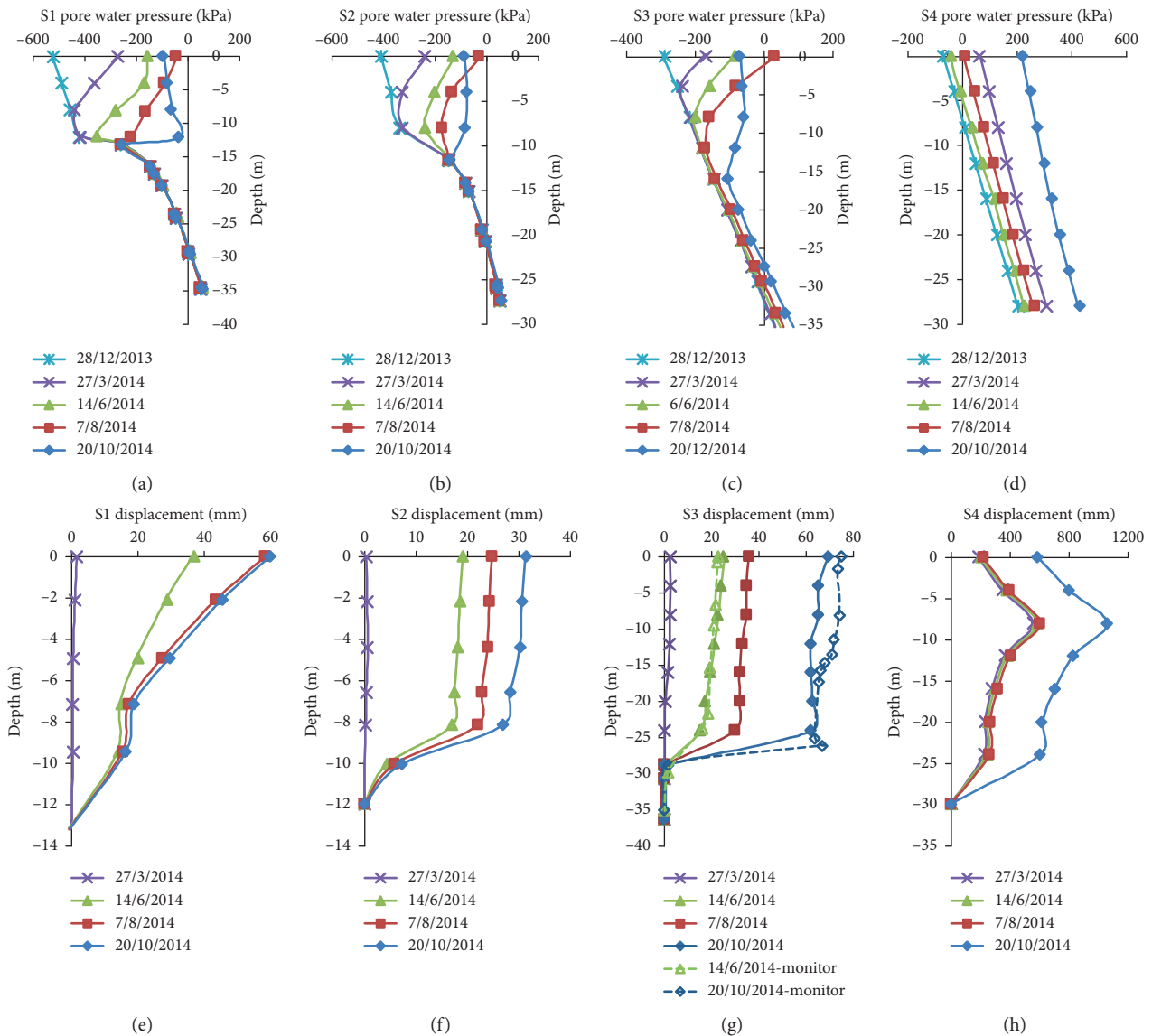


FIGURE 11: Simulated pore water pressure and displacement over time along sections of the Baishuihe landslide.

the landslide associated with the in-field observations. The conclusions from the study are as follows:

- (1) The SNMR technology provides a strategy for obtaining a series of relatively reliable spatial measurements of hydrological parameters of landslide fields using a noninvasive method. The estimation

should be calibrated according to the field tests measurements.

- (2) The estimated K_s values for the overall landslide mass site are log-normally distributed within a wide range between 3.00×10^{-6} cm/s and 7.80×10^{-3} cm/s and are associated with the CV of 34%. The variogram



FIGURE 12: Large deformation observations in the Baishuihe landslide site. (a) Great fissure at the intermediate platform. (b) Small collapse at the top section of the landslide.

analysis considering the scale effect caused by the different data intervals along different directions shows that the nested variogram has A of 298.89 m and 65.56 m, respectively, for the overall site and major cross-sectional analysis. The spatial variation of K_s is mainly dependent on the structure of the deposit.

- (3) The displacement time history as well as the pore water pressure and displacement of the studied sections based on the finite-element seepage-stress analysis of a Kriging-interpolated spatial variable K_s value calculation model provide important insights into the deformation behavior of the landslide associated with the in-field observations and monitoring data. All of the results indicate that the Baishuihe landslide is a progressive landslide with significant secondary sliding at the front section and superficial deformation at the back section. The available information indicates the main factor influencing the landslide deformation is rainfall and reservoir water fluctuation.

This study provides an unconventional framework for studying the heterogeneous geomaterial and contributes to a better understanding of the spatial variability of the hydraulic property of accumulation reservoir landslides at a field scale.

Data Availability

The data used to support the findings of this study are available from the corresponding author upon request.

Conflicts of Interest

The authors declare that there are no conflicts of interest regarding the publication of this article.

Acknowledgments

This research was supported by the National Key R&D Program of China (No. 2017YFC1501304), the China Postdoctoral Science Foundation (No. 2016M592411), and the National Natural Science Foundation of China (Nos. 41572279, 41807271, and 41877259).

References

- [1] J. E. Wang, W. Xiang, and L. Ning, "Landsliding triggered by reservoir operation: a general conceptual model with a case study at Three Gorges Reservoir," *Acta Geotechnica*, vol. 9, no. 5, pp. 771–788, 2014.
- [2] H. M. Tang, C. D. Li, X. L. Hu et al., "Deformation response of the Huangtupo landslide to rainfall and the changing levels of the Three Gorges Reservoir," *Bulletin of Engineering Geology and the Environment*, vol. 74, no. 3, pp. 933–942, 2015.
- [3] A. Perrone, R. Vassallo, V. Lapenna, and D. M. Caterina, "Pore water pressure and slope stability: a joint geophysical and geotechnical analysis," *Journal of Geophysics and Engineering*, vol. 5, no. 3, pp. 323–337, 2008.
- [4] Q. Zhai and H. Rahardjo, "Estimation of permeability function from the soil–water characteristic curve," *Engineering Geology*, vol. 199, pp. 148–156, 2015.
- [5] H. Q. Dou, T. C. Han, X. N. Gong, Z. Y. Qiu, and Z. N. Li, "Effects of the spatial variability of permeability on rainfall-induced landslides," *Engineering Geology*, vol. 192, pp. 92–100, 2015.
- [6] Z. X. Zou, C. R. Xiong, Y. K. Wang, H. M. Tang, and J. E. Wang, "An approach to obtain saturated hydraulic conductivity of reservoir landslide," *Geotechnical and Geological Engineering*, vol. 36, no. 2, pp. 1185–1196, 2018.
- [7] S. Zhang, H. M. Tang, X. Liu, Q. W. Tan, and Y. S. Xia-hou, "Seepage and instability characteristics of slope based on spatial variation structure of saturated hydraulic conductivity," *Earth Science-Journal of China University of Geosciences*, vol. 43, no. 2, pp. 622–634, 2018, in Chinese.
- [8] J. A. Sobieraj, H. Elsenbeer, and G. Cameron, "Scale dependency in spatial patterns of saturated hydraulic conductivity," *CATENA*, vol. 55, no. 1, pp. 49–77, 2004.
- [9] A. Zimmermann, D. S. Schinn, T. Francke, H. Elsenbeer, and B. Zimmermann, "Uncovering patterns of near-surface saturated hydraulic conductivity in an overland flow-controlled landscape," *Geoderma*, vol. 195–196, pp. 1–11, 2013.
- [10] Y. Wang, M. A. Shao, Z. Liu, and R. Horton, "Regional-scale variation and distribution patterns of soil saturated hydraulic conductivities in surface and subsurface layers in the loessial soils of China," *Journal of Hydrology*, vol. 487, pp. 13–23, 2013.
- [11] W. Wang, Y. Wang, Q. M. Sun, M. Zhang, Y. X. Qiang, and M. M. Liu, "Spatial variation of saturated hydraulic conductivity of a loess slope in the South Jingyang Plateau, China," *Engineering Geology*, vol. 236, pp. 70–78, 2018.
- [12] X. H. Chen, "Statistical and geostatistical features of streambed hydraulic conductivities in the Platte River, Nebraska," *Environmental Geology*, vol. 48, no. 6, pp. 693–701, 2005.

- [13] X. Chen, H. Mi, H. He et al., "Hydraulic conductivity variation within and between layers of a high floodplain profile," *Journal of Hydrology*, vol. 515, pp. 147–155, 2014.
- [14] D. H. Cheng, X. H. Chen, A. D. Huo, M. Gao, and W. K. Wang, "Influence of bedding orientation on the anisotropy of hydraulic conductivity in a well-sorted fluvial sediment," *International Journal of Sediment Research*, vol. 28, no. 1, pp. 118–125, 2013.
- [15] R. B. Miller, D. M. Heeren, G. A. Fox, T. Halihan, D. E. Storm, and A. R. Mittelstet, "The hydraulic conductivity structure of gravel-dominated vadose zones within alluvial floodplains," *Journal of Hydrology*, vol. 513, pp. 229–240, 2014.
- [16] J. Bevington, D. Piragnolo, P. Teatini, G. Vellidis, and F. Morari, "On the spatial variability of soil hydraulic properties in a Holocene coastal farmland," *Geoderma*, vol. 262, pp. 294–305, 2016.
- [17] C. M. Regalado and R. Muñoz-Carpena, "Estimating the saturated hydraulic conductivity in a spatially variable soil with different permeameters: a stochastic Kozeny-Carman relation," *Soil and Tillage Research*, vol. 77, no. 2, pp. 189–202, 2004.
- [18] J. O. Walbrecker and A. A. Behroozmand, "Surface-NMR measurements of the longitudinal relaxation time T1 in a homogeneous sand aquifer in Skive, Denmark," *Journal of Applied Geophysics*, vol. 87, pp. 46–52, 2012.
- [19] A. A. Behroozmand, K. Keating, and E. Auken, "A review of the principles and applications of the NMR technique for near-surface characterization," *Surveys in Geophysics*, vol. 36, no. 1, pp. 27–85, 2015.
- [20] M. A. Meju, P. Denton, and P. Fenning, "Surface NMR sounding and inversion to detect groundwater in key aquifers in England: comparisons with VES-TEM methods," *Journal of Applied Geophysics*, vol. 50, no. 1-2, pp. 95–111, 2002.
- [21] R. Knight, E. Grunewald, T. Irons et al., "Field experiment provides ground truth for surface nuclear magnetic resonance measurement," *Geophysical Research Letters*, vol. 39, no. 3, pp. 1–7, 2012.
- [22] E. Grunewald, R. Knight, and D. Walsh, "Advancement and validation of surface nuclear magnetic resonance spin-echo measurements of T2," *Geophysics*, vol. 79, no. 2, pp. EN15–EN23, 2013.
- [23] X. L. Hu, H. M. Tang, S. Z. Ma, and G. C. Zhang, "Numerical simulation of the 3D landslide stability in three gorges area based on NMR," *Earth Science-Journal of China University of Geosciences*, vol. 31, no. 2, pp. 279–284, 2006.
- [24] M. Hertrich, "Imaging of groundwater with nuclear magnetic resonance," *Magnetic Resonance Spectroscopy*, vol. 53, no. 4, pp. 227–248, 2008.
- [25] W. E. Kenyon, P. I. Day, C. Straley, and J. F. Willemsen, "A three-part study of NMR longitudinal relaxation properties of water-saturated sandstones," *SPE Formation Evaluation*, vol. 3, no. 3, pp. 622–636, 1988.
- [26] D. O. SeEVERS, "A nuclear magnetic method for determining the permeability of sandstones," in *Proceedings of SPWLA 7th Annual Logging Symposium*, Tulsa, OK, USA, May 1966.
- [27] A. Weller, S. Nordsiek, and W. Debschütz, "Estimating permeability of sandstone samples by nuclear magnetic resonance and spectral-induced polarization," *Geophysics*, vol. 75, no. 6, pp. E215–E226, 2010.
- [28] R. Dlugosch, T. Günther, M. Müller-Petke, and U. Yaramanci, "Improved prediction of hydraulic conductivity for coarse-grained, unconsolidated material from nuclear magnetic resonance," *Geophysics*, vol. 78, no. 4, pp. EN55–EN64, 2013.
- [29] R. Knight, D. O. Walsh, J. J. Butler et al., "NMR logging to estimate hydraulic conductivity in unconsolidated aquifers," *Groundwater*, vol. 54, no. 1, pp. 104–114, 2016.
- [30] D. Y. Li, K. L. Yin, and C. Leo, "Analysis of Baishuihe landslide influenced by the effects of reservoir water and rainfall," *Environmental Earth Sciences*, vol. 60, no. 4, pp. 677–687, 2010.
- [31] J. Du, K. L. Yin, and S. Lasasse, "Displacement prediction in colluvial landslides, three gorges reservoir, China," *Landslides*, vol. 10, no. 2, pp. 203–218, 2013.
- [32] Y. Liu, D. Liu, Z. M. Qin, F. B. Liu, and L. B. Liu, "Rainfall data feature extraction and its verification in displacement prediction of Baishuihe landslide in China," *Bulletin of Engineering Geology and the Environment*, vol. 75, no. 3, pp. 897–907, 2016.
- [33] F. S. Miao, Y. P. Wu, Y. H. Xie, and Y. N. Li, "Prediction of landslide displacement with step-like behavior based on multialgorithm optimization and a support vector regression model," *Landslides*, vol. 15, no. 3, pp. 475–488, 2018.
- [34] S. Zhang, H. M. Tang, H. B. Zhan, G. P. Lei, and H. Cheng, "Investigation of scale effect of numerical unconfined compression strengths of virtual colluvial-deluvial soil-rock mixture," *International Journal of Rock Mechanics & Mining Sciences*, vol. 77, pp. 208–219, 2015.
- [35] X. H. Long, J. Zhao, Z. P. Liu et al., "Applying geostatistics to determine the soil quality improvement by Jerusalem artichoke in coastal saline zone," *Ecological Engineering*, vol. 70, pp. 319–326, 2014.
- [36] J. P. Chiles and D. Pierre, *Geostatistics: Modeling Spatial Uncertainty*, Wiley, New York, NY, USA, 1999.
- [37] P. Goovaerts, *Geostatistics for Natural Resources Evaluation*, Oxford University Press, New York, NY, USA, 1997.
- [38] J. M. Wang, R. X. Yang, and Z. K. Bai, "Spatial variability and sampling optimization of soil organic carbon and total nitrogen for Minesoils of the Loess Plateau using geostatistics," *Ecological Engineering*, vol. 82, pp. 159–164, 2015.
- [39] Geo-Slope International Ltd., *Seep/W for Finite Element Seepage Analysis User's Manual*, Geo-Slope International Ltd., Calgary, AB, Canada, 1998.
- [40] M. Aubertin, M. Mbonimpa, B. Bussiere, and R. P. Chapuis, "A model to predict the water retention curve from basic geotechnical properties," *Canadian Geotechnical Journal*, vol. 40, no. 6, pp. 1140–1122, 2003.

Research Article

Shearing Performance of Lime-Reinforced Iron Tailing Powder Based on Energy Dissipation

Ping Jiang ¹, Lingqi Qiu,¹ Na Li ¹, Wei Wang ¹, Aizhao Zhou,² and Jingping Xiao³

¹School of Civil Engineering, Shaoxing University, Shaoxing, Zhejiang 312000, China

²Department of Civil and Architecture Engineering, Jiangsu University of Science and Technology, Zhenjiang, Jiangsu 212003, China

³Huahui Engineering Design Group Co. Ltd, Shaoxing, Zhejiang 312000, China

Correspondence should be addressed to Wei Wang; wangwells@qq.com

Received 15 June 2018; Accepted 10 September 2018; Published 21 October 2018

Guest Editor: Yonggui Chen

Copyright © 2018 Ping Jiang et al. This is an open access article distributed under the Creative Commons Attribution License, which permits unrestricted use, distribution, and reproduction in any medium, provided the original work is properly cited.

The resource utilization of iron tailing powder is an effective measure to reduce the risk of tailing stacking. Based on the research findings on lime soil, a method for using lime to strengthen iron tailing powder was proposed. $F-s$ curves and c and φ values of iron tailing powder with 0%, 2%, 4%, 8%, and 10% lime were obtained through direct shear tests. The back propagation (BP) neural network algorithm was used to fit the $F-s$ curve, and the fitting equation that met the accuracy requirement was obtained. Based on the energy dissipation theory, the shear failure energy dissipation of iron tailing powder with different lime doses was achieved in the form of definite integrals under different normal stresses of 100 kPa, 200 kPa, 300 kPa, and 400 kPa, respectively. It was concluded that the addition of lime could increase the shear energy dissipation of iron tailing powder. The shear energy dissipation of iron tailing powder first increased and then decreased with the increase in lime dose. The maximum value was reached with 4% lime, and the energy dissipation increased linearly with increasing normal stress. In this study, the shear performance of lime-reinforced iron tailing powder was studied through the direct shear test combined with the energy dissipation theory, providing a theoretical basis for the resource utilization of iron tailing powder.

1. Introduction

Iron tailing powder is one of the products of iron ore sorting operation. Not only it has an impact on the surrounding environment, the tailing stacking also seriously threatens the lives and property of the people downstream of the reservoir area. Therefore, how to use tailings and turn waste into treasure is a matter of great concern to local governments. By the end of 2017, the total stock of various types of tailings in China reached 16 billion tons, of which iron tailings account for one-third of all tailings. Taking Zhejiang Lizhu Iron Ore as an example, about 200,000 tons of dehydrated tailings are produced each year. More than 20 million tons of tailings accumulate in the existing tailing dam storage yard, and the iron tailings occupy a large proportion of land resources with a risk of dam break.

Many studies were conducted on the resource utilization of iron tailing powder, including concrete fine aggregates [1],

wastewater treatment [2], filling materials of composite material [3], recovery of iron ore [4], and use as a road material [5]. The particles with larger particle sizes in Lizhu iron tailings can be used as building materials, bringing economic benefits. However, the tailing particles with a particle size of less than 0.075 mm are small, nonviscous, nonphysicochemically active, and difficult to utilize and transform. Therefore, certain strategies are needed to increase the degree of resource utilization.

Lime-reinforced soil is a building material with a long history; its mechanical properties have been previously explored. Based on the unconfined compressive strength and splitting strength of lime soil, the Mohr-Coulomb destruction envelope curve of lime soil was investigated by Consoli using lime content and porosity as basic parameters [6]. A series of studies were conducted by Wang, including size effect on cementitious aggregates during curing of calcined soil; thermal conductivity, suction, and microstructural changes

during curing; and the effect of aggregate size on the compressibility and air permeability of lime-treated fine-grained soils [7–9]. Jha studied the volume change behavior and strength growth mechanism of lime-treated gypseous soil from the perspective of mineralogy and microstructure [10, 11]. The short-term effects of the physical properties of lime-treated kaolin were studied by Vitale [12]. The aforementioned findings indicated that lime could fill the pores between soil particles to a certain extent and react with the active silica and other components in the soil to improve their mechanical properties.

Therefore, lime soil research findings can be used for reference. The iron tailing powder can be modified with lime to form a new composite soil material, which can be used in practical engineering. Energy dissipation is a commonly used method for studying material failure performance such as the factor of safety (FS) of 3D stepped slopes [13], constitutive model for geotechnical materials [14, 15], soil-sweep interaction [16], mechanical behaviors of soil [17, 18], and cement soil [19, 20]. Shearing performance is the most basic mechanical property of geotechnical materials. Therefore, the research findings on lime soil can be used to study the shear properties of lime-reinforced iron tailing powder based on energy dissipation theory.

2. Physicochemical Properties of Iron Tailing Powder

The test samples were obtained from Zhejiang Lizhu Iron Ore (Figure 1). The chemical composition, physical properties, and particle composition were tested separately. The test results were as follows.

According to the chemical analysis method of GB/T176-2008, the content of SiO_2 and MgO was higher (41.11% and 16.7%, resp.). The contents of SO_3 and Na_2O were lower (0.46% and 0.29%, resp.). The iron ore tailings contained 10.8% Fe_2O_3 . The main chemical composition of iron tailing powder is shown in Table 1.

Loss on ignition, chloride ion, total alkali content, specific gravity, and specific surface area of iron tailing powder were tested. The test results are shown in Table 2.

Since the iron tailing powder contained fine particles after sorting, the particle size analysis of iron tailing powder (less than $45\ \mu\text{m}$, $45\text{--}75\ \mu\text{m}$, $75\text{--}100\ \mu\text{m}$, $100\text{--}150\ \mu\text{m}$, and more than $150\ \mu\text{m}$) was conducted using a Mastersizer2000 laser particle size analyzer. The results are shown in Figure 2.

3. Direct Shear Test

Lizhu iron tailing powder has a certain content of SiO_2 . However, the particle size of iron tailings is less than $45\ \mu\text{m}$. Therefore, a method of using lime to strengthen iron tailing powder was proposed to increase the resource utilization of Lizhu iron tailing powder. The shear performance of the material was the basic mechanical index. The direct shear test was used to study the shear properties of lime-reinforced tailing powder.

3.1. Sample Preparation and Testing. The sample was quicklime, and the lime dose was the percentage of the dry mass of lime relative to iron tailing powder. The doses were 0%, 2%, 4%, 8%, and 10%. These percentages were chosen considering both international and China experience with soil-lime mixtures in experimental work [6–9]. In the preparation process, quicklime and iron tailing powders were first stirred for 3 min. Then, 17% of water was added and stirred for another 3 min. After standing for 24 h, they were put into a ring knife with a diameter of 61.8 mm and a height of 20 mm. A layer of petroleum jelly was smeared to the interior of the ring knife. The sample was formed by compaction, and the upper and lower surfaces of the sample were leveled. After leaving for 2 h, demolding was performed and the weight of each sample was determined. The weight of the sample should be controlled at $146\ \text{g} \pm 2\ \text{g}$. The samples were wrapped in a natural environment for 24 h using a plastic wrap (Figure 3) and subjected to direct shear test.

The test equipment was a fully automatic quadruple direct shear apparatus (Figure 4) produced by Nanjing TKA Technology Co., Ltd. It could perform direct shear tests under the action of four normal stresses simultaneously, ensure the test accuracy, and improve the test efficiency. The normal stresses were 100 kPa, 200 kPa, 300 kPa, and 400 kPa, and the shear rate was 1 mm/min. Six shear forces (F) and corresponding shear displacements (s) were recorded every second during the test.

3.2. Test Results and Analysis. Based on the test results, the shear force versus displacement curves of lime-reinforced iron tailings under different normal stresses were plotted, as shown in Figure 5.

The peak force F_{\max} was extracted and the peak shear strength τ_{\max} was calculated using the F - s curve according to Equation (1). The cohesion c and the internal friction angle φ of lime-reinforced iron tailings powder with different lime doses were calculated according to the Mohr-Coulomb principle (Equation (2)) and are plotted in Figure 6:

$$\tau_{\max} = \frac{F_{\max}}{A}, \quad (1)$$

$$\tau = c + \sigma \tan \varphi. \quad (2)$$

Figure 6 shows that the internal friction angle of iron tailing powder increased with increasing lime dose to some extent. When the lime dose increased from 0% to 8%, the internal friction angle increased from 31.7° to 34.7° . From 8% to 10%, the internal friction angle increased obviously from 34.7° to 42.7° , indicating that the addition of quicklime enhanced the friction force between tailing particles to some extent.

The cohesive force of iron tailing powder with added lime first increased and then decreased with increasing amount of quicklime. When the lime dose increased from 0% to 8%, the cohesive force increased from 12.3 kPa to 96.5 kPa with obvious growth about seven times. However, when the lime dose increased from 8% to 10%, the cohesion



FIGURE 1: The position of Zhejiang Lizhu Iron tailings.

TABLE 1: Chemical composition of iron tailings powder.

Composition	SiO ₂	Fe ₂ O ₃	Al ₂ O ₃	CaO	MgO	SO ₃	K ₂ O	Na ₂ O
Mass fraction (%)	41.11	10.8	8.19	13.99	16.7	0.46	0.72	0.29

TABLE 2: Main physical parameters of iron tailings powder.

Composition	LOI	CI	Total alkali content	Specific gravity	Specific surface area (m ² /kg)
Parameter	7.01	0.21	0.76	3.06	379

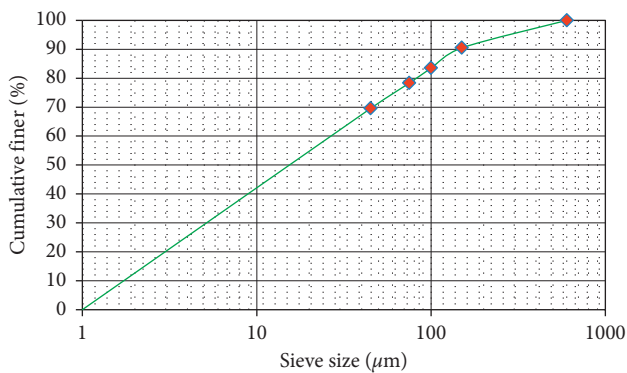


FIGURE 2: Iron tailings powder distribution curve.

decreased from 96.5 kPa to 36.3 kPa. It showed that quicklime could improve the cohesion of iron tailing powder when the lime dose increased from 0% to 8%, but the

cohesion decreases when the lime dose increased from 8% to 10%.

Since the particle size of the quicklime particles was about 1 μm, and iron tailing powder comprised particles smaller than 45 μm, the quicklime particles could fill gaps between the iron tailing powder particles to some extent, thereby improving their adhesion. When the lime dose was between 2% and 8%, the cohesion of lime-reinforced iron tailing powder increased. As quicklime particles were fine and easy to slide, the frictional effect between iron tailing powder particles was not obvious. Therefore, the shear strength of lime-reinforced iron tailings powder increased within a certain range of lime dose. When the amount of quicklime reached 10%, there produces one or several layers of the lime closely and continuously around the outside surface of the iron tailings powder particles, which just like a “lime film” forming around the iron tailing powder particles, decreasing the cohesion of the iron



FIGURE 3: Iron ore tailings direct shear sample.



FIGURE 4: Fully automatic quadruple direct shear apparatus.

tailing powder particles and increasing the internal friction angle.

4. Energy Dissipation

The direct shear test results of lime-reinforced iron tailing powder indicated that a certain amount of quicklime could improve the cohesion and internal friction of the tailing powder, thereby improving its shear resistance. However, it is difficult to comprehensively evaluate the effect of lime dose on the shear performance of iron tailing powder due to two independent parameters of cohesion and internal friction angle. The failure process of the sample direct shear test is actually an energy-dissipating process. Therefore, the characteristics of the direct shear test indicate that the energy dissipation can be used to characterize the sample failure process. That is, the characteristics of the F - s curve show that the work done by the shear force is the energy dissipation of sample failure. Due to the limited discrete data points obtained during the direct shear test, it is necessary to accurately obtain the F - s function relationship to accurately obtain the energy dissipation by the test sample. BP neural network is a common data-fitting method. A reasonable neural network structure can simulate almost any nonlinear function [21, 22]. The BP neural network

algorithm was used in this study to fit the F - s curve, and then the definite integral method was used to achieve the shear energy dissipation of lime-reinforced iron tailings powder.

4.1. BP Neural Network Curve Fitting. A BP neural network structure with one hidden-layer and two hidden-layer nodes was chosen: input node and output node. Hidden-layer transfer functions are expressed as in Equation (3), output-layer transfer functions as in Equation (4), and BP neural network information transfer as in Equation (5):

$$f(v) = \frac{1}{e^{-v} + 1}, \quad (3)$$

$$f(v) = v, \quad (4)$$

$$f(v) = \frac{\omega_2}{e^{-(\omega_1 v + b_1)} + 1} + b_2, \quad (5)$$

where $\omega_{1(2 \times 1)}$ and $b_{1(2 \times 1)}$ are the weights and offsets of the input layer, respectively, and $\omega_{2(1 \times 2)}$ and $b_{2(1 \times 1)}$ are the weights and offsets of the hidden layers, respectively. The use of BP neural network was based on experimental data by error reverse transforming and constantly updating weights and offsets to meet the fitting accuracy.

The original data is needed to be normalized according to the following equation to ensure the fitting accuracy, so that the input and output data were all between $[-1, 1]$:

$$y = \frac{2(x - x_{\min})}{x_{\max} - x_{\min}} - 1, \quad (6)$$

where x_{\max} and x_{\min} are the maximum and minimum values of the data to be converted, respectively, x and y denote the data to be converted and the converted data, respectively. Obviously, $-1 \leq y \leq 1$.

After BP neural network fitted the functional relationship that satisfied the accuracy, the calculation data were converted into the original data according to the following equation:

$$x = \frac{(x_{\max} - x_{\min})(y + 1)}{2} + x_{\min}. \quad (7)$$

Combining Equations (5), (6), and (7), a more accurate F - s fitting equation was obtained, as shown in the following equation:

$$F = \frac{C_1}{e^{-C_2 s - C_3} + 1} + \frac{C_4}{e^{-C_5 s - C_6} + 1} + C_7, \quad (8)$$

where $C_1 = (F_{\max} \omega_{21})/2$, $C_2 = 2\omega_{11}/s_{\max}$, $C_3 = b_{11} - \omega_{11}$, $C_4 = (F_{\max} \omega_{22})/2$, $C_5 = 2\omega_{12}/s_{\max}$, $C_6 = b_{12} - \omega_{12}$, and $C_7 = (F_{\max}/2)(b_2 + 1)$.

Using the F - s experimental data obtained through the direct shear test, F - s fitting equations under different normal stresses with different lime doses were obtained by means of the BP neural network algorithm. The calculation data are shown in Table 3.

The fitting curve with 4% lime is shown in Figure 7.

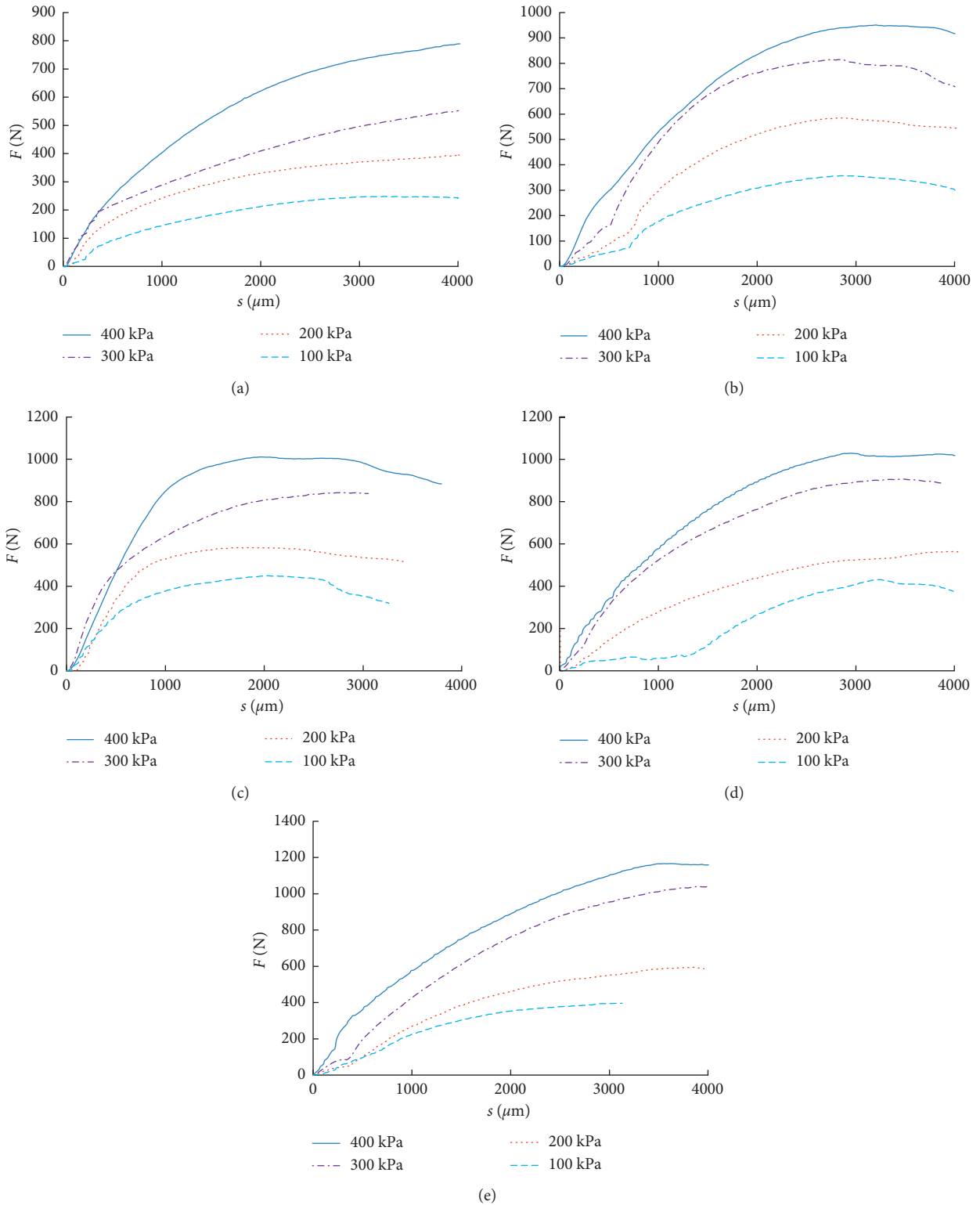


FIGURE 5: F - s curve of iron tailing powder with different lime doses. (a) 0% lime, (b) 2% lime, (c) 4% lime, (d) 8% lime, and (e) 10% lime.

Table 3 and Figure 7 show that the BP neural network algorithm provided a more accurate F - s fitting function with an average relative error less than 10%. Therefore, the BP neural network algorithm was used to fit the F - s function relationship.

4.2. Energy Dissipation Calculation. According to the fitting formula, the definite integral was used to obtain the shear energy dissipation of iron tailing powder with different lime doses under different normal stresses, as shown in the following equation:

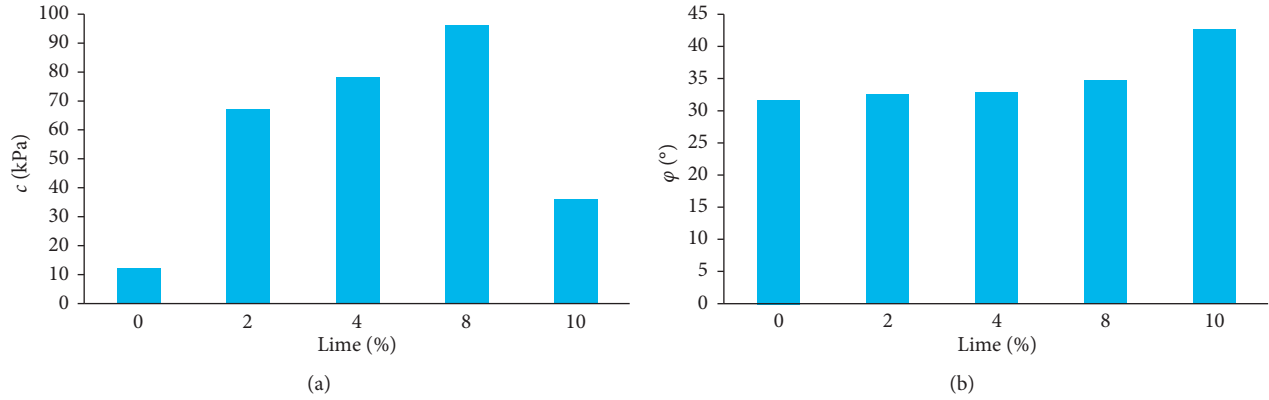


FIGURE 6: (a) Cohesion and (b) internal friction angle of iron tailing powder with different lime doses.

TABLE 3: BP neural network fitting results.

Lime dosage (%)	Normal stress (kPa)	C_1	C_2	C_3	C_4	C_5	C_6	C_7	Average relative error
0	100	-49.93	0.0023	-9.71	727324	0.00077	7.87	-727051	0.03
	200	-19.77	0.0055	-29.97	-4557279	-0.00091	-9.36	399	0.06
	300	-14.06	0.0033	-17.77	317668	0.00037	6.33	-317062	0.05
	400	24.61	-0.0062	34.9	-38062	-0.00067	-3.79	823	0.02
2	100	101.72	-0.0041	16.19	427.	0.002	-1.82	-168	0.06
	200	-319	0.0013	-6.87	660	0.0022	-2.31	-64	0.05
	300	143	-0.0047	17.77	-965	-0.0024	1.78	668	0.02
	400	121	-0.0031	10.99	-2121805	-0.00077	-7.68	863	0.05
4	100	125	-0.0075	20.69	-2002	-0.0021	-1.16	327	0.02
	200	57.6	-0.0054	14.85	756	0.0044	-1.48	-236	0.12
	300	634	0.0019	-1.23	458	0.0095	-1.54	-240	0.01
	400	152.46	-0.0036	11.99	-1363	-0.0031	1.16	863	0.01
8	100	-243	0.0018	-3.41	-571	-0.0031	3.48	581	0.09
	200	-537	-0.0013	1.41	-134	-0.0067	3.18	572	0.08
	300	-70.42	0.0055	-19.89	331411	0.00075	5.78	-330411	0.03
	400	-1162	0.00088	-3.73	89179	0.0003	3.69	-86966	0.06
10	100	587	0.0015	-0.68	-24.39	-0.023	17.96	-181	0.03
	200	533	0.0012	-1.5	183	0.0046	-3.28	-103	0.04
	300	-1350	-0.0011	1.06	-86.05	-0.013	7.37	1086	0.03
	400	-356	-0.0023	6.55	-942	-0.002	1.91	1173	0.03

$$W = \int_0^{s_{\max}} F(s) ds, \quad (9)$$

where s_{\max} is taken as 4 mm consistent with the provisions of 4.7 in Test Method of Soils for Highway Engineering (JTG E40-2007) [23]. The calculation results of the shear energy dissipation of iron tailing powder with different lime doses under different normal stresses are shown in Table 4.

Figure 8 shows that the shear energy dissipation of iron tailing powder with different lime doses increased linearly with increasing normal stress. The shear energy dissipation of lime-reinforced iron tailing powder was higher than that of normal iron tailing powder, and the iron tailing powder with 4% lime had the largest energy dissipation value.

Figure 9 shows that under different normal stresses, the shear energy dissipation of lime-reinforced iron tailing powder had the same variation tendency with increasing

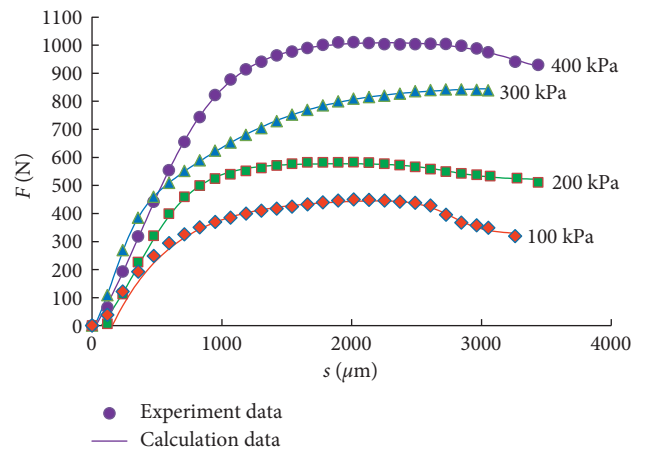


FIGURE 7: F - s fitting curve of iron tailing powder with 4% lime.

TABLE 4: Shear energy dissipation of iron tailing powder with different lime doses under different normal stresses (J).

Lime (%)	Normal stress (kPa)			
	100	200	300	400
0	0.74	1.18	1.24	2.2
2	0.99	1.62	2.44	2.67
4	1.4	1.95	2.82	3.33
8	1.18	1.54	2.68	2.39
10	1.18	1.1	2.68	2.71

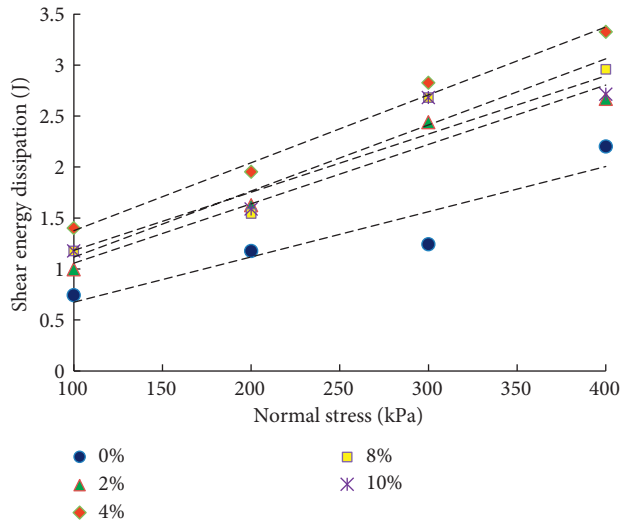


FIGURE 8: Shear energy dissipation of lime-reinforced iron tailing powder under different normal stresses.

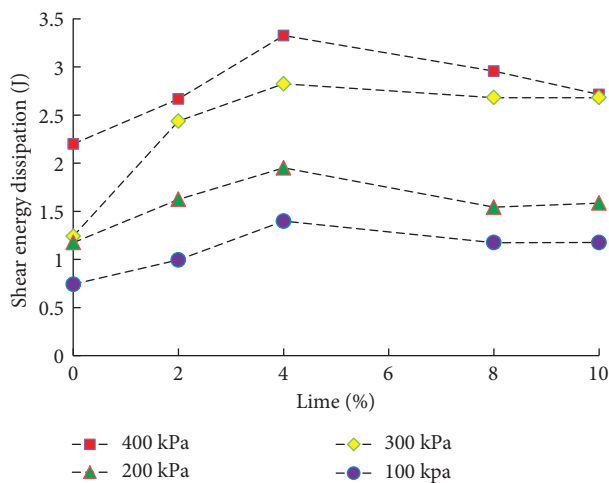


FIGURE 9: Shear energy dissipation of lime-reinforced iron tailing powder with different lime doses.

lime dose. That is, the shear energy dissipation first increased and then decreased gradually with increasing lime dose. When the lime dosage was 4%, the shear energy dissipation value was the largest. Therefore, it was concluded that 4% lime provided the best ratio.

5. Conclusions

This study proposed a method for using lime to strengthen iron tailing powder based on the research findings on the lime soil. The F - s curves and c and ϕ values of iron tailing powders with 0%, 2%, 4%, 8%, and 10% lime content were obtained through direct shear tests. The BP neural network algorithm was used to fit the F - s curve. Based on the energy dissipation theory, the shear failure energy dissipation of iron tailing powder with different lime doses under different normal stresses of 100 kPa, 200 kPa, 300 kPa, and 400 kPa was achieved in the form of a definite integral. Several conclusions are drawn as follows:

- (1) BP neural network algorithm has a good fitting accuracy and can be used to fit the F - s curve in the direct shear test.
- (2) The cohesion of lime-reinforced iron tailing powder first increases and then decreases with increasing lime dose. Also, the internal friction angle increases with increasing lime dose.
- (3) The incorporation of lime can increase the shear energy dissipation of iron tailing powder. With the increase in lime dose, the shear energy dissipation of iron tailing powder first increases and then decreases, reaching the maximum with 4% lime. Furthermore, the energy dissipation increases linearly with increasing normal stress.

Data Availability

All the data used to support the findings of this study are included within the article.

Conflicts of Interest

The authors declare that they have no conflicts of interest.

Acknowledgments

This work was supported by the National Natural Science Foundation of China (41772311 and 51579199), Zhejiang Provincial Natural Science Foundation of China (LY17E080016), and the Research Fund of Zhejiang Provincial Department of Housing and Urban-Rural Development (2017K179, 2016K130).

References

- [1] F. H. Han, L. Li, S. M. Song, and J. Liu, "Early-age hydration characteristics of composite binder containing iron tailing powder," *Powder Technology*, vol. 315, pp. 322–331, 2017.
- [2] P. Duan, C. Yan, W. Zhou, and D. Ren, "Development of fly ash and iron ore tailing based porous geopolymer for removal of Cu(II) from wastewater," *Ceramics International*, vol. 42, no. 12, pp. 13507–13518, 2016.
- [3] M. A. Onitiriand and E. T. Akinlabi, "Effects of particle size and particle loading on the tensile properties of iron-ore-tailing-filled epoxy and polypropylene composites," *Mechanics of Composite Materials*, vol. 52, no. 6, pp. 817–828, 2017.

- [4] L. Panda, S. K. Biswal, R. Venugopaland, and N. R. Mandre, "Recovery of ultra-fine iron ore from iron ore tailings," *Transactions of the Indian Institute of Metals*, vol. 71, no. 2, pp. 463–468, 2018.
- [5] L. A. D. C. Bastos, G. C. Silva, J. C. Mendes, and R. A. F. Peixoto, "Using iron ore tailings from tailing dams as road material," *Journal of Materials in Civil Engineering*, vol. 28, no. 10, article 04016102, 2016.
- [6] N. C. Consoli, L. Da Silva Lopes Jr, B. S. Consoli, and L. Festugato, "Mohr–Coulomb failure envelopes of lime-treated soils," *Géotechnique*, vol. 64, no. 2, pp. 165–170, 2014.
- [7] Y. Wang, M. Duc, Y. J. Cui et al., "Aggregate size effect on the development of cementitious compounds in a lime-treated soil during curing," *Applied Clay Science*, vol. 136, pp. 58–66, 2017.
- [8] Y. Wang, Y. J. Cui, A. M. Tang, C. S. Tang, and N. Benahmed, "Changes in thermal conductivity, suction and microstructure of a compacted lime-treated silty soil during curing," *Engineering Geology*, vol. 202, pp. 114–121, 2016.
- [9] Y. Wang, Y. J. Cui, A. M. Tang, N. Benahmed, and M. Duc, "Effects of aggregate size on the compressibility and air permeability of lime-treated fine-grained soil," *Engineering Geology*, vol. 228, pp. 167–172, 2017.
- [10] A. K. Jhaand and P. V. Sivapullaiah, "Volume change behavior of lime treated gypseous soil -influence of mineralogy and microstructure," *Applied Clay Science*, vol. 119, pp. 202–212, 2016.
- [11] A. K. Jhaand and P. V. Sivapullaiah, "Physical and strength development in lime treated gypseous soil with fly ash-micro-analyses," *Applied Clay Science*, vol. 145, no. 1, pp. 17–27, 2017.
- [12] E. Vitale, D. Deneele, G. Russoand, and G. Ouvrard, "Short-term effects on physical properties of lime treated kaolin," *Applied Clay Science*, vol. 132-133, pp. 223–231, 2016.
- [13] X. L. Yang and Z. W. Li, "Factor of safety of three-dimensional stepped slopes," *International Journal of Geomechanics*, vol. 18, no. 6, article 04018036, 2018.
- [14] Z. G. Zhang, Y. Q. Chen, and Z. P. Huang, "A novel constitutive model for geomaterials in hyperplasticity," *Computers and Geotechnics*, vol. 98, pp. 102–113, 2018.
- [15] S. Nadimi and J. Fonseca, "A micro finite-element model for soil behavior: numerical validation," *Géotechnique*, vol. 68, no. 4, pp. 364–369, 2018.
- [16] K. Tamas, "The role of bond and damping in the discrete element model of soil-sweep interaction," *Biosystems Engineering*, vol. 169, pp. 57–70, 2018.
- [17] K. J. Hanley, X. Huang, and C. Q'Sullivan, "Energy dissipation in soil samples during drained triaxial shearing," *Géotechnique*, vol. 68, no. 5, pp. 421–433, 2018.
- [18] Z. W. Zhou, W. Ma, S. J. Zhang, Y. H. Mu, and G. Y. Li, "Effect of freeze-thaw cycles in mechanical behaviors of frozen loess," *Cold Regions Science and Technology*, vol. 146, pp. 9–18, 2017.
- [19] W. Wang, N. Li, F. Zhang, A. Zhou, and S. Chi, "Experimental and mathematical investigations on unconfined compressive behavior of coastal soft soil under complicated freezing processes," *Polish Maritime Research*, vol. 23, no. 4, pp. 112–116, 2016.
- [20] Y. Liu, Y. Jiang, H. Xiao, and F. H. Lee, "Determination of representative strength of deep cement-mixed clay from core strength data," *Géotechnique*, vol. 67, no. 4, pp. 350–364, 2017.
- [21] F. He and L. Zhang, "Prediction model of end-point phosphorus content in BOF steelmaking process based on PCA and BP neural network," *Journal of Process Control*, vol. 66, pp. 51–58, 2018.
- [22] X. Yu, J. Han, L. Shi, Y. Wang, and Y. Zhao, "Application of a BP neural network in predicting destroyed floor depth caused by underground pressure," *Environmental Earth Sciences*, vol. 76, no. 15, p. 535, 2017.
- [23] Profession Standard Of The People's Republic Of China, *Test Method of Soils for Highway Engineering (JTG E40-2007)*, People's Communications Press, Beijing, China, 2007.

Research Article

Numerical Modeling of Thermal-Dependent Creep Behavior of Soft Clays under One-Dimensional Condition

Qi-Yin Zhu  and Ping Qi

State Key Laboratory for Geomechanics and Deep Underground Engineering, China University of Mining and Technology, Xuzhou 221008, China

Correspondence should be addressed to Qi-Yin Zhu; qiyin.zhu@gmail.com

Received 29 June 2018; Revised 20 September 2018; Accepted 25 September 2018; Published 17 October 2018

Academic Editor: Dingwen Zhang

Copyright © 2018 Qi-Yin Zhu and Ping Qi. This is an open access article distributed under the Creative Commons Attribution License, which permits unrestricted use, distribution, and reproduction in any medium, provided the original work is properly cited.

Creep is a common phenomenon for soft clays. The paper focuses on investigating the influence of temperature on the time-dependent stress-strain evolution. For this purpose, the temperature-dependent creep behavior for the soft clay has been investigated based on experimental observations. A thermally related equation is proposed to bridge the thermal creep coefficient with temperature. By incorporating the equation to a selected one-dimensional (1D) elastic viscoplastic (EVP) model, a thermal creep-based EVP model was developed which takes into account the influence of temperature on creep. Simulations of oedometer tests on reconstituted clay are made through coupled consolidation analysis. The bonding effect of the soil structure on compressive behavior for intact clay is studied. By incorporating the influence of the soil structure, the thermal creep EVP model is extended for intact clay. Experimental predictions for thermal creep oedometer tests are simulated at different temperatures and compared to that obtained from reconstituted clay. The results show that the influence of temperature on the creep behavior for intact clay is significant, and the model, this paper proposed, can successfully reproduce the thermal creep behavior of the soft clay under the 1D loading condition.

1. Introduction

It is well known that soft clays exhibit time-dependent behavior due to their viscosity. The long-term settlement of these clays after the dissipation of excess pore water pressure, which is sometimes called creep deformation, has been an important issue in geotechnical engineering. The creep behavior of the soft clay has been investigated experimentally in [1–5]. Based on that, some practical models have been developed [6–9].

Due to the deposition effect, interparticle bonds are usually formed in soft clays referred as the soil structure. When suffering loading for the soft clay, a significant progressive loss of bonds will happen. By comparing the compression curves in $e - \log \sigma'_v$ (void ratio versus vertical effective stress in the log scale) for intact and reconstituted samples, the large differences observed are induced by the bond elimination. In addition, the bond elimination effect

on the creep behavior of soft clays has been studied in [10, 11].

Soft clays are also subjected to the action of heat under many circumstances, for example, the nuclear waste isolation, heat energy storage, and geothermal development. Studies show that the creep behavior of soft clays is strongly related not only to the bonding structure but also to temperature. The creep behavior of these clays will be changed accordingly [12–16]. However, the effect of temperature on the creep behavior was somehow showed, but not well documented. It will be nice if there exists a direct way for modeling the thermal creep behavior.

For this purpose, we focus on the 1D behavior which can bring fundamental features for more mechanical behavior. Firstly, the temperature dependency behavior of creep is studied based on the experimental observations. Then, a thermally related EVP model for reconstituted clay is proposed by incorporating the effect of temperature.

Furthermore, the bonding elimination of the structure is incorporated into the thermal-based model. Finally, the prediction ability of the proposed model is shown by simulations at different conditions.

2. Temperature Dependency of Creep of Soil

2.1. Experimental Observations. The consolidation process of soil is usually divided into primary consolidation and secondary consolidation, and the boundary point is whether the excess pore pressure completely dissipates. Similarly, thermal secondary consolidation occurs for thermal consolidation after the dissipation of excess pore pressure [13]. Figure 1 shows an idealized thermal consolidation test result. Actually, thermal secondary consolidation occurs throughout the thermal consolidation process, and the induced deformation only relates to time and temperature. Thus, thermal creep used in this paper is more suitable for the process. The slope of the linear portion of the thermal consolidation curve is the thermal creep coefficient ψ_T , given in void ratio per log cycle.

A number of studies demonstrate that the temperature affects significantly the thermal creep coefficient. For example, Figure 2 presents the evolution of the thermal creep coefficient with increasing temperature for intact Pacific illite conducted by Houston et al. [13]. The values range from about 0.01 at 40°C to about 0.06 at 200°C. The increase in the rate of thermal creep deformation at the elevated temperatures was quite significant. Additionally, the creep-temperature tests on peats conducted by Fox and Edil [12] also show that creep dominates the consolidation process and temperature influences the creep rate significantly. Thus, it can be concluded that it is necessary to account for the effect of temperature on creep for soft intact clay.

2.2. Proposed Thermal Creep Equation. Based on the experiments, different expressions were given to describe the temperature-dependent behavior of the thermal creep coefficient. The relationship between thermal creep coefficient and temperature can be linearly functioned by Houston et al. [13]. That is,

$$\psi_T = A \cdot T, \quad (1)$$

where ψ_T is the thermal creep coefficient under temperature T and A is the thermal relate parameter, which can be obtained by correlating the results as shown in Figure 2. Equation (1) describes ψ increasing linearly with temperature straightforwardly. However, we can observe that ψ_T will be zero when the temperature decreases to zero and ψ_T will be negative if the temperature still decreases and is unreasonable.

Based on the experimental results on peat, the following equation is used by Fox and Edil [12] to predict the value of ψ_T , due to a change in soil temperature:

$$\psi_T = \psi_{T_r} \exp[B(T - T_r)], \quad (2)$$

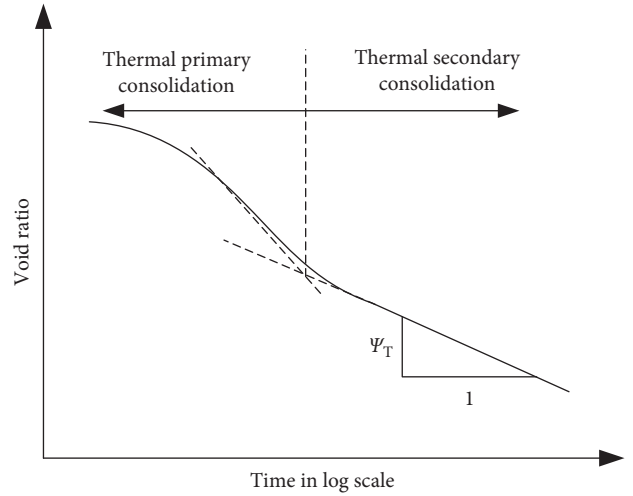


FIGURE 1: Definition of the thermal creep coefficient.

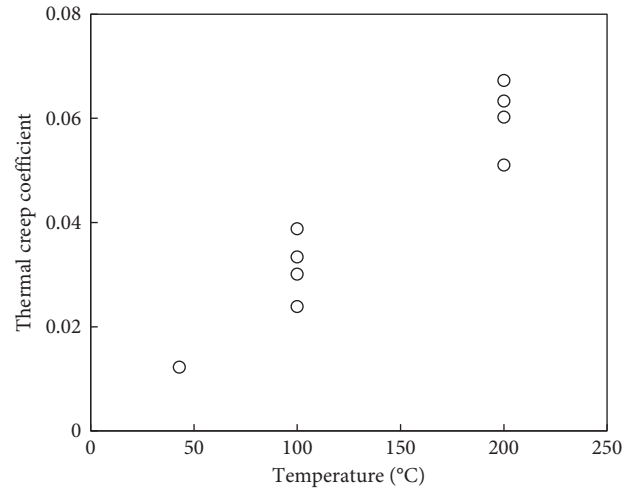


FIGURE 2: Evolution of the thermal creep coefficient of Pacific illite [13].

where ψ_{T_r} is the reference thermal creep coefficient under the reference temperature T_r , thermal relate parameter B is equal to $0.25 \pm 0.02/^\circ\text{C}$ for the peat in [12], and the parameter is independent of vertical effective stress and the magnitude of temperature change. Equation (2) describes that ψ increases nonlinearly with temperature. However, due to its mathematic structure, Equation (2) will deduce a very large number of ψ at a higher temperature, far beyond the normal range.

In this study, we propose a new equation to describe the nonlinear increase of the thermal creep coefficient with temperature, which can be written as

$$\psi_T = \psi_{T_r} \left(\frac{T}{T_r} \right)^{C_T}, \quad (3)$$

where C_T is the thermal relate parameter which can be correlated with the experiment results. This equation can overcome the deficiency exposed by Equations (1) and (2). Figure 3 plots the comparisons of the three equations

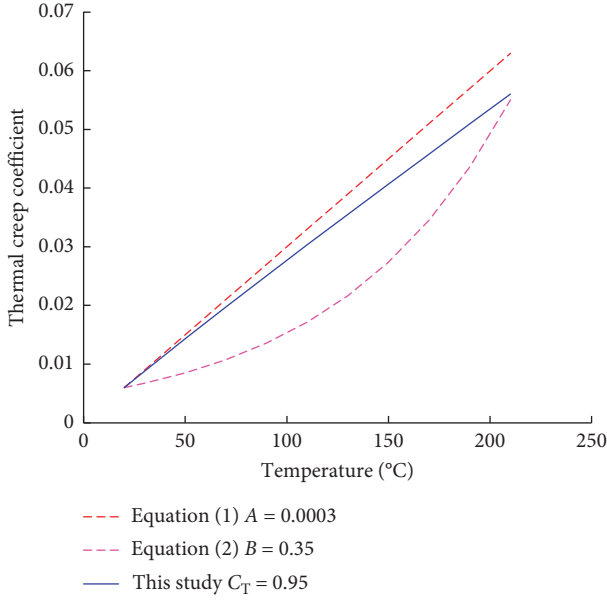


FIGURE 3: Comparisons of the equations describing the relationship between thermal creep coefficient and temperature.

describing the relationship between thermal creep coefficient and temperature. The point $T = 20^\circ\text{C}$ and $\psi(20) = 0.006$ is adopted as the reference. As indicated, three equations give different shape curves. Overall, the curve plotted from Equation (3) is more practical than the others.

3. EVP Model considering the Temperature Effect on Creep

3.1. Adopted One-Dimensional Elastic Viscoplastic Model. First, a time-dependent stress-strain model without the thermal effect needs to be selected as a base [6]. The adopted model is presented briefly in this part.

Following the classic elastic viscoplastic approach, the total strain rate contains the elastic and viscoplastic strains rate, that is,

$$\dot{\epsilon}_v = \dot{\epsilon}_v^e + \dot{\epsilon}_v^{vp}, \quad (4)$$

where $\dot{\epsilon}_v$ represents the total strain rate and the superscripts “e” and “vp” denote the elastic and viscoplastic parts, respectively. The elastic strain rate is expressed as

$$\dot{\epsilon}_v^e = \frac{\kappa}{1 + e_0} \frac{\dot{\sigma}_v'}{\sigma_v'}, \quad (5)$$

where e_0 is the initial void ratio, σ_v' is the effective vertical stress, and κ is the slope of recompression lines in $e - \ln \sigma_v'$ space.

For the viscoplastic strain rate, a one-dimensional formulation proposed by Kutter and Sathialingam [17] was adopted based on the creep coefficient ψ :

$$\dot{\epsilon}_v^{vp} = \frac{\psi}{(1 + e_0)\tau} \left(\frac{\sigma_v'}{\sigma_v'^r} \right)^{\lambda - \kappa/\psi}, \quad (6)$$

where λ denotes the slope of the normal compression line in $e - \ln \sigma_v'$ space; τ is the reference time, and it equals to the

duration of each load increment in the oedometer test; and $\sigma_v'^r$ is the reference stress corresponding to the incremental time τ and increases with the development of the viscoplastic strain according to

$$\sigma_v'^r = \sigma_p'^r \exp\left(\frac{1 + e_0}{\lambda - \kappa} \epsilon_v^{vp}\right), \quad (7)$$

where $\sigma_p'^r$ denotes the preconsolidation pressure.

The above relationships have been suggested in [18–20] and validated in [6, 10].

3.2. Incorporation of the Thermal Effect. The effects of temperature on the stress-strain behavior of clay have been observed in the laboratory [12, 13], which are helpful to discuss the thermal effect on the parameters in the above constitutive model. Increase and decrease in temperature may produce changes in the bonding of clay particles and the viscosity of absorbed water. These changes alternately produce more or fewer changes in compressibility. However, the experiments conducted in [15, 21, 22] show that the variations of λ and κ with temperature are negligible. Furthermore, a volume change due to elastic expansion of the clay particle will occur during the drainage of thermal consolidation. Considering that the strain under a constant effective stress remains small [14, 23, 24] and the emphasis of this paper, the parameters λ , κ , and e_0 will remain constant when clays suffering a change of temperature.

The thermal creep coefficient can be incorporated into the basic EVP model directly. By substituting the parameter ψ in Equation (6) by Equation (3), the 1D thermal-related viscoplastic strain rate changes to

$$\dot{\epsilon}_v^{vp} = \frac{\psi_{T_r}}{(1 + e_0)\tau} \left(\frac{T}{T_r} \right)^{C_T} \left(\frac{\sigma_v'}{\sigma_v'^r} \right)^{(\lambda - \kappa)/(\psi_{T_r})} (T_r/T)^{C_T}. \quad (8)$$

Actually, the preconsolidation pressure σ_p' also varies with temperature. The thermal-dependent behavior of σ_p' has been studied from the oedometer tests or isotropic compression tests with variable temperatures. All of the results indicate that σ_p' will decrease with an elevated temperature [25–29]. Based on the data collected from literature, Figure 4 plots the relationship between the normalized preconsolidation pressure and temperature. The regression analyses show that it is also reasonable to assume a linear relationship between $\log(\sigma_p'/\sigma_p'^r)$ and $\log(T/T_r)$, firstly proposed by [28]. Thus, the relationship between the preconsolidation pressure and temperature can be fitted by

$$\frac{\sigma_p'}{\sigma_p'^r} = \left(\frac{T}{T_r} \right)^\theta, \quad (9)$$

where θ is a thermal parameter and σ_p' and $\sigma_p'^r$ are the preconsolidation pressures at temperature T and the reference temperature T_r , respectively. The present model has no elastic limit, which is different from Perzyna’s overstress method [30].

3.3. Coupled Consolidation Analysis. In the following numerical simulations of the conventional oedometer tests,

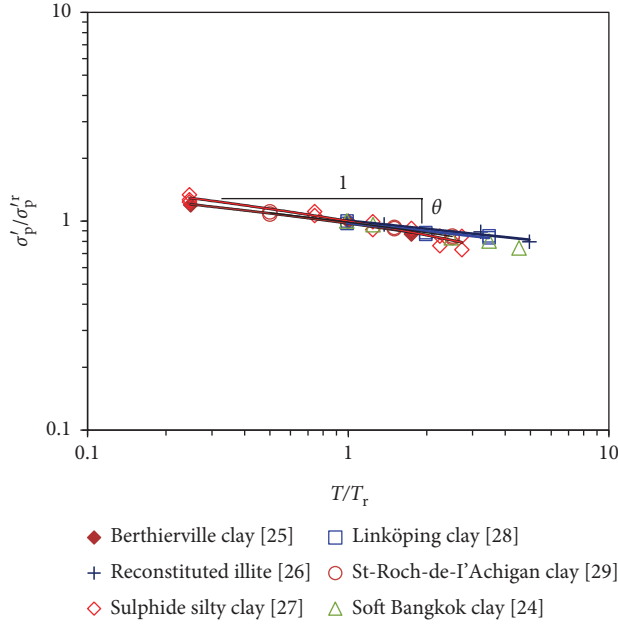


FIGURE 4: Temperature dependency of preconsolidation pressure.

soil-water coupling analysis will be performed. Darcy's law was adopted for the consolidation process:

$$-\frac{\partial \varepsilon_v}{\partial t} = \frac{1 + e_0}{\gamma_w} \frac{\partial}{\partial z} \left(\frac{k}{1 + e} \right) \frac{\partial u}{\partial z}, \quad (10)$$

where z is the vertical depth, u is the excess pore pressure, and k is the hydraulic conductivity. Actually, k is also influenced by temperature. A decrease in pore water viscosity will happen with increasing temperature, which will result in an increase in the permeability of the soil. Thus, increasing temperature will speed up the consolidation process. Considering the emphasis of this paper, only the void ratio-dependent behavior of k is considered, and according to experimental results, the evolution of k can be expressed as

$$k = k_0 10^{(e - e_0)/c_k}, \quad (11)$$

where the initial hydraulic conductivity k_0 is corresponding to e_0 and the permeability coefficient c_k can be easily measured from the oedometer test results by plotting $e - \log k$.

The above equations were implemented in finite element software PLAXIS Version 8, but in 1D, finite element simulations can be established for modeling the primary consolidation and the creep process in an oedometer test. Details of coupled consolidation and creep analysis can be found in [19, 31] and are not repeated here.

3.4. Simulated One-Dimensional Behavior. In order to validate the proposed thermal-dependent EVP model, numerical simulations for the assumed oedometer creep tests were performed at three temperatures ($T = 20^\circ\text{C}$, 50°C , and 80°C). The results are shown in Figure 5, and the parameters adopted for these simulations are listed in Figure 5(a). The

simulated temperature behavior agrees with the common experimental phenomena on unstructured clay, as expected by the model's principle. For example, the simulated relationship between the preconsolidation pressure and temperature corresponds to the input value of θ .

Take the simulated test on $T = 80^\circ\text{C}$; for example, the compression behavior for each load increment is presented in Figure 5(b). The simulated thermal creep coefficient $\psi = 0.013$ agrees well with that obtained from Equation (3) with $T_r = 20^\circ\text{C}$ and $\psi_{T_r} = 0.0065$.

4. Thermal-Dependent EVP Model for Intact Clay

4.1. Bonding Effect on Compression Behavior. During the oedometer tests, the difference of the compression curves obtained on intact and reconstituted clay is caused by bonding elimination as shown in Figure 6(a) for Wenzhou clay [32]. The structures between soil particles for intact clay will be eliminated gradually during compressing. The tests conducted under variable temperatures show that the shape of the compression curves does not change with temperature, for instance, tests on intact Berthierville clay [25] and Linköping clay [28]. Thus, we assume that the process of bonding elimination is thermal independent but only relates to the strain level. Figure 6(b) presents the schematic plot of the stress-strain curve at an arbitrary temperature T for soft intact clay. For a given viscoplastic strain level ε_v^{vp} , the bond elimination results in the current stress σ'_v reaching point D for intact clay. Corresponding to the same viscoplastic strain, we define an intrinsic stress σ'_{vi} on the reconstituted sample. We assume that the difference between the current stress and intrinsic stress is due to the existing of the soil structure, based on which a bonding ratio $\chi = \sigma'_v/\sigma'_{vi} - 1$ can be proposed. Thus, the current stress σ'_v during straining can be expressed as

$$\sigma'_v = (1 + \chi)\sigma'_{vi}. \quad (12)$$

Initially, the bonding ratio $\chi = \chi_0 = \sigma'_p/\sigma'_{pi} - 1$. Following the increasing of strain, the bonds are broken gradually and χ decreases from its initial value χ_0 ultimately towards zero when the bonds are completely eliminated as plotting in Figure 6(a). According to the definition, bonding ratio and the corresponding viscoplastic strain during compression is measured and plotted in Figure 6(c) for Wenzhou clay. Based on the results, we propose the following relationship to express the attenuation of bonding ratio:

$$\chi = \chi_0 e^{-\zeta \varepsilon_v^{vp}}, \quad (13)$$

where the parameter ζ controls the rate of bonding elimination ($\zeta = 8.0$ for Wenzhou clay in Figure 6(c)). Actually, the intrinsic stress σ'_{vi} in Equation (12) can be regarded as the reference stress as indicated in Equation (8), and the bonding ratio can be regarded as the scaling parameter. Thus, the present model is then composed of Equations (8), (9), and (12). Combining with the elastic strain rate in Equation (5), the stress-strain curve for a given temperature can be obtained.

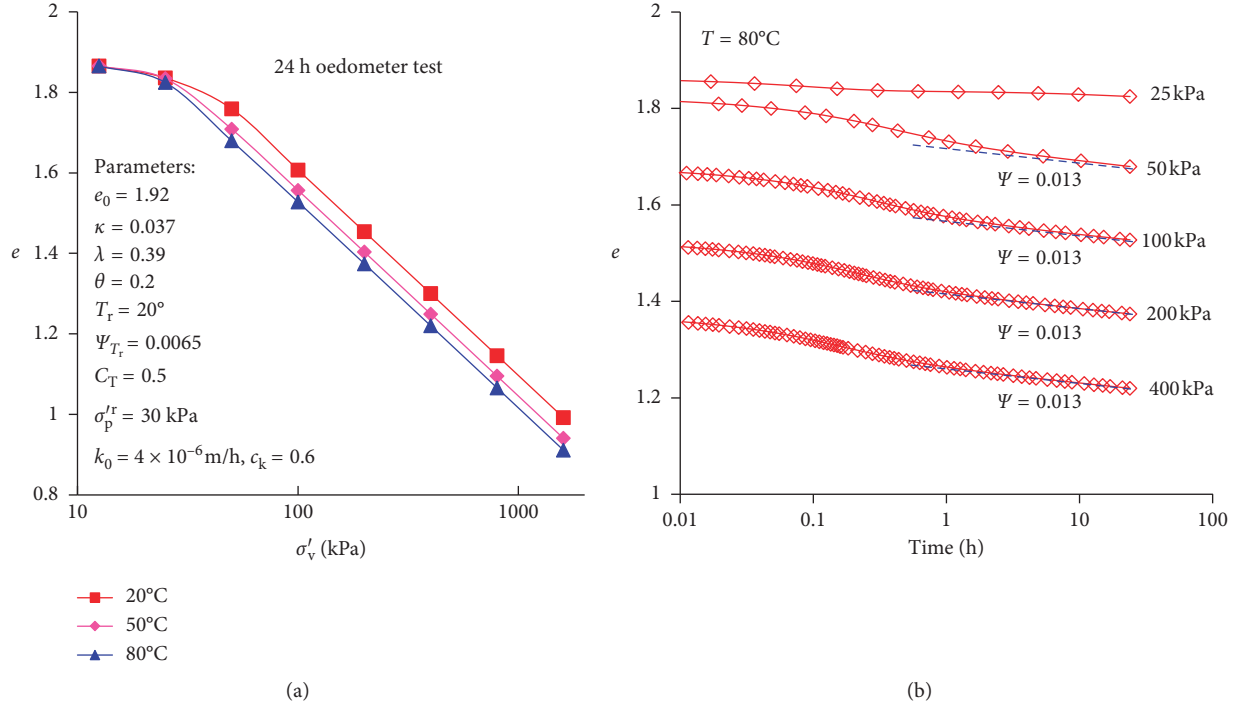


FIGURE 5: Simulations for 24 h oedometer tests: (a) compression curves at different temperatures; (b) compression behavior at each load increment for the test simulated at $T = 80^\circ\text{C}$.

4.2. Model Parameters. The present model that combined creep and temperature involves a number of parameters which can be divided into four groups:

- Parameters related to compressibility: initial void ratio (e_0), the intrinsic slope of the compression line (λ_i), and the slope of the recompression line (κ). The values of λ_i and κ can be measured from the oedometer tests on the reconstituted and intact samples, respectively. As the thermal expansion and contraction are neglected in this paper, e_0 can be measured initially at the reference temperature.
- Parameter related to bonding elimination: the initial bonding ratio (χ_0) and the parameter ζ . The value of χ_0 can be measured from the oedometer tests on the intact and reconstituted samples conducted at the same temperature. It needs to point out that, for χ_0 , high-quality intact samples are needed. The parameter ζ representing the bonding elimination rate can be derived from Equations (12) and (13):

$$\zeta = -\ln \left\{ \frac{1}{\chi_0} \left[\frac{\sigma'_v}{\sigma'_{vi}} - 1 \right] \right\} \frac{1}{\varepsilon_v^{\text{vp}}}, \quad (14)$$

where $\varepsilon_v^{\text{vp}}$ is the volumetric viscoplastic strain corresponding to σ'_v (Figure 6(b)) at an arbitrary temperature. Thus, ζ can be calculated by selecting a point on the postyield curve.

- Parameters of creep: reference thermal creep coefficient (ψ_{T_r}) and thermal parameter (C_T). ψ_{T_r} can be measured directly from the oedometer tests on

reconstituted at a reference temperature (T_r). C_T can be obtained by correlating ψ_{T_r} with temperature.

Parameters related to preconsolidation pressure: the reference preconsolidation pressure (σ_p^r) at the reference temperature T_r and the thermal parameter (θ). σ_p^r can be obtained at the intersection of the compression curves for the reconstituted and intact samples, as shown in Figure 6(b). θ can be obtained directly from the oedometer tests on the reconstituted or intact samples at different temperatures. Wang et al. [33] investigated the value of θ for seven clays and summarized that θ varies from 0.125 to 0.194. Furthermore, θ can be obtained by the empirical correlation of liquid limit (w_L) expressed as

$$\theta = 0.1072 + 0.0008w_L. \quad (15)$$

Thus, θ can be obtained by correlating without carrying out the temperature-controlled tests.

Thus, ten model parameters (e_0 , κ , λ , θ , T_r , C_T , ψ_{T_r} , σ_p^r , χ_0 , and ζ) are required for the model, and all of the parameters can be determined straightforwardly from the temperature-controlled oedometer test.

5. Calibration and Validation

5.1. Predictions on Wenzhou Clay. The thermal creep coefficient ψ is also influenced by the bonding elimination process during straining. In order to evaluate the model ability to reproduce the behavior of soft intact clay, simulations were performed for the thermal oedometer tests with different temperatures. The input ordinary parameters are the same as those given in Table 1. For intact clay, two

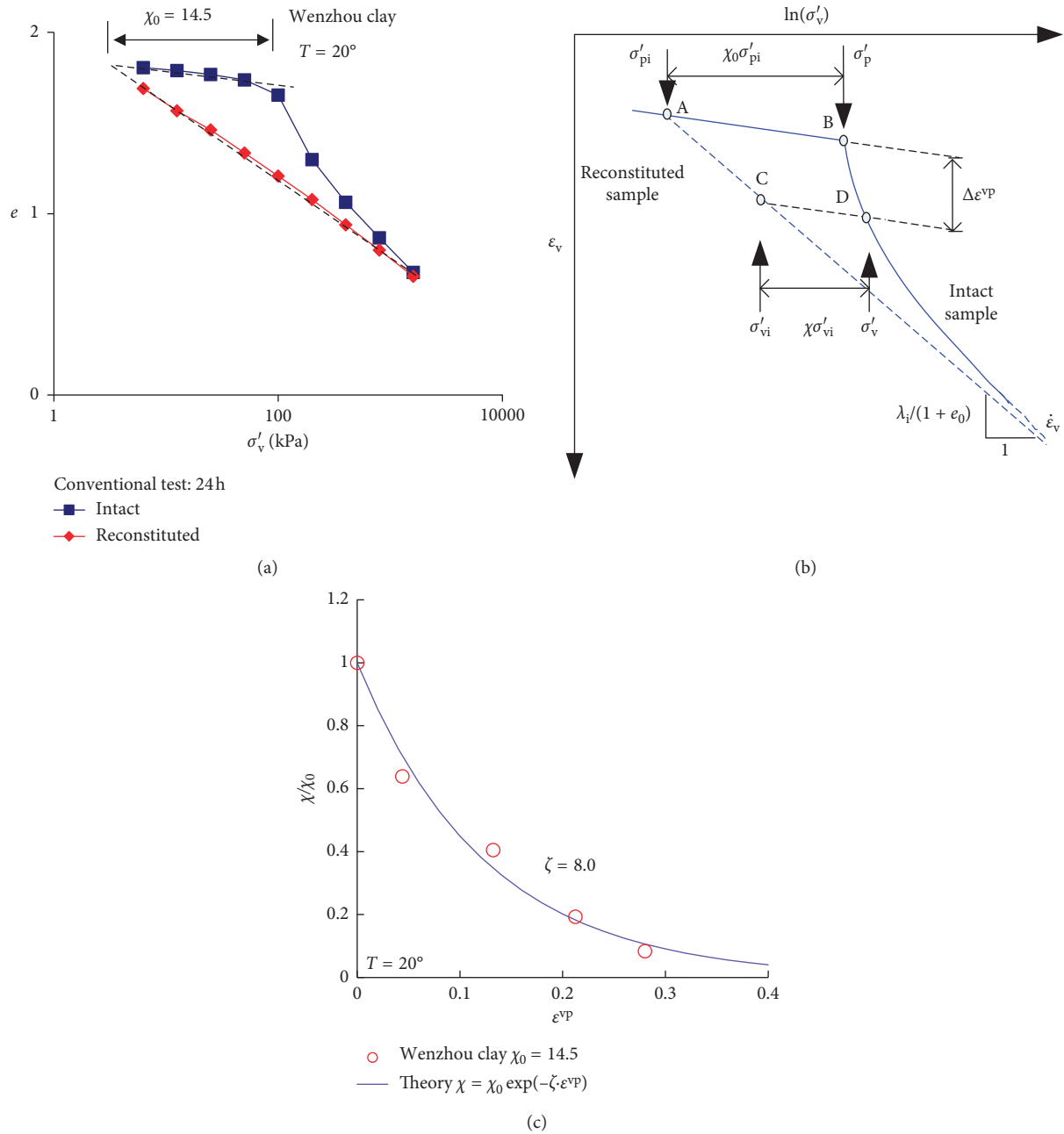


FIGURE 6: Bonding effect on the compressibility and the evolution of bonding ratio: (a) compression curves for intact and reconstituted Wenzhou clay at $T = 20^\circ\text{C}$; (b) illustration of the bonding elimination with viscoplastic strain; (c) evolution of bonding ratio with viscoplastic strain.

TABLE 1: Values of model parameters and state variables for selected clays.

clay	$\lambda\Lambda$	κ	e_0	σ'_p kPa	χ_0	ζ	θ	T_r	ψ_{T_r}	C_T	k (m/h)	c_k
Wenzhou	0.39	0.037	1.92	30	3.5	8	0.2	70	0.006	0.5	4×10^{-6}	0.6
Utby	0.18	0.03	1.98	55	54	15	0.15	20	0.02	0.31	2×10^{-6}	0.99
Tokyo bay	0.36	0.05	2.4	79	0.4	7	0.17	20	0.031	—	1×10^{-7}	1.2

parameters $\chi_0 = 3.5$ and $\zeta = 8$ were used. Three temperatures with $T = 20^\circ\text{C}$, 50°C , and 80°C are adopted in the simulations.

Figure 7 shows typical results of the thermal oedometer tests in natural intact clay simulated by the new model:

- (1) In Figure 7(a), the compression curves in different temperatures are similar to the oedometer test on intact Wenzhou clay (Figure 6(a)). The pre-consolidation pressure is influenced significantly by

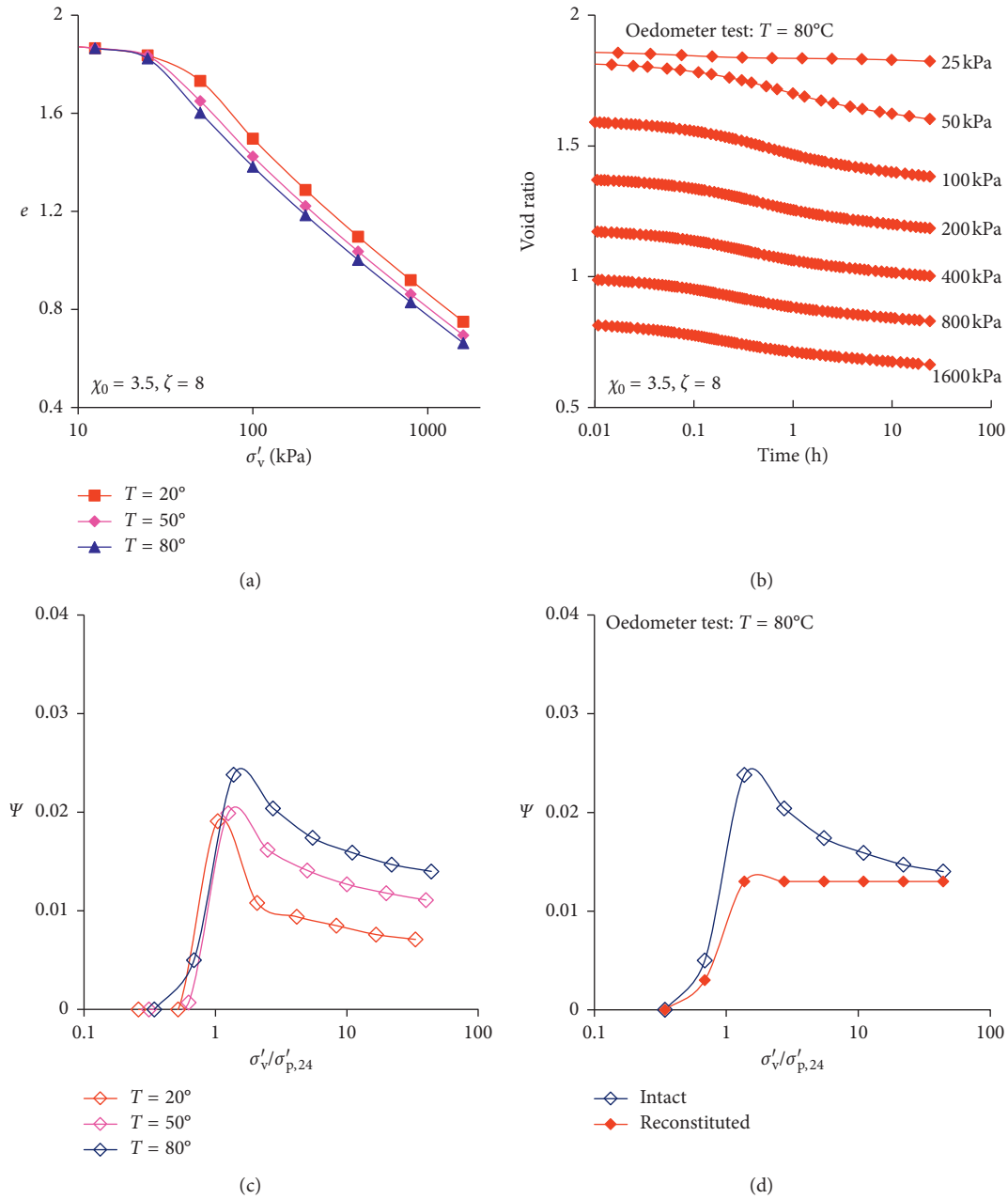


FIGURE 7: Predictions of the thermal oedometer test on Wenzhou clay with different temperatures: (a) compression curves at different temperatures; (b) strain-time curves for the case with $T = 80^\circ\text{C}$; (c) evolution of the thermal creep coefficient with normalized vertical stress; (d) comparisons of the thermal creep coefficient between intact and reconstituted clay.

the temperature as presented in Figure 5 on reconstituted clay.

- (2) In Figure 7(b), the typical curves of strain versus time were reproduced for natural intact clay, where the thermal creep coefficient ψ can be obtained at the end of each load; here, only the simulation results for $T = 80^\circ\text{C}$ are presented.
- (3) In Figure 7(c), the measured ψ at three temperatures were plotted versus the normalized applied stress by the preconsolidation pressure. Here, the preconsolidation pressure is different for the three tests. The value ψ for intact clay increases rapidly with the

applied stress, and when the stress reaches the preconsolidation pressure, ψ reaches a peak value and then decreases. The difference between these curves is due to the combined influence of temperature and bonding elimination.

- (4) In Figure 7(d), the measured ψ for intact and reconstituted clay are compared for the test at $T = 80^\circ\text{C}$. The difference between the two curves is due to the existence of bonding and its elimination.

5.2. Predictions on Utby Clay. Li et al. [34] presented a set of the long-term oedometer tests on Utby clay (6 m depth) with

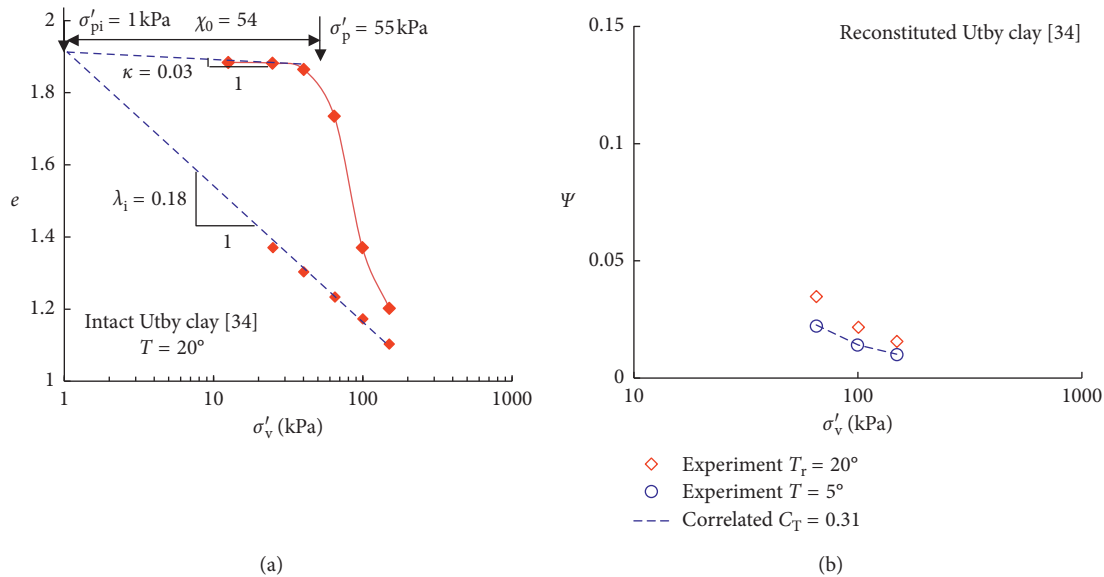


FIGURE 8: Determination of parameters from the thermal oedometer test: (a) compression parameters at $T = 20^\circ$; (b) the thermal creep coefficient based on the experiment on the reconstituted sample.

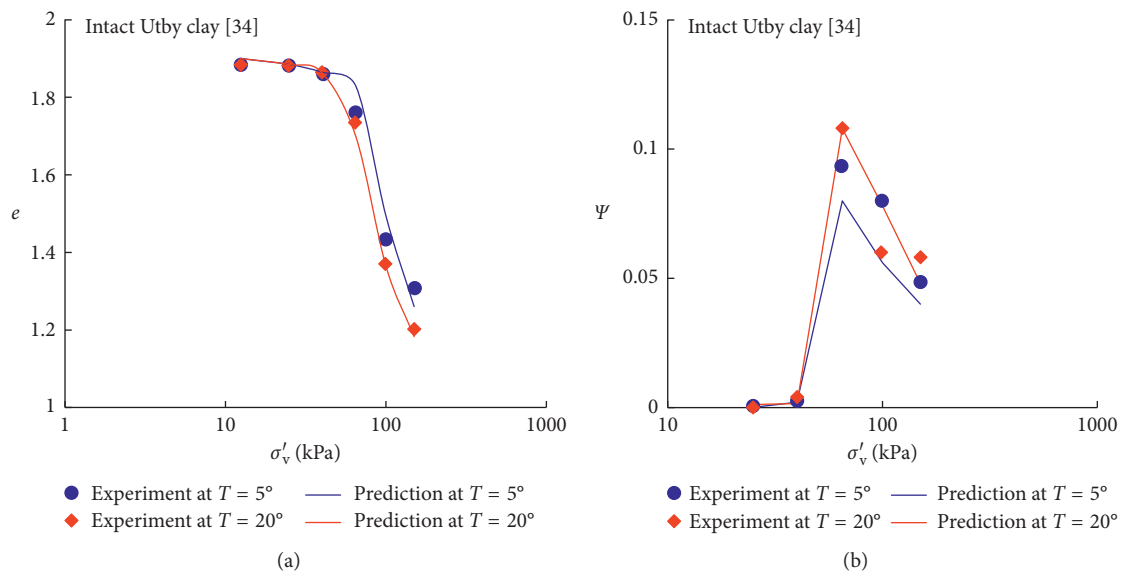


FIGURE 9: Predictions of the thermal oedometer test on intact Utby clay (depth = 6 m) with different temperatures: (a) compression curves; (b) creep coefficient.

different temperatures for both intact and reconstituted samples. The clay properties are as follows: liquid limit $w = 55\%$, $e_0 = 1.977$, and $\sigma'_p = 55$ kPa for the intact sample at the reference room temperature $T = 20^\circ$. The other parameters for the model were correlated with thermal oedometer tests results. Figure 8(a) shows the compression tests on intact and reconstituted samples at $T_r = 20^\circ$. The parameter $\lambda_i = 0.18$ is determined based on the results of the reconstituted sample. The parameter $\kappa = 0.003$ is correlated from the recompression curve. Bonding ratio $\chi_0 = 54$ is obtained based on the method described above. The value of $\zeta = 15$ was determined by selected a stress-strain point in Figure 8(a) and using Equation (14). Figure 8(b) presents the variation of the

thermal creep coefficient with temperature. Adopting ψ_T at $T = 20^\circ$ as a reference, the predicted values of ψ_T for $T = 5^\circ$ agree well with the experimental results with $C_T = 0.31$. Furthermore, an average value of $\psi_{T_r} = 0.02$ is used based on the experimental results at $T = 20^\circ$. With Equation (15), $\theta = 0.15$ is adopted in the simulation. To simulate the long-term creep test, the permeability of soil was taken as 4×10^{-6} m/h estimated from the consolidation curves of vertical strains versus time. The value of c_k was equal to $e_0/2$, as suggested by Tavenas et al. [35] based on observations on soft marine clays. All of the parameters are summarized in Table 1.

Figure 9 shows the comparison between experimental and simulation results. The predicted compression behavior

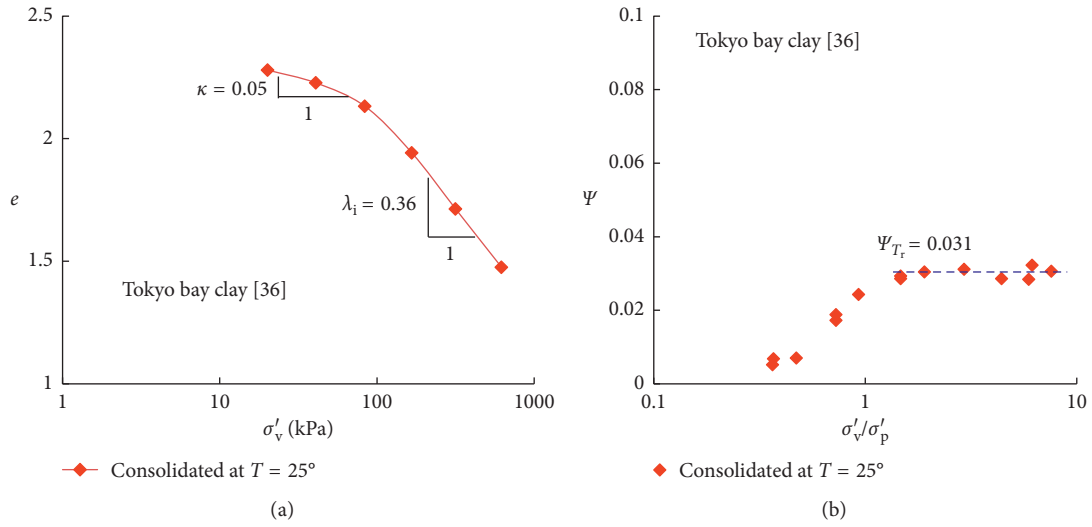


FIGURE 10: Determination of parameters from the oedometer tests for the sample consolidated at room temperature: (a) compression curves; (b) creep coefficient versus vertical stress.

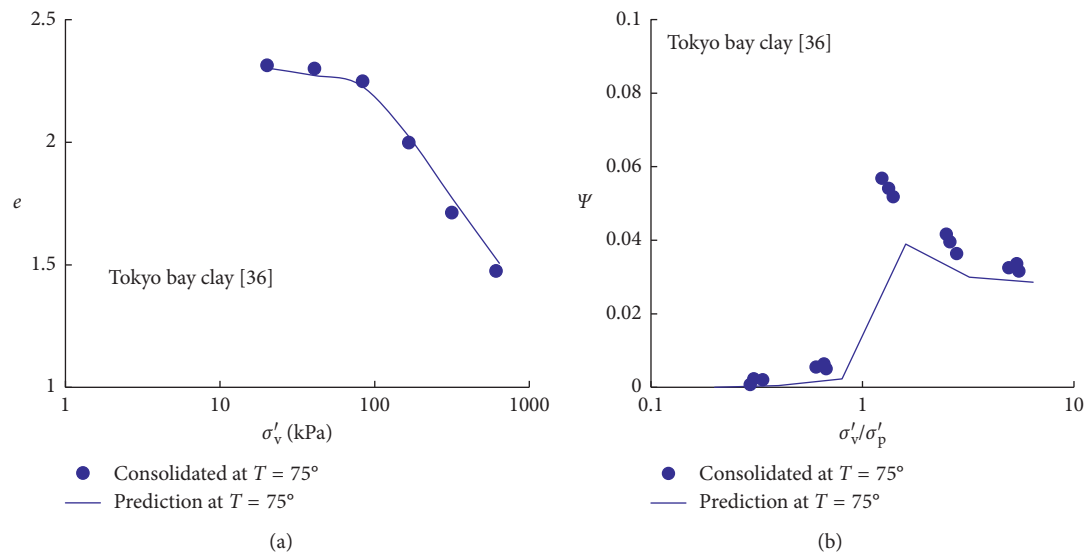


FIGURE 11: Predictions of the oedometer test on Tokyo bay clay consolidated at high temperatures: (a) compression curves; (b) creep coefficient versus normalized vertical stress.

at different temperatures shows good agreement with the experimental results for the values of the preconsolidation pressures and for the shape of the compression curves (Figure 9(a)). Furthermore, the predicted thermal creep coefficient also agrees well with the experimental results. For the values of vertical stress equal to the preconsolidation pressure, the thermal creep coefficient reaches to the maximum value (Figure 9(b)). It can be concluded that it is necessary to account for the coupling effect of temperature and destructuration for accurate predictions of the thermal compression behavior of the soft clay.

5.3. Predictions on Tokyo Bay Clay. Tsuchida et al. [36] conducted the oedometer tests on Tokyo bay clays which are

consolidated at room temperature (25°) and at high temperature (75°), respectively. The sample which is suffered consolidating at a high temperature and cooled after the completion consolidation will behave like the lightly aged clay. Adopting the sample consolidated at room temperature as a reference, the properties are as follows: liquid limit $w = 78\%$ and $e_0 = 2.4$. From the experimental results on the sample consolidated at room temperature (Figure 10(a)), the parameter $\lambda_1 = 0.36$, $\kappa = 0.05$, and $\sigma'_p = 79$ kPa can be obtained. In addition, the reference $\psi_{T_r} = 0.031$ is averaged for the vertical stress larger than preconsolidation pressure (Figure 10(b)). Also, the parameter $\theta = 0.17$ can be calculated by Equation (15). $\chi_0 = 0.2$ is obtained by the increase of preconsolidation pressure due to the cooling of the sample after high temperature consolidation. Similarly, $\zeta = 7$ is

correlated based the compression curve, and the consolidation-related parameters $k = 1 \times 10^{-7}$ m/h, $c_k = 1.2$. All of the parameters are collected in Table 1.

Figure 11(a) shows that the predicted compressibility of Tokyo bay clay consolidated at a high temperature agrees well with the experiment. Furthermore, the predicted thermal creep coefficient has the same shape with experiment. The predicted values are a little smaller than the experimental results (Figure 11(b)). Overall speaking, the model can reproduce well the thermal creep behavior for the soft clay.

6. Conclusions

The temperature-dependent behavior of creep for soft intact clay has been investigated based on experimental observations from experimental results. A thermally related equation is proposed to bridge the thermal creep coefficient with temperature. By incorporating the equation to a selected one-dimensional EVP model, a thermal creep-based EVP model is developed taking into account the temperature dependency of creep. The determination of the model parameters is straightforward. Numerical simulations have been conducted to examine the predictive ability of the model for the soft clay.

Experimental predictions have carried out the thermal oedometer tests at different temperatures. The bonding elimination effect on the evolution of the thermal creep coefficient has been highlighted by comparing predictions with and without considering bonding elimination.

The results demonstrate that the proposed model can well reproduce temperature-dependent creep behavior of soft intact clay under the one-dimensional loading condition. Future work will be done to extend the proposed model to three-dimensional general stress space.

Data Availability

No data were used to support this study.

Conflicts of Interest

The authors declare that there are no conflicts of interests regarding the publication of this article.

Acknowledgments

We acknowledge with gratitude the financial support provided by the Fundamental Research Funds for the Central Universities (2015QNA64).

References

- [1] G. Mesri and P. Godlewski, "Time and stress-compressibility interrelationship," *Journal of the Geotechnical Engineering Division*, vol. 103, no. 5, pp. 417–430, 1977.
- [2] S. Leroueil, M. Kabbaj, F. Tavenas, and R. Bouchard, "Stress-strain-strain rate relation for the compressibility of sensitive natural clays," *Géotechnique*, vol. 35, no. 2, pp. 159–180, 1985.
- [3] J. H. Yin, J. G. Zhu, and J. Graham, "A new elastic viscoplastic model for time-dependent behaviour of normally and over-consolidated clays: theory and verification," *Canadian Geotechnical Journal*, vol. 39, no. 1, pp. 157–173, 2002.
- [4] Q. Y. Zhu, Z. Y. Yin, P. Y. Hicher, and S. L. Shen, "Non-linearity of one-dimensional creep characteristics of soft clays," *Acta Geotechnica*, vol. 11, no. 4, pp. 887–900, 2016.
- [5] Z. Y. Yin, M. Hattab, and P. Y. Hicher, "Multiscale modeling of a sensitive marine clay," *International Journal for Numerical and Analytical Methods in Geomechanics*, vol. 35, no. 15, pp. 1682–1702, 2011.
- [6] Z. Y. Yin and J. H. Wang, "A one-dimensional strain-rate based model for soft structured clays," *Science China Technological Sciences*, vol. 55, no. 1, pp. 90–100, 2012.
- [7] Z. Y. Yin, M. Karstunen, C. S. Chang, M. Koskinen, and M. Lojander, "Modeling time-dependent behavior of soft sensitive clay," *Journal of Geotechnical and Geoenvironmental Engineering*, vol. 137, no. 11, pp. 1103–1113, 2011.
- [8] J. H. Yin and J. Graham, "Elastic visco-plastic modelling of one-dimensional consolidation," *Geotechnique*, vol. 46, no. 3, pp. 515–527, 1996.
- [9] Z. Y. Yin, Q. Y. Zhu, J. H. Yin, and Q. Ni, "Stress relaxation coefficient and formulation for soft soils," *Géotechnique Letters*, vol. 4, no. 1, pp. 45–51, 2014.
- [10] Q. Y. Zhu, Z. Y. Yin, D. M. Zhang, and H. W. Huang, "Numerical modeling of creep degradation of natural soft clays under one-dimensional condition," *KSCSE Journal of Civil Engineering*, vol. 21, no. 5, pp. 1668–1678, 2017.
- [11] Z.-Y. Yin, Q. Y. Zhu, and D. M. Zhang, "Comparison of two creep degradation modeling approaches for soft structured soils," *Acta Geotechnica*, vol. 12, no. 6, pp. 1395–1413, 2017.
- [12] P. J. Fox and T. B. Edil, "Effects of stress and temperature on secondary compression of peat," *Canadian Geotechnical Journal*, vol. 33, no. 3, pp. 405–415, 1996.
- [13] S. L. Houston, W. N. Houston, and N. D. Williams, "ThermoMechanical behavior of seafloor sediments," *Journal of Geotechnical Engineering*, vol. 111, no. 11, pp. 1249–1263, 1985.
- [14] C. J. R. Coccia and J. S. McCartney, "Thermal volume change of poorly draining soils I: critical assessment of volume change mechanisms," *Computers and Geotechnics*, vol. 80, pp. 26–40, 2016.
- [15] N. Jarad, O. Cuisinier, and F. Masrouri, "Effect of temperature and strain rate on the consolidation behaviour of compacted clayey soils," *European Journal of Environmental & Civil Engineering*, vol. 3, pp. 1–18, 2017.
- [16] L. Laloui, S. Leroueil, and S. Chalindar, "Modelling the combined effect of strain rate and temperature on one-dimensional compression of soils," *Canadian Geotechnical Journal*, vol. 45, no. 12, pp. 1765–1777, 2008.
- [17] B. L. Kutter and N. Sathialingam, "Elastic viscoplastic modelling of the rate-dependent behaviour of clays," *Géotechnique*, vol. 42, no. 3, pp. 427–441, 1992.
- [18] P. A. Vermeer and H. P. Neher, "A soft soil model that accounts for creep," in *Proceedings of Plaxis Symposium Beyond 2000 in Computational Geotechnics*, Amsterdam, Netherlands, March 1999.
- [19] D. F. E. Stolle, P. A. Vermeer, and P. G. Bonnier, "Time integration of a constitutive law for soft clays," *Communications in Numerical Methods in Engineering*, vol. 15, no. 8, pp. 603–609, 1999.
- [20] M. Leoni, M. Karstunen, and P. A. Vermeer, "Anisotropic creep model for soft soils," *Géotechnique*, vol. 58, no. 3, pp. 215–226, 2008.

- [21] R. G. Campanella and J. K. Mitchell, "Influence of temperature variation on soil behavior," *Journal of Soil Mechanics and Foundation Division*, vol. 94, pp. 609–734, 1968.
- [22] A. Tsutsumi and H. Tanaka, "Combined effects of strain rate and temperature on consolidation behavior of clayey soils," *Soils and Foundations*, vol. 52, no. 2, pp. 207–215, 2012.
- [23] C. Cekerevac and L. Laloui, "Experimental study of thermal effects on the mechanical behaviour of a clay," *International Journal for Numerical and Analytical Methods in Geomechanics*, vol. 28, no. 3, pp. 209–228, 2004.
- [24] H. M. Abuel-Naga, D. T. Bergado, A. Bouazza, and G. V. Ramana, "Volume change behaviour of saturated clays under drained heating conditions: experimental results and constitutive modeling," *Canadian Geotechnical Journal*, vol. 44, no. 8, pp. 942–956, 2007.
- [25] M. Boudali, S. Leroueil, and B. R. Srinivasa Murthy, "Viscous behaviour of natural clays," in *Proceedings of the 13th International Conference on Soil Mechanics and Foundation Engineering*, pp. 411–416, A. A. Balkema, Rotterdam, Netherlands, 1994.
- [26] N. Tanaka, "Thermal elastic plastic behaviour and modelling of saturated clays," Doctoral thesis, University of Manitoba, Winnipeg, Manitoba, Canada, 1995.
- [27] L. G. Eriksson, "Temperature effects on consolidation properties of sulfide clays," in *Proceedings of the 12th International Conference on Soil Mechanics and Foundation Engineering*, pp. 2084–2090, A. A. Balkema, Rotterdam, Netherlands, 1989.
- [28] L. Moritz, "Geotechnical properties of clay at elevated temperatures," Report: 47, Swedish Geotechnical Institute, Linköping, Sweden, 1995.
- [29] M. E. S. Marques and S. Leroueil, "Viscous behaviour of St-Roch-de-l'Achigan clay, Quebec," *Canadian Geotechnical Journal*, vol. 41, no. 1, pp. 25–38, 2004.
- [30] P. Perzyna, "Fundamental problems in viscoplasticity," *Advances in Applied Mechanics*, vol. 9, no. 2, pp. 243–377, 1966.
- [31] Y. Kim and S. Leroueil, "Modeling the viscoplastic behaviour of clays during consolidation: application to Berthierville clay in both laboratory and field conditions," *Canadian Geotechnical Journal*, vol. 38, no. 3, pp. 484–797, 2001.
- [32] L. L. Zeng, Z. S. Hong, S. Y. Liu et al., "Variation law and quantitative evaluation of secondary consolidation behavior for remolded clays," *Chinese Journal of Geotechnical and Engineering*, vol. 34, no. 8, pp. 1496–1500, 2012.
- [33] L. Z. Wang, K. J. Wang, and Y. Hong, "Modeling temperature-dependent behavior of soft clay," *Journal of Engineering Mechanics*, vol. 142, no. 8, article 04016054, 2016.
- [34] Y. L. Li, J. Dijkstra, and M. Karstunen, "Thermomechanical creep in sensitive clays," *Journal of Geotechnical and Geoenvironmental Engineering*, vol. 144, no. 11, article 04018085, 2018.
- [35] F. Tavenas, P. Leblond, and S. Leroueil, "The permeability of natural soft clay, part II. permeability characteristics," *Canadian Geotechnical Journal*, vol. 20, no. 4, pp. 645–660, 1983.
- [36] A. Tsutsumi and H. Tanaka, "Combined effects of strain rate and temperature on consolidation behavior of clayey soils," *Soils and Foundations*, vol. 52, no. 2, pp. 207–215, 2012.

Research Article

Effect of Colluvial Soil Slope Fracture's Anisotropy Characteristics on Rainwater Infiltration Process

Ling Zeng,^{1,2} Jie Liu,³ Jun-hui Zhang ,^{3,4} Han-bing Bian,² and Wei-hua Lu⁵

¹Engineering Laboratory of Spatial Information Technology of Highway Geological Disaster Early Warning in Hunan Province, Changsha University of Science & Technology, Changsha 410114, China

²School of Civil Engineering, Changsha University of Science & Technology, Changsha 410114, China

³School of Traffic and Transportation Engineering, Changsha University of Science & Technology, Changsha 410114, China

⁴National Engineering Laboratory of Highway Maintenance Technology, Changsha University of Science & Technology, Changsha 410114, China

⁵School of Civil Engineering, Nanjing Forestry University, Nanjing 210037, China

Correspondence should be addressed to Jun-hui Zhang; zjhseu@csust.edu.cn

Received 26 June 2018; Accepted 10 September 2018; Published 17 October 2018

Academic Editor: Annan Zhou

Copyright © 2018 Ling Zeng et al. This is an open access article distributed under the Creative Commons Attribution License, which permits unrestricted use, distribution, and reproduction in any medium, provided the original work is properly cited.

The SEEP/W module of finite element software GEO-slope is used to analyze the effects of fracture depth, permeability coefficient ratio, fracture angle, and fracture number on the rainwater infiltration process. Moreover, the effect of fracture seepage anisotropy on slope stability is discussed combining with unsaturated seepage theory. The results show that the pore water pressure in the fracture increases rapidly with the rainfall until it changes from negative pressure to positive pressure. The greater the fracture depth is, the greater the pore water pressure in the fracture is, and the greater the infiltration depth at the time of rainfall stopping is. When the permeability coefficient is greater than the rainfall intensity, the permeability coefficient ratio has a great influence on the infiltration process of rainwater. The smaller the fracture angle is, the greater the maximum pore water pressure is in the fracture depth range, and the greater the depth of the positive pore water pressure is. However, with the increase of fracture angle, the infiltration depth decreases, and the range of the surface saturation area of slope increases obviously. With the increase of fracture density, the saturated positive pressure region is connected to each other in the slope. The influence range and the degree of the rainwater on the seepage field are larger and larger. There is a power relation between the saturation area and the fracture number, and also the concentration distribution of long fractures directly forms the large-connected saturated zone and raises groundwater. The range of the saturated zone and variation law of the pore water pressure under fracture seepage are obtained, which provide a reference for the parameter partition assignment of slope stability analysis under fracture seepage.

1. Introduction

Colluvial soil slope whose soil layer thickness is within 7 m is widely distributed in the southern part of China [1]. Under the influence of rainfall, it can easily bring shallow landslide or debris flow which is the main geological hazard in southern China. A large number of engineering practices and tests have proved that the strength of slope soil has the characteristics of deterioration with increase of water content [2]. Therefore, mastering the occurrence state of rainwater in slope soil becomes the precondition for studying the stability of slope. Because the slope soil has the

characteristics of low strength and strong evaporation, the peristalsis and uneven evaporation of the upper and lower layers occur after rainfall infiltration in the diluvial layer, thus causing a clear fracture. In addition, the fracture's permeability is obviously different from the surrounding soil, which induces water to infiltrate into the slope soil more quickly and expand the infiltration range. In particular, when the permeability of the undisturbed slope soil is low, the infiltrated water may change the whole seepage field of the slope above the bedrock. Therefore, the process of rainwater anisotropic infiltration induced by fractures should be analyzed in the design of drainage

measures for colluvial soil slope. The anisotropic seepage is mainly caused by the following aspects: (1) fracture depth, (2) ratio of the permeability coefficient along the fracture direction to vertical fracture direction (permeability ratio μ), (3) angle of fracture distribution (θ), and (4) fracture density.

At present, scholars worldwide have conducted a significant amount of research on fracture seepage. Ju et al. [3] and Qian et al. [4] studied the seepage properties of fractured rocks under different confining pressures. Chen et al. [5] and Huang et al. [6] studied the numerical calculation method of the discrete fracture model for two-dimensional seepage in fractured rock. Yang et al. [7] and Chai and Xu [8] studied the composite element model of rock fracture seepage coupling with normal stress. Su et al. [9] and Zeng et al. [10] have carried out a rough single fracture percolation-dissolution coupling model controlled by the surface reaction and diffusion migration. Ju et al. analyzed the variation of seepage properties with fracture roughness and the influence of the rough structure on seepage mechanism through laboratory tests. In addition, the fractal model of relationship between water flow resistance and fracture roughness was obtained [3]. Liu et al. used the DFN-GEN program to generate the fracture-rock calculation model, studied the hydraulic characteristics of the fractured rock mass, and discussed the influence law of stress on the equivalent permeability coefficient of the fractured rock mass [11]. Chen and Song carried out a numerical calculation method for the discrete fracture network model for flow and heat transfer in two-dimensional fractured rocks. The model is used to simulate a randomly generated fracture network to study the characteristics of flow and heat transfer in fractured rock [12]. Leung and Zimmerman studied the fluid flow in a random two-dimensional fracture network and established a macroscopic effective hydraulic conductivity estimation method based on the fracture network parameters [13]. Xue and Chen established a composite element model considering the coupling of rock fracture seepage and normal stress. The analysis shows that the normal stress causes the seepage uneven penetration of the fractured rocks; that is, the osmotic gradient, the uplift pressure, and seepage velocity of the local area increase significantly [14]. Chen et al. discussed the seepage properties of the joint surface and derived the normal and tangential stiffness coefficient formulas of the joint plane and the equivalent permeability coefficient formula of the joint system [15]. Huo et al. established a rough single-fracture seepage-dissolution coupling model controlled by the surface reaction and diffusion migration. The results show that the distribution of aperture, flow velocity, and concentration of Ca^{2+} appeared as inhomogeneous wormholes. The flow through the fracture increased during the whole period of simulation, and the factor controlling the chemical reaction varied during the dissolution [16]. Su et al. believe that the overall permeability of the fracture increases slowly at the initial moment. As the aperture increases and penetrates, the dissolution rate will gradually increase, which is an accelerated process [9].

Song et al. studied the influence of fluid-solid coupling on shale mechanics and seepage laws. The shale seepage tests under different saturations show that, under fluid-solid coupling conditions, the higher the saturation, the higher the propagation and the seepage ability of microcracks under pressure [17]. Huang et al. carried out numerical analysis on the hydrothermal coupling model of low-temperature fractured rocks. It is believed that both the fracture width and delivery head of fracture water affect completed freezing time. The completed freezing time increases with the increase of fracture width and delivery head of fracture water [6]. Zeng et al. studied the seepage law considering the formation dip angle, established the modified radial flow formula of the inclination angle, and obtained the formation pressure distribution and the production formula of the inclined formation by the plane radial seepage theory [18].

From the above studies, we can see that the existing researches mainly focus on the fracture seepage test method, numerical calculation theory, and the establishment of the constitutive model, and the research object is mostly rock fissure seepage. However, the research on soil slope fracture seepage is seldom carried out. In the last two years, the frequency of soil slope instability caused by rainfall was increasing. Therefore, the fracture causing the change of the seepage field of soil slope and leading to slope instability phenomenon ultimately cannot be ignored. This paper intends to study the influence of slope fracture anisotropy on the rainwater infiltration process in colluvial soil slope. What's more, the occurrence characteristics of rainwater under the influence of fracture anisotropy are obtained to provide a reference for slope stability analysis and design of drainage measures when fractures exist.

2. Numerical Realization of Fracture Anisotropy

In this paper, the SEEP/W module of finite element software GEO-slope is used to calculate the seepage process of rainwater [19]. The fracture depth, fracture angle, permeability coefficient ratio, and fracture density are simulated by the following methods [20–22]: (1) a solid element is established equivalent to a fracture in the model, and a fracture is defined as another material different from the colluvial soil; (2) to simulate the distribution of fractures by changing the length, angle, and spacing of the established fracture solid element; (3) the anisotropy of the fracture unit is simulated by defining the ratio (μ) of the permeability coefficient (k'_y) along the direction of fracture and the permeability coefficient (k'_x) in the direction of vertical fracture. The angle of fractures distribution (θ) should also be taken into account here. The schematic diagram is shown in Figure 1.

In Figure 1, the fracture angle (θ), the fracture permeability coefficient (k'_x and k'_y), and the actual set fracture permeability coefficient (k_x and k_y) satisfy the following formula:

$$\begin{pmatrix} k_x \\ k_y \end{pmatrix} = \begin{bmatrix} \cos \theta & \sin \theta \\ -\sin \theta & \cos \theta \end{bmatrix} \begin{pmatrix} k'_x \\ k'_y \end{pmatrix}, \quad (0 \leq \theta \leq 90^\circ), \quad (1)$$

$$\begin{pmatrix} k_x \\ k_y \end{pmatrix} = \begin{bmatrix} \cos \theta & \sin \theta \\ \sin \theta & \cos \theta \end{bmatrix} \begin{pmatrix} k'_x \\ k'_y \end{pmatrix}, \quad (\theta = 90^\circ), \quad (2)$$

where θ is the angle between the crack and the vertical direction, k'_x and k'_y are the permeability coefficients in the direction of vertical fracture and permeability coefficient along the direction of fracture, respectively, and k_x and k_y are the permeability coefficients along the X and Y directions in the global coordinate system, respectively.

3. Numerical Model and Calculation Scheme

3.1. Numerical Model and Boundary Conditions. A simple slope with a height of 20 m and an angle of 30° is used in the calculation. The fracture is considered within a depth of seven meters on the surface of the slope. The fracture is designed at the middle and top of the slope. The length of fracture is 1 m, 3 m, and 5 m, and the angle of fracture is 0° , 30° , and 60° . As shown in Figure 2, the influence of the number of fractures on the seepage process is considered according to the uniform distribution of fractures in the middle and top of the slope. The numbers of fracture are 1, 2, 3, 4, and 5. In the calculation of rainfall infiltration, when the rainfall intensity is less than the saturation permeability coefficient of slope surface soil, the slope surface adopts the unit flow boundary, which is controlled by the rainfall intensity. When the rainfall intensity is greater than the permeability coefficient of slope surface soil, the slope surface is set as the head boundary.

The calculation of saturated-unsaturated seepage under rainfall condition requires an initial condition, and the infiltration of rainwater is transient seepage based on the initial condition. In the natural state, the area above the groundwater level is generally unsaturated. According to the Van Genuchten (VG) model, the natural state determines the distribution of the initial matrix suction field in the slope. However, the permeability coefficient of the unsaturated region is much smaller than that of the saturated permeability coefficient because of the existence of matrix suction. The continuous infiltration of rainwater in the slope is controlled by the permeability coefficient of the unsaturated region. Therefore, the accurate determination of the initial state is the key to simulate the rainwater infiltration process. At present, there are two representative methods for the simulation of the unsaturated region in the initial state [23]: (1) the above area of the groundwater level shall be linearly assigned according to the hydrostatic pressure, which will result in a large difference in the negative pore water pressure at different positions of the slope surface, and (2) the pore water pressure below the groundwater is calculated according to hydrostatic pressure. The pore water pressure on the underground water level is 0 kPa. The pore water pressure in the area above the underground water level is fitted by using the VG model. However, the negative pore water pressure on the slope in contact with the atmosphere should be the same.

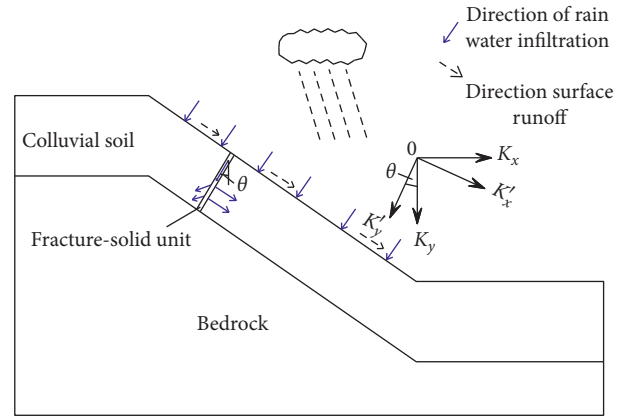


FIGURE 1: Fracture permeability coefficient and global coordinate system conversion.

As far as the literature is concerned, most scholars use the first method to simulate the initial seepage field. In fact, since the surface of slope is in contact with the atmosphere, the drought-wet degree of the slope surface is close, and the negative pore water pressure is basically the same. Therefore, the second method is used to simulate the initial seepage field of slope, as shown in Figure 3.

3.2. Calculation Parameters and Schemes. The actual project supported in this paper is the slope of K107 + 670 of the Rucheng-Chenzhou expressway in Hunan Province, so the parameters used in the calculation are derived from the test of undisturbed soil [24]. To obtain the permeability of weakly weathered limestone, the borehole water pressure test was carried out on the rock. According to the test results, $k_x = k_y = 1.0 \times 10^{-9}$ m/s. The saturated permeability coefficient of homogeneous (gravel) silty clay was obtained by the laboratory test, and $k_x = 1.0 \times 10^{-7}$ m/s, and $k_y = 0.83 \times 10^{-7}$ m/s. The saturated water content is measured by the laboratory test of the original sample. The saturated water content of silty clay is 0.35, and that of weakly weathered limestone is 0.05. The residual water content (w_r) of silty clay which is acquired by the laboratory test is 0.02.

The permeability coefficient in the direction of vertical fracture is $k'_x = 2.83 \times 10^{-2}$ m/s. The permeability coefficients along the direction of fracture are $k'_y = 1k'_x, 10k'_x, 100k'_x,$ and $1000k'_x$, respectively, and μ are 1, 10, 100, and 1000 [25]. Then, k_x and k_y in the global coordinate system with different permeability coefficient ratios (μ) and fracture angles (θ) are calculated according to Equations (1) and (2). The results are shown in Figure 4.

To simulate the most unfavorable rainfall conditions, the rainfall intensity value was calculated by using the maximum rainfall of 7 days in the last 20 years in the Rucheng-Chenzhou area, Hunan Province. The rainfall is 585 mm (9.67×10^{-7} m/s) [26]. To consider the influence of fracture length, fracture angle, fracture permeability coefficient ratio, and fracture density on the rainwater seepage process, the designed calculation scheme is shown in Table 1.

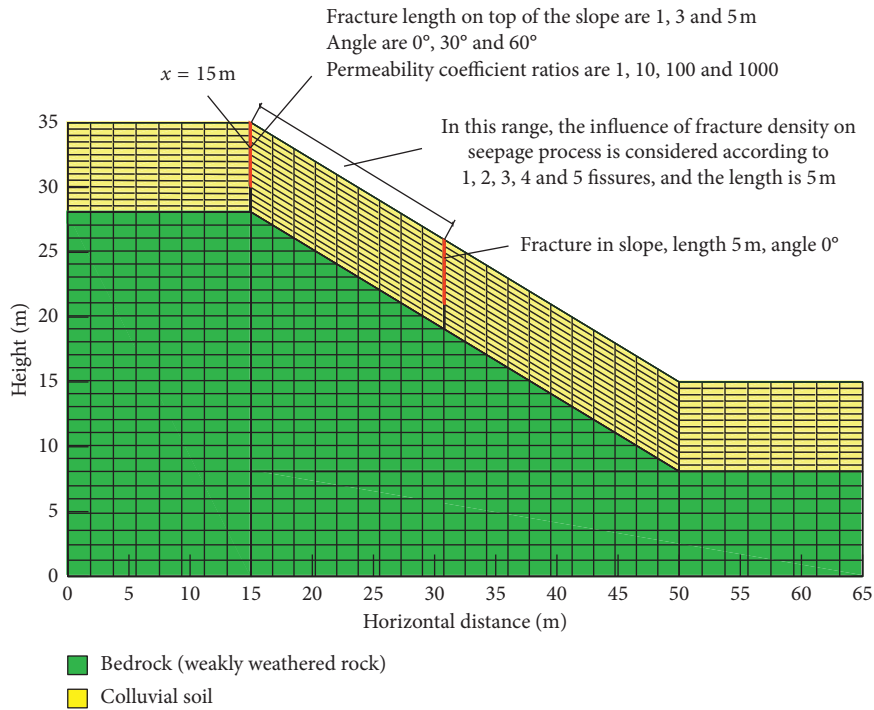


FIGURE 2: Numerical calculation model.

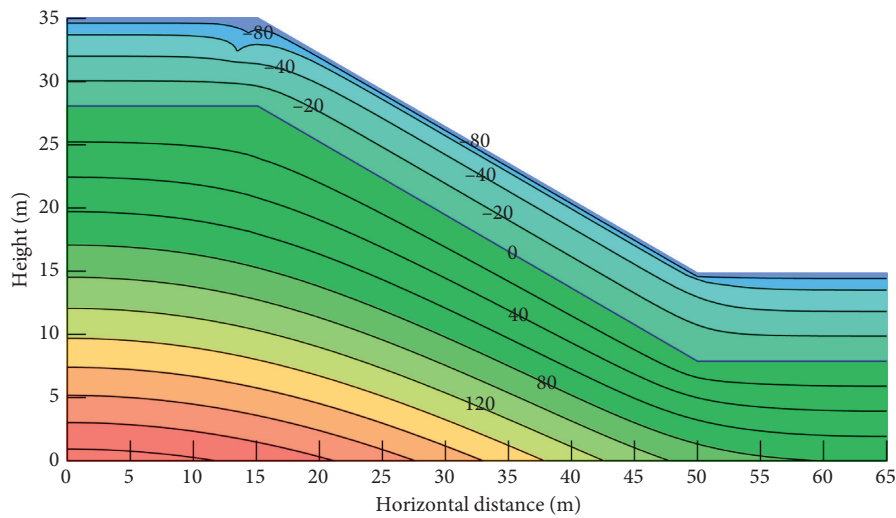


FIGURE 3: Initial pore water pressure distribution in slope (unit: kPa).

4. Results and Discussion

4.1. Influence of Fracture Anisotropy Degree on the Rainwater Infiltration Process

4.1.1. Influence of Fracture Depth. Figure 5 shows the distribution of pore water pressure of different fracture depths along the section ($x = 15\text{ m}$) at 1 and 7 days of continuous rainfall. It can be seen that the pore water pressure in the fracture increases rapidly with the rainfall until it changes

from negative pressure to positive pressure. When fracture depth is 1 m and the duration of rainfall is 1 d, the maximum pore water pressure in the fracture is 9.69 kPa, and the infiltration depth of rainwater along the bottom of the fracture is 0.5 m. However, the maximum pore water pressure in the fracture is 9.70 kPa, and the infiltration depth of rainwater along the bottom of the fracture is 1.5 m when rainfall falls for 7 days. For 3 m fracture and 5 m fracture, the variation of pore water pressure is similar to that of 1 m fracture. Both show that pore water pressure of

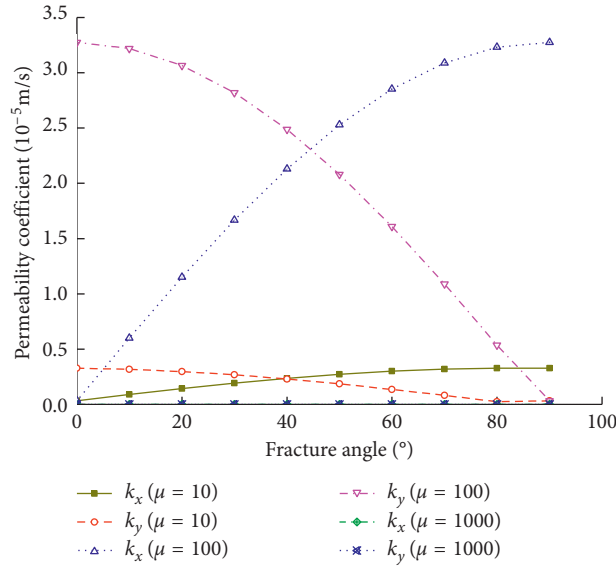


FIGURE 4: Fracture permeability coefficient in the global coordinate system.

TABLE 1: Schemes for numerical analysis.

Scheme number	A1~A3	B1~B4	C1~C3	D1~D4
Fracture position	Top of the slope	Top of the slope	Top of the slope	From the top to the middle of the slope
Fracture angle (°)	0	0	0, 30, and 60	0
Fracture depth (m)	1, 3, and 5	3	3	5
Permeability coefficient ratio, μ	100	1, 10, 100, and 1000	100	100
Fracture density	Single fracture	Single fracture	Single fracture	1, 2, 3, 4, and 5 fractures
Boundary condition	Rainfall intensity (m/s) Rainfall duration/numerical time (h)	585 mm (9.67 × 10 ⁻⁷ m/s) 7 days		
Analysis content	Fracture depth	Permeability coefficient ratio	Fracture angle	Fracture density

the fracture section is almost equal when rainfall is 1 d and 7 d, respectively. The infiltration depth at 7 days of rainfall is obviously greater than that at 1 day, which is 2.0 m and 1.7 m, respectively. The infiltration depths are greater than that of 1 m fracture. The results show that, after 1 day of rainfall, the fracture is almost filled with the infiltration rainwater. However, the rainwater infiltration depth is related to rainfall duration, soil permeability coefficient, and seepage boundary condition.

By analyzing the reason, because of the large permeability coefficient of the fracture, the infiltration rainwater on the slope will enter into the fracture quickly. However, because of the small permeability coefficient of soil, the rainwater in the fracture is not easy to seep out the slope soil. Rainwater will converge inside the fracture until the fracture is completely filled with rainwater. The pressure head is almost the same as the fracture depth in the fracture. When the fissure is filled with rainwater, the infiltration of fracture rainwater into the slope will be changed into pressure permeability. Therefore, the greater the fracture depth, the greater the pore water pressure in the fracture, and the greater the infiltration depth at the time of rainfall stopping.

Figure 6 shows the distribution of the saturation line around fractures at different fracture depths (7 days of rainfall). The area around the fracture is saturated after seven days of rainfall. The size of the saturated region is positively correlated with the depth of the fracture. The continuous saturation zone is not formed in the slope except the fracture. In particular, when the fracture depth is 5 m, the saturation line down the fracture has merged with the underground water line. The saturated area increases rapidly and eventually leads to the rise of the groundwater level, which affects the seepage field of the slope to a greater extent. In conclusion, under the same conditions, the fracture depth determines the size of the saturated area around the fracture. The formation of the rapid seepage path is the direct cause of the rise of the groundwater level in the fractured slope.

4.1.2. Influence of Fracture Permeability Coefficient Ratio.

Figure 7 shows the distribution curves of pore water pressure with buried depth of fracture at different fracture permeability ratios. As shown in Figure 7, after 7 days of rainfall, the pore water pressure of each scheme fracture section

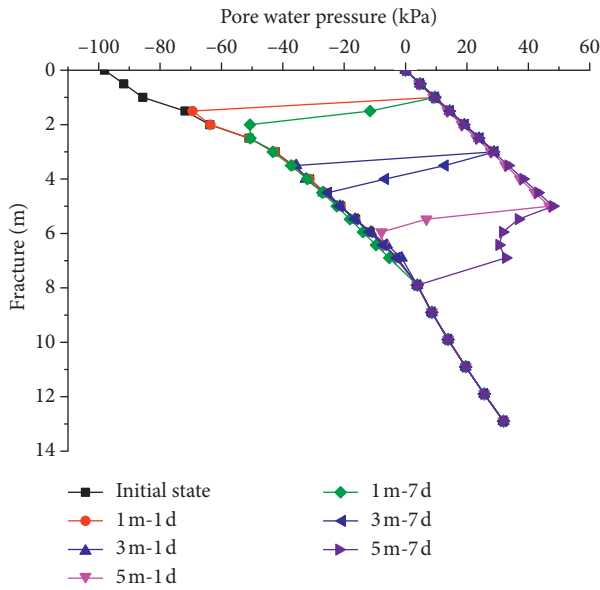


FIGURE 5: Distribution curves of pore water pressure with depth in different fracture depths ($x = 15$ m).

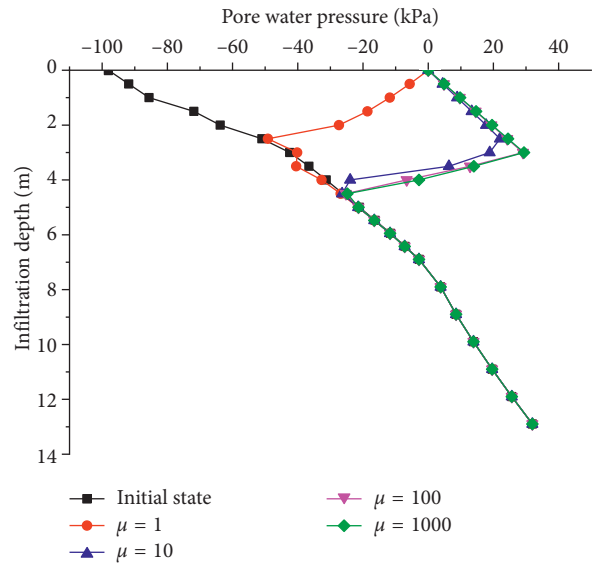


FIGURE 7: Distribution curves of pore water pressure with depth in different fracture permeability coefficient ratios ($x = 15$ m).

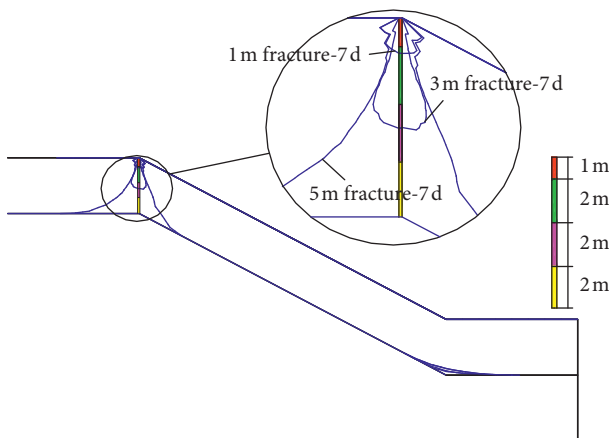


FIGURE 6: Distribution of the infiltration line around the fracture in different fracture depth (7 days of rain).

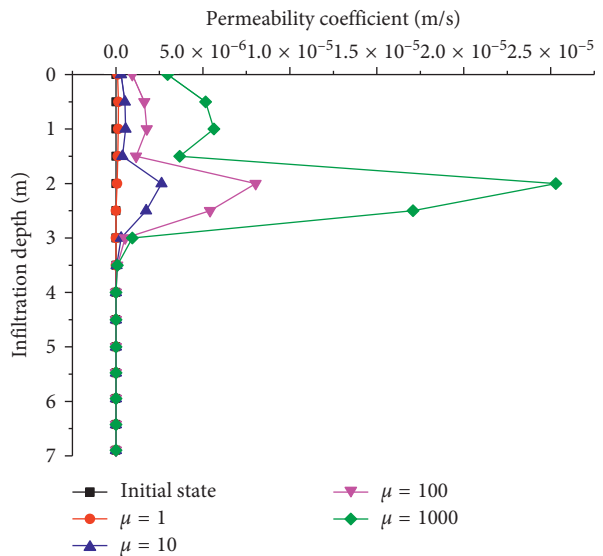


FIGURE 8: Distribution curve of the permeability coefficient with depth in different fracture permeability coefficient ratios ($x = 15$ m).

increases to a certain extent. When $\mu = 1$, the pore water pressure decreases gradually with the increase of buried depth in the fracture range, and it is always in a negative pressure. When $\mu \geq 10$, the pore water pressure increases gradually with the increase of buried depth in the fracture range. Their pore water pressure distribution law is basically consistent, and the numerical difference is small. Figure 8 shows the distribution curve of the fracture permeability coefficient with buried depth when rainfall stops. When $\mu \geq 10$, the permeability coefficient is obviously larger than that of the initial state and $\mu = 1$.

Combined with the analysis of Figures 7 and 8, it is not difficult to find the reasons for the above phenomenon. When $\mu = 1$, the unsaturated state is always maintained in the fracture range. The maximum permeability coefficient in the fracture range is 1.51×10^{-7} m/s, which is less than 9.67×10^{-7} m/s of rainfall intensity. Therefore, the infiltration

process of rainfall is actually controlled by the soil permeability coefficient. However, when $\mu \geq 10$, the vertical permeability coefficient of fracture increases significantly relative to $\mu = 1$. The fracture is saturated rapidly. The unsaturated permeability coefficient is changed to the saturation permeability coefficient. The permeation coefficient is much larger than the rainfall intensity, and the infiltration process of rainwater is controlled by the rainfall intensity. Therefore, when $\mu \geq 10$, the distribution of pore water pressure is basically the same, and the numerical difference is small.

Figure 9 shows a cloud map of pore water pressure in the fracture area with different permeability coefficient ratios. For convenience of analysis, only the fracture area is displayed. It can be seen that when $\mu = 1$, the whole fracture area

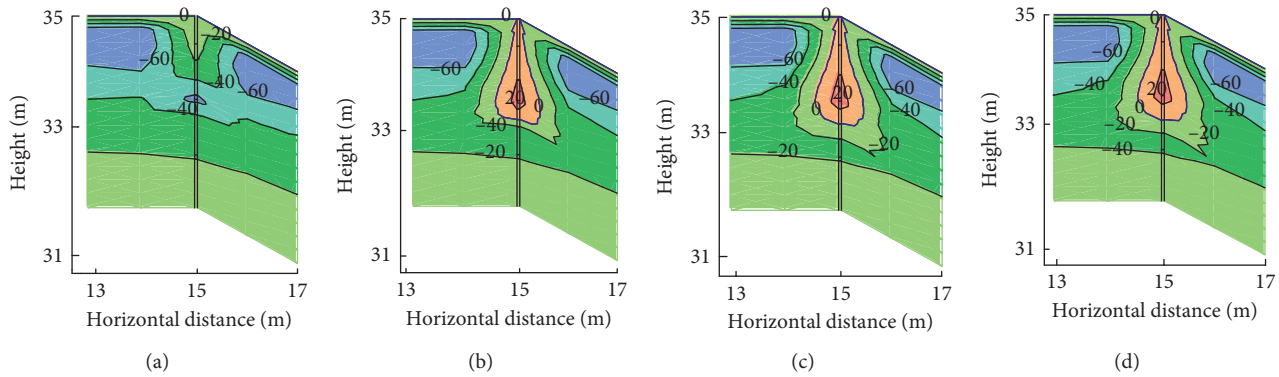


FIGURE 9: Pore water pressure cloud images of the fracture zone with different permeability coefficient ratios (fracture depth 3 m, unit: kPa): (a) $\mu = 1$; (b) $\mu = 10$; (c) $\mu = 100$; (d) $\mu = 1000$.

is the negative pressure area after 7 days of rainfall. When $\mu \geq 10$, a certain range of the saturation zone appears along the fracture. The maximum pore water pressure in this area is above 20 kPa. The distribution of the saturated area is similar, which further shows that the distribution of pore water pressure in Figure 7 is objective.

In conclusion, the influence of the fracture permeability coefficient on the rainfall infiltration process is mainly related to the relative magnitudes of the permeability coefficient and rainfall intensity. When the permeability coefficient of the fracture is less than the rainfall intensity, the permeability coefficient ratio has little effect on the infiltration process. When the permeability coefficient is greater than the rainfall intensity, the permeability coefficient ratio has a great influence on the infiltration process of rainwater. However, with the increasing of the permeability coefficient ratio, the influence of rainwater on the seepage process is not obvious.

4.2. Influence of Anisotropic Direction of Fracture on the Rainwater Infiltration Process. Figure 10 shows the variation of pore water pressure along the fracture section with buried depth at different fracture angles after rainfall. The following can be seen from the graph: (1) the pore water pressure caused by rainfall in the range of fracture depth changes from the negative value of the initial state to the positive value. The value increases linearly with the increase of buried depth. The difference of the pore water pressure distribution curve with different fracture angles is small. The pore water pressure distribution curve is parallel to that of the initial state. The results show that different fracture angles have little effect on distribution of pore water pressure. (2) The smaller the fracture angle is, the greater the maximum pore water pressure in the fracture depth range is, and the greater the depth of the positive pore water pressure is. Figure 11 shows the distribution of pore water pressure in the top of the slope at different fracture angles. It can be seen that, with the increase of fracture angle, the depth of infiltration decreases, but the range of the surface saturation area of slope increases obviously. The results show that the influence of fracture angle on the infiltration process of rainwater is

mainly reflected on infiltration depth and the range of the surface saturation area.

From the above analysis, it can be seen that the influence of different fracture angles on the seepage field of the slope is mainly reflected in the infiltration depth, influence range, and degree. When the fracture angle is small, the influence depth of rainwater infiltration is greater, but it has little influence on the surface seepage field of the slope. However, when the fracture angle is large, the influence depth of rainwater infiltration is relatively small, but the influence on the surface seepage field of the slope is greater.

The reasons for this can be summarized as follows: (1) after a long period of rainfall, the fractures gradually reached saturation. The saturation permeability coefficient is much larger than the rainfall intensity, and the infiltration process is controlled by the rainfall intensity. Under the same condition of rainfall, almost all of rainwater is infiltrated. Therefore, the fracture angles have little effect on the distribution of pore water pressure with buried depth. (2) The smaller the fracture angle is, the greater the vertical permeability coefficient is. As a result, rainwater is more likely to cause saturation in the deep fracture areas. Accordingly, the surface saturation area of slope is relatively small. When the fracture angle increases, the vertical permeability coefficient becomes smaller and the horizontal permeability coefficient becomes larger. The rainwater is easy to gather in the shallow layer of the slope and seepage along the horizontal direction, which causes the saturation region of the slope surface to increase obviously.

4.3. Influence of Fracture Density on the Rainwater Infiltration Process. The size of fracture density often determines the stability of the slope. Especially, when the fracture depth is large, rainwater easily enters the deep slope directly, which has great influence on slope stability. Hence, in the middle to the top of the model, a different number of fractures whose length is 5 m are set up. In each of the five schemes, there are 1, 2, 3, 4, and 5 fissures, respectively. The five schemes are used to analyze the influence of fracture density on the rainwater infiltration process. Figure 12 shows the distribution of pore water pressure at different number of fractures. It can

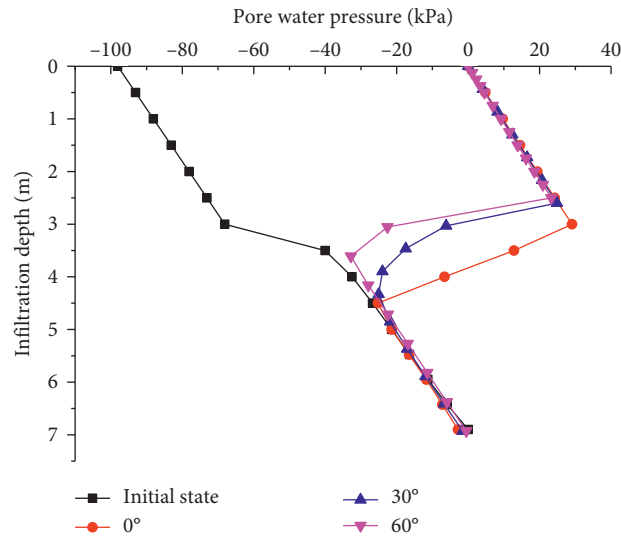


FIGURE 10: Distribution curves of pore water pressure with depth in different fracture angles (fracture depth 3 m).

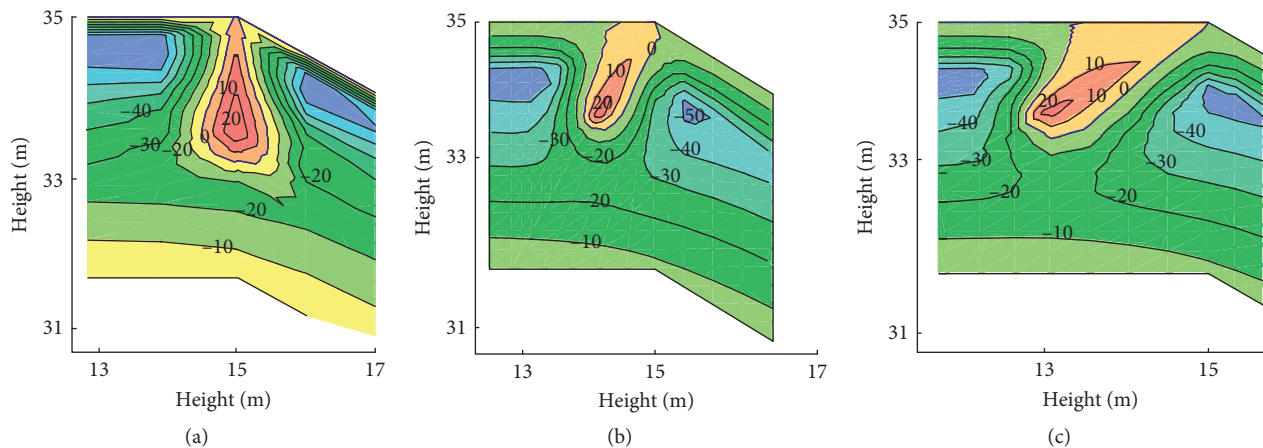


FIGURE 11: Pore water pressure in the fracture zone with different fracture angles (fracture depth 3 m, unit: kPa): (a) $\theta = 0^\circ$; (b) $\theta = 30^\circ$; (c) $\theta = 60^\circ$.

be seen from Figure 12 that when there is no fracture, the slope still maintains the negative pressure state after rainfall, and there is no saturation zone. When there is a fracture, rainwater infiltrates along the fracture and forms a saturated positive pressure zone inside the slope. With the increase of fracture density, the saturated positive pressure region is connected to each other in the slope. The influence range and the degree of the rainwater on the seepage field are larger and larger. The range of the saturated zone formed by 1 to 5 fractures is 16.4 m^2 , 34.7 m^2 , 60.9 m^2 , 75.6 m^2 , and 110.7 m^2 , respectively. The area of the saturated area increases with the number of fractures in the form of the formula $y = 15.968x^{1.2073}$, as shown in Figure 13. Figure 14 shows the variation process of the saturation line in the fracture with rainfall time when 5 m long fissures are distributed in the middle and upper parts of the slope. The saturation zone formed by each fracture exists independently during 2 days of rainfall. After 3 days of rainfall, the saturated area of the lower part of the single fracture began

to merge and connect gradually. The saturation line increases obviously with the continuous rainfall.

In conclusion, the existence of long fractures as the dominant seepage path will help rainwater enter the slope quickly. Rainfall can directly recharge the slope groundwater and form a large area of the saturation area. The existence of the saturated zone increases the weight of soil and reduces the unsaturated strength of soil. Especially when there are many fractures in the slope at the same time, the influence area of rainwater infiltration will be further enlarged, which will be unfavorable to the slope stability.

4.4. Analysis of Influence of Fracture on Slope Stability.

The formation of cracks in soil slopes, especially loose slopes, mainly comes from two aspects: (1) slip of slope soil; (2) when the upper soil evaporates and shrinks, the lower soil cannot synchronize, so the upper and lower soil shrinkage is

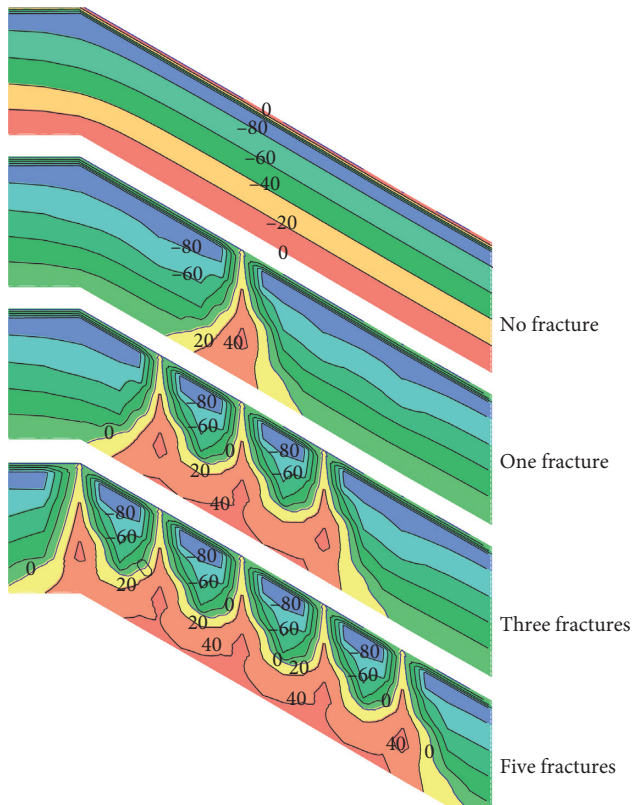


FIGURE 12: Effect of fracture quantity on pore water pressure field (fracture depth 3 m, unit: kPa).

uneven, resulting in cracks. The existence of a fracture causes it to lose its original strength on the surface of a fracture [27]. When the crack develops to a certain extent, it will inevitably affect the slope stability [28]. Specifically, the most important causes of soil slope instability caused by fractures can be summarized in three aspects: (1) as far as the fracture itself is concerned, the degree of development of the fracture will determine the strength of the soil, which includes the density, depth, and width of the fracture. At present, there is not a criterion of how the degree of crack development affects the strength of soil, but some useful research has been carried out [29]. (2) The pore water pressure and water content increase due to rainwater entering the fractures and slope soil. The unsaturated strength of the soil will be reduced. At the same time, the gravity of the soil will be increased, which will lead to the increase of the sliding force. (3) For colluvial soil slope, the lower part of the slope is impervious bedrock. When rainwater enters the fracture and surrounding soil, the hydrodynamic pressure will be generated in the sliding body of the upper part of the bedrock, and the slope sliding moment will be significantly increased.

In view of the fact that fracture affects slope stability, the influences of the fracture depth, fracture angle, and fracture density on the rainwater infiltration process are analyzed. The results show that the pore water pressure of the soil around the fracture increases under the condition of rainfall. The soil reaches the saturation state (water content increases). When the fracture density is high, the continuous saturation zone is

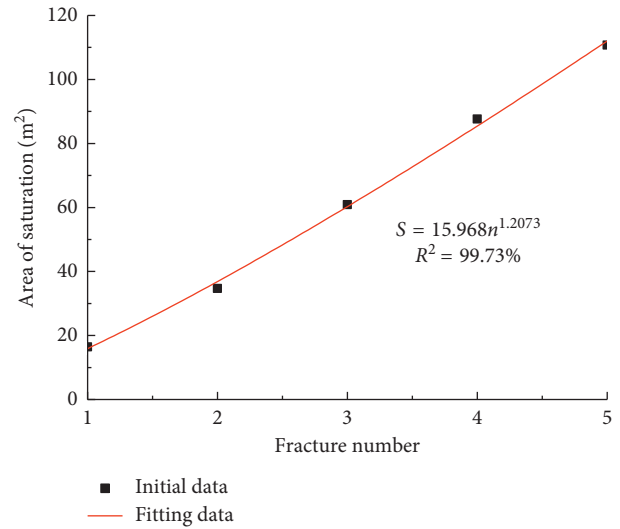


FIGURE 13: The relationship between the fracture numbers and the area of saturation.

formed inside the slope. According to bivariate unsaturated shear strength formula put forward by Fredlund et al. [30], the strength of unsaturated soil is determined by several factors [31, 32] such as effective shear strength parameters (c' and ϕ'), matrix suction ($u_a - u_w$), and ϕ_b . When the soil is saturated, the effective shear strength parameters (c' and ϕ') decrease, the matrix suction almost disappears in the saturated region, and ϕ_b decreases accordingly. As a result, the strength of unsaturated soil decreases significantly. Moreover, when rainwater enters the soil along the fractures, the weight of soil will increase, which leads to the increase of slope sliding force. Combining the calculation results with the theory of unsaturated shear strength shows that fracture can enhance the infiltration of rainwater in the slope soil and thus affects the slope stability significantly. The range of the saturated zone and variation law of the pore water pressure under fracture seepage are obtained, which provides a reference for the parameter partition assignment of slope stability analysis under fracture seepage.

5. Conclusions

The influence of anisotropy of slope fracture on the rainwater infiltration process of slope soil is simulated by the numerical method, and the following conclusions are obtained:

- (1) The fracture depth, permeability coefficient ratio, fracture angle, and fracture density all affect the infiltration of rainwater to a certain extent and mainly reflect in the influence on pore water pressure, infiltration rate of rainwater, infiltration depth, and infiltration range. It is worth considering in slope stability analysis and slope drainage design.
- (2) Under the same rainfall conditions, the greater the fracture depth, the greater the pore water pressure in the fissure, and the greater the influence range on the slope. The effect of the permeability coefficient ratio

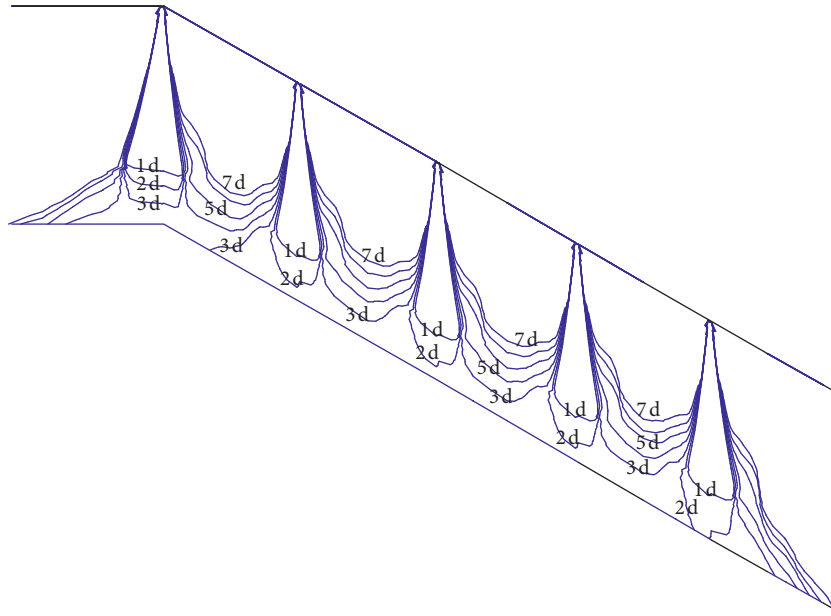


FIGURE 14: The distribution of the phreatic line with the rainfall time when the fracture density is 5 (fracture depth 3 m).

on the infiltration process of rainwater is mainly related to the relative size of the permeability coefficient and rainfall intensity. When the permeability coefficient is less than the rainfall intensity, the influence of μ on the infiltration process of rainwater is small. While the permeability coefficient is greater than the rainfall intensity, the influence of μ on the infiltration process of rainwater becomes more and more significant.

- (3) Fracture angle has little effect on the distribution law of pore water pressure. The influence of rainwater on the surface layer of slope is big when the angle is large. For small fracture angle, rainwater has a greater infiltration depth.
- (4) Under the same rainfall condition, the area of the saturated zone increases exponentially with the number of fractures. The concentrated distribution of long fractures is the direct cause of the large-scale connected saturated zone in the slope and the rise of the groundwater level.

Data Availability

The data used to support the findings of this study are available from the corresponding author upon request.

Conflicts of Interest

The authors declare that there are no conflicts of interest regarding the publication of this paper.

Acknowledgments

The authors gratefully acknowledge the National Key Research and Development Program of China (2017YFC0805307), National Natural Science Foundation of China (51878078,

51838001, 51878070, 51508040, and 51678074), Excellent Youth Foundation of Natural Science Foundation of Hunan Province (2018JJ1026), Jiangsu Provincial Natural Science Fund Projects (BK20150885), and Open Fund of Engineering Laboratory of Spatial Information Technology of Highway Geological Disaster Early Warning in Hunan Province (Changsha University of Science and Technology), China (KFJ160601).

References

- [1] L. T. Zhan, H. Li, Y. M. Chen, and D. G. Fredlund, "Parametric analyses of intensity-duration curve for predicting rainfall-induced landslides in residual soil slope in southeastern coastal areas of China," *Rock and Soil Mechanics*, vol. 33, no. 3, pp. 872–880, 2012, in Chinese.
- [2] R. I. Borja and J. A. White, "Continuum deformation and stability analyses of a steep hillside slope under rainfall infiltration," *Acta Geotechnica*, vol. 5, no. 1, pp. 1–14, 2010.
- [3] Y. Ju, Q. G. Zhang, Y. M. Yang, H. P. Xie, F. Gao, and H. J. Wang, "An experimental investigation on the mechanism of fluid flow through single rough fracture of rock," *Science China Technological Sciences*, vol. 56, no. 8, pp. 2070–2080, 2013.
- [4] J. Qian, Z. Chen, H. Zhan, and H. Guan, "Experimental study of the effect of roughness and Reynolds number on fluid flow in rough-walled single fractures: a check of local cubic law," *Hydrological Processes*, vol. 25, no. 4, pp. 614–622, 2011.
- [5] S. Chen, F. Liu, and K. Burrage, "Numerical simulation of a new two-dimensional variable-order fractional percolation equation in non-homogeneous porous media," *Computers & Mathematics with Applications*, vol. 68, no. 12, pp. 2133–2141, 2014.
- [6] S. B. Huang, Q. S. Liu, A. P. Cheng, and Y. Z. Liu, "A coupled hydro-thermal model of fractured rock mass under low temperature and its numerical analysis," *Rock and Soil Mechanics*, vol. 39, no. 2, pp. 735–744, 2018.

- [7] T. H. Yang, P. Jia, W. H. Shi, P. T. Wang, H. L. Liu, and Q. L. Yu, "Seepage-stress coupled analysis on anisotropic characteristics of the fractured rock mass around roadway," *Tunnelling and Underground Space Technology Incorporating Trenchless Technology Research*, vol. 43, pp. 11–19, 2014.
- [8] J. R. Chai and W. S. Xu, "Coupling analysis of unsteady seepage and stress fields in discrete fractures network of rock mass in dam foundation," *Science China Technological Sciences*, vol. 54, no. 1, pp. 133–139, 2011.
- [9] B. Y. Su, W. J. Zhang, J. C. Sheng, X. C. Xu, M. L. Zhan, and J. S. Liu, "Study of permeability in single fracture under effects of coupled fluid flow and chemical dissolution," *Rock and Soil Mechanics*, vol. 31, no. 11, pp. 3361–3366, 2010, in Chinese.
- [10] L. Zeng, H. B. Bian, Z. N. Shi, and Z. M. He, "Forming condition of transient saturated zone and its distribution in residual slope under rainfall conditions," *Journal of Central South University*, vol. 24, no. 8, pp. 1866–1880, 2017.
- [11] Q. S. Liu, Y. X. Wu, and B. Liu, "Discrete element analysis of effect of stress on equivalent permeability of fractured rockmass," *Chinese Journal of Rock Mechanics and Engineering*, vol. 30, no. 1, pp. 176–183, 2011, in Chinese.
- [12] B. G. Chen and E. X. Song, "A numerical method for discrete fracture network model for flow and heat transfer in two-dimensional fractured rocks," *Chinese Journal of Rock Mechanics and Engineering*, vol. 33, no. 1, pp. 43–51, 2014, in Chinese.
- [13] C. T. O. Leung and R. W. Zimmerman, "Estimating the hydraulic conductivity of two-dimensional fracture networks using network geometric properties," *Transport in Porous Media*, vol. 93, no. 3, pp. 777–797, 2012.
- [14] L. L. Xue and S. H. Chen, "Composite element model of seepage-normal stress coupling for rock fractures," *Chinese Journal of Rock Mechanics and Engineering*, vol. 26, no. 1, pp. 2613–2619, 2007, in Chinese.
- [15] S. H. Chen, H. R. Wang, and W. L. Xiong, "Study of the seepage characteristics of joint surface," *Journal of Wuhan University of Hydraulic and Electric Engineering*, vol. 22, no. 1, pp. 53–60, 1989, in Chinese.
- [16] J. X. Huo, H. Z. Song, J. N. Du, and Q. C. Guan, "Coupled fluid flow and chemical dissolution model based on surface reaction and mass transfer control in a rough fracture," *Chinese Journal of Rock Mechanics and Engineering*, vol. 34, no. 5, pp. 1013–1021, 2015, in Chinese.
- [17] F. Q. Song, X. Hu, K. Ji, and X. Huang, "Effect of fluid–solid coupling on shale mechanics and seepage laws," *Natural Gas Industry B*, vol. 5, no. 1, pp. 41–47, 2018.
- [18] Y. Zeng, X. D. Kang, X. Q. Xie, E. Tang, and C. Liu, "Studies on seepage law considering stratigraphic dips," *Petroleum*, vol. 3, no. 4, pp. 470–475, 2017.
- [19] S. Ou, L. Wang, P. Wang, Z. Wang, J. Huang, and D. L. Zhou, "Numerical analysis of seepage flow characteristic of collapse column under the influence of mining," *International Journal of Mining Science and Technology*, vol. 23, no. 2, pp. 237–244, 2013.
- [20] Z. Wang, J. Pan, Q. Hou, B. Yu, M. Li, and Q. H. Niu, "Anisotropic characteristics of low-rank coal fractures in the Fukang mining area, China," *Fuel*, vol. 211, pp. 182–193, 2018.
- [21] S. Liu, W. Li, Q. Wang, Z. Wu, and Z. Yang, "Numerical simulation on crack propagation of rock mass with a single crack under seepage water pressure," *Advances in Mechanical Engineering*, vol. 9, no. 10, article 168781401773289, 2017.
- [22] Z. Y. Ye, Q. H. Jiang, C. B. Zhou, and Y. Z. Liu, "Numerical analysis of unsaturated seepage flow in two-dimensional fracture networks," *International Journal of Geomechanics*, vol. 17, no. 5, article 04016118, 2016.
- [23] Z. M. Jiang, J. Tang, G. Xie, and W. J. Chen, "Water pressure test of rock permeability of the slope in Ruchen expressway," *Highway & Auto-Motive Application*, vol. 11, no. 6, pp. 101–104, 2010, in Chinese.
- [24] X. Wu, Y. Wei, J. Wang, J. Xia, C. Cai, and Z. Wei, "Effects of soil type and rainfall intensity on sheet erosion processes and sediment characteristics along the climatic gradient in central-south China," *Science of the Total Environment*, vol. 621, pp. 54–66, 2018.
- [25] J. P. Yuan, Y. L. Lin, P. Ding, and C. L. Han, "Influence of anisotropy induced by fissures on rainfall infiltration of slopes," *Chinese Journal of Geotechnical Engineering*, vol. 38, no. 1, pp. 76–82, 2016, in Chinese.
- [26] L. Scholtès and F. V. Donzé, "Modelling progressive failure in fractured rock masses using a 3D discrete element method," *International Journal of Rock Mechanics and Mining Sciences*, vol. 52, pp. 18–30, 2012.
- [27] J. H. Zhang, J. Li, Y. S. Yao, J. L. Zheng, and F. Gu, "Geometric anisotropy modeling and shear behavior evaluation of graded crushed rocks," *Construction and Building Materials*, vol. 183, pp. 346–355, 2018.
- [28] L. J. Munkholm, R. J. Heck, B. Deen, and T. Zidar, "Relationship between soil aggregate strength, shape and porosity for soils under different long-term management," *Geoderma*, vol. 268, pp. 52–59, 2016.
- [29] Z. Z. Yin, J. P. Yuan, and J. Wei, "Influences of fissures on slope stability of expansive soil," *Chinese Journal of Geotechnical Engineering*, vol. 34, no. 12, pp. 2155–2161, 2012, in Chinese.
- [30] D. G. Fredlund, N. R. Morgenstern, and R. A. Widger, "The shear strength of unsaturated soils," *Canadian Geotechnical Journal*, vol. 15, no. 3, pp. 313–321, 2002.
- [31] J. H. Zhang, J. H. Peng, J. L. Zheng, and Y. S. Yao, "Characterisation of stress and moisture-dependent resilient behaviour for compacted clays in South China," *Road Materials and Pavement Design*, pp. 1–14, 2018.
- [32] J. H. Zhang, J. H. Peng, J. Li, and J. L. Zheng, "Variation of resilient modulus with soil suction for cohesive soils in South China," *International Journal of Civil Engineering*, pp. 1–13, 2018.

Research Article

Experimental Study on the Fine-Grained Uranium Tailings Reinforced by MICP

Rong Gui ^{1,2}, Yu-xiang Pan ^{1,2}, De-xin Ding,^{1,2} Yong Liu,² and Zhi-jun Zhang ²

¹Key Discipline Laboratory for National Defense for Biotechnology in Uranium Mining and Hydrometallurgy, University of South China, Hengyang, Hunan 421001, China

²Nuclear Resource Engineering College, University of South China, Hengyang, Hunan 421001, China

Correspondence should be addressed to Zhi-jun Zhang; zzz181@163.com

Received 15 June 2018; Accepted 5 September 2018; Published 17 October 2018

Guest Editor: Xinbao Yu

Copyright © 2018 Rong Gui et al. This is an open access article distributed under the Creative Commons Attribution License, which permits unrestricted use, distribution, and reproduction in any medium, provided the original work is properly cited.

Sporosarcina Pasteurii was chosen for the experiment to study the effect and mechanism of fine-grained uranium tailings reinforced by MICP. The biochemical characteristics of strains and microbial immobilization in uranium tailings were analyzed. The results showed that the CaCO_3 production rate is positively correlated with the physiological activity of *Sporosarcina Pasteurii* and the concentration of calcium sources, and the higher the solution concentration of CaCl_2 , the lower the discharge rate of bacterial liquid from the sand column, but high concentration of CaCl_2 solution will affect the uniform distribution and migration of bacteria in the uranium tailings. After 16 days, the direct shear was used to test the reinforcement effects of fine-grained uranium tailings by MICP. The cohesive force and the internal friction angle of fine-grained uranium tailings were increased by 140.1% and 46.7%. The production amount of CaCO_3 is 138.89 kg/m^3 . The results showed that the MICP-reinforced technology can effectively improve the shear strength of the uranium tailings, and the experiment provides a new method for the reinforcement of the fine-grained uranium tailings dam.

1. Introduction

With the rapid development of nuclear industry in China, the demand for nuclear fuel increased rapidly. However, a large amount of radioactive waste was produced during the mining and metallurgy process of uranium, and many tailings reservoirs have been built to store them. As a special hydraulic structure, the safety of tailings reservoir has always been the focus of social attention. However, there were numerous serious accidents caused by failure of tailings dam at home and abroad for various reasons [1, 2]. On September 8, 2008, a catastrophic failure accident occurred in the tailings reservoir of Xinta Mining Ltd. Co. Xiangfen County, Shanxi Province, China, that killed 281 people and claim a direct economic loss of 96.91 million yuan. On July 19, 1985, a fluorite tailings dam of Prealpi Mineraia failed at Stava, Trento, Italy. $200,000 \text{ m}^3$ of tailings flowed 4.2 km downstream at a speed of up to 90 km/h that killed 268 people and destroyed 62 buildings. However, due to the

uranium tailings contain radionuclide such as uranium and radium, the catastrophe caused by failure of uranium tailings dam could be even more serious than other tailings dam, which also will cause severe radioactive pollution to the surrounding water and soil. Therefore, in order to ensure the stability of the uranium tailings dam, it is necessary to study the reinforcement technology of uranium tailings.

Traditional soil reinforcement techniques use sodium silicate, cement, and other chemical pulp as grouting materials which have some obstacles such as high cost, high-energy consumption, and permanent soil pollution [3–5]. Whiffin was first proposed to apply microbial diagenesis to cement the loose sand particles and achieved good effect in 2004 [6]. This has led to a research boom in the reinforcement of rock and soil by MICP technology. Paassen et al. applied the MICP technology to reinforce 100 m^3 in situ sand base, and the unconfined compressive strength and stiffness of the treated sand base have a significant improvement [7]. Paassen applied the MICP technology to

reinforce the 3–20 m gravel layer under the surface in the Netherlands, and no collapse happened in the reinforced gravel layer in the horizontal directional drilling and the gas pipeline laying [8]. Burbank et al. use the indigenous diagenetic microorganisms to reinforce the soil in the laboratory. The results show that calcium carbonate production in the soil was 20–48 kg/m³, and the static penetration value of the reinforced soil increased by 2.2 times [9]. Soon et al. [10] applied the MICP technology to reinforce the low-permeability soils and proved that the technology can also improve the mechanical properties of clay or silt. Canakci et al. applied the MICP technology to treat the peat soils with the low-strength and high-compression. After treatment, the shear strength and erosion resistance of reinforced peat soils increased, and calcium carbonate production in peat soil is 16% of the weight of the soil [11]. Mahawish et al. studied the feasibility of applying MICP technology to improve the mechanical properties of coarse sand and applying MICP technology to reinforce the gravel piles, sand piles, and bauxite columns. The uniaxial compressive strength of reinforced piles was up to 8.9 MPa–2.3 GPa [12]. Pusadkar et al. reinforced the sand slop in the laboratory by injecting bacteria (*S. Pasteurii*) and cement solution in sand, and the bearing capacity of slope footing increased significantly after MICP treatment [13]. Grabiec et al. applied the MICP technology to reinforce the incompletely compacted silty clays, and found that MICP technology can make diagenesis in the silty clays and significantly improve the soil stiffness [14].

The biological reinforcement technology aim at improving soil mechanical properties, and erosion resistance precipitate calcium carbonate crystals by the microbial biochemical activities. This technology is often referred to as microbial-induced calcite precipitation (MICP) [15]. At present, MICP technology has been successfully applied to solve geotechnical engineering problems, such as strengthening the bearing capacity of foundation soil, reducing the liquefaction of soils caused by earthquakes, reducing the swelling potential of foundations and roads, and reducing the permeability of tunnel walls and soils [7, 16–20]. These researches have shown that the MICP technology has the advantages over the traditional reinforcement technology which not only reduced the disturbance of chemical grouting reinforcement but also has the advantages of economy, the environmental protection, and large curing radius.

Because the uranium tailings contain radionuclides and have different particle gradations from other porous media, so it is necessary to verify the feasibility of using the MICP technology to reinforce the fine-grained uranium tailings. Therefore, it is necessary to verify the feasibility of using the MICP technology to reinforce the fine-grained uranium tailings.

2. Materials and Methods

2.1. Strains and Culture Medium. The *Sporosarcina Pasteurii* used in the experiment was from the China General Microbiological Culture Collection Center (No. ATCC 11859).

The components of culture medium are shown in Table 1. Firstly, the urea solution was filtered by a steel sterilizing filter with 0.45 μm and 0.22 μm microporous permeable membranes. The urea solution was prepared separately during the sterilization because the urea is easy to decompose under high temperature. Then, the rest of the components were sterilized by pressurized steam sterilization at 121°C for 20 minutes. After preparation, the two solutions were mixed in proportion to get the required solution.

2.2. Uranium Tailings Samples. The samples were from a uranium tailings reservoir in south China. The screening test showed that the gradation parameters d_{10} of the samples is 0.067 mm, d_{30} is 0.117 mm, d_{60} is 0.208 mm, the non-uniform coefficient C_u is 2.663, the curvature coefficient C_c is 0.893, the relative density G_s is 2.67, the density ρ is 1.454 g/cm³, and the void ratio e is 0.752.

2.3. Fixative Solution and Cement Solution. The bacterial liquid is easily discharged from uranium tailings because the *Sporosarcina Pasteurii* has a diameter size within 0.5–3.0 μm . In order to reduce the discharge rate (the ratio of the OD600 value of the discharged bacterial liquid to the OD600 value of the inoculated bacterial liquid) of bacterial liquid from the sand column, CaCl₂ was chosen as the fixative solution. According to related references [9, 13], the higher the concentration of the fixative solution was, the lower the discharge rate of the bacterial liquid was. But under a certain concentration of CaCl₂, the inoculated bacterial liquid will form the flocules, and its diameter sizes enlarged with the increasing concentration of CaCl₂ and blocked the pores between the uranium tailings, resulting in nonuniform distribution of bacterial liquid and unstable transmission of cement solution in the sand column. It indicated that the fixation and uniform distribution of the bacterial liquid in the sand column cannot simultaneously reach their optimum value, especially to different sand samples. So it is necessary to conduct the experimental analysis according to actual needs.

Therefore, in order to study the effects of different concentrations of the fixative solution on the fixation and migration of *Sporosarcina Pasteurii* in uranium tailings, five different concentrations of CaCl₂ solution (0.005 mol/L, 0.015 mol/L, 0.025 mol/L, 0.035 mol/L, and 0.045 mol/L) were set to in the experiment. Based on the experimental results, the cement solution was determined with 0.5 mol/L urea and 0.5 mol/L CaCl₂ solution (equivalent volume mixture).

2.4. Physical Model. The physical model of the sand columns were constructed of polyvinyl chloride (PVC) 7 cm height with an inner diameter of 6.18 cm (the same as the diameter size of the sand samples in the direct shear test). The upper part of the experimental device have a grouting port connected to the sealed plastic bottle with a rubber hose and a reserved vent. The grouting pipe and the outlet pipe have

TABLE 1: Composition of culture medium used in the experiment.

Medium name	pH	Components
CASO liquid medium	7.3	Casein 15 g, soy peptone 5 g, sodium chloride 5 g, urea 20 g, nickel chloride 0.0013 g, deionized water 1000 mL
CASO solid medium	7.3	Casein 15 g, soy peptone 5 g, sodium chloride 5 g, urea 20 g, nickel chloride 0.0013 g, 20 g agar powder, deionized water 1000 mL
Mixed medium	7.3	Casein 15 g, soy peptone 5 g, sodium chloride 5 g, urea 30 g (0.5 mol/L), nickel chloride 0.0013 g, calcium chloride 55.5 g (0.5 mol/L), deionized water 1000 mL

a rubber pipe with a water stop valve. In order to prevent the sand from entering the grouting pipe and outlet pipe, two gauze layers were set on both sides of the sand columns. And, two gravel layers (particle size 2 ± 0.5 mm) were laid on both sides of the sand column to avoid scouring the uranium tailings and clogging of the grouting mouth during the experiment. The experimental device is shown in Figure 1 and Figure 2.

3. Test Procedure and Methods

3.1. Activation and Propagation of *Sporosarcina Pasteurii* Strains. An inoculating loop was used to scrape the strains into a tube which contains 10 mL CASO liquid medium, and the tube was kept in a constant-temperature shaking incubator which was set at 30°C for 2 days. Then, an inoculating loop was used to take the culture supernatant and perform streak inoculation on a solid medium plate. Place the inoculated plate in a constant-temperature incubator which was set at 30°C for 2 days. After 2 days, the milky colonies formed on the solid medium (Figure 3). An inoculating loop was used to scrape the strains from the solid medium into a conical flask with 100 mL of CASO liquid medium. Place the conical flask in a constant-temperature shaking incubator which was set at 30°C for 2 days. The rotation speed was controlled at 130 r/min. From Figure 4, obvious turbidness was observed in the inoculated conical flask compared with the blank reference after 48 h.

3.2. Biochemical Characteristics of the Strains under Cement Solution

3.2.1. Experiment Method. 200 mL of cement solution was poured into three 250 ml of conical flasks. The OD_{600} value of bacterial liquid was diluted to 1.0 with CASO liquid medium. Then, 2 mL of the diluted bacterial liquid inoculated in the conical flask (inoculation amount was 1% (v/v)) which was placed in a constant-temperature shaking incubator which was set at 30°C . The rotation speed was controlled at 130 r/min. Then determine the number of bacteria in culture fluid, ammonia concentration, pH value, and CaCO_3 production after being cultured for 2 h, 4 h, 8 h, 12 h, 18 h, 24 h, and 36 h.

3.2.2. Detection Method

(1) *Number of Bacteria.* In this experiment, the protein nucleic acid analyzer was used to determine the OD_{600} value of the bacterial liquid and substitute the value into formula (1) [21] to calculate the total number of bacteria in the bacterial liquid.

$$Y = 8.59 \times 10^4 Z^{1.3627}, \quad (1)$$

Where Z is the value of OD_{600} and Y is the concentration of bacterial liquid (units/ μL).

However, this formula is valid for the OD_{600} value between 0.2 and 0.8. Bacterial liquid should be diluted and then converted if it exceeds this range.

(2) *Ammonia Concentration.* Take 40 mL of culture supernatant for different culture periods with a centrifuge tube and place them in a refrigerated centrifuge at a speed of 8000 r/min for 20 minutes. Pipette 10 mL of centrifuge supernatant into the colorimetric tube, and the ammonia concentration was determined by the spectrophotometric method.

(3) *pH Value.* The pH value of the culture solution was measured by precision bench-top pH meter.

(4) *CaCO_3 Production.* The acid dissolution method was adopted to determine the calcium carbonate content in the mixed medium as follows: the culture liquid in the conical flask was filtered with filter paper after incubating in a constant-temperature shaking incubator for a period of time, and then put the filtered paper containing residues and the conical flask into a beaker at 70°C for 24 hours. The residues in the conical flask and the filter paper after drying are shown in Figure 5. The total mass of filter paper, beaker, and conical flask is W_1 .

100 mL dilute hydrochloric acid (2 mol/L) was slowly added to the conical flask and to the beaker containing the filter paper, and stirred with a glass rod until no gas generated. After drying, the process was repeated once more, and the total mass of filter paper, beaker, and conical flask is W_2 . According to chemical reaction formula (2), the difference in mass between W_2 and W_1 before and after the reaction is the difference between CaCO_3 and CaCl_2 . The content of CaCO_3 can be calculated by the following formula:

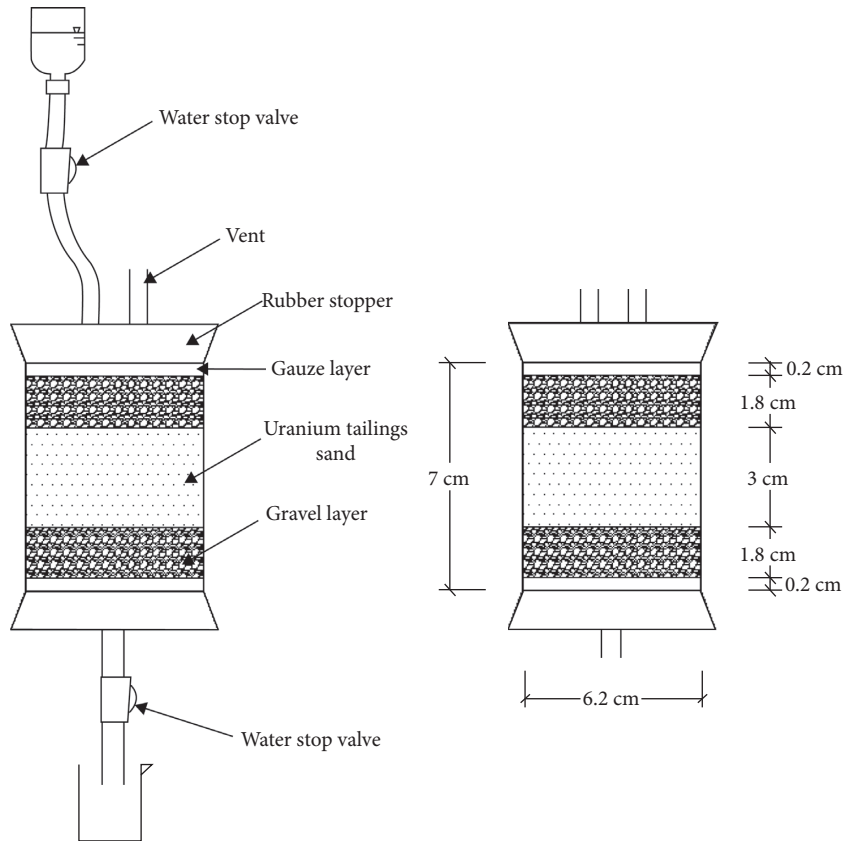


FIGURE 1: Schematic diagram of the MICP experimental device.



FIGURE 2: Physical model of the MICP experimental device.



FIGURE 3: *Sporosarcina Pasteurii* strains on solid medium.

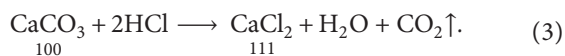


FIGURE 4: *Sporosarcina Pasteurii* strains were cultured in liquid medium for 2 days (left side is inoculated conical flask and the right side is blank reference).



FIGURE 5: The residues in the conical flask and on the filter paper after drying.

$$m_{\text{CaCO}_3} = 100 \times \frac{W_2 - W_1}{(111 - 100)}, \quad (2)$$



3.3. Domestication of *Sporosarcina Pasteurii* in the Radioactive Effluent of Uranium Tailings. 2 ml bacterial suspension was inoculated into the conical flask which contains 10 mL CASO liquid medium and 100 ml sterilized radioactive effluent of uranium tailings. The flask was placed in the constant-temperature shaking incubator for 24 h which was set at 30°C, and the rotation speed was controlled at 200 r/min. The domesticated culture medium was taken by an inoculating loop and inoculated on a solid medium plate. Place the inoculated plate in a constant-temperature incubator which was set at 30°C for 2 days. After the strains grew up, they were added to the mixed medium again. The strains were domesticated once every 5 days for 8 successive generations.

3.4. Fine-Grained Uranium Tailings Bacterial Liquid Fixing Test. Firstly, the deionized water was slowly injected into the

sand column to discharge the gas and to saturate the sand samples. The flow rate of the deionized water was controlled to 2 mL/min by adjusting the stop valve at the injection port. The OD₆₀₀ value of the outflow liquid was detected and reached zero after 12 h. The water content of the saturated sand column is 38.9 mL by calculating the pore volume. According to related references, the inoculated amount of bacterial liquid is 1.2 times of water content of the saturated sand (50 mL). Bacterial liquid and CaCl₂ solution were mixed at a ratio of 1 : 1, and the flow rate of mixed liquid was adjusted to 1 mL/min. After 12 h, the outlet water stop valve was opened, and 5 mL of effluent was collected to determine the OD₆₀₀ value.

3.5. Fine-Grained Uranium Tailings Reinforcement Test. 25 mL bacterial liquid (OD₆₀₀ = 1.1) and CaCl₂ solution were injected into the sand column with equal volume each day, and the injection flow rate was controlled at 1 mL/min. Eight sand column models inoculated with bacterial liquid were prepared for experiment, and another eight sand column models as a blank reference. Two molds were detached on the 4th, 8th, 12th, and 16th days, respectively; the uranium tailings reinforced by MICP is shown in Figure 6.

After the sand column was vertically and smoothly placed into the geotechnical ring cutter, 0.5 cm × 0.5 cm × 0.5 cm sand samples were takeout with a soil spatula, and it was placed in a thermostatic oven dried for 24 hours at 105°C. The microstructure of the reinforced sand samples was observed by scanning electron microscopy (SEM) to observe the precipitation structure of CaCO₃ and to analyze reinforcement mechanism of MICP.

The geotechnical tests were conducted to determine the reinforcement effects of fine-grained uranium tailings by MICP, and the reinforced sand samples were loaded into the shear box to test the shear strength. The vertical normal stress is 50 kPa and 100 kPa. The control shear rate is 0.8 mm/min. The direct shear test is shown in Figure 7.

The sand samples after the test were ground with a grinder and dried in a thermostatic oven for 24 hours. 50 g of sand samples after grinding and 100 mL hydrochloric acid (2 mol/L) was added slowly into a beaker and stirred with a glass rod until no gas generated. Then, place it in a thermostatic oven for 24 hours, and the process was repeated once more. After drying, the sand samples were weighed in m' .

The mass difference between m' and 50 before and after the reaction were the mass difference between CaCO₃ and CaCl₂. According to the chemical equation, the mass of CaCO₃ can be calculated by the following:

$$m_{\text{CaCO}_3} = 100 \times \frac{m' - 50}{(111 - 100)}. \quad (4)$$

The calculated mass of CaCO₃ subtracted with the original mass of CaCO₃ was the mass of CaCO₃ generated in each sand column. The volume of sand samples was



FIGURE 6: Uranium tailings reinforced by MICP.

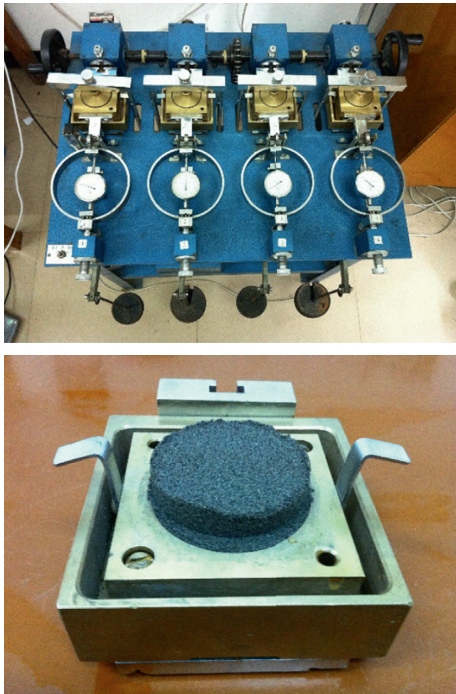


FIGURE 7: Direct shear test and shear failure of specimen.

calculated according to the density of each sand column, so the mass of CaCO_3 produced per unit volume can be calculated.

4. Test results

4.1. Physiological and Biochemical Characteristics of Strains in the Environment of Cement

4.1.1. The Changes in Bacterial Number and pH Value as Function of Time. The changes in bacterial number and pH value in mixed media as function of time was obtained by culturing *Sporosarcina Pasteurii* for 36 h in a shake flask, as shown in Figure 8. The growth curve of bacterial number basically conforms to the Gompertz–Richards model and

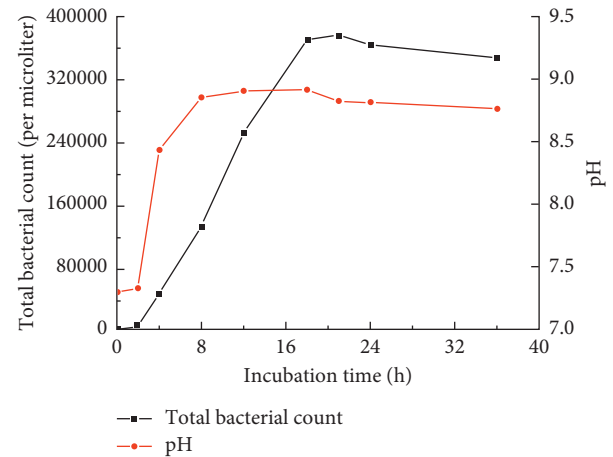


FIGURE 8: Changes in bacterial density and pH value in mixed media as function of time.

could be divided into three stages. The lag stage phase (0–2 h) is not very obvious for the *Sporosarcina Pasteurii* chosen for the experiment is excellent and has adapted to the test by cycle culturing. In this stage, the pH value of the solution did not change substantially. Almost no increase in the number of *Sporosarcina Pasteurii* was observed, but its anabolism was active to provide sufficient enzymes, energy, and intermediate metabolites for subsequent growth and reproduction of bacteria.

In the logarithmic phase (2–18 h), the number of bacteria has a steady geometric growth. The biological morphology was typical, and the biological activity was strong. A large number of urease was produced to decompose the urea into carbonate and ammonium ions, so the pH value of solution rises from 7.3 to about 9.0. Therefore, it is suitable for choosing the strains in this phase for the following inoculation experiment.

In the stationary phase (18–24 h), the number of bacteria reached a peak and tended to be stable, but high activity of the strains was maintained. Some adverse effects have been appeared such as the overconsumption of nutrients in the medium, the accumulation of toxic metabolites (such as alcohol and H_2O_2), the increase of pH causing changes in bacterial morphology and biological activity, decreased bacterial growth rate, and increased relative death of bacteria, but bacterial number attains equilibrium between proliferation and death, and the spores began to form in this phase.

In the decline phase (after 24 h), the bacterial number tended to increase slowly and the number of dead bacteria increased significantly. The number of live bacteria was inversely related with the culture time, and the pH value of the solution was slightly declined, and the physiological metabolic activity tends to stagnant.

4.1.2. The Changes in Ammonia Nitrogen Concentration and CaCO_3 Production as Function of Time. The changes in ammonia nitrogen concentration and CaCO_3 production as function of time was obtained by shaking flask experiments

in cement solution, as shown in Figure 9. After inoculating the *Sporosarcina Pasteurii* into the mixed culture medium for 4 hours, the concentration of ammonia nitrogen rose rapidly, which indicated that *Sporosarcina Pasteurii* had a high urease activity in the initial state, but the production rate of CaCO_3 increase slowly because of the bacteria are still in the lag phase or logarithmic phase which have insufficient bacteria and urease. In the following 14 hours, the bacteria maintained a high level of physiological activity which resulted in a continuous increase of CaCO_3 production. And, the ammonia nitrogen production began to decline because ammonia nitrogen volatilize to the outside during the shaking culture.

At 18 h after inoculation, production rate of the calcium carbonate slows down. On the one hand, the ratio of calcium ions converted into crystals in the solution reached 80%, and calcium ion concentration has become the limiting factor to affect the process of microbial mineralization. On the other hand, the activity of the bacteria decreased because of limited nutrients and deteriorated external conditions in the culture medium. Especially, the amount of calcium carbonate remains stable as the bacteria entered the decline stage after 24 h. The results showed the following: CaCO_3 production of *Sporosarcina Pasteurii* in the cement solution was positively correlated with its physiological activity and calcium concentration.

4.2. Test Results of Bacterial Liquid Fixation in Uranium Tailings Sand. Different concentrations of CaCl_2 solution and bacterial liquid were injected into the sand column 12 h later, the effluent was collected, its concentrations of CaCl_2 and the OD_{600} value were determined, and the results are shown in Figure 10. We can see that the higher the concentration of CaCl_2 solution is, the lower the OD_{600} value of the effluent is, and the value was followed by a logarithmic decrease. However, considering the low concentration of CaCl_2 solution is conducive to the transmission of bacteria liquid, 0.025 mol/L CaCl_2 solution was chosen as the fixative solution in the experiment, and the fixation rate of bacterial liquid was 92.14% by experiment (the fixation rate was higher than 90%).

4.3. Test of Uranium Tailings Reinforced by MICP

4.3.1. Changes of Shear Strength of Reinforced Uranium Tailings. The direct shear was used to test the variation of shear properties of reinforced uranium tailings over time. The results are shown in Figure 11; we can see the internal friction angle, cohesive force, and shear strength of uranium tailings reinforced by MICP were significantly increased. And, the shear strength growth rate of grouting reinforcement from 8 to 12 days is the highest due to the calcium carbonate crystals binds sand particles together and reinforces the structure strength of the sand. After 16 days, the cohesion of reinforced uranium tailings increased from 9.59 kPa to 23.03 kPa, the growth rate was 140.1%, the internal friction angle of reinforced uranium tailings increased from 29.1° to 42.7°, and the growth rate

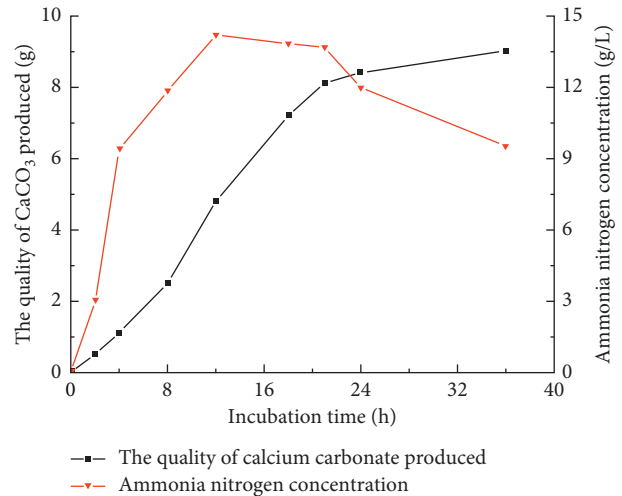


FIGURE 9: The changes in ammonia nitrogen concentration and CaCO_3 production as function of time.

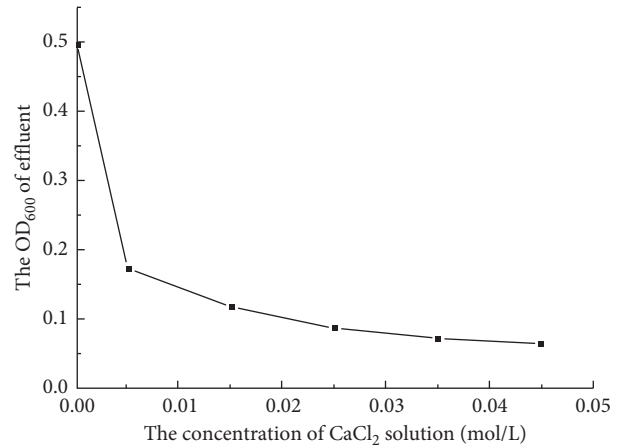


FIGURE 10: Curve of the OD_{600} value of effluent with the concentration of CaCl_2 solution.

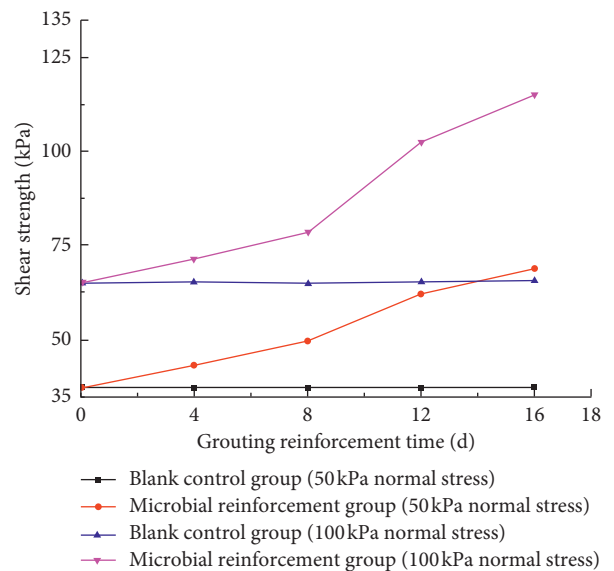


FIGURE 11: The changes in shear strength of uranium tailings reinforced by MICP as function of time.

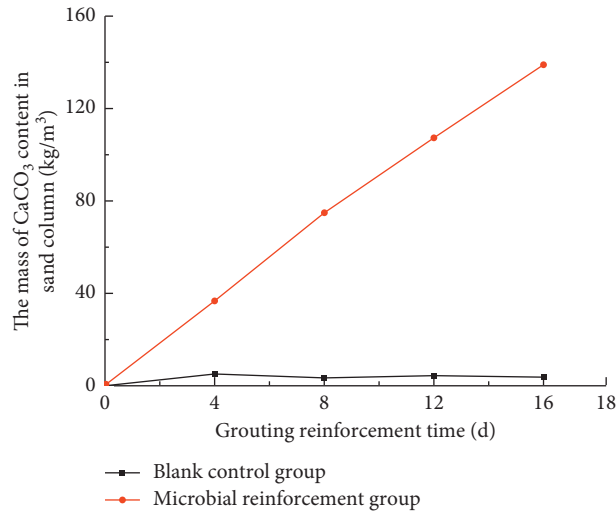


FIGURE 12: The changes in CaCO_3 production of uranium tailings reinforced by MICP as function of time.

was 46.7%. Under the normal stress of 50 kPa, the shear strength increased from 37.42 kPa to 69.02 kPa, and the growth rate was 84.6%. Under the normal stress of 100 kPa, the shear strength increased from 65.25 kPa to 115.14 kPa, and the growth rate was 76.5%. However, the shear strength of the blank reference group did not change substantially. The results showed that MICP technology can increase shear strength of uranium tailings effectively.

4.3.2. The Change in CaCO_3 Production in Uranium Tailings as Function of Time. The change of CaCO_3 production was determined by the acid dissolution method, the changes in CaCO_3 production as a function of time are shown in Figure 12, and utilization rate of calcium ion of MICP was calculated after experiment; the results are shown in Table 2, about 65%. We can see that the inoculated group has more CaCO_3 production and higher calcium ion utilization rate than blank reference group. However, the utilization rate should be improved compared with the 90% utilization rate of shaking flask experiment in the cement liquid in 4.1.

To further research the differences in CaCO_3 production of MICP between the uranium tailings environment and the cement liquid environment, detaching the molds and observing the cementation of different layers of sand column after grouting (Figure 13), a lot of CaCO_3 crystal deposits were found in the buffer gravel layer in the grouting hole and in the gauze layer. Therefore, the reason for the low utilization rate of calcium ion in uranium tailings is that CaCO_3 particles were deposited in the gravel layer and gauze layer, or the bacteria were washed away during the grouting process, resulting in insufficient nucleus to form the CaCO_3 .

4.3.3. SEM Results and Analysis of Reinforcement Mechanism. To research the reinforcement mechanism of uranium tailings reinforced by MICP, SEM images were observed for sand samples after the experiment. The

scanning electron micrographs are presented in Figure 14; it can be observed that, between the uranium tailings, particles were filled with a large number of white calcite crystals which are irregular particles, and there are overlapping phenomena. These crystals bind uranium tailings together and form bio-sandstones, which reduces the porosity of sand samples, and greatly improve their shear strength.

5. Conclusion

In this paper, *Sporosarcina Pasteurii* was chosen for the experiment to study the effect and mechanism of fine-grained uranium tailings reinforced by MICP. The experiments were performed in shaking cement solution and in sand column, and biochemical properties and mineralization efficiency were analyzed. The effect and mechanism of uranium tailings reinforced by MICP were discussed by direct shear test and SEM. The results obtained are as follows:

- (1) The growth curve of bacterial number basically conforms with the Gompertz–Richards model. The lag stage phase of curve is not very obvious which indicated that the *Sporosarcina Pasteurii* chosen for the experiment is excellent. Through shaking flask experiments in cement solution, it indicated that the CaCO_3 production of *Sporosarcina Pasteurii* in the cement solution was positively correlated with its physiological activity and the concentration of calcium sources, and it showed an increase at the first and then tended to be stable.
- (2) The following can be found from the microbial immobilization experiments: the higher the solution concentration of CaCl_2 , the lower the discharge rate of bacterial liquid from the sand column, but high concentration of CaCl_2 solution will affect the uniform distribution and migration of bacteria in the uranium tailings.

TABLE 2: Table of calcium ion utilization.

Curing time	4 d	8 d	12 d	16 d
Calcium ion utilization rate of MICP	65.56%	67.34%	64.31%	62.46%
Calcium ion utilization rate of blank reference	9.55%	2.93%	2.78%	1.78%

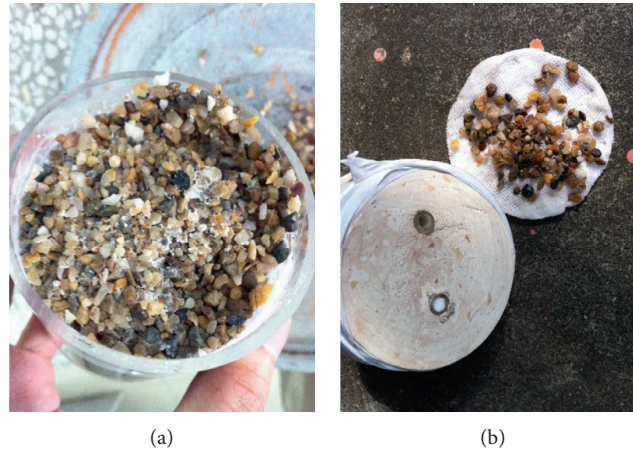
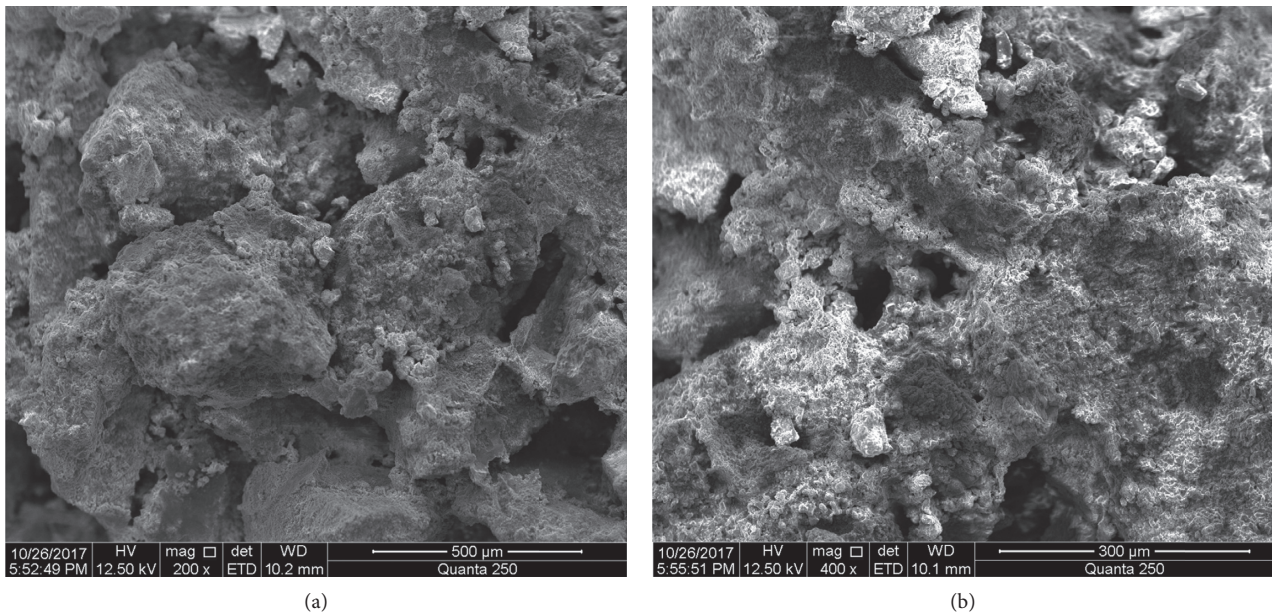
FIGURE 13: Deposition of CaCO_3 in gravel layers and gauze layers: (a) buffer gravel layer; (b) grouting mouth and gauze layer.

FIGURE 14: SEM images of uranium tailings reinforced by MICP at the end of experiment (200x: a; 400x: b).

(3) *Sporosarcina Pasteurii* was chosen for MICP experiment for 16 d, and the shear strength of uranium tailings increased by 84.6% and 76.5%, respectively, under 50 kPa and 100 kPa normal press. The results show that the MICP technology can increase the shear strength of fine-grained uranium tailings effectively. Through the scanning electron micrographs, the mechanism of uranium tailings reinforced by MICP was that calcite crystals produced by *Sporosarcina*

Pasteurii bind the uranium tailings particles together and form biological sandstones.

(4) The physical model and grouting mode should be further optimized to improve the production rate of CaCO_3 . And, the external factors (e.g., temperature and pressure) that influence the reinforced effect of uranium tailings by MICP should be considered, and the reinforcement depth should be further studied in the following experiments.

Data Availability

The data that support the findings of this study are available from the corresponding author upon reasonable request.

Conflicts of Interest

The authors declare no conflicts of interest.

Acknowledgments

This study was supported by the National Natural Science Foundation of China (51774187), Science and Technology Department Key R&D Plan Project of Hunan Province (2017SK2280), Nuclear and Radiation Safety Supervision Project of Ministry of Environmental Protection (1728-21), and Uranium Tailings Depot Resiliency Engineering Technology Research Center of Hunan Province.

References

- [1] G. D. Mei, *Research on Mechanism and Online Early-Warning Method for Tailings Dam Failure*, University of Science and Technology Beijing, Beijing, China, 2015.
- [2] H. D. Xu, "Statistical analyses of tailing reservoir disease accidents in China," *Industrial Construction*, vol. 31, no. 1, pp. 69–71, 2001.
- [3] H. L. Liu and M. H. Zhao, "Review of ground improvement technical and its application in China," *China Civil Engineering Journal*, vol. 49, no. 1, pp. 96–115, 2016.
- [4] C. X. Qian, A. H. Wang, and X. Wang, "Advances of soil improvement with bio-grouting," *Rock and Soil Mechanics*, vol. 36, no. 6, pp. 1537–1548, 2015.
- [5] C. Q. Wang, K. F. Tan, P. X. Wang, and X. X. Xu, "Research status on grouting materials in China," *Adhesion*, vol. 11, pp. 87–91, 2013.
- [6] V. S. Whiffin, *Microbial CaCO₃ Precipitation for the Production of Biocement*, Murdoch University, Perth, Australia, 2004.
- [7] L. A. V. Paassen, R. Ghose, T. J. M. van der Linden, W. R. L. van der Star, and M. C. M. van Loosdrecht, "Quantifying biomediated ground improvement by ureolysis: large-scale biogrout experiment," *Journal of Geotechnical and Geoenvironmental Engineering*, vol. 136, no. 12, pp. 1721–1728, 2010.
- [8] L. A. V. Paassen, "Bio-mediated ground improvement: from laboratory experiment to pilot applications," in *Proceedings of Geo-Frontiers Congress*, pp. 4099–4108, Dallas, Texas, March 2011.
- [9] M. B. Burbank, T. J. Weaver, T. L. Green, B. C. Williams, and R. L. Crawford, "Precipitation of calcite by indigenous microorganisms to strengthen liquefiable soils," *Geomicrobiology Journal*, vol. 28, no. 4, pp. 301–312, 2011.
- [10] N. W. Soon, L. M. Lee, T. C. Khun, and H. S. Ling, "Factors affecting improvement in engineering properties of residual soil through microbial-induced calcite precipitation," *Journal of Geotechnical and Geoenvironmental Engineering*, vol. 140, no. 5, article 04014006, 2014.
- [11] H. Canakci, W. Sidik, and I. H. Kilic, "Bacterail calcium carbonate precipitation in peat," *Arabian Journal for Science and Engineering*, vol. 40, no. 8, pp. 2251–2260, 2015.
- [12] A. Mahawish, A. Bouazza, and W. P. Gates, "Biogrouting coarse materials using soil-lift treatment strategy," *Canadian Geotechnical Journal*, vol. 53, no. 12, pp. 2080–2085, 2016.
- [13] D. S. S. Pusadkar, R. N. Tawalare, and D. A. I. Dhattrak, "Performance of footing on MICP induced slope," *IOSR Journal of Mechanical and Civil Engineering*, vol. 14, no. 3, pp. 100–105, 2017.
- [14] A. M. Grabiec, J. Starzyk, K. Stefaniak, J. Wierzbicki, and D. Zawal, "On possibility of improvement of compacted silty soils using biodeposition method," *Construction and Building Materials*, vol. 138, pp. 134–140, 2017.
- [15] J. T. DeJong, M. B. Fritzges, and K. Nusslein, "Microbially induced cementation to control sand response to undrained shear," *Journal of Geotechnical and Geoenvironmental Engineering*, vol. 132, no. 11, pp. 1381–1392, 2006.
- [16] X. H. Cheng, Q. Ma, Z. Yang, Z. C. Zhang, and M. Li, "Dynamic response of liquefiable sand foundation improved by bio-grouting," *Chinese Journal of Geotechnical Engineering*, vol. 35, no. 8, pp. 1486–1495, 2013.
- [17] N. K. Dhami, M. S. Reddy, and A. Mukherjee, "Bio-mineralization of calcium carbonates and their engineered applications: a review," *Frontiers in Microbiology*, vol. 4, no. 314, 2013.
- [18] M. P. Harkes, L. A. van Paassen, J. L. Booster, V. S. Whiffin, and M. C. M. van Loosdrecht, "Fixation and distribution of bacterial activity in sand to induce carbonate precipitation for ground reinforcement," *Ecological Engineering*, vol. 36, no. 2, pp. 112–117, 2010.
- [19] W. S. Ng, M. L. Lee, and S. L. Hii, "An overview of the factors affecting microbial-induced calcite precipitation and its potential application in soil improvement," *World Academy of Science*, vol. 6, no. 2, pp. 723–729, 2012.
- [20] H. Rong, *Preparation and Binding Mechanism of Microbe Cement*, Southeast University, Nanjing, China, 2014.
- [21] S. K. Ramachandran, "Remediation of concrete using microorganisms," *ACI Material Journal*, vol. 98, no. 1, pp. 3–9, 2001.

Research Article

Crystalline Swelling Process of Mg-Exchanged Montmorillonite: Effect of External Environmental Solicitation

Marwa Ammar and Walid Oueslati 

UR13ES46 Physique des Matériaux Lamellaires et Nano-Matériaux Hybrides (PMLNMH), Faculté des Sciences de Bizerte, 7021 Zarzouna, Tunisia

Correspondence should be addressed to Walid Oueslati; walidoueslati@gmail.com

Received 8 May 2018; Revised 9 August 2018; Accepted 9 September 2018; Published 16 October 2018

Academic Editor: Dingwen Zhang

Copyright © 2018 Marwa Ammar and Walid Oueslati. This is an open access article distributed under the Creative Commons Attribution License, which permits unrestricted use, distribution, and reproduction in any medium, provided the original work is properly cited.

This work reports characterization of the possible effects that might distress the hydration properties of Mg-exchanged low-charge montmorillonite (SWy-2) when it undergoes external environmental solicitation. This perturbation was created by an alteration of relative humidity rates (i.e., RH%) over two hydration-dehydration cycles with different sequence orientations. Structural characterization is mainly based on the X-ray diffraction (XRD) profile-modeling approach achieved by comparing the “in situ” obtained experimental 00l reflections with other ones calculated from theoretical models. This method allows assessing the evolution of the interlayer water retention mechanism and the progress of diverse hydration state’s contributions versus external strain. Obtained results prove that the hydration behavior of the studied materials is strongly dependent on the RH sequence orientation which varied over cycles. The interlayer organization of Mg-exchanged montmorillonite (i.e., SWy-2-Mg) is characterized by a heterogeneous hydration behavior, which is systematically observed at different stages of both cycles. By comparing the interlayer water process evolution of Mg-exchanged montmorillonite with the observed SWy-2-Ni sample hydration behaviors, a same hysteresis thickness characterized by obvious fluctuations of interlayer water molecule abundances is observed. Nevertheless, in the case of Hg and Ba-saturated montmorillonite, the retention water process versus the applied cycles was steadier comparing with Mg ions.

1. Introduction

Smectites are swelling clay minerals that belong to the family of the phyllosilicates 2:1, which naturally occur in both terrestrial and marine environments [1] where they often represent the most effective components. In fact, by dint of its significant intrinsic physical and chemical properties, mainly the high specific surface areas (up to $760 \text{ m}^2 \cdot \text{g}^{-1}$), the cation-exchange capacities as well as the high sorption efficiency of cations, and its strong mechanical stability [2], these materials were used in many extensive exploitation. Indeed, it plays an important role in many geological processes, the phenomena of the petroleum migration, greenhouse gas sequestration, oilfield [3], and in engineering. Moreover, for last decades, the smectites were widely used as crucial components for elaboration of natural barriers to isolate the hazardous wastes and for the removal

of heavy metal cations from various effluents of industrial and wastewater treatment [4–12] and also proposed as geotechnical barriers in many nuclear waste disposal concepts in order to retard the potential transport of radionuclides towards the biosphere [13–15].

Notwithstanding the diverse beneficial effects of smectites, the hydration behavior of these mineral is very sensitive to the change of the environmental surrounding conditions (i.e., temperature, pressure, and RH), which may influence the stability of the clay microstructure therefore the stability of the geotechnical barrier. Hence, the well understanding of swelling smectites properties (the hydration and the dehydration mechanism) is of paramount importance for many natural processes and for such applications.

The water-metal-smectites system was the subject of diverse studies, and it was extensively studied at different scales using several characterization methods [16–26]. At

nanometer scale, the swelling process corresponds to the presence of hydrated chemical species on the interlayer space. This process depends on several factors including composition such as the layer charge amount, the charge location and distribution [27–30], the interlayer cation type, the interlayer cation valence, and the hydration energy [31] and also on the environment conditions such as the relative humidity, temperature, and H₂O pressure [32–37]. The pioneering studies focusing the crystalline swelling was performed using X-ray diffraction technique. By following the evolution of d_{001} basal-spacing value, different hydration states were defined with the insertion of 0, 1, 2, or 3 planes of H₂O molecules in the interlamellar spaces leading to growth of the spacing values as function of RH% [28,38–40].

Furthermore, the development of the XRD profile-modeling procedures and the methodology proposed by [41] allows the characterization of the structural modifications that occur during smectite swelling process. In addition, by using the XRD modeling approach, the quantification of hydration heterogeneity becomes easier especially when different layer hydration state types coexist in the same smectite structure. Several studies used this modeling approach tools to study the hydration properties of different smectite sample types and demonstrate systematic hydration heterogeneity whatever the interlayer cation, the RH%, the amount, the layer charge location, and the surrounding temperature [40,42–46].

According to this method, the present work focuses the damage that may affect the structural properties of the host materials and the hydrous behavior of an Mg-saturated smectite (i.e., montmorillonite: SWy-2) when it was submitted to a continuous variation of an environmental surroundings condition (i.e, variable RH%). This environmental solicitation is performed by varying “in situ” the RH% in reverse sequence orientation upon two hydration/dehydration cycles. Upon the applied cycles and under controlled atmosphere, a complex progress of the interlamellar space configuration of SWy-2-Mg sample is followed and quantified. After that the obtained results are compared with the earlier studies related to the same studied specimen which is saturated with other bivalent cations (Hg, Ba, and Ni) and submitted to the same climatic changes over the hydration-dehydration cycles for the purpose of discriminating the effect of the ionic potential on the crystalline swelling.

2. Materials and Methods

2.1. Host Materials. A dioctahedral smectite SWy-2 originated from bentonites of Wyoming (USA) is selected for the present study. Clay fraction is supplied by the Source Clay Minerals Repository Collection of the Clay Minerals Society and characterized by the following half-cell structural formula [47]:

The cation-exchange capacity (CEC) of this smectite is 101 meq/100 g where the charge deficit is majority resulting from cationic substitutions in the octahedral sheet and extremely limited tetrahedral ones.

2.2. Sample Treatments. To saturate all exchangeable sites by homoionic cations (Na⁺) and to guarantee better colloidal

dispersion, a pretreatment of the host material is carried out in order to prepare a Na-rich montmorillonite suspension. This aims is based on a classical protocol of an exchange process [48] which consists of dispersing ~20 g of solid in ~200 ml of NaCl solution (1 M) and stirring mechanically for 24 h. A SIGMA laboratory centrifuge is used for the separation of the solid fraction at 4000 rpm speed. These steps were repeated five times to ensure saturation of all exchangeable sites by Na⁺ cations. Excess chloride was removed by washing with distilled water five times, and the separation of the solid-liquid was performed by centrifugation at 8000 rpm speed. The same ionic exchange procedure was followed to prepare Mg-rich montmorillonite suspension using MgCl₂ solution (1M), and the final obtained clay suspension was labeled SWy-2-Mg.

Two oriented slides were prepared for the obtained samples (SWy-2-Mg) to be analyzed by XRD technique. For that the specimen suspension was deposited on a glass slide and then dried at room temperature for 24 hours to obtain an air-dried preparation [49].

2.3. “In Situ” XRD Analysis. The “in situ” XRD patterns produced by SWy-2-Mg sample are obtained upon two overturn hydration-dehydration cycles. These cycles were created by varying gradually the RH% in reverse orientation with a 10% step. For that an Anton Paar TTK 450 chamber coupled with a D8 Advance Brüker installation (Cu-K α radiation) equipped with solid-state detector and operating at 40 KV and 30 mA was used. The reflection setting diffractometer installation is equipped with an Ansyco rh-plus 2250 humidity control device used to vary manually the RH%. The hydration-dehydration cycle orientations were detailed in Figure 1 and can be resumed as follows.

Both applied cycles were performed in three successive processes starting from 40% RH, which coincides with the relative humidity value of the room condition (297 K and ~40% RH).

The first cycle is divided into three domains summarized as follows.

The first one (I) consists of a hydration process realized by increasing the RH% from 40 to almost saturated condition (80%) followed by a dehydration procedure (II) assured by the decrease of the RH% towards extremely dry condition (10%). Finally, a rehydration process (III) was performed to a second return to 40% RH (Figure 1).

The sequential RH orientation was accomplished in an inverse way for the second cycle. Indeed, starting from 40% RH, a dehydration process was performed decreasing the RH% to 10%, followed by a hydration procedure reaching 80% RH and to finish with a second dehydration process by lessening the RH% to 40% (Figure 1).

Over these applied cycles, experimental XRD patterns were registered, in situ, every 10% at the fixed relative humidity condition values where the usual scanning parameters were 0.04°2 θ as step size and 6 s as counting time per step over the angular range 2–40°2 θ . In total, sixteen experimental patterns were recorded per cycle, and for all obtained 001 reflection, quantitative and qualitative XRD analyses are performed.

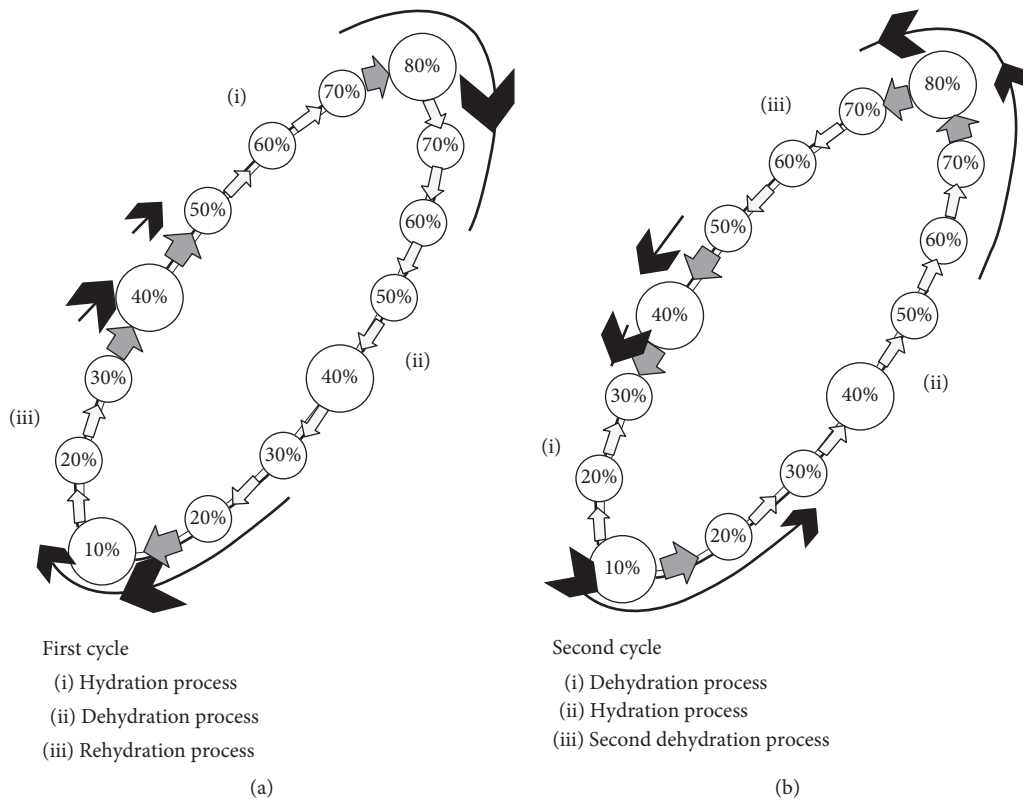


FIGURE 1: Sequence variation of the RH% during different hydration-dehydration cycles.

2.3.1. Qualitative XRD Pattern Investigations. A primeval interpretation about the hydration states of the studied samples can be obtained from a qualitative XRD analysis of the experimental profile. This information was deduced through the d_{001} basal-spacing values and a description of the 001 reflection profile geometry (pics symmetry and/or asymmetry). In addition, the correlation between the calculated parameters including the full width at half maximum intensity (FWHM) for the 001 reflections and ξ parameters [42, 50] can supply information about the hydration character of the studied samples (homogenous or interstratified). Nevertheless, the qualitative examination cannot provide information about structural transformation related to the position and organization of H_2O molecule and the exchangeable cations along the c^* axis. In addition, it is impossible to distinguish the nature and the relative contributions of different hydration phases at different RH values varied over the cycles. Thus, a quantitative evaluation of diverse changes which occurs within the smectite structure was required to accomplish the aims of the studies.

2.3.2. XRD Profile-Modeling Approach. The quantitative analysis is based on the XRD profile-modeling approach in order to propose theoretical structural models estimating, respectively, the gradual evolution of the interlamellar space content versus the hydration sequences, the nature of the different layer types coexisting within crystallites, and their proportion and their structural composition at different stages of both the applied cycles.

This method consists of adjusting the experimental XRD patterns (001 reflection) to theoretical ones where the

calculated intensity is based on the algorithms developed by [41]. The theoretical matrix formalism was detailed by [41]. The used Z atomic coordinates of the interlayer space correspond to those proposed by [41]. The abundances of the different types of layers (W_i), the mode of stacking of the different kinds of layers, and the mean number of layers per coherent scattering domain (CSD) [51] can be determined also through XRD profile-modeling approach. The layer-type stacking is described by a set of junction probabilities (P_{ij}) where the relationships between these probabilities and the abundances W_i of the different types of layers were given by [41]. A detailed description of the fitting strategy was detailed in the work of [37, 40]. Indeed, XRD pattern-modeling was performed assuming the possible presence of different layer types. These different layer types correspond to the different hydration states commonly reported in smectites as a function of relative humidity. In the fitting process, we have introduced dehydrated layers (0W layers, layer thickness at 9.6–10.0 Å), monohydrated layers with one plane of H_2O molecules in the interlayer (1W layers at 11.5–13.0 Å), bihydrated layers with two planes of H_2O molecules in the interlayer (2W layers at 13.9–15.8 Å), and trihydrated layers (3W layers at 18.0–18.5 Å).

3. Results

3.1. Quantifying Interlamellar Space Content during the First Cycle

3.1.1. Qualitative XRD Analysis. All experimental XRD patterns produced by the SWy-2-Mg sample during the first

cycle are presented in Figure 2 with the calculated profile, obtained using the corresponding contributions of the various mixed-layer structures (MLSs).

A qualitative investigation was performed providing preliminary information about the hydration property evolution. In fact, a homogenous hydration character is observed at the highest RH range extending between 70% (hydration process) \leq RH \leq 60% (dehydration process). This description is confirmed by the low value of the calculated FWHM, the ξ parameter (Table 1) of the 001 reflection positions over the RH fields. On the contrary, a heterogeneous hydration behavior was deduced at the lowest RH range justified by the irrationality, for all measurable reflection positions, characterized by high ξ parameter values (Table 1).

The gradual evolution of the d_{001} basal-spacing values as function of RH% (Figure 3(a)) shows a clear hysteresis between 40% \leq RH \leq 10%. For this RH range, the structure is dominated by an interstratified hydration behavior between 1W and 2W layer types. However, the variation of the d_{001} spacing between 80 and 40% RH tails the same roads which can be interpreted by a hydrous stability on the interlayer spaces.

3.1.2. Theoretical Models and the Hydration Properties. The structural parameters used to reproduce experimental patterns of SWy-2-Mg as a function of RH% were regrouped in Table 2. Results derived from the quantitative XRD investigation demonstrate that the studied structure (i.e., SWy-2-Mg) changes, all over the cycle, with an interstratified hydration behavior. Indeed, all proposed models are described by a main structure composed by diverse hydration state contributions (0W, 1W, 2W, and 3W) at different RH values (Figure 2).

These heterogeneous hydration behaviors can be explained by sequential transitions between different hydration states induced by the continuous variation of the RH%. The evolution of different relative layer-type proportions as a function of the RH% (Figure 4) shows a continuous diffusion of H₂O molecules in the interlamellar spaces during the hydration process leading to progressive and continuous 1W \rightarrow 2W and 2W \rightarrow 3W transitions.

In fact, at the beginning of the cycle (40% RH), the studied sample (SWy-2-Mg) was characterized by a main structure composed by 21% of 1W layer types with major contribution of the bihydrated ones (79%). By reaching 80% RH, a different configuration composed by 7%, 65%, and 28% attributed, respectively, to 1W, 2W, and 3W hydration states is manifested (Figure 4). On the contrary, along the dehydration process, the decrease of the RH values from 80% to 30% leads to a gradual emptying of the microscopic porosity corresponding to the reduction of the interlamellar water molecule abundances. Indeed, successive 3W \rightarrow 2W and 2W \rightarrow 1W transitions are observed over this RH range, where the structure is composed at 30% RH by 19%, 75%, and 6%, respectively, for 1W, 2W, and 3W layer types. An obvious transformation on the structural composition and a notable change on the hydration

behavior were distinguished towards the lowest RH domain starting from 20% RH (rehydration process) to the end of the cycle at 40% RH (rehydration process). In fact, fast emptying of the interlamellar spaces from water planes was noted by decreasing the % RH rates during the dehydration procedure where the 2W layer-type contribution decreases rapidly with a complete disappearance of the 3W layer from the structure (Figure 4). Over this RH range, fast increasing of the 1W layer-type contribution was noted, which dominates the structure until the end of the cycle (Figure 4).

3.2. Quantifying Interlamellar Space Content during the Second Cycle

3.2.1. Qualitative XRD Investigation. Experimental XRD patterns obtained under controlled RH condition along the second cycle are represented with the respective contributions of the various MLSs used to calculate profiles in Figure 5.

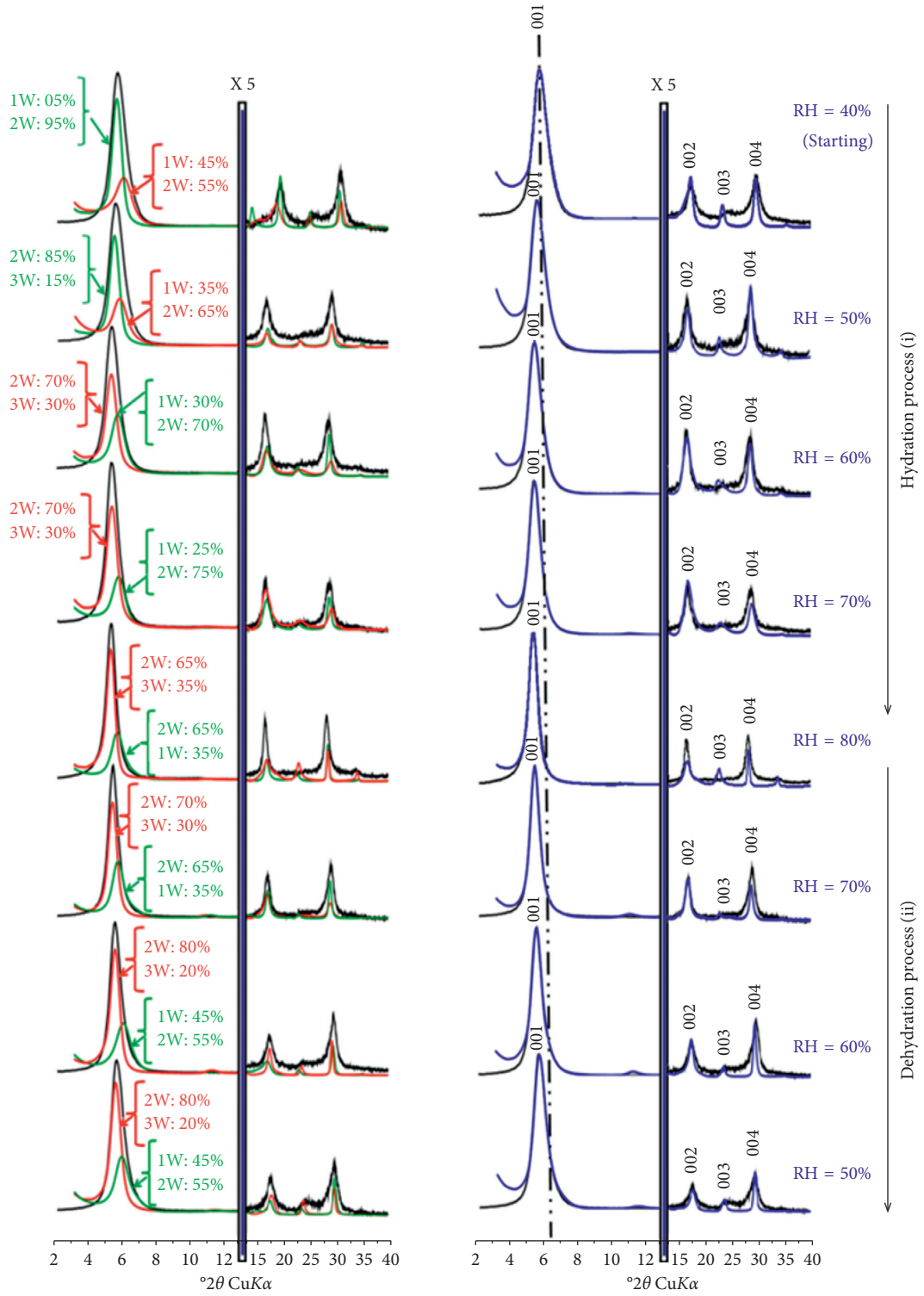
The correlation between FWHM and the ξ parameter (Table 3) proposes that over a large RH range extending between 30% (dehydration process) \leq RH \leq 70% RH (hydration procedure), the structure is characterized by an interstratified hydration character. However, the study suggests homogenous hydration behaviors with decreasing the RH values from 80% to 40% over the second dehydration procedure (Table 3).

Evolution of the layer thickness (d_{001}) as function of the RH%, along the second cycle, was characterized by the appearance of a clear hysteresis at the RH range extending between 40% and 10% (Figure 3). Indeed, a fast shift of the d_{001} spacing values from 15.39 Å at 40% RH to 12.90 Å at 10% RH was observed. However, a slow d_{001} value progress is noted by inverting the RH% orientation. Over these RH domains, the d_{001} is attributed to an interstratified 2W-1W hydration state.

3.2.2. Theoretical Models and the Hydration Properties. Optimum structural parameters used to fit experimental XRD patterns in the case of the second cycle are summarized in Table 4. The quantitative XRD investigation demonstrates that all calculated theoretical models which allow reproducing the 001 reflections are characterized by heterogeneous hydration states composed of two different MLSs with diverse relative proportions of layer types (Figures 5(a) and 5(b)).

Evolution of different layer type contributions as a function of RH is detailed in Figure 6. With decreasing the RH% during the first dehydration procedure, a slow transition from the 2W to 1W state was observed between 40% RH and 20% RH where the smectite crystallite presents major contributions of the 2W layer types.

A notable increase of the 1W layer proportion, towards the lowest RH condition (i.e., 10% RH), is detected. At this RH rate, the structure is reproduced by 70% of the monohydrated states (1W) and 30% of the bihydrated ones (Figure 6).



(a)
FIGURE 2: Continued.

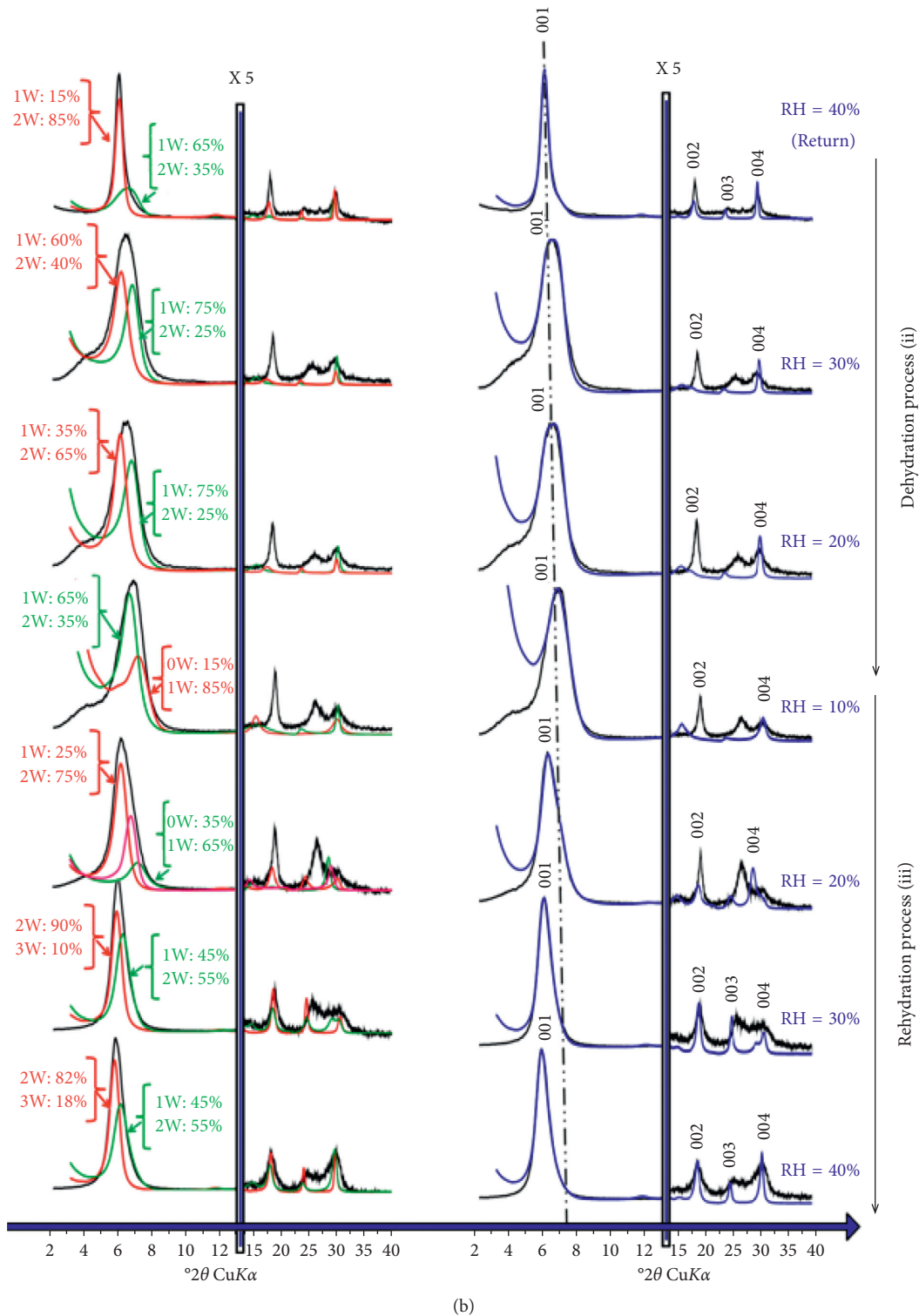


FIGURE 2: Best agreement between experimental (black line) and calculated (blue line) XRD patterns obtained using the respective contributions of the various MLSs (red and green line) in the case of the first cycle. (a) Hydration-dehydration. (b) Dehydration-hydration.

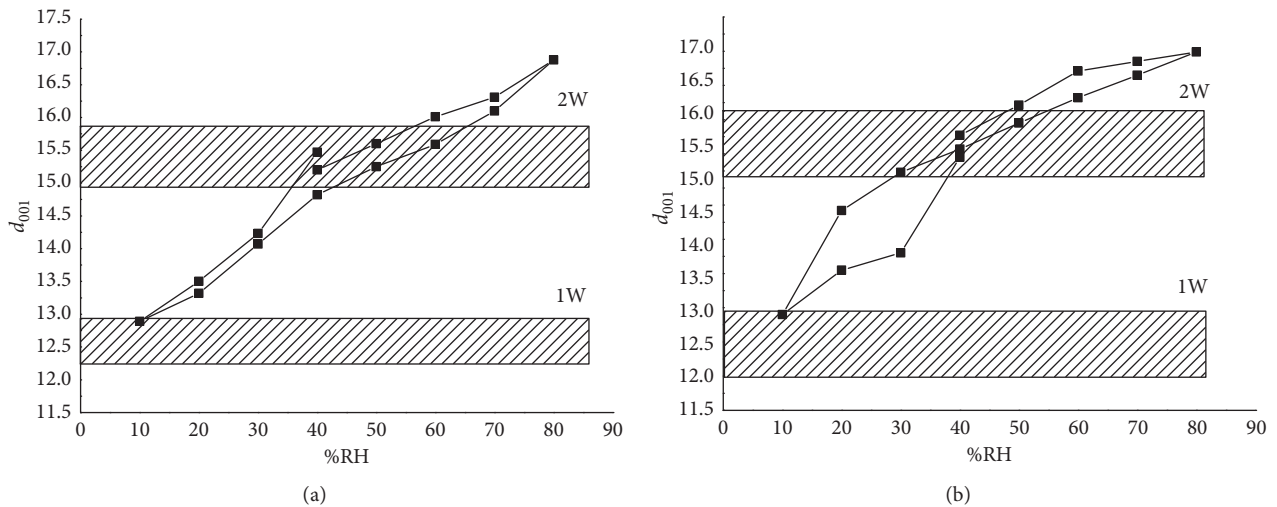
Progressive intercalation of water planes is noted during the hydration procedure. This accelerated intercalation is achieved by a continuous transition from the 1W to the 2W layer types between 20 and 40% RH. Reaching 50% RH, the insertion of the H_2O molecules

becomes more easier; indeed, the 3W state appears at this stage and persists in the structure for a wide RH field extending between 50 and 60% RH (dehydration procedure) (Figure 6). Over these RH domains, the structure grows gradually containing different contributions of the

TABLE 1: Qualitative XRD investigation versus % RH in the case of the first hydration-dehydration cycle.

	% RH	d_{001}	FWHM	ξ	Character
Hydration process	40	15.52	1.03	0.77	I
	50	15.96	1.09	0.67	I
	60	16.46	0.94	0.47	I
	70	16.60	0.82	0.34	H
	80	16.74	0.68	0.21	H
Dehydration process	70	16.40	0.70	0.13	H
	60	16.07	0.78	0.18	H
	50	15.70	0.89	0.15	H
	40	15.32	0.91	0.26	H
	30	14.98	0.95	0.41	I
	20	14.42	1.34	0.48	I
Rehydration process	10	12.90	1.50	0.72	I
	20	13.55	1.54	0.53	I
	30	13.80	1.50	0.83	I
	40	15.20	1.48	0.20	I

Note: position d_{001} and FWHM of the 001 reflection are given in angstroms and in $^{\circ}2\theta$ CuK α , respectively. The ξ parameter which accounts for the departure from rationality of the 001 reflection series is calculated as the standard deviation of the $l \times d_{001}$ values calculated for the Xi measurable reflections (Xi = 3 in this case) over the 2–40 $^{\circ}2\theta$ CuK α angular range. (I) and (H) indicate Interstratified hydration character and Homogeneous hydration character.

FIGURE 3: Evolution of the given d_{001} spacing values according to % RH values during the first and the second cycle.

three layer types including 1W, 2W, and 3W with a clear dominance of the bihydrated phases (2W). During the second dehydration procedure performed by decreasing the RH% from the highest RH value (i.e., 80% RH) to the starting point (i.e., 40% RH), a gradual emptying of the interlamellar spaces from water is noted. Theoretical models propose structures characterized by the major proportion of the 2W layer types which kept the highest proportion until the end of the cycle (Figure 6).

4. Discussion

4.1. RH, Interlamellar Water Amounts, and Ionic Radius. The continuous variation of the RH values along both cycles automatically brings a sequential transition between

different hydration states in the interlayer spaces of SWy-2-Mg complex, which logically leads to a continuous change on the interlayer water amount and distribution.

Figure 7 represents a comparison between the interlamellar water molecule content evolution along the first and the second cycle, which establishes the dependence of the hydration behavior progression on the sequence variation and orientation of the RH values clearly. In fact, a dissimilar progression of the water amount was perceived in three principal RH fields: Over the first RH section spreading between 50% RH and 80% RH, labeled (I), the interlayer water amounts retained in the structure were more important in the case of first hydration-dehydration cycle than in the second one. An analogous hydration behavior of the studied complex is observed in the short RH domain over the second domain

TABLE 2: Structural parameters used to reproduce experimental patterns of SWy-2-Mg complex as a function of RH along the first hydration-dehydration cycle.

	% RH	% of MLS	% of 0W/1W/2W/3W-R*	L.Th	nH_2O	ZH ₂ O	Z _{Mg}	M	
				0W	0W	0W	0W		
				1W	1W	1W	1W		
				2W	2W	2W	2W		
				3W	3W	3W	3W		
Hydration	40 (start)	65	0/45/55/0-R0	—	—	—	—	8	
		35	0/05/95/0-R0	12.30	2	09.60	09.60		
				15.65	4	10.00/14.50	12.40		
	50	70	0/35/65/0-R1	—	—	—	—	8	
		30	0/0/85/15-R0	12.30	2	09.70	09.70		
				15.75	4	10.00/14.50	12.40		
	60	60	0/0/70/30-R0	—	—	—	—	7	
		40	0/30/70/0-R1	12.40	2.5	09.80	09.80		
				15.75	5	10.00/14.70	12.40		
	70	80	0/0/70/30-R0	—	—	—	—	8	
		20	0/25/5/0-R1	12.65	2.5	09.80	09.80		
				15.80	5.6	10.00/14.85	12.60		
	80	80	0/0/65/35-R1	—	—	—	—	11	
		20	0/65/35/0-R1	12.65	3	10.40	09.60		
				15.80	6	10.00/14.50	12.70		
	Dehydration	70	70	0/0/70/30-R0	—	—	—	—	10
			30	0/35/65/0-R0	12.40	2.5	10.20	09.20	
					15.75	6	10.00/14.90	12.60	
60		60	0/0/80/20-R1	—	—	—	—	10	
		35	0/45/55/0-R1	12.15	2.5	10.30	10.30		
				15.50	5	09.50/14.70	12.50		
50		50	0/0/80/20-R0	—	—	—	—	10	
		50	0/45/55/0-R1	12.00	2.5	10.30	10.30		
				15.20	4	09.60/14.50	12.40		
40		58	0/0/82/18-R1	—	—	—	—	10	
		42	0/45/55/0-R1	12.30	2.5	10.00	10.00		
				14.95	4	09.70/14.90	12.60		
30		58	0/0/90/10-R0	—	—	—	—	10	
		42	0/45/55/0-R1	12.50	2	10.00	10.00		
				14.95	3.2	10.30/14.50	12.60		
20		40	35/65/0/0-R1	10.70	—	—	9.00	9	
		37.80	0/25/75/0-R1	12.50	2	09.70	09.70		
		22.20	0/80/20/0-R0	14.75	3.6	10.30/14.50	12.40		
10	60	15/85/0/0-R0	10.20	—	09.00	9.00	7		
	40	0/65/35/0-R0	12.00	1.5	09.70	09.70			
			14.75	3.6	10.30/14.00	12.40			

TABLE 2: Continued.

% RH	% of MLS	% of 0W/1W/2W/3W-R*	L.Th	nH_2O	Z_{H_2O}	Z_{Mg}	M	
			0W	0W	0W	0W		
Rehydration	20	78	1W	1W	1W	1W	9	
			2W	2W	2W	2W		
			3W	3W	3W	3W		
	30	35	0/75/25/0-R0	—	—	—	—	10
			0/35/65/0-R0	12.00	1.5	09.50	09.50	
			—	15.00	3.6	10.30/14.00	12.50	
			—	—	—	—	—	
			0/75/25/0-R0	—	—	—	—	
			0/60/40/0-R0	12.00	1.8	09.50	09.50	
	40 (return)	42	0/30/70/0-R1	—	—	—	—	7
			0/55/45/0-R1	12.40	1.8	10.20	10.50	
			—	15.80	4	11.00-14.60	12.20	

Note: 3W, 2W, 1W, and 0W are attributed to the layer hydration state. R*: Reichweit (R)^{1/2} factor. R0 and R1 describe the MLS with random interstratifications or with partial segregation, respectively. L.Th: layer thickness in Å. nH_2O : number of H₂O molecule per half unit cell. Z_{H_2O} : position along c* axis of H₂O molecule. Z_{Mg} : position of exchangeable cations per half unit cell calculated along c* axis. M: average layer number per stacking. n_{Mg} : number of H₂O molecule per half unit cell fixed to 0.15, indicating full saturation of the cationic exchange capacity CEC of the minerals.

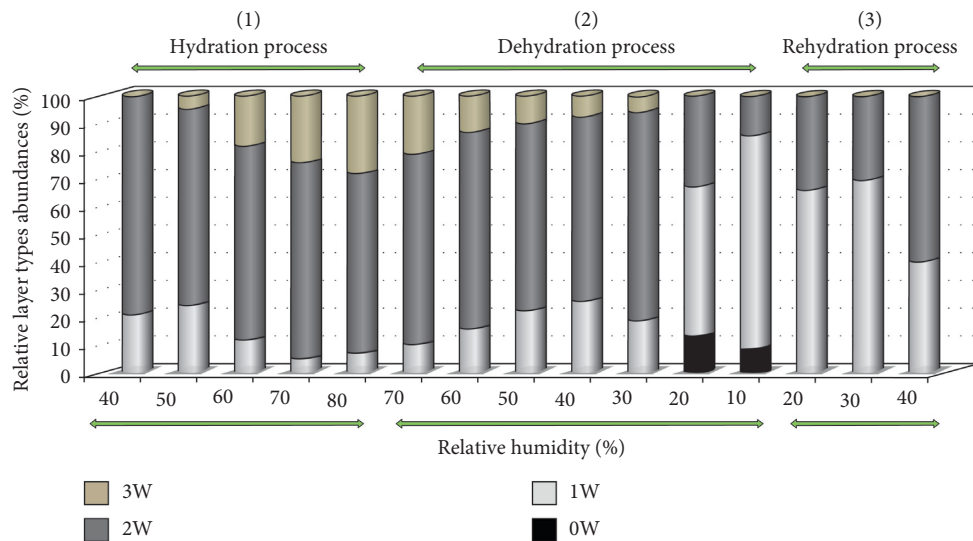


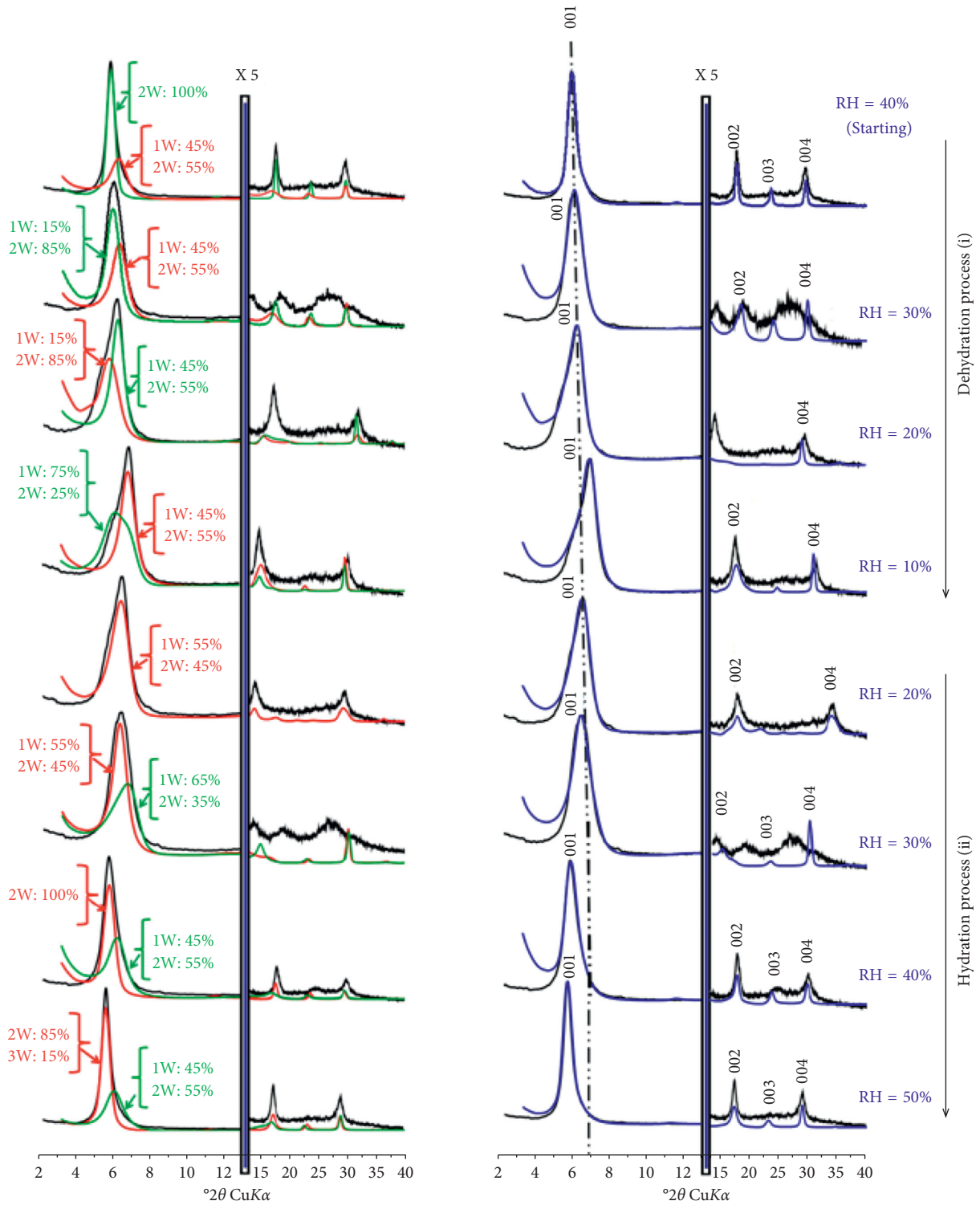
FIGURE 4: Relative contribution progress of the different layer types (summing up all mixed-layer structures) as function of the RH % along the first cycle.

(II) between 50 and 40% RH of both cycles. However, at the lower RH fields (III), quantitative results prove that the calculated interlamellar water amounts were more important in the case of the second cycle than the first one.

Such obtained result is in concordance with the previous work [52–54] where the same studied montmorillonite was saturated with other bivalent cations characterized by different ionic radius (Ni²⁺, Hg²⁺, and Ba²⁺) and have undergone the same “in situ” adsorption/desorption sequences. Results derived from modeling of X-ray diffraction (XRD) patterns related to the cited study have proven that the hydration

mechanism at crystal scale of diverse samples was found to evolve gradually in different ways as a function of the applied cycles, thus proving the dependence of the progress of the swelling property of the montmorillonite on the sequence orientation, which means problem related to how the RH rates varied over the cycle.

On the contrary, the comparison between the development of the interlayer H₂O molecule retained in the interlamellar spaces for the montmorillonite saturated by diverse bivalent cations (Ba²⁺, Ni²⁺, Hg²⁺, and Mg²⁺) upon the first cycle and the second one (Figure 8) shows an analogous hydration performance between the SWy-2-



(a)
FIGURE 5: Continued.

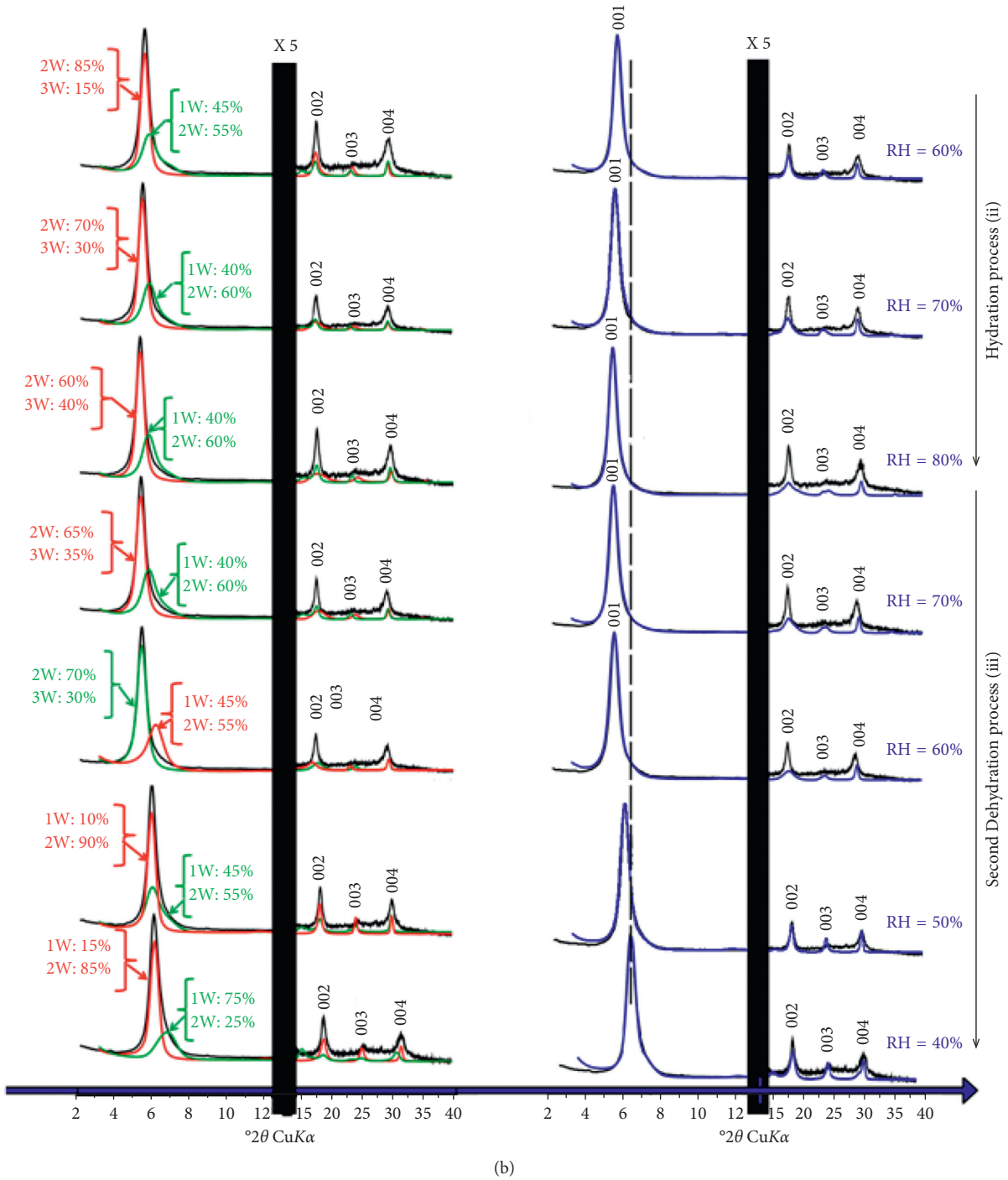


FIGURE 5: Best agreement between experimental (black line) and calculated (blue line) XRD patterns obtained using the respective contributions of the various MLSs (red and green line) in the case of the second cycle.

Ni and SWy-2-Mg. In fact, a clear hysteresis is observed in both cases indicating irreversible interlayer water progress during the hydration-dehydration cycles. However, location of Ba²⁺ and Hg²⁺ in exchangeable sites of the same matrix leads to more stability in interlamellar spaces of both structures; thus, the evolution of the interlayer water contents was more respected during the applied

cycles. The assessment of these results revealed that the environmental solicitation performed by the continuous change of the RH% affects deeply the hydration performance of the host materials (SWy-2) especially in presence of bivalent cations with the lowest ionic radius in their exchangeable sites. In fact, unlike the cations with little size (Mg²⁺ and Ni²⁺), the huge size of Ba²⁺ and Hg²⁺ favors

TABLE 3: Qualitative XRD investigation versus RH% in the case of the second hydration-dehydration cycle.

	% RH	d_{001} (Å)	FWHM ($^{\circ}2\theta$)	ξ	Character
Dehydration process	40 (start)	15.47	1.40		I
	30	14.23	1.44	0.16	I
	20	13.50	1.55	0.18	I
	10	12.89	1.76	0.10	I
Hydration process	20	13.32	1.69	0.53	I
	30	14.07	1.67	0.51	I
	40	14.82	1.72	0.80	I
	50	15.25	1.63	0.36	I
	60	15.59	1.60	0.15	I
	70	16.10	1.04	0.20	I
Second dehydration process	80	16.88	1.00	0.49	I
	70	16.31	0.95	0.20	H
	60	16.01	1.19	0.18	I
	50	15.60	1.46	0.15	I
	40 (return)	15.20	1.60	0.10	I

a decrease of the hydration heterogeneities degree and thus establish more stability of the crystal structure. Thus, the ionic radius of the bivalent compensator ions represents an intrinsic parameter which has important impact on the evolution of the hydration behaviors of the studied smectite.

The hydrous disruption that appears on the interlamellar spaces can be interpreted by the appearance of structural perturbation and new organization at the crystal scale versus the applied hydrous strain. Indeed, the hydration heterogeneity was explained in many studies by the disorder distribution of the surface charge sites which leads to heterogeneous structural composition responsible for such behaviors [55, 56].

Such structural perturbation is justified in the present work through quantitative XRD investigation. Indeed, all theoretical structural models suggest the coexistence of more than one mixed-layer structure (MLS) and propose continuous variations of the interlamellar spaces configurations whatever the interlayer bivalent cations nature (i.e., Mg^{2+} , Hg^{2+} , Ba^{2+} , and Ni^{2+}) and whatever the relative humidity rates that varied upon the applied cycles [52–54].

However, the unsteadiness of the material behavior face to the environmental surroundings changes represent inconvenience when using such mineral as natural barriers in industrial wastes and radioactive treatment specially in long-live storage application.

Indeed, [45] demonstrates that the cation-exchange process of Na-rich montmorillonite in contact with solution containing bivalent cations (Cu^{2+} and Co^{2+}) was affected when applied 15 hydration-dehydration cycles, created by continuous variation of RH% rates. In this case, results derivated from quantitative XRD analysis prove that the hydrous strain was accompanied by an obvious structural change characterized by a decrease in the amount of exchangeable sites which affect the selective exchange process.

In this regard, taking into account the change of surrounding environmental condition is crucial to avoid its

consequence on the microstructure stability of the geotechnical barrier especially in long term.

4.2. Hydration Hysteresis. The comparison between the average hydration hysteresis and the evolution of the calculated standard deviation (SD) for all specimens along both cases of cycles were reported in Figure 9. The SD is generally used to quantify the amount of variation or dispersion of a set of data values. The comparison shows that every sample was characterized by different average hydration hysteresis as well as their associated SD as function of the applied cycle. This result confirms the impact of the RH sequence orientation on the hydration behavior of the studied montmorillonite whatever the nature of the bivalent cation present in their exchangeable sites.

Moreover, the evolution of the SD parameter versus RH% over both cycles (Figure 10) indicate that for all studied complexes, the calculated SD values were more important for the major parts of the RH field in the case of the second cycle than in the first one. The high SD values can be interpreted by the appearance of important structural fluctuations and perturbation on the hydration properties over the second cycle comparing with the first one. However, when focusing the progress of the SD values' evolution during the first cycle, the obtained results show that the calculated SD decreases gradually for different samples when increasing RH values, which indicates more structural stability trends for all studied complexes at the highest RH fields.

On the contrary, according to the literature [20, 28, 33], the classification of the divalent cations used in this work (based on their ionic potential) should respect the following order: $Mg^{2+} > Ni^{2+} > Hg^{2+} > Ba^{2+}$. However, the exploitation of Figure 9, by following the evolution of different average hydration hysteresis as function of the % RH, indicates that this classification was low respected in major parts of the explored RH fields and in both cycle types. Indeed, at the exception of narrow RH fields

TABLE 4: Structural parameters used to fit experimental patterns of SWy-2-Mg complex as a function of RH along the second hydration-dehydration cycle.

	% RH	% of MLS	% of 0W/1W/2W/3W-R*	L.Th		nH_2O		ZH_2O		Z_{Mg}		M	
				0W	1W	0W	1W	0W	1W	0W	1W		
Dehydration	40 (start)	60	0/0/100/0-R0	—	—	—	—	—	—	—	—	9	
		40	0/45/55/0-R0	12.35	2	10.60	10.60	10.00/14.50	12.40	—	—		
				15.55	4	—	—	—	—	—	—		
	30	55	0/15/85/0-R0	—	—	—	—	—	—	—	—	8	
		45	0/45/55/0-R0	12.30	2	10.60	10.60	10.00/14.50	12.40	—	—		
	20	62	0/45/55/0-R0	—	—	—	—	—	—	—	—	10	
		38	0/15/85/0-R0	12.30	1.8	10.60	10.60	09.00/13.50	12.40	—	—		
	10	75	0/75/25/0-R0	—	—	—	—	—	—	—	—	11	
		25	0/55/45/0-R0	12.25	1	10.60	10.60	09.00/13.50	12.60	—	—		
	Hydration	20	100	0/55/45/0-R0	—	—	—	—	—	—	—	—	10
					12.15	2	10.70	10.70	09.90/13.00	12.60	—	—	
					15.15	3.6	—	—	—	—	—	—	
30		55	0/55/45/0-R0	—	—	—	—	—	—	—	—	10	
		45	0/65/35/0-R1	12.20	2	10.30	10.30	09.00/13.50	12.40	—	—		
40		55	0/0/100/0	—	—	—	—	—	—	—	—	7	
		45	0/45/55/0-R0	12.20	2	10.60	10.60	10.00/14.50	12.50	—	—		
50		70	0/0/85/15-R0	—	—	—	—	—	—	—	—	8	
		30	0/45/55/0-R1	12.20	2	10.30	10.30	10.00/14.80	12.50	—	—		
				15.60	4	10.00/14.80	12.50	09.90/14.50/16.70	14.50	—	—		
60		85	0/0/70/30-R0	—	—	—	—	—	—	—	—	10	
		15	0/45/55/0-R0	12.20	2	10.70	10.70	10.00/14.60	12.40	—	—		
70	75	0/0/65/35-R0	12.30	2	10.70	10.70	—	—	—	—	11		
	25	0/40/60/0-R1	15.70	4	10.50/14.90	12.40	10.60/14.50/16.20	14.50	—	—			
80	75	0/0/60/40-R0	—	—	—	—	—	—	—	—	12		
	25	0/40/60/0-R1	12.30	2.2	10.30	10.30	10.50/14.90	12.50	—	—			
			15.70	4.4	10.50/14.90	12.50	10.50/14.60/16.20	14.60	—	—			

TABLE 4: Continued.

% RH	% of MLS	% of 0W/1W/2W/3W-R*	L.Th	n_{H_2O}	Z_{H_2O}	Z_{Mg}	M	
			0W	0W	0W	0W		
			1W	1W	1W	1W		
			2W	2W	2W	2W		
			3W	3W	3W	3W		
Dehydration	70	65	0/0/70/30-R0	—	—	—	—	12
		35	0/60/40/0-R1	12.20	2.2	10.30	10.30	
				15.70	4.4	10.50/14.90	12.50	
	60	65	0/0/85/15-R0	—	—	—	—	11
		35	0/45/55/0-R1	12.30	2	10.20	10.20	
				15.70	4	10.50/14.80	12.50	
	50	55	0/10/90/0-R0	—	—	—	—	11
		45	0/45/55/0-R1	12.20	2	10.20	10.20	
				15.15	4	10.50/14.80	12.50	
	40 (return)	66	0/15/85/0-R0	—	—	—	—	12
		34	0/65/35/0-R1	12.00	2	09.70	09.70	
				15.15	4	10.00/14.50	12.40	
			—	—	—	—		

n_{Mg} : number of H₂O molecule per half unit cell fixed to 0.15, indicating full saturation of the cationic exchange capacity CEC of the minerals.

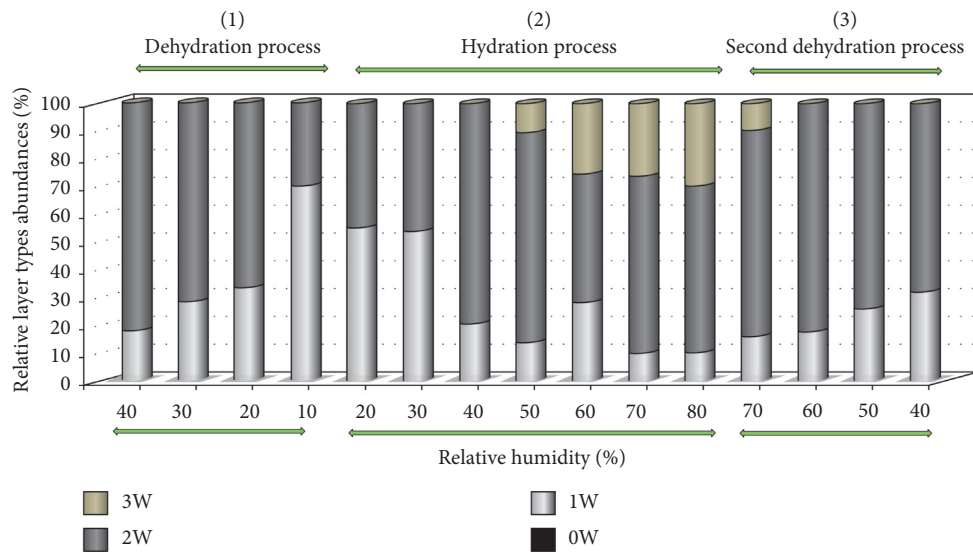


FIGURE 6: Evolution of the relative contribution of the different layer types (summing up all MLSs) as function of the RH% in the case of the second cycle.

extending between 10% and 30% during the second cycle (Figure 9), the classification varied arbitrarily between different cations and changed randomly from an RH field to others ones.

As a consequence of this last result, the ionic potential cannot explain or justify the hydration behavior evolution of the montmorillonite saturated with bivalent cations when submitted to continuous changes of the RH%. In this regard, the water retention mechanism and the crystalline swelling of this smectite became more complex phenomenon under this type of environmental surrounding condition

change. In fact, several factors contribute simultaneously to govern the interlamellar hydration processes, and their combined impacts complicate the well understanding of the interlayer swelling process.

5. Conclusion

This work focuses on the detailed hydration behavior response of an Mg-rich montmorillonite when it undergoes an environmental sollicitation created by continuous variation of the RH% along two different hydration-dehydration

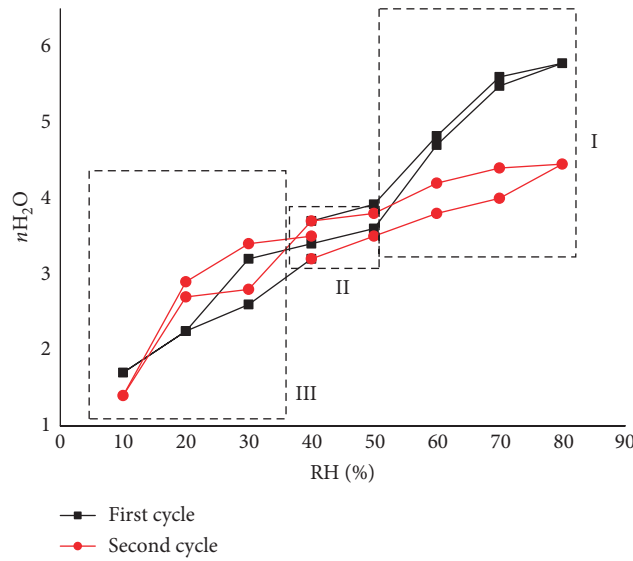


FIGURE 7: Development of the interlayer water contents as function of the RH% along the first and the second cycles in the case of SWy-2-Mg complex.

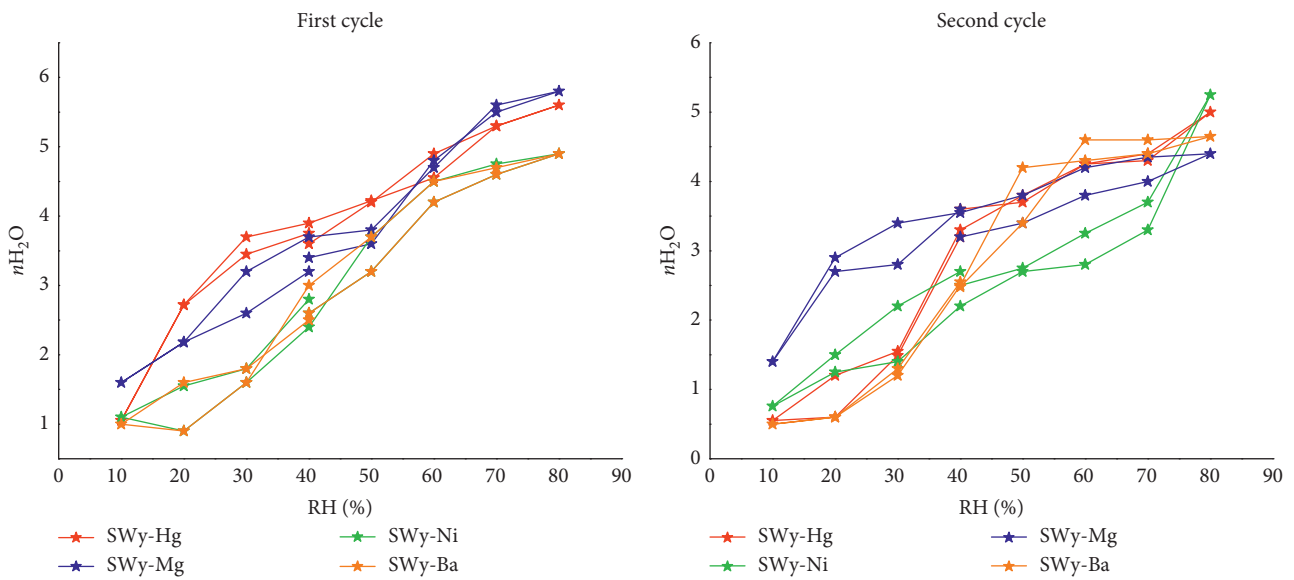


FIGURE 8: Comparison between the evolutions of the interlamellar water amount of the montmorillonite exchanged with different bivalent cations during the cycles.

cycles. Quantitative analysis is mainly based on XRD-modeling approach. The evolution of the hydration properties of the studied sample is quantified and followed every 10% RH upon both cycles. The obtained results are compared with the hydration behaviors of Hg-, Ba-, and Ni-rich montmorillonite studied in the same environmental condition changes.

The main results obtained through quantitative XRD investigation shows the following:

(i) The hydration behavior of the studied sample (i.e., SWy-2-Mg) strongly depended on the sequence orientation of the RH that varied over cycles.

(ii) The proposed theoretical models describing the evolution of the structural properties suggests the coexistence of more than one MLS indicating the hydration heterogeneity character for the SWy-2-Mg whatever the RH% sequence orientation.

(iii) The montmorillonite's interlamellar water content growth was dependent on the nature of the bivalent exchangeable cations. In fact, the presence of Mg^{2+} as well as Ni^{2+} ions in the structure leads an irreversible interlayer water content process confirmed by the appearance of a hydration hysteresis. However, the location of cations with largest ionic radius like Ba^{2+} and Hg^{2+} , in exchangeable sites, was

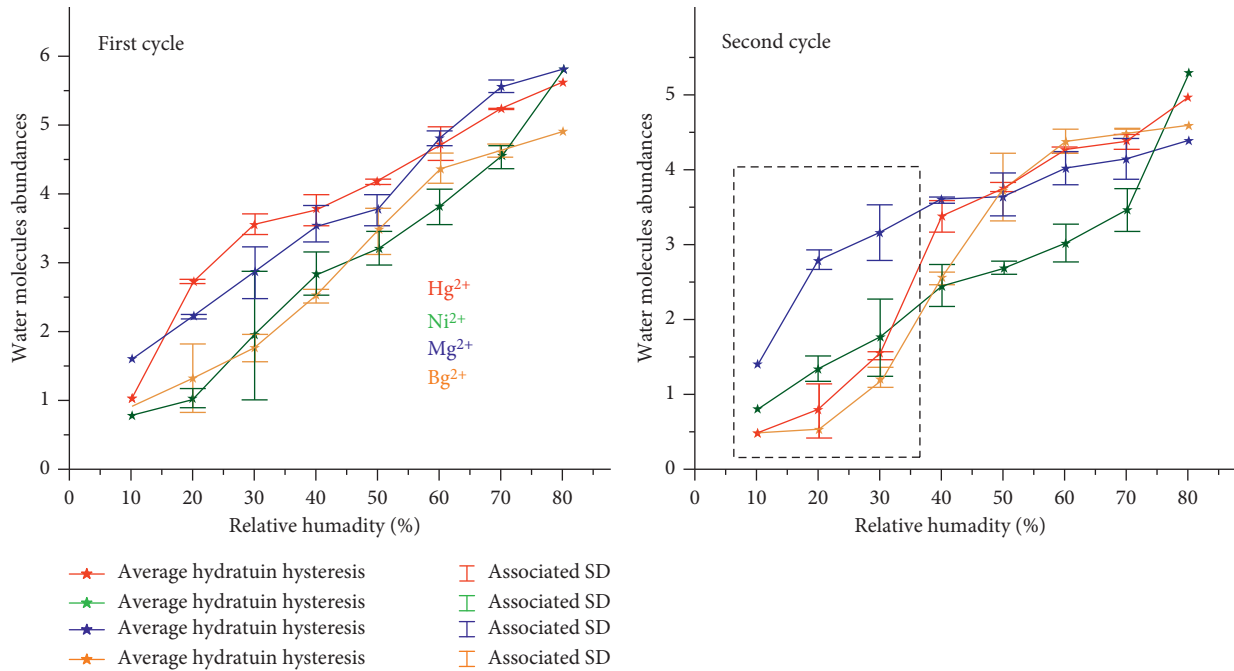


FIGURE 9: Average hydration hysteresis and the associated SD for the montmorillonite saturated with different bivalent cations in the cases of the first and the second cycles.

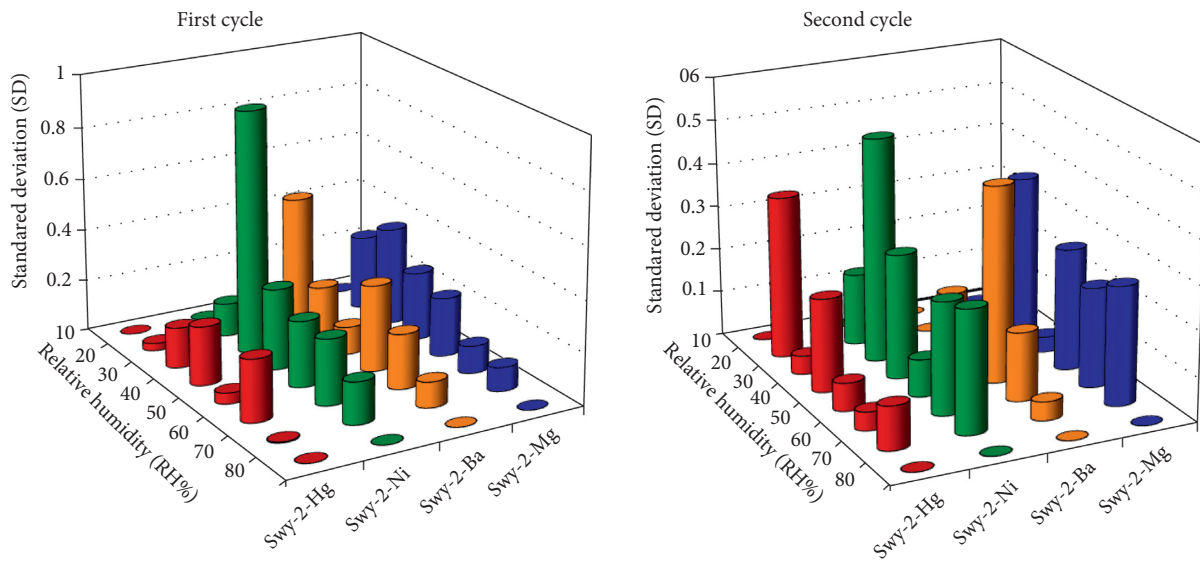


FIGURE 10: Stacked histogram of the hydration SD for the montmorillonite exchanged with divers cations during the hydration-dehydration cycle.

accompanied by more orderliness of systems and decrease in the water-content fluctuation.

- (iv) The effect of the ionic potential parameter on the interlayer water retention mechanism, under controlled atmosphere (i.e, variable RH), is not justified and cannot give a logical explanation on the progress of hydration behaviors of different complex.

Data Availability

No data were used to support this study.

Conflicts of Interest

The authors declare that they have no conflicts of interest.

Acknowledgments

The results presented are a part of the Ph.D. thesis of Marwa Ammar realized at the PMLNMH (UR05/13-01) Faculty of Science of Bizerte, Tunisia, cosupervised by Dr. Walid Oueslati and Prof. Abdesslem Ben Haj Amara. Marwa Ammar acknowledges Dr. W. Oueslati for the fruitful

discussions about smectite hydration, her main contribution in the XRD modeling approach, and the proof reading of the manuscript.

References

- [1] D. Charpentier, M. D. Buatier, E. Jacquot, A. Gaudin, and C. G. Wheat, "Conditions and mechanism for the formation of iron-rich Montmorillonite in deep sea sediments (Costa Rica margin): coupling high resolution mineralogical characterization and geochemical modeling," *Geochimica et Cosmochimica Acta*, vol. 75, no. 6, pp. 1397–1410, 2011.
- [2] O. Karnland, S. Olsson, and U. Nilsson, "Mineralogy and sealing properties of various bentonites and smectite-rich clay materials," SKB internal report TR-06-30, 2006.
- [3] R. L. Anderson, I. Ratcliffe, H. C. Greenwell, P. A. Williams, S. Cliffe, and P. V. Coveney, "Clay swelling—a challenge in the oilfield," *Earth-Science Reviews*, vol. 98, no. 3-4, pp. 201–216, 2010.
- [4] N. G. Turan and O. Ozgonenel, "Study of montmorillonite clay for the removal of copper(II) by adsorption: full factorial design approach and cascade forward neural network," *Scientific World Journal*, vol. 2013, 342628, 11 pages, 2013.
- [5] T. D. Pham, H. H. Nguyen, N. V. Nguyen et al., "Adsorptive removal of copper by using surfactant modified laterite soil," *Journal of Chemistry*, vol. 2017, Article ID 1986071, 10 pages, 2017.
- [6] X. Gu, L. J. Evans, and S. J. Barabash, "Modeling the adsorption of Cd(II), Cu(II), Ni(II), Pb(II) and Zn(II) onto montmorillonite," *Geochimica et Cosmochimica Acta*, vol. 74, no. 20, pp. 5718–5728, 2010.
- [7] K. L. Wasewar, P. Kumar, S. Chand, B. N. Padmini, and T. T. Teng, "Adsorption of cadmium ions from aqueous solution using granular activated carbon and activated clay," *Clean: Soil, Air, Water*, vol. 38, no. 7, pp. 649–656, 2010.
- [8] M. M. Akafia, T. J. Reich, and C. M. Koretsky, "Assessing Cd, Co, Cu, Ni, and Pb sorption on montmorillonite using surface complexation models," *Applied Geochemistry*, vol. 26, pp. S154–S157, 2011.
- [9] B. Doua, V. Dupont, W. Panc, and B. Chenc, "Removal of aqueous toxic Hg(II) by synthesized TiO₂ nanoparticles and TiO₂/montmorillonite," *Chemical Engineering Journal*, vol. 166, no. 2, pp. 631–638, 2011.
- [10] S. N. Rajurkar, N. A. Gokarn, and K. Dimya, "Adsorption of chromium(III), nickel(II), and copper(II) from aqueous solution by activated alumina," *Clean: Soil, Air, Water*, vol. 39, no. 8, pp. 767–773, 2011.
- [11] J. Zhu, V. Cozzolino, M. Pigna, Q. Huang, A. G. Caporale, and A. Violante, "Sorption of Cu, Pb and Cr on Na-montmorillonite: competition and effect of major elements," *Chemosphere*, vol. 84, no. 4, pp. 484–489, 2011.
- [12] J. L. Suter, M. Sprik, and E. S. Boek, "Free energies of adsorption of alkali ions onto beidellite and montmorillonite surfaces from constrained molecular dynamics simulations," *Geochimica et Cosmochimica Acta*, vol. 91, pp. 109–119, 2012.
- [13] Y. Tachi and K. Yotsuji, "Diffusion and sorption of Cs⁺, Na⁺, I⁻ and HTO in compacted sodium montmorillonite as a function of porewater salinity: Integrated sorption and diffusion model," *Geochimica et Cosmochimica Acta*, vol. 132, pp. 75–93, 2014.
- [14] F.M. Huber, S. Heck, L. Truche et al., "Radionuclide desorption kinetics on synthetic Zn/Ni-labeled montmorillonite nanoparticles," *Geochimica et Cosmochimica Acta*, vol. 148, pp. 426–441, 2015.
- [15] K. K. Norrfors, M. Bouby, S. Heck et al., "Montmorillonite colloids: I. Characterization and stability of dispersions with different size fractions," *Applied Clay Science*, vol. 114, pp. 179–189, 2015.
- [16] Z. Y. Li, Z. W. Ma, T. J. Kuijp, Z. W. Yuan, and L. Huang, "A review of soil heavy metal pollution from mines in China: pollution and health risk assessment," *Science of the Total Environment*, vol. 468-469, pp. 843–853, 2014.
- [17] A. E. Burakov, E. V. Galunin, I. V. Burakova et al., "Adsorption of heavy metals on conventional and nanostructured materials for wastewater treatment purposes: a review," *Ecotoxicology and Environmental Safety*, vol. 148, pp. 702–712, 2018.
- [18] T. Nguyen, H. Ngo, W. Guo et al., "Applicability of agricultural waste and by-products for adsorptive removal of heavy metals from wastewater," *Bioresource Technology*, vol. 148, pp. 574–585, 2013.
- [19] D. A. Glatstein and F. M. Francisca, "Influence of pH and ionic strength on Cd, Cu and Pb removal from water by adsorption in Na-Bentonite," *Applied Clay Science*, vol. 118, pp. 61–67, 2015.
- [20] B. Alyüz and S. Veli, "Kinetics and equilibrium studies for the removal of nickel and zinc from aqueous solutions by ion exchange resins," *Journal of Hazardous Materials*, vol. 167, no. 1–3, pp. 482–488, 2009.
- [21] N. Malikova, A. Cadène, E. Dubois et al., "Water diffusion by quasi-elastic neutron scattering in a synthetic hectorite—a model clay system," *Journal of Physical Chemistry C*, vol. 111, no. 47, pp. 17603–17611, 2007.
- [22] B. Rotenberg, V. Marry, R. Vuilleumier, N. Malikova, C. Simon, and P. Turq, "Water and ions in clays: unraveling the interlayer/micropore exchange using molecular dynamics," *Geochimica et Cosmochimica Acta*, vol. 71, no. 21, pp. 5089–5101, 2007.
- [23] E. Ferrage, B. Lanson, L. J. Michot, and J. L. Robert, "Hydration properties and interlayer organization of water and ions in synthetic Na-smectite with tetrahedral layer charge. Part 1. Results from X-ray diffraction profile modeling," *Journal of Physical Chemistry C*, vol. 114, no. 10, pp. 4515–4526, 2010.
- [24] A. Derkowski, V. A. Drits, and D. K. McCarty, "Rehydration of dehydrated-dehydroxylated smectite in a low water vapor environment," *Mineralogical Society of America*, vol. 97, no. 1, pp. 110–127, 2012.
- [25] M. Fleury, E. Kohler, F. Norrant, S. Gautier, J. M'Hamdi, and L. Barre, "Characterization and quantification of water in smectites with low-field NMR," *Journal of Physical Chemistry C*, vol. 117, no. 9, pp. 4551–4560, 2013.
- [26] F. Salles, J. M. Douillarda, O. Bildsteinb et al., "Driving force for the hydration of the swelling clays: case of montmorillonites saturated with alkaline-earth cations," *Journal of Colloid and Interface Science*, vol. 395, pp. 269–276, 2013.
- [27] B. Dazas, B. Lanson, A. Delville et al., "Influence of tetrahedral layer charge on the organization of interlayer water and ions in synthetic Na-saturated smectites," *Journal of Physical Chemistry C*, vol. 119, no. 8, pp. 4158–4172, 2015.
- [28] B. Lanson, S. Lantenois, P. Van Aken, A. Bauer, and A. Plançon, "Experimental investigation of smectite interaction with metal iron at 80°C: structural characterization of newly-formed Fe-rich phyllosilicates," *American Mineralogist*, vol. 97, no. 5-6, pp. 864–871, 2012.
- [29] L. J. Michot, I. Bihannic, M. Pelletier, E. Rinnert, and J. L. Robert, "Hydration and swelling of synthetic Na-saponites: influence of layer charge," *American Mineralogist*, vol. 90, no. 1, pp. 166–172, 2005.

- [30] D. A. Laird, "Influence of layer charge on swelling of smectites," *Applied Clay Science*, vol. 34, no. 1–4, pp. 74–87, 2006.
- [31] M. S. Karmous, H. Ben Rhaiem, J.-L. Robert, B. Lanson, and A. Ben Haj Amara, "Charge location effect on the hydration properties of synthetic saponite and hectorite saturated by Na⁺, Ca²⁺ cations: XRD investigation," *Applied Clay Science*, vol. 46, no. 1, pp. 43–50, 2009.
- [32] K. U. Mohammad, "A review on the adsorption of heavy metals by clay minerals, with special focus on the past decade," *Chemical Engineering Journal*, vol. 308, pp. 438–462, 2017.
- [33] V. Masindi and W. M. Gitari, "Simultaneous removal of metal species from acidic aqueous solutions using cryptocrystalline magnesite/bentonite clay composite: an experimental and modelling approach," *Journal of Cleaner Production*, vol. 112, pp. 1077–1085, 2016.
- [34] G. M. Joziane, P. M. Murilo, K. Thirugnanasambandham et al., "Preparation and characterization of calcium treated bentonite clay and its application for the removal of lead and cadmium ions: adsorption and thermodynamic modeling," *Process Safety and Environmental Protection*, vol. 111, no. #, pp. 244–252, 2017.
- [35] M. V. Villar and A. Loret, "Influence of temperature on the hydro-mechanical behavior of a compacted bentonites," *Applied Clay Science*, vol. 26, no. 1–4, pp. 337–350, 2004.
- [36] W. Oueslati, H. Ben Rhaiem, and A. Ben Haj Amara, "XRD investigations of hydrated homoionic montmorillonite saturated by several heavy metal cations," *Desalination*, vol. 271, no. 1–3, pp. 139–149, 2011.
- [37] R. Chalhaf, W. Oueslati, M. Ammara, H. Ben Rhaiema, and A. Ben Haj Amara, "Effect of temperature and pH value on cation exchange performance of natural clay for selective (Cu²⁺, Co²⁺) removal: equilibrium, sorption and kinetics," *Progress in Natural Science: Materials International*, vol. 23, no. 1, pp. 23–35, 2013.
- [38] B. Lanson, "Modelling of X-ray diffraction profiles: investigation of defective lamellar structure crystal chemistry," *EMU Notes in Mineralogy*, vol. 11, pp. 151–202, 2011.
- [39] B. Lanson, "Crystal structure of mixed-layer minerals and their X-ray identification: new insights from X-ray diffraction profile modelling," *Clay Science*, vol. 12, no. 1, pp. 1–5, 2005.
- [40] E. Ferrage, B. Lanson, N. Malikova, A. Planc, B. A. Sakharov, and V. A. Drits, "New insights on the distribution of interlayer water in bi-hydrated smectite from X-ray diffraction profile modeling of 001 reflections," *Chemistry of Materials*, vol. 17, no. 13, pp. 3499–3512, 2005.
- [41] V. A. Drits and C. Tchoubar, *X-ray Diffraction by Disordered Lamellar Structures: Theory and Applications to Microdivided Silicates and Carbons*, Springer-Verlag, Berlin, Germany, 1990.
- [42] E. Ferrage, B. Lanson, B. A. Sakharov, and V. A. Drits, "Investigation of smectite hydration properties by modeling of X-ray diffraction profiles. Part 1. Montmorillonite hydration properties," *American Mineralogist*, vol. 90, no. 8–9, pp. 1358–1374, 2005b.
- [43] E. Ferrage, C.A. Kirk, G. Cressey, and J. Cuadros, "Dehydration of Ca-montmorillonite at the crystal scale. Part 2. Mechanisms and kinetics," *American Mineralogist*, vol. 92, no. 7, pp. 1007–1017, 2007.
- [44] E. Ferrage, B. A. Sakharov, L. J. Michot et al., "Hydration properties and interlayer organization of water and ions in synthetic Na smectite with tetrahedral layer charge. Part 2. Toward a precise coupling between molecular simulations and diffraction data," *Journal of Physical Chemistry C*, vol. 115, no. 5, pp. 1867–1881, 2011.
- [45] R. Chalhaf, W. Oueslati, M. Ammar, H. Ben Rhaiem, and A. Ben Haj Amara, "Effect of an in situ hydrous strain on the ionic exchange process of dioctahedral smectite: case of solution containing (Cu²⁺, Co²⁺) cations," *Applied Surface Science*, vol. 258, no. 22, pp. 9032–9040, 2012.
- [46] W. Oueslati, H. Ben Rhaiem, and A. Ben Haj Amara, "Effect of relative humidity constraint on the metal exchanged montmorillonite performance: An XRD profile modeling approach," *Applied Surface Science*, vol. 261, pp. 396–404, 2012.
- [47] W.F. Moll, "Baseline studies of the clay minerals society source clays: Geological origin," *Clays and Clay Minerals*, vol. 49, no. 5, pp. 374–380, 2001.
- [48] A. Sari and M. Tuzen, "Cd(II) adsorption from aqueous solution by raw and modified kaolinite," *Applied Clay Science*, vol. 88–89, pp. 63–72, 2014.
- [49] W. Oueslati, N. Chorfi, and M. Abdelwahed, "Effect of mechanical constraint on the hydration properties of Na-montmorillonite: study under extreme relative humidity conditions," *Powder Diffraction*, vol. 32, no. S1, pp. S160–S167, 2017.
- [50] S. Lantenois, B. Lanson, F. Muller, A. Bauer, M. Jullien, and A. Plançon, "Experimental study of smectite interaction with metal iron at low temperature. 1. Smectite destabilization," *Clays and Clay Minerals*, vol. 53, no. 6, pp. 597–612, 2005.
- [51] H. Ben Rhaiem, D. Tessier, and A. Ben Haj Amara, "Mineralogy of the <2 mm fraction of three mixed-layer clays from southern and central Tunisia," *Clay Minerals*, vol. 35, no. 2, pp. 375–381, 2000.
- [52] M. Ammar, W. Oueslati, H. Ben Rhaiem, and A. Ben Haj Amara, "Effect of the hydration sequence orientation on the structural properties of Hg exchanged montmorillonite: quantitative XRD analysis," *Journal of Environmental Chemical Engineering*, vol. 2, no. 3, pp. 1604–1611, 2014.
- [53] M. Ammar, W. Oueslati, N. Chorfi, and H. B. Rhaiem, "Interlamellar space configuration under variable environmental conditions in the case of Ni-exchanged montmorillonite: quantitative XRD analysis," *Journal of Nanomaterials*, vol. 2014, Article ID 284612, 13 pages, 2014.
- [54] W. Oueslati, M. Ammar, and N. Chorfi, "Quantitative XRD analysis of the structural changes of Ba-exchanged montmorillonite: effect of an in situ hydrous perturbation," *Minerals*, vol. 5, no. 3, pp. 507–526, 2015.
- [55] G. Christidis and A. C. Dunham, "Compositional variations in smectites. Part II: alteration of acidic precursors—a case study from Milos Island, Greece," *Clay Minerals*, vol. 32, no. 2, pp. 255–273, 1997.
- [56] C. I. Sainz Diaz, J. Cuadros, and A. Hernandez Laguna, "Analysis of cation distribution in the octahedral sheet of dioctahedral 2:1 phyllosilicates by using inverse Monte Carlo methods," *Physics and Chemistry of Minerals*, vol. 28, pp. 445–454, 2001.

Research Article

Effect of Osmotic Pressure on Migration Behavior of nZnO in GCLs

Ping Yang,¹ Tao Jiang ,² Youlong Zhang,³ and Zhicheng Li⁴

¹Key Laboratory of Geotechnical and Underground Engineering of Ministry of Education, Tongji University, Shanghai, China

²Department of Geotechnical Engineering, Tongji University, Shanghai, China

³China Aviation International Construction and Investment Co. Ltd, Beijing, China

⁴Department of Geotechnical Engineering, Tongji University, Shanghai, China

Correspondence should be addressed to Tao Jiang; 1530834@tongji.edu.cn

Received 14 June 2018; Revised 21 August 2018; Accepted 18 September 2018; Published 16 October 2018

Academic Editor: Annan Zhou

Copyright © 2018 Ping Yang et al. This is an open access article distributed under the Creative Commons Attribution License, which permits unrestricted use, distribution, and reproduction in any medium, provided the original work is properly cited.

The migration of zinc oxide nanoparticles (nZnO) in geosynthetic clay liners (GCLs) under different osmotic pressures was conducted using a self-developed geosynthetic clay liner osmometer. The effects of the osmotic pressure on the migration behavior of nZnO in GCLs were analyzed. The results showed that, with an increase of osmotic pressure, the retention rate of nZnO increased greatly, the particle size increased, the stability of the soliquoid declined, GCLs pores were compressed, the infiltration coefficient of GCLs reduced, and the interception effect of GCLs on nZnO particles strengthened. The two-site model can simulate the migration behavior of nZnO in GCLs very well. The correlativity between the maximum migration distance (L_{\max}) of nZnO in GCLs and the osmotic pressure was negative.

1. Introduction

Zinc oxide nanoparticles (nZnO) are a high-performance inorganic product and are currently one of the most widely used engineered nanoparticles (ENPs) in the world [1, 2]. However, Collins [3] reported that nZnO can affect the survival of organisms in the soil and can even change their community structure. At concentrations of 50 and 100 mg/L, nZnO exhibited cytotoxicity in Neuro-2A cells [4]. Moreover, nZnO can reach the membranes of human aortic endothelial cells (HAECs) and can be absorbed. At a concentration of 10 mg/L, nZnO induced a conspicuous inflammatory response in HAECs. At higher concentrations, nZnO could lead to HAEC necrosis [5]. The toxic effects of nZnO on human lung adenocarcinoma cells (A549) were concentration-dependent and time-dependent [6]. Deng [7] holded that the cytotoxicity of nZnO was mainly caused by the dissolved zinc ions.

Solid waste landfill leaking is a key path for nanoparticles to enter the natural environment [8]. With increasing application of nano materials, large amounts of nanoparticles

have entered landfills as three types of waste [9]. Nanoparticles in liquid waste can easily enter the leachate of landfill. Bolyard et al. [10] and Khan et al. [11] have found that nanoparticles suspended in leachate can migrate successfully through garbage soil. Current studies have mostly adopted column elution tests to simulate nanoparticle migration in the soil. The testing systems mainly consisted of a suspension of nZnO particles (nZnO suspension) and a porous medium [12]. The porous medium was typically composed of quartz sand, silica sand, and glass beads, which serve as a simplified replacement of natural soil. The physical and chemical properties of the porous medium are distinctively different from those of natural soil. Research results showed that the migration of carbon nanotubes was weaker in quartz sand than in glass beads [13]. The smaller the particle size of quartz sand is, the weaker the migration of nanoparticles is. When the particle size of quartz sand decreased from 0.106 mm to 0.043 mm, the concentration of nanoparticles in the effluent declined by 60% [14]. Similar patterns have also been observed in nTiO₂ and nAg in subsequent studies [15]. The interception ratio of nC60 in

clay-containing soil specimens was far higher than that in quartz sand and glass beads. The interception in soil specimens was irreversible [16]. The findings indicated that soil properties exert significant influence on nanoparticle migration in soil. In addition, specific chemical properties of the suspension (e.g., ionic strength, organic matter content, surface active agents, and pH values) can indirectly affect the migration behavior of nanoparticles in a porous medium by influencing nanoparticle scattering and suspension stability [17, 18, 19, 20].

Aforementioned research on the migration of nanoparticles in ideal porous media (e.g., glass beads and quartz sand) or sand obtained preliminary results [21, 22]. The NPs migration and sorption processes are related to the soil properties differentiation [23]. Until now, no published studies have considered the influence of osmotic pressure on the migration properties of nanoparticles in a porous medium. A previous test conducted at landfill sites indicated that the water level of leachate inside landfills could be as high as 20 m–30 m [24]. Geosynthetic clay liner (GCL) was used as the last barrier preventing garbage leachate to enter the natural environment [25]. Whether can GCLs effectively intercept nanoparticles under high osmotic pressure? Therefore, it is an important issue that how osmotic pressure in landfill leachate impacts on migration behaviors of nZnO particles from GCLs to the groundwater.

2. Experimental Materials and Methods

2.1. Material

2.1.1. Geosynthetic Clay Liner. The GCL was prepared by stitching sodium bentonite particles between two layers of geotextiles. According to the data provided by the GCL manufacturer, the bottom layer was woven geotextile with a unit mass of 221 g/m², the top layer was nonwoven geotextile with a unit mass of 112 g/m², and the middle layer was bentonite. The performance of GCL and properties of bentonite are shown in Tables 1 and 2, respectively. The structural representation of the GCL is shown in Figure 1.

2.1.2. Preparation of the nZnO Suspension. nZnO particles were synthesized by a solid reaction process in this experiment. The specific processes are as follows:

- (1) After a specific amount of nZnO had been scattered in an adequate amount of deionized water, the mixture was subjected to an ultrasonic crusher. The nZnO suspension achieved optimal scattering when the frequency, temperature, and time of the ultrasonic crusher were set at 28 kHz, 50°C, and 25 min, respectively [26].
- (2) The experiment employed inductively coupled plasma mass spectrometry (ICP) to measure the concentrations of nZnO suspensions. When the concentrations of elements differed, the suspensions emitted characteristic lights of varying intensity. Quantitative analysis was conducted using this property. The measuring process included the

TABLE 1: Basic performance of GCLs.

Parameters	
Mass per unit area (kg/m ²)	5.56
Thickness (mm)	6.78
Longitudinal breaking strength (kN/m)	11.85
Transverse breaking strength (kN/m)	10.28
Longitudinal breaking elongation (%)	19.50
Transverse breaking elongation (%)	10.67
Vertical permeability coefficient (m/s)	2.69×10^{-9}
Sodium bentonite content (kg/m ²)	5.32

TABLE 2: Basic properties of bentonite.

	Montmorillonite	67
Mineral composition (%)	Kaolinite	14
	Illite	12
	Orthoclase	4
	Quartz	2
Chemical composition (%)	SiO ₂	57.2
	Al ₂ O ₃	16.5
	CaO	3.4
	TiO ₂	0.8
	Fe ₂ O ₃	5.7
	Na ₂ O	3.3
	K ₂ O	0.7
	MgO	3.7
Ion exchange capacity (mmol/g)	Na ⁺	0.445
	K ⁺	0.010
	Ca ²⁺	0.159
	Mg ²⁺	0.017
Initial water content (%)		17.0
Initial thickness (mm)		6.65
pH		9.89~10.67

following steps: (i) tetraacetic acid digestion to process the dispersion (the acid converted nZnO to zinc ions; the acid also dissolved soil and other impurities); (ii) ICP to measure the concentration of zinc ions and to calculate the concentration of nZnO suspension; and (iii) ZetaPALS to measure the zeta potential of the solution. The zeta potential is a measurement of the intensity of mutual repulsion or attraction among particles. The zeta potential represents the stability of colloidal dispersion. Table 3 shows the dispersion properties of nZnO suspension which is gotten as described above.

2.2. Experimental Setup. The osmometer self-developed comprised a pressure control system (composed of a pressure controller, an air pressure pump, and a pressure gauge), a temperature control system (a constant temperature sink), an infiltration chamber, and an automatic collector. The various parts of the system were connected by plexiglass hollow tubes to form a closed system (Figure 2). Osmotic pressure could be adjusted from 0.1 MPa to 0.5 MPa using a pneumatic pump.

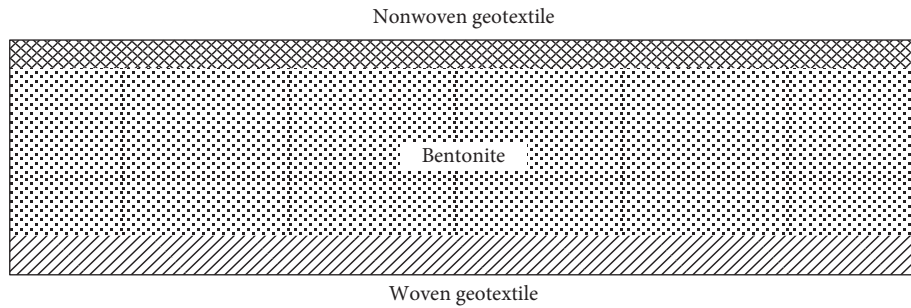


FIGURE 1: Structural representation of the GCL.

TABLE 3: The basic properties of nZnO suspensions.

Component	State	Particle distribution range	Dispersive medium	pH	Zeta potential	Concentration
nZnO	Pure white uniform colloid	2~40 nm	Deionized water	10~11	37 mV	50 mg/L

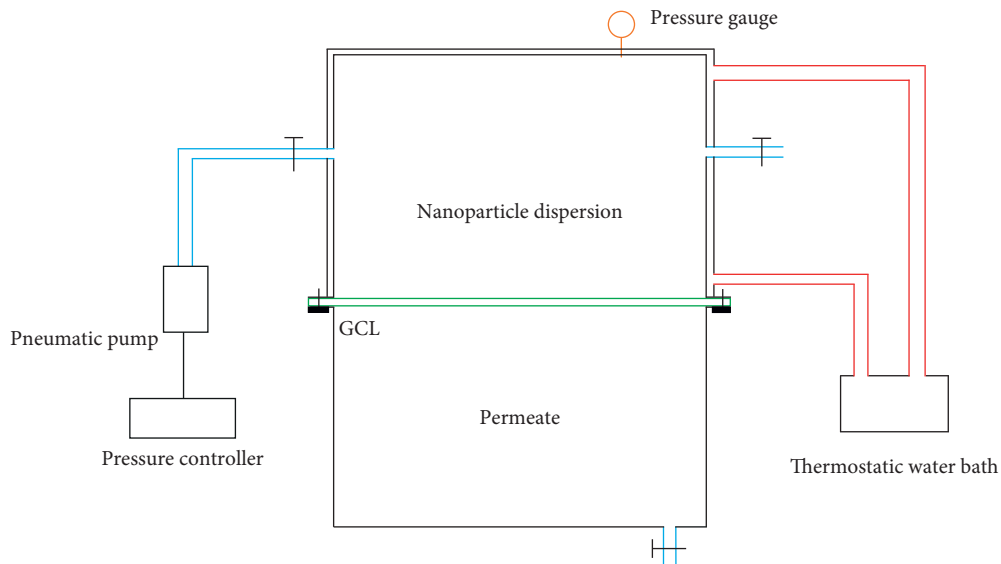


FIGURE 2: Schematic diagram of GCLs permeameter.

2.3. *Experimental Methods.* To investigate the effects of varying osmotic pressure on the migration of nZnO particles in GCLs, five osmotic pressure levels were set according to the water level of landfill leachate. Table 4 shows the experimental parameters.

The experiment steps were as follows:

- (1) Inject 20 pore volumes (PV, obtained by dividing exudate volume by GCLs pore volume) of deionized water into the infiltration chamber and infiltrate GCLs under a specific pressure.
- (2) Mix nZnO granule stock solution with a suitable amount of background solution at a specific proportion and use a magnetic stirrer to stir for 3 h to ensure complete mixing.
- (3) Inject uniformly mixed nZnO granule suspension into the infiltration chamber and set a corresponding osmotic pressure using the control system.
- (4) Collect exudate every 1/3 PV.

TABLE 4: The parameters of experiment.

Experimental condition	Osmotic pressure
Initial concentration 50 mg/L	From 0.1 to 0.5 MPa
Ionic strength 1 mmol/L	
Organic content 1 mg/L	
Temperature 30°C	

Note. C = degrees centigrade.

- (5) When 15 PV of exudate have been collected, elute nZnO particles that have been intercepted in the GCLs using 5 PV of deionized water.
- (6) Collect the exudate at the bottom of the infiltration chamber by using an automatic collector and centrifuge tubes. All exudate samples obtained through infiltration and elution were collected in 5 mL centrifuge tubes.
- (7) Measure nZnO particle concentration using ICP.

Mark the concentration of nZnO particles before infiltrating GCLs as C_0 and that in the exudate collected after infiltrating GCLs as C . After the experiment has been completed, adopt the PV number as the abscissa and C/C_0 as the ordinate to plot a breakthrough curve (BTC) of nZnO particles. The maximum C/C_0 indicates maximum breakthrough equilibrium concentration (C_{max}). When at least three consecutive C/C_0 values are ≥ 95 percent of the C_{max} , it is defined as equilibrium in the breakthrough curve. The smallest PV value corresponding to C_{max} is defined as the equilibrium critical PV.

The compression test and infiltration test of GCLs were conducted with Chinese standard for soil test method (GB/T 50123-1999).

2.4. Theoretical Model. This study adopted a two-site kinetic attachment model in porous media proposed by van Genuchten and Wagenet [27] to analyze the migration of nanoparticles in porous media. The dimensionless form of the two-site kinetic attachment model can be expressed as:

$$\frac{\partial C_1}{\partial T} + (\beta R - 1) \frac{\partial C_1}{\partial T} + (1 - \beta) R \frac{\partial S}{\partial T} = \frac{1}{Pe} \frac{\partial^2 C_1}{\partial X^2} - \frac{\partial C_1}{\partial X}, \quad (1)$$

$$(1 - \beta) R \frac{\partial S}{\partial T} = \omega (C_1 - S),$$

where C_1 is the relative concentration C/C_0 ; β is the fraction of instantaneous retardation, denoting the distribution of instantaneous equilibrium and rate-limited site types; ω is the Damköhler number, which is the ratio between the retention time and the characteristic absorption time in hydrodynamics; T is the number of pore volumes; S is the total adsorption; Pe is the Péclet number, which is a dimensionless number designating the ratio between the convection rate and the diffusion rate; and R is the retardation factor, reflecting the characteristics of retardation nanoparticles exhibit in migrating through the porous medium.

3. Analysis of Experimental Results

3.1. BTC of nZnO Particles under Varying Osmotic Pressures. Figure 3 shows the breakthrough curve of nZnO particles at varying pressures. The parameters of the BTC are shown in Table 5.

When the pressure rises from 0.1 MPa to 0.5 MPa, the critical PV rises from 7.5 to 9.8. As pressure increases, the maximum equilibrium concentration C_{max} declines, and the interception ratio increases. When the osmotic pressure rises from 0.1 MPa to 0.5 MPa, the maximum equilibrium concentration C_{max} drops from 40.04 mg/L to 20.145 mg/L. At the same time, the total rejection rate of nZnO particles in GCLs increases from 48.21% to 82.04%. In the experiments, the interception ratio was 82.04% under an osmotic pressure of 0.5 MPa, meaning that a substantial quantity of nZnO particles deposited in GCLs, with only 17.96% of the particles migrating from GCLs and only 0.18% of the particles migrating out of the GCLs. Both the maximum equilibrium

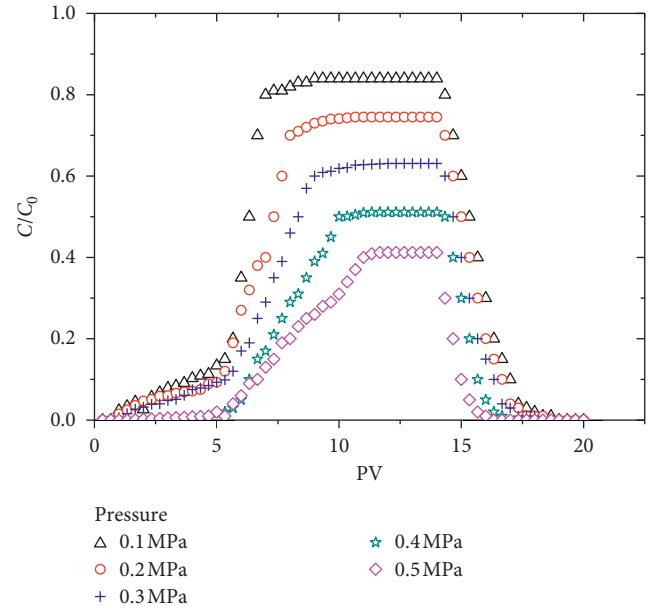


FIGURE 3: BTC of nZnO particles under different osmotic pressures.

concentration C_{max} and interception ratio of nZnO particles under varying osmotic pressures indicated that the migration properties of nZnO particles in GCLs weakened when osmotic pressure increased.

3.2. Effect of Varying Osmotic Pressure on Transportation Parameters

3.2.1. Effect of Osmotic Pressure on the Stability of nZnO Suspension. The test results of the particles size and zeta potential of the nZnO particle suspensions under different osmotic pressures are shown in Figure 4. The results indicated that pressure can cause nZnO particles to grow in size and agglomerate and reduce the scattering stability of the nZnO suspension. The test results revealed that when the osmotic pressure rose from 0.1 MPa to 0.5 MPa, the zeta potential of the nZnO suspension rose from -38.6 mV to -34.2 mV and the size of nZnO particles increased by 5.8% from 317.1 nm to 335.5 nm.

3.2.2. Effect of Osmotic Pressure on the Microstructure and Infiltration Properties of GCLs. Under pressure changes, the porosity ratios of GCLs change accordingly. This study performed a compression test on the GCLs to obtain a compression curve (Figure 5). When the pressure rose from 0.1 MPa to 0.5 MPa, the GCLs porosity ratio decreased from 7.9 to 2.1. Specifically, at the initial stage of pressure application (0.05–0.20 MPa), the extent of change in the porosity ratio was relatively small because the pressure exerted relatively little force on the internal structure of GCLs. When the pressure increased from 0.2 MPa to 0.35 MPa, relatively high pressure accelerated the GCLs porosity change rate, causing the porosity ratio to decrease by 62.5% (i.e., from 6.4 to 2.4), the pressure had a relatively

TABLE 5: Parameters of the BTC.

Osmotic pressure (MPa)	Critical PV	C_{max} (mg/L)	Total rejection rate (%)	Desorption rate/reversible rejection rate (%)
0.1	7.5	40.04	48.21	3.91
0.2	7.8	40.515	57.00	2.78
0.3	8.3	30.095	65.48	1.89
0.4	8.4	30.54	75.38	0.84
0.5	9.8	20.145	82.04	0.18

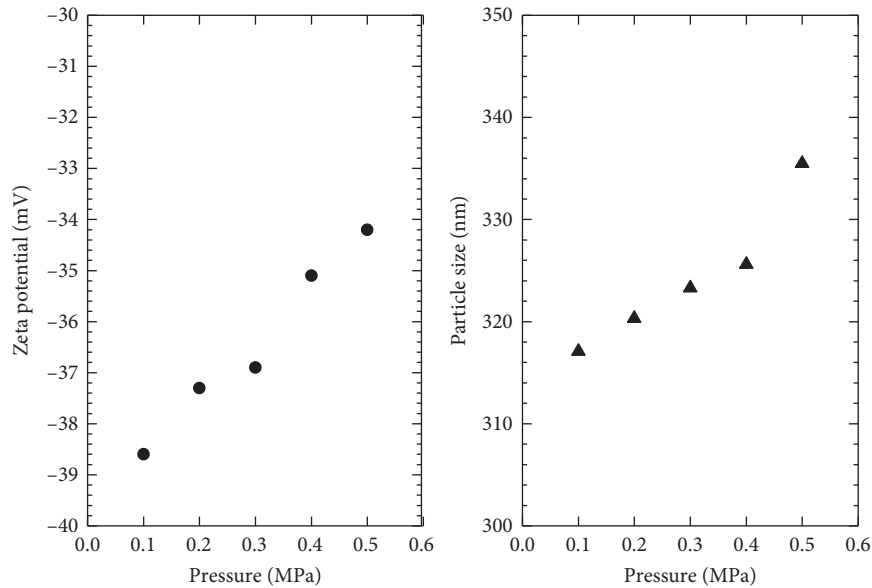


FIGURE 4: (a) Zeta potential of nZnO suspension and (b) particle size of nZnO particles under different osmotic pressures.

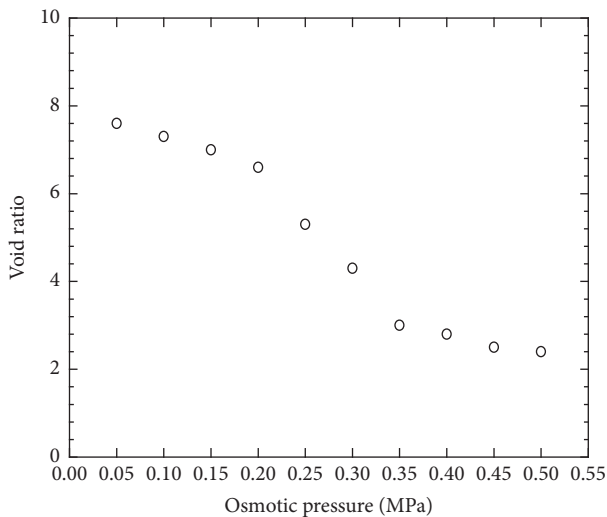


FIGURE 5: GCLs compression curve.

large effect on the internal structure of GCLs. Finally, because the consolidation effect in the preceding stages had fully compressed the GCLs, changes in the GCLs porosity ratio were inconspicuous in the last stage of compression (0.35–0.5 MPa), and the porosity ratio remained between 2.0

and 2.4. Therefore, osmotic pressure exerted notable effects on GCLs microstructure.

The GCLs infiltration coefficients under varying pressures were tested using the infiltration test (Figure 6). The test results indicated that, with continual increases in osmotic pressure, GCLs infiltration coefficients continually decreased. When the osmotic pressure reached 0.35 MPa, the extent of change in infiltration coefficients was reduced.

The effect of pressure on the migration performance of nZnO particles in GCLs has a certain effect. The migration performance of nZnO particles deteriorates as the pressure increases. This is mainly due to the fact that nZnO particles tend to agglomerate in suspension as the pressure increases, and the nZnO particle size becomes larger, which is not conducive to its migration in porous media. In addition, pressure affects the microstructure of GCLs. Pressure causes the GCLs pores to decrease and the permeability to decrease. The retention of nZnO particles by GCLs is enhanced.

3.3. Mechanism of Effect of Osmotic Pressure on nZnO Particle Migration in GCLs. The two-site model was used to fit the breakthrough curves of nZnO particles in GCLs under different osmotic pressures. The results of the simulation are shown in Figure 7. The coincidence between the fitting curve and the measured data is good. When the pressure was lower

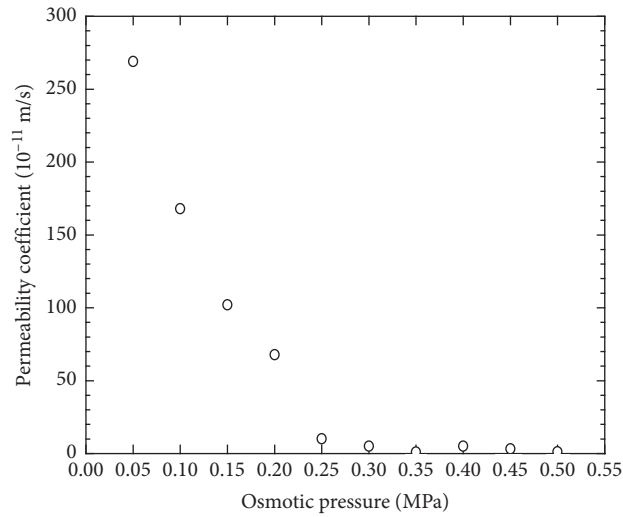


FIGURE 6: GCLs permeability coefficient under different osmotic pressures.

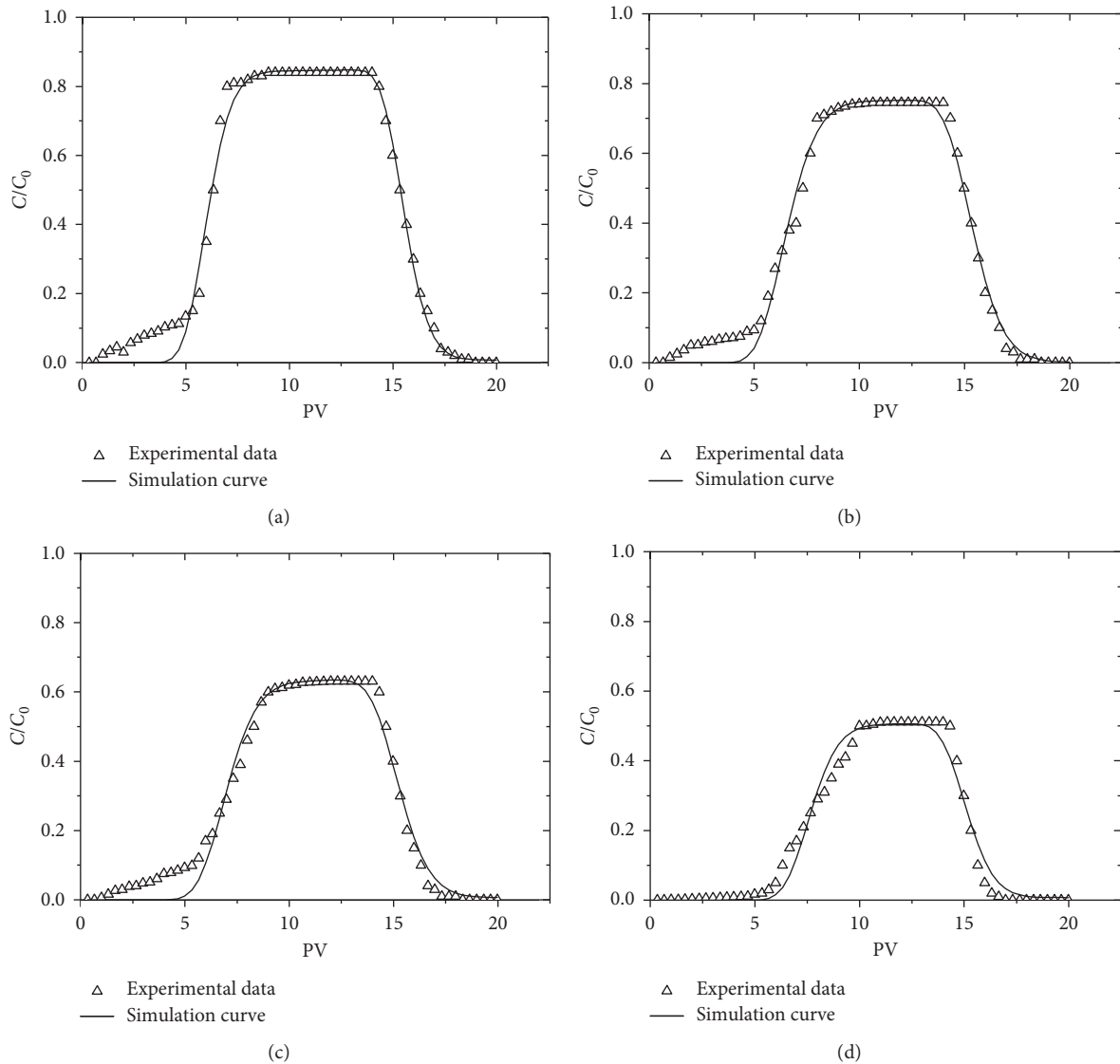


FIGURE 7: Continued.

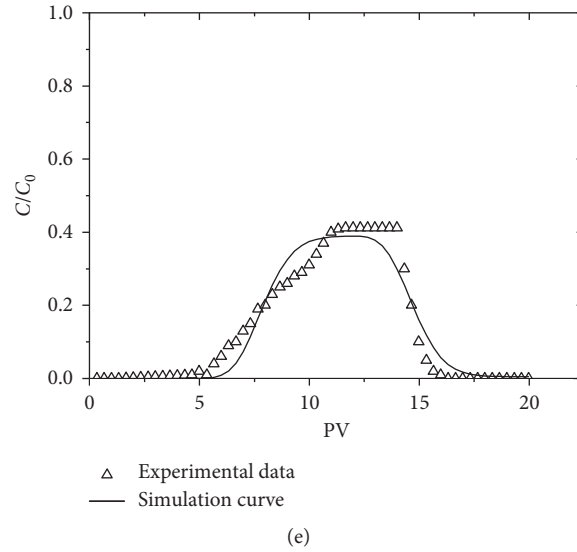


FIGURE 7: The two-site model simulation results. Pressure: (a) 0.1 MPa; (b) 0.2 MPa; (c) 0.3 MPa; (d) 0.4 MPa; (e) 0.5 MPa.

than 0.3 MPa, the infiltration coefficients and void ratio of GCLs decrease quickly with increase of pressure. So, in the first 5 PV, the coincidence between the fitting curve and the measured data is relatively low. This indicates that the two-site model can describe the migration process very well. In addition, the coefficient of correlation (R^2) also notes that the two-site model has a better fitting effectiveness for the migration process, as shown in Table 6, R^2 are all above 0.945. Of the four dimensionless parameters, pressure had relatively large influences on the Pe , R , and ω . Specifically, Pe dropped when pressure rose, which indicated that the convection effect of nZnO particles weakened in the GCLs. This phenomenon happened because pressure reduced GCLs porosity so that the flow rate of the suspension slowed in the GCLs. R was positively correlated with pressure. Greater values of R indicated that the nanoparticles encountered greater retardation when nanoparticles migrated in the porous medium. Therefore, the retardation effect of GCLs on nZnO particles became increasingly conspicuous as pressure increased.

3.4. Maximum Migration Distance of Nanoparticles. The maximum migration distance (L_{max}) of nanoparticles in porous media is defined as the migration distance when 99% of nanoparticles (i.e., $c/c_0 = 0.01$) are trapped. The two-site model can accurately describe the migration process of nZnO particles in GCLs. Therefore, we adopted the two-site model to simulate the relationship between C/C_0 of nZnO particles and the migration distance (z) in GCLs under different experimental conditions by the CXTFIT module of the STANMOD software and to acquire the L_{max} . The results of the simulation are shown in Figure 8. From the simulation results, the correlativity between L_{max} and osmotic pressure is negative. It is also proved that the migration properties of nZnO particles in GCLs drop down with the osmotic pressure increasing.

TABLE 6: The fitting values of the dimensionless parameters in the two-site model.

Osmotic pressure (MPa)	Pe	R	β	ω	R^2
0.1	251.2448	61.9311	0.4014	0.0632	0.988
0.2	229.2961	128.8189	0.3910	0.0981	0.988
0.3	69.3585	170.7667	0.3244	0.5214	0.979
0.4	62.3821	385.2743	0.3065	1.1122	0.977
0.5	36.7632	501.5935	0.3874	2.3723	0.945

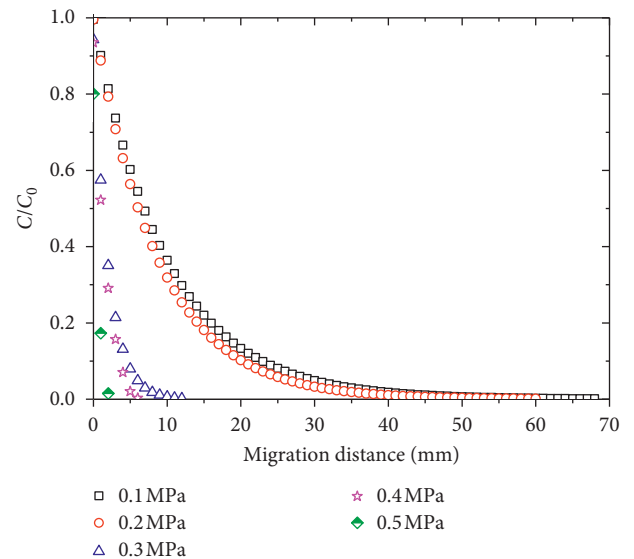


FIGURE 8: Migration distance simulation results.

4. Conclusion

Along with increasing pressure, the zeta potential among nZnO particles decreased, the maximum energy barrier

(Φ_{\max}) reduced gradually, the agglomeration properties of nZnO strengthened, and the tension-induced interception of nZnO particles in GCLs increased.

Along with increasing pressure, GCLs pores were compressed, the infiltration coefficient of GCLs reduced, and the interception effect of GCLs on nZnO particles strengthened.

The two-site model can accurately describe the migration process of nZnO particles in GCLs. The migration properties of nZnO particles in GCLs drop down with the osmotic pressure increasing.

The correlativity between L_{\max} and osmotic pressure is negative. It is also proved that the migration properties of nZnO particles in GCLs drop down with the osmotic pressure increasing.

Because of the complex environmental conditions of landfills, the actual conditions of such sites could not be accurately simulated in this study. However, the aforementioned results can serve as a reference for future research on the migration behaviors and mechanisms of nanoparticles in landfills.

Data Availability

The data used to support the findings of this study are included within the article.

Conflicts of Interest

The authors declare that they have no conflicts of interest.

Acknowledgments

This investigation was supported by the National Natural Science Foundation of China (projects nos. 41672274 and 41002093); the Fundamental Research Funds for the Central Universities (projects no. 22120180233); and Opening fund of State Key Laboratory of Geohazard Prevention and Geoenvironment Protection (Chengdu University of Technology) (project no. SKLGP 2014K013). The authors are extremely grateful for the financial support from these four organizations.

References

- [1] M. F. Peterson, "Progress in preparation and application of one-dimensional nano zinc oxide," *Journal of Materials Engineering*, vol. 43, no. 2, pp. 103–112, 2015.
- [2] P. Sun, A. Shijirbaatar, J. Fang, G. Owens, D. Lin, and K. Zhang, "Distinguishable transport behavior of zinc oxide nanoparticles in silica sand and soil columns," *Science of the Total Environment*, vol. 505, pp. 189–198, 2015.
- [3] D. Collins, T. Luxton, N. Kumar, S. Shah, V. K. Walker, and V. Shah, "Assessing the impact of copper and zinc oxide nanoparticles on soil: a field study," *Plos One*, vol. 7, no. 8, p. e42663, 2012.
- [4] H. A. Jeng and J. Swanson, "Toxicity of metal oxide nanoparticles in mammalian cells," *Journal of Environmental Science and Health Part A Toxic/hazardous Substances and Environmental Engineering*, vol. 41, no. 12, pp. 2699–2711, 2006.
- [5] A. Gojova, B. Guo, R. S. Kota, J. C. Rutledge, I. M. Kennedy, and A. I. Barakat, "Induction of inflammation in vascular endothelial cells by metal oxide nanoparticles: effect of particle composition," *Environmental Health Perspectives*, vol. 115, no. 3, pp. 403–409, 2007.
- [6] W. Lin, Y. Xu, C.-C. Huang et al., "Toxicity of nano- and micro-sized ZnO particles in human lung epithelial cells," *Journal of Nanoparticle Research*, vol. 11, no. 1, pp. 25–39, 2009.
- [7] X. Deng, Q. Luan, W. Chen et al., "Nanosized zinc oxide particles induce neural stem cell apoptosis," *Nanotechnology*, vol. 20, no. 11, article 115101, 2009.
- [8] D. Wang, M. Paradelo, S. A. Bradford et al., "Facilitated transport of Cu with hydroxyapatite nanoparticles in saturated sand: effects of solution ionic strength and composition," *Water Research*, vol. 45, no. 18, pp. 5905–5915, 2011.
- [9] G. S. Yazici, B. Alan, E. Adar, and M. S. Bilgili, "The impact of nanoparticles on aerobic degradation of municipal solid waste," *Waste Management and Research*, vol. 35, no. 4, pp. 426–436, 2017.
- [10] S. C. Bolyard, D. R. Reinhart, and S. Santra, "Behavior of engineered nanoparticles in landfill leachate," *Environmental Science and Technology*, vol. 47, no. 15, p. 8114, 2013.
- [11] I. A. Khan, N. D. Berge, T. Sabo-Attwood, P. Lee Ferguson, and N. B. Saleh, "Single-walled carbon nanotube transport in representative municipal solid waste landfill conditions," *Environmental Science and Technology*, vol. 47, no. 15, pp. 8425–433, 2013.
- [12] Y. Zhang, P. Yang, and S. Xue, "Researching advances in transportation of nanomaterial contaminants in soil," *Environmental Engineering*, vol. 3, pp. 88–91, 2015, in Chinese.
- [13] X. Liu, D. M. O'Carroll, E. J. Petersen, Q. Huang, and C. L. Anderson, "Mobility of multiwalled carbon nanotubes in porous media," *Environmental Science & Technology*, vol. 43, no. 21, pp. 8153–8158, 2009.
- [14] N. T. Mattison, D. M. O'Carroll, R. K. Rowe, and E. J. Petersen, "Impact of porous media grain size on the transport of multi-walled carbon nanotubes," *Environmental Science and Technology*, vol. 45, no. 22, pp. 9765–9775, 2011.
- [15] Y. Liang, S. A. Bradford, J. Simunek, H. Vereecken, and E. Klumpp, "Sensitivity of the transport and retention of stabilized silver nanoparticles to physicochemical factors," *Water Research*, vol. 47, no. 7, pp. 2572–2582, 2013.
- [16] K. Wang, J. Liu, L. Liu, and D. Sun, "Biocompatibility of graphene oxide," *Nanoscale Research Letters*, vol. 6, no. 1, pp. 1–8, 2011.
- [17] D. Bouchard, W. Zhang, and X. Chang, "A rapid screening technique for estimating nanoparticle transport in porous media," *Water Research*, vol. 47, no. 12, p. 4086, 2013.
- [18] I. G. Godinez and C. J. Darnault, "Aggregation and transport of nano-TiO₂ in saturated porous media: effects of pH, surfactants and flow velocity," *Water Research*, vol. 45, no. 2, pp. 839–851, 2011.
- [19] D. H. Lin, X. Tian, F. Wu, and B. Xing, "Fate and transport of engineered nanomaterials in the environment," *Journal of Environmental Quality*, vol. 39, no. 6, p. 1896, 2010.
- [20] T. Rahman, J. George, and H. J. Shipley, "Transport of aluminum oxide nanoparticles in saturated sand: effects of ionic strength, flow rate, and nanoparticle concentration," *Science of the Total Environment*, vol. 499, no. 5, pp. 565–571, 2014.
- [21] A. Braun, E. Klumpp, R. Azzam, and C. Neukum, "Transport and deposition of stabilized engineered silver nanoparticles in water saturated loamy sand and silty loam," *Science of the Total Environment*, vol. 535, p. 102, 2015.

- [22] D. Wang, C. Su, W. Zhang et al., "Laboratory assessment of the mobility of water-dispersed engineered nanoparticles in a red soil (Ultisol)," *Journal of Hydrology*, vol. 519, pp. 1677–1687, 2014.
- [23] S. P. Kulizhskiy, S. V. Loiko, Y. N. Morgalev, G. I. Istigechev, A. V. Rodikova, and T. A. Maron, "Investigation of platinum and nickel nanoparticles migration and accumulation in soils within the South eastern part of West Siberia," *Nano Hybrids and Composites*, vol. 13, pp. 115–122, 2017.
- [24] W. Zhang, *Experimental and Numerical Study on Water/Leachate Transport in Landfill of Municipal Solid Waste.D.*, Zhejiang University, Hangzhou, China, 2007, in Chinese.
- [25] J. Liu and X. J. Kong, "Seismic stability and permanent displacement analysis of a solid waste landfill slope containing geomembrane," *Rock and Soil Mechanics*, vol. 25, no. 5, pp. 778–782, 2004.
- [26] G. K. Wang and Y. X. Yang, "Infection of different ultra audible frequency and temperature to dispersive property of ZnO nanometre granule," *Sichuan Textile Technology*, 2005, in Chinese.
- [27] M. Th. van Genuchten and R. J. Wagenet, "Two-site/two-region models for pesticide transport and degradation: theoretical development and analytical solutions," *Soil Science Society of America Journal*, vol. 53, no. 5, pp. 1303–1310, 1989.

Research Article

Consolidated Undrained Triaxial Compression Tests and Strength Criterion of Solidified Dredged Materials

Jianwen Ding ¹, Xusong Feng,² Yupeng Cao ³, Sen Qian ⁴, and Feng Ji⁵

¹Ph.D, Associate Professor, Institute of Geotechnical Engineering, School of Transportation, Southeast University, Nanjing 210096, China

²Ph.D, Jiangsu Water Resources Company Limited, The Water Diversion Project from South to North in China, Nanjing 210029, China

³Ph.D, Lecturer, College of Transportation, Shandong University of Science and Technology, Qingdao 266590, China

⁴Ph.D Candidate, Institute of Geotechnical Engineering, School of Transportation, Southeast University, Nanjing 210096, China

⁵Ph.D, Jiangsu Water Resources Company Limited, The Water Diversion Project from South to North in China, Nanjing 210029, China

Correspondence should be addressed to Jianwen Ding; jwding2006@163.com

Received 14 May 2018; Accepted 18 August 2018; Published 15 October 2018

Academic Editor: Yonggui Chen

Copyright © 2018 Jianwen Ding et al. This is an open access article distributed under the Creative Commons Attribution License, which permits unrestricted use, distribution, and reproduction in any medium, provided the original work is properly cited.

Consolidated undrained triaxial compression tests were performed to investigate the shear strength behavior of the solidified dredged materials (SDM). The variation law of deviator stress and excess pore water pressure with the increase of the applied confining pressure was investigated. It is found that the shear strength envelope is consisted of two lines, and there exists a transitional stress on the intersection point. The undrained shear strength develops slightly with the increase of applied normal stress in the preyield state. However, the undrained shear strength increases significantly in the postyield state, and the strength envelope is nearly a straight line with the extension through the origin. Based on the triaxial test data and the binary medium model, a strength criterion considering strength evolution mechanism is proposed and the relevant parameters of the strength criterion were discussed. Comparisons of the predicted results and experimental data demonstrate that the proposed strength criterion can properly describe the strength evolution rules of the SDM.

1. Introduction

Large volumes of sediment are dredged annually to maintain the navigational depth of channels and harbors, to prevent rivers from flooding, and to restore the ecosystem of degenerative water bodies [1–6]. How to deal with the vast amounts of dredged materials (DM) becomes an important issue in engineering practice. Many studies have been conducted regarding the use of DM as land reclamations backfill or engineering construction materials [2, 5, 7–9]. Solidification/stabilization is an ideal way that can improve the engineering properties of the abandoned DM [5] (Kamon et al. 2005) [6, 8, 10], showing economical and environmental advantages and avoiding borrowing soils from elsewhere.

The strength properties of structured clays are different from remolded clays [11–15]. However, the existing strength criteria are mostly established on the basis of the properties of reconstituted soils [16–19] that cannot well reflect the influence of soil structures on the properties of structured soils [14]. It has been well reported by researchers [15, 20] that the strength envelope of the natural structured sedimentary clays can be divided into two parts in terms of the structure yield stress (i.e., preyield state and postyield state). And there also exists a transitional stress on the strength envelope of the cement-treated soil [21, 22]. The structure formation of natural soil is attributed to the soil structure development during depositional and post-depositional processes [23–26]. Similar to natural structured soils, the observed high yield stresses are evidences for the

structure of cement-treated soil [1, 2, 22, 27, 28]. The structure of the SDM is formed by cement hydration and pozzolanic reaction, and a mechanically stable soil matrix was produced due to cementation bonds [1, 6, 21, 28, 29]. Hence, the SDM can be considered as an artificially structured soil, and it can exhibit strongly stable structure and higher yield stress compared with the untreated DM.

The objectives of this study are (1) to investigate shear strength behavior of the SDM, (2) to establish strength criterion for the SDM, and (3) to verify the validity of the proposed strength criterion and discuss the relevant parameters.

2. Materials and Test Method

2.1. Materials. The dredged material (DM, as shown in Figure 1) used in this study was taken from the bottom of the Baima Lake located in Huaian, Jiangsu Province, China (sampling site as shown in Figure 2). The basic physical properties of the DM are summarized in Table 1. The liquid limit and plastic limit are 66.1% and 26.6%, respectively. According to the Unified Soil Classification System, the DM is classified as high plasticity clay.

Based on the conventional cement-treated method, in this study, phosphogypsum was used together with cement to stabilize the DM at high water content. It should be mentioned that phosphogypsum is a by-product of the production of phosphoric acid, only a small portion can be recycled, other most is deposited without any prior treatment. Deserted phosphogypsum occupies land areas and possibly causes serious environmental contamination [31–33]. Type I ordinary Portland cement was used in this study, and phosphogypsum (as shown in Figure 3) used here was taken from a chemical company in Nanjing, China.

2.2. Sample Preparing and Test Method. Mixing proportion design of the SDM is presented in Table 2, and current dredging method characterized with high water content of the DM [34] has been taken into account. In Table 2, the mixing proportion can be expressed as 2.5W+C100+P40 and so on. In the expression, 2.5W denotes the water content of DM slurry is 2.5 times the liquid limit, C100 denotes the cement content is 100 kg for 1 m³ DM slurry (i.e., 100 kg/m³), and P40 denotes the weight of phosphogypsum is 40% of the cement. All triaxial tests were performed at the curing period of 28 days, and the confining pressure is designed in the range of 100–1200 kPa, which are shown in Table 2.

The specimens were prepared by mixing the DM slurries with dry cement powder and phosphogypsum powder. Then, the uniform paste was placed into a cylindrical mold. The bottom of the mold is specially designed which can be dismantled freely so that the sample is easy to dismantle. Friction was minimized by using a polished inner wall and smeared with a thin film of grease. The cylindrical specimens were dismantled after 24 hours, wrapped with plastic bags, and then stored in a standard curing room with a constant ambient temperature of $20 \pm 2^\circ\text{C}$ and a relative humidity

above 95%. The dimension of all specimens (as shown in Figure 4) is 39.1 mm in diameter and 80 mm in height.

Consolidated undrained triaxial compression tests were conducted at the designed curing period of 28 days. Before installation in the triaxial cell, the specimens were placed in a vacuum chamber filled with distilled water for saturation at least 24 hours. After installation, undrained isotropic loading was used to check the pore pressure coefficient “B.” The triaxial tests were conducted at an axial compression rate of 0.073 mm/min. Excess pore water pressure was measured during the shear phase. It should be mentioned that even adopted with a back pressure of 200 kPa after vacuum saturation, the measured pore pressure parameter “B” was only around 0.9, which is in agreement with the phenomenon reported by Kamruzzaman et al. [28].

3. Results and Discussion

The variation of deviator stress under different confining pressures is shown in Figure 5. It can be seen that there exists a peak deviator stress for all SDM samples, which is similar to the overconsolidated soils [28, 35–39]. Figure 5 illustrates that the peak deviator stress increases with the applied confining pressure and the failure strain also increases with the increase in confining pressure. It is interesting to note that the increment of the peak deviator stress is different under different stress levels. The peak deviator stress increases very small when the confining pressure is less than 400 kPa, which is similar to the observations reported by other researchers [21, 28]. The change of the fabric in the consolidation process is insignificant at low confining pressures, and the peak strength is mainly governed by the soil structure resistance [15, 21]. However, the peak strength significantly increases when the confining pressure is more than 400 kPa, for the cementation bond begins to break and its artificial structure disappears progressively at high confining pressures, and the shear strength mainly depends on the applied stress level. Hence, the behavior of the SDM is similar to heavily over-consolidated natural structured clays, although its structure yield stress is related to bonding and not to stress history [1, 22, 28, 40].

The variation of excess pore water pressure under different confining stress is shown in Figure 6. It can be seen that there exists a peak value when the confining pressure is lower than 400 kPa; however, the peak value becomes insignificant when the confining pressure is greater than 400 kPa. Similar results were observed by other researchers on cement-treated or untreated clays [28, 41, 42]. The change law of excess pore water pressure with the confining pressure is different with the deviator stress, the peak pore water pressure increases notably with an increase in confining pressure, both in the lower stress level stage and in the higher stress level stage. Similar results were reported by other researchers on cement-treated clays [28, 41].

The relationship between undrained shear strength and applied normal stress is shown in Figure 7. It can be seen that the undrained shear strength envelope is approximately consisted of two straight lines, and there is a transitional



FIGURE 1: Dredged material.



FIGURE 3: Phosphogypsum.

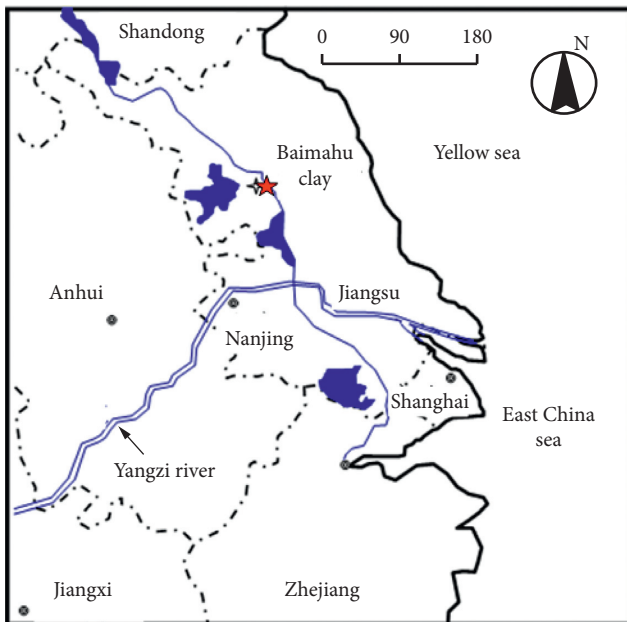


FIGURE 2: Sampling site [30].

TABLE 1: Basic physical properties of the dredged material.

Properties	Values
Specific gravity, G_s	2.68
Liquid limit, LL (%)	66.1
Plastic limit, PL (%)	26.6
Plasticity index, PI (%)	39.5
Sand (>0.074 mm) content (%)	9.0
Silt (0.074–0.005 mm) content (%)	59.4
Clay (<0.005 mm) content (%)	31.6
Organic content (%)	2.2

stress at the intersection point of the two straight lines on the strength envelope. Such a bilinear strength envelope for natural sedimentary clays has been well reported by other researchers [15, 20].

In Figure 7, it can be seen that the undrained shear strength increases slightly with the increase in applied normal stress at first (i.e., in the preyield state), which indicates that the shear strength of the SDM is mainly affected

TABLE 2: Programme of triaxial test.

Mixing proportion	Confining pressure (kPa)
2.5W+C100+P40	100, 200, 400, 600, 800, 1000, 1200
3.0W+C100+P70	100, 200, 400, 600, 800, 1000, 1200
3.0W+C200	100, 200, 400, 600, 800, 1000, 1200
3.0W+C200+P50	100, 200, 400, 600, 800, 1000, 1200



FIGURE 4: Specimens.

by the soil structure resistance when the applied stress is smaller than the yield stress. However, the shear strength increases significantly when the applied normal stress is greater than yield stress (i.e., in the postyield state). It is interesting to note that all the strength envelopes are nearly a straight line with the extension through the origin, which is consistent with the observation of other researchers [15, 22]. It indicates that the undrained shear strength mainly depends on the applied normal stress in the postyield stage, for the cementation bond is progressively destroyed and the soil structure resistance gradually vanishes when the stress level exceeds its yield stress [28, 40].

4. Strength Criterion for the SDM

Based on the homogenization theory of heterogeneous materials [43] and considering the breakage mechanics of geomaterials [44], Shen [45] proposed the binary medium model for structured soil and suggested a basic equation for the mean stress tensor $\{\bar{\sigma}\}$ as Equation (1). In the model, the

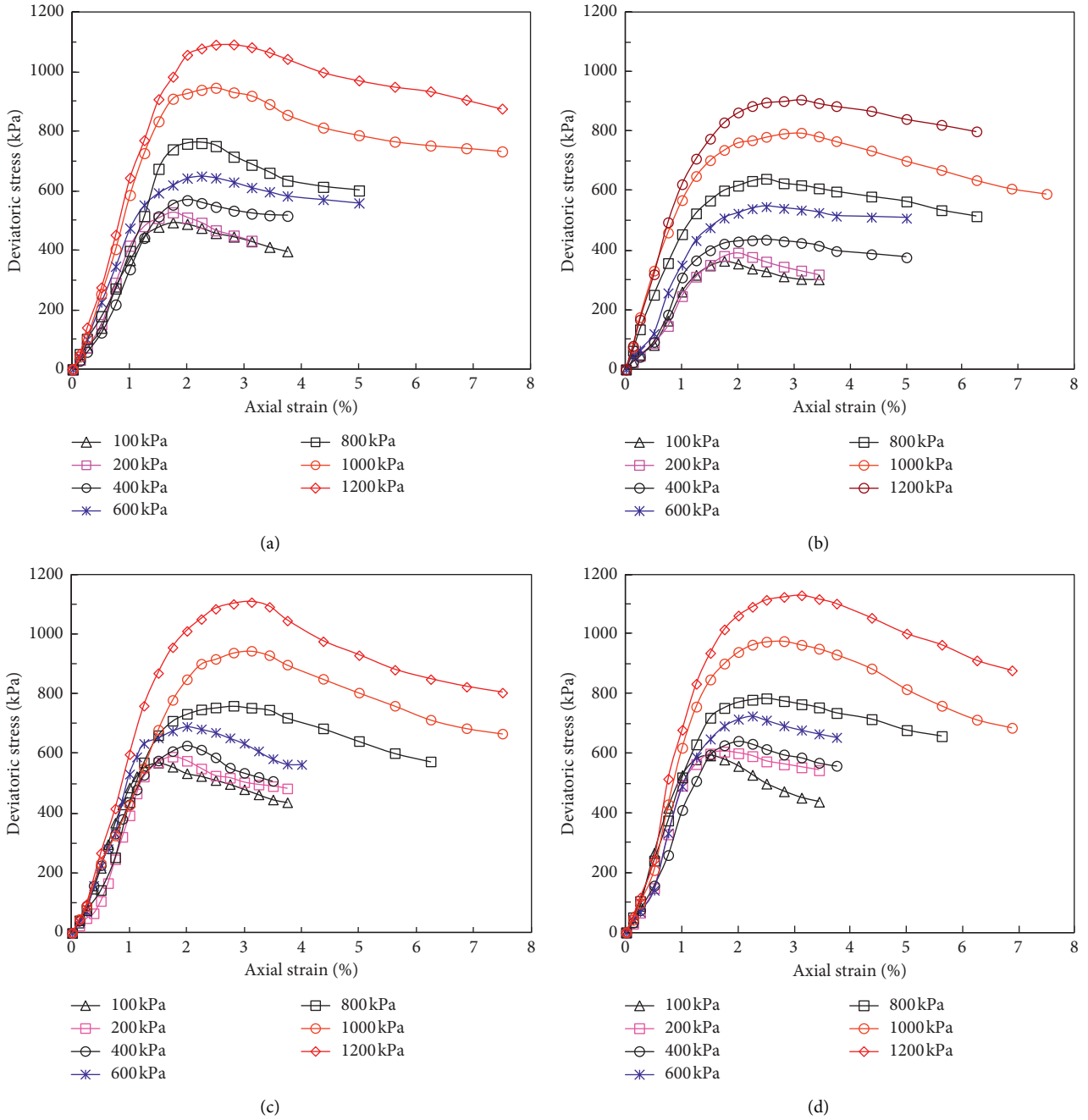


FIGURE 5: Relationship between deviatoric stress and axial strain at different applied confining pressures: (a) 2.5W+C100+P40, (b) 3.0W+C100+P70, (c) 3.0W+C200, and (d) 3.0W+C200+P50.

structured soil is conceptualized as binary medium consisting of bonding element and frictional element:

$$\{\bar{\sigma}\} = (1 - b)\{\sigma_i\}b + \{\sigma_f\}, \quad (1)$$

where $\{\bar{\sigma}_i\}$ is the mean stress tensor of the bonding element and $\{\bar{\sigma}_f\}$ is the mean stress tensor of the frictional element, respectively, and b is the resistance share ratio.

In addition, according to the basic theory of soil mechanics, cohesion is independent of the normal stress, whereas internal friction is the proportional function of

normal stress in the shear surface. Hence, the shear strength of the SDM can be expressed as

$$\tau = f(\tau_b) + f(\tau_f), \quad (2)$$

where $f(\tau_b)$ is the shear strength provided by the bonding element and $f(\tau_f)$ is the shear strength provided by the frictional element.

Substituting Equation (1) into (2), the shear strength of solidified soil can be expressed as

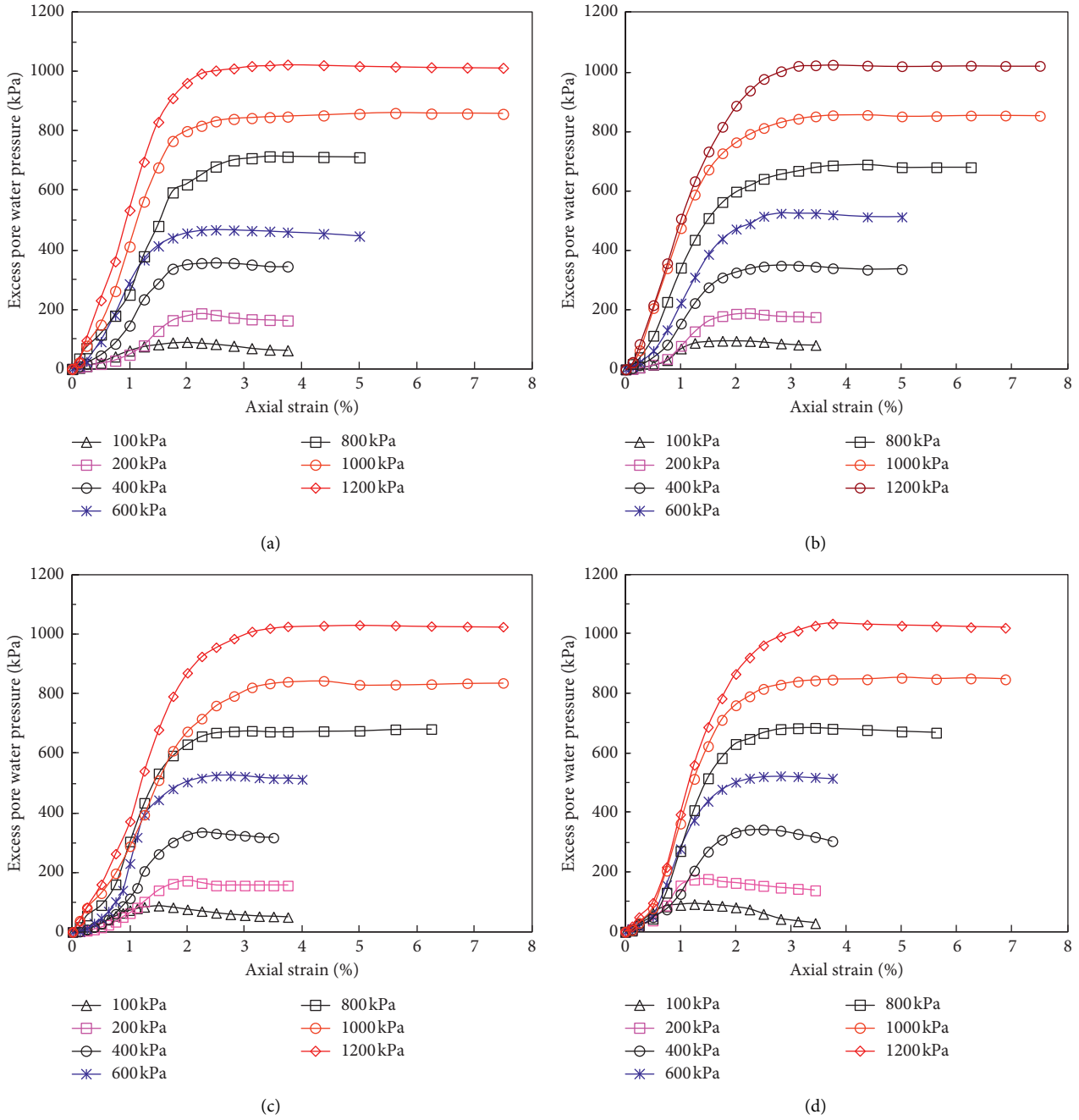


FIGURE 6: Relationship between excess pore water pressure and axial strain at different applied confining pressures: (a) 2.5W+C100+P40, (b) 3.0W+C100+P70, (c) 3.0W+C200, and (d) 3.0W+C200+P50.

$$\tau = (1 - \beta)\tau_b + \beta\tau_f, \quad (3)$$

where τ_b and τ_f are the shear strengths provided by bonding element and frictional element, respectively, and β is the shear resistance share ratio.

It has been well documented that atmospheric pressure can be used in the strength reference framework to investigate the strength of the solidified soil [14, 46, 47]. The expression of shear strength provided by bonding element is assumed as follows:

$$\tau_b = \frac{q_u}{2} (\sigma_{bm}/P_a)^n, \quad (4)$$

where q_u is the unconfined compressive strength, $\sigma_{bm} = (\sigma_{1b} + \sigma_{2b} + \sigma_{3b})/3$ is the mean stress of bonding element, P_a is the standard atmospheric pressure, and n is an undetermined constant.

The shear strength provided by frictional element follows the Mohr–Coulomb criterion. It is the proportional function of normal stress and can be expressed as

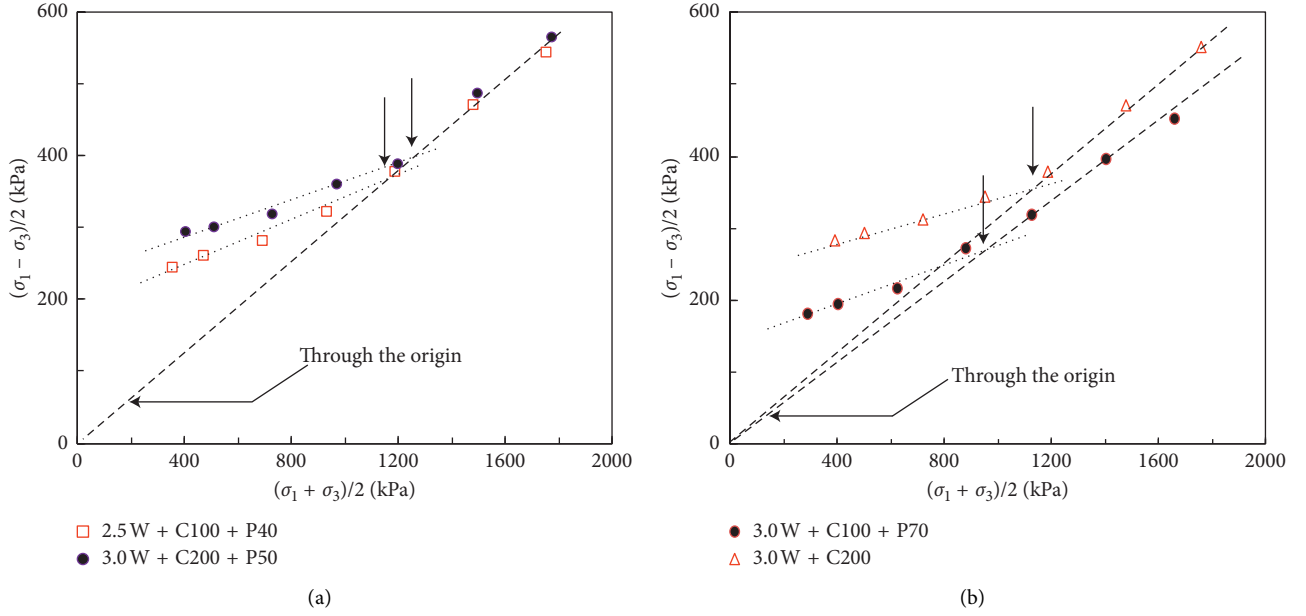


FIGURE 7: Undrained shear strength versus normal stress: (a) 2.5W+C100+P40 and 3.0W+C200+P50; (b) 3.0W+C100+P70 and 3.0W+C200.

$$\tau_f = \sigma_f \tan \varphi, \quad (5)$$

where φ is the internal friction angle of frictional elements and $\sigma_f = (\sigma_{1f} + \sigma_{3f})/3$ is the average of the minor principal stress and the major principal stress.

According to the triaxial tests data, the evolution law of shear strength is significantly different between the preyield state and the postyield state. The parameter β used here is introduced from the expression suggested by Liu and Shen [14], as shown in Equation (6):

$$\beta = 1 - e^{-(\sigma_3/\sigma_{vy})^m}, \quad (6)$$

where σ_{vy} is the structure yield stress which can be obtained from oedometer test and also can be indirectly derived from unconfined compression test according to the empirical relationship suggested by some researchers [27, 48, 49], σ_3 is the minor principal stress, and m is an undetermined constant.

Substituting Equations (4)–(6) into Equation (3), the shear strength criterion of the SDM can be expressed as follows:

$$\tau = e^{-(\sigma_3/\sigma_{vy})^m} \frac{q_u}{2} (\sigma_m/P_a)^n + \left[1 - e^{-(\sigma_3/\sigma_{vy})^m} \right] \sigma \tan \varphi, \quad (7)$$

where q_u is the unconfined compressive strength, $\sigma_m = (\sigma_1 + \sigma_2 + \sigma_3)/3$, and $\sigma = (\sigma_1 + \sigma_3)/2$.

5. Parameters Discussion and Strength Criterion Verification

5.1. Parameters Discussion. The influence of parameters m and n is discussed as follows. First, the influence of m is discussed with the assumption that n is a constant of 0.2 referenced the value suggested by Liu and Shen [14]. Other

TABLE 3: Values of other parameters for “ m ” discussion.

P_a (kPa)	q_u (kPa)	σ_{vy} (kPa)	φ (°)
101.4	400	550	18

parameters are listed in Table 3. The influence of the parameter m to evolution laws of shear strength is shown in Figure 8. It can be seen that when $m = 0.1$, shear resistance is nearly one straight line and similar with the conventional Mohr–Coulomb criterion. In addition, it is interesting to note that when $m \geq 3$, not only all curves are very close but also the extensions of strength envelope are nearly through the origin in the postyield state. By comparison, the shape of curve is closer to the experimental curve when $m = 3$. Hence, $m = 3$ is suggested in this paper.

Subsequently, the value of n was discussed with the assumption that m is a constant of 3, and the other parameters are shown in Table 3. The influence of the parameter n to evolution laws of shear strength is shown in Figure 9. It can be seen that the parameter n has more significant influence when the stress level is lower; however, when the stress level is higher, the parameter n almost has no effect on shear resistance and all curves nearly concentrate to one straight line, what is more, with the extension of the strength envelope through the origin in the postyield state. Figure 9 indicates that the cohesion of bonding element gradually vanishes, and the shear resistance is mainly provided by the frictional element after structure yield. Hence, the proposed strength criterion can well describe the evolution laws of shear strength for the SDM.

5.2. Strength Criterion Verification. In order to further verify the validity of the proposed shear strength criterion,

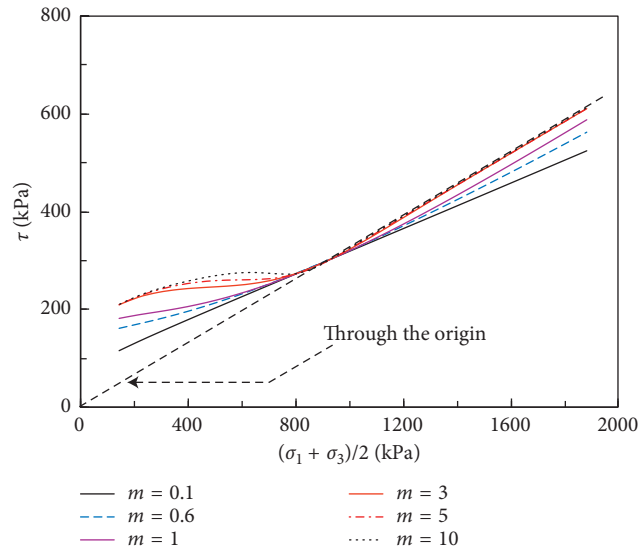


FIGURE 8: Influence of parameter m to evolution laws of shear strength.

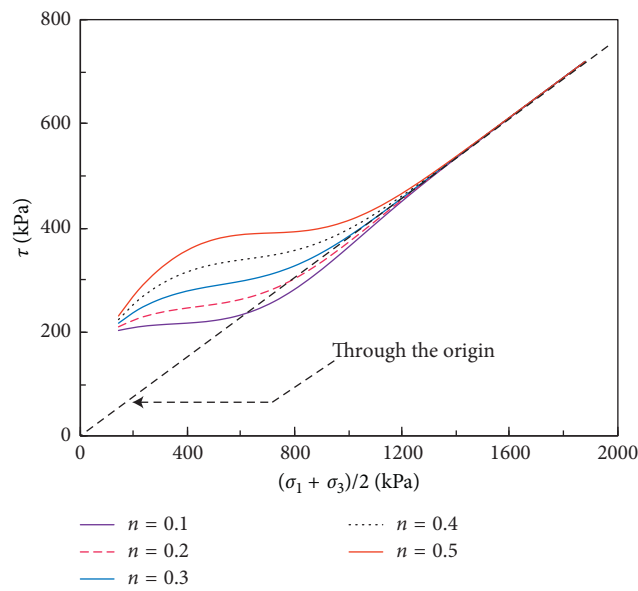


FIGURE 9: Influence of parameter (n) to evolution laws of shear strength.

comparisons between the simulation results obtained from the proposed strength criterion and the experimental data from triaxial tests are plotted in Figure 10. The parameters are determined as follows: $m = 3$, $P_a = 101.4$ kPa, σ_{vy} is determined according to one-dimensional compression test [27], q_u is determined according to unconfined compression test [50], φ is determined according to triaxial test in the postyield state, and n is an undetermined constant. The values of main parameters are summarized in Table 4.

Figure 10 presents comparisons of shear strength between simulation results and experimental data. The curve is mainly composed of two segments, the former is a slightly upward curve and the latter is nearly one

straight line. The suggested range of n is 0.1–0.3. And it can be seen that the extension of strength envelope is nearly through the origin when stress level is higher. The comparisons between predicted results and experimental data demonstrate that the proposed strength criterion is valid, and it can well describe the mechanical features and shear strength evolution laws.

Figure 11 presents the evolution laws of percentage of cohesion and internal friction with the increase in the normal stress for the mixing proportion of 2.5W+C100+P40, and the others are same. It can be seen that the total shear resistance is all provided by the bonding element at first, and the percentage of cohesion decreases gradually with the increase in the stress level. However, the

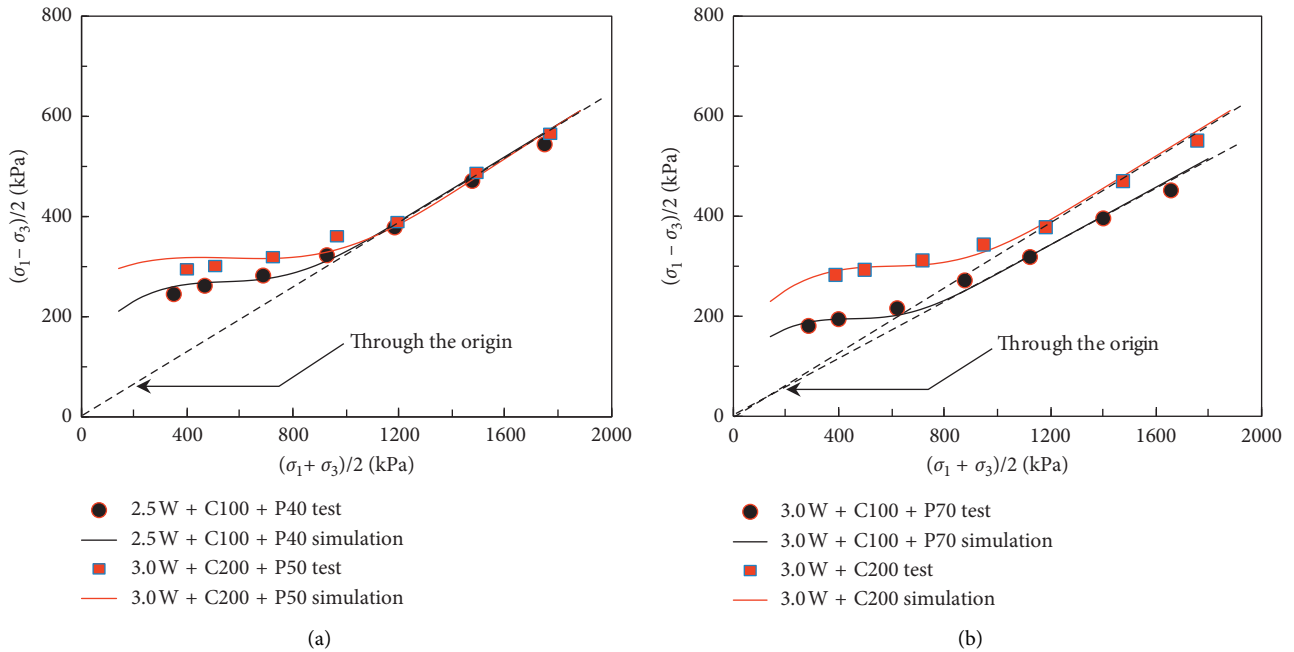


FIGURE 10: Comparisons between simulation results and test data: (a) 2.5W+C100+P40 and 3.0W+C200+P50; (b) 3.0W+C100+P70 and 3.0W+C200.

TABLE 4: Values of parameters for strength criterion verification.

Mixing proportion	Curing period	m	n	q_u (kPa)	σ_{vy} (kPa)	$\varphi(^{\circ})$
2.5W+C100+P40	28	3	0.3	392	510	18
3.0W+C100+P70	28	3	0.3	305	436	16
3.0W+C200	28	3	0.3	426	559	18
3.0W+C200+P50	28	3	0.1	621	760	18

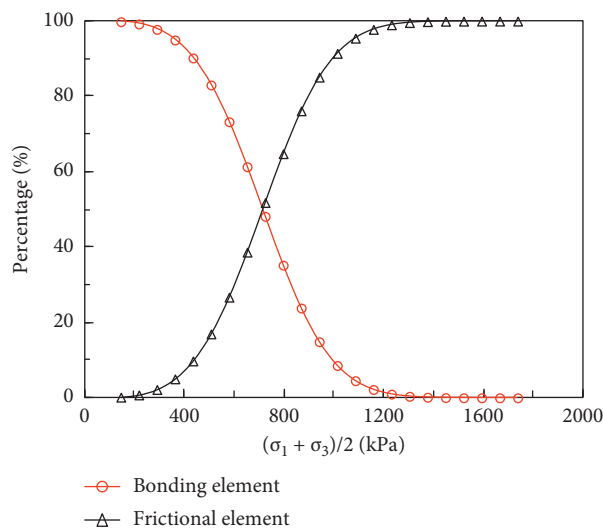


FIGURE 11: Percentage of cohesion and internal friction versus normal stress.

percentage of the internal friction increases with the increase in the stress level. Finally, with the bonding elements broken completely, the total shear resistance is fully provided by the frictional elements. Figure 11

indicates that the internal friction increases gradually with the increase in the stress level because of the bonding elements progressively breaking down and turning into frictional elements in essence.

6. Conclusions

The main conclusions obtained in this study are summarized as follows:

- (1) The peak deviator stress increases small when the confining pressure is low, for the change of the fabric in the consolidation process is insignificant at low confining pressures.
- (2) The undrained shear strength envelope is approximately consisted of two straight lines. The strength increases slightly with the increase in normal stress in preyield state; however, it increases significantly in postyield state with the extension of the strength envelope nearly through the origin.
- (3) In preyield state, the shear strength of the SDM is mainly affected by cementation bonding effect and governed by structure resistance; however, in postyield state, it is mainly attributed to internal friction and controlled by the applied normal stress.
- (4) A strength criterion considering strength evolution mechanism is proposed for the SDM. Comparisons of the predicted results and experimental data demonstrate that the proposed strength criterion can properly describe the mechanical features and strength evolution laws.

Data Availability

The data used to support the findings of this study are available from the corresponding author upon request.

Conflicts of Interest

The authors declare that they have no conflicts of interest.

Acknowledgments

This study was partially supported by the National Science and Technology Support Program Fund of China (Grant no. 2015BAB07B06), National Natural Science Foundation of China (Grant nos. 51378118 and 51608312), and Ministry of Water Resources Special Fund of China (Grant no. 201401006). The authors are grateful to Dr. Tao Cheng and Dr. Dong Tang for their constructive discussions, which are essential to the successful completion of this manuscript.

References

- [1] C. I. Chiu, W. Zhu, and C. L. Zhang, "Yielding and shear behaviour of cement-treated dredged materials," *Engineering Geology*, vol. 103, no. 1, pp. 1–12, 2008.
- [2] J. W. Ding, Z. S. Hong, and S. Y. Liu, "Triaxial shear test of flow-solidified soil of dredged clays," *Journal of Southeast University (Natural Science Edition)*, vol. 41, no. 5, pp. 1070–1074, 2011, in Chinese.
- [3] V. Dubois, N. E. Abriak, R. Zentar, and G. Ballivy, "The use of marine sediments as a pavement base material," *Waste Management*, vol. 29, no. 2, pp. 774–782, 2009.
- [4] Y. T. Kim, J. Ahn, W. J. Han, and M. A. Gabr, "Experimental evaluation of strength characteristics of stabilized dredged soil," *Journal of materials in civil engineering*, vol. 22, no. 5, pp. 539–544, 2009.
- [5] Y. Tang, Y. Miyazaki, and T. Tsuchida, "Practices of reused dredgings by cement treatment," *Soils and Foundations*, vol. 41, no. 5, pp. 129–143, 2001.
- [6] W. Zhu, C. L. Zhang, and A. C. Chiu, "Soil-water transfer mechanism for solidified dredged materials," *Journal of Geotechnical and Geoenvironmental Engineering*, vol. 133, no. 5, pp. 588–598, 2007.
- [7] D. G. Grubb, M. Chrysochoou, C. J. Smith, and N. E. Malasavage, "Stabilized Dredged Material. I: Parametric Study," *Journal of Geotechnical and Geoenvironmental Engineering*, vol. 136, no. 8, pp. 1011–1024, 2010.
- [8] K. Siham, B. Fabrice, A. N. Edine, and D. Patrick, "Marine dredged sediments as new materials resource for road construction," *Waste Management*, vol. 28, no. 5, pp. 919–928, 2008.
- [9] L. L. Zeng, Z. S. Hong, and Y. J. Cui, "On the volumetric strain-time curve patterns of dredged clays during primary consolidation," *Géotechnique*, vol. 65, no. 12, pp. 1023–1028, 2015.
- [10] M. Kamon, J. Jeoung, and T. Inui, "Alkalinity control properties of the solidified/stabilized sludge by a low alkalinity additive," *Soils and Foundations*, vol. 45, no. 1, pp. 87–98, 2005.
- [11] J. K. Mitchell, "Practical problems from surprising soil behavior," *Journal of Geotechnical Engineering*, vol. 112, no. 3, pp. 259–289, 1986.
- [12] J. B. Burland, "On the compressibility and shear strength of natural clays," *Géotechnique*, vol. 40, no. 3, pp. 329–378, 1990.
- [13] F. Cotecchia and R. J. Chandler, "A general framework for the mechanical behaviour of clays," *Géotechnique*, vol. 50, no. 4, pp. 431–447, 2000.
- [14] E. Liu and Z. Shen, "On the strength criterion for the structured soils," *Engineering Mechanics*, vol. 24, no. 2, pp. 50–55, 2007, in Chinese.
- [15] Z. Hong, S. Shen, Y. Deng, and T. Negami, "Loss of soil structure for natural sedimentary clays," *Proceedings of the Institution of Civil Engineers-Geotechnical Engineering*, vol. 160, no. 3, pp. 153–159, 2007.
- [16] H. Matsuoka and T. Nakai, "Stress-deformation and strength characteristics of soil under three different principal stresses," *Proceedings of the Japan Society of Civil Engineers*, vol. 232, pp. 59–70, 1974.
- [17] Y. P. Yao, D. Lu, A. N. Zhou, and B. Zou, "Generalized non-linear strength theory and transformed stress space," *Science in China Series E: Technological Sciences*, vol. 47, pp. 691–709, 2004.
- [18] Y. P. Yao, J. Hu, A. N. Zhou, T. Luo, and N. Wang, "Unified strength criterion for soils, gravels, rocks, and concretes," *Acta Geotechnica*, vol. 10, pp. 749–759, 2015.
- [19] A. N. Zhou, R.-Q. Huang, and D. Sheng, "Capillary water retention curve and shear strength of unsaturated soils," *Canadian Geotechnical Journal*, vol. 53, pp. 974–987, 2016.
- [20] H. Hanzawa and K. Adachi, "Overconsolidation of alluvial clays," *Soils and Foundations*, vol. 23, no. 4, pp. 106–118, 1983.
- [21] S. Horpibulsuk, N. Miura, and D. T. Bergado, "Undrained shear behavior of cement admixed clay at high water content," *Journal of Geotechnical and Geoenvironmental Engineering*, vol. 130, no. 10, pp. 1096–1105, 2004.
- [22] Y. Huang, W. Zhu, X. Qian, N. Zhang, and X. Zhou, "Change of mechanical behavior between solidified and remolded

- solidified dredged materials,” *Engineering Geology*, vol. 119, no. 3, pp. 112–119, 2011.
- [23] D. W. Hight, R. Böese, A. P. Butcher, C. R. I. Clayton, and P. R. Smith, “Disturbance of the Bothkennar clay prior to laboratory testing,” *Géotechnique*, vol. 42, no. 2, pp. 199–217, 1992.
- [24] Z. Hong and T. Tsuchida, “On compression characteristics of Ariake clays,” *Canadian Geotechnical Journal*, vol. 36, no. 5, pp. 807–814, 1999.
- [25] S. Leroueil and P. Vaughan, “The general and congruent effects of structure in natural soils and weak rocks,” *Géotechnique*, vol. 40, no. 3, pp. 467–488, 1990.
- [26] J. H. Schmertmann, “The mechanical aging of soils,” *Journal of Geotechnical Engineering*, vol. 117, no. 9, pp. 1288–1330, 1991.
- [27] J. W. Ding, X. C. Wu, H. Li, X. Bie, and F. Ji, “Compression properties and structure yield stress for solidified soil of dredged clays,” *Journal of Engineering Geology*, vol. 20, no. 4, pp. 627–632, 2012, in Chinese.
- [28] A. H. M. Kamruzzaman, S. H. Chew, and F. H. Lee, “Structuration and destructuration behaviour of cement-treated Singapore marine clay,” *Journal of Geotechnical and Geoenvironmental Engineering*, vol. 135, no. 4, pp. 573–589, 2009.
- [29] S. H. Chew, A. H. M. Kamruzzaman, and F. H. Lee, “Physicochemical and engineering behaviour of cement treated clays,” *Journal of Geotechnical and Geoenvironmental Engineering*, vol. 130, no. 7, pp. 696–706, 2004.
- [30] Z. S. Hong, J. Yin, and Y. J. Cui, “Compression behaviour of reconstituted soils at high initial water contents,” *Géotechnique*, vol. 60, no. 9, pp. 691–700, 2010.
- [31] A. B. Parreira, A. R. K. Kobayashi, and O. B. Silvestre Jr., “Influence of Portland cement type on unconfined compressive strength and linear expansion of cement-stabilized phosphogypsum,” *Journal of Geoenvironmental Engineering*, vol. 129, no. 10, pp. 956–960, 2003.
- [32] W. Shen, M. Zhou, and Q. Zhao, “Study on lime-fly ash-phosphogypsum binder,” *Construction and Building Materials*, vol. 21, no. 7, pp. 1480–1485, 2007.
- [33] H. Tayibi, M. Choura, F. A. López, F. J. Alguacil, and A. López-Delgado, “Environmental impact and management of phosphogypsum,” *Journal of Geoenvironmental Engineering*, vol. 90, no. 8, pp. 2377–2386, 2009.
- [34] G. Xu, F. Gao, Z. Hong, and J. Ding, “Sedimentation behavior of four dredged slurries in China,” *Marine Georesources and Geotechnology*, vol. 30, no. 2, pp. 143–156, 2012.
- [35] T. Luo, Y. P. Yao, A. N. Zhou, and X. G. Tian, “A three-dimensional criterion for asymptotic states,” *Computers and Geotechnics*, vol. 41, pp. 90–94, 2012.
- [36] J. K. Mitchell, *Fundamentals of Soil Behavior*, Wiley, New York, NY, USA, 2nd edition, 1992.
- [37] Y. P. Yao, W. Hou, and A. N. Zhou, “Constitutive model for overconsolidated clays,” *Science in China Series E: Technological Sciences*, vol. 51, pp. 179–191, 2008.
- [38] Y. P. Yao, W. Hou, and A. N. Zhou, “UH model: three-dimensional unified hardening model for overconsolidated clays,” *Géotechnique*, vol. 59, pp. 451–469, 2009.
- [39] Y. P. Yao and A. N. Zhou, “Non-isothermal unified hardening model: a thermo-elastoplastic model for clays,” *Géotechnique*, vol. 63, pp. 1328–1345, 2013.
- [40] S. M. Rao and P. Shivananda, “Compressibility behaviour of lime-stabilized clay,” *Geotechnical and Geological Engineering*, vol. 23, no. 3, pp. 309–319, 2005.
- [41] F. Sariosseiri and B. Muhunthan, “Effect of cement treatment on geotechnical properties of some Washington state soils,” *Engineering Geology*, vol. 104, no. 1, pp. 119–125, 2009.
- [42] J. Suebsuk, S. Horpibulsuk, and M. D. Liu, “Modified structured cam clay: a generalised critical state model for destructured, naturally structured and artificially structured clays,” *Computers and Geotechnics*, vol. 37, no. 7, pp. 956–968, 2010.
- [43] J. Wang, C. Leung, and Y. Ichikawa, “A simplified homogenisation method for composite soils,” *Computers and Geotechnics*, vol. 29, no. 6, pp. 477–500, 2002.
- [44] Y. G. Chen, L. Y. Jia, W. M. Ye, B. Chen, and Y. J. Cui, “Advances on experimental investigation on hydraulic fracturing behavior of bentonite-based materials used for HLW disposal,” *Environmental Earth Sciences*, vol. 75, pp. 787–800, 2016.
- [45] Z. Shen, “Breakage mechanics for geological materials: An ideal brittle-elastic-plastic model,” *Chinese Journal of Geotechnical Engineering*, vol. 25, no. 3, pp. 253–257, 2003, in Chinese.
- [46] G. A. Lorenzo and D. T. Bergado, “Fundamental parameters of cement-admixed clay-new approach,” *Journal of Geotechnical and Geoenvironmental Engineering*, vol. 130, no. 10, pp. 1042–1050, 2004.
- [47] P. Jongpradist, S. Youwai, and C. Jaturapitakkul, “Effective void ratio for assessing the mechanical properties of cement-clay admixtures at high water content,” *Journal of Geotechnical and Geoenvironmental Engineering*, vol. 137, no. 6, pp. 621–627, 2011.
- [48] S. Horpibulsuk, D. T. Bergado, and G. A. Lorenzo, “Compressibility of cement-admixed clays at high water content,” *Géotechnique*, vol. 54, no. 2, pp. 151–154, 2004.
- [49] Y. Tang, H. Liu, and W. Zhu, “Study on engineering properties of cement-stabilized soil,” *Chinese Journal of Geotechnical Engineering*, vol. 22, no. 5, pp. 549–554, 2000, in Chinese.
- [50] J. W. Ding, T. P. Liu, Y. P. Cao, R. M. Yang, and G. Wang, “Unconfined compression tests and strength prediction method for solidified soils of dredged clays with high water content,” *Chinese Journal of Geotechnical Engineering*, vol. 35, no. 2, pp. 55–60, 2013, in Chinese.

Research Article

Studying Shear Performance of Flax Fiber-Reinforced Clay by Triaxial Test

Qiang Ma , Yicong Yang , Henglin Xiao , and Wenwen Xing 

Hubei University of Technology, School of Civil Architecture and Environment, Wuhan 430068, China

Correspondence should be addressed to Henglin Xiao; xiao-henglin@163.com

Received 22 June 2018; Accepted 4 September 2018; Published 15 October 2018

Guest Editor: Yonggui Chen

Copyright © 2018 Qiang Ma et al. This is an open access article distributed under the Creative Commons Attribution License, which permits unrestricted use, distribution, and reproduction in any medium, provided the original work is properly cited.

Laboratory triaxial tests were carried out to investigate the reinforcement mechanism, to study the characteristics of flax fiber-reinforced clay, and to discuss the effect on stress-strain relationship and shear strength parameters of flax fiber-reinforced clay in different flax fiber content and different confining pressure. Respectively, the ratio of fiber content to clay by weight is 0.2%, 0.4%, 0.6%, 0.8%, and 1.0%, and the confining pressure is 100 kPa, 200 kPa, and 300 kPa in triaxial test. The test results show that, the shear strength of flax fiber-reinforced clay is greater than that of pure clay. Compared with the pure clay, the shear strength of flax fiber-reinforced clay increased as the cohesion and friction increased; while the increase of the friction is relatively small, the increase of cohesion is large. The shear strength firstly increased and then reduced with the increase of flax fiber content. When the fiber content was 0.8%, the shear strength reached a peak value, and the shear strength reduced with the further increase of fiber content.

1. Introduction

The strength and antideformation capacity of natural plain soil are often insufficient to meet engineering requirements of soil. The addition of reinforcement to soil can restrict the deformation and increase the strength of soil. At present, the normally used reinforcing materials in soil are fiber, metal bar, and geosynthetics. Among them, the fiber is beneficial to tensile and crack resistances, as it can be evenly distributed in soil, which makes the mechanical properties of fiber-reinforced soil approach to isotropy and effectively make up for the deficiency of traditional reinforced soil [1, 2]. Fiber reinforcement technology is always a hot topic in the research field of soil improvement [3–6]. The results of the previous studies show that the compression strength, the shear strength, the tensile capacity, and the bearing capacity of soil can be effectively improved by the reinforcement of polypropylene and other synthetic fibers. Besides, the strain of soil under failure can be also increased, and the loss of strength can be reduced, which makes the soil sample represent higher toughness [7, 8].

Shear failure of soil often cause disaster in geotechnical engineering. The shear strength of soil can be improved by

adding certain amount of fiber. Prabakar and Sridhar [9] and Consoli et al. [10] compared the shear strength index of plain soil with that of fiber-reinforced soil by experiments; the results show that the addition of fiber can increase the shear strength of soil. Yetimoglu and Salbas [11] mentioned that fiber reinforcement had no significant effect on the peak shear strength, but the residual shear strength of sand increased. Zhu et al. [12] studied the interaction between fiber and surrounding soil through shear tests, and then analyzed the reinforcement process and its mechanism of short fiber. In general, direct shear tests and triaxial compression tests are carried out to investigate the shear strength characteristics of fiber-reinforced soil. In terms of direct shear tests, Garry and Ohashi [13] studied the effects of different fiber inclining angles on the working mechanism of fiber-reinforced sand. Welker and Josten [14] conducted a series of direct shear tests to study the shear strength properties of polypropylene fiber-reinforced soil, and the optimum fiber content was determined to be 0.2%. Tang et al. [15] studied the strength characteristics of the fiber-reinforced cement soil. In terms of triaxial compression tests, Gray and Alrefeai [16] carried out triaxial tests on the stress-strain performance of fiber-reinforced sand with

nondiscrete distribution, and the test results show that the fiber increases the axial strain of reinforced sand when it is destroyed, and reduces the loss of postpeak strength. Ranjan et al. [17] carried out triaxial tests on medium and coarse sand reinforced with fiber, and the results show that the peak strength of fiber-reinforced soil is enhanced with the increase of fiber content, and the residual strength is higher than that of plain soil. In addition, the shear strength of fiber-reinforced soil is linearly correlated with the content of fiber. Yetimoglu et al. [18] carried out triaxial tests on fiber-reinforced sand, and the results show that the shear strength of fiber-reinforced sand was obviously increased compared with that of nonreinforced sand. Botero et al. [19] put regenerated polyester resin (PET) fiber into silt and studied the stress-strain characteristics of fiber-reinforced soil by unconsolidated and undrained shear test. The results show that PET fiber can greatly improve the ability of soil to resist deformation. The results of the previously mentioned studies and some other studies show that the strength of fiber-reinforced soil is related to many factors, such as fiber type, content, thickness, length, and so on [20–23].

The aforementioned fiber used in reinforcing soil is mainly artificial synthetic fiber. Although artificial synthetic fiber has the characteristics of high strength, acid and alkali resistance, it is costly and not green in manufacturing and transporting. At the same time, due to the increasingly severe global energy and environmental problems, more and more attention has been paid to the research of natural reinforced materials with the development of ecological civilization [24]. Endo [25] and Wu et al. [26] found that the horizontal and vertical roots of plants could improve the shear strength of soil by laboratory experiments. Ma'Ruf [27] conducted direct shear tests on soil containing plant roots to study the effects of roots of bamboo on the shear strength of soil. Bergado and Bukkanasuta [28] selected bamboo as reinforced material; its reinforcement effect was studied by direct shear tests and pull out tests in laboratory, and the results show that the reinforcement effect of bamboo net is slightly better than that of geogrid. Prabakar and Sridhar [9] used sisal fiber to reinforce silty clay; the effects of fiber content, length, and other factors on the strength parameters and compaction characteristics were investigated by triaxial test and compaction test, and the results showed that sisal fiber can effectively increase the maximum deviatoric stress of clay. Suits et al. [29] carried out triaxial unconsolidated undrained tests on coconut shell fiber-reinforced soft clay, and the tests results showed that 1% is the optimal fiber reinforcement ratio, and the reinforcement effect is more obvious under high confining pressure. Adili et al. [30] pointed out that the friction and cohesion of silt with sandy reached the maximum value when reinforcement ratio of papyrus reaches 10%. Mohamed et al. [31] studied the use of hay fiber to improve the properties of expansive clay. Zekkos et al. [32] tested the mixed soil consists of cardboard and plastic fiber, wood fiber, municipal solid waste, and other fiber, which proves that wood fiber is the best to improve the shear resistance of soil. Anggraini et al. [33] took coconut shell fiber as reinforced material, and considered that fiber content is the main factor affecting the strength of reinforced

soil. The abovementioned studies show that natural fiber also performs good reinforcement effects. The acquisition and selection of natural fibers is mostly based on the ecological environment of the project, and there are many kinds of materials that can be selected locally [34]. These studies expand the sources and fields of reinforced material; however, there are relatively few research studies on the behavior of flax fiber-reinforced clay at present.

In this paper, the laboratory triaxial tests were carried out to investigate the mechanical properties and failure characteristics of flax fiber-reinforced clay, by controlling the reinforcement ratio and confining pressure. On the basis of triaxial tests, the relationship between the parameters (principal stress difference, shear strength, cohesion, and fraction) with reinforcement ratio and confining pressure of flax fiber-reinforced clay were investigated. Furthermore, the reinforcement mechanism of flax fiber was also discussed.

2. Materials and Methods

2.1. Materials. The clay used in the triaxial tests was taken from a 9 m deep foundation pit located at Han street in Wuhan, and its physical parameters are listed in Table 1. The fibers used in the test were flax fibers, which were taken from the flax trees on the campus of Hubei University of Technology. The tensile force and deformation curve of the fiber was obtained by a series of tensile tests, the mean values of which are shown in Figure 1, and the mean values of the parameters of the flax fiber are listed in Table 2.

2.2. Methods. TSZ-2 automatic triaxial apparatus (produced by Nanjing soil instrument factory Co., Ltd.) was adopted for the tests. As shown in Figure 2, the apparatus is composed of triaxial instrument and data acquisition system. The triaxial tests of flax fiber-reinforced clay under unconsolidated and undrained (UU) condition were carried out; the loading rate was controlled at 0.50 mm/min; the reinforcement effect of flax fiber on clay was investigated by controlling the fiber content and confining pressure of the sample.

According to the requirements of the Chinese Highway Geotechnical Test Code [35], the samples were prepared for triaxial tests. Flax fibers with the diameter about 0.2 mm~0.4 mm were gathered from natural state; then sheared in length of 20 mm; and the selected clay was dried, mashed, and sifted. The weighed dry clay was mixed with the flax fiber evenly, and the moisture content of the sample was controlled at 15% by adding water. Then the flax fiber-reinforced clay was cured for 24 hours to make its moisture content stable. The reinforced clay weighing 175 g is used for the preparation of each sample, which was compacted in 5 layers by a unified compaction hammer from the same height, and the compaction degree of the samples was controlled; the final size of the samples was 39.1 mm in diameter and 90 mm in height. In order to study the effect of the mass percentage of flax fiber on the strength of reinforced clay, the tests were carried out with 0.2% (0.35 g), 0.4% (0.7 g), 0.6% (1.05 g), 0.8% (1.4 g), and 1.0% (1.75 g) of

TABLE 1: Parameters of clay.

Natural density (g/cm^3)	Natural moisture content (%)	Liquid limit (%)	Plastic limit (%)
2.027	21.9	38.946	20.4314

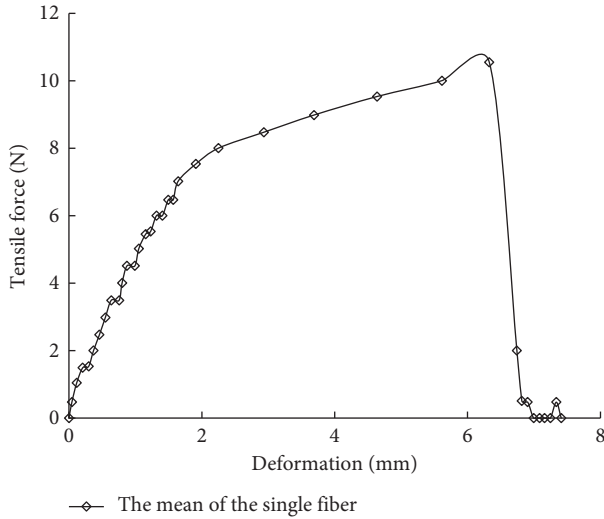


FIGURE 1: Tensile force versus deformation of flax fiber.

TABLE 2: Parameters of flax fiber.

Fiber length (mm)	Fiber diameter (mm)	Interface morphology	Ultimate tensile strength (MPa)	Modulus (GPa)
20	0.35	Sub-circular	127.54	0.51

flax fiber, respectively. In order to study the effect of confining pressure on the strength of reinforced clay, the tests were carried out for each group of samples at 100 kPa, 200 kPa, and 300 kPa, and there were 18 group tests in total in this study.

3. Results and Discussion

3.1. The Relationship between Principal Stress Difference ($\sigma_1 - \sigma_3$) and Axial Strain (ϵ_1). The testing results show that the axial strains of the samples are less than 15%. Figure 3 shows the relationship between the principal stress difference ($\sigma_1 - \sigma_3$) and the axial strain (ϵ_1) of pure clay and reinforced clay with fiber content of 0.2% at the confining pressure of 100 kPa, 200 kPa, and 300 kPa, respectively.

As it can be seen from Figure 3, (1) the difference of principal stress difference ($\sigma_1 - \sigma_3$) between pure clay and flax fiber-reinforced clay is smaller, and the curves are closer when the axial strain is small ($\epsilon_1 \leq 1\%$). With the increase of axial strain, the curves are gradually pulling away, and the principal stress difference of the flax fiber-reinforced clay is obviously larger than that of pure clay. (2) The principal stress difference of pure clay peaked at the axial strain less 15%, but that of the flax fiber-reinforced clay did not peak. The principal stress difference and axial strain curve of pure clay presents softening regulation; however, the curve



FIGURE 2: TSZ automatic triaxial test apparatus.

of principal stress difference and axial strain of flax fiber-reinforced clay presents hardening regulation, which indicates that the addition of flax fiber affects the strength and deformation resistance of clay.

Figure 4 shows the principal stress difference and axial strain relation curve of the flax fiber-reinforced clay under different confining pressures. As it can be seen from Figure 4, (1) the principal stress difference and axial strain curves of the flax fiber-reinforced clay are influenced by confining pressure, namely, the confining pressure affects the shear strength and deformation resistance of flax fiber-reinforced clay. (2) The curves of the flax fiber-reinforced clay are very close under different confining pressures when the axial strain is small ($\epsilon_1 \leq 1\%$). But with the increasing of the axial strain, the distance of the curves of flax fiber-reinforced clay under different confining pressures is gradually drawn apart and increased, which indicates that the influence of confining pressure on the principal stress difference of flax fiber-reinforced clay is becoming more obvious when the axial strain increases.

Comparing Figure 3 with Figure 4, it can be seen that (1) the difference of principal stress of flax fiber-reinforced clay increases with the increasing of the content of flax fiber, which indicates that fiber content affects the strength and deformation resistance of reinforced clay. (2) When the axial strain is less than 15%, under the confining pressure of 100 kPa, the content of flax fiber increases from 0.2% to 0.8%, the corresponding increments of principal stress difference are 58.38 kPa, 36.14 kPa, and 23.6 kPa, respectively. Under the confining pressure of 200 kPa, the increments of principal stress difference are 83.32 kPa, 86.33 kPa, and 38.9 kPa, respectively. Under the confining pressure of 300 kPa, the increments of principal stress difference are 38.36 kPa, 111.14 kPa, and 120.74 kPa,

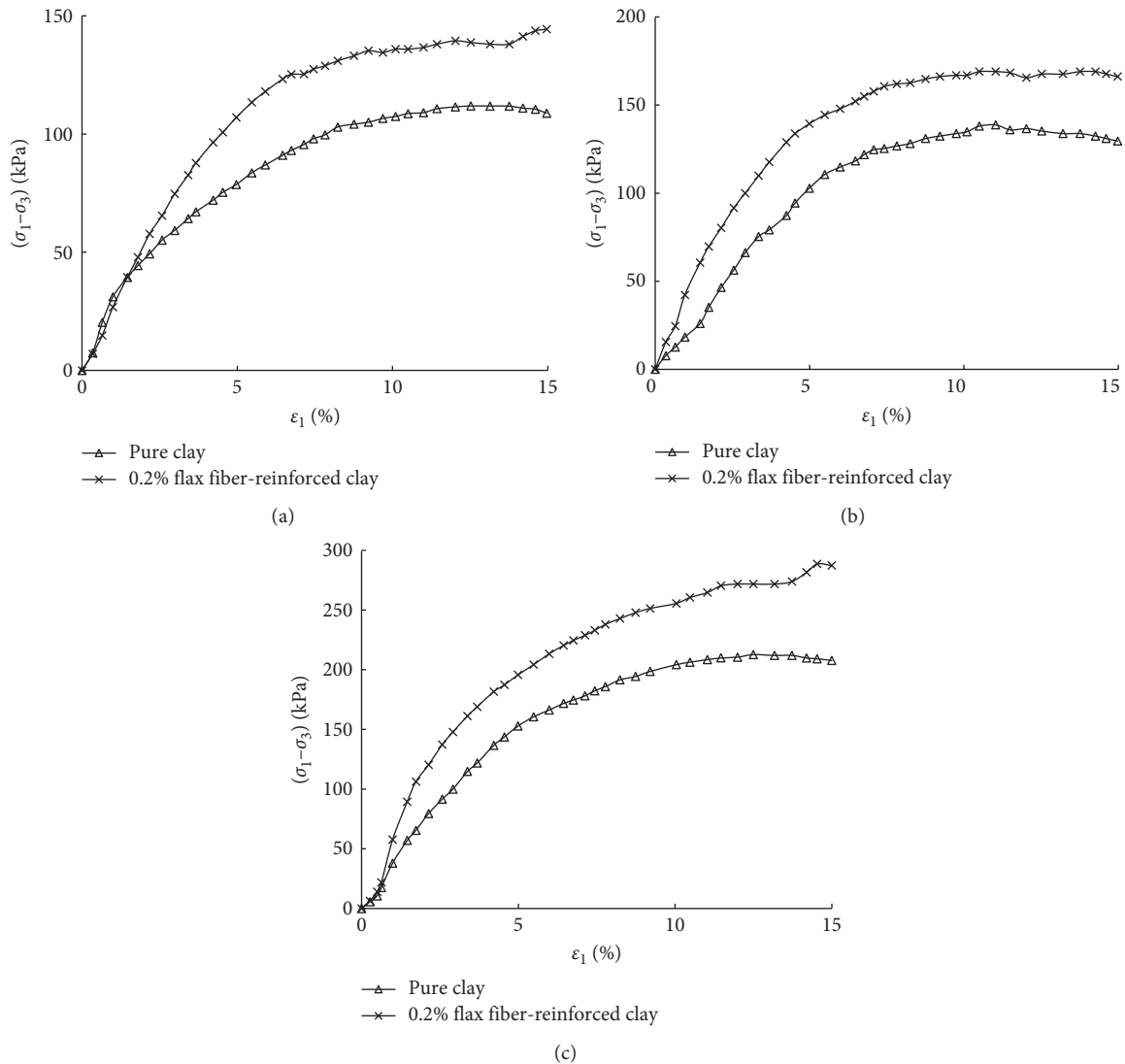


FIGURE 3: $(\sigma_1 - \sigma_3)$ versus ϵ_1 of pure clay and reinforced clay. (a) 100 kPa confining pressure; (b) 200 kPa confining pressure; (c) 300 kPa confining pressure.

respectively. It shows that the effect of the reinforcement ratio on the strength of reinforced clay is different, and the principal stress difference of flax fiber-reinforced clay changes nonlinearly with the increase of fiber content.

Figure 5 shows the principal stress difference and axial strain relation curves of the tested samples with different flax fiber content at the confining pressure of 200 kPa.

As it can be seen from Figure 5, (1) when the axial strain is small ($\epsilon_1 \leq 1\%$), the principal stress difference and axial strain relation curves of the pure clay and flax fiber-reinforced clay are closer, but with the increase of axial strain, the distance of the curves of the pure clay and flax fiber-reinforced clay was gradually drawn apart and increased. The results indicate that the reinforcing effect of flax fiber is becoming remarkable when the axial strain increases. (2) Compared with pure clay, the difference of principal stress of flax fiber-reinforced clay is higher, which indicates that flax fiber reinforcement can improve the shear strength of clay. (3) The principal stress difference and axial strain

curves of pure clay present softening regulation, but the curves of flax fiber-reinforced clay present hardening regulation; it indicates that the strength and deformation resistance of clay are enhanced by adding flax fiber. (4) The effects of different content of flax fiber on the strength of reinforced clay are different; the difference of principal stress of flax fiber-reinforced clay increases first and then decreases with the increasing of fiber content, which indicates that the best content of flax fiber-reinforced clay exists. (5) When the content of flax fiber is 0.8%, the relative principal stress difference of flax fiber-reinforced clay reaches a peak value; hence, the optimum content of flax fiber-reinforced clay is 0.8%.

3.2. *The Relationship between Principal Stress Difference $(\sigma_1 - \sigma_3)$ and Content of Flax Fiber.* Figure 6 shows the relationship between the difference of principal stress and the content of flax fiber. It can be seen that there is a nonlinear

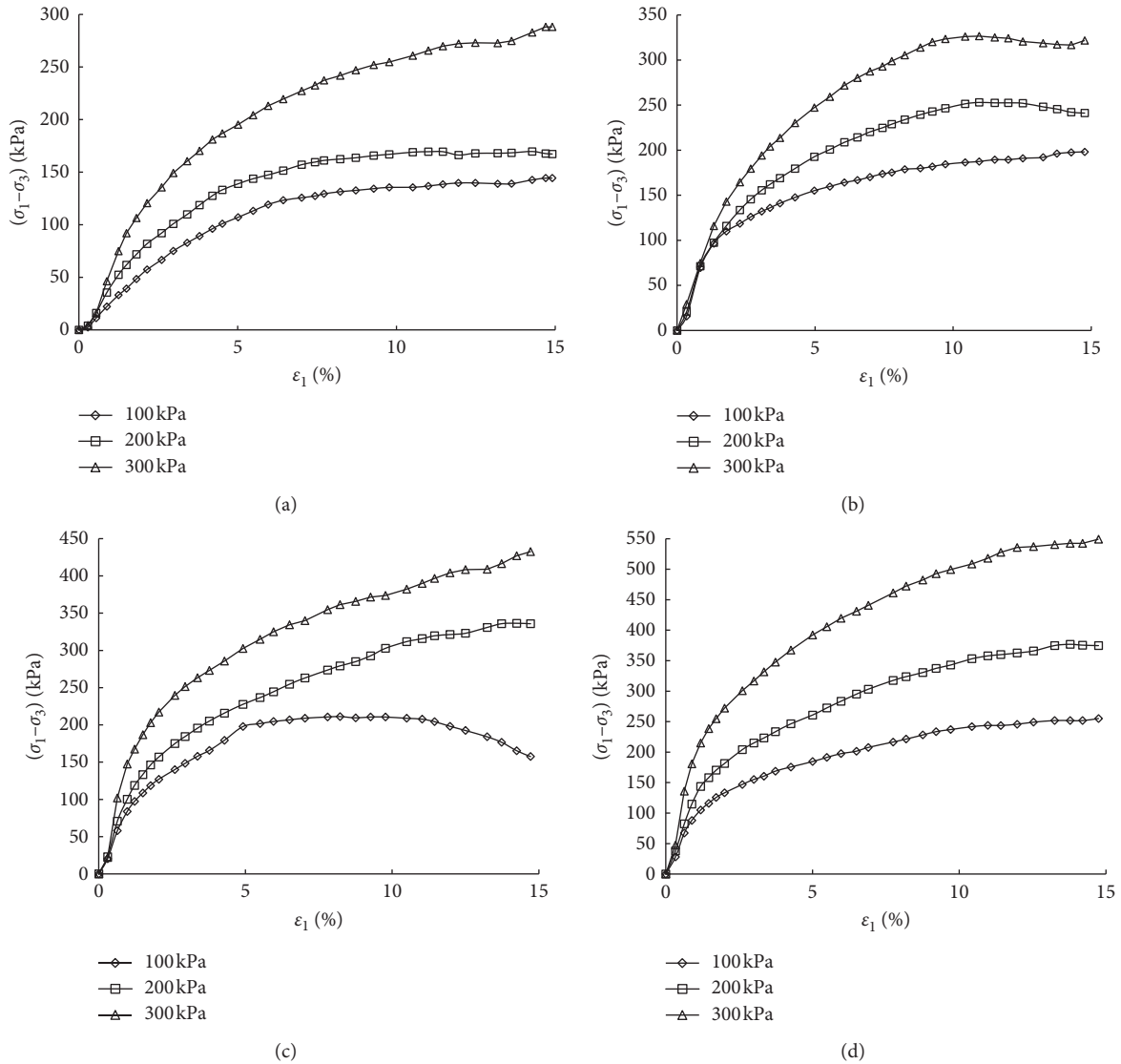


FIGURE 4: $(\sigma_1 - \sigma_3)$ versus ϵ_1 of soil with various confining pressure. (a) 0.2% reinforcement, (b) 0.4% reinforcement, (c) 0.6% reinforcement, and (d) 0.8% reinforcement.

relationship between the principal stress difference and the content of flax fiber under the same confining pressure, with the increase of content of flax fiber; the principal stress difference of reinforced clay first increases and then decreases, and there exists a peak value, that is the optimum content of flax fiber, and the optimum content of flax fiber measured at this test is 0.8%. When the content of flax fiber in clay is less, the contact area between clay and fiber is smaller. However, with the increase of fiber content, the contact area between fiber and clay extends, the friction resistance between them increases, and the axial deformation decreases, the reinforcing effect of flax fiber is more obvious. The difference of principal stress in the same axial strain is higher than that of the pure clay, and this value increases with the increase of the content of flax fiber until the peak value is reached; when the content of flax fiber exceeds the peak, because of the excessive content of flax fiber, flax fiber accumulates in the clay, which makes the flax

fiber not fully be in contact with clay to play the role of reinforcement and forms a kind of “barrier layer,” which interrupts the integrity of clay; after reaching the peak value, the principal stress difference decreases with the increase of the content of flax fiber.

3.3. Shear Strength of Flax Fiber-Reinforced Clay. Under the confining pressure of 100 kPa, 200 kPa, and 300 kPa, according to the test results of multiple samples, the mean value was used to draw the Mohr stress circle envelope, and the shear strength indexes of reinforced clay with different flax fiber contents were obtained. Taking the reinforced clay with 0.8% flax fiber as an example, Figure 7 is the Mohr stress circle envelope of reinforced soil with 0.8% content of flax fiber.

The cohesion c and friction angle φ can be obtained by combining the whole test, as listed in Table 3. As it can be

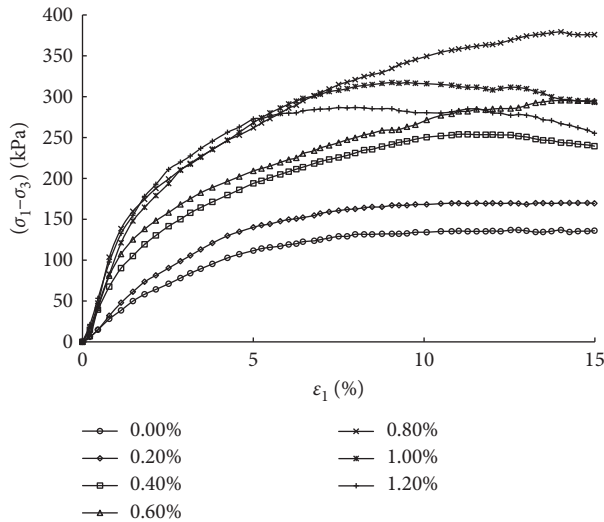


FIGURE 5: $(\sigma_1 - \sigma_3)$ versus ε_1 of reinforced clay.

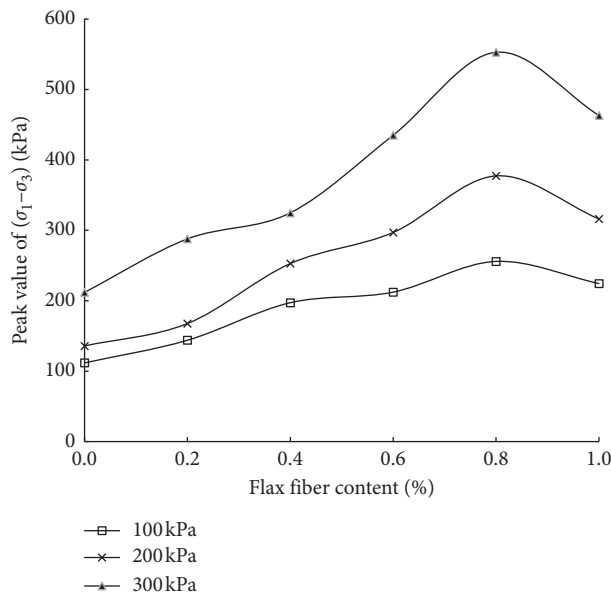


FIGURE 6: Peak value of $(\sigma_1 - \sigma_3)$ versus flax fiber content.

seen in Table 3, the cohesion and friction angle of flax fiber-reinforced clay are improved compared with pure clay; the increase of cohesion is higher, but the increase of friction angle is smaller. When the content of flax fiber is 0.20%, the cohesion of reinforced clay is increased by 3.04%, and the friction angle is only increased by 1.57%. When the content of flax fiber is 0.40%, the cohesion of reinforced clay is increased by 18.22%, and the friction angle is only increased by 10.59%. When the content of flax fiber is 0.60%, the cohesion of reinforced clay is increased by 28.40%, and the friction angle is only increased by 17.65%. When the content of flax fiber is 0.80%, the cohesion of reinforced clay is increased by 39.68%, and the friction angle is only increased by 6.67%. When the content of flax fiber is 1.00%, the cohesion of reinforced clay is increased by 31.00%, and the friction angle is only increased by 3.92%. That is to say, when

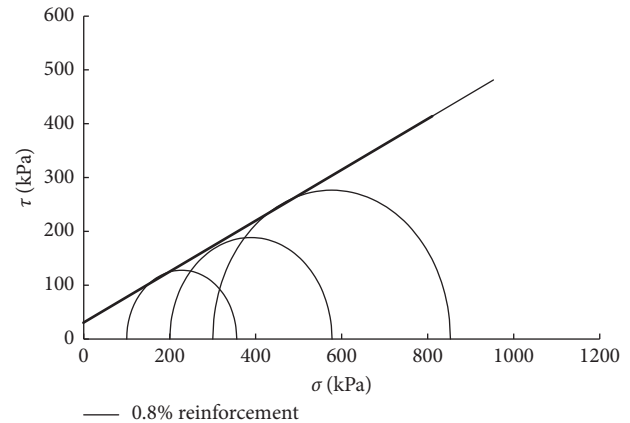


FIGURE 7: Mohr stress circle envelope of 0.8% reinforcement.

TABLE 3: Shear strength parameters.

Flax fiber content (%)	Shear strength index C (kPa)	φ ($^\circ$)
0.0	34.9	25.5
0.2	35.96	25.9
0.4	41.26	28.2
0.6	44.81	30
0.8	48.75	27.2
1.0	45.72	26.5

the content of flax fiber is greater than 0.80%, the cohesion of reinforced clay is mostly increased, and the friction angle is slightly increased; it shows that the effect of flax fiber-reinforced clay is mainly reflected in the increase of cohesion.

3.4. Discussion on Reinforcement Mechanism of Flax Fiber-Reinforced Clay. By analyzing the results of triaxial tests, it can be seen that the mechanical properties of flax fiber-reinforced clay have been improved; its shear strength parameters have been enhanced, namely, the cohesion and friction angle of the clay have been increased by adding flax fiber. The increment of cohesion is higher and the increment of friction angle is smaller, which indicates that the reinforcement of flax fiber mainly affects the cohesion of reinforced clay.

The reinforcement mechanism of flax fiber-reinforced clay can be explained by analyzing the state of fiber in reinforced clay. Flax fiber is randomly distributed in clay in the state shown in Figure 8, and the clay particles in the tests are discrete under a certain degree of compaction, the pores among particles are compressed, and the particles are mainly in surface contact state. When flax fibers are mixed in clay, it connects with clay particles; hence, the bonding between particles is strengthened. Besides, the integrity of reinforced clay is enhanced, the deformation and displacement of clay particles are effectively constrained, and the cohesion of reinforced clay increases. Thus, the shear strength of reinforced clay is improved. When the content of flax fiber is not high, the main distribution state of flax fiber in clay is as shown in Figures 8(a) and 8(b), and the distribution of flax

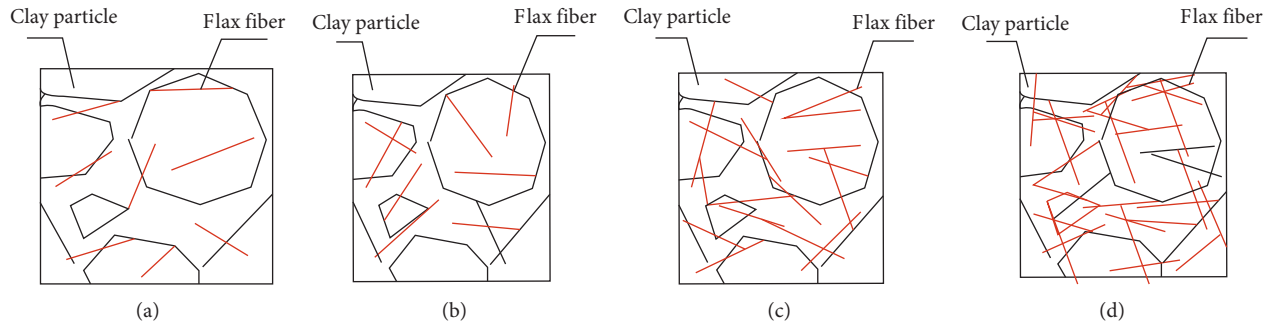


FIGURE 8: Distribution diagram of flax fiber. (a) Low content, (b) lower content, (c) optimum content, and (d) excessive content.

fiber in clay is more uniform, in a state of disjoint and partial or local intersecting; therefore, the tension of flax fiber strengthens the bond among clay particles, which enhances the shear strength of clay. When the content of flax fiber approaches the optimum content, the main distribution state of flax fiber in clay is as shown in Figure 8(c), the agglomeration of flax fiber in clay increases, and the interlacing among flax fiber is more obvious. Therefore, the flax fiber interlaces with each other and forms a network structure, and the local strengthening cell is formed; hence, the integrity of the clay sample increases, and the movements of the interlacing points caused by external force can be limited by the adjacent flax fiber when one of the fiber is stripped, so that the external forces can be transferred among the flax fibers. The flax fiber can withstand tension in all directions, realizing the decomposition of the force, promoting in the redistribution of internal forces in the sample. When the fiber content is more than the optimum content, the distribution of the fiber in the clay is obviously uneven, compared with the previous low content, as shown in Figure 8(d), part of the fibers is locally concentrated in clay, most of the fibers cannot contact with the clay particles, and thus they cannot fully play the role of reinforcement; these fibers separate the clay particles, and the integrity of clay is destroyed.

The flax fiber is randomly distributed in the clay, forming numerous interrelated local reinforcing cells in the clay; the reinforcing effect of this kind of local reinforcing cell mainly comes from the friction resistance between the fiber and clay and the spatial constraint of the fibrous network formed by the flax fiber.

4. Conclusions

The flax fiber reinforcement can both improve the properties of clay and reduce the engineering cost as it is a natural reinforcement material. From the laboratory triaxial test of flax fiber-reinforced clay, the following conclusions can be drawn.

- (1) As a reinforcement material, flax fiber can improve the strength and resist deformation of clay; the reinforcement effect of flax fiber is more obvious when the axial strain is larger.
- (2) The cohesion and friction angle of the reinforced clay are increased, but the increase of friction angle is smaller than that of the pure clay.
- (3) There is a nonlinear relationship between principal stress difference, shear strength, and fiber content. With the increasing of fiber content, the difference of principal stress and shear strength increase first and then decrease, and there exists a peak value, which is corresponding to the optimum flax fiber content of reinforced clay, and the optimum content is 0.8% at the confining pressure of 200 kPa.
- (4) The reinforcement mechanism of flax fiber is that the randomly distributed fiber in clay bend and interweave to form “local strengthening cell,” and the reinforcing effect of this kind of “local strengthening cell” mainly comes from the friction resistance between the fiber and clay and the spatial constraint of the fibrous network formed by the flax fiber.

Data Availability

The data used to support the findings of this study are available from the corresponding author upon request.

Conflicts of Interest

The authors declare that there are no conflicts of interest regarding the publication of this article.

Acknowledgments

This work was supported by grants from National Key R&D Program of China (No. 2016YFC0502208), National Natural Science Foundation of China (NSFC) (Nos. 51678223 and 51608181), and Green Industrial Project of Hubei University of Technology (YXQN2017001 and BSQD12153). The authors would like to express their appreciation to these financial assistances.

References

- [1] B. Fatahi, B. Fatahi, T. M. Le, and H. Khabbaz, “Small-strain properties of soft clay treated with fiber and cement,” *Geosynthetics International*, vol. 20, no. 4, pp. 286–300, 2013.
- [2] I. M. C. F. G. Falorca and M. I. M. Pinto, “Effect of short, randomly distributed, polypropylene microfibres on shear strength behaviour of soils,” *Geosynthetics International*, vol. 18, no. 1, pp. 2–11, 2011.
- [3] M. Jamei, P. Villard, and H. Guiras, “Shear failure criterion based on experimental and modeling results for fiber-

- reinforced clay,” *International Journal of Geomechanics*, vol. 13, no. 6, pp. 882–893, 2013.
- [4] C. S. Tang, B. Shi, and L. Z. Zhao, “Interfacial shear strength of fiber reinforced soil,” *Geotextiles and Geomembranes*, vol. 28, no. 1, pp. 54–62, 2010.
- [5] C. S. Tang, B. Shi, Y. J. Cui, and K. Gu, “Desiccation cracking behavior of polypropylene fiber-reinforced clayey soil,” *Canadian Geotechnical Journal*, vol. 49, no. 9, pp. 1088–1101, 2012.
- [6] M. Chen, S. L. Shen, A. Arulrajah, H. N. Wu, D. W. Hou, and Y. S. Xu, “Laboratory evaluation on the effectiveness of polypropylene fibers on the strength of fiber-reinforced and cement-stabilized Shanghai soft clay,” *Geotextiles and Geomembranes*, vol. 43, no. 6, pp. 515–523, 2015.
- [7] S. S. Kutanaei and A. J. Choobbasti, “Triaxial behavior of fiber-reinforced cemented sand,” *Journal of Adhesion Science and Technology*, vol. 30, no. 6, pp. 579–593, 2016.
- [8] C. S. Tang, D. Y. Wang, Y. J. Cui, B. Shi, and J. Li, “Tensile strength of fiber reinforced soil,” *Journal of Materials in Civil Engineering*, vol. 28, no. 7, article 04016031, 2016.
- [9] J. Prabakar and R. S. Sridhar, “Effect of random inclusion of sisal fibre on strength behaviour of soil,” *Construction and Building Materials*, vol. 16, no. 2, pp. 123–131, 2002.
- [10] N. C. Consoli, M. Casagrande, P. Prietto, and A. Thomé, “Plate load test on fiber-reinforced soil,” *Journal of Geotechnical and Geoenvironmental Engineering*, vol. 129, no. 10, pp. 951–955, 2003.
- [11] T. Yetimoglu and O. Salbas, “A study on shear strength of sands reinforced with randomly distributed discrete fibers,” *Geotextiles and Geomembranes*, vol. 21, no. 2, pp. 103–110, 2003.
- [12] H. H. Zhu, C. C. Zhang, C. S. Tang, B. Shi, and B. J. Wang, “Modeling the pullout behavior of short fiber in reinforced soil,” *Geotextiles and Geomembranes*, vol. 42, no. 4, pp. 329–338, 2014.
- [13] D. H. Garry and H. Ohashi, “Mechanics of fiber reinforcement in sand,” *Journal of Geotechnical Engineering*, vol. 109, no. 3, pp. 335–353, 1983.
- [14] A. L. Welker and N. Josten, “Interface friction of a geomembrane with a fiber reinforced soil,” in *Proceedings of Geo-Frontiers Congress 2005*, pp. 1–8, Austin, TX, USA, October 2005.
- [15] C. S. Tang, B. Shi, W. Gao, F. Chen, and Y. Cai, “Strength and mechanical behavior of short polypropylene fiber-reinforced and cement stabilized clayey soil,” *Geotextiles and Geomembranes*, vol. 25, no. 3, pp. 194–202, 2007.
- [16] D. H. Gray and T. Alrefeai, “Behavior of fabric-versus fiber-reinforced sand,” *Journal of the Geotechnical Engineering*, vol. 112, no. 8, pp. 804–820, 1986.
- [17] G. Ranjan, R. M. Vasani, and H. D. Charan, “Probabilistic analysis of randomly distributed fiber-reinforced soil,” *Journal of Geotechnical Engineering*, vol. 122, no. 6, pp. 419–426, 1996.
- [18] T. Yetimoglu, M. Iaanir, and O. E. Inanir, “A study on bearing capacity of randomly distributed fiber-reinforced sand fills overlying soft clay,” *Geotextiles and Geomembranes*, vol. 23, no. 2, pp. 174–183, 2005.
- [19] E. Botero, A. Ossa, G. Sherwell et al., “Stress-strain behavior of a silty soil reinforced with polyethylene terephthalate (PET),” *Geotextiles and Geomembranes*, vol. 43, no. 4, pp. 363–369, 2015.
- [20] N. Cristelo, V. M. C. F. Cunha, M. Dias, A. T. Gomes, T. Miranda, and N. Araújo, “Influence of discrete fiber reinforcement on the uniaxial compression response and seismic wave velocity of a cement-stabilised sandy-clay,” *Geotextiles and Geomembranes*, vol. 43, no. 1, pp. 1–13, 2015.
- [21] O. Plé and T. N. H. Lê, “Effect of polypropylene fiber-reinforcement on the mechanical behavior of silty clay,” *Geotextiles and Geomembranes*, vol. 32, no. 2, pp. 111–116, 2012.
- [22] C. A. Anagnostopoulos, D. Tzetzis, and K. Berketis, “Shear strength behaviour of polypropylene fibre reinforced cohesive soils,” *Geomechanics and Geoengineering*, vol. 9, no. 3, pp. 241–251, 2014.
- [23] L. Festugato, E. Menger, F. Benezra, E. A. Kipper, and N. C. Consoli, “Fiber-reinforced cemented soils compressive and tensile strength assessment as a function of filament length,” *Geotextiles and Geomembranes*, vol. 45, no. 1, pp. 77–82, 2017.
- [24] S. Gowthaman, K. Nakashima, and S. Kawasaki, “A state-of-the-art review on soil reinforcement technology using natural plant fiber materials: past findings, present trends and future directions,” *Materials*, vol. 11, no. 4, p. 553, 2018.
- [25] T. Endo, “Effect of tree roots upon the shear strength of soil,” *Japan Agricultural Research Quarterly*, vol. 14, no. 2, pp. 112–115, 1980.
- [26] T. H. Wu, P. E. Beal, and C. Lan, “In-situ shear test of soil-root systems,” *Journal of Geotechnical Engineering*, vol. 114, no. 12, pp. 1376–1394, 1988.
- [27] M. F. Ma’Ruf, “Shear strength of Apus bamboo root reinforced soil,” *Ecological Engineering*, vol. 41, no. 4, pp. 84–86, 2012.
- [28] D. T. Bergado and A. Bukkanasuta, “Laboratory pull-out tests using bamboo and polymer geogrids including a case study,” *Geotextiles and Geomembranes*, vol. 5, no. 3, pp. 153–189, 1987.
- [29] L. D. Suits, T. C. Sheahan, P. Vinod, A. Bhaskar, and C. S. Lekshmi, “Triaxial compression of clay reinforced with sand-coir fiber core,” *Geotechnical Testing Journal*, vol. 30, no. 4, pp. 333–336, 2007.
- [30] A. A. Adili, R. Azzam, G. Spagnoli, and J. Schrader, “Strength of soil reinforced with fiber materials (papyrus),” *Soil Mechanics and Foundation Engineering*, vol. 48, no. 6, pp. 241–247, 2012.
- [31] A. E. M. K. Mohamed, “Improvement of swelling clay properties using hay fibers,” *Construction and Building Materials*, vol. 38, no. 1, pp. 242–247, 2013.
- [32] D. Zekkos, A. Grizi, and G. Athanasopoulos, “Experimental investigation of the effect of fibrous reinforcement on shear resistance of soil-waste mixtures,” *Geotechnical Testing Journal*, vol. 36, no. 6, article 20120190, 2013.
- [33] V. Anggraini, B. B. K. Huat, A. Asadi, and H. Nahazanan, “Effect of coir fibers on the tensile and flexural strength of soft marine clay,” *Journal of Natural Fibers*, vol. 12, no. 2, pp. 185–200, 2015.
- [34] V. Sharma, H. K. Vinayak, and B. M. Marwaha, “Enhancing compressive strength of soil using natural fibers,” *Construction and Building Materials*, vol. 93, pp. 943–949, 2015.
- [35] The Professional Standards Compilation Group of People’s Republic of China, *JTG E40-2007, Highway Geotechnical Test Rules*, People’s Communications Press, Beijing, China, 2007.

Research Article

Investigating the Factors Affecting the Properties of Coral Sand Treated with Microbially Induced Calcite Precipitation

Wenni Deng  and Yue Wang 

School of Civil Engineering, Southeast University, Nanjing 211189, China

Correspondence should be addressed to Wenni Deng; wdeng@seu.edu.cn

Received 15 June 2018; Revised 28 August 2018; Accepted 18 September 2018; Published 15 October 2018

Guest Editor: Yonggui Chen

Copyright © 2018 Wenni Deng and Yue Wang. This is an open access article distributed under the Creative Commons Attribution License, which permits unrestricted use, distribution, and reproduction in any medium, provided the original work is properly cited.

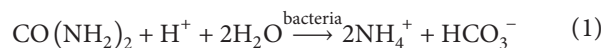
Microbial-induced carbonate precipitation (MICP) can be used to cement coral sand to improve its engineering properties to protect coastal structures. In this study, a series of laboratory tests were conducted to test the effect of the MICP method by using an ureolytic bacterium (*Sporosarcina pasteurii*). In order to determine the activity of bacteria, the growth properties of the microbial strain were observed under different culture conditions (different pH and temperature). The effect of partial size distribution and nutrient concentration on the soil permeability and unconfined compressive strength was then examined in coral sand. The results showed that the pH had less effect on the bacteria growth compared to temperature. The bacteria can growth well at pH over 8 and temperature higher than 20°C. The well-degraded soil has higher unconfined compressive strength (1.91–2.61 MPa) than poor-degraded soil (1.31 MPa). The similar trend was also found in permeability reduction. The unconfined compressive strength increased as the biocement solution concentration increased to 1 mol/L and then decreased at 1.5 mol/L.

1. Introduction

Coral sand is widely distributed on coral reefs and seashores in South China Sea. In coastal engineering, there are many buildings and breakwaters or other structures constructed on coral sand, or using coral sand as backfill materials for road embankment or airport runways. However, the coral sands consist of shells and corals with high void ratio. The strength is rather low compared to silica sand and can be easily crushed under load. So it is necessary to improve its strength before it is used as foundation or backfill materials. There are many traditional technologies such as pile driving, grouting, and vibrocompaction, which have been successfully applied to other soils. However, these methods are ineffective when applied to calcareous sand due to its high carbonate contents and low strength. For the grouting method, it may also cause pollution to the marine environment. Other methods may cause the breakdown of coral sand [1, 2].

In recent years, a novel ground improving method was proposed to minimize the environmental problems by microbial-induced carbonate precipitation (MICP [3, 4]).

The MICP technique involves two biochemical reactions: (1) the hydrolysis of urea by the urease enzyme produced by bacteria and (2) the precipitation of calcite with the presence of Ca^{2+} . With the production of calcite, the soil properties were changed. The chemical reaction equation can be expressed as follows:



MICP has a broad application in various conditions because it can reduce the permeability of soil and improve soil strength, mitigating liquefaction, and stabilizing costal sand dunes [5–14].

It has been well studied by the researchers to optimize the treatment in the laboratory or field experiments on silicon sand [7]. Harkes et al. reported that the unconfined compression strength (UCS) varied from 0.2 to 20 MPa according to the amount of calcite precipitation [15]. Others also found similar results that the UCS ranges from 1 to

12 MPa for silicon sand [16]. Meanwhile, the MICP effect quite relied on the experimental conditions, such as the pH, temperatures, and chemical species concentrations [6, 8, 17]. The change of the conditions can influence both the activity of the bacteria and the chemical reaction rate and then affect the precipitation of calcite. It is difficult to develop an injection approach that can generate homogeneous distributed calcite in the soil. Previous studies have reported non-homogeneous distribution of calcite in soil especially in long distance injection. In order to achieve a homogeneous calcite fill in the soil, they have tried to slow down the injection flow or inject with some fixation solution with bacteria. But these works did not completely solve the problem, more detailed researches are still required to get a better strategy.

Although soil improvement using MICP has shown a great promise in silicon sand, a few studies have been reported to apply the MICP effect on coral sand [13, 18, 19]. Based on the previous studies of the silicon sand, this study aimed at determining the efficiency of MICP treatment to improve the properties of coral sand. First, the growth characteristics of the bacteria were measured under various culture conditions. Then, a series of tests were conducted to explore the effect of particle size distribution and cementation solutions on the efficacy of MICP. Soil permeability and UCS tests were conducted on the biocemented soil columns.

2. Materials and Methods

2.1. Bacteria Cultivation. The test bacteria *Sporosarcina pasteurii* (ATCC 11859) was used in this study. The bacterial strain was cultured in the liquid medium under various conditions (pH and temperature) and found the optimal growth conditions. The cell density was quantified by measuring the absorbance of the suspension using a spectrophotometer at 600 nm wavelength (OD_{600}). The bacteria were first grown on the plate media and incubated at 30°C. The cultivation solution ingredients are listed in Table 1. After the plate growth, the bacteria were harvested and inoculated in the liquid media to grow for 24 h at 180 rpm with an aeration of 1 : 2.5 (200 mL of the media in a 500 mL flask) to an optical density of 600 nm (OD_{600}) of 1–1.3. This OD_{600} value can ensure the bacteria had high urease activity during the experiment.

The following two factors were analyzed to investigate the growth condition of the bacterial strain: (1) the pH of the liquid culture media ranged from 8 to 11 and (2) the culturing temperature varied from 5 to 35°C.

2.2. Soil Column Preparation. The sands used in this study were collected from Nansha Island. The sands were crushed down and sieved through 5 mm sieve to be used in the experiments. Three different particle size distributions (PSDs) were prepared by mixing different size sands. In Figure 1, soil #1 and #2 are classified as well graded, and #3 is poorly graded. The mean particle size of soil #1 is fine, and #3 is coarse. The summary of the properties (porosity e , dry density ρ_d , coefficient of uniformity C_u , and coefficient of

TABLE 1: Summary of the microbial-induced carbonate precipitation recipe.

Solution	Constituents
Growth media	0.5% peptone
	0.3% yeast extract 2% urea 10 mg/L $MnSO_4 \cdot H_2O$ with agar for plate growth
Cementation media	$CaCl_2$
	Urea

curvature C_c) is presented in Table 2. The relative density of soil was around 2.7–2.85 g/cm³.

The soil columns were prepared in a PVC column with 50 mm in diameter and 120 mm in height. A mesh and filter paper were placed at the bottom of the column to minimize the loss of soil particles during the test.

2.3. MICP Treatment. A peristaltic pump was used to inject the bacteria and cementation solutions to the soil column from the bottom to the top and then let it drain from the top to the bottom. The flow rate was set to 1 mL/min. Each sample was flushed by 1.5 pore volumes of bacteria-0.5 M $CaCl_2$ solution first. The bacteria- $CaCl_2$ solution was kept within the sample for 6 h to allow the bacteria to attach to the soil surface. Then, 1.5 pore volume cementation solutions (urea and $CaCl_2$) were pumped to the soil sample and kept for 12 h. The bacteria and cementation solution were injected four times as described before.

To determine the effect of various conditions on the UCS of the specimen, the following conditions were considered: the concentrations of urea and $CaCl_2$ used were 0.5 mol/L, 1.0 mol/L, and 1.5 mol/L. Each sample was prepared in triplicates.

3. Results and Discussion

3.1. Bacteria Growth Conditions Tests. The growth curve of the microbial strain in different culture conditions (pH and temperature) was obtained to investigate the effects of various conditions on bacterial growth.

3.1.1. The Effect of pH. The cell densities were reflected by the value of OD_{600} . OD_{600} obtained at different pH values from 8 to 11 is shown in Figure 2. The results showed that the OD_{600} can reach to above 1 after about 8 h. The data presented showed that there is only a slight difference between pH over 9 especially at the stable stage of the bacteria growth curve. It means that these bacteria prefer alkaline environment and can be used in the environmental pH at 9–11. For the biochemical reaction, the calcium carbonate precipitated when pH is above 8.3 and increased up to 9, and the pH tends to lower back to neutral afterwards [10, 20]. As the coral sand mainly exists in seawater, the pH is always larger than 7. So it is possible to apply these bacteria to coral sand from the aspect of the pH value.

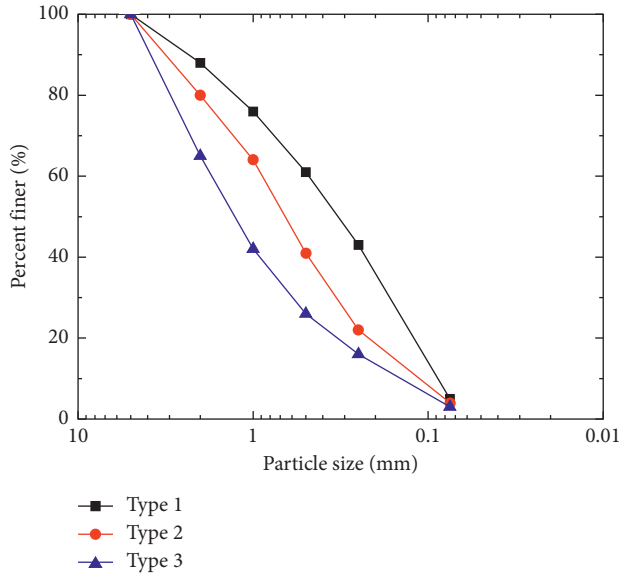


FIGURE 1: The soil particle distribution curve for 3 types of soil.

TABLE 2: Initial porosity and parameters for soils.

Parameter	Soil #1	Soil #2	Soil #3
e	0.91	0.85	1.11
ρ_d	1.46	1.51	1.35
C_u	4.82	6.93	9.56
C_c	1.03	1.30	1.38

3.1.2. *The Effect of Temperature.* In the tests, the bacteria were cultured at 5, 10, 20, 30, and 35°C to measure the growth curve. The bacteria densities increased with the increase in temperature. As shown in Figure 3, at low temperatures (5–10°C), the final OD₆₀₀ was less than 1.0, which was rather low to apply in soil. The best temperature for the bacteria growth is 30–35°C. It has also been reported by Whiffin [21] and van Paassen [16] that the urease activity increased with temperature up to 60°C.

From the aspect of temperature, the bacteria are not applicable to deep seabed but can be used in the offshore area. Or indigenous bacteria which can produce urease enzyme may be used to precipitate calcite in deep seabed.

The temperature had a more significant influence on the bacteria growth ability compared to the pH value (comparing Figures 2 and 3). So it is more important to control the temperature when applying the MICP technique in engineering applications. Thus, the bacteria used in the following soil column experiments were grown at 30°C with pH at 9.

3.2. *Permeability.* The soil permeability was measured during the MICP process after each injection of cementation solution.

3.2.1. *The Effect of Sand Particle Distribution.* Three different SPDs of coral sand were used in the experiments. The concentration of the cementation solution in these tests was

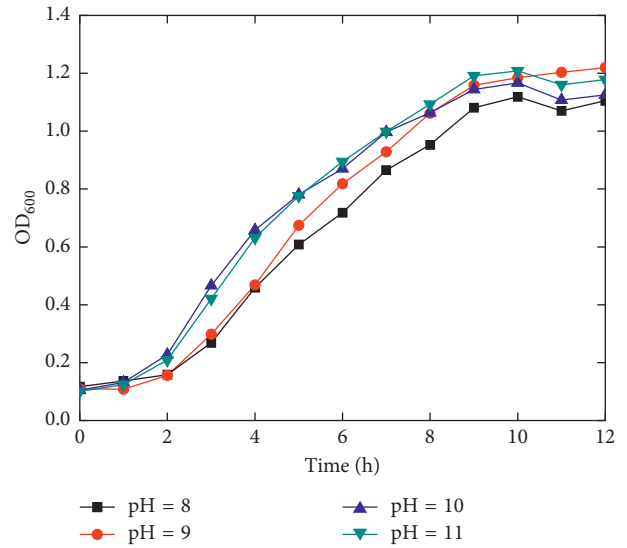


FIGURE 2: The OD₆₀₀ value of the bacteria solution at different pH values.

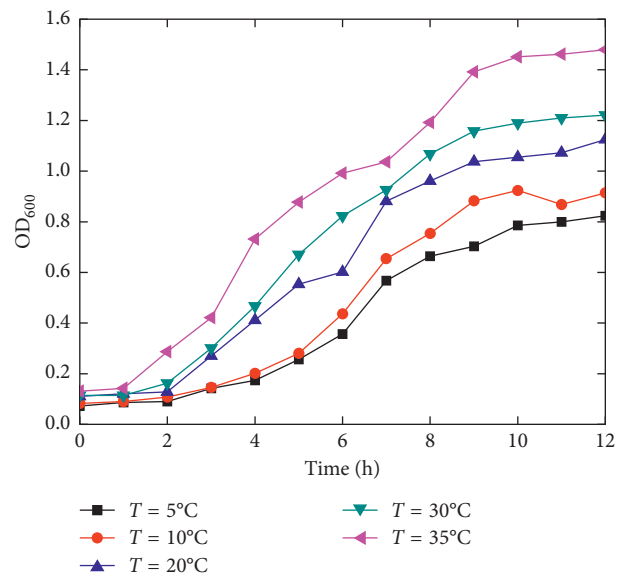


FIGURE 3: The OD₆₀₀ value of the bacteria solution at different temperatures.

1 mol/L. Figure 4 shows the cemented samples after the MICP process of three soil types. The loose sand was cemented together by the MICP. However, the cementation effect was not that good as there are still some pores at the surface, and the bonding between particles was weak. There were more calcite precipitated at the top of the column and less at the middle and bottom.

The permeability of three soils during the MICP process is shown in Figure 5. There was a significant reduction in soil #2 and a slight reduction in soil #1. For soil #3, the permeability almost remained the same before the MICP process. That was because soil #3 had a high initial porosity and larger particle size. The bacteria were difficult to attach

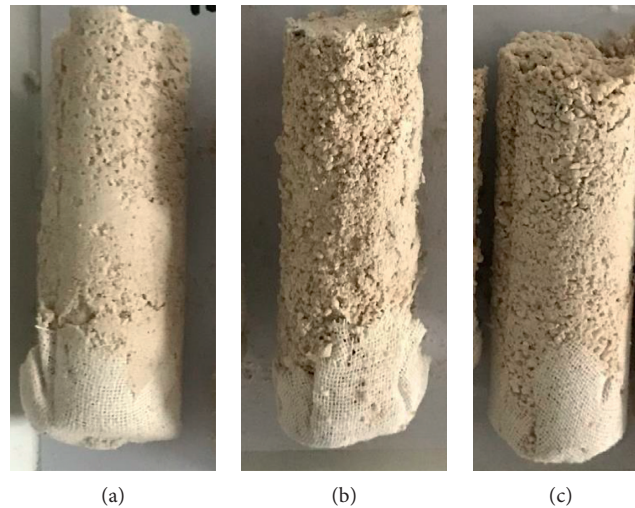


FIGURE 4: The soil column after the MICP process with different soil particle distributions: (a) soil #1; (b) soil #2; (c) soil #3.

to the soil particles and can be washed off by the injection flow even at very low flow rate. Meanwhile, even there were calcite precipitated between the soil particles, the pore space was not completely occupied to block the flow of water. For low porosity and finer sand particles, the soil pore space can easily be blocked by the calcite and then affect the biocementation effect. To reach a better cementation effect, the initial pore space cannot be too large or too small. Previous studies had reported that the optimal grain size for the biocementation process is between 50 and 400 μm for sand [22]. The MICP cannot take place in very fine sand, and larger amount of nutrients were required in coarser sand. However, there was less report about the effect of PSD.

3.2.2. The Effect of Solution Concentrations. Figure 6 shows that the cemented samples after the MICP process at three different solution concentrations of 0.5, 1, and 1.5 mol/L. The soil used in these experiments was soil #2. The biocementation effect of 1 mol/L and 1.5 mol/L was better than 0.5 mol/L as illustrated in Figure 6.

Figure 7 shows the permeability of soil #2 cemented at three different solution concentrations. The permeability was reduced after the biocementation process. When the solution concentrations were low at 0.5 mol/L, the calcite amount in soil was low. The permeability only changed slightly. For 1.0 and 1.5 mol/L, the permeability change almost had the same trend. The higher the solution concentration injected, the better the MICP effect.

3.3. Unconfined Compressive Strength

3.3.1. The Effect of Sand Particle Distribution. The soil was taken out from the column and dried for 7 days after the permeability test for the unconfined compressive strength test. Table 3 shows the UCS strength of three soils during the test. Unconfined compressive strengths were not obtained for every sample due to the poor cementation effect of some samples. Soil 2# was cemented the best compared to 1# and

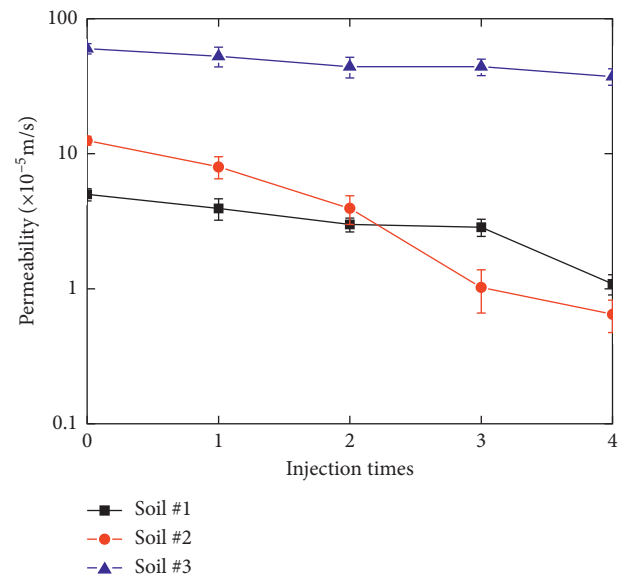


FIGURE 5: Soil permeability after each injection of the bacteria and cementation solution with different soil particle distributions.

3#. There were visible voids or deflections in soil 3# as the pores were larger. The UCS value was larger in soil 2# to about 2.61 MPa and 1.31 MPa for soil 3#. During the experiments, the same amounts of nutrients were injected to the column, but soil #1 and #3 had larger pore volumes than soil #2.

3.3.2. The Effect of Cementation Solution Concentration.

To investigate the effect of cementation solution concentration on MICP-treated coral sand, the sand column was prepared under three different cementation solution concentrations using soil #2. The soil was selected because of its best MICP efficiency as described before. Table 4 shows the UCS strength of soil biocemented with three solution concentrations. The biocementation effect of 1 mol/L and

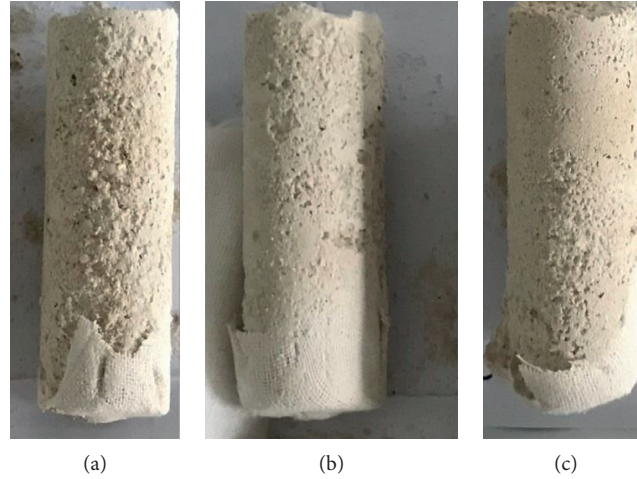


FIGURE 6: The soil column after the MICP process with different solution concentrations: (a) 0.5 mol/L; (b) 1 mol/L; (c) 1.5 mol/L.

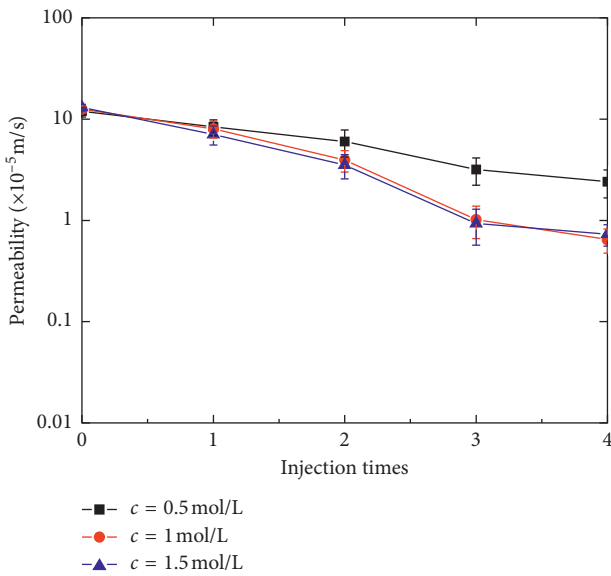


FIGURE 7: Soil permeability after each injection of the bacteria and cementation solution with different cementation solution concentrations.

TABLE 3: Soil UCS after the biocement process for 3 soil types.

Soil type	UCS (MPa)
Soil #1	1.93 ± 0.32
Soil #2	2.61 ± 0.51
Soil #3	1.31 ± 0.45

1.5 mol/L was better than 0.5 mol/L. Although the amount of calcite increased as the concentrations increased, the distribution pattern at the pore scale was also affected by the concentration. At higher concentration (1.5 mol/L), there were more calcite deposited at the inlet, while at lower concentration (mol/L), calcite distribution was more homogeneous.

TABLE 4: Soil UCS after the biocement process for 3 soil types.

Solution concentration (mol/L)	UCS (MPa)
0.5	1.53 ± 0.34
1	2.61 ± 0.55
1.5	2.31 ± 0.47

4. Conclusions

MICP is a complex biochemical process which has been used to improve coral sand properties. Identification of different factors enables the control of MICP in geotechnical engineering. Understanding how different treatments and sand properties could affect MICP is very important. This study describes the influence of pH and temperature on bacteria growth, soil particle size distribution, and solution concentrations on soil permeability and strength. Based on the experimental data, the following conclusions were drawn:

- (1) The pH values within 8–11 had little effect on the growth of bacteria.
- (2) The temperature had greater effect on the bacteria activity: at low temperature, the bacteria did not have high enough density for the MICP application. The best temperature is over 30–35°C.
- (3) The permeability of biocemented coral sand was reduced after the MICP process. However, the well-graded sand and medium porosity sand has a larger reduction in the permeability.
- (4) The results of UCS showed that the SPD and solution concentrations have an obvious effect on the MICP-treated coral sand. For well-cemented coral sand, the UCS can reach up to 2.6 MPa.

The MICP process was very complex. The results reported in this paper will be employed to further investigate the use of MICP on improving the soil strength.

Data Availability

All the data supporting the conclusions of this study are presented in the tables of the article.

Conflicts of Interest

The authors declare that they have no conflicts of interest.

Acknowledgments

This research project was financially supported by the National Natural Science Foundation of China (Grant no. 51508092), Jiangsu Province Science Foundation for Youths (Grant no. BK20150611), and a project funded by the Priority Academic Program Development of Jiangsu Higher Education Institutions.

References

- [1] Y. Xiao, H. Liu, P. Xiao, and J. Xiang, "Fractal crushing of carbonate sands under impact loading," *Geotechnique Letters*, vol. 6, no. 3, pp. 199–204, 2016.
- [2] P. Xiao, H. L. Liu, Y. Xiao, A. W. Stuedlein, and T. M. Evans, "Liquefaction resistance of bio-cemented calcareous sand," *Soil Dynamics and Earthquake Engineering*, vol. 107, pp. 9–19, 2018.
- [3] Z. Y. Wang, N. Zhang, G. J. Cai, Y. Jin, N. Ding, and D. Shen, "Review of ground improvement using microbial induced carbonate precipitation (micp)," *Marine Georesources & Geotechnology*, vol. 35, no. 8, pp. 1135–1146, 2017.
- [4] V. Achal and S. Kawasaki, "Biogrout: a novel binding material for soil improvement and concrete repair," *Frontiers in Microbiology*, vol. 7, 2016.
- [5] J. He, J. Chu, and V. Ivanov, "Mitigation of liquefaction of saturated sand using biogas," *Geotechnique*, vol. 63, no. 4, pp. 267–275, 2013.
- [6] W. K. Van Wijngaarden, F. J. Vermolen, G. A. M. Van Meurs, and C. Vuik, "Modelling biogrout: a new ground improvement method based on microbial-induced carbonate precipitation," *Transport in Porous Media*, vol. 87, no. 2, pp. 397–420, 2011.
- [7] L. Van Paassen, "Bio-mediated ground improvement: from laboratory experiment to pilot applications," in *Proceedings of Geo-Frontiers*, pp. 4099–4108, Dallas, TX, USA, March 2011.
- [8] J. T. Dejong, B. M. Mortensen, B. C. Martinez, and D. C. Nelson, "Bio-mediated soil improvement," *Ecological Engineering*, vol. 36, no. 2, pp. 197–210, 2010.
- [9] V. S. Whiffin, L. A. Van Paassen, and M. P. Harkes, "Microbial carbonate precipitation as a soil improvement technique," *Geomicrobiology Journal*, vol. 24, no. 5, pp. 417–423, 2007.
- [10] J. T. Dejong, M. B. Fritzges, and K. Nusslein, "Microbially induced cementation to control sand response to undrained shear," *Journal of Geotechnical and Geoenvironmental Engineering*, vol. 132, no. 11, pp. 1381–1392, 2006.
- [11] J. T. Dejong, B. M. Montoya, and R. W. Boulanger, "Dynamic response of liquefiable sand improved by microbial-induced calcite precipitation," *Geotechnique*, vol. 63, no. 4, pp. 302–312, 2013.
- [12] J. Chu, V. Ivanov, M. Naeimi, V. Stabnikov, and H.-L. Liu, "Optimization of calcium-based bioclogging and biocementation of sand," *Acta Geotechnica*, vol. 9, no. 2, pp. 277–285, 2014.
- [13] C. M. Bu, K. J. Wen, S. H. Liu, U. Ogbonnaya, and L. Li, "Development of bio-cemented constructional materials through microbial induced calcite precipitation," *Materials and Structures*, vol. 51, no. 1, 2018.
- [14] E. Salifu, E. Maclachlan, K. R. Iyer, C. W. Knapp, and A. Tarantino, "Application of microbially induced calcite precipitation in erosion mitigation and stabilisation of sandy soil foreshore slopes: a preliminary investigation," *Engineering Geology*, vol. 201, pp. 96–105, 2016.
- [15] M. P. Harkes, L. A. Van Paassen, J. L. Booster, V. S. Whiffin, and M. C. M. van Loosdrecht, "Fixation and distribution of bacterial activity in sand to induce carbonate precipitation for ground reinforcement," *Ecological Engineering*, vol. 36, no. 2, pp. 112–117, 2010.
- [16] L. A. van Paassen, *Biogrout, Ground Improvement by Microbially Induced Carbonate Precipitation*, Delft University of Technology, Delft, Netherlands, 2009.
- [17] A. R. Sotoudehfar, M. M. Sadeghi, E. Mokhtari, and F. Shafiei, "Assessment of the parameters influencing microbial calcite precipitation in injection experiments using taguchi methodology," *Geomicrobiology Journal*, vol. 33, no. 2, pp. 163–172, 2016.
- [18] M. N. H. Khan, G. G. N. N. Amarakoon, S. Shimazaki, and S. Kawasaki, "Coral sand solidification test based on microbially induced carbonate precipitation using ureolytic bacteria," *Materials Transactions*, vol. 56, no. 10, pp. 1725–1732, 2015.
- [19] M. N. H. Khan, S. Shimazaki, and S. Kawasaki, "Coral sand solidification test through microbial calcium carbonate precipitation using *pararhodobacter* sp.," *International Journal of Geomate*, vol. 11, no. 26, pp. 2665–2670, 2016.
- [20] S. Stocks-Fischer, J. K. Galinat, and S. S. Bang, "Microbiological precipitation of CaCO₃," *Soil Biology & Biochemistry*, vol. 31, no. 11, pp. 1563–1571, 1999.
- [21] V. S. Whiffin, *Microbial CaCO₃ Precipitation for the Production of Biocement*, Murdoch University, Murdoch, WA, Australia, 2004.
- [22] V. Rebata-Landa, *Microbial Activity in Sediments: Effects on Soil Behavior*, Georgia Institute of Technology, Atlanta, Georgia, 2007.

Research Article

Effect on the Resistance of Concrete Acid Corrosion in Superficial Soil Layers

Jihong Wei ¹, Jin Liu ¹, Yuxia Bai, ¹ Zezhuo Song, ¹ Qiao Feng, ¹ Yi Lu, ² and Shaorui Sun ¹

¹School of Earth Sciences and Engineering, Hohai University, Nanjing 210098, China

²Key Laboratory of Earth Fissures Geological Disaster, Ministry of Land and Resource (Geological Survey of Jiangsu Province), Jiangsu 210049, China

Correspondence should be addressed to Jin Liu; jinliu920@163.com

Received 17 April 2018; Accepted 25 September 2018; Published 15 October 2018

Guest Editor: Yongfeng Deng

Copyright © 2018 Jihong Wei et al. This is an open access article distributed under the Creative Commons Attribution License, which permits unrestricted use, distribution, and reproduction in any medium, provided the original work is properly cited.

To understand the effect and mechanism of urban heat island (UHI) and the acid corrosion of concrete on the strength of concrete in superficial soil layers from Nanjing area, both laboratory and field tests of accelerated corrosion of concrete were carried out and analyzed. The laboratory test results indicate that the concrete corrosion depends on acid concentration, tested time, and also on the temperature. The maximum corrosion coefficient (*K*-value) of 45.86%, as observed at 10% of acid concentration, 40°C of tested temperature, and 90 days of tested time, was about 2 times that of specimens with 10% of acid concentration, 5°C tested temperature, and tested after 90 days. The field test showed that the compressive strength of specimens in urban station was lower than that of specimens in rural station. The *K*-value of specimens with same acid concentration observed at urban area was higher than that of specimens at rural area. Both the laboratory and field tests showed that the temperature has an increasingly powerful influence on the concrete corrosion under acid environment. Therefore, the UHI effect will accelerate the acid corrosion in concrete construction and may affect the stability and durability of buildings in urban areas. The safety and life assessment of concrete buildings therefore require great attention.

1. Introduction

Urban heat island (UHI) means that the temperature in urban areas is considerably higher than that in surrounding rural areas. It is becoming more and more significant in many major cities [1–3]. Recently, UHI effect and its corresponding environmental problems are increasing with the rapid development of worldwide urbanization [4, 5]. The urban heat island intensity (UHII), which is the temperature difference between the urban area and the surrounding rural areas, was used to quantitatively describe the UHI effect [6]. It was demonstrated that the UHII in some major cities was as follows: 7.8°C in Mexico [7], 8.0°C in New York [8], 2.2°C in Alaska [9], 4.0°C in Singapore [10], 7.4°C in Shanghai [11], 3.3°C in Beijing [12], and 3.1°C in Nanjing [13]. Variation in temperature affects the engineering properties of soil in urban area, and consequently, the strength and stability of various engineered structures differ [14]. Many previous studies have shown that the increasing superficial soil

temperature influenced the soil permeability, suction of unsaturated soils, and shear strength of soil [15–17].

Most of the buildings in urban and rural areas are made up of concrete. The durability of the concrete constructions is of great concern for the construction industry [18, 19]. Among others, the acid corrosion is an important degradation process that affects the durability of concrete constructions [20–23]. Acid corrosion is the gradual destruction, or the wearing away, of materials by acidic compounds. The acids in superficial soil layers may come from the atmosphere, soil, or groundwater [24]. The concrete materials in the superficial soil layers are exposed to these acid environments whilst the temperature change will accelerate the acid corrosion of concrete construction [25–29]. Over the past century, many studies related to concrete deterioration in sulfate solution or chloride solution were widely conducted [30–32]. Tumidajski and Chan [33] proposed that the chloride penetration and diffusivity in the slag concrete increased the presence of sulfate ions.

However, limited studies have paid attention to the effects of "heat island" on the acid corrosion of concrete construction in superficial soil layers [13, 14, 34].

The main objective of this study is to evaluate the acid corrosion process of concrete in the superficial soil layers of urban area, which have higher ground temperature owing to the urban heat island effect. Laboratory and field tests of accelerated corrosion of concrete were carried out. The compressive strength properties of concrete specimens, cured at different temperatures (5°C, 20°C, and 40°C), different acid concentrations (0%, 5%, and 10%), and different tested times (30 days and 90 days), were studied by laboratory tests. The field contrast tests on the concrete specimens with three different concentrations of corrosion medium and different tested times were carried out in urban and rural observation stations. Finally, the mechanism of concrete acid corrosion and the urban heat island effect on the concrete strength of superficial soil layers in Nanjing area were analyzed.

2. Materials and Test Methods

2.1. Materials. In this study, sulfuric acid was selected as an aggressive medium for the test of accelerated acid attack. The different concentrations of sulfuric acid were prepared through dilution from concentrated sulfuric acid. A kind of quartz sand obtained from Nanjing city of China was used for this test. The range of particle size is 0.1~1 mm, and the physical properties of sand are presented in Table 1. Ordinary Portland cement (OPC, Jiangsu Sincerity Cement Co. Ltd., Xuzhou, China) was selected, and its chemical compositions and the physical properties are shown in Table 2.

2.2. Test Methods. In order to understand the effect of urban heat island (UHI) on the resistance of mortar to acid attack in superficial soil layers, both laboratory and field tests of accelerated acid attack on cement mortar were carried out. The UHI effect was evaluated by the variation of compressive strength of concrete specimens tested in acid solution at different temperatures. The mortar with cement to sand ratio of 0.4 was prepared for tests. The moisture content and dry density of the prepared samples were 10% and 1.70 g/cm³, respectively. The details of specimens for acid attack are given in Tables 3 and 4. Sand was mixed homogeneously with cement powder, and then predetermined amount of water was added. After that, sample was casted into moulds of 50 mm diameter and 80 mm height to prepare cylindrical specimens. After demoulding, all the specimens were cured in cement maintenance box for 28 days.

Nine groups of the specimens were tested in the laboratory, and another six groups were used for field test. In the laboratory, three different temperatures (5°C, 20°C and 40°C) and three different acid concentrations (0%, 5% and 10%) were applied. Each group of specimens was placed in plastic box that was filled with acid solution; subsequently, every three groups of specimens with different acid concentrations were kept in a temperature cabinet with constant temperature for 30 and 90 days, respectively, and then the compressive strengths were tested.

In the field, two different locations built with long-term observation stations in Nanjing, China, were selected, as illustrated in Figure 1. The temperatures of underground soil (0–300 cm depth) were recorded continuously. The urban observation station was located in an open yard near Hongshan Road, where the UHI was observed to be more specific [35]. The rural observation station is about 40 km away from the urban station, located in Gaomiao village, and generally surrounded by agricultural land. Three groups of specimens with three different concentrations of corrosion medium were placed in urban observation station, and the other three groups were placed in rural observation station. All the specimens were buried in superficial soil layers, and the schematic diagram of burial depth condition is shown in Figure 2. The compressive strength of each group of specimens was determined at 3 months, 6 months, 9 months, and 12 months. This field test was performed during April 1, 2011, to March 31, 2012. The compressive strength tests were carried out on June 30, September 30, and December 31 of the year 2011 and March 31, 2012.

The unconfined compressive strength (UCS) of sample after attack was determined in triplicate using a rock press apparatus, and the average value was used to calculate the coefficient of corrosion (K) according to the formula as follows:

$$K = \left[\frac{(R_1 - R_2)}{R_1} \right] * 100\%. \quad (1)$$

where K is defined as the corrosion index of concrete specimen and R_1 and R_2 are the UCS of the uncorroded and corroded concrete specimens under the same temperature condition.

3. Test Results and Analyses

3.1. Laboratory Test Results. UCS of specimens with different acid corrosion medium concentration, ambient temperature, and tested time are presented in Table 3. The variation of compressive strength of concrete specimens with temperature and acid concentration is shown in Figures 3 and 4. As can be seen in Figure 3, the compressive strengths of all specimens tested after 30 days and 90 days increase with increasing tested temperature. The tendency of uncorroded specimens is more significant than the other specimens with acid concentration of 5% and 10%. As seen in Figure 4, the compressive strengths of specimens tested after 30 days and 90 days decreased with increasing concentration of acid medium. This tendency is more apparent at higher ambient temperature.

Corrosion coefficient (K) of specimens tested after 30 and 90 days is presented in Table 3. The variation of K with ambient temperature is illustrated in Figure 5. As seen, the K -value of specimens for both tested time 30 and 90 days increases with the increase in ambient temperature. The maximum K -value is observed to be 45.86% at 10% of acid corrosion concentration, 40°C of tested temperature, and 90 days of tested time, which is about 2 times that of specimen with 10% of acid concentration, 5°C of tested temperature, and 90 days of tested time. With the same acid concentration,

TABLE 1: Physical properties of sand.

Quality percentage of different size particles			Constrained grain size (D_{60})	Intermediate particle diameter (D_{30})	Effective size (D_{10})	Uniformity coefficient (C_u)	Curvature coefficient (C_c)	Specific gravity (G_s)
1~0.5 (mm)	0.5~0.25 (mm)	0.25~0.1 (mm)						
12%	62%	26%	0.38	0.29	0.17	2.24	1.30	2.65

TABLE 2: Chemical composition and physical properties of cement.

SiO ₂	Al ₂ O ₃	Fe ₂ O ₃	CaO	MgO	SO ₃	Others	Specific surface area	Compressive strength (standard curing)
20.3%	4.3%	3.5%	62.4%	2.8%	3.3%	1.6%	387 m ² /kg	32.5 MPa

TABLE 3: The compressive strengths of corrosion concrete with various temperatures.

Container number	Sample number	Temperature (°C)	SO ₄ ²⁻ (%)	Compressive strength (MPa)		Corrosion index K (%)	
				30 days	90 days	30 days	90 days
L-1	6	5	0	23.73	26.34	0	0
L-2	6	20	0	29.59	30.19	0	0
L-3	6	40	0	38.24	38.92	0	0
L-4	6	5	5	20.07	21.89	15.42	16.89
L-5	6	20	5	22.91	21.87	22.57	27.56
L-6	6	40	5	28.84	23.66	24.58	39.20
L-7	6	5	10	18.31	19.87	22.84	24.56
L-8	6	20	10	20.32	20.12	31.33	33.35
L-9	6	40	10	20.95	21.07	45.21	45.86

TABLE 4: The corrosion test results of concrete at urban and rural observation stations.

Number	Sample numbers	Stations	SO ₄ ²⁻ (%)	Compressive strength (MPa)				Corrosion index K (%)			
				3 months	6 months	9 months	12 months	3 months	6 months	9 months	12 months
F-1	12	Urban	0	15.79	15.84	15.71	15.83	0	0	0	0
F-2	12		5	14.34	12.92	10.87	9.70	9.20	18.45	30.81	38.73
F-3	12		10	12.32	9.86	7.85	6.81	21.96	37.75	50.00	56.95
F-4	12	Rural	0	15.98	15.99	15.88	15.97	0	0	0	0
F-5	12		5	14.97	14.53	12.26	10.96	6.34	9.13	22.79	31.40
F-6	12		10	14.16	11.99	10.25	9.45	11.40	25.00	35.48	40.83

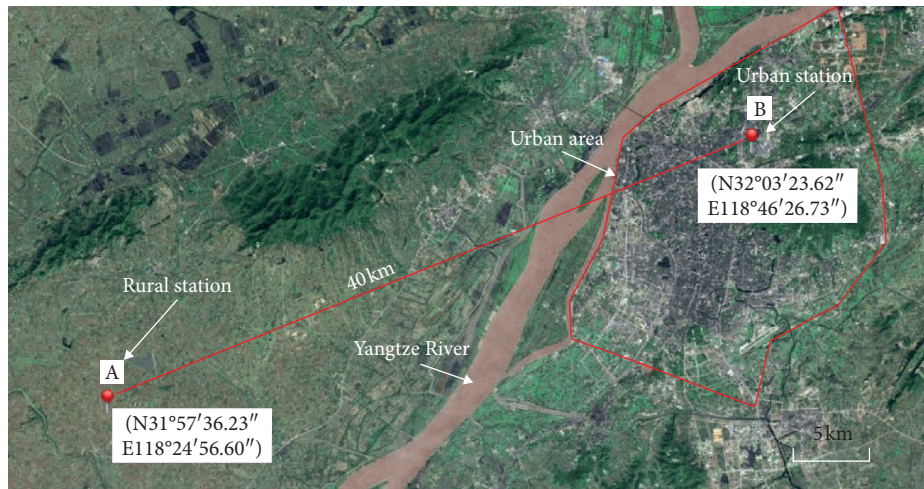


FIGURE 1: Locations of the urban and rural observation stations.

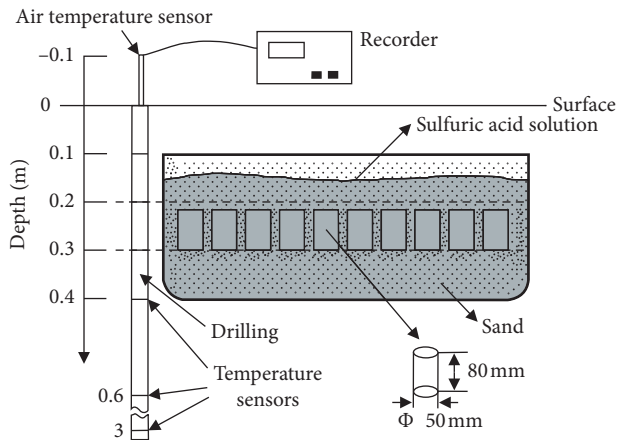


FIGURE 2: Schematic diagram of field test.

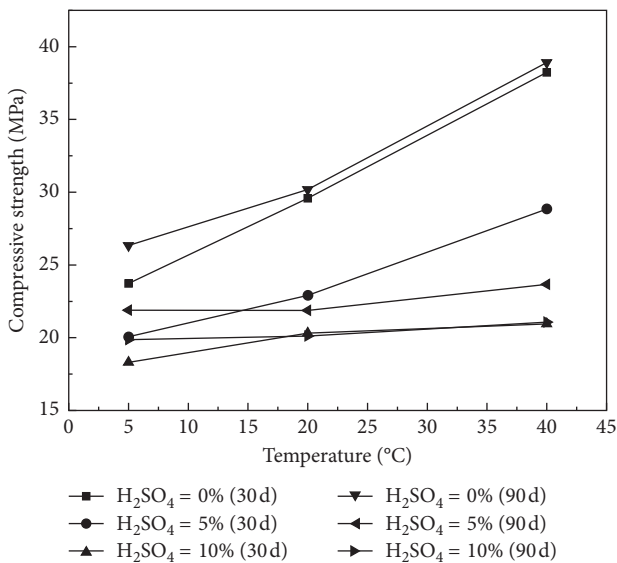


FIGURE 3: Variation of compressive strength of concrete specimens with temperature.

the *K*-value of specimens tested at tested time of 90 days is higher than that of specimens tested at tested time of 30 days. Compared with the 5% acid concentration, the specimens with 10% acid concentration have greater corrosion and higher *K*-value. With the acid concentration of 10% as an example, the *K*-value of specimen tested at 90 days with tested temperatures 5°C, 20°C, and 40°C is 24.56%, 33.35%, and 45.86%, respectively.

It can be calculated from Table 3 that within 5°C to 40°C, the corrosion index *K*-value of specimens tested after 90 days with the acid concentration of 5% and 10% increases about 0.64% and 0.61%, respectively, while temperature rising every once.

3.2. Field Test Results. The compressive strength results of field test are presented in Table 4. It was found that UCS of specimens with the same acid concentration in urban station is lower than that of specimens in rural station. The

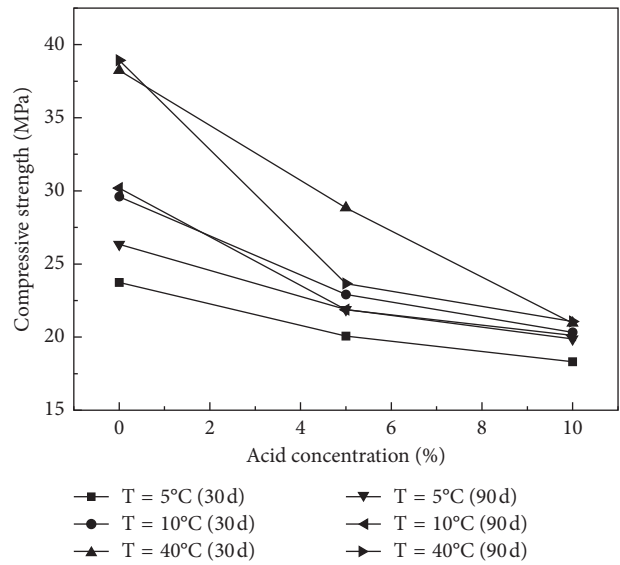


FIGURE 4: Variation of compressive strengths of concrete specimens with acid concentration.

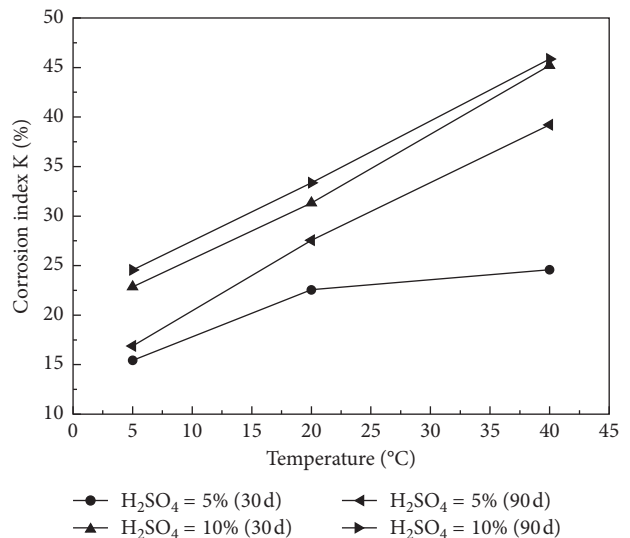


FIGURE 5: Variation of *K*-value with tested temperature.

compressive strengths of specimens at both urban as well as rural stations reduce as acid concentration increases. It also can be seen from Table 4 that the *K*-values of specimens with the same tested time increase with increasing acid concentration, and the specimens of urban area have stronger tendency. In addition, it is apparent that the corrosion coefficients (*K*-value) of specimens with same acid concentration observed at urban area are higher than that of specimens at rural area. As observed with the acid concentration of 10% (Figure 6), the *K*-values of urban specimens at age of 3, 6, 9, and 12 months are significantly higher than that of rural specimens. The *K*-value of specimens with the acid concentration 10% and tested time of 12 months at urban and rural area is 56.95% and 40.83%, respectively. The *K*-value obtained at urban area is about 1.39 times than that of specimens tested at rural area.

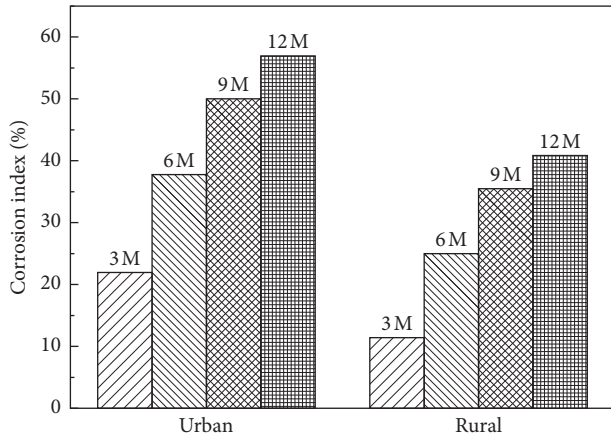


FIGURE 6: Corrosion index of urban and rural specimens.

The variation of corrosion index *K*-value with the tested time is illustrated in Figure 7. As observed, the corrosion index of both urban and rural specimens increases with the increase in the tested time. The increasing tendency of specimen with acid concentration of 10% is stronger than the specimen with acid concentration of 5%. With the same acid concentration, the corrosion index of specimens at urban station is larger than that of specimens at rural station in the whole test process.

3.3. UHI Effect on Concrete Corrosion. The average monthly temperatures (T_m) from April 1, 2011, to March 31, 2012, were calculated for both urban ($T_{m,u}$) and rural ($T_{m,r}$) soils at different depths and are presented in Table 5. In this study, the range of depths 0–40 cm is considered to explore the UHI effect on concrete corrosion. The average monthly temperatures (T_m) for urban and rural soil during the depths of 0–40 cm calculated from Table 5 are shown in Figure 8. The maximum T_m is observed in August as 29.28°C in the urban area and 26.59°C in the rural area. The minimum T_m values of urban and rural areas as observed in February are 7.61°C and 4.55°C, respectively. It can be seen from Figure 8 that the monthly temperatures of both urban and rural areas have a similar tendency of increase to the maximum value from April to August, and then the value begins to decrease and reaches the minimum value in February of the next year. At last, it rises to a higher value for the next monthly temperature cycle.

The urban heat island intensity (UHII) is defined as the temperature difference between the urban and surrounding rural locations. Based on this data, the differences of soil temperature at different time scales were calculated to examine the UHII patterns, such as monthly averages, 3-monthly averages, and yearly averages. The monthly, 3-monthly, and yearly UHII in the depth range of 0–40 cm is given in Table 5. As observed, the maximum monthly UHII is observed in November as 3.67°C, and the minimum monthly UHII is observed in July as 0.49°C; the 3-monthly UHII in the tested time is 1.25°C, 1.91°C, 3.61°C, and 3.26°C, respectively; and the yearly UHII is 2.51°C.

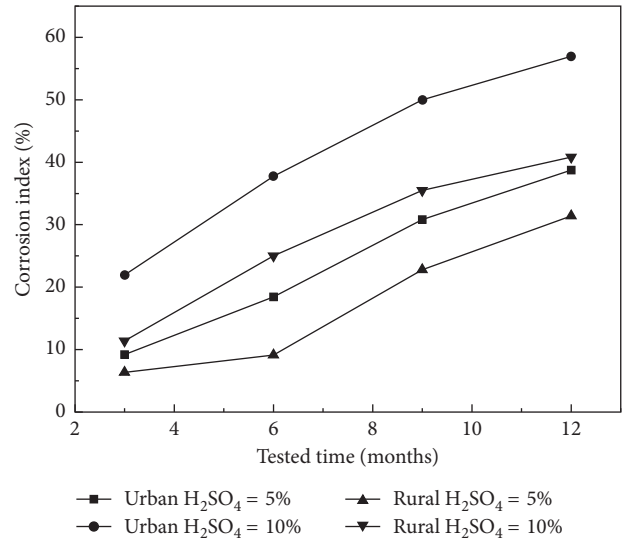


FIGURE 7: Variation of corrosion index *K*-value with the tested time.

The temperature corrosion effect (TCE) is defined as the rising range of the corrosion index *K*-value of concrete specimens with every temperature rise. The laboratory test results show that within 5°C to 40°C, the TCE values of specimens with the acid concentration of 5% and 10% are about 0.64%/°C and 0.61%/°C, respectively. The field test results show that the corrosion differences between the urban and rural locations at tested 3, 6, 9, and 12 months period are 2.86%, 9.32%, 8.02%, and 7.33%, respectively, for specimens with the acid concentration of 5% and are 10.56%, 12.75%, 14.52%, and 16.12%, respectively, for specimens with the acid concentration of 10%. The 3-, 6-, 9-, and 12-monthly UHII is 1.25°C, 1.58°C, 2.26°C, and 2.51°C, respectively. Therefore, the TCE caused by UHII is 2.29%/°C, 5.90%/°C, 3.55%/°C, and 2.92%/°C for specimens with the acid concentration of 5% and are 8.45%/°C, 8.07%/°C, 6.43%/°C, and 6.42%/°C for specimens with the acid concentration of 10%.

The above results obtained from both laboratory and field tests indicate that the temperature has an accelerated influence on the concrete corrosion under acid environment. Therefore, the urban heat island (UHI) will accelerate the acid corrosion of concrete construction and may affect the stability and durability of buildings in urban areas. The safety and life assessment of concrete buildings must require more attention.

4. Mechanism Analysis

Dissolution and decomposition are two kinds of concrete corrosion in acid medium. The dissolution type of corrosion is defined as the dissolution of composition of cement, such as calcium hydroxide being precipitated in the form of corrosion damage. Decomposable corrosion is defined as the chemical reaction between corrosive medium and cement hydrates. Usually, the decomposed corrosion occurs primarily on the surface layer of cement concrete, and its

TABLE 5: The average monthly temperatures of urban and rural soil at different depths.

Date	Average monthly temperatures of urban soil (°C)					Average monthly temperatures of rural soil (°C)					Monthly UHII (0-40 cm)/°C	3-monthly UHII (0-40 cm)/°C	Yearly UHII (0-40 cm)/°C		
	0 cm	10 cm	20 cm	30 cm	40 cm	Average (0-40 cm)	0 cm	10 cm	20 cm	30 cm				40 cm	Average (0-40 cm)
2011-04	18.28	19.21	18.6	18.08	17.45	18.32	17.25	16.59	15.82	15.46	14.98	16.02	2.3		
2011-05	22.85	22.46	21.71	21.29	20.7	21.8	22.05	21.08	20.75	20.43	19.94	20.85	0.95	1.25	
2011-06	24.78	23.76	23.29	22.91	22.39	23.43	24.17	23.38	22.7	22.41	21.94	22.92	0.51		
2011-07	28.12	27.32	26.76	26.24	25.58	26.8	27.76	26.96	26.11	25.69	25.04	26.31	0.49		
2011-08	29.9	29.21	29.19	29.1	28.99	29.28	27.16	26.99	26.48	26.37	25.95	26.59	2.69	1.91	
2011-09	25.91	25.62	25.88	26.15	26.33	25.98	23.27	23.55	23.35	23.55	23.48	23.44	2.54		
2012-10	21.51	21.06	21.52	22	22.42	21.7	16.81	17.86	18.12	18.71	19.04	18.11	3.59		2.51
2012-11	17.79	17.71	18.27	18.81	19.3	18.38	13.34	14.36	14.71	15.37	15.79	14.71	3.67	3.61	
2012-12	8.46	8.89	10.03	11.02	12.17	10.11	3.69	5.67	6.6	7.84	8.83	6.53	3.58		
2012-01	7.01	7.31	8.13	8.86	9.65	8.19	2.88	4.26	4.77	5.62	6.29	4.76	3.43		
2012-02	6.83	6.87	7.53	8.1	8.72	7.61	3.06	4.21	4.54	5.21	5.71	4.55	3.06	3.26	
2012-03	12.42	11.73	11.75	11.83	11.91	11.93	8.81	8.75	8.47	8.58	8.54	8.63	3.3		

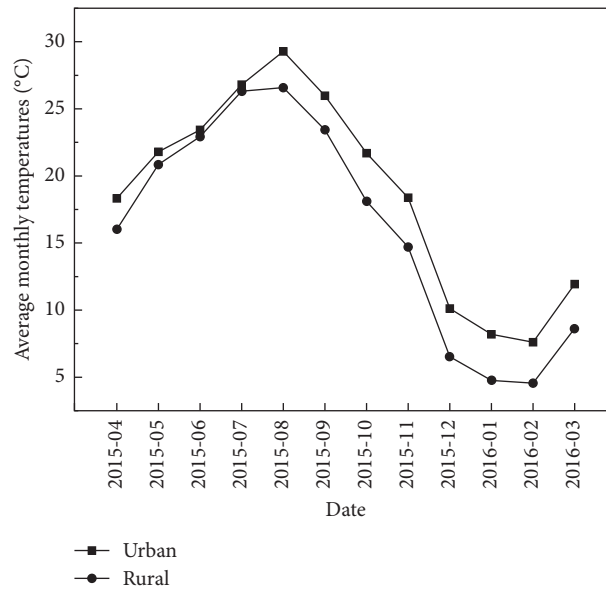
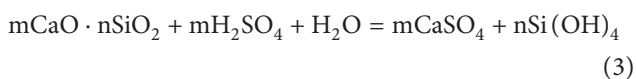
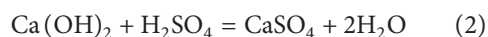


FIGURE 8: Average monthly temperatures for urban and rural soils in the depth ranges of 0–40 cm.

internal structure remains intact. In this study, the failure mode of specimens indicates that the decomposed corrosion is the main form of the sulfuric acid corrosion of concrete specimens.

The variation in microstructure of concrete specimen was observed by scanning electron microscopy (SEM, SU3500, Hitachi) at an acceleration voltage of 5 kV and a beam current of 100 μ A. The specimen is fixed on the object stage and connected with the conductive silver paste. Subsequently, the specimen surface is sputtered with gold with a voltage of 700 V for a minute by the ion sputter (E-1010, Hitachi). The photomicrographs of scanning electron microscope (SEM) of the concrete specimen with tested time of 6 months, acid concentration of 5%, and buried in urban soil are shown in Figure 9. As seen, the internal structures of specimens still maintain intact (Figure 9(a)). The outer layer of cement hydration product is corroded (Figure 9(c)), and an obvious corrosion boundary is present between inner and outer layers (Figure 9(b)). As a consequence, the structure became loose, and the strength of the concrete specimen reduced.

The corrosion process is that the acid medium penetrates through the matrix of concrete specimen to react with Ca(OH)₂ and calcium silicate hydrate (C-S-H) to form calcium salts. The reaction process is shown in the following chemical Equations (2) and (3).



This chemical reaction accelerates with the increasing sulfuric acid concentration and environment temperature. The increase of acid concentration or the temperature can induce the accelerated penetration rate of sulfuric acid into mortar sample, higher solubility, and activity of ions.

Therefore, the compressive strengths of concrete specimens reduce with the increasing acid concentration or the temperature in the tests.

The UHI effect in soil is actually equivalent to an additional temperature field in natural soil. The corrosion rate of the concrete materials in urban acid environment is accelerated due to UHI effect. These results have been demonstrated in the above field test.

5. Conclusions

A series of laboratory and field tests were performed to study urban heat island effect on the concrete acid corrosion. The effects of the acid concentration and environment temperature on the compressive strength and corrosion index of concrete specimens were investigated. The main conclusions from the present study can be summarized as follows:

- (1) It is observed from laboratory testing that the concrete corrosion varies and depends on the acid concentration, tested time, and also on the temperature. The concrete corrosion index K -value increases with the increasing acid concentration, tested time, and ambient temperature. The maximum K -value of 45.86% is observed at 10% of acid concentration, 40°C of ambient temperature, and 90 days of tested time, which is about 2 times of that of specimens with 10% of acid, 5°C of temperature, and 90 days tested. Within 5°C to 40°C, the corrosion index K -value of specimens tested after 90 days, with the acid concentration of 5% and 10%, increases about 0.61% and 0.63%, respectively, while temperature rising every once.
- (2) The field test shows that the compressive strength of specimens in the urban station is lower than that of specimens in the rural station. The compressive strength of specimens at both urban and

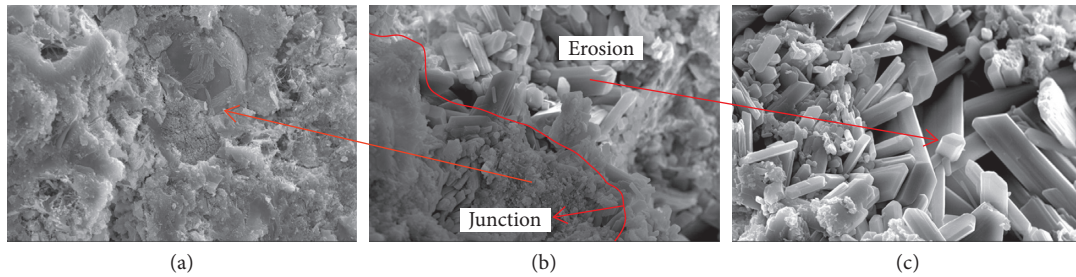


FIGURE 9: Photomicrographs of SEM of acid corrosion concrete specimen: (a) centre of the specimen with magnification 1500x; (b) junction of the specimen with magnification 1500x; (c) erosion of the specimen with magnification 2000x.

rural stations reduces with the increasing acid concentration. The K -values of specimens with some tested time increase with increasing acid concentration, and the specimens of urban area have stronger tendency. The corrosion coefficient K -value of specimens with same acid concentration observed at urban area is higher than that of specimens at rural area. The corrosion index of both urban and rural specimens increases with the increasing test time.

- (3) SEM images indicate that the decomposed corrosion is a main form of the sulfuric acid corrosion of concrete specimens. The internal structure of specimens still maintains intact, the outer layer of cement hydration product is corroded, and an obvious corrosion boundary is observed between internal and outer layers. The structure becomes loose, and the strength of the concrete specimen may reduce.
- (4) The soil profile temperature (within 40 cm depth) data during the period of April 1, 2011, to March 31, 2012, are obtained from two observation stations set up in urban and rural areas of Nanjing city, China. The maximum monthly UHII is observed in November as 3.67°C , and the minimum monthly UHII is observed in July as 0.49°C ; the 3-monthly UHII in the tested time is 1.25°C , 1.91°C , 3.61°C and 3.26°C respectively, and the yearly UHII is 2.51°C . The corrosion differences between the urban and rural locations at tested 3, 6, 9, and 12 months period are 2.86%, 9.32%, 8.02%, and 7.33%, respectively, for specimens with the acid concentration of 5% and are 10.56%, 12.75%, 14.52% and 16.12%, respectively, for specimens with the acid concentration of 10%.
- (5) Laboratory and field test results indicate that the temperature has an increasingly powerful influence on the concrete corrosion under acid environment. Therefore, the urban heat island (UHI) will accelerate the acid corrosion of concrete construction and may affect the stability and durability of buildings in urban areas. The safety and life assessment of concrete buildings must require great attention.

Data Availability

The data used to support the findings of this study are included within the article.

Conflicts of Interest

The authors declare that there are no conflicts of interest regarding the publication of this paper.

Acknowledgments

This research was financially supported by the Water Conservancy Science and Technology Project of Jiangsu Province, China (Grant no. 2017010), the National Natural Science Foundation of China (Grant no. 41472241), and the Fundamental Research Funds for the Central Universities (Grant no. 2016B05914). The authors gratefully acknowledge Dr. Bin Shi, Professor in the School of Earth Sciences and Engineering, Nanjing University, China, and Dr. Kai Gu, Associate Professor in the School of Earth Sciences and Engineering, Nanjing University, China, for their help and comments on this work.

References

- [1] T. R. Oke, *Boundary Layer Climate*, Methuen, London, UK, 1987.
- [2] H. S. Shang, Y. P. Song, and L. K. Qin, "Experimental study on strength and deformation of plain concrete under triaxial compression after freeze-thaw cycles," *Building and Environment*, vol. 43, no. 7, pp. 1197–1204, 2008.
- [3] S. P. Huang, M. Taniguchi, M. Yamano, and C. H. Wang, "Detecting urbanization effects on surface and subsurface thermal environment—a case study of Osaka," *Science of the Total Environment*, vol. 407, no. 9, pp. 3142–3152, 2009.
- [4] F. Al-Ajmi, D. L. Loveday, and V. I. Hanby, "The cooling potential of earth-air heat exchangers for domestic buildings in a desert climate," *Building and Environment*, vol. 41, no. 3, pp. 235–244, 2006.
- [5] P. A. Mirzaei and F. Haghighat, "Approaches to study urban heat island-abilities and limitations," *Building and Environment*, vol. 45, no. 10, pp. 192–201, 2010.
- [6] A. M. Rizwan, Y. C. L. Dennis, and C. H. Liu, "A review on the generation, determination and mitigation of Urban Heat Island," *Journal of Environmental Sciences-China*, vol. 20, no. 1, pp. 120–128, 2008.
- [7] E. Jauregui, "Heat island development in Mexico City," *Atmospheric Environment*, vol. 31, no. 22, pp. 3821–3831, 1997.
- [8] S. D. Gedzelman, S. Austin, R. Cermak et al., "Mesoscale aspects of the urban heat island around New York City," *Theoretical and Applied Climatology*, vol. 75, no. 1–2, pp. 29–42, 2003.

- [9] K. M. Hinkel, F. E. N. Nelson, A. E. Klene, and J. H. Bell, "The urban heat island in winter at barrow, Alaska," *International Journal of Climatology*, vol. 23, no. 15, pp. 1889–1905, 2003.
- [10] N. H. Wong and C. Yu, "Study of green areas and urban heat island in a tropical city," *Habitat International*, vol. 29, no. 3, pp. 547–558, 2005.
- [11] J. Shu, T. H. Jiang, and X. M. Yang, "Temporal characteristics of urban heat island in Shanghai," *Shanghai Environmental Sciences*, vol. 19, no. 11, pp. 532–534, 2000.
- [12] J. H. Zhang, Y. Y. Hou, G. C. Li, H. Yan, L. M. Yang, and F. M. Yao, "The diurnal and seasonal characteristics of urban heat island variation in Beijing city and surrounding areas and impact factors based on remote sensing satellite data," *Science in China Series D-Earth Sciences*, vol. 48, no. S2, pp. 220–229, 2005.
- [13] B. Shi, C. S. Tang, L. Gao, C. Liu, and B. J. Wang, "Observation and analysis of the urban heat island effect on soil in Nanjing, China," *Environment Earth Sciences*, vol. 67, no. 1, pp. 215–229, 2012.
- [14] C. Liu, B. Shi, C. S. Tang, and L. Gao, "A numerical and field investigation of underground temperatures under urban heat island," *Building and Environment*, vol. 46, no. 5, pp. 1205–1210, 2011.
- [15] D. Li and J. Fan, "A study of mechanical property of artificial frozen clay under dynamic load," *Advances in Civil Engineering*, vol. 2018, Article ID 5392641, 8 pages, 2018.
- [16] H. Jansen, J. Carmeliet, and H. Hens, "The influence of soil moisture transfer on building heat loss via the ground," *Building and Environment*, vol. 39, no. 7, pp. 825–836, 2004.
- [17] A. C. Jacinto, M. V. Villar, and R. Gomez-Espina, "Adaptation of the van Genuchten expression to the effects of temperature and density for compacted bentonites," *Applied Clay Science*, vol. 42, no. 3–4, pp. 575–582, 2009.
- [18] R. V. Balendran and W. H. Martin-Buades, "The influence of high temperature curing on the compressive, tensile and flexural strength of pulverized fuel ash concrete," *Building and Environment*, vol. 35, no. 5, pp. 415–423, 2000.
- [19] C. D. Atis and C. Bilim, "Wet and dry cured compressive strength of concrete containing ground granulated blast-furnace slag," *Building and Environment*, vol. 42, no. 8, pp. 3060–3065, 2007.
- [20] M. Mohammed and C. L. Page, "Effect of temperature and salt contamination on carbonation of cements," *Journal of Materials in Civil Engineering*, vol. 8, no. 2, pp. 63–69, 1996.
- [21] O. S. B. Al-Amoudi, M. Maslehuddin, A. N. Lashari, and A. A. Almusallam, "Effectiveness of corrosion inhibitors in contaminated concrete," *Cement and Concrete Composites*, vol. 25, no. 4–5, pp. 439–449, 2003.
- [22] S. Aydın, H. Yazıcı, H. Yigiter, and B. Baradan, "Sulfuric acid resistance of high-volume fly ash concrete," *Building and Environment*, vol. 42, no. 2, pp. 717–721, 2007.
- [23] J. O. Okeniyi, A. P. I. Popoola, C. A. Loto, O. A. Omotosho, S. O. Okpala, and I. J. Ambrose, "Effect of NaNO_2 and $\text{C}_6\text{H}_{15}\text{NO}_3$ synergistic admixtures on steel-rebar corrosion in concrete immersed in aggressive environments," *Advances in Materials Science and Engineering*, vol. 2015, Article ID 540395, 11 pages, 2015.
- [24] M. Laura and M. H. Carolyn, "Influence of cation on Corrosion behavior of reinforcing steel in high-pH sulfate solutions," *ACI Materials Journal*, vol. 102, no. 4, pp. 279–286, 2005.
- [25] X. S. Wang, B. S. Wu, and Q. Y. Wang, "Online SEM investigation of microcrack characteristics of concretes at various temperatures," *Cement and Concrete Research*, vol. 35, no. 7, pp. 1385–1390, 2005.
- [26] M. J. Terro, "Properties of concrete made with recycled crushed glass at elevated temperatures," *Building and Environment*, vol. 41, no. 5, pp. 633–639, 2006.
- [27] Y. B. Jiao, H. B. Liu, X. Q. Wang, Y. W. Zhang, G. B. Luo, and Y. F. Gong, "Temperature effect on mechanical properties and damage identification of concrete structure," *Advances in Materials Science and Engineering*, vol. 2014, Article ID 191360, 10 pages, 2014.
- [28] S. M. Chang, S. K. Oh, D. S. Seo, and S. M. Choi, "Characteristics of humidity-temperature changing in the below-grade concrete structure by applying waterproofing materials on the exterior wall," *Advances in Materials Science and Engineering*, vol. 2015, Article ID 959502, 10 pages, 2015.
- [29] K. C. He, R. X. Guo, Q. M. Ma, F. Yan, Z. W. Lin, and Y. L. Sun, "Experimental research on high temperature resistance of modified lightweight concrete after exposure to elevated temperatures," *Advances in Materials Science and Engineering*, vol. 2016, Article ID 5972570, 6 pages, 2016.
- [30] L. X. Liu, "Brief Introduction on the study of erosion and prevention of concrete in Salt Lake and saline soil area of Chaerhan, Chaidamu," *Journal of Building Materials*, vol. 4, no. 4, pp. 395–400, 2001.
- [31] M. S. Menashi, D. Cohen, and J. Olek, "Mechanism of sulfate attack: a fresh look part 1. Summary of experimental results," *Cement and Concrete Research*, vol. 32, no. 6, pp. 915–921, 2002.
- [32] C. Argiz, M. Á. Sanjuán, P. Castro, and E. Álvarez, "Modeling of corrosion rate and resistivity of steel reinforcement of calcium aluminate cement mortar," *Advances in Civil Engineering*, vol. 2018, Article ID 1096282, 9 pages, 2018.
- [33] P. J. Tumidajski and G. W. Chan, "Effect of sulfate and carbon dioxide on chloride diffusivity," *Cement and Concrete Research*, vol. 26, no. 4, pp. 551–556, 1996.
- [34] A. M. Tang and Y. J. Cui, "Controlling suction by the vapour equilibrium technique at different temperatures and its application in determining the water retention properties of MX80 clay," *Canadian Geotechnical Journal*, vol. 42, no. 1, pp. 287–296, 2005.
- [35] Y. Yang, W. Su, and N. Jiang, "Time-space character analysis of urban heat island effect in Nanjing city using remote sensing," *Remote Sensing Technology and Application*, vol. 21, no. 6, pp. 488–492, 2006.

Research Article

Research on the Slurry for Long-Distance Large-Diameter Pipe Jacking in Expansive Soil

Xian Yang ^{1,2}, Yang Liu,³ and Chao Yang³

¹School of Resource and Safety Engineering, Central South University, Changsha 410083, China

²School of Resource, Environment and Safety Engineering, Hunan University of Science and Technology, Xiangtan 411201, China

³Hunan Provincial Key Laboratory of Shale Gas Resource Utilization, Hunan University of Science and Technology, Xiangtan 411201, China

Correspondence should be addressed to Xian Yang; yangxj@163.com

Received 12 June 2018; Accepted 27 August 2018; Published 14 October 2018

Academic Editor: Yonggui Chen

Copyright © 2018 Xian Yang et al. This is an open access article distributed under the Creative Commons Attribution License, which permits unrestricted use, distribution, and reproduction in any medium, provided the original work is properly cited.

When the pipe jacking technology is applied in expansive formation, the soil around the pipe will easily absorb water from the slurry and expand to wrap up the pipe, producing an excessive pipe jacking force. A water-based slurry formula suitable for pipe jacking in expansive soil layer was proposed in this paper. Firstly, the key design points of pipe jacking slurry in expansive soil were put forward. Secondly, plant glue, potassium humate, Na-CMC, and graphite powder were chosen as treating agents to improve the slurry performance. The effect of addition levels of different treating agents on the funnel viscosity, filter loss, expansion ratio, friction coefficient and water dissociation rate of the slurry were tested. Thirdly, based on the results of single-factor tests, a water-based slurry formula suitable for pipe jacking in expansive soil was obtained. Finally, the slurry formula was applied in a practical pipe jacking project in expansive formation, and the jacking force was controlled well in the whole jacking process. The new water-based slurry is cheap and practical and has no pollution to environment. Furthermore, a simple and practical calculating method of the pipe jacking force was presented. The comparison of the calculated and measured pipe jacking force shows that the simple calculating method can estimate the jacking force well. Improving slurry performance to reduce jacking force in pipe jacking and predicting pipe jacking force accurately can help reducing the investment for counterforce wall and jacking system in pipe jacking engineering.

1. Introduction

The interaction between clay minerals and water leads to the expansibility, dispersion, thixotropy, plasticity, and impermeability of clay. Therefore, clay materials have been widely used in engineering fields, such as high-level radioactive waste disposal [1–3], dam clay core wall [4], drilling fluid [5], and so on. In the pipe jacking project, clay is always used to make thixotropic slurry for lubrication. Proper pipe jacking slurry can significantly reduce the pipe jacking force and reduce the investment of the reaction wall and relay stations. Especially in long-distance large-diameter pipe jacking engineering, excellent lubrication effect of slurry is essential. The poor lubrication effect will result in the increase of pipe jacking force, which will damage the reaction wall or the pipe

[6, 7]. High-quality bentonite slurry with some treating agents was always used in pipe jacking in general formation [8]. However, when it comes to the expansive soil, the conventional slurry will lose the lubrication effect. The soil around the pipe will absorb the water from the slurry and expand to wrap up the pipe tightly, resulting in a sharp increase of pipe jacking force and the failure of the pipe jacking project.

At present, there are a lot of studies on the drilling slurry in the expansive formation. During drilling in expansive formations such as mudstone and shale, clay particles in the formation hydrated and dispersed into the drilling slurry, which not only increases the viscosity of the slurry, deteriorates the rheological properties, but also causes the expansion of the formation, shrink, or even collapse of the

hole. Therefore, in the expansive formation, enhancing the inhibition of drilling slurry is most important. Inhibitory drilling fluid includes oil-based drilling fluid [9], synthetic-based drilling fluid [10], and water-based drilling fluid [11]. Oil-based drilling fluids and synthetic-based drilling fluids have good inhibition effect, but they cost highly and have adverse impact on environment. So, inhibitory water-based drilling fluids have been widely used. The most frequently used slurry includes calcium-treated mud [12] and potassium-based mud [11].

Good lubrication is the common requirement for pipe jacking slurry and drilling mud. In addition to lubrication, pipe jacking slurry also plays an important role in filling the gap between pipe and soil to support formation and reduce settlement. Drilling mud needs cooling bit and carrying the drilling debris by reciprocating cycle. From the above, it is seen that there are many different demands for the pipe jacking slurry and drilling mud. Therefore, there are similarities and differences as well between inhibitory drilling mud and pipe jacking slurry. We can learn from the design idea of inhibitory drilling mud to design pipe jacking slurry in expansive soil. At the same time, they should be considered the different functions to design their different characteristic parameters.

There are also many research studies on pipe jacking slurry, mainly focusing on the slurry formulation in general formation, the influence of lubricity and thixotropy of slurry on pipe jacking force [13] and so on. However, there are not many research studies on the formula of the pipe jacking water-based slurry in expansive soil. Wang et al. [14] indicated that the diesel base slurry was a good solution for clay hydration and dispersion in the expanding soil. Diesel base slurry has good lubricity and is conducive to formation stability, but the diesel can produce toxic aromatics that will badly affect the groundwater systems. In addition, large amount of slurry will be required for a long-distance large-diameter pipe jacking project; this will lead to high cost when using oil base slurry.

In this paper, the key design points of pipe jacking slurry for pipe jacking in expansive soil were put forward by reference to the study on water-based drilling mud and the requirements for pipe jacking slurry in general formation. Several treatment agents were selected for single-factor test, and the effects of various treatment agents on the viscosity, water loss, expansion ratio, friction coefficient, and water dissociation rate were analyzed. Based on the results of single-factor test, a kind of water-based slurry suitable for pipe jacking in expansive soil was obtained, and the water base slurry gained good application effect in a practical project. Furthermore, a practical calculating method of the pipe jacking force was presented. Improving slurry performance to reduce jacking force in pipe jacking and predicting jacking force accurately can significantly reduce investment in pipe jacking engineering.

2. Materials and Methods

2.1. The Key Points of Slurry Formula Design. It is known that there are a large number of clay minerals in the expansive

soil, especially the montmorillonite mineral. This will make the soil around the pipe absorb water from the slurry. The clay particles disperse into the gap between the pipe and the formation. Then the gap size will get smaller, or even the formation will collapse to wrap up the pipe tightly, leading to the failure of pipe jacking. For the pipe jacking in the expansive soil, decreasing the water penetration into the formation is very important, which can prevent the clay minerals dispersing into the gap between the pipe and the formation. Comprehensively, considering all kinds of performance requirements for the slurry in expansive soil, the following key points of slurry formula designs are put forward according to the requirements for the drilling mud in expansive formation and the pipe jacking slurry in general formation:

- (1) Improve the inhibitory action of slurry. The addition of inhibitory additives into the slurry can reduce the dispersion of clay minerals and maintain the stability of the formation. During the shale drilling, the expansion ratio of shale should be generally controlled within 10%, which can ensure the stability of the formation without sticking to the drill tools. Compared with the common core-drilling technology, pipe diameter in the pipe jacking is larger, and the gap between the pipe and the formation is larger as well. Also, the admissible expansion ratio in pipe jacking will be larger than that in the core-drilling technology. Therefore, the expansion ratio of formation is required to be controlled at 15% in this test.
- (2) Improve the slurry viscosity. The higher the slurry viscosity, the lower the water penetration rate into the soil will be. The viscosity of pipe jacking slurry is always larger than the drilling mud. The funnel viscosity of thixotropic slurry is required to be ranged from 40 s to 65 s in general pipe jacking project. In this range, it can ensure the slurry's fluidity and fill the gap effectively but will not spread too much into the formation to result in surface deformation. In the expansive formation, the viscosity of the slurry should be relatively larger. In this test, the viscosity of slurry is required to be greater than 55 s.
- (3) Reduce the filter loss of slurry. The filter loss reducing agents can increase the thickness of the hydration film and increase the permeability resistance. Besides, they can improve the quality of filter cake obviously. The filter loss is always required to be less than 25 ml/30 min in the pipe jacking. In expansive soil formation, the filter loss should be smaller. In this test, it is required to be no more than 10 ml/30 min.
- (4) Reduce the water dissociation. After the slurry is prepared, the ratio of the water dissociated from the slurry to the volume of the original slurry within 24 h is called water dissociation rate. This parameter can reflect the stability of the slurry. The water dissociation rate of thixotropic slurry in the pipe jacking is required to be 0.

- (5) Improve the slurry lubricity. The friction coefficient of water-based drilling mud tested by the extreme pressure lubrication instrument is commonly between 0.2 and 0.35. The friction coefficient can be properly reduced when adding some lubricant agents. Considering the high requirements of long-distance large-diameter pipe jacking on slurry lubrication, the friction coefficient in this test is required to be controlled within 0.25. (The materials contacted with the slurry in the test instrument are different from those in the practical project, so the friction coefficient obtained by the extreme pressure lubrication instrument cannot be directly used in the pipe jacking project).

2.2. Selection of Treating Agents. Considering the particularity of the expansive soil and the high requirement for the lubricity in pipe jacking, some corresponding treating agents must be added into the slurry system. In view of the economy and efficiency of the treatment agents, some materials were selected as follows.

2.2.1. Potassium Humate. Potassium humate is a high molecular compound aromatic hydroxy carboxylate and is soluble in water. Because the potassium humate contains many active functional groups such as the carboxyl group, the phenol hydroxyl group, the alcohol hydroxyl group, the carbonyl group, and the methoxy group, it can be strongly adsorbed by clay particles to form thin and elastic filter cake to reduce the filter loss. At the same time, because the special size of k^+ has, it can generate fixed effects on the crystal lattice of the clay mineral and result in inhibiting the clay hydration. The amount of potassium humate in the slurry is generally 2-3%.

2.2.2. Plant Glue. Plant glue has good performances in tackifying and adjusting the slurry rheological property. The amount used in slurry is usually 2-3%.

2.2.3. Low-Viscosity Na-CMC. It can help to form dense, firm, and low permeability filter cake on the surface of the formation to prevent the free water from slurry into the expansive soil formation. In addition to the filter loss reducing effect, the Na-CMC has a certain performance in tackifying, and it is also good for the slurry stability. The general amount used in slurry is about 0.1%-0.2%.

2.2.4. Graphite Powder. The graphite powder is selected as the lubricant in this test. Graphite powder can be firmly adsorbed on the pipe and the formation surface, thereby changing the friction state between the friction pairs and reducing the friction resistance. In addition to the good lubrication performance, the particles of the graphite powder can also enter the microcracks in the formation to block the cracks, which can prevent the free water from slurry into the soil and reduce the hydration of the clay

minerals. The general addition amount of graphite powder is about 0.5%–1%.

2.3. Single Factor Test

2.3.1. Test Instruments and Methods. The tests mainly aim at revealing the effect of different addition levels of different treating agents on the viscosity, filter loss, expansion rate, friction coefficient, and the water dissociation rate. Firstly, the base slurry was determined to be 8% bentonite powder +0.3% $NaCO_3$. Then, a different additive was added into the base slurry separately. The variation rules of the viscosity, the filter loss rate, the expansion ratio, the friction coefficient, and the water dissociation rate of the several kinds of new slurry were studied. Figure 1 shows the test instruments.

(1) *Swelling Tests.* The silty clay encountered in an actual project was selected in the test. After drying, grinding, and sieving, the silty clay was made into mud powder. 12 g mud powder was loaded into the test tube and was compacted with 8 MPa pressure to make a stand-by cylinder. Then the cylinder was put into the prepared slurry, and the linear expansion ratio of the cylinder was measured with expansion-testing equipment (Figure 1(a)).

(2) *Filter Loss Tests.* Slurry filter loss was tested by using the filter loss test instrument. The slurry was filled into the slurry cup, and the slurry cup was installed on the tee joint. Keeping the atmospheric pressure in the slurry cup at 0.69 MPa, the slurry's filtration volume in 30 minutes was measured, which was the filter loss (Figure 1(b)).

(3) *Funnel Viscosity Tests.* 500 ml and 200 ml slurry were measured by the steel measuring cylinder of Markov funnel viscometer and was poured into the funnel. Then, the time required for 500 ml slurry to flow out was recorded, which was the slurry's funnel viscosity (Figure 1(c)).

(4) *Lubricity Tests.* The friction coefficient of the slurry was tested by using the extreme pressure lubrication instrument. The slurry was filled into the test cup, the motor was turned on, and the pressure was set to 16.95 N·m. After the system had run for 5 minutes, the ammeter reading was recorded to calculate the slurry friction coefficient (Figure 1(d)).

(5) *Stability Tests of the Slurry.* After being prepared, the slurry was kept undisturbed for 24 h. Then, the volume of water dissociated from the slurry was recorded to calculate the water dissociation rate of the slurry (Figure 1(e)).

2.3.2. Test Results and Analysis. The water dissociation rate of the base slurry is 0.05. After adding some treating agents, the water dissociation rate is easy to be controlled to be 0. So, the effect of treatment agents on the water dissociation rate will not be analyzed more. The effect of the treatment agents on the viscosity, the filter loss rate, the expansion rate, and the friction coefficient of slurry is analyzed as follows:

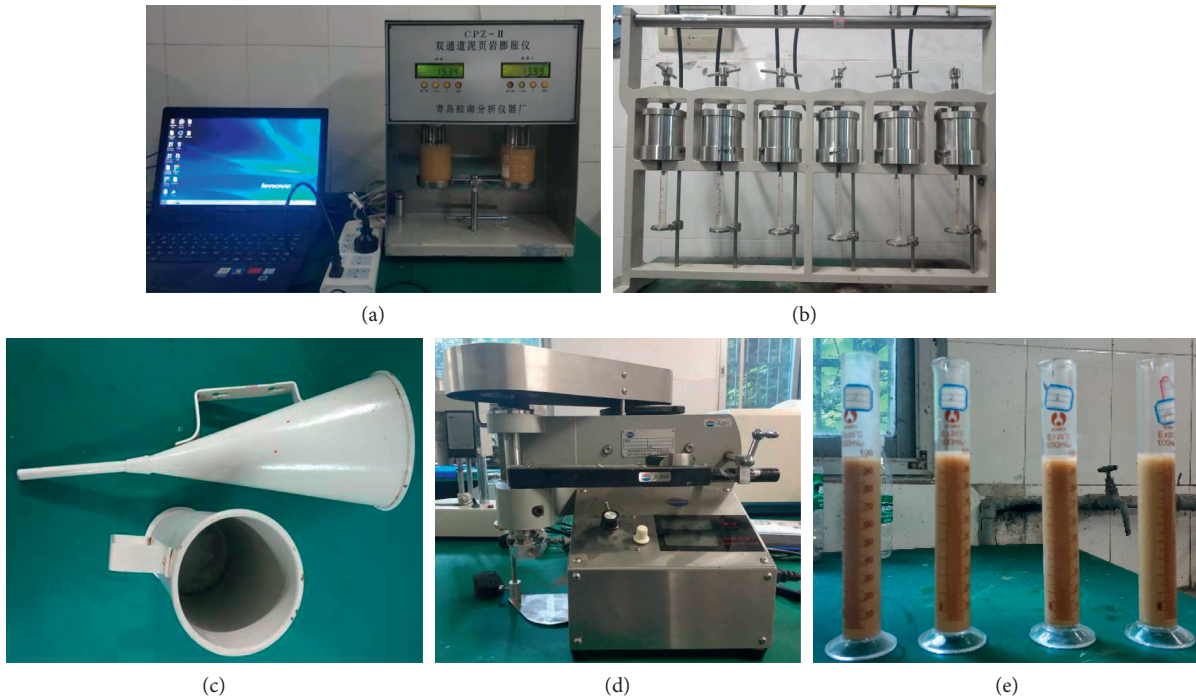


FIGURE 1: Tests of the slurry properties. (a) Swelling test. (b) Filter loss test. (c) Funnel viscosity test. (d) Lubricity test. (e) Stability test.

- (1) The effect of plant glue on the slurry properties: as shown in Figure 2, with the increase of the plant glue, the funnel viscosity of the slurry increases, but the increasing tendency is getting smaller. The filter loss is not affected. Also, the expansion ratio of slurry decreases, but the decreasing tendency is not obvious. The plant glue has a slight beneficial effect on the slurry lubricity.
- (2) The effect of potassium humate on the slurry properties: as we can see from Figure 3, the filter loss of the slurry is getting smaller with the increase of the potassium humate. And, the depressed tendency changes significantly when the addition amount of the potassium humate exceeds 2.5%. Besides, the potassium humate has no effect on the slurry funnel viscosity. The expansion ratio decreases significantly with the increase of the potassium humate. And, it has a slight beneficial effect on the slurry lubricity.
- (3) The effect of Na-CMC on the slurry properties: as shown in Figure 4, with the increase of Na-CMC, the filter loss of slurry is getting smaller, and the viscosity is getting larger. Besides, the expansion ratio declines slightly. The Na-CMC has no effect on the slurry lubricity.
- (4) The effect of graphite powder on the slurry properties: as shown in Figure 5, the higher the amount of graphite powder, the better the slurry lubricity will be. However, the increase of graphite powder will have a slight adverse effect on the filter loss.

2.4. Slurry Formula Design and Performance Tests. The aim of the slurry formula is to meet the requirements when

applying the long-distance large-diameter pipe jacking technology in the expansive formation. Based on the single-factor tests, the additive amount of all kinds of treating agents could be selected. Considering the interaction between each single factor, the addition amount of all the treating agents had been adjusted. Finally, three kinds of slurry formulas had been proposed, and the performance tests of these three formulas were conducted. The slurry formulas were as follows:

$$\begin{aligned} & \text{base slurry} + 2\% \text{ potassium humate} + 2\% \text{ plant glue} \\ & + 0.1\% \text{ Na-CMC} + 0.75\% \text{ graphite powder,} \end{aligned} \quad (1)$$

$$\begin{aligned} & \text{base slurry} + 2.5\% \text{ potassium humate} + 2\% \text{ plant glue} \\ & + 0.15\% \text{ Na-CMC} + 0.75\% \text{ graphite powder,} \end{aligned} \quad (2)$$

$$\begin{aligned} & \text{base slurry} + 3\% \text{ potassium humate} + 2.5\% \text{ plant glue} \\ & + 0.2\% \text{ Na-CMC} + 1\% \text{ graphite powder.} \end{aligned} \quad (3)$$

In addition to the five tests that were the same as the single-factor tests, we also measured initial and final static shear-stress of the three kinds of slurry formulas by the six-speed rotating viscometer (Figure 6). Static shear-stress refers to the strength of gel structure formed after the slurry is kept static for a while. The value of static shear-stress is determined by the number of structural chains in a unit volume of fluid and the strength of a single structural chain. The sequence of fluid structure gradually tends to be stable, and the structural development tends to be perfect, and the

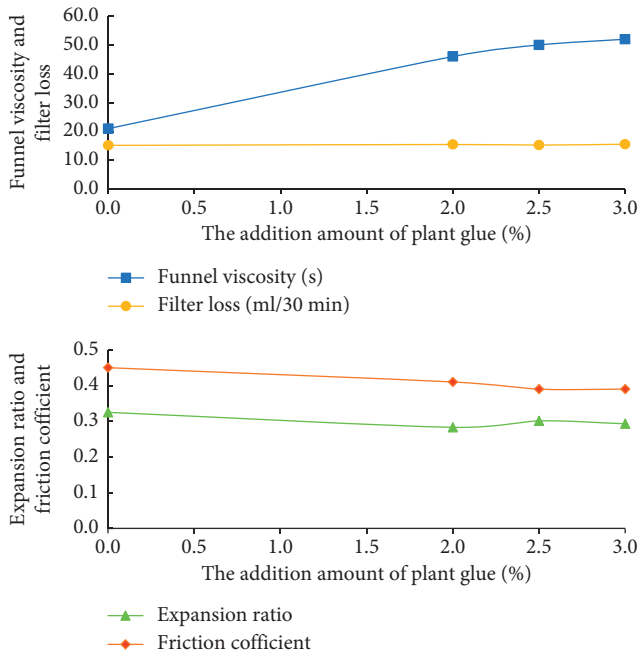


FIGURE 2: The effect of plant glue on the slurry properties.

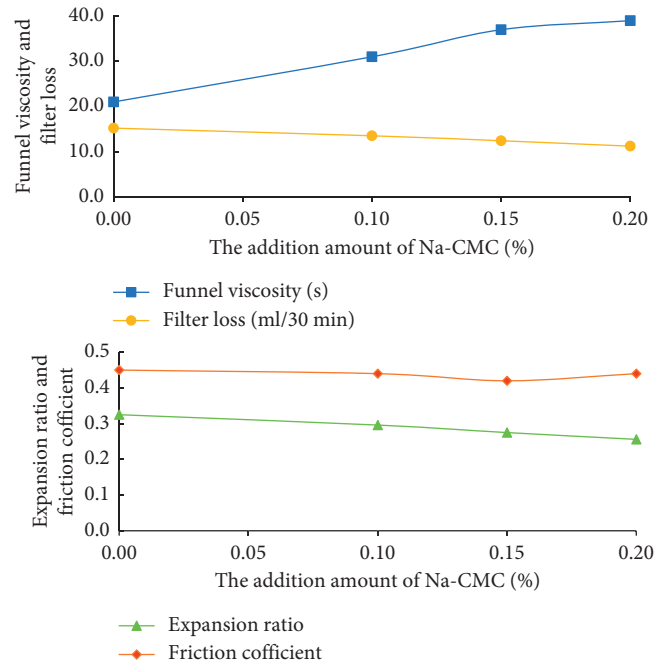


FIGURE 4: The effect of Na-CMC on the slurry properties.

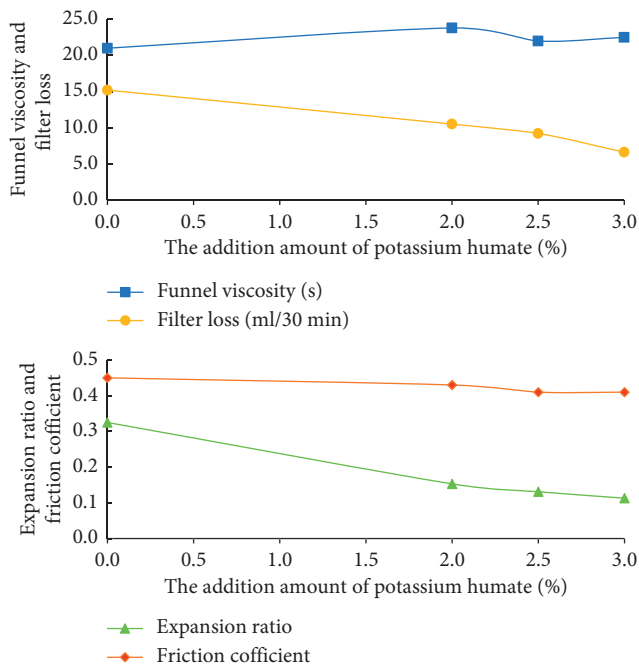


FIGURE 3: The effect of potassium humate on the slurry properties.

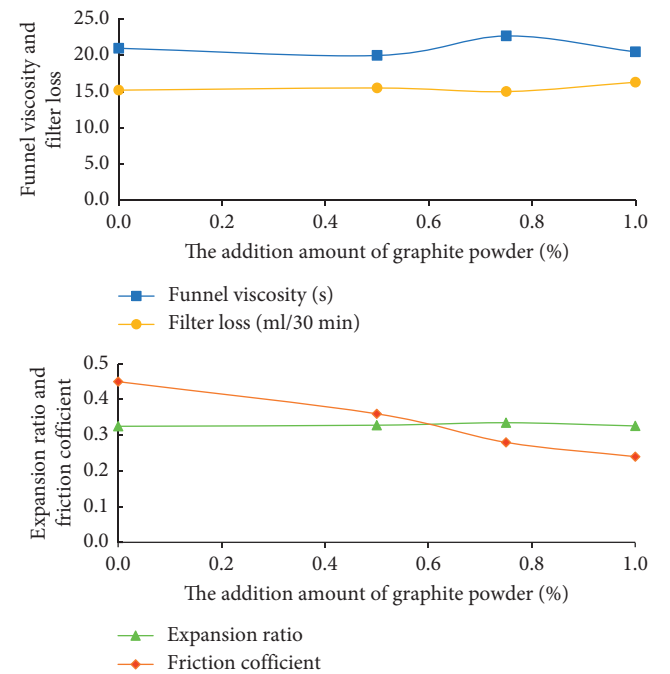


FIGURE 5: The effect of graphite powder on the slurry properties.

static shear-stress also increases. To measure the growth rate of gel strength, static shear-stress must be measured twice. According to the API standard, static shear-stress of 10 seconds and 10 minutes at rest is measured, which is called initial shear-stress and final shear-stress respectively. For thixotropic pipe jacking slurry, the greater static shear-stress means that when the pipe jacking stops and starts again, it needs greater pipe jacking force to overcome the network structure inside the slurry. Therefore, the jacking force is

always larger than that in the normal pipe jacking state when the pipe is restarted. Too large shear-stress also causes higher pump pressure. However, the static shear-stress should not be too small. If the static shear-stress is too small, when the pipe jacking stops, the slurry fluidity is still too large, which is unfavorable for filling the gap between the pipe and formation and maintaining the formation stability. There is a great relationship between slurry shear-stress and viscosity.



FIGURE 6: The six-speed rotating viscometer test.

Both Plant glue and Na-CMC can affect the static shear-stress in the three kinds of slurry formula.

As shown in Table 1, both Formulas (2) and (3) can meet the design requirements mentioned in 2.1. So, the static shear-stress will be a key factor to select the better slurry formula. The static shear-stress of Formula (2) is more suitable, which is not too small or too large. Therefore, Formula (2) is selected when applying the long-distance large-diameter pipe jacking technology in an expansive soil formation.

3. Results and Discussion

3.1. Overview of the Slurry Application in a Practical Pipe Jacking Project

3.1.1. Geological Situation. It is a water supply pipeline along a road constructed by pipe jacking technology. In this project, the outer diameter of the steel pipe is 1500 mm. The thickness of the pipe is 24 mm. The total length of the pipeline is 492 m. The overburden height is 3.2–4.8 m. The underground water level is 6.4 m. According to the geological survey report, the strata in this area from the top to the bottom are plain fill soil, clay, silty clay, silty clay sand inclusion layer, and gravel layer, respectively. The pipe jacking project is in the silty clay layer. The characteristics of the silty clay: brown red, hard plastic, high toughness, and visible cracks. The soil mass is 18.6 kN/m^3 , the cohesion is 24 kPa, and the internal friction angle is 18° . The compression coefficient is 0.13 MPa^{-1} , which belongs to medium compressibility soil. According to the expansion test, the average free expansion ratio of the soil is 51.4%, but the largest free expansion ratio reaches 64.3%. The potential of expansion is weak, and the potential of local expansion is medium.

3.1.2. The Pipe Jacking and Slurry System. The earth pressure balance jacking machine was used in this pipe jacking project. Four jacks with 2000 kN oil cylinders were applied. The maximum bearing capacity of the reaction wall in the departure working shaft was 8000 kN. The pipes were made of steel tubes with strength grade Q235-B.

To reduce friction, slurry Formula (2) was selected to be used in this project. The synchronous grouting method was adopted at the rear of the driving machine to reduce the friction between pipe and formation in this project. In the front of each pipe, four grouting holes were arranged on a section (Figure 7). By using the BW-200 slurry pump, the lubrication slurry was injected into the gap between the pipe and the formation through the main pipe, the branch pipe, the ball valve, and the reserved grouting holes on the pipe. During the construction process, the grouting quantity was 1.5 times of the volume of the gap between the pipe and the formation, and the grouting pressure was 25–45 kPa.

According to the calculation result of pipe jacking force, a relay jacking ring had been designed in this project to provide enough pipe jacking force. But during the actual construction process, due to the good lubrication effect of slurry, the jacking force was smaller, so the jacking pipe construction was finally completed without using the relay jacking ring. Good lubrication results effectively simplified the operation procedure and reduced investment.

3.2. Calculation and Monitoring of the Pipe Jacking Force

3.2.1. Calculation Method of the Jacking Force. During the pipe jacking, the ideal situation is that the slurry forms a stable and closed sleeve at the outer surface of the pipe. In this case, the solid-liquid contact model can be used to calculate the jacking force. However, in the actual pipe jacking process, it is often difficult to achieve complete solid-liquid contact and to avoid the direct contact between the pipe and the soil. Besides, due to the existence of the gap between the pipe and the formation, if the soil is stable and does not collapse, the complete pipe-soil contact will not exist, too. Therefore, the actual pipe jacking contact should be a complex contact mode combining partial pipe-soil contact with partial pipe-slurry-soil contact.

As found in some domestic and foreign relevant specifications, complete pipe-soil contact model was mostly used to calculate the pipe jacking force. In this model, the gap between the pipe and the formation is not considered, and it indicates that the jacking force is equal to the frictional resistance caused by the soil pressure on the pipe. And many monitoring results showed that the jacking force is much smaller than the jacking force calculated by this model. If that the pipe was completely covered by slurry sleeve in the process of pipe jacking, Ye et al. [15] proposed a solid-liquid contact model to calculate the pipe jacking force. Zhang et al. [16] divided the contact outside the pipe into the pipe-soil contact and the pipe-slurry-soil contact to calculate the contact friction force of the two parts, respectively. However, there is an implicit condition in Zhang's model [16]. In Zhang's model [16], the stratum is a completely self-stability

TABLE 1: The properties of the slurry.

Slurry formulas	Funnel viscosity (s)	Initial static shear-stress (kPa)	Final static shear-stress (kPa)	Filter loss (ml/30 min)	Expansion ratio (%)	Friction coefficient	Water dissociation rate
Base slurry	21	5.18	6.5	15.2	32.5	0.45	0.05
Formula (1)	52	5.66	7.98	8.6	12.5	0.28	0
Formula (2)	57	5.78	8.24	7.2	11.8	0.25	0
Formula (3)	62	6.14	9.65	7.1	11.3	0.23	0

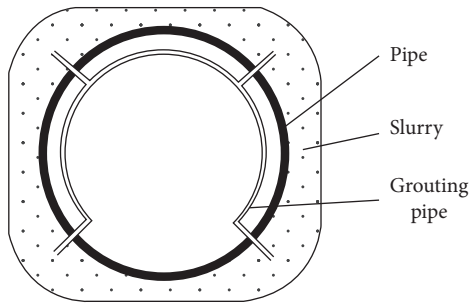


FIGURE 7: The schematic diagram of grouting in pipe jacking.

system, that is, there is no earth pressure on the pipe absolutely. Therefore, when the friction coefficient was supposed to be 0.5, the calculated jacking force was in good agreement with the measured jacking force in Zhang's research [16]. However, according to the test results of the slurry friction coefficient tests, the friction coefficient is generally less than 0.5, which indicates that when earth pressure is not considered, the calculated jacking force by using Zhang's method [16] is relatively smaller.

Combining with Zhang's research [16] and Terzaghi loose earth theory [17], a practical calculating method for the pipe jacking force is presented based on the pipe-soil and pipe-slurry-soil combinative contact model (Figure 8). According to angle calculation formula in Persson contact model, it is concluded that the pipe-soil contact angle can be approximately 180° , that is, the upper part of the contact model is the pipe-slurry-soil contact, and the lower part is the pipe-soil contact [16].

When calculating the jacking force of the upper part, it is considered that the slurry in the gap between the pipe and the formation only transmits hydrostatic pressure. The contact friction per unit length is calculated as follows:

$$f_{\text{pipe-slurry}} = \frac{(p_m \mu_1 + c_1) \pi D}{2}, \quad (4)$$

where $f_{\text{pipe-slurry}}$ is the friction per unit length between the pipe and slurry, kN. p_m is the slurry pressure outside the pipe, kPa. Usually, the value is supposed to be equal to the hydrostatic pressure on the pipe plus 20 kPa. D is the external diameter of pipe, m. μ_1 is the friction coefficient between the pipe and the slurry. c_1 is the cohesion between the pipe and the slurry, kPa, which can be ignored due to the good lubrication performance of the slurry.

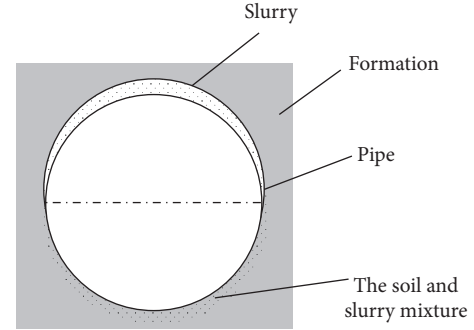


FIGURE 8: The schematic of diagram the pipe-soil and pipe-slurry combinative contact model [16].

When calculating the jacking force of the lower part, it is considered that the steel pipe gravity and the soil pressure on the pipe are loaded onto the soil under the steel pipe. Terzaghi loose earth theory [17] is used to calculate the earth pressure on the pipe (Figure 9):

$$\sigma_z = \frac{B(\gamma - c/B)}{k_0 \tan \varphi} \left(1 - e^{-k_0 \tan \varphi H/B} \right), \quad (5)$$

where σ_z is the earth pressure on the pipe, kPa. k_0 is the Rankine active earth pressure coefficient. c is the cohesion of soil, kPa. B is half of the width of the soil damage line, m. γ is the soil mass, kN/m^3 . φ is the internal friction angle of soil, $^\circ$. H is the buried depth, m. Calculation formula of pipe-soil friction is

$$f_{\text{pipe-soil}} = \left(\frac{\sigma_z \pi D}{2} + G \right) \mu_2 + \frac{c_2 \pi D}{2}, \quad (6)$$

where $f_{\text{pipe-soil}}$ is the friction per unit length between the pipe and soil, kN. G is the pipe weight per unit length, kN. μ_2 is the friction coefficient between the pipe and slurry-soil mixture. c_2 is the cohesion between the pipe and slurry-soil mixture, kPa. Because graphite powder is mixed into the slurry, the lubricity of the slurry-soil mixture is good, so the cohesive force is ignored.

Therefore, the calculation formula of the pipe jacking force per unit length is as follows:

$$f = f_{\text{pipe-slurry}} + f_{\text{pipe-soil}}, \quad (7)$$

where f is the whole friction per unit length, kN.

The friction coefficient is usually in the range of 0.07–0.10 [7]. And, it is related to the grouting amount, grouting

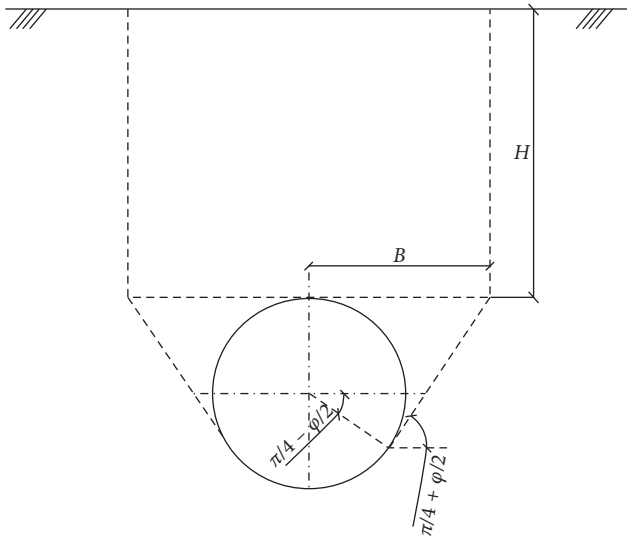


FIGURE 9: The schematic diagram of the Terzaghi loose earth theory [17].

uniformity, slurry sleeve integrity, etc. It is also found that the lower value will be taken when the lubrication effect is good. On the contrary, the higher value will be taken, but usually the value will be no more than 0.2. Besides, the friction coefficient is approximately equal to $\tan \varphi$ without grouting [7]. Therefore, in this calculation, the friction coefficient of the pipe-slurry contact part is set as 0.1. In the pipe-soil contact, there is some slurry mixed with the soil, so the friction coefficient of the mixture is approximately set as follows:

$$\mu_2 = \frac{(0.2 + \tan \varphi)}{2}. \quad (8)$$

The average overburden height is 4 m. In this pipe jacking project, the calculated jacking force per unit length is 16.56 kN.

3.2.2. Comparison and Discussion. The jacking force is monitored throughout the whole jacking process. Figure 10 shows the monitoring results of the initial 100 m construction in the pipe jacking project. It is found that the measured jacking force is about 10% smaller than the calculated jacking force. At the initial stage of the jacking process and the pipe jacking section between 40 and 50 m (the pipe jacking was paused and restarted during this period), the jacking force is significantly larger. The main reason is that in these two construction sections, the slurry is changed from the liquid state to the gelatinous state after keeping static for some time, and the static shear-stress increased. When the pipe jacking construction is restarted, it is required to overcome the static shear-stress of the slurry, resulting in an increase of the pipe jacking force.

The monitoring results showed that the selection of slurry Formula (2) had provided good lubrication for the long-distance large-diameter pipe jacking in the expansive soil. Under normal lubrication condition, the pipe jacking

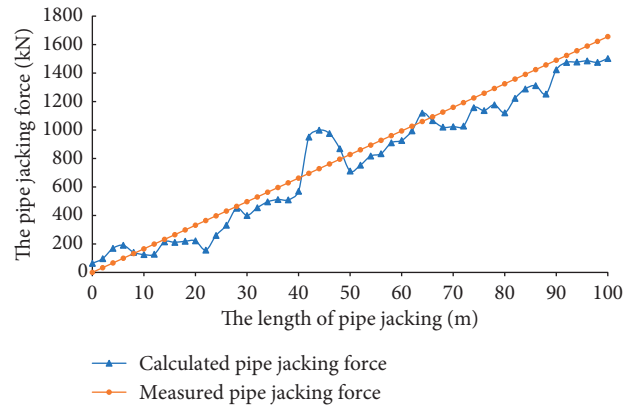


FIGURE 10: The calculated and measured pipe jacking force.

force had been controlled well. Meanwhile, the actual contact situation of pipe jacking was fully considered in the pipe jacking calculated method. So, the more accurate prediction of pipe jacking force had been obtained with the method.

4. Conclusions

- (1) Combined with the requirements for the pipe jacking slurry in general formation and the drilling mud in expansive formation, the key design points of slurry for the long-distance large-diameter pipe jacking project in expansive soil were put forward.
- (2) Based on the laboratory tests, the thixotropic slurry properties change rules were obtained, as the addition amount of plant glue, potassium humate, Na-CMC, and graphite powder changed. According to the results of single-factor tests, three kinds of inhibitive slurry formulas were prepared, and their properties were comprehensively tested. Both Formulas (2) and (3) could fully meet the requirements for the long-distance large-diameter pipe jacking project in the expansion formation. Because the static shear-stress of Formula (2) was more suitable, the Formula (2) was selected to be used in a practical project. The monitoring results showed that the slurry Formula (2) had a great lubrication effect in the expansive formation.
- (3) Combined with the Terzaghi loose earth theory and the actual contact situation of pipe jacking, a practical calculated method of the pipe jacking force was presented. The calculated jacking force per unit length was 16.56 kN according to the new method. And the actual jacking force was about 10% smaller than the calculated pipe jacking force. It proved that the new method could accurately predict the pipe jacking force.

Data Availability

The numerical data used to support the findings of this study are included within the article. All the lab test data and calculation results data used to support the findings of this study are also available.

Conflicts of Interest

The authors declare that they have no conflicts of interest.

Acknowledgments

The authors are grateful to the National Natural Science Foundation of China (41702323 and 51608192), the Natural Science Foundation of Hunan Province (2016JJ3062), and the Postdoctoral Science Foundation of Central South University (160320001 and 140050007).

References

- [1] Y. G. Chen, L. Y. Jia, Q. Li, W. M. Ye, Y. J. Cui, and B. Chen, "Swelling deformation of compacted GMZ bentonite experiencing chemical cycles of sodium-calcium exchange and salinization-desalinization effect," *Applied Clay Science*, vol. 141, pp. 55–63, 2017.
- [2] Y. G. Chen, C. M. Zhu, W. M. Ye, Y. J. Cui, and Q. Wang, "Swelling pressure and hydraulic conductivity of compacted GMZ01 bentonite under salinization–desalinization cycle conditions," *Applied Clay Science*, vol. 114, pp. 454–460, 2015.
- [3] Y. G. Chen, Y. J. Cui, A. M. Tang, Q. Wang, and W. M. Ye, "A preliminary study on hydraulic resistance of bentonite/host-rock seal interface," *Geotechnique*, vol. 64, no. 12, pp. 997–1002, 2014.
- [4] K. D. Liu, "Research on structure force of clay core wall stone slag dam," *Applied Mechanics and Materials*, vol. 394, pp. 376–380, 2013.
- [5] C. G. Struchtemeyer, J. P. Davis, and M. S. Elshahed, "Influence of the drilling mud formulation process on the bacterial communities in thermogenic natural gas wells of the barnett shale," *Applied and Environmental Microbiology*, vol. 77, no. 14, pp. 4744–4753, 2011.
- [6] J. Yen and K. Shou, "Numerical simulation for the estimation the jacking force of pipe jacking," *Tunnelling and Underground Space Technology*, vol. 49, pp. 218–229, 2015.
- [7] A. L. Pellet Beaucour and R. Kastner, "Experimental and analytical study of friction forces during microtunneling operations," *Tunnelling and Underground Space Technology Incorporating Trenchless Technology Research*, vol. 17, no. 1, pp. 83–97, 2002.
- [8] C. C. Reilly and T. L. L. Orr, "Physical modelling of the effect of lubricants in pipe jacking," *Tunnelling and Underground Space Technology*, vol. 63, pp. 44–53, 2017.
- [9] T. Elshehabi and I. Bilgesu, "Impact of drilling with oil based mud on well control in horizontal shale gas wells," in *Proceedings of SPE Eastern Regional Meeting*, Morgantown, WV, USA, October 2015.
- [10] M. S. Zazarli Shah, A. Sauki, W. Z. W. Bakar, N. A. Ghazali, and A. Azizi, "Drilling fluid design for shale gas drilling," *Advanced Materials Research*, vol. 1113, pp. 617–624, 2015.
- [11] A. Aftab, A. R. Ismail, and Z. H. Ibupoto, "Enhancing the rheological properties and shale inhibition behavior of water-based mud using nanosilica, multi-walled carbon nanotube, and graphene nanoplatelet," *Egyptian Journal of Petroleum*, vol. 26, no. 2, pp. 291–299, 2016.
- [12] A. Babajide, O. Adebawale, F. Adesina et al., "Effects of temperature and pressure on shale cuttings dispersion in water based mud WBM using NaCl, CaCl₂, KCl salts as primary inhibiting agents and polymer XCD xanthan gum as secondary inhibiting agent," in *Proceedings of SPE Nigeria International Conference and Exhibition*, Lagos, Nigeria, August 2016.
- [13] H. Shimada, S. Khazaei, and K. Matsui, "Small diameter tunnel excavation method using slurry pipe-jacking," *Geotechnical and Geological Engineering*, vol. 22, no. 2, pp. 161–186, 2004.
- [14] M. Y. Wang, H. Li, and B. J. Geng, "Analysis on the practical application of pipe engineering in expansive soil," *Shan Dong Water Resource*, vol. 8, pp. 32–33, 2009, in Chinese.
- [15] Y. C. Ye, L. M. Peng, W. C. Yang et al., "Calculation of jacking force for pipe-jacking considering mud slurry thixotropy," *Chinese Journal of Geo-technical Engineering*, vol. 37, pp. 1653–1659, 2015, in Chinese.
- [16] P. Zhang, B. S. Ma, C. Zeng et al., "Numerical model for jacking force based on pipe-soil contact characteristics," *Chinese Journal of Geo-technical Engineering*, vol. 39, pp. 244–249, 2017, in Chinese.
- [17] K. Terzaghi, *Theoretical Soil Mechanics*, John-Wiley and Sons, Hoboken, NJ, USA, 1943.

Research Article

Deformation and Damping Characteristics of Lightweight Clay-EPS Soil under Cyclic Loading

Yundong Zhou,¹ Mingdong Li ,² Qibao He,¹ and Kejun Wen ³

¹Key Laboratory of Ministry of Education for Geomechanics and Embankment Engineering, Hohai University, Nanjing 210098, China

²School of Civil Engineering and Architecture, East China University of Technology, Nanchang 330013, China

³Department of Civil and Environmental Engineering, Jackson State University, Jackson, MS 39217, USA

Correspondence should be addressed to Mingdong Li; lmd@ecit.edu.cn

Received 14 June 2018; Revised 23 August 2018; Accepted 13 September 2018; Published 10 October 2018

Guest Editor: Yongfeng Deng

Copyright © 2018 Yundong Zhou et al. This is an open access article distributed under the Creative Commons Attribution License, which permits unrestricted use, distribution, and reproduction in any medium, provided the original work is properly cited.

Lightweight Clay-EPS Soil (LCES) is a newly developed material which has many merits such as the adjustability of strength and density, simplicity for construction, and economical efficiency. It has been widely applied in practical engineering, e.g., soft ground improvement, the solvent of bridge head jump, earthfill of pipeline, and broadening of highway. Meanwhile, construction castoff and industrial waste can be recycled as a major ingredient in LCES. The dynamic deformation characteristics of LCES and clay were comprehensively studied using laboratory dynamic triaxial tests. It was found that the compressive strain of LCES increased while the growth rate of strain decreased with the increasing number of cycles, which conformed to a hyperbola model. The dynamic secant elastic modulus of LCES decreased with the increase of dynamic strain, which was represented by strain softening. The dynamic modulus of clay decreased sharply, while that of LCES decreased marginally. Moreover, the damping ratio of LCES tended to increase with the increasing dynamic strain. The damping ratio of LCES was lower than that of clay at the same strain level. It was also found that cement content had a negative relationship with the damping ratio of LCES, while the effect of EPS beads content was adverse. The damping ratio of both LCES and clay decreased moderately.

1. Introduction

Public infrastructures, such as the highway, railway, and city subway, have confronted many challenges, including the bumping at the bridge-head in highway, undue settlement of soft foundation, unstable retaining wall, etc. The overweight of soil can be one of the major causes. Expanded polystyrene (EPS) composite soil is a type of artificial material that consists of soil, EPS bead, water, and cementing material (e.g., cement and fly ash) [1, 2]. The EPS composite soil had been applied in many engineering constructions in Japan since the 1980s, and both the density and strength performance of EPS composite soil can achieve the engineering requirement [3, 4]. Lightweight Clay-EPS Soil (LCES) is a kind of geotechnical material which has many merits such as the lightness, adjustability of strength and density, and fluidity. It has been widely applied in many engineering

practice, including the treatments of soft foundation, vehicle jump at bridge head, backfill of pipelines, and broadening of highway, as shown in Figure 1. The waste soils generated from engineering constructions can be reused as the major ingredient in LCES by using the curing agent and lightweight filler. Recycling of the waste soils could significantly reduce the cost of engineering construction. Cement mixed with fly ash, lime, and waste gypsum were normally adopted as curing agent to improve the mechanical performance of LCES. Meanwhile, the household waste such as foam plastic and tire beads could be used as the lightweight filler. Moreover, the LCES was widely applied in many engineering projects in China, such as the road foundation reinforcement, slope stability, and construction backfill [5, 6].

There are many research achievements on lightweight soil, especially on its static characteristics. Dry density of LCES decreases dramatically with the increase of EPS beads

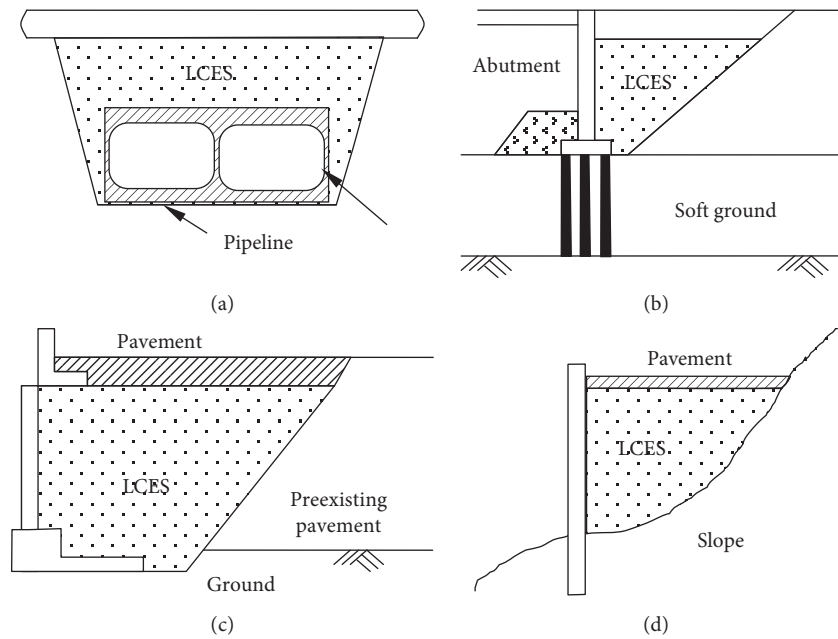


FIGURE 1: The engineering applications of LCES. (a) Pipeline backfill. (b) Solvent of bridge head jump. (c) Road widening. (d) Slope earthfill.

volumetric content, while it increases slightly with the increase of cement content. Unconfined compressive strength increases dramatically in a parabolic relationship with the increase of cement content, while decreases with the increase of EPS beads volumetric content in a hyperbolic relationship. Cohesion increases with the increase of cement content because it is mainly caused by the bonding function of hydration products of cement. Friction angle decreases with the increase of EPS beads volumetric content, which is caused by the smoother surfaces of EPS beads than sand grains. Quantitative relationships between physico-mechanical properties of sand-EPS beads soil and material proportion were provided [7]. Cohesion decreases with the increase of the EPS size, which was theoretically proved. According to the fact that the strength reduction rate is far below the reduction rate of unit price, EPS beads with diameter of 3–5 mm can be used in construction [8]. A model for compaction density of sand-EPS beads soil was established based on material composition and the physical essence of soil compaction. It was verified by lab tests that the predicted value was close to the measured wet density with relative error between 0.282% and 5.267% under different compaction conditions [9]. The volume ratio of EPS beads to the soil, initial average effective consolidation pressure, initial consolidation stress ratio, initial intermediate principal stress coefficient, and initial principal stress direction angle had great effects on the maximum dynamic shear modulus and the reference shear strain [10, 11]. The stress increased when LCES was considered as viscous elastic material instead of elastic material [12]. The shear stress attenuated more rapidly with the depth [13]. The damage caused by dynamic loading could be effectively reduced by LCES [14]. Data from stress-controlled cyclic uniaxial tests showed a logarithmic decrease in the damping ratio of EPS geofoam with the increasing axial strain amplitude. For

cyclic axial strain amplitudes greater than 1.0%, LCES exhibited a viscoelastoplastic behavior associated with the occurrence of permanent plastic strains at the end of the cyclic tests [15]. The simulation study on the process of falling rocks found that LCES could reduce the impact of falling rocks [16]. Gao et al. applied EPS composite soil as backfills and found that the dynamic deformation mode of EPS composite soil was different from that of fine sand [2].

To investigate the deformation and damping characteristics of LCES, a series of cyclic triaxial tests on LCES with different proportions were carried out by using the multifunctional indoor triaxial apparatus. The dynamic deformation characteristics of LCES were obtained. The influences of cement content, EPS beads content, and confining pressure on the dynamic modulus and damping ratio of LCES were analyzed and compared with the dynamic deformation characteristics of clay.

2. Materials and Methods

2.1. Clay. The clay adopted in this study was collected from 6 meters below the ground surface of Olympic Sports Center, located in Hexi, Nanjing. The geotechnical properties of this clay are shown in Table 1, and its particle size distribution is shown in Figure 2. The clay soil is classified as Lean Clay (CL) based on Unified Soil Classification System standard.

2.2. Cement. The binder used in the experiment was 32.5# Portland cement produced in Nanjing, China.

2.3. Expanded Polystyrene (EPS) Beads. EPS is a macromolecule polymer with prior lightweight properties. During the forming process of EPS beads, a large number of individual pores were formed because of expanding of blowing

TABLE 1: Geotechnical properties of clay.

Unit weight γ ($\text{kN}\cdot\text{m}^{-3}$)	Water content ω (%)	Void ratio e	Specific gravity G_s	Degree of saturation S_r (%)	Plastic limit ω_p (%)	Liquid limit ω_L (%)	Plastic index I_P	Liquid index I_L
16.4	62.3	1.70	2.73	100	27.3	47.5	20.2	1.73

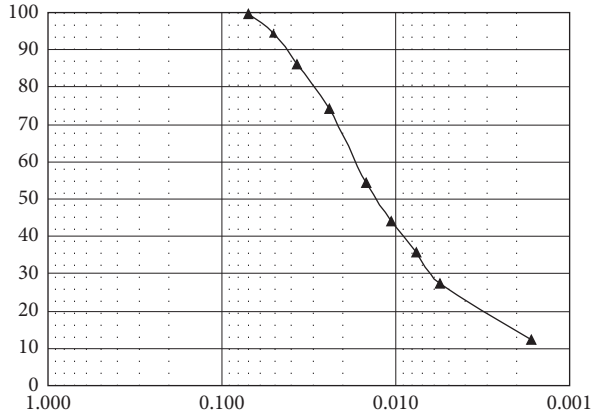


FIGURE 2: Particle size distribution of clay.

agent, resulting in the increase in volume by up to 40 times. The EPS Beads adopted in this study was provided by Nanjing Youbang Foamed Plastic Co. Ltd, with 0.023 g/cm^3 in density and 3 mm in average diameter.

2.4. Test Design. To investigate the effect of material proportion on the deformation and damping characteristics of LCES under cyclic loading, totally 9 dosages of LCES were selected in this study, as listed in Table 2. Different ratios of cement and EPS beads were added to clay soil to prepare LCES with different material proportions. Four specimens were prepared for each dosage of additive. The value of α indicates the cement addition ratio by weight of dry soil, while β means the EPS addition ratio by weight of dry soil.

2.5. Preparation of Specimens. The materials were prepared and weighed before being mixed thoroughly with a blender at 100 rot/min. The mixtures were then put into the mold and compacted through 5 layers. The specimen was 61.8 mm in diameter and 140 mm in height. The specimens were cured in a curing box at $20 \pm 2^\circ\text{C}$ and 99% humidity continuously for 27 d. The cross sections of T11, T12, and T13 are shown in Figure 3. The specimens were placed in air extractor, and vacuumized for 20 min at a vacuum degree of -0.1 MPa . Finally, the specimens were fully saturated through opening the water inlet valve. The saturated specimens were set in water environment for another 24 hours before the dynamic triaxial test.

2.6. Test Methods. The specimens were tested by a multi-functional automatic dynamic triaxial apparatus which was developed by Hohai University and Japan Round Well Co., LTD. The dynamic triaxial test of LCES was conducted in accordance with the dynamic triaxial method in

TABLE 2: Proportions of cement and EPS.

Maker	α (%)	β (%)
T11	5	2
T12	5	3
T13	5	4
T21	10	2
T22	10	3
T23	10	4
T31	20	2
T32	20	3
T33	30	4
T00*	0	0

*T00 is the control test with material clay.



FIGURE 3: Cross sections of T11, T12, and T13.

geotechnical test procedures. The specimens removed from water were placed in a triaxial cell which connects with vibration equipment. A cell pressure (20 kPa) was applied to saturate the pipe line around 30 min until there was no air bubble in the drainage pipe. The back pressure (100 kPa) was then applied to fully saturate the specimens. Certain confining pressures (30 kPa, 60 kPa, and 90 kPa) were applied to the specimen for consolidation. The consolidation process was finished when the volume change of the specimen had been less than 0.1 mL in 5 min. After consolidation, undrained shear tests were conducted until dynamic strain exceeds 5%.

The dynamic load applied in this test was in the form of sine wave with a frequency of 0.1 Hz. The amplitude was controlled by the dynamic shear stress ratio (s), as shown in Equation (1). The dynamic shear stress ratio of LCES was applied, and 10 cycles was loaded.

$$s = \frac{\tau_d}{\sigma_c} = \frac{\sigma_d}{2\sigma_c} = 0.5, \quad (1)$$

where s is the dynamic shear stress ratio, i.e., the ratio of shear stress with respect to confining stress in the 45° surface of the specimen; τ_d is the dynamic shear stress amplitude in the 45° surface of the specimen; σ_c is the consolidation confining pressure; and σ_d is the amplitude of axial dynamic load.

3. Results and Discussion

3.1. Time History Character Curve of Strain of LCES. The dynamic strain versus time curve is shown in Figure 4. When dynamic shear stress was 0.5, the strain of LCES was mainly compressive strain compared with clay soil. The strain scope of LCES was affected by the cement content. When the cement content was 5%, the strain scope is around 6-7%. However, the strain scope reduced to 4% as the cement content reached 15%. This might be caused by the strong cementation force of cement, which improved LCES' ability to resist stress.

The relationship between the dynamic strain of LCES and the number of load cycles is presented in Figure 5. The compression strain of LCES tended to increase with the increase of load cycles. This might be caused by the reduction of void space and volume shrinkage of EPS beads under compression stress. In addition, it was found that the growth rate of strain decreased with the increase of cycle numbers, but the dynamic strain leveled off. This finding indicated that the strength of the dynamic load was lower than the critical dynamic strength, when the dynamic shear stress ratio of LCES was 0.5. In this case, there were no or minor damages of soil structure, and the soil structure did not enter the stage of shear vibration and vibration failure. Soil deformation was mainly caused by the vibration and compaction of soil beads which was caused by vertical displacement. Yan et al. found a different trend on clay soil that ε_d initially increased slowly with N , followed by a more rapid increase [17].

3.2. Dynamic Secant Elastic Modulus of LCES. The hysteresis curve of LCES under cyclic loading is shown in Figure 6. The curve moved from point O along arc OA to point A with the increase of stress during the loading process. However, the curve moved from point A along the arc ABC to point B during the unloading process. Meanwhile, point B moved along arc BCD to point D in the process of reverse loading and unloading, and point D did not coincide with point O, which indicated that the deformation of LCES under dynamic load included elastic deformation and plastic deformation. The $\Delta\varepsilon_d$ presented in Figure 6 is the plastic deformation after 7 days of loading. A uniform plastic deformation $\Delta\varepsilon_d$ was assumed since the plastic deformation ran through the whole loading process. The plastic deformation was uniformly distributed to all the points on the curve, and the corrected hysteresis loop was obtained by subtracting the amount of evenly distributed plastic deformation from the collected deformation, as shown by the dash line in Figure 6. The corrected hysteresis loop was occlusive, and it was the same as that of ordinary soil. For clay soil, the slope of the line from the point of origin to the point of the hysteresis loop was taken as the equivalent dynamic modulus of elasticity. It was not appropriate to apply the equivalent dynamic elastic modulus to LCES since the cumulative deformation of LCES was large and the hysteresis loop deviated too much from the origin. Therefore, the dynamic secant elastic modulus E_{sec} was adopted

for analysis as shown in Figure 7. The slope of the vertex connection line of the hysteresis loop corresponding to various loads was the same as the equivalent dynamic elastic modulus of clay.

The curves of $E_{sec} \sim \varepsilon_d$ under different confining pressures are shown in Figure 8. In general, the dynamic secant elastic modulus of LCES decreased with the increase of dynamic strain, which was represented by strain softening and exhibited a good hyperbolic relationship. The main reason was that the rigidity of LCES mainly came from cementing of cement hydrate. With the increase of the strain, the effect of cementing was gradually damaged and the rigidity of LCES was reduced. In the same proportion of LCES, the motion-cutting line modulus increased with the increase of confining pressure. This might be explained by the fact that the greater confining pressure caused a denser specimen and achieved a higher stiffness. This finding is the same as the performance of conventional soil.

The curve of $E_{sec} \sim \varepsilon_d$ on different cement content is shown in Figure 9. In the same EPS beads content and confining pressure, the elastic modulus of the moving secant modulus of LCES gradually increased with the increase of cement content, which indicated that the addition of cement could improve the dynamic stiffness of LCES. Higher cement content achieves better cementation function of particles and more reduction of porosity ratio. The E_{sec} of LCES decreased slower with the increase of ε_d than that in ordinary clay. When the cement content increased, the $E_{sec} \sim \varepsilon_d$ curve approached a linear relationship which indicated that LCES had a better deformation resistance than ordinary clay under dynamic force. This can be attributed to the fact that cement hydrate cementation enhanced the deformation resistance under dynamic force after the soil and cement were completely mixed.

The curve of $E_{sec} \sim \varepsilon_d$ on different EPS beads content is shown in Figure 10. When cement content was 10%, there was no remarkable difference in E_{sec} with the increase of EPS beads content, which indicated that the effect of the relative cement content and the EPS volumetric content on dynamic stiffness was negligible. This also indicated that 10% cement mixed clay and EPS beads had similar stiffness. Meanwhile, E_{sec} decreased with the increase of EPS content when cement content increased to 15%. It was illustrated that the cement cementation was enhanced under high cement content, and the stiffness of soil-cement was significantly greater than that of EPS beads. In this case, the content of cement relatively decreased due to the increase of EPS beads content, which resulted in the reduction of the overall motion-cutting line modulus.

3.3. Damping Ratio of LCES. The damping ratio, D , represented the viscous property of soil, which was an important index to measure the vibration damping property of soil and had a significant influence on the dynamic response of soil. D in this study was defined as the ratio of the actual damping coefficient to the critical damping coefficient as shown in Equation (2), where A_L is the area of the hysteresis loop and A_T is the area of the shadow triangle as shown in Figure 11.

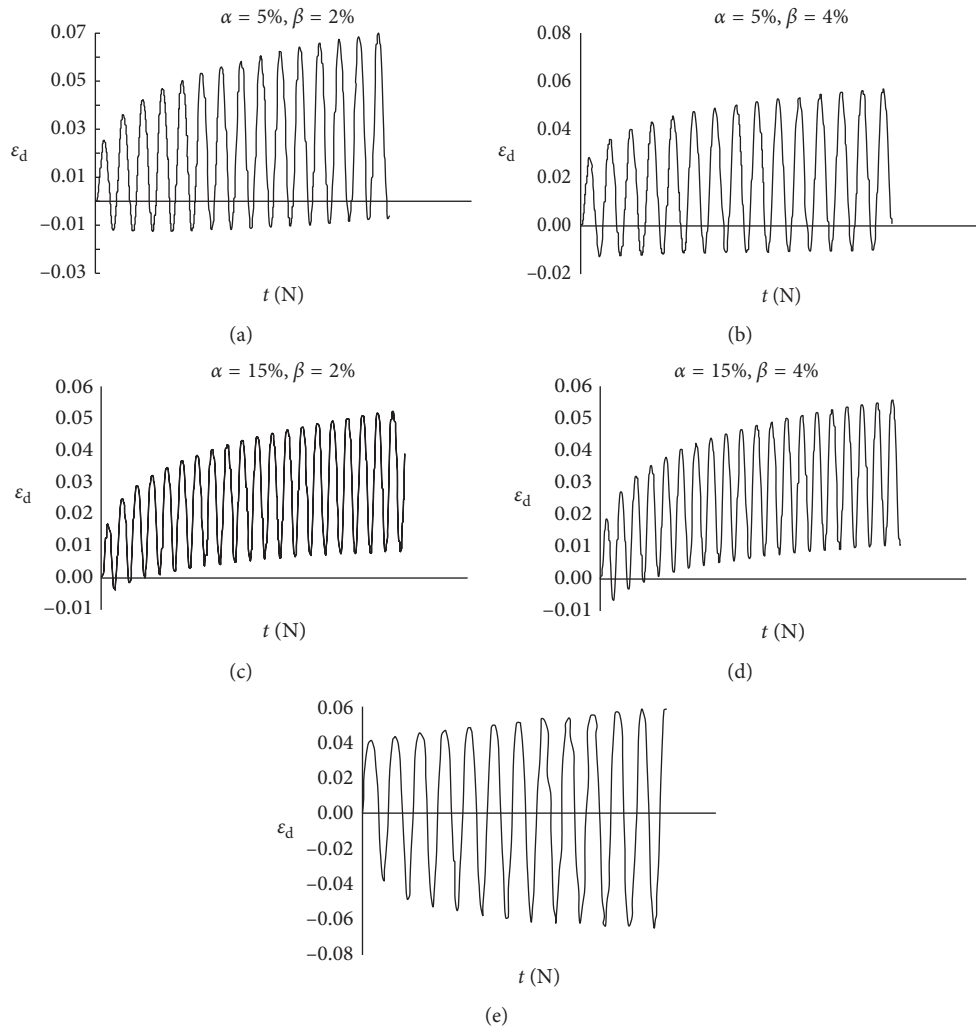


FIGURE 4: Typical dynamic strain time history character curves of LCES. (a) T11, (b) T13, (c) T31, (d) T33, and (e) T00 (material clay).

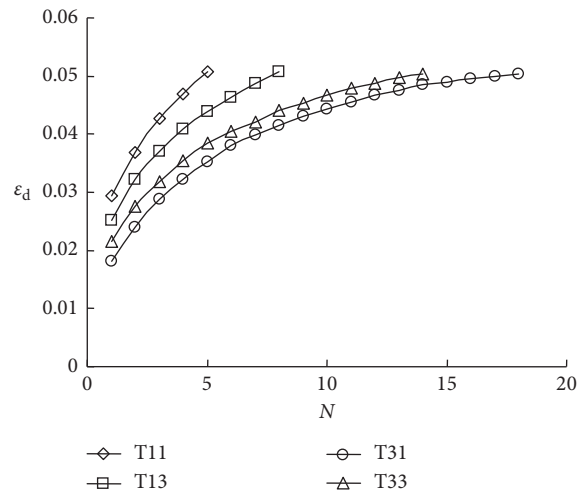


FIGURE 5: The dynamic strain behavior of LCES as a function of the number of load cycles.

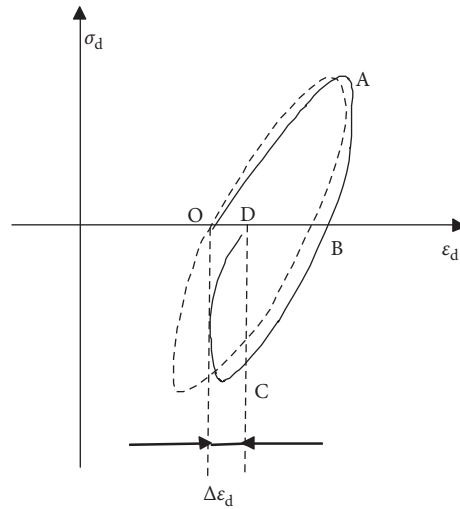


FIGURE 6: The hysteresis curve of LCES.

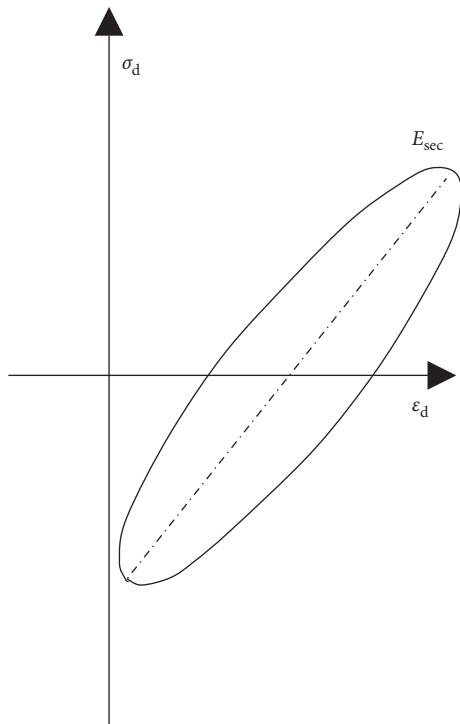


FIGURE 7: Dynamic secant elastic modulus E_{sec} .

$$D = \frac{A_L}{4\pi A_T} \quad (2)$$

Figure 12 presents the relationships between the damping ratio and dynamic strain of LCES and clay at different cement content. The damping ratio of LCES and clay increased gradually as the dynamic strain increased. Maher et al. also found similar results that the damping ratio of cement-treated sand was increased with the increase of shear strain [18]. Cement content had significant effects on the LCES damping ratio. The damping ratio of LCES was lower than that of clay, and it decreased with the increase of

cement content which indicated that the damping ratio of LCES could be controlled by adjusting the cement content. This might be caused by that cement hydrate increased the stiffness of soil and reduced the viscosity of soil, which resulted in the decrease of the damping ratio.

Figure 13 presents the relationship between the damping ratio and dynamic strain of LCES and clay at different beads content. The damping ratio of LCES increased with the increase of EPS beads content, which indicated that EPS beads could absorb more vibration energy. This might be due to the fact that EPS beads were soft and nonlinear elastic. When EPS beads content increased, the cement content decreased correspondingly, which might weaken the effect of cement hydrate on the damping ratio of LCES. Gao et al. found that there was no significant different on the damping ratio with different EPS content when shear strain was less than 0.5% [19]. When shear strain exceeded 0.5%, the larger the EPS beads content, the larger the damping ratio. They believed that larger EPS bead content generated more weak interfaces between EPS beads and cemented soil [19].

Figure 14 presents the relationship between the damping ratio and dynamic strain of LCES and clay under different confining pressures. The damping ratio of LCES and clay decreased slightly with the increase of the confining pressure in the range of 30 kPa to 90 kPa.

4. Conclusions

For LCES with cement content between 5% and 15%, EPS beads content was between 2% and 4%, confining pressure was between 30 kPa and 90 kPa, and dynamic shear stress ratio was 0.5, the following dynamic deformation characteristics were found:

- (1) The compressive strain of LCES was significantly greater than the tensile strain. The tensile strain decreased with the increase of cement content. There was almost no tensile strain occurred when the cement content increased to 15%.

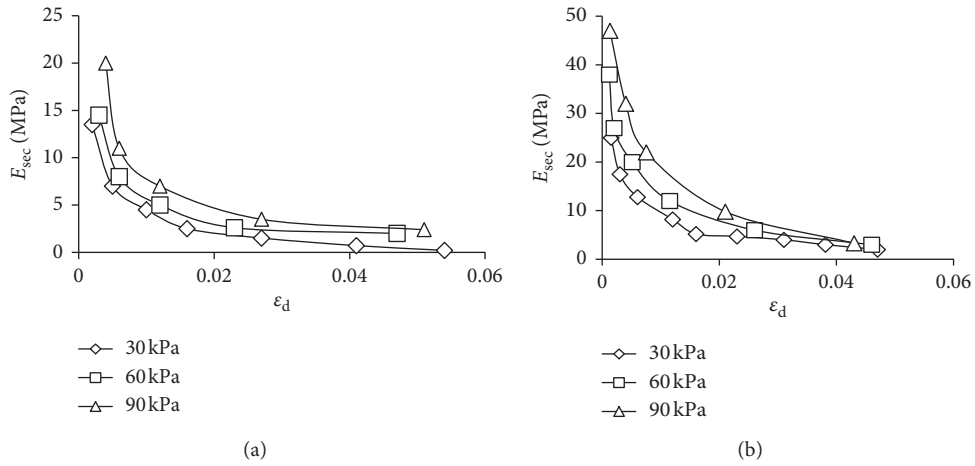


FIGURE 8: The curve of $E_{sec} \sim \epsilon_d$ under different confining pressures. (a) T13; (b) T31.

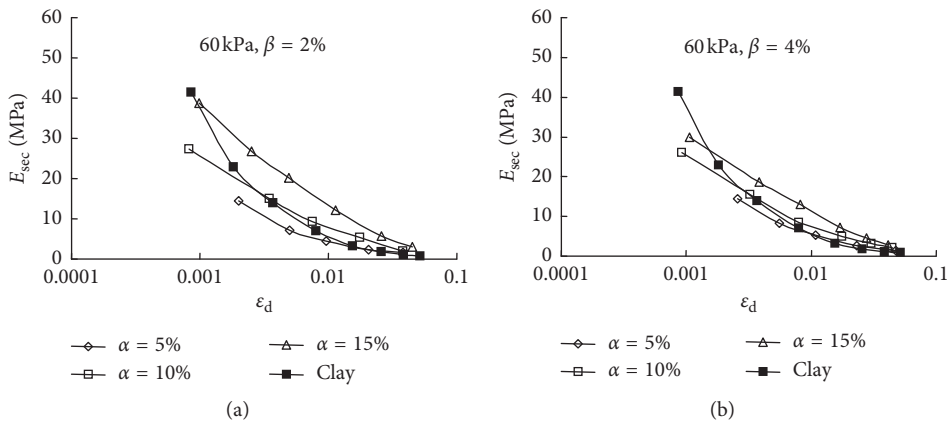


FIGURE 9: The curve of $E_{sec} \sim \epsilon_d$ on different cement content.

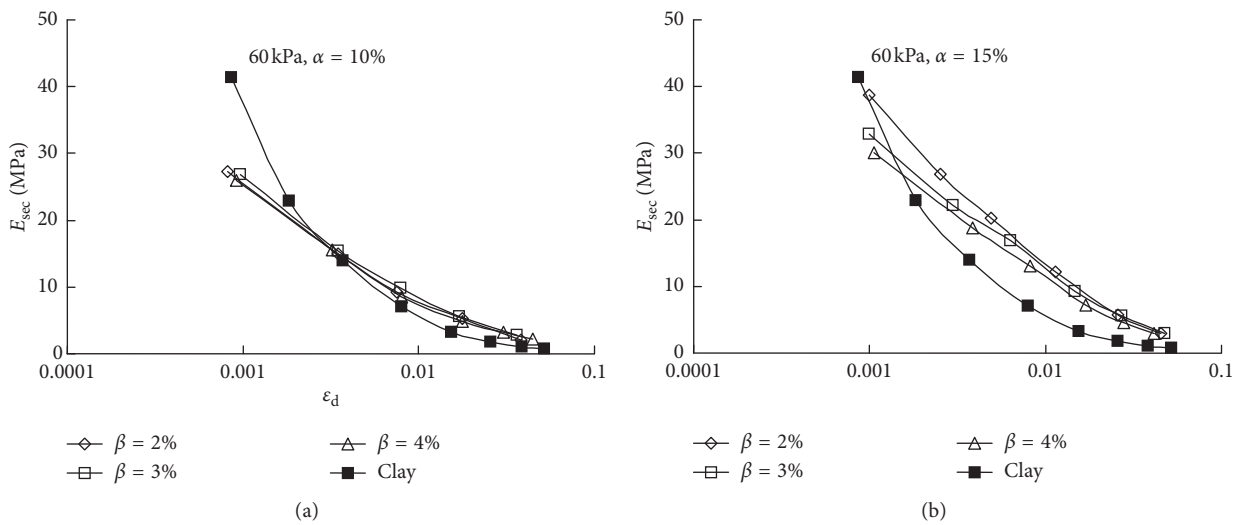


FIGURE 10: The curve of $E_{sec} \sim \epsilon_d$ on different EPS beads content.

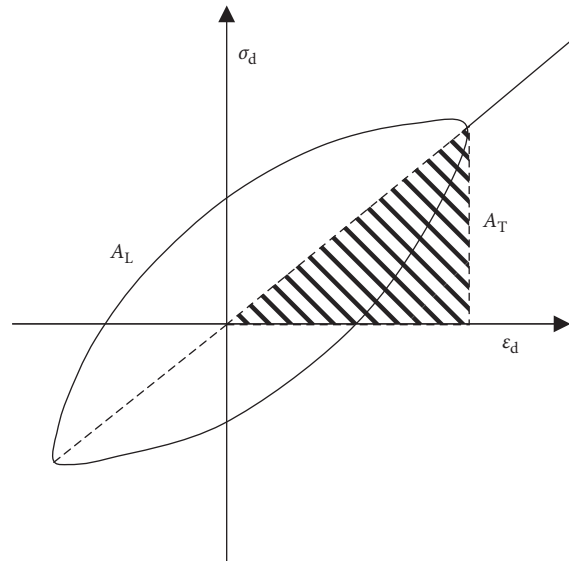


FIGURE 11: Definition of damping ratio.

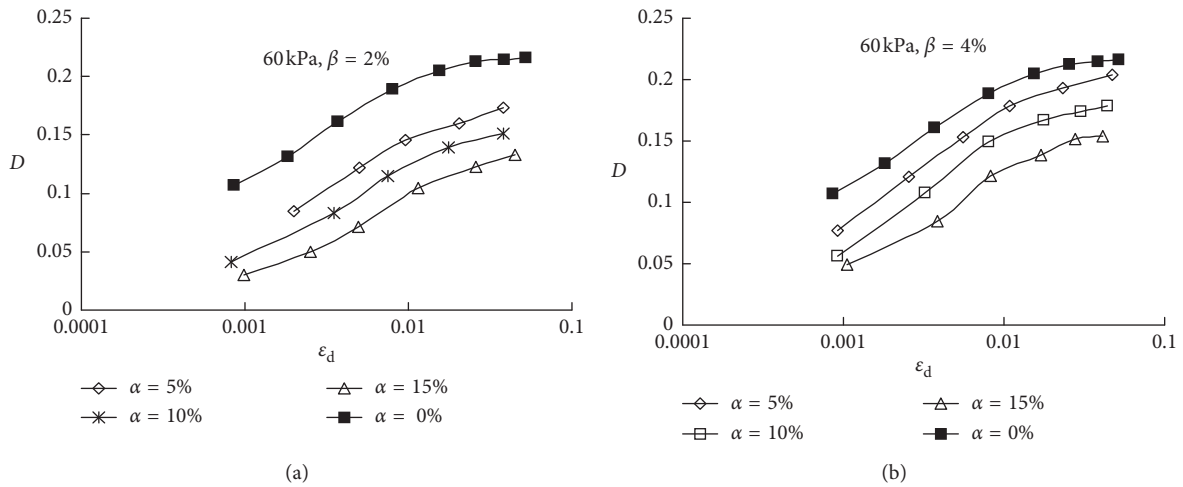


FIGURE 12: Relationship between the damping ratio and dynamic strain of LCES and clay at different cement content.

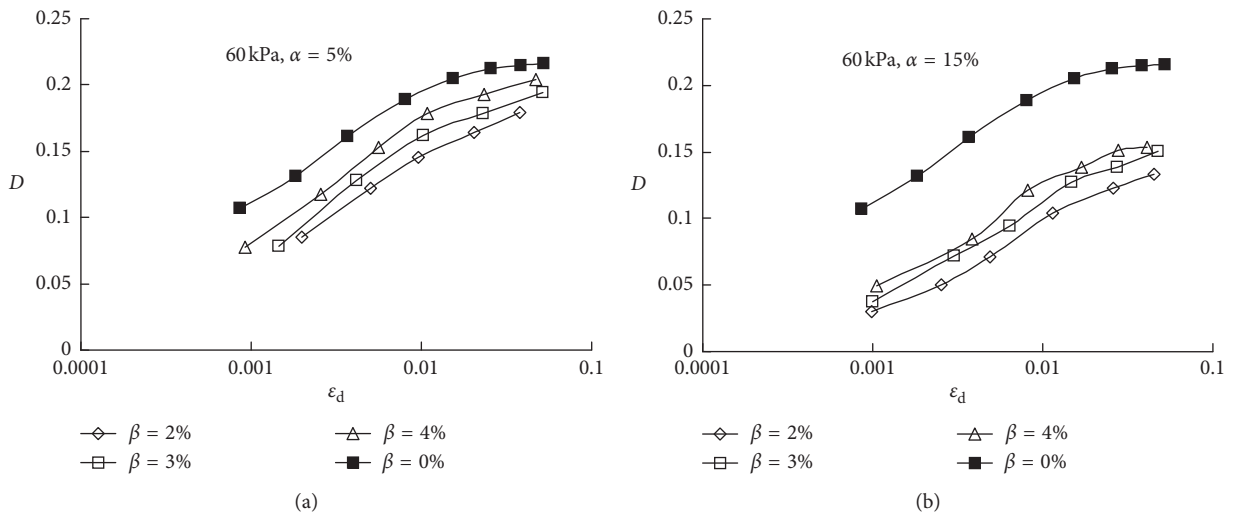


FIGURE 13: Relationship between the damping ratio and dynamic strain of LCES and clay at different beads content.

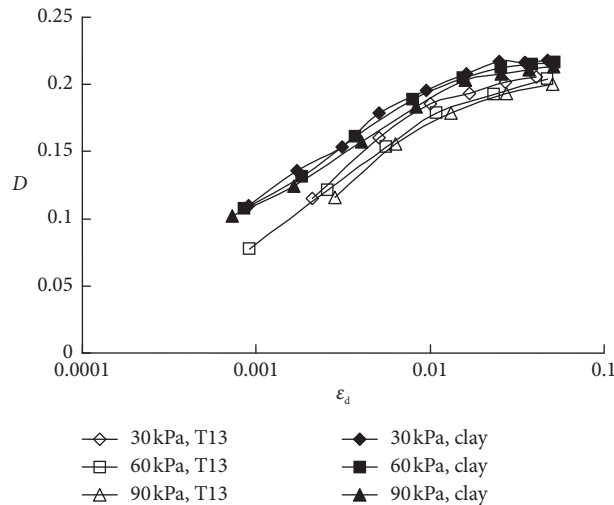


FIGURE 14: Relationship between the damping ratio and dynamic strain of LCES and clay under different confining pressures.

- (2) The compressive strain of LCES gradually increased with the increase of load cycles. The strain growth rate decreased with the increase of load cycles. The dynamic strain leveled off, which was consistent with the rule of the hyperbola model.
- (3) The dynamic secant elastic modulus of LCES decreased with the increase of dynamic strain, which was represented by strain softening and exhibited a good hyperbolic relationship. The dynamic modulus of clay decreased rapidly, but that of LCES decreased relatively slower. In addition, the dynamic modulus increased with the increase of confining pressure.
- (4) The damping ratio of LCES and clay increased with the increase of dynamic strain. The damping ratio of LCES was lower than that of clay. It decreased significantly with the increase of cement content, increased with the increase of EPS beads content, and decreased slightly with the increase of confining pressure.

Data Availability

The data used to support the findings of this study are available from the corresponding author upon request.

Conflicts of Interest

The authors declare that they have no conflicts of interest.

Acknowledgments

This study was supported by the National Foundation of China under Grant Nos. 51609093 and 51869001, the Science Foundation of Jiangsu Education Ministry under Grant No. 16KJB560002, China Postdoctoral Research Funds under Grant No. 2017M611675 for 168401, and Jiangsu Planned Projects for Postdoctoral Research Funds under Grant No.

1601007A. These supports are gratefully acknowledged. The assistance from Yifei Sun in improving the English writing of this study is appreciated.

References

- [1] Y. Kikuchi, T. Nagatome, T. A. Mizutani, and H. Yoshino, "The effect of air foam inclusion on the permeability and absorption properties of light weight soil," *Soils and Foundations*, vol. 51, no. 1, pp. 151–165, 2011.
- [2] H. Gao, Y. Hu, Z. Wang, C. Wang, and G. Chen, "Shaking table tests on the seismic performance of a flexible wall retaining EPS composite soil," *Bulletin of Earthquake Engineering*, vol. 15, no. 12, pp. 5481–5510, 2017.
- [3] K. Nagase and H. Kobayashi, "Development of a lightweight soil with styrofoam," *Soil and Foundations*, vol. 48, no. 6, pp. 13–15, 2000.
- [4] K. Tsuchida and H. Tougi, "Application of light-weight soil mixture made from clay and construction soil in coastal engineering," *Japan Civil Engineering Society*, vol. 20, no. 3, pp. 13–23, 2000.
- [5] M. Li, W. Zhu, D. Ma, and F. Ji, "Construction technology and application in-situ of expanded polystyrene treated light-weight soil," *Chinese Journal of Geotechnical Engineering*, vol. 28, no. 4, pp. 533–536, 2006, in Chinese.
- [6] H. Liu, "Technological innovation methods and practices in geotechnical engineering," *Chinese Journal of Geotechnical Engineering*, vol. 35, no. 1, pp. 34–58, 2013.
- [7] M. Li, K. Wen, L. Li, and A. Tian, "Mechanical properties of expanded polystyrene beads stabilized lightweight soil," *Geomechanics and Engineering*, vol. 13, no. 3, pp. 459–474, 2017.
- [8] T. Hou, "Influence of expanded polystyrene size on deformation characteristics of light weight soil," *Journal of Central South University*, vol. 19, no. 11, pp. 3320–3328, 2012.
- [9] T. Hou, "Model for compaction density and engineering properties of light weight soil," *Chinese Journal of Geotechnical Engineering*, vol. 36, no. 11, pp. 2127–2135, 2014, in Chinese.
- [10] H. Gao, R. Chen, F. Tong, G. Chen, and X. Cai, "Dynamic modulus and damping ratio of EPS bead composite soil under

- complex stress conditions,” *Journal of Disaster Prevention and Mitigation Engineering*, vol. 35, no. 2, pp. 166–198, 2015.
- [11] H. Gao, J. Liu, and H. Liu, “Geotechnical properties of EPS composite soil,” *International Journal of Geotechnical Engineering*, vol. 5, no. 1, pp. 69–77, 2011.
- [12] X. Cai, H. Gao, H. Zhao, G. Chen, and R. Chen, “Dynamic characteristics of EPS beads composite lightweight soil under railway loading,” *Journal of Disaster Prevention and Mitigation Engineering*, vol. 35, no. 5, pp. 651–658, 2015.
- [13] R. J. Bathurst, S. Zarnani, and A. Gaskinc, “Shaking table testing of geofoam seismic buffers,” *Soil Dynamics and Earthquake Engineering*, vol. 27, no. 4, pp. 324–332, 2007.
- [14] A. C. Trandair, S. F. Bartlett, and B. N. Lingwall, “Behavior of EPS geofoam in stress-controlled cyclic uniaxial tests,” *Geotextiles and Geomembranes*, vol. 28, no. 6, pp. 514–524, 2010.
- [15] J. Wang, X. Zhou, S. Wang, and J. Liu, “Study on energy dissipation measures of open cut tunnel under rockfall impact,” *Journal of Highway Communication Technology*, vol. 32, no. 9, pp. 103–108, 2015.
- [16] B. M. Das and Z. Luo, “Principles of soil dynamics,” in *Soil Dynamics and Earthquake Engineering*, vol. 13, Cengage Learning, Boston, MA, USA, 3rd edition, 2017.
- [17] C. Yan, X. Xu, and L. Huang, “Identifying the impact factors of the dynamic strength of mudded intercalations during cyclic loading,” *Advances in Civil Engineering*, vol. 2018, Article ID 5805294, 9 pages, 2018.
- [18] M. H. Maher, K. S. Ro, and J. P. Welsh, “High strain dynamic modulus and damping of chemically grouted sand,” *Soil Dynamics and Earthquake Engineering*, vol. 13, no. 2, pp. 131–138, 1994.
- [19] H. Gao, C. Bu, Z. Wang, Y. Shen, and G. Chen, “Dynamic characteristics of expanded polystyrene composite soil under traffic loadings considering initial consolidation state,” *Soil Dynamics and Earthquake Engineering*, vol. 102, pp. 86–98, 2017.

Research Article

Utilization of Electroplating Sludge as Subgrade Backfill Materials: Mechanical and Environmental Risk Evaluation

Yu Zhang, Peixin Shi , Lijuan Chen, and Qiang Tang 

School of Rail Transportation, Soochow University, Suzhou, China

Correspondence should be addressed to Peixin Shi; pxshi@suda.edu.cn

Received 7 June 2018; Revised 1 September 2018; Accepted 17 September 2018; Published 10 October 2018

Academic Editor: Dingwen Zhang

Copyright © 2018 Yu Zhang et al. This is an open access article distributed under the Creative Commons Attribution License, which permits unrestricted use, distribution, and reproduction in any medium, provided the original work is properly cited.

The electroplating sludge may pose serious threat to human health and surrounding environment without safe treatment. This paper investigated the feasibility of using electroplating sludge as subgrade backfill materials, by evaluating the mechanical properties and environmental risk of the cement-coal fly ash solidified sludge. In this study, Portland cement and coal fly ash are used to solidify/stabilize the sludge. After curing for 7, 14, and 28 days, the stabilization/solidification sludge specimens were subject to a series of mechanical, leaching, and microcosmic tests. It was found that the compressive strength increased with the increase of cement content, curing time, and the cement replacement by coal fly ash besides water content. Among these factors, the impact of water content on the compressive strength is most noticeable. It was observed that the compressive strength declined by 87.1% when the water content increased from 0% to 10%. Besides, leaching tests showed that the amount of leaching heavy metals were under the standard limit. These results demonstrated utilization of electroplating sludge in subgrade backfill material may provide an alternative for the treatment of electroplating sludge.

1. Introduction

Electroplating industries generate the increasing amount of contaminated water, which requires treatment before being discharged to mitigate the impact on the environment [1]. However, as a product from the process of the wastewater treatment, a great deal of highly hazardous sludge is produced [2]. Every year, about 100,000 tonnes of electroplating sludge (ES) have been generated in China [3]. ES is an extremely complex mixture that contains a huge amount of heavy metals, pathogenic microorganisms, and organic pollutants [4]. These harmful ingredients, especially various heavy metals, have serious biological toxicity and can pose serious threat to human health [5–7]. Thus, the appropriate disposal of ES is becoming more urgent for the electroplating industry and environmental engineering [8].

Solidification/stabilization (S/S) techniques are widely used in the treatment for metal-contained hazardous waste. The S/S method mixes contaminants with binders to convert the hazardous waste into the immobile and low toxic form [9]. Several binders are currently used for S/S [10, 11].

Portland cement is one of the mostly used binders in the S/S matrix due to its easy availability and low cost. It can readily wrap wet wastes, and its alkalinity condition decreases the solubility of many inorganic toxic or hazardous metals [12, 13]. However, the S/S of sewage sludge by cement is affected adversely by (1) the high internal porosity of cement-solidified matrix that results in higher leaching rate, and (2) the increase in volume of the solidified matrix [14, 15].

Other techniques for sludge disposal are also found in the literature, for example, incorporation into coal fly ash. Coal fly ash is currently one of the most common binding supplemental materials in waste stabilization. It is mainly used in mixture with Portland cement or lime and serves as a bulking agent and a pozzolan [10]. Coal fly ash is rich in silica (SiO_2) and calcium oxide (CaO). The SiO_2 reacts with calcium hydroxide formed from the hydration process of CaO to produce calcium silicate hydrate [12]. The pozzolanic properties enable it to be used in some engineering applications instead of cement [16]. Incorporation of fly ash into the binder can improve the long-term durability of mixed

cement stabilized product by decreasing the penetration of aggressive agents such as chloride ions [17]. Hardened fly ash-cement mixture, when properly designed, acts with increased strength and decreased permeability. Additionally, replacing parts of cement by fly ash can reduce the cost of production [18, 19].

Generally, cement-solidified products are always ultimately treated by landfilling [20]. However, the limited land area and the negative impact on environment have made it more essential to develop the effective and feasible treatment techniques [15]. Some researchers have studied the stability of cement-solidified forms disposed in landfills [21–25]. Tang et al. suggested that the leaching of heavy metals from cement-solidified products can be regarded as a pH-dependent controlled process, and the solubility and leachability of some solidified heavy metals increased when the pH value decreased [15]. Accordingly, some viable alternatives of reusing the sludge containing heavy metals should be encouraged to discover, helping to decrease landfill-space consumption and save resources [26].

As a waste-to-resource technique, recycling waste sludge for geotechnical works material and incorporation into construction materials can play a significant role in sustainable natural resource use [27]. Moreover, if the utilization of waste sludge in suitable geotechnical and construction material systems can be more beneficial to the stabilization of hazardous heavy metals, it will simultaneously alleviate the environmental damages. Therefore, this current work evaluated the potential utilization of solidified electroplating sludge for subgrade backfill materials. The impacts of binder formulation (different portions of Portland cement and coal fly ash), water content, and curing time on the physical properties of the solidified sludge specimens were explored. Microstructure characteristics were investigated on specimens with different formulation of the binders. In addition, the leachability of hazardous metals from the solidified sludge was evaluated for ensuring the environmental safety. The optimum proportion of substitution for meeting technical requirement and environmental standards were also determined.

2. Materials and Methods

2.1. Materials. The waste sludge (Figure 1(a)), as the byproduct generated from wastewater treatment processes, was collected from a diode plant located in Suzhou, China, and its physical and chemical properties are listed in Table 1. The elemental composition of the sludge was analyzed through X-ray fluorescence spectroscopy (XRF) analysis (JSX-3400R, JEOL, Japan). As shown in Table 1, the main elements in the sludge were copper (Cu), rhodium (Rh), and calcium (Ca), with an average composition of 23.17, 23.22, and 25.29%, respectively. The first two were directly related to the production process of diode. The Ca is generated during the wastewater treatment process, in which calcite is used as a coagulant agent (CaCO_3) [28]. The Cu is the main contamination, and the toxicity degree of Cu is critical.

Moisture and density were determined for select sludges. The sludge was acidic (pH 4.8), with a moisture content around 70% and a density about 1.05 g/cm^3 . Table 1 shows the mean values of three parallel samples used in the analysis. Moisture was measured following the method described by EN 14346: 2006 [29]. Density was determined by introducing a certain amount of sludge in water and measuring the volume on exchanging with water [30].

Portland cement (PC), coal fly ash (CFA), and water were used as binding materials. The PC was purchased from a local cement plant in Suzhou, China, mainly consisting of 6–15% active additive and 85–94% cement. The CFA was supplied by a coal-fired power plant located in Anhui, China (Figure 1(b)). The physical properties and chemical compositions of the cementitious materials are summarized in Table 1. Physically, CFA is in a form of fine particles with a medium density (2.9 g/cm^3) and has a high surface area ($3413 \text{ cm}^2/\text{g}$). The pH value of CFA shows alkalinity (pH = 10.36). In terms of chemical compositions, high contents of Si and Al were observed in CFA, which was in close agreement with the results of studies in other literatures [31, 32]. Water used in this study was deionized and was prepared from tap water via distillation (RFD240NA, Advantec, Japan).

2.2. Sample Preparation. During sample preparation, the homogeneity of CFA and sludge need to be guaranteed. The sludge was grinded to aid workability of the sludge-ash-cement matrix during casting. Prior to mixture, the CFA and PC were oven dried (101-A, Leao, China) at a temperature of 105°C for at least 24 hours and then cooled down naturally. The designed amounts of sludge, PC, CFA, and water were mixed together manually with certain care. Table 2 lists the detailed composition of sludge-ash-cement samples. Sludge was prepared with different water, PC, and CFA amounts in order to examine the effect of the PC replacement, water content, and cement content on the mechanical and leaching properties of mixtures. The proportions of cement were 10, 15, and 20% by total weight of solid materials. In terms of PC replacement, the S/S sludge specimens were prepared with a constant binder content (PC + CFA) of 30%, including 20% PC + 10% CFA (i.e., 33% PC replacement) and 15% cement + 15% CFA (i.e., 50% PC replacement). In particular, the water content used in this study is the additional added amount of water that excludes moisture contained originally in the raw sludge. Specimens in the unconfined compressive strength (UCS) test were prepared with water content of 0, 5, and 10%, while the water content in the leachability test was 8.5%. In order to achieve sufficient cement hydration, the amount of water must be considered. Excessive water may cause the loss of effective components of cement, resulting in difficulty in forming stable and uniform cement-solidified mixtures. However, when the water is inadequate, cement-sludge mixture cannot be mixed evenly, and the effective utilization rate of cement would be reduced. After designed days of curing, the samples were tested for strength and leachability. Each test was performed on three parallel samples with the same composition.



FIGURE 1: Industrial sludge and CFA used in the study.

TABLE 1: Physical characteristics and chemical composition of sludge, fly ash, and cement.

	Sludge	Coal fly ash	Portland cement
<i>Physical characteristics</i>			
Moisture (%)	70	20	0.5
Density (g/cm ³)	1.05	2.9	3.18
pH	4.8	10.36	13
Specific gravity (g/cm ³)	2.65	2.34	3.13
Specific surface area (cm ² /g)	3400	3413	3550
<i>Chemical composition (%)</i>			
Cu	23.17	—	—
Fe	2.12	2.95	2.34
Al	0.43	15.46	3.07
Ca	25.29	3.53	47.0
Si	0.4	25.24	9.4
S	1.16	0.69	1.08
Zn	2.53	—	-
Pb	1.03	—	-
Mg	0.40	—	0.50
Cr	2.5	—	—
Mn	1.62	—	—
Rh	23.22	—	—
V	12.93	—	—
Sr	2.6	—	—
Ti	—	0.40	—
Na	—	—	3.19
K	—	—	0.42
Cl	—	—	0.005

2.3. Test Methods

2.3.1. Unconfined Compressive Strength. To measure the UCS, the mixture was filled into the mold (4 cm in diameter, 8 cm in height). To ensure uniformity, samples were compacted in four equal layers, and each layer was dropped by rammer with the same hammer times. After that, the specimens were demolded and cured at 95% humidity and 27°C temperature for 7, 14, and 28 days in a curing box (HBV-15B, Donghua, China). The UCS testing was

TABLE 2: Experimental tests carried out.

Mixture	Binder (%)			Mixture	Binder (%)		
	PC	CFA	Water		PC	CFA	Water
<i>UCS</i>				<i>Leaching</i>			
1	15	0	5	1	0	0	0
2	20	0	5	2	10	0	8.5
3	30	0	5	3	15	0	8.5
4	15	15	0	4	20	0	8.5
5	20	10	0	5	30	0	8.5
6	15	15	5	6	10	20	8.5
7	20	10	5	7	15	15	8.5
8	15	15	10	8	20	10	8.5
9	20	10	10	—	—	—	—

performed with a microcomputer-controlled electronic machine (LDS-50, Chenda, China) with a fixed strain rate of 1%/min according to ASTM D4219.

2.3.2. Leaching Test. The sample preparation for the leaching test is the same as that for the UCS test, besides the curing time being 14 days. After that, the leaching tests were carried out according to the USEPA TCLP method (method no: 1311) [33]. All the specimens were oven dried at 105°C for 24 hrs and then manually crushed to < 9.5 mm for the TCLP. The pulverized mixture was weighed and mixed with deionized water at a liquid-to-solid ratio of 20 by weight. The pH value of the samples was adjusted to 2.88 ± 0.05 by adding 0.1 M acetic acid, and then the samples were vibrated at 30 rpm for 18 hrs before passing them through 0.6–0.8 μm glass fiber filters. Subsequently, the targeted heavy metal in the filtrate solution was analyzed by atomic absorption spectroscopy (AAS) (TAS-990, Persee General, China) to assess its potential leachability.

2.3.3. Microscopic Characteristics Test. The shape, size, and morphology of the S/S samples were observed through a SU-8020 scanning electron microscope (SEM). During SEM, the

samples were firstly crushed, dried at 65°C, and then mounted on Al-stubs and gilt with Au, with a working voltage of 15 kV.

3. Testing Results and Discussion

3.1. UCS. The UCS is one of the important factors affecting the solidified effect. To date, most countries do not have concrete strength index for sludge landfill, except for Germany where a minimum requirement for UCS is set at 50 kPa [34, 35]. Figure 2 shows that the UCS of all solidified sludge treated by the blended cement meets the acceptance criterion for landfilling. As shown in Figure 2, the UCS of solidified sludge varied depending on the PC content. For example, in the case of the mixtures containing 15, 20, and 30% of PC by weight, after 28-day curing, the UCS was 0.17, 0.20, and 0.21 MPa, respectively. It shows that, with the increase of the proportion of PC, the sludge strength increases. It is supposed that the cement hydration provides the formation of calcium silicate hydrated (C-S-H) and calcium hydroxide (CH), which is the gels in cement responsible for strength development [36, 37]. It can be seen from Figure 2, the UCS of the cement-sludge mixtures was not obviously increased in the early stage of experiment. This may due to the presence of a large number of Cu atoms, which is reported to contribute to the retardation of cement hydration [38]. Cu may exist as hydroxides or interactions with calcium to form a series of complex compounds in the cement-solidified materials [39]. These detrimental compounds can wrap the binder particles and restrict further pozzolanic activity and the generation of cementitious gels. Such changes would play a negative influence on the strength of S/S mixtures [40]. Figure 2 shows an unusual phenomenon that was based on the 0% water content; the UCS of the cement-solidified sludge decreased with the increasing amount of cement after 7-day and 14-day curing. This can be explained that the water required for cement hydration comes only from moisture contained originally in the raw sludge, resulting in an insufficient hydrated reaction. Some cement particles without hydration, acting as filling materials, were filled in the pores between the soil particles and even weakened the cementation between soil particles and cement hydration products, furthermore resulting in the decrease of UCS.

As can be observed in Figure 2, the UCS of the solidified matrix increases with curing time. Compared to 7 days, the 28-day UCS of solidified mixtures with 15, 20, and 30% of PC increases by 21.4, 81.8, and 163%, respectively. The increasing strength values over time reflected the ongoing hydration reaction during which the strong adhesive products were produced, providing strong loading resistance [41]. Tang et al. concluded that the hydration reaction is more sufficient with the increase of curing time [15]. In addition, at the later hydration age, the hydration of residual cement particles may take place by the solid-state reactions and the transport of ions in the solution becomes limited [24, 42]. It can be seen that the setting time of cement paste plays an important role in the S/S process.

The adverse impact of water on strength development is given in Figure 3, where the change of relation between the

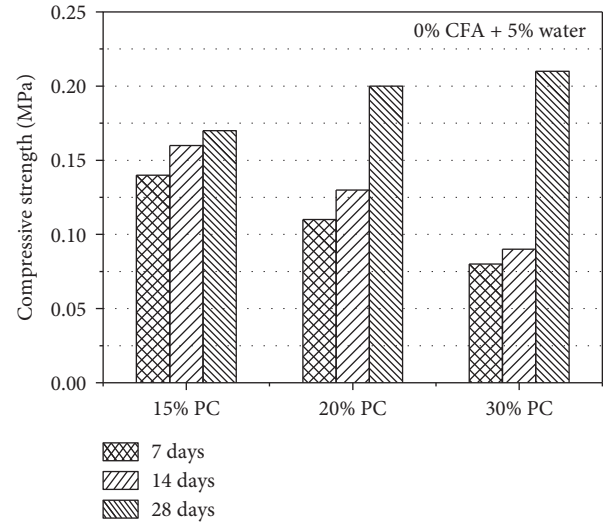


FIGURE 2: Compressive strength of solidified sludge with different amounts of PC.

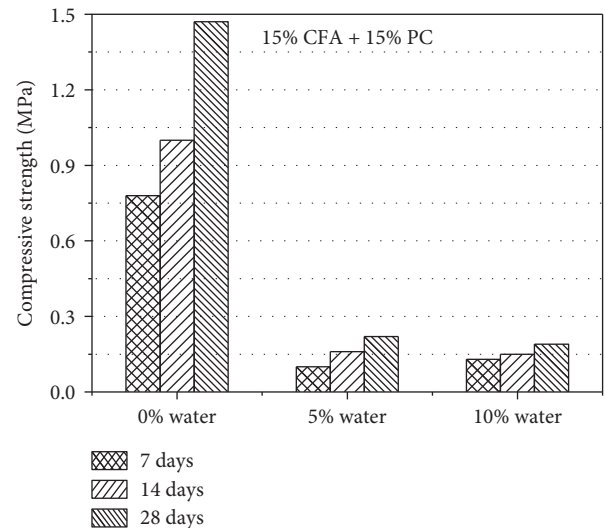


FIGURE 3: Compressive strength of solidified sludge with different water contents.

UCS and water content is depicted. Obviously, the experimental results revealed that the strength values of all time periods decreased as water content increased. For example, the UCS of cement-based matrices (water content = 0, 5, and 10%) after 28 days of solidification are 1.47, 0.22, and 0.19 MPa, respectively. Wang et al. explained that the higher water content increases the lubrication between sludge particles and reduces the friction force, which leads to the decrease of the strength [43]. Besides, the initial moisture content of the sludge is also an important factor that restricts the UCS of the solidified sludge. Table 1 shows that the initial moisture content of the sludge used in this study is 70% which is very high. It is generally very difficult to consolidate the sludge material in practice. To reduce the detrimental influence of moisture on the strength of specimens, cement

was used as a material that, by consuming large quantities of water as a result of the pozzolanic reactions, results in a rise of the strength of the mixture [44].

Figure 4 shows the effect of CFA on the UCS of the cement-solidified mixtures. It shows that, with 0, 5, and 10% of water content, the 28-day UCS of the sludge blocks stabilized/solidified by 20% PC+10% CFA (i.e., 33% PC replacement) and 15% cement+15% CFA (i.e., 50% PC replacement) are (0.93 MPa, 1.47 MPa), (0.1 MPa, 0.22 MPa), and (0.13 MPa, 0.19 MPa), respectively. The results revealed that the PC replacement by CFA increased the mechanical strength. The hydration of CFA leads to consumption of cement hydrates and packs the pore structure already established by its own hydration product, thus helping to achieve a tighter pore structure and greater intensity for cement-based mixtures. Now in China, for the safe use of stabilized materials in the highway construction, a standard called *Technical Guidelines for Construction of Highway Roadbases* (JTG/T F20-2015) was established. In this highway construction technical specification, there is a specific regulation on unconfined compression strength of lime-coal fly ash stabilized, which is shown in Table 3. Based on Figure 4, it can be seen that the UCS of 14-day and 28-day solidified matrix with 0% water all can satisfy the design value (1.1 MPa, which is required in the standard).

3.2. TCLP Results. The TCLP technique determines the pollutants' migration in a sample and the toxic degree that allows the classification of the material as "dangerous." It can be seen from Table 1 that the content of Cu in sludge dominates the leading position. The effect of different heavy metal ions types on cement hydration have been studied extensively in recent years. Qiao et al. investigated that copper ions leading to a high degree of inhibition in the cement hydration, indicating that the curing effect of Cu is worse than that of other heavy metals [45]. According to scanning electron microscope results of Wang et al., the existence of copper allows an offset in the C-S-H gel diffraction peak, and thereby decreases the crystallinity of C-S-H [46]. Therefore, monitoring the leachability of Cu plays a guiding role in this research. The results of the TCLP tests are presented in Figure 5. The average leached Cu concentrations of untreated samples are 29.9 mg/L, suggesting its high mobility in the untreated soil. Figure 5 shows the effect of the amount of PC on the leaching characterization of solidified sludge. The Cu leaching concentration for all stabilized samples is noticeably decreased after PC treatment. In addition, increasing PC content is found to significantly reduce the Cu leachability. Because of the high-alkalinity environments in the cement-based matrix, these metals might exist in the form of metal hydrated phases, metal hydroxides, and calcium-metal compounds [47]. Roy and Cartledge investigated the speciation of Cu in the cement-solidified ES [48]. It was found that the main copper-bearing phase was a copper-hydrated phase when Cu was added as copper nitrate in the matrix. Cu may also exist in the form of hydroxides or react with calcium to generate complex compounds in the cement-based materials.

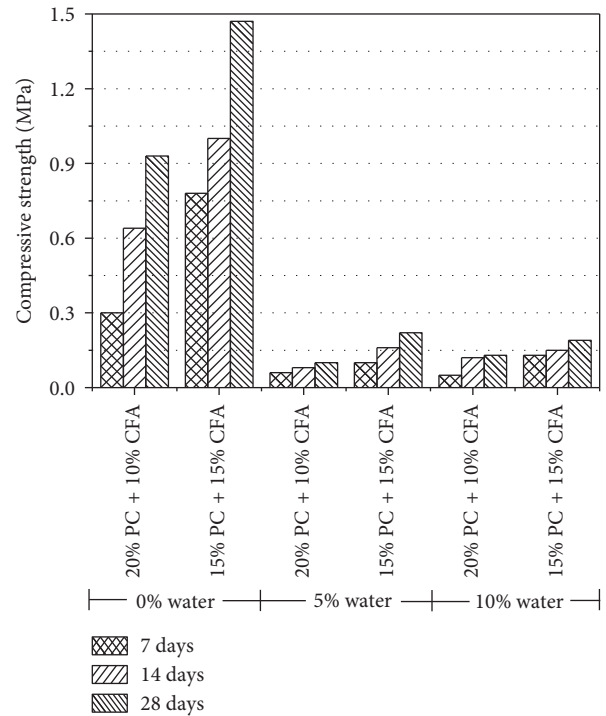


FIGURE 4: Compressive strength of solidified sludge with different contents of CFA.

In China, for the safe utilization of heavy metal-contained materials in the road construction, the relevant standard titled "*Specifications for environmental impact assessment of highways*" (JTG B03.2006) was established based on the characteristics of highway engineering. Considering the heavy metals in the solidified sludge will eventually permeate into the soil, the water quality evaluation in highway engineering of the this standard is the same as the standard "*Soil environmental quality standard*" (GB 15618-1995). So, the standard GB 15618-1995 was adopted to evaluate the acceptable leaching of the treated sludge as a roadbed material. The limit values of soil environmental quality are presented in Table 4. The leaching characteristic of the sludge stabilized/solidified by PC + CFA is also illustrated in Figure 5. Obviously, the leaching values of the targeted heavy metal were far below the limit, although the addition of CFA increased the leaching concentration. For example, with the presence of 30% binder, all the leaching concentration of 10% CFA + 20% PC (1.3 mg/L), 15% CFA + 15% PC (13.9 mg/L), and 20% CFA + 10% PC (16.1 mg/L) far exceeded the leaching of 30% PC (0.8 mg/L). It may be because C-S-H gel generated by the hydration of CFA was insufficient to make up the loss of cement hydration [49]. Based on the foregoing results, CFA geopolymers solidification of heavy metals was a choice. Qian et al. considered that heavy metal ions are not only in the form of physical enclosure but also via special solidifying structures of adsorption and even bonding with matrix materials [12]. Hence, it can be firmly fixed in the geopolymers.

Scanning electron micrographs of the cement-sludge (20% PC) and cement-fly ash-sludge mixtures (20% PC + 10% CFA) aged 14 days are shown in Figures 6(a) and 6(b),

TABLE 3: Unconfined compression strength of lime-coal fly ash stabilized materials (MPa).

Structure layer	Highway grade	Special heavy traffic	Heavy traffic	Light traffic
Base	Motorways and first-grade highway	≥1.1	≥1.0	≥0.9
	Second-grade and under second-grade highway	≥0.9	≥0.8	≥0.7
Sub-base	Motorways and first-grade highway	≥0.8	≥0.7	≥0.6
	Second-grade and under second-grade highway	≥0.7	≥0.6	≥0.5

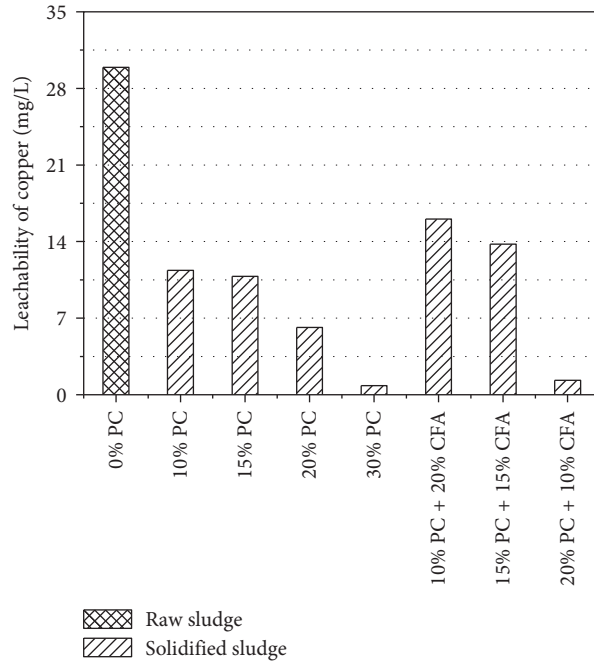


FIGURE 5: TCLP leachability of solidified sludge with different binder formulations.

TABLE 4: Standard values of soil environmental quality (mg/L).

Heavy metals	Grade I ^a		Grade II		Grade III ^c
	Natural	pH < 6.5	pH 6.5–7.5	pH > 7.5	pH > 6.5
Cu (farmland)	35	50	100	100	400
Cu (orchard)	—	150	200	200	400

^aLimit values for protecting natural ecology and maintaining the soil quality in the natural setting. ^bLimit values for protecting agricultural productions and human health. ^cLimit values for protecting the normal growth of plants.

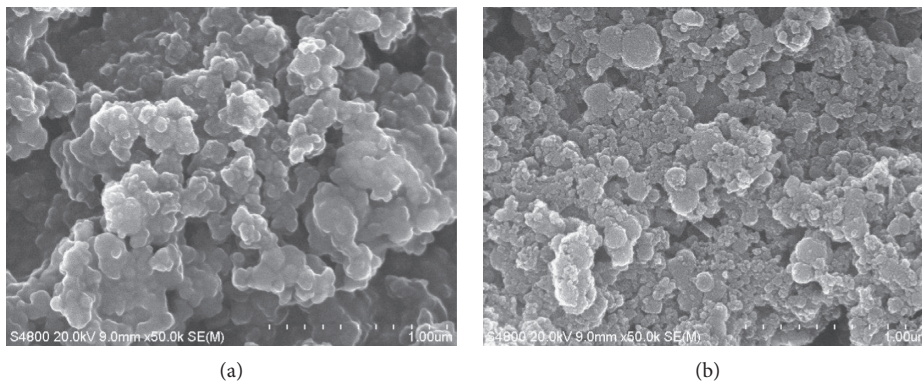


FIGURE 6: SEM micrographs of 14-day cured solidified sludge with different binder formulation. (a) 20% PC. (b) 20% PC + 10% CFA.

respectively. A great quantity of smooth spherical particles exists in the CFA, and they were primarily fly ash glassy spheres, acting as lubricating agent, helping to improve the rheological properties of fresh paste before setting [50, 51]. Compared with Figure 6(a), the microstructure of the sample in Figure 6(b) showed a clear change. A high concentration of white globule of C-S-H was found in a denser structure, and these results corresponded to those of Li and Poon [36]. The CFA is believed to have pozzolanic reaction after the age of 3 days as blended with PC, forming geopolymer gel and filling between the inner portion of unreacted fly ash spheres as well as the gap of particles, thus resulting in higher densification of the matrix [51]. Recent research reveals that the main hydrate of cement and fly ash, calcium silicate hydrate (C-S-H), adopts two distinct morphologies: a low density C-S-H at the surface of cement and fly ash particles and a high density C-S-H deeper into the particles [52]. However, as shown in Figure 6(a), the gel structure of solidified matrix was loose and the density was reduced, which may increase the permeability and ionic diffusion of heavy metals in the solidified matrix. As shown in Figure 5, the leaching concentration of the sample solidified with 20% PC + 10% CFA (1.3 mg/L) is lower than that solidified with 20% PC (6.1 mg/L). Consequently, CFA can improve cement packing, block capillary pores, and reduce the permeability of heavy metals in the samples.

4. Conclusions

This study has provided a feasible strategy for the utilization of electroplating sludge as the subgrade backfill materials. PC and CFA were acted as curing agents in the S/S treatment of electroplating sludge. It concluded that all the studied parameters (PC content, curing time, water content, and CFA/PC ratio) dramatically affect the effectiveness of the S/S process.

The UCS of stabilized sludge with 0% water content meets the highway construction technical specification and increased fast with the increase of cement content, curing time, and CFA/PC ratio. The increment in strength for cement/coal fly ash-treated samples could be largely due to the main hydrate of cement and fly ash, a high density C-S-H deeper into the cement and fly ash particles, helping to achieve a tighter pore structure and greater intensity for cement-solidified mixtures. The water content produces a detrimental effect on the UCS of cement-solidified sludge, which retarded the development of strength or even reduced the final strength. This can be explained that the higher water content increases the lubrication between sludge particles and reduces the friction force. In terms of the leaching test results, it was shown that CFA can act as a filler to plug capillary pores and reduce the permeability of heavy metals in the samples.

Data Availability

We declare that all the data presented in the manuscript were obtained from laboratory tests at Soochow University in

Suzhou, China. All the laboratory testing data were presented in the figures and the tables in the manuscript. We will be very pleased to share our all the raw data. If needed, please contact us via email: pxshi@suda.edu.cn.

Conflicts of Interest

The authors declare that they have no conflicts of interest.

Acknowledgments

This study was supported by the National Natural Science Foundation of China (51778386 and 51708377), Natural Science Foundation of Jiangsu Province (BK20170339 and BK20160320), and project from Jiangsu Provincial Department of Housing, Urban-Rural Development (2016ZD18 and 2017ZD002).

References

- [1] I. C. Chou, Y. M. Kuo, C. Lin, J. W. Wang, C. T. Wang, and G. P. Chang-Chien, "Electroplating sludge metal recovering with vitrification using mineral powder additive," *Resources, Conservation and Recycling*, vol. 58, pp. 45–49, 2012.
- [2] M. Zhang, C. Chen, L. Mao, and Q. Wu, "Use of electroplating sludge in production of fired clay bricks: characterization and environmental risk evaluation," *Construction and Building Materials*, vol. 159, pp. 27–36, 2018.
- [3] C. Zhang, J. Song, J. Zhang, J. Zhang, J. Xing, and D. Hu, "Understanding and application of an electroplating sludge-derived catalyst with an active texture for improved NO reduction," *Science of the Total Environment*, vol. 631–632, pp. 308–316, 2018.
- [4] H. Lyu, Y. Gong, J. Tang, Y. Huang, and Q. Wang, "Immobilization of heavy metals in electroplating sludge by biochar and iron sulfide," *Environmental Science and Pollution Research*, vol. 23, no. 14, pp. 14472–14488, 2016.
- [5] Q. Tang, F. Gu, Y. Zhang, Y. Q. Zhang, and J. L. Mo, "Impact of biological clogging on the barrier performance of landfill liners," *Journal of Environmental Management*, vol. 222, pp. 44–53, 2018.
- [6] Q. Tang, H. J. Kim, K. Endo, T. Katsumi, and T. Inui, "Size effect on lysimeter test evaluating the properties of construction and demolition waste leachate," *Soils and Foundations*, vol. 55, no. 4, pp. 720–736, 2015.
- [7] Q. Tang, T. Katsumi, T. Inui, and Z. Z. Li, "Membrane behavior of bentonite amended compacted clay," *Soils and Foundations*, vol. 54, no. 3, pp. 329–344, 2014.
- [8] L. Q. Mao, R. Z. Tang, Y. C. Wang, Y. N. Guo, P. Su, and W. Y. Zhang, "Stabilization of electroplating sludge with iron sludge by thermal treatment via incorporating heavy metals into spinel phase," *Journal of Cleaner Production*, vol. 187, no. 20, pp. 616–624, 2018.
- [9] S. Ucaroglu and I. Talinli, "Recovery and safer disposal of phosphate coating sludge by solidification/stabilization," *Journal of Environmental Management*, vol. 105, pp. 131–137, 2012.
- [10] W. Y. Xia, Y. J. Du, K. R. Reddy, and Y. S. Feng, "Solidification/stabilization of Pb, Zn and Cd contaminated industrial site soil using KMP binder: strength, leaching and microstructure characterization," *Journal of Materials in Civil Engineering*, vol. 30, no. 6, article 04018080, 2018.

- [11] W. Y. Xia, Y. S. Feng, F. Jin, L. M. Zhang, and Y. J. Du, "Stabilization and solidification of a heavy metal contaminated site soil using a hydroxyapatite based binder," *Construction and Building Materials*, vol. 156, pp. 199–207, 2017.
- [12] G. Qian, Y. Cao, P. Chui, and J. Tay, "Utilization of MSWI fly ash for stabilization/solidification of industrial waste sludge," *Journal of Hazardous Materials*, vol. 129, no. 1–3, pp. 274–281, 2006.
- [13] J. Ma, Y. Zhao, J. Wang, and W. Li, "Effect of magnesium oxychloride cement on stabilization/solidification of sewage sludge," *Construction and Building Materials*, vol. 24, no. 1, pp. 79–83, 2010.
- [14] G. E. Voglar and D. Leštan, "Equilibrium leaching of toxic elements from cement stabilized soil," *Journal of Hazardous Materials*, vol. 246–247, no. 4, pp. 18–25, 2013.
- [15] Q. Tang, Y. Zhang, Y. Gao, and F. Gu, "Use of cement-chelated solidified MSWI fly ash for pavement material: mechanical and environmental evaluations," *Canadian Geotechnical Journal*, vol. 54, no. 11, pp. 1553–1566, 2017.
- [16] A. González, R. Navia, and N. Moreno, "Fly ashes from coal and petroleum coke combustion: current and innovative potential applications," *Waste Management & Research*, vol. 27, pp. 976–987, 2009.
- [17] P. Nath and P. Sarker, "Effect of fly ash on the durability properties of high strength concrete," *Procedia Engineering*, vol. 14, pp. 1149–1156, 2011.
- [18] Z. T. Yao, X. S. Ji, P. K. Sarker, J. H. Tang, L. Q. Ge, and M. S. Xia, "A comprehensive review on the applications of coal fly ash," *Earth-Science Reviews*, vol. 141, pp. 105–121, 2015.
- [19] Y. Chao, S. Y. Liu, and Y. F. Deng, "Experimental research for the application of mining waste in the trench cutting remixing deep wall method," *Advances in Materials Science and Engineering*, vol. 2015, Article ID 202848, 9 pages, 2015.
- [20] Y. L. Chen, M. S. Ko, Y. C. Lai, and J. E. Chang, "Hydration and leaching characteristics of cement pastes made from electroplating sludge," *Waste Management*, vol. 31, no. 6, pp. 1357–1363, 2011.
- [21] J. Monteny, E. Vincke, A. Beeldens et al., "Chemical, microbiological, and in situ test methods for biogenic sulfuric acid corrosion of concrete," *Cement and Concrete Research*, vol. 30, pp. 623–634, 2000.
- [22] Q. Chen, L. Zhang, Y. Ke, C. Hills, and Y. Kang, "Influence of carbonation on the acid neutralization capacity of cements and cement-solidified/stabilized electroplating sludge," *Chemosphere*, vol. 74, no. 6, pp. 758–764, 2009.
- [23] Y. J. Du, N. J. Jiang, S. L. Shen, and F. Jin, "Experimental investigation of influence of acid rain on leaching and hydraulic characteristics of cement-based solidified/stabilized lead contaminated clay," *Journal of Hazardous Materials*, vol. 225–226, no. 10, pp. 195–201, 2012.
- [24] Q. Tang, Y. Liu, F. Gu, and T. Zhou, "Solidification/stabilization of fly ash from a municipal solid waste incineration facility using Portland cement," *Advances in Materials Science and Engineering*, vol. 2016, Article ID 7101243, 10 pages, 2016.
- [25] Q. Tang, F. Gu, Y. F. Gao, T. Inui, and T. Katsumi, "Desorption characteristics of Cr(III), Mn(II) and Ni(II) in contaminated soil using citric acid and citric acid containing wastewater," *Soils and Foundations*, vol. 58, no. 1, pp. 50–64, 2018.
- [26] Y. Tang, S. W. Chan, and K. Shih, "Copper stabilization in beneficial use of waterworks sludge and copper-laden electroplating sludge for ceramic materials," *Waste Management*, vol. 34, no. 6, pp. 1085–1091, 2014.
- [27] A. O. Babatunde and Y. Q. Zhao, "Constructive approaches toward water treatment works sludge management: an international review of beneficial reuses," *Critical Reviews in Environmental Science and Technology*, vol. 37, no. 2, pp. 129–164, 2007.
- [28] J. J. C. Bocanegra, E. E. Mora, and G. I. C. González, "Encapsulation in ceramic material of the metals Cr, Ni, and Cu contained in galvanic sludge via the solidification/stabilization method," *Journal of Environmental Chemical Engineering*, vol. 5, no. 4, pp. 3834–3843, 2017.
- [29] EN 14346, *Characterization of Waste e Calculation of Dry Matter by Determination of Dry Residue or Water Content*, European Norm, Germany, 2006.
- [30] M. T. Montañés, R. Sáncheztovar, and M. S. Roux, "The effectiveness of the stabilization/solidification process on the leachability and toxicity of the tannery sludge chromium," *Journal of Environmental Management*, vol. 143, no. 10, pp. 71–79, 2014.
- [31] G. Cheng, Q. Li, Z. Su, S. Sheng, and J. Fu, "Preparation, optimization, and application of sustainable ceramicsite substrate from coal fly ash/waterworks sludge/oyster shell for phosphorus immobilization in constructed wetlands," *Journal of Cleaner Production*, vol. 175, pp. 572–581, 2018.
- [32] F. Tomonori, H. Akira, D. K. Achmad, M. Norio, A. N. Huang, and K. Fukui, "Utilization of incineration fly ash from biomass power plants for zeolite synthesis from coal fly ash by microwave hydrothermal treatment," *Advanced Powder Technology*, vol. 29, no. 3, pp. 450–456, 2018.
- [33] United States Environmental Protection Agency, *US EPA Method 1311: Toxicity Characteristic Leaching Procedure*, US EPA, Washington, DC, USA, 1992.
- [34] A. Koenig, J. N. Kay, and L. M. Wan, "Physical properties of dewatered wastewater sludge for landfilling," *Water Science and Technology*, vol. 34, pp. 533–540, 1996.
- [35] German Federal Government, *Technical Guidelines for Municipal Waste of 14 May 1993*, German Federal Government, Germany, 1993, in German.
- [36] J. Li and C. S. Poon, "Innovative solidification/stabilization of lead contaminated soil using incineration sewage sludge ash," *Chemosphere*, vol. 173, pp. 143–152, 2017.
- [37] D. W. Zhang, Z. G. Cao, L. B. Fan, and Y. F. Deng, "Effect of chloride salt concentration on unconfined compression strength of cement-treated lianyungang soft marine clay," *Journal of Southeast University*, vol. 29, no. 1, pp. 79–83, 2013.
- [38] Y. J. Du, N. J. Jiang, S. Y. Liu, F. Jin, D. N. Singh, and A. J. Puppala, "Engineering properties and microstructural characteristics of cement-stabilized zinc contaminated kaolin," *Canadian Geotechnical Journal*, vol. 51, pp. 289–302, 2013.
- [39] D. H. Moon, J. R. Lee, D. G. Grubb, and J. H. Park, "An assessment of Portland cement, cement kiln dust and Class C fly ash for the immobilization of Zn in contaminated soils," *Environmental Earth Sciences*, vol. 61, pp. 1745–1750, 2010.
- [40] A. R. Goodarzi and M. H. Zandi, "Assessing geo-mechanical and leaching behavior of cement-silica-fume-stabilized heavy metal-contaminated clayey soil," *Environmental Earth Sciences*, vol. 75, no. 10, pp. 1–17, 2016.
- [41] Y. S. Wang, J. G. Dai, L. Wang, D. Tsang, and C. S. Poon, "Influence of lead on stabilization/solidification by ordinary Portland cement and magnesium phosphate cement," *Chemosphere*, vol. 190, pp. 90–96, 2017.

- [42] P. K. Mehta and P. J. M. Monteiro, *Concrete: Microstructure, Properties, and Materials*, McGraw-Hill Education, New York, NY, USA, 4th edition, 2014.
- [43] P. Wang, C. S. Tang, K. Q. Sun, Z. G. Chen, S. K. Xu, and B. Shi, "Advances on solidification/stabilization of sludge disposal," *Journal of Engineering Geology*, vol. 24, no. 4, pp. 649–660, 2016, in Chinese.
- [44] C. A. Anagnostopoulos, "Strength properties of an epoxy resin and cement-stabilized silty clay soil," *Applied Clay Science*, vol. 114, pp. 517–529, 2015.
- [45] B. Qiao, Z. H. Zhao, S. Wang, H. X. Guo, and C. Jiang, "Laboratory study on diffusion of heavy metals in cement treated dredged material," *Hennan Sciencevol*, 35, no. 3, pp. 452–459, 2017, in Chinese.
- [46] L. Wang, B. Yan, X. Wang, C. Liu, and J. Liu, "Research on effect of different heavy metal ions on C-S-H Gel and its stability," *Journal of Building Materials*, vol. 17, no. 5, pp. 790–796, 2014, in Chinese.
- [47] C. A. Johnson, M. Kersten, F. Ziegler, and H. C. Moor, "Leaching behaviour and solubility-controlling solid phases of heavy metals in municipal solid waste incinerator ash," *Waste Management*, vol. 16, pp. 129–134, 1996.
- [48] A. Roy and F. K. Cartledge, "Long-term behavior of a Portland cement-electroplating sludge waste form in presence of copper nitrate," *Journal of Hazardous Materials*, vol. 52, pp. 265–286, 1997.
- [49] L. Wang, J. S. H. Kwok, D. C. W. Tsang, and C. S. Poon, "Mixture design and treatment methods for recycling contaminated sediment," *Journal of Hazardous Materials*, vol. 283, pp. 623–632, 2015.
- [50] Y. Wang, F. Han, and J. Mu, "Solidification/stabilization mechanism of Pb(II), Cd(II), Mn(II) and Cr(III) in fly ash based geopolymers," *Construction and Building Materials*, vol. 160, pp. 818–827, 2017.
- [51] V. G. Papadakis, "Effect of fly ash on Portland cement systems Part I: low-calcium fly ash," *Cement and Concrete Research*, vol. 29, pp. 1727–1736, 1999.
- [52] C. Li, H. Sun, and L. Li, "A review: the comparison between alkali-activated slag (Si + Ca) and metakaolin (Si + Al) cements," *Cement and Concrete Research*, vol. 40, pp. 1341–1349, 2010.

Research Article

Lab Study on the Effect of Cation Exchange Capacity on Slurry Performance in Slurry Shields

By Pinghe Sun,^{1,2,3,4} Binkui Zhao,^{1,2} Han Cao ,^{1,2,3,4} Jingyuan Wang,^{1,2} Dingqiang Mo,^{1,2} and Shaoh Zhang^{1,2}

¹School of Geosciences and Information Physics, Central South University, Changsha 410083, China

²Key Laboratory of Metallogenic Prediction and Geoenvironmental Monitoring of Ministry of Education, Central South University, Changsha 410083, China

³State Key Laboratory of Oil and Gas Reservoir Geology and Exploitation, Southwest Petroleum University, Chengdu, Sichuan, China

⁴Arizona State University, Tempe, AZ 85287, USA

Correspondence should be addressed to Han Cao; hancao@csu.edu.cn

Received 10 June 2018; Accepted 30 August 2018; Published 3 October 2018

Academic Editor: Yonggui Chen

Copyright © 2018 By Pinghe Sun et al. This is an open access article distributed under the Creative Commons Attribution License, which permits unrestricted use, distribution, and reproduction in any medium, provided the original work is properly cited.

Ion stabilizers can enhance the reinforcement slurry effect on the wall and stabilize the wall actively in slurry shields. This paper presents different cation exchange capacities obtained by changing the content of the ion stabilizer (1.5%, 2.0%, 2.5%, 3.0%, 3.5%, 4.0%, 4.5%, 5.0%, 5.5%, and 6.0%) in slurry associated with the basis of the existing slurry formula through the laboratory tests. In order to study the effect of the cation exchange capacity on the performance of slurry properties, the rheological properties of the slurry are analyzed and evaluated by the power law model. Results indicate that the cation exchange capacity of the slurry decreases first and then increases with the increase of the ion stabilizer content. When the content of the ion stabilizer is maintained at 3.50%, the cation exchange capacity reaches the minimum value of 2.92. The filtration volumes, pH values, and rheological parameters of the slurry also indicate an obvious linear change with the change of the cation exchange capacity. The minimum filtration volume is 9.70 mL/30 min when the ion stabilizer content reaches 3.50%. However, the pH value reaches the maximum, that is, 11.34 which is changed from 10, and the change could be considered as a constant value in the field work. When the cation exchange capacity increases, the continuity of polymer structure in the slurry decreases first and then increases, the flow index and consistency coefficient are located within a reasonable range, and the rheological properties of the slurry meet the design requirements of the standards.

1. Introduction

Slurry shields are TBM fitted with a full-face cutterhead which provides face support by pressurizing boring fluid inside the cutterhead chamber. The pressurized slurry system plays an important role in the stability of the excavation face associated with filter cake in slurry shields [1–4]. The slurry should be able to create an impermeable membrane at the ground interface. Once the ground interface becomes impermeable, the slurry can develop an adequate confinement pressure. Polymers, sands, vermiculites, even micro-organism, and other additives are usually added into the slurry to improve the performance of slurry in practical

construction engineerings [5–9]. Slurry shields in rock would generally require slurry with properties related mostly to its basic functions as lubrication, transport of cuttings. Slurry shields in soil would require slurry with properties related to primary functions, such as marsh funnel and plastic viscosity, pH, yield point, and filter cake properties. When slurry shields in mix ground conditions, it requires slurry with both primary functions and specific properties which are not simply the one applying to the worst soil conditions encountered at the face. There are new factors to consider, which exist only in mix face conditions, and cation exchange capacity of the slurry is one of them. The cation exchange capacity (CEC) is usually called methylene blue

capacity that is an important parameter representing the exchangeable ion quantity of the slurry such as ion stabilizer slurry fluid, which directly reflects the ion exchange capacity of the slurry fluid. It can be obtained according to the methylene blue titration test, a major international measurement method first proposed by the American Petroleum Society (API), and the total cation exchange capacity in the slurry fluid could be calculated. The bentonite-free slurry fluid formulation system composed of plant gum, poly-anionic cellulose, liquid ion stabilizer, graphite powder, and barite is selected on the basis of existing research because the bentonite itself has a certain cation exchange capacity, and the polymeric materials can meet the design requirements of viscosity, rheology, and filtration loss. Different cation exchange capacities are obtained by changing the content of the ion stabilizer in the slurry fluid, and the rheology performance of slurry is analyzed and evaluated by the power law model on the basis of the existing formula.

In formation evaluation, it is the contribution of cation exchange sites to the formation of electrical properties that is important or required to determine the clay types and dry clay parameters. In slurry shields, most studies are focused on the filter cake properties [10–13]. Because it is easy for slurry to penetrate into the stratum, causing a large amount of fluid loss when slurry shields cut through strong permeability stratum, resulting in poor filter cake on the excavation face, which is incapable of providing enough support required for the stability of the excavation surface [14–17]. Several factors control the formation of filter cake, such as the permeability of the rock and soil, the pressure, and properties of slurry (density, rheological properties, grain size distribution, etc.) [18–22]. Watanabe and Yamazaki and Wang and Zhu [23, 24] investigated the effects of density of slurry on the fluid loss in the highly permeable soils, and they found that the proportion of sand in the slurry played an important role in the fluid loss of slurry during the formation of filter cake. Cheng et al. [18] performed laboratory model tests on pure bentonite suspensions in medium coarse sands, and results indicated that the viscosity of suspensions had a significant influence on the filter cake properties. Fritz et al. [15] and Heinz [20] developed an apparatus for measuring the support pressure of slurry and performed the support pressure tests to evaluate the best combination of additives in slurries. Han et al. [19] evaluated the factors that control the formation of filter cake based on some laboratory tests; the results showed that the higher the viscosity of the slurry was, the easier for the filter cake to form, and the filter cake formed was thin and compactable. If there was less fluid loss in the process of formation of the filter cake, it indicated that the filter cake is easy to form. However, if there was less fluid loss after the filter cake formed, it indicated that the filter cake was compactable. Min et al. [25] investigated the processing of filter cake formed on the surface of coarse grained sandstone with high pressure, and the results indicated that the formation of filter cake was affected by the properties of slurry, especially particle size and density. Filz et al. [26] presented formed criteria of filter cake in sandy formation, and the results indicated that the percolation range had much more

effects on the strength of coarse granular soil due to the poor filter cake. Amorim et al. [27] investigated the influence of ionic strength on the apparent and plastic viscosities and water loss in sodium bentonite suspension with polymers, and the results could be concluded that the presence of salt and the increase of salinity in these suspensions strongly affect the plastic and apparent viscosities and water loss after polymers added. Liu and Santamarina [28] advanced a comprehensive filter cake growth model for water-based slurry implemented with robust, physically informed constitutive equations in their study, and they also obtained the results that environmental factors such as temperature, pH, ionic concentration, and cation contamination have a significant influence on filter cake properties. In this paper, further studies show the effect of ion exchange in slurry on its properties based on the current study mentioned above. Bentonite is composed of two tetrahedrally coordinated sheets of silicon ions surrounding an octahedrally coordinated sheet of aluminum ions, the isomorphous substitution of Al^{3+} for Si^{4+} in the tetrahedral layer and Mg^{2+} or Fe^{3+} for Al^{3+} in the octahedral layer results in a net negative surface charge on the layer, which makes it hold its physical and chemical properties, i.e., large specific surface area, cation exchange capacity, and adsorptive affinity for organic and inorganic ions [29, 30]. When the bentonite contained in the stratum dissolve in the slurry, the cations in the slurry (such as Ca^{2+} , Na^+ , and Mg^{2+}) will lead to chemical deterioration on the filter cake associated with slurry circulation, and the interaction between these charged ions can create an electrostatic field around them [31]. That is, the slurry will be converted from the well-suspended dispersion to the agglutination state and resulted in the increase of particle size. At the same time, the poor quality of the filter cake will appear and the slurry will lose its basic functions [32, 33]. In order to regulate the performance of slurry based on the micro- and macropoint, it is essential to study the effect of the cation exchange capacity on the performance of slurry. In this case, a dense, low permeability filter cake can be formed on the cutting face and improve the stability of the wall during excavation.

The ion stabilizer is one kind of advanced material and widely used to improve the physical and mechanical properties of stratum in many fields to meet the requirements of engineering technology, such as slope protection, water conservancy construction, road subgrade, and trenchless [34]. The ion stabilizer has strong practicability, stable performance, and low cost, as a new kind of chemical material. A proper amount of the ion stabilizer dissolves in the slurry fluid can form ionic solutions; that is, a liquid organic salt composed of cations and anions [35], which contains the basic properties of shield slurry. The ion stabilizer mainly forms high valence ions and water compounds with low water binding and high cohesive force in solution by ion exchange as an additive in the slurry fluid. The high valence cations in the solution are adsorbed by clay particles in the stratum, with neutralizing the negative charge on the surface of particles, reducing the repelling force between the clay particles, and effectively restraining the stratum hydration and expansion to improve the stability of the

excavation. The water compounds formed in the solution can effectively seal the cracks in the wall, reducing the invasion of filtrate, and improve the mechanical strength and impermeability of the rock and soil near the wall at the same time [36].

2. Materials and Methods

2.1. Materials. The test materials include ENI ion stabilizer, methylene blue titration materials and basic slurry fluid formulation materials consist of solvent (water), vegetable gum (CT), polyanion cellulose (PAC), graphite powder, and barite. The ENI ion stabilizer is mainly composed of petroleum sulfonated agent, modified sodium silicate, modified polymer surface active agent, and other materials, and it can decompose the clay mineral and nonclay particles in the stratum. It also can recrystallize the clay mineral particles and reduce the invasion of filtrate rely on making use of bonding and winding between polymer compounds and leaving the particles hydrophobic and dense. Its appearance is light yellow as shown in Figure 1. The positive charges in methylene blue solution are alkaline, which are unstable and able to react with most inorganic salts to produce compound salts. 0.01 mol/L methylene blue water solution, 3% hydrogen peroxide solution, and 2.5 mol/L dilute sulfuric acid solution were used as the methylene blue titration experiment materials in this study, as shown in Figure 2.

2.2. Methods. Different cation exchange capacities were obtained by changing the content of ion stabilizers in the slurry fluid based on the existing formula, and the designed addition of the ion stabilizer in the experiment was 1.5%, 2.0%, 2.5%, 3.0%, 3.5%, 4.0%, 4.5%, 5.0%, 5.5%, and 6.0% (Group 1–10). The same slurry fluid basic formula was used in each group in order to obtain the degree of influence of the ion stabilizer.

The slurry fluids with different ion stabilizer contents were prepared according to the API standard in the experiment. The slurry performance parameters of each group were measured by the ZNN-D6 digital display rotary viscometer, and the data were recorded. According to the standard analysis method, the rheological parameters of each group could be calculated with the data. The pH values of slurry were measured three times in each group by precision acidity and alkalinity tester, and then the average of these data was calculated. The tests of filtrate volume were carried out according to the API RP 13B-12009 standard, and the control pressure value was maintained at 0.69 MPa. The methylene blue titration tests were carried out three times for each group of slurry fluids according to the standard GB/T16783.1-2006, and the average CEC values were obtained. The mathematical formula for the calculation is as follows [37, 38]:

$$CEC = \frac{V_M}{V_D}, \quad (1)$$

where CEC is the cation exchange capacity of the slurry fluids (dimensionless unit), V_M is the consumption of methylene blue standard solution (mL), and V_D is the amount of slurry fluid samples (mL).

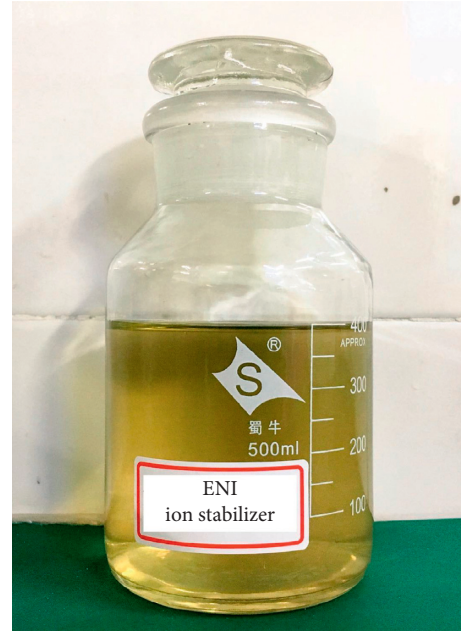


FIGURE 1: The actual picture of ENI ion stabilizer.



FIGURE 2: The reagent used for the methylene blue titration test.

3. Results and Discussions

All the pH test, methylene blue solution titration test (CEC), and filtrate test (FL_{API}) of slurry fluids were performed in the drilling fluid lab in Central South University, and the test results obtained are shown in Table 1.

3.1. Relationship between Cation Exchange Capacity of the Slurry Fluid and Its Content of Ionic Stabilizer. The relationship between the cation exchange capacity of the slurry fluid and its content of the ion stabilizer is indicated in Figure 3. The cation exchange capacity of the slurry fluid decreases first and then increases with the increase of the content of the ion stabilizer, and the cation exchange capacity of the slurry fluid is minimum when the stabilizer content is 3.5%.

TABLE 1: Experimental results of slurry fluids with different contents of ionic stabilizer.

Content (%)	PAC (%)	CT (%)	Graphite powder (%)	CEC	FL_{API} (mL)	pH
1.50				4.75	11.30	10.99
2.00				4.25	10.60	11.16
2.50				3.58	10.30	11.21
3.00				3.25	10.20	11.26
3.50	0.30	2.50	0.50	2.92	9.70	11.34
4.00				3.42	10.50	11.26
4.50				4.92	10.60	11.02
5.00				6.00	10.90	11.08
5.50				6.83	11.30	11.09
6.00				7.67	11.50	11.12

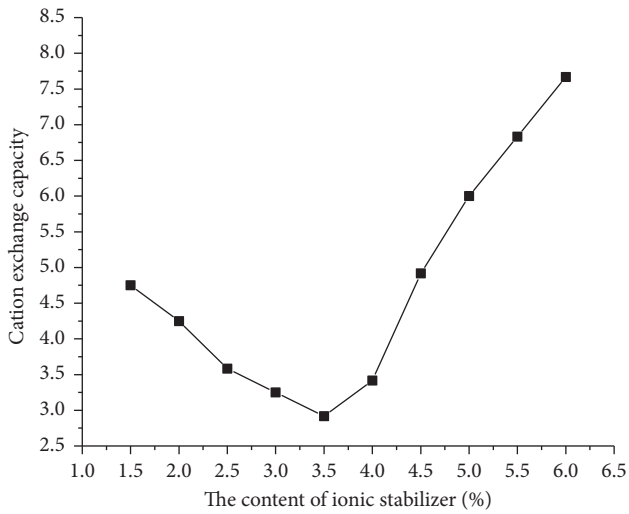


FIGURE 3: Curve of cation exchange capacity of the slurry fluid.

3.2. Effect of Cation Exchange Capacity on Filtrate and pH.

Figure 4 shows the relationship between the cation exchange capacity of the slurry fluid and the filtrate volume. As the cation exchange capacity of the slurry fluid increases, filtrate volume also increases with it. The residue deposits on a permeable stratum when the slurry is forced against the stratum under a pressure. Filtrate is the liquid that passes through the stratum, leaving the filter cake on the cutting surface. When the filter cake formed, it has an important effect on filtration, mainly including inherent resistance and adsorption resistance. The inherent resistance of the filter cake can be considered as a constant in this experiment, which is generally related to the concentration of the slurry fluid and the characteristics of the filter. The adsorption resistance is greatly influenced by the adsorption capacity, which increases as the ion exchange capacity of the slurry fluid increases. According to the calculation model of adsorption resistance, the adsorption differential pressure increases as the viscosity of the slurry fluid is constant, which indirectly leads to the increase of the filtrate volume of the slurry fluid.

Figure 5 shows the relationship between the cation exchange capacity and its pH values of the slurry fluid. The

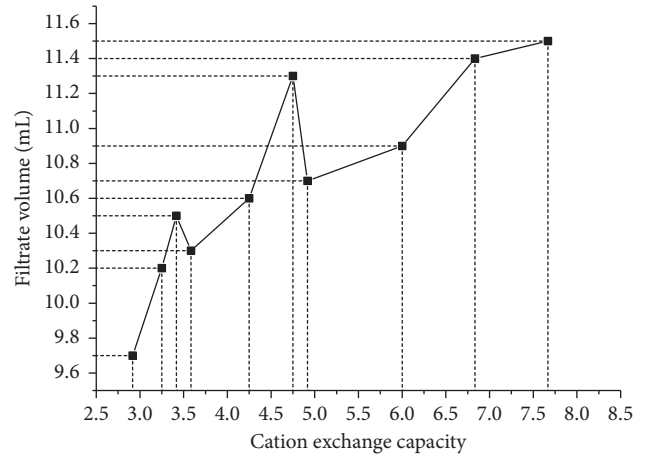


FIGURE 4: Curve of filtration volume.

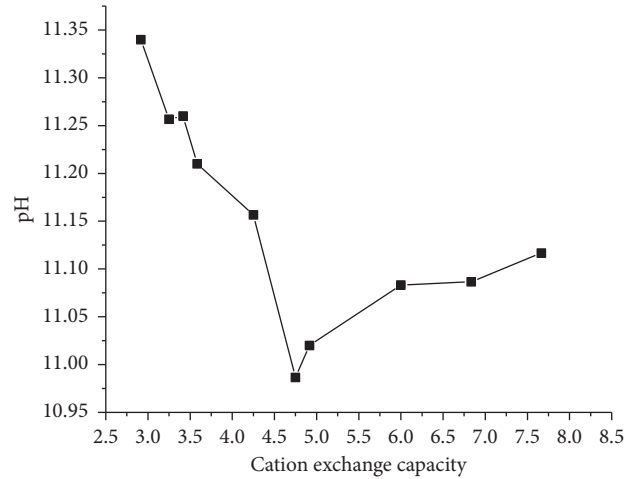


FIGURE 5: Curve of pH change in the slurry fluid.

pH value decreases first and then increases with the cation exchange capacity increasing. A solution with a concentration of hydrogen ions higher than 10^{-7} mol/L is acidic, and a solution with a lower concentration is alkaline, which indicates that hydrogen ions concentration in the slurry is less than 10^{-10} mol/L. So, it is easy to learn that the slurry fluid is still an alkaline solution of $\text{pH} > 10$ from the diagram. However, the change of pH is relatively small, which can be seen as a constant in practical engineering.

3.3. Effect of Cation Exchange Capacity of the Slurry Fluid on Its Rheological Properties. The rheology is the characteristics of slurry fluid flow and deformation under the action of external forces, which is generally expressed by different rheological models and parameters.

The rheological parameters of the slurry fluid are tested and calculated according to the API standard. The rheological model discrimination coefficient (F) under different cation exchange capacities is calculated by Equation (2), and the results are shown in Table 2.

TABLE 2: Rheological model discriminant coefficient (F).

CEC	2.92	3.25	3.42	3.58	4.25	4.75	4.92	6.00	6.83	7.67
F	0.56	0.54	0.46	0.48	0.55	0.56	0.33	0.47	0.49	0.39

$$F = \frac{\theta_{200} - \theta_{100}}{\theta_{300} - \theta_{100}}, \quad (2)$$

where F is the rheological model discriminant coefficient. When $F = 0.5 \pm 0.03$, it is defined as the Bingham model; otherwise, the power law model is applied. θ_N is the dial value of viscometer when the speed is N (mPa·s).

According to above discriminant coefficients, the slurry fluid could be defined as the power law model with different cation exchange capacities. Power law fluid is non-Newtonian model, which usually includes pseudoplastic fluid and expansion plastic fluid. The rheological properties of the slurry fluid can be characterized by rheological parameters such as the flow index, consistency coefficient, apparent viscosity, plastic viscosity, and static shear force, as shown in Table 3.

3.3.1. Power Law Model. The variation tendency of flow behavior index and consistency coefficient indicate a highly symmetrical relationship, as shown in Figure 6 and Figure 7, respectively. The amount of negative charges in the slurry fluid increases with the increase of the cation exchange capacity. The high valence cations in the slurry fluid can be hydrated and flocculated when the cation exchange capacity is less than 4.75, which inhibits the ion exchange in the ionic solution. The interaction between entanglement of polymer molecular chains and the adsorbent groups on the molecular chain is weakened in the slurry fluid, and the continuity of the formed polymer spatial structure is poor, which leads to the increase of the flow behavior index and the decrease of the consistency coefficient. When the cation exchange capacity reaches 4.75, the amount of coagulation in the slurry fluid is maximum. At the time, flow behavior index and consistency coefficient reach an interval maximum value and the filtration volume also fluctuates greatly. The cationic flocculation reaction in the slurry fluid reaches a dynamic equilibrium. The flow behavior index and consistency coefficient remain constant when the cation exchange capacity reaches 4.92. The dynamic equilibrium is upset after the cation exchange capacity exceeds 6.00. Because there are a lot of free high-valence cations in the slurry fluid due to the dissolution of coagulation, the ion exchange effect in the solution is enhanced, and as the coefficient of consistency increases sharply, the flow behavior index decreases. There are too many polymers with continuous spatial structure formed in the slurry fluid which reduces the slurry fluid dispersion and decreases the water retention property, resulting in the increase of filtrate volume. Normally, the smaller the flow index is, the better the shear dilution performance of the fluid is under the power law model. However, it is not the smaller, the better when it comes to the matter of the overall performance of slurry fluid. The filtrate value of slurry fluid is the largest when the flow behavior

index is the smallest, which is indicated in Figures 4 and 6. The flow behavior index and consistency coefficient are close to the median value which is convenient to adjust related parameters, and the filtrate volume is the smallest when the cation exchange capacity reaches the minimum value.

3.3.2. Effect of Cation Exchange Capacity of Slurry Fluid on Its Viscosities. The apparent viscosity, shear stress, and shear rate of the slurry fluid with different cation exchange capacities are calculated according to the data obtained from the viscometer and Equations (3)–(5) [39, 40], and shear rate obtained is the average value to improve the accuracy:

$$\mu_{AV} = \frac{\tau}{D}, \quad (3)$$

$$\tau = 0.511\theta_N, \quad (4)$$

$$D = \frac{21936.7646N}{13750.3615 - 901.2775m + 38.5114m^2 - m^3}, \quad (5)$$

where μ_{AV} is the apparent viscosity of slurry fluid (mPa·s), τ is the shear stress (Pa), θ_N is the dial reading of viscometer when the speed is N (mPa·s), D is the shear rate (s^{-1}), N is the speed of viscometer (r/min), m is the calculation constant, and $m = 1/n$, n is the flow behavior index of the slurry fluid.

Figure 8 shows the relationship between the cation exchange capacity and slurry viscosities. They all show a highly consistent trend, decreasing first and then increasing as the cation exchange capacity increases. Finally they show a gradually decreasing trend. When the cation exchange capacity is less than 4.75, with the increase of the flocculation degree in the slurry fluid, the ion exchange effect and the dispersion degree in the solution are weakened. At the same time, as the viscosity increases, the frictional resistance between the flocculant, the polymer and the liquid phase increases at the macroscopic scale. The flocculation amount reaches the maximum and the viscosities reach the peak value while the cation exchange capacity is 4.75. And the cationic flocculation reaction in the slurry fluid reaches a dynamic equilibrium. In this case, its viscosities remain relatively constant when the cation exchange capacity is between 4.92 and 6.00. Then, the dynamic equilibrium of flocculation is tipped when the cation exchange capacity exceeds 6, and the dispersity of the slurry fluid decreases, resulting in the decrease of viscosities.

Figure 9 shows the rheological curves of slurry fluids with different cation exchange capacities. It can be learned from Equation (3) that apparent viscosity is the ratio of shear stress to shear rate at a certain shear rate; that is, apparent viscosity is the slope of the line section of the curve in Figure 8. The diminished amplitude of the slope of the curve (i.e., apparent viscosity) is maximum with the increase of the shear rate when the cation exchange capacity is the smallest, indicating that the shear dilution ability of the slurry fluid is the strongest at this time.

3.3.3. Effect of Cation Exchange Capacity of Slurry Fluid on Its Static Shear Force. The static shear force is determined by

TABLE 3: Rheological parameters of slurry fluid with different cation exchange capacities.

CEC	Flow behavior index	Consistency coefficient (Pa·s ⁿ)	Apparent viscosity (mPa·s)	Plastic viscosity (mPa·s)	Initial shear force (Pa)	Final shear force (Pa)
2.92	0.64	0.31	25.33	18.14	0.81	1.32
3.25	0.64	0.28	22.63	16.17	0.72	0.84
3.42	0.64	0.29	23.33	16.69	0.58	0.49
3.58	0.68	0.21	23.12	17.35	0.76	0.63
4.25	0.68	0.23	24.08	18.02	0.85	0.94
4.75	0.70	0.19	24.66	18.99	0.99	0.89
4.92	0.65	0.26	22.62	16.31	1.12	1.26
6.00	0.65	0.25	21.53	15.54	1.35	1.26
6.83	0.53	0.50	19.50	12.05	1.23	0.82
7.67	0.52	0.51	18.61	11.30	0.54	0.18

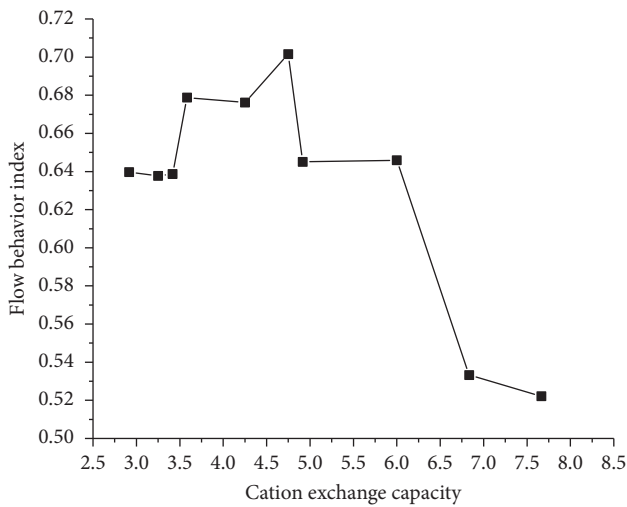


FIGURE 6: Curve of flow behavior index of slurry fluid.

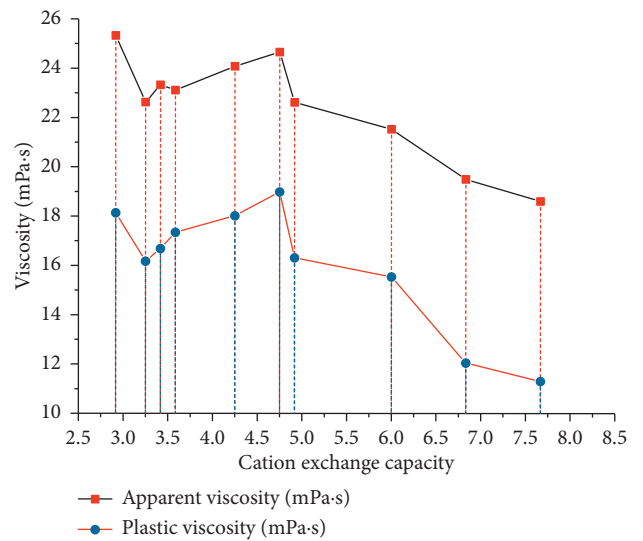


FIGURE 8: Curve of viscosities of the slurry fluid.

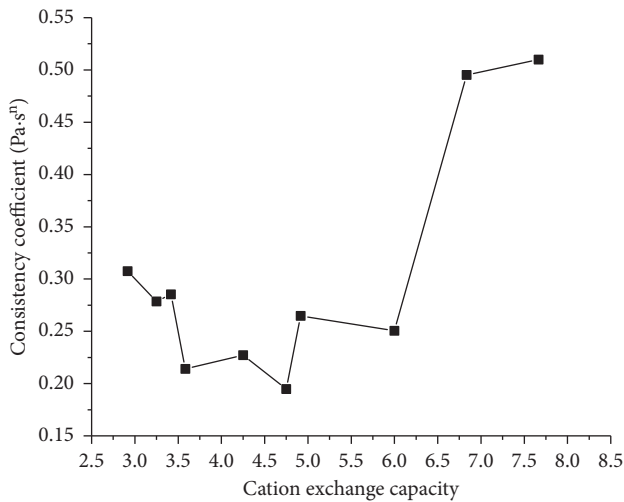


FIGURE 7: Curve of consistency coefficient of slurry fluid.

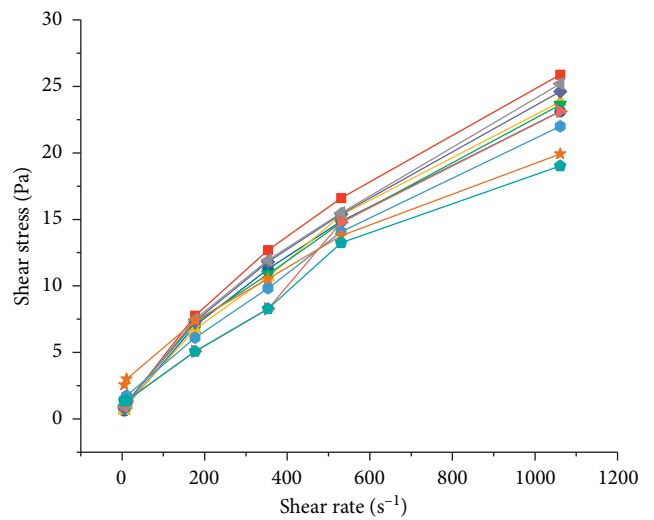


FIGURE 9: Rheological curves of slurry fluids.

the number of structural chains and the strength of the single structure chain in the unit volume. The value of static shear force mainly reflects the suspension capacity of the slurry, so the larger the static shear force is, indicating the slurry structure more stable, the better its suspension capacity is.

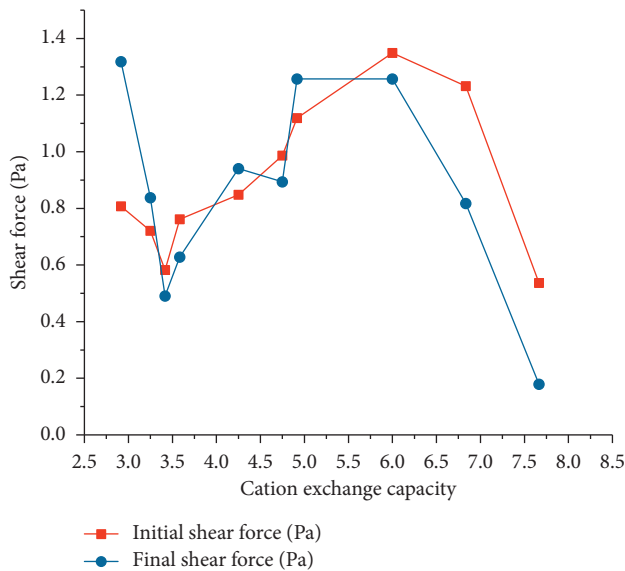


FIGURE 10: Curve of static shear force of slurry fluid.

The varying regularity with the cation exchange capacity is shown in Figure 10. The structure formation of the polymer space is hindered by the hydration and flocculation of high valence cation with the increase of the cation exchange capacity, and the static shear force of the slurry fluid drops sharply when the cation exchange capacity is less than 3.42. The floc and the polymer can form a complex with a certain spatial structure and strength with the flocculation reaction, which leads to the gradual increase of the static shear force when the cation exchange capacity is between 3.42 and 6.00. The dynamic equilibrium of the flocculation reaction is tipped after the cation exchange capacity exceeds 6.00. Then the structures of the complex begin to break down with the ion exchange enhanced in the solution. When the continuous polymer of excessive space structure is formed, it will result in diminish in dispersion of the slurry fluid, which makes the static shear force reduce abruptly.

4. Conclusions

Ion stabilizers can enhance the reinforcement slurry effect on the wall and stabilize the wall actively in slurry shields. This paper presents the effect on the slurry fluid from different cation exchange capacities.

The cation exchange capacity of the slurry fluid decreases first and then increases following the increase of the ion stabilizer content in the slurry fluid. And the filtration volume, pH value, and rheological parameters of the slurry fluid indicate a linear trend obviously as the cation exchange capacity increases.

With the increase of the cation exchange capacity, the continuity of the spatial structure formed by the polymer in the slurry fluid decreases first and then increases, which directly leads to the change of the flow behavior index. The viscosity and static shear force of the slurry fluid present a corresponding regular change with the continuity of the polymer spatial structure too.

The test results also indicate that the filtrate of the slurry fluid is minimum when the cation exchange capacity reaches the smallest. This is beneficial to restrain the hydration expansion of rock and soil, maintaining the stability of the excavation face. Slurry filtrate volume and rheological parameters such as viscosity, static shear, flow behavior index, and consistency coefficient are present with ideal values following with smallest value of the cation exchange capacity. The spatial structure of the polymer in the slurry fluid is relatively continuous, which is beneficial to cation transporting in the fluid system. These cations can neutralize the negative electricity of the clay in the cutting face and strengthen the stability of the wall. In this case, the overall performance of the slurry fluid reaches a relatively ideal state.

Data Availability

The data used to support the findings of this study are available from the corresponding author upon request.

Conflicts of Interest

The authors declare that they have no conflicts of interest.

Acknowledgments

The authors gratefully acknowledge the financial support from the National Natural Science Foundation (41602372), the open fund project of the Key Laboratory of the Complex Conditions for Slurry and Mining of the Ministry of Land and Resources (DET201612), the National Key Laboratory of Oil and Gas Reservoir Geology and Development Engineering (Southwest Petroleum University) open fund project (PLN201607 and PLN201609), the National Study Fund Visiting Scholar Project (201706375018), and the Fundamental Research Funds for the Central Universities of Central South University (No. 2018zzts697).

References

- [1] S. Chen, "Slurry ratio for shield machine construction in complex formation and its application," *Railway Construction Technology*, vol. 8, pp. 83–86, 2016.
- [2] G. Anagnostou and K. Kovfiki, "The face stability of slurry shield driven tunnels with ideal face membrane-drained case," *Tunnelling and Underground Space Technology*, vol. 9, no. 2, pp. 165–174, 1994.
- [3] S. H. Kim and F. Tonon, "Face stability and required support pressure for TBM driven tunnels with ideal face membrane-drained case," *Tunnelling and Underground Space Technology*, vol. 25, no. 5, pp. 526–542, 2010.
- [4] W. Broere, "Influence of excess pore pressures on the stability of the tunnel face," in *Geotechnical Aspects of Underground Construction in Soft Ground*, R. Kastner, F. Emeriault, D. Dias, and A. Guilloux, Eds., pp. 179–184, Balkema, Toulouse, France, 2002.
- [5] L. H. Babendererde, "Developments in polymer application for soil conditioning in EPB-TBMs," in *Tunnels and Metropolises*, A. Negro Jr and A. A. Ferreira, Eds., pp. 691–695, Balkema, Rotterdam, Netherlands, 1998.

- [6] G. T. Houlsby and S. Psomas, "Soil conditioning for pipejacking and tunnelling: properties of sand/foam mixtures," in *Proceedings of Underground Construction*, pp. 128–138, London, UK, 2001.
- [7] P. Fritz, "Additives for slurry shields in highly permeable ground," *Rock Mechanics and Rock Engineering*, vol. 40, no. 1, pp. 81–95, 2007.
- [8] T. Leinala, M. Grabinsky, and K. Klein, "A review of soil conditioning agents for EPBM tunneling," in *Proceedings of 17th Tunnelling Association of Canada Conference*, Toronto, Canada, 2002.
- [9] B. K. Halder and A. M. Palomino, *The Shear Strength of "Tunable" Clay-Polymer Composite under Various Ionic Concentrations*, Geo-Chicago, Chicago, USA, 2016, pp. 61–72.
- [10] G. W. E. Milligan, *Lubrication and Soil Conditioning in Tunneling, Pipe Jacking and Micro-Tunneling: A State-of-the-art Review*, Geotechnical Consulting Group, London, UK, 2000.
- [11] S. A. Jefferis, "Water-soluble polymers in tunnelling and slurry supported excavations," in *Cellulose and Cellulose Derivatives: Physico-chemical aspects and industrial applications*, J. F. Kennedy, G. O. Phillips, and P. A. William, Eds., Woodhead Publishing Ltd, Cambridge, UK, 1995.
- [12] G. W. E. Milligan, "Soil conditioning and lubricating agents in tunnelling and pipe jacking," in *Proceedings of Underground Construction Conference*, pp. 105–116, London, UK, 2001.
- [13] EFNARC, *Specification and Guidelines for the Use of Specialist Products for Soft Ground Tunnelling*, European Federation for Specialist Construction Chemicals and Concrete Systems, Surry, UK, 2005.
- [14] T. Wang and M.S. thesis, *A Study on Preparation of Environment Friendly Slurry and its Adaption during Slurry Shield Tunneling in High Permeability Stratum*, Beijing Jiaotong University, Beijing, China, 2015.
- [15] P. Fritz, R. Hermanns Stengele, and A. Heinz, "Modified bentonite slurries for slurry shields in highly permeable soils," in *Proceedings of 4th International Symposium on Geotechnical Aspects of Underground Construction in Soft Ground*, France, Toulouse, 2002.
- [16] J. Jebelli, M. A. Meguid, and M. K. Sedghinejad, "Excavation failure during micro-tunneling in fine sands: a case study," *Tunnelling & Underground Space Technology Incorporating Trenchless Technology Research*, vol. 25, no. 6, pp. 811–18, 2010.
- [17] M. Bayati and J. K. Hamidi, "A case study on TBM tunnelling in fault zones and lessons learned from ground improvement," *Tunnelling & Underground Space Technology*, vol. 63, pp. 162–170, 2017.
- [18] Z. L. Cheng, Z. M. Wu, and Y. Y. Xu, "Experimental study on stability of excavation face of slurry shield tunnel construction in sandy ground," *Journal of Yangtze River Scientific Research Institute*, vol. 18, no. 5, pp. 53–55, 2001.
- [19] X. R. Han, W. Zhu, W. Q. Liu, X. C. Zhong, and F. L. Min, "Influence of slurry property on filter-cake quality on working face of slurry shield," *Rock and Soil Mechanics*, vol. 29, no. s1, pp. 288–292, 2008.
- [20] A. Heinz, "Modifizierte bentonitsuspensionen für geotechnische bauverfahren in böden hoher durchlässigkeit," Ph. D. thesis, Swiss Federal Institute of Technology ETH, Zurich, Switzerland, 2006.
- [21] P. G. Harding, "High density slurry shield extends Japanese technology," *Tunnels and Tunnelling International*, vol. 14, pp. 55–56, 1982.
- [22] T. B. Nguyen, C. Lee, and H. Choi, "Slug test analysis in vertical cutoff walls with consideration of filter cake," *Journal of Geotechnical & Geoenvironmental Engineering*, vol. 137, no. 8, pp. 785–797, 2011.
- [23] T. Watanabe and H. Yamazaki, "Giant size slurry shield is a success in Tokyo," *Tunnels and Tunnelling International*, vol. 13, no. 1, pp. 13–17, 1981.
- [24] Q. Wang and D. Y. Zhu, "Effect of slurry density on slurry consumption slurry shield tunneling," *Journal of China Three Gorges University (Natural Sciences)*, vol. 39, no. 3, pp. 62–65, 2017.
- [25] F. L. Min, W. Zhu, and X. R. Han, "Filter cake formation for slurry shield tunneling in highly permeable sand," *Tunnelling and Underground Space Technology*, vol. 38, no. 3, pp. 423–430, 2013.
- [26] G. M. Filz, T. Adams, and R. R. Davidson, "Stability of long trenches in sand supported by bentonite-water slurry," *Journal of Geotechnical and Geoenvironmental Engineering*, vol. 130, no. 9, pp. 915–921, 2004.
- [27] L. V. Amorim, M. I. R. Barbosa, H. L. Lira, and H. C. Ferreira, "Influence of ionic strength on the viscosities and water loss of bentonite suspensions containing polymers," *Materials Research*, vol. 10, no. 1, pp. 53–56, 2007.
- [28] Q. Liu and J. C. Santamarina, "Mudcake growth: model and implications," *Journal of Petroleum Science and Engineering*, vol. 162, pp. 251–259, 2017.
- [29] Y. G. Chen, B. H. Zhu, D. B. Wu et al., "Eu(III) adsorption using di(2-thylhexyl) phosphoric acid-immobilized magnetic GMZ bentonite," *Chemical Engineering Journal*, vol. 181–182, pp. 387–396, 2012.
- [30] Y. G. Chen, Y. He, W. M. Ye, and L. Y. Jia, "Competitive adsorption characteristics of Na(I)/Cr(III) and Cu(II)/Cr(III) on GMZ bentonite in their binary solution," *Journal of Industrial and Engineering Chemistry*, vol. 26, pp. 335–339, 2014.
- [31] Y. G. Chen, Z. Sun, W. M. Ye, and Y. J. Cui, "Adsorptive removal of Eu(III) from simulated groundwater by GMZ bentonite on the repository conditions," *Journal of Radio-analytical & Nuclear Chemistry*, vol. 311, no. 3, pp. 1839–1847, 2017.
- [32] P. H. Xu, *Slurry Performance and Measurement Method for slurry balanced shield construction*, Wisdom City and Rail Transit of Chinese Society for Urban Studies, Shenyang, China, 2015.
- [33] Y. Wang and H. Shen, "Study on slurry preparation for slurry shield crossing high permeability formation," *Sichuan Cement*, vol. 6, p. 300, 2015.
- [34] S. J. Han, Y. T. Li, and X. H. Wu, "Discussion on using SR solidified soil as a canal seepage proof material," *Journal of Water Resources and Architectural Engineering*, vol. 6, no. 3, pp. 19–21, 2000.
- [35] Z. H. Luo, L. X. Wang, and B. R. Xia, "Effect of an ionic liquid with an imidazole cation on shale inhibitive property in water-based drilling fluids and its mechanism," *Chemical Industry and Engineering Progress*, vol. 36, no. 11, pp. 4209–4215, 2017.
- [36] P. H. Sun, M. J. Tian, H. Cao, L. X. Niu, and S. H. Zhang, "Study on the mechanism of ENI action on preventing drilling fluid overflowing in HDD," *Tunnelling and Underground Space Technology*, vol. 77, pp. 94–102, 2018.
- [37] American Petroleum Institute, *Recommended Practice for Field Testing of Water-Based Drilling Fluids: API RP 13B-1*, American Petroleum Institute, Washington, DC, USA, 4 edition, 2009.

- [38] N. Su, G. Z. Qi, and M. Z. Ma, "Probe into the methylene blue capacity and bentonite of drilling fluids," *Xinjiang Oil and Gas*, vol. 7, no. 3, pp. 42–45, 2011.
- [39] K. Q. Liu, Z. S. Qiu, J. Cao, Y. Luo, and M. L. Cui, "Derivation and verification of shear equation for non-newtonian drilling fluid," *Drilling Fluid and Completion Fluid*, vol. 31, no. 4, pp. 33–35, 2014.
- [40] Y. G. Chen, B. H. Zhu, D. B. Wu, Y. H. Yang, W. M. Ye, and J. F. Guo, "Eu (III) adsorption using di (2-thylhexyl) phosphoric acid-immobilized magnetic GMZ bentonite," *Chemical Engineering Journal*, vol. 181-182, pp. 387–396, 2012.

Research Article

Optimization of Stope Structural Parameters Based on Mathews Stability Graph Probability Model

Long Zhang ¹, Jian-hua Hu ¹, Xue-liang Wang,² and Lei Zhao²

¹School of Resources and Safety Engineering, Central South University, Changsha 410083, China

²Hubei Sanning Mining Co., Ltd., Yichang, Hubei 443100, China

Correspondence should be addressed to Jian-hua Hu; hujh21@csu.edu.cn

Received 30 June 2018; Revised 23 August 2018; Accepted 6 September 2018; Published 1 October 2018

Academic Editor: Dingwen Zhang

Copyright © 2018 Long Zhang et al. This is an open access article distributed under the Creative Commons Attribution License, which permits unrestricted use, distribution, and reproduction in any medium, provided the original work is properly cited.

Strip mining with subsequent filling is one of the main mining methods for gently inclined thin ore bodies. The production process of excavating alternate strips is beneficial to the safety of mining. Reasonable stope structural parameters are key to achieving safe and efficient mining. The Tiaoshuihe phosphate mine of Sanning Mining is taken as an example in this study. Based on precision finite element modeling and simulation, a reasonable width range and the interval value of the strip are determined. A reliable and efficient strip width is calculated by using the probability model of the improved Mathews stability graph method. The results show the following. Firstly, under the geological conditions and backfill environment of the Tiaoshuihe phosphate mine, the reasonable and safe strip width interval is 7–9 m. Secondly, the probabilities of open stope stability with strip widths of 7, 8, and 9 m are 88.55%, 86.76%, and 84.94%, respectively. The reasonable probabilities of stope stability with strip widths of 7 and 8 m are higher than 85%. Thirdly, combining this with the drilling equipment operation parameters, it is suggested that the best strip width is 7 m without increasing the strength of the backfill.

1. Introduction

At present, the filling mining method is becoming increasingly widely used. It is a safe and efficient method to apply strip mining with subsequent filling for gently inclined thin ore bodies [1]. The structural parameters of the stope are closely related to its productivity and recovery rate, as well as the stability of the goaf. Meanwhile, the mining equipment level and technology are required to consist with the structural parameters of the stope [2]. Gao-hui et al. [3] combined an engineering geological evaluation with a numerical simulation to determine the stope height, chamber width, and spike diameter in Baiyang ore block. Ning and Hu [4]. used Mathews stability graph method and an orthogonal numerical simulation to determine the limit exposure area of zinc-copper ore body of Dachang Tongkeng Mine. Li and Li [5] applied the 3D-sigma numerical simulation method to analyze the surrounding rock stability in different stope structure parameters and designed the reasonable size of room and pillar for a phosphate mine. Guo et al. [6] adopted the fuzzy comprehensive evaluation method to prove that the

optimal stope structural parameter is 10 m × 10 m for safety and high-efficiency mine operation in Sanshandao Gold Mine. Chen et al. [7] optimized the structural parameters of Yongping Copper Mine with FLAC3D and analyzed plastic zone, displacement, and stress distribution after excavation. Li et al. [8] performed a series of three-dimensional simulation and studied the relationship between mining safety-rock movement parameters and the design parameters and then obtained the reliable structural parameters of the stope.

However, the traditional single computational analysis method has some limitations. For uncertain rock mechanics parameters, the probability of its stability has an important influence on the optimization of engineering parameters. In this study, with finite element numerical simulation determining the width range of the strip, the overall stability of the goaf is calculated by using the Mathews binary linear regression model, and the stability probability of goaf is quantized for different strip widths. Taking the parameters of underground equipment into consideration, a reasonable strip width for the Tiaoshuihe phosphate mining was determined by comparing the stability probability finally.

2. Project Profile

The phosphate ore bodies of the Tiaoshuihe phosphate mine of Sanning Mining are divided into the middle phosphate layer (Ph^2) and the lower phosphate layer (Ph_1^3), and the average interval between the two layers is 10 m. The middle phosphate layer currently being mined is 1.63–6.79 m in thickness, with an average thickness of 3.22 m and an inclined angle of 15° . Its burial depth is 81.67–614.75 m, with an average burial depth of 254.27 m. The folds in the mine area are not well developed, while the fault structure in the area is relatively developed. Considering the limited space in the thin ore body, the DD211L low-type drilling rig manufactured by Sandvik was purchased and used in the mine, and the maximum drilling width of this rig is 7.6 m for a single-drilling application.

Full-thickness panel strip mining is adopted in this mine, with the sequence of excavating alternate strips. The waste rock is cemented with tailings filling into the open stope. At present, the method of exploiting a strip width of 5 m and leaving 5.5 m is used in the mine. To improve the production capacity of the stope and reduce the construction involved in the mining, the strip width of the stope is proposed to be enlarged, so as to enhance the recovery rate of the stope. The mechanical parameters of the rock body in the Tiaoshuihe phosphate mine are obtained by a standard reduction of the rock mechanical parameters tested in the laboratory [9], as shown in Table 1.

3. Determination of Strip Width Range

3.1. Accurate Finite Element Model and Simulation Schemes. FLAC3D is a type of simulation software developed by the ITASCA of America and is widely used in rock and soil mechanics calculation [10–12]. Since it comprises 11 kinds of original constitutive models of elastoplastic materials, such as seepage, static, creep, dynamic, and temperature calculation models, it is appropriate for many scientific research fields like geotechnical engineering, geological engineering, and mining engineering [13–15]. Furthermore, it can get the accurate data and graph of stress, displacement, and plastic zone after caving and filling. Hence, FLAC3D can meet the requirements of this paper.

To ensure the accuracy and authenticity of the finite element analysis, the ore body model has the same thickness as the average three-dimensional ore body extracted from the Tiaoshuihe phosphate mine in DIMINE software. Four model groups with strip widths of 6, 7, 8, and 9 m and the length of 50 m were established, in which the roadway widths were 4.5 m and the left and right sides of the roadway each contained five strips. Figure 1 shows the model with strip width of 9 m as an example, and ten strips are numbered 1–10. The intercepted ore body was meshed using a DIMINE-CAD-MIDAS/GTS coupling operation and imported into the numerical simulation software FLAC3D for calculation [16, 17].

The calculation steps of exploiting-filling-exploiting are designed according to the four sets of models established, and each model corresponds to one scheme. The simulation

consists of three main steps in each scheme: the first step (I) is the exploitation of strips 3, 4, 7, and 8. The second step (II) is the filling of strips 3, 4, 7, and 8. The third step (III) is the exploitation of strips 1, 2, 5, 6, 9, and 10. The four simulation schemes of different strip widths are shown in Table 2.

3.2. Simulation Results

3.2.1. Displacement and Stress Analysis of the Roof. In the simulation process, it is found that the stability of the stope after the third step is the worst. Therefore, the displacement and stress of the roof after the third step in the four schemes are analyzed. The specific values are shown in Table 3.

Comparing these parameters in Table 3 with the maximum bearing capacity of the roof in Table 1, it can be concluded that the roof in the stope of the four schemes will not be damaged.

3.2.2. Plastic Failure Analysis of the Backfill. After the third step, both sides of the backfill are goaf. When the pressure exerted by the roof on the backfill exceeds the compressive strength of the backfill, plastic failure will lead to overall collapse of the backfill [18]. Table 4 shows the plastic failure volumes of the backfill after the third step of the four schemes. Shear failure is mainly caused by the pressure exerted on the backfill by the top plate exceeding the compressive strength of the backfill. When the shear failure area is too large, the backfill will perforate. And the tensile failure is mainly located in the center of the roof, which is caused by the self-gravity stress of the overlying strata.

It can be concluded from Table 4 that the tensile failure volume is sufficiently small that it does not affect the stability of the backfill. Therefore, the shear failure is mainly analyzed as follows. The change curve of shear failure volume with strip width is shown in Figure 2.

As shown in Figure 2, the shear failure volume of the backfills in schemes 2, 3, and 4 exhibits a significant change compared with that of scheme 1, with a decrease of more than 1000 m^3 . The overall stabilities of the backfills of these three schemes are better than that of scheme 1. As can be seen from Figure 3, the shear failure plastic zone passes through the backfill; thus, the backfill will lose its stability. “shear- n ” in Figure 3 means the backfill is in plastic state now, which is the main factor of influencing the stability of the backfill. “shear- n ” in schemes 2, 3, and 4 is far less than that in scheme 1.

In the two-step stopping process, there are two main forms of stope instability damage [19]. The first is when the deformation of the roof exceeds the allowable range, leading to collapse failure of the roof, or when the tensile stress produced by the roof exceeds its ultimate tensile strength, resulting in tensile failure. The second is when plastic penetration failure occurs when the pressure of the backfill exceeds its compressive strength, and the whole backfill collapses.

It can be concluded that when the width of the strip is 6 m, the overall strength of the backfill after the third step is smaller than that of the 7, 8, and 9 m strips, and plastic zone

TABLE 1: Mechanical parameters of rock mass and the backfill.

Rock layer	P (g·cm ⁻³)	K (GPa)	G (GPa)	φ (°)	C (MPa)	T (MPa)
The upper surrounding rock	2.845	45.319	11.289	50.58	4.808	5.494
The phosphate rock layer	3.021	14.219	8.5740	60.76	1.052	2.010
The lower surrounding rock	2.846	25.786	16.599	53.60	1.732	3.643
Backfill	2.200	18.788	12.432	40.00	0.200	0.300

T , tensile strength; C , cohesion; φ , internal friction angle; K , bulk modulus; G , shear modulus; ρ , density.

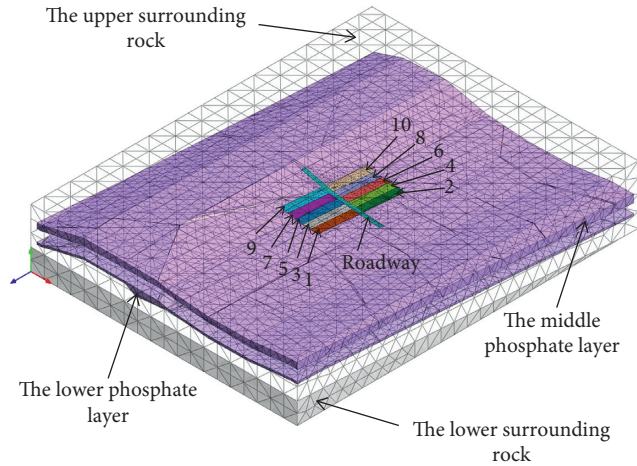


FIGURE 1: Model with strip width of 9 m.

TABLE 2: Simulation schemes.

Schemes	Strip width (m)	Steps
Scheme 1	6	I, II, and III
Scheme 2	7	I, II, and III
Scheme 3	8	I, II, and III
Scheme 4	9	I, II, and III

TABLE 3: Roof displacement and stress values of the four schemes after the third step.

Schemes	Displacement (mm)	Shear stress (MPa)	Tensile stress (MPa)	Compressive stress (MPa)
Scheme 1	2.56	7.92	2.46	18.21
Scheme 2	2.42	8.23	2.28	20.67
Scheme 3	2.68	8.24	2.39	20.94
Scheme 4	2.55	8.51	2.07	20.22

penetration failure occurs. Therefore, the analysis shows that 7, 8, and 9 m may be stable strip widths.

4. Calculation of Mathews Stability Graph Probability Model

According to the previous finite element analysis, 7, 8, and 9 m are the strip widths that are likely to be applicable. The

TABLE 4: Volume of the plastic zone after the third step.

Schemes	Shear failure volume (m ³)	Tensile failure volume (m ³)
Scheme 1	1212.54	0.00094
Scheme 2	164.886	0.00170
Scheme 3	177.965	0.00127
Scheme 4	157.505	0.00470

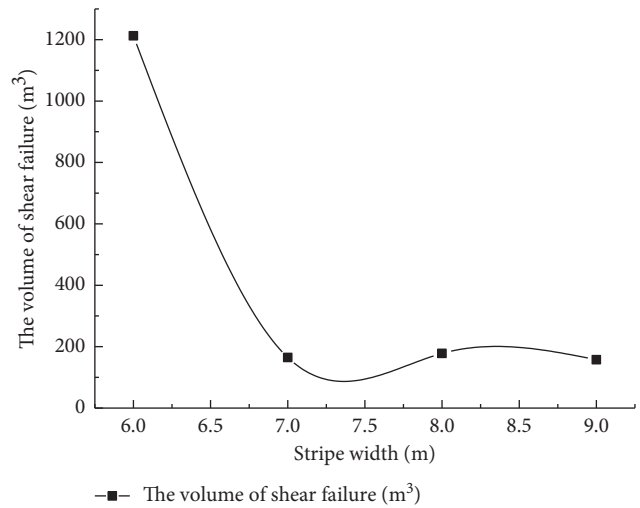


FIGURE 2: Volume of shear failure variation after the third step.

probability model of Mathews stability graph is used to further optimize the three strip widths.

4.1. Mathews Stability Graph Probability Model. The original Mathews stability graph was divided into stable, potentially unstable, and potential caving zones according to the scatter of the stability data in Figure 4. The initial stability zones and graph devised by Mathews et al. were based on 50 cases [20].

After 1980, researchers like Potvin, Stewart, Forsyth, and Tureman redrew the Mathews stability graph by increasing the number of projects evaluated to 500 [21]. Mawdesley applied mathematical statistics to explain the Mathews stability graph in 2001 and 2002 [22, 23]. In 2004, Mawdesley adopted the method of logarithmic regression analysis, redefining the stability area and great destruction zone. Parallel lines in the equal probability graph are drawn to divide the stable area, unstable area, and caving zone [24].

The Mathews method is based on a stability graph relating two calculated factors: the Mathews stability number (N), which represents the competency of the rock mass for a given

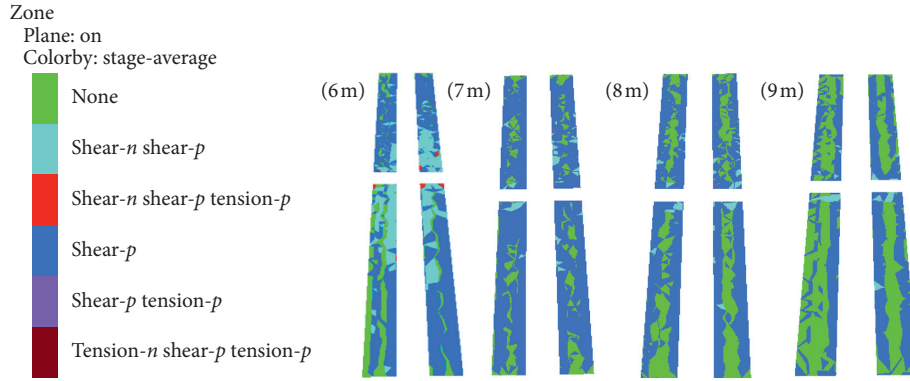


FIGURE 3: Plastic failure in the backfill after the third step.

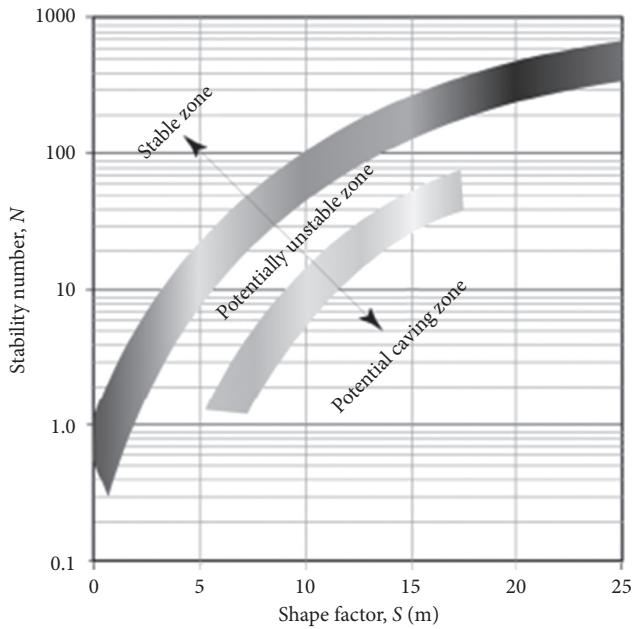


FIGURE 4: Three stability zones of the original Mathews stability graph.

stress condition, and the shape factor (S), or hydraulic radius, which accounts for the geometry of the surface.

The logistic regression line defining the stability boundaries is defined by Equations (1) and (2), where $f(z)$ is the logit value. The logit value is analogous to the response variable in a linear regression model and is determined for each data point based on the shape factor and the stability parameter [25, 26]:

$$Z = \alpha + \beta_1 x_1 + \beta_2 x_2 + \dots + \beta_n x_n, \quad (1)$$

$$f(z) = \frac{1}{1 + \exp(-z)}, \quad (2)$$

where Z is the predicted log odds value, α is a constant, $\beta_{1,2}$ are numerical coefficients, and $f(z)$ is the predicted logit probability value.

In the logit model of the stability data, the probability of stability is expressed as a linear function of the shape factor, the Mathews stability number, and a constant, represented by

$$Z = 2.9603 - 1.4427 \ln S + 0.7928 \ln N, \quad (3)$$

where S and N are the shape factor and stability parameter, respectively.

4.2. Parameters Determination

4.2.1. Calculation of Stability Parameter N . The calculation formula of stability index N is as follows [27]:

$$N = Q' \times A \times B \times C, \quad (4)$$

where Q' is the modified Q -value, A is the stress factor, B is the joint orientation factor, and C is the surface orientation factor. The modified Q -value is calculated using the following equation:

$$Q = e^{((RMR-44)/9)}, \quad (5)$$

where RMR is the rock mass rating system and Q is the tunneling quality index system [28].

The indicators were graded by consulting the relevant data of the geological report of the Tiaoshuihe phosphate mine: (1) rock compressive strength is 205.70 MPa, scoring 12 points; (2) rock mass quality indicator RQD is 79.18%, scoring 17 points; (3) joint spacing scores 10 points; (4) joint state scores 10 points; (5) state of groundwater on average is 15 L/min, scoring 7 points; and (6) joint bearing scores -5 points:

$$RMR = 12 + 17 + 10 + 10 + 7 - 5 = 51. \quad (6)$$

In summary, the RMR points of the surrounding rocks of the up panel can be obtained by Equation (6), and Q is calculated from the following equation:

$$Q = e^{((51-44)/9)} = 2.18. \quad (7)$$

Q' approximates the value of Q as 2.18.

Figure 5 shows how to calculate the parameters of A , B , and C [23]. A is determined from the ratio of the intact rock strength (unconfined compressive strength) to the induced stress at the center-line of the slope surface. The intact rock strength is 205.70 MPa, and the induced stress at the center-line of the slope surface is less than 20.5 MPa. Thus, the value of A is 1.

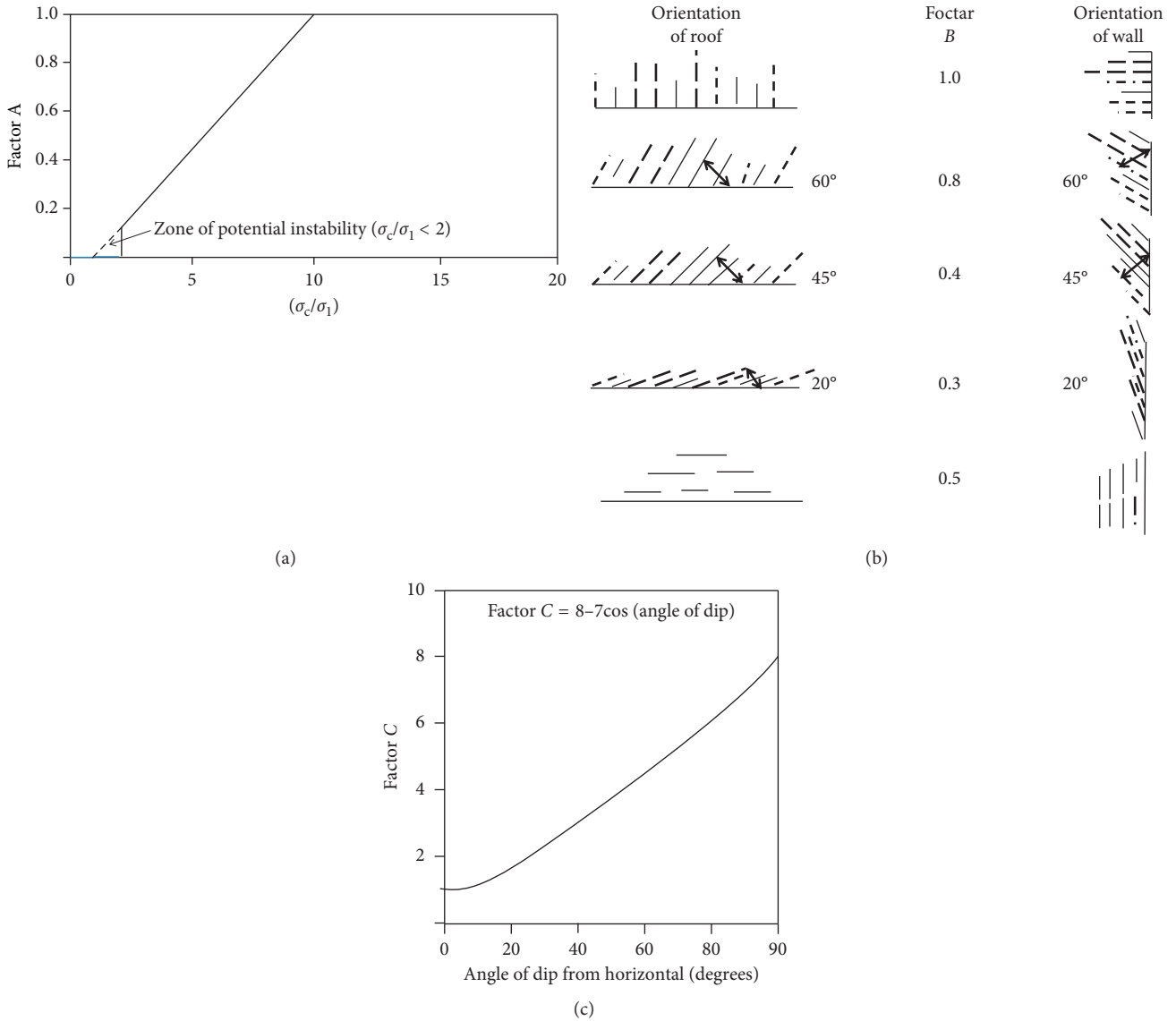


FIGURE 5: Adjustment factors for determining the Mathews stability number: (a) A (stress factor) (b) B (joint orientation factor), and (c) C (surface orientation factor). σ_c is the uniaxial compressive strength of intact rock and σ_1 is the induced compressive stress.

According to the actual project, the value of B is 0.9.
C is the surface orientation factor:

$$C = 8 - 7 \cos \alpha, \tag{8}$$

where α is the angle of dip.

For the ore body in the Tiaoshuihe phosphate mine, α is 15°. Thus, the value of C is 1.24.

Substituting these results into Equation (4) and taking the value of Q' as 2.18 determine the stability number (N) of the surrounding rock of the upper panel. N is calculated by the following equation:

$$N = 2.18 \times 1 \times 0.9 \times 1.24 = 2.43. \tag{9}$$

4.2.2. Calculation of Shape Parameter S. The shape factor S (or hydraulic radius R) reflects the shape and size of the stope. It can be calculated by the following equation:

$$S = \frac{XY}{2(X + Y)}, \tag{10}$$

where X and Y are the width and length of the stope, respectively.

Since the length of the ore chamber is set as 50 m, the widths of the ore chamber are 7, 8, and 9 m, and the obtained shape coefficients S are 3.07, 3.45, and 3.81, respectively.

4.3. Analysis of Calculation Results. According to the previous Mathews stability probability model of Equations (2) and (3), the lines of any probabilistic model can be represented in the Mathews stability diagram. Set any probability value $f(z)$, the corresponding z can be got. Then, Equation (3) will be a linear function between N and S . In Figure 6, different lines can represent different stable probabilities. The model is straight line, which is different from the

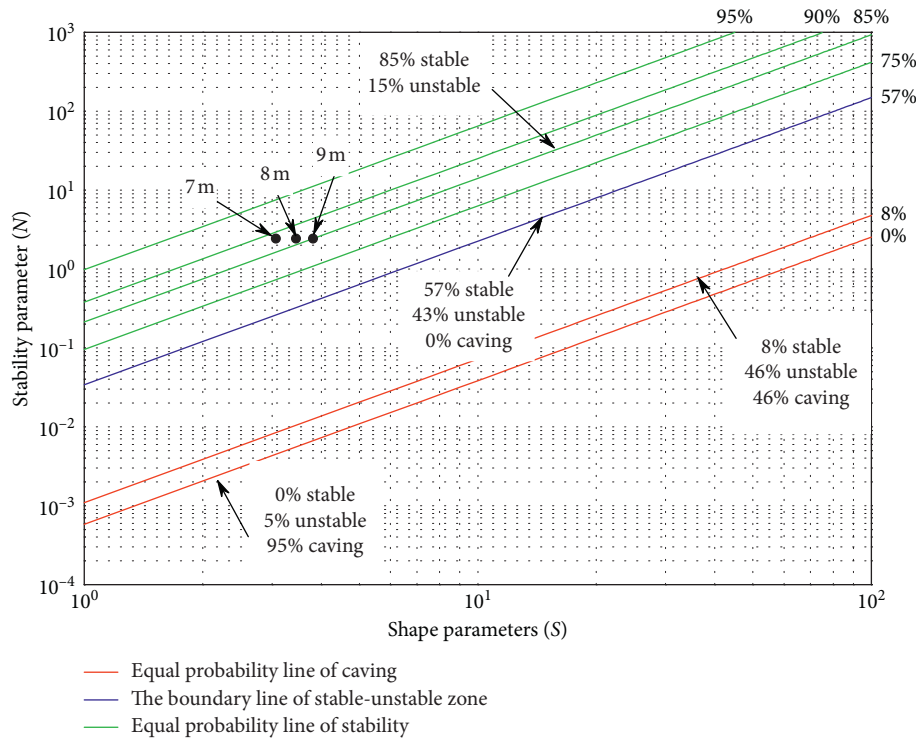


FIGURE 6: Improved Mathews stability probability graph.

traditional curve graph. The three points on the graph correspond to the stable probabilities when the widths of the strip are 7, 8, and 9 m.

Comparison of the coordinate points corresponding to the strip widths of 7, 8, and 9 m in Figure 6 shows that when the strip width is 9 m, the probability of stope stability is lower than 85%. Moreover, when the strip width is 7 or 8 m, the stability probability of the stope is above 85%, and the stability of the strip width of 7 m is better than that of 8 m; thus, the stability of the strip width of 9 m is the worst.

The stability probabilities can be quantified according to Equations (2) and (3), using a strip width of 7 m as an example:

$$Z = 2.9603 - 1.4427 \ln 3.07 + 0.7928 \ln 2.43 = 2.046, \quad (11)$$

$$p = \frac{1}{1 + e^{-2.046}} = 88.55\%. \quad (12)$$

It is calculated in Equations (11) and (12) that when the strip width is 7 m, the probabilities of stope stability and failure are 88.55% and 11.45%, respectively. Similarly, when the strip width is 8 m, the probabilities of stope stability and failure are 86.76% and 13.24%, respectively. When the strip width is 9 m, the probabilities of stope stability and failure are 84.94% and 15.06%, respectively.

The Mathews stability probability model is used to study the structural parameters of the mining field of the Tiaoshuihe phosphate mine. Moreover, the stability probability of the strip width of 9 m is lower than 85%, and the possibility of stope failure is more than 15%. Based on

previous engineering experience, the unstable probability more than 15% is dangerous. Therefore, the strip width of 9 m is not suitable. Considering that the maximum width of a single drilling application is 7.6 m for the DD211L low-type drilling rig in the underground, it is suggested that the best strip width is 7 m. It is being applied well in Tiaoshuihe phosphate mine now, and the engineering practice proves that this parameter is suitable.

5. Conclusions

- (1) An accurate finite element model was established for the Tiaoshuihe phosphate mine, and the rock mechanics parameters were based on engineering specifications. It is concluded that when the width of the strip is 6 m, the overall strength of the backfill is the worst after the third step, and plastic penetration failure occurs easily. Strip widths of 7, 8, and 9 m may be applicable.
- (2) The study of the Mathews stability probability model, generation of the logarithmic coordinate graph, and calculation of the quantitative probability indicate that the stability of the goaf decreases gradually when the strip width ranged from 7, 8, to 9 m. When the width of the strip is 9 m, the probability of goaf instability is greater than 15%, which is dangerous.
- (3) Comprehensively considering that the maximum width of a single drilling application is 7.6 m for the DD211L low-type drilling rig in the Tiaoshuihe phosphate mine, and that the stability of the 7 m strip

width is higher than that of the 8 m according to the results calculated previously, a strip width of 7 m is recommended.

Data Availability

The data used to support the findings of this study are available from the corresponding author upon request.

Conflicts of Interest

The authors declare that they have no conflicts of interest.

Acknowledgments

The support from National Natural Science Foundation of China (Grant no. 41672298) is sincerely appreciated.

References

- [1] N. Meng, Y.-Q. Zhang, L. Yan et al., "Environmental effects of mining subsidence and its ecological restoration techniques," *Energy Technology and Management*, vol. 46, no. 2, pp. 119–121, 2011.
- [2] H.-G. Ren, Z.-Y. Tan, C. Xue-feng et al., "AHP-fuzzy optimization of structural parameters in sublevel open stope succedent filling method," *Journal of University of Science and Technology Beijing*, vol. 33, no. 4, pp. 400–405, 2011.
- [3] Y. Gao-hui, A.-X. Wu, Y.-M. Wang et al., "Stability analysis of stope retention pillars in broken rock conditions," *Journal of University of Science and Technology Beijing*, vol. 33, no. 4, pp. 400–405, 2011.
- [4] Y.-L. Ning and J.-H. Hu, "Maximum exposed area of stope with gently inclined thin orebody and parameters optimization," *Mining and Metallurgical Engineering*, vol. 34, no. 1, pp. 14–17, 2014.
- [5] X. X. Li and K. G. Li, "Optimization of stope structural parameters in phosphorite mine and its stability analysis," *Applied Mechanics and Materials*, vol. 580–583, pp. 1268–1272, 2014.
- [6] Q. F. Guo, F. H. Ren, S. J. Miao, and X. Chen, "Application of fuzzy comprehensive evaluation in stope structural parameters optimization," *Applied Mechanics and Materials*, vol. 256–259, pp. 271–275, 2013.
- [7] S. Chen, Z. Tan, X. Cai, and H. Ren, "Optimization of structural parameters of underground mining caverns with FLAC3D," in *Proceedings of 2nd ISRM International Young Scholars' Symposium on Rock Mechanics*, Beijing, China, September 2011.
- [8] X. Li, Q. Gao, S. H. Zhai, and S. Nan, "Optimization of structural parameters for mining large iron ore stope by filling method," in *Proceedings of 2nd ISRM International Young Scholars' Symposium on Rock Mechanics*, Beijing, China, October 2011.
- [9] Y. Hai-wang, J. Chang, and L. Zhou, "Parameters optimization of stope structure based on FLAC3D," *Metal Mine*, no. 12, pp. 6–8, 2010.
- [10] J. Wang, J. Liu, L. Qiao, and X. Ouyang, "Dynamic response to seismic waves at the shallow slope supported by bolts," *Geotechnical and Geological Engineering*, vol. 36, no. 4, pp. 1991–2001, 2018.
- [11] C. Ma, P. Wang, and L. Jiang, "Deformation and control countermeasure of surrounding rocks for water-dripping roadway below a contiguous," *Processes*, vol. 6, no. 7, pp. 77 pages, 2018.
- [12] L.-L. Guo, Y.-B. Zhang, Y.-J. Zhang, Z.-W. Yu, and J.-N. Zhang, "Experimental investigation of granite properties under different temperatures and pressures and numerical analysis of damage effect in enhanced geothermal system," *Renewable Energy*, vol. 126, pp. 107–125, 2018.
- [13] P. Zorany Agudelo, S. Jose Antonio, C. D. H. C. Tsuha, D. Dias, and L. Thorel, "Numerical and experimental study on influence of installation effects on behaviour of helical anchors in very dense sand," *Canadian Geotechnical Journal*, vol. 55, no. 8, pp. 1067–1080, 2018.
- [14] A. M. A. N. Karunarathne, M. Fardipour, E. F. Gad et al., "Modelling of climate induced moisture variations and subsequent ground movements in expansive soils," *Geotechnical and Geological Engineering*, vol. 36, no. 4, pp. 2455–2477, 2018.
- [15] J.-F. Zou and Q. Ze-hang, "Face-stability analysis of tunnels excavated below groundwater considering coupled flow deformation," *International Journal of Geomechanics*, vol. 18, no. 8, article 04018089, 2018.
- [16] Y. Sun, L.-M. Luo, and H.-W. Deng, "Stability analysis and parameter optimization of stope in deep metal mines," *Gold Science and Technology*, vol. 25, no. 1, pp. 99–105, 2017.
- [17] X. Luo, W. Jun, and F. Gao, "Optimization of stope width for steeply inclined thick ore-body in deep mine," *Metal Mine*, no. 6, pp. 7–10, 2018.
- [18] L. Zhi-yi, L.-C. Zhang, G.-Y. Zhao et al., "Structural parameters optimization and engineering application of the second-step stope based on FLAC3D," *Metal Mine*, no. 10, pp. 6–10, 2015.
- [19] X. Hong-liang, L. Zhao-sheng, S. Lu et al., "Optimizing the stope structural parameters using Mathews empirical analysis method and numerical analysis method," *Metal Mine*, no. 12, pp. 19–23, 2015.
- [20] F. Xing-long, L.-G. Wang, B. Lin et al., "Collapsibility of orebody based on Mathews stability graph approach," *Chinese Journal of Geotechnical Engineering*, no. 4, pp. 600–604, 2008.
- [21] E. T. Brown, *Block Caving Geomechanics*, Julius Kruttschnitt Mineral Centre, Indooroopilly, QLD, Australia, 2003.
- [22] R. Trueman, P. Mikula, C. Mawdesley, and N. Harries, "Experience in Australia with the application of the Mathews method for open stope design," *CIM Bulletin*, vol. 93, no. 2, pp. 162–167, 2000.
- [23] C. Mawdesley, R. Trueman, and W. J. Whiten, "Extending the Mathews stability graph for open-stope design," *Transactions of the Institution of Mining and Metallurgy*, vol. 10, no. 1, pp. 27–39, 2001.
- [24] C. Mawdesley, "Using logistic regression to investigate and improve an empirical design method," *International Journal of Rock Mechanics and Mining Sciences*, vol. 41, no. 1, pp. 756–761, 2004.
- [25] T.-B. Yin and M.-L. Zhang, "Determination on the exposure area in stope based on Mathews stability graphic method," *Modern Mining*, vol. 31, no. 6, pp. 8–10, 2015.
- [26] Y. Zhao, Y. Tian-hong, X.-R. Wang et al., "Stability evaluation of stope based on Mathews graph method," *Journal of Northeastern University*, vol. 37, no. 1, pp. 74–78, 2016.
- [27] F. Tawiah Suorineni, "Empirical methods in mining geomechanics—reflections on current state-of-the-art," in *Proceedings of 1st International Conference on Applied Empirical Design*, June 2014.
- [28] E. Akbar, M. Reza, S. Erfan et al., "Prediction of rock mass rating using TSP method and statistical analysis in Semnan Rooziyeh spring conveyance tunnel," *Tunnelling and Underground Space Technology*, vol. 5, no. 79, pp. 224–230, 2018.

Research Article

Fractal Pattern of Particle Crushing of Granular Geomaterials during One-Dimensional Compression

Jiru Zhang  and Biwen Zhang 

School of Civil Engineering and Architecture, Wuhan University of Technology, Wuhan 430070, China

Correspondence should be addressed to Jiru Zhang; zhangjr1964@sohu.com

Received 25 May 2018; Accepted 29 July 2018; Published 25 September 2018

Academic Editor: Yongfeng Deng

Copyright © 2018 Jiru Zhang and Biwen Zhang. This is an open access article distributed under the Creative Commons Attribution License, which permits unrestricted use, distribution, and reproduction in any medium, provided the original work is properly cited.

This paper focuses on the effect of particle crushing on the behavior of granular geomaterials. Series of high-pressure one-dimensional compression tests were carried out on a quartz sand-gravel. A detail investigation was performed primarily on the compression behavior, the evolution of particle-size distribution (PSD), the fractal pattern of the grading curve, and the amount of particle crushing. It was found that both the yielding state and the state at the maximum compressibility are closely associated with the evolution of PSD and the fractal pattern of particle crushing. As the vertical stress increases, the fractal characteristic of the grading curve appears only within the finer part at first, evolves into bifractal within the overall measurable grading curve late, and translates into monofractal finally. Furthermore, a pair of particle crushing indexes B_{e1} and B_{e2} considering different particle size scales were proposed. The reasonability of using B_{e1} and B_{e2} to describe the amount of crushing corresponding to the scale of particles was discussed. Finally, it was found that the value of the ratio between the volumetric strain and the crushing index B_{e1} is constant and independent of the initial particle size and the initial PSD when the vertical stress is larger than the stress at the maximum compressibility or the coarser part of the grading curve is evolved into fractal.

1. Introduction

Particle crushing (a confluent terminology describing all types of fragmentation and breakage), which is triggered when the applied stresses of particles exceed their strength, essentially generates a new complicated system with smaller sized and various shaped particles and consequently influences mechanical properties and behaviors of soils. This theme appears to play a vitally significant role associated with several natural disasters, such as landslides, earthquakes, debris flows, and surface collapses, and engineering applications; for instance, how to drive long offshore piles into bioclastic, calcareous soils or how to choose an applicable PSD of materials in constructing large earth and rockfill dams [1–9]. Hence, whatever the behaviors of single particle compression [10, 11], one-dimensional compression [12–14], ring shear tests [15–18], plane strain tests [19], or triaxial tests [6, 20–22], it attracts extensive and special attention in geotechnical engineering owing to the complex

mechanism involved. Totally, it is important and necessary to improve our understanding of the internal mechanism between particle crushing and soil behavior from the perspective of scientific research and the practical view of engineering problems.

By means of either laboratory tests or discrete element modeling [13, 15, 23–34], several studies focused on the significant role of PSD in the basic constitutive properties of granular materials, especially in the critical states. Particle crushing which produces a new PSD depends not only on the nature of the crushable particle, but also to a relatively great extent on the surroundings involving the sizes and shapes of adjacent particles and the force chains exerted to the focused objective. Although the particle-crushing-induced complicated system during compression or shearing depends on manifold factors, such as mineralogies, morphology, stress-strain state, void ratio, water content, and test methodologies, but it is consistent with fractal theory in many cases. Some previous studies confirmed in

broad agreement that both the crushing of a single particle and the continuous crushing of granular aggregates result in an increasing tendency towards a monofractal PSD with a single fractal dimension D [10, 35–39]. Also, the bifractal behavior of geomaterials during crushing was observed [18]. Consequently, a question which arises is what role particle crushing plays in influencing the fractal behavior, especially in the development of fractal. This has not been detailed in studies yet. No researchers so far have examined the relationship between the crushing of particles and the varying fractal characteristics of grading curves, especially at different scales. A detailed investigation of particle-crushing-induced fractal development of grading curves will return us with a higher cognition of the sensibility of crushing of soils and of the nature of behavior of granular materials.

According to the data of one-dimensional compression tests on quartz sand-gravel up to 204.8 MPa [39], the present paper examined the effects of particle size and initial PSD on the compression and crushing behaviors of granular geomaterials. In addition, the fractal dimensions of varying grading curves taking different scales into account were calculated to explore the fractal mechanism of particle crushing. Due to the fact that particle crushing generally exists in overall mechanical behaviors of crushable soils, even though the findings are obtained from one-dimensional compression tests, it still improves our understanding of the nature of particle crushing implicated in the fractal theory and may open the door to the intelligent interpretation of soil behaviors considering the effect of crushing.

2. Materials and Test Methods

Tests in this paper were performed on a type of crushable granular geomaterial which is a mixture of sand and gravel from the Yangtze River in China. The percent content of main component is 89.72% of SiO_2 by means of X-ray diffraction experiments. Hence, it is named as quartz sand-gravel (QS). Before tests, the materials were dry-sieved into fractions to make various specimens involving uniformly graded specimens (marked as QS1 and QS2) and natural graded specimens (marked as QS3). The initial grading curves of all types of specimens are shown in Figure 1. As shown in Figure 2, a self-made confined compression device [37] with a 79.8 mm diameter and 20 mm height cylindrical specimen was used to reach very high vertical stress up to the maximum 204.8 MPa. All types of specimens were prepared by tamping using various energy levels to achieve a similar value of the initial void ratio $e_0 = 0.78 \pm 0.03$. The use of organo-silicic oil coating applied to the bottom of the piston minimized the effect of boundary friction. The dial indicators fixed to the piston were applied to measure compressive deformation of the specimens, where each value was the average of two measurements. In order to insight the evolution of PSD during crushing, these one-dimensional compression tests were terminated at nine vertical stress levels from 0.8 MPa to 204.8 MPa with one as the constant loading increment ratio. The details of the initial PSDs of all

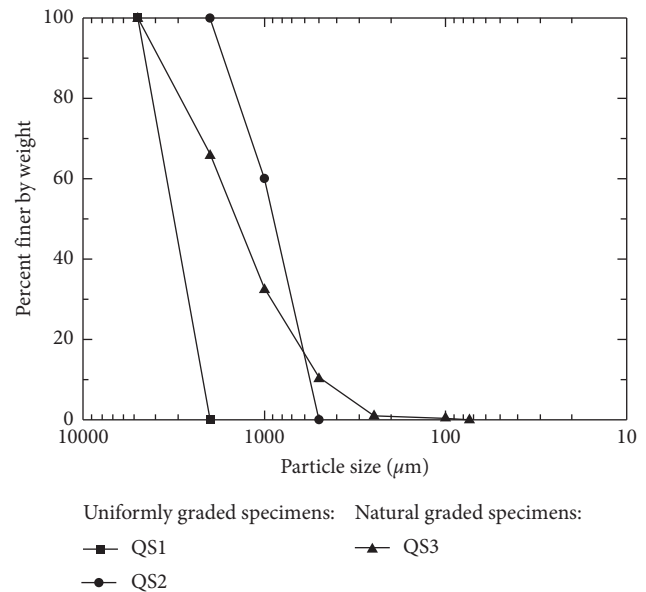


FIGURE 1: Initial grading curves.

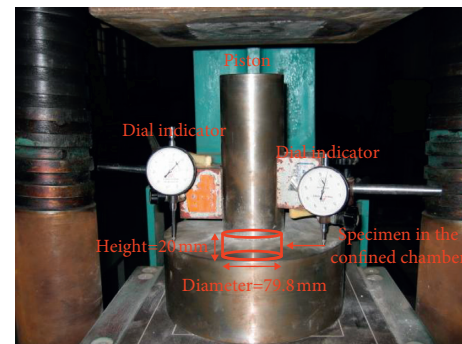


FIGURE 2: Test device.

types of specimens and parameters of tests are summarized in Table 1.

After one-dimensional compression tests, the grading curves of all precrushed specimens were determined by means of the sieve shaker and the laser particle analyzer. On one hand, the sieve shaker was used to obtain the first part of PSD, in which particles are ranged from $74 \mu\text{m}$ to the largest particle size, from the part of specimens retaining on the $74 \mu\text{m}$ sieve pore. On the other hand, the laser particle analyzer was used to obtain the second part of PSD, in which particles are ranged from the minimum measurable size $1 \mu\text{m}$ to $74 \mu\text{m}$, from the balance passing through the $74 \mu\text{m}$ sieve pore. The data obtained by these two methods were summed up, and the whole measurable grading curves of the specimens after tests were calculated. Because the method of the laser particle analyzer to obtain the corresponding PSD is based on the equivalent diameter analysis, the accuracy will not be enough if the shapes of the considered particles are flake-like or needle-like. Fortunately, according to the shape factor data of precrushed geomaterials, such as quartz sand and carbonate sand [40] and the scanning electron microscope (SEM) images of the generated particles after crushing

TABLE 1: Details of initial PSDs of the specimens and parameters of the tests.

Geomaterials	Specimen number	Initial PSD (%)					Specimen dimension $D \times H$ (mm \times mm)	Initial void ratio e_0	Specific weight G_s	Vertical stress level σ_v (MPa)
		5000~2000 (μm)	2000~1000 (μm)	1000~500 (μm)	500~250 (μm)	250~100 (μm)				
Quartz sand and gravel (QS)	QS1	100	0	0	0	0	0	0.78 \pm 0.03	2.67	0, 0.8, 1.6, 3.2, 6.4, 12.8, 25.6, 51.2, 102.4, 204.8
	QS2	0	60	40	0	0	0			
	QS3	34.2	33.3	22.3	9.4	0.3	0.5			

[41], the ratios between the 3D of the created particles by crushing are not much different. Hence, it is reasonable to guarantee the validity of using the laser particle analyzer to describe that part of PSD. It is also shown that the ratios between the 3D of most particles generated from crushing, whose sizes are smaller than $74\ \mu\text{m}$, are similar.

3. Results and Discussion

3.1. One-Dimensional Compression Behavior. The data points in Figure 3 show the decreasing tendency of the void ratio e with increasing logarithm of vertical stress σ_v for all types of specimens. The continuous reduction of the value of the void ratio e is mainly due to successive particle crushing and rearrangement. With almost the identical initial void ratio e_0 , the reduction of the value of the void ratio e is largest for QS1, intermediate for QS2, and lowest for QS3 at the same vertical stress levels. The reasonable interpretation of the above observation is as following [14, 36]. The crushing strength of the larger particle is lower because there are more interior flaws in it. Hence, QS1 with larger particle sizes produces more crushing and rearrangement for uniformly graded specimens. Meanwhile, the natural graded specimen QS3 is well graded comparing to the uniformly graded specimens. The particles in QS3 are protected by more surrounding contact points. Hence, the probability of the particle crushing of QS3 is lower and less void ratio produced by crushing is used for particle rearrangement.

On the other hand, as shown in Figure 3, we are obliged to select the smooth B-spline to describe e versus $\log \sigma_v$ relationship with unimportant error within the maximum testing load because the decreasing tendency above is actually a continuous process. According to [14], two states on the one-dimensional compression are defined. One is the yielding state which corresponds to the state when the curvature of the relation between the void ratio e and the logarithmic of the vertical stress σ_v is maximum. Another is the state at the maximum compressibility, which corresponds to the state when the compression index C_c is maximum. Hence, in Figure 3, the yielding states are marked as the hollow legends and the states at the maximum compressibility are marked as the semihollow legends for all types of the specimens. The stress σ_{v_y} corresponds to the stress at the yielding state, and the stress σ_{v_c} corresponds to the stress at the state when the compression index C_c is maximum. With respect to these two indexes σ_{v_y} and σ_{v_c} , three situations can be observed from Figure 3: (i) for uniformly graded specimens, the specimen QS1 with larger particle size has higher σ_{v_y} and σ_{v_c} ; (ii) both σ_{v_y} and σ_{v_c} of uniformly graded specimens QS1 and QS2 are lower than those of the natural graded specimen QS3; and (iii) for a given specimen, σ_{v_c} is higher than σ_{v_y} . The first situation manifests that specimens with smaller particle size are more difficult to yield and are more difficult to show the maximum compressibility for uniformly graded specimens. Analogously, the second situation indicates that uniformly graded specimens are easier to yield and are easier to show the maximum compressibility comparing with well-graded specimens. Hence, the yield state and the state at the maximum

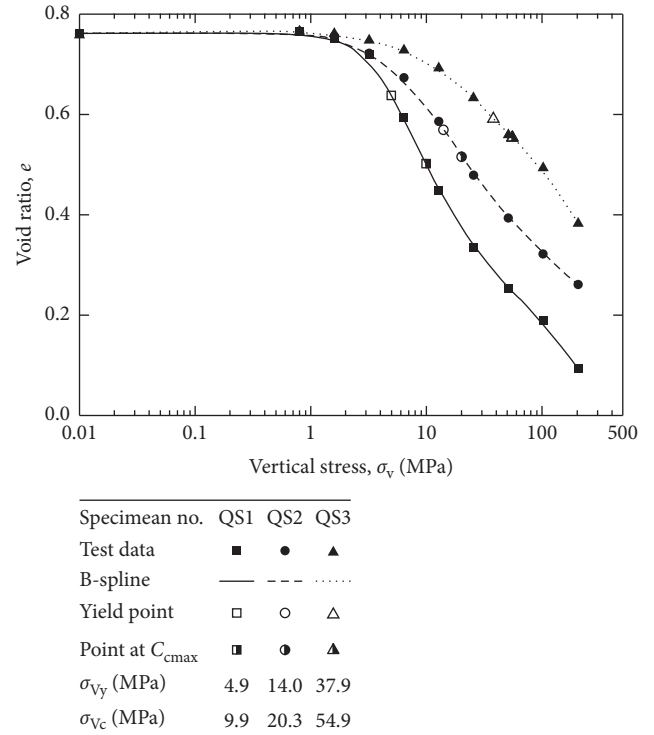


FIGURE 3: Relationship between e and σ_v .

compressibility depend not only on the nature of particles but also on the packing of multitudinous particles. The last situation expresses that the state at the maximum compressibility is always after the yielding state. It also implied that the gradient in the e - $\log \sigma_v$ relationship increases after yielding and then gradually decreases to a relative steady value after showing the maximum compressibility, combining with the shapes of the B-splines in Figure 3.

Figure 4 shows the relationship between the vertical strain or the volumetric strain ε_v (in the one-dimensional compression tests of this paper, the vertical strain is identical with the volumetric strain because of the constant cross section of the specimen) and the vertical stress σ_v . It can be observed that the value of ε_v increases rapidly at relative small stress levels, then increases less rapidly after the vertical stress σ_v passes beyond σ_{v_c} and gradually approaches stabilization at relative high stress levels for all types of specimens. The implications of the yielding state and the state at the maximum compressibility are further investigated in the following part.

3.2. Evolution of PSD. The grading curves of all the specimens after one-dimensional compression tests terminated at each preset vertical stress level are plotted in Figure 5, with semilogarithmic coordinates on the left pictures and double-logarithmic coordinates on the right pictures. Meanwhile, it is assumed that the grading curve at the preset stress level which is closest to σ_{v_y} or σ_{v_c} can be approximately regarded as the grading curve at the stress equal to σ_{v_y} or σ_{v_c} , respectively, with unimportant error. The dashed dotted line is the referenced ultimate fractal grading curve with a fractal

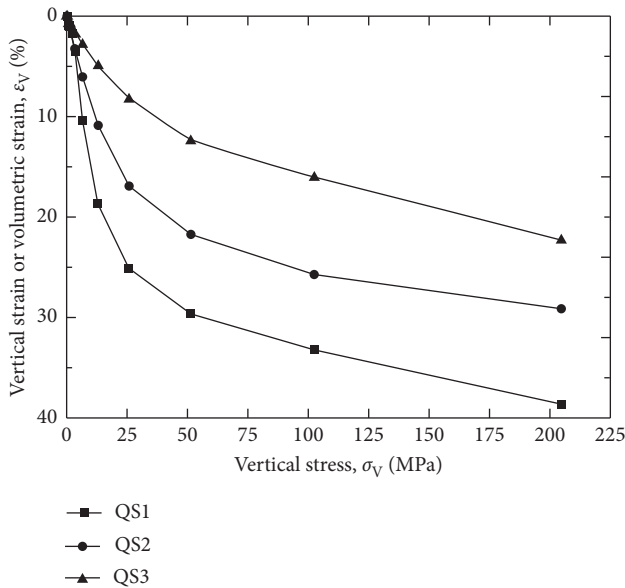


FIGURE 4: Relationship between ε_V and σ_V .

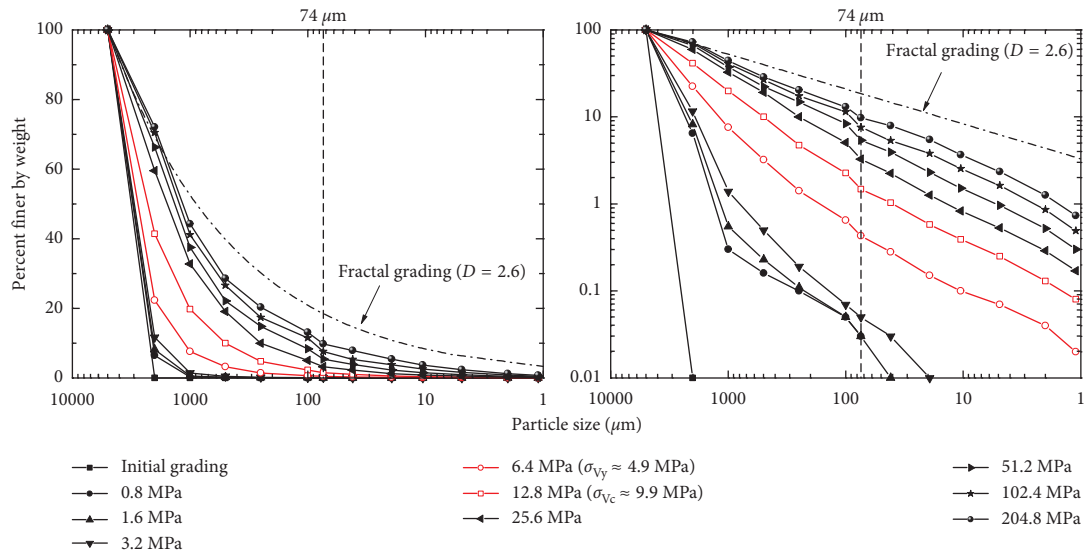
dimension $D=2.6$ [23]. Examination of Figure 5 shows a similarity for all types of specimens that the proportion of particles finer than $74 \mu\text{m}$ increases markedly as the vertical stress σ_V increases; however, part of the largest particles of initial specimens still exist even at the maximum vertical stress level. In the semilogarithmic coordinates of Figure 5, the curve gradually rises up and the degree of concave upward of the curve gradually decreases, in particular, after the vertical stress σ_V exceeds σ_{Vy} . It indicates that the degree of crushing increases markedly after yielding. Meanwhile, in the double-logarithmic coordinates of Figure 5, the curve is gradually transformed into approximately a straight line, especially after the vertical stress σ_V exceeds a definite extent to σ_{Vc} . It indicates that the grading curve is gradually equipped with fractal characteristic, especially after the specimen shows the maximum compressibility. Therefore, it may be reasonable to regard σ_{Vc} as a transition point of the grading curve to be equipped with the fractal characteristic. In a similar fashion, it should be noted that when the vertical stress σ_V passes σ_{Vy} , the shape of the grading curve within the particle size interval finer than $74 \mu\text{m}$ becomes a straight line, which indicates that the finer part of the grading curve may be previously equipped with fractal characteristic. Hence, we can deduce that σ_{Vy} can at least be regarded as another transition point to be equipped with fractal characteristic within the finer part of the grading curve. Also, the reasonability of the above deductions is verified in the next part.

3.3. Fractal Pattern. A simplex fractal dimension is usually used to describe the PSD of soil, and this fractal parameter can be used as a constant in models of soil-water characteristic curves (SWCCs) or particle crushing [33, 42–47]. However, according to the data in this paper and other relevant literatures [18, 48], a simplex fractal dimension

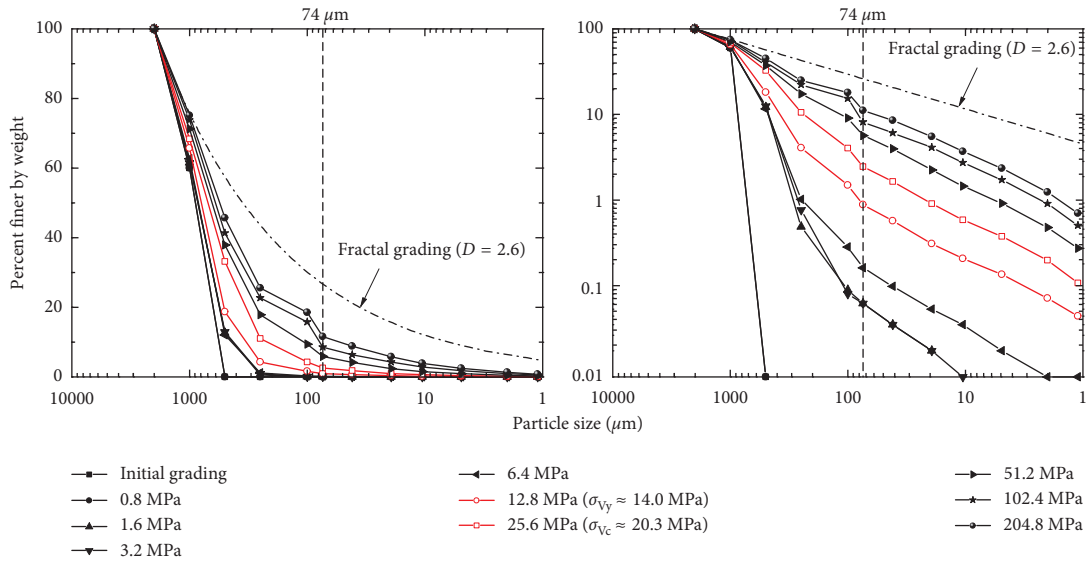
sometimes does not adequately describe the fractal characteristics of the whole PSD. The evolution pattern of fractals requires further study.

By assuming the referenced particle size as d , the largest particle size as d_M , the mass of particles finer than d as $M(\delta < d)$, and the total mass of a specimen as M_T , if there is a linear relationship between $\log(d/d_M)$ and $\log[M(\delta < d)/M_T]$ with a slope k , we can deem that the grading curve is fractal with the fractal dimension $D=3-k$. The results of linear fitting between $\lg[M(\delta < d)/M_T]$ and $\lg(d/d_M)$ are shown in Figure 6. The left pictures of Figure 6 regard particle size intervals which are finer than $74 \mu\text{m}$ and coarser than $74 \mu\text{m}$ as fitting intervals, respectively. And the middle pictures of Figure 6 regard the whole measurable particle size interval as the only fitting interval. Actually, not all the grading curves after tests are equipped with fractal characteristics. Hence, we are obliged to assume a value of determination coefficients R^2 of linear fitting as a transformation point to make a decision that whether or not the fractal of the grading curve is relative strict. By examination of the right pictures of Figure 6, which show the histograms of determination coefficients R^2 of these three aforementioned linear fittings at each stress level, the value of R^2 equal to 0.98 may be a plausible and relative high value to represent this transformation point. Therefore, in the left and middle pictures in Figure 6, fitting lines having relative high significance level with $R^2 > 0.98$ are presented by the solid lines, and those having relative low significance level with $R^2 < 0.98$ are presented by the dashed lines. In addition, the values of the fractal dimensions of the fitting lines are labeled beside with D_1 for those when d is coarser than $74 \mu\text{m}$, D_2 for those when d is finer than $74 \mu\text{m}$, and D for those of the whole measurable size interval.

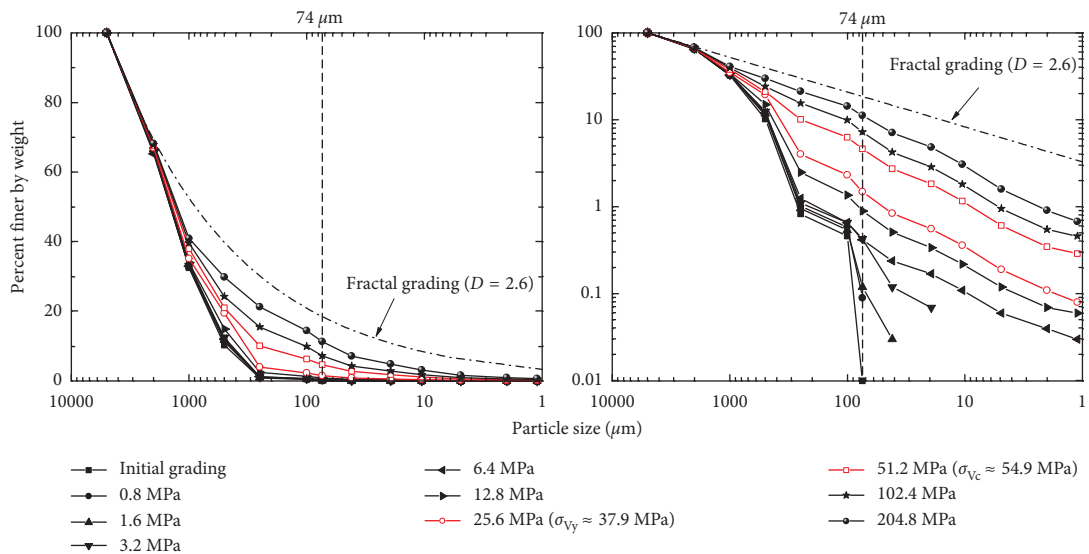
The detailed examination of the left and right pictures of Figure 6 shows that the fractal characteristic of the finer particle size interval is not relatively strict when the vertical stress σ_V is lower than σ_{Vy} for all types of specimens. However, the fractal characteristic of the above part is relatively strict when the vertical stress σ_V is greater than σ_{Vy} . Nevertheless, the similar result of the coarser particle size interval appears when the vertical stress σ_V is greater than σ_{Vc} . The narration above at least implies that the fractal characteristic previously appears on the finer particle size interval after yielding and subsequently appears on the coarser interval after the specimen shows the maximum compressibility. By means of the middle and right pictures of Figure 6, the whole measurable grading curves of all types of specimens are equipped with monofractal characteristic only when the vertical stress σ_V exceeds a certain degree to σ_{Vc} . Hence, three particle size regions should be differentiated. In the first region ranged between $1 \mu\text{m}$ and an uncertain size which may be finer than $74 \mu\text{m}$, the grading curve is fractal when the vertical stress σ_V passes through σ_{Vy} . In the second region ranged between the largest particle size and another uncertain size which may be coarser than $74 \mu\text{m}$, the grading curve is fractal when the vertical stress σ_V passes through σ_{Vc} . And the third region ranged between these two uncertain sizes represents a transition region from the fractal characteristic in the coarser region to that in the finer region.



(a)



(b)



(c)

FIGURE 5: Grading curves after tests terminated at each preset stress level for (a) QS1, (b) QS2, and (c) QS3.

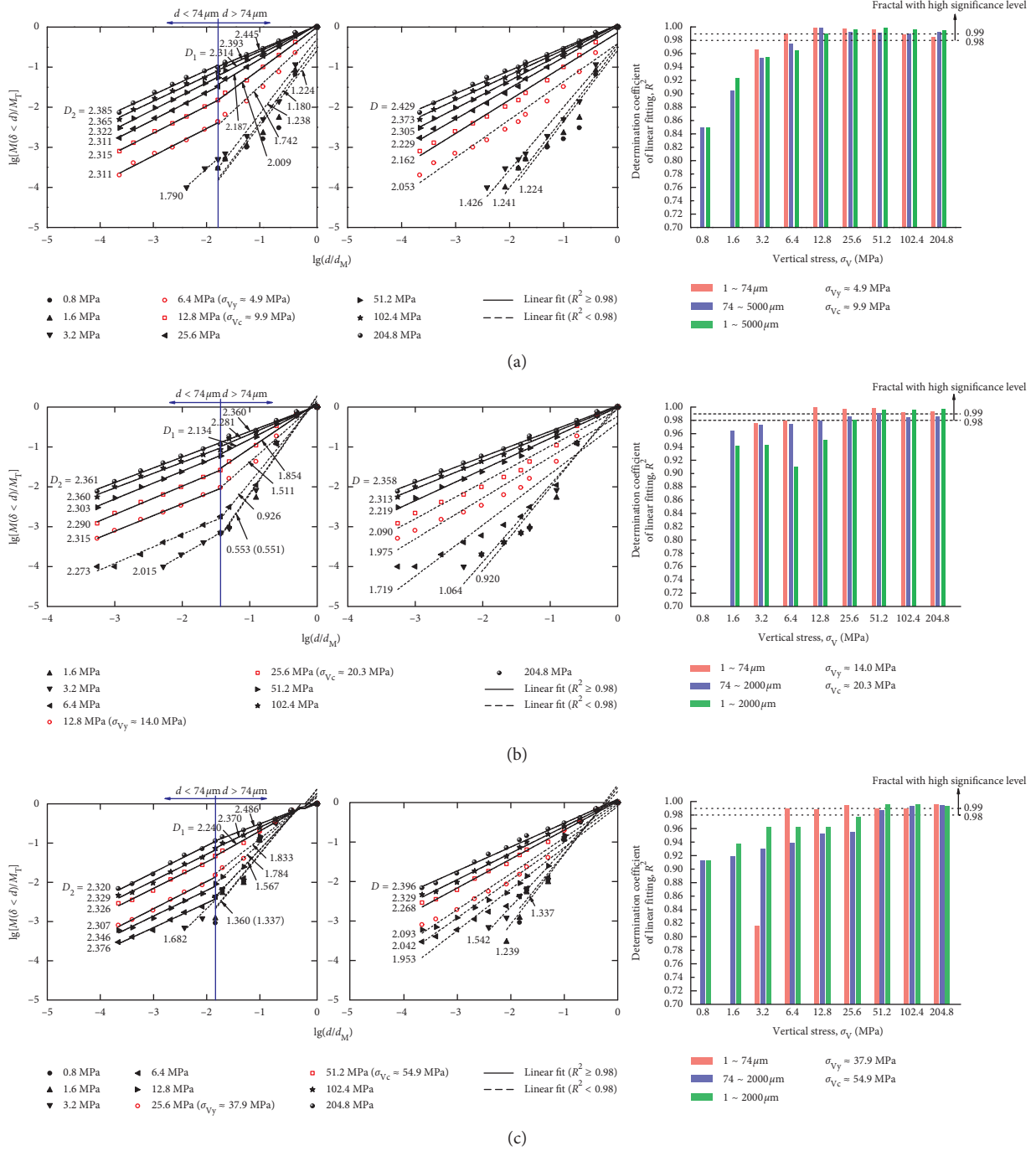


FIGURE 6: Linear fitting between $\lg[M(\delta < d)/M_T]$ and $\lg(d/d_M)$ with the left picture regarding particle size finer than $74 \mu\text{m}$ and coarser than $74 \mu\text{m}$ as a fitting range, respectively, with the middle picture regarding the whole measurable particle size interval as the only fitting range, and with the right picture expressing the histograms of determination coefficients R^2 of these three linear fittings at each preset vertical stress level for (a) QS1, (b) QS2, and (c) QS3.

The existence of this transition region makes the problem extremely complicated. In order to simplify the analysis, the existence of this transition region is disregarded, and the transition particle size between the two fractal regions is assumed to be $74 \mu\text{m}$. In addition, as shown in Figures 7(a) and 7(b), despite the different initial PSDs and particle sizes between all types of specimens, the PSD data of the finer

region in which the values of fractal dimensions exceed 2.29 are shown to be strictly self-similar, and those of the coarser region in which the values of fractal dimensions exceed 1.85 are shown to be strictly self-similar. Therefore, the values of 2.29 and 1.85 can be considered as the lower limits of the fractal dimensions corresponding to the finer and coarser regions, respectively. In a similar fashion, the value of 1.96

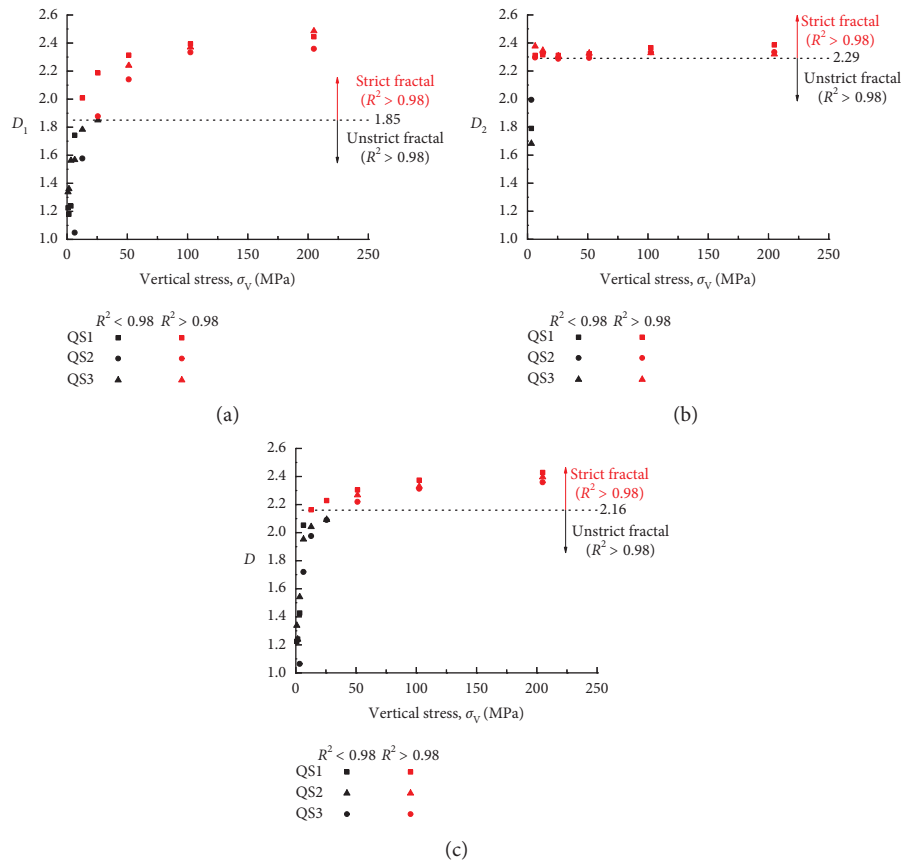


FIGURE 7: Relationship between vertical stress σ_v and fractal dimensions (a) D_1 , (b) D_2 , and (c) D .

can be considered as the lower limit of the fractal dimension for the whole measurable PSD, as shown in Figure 7(c).

In general, during one-dimensional compression, when the vertical stress σ_v is between σ_{vY} and σ_{vC} , the fractal characteristic exists only in the finer interval of the grading curve, in which particle sizes are finer than $74\mu\text{m}$. Subsequently, the bifractal characteristic exists in the whole measurable grading curve when the vertical stress σ_v is immediately larger than σ_{vC} . And $74\mu\text{m}$ should be the transition particle size point between the different fractal characteristics of the finer and coarser intervals. Finally, the whole measurable grading curve is monofractal when the vertical stress exceeds a certain degree to σ_{vC} . The evolution of the fractal characteristic above consists of the fractal pattern during one-dimensional compression.

3.4. Particle Crushing. Based on the different PSDs before and after crushing, some scholars put forward series of quantitative indexes to represent the degree of particle crushing. As a whole, those indexes may be divided into two principal groups: one is based on the change of one or several characteristic particle sizes before and after crushing, such as B_{10} , B_{15} , and B_M as depicted in Figure 8 [1, 3, 49]. The other one is based on the relative change of the whole PSD before and after crushing, which are primarily represented by B_r and B_e proposed by Hardin [50] and Einav [51], respectively,

as depicted in Figure 9. The difference between B_r and B_e lies in the assumption of the ultimate state of particle crushing. Hardin [50] assumed that particle crushing eventually formed a uniform distribution system with particle sizes less than $74\mu\text{m}$. However, Einav [51] assumed that the ultimate distribution was a monofractal distribution with scale invariance or self-similarity. It should be noted that most properties of soil may depend on the overall PSDs, such as void ratio, volumetric strain, constitutive relation, and critical state. Actually, particle crushing is not an active process like gravity, which is always fully active and forever produces its total effect, but can be denoted by a passive quantity which can be measured by the relative distance to its ultimate state indicating the elimination of possibility for any further crushing. From this point of view, particle crushing, which resembles internal friction and cohesion of soils, has to be mobilized by external conditions until the potential of crushing approaches zero. Therefore, comparing with the indexes of the first group which depend on just one or several characteristic particle sizes, B_r and B_e chosen in this study may be more appropriate for representing the amount of crushing not only owing to their clear concepts and clearly defined assumptions but also due to considering the changes of distribution in almost overall particle size range.

On the other hand, with the above fractal pattern of particle crushing in mind, it is advisable to separate the

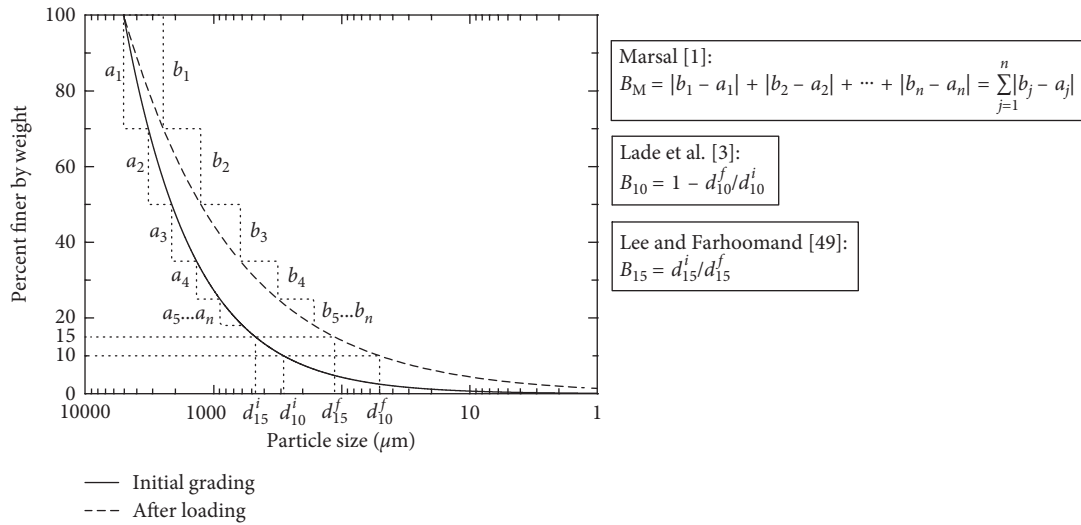


FIGURE 8: Definitions of the particle crushing indexes B_M [1], B_{10} [3], and B_{15} [49].

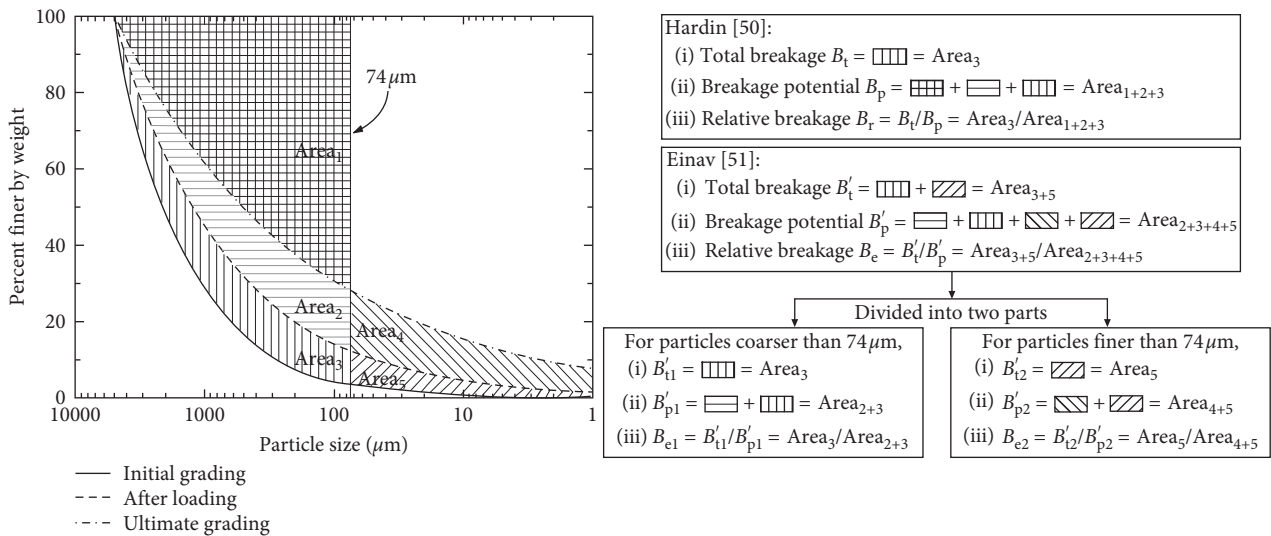
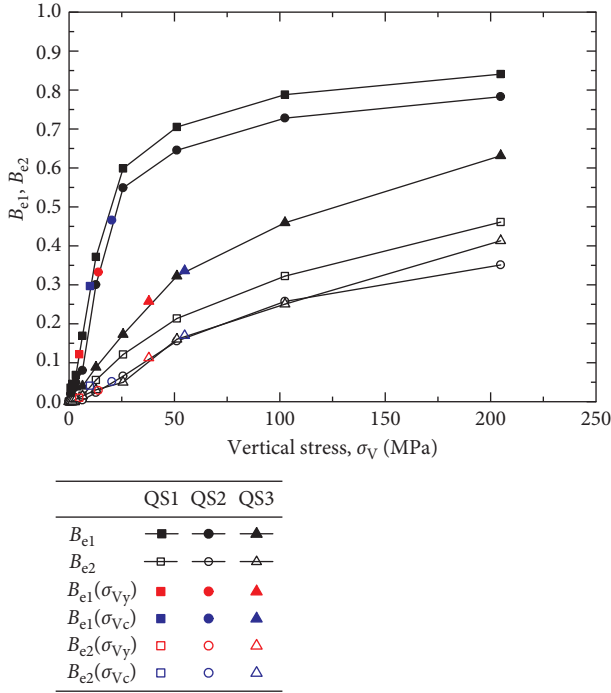
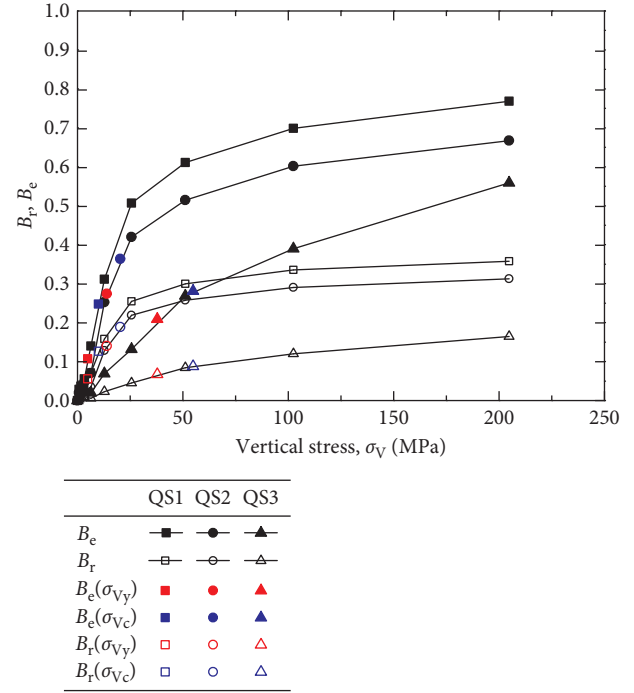


FIGURE 9: Definitions of the particle crushing indexes B_r [50] and B_e [51] and the division of B_e .

relative breakage B_e proposed by Einav [51] into two parts considering different scales. These different scales are the two ranges of the overall measurable PSD corresponding to the aforementioned bifractal characteristic. To achieve this objective, as defined in Figure 9, the total potential breakage B'_p is divided into two parts B'_{p1} and B'_{p2} to represent the corresponding potential breakage whose particle sizes are ranged coarser and finer than $74 \mu\text{m}$, respectively. And the total breakage B'_t is also divided into two parts B'_{t1} and B'_{t2} to represent the corresponding total breakage whose particle sizes are ranged coarser and finer than $74 \mu\text{m}$, respectively. Then, defining $B_{e1} = B'_{t1} / B'_{p1}$ to represent the relative breakage of particles coarser than $74 \mu\text{m}$ and defining $B_{e2} = B'_{t2} / B'_{p2}$ to represent the relative breakage of particles finer than $74 \mu\text{m}$. The aim of this division is to apply the divided indexes to investigate the amounts of crushing in different particle scales.

Figure 10 shows the relationship between vertical stress σ_v and B_{e1} or B_{e2} . For all types of specimens, as the vertical stress σ_v increases, both of the values of B_{e1} and B_{e2} increase rapidly, when the vertical stress σ_v is smaller than σ_{vc} . Then, when the vertical stress σ_v is larger than σ_{vc} , both of the values of B_{e1} and B_{e2} gradually approach a relatively steady state. However, the increasing rate of B_{e2} is obviously faster than that of B_{e1} . This is because the value of B_{e1} is closer to unity than that of B_{e2} , such as the values of B_{e1} at the maximum vertical stress 204.8 MPa for QS1 and QS2 are even 0.84 and 0.78, respectively, but the values of B_{e2} at that state for QS1 and QS2 are merely 0.46 and 0.35, respectively. It implies that the breakage potential in the scale of particles larger than $74 \mu\text{m}$ is not much left; however, the breakage potential in the scale of particles finer than $74 \mu\text{m}$ is still a lot at that state. Hence, the probability of crushing in the finer scale is higher. This difference also implies the reasonability of the division of B_e . Comparing to the natural graded

FIGURE 10: Relationship between σ_V and B_{e1} or B_{e2} .FIGURE 11: Relationship between σ_V and B_e or B_r .

specimen QS3, this increasing tendency of the value of B_{e1} is more significant for the uniformly graded specimens QS1 and QS2. This is because that the cushioning effect of surrounding contacts of coarser particles in the natural graded specimen QS3 is more significant; therefore, the higher degree of particle crushing of the coarser particles is induced in the uniformly graded specimens QS1 and QS2. As shown in Figure 9, with respect to B_r and B_{e1} , the value of B_t is equal to that of B'_{t1} , and the value of B_p is equal to the sum of B'_{p1} and $Area_1$. Hence, the difference between the values of B_r and B_{e1} is only due to the difference between their denominators. With respect to B_e and B_{e1} , although the value of B'_p is larger than that of B'_{p1} by B'_{p2} , the value of B'_{t2} is mostly only a very small fraction of the value of B'_t . The difference between the values of B_e and B_{e1} is also due to the difference between their denominators with not much important error. Hence, the variation tendencies of B_e and B_r in Figure 11, which show the relationship between the vertical stress σ_V and B_e or B_r , are similar to those of B_{e1} in Figure 10.

Hence, we can deduce that, at an extremely large vertical stress, the coarser part of the uniformly graded specimens is faster than the finer part to reach the ultimate state of particle crushing, although this deduction can only be executed by mental operations due to the limitation of laboratory tests. In addition, the effect of the increasing vertical stress σ_V on the evolution of B_e and B_r should be identical with that on the evolution of B_{e1} ; hence, these three crushing indexes B_e , B_r , and B_{e1} are reasonable for describing the amount of crushing in which particles are coarser than $74 \mu\text{m}$ with unimportant error, but the most accurate index should be B_{e1} .

Nevertheless, as shown in Figure 10, the increasing tendency of the value of B_{e2} in the uniformly graded

specimens QS1 and QS2 is less rapid than that in the natural graded specimen QS3. This may be resulted from that the average number of contact points of finer particles in QS3 is less than those in QS1 and QS2, and the contact cushioning effect exceeds the crushing strength effect on particle crushing. Hence, the probabilities of crushing of the finer “parent” particles (i.e., the finer particles which have not been crushed) and the finer and finer particles produced by previous rounds of particle crushing in QS3 are higher than the probabilities of crushing of those in QS1 and QS2. In addition, the pronounced different increasing tendencies between B_{e2} and B_{e1} represent that the reasonable index of particle crushing for describing the corresponding relative breakage, in which particles are finer than $74 \mu\text{m}$, should be B_{e2} which is essentially different from B_e , B_{e1} , and B_r .

Figure 12 shows the relationship between the vertical stress σ_V and the ratio ε_V/B_{e1} or ε_V/B_{e2} . Meanwhile, Figure 13 shows the relationship between the vertical stress σ_V and the ratio ε_V/B_e or ε_V/B_r . From ring shear tests [15] and triaxial tests [16], the phenomenon that the value of ε_V/B_r has been constant is observed almost at the critical state of soils. However, from Figures 12 and 13, it can be observed that both the values of ε_V/B_{e1} and ε_V/B_e are already constant, respectively, after the vertical stress σ_V exceeds σ_{Vc} . The values of the constants of ε_V/B_{e1} and ε_V/B_e are 0.391 and 0.461, respectively. From the previous part of this paper, when the vertical stress σ_V is larger than σ_{Vc} , it marks that the coarser part of PSD, in which particles are larger than $74 \mu\text{m}$, is fractal. Hence, it indicates that the coarser part of PSD is equipped with the fractal characteristic can be regarded as a token of that the values of ε_V/B_{e1} and ε_V/B_e are constant. On the other hand, the values

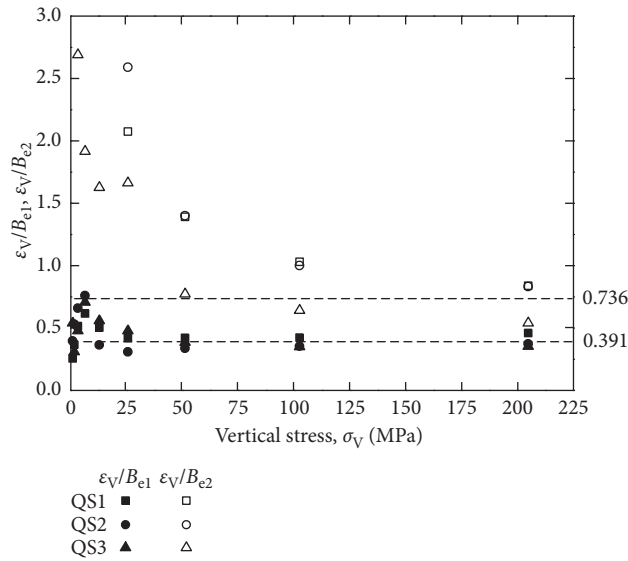


FIGURE 12: Relationship between σ_V and ϵ_V/B_{e1} or ϵ_V/B_{e2} .

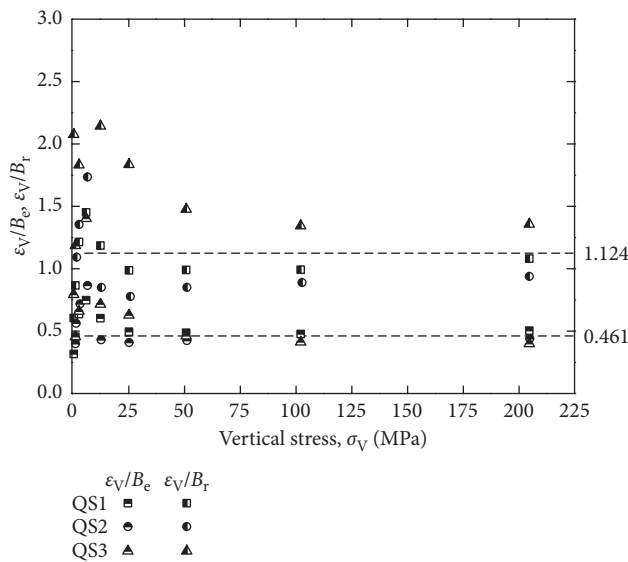


FIGURE 13: Relationship between σ_V and ϵ_V/B_e or ϵ_V/B_r .

of ϵ_V/B_{e2} and ϵ_V/B_r also have a tendency to be constant as the vertical stress σ_V increases; however, the prominence of this tendency is far inferior to that for the values of ϵ_V/B_{e1} and ϵ_V/B_e . With respect to ϵ_V/B_{e1} and ϵ_V/B_e , the constants for both are determined by the average of the ordinates of data points, which are all at a state after the maximum compressibility, as shown in Figures 12 and 13. The relevant statistical parameters are summarized in Table 2. It can be found that the square deviation of the values of ϵ_V/B_{e1} is very small and equal to 0.00287 which is even slightly lower than that of ϵ_V/B_e . Hence, comparing to ϵ_V/B_e , the more appropriate physical quantity to represent the physical phenomenon that the ratio of the volumetric strain to the relative breakage is a constant should be ϵ_V/B_{e1} . Hence, during one-dimensional compression, once the coarser part of PSD has been reached to fractal or the vertical stress

σ_V has been larger than σ_{Vc} , the prediction of the relative breakage can be accomplished by means of the measurable volumetric strain ϵ_V and the constant of the value of ϵ_V/B_{e1} obtained from tests.

4. Conclusion

To clarify the influence of particle crushing on the behavior of granular geomaterials, a series of one-dimensional compression tests were conducted on quartz sand-gravel up to 204.8 MPa. The detailed investigations were mainly on the compression behavior, the evolution of PSD, the fractal pattern of grading curve, and the degree of particle crushing. The major findings can be drawn as follows.

As the vertical stress increases, both the yielding state and the state at the maximum compressibility of uniformly

TABLE 2: Statistical parameters of the values of ε_V/B_{e1} and ε_V/B_e for all types of specimens when $\sigma_V \geq \sigma_{Vc}$.

Vertical stress, σ_V (MPa)	ε_V/B_{e1}			ε_V/B_e		
	QS1 ($\sigma_{Vc} \approx 9.9$ MPa)	QS2 ($\sigma_{Vc} \approx 20.3$ MPa)	QS3 ($\sigma_{Vc} \approx 54.9$ MPa)	QS1 ($\sigma_{Vc} \approx 9.9$ MPa)	QS2 ($\sigma_{Vc} \approx 20.3$ MPa)	QS3 ($\sigma_{Vc} \approx 54.9$ MPa)
12.8	0.50349	—	—	0.6019	—	—
25.6	0.41932	0.30881	—	0.49532	0.40419	—
51.2	0.42075	0.33716	0.38471	0.4859	0.42325	0.46193
102.4	0.42174	0.35402	0.3502	0.47581	0.42814	0.41262
204.8	0.4594	0.37241	0.35382	0.5031	0.43703	0.39979
Mean value	—	0.39049	—	—	0.46075	—
Square deviation	—	0.00287	—	—	0.00300	—

graded specimens are easier to be reached than those of the well-graded specimens. For uniformly graded specimens, the smaller the particle sizes are, the more difficult these two states are to be reached. For a given specimen, the yielding state is always previous to the state at the maximum compressibility. In addition, these two states are closely associated with the evolution of PSD and the fractal pattern of particle crushing.

During one-dimensional compression, the evolution of PSD induced by particle crushing is described as follows: for each type of specimens, the finer part, in which particles are finer than $74\mu\text{m}$, of the grading curve tends to be approximately a straight line after the yielding state in the double-logarithmic coordinates. However, the coarser part, in which particles are coarser than $74\mu\text{m}$, of the grading curve tends to be approximately another straight line after the state at the maximum compressibility. The whole grading curve tends to be a straight line when the vertical stress exceeds a definite extent to the stress at the maximum compressibility state.

On one-dimensional compression, the fractal pattern of particle crushing is described as follows: the fractal first appears on the finer part of a grading curve after the yielding state. Then the bifractal appears on the whole grading curve with $74\mu\text{m}$ as the transition particle size, which is utilized to distinguish the different fractal characteristics between the finer and coarser parts, after the state at the maximum compressibility. Finally, the entire grading curve evolves into monofractal when the vertical stress exceeds a certain degree to the stress at the maximum compressibility. In addition, the values of 2.29, 1.85, and 2.16 are considered as the lower limits of the fractal dimensions for the finer, the coarser, and the whole parts of a grading curve, respectively.

With the fractal pattern of particle crushing in mind, a pair of crushing indexes B_{e1} and B_{e2} by means of the division of the relative breakage B_e are proposed for representing the relative breakages of particles coarser than $74\mu\text{m}$ and finer than $74\mu\text{m}$, respectively. The division of the relative breakage B_e is reasonable due to the relatively large difference between the values of B_{e1} and B_{e2} during crushing.

Either that the vertical stress is larger than the stress at the maximum compressibility or that the coarser part of PSD is evolved into fractal can be regarded as a token of the physical phenomenon that the ratio between the volumetric strain and the relative breakage is a constant. Hence, the

prediction of the relative breakage can be accomplished by means of the volumetric strain and the constant which are available from one-dimensional compression tests.

Data Availability

The data used to support the findings of this study are available from the corresponding author upon request.

Conflicts of Interest

The authors declare that they have no conflicts of interest.

Acknowledgments

The National Natural Science Foundation Funded Project of China (Grant no. 41272334) and Fundamental Research Fund for the Central Universities of China (Grant no. 2014-yb-019) are gratefully acknowledged.

References

- [1] R. J. Marsal, "Large scale testing of rockfill materials," *Journal of the Soil Mechanics and Foundations Division*, vol. 93, no. 2, pp. 27–43, 1967.
- [2] M. F. Randolph, "The axial capacity of deep foundations in calcareous soil," in *Proceedings of International Conference on Calcareous Sediments*, pp. 837–857, Perth, Australia, March 1988.
- [3] P. V. Lade, J. A. Yamamuro, and P. A. Bopp, "Significance of particle crushing in granular materials," *Journal of Geotechnical Engineering*, vol. 122, no. 4, pp. 309–316, 1996.
- [4] K. Sassa, H. Fukuoka, G. Scarascia-Mugnozza, and S. Evans, "Earthquake-induced landslides: distribution, motion and mechanisms," *Soils and Foundations*, vol. 54, no. 4, pp. 544–559, 2014.
- [5] M. Kikumoto, D. M. Wood, and A. Russell, "Particle crushing and deformation behavior," *Soils and Foundations*, vol. 50, no. 4, pp. 547–563, 2010.
- [6] F. W. Yu and L. J. Su, "Particle breakage and the mobilized drained shear strengths of sand," *Journal of Mountain Science*, vol. 13, no. 8, pp. 1481–1488, 2016.
- [7] Y. P. Yao, J. Hu, A. N. Zhou, T. Luo, and N. Wang, "Unified strength criterion for soils, gravels, rocks, and concretes," *Acta Geotechnica*, vol. 10, no. 6, pp. 749–759, 2015.
- [8] D. Lu, X. Du, G. Wang, A. N. Zhou, and A. Li, "A three-dimensional elastoplastic constitutive model for concrete," *Computers & Structures*, vol. 163, pp. 41–55, 2016.

- [9] A. N. Zhou, C. Q. Li, and J. Huang, "Failure analysis of an infinite unsaturated soil slope," *Proceedings of the Institution of Civil Engineers-Geotechnical Engineering*, vol. 169, no. 5, pp. 410–420, 2016.
- [10] B. Zhao, J. Wang, M. R. Coop, G. Viggiani, and M. Jiang, "An investigation of single sand particle fracture using X-ray micro-tomography," *Geotechnique*, vol. 65, no. 8, pp. 625–641, 2015.
- [11] W. Wang and M. R. Coop, "An investigation of breakage behaviour of single sand particles using a high-speed microscope camera," *Geotechnique*, vol. 66, no. 12, pp. 984–998, 2016.
- [12] J. A. Yarnamuro, "One-dimensional compression of sands at high pressures," *Journal of Geotechnical Engineering*, vol. 122, no. 2, pp. 147–154, 1996.
- [13] G. R. McDowell and M. D. Bolton, "On the micro mechanics of crushable aggregates," *Geotechnique*, vol. 48, no. 5, pp. 667–679, 1998.
- [14] Y. Nakata, M. Hyodo, A. F. L. Hyde, Y. Kato, and H. Murata, "Microscopic particle crushing of sand subjected to high pressure one-dimensional compression," *Soils and Foundations*, vol. 41, no. 1, pp. 69–82, 2001.
- [15] L. Luzzani and M. R. Coop, "On the relationship between particle breakage and the critical state of sands," *Soils and Foundations*, vol. 42, no. 2, pp. 71–82, 2002.
- [16] M. R. Coop, K. K. Sorensen, T. B. Freitas, and G. Georgoutsos, "Particle breakage during shearing of a carbonate sand," *Geotechnique*, vol. 54, no. 3, pp. 157–163, 2004.
- [17] O. Igwe, K. Sassa, and F. W. Wang, "The influence of grading on the shear strength of loose sands in stress-controlled ring shear tests," *Landslides*, vol. 4, no. 1, pp. 43–51, 2007.
- [18] G. Miao and D. Airey, "Breakage and ultimate states for a carbonate sand," *Geotechnique*, vol. 63, no. 14, pp. 1221–1229, 2013.
- [19] E. Becker, C. K. Chan, and H. B. Seed, "Strength and deformation characteristics of rockfill materials in plane strain and triaxial compression tests," *Science*, vol. 34, no. 878, p. 576, 1972.
- [20] S. Donohue, C. O'Sullivan, and M. Long, "Particle breakage during cyclic triaxial loading of a carbonate sand," *Geotechnique*, vol. 59, no. 5, pp. 477–482, 2009.
- [21] T. Luo, Y. P. Yao, A. N. Zhou, and X. G. Tian, "A three-dimensional criterion for asymptotic states," *Computers and Geotechnics*, vol. 41, pp. 90–94, 2012.
- [22] Y. P. Yao, W. Hou, and A. N. Zhou, "Constitutive model for overconsolidated clays," *Science in China, Series E: Technological Sciences*, vol. 51, no. 2, pp. 179–191, 2008.
- [23] S. J. Steacy and C. G. Sammis, "An automaton for fractal patterns of fragmentation," *Nature*, vol. 353, no. 6341, pp. 250–252, 1991.
- [24] E. U. Klotz and M. R. Coop, "An investigation of the effect of soil state on the capacity of driven piles in sands," *Geotechnique*, vol. 51, no. 9, pp. 733–751, 2001.
- [25] S. Lirer, A. Flora, and M. V. Nicotera, "Some remarks on the coefficient of earth pressure at rest in compacted sandy gravel," *Acta Geotechnica*, vol. 6, no. 1, pp. 1–12, 2011.
- [26] G. Ma, W. Zhou, T. T. Ng, Y. G. Cheng, and X. L. Chang, "Microscopic modeling of the creep behavior of rockfills with a delayed particle breakage model," *Acta Geotechnica*, vol. 10, no. 4, pp. 481–496, 2015.
- [27] E. E. Alonso, E. E. Romero, and E. Ortega, "Yielding of rockfill in relative humidity-controlled triaxial experiments," *Acta Geotechnica*, vol. 11, no. 3, pp. 455–477, 2016.
- [28] S. Feia, J. Sulem, J. Canou, S. Ghabezloo, and X. Clain, "Changes in permeability of sand during triaxial loading: effect of fine particles production," *Acta Geotechnica*, vol. 11, no. 1, pp. 1–19, 2016.
- [29] Y. P. Yao and A. N. Zhou, "Non-isothermal unified hardening model: a thermo-elasto-plastic model for clays," *Geotechnique*, vol. 63, no. 15, pp. 1328–1345, 2013.
- [30] Y. P. Yao, W. Hou, and A. N. Zhou, "UH model: three-dimensional unified hardening model for overconsolidated clays," *Geotechnique*, vol. 59, no. 5, pp. 451–469, 2009.
- [31] Y. P. Yao, D. C. Lu, A. N. Zhou, and B. Zou, "Generalized non-linear strength theory and transformed stress space," *Science in China Series E: Technological Sciences*, vol. 47, pp. 691–709, 2004.
- [32] Y. P. Yao, A. N. Zhou, and D. C. Lu, "Extended transformed stress space for geomaterials and its application," *Journal of Engineering Mechanics*, vol. 133, pp. 1115–1123, 2007.
- [33] J. G. Qian, J. B. Gu, X. Q. Gu, and M. S. Huang, "Discrete numerical modeling of granular materials considering crushability," *Journal of Mountain Science*, vol. 14, no. 4, pp. 758–770, 2017.
- [34] Y. P. Cheng, M. D. Bolton, and Y. Nakata, "Crushing and plastic deformation of soils simulated using DEM," *Geotechnique*, vol. 54, no. 2, pp. 131–141, 2004.
- [35] D. L. Turcotte, "Fractals and fragmentation," *Journal of Geophysical Research*, vol. 91, no. 2, pp. 1921–1926, 1986.
- [36] G. R. McDowell, M. D. Bolton, and D. Robertson, "The fractal crushing of granular materials," *Journal of the Mechanics and Physics of Solids*, vol. 44, no. 12, pp. 2079–2102, 1996.
- [37] J. R. Zhang, J. Zhu, and W. J. Huang, "Crushing and fractal behaviors of quartz sand-gravel particles under confined compression," *Chinese Journal of Geotechnical Engineering*, vol. 30, no. 6, pp. 783–789, 2008.
- [38] F. Altuhafi and B. A. Baudet, "A hypothesis on the relative roles of crushing and abrasion in the mechanical genesis of a glacial sediment," *Engineering Geology*, vol. 120, no. 1, pp. 1–9, 2011.
- [39] J. R. Zhang, Y. Hu, B. W. Zhang, and Y. Z. Liu, "Fractal behavior of particle-size distribution during particle crushing of a quartz sand and gravel," *Chinese Journal of Geotechnical Engineering*, vol. 37, no. 5, pp. 784–791, 2015.
- [40] F. N. Altuhafi and M. R. Coop, "Changes to particle characteristics associated with the compression of sands," *Geotechnique*, vol. 61, no. 6, pp. 459–471, 2011.
- [41] F. N. Altuhafi, B. A. Baudet, and P. Sammonds, "On the particle size distribution of a basaltic till," *Soils and Foundations*, vol. 51, no. 1, pp. 113–121, 2011.
- [42] Y. F. Xu, X. B. Feng, H. G. Zhu, and F. F. Chu, "Fractal model for rockfill shear strength based on particle fragmentation," *Granular Matter*, vol. 17, no. 6, pp. 753–761, 2015.
- [43] A. Zhou, R. Q. Huang, and D. Sheng, "Capillary water retention curve and shear strength of unsaturated soils," *Canadian Geotechnical Journal*, vol. 53, no. 6, pp. 974–987, 2016.
- [44] A. N. Zhou, "A contact angle-dependent hysteresis model for soil-water retention behaviour," *Computers and Geotechnics*, vol. 49, pp. 36–42, 2013.
- [45] A. N. Zhou, D. Sheng, and J. P. Carter, "Modelling the effect of initial density on soil-water characteristic curves," *Geotechnique*, vol. 62, no. 8, pp. 669–680, 2012.
- [46] A. N. Zhou, D. Sheng, and J. Li, "Modelling water retention and volume change behaviours of unsaturated soils in non-isothermal conditions," *Computers and Geotechnics*, vol. 55, pp. 1–13, 2014.
- [47] A. Zhou, S. Wu, J. Li, and D. Sheng, "Including degree of capillary saturation into constitutive modelling of unsaturated soils," *Computers and Geotechnics*, vol. 95, pp. 82–98, 2018.

- [48] J. R. Zhang, Y. Hu, H. L. Yu, and G. L. Tao, "Predicting soil-water characteristic curve from multi-fractal particle-size distribution of clay," *Journal of Hydraulic Engineering*, vol. 46, no. 6, pp. 650–657, 2015.
- [49] K. L. Lee and I. Farhoomand, "Compressibility and crushing of granular soil in anisotropic triaxial compression," *Canadian Geotechnical Journal*, vol. 4, no. 1, pp. 68–86, 1967.
- [50] B. O. Hardin, "Crushing of soil particles," *Journal of Geotechnical Engineering*, vol. 111, no. 10, pp. 1177–1192, 1985.
- [51] I. Einav, "Breakage mechanics—part I: theory," *Journal of the Mechanics and Physics of Solids*, vol. 55, no. 6, pp. 1274–1297, 2007.

Research Article

Practical Approach to Predicting the K_0 Behavior of In Situ Sandy Gravel

Ming-Jie Jiang ¹, Jun-Gao Zhu ^{1,2}, En-yue Ji,³ Ying-qi Wei,⁴ and Zhi-zhou Geng¹

¹Key Laboratory of Ministry of Education for Geomechanics and Embankment Engineering, Hohai University, 01 Xikang Road, Nanjing 210098, China

²Key Laboratory of Failure Mechanism and Safety Control Techniques of Earth-Rockfill Dam of the Ministry of Water Resources, Nanjing Hydraulic Research Institute, 223# Guangzhou Road, Nanjing 210029, China

³Key Laboratory of Failure Mechanism and Safety Control Techniques of Earth-Rock Dam of the Ministry of Water Resources, Nanjing Hydraulic Research Institute, 34 Hujuguan Road, Nanjing 210029, China

⁴State Key Laboratory of Simulation and Regulation of Water Cycle in River Basin, China Institute of Water Resources and Hydropower Research, Beijing 100048, China

Correspondence should be addressed to Jun-Gao Zhu; zhujungao@hhu.edu.cn

Received 29 May 2018; Accepted 19 August 2018; Published 24 September 2018

Academic Editor: Yongfeng Deng

Copyright © 2018 Ming-Jie Jiang et al. This is an open access article distributed under the Creative Commons Attribution License, which permits unrestricted use, distribution, and reproduction in any medium, provided the original work is properly cited.

To investigate the scale effect on at-rest earth pressure coefficient K_0 for sandy gravel, a number of K_0 tests for sandy gravel were performed by using a new-developed large-size K_0 apparatus. The test samples with different maximum particle size d_M are prepared by different techniques, and the scale effect on K_0 behavior of sandy gravels is investigated. It is found that the vertical stress σ_v , preparation technique and d_M all have some influence on the value of K_0 for the tested sandy gravels. Since different d_M or preparation techniques all induce the scale effect, the scale effect on K_0 of sandy gravel can not be ignored. Based on the test data of sandy gravel, a description of K_0 considering scale effect as well as σ_v is proposed and an approach to predict the K_0 behavior of sandy gravel in situ is obtained. Furthermore, the accuracy and applicability of the approach is verified.

1. Introduction

The at-rest earth pressure coefficient K_0 is defined as the ratio of the effective horizontal stress versus vertical stress. It is a basic mechanic parameter of the soils in many practical engineering works such as slope [1] and tunnel [2] but is relatively difficult to determine.

The mechanical properties of soil essentially depend upon the stress state, and therefore, accurate measurement of the initial stress state plays an important role in analyzing and designing the earthworks. In general, the vertical stress, σ'_v , of a ground is calculated according to the bulk density of soil and the depth, and then the evaluation of initial stress state can be done by using the K_0 value. In fact, sandy gravels are usually adopted as filling materials in many earthworks such as heavily loaded railway and earth dam, and the evaluation of K_0 of sandy gravel is important in the analysis and design of the earthworks. Therefore, the investigation to

K_0 behavior of sandy gravels has great theoretical significance and practical value.

In the actual project, for example, earth rockfill dam, the maximum grain size d_M of sandy gravel can reach 800~1200 mm [3]. Due to the dimensional limitation of the laboratory instruments, preparation techniques, such as scalping technique [4], replacement technique [5], and parallel gradation technique [6], are used to reduce the grain size distribution (GSD) of in situ sandy gravel. In scalping technique, the oversize particles were removed from the soil in situ. In replacement technique, the oversize particles are replaced in proportion by the particles with the size less than d_M and more than 5 mm. In parallel gradation technique, the GSD of reduced particle size tested specimen is parallel to that of the soil in situ.

Due to the difference between GSD of test specimens and that of sandy gravel in situ, the mechanical properties of test specimen are always different from that of sandy gravel in situ, which is called scale effect [7].

Wide ranges of investigations to the scale effect on mechanical properties of soil have been published. Some researchers [8–11] have studied the scale effect on the shear strength of soil. Abu-Farsakh and Yu [12] and Wei et al. [13] have found that there is a big difference between the compression behavior of in situ soil and that measured in the laboratory. The published works [14, 15] point out that the scale effect on the particle crushing of sandstone particle mixtures is obvious. Chang et al. [16] have investigated the scale effect on the minimum void ratio of granular soil. Wang et al. [17] used PFC2D to analyze the scale effect on the key physical parameters of soil such as maximum dry density, initial elasticity modulus, and bulk modulus of coarse-grained soil. However, the relevant research about the scale effect on K_0 of sandy gravel is almost blank. Therefore, the investigation to scale effect on K_0 of sandy gravel still needs to make further studies.

In this study, K_0 tests for sandy gravel were conducted using a new-developed K_0 test apparatus. Based on the test results, the scale effect on K_0 of sandy gravel is investigated, and an approach to predict the K_0 behavior of sandy gravel is studied.

2. Testing Apparatus and Programme

2.1. Testing Apparatus. In this study, the K_0 test apparatus is newly developed by the authors and can be used for the most soils including sandy gravel. The apparatus, as shown in Figure 1, is similar to the oedometer, and its test principle will be introduced as follows.

In Figure 1, four force sensors (10) are adopted to fix the two rigid cylinders (6) and measure the total pressure N_h loaded on the test specimen, and the effective Horizontal stress σ'_h loaded on the test specimen can be expressed as

$$\sigma'_h = \frac{N_h}{(h - \Delta h)d}, \quad (1)$$

where d and h are the diameter and initial height of test specimen, respectively and Δh is the compression of test specimen during test, and obtained by the displacement sensor (11).

To diminish the influence of sidewall friction F between the rigid cylinders (6) and test specimen, according to Wang et al. [18], the arithmetic average of top and bottom effective vertical pressure is used as the vertical pressure applied to the test specimen, and the effective vertical stress σ'_v loaded on the test specimen can be calculated as

$$\sigma'_v = \frac{N_v + (N_v - F)}{2A} = \frac{4(N_v - F/2)}{\pi d^2}, \quad (2)$$

where N_v is the vertical pressure loaded on the top surface of test specimen and measured by load sensor (12). F is the sidewall friction and measured by four load sensor (3). $(N_v - F)$ is the vertical pressure loaded on the bottom surface of test specimen.

As a result, the K_0 value can be obtained according to Equation (3). For the detailed introduction and the calibration of this apparatus, it can be seen in the work [19].

$$K_0 = \frac{\sigma'_h}{\sigma'_v} = \frac{(N_h / (h - \Delta h)d)}{(4(N_v - F/2) / \pi d^2)}. \quad (3)$$

2.2. Programme and Testing Methods. The soil tested is a calcareous fluvial gravel with rounded grains, which is retrieved from Cihaxia rockfill dam, located in western China, as shown in Figure 2.

Due to the large particle size, the GSD of sandy gravel in situ is reduced to GSDs with different d_M ranging from 10 mm to 60 mm for lab test of this paper. The scalping technique [4], replacement technique [5], and parallel gradation technique [6] are used to reduce the GSD, and the test specimens are referred to as S1~S4 (series of test specimens prepared by scalping technique, called “S series”), P1~P4 (ones by parallel gradation technique, called “P series”) and R1~R4 (ones by replacement technique, called “R series”), respectively. The GSD and corresponding maximum grain size d_M of each test specimen are given in Table 1.

The height and diameter of test specimen is 30 cm and 40 cm, respectively, and all test specimens are air-dried and uncompacted. Since the difference, between the initial dry density of every test specimen and the test data of minimum dry density test, is less than 1%, the relative density of each test specimen can be seen as 0. The initial dry density of every test specimen is shown in Table 1 and Figure 3.

During test, with 10 kPa/min, σ'_v loaded on the test specimen from 100 kPa to 2000 kPa was applied step by step. When σ'_v reached the predetermined value, σ'_v was kept constant for 15 minutes and then the reading of each sensor was recorded. When σ'_v reached 2000 kPa, σ'_v was kept constant for 150 minutes, and then, the reading of each sensor was recorded. Afterward, σ'_v was reduced to zero with unloading stress rate of 10 kPa/min. When σ'_v reached the predetermined load during unloading, σ'_v was kept constant for 15 minutes and then reading of each sensor was recorded.

3. Interpretation of Experimental Results

Based on the K_0 test results of S1~S4 (S series), P1~P4 (P series), and R1~R4 (R series), the K_0 behavior of sandy gravel is investigated. The relationship between K_0 and σ'_v are plotted in Figures 4(a)–4(c), respectively. Figure 4 shows that the K_0 value of every test specimen tends to decrease with the increment of σ'_v , which is consistent with the published works [20–25]. Therefore, studying the relationship of K_0 and σ'_v has important theoretical significance. Based on the test data of sandy gravels, Zhu et al. [25] proposed a $K_0 - \sigma'_v$ correlation for sandy gravel:

$$K_0 = \frac{K_{0\max} + K_{0\min} \sqrt{\sigma'_v / p_a}}{\sqrt{\sigma'_v / p_a} + 1}, \quad (4)$$

where p_a is standard atmospheric pressure, $K_{0\max}$ and $K_{0\min}$ are fitting parameters. The physical meanings of $K_{0\max}$ and $K_{0\min}$ are the K_0 value when $\sigma'_v = 0$ and $\sigma'_v \rightarrow \infty$, respectively.

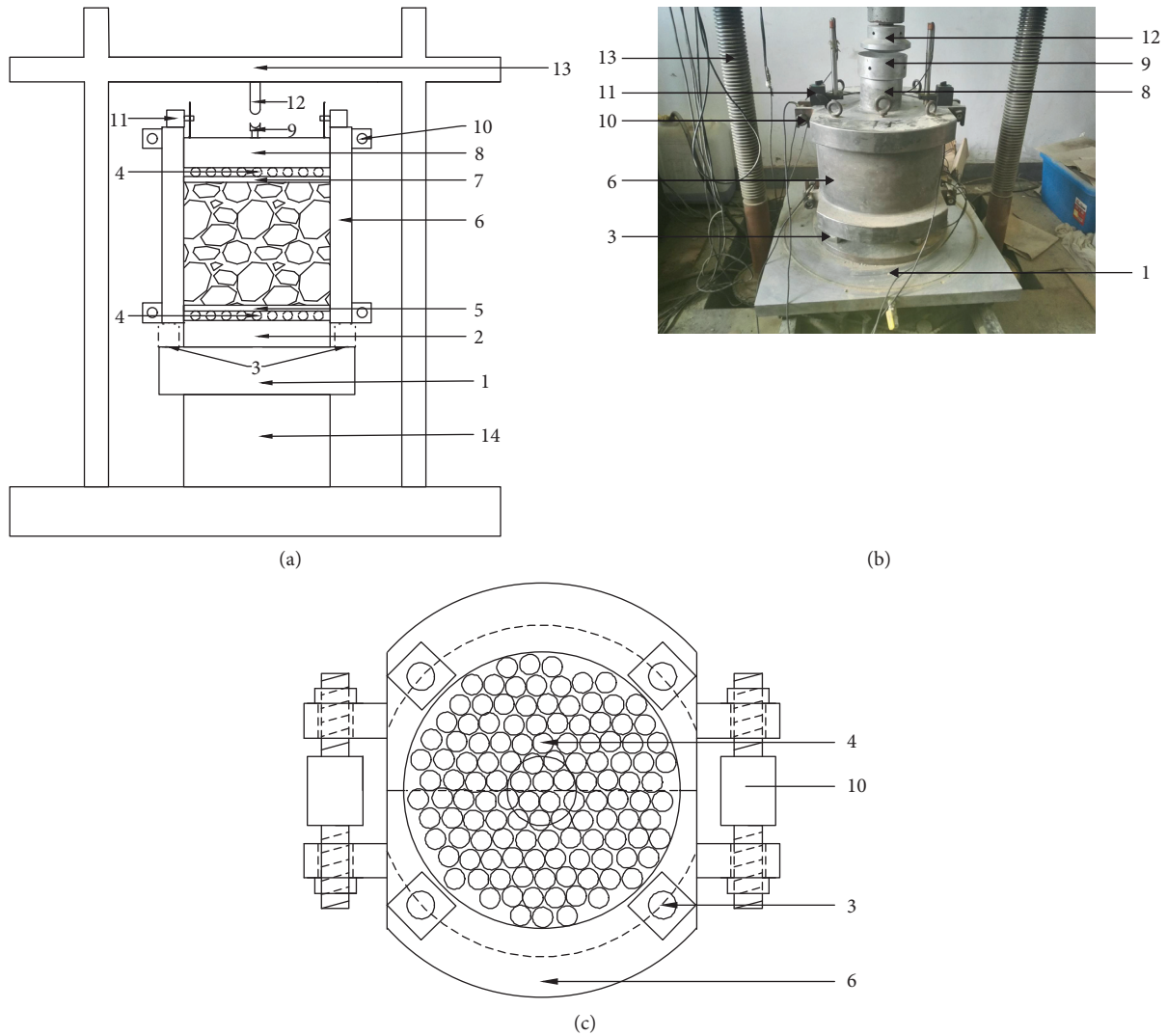


FIGURE 1: Sketch map of test equipment. (a) Sketch map of the apparatus. (b) Photo of the apparatus. (c) Top view of the apparatus (1, base; 2, baseplate; 3, load sensor; 4, steel ball; 5, the bottom force transmission plate; 6, semicircle rigid cylinders; 7, the top force transmission plate; 8, pressure plate; 9, compression plate; 10, pull pressure sensor; 11, displacement sensor; 12, load sensor; 13, loading frame; 14, load cylinder).

In order to verify Equation (4), the test data of S1~S4, R1~R4 and P1~P4 are fitted by Equation (4), and the fitting parameters and curves are shown in Table 2 and Figure 4, respectively. It can be seen from Figure 4 that the fitting curves agree well with the corresponding test data. Compared with the corresponding test data, the errors of the K_0 value predicted by Equation (4) are mostly below 2% and the maximum error is only 5.9%. Therefore, Equation (4) can describe well the relationship of K_0 and σ'_v .

To analyze the influence of d_M on K_0 of sandy gravel, the K_0 behaviours of test specimens in terms of d_M are investigated as plotted in Figures 4(a)–4(c). Figures 4(a)–4(c) show that increasing d_M tends to decrease the K_0 value with the same σ'_v loaded on test specimen, which means that d_M has a significant effect on the K_0 .

To investigate the influence of preparation technique on K_0 of sandy gravel. The $K_0 - \sigma'_v$ curves of the tested specimens modified by different preparation techniques with the



FIGURE 2: Photo of tested sample ($40 \text{ mm} < d_M < 60 \text{ mm}$).

same d_M are presented in Figure 5. Due to limited space, only the tested specimens with $d_M = 20 \text{ mm}$ are plotted in Figure 5, and the test results of test specimens with $d_M = 10 \text{ mm}$ and 40 mm indicate a consistent trend. It can be

TABLE 1: Basic property of tested soil and specimens.

Test specimen	d_M (mm)	Initial dry density (g/cm ³)	Grain groups content (%)					
			100~60	60~40	40~20	20~10	10~5	<5
Original GSD*	100	—	21.87	12.25	16.51	12.76	8.14	28.46
S1	60	2.05	—	15.68	21.13	16.33	10.42	36.43
S2	40	2.03	—	—	25.06	19.39	12.36	43.20
S3	20	1.96	—	—	—	25.85	16.49	57.66
S4	10	1.90	—	—	—	—	22.23	77.74
R1	60	2.01	—	17.64	23.79	18.38	11.73	28.46
R2	40	2.01	—	—	31.58	24.39	15.56	28.46
R3	20	1.94	—	—	—	43.68	27.86	28.46
R4	10	1.91	—	—	—	—	71.54	28.46
P1	60	2.01	—	18.30	21.00	14.20	12.30	34.20
P2	40	1.95	—	—	27.60	18.90	13.70	39.80
P3	20	1.89	—	—	—	27.60	18.50	53.90
P4	10	1.82	—	—	—	—	27.60	72.40

Note. Original GSD represents the GSD of the soil in situ.

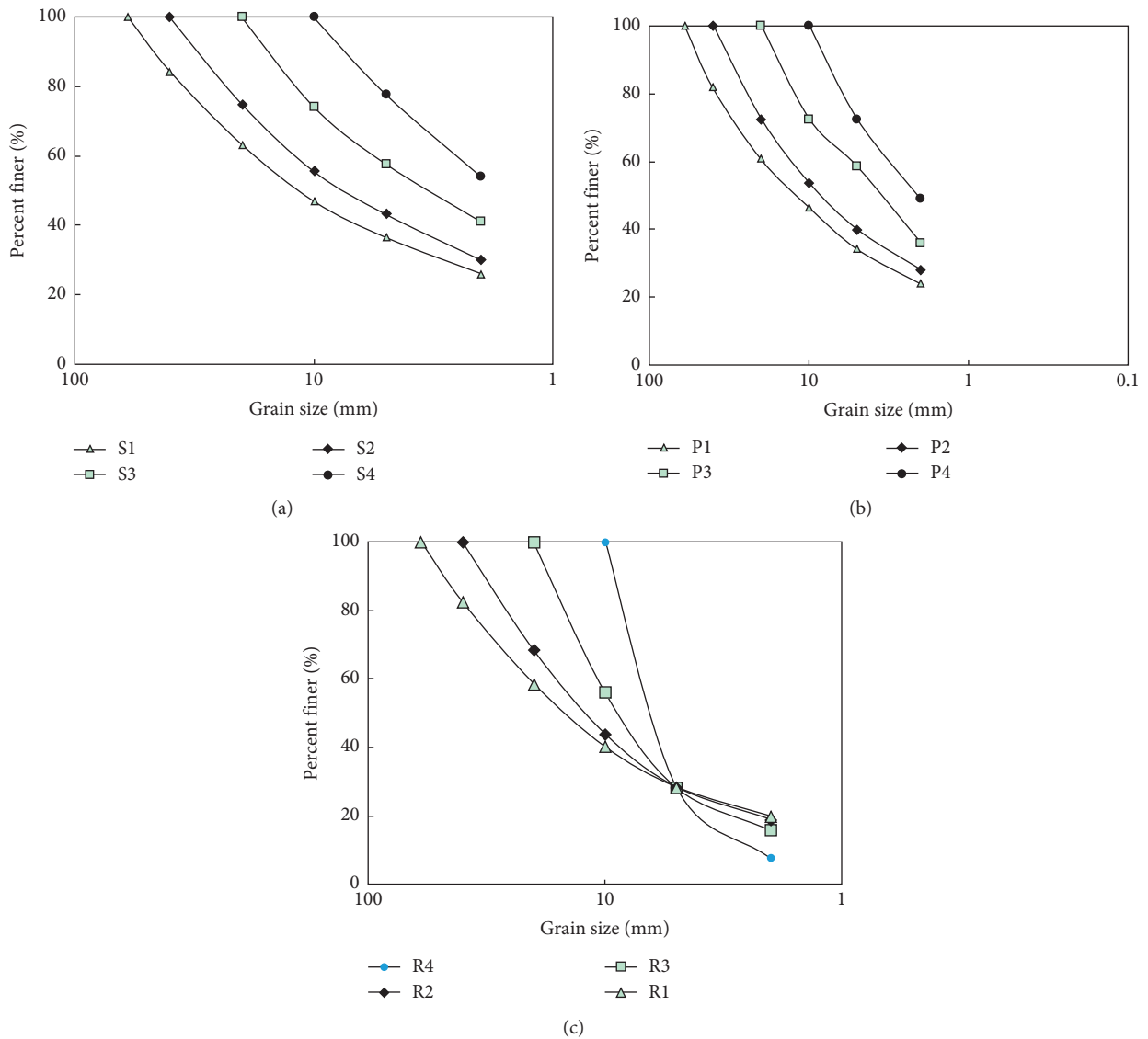


FIGURE 3: Grain size distribution (PSD) curves of tested materials. (a) S1~S4, (b) P1~P4, and (c) R1~R4.

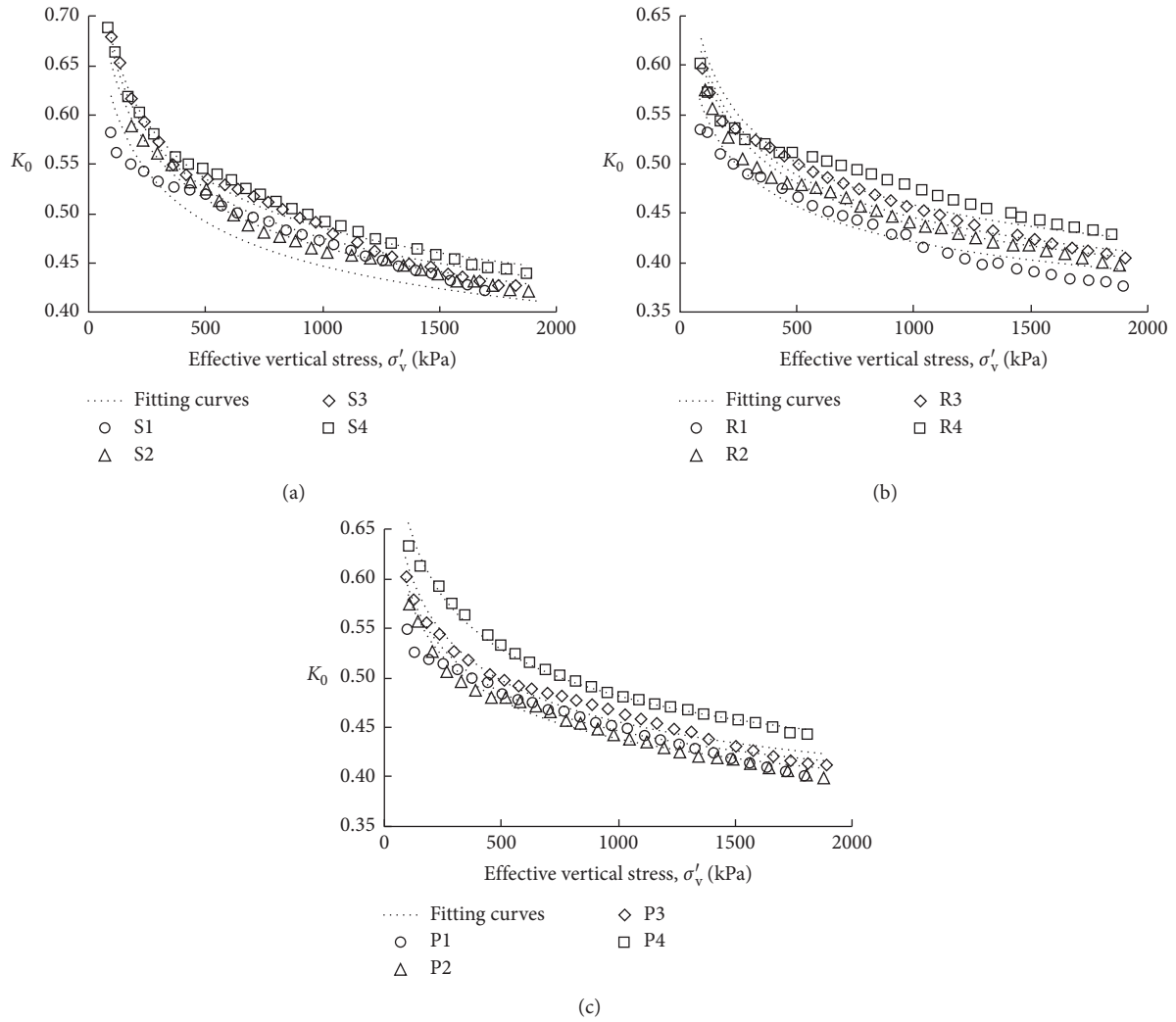


FIGURE 4: $K_0 - \sigma'_v$ curves. (a) S1~S4, (b) R1~R4, and (c) P1~P4.

seen from Figure 5 that there is a certain difference between the K_0 values of the test specimens prepared by different preparation techniques and the maximum difference can reach 22%. Therefore, preparation technique has some influence on the K_0 behavior of sandy gravel.

As discussed above, d_M and preparation technique all have some influence on K_0 of test specimen, and different d_M or preparation techniques all induce the scale effect. Therefore, the scale effect on K_0 of sandy gravel can not be ignored. This observation indicates that the laboratory test data can not reflect the accurate K_0 value of sandy gravel in situ, and therefore, the approach to accurately predict the K_0 behavior of in situ sandy gravel based on the laboratory test data is investigated in the next section.

4. The Approach to Predict K_0 Behavior of Sandy Gravel In Situ

As mentioned above, K_0 of each test specimen varies evidently with the variations of d_M or preparation technique. This means that there is some relationship between K_0 and

TABLE 2: K_{0max} and K_{0min} of the test specimens.

Preparation technique	d_M (mm)	10	20	40	60
Scalping technique	Test specimen	S4	S3	S2	S1
	K_{0max}	1.042	1.006	0.972	0.953
	K_{0min}	0.312	0.304	0.296	0.291
	R^2	0.998	0.997	0.997	0.975
Replacement technique	Test specimen	R4	R3	R2	R1
	K_{0max}	0.935	0.914	0.892	0.880
	K_{0min}	0.311	0.297	0.284	0.277
	R^2	0.997	0.997	0.994	0.997
Parallel gradation technique	Test specimen	P4	P3	P2	P1
	K_{0max}	0.970	0.926	0.885	0.861
	K_{0min}	0.324	0.313	0.302	0.296
	R^2	0.999	0.996	0.997	0.995

GSD of sandy gravel. On the other hand, for a given in situ sandy gravel, if the preparation technique is the same, the GSD of test specimen are principally determined by d_M [26],

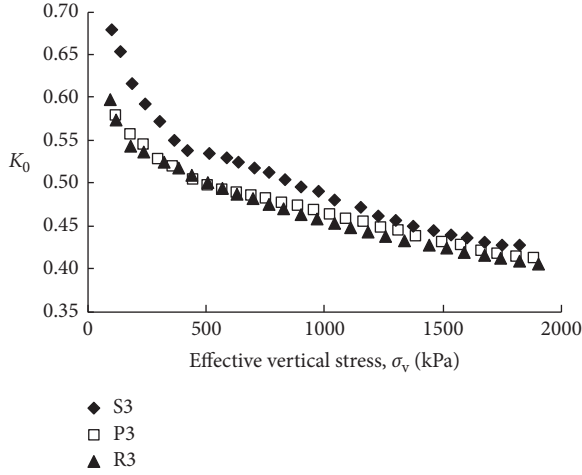


FIGURE 5: $K_0 - \sigma'_v$ curves under different preparation techniques ($d_M = 20$ mm).

and therefore, there may be some relationship of K_0 and d_M for test specimens prepared by the same preparation technique. If the relationship of K_0 and d_M can be obtained, the K_0 behavior of the sandy gravel in situ can be extrapolated by using the $K_0 - d_M$ relation. In theory, extrapolating may not be reliable. However, due to the large particle size, the laboratory K_0 test for sandy gravel with original GSD can not be performed directly, and extrapolating is adopted by some scholars [27, 28] as an acceptable approach.

According to Equation (4), if $K_{0\max}$ and $K_{0\min}$ of in situ sandy gravel is determined, the K_0 behavior of in situ sandy gravel can then be predicted. Therefore, if the relationship of $K_{0\max}$ and $K_{0\min}$ versus d_M can be obtained, the $K_{0\max}$ and $K_{0\min}$ of the sandy gravel in situ can be extrapolated by using this relation from test data, and the K_0 behavior of the sandy gravel in situ can be predicted using Equation (4) with the corresponding $K_{0\max}$ and $K_{0\min}$.

To further study the relationship of $K_{0\max}$ and d_M , the test results of specimens prepared by scalping technique and replacement technique, i.e., the S series tests and R series tests, are illustrated in $(1 - (d_{M1}/d_{M2})) \sim \ln(K_{0\max1}/K_{0\max2})$ plane, as shown in Figure 6, where $K_{0\max1}$ and $K_{0\max2}$ are the $K_{0\max}$ value of test specimen with d_{M1} and d_{M2} , respectively. Figure 6 shows that the relationship between $(1 - (d_{M1}/d_{M2}))$ and $\ln(K_{0\max1}/K_{0\max2})$ is nonlinear and positive. Fitting with a power function curve to data points, the fitting curves are plotted in Figure 6. As shown in Figure 6, the fitting curves have a good agreement with the corresponding test data. Compared with the test data, the maximum errors of predicted value is less than 10%. Therefore, an equation, to describe the relationship of $K_{0\max}$ and d_M , is obtained:

$$\ln \frac{K_{0\max1}}{K_{0\max2}} = c_0 \left(1 - \frac{d_{M1}}{d_{M2}} \right)^{c_1}, \quad (5)$$

where d_{M1} and d_{M2} are the maximum particle size of test specimens with different GSD prepared by the same preparation technique, and $d_{M1} < d_{M2}$; $K_{0\max1}$ and $K_{0\max2}$ are

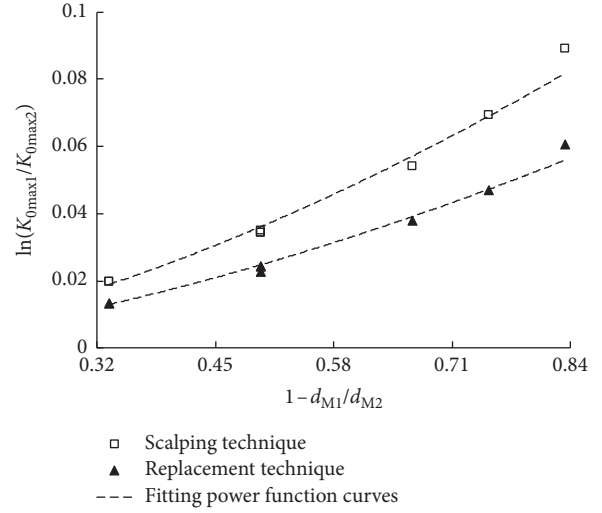


FIGURE 6: $(1 - (d_{M1}/d_{M2})) \sim \ln(K_{0\max1}/K_{0\max2})$ fitting curves for S1~S4 and R1~R4.

the $K_{0\max}$ value of test specimen with d_{M1} and d_{M2} ; and c_0 and c_1 are fitting parameters.

In a similar way, the relationship of $K_{0\min}$ in Equation (4) and d_M may be expressed as

$$\ln \frac{K_{0\min1}}{K_{0\min2}} = c_2 \left(1 - \frac{d_{M1}}{d_{M2}} \right)^{c_3}, \quad (6)$$

where d_{M1} and d_{M2} are the maximum particle size of test specimens with different GSD prepared by the same preparation technique, and $d_{M1} < d_{M2}$; $K_{0\min1}$ and $K_{0\min2}$ are the $K_{0\min}$ value of test specimen with d_{M1} and d_{M2} ; and c_2 and c_3 are fitting parameters.

To verify Equations (5) and (6), $K_{0\max}$ and $K_{0\min}$ and corresponding d_M of P1, P2, and P4 test specimens with $d_M = 10, 40,$ and 60 mm prepared by parallel gradation technique are put into Equations (5) and (6), respectively, and the corresponding $c_0, c_1, c_2,$ and c_3 are determined. For example, for $d_{M1} = 10$ mm and $d_{M2} = 40$ mm, the corresponding $K_{0\max}$ are 0.97 and 0.885 (Table 2), and substituting in Equation (5), an equation with unknowns of c_0 and c_1 is established. Similarly, for $d_{M1} = 10$ mm and $d_{M2} = 60$ mm, another equation is established. Combining these two equations, c_0 and c_1 can be found, and they are 0.115 and 1.609. In a similar way, for Equation (6), c_2 and c_3 are determined, and they are 0.117 and 1.603.

Using Equations (5) and (6) with $K_{0\max}, K_{0\min},$ and corresponding d_M of P1, P2, and P4, when $c_0, c_1, c_2,$ and c_3 are determined, $K_{0\max}$ and $K_{0\min}$ of P3 can be listed in Table 3. It can be seen from Table 3 that based on the test results of P1, P2, and P4, the predicted $K_{0\max}$ and $K_{0\min}$ of P3 are almost the same. Compared with the fitting value given by Equation (4), the maximum error of predicted value is only 1%. Therefore, Equations (5) and (6) are applicable to describe the relationship of $K_{0\max}$ and $K_{0\min}$ versus d_M , respectively.

The arithmetic average of three groups of values predicted by Equations (5) and (6) is used as the predicted

TABLE 3: Predicted $K_{0\max}$ and $K_{0\min}$ of P3.

	P1	P2	P4	Eq. (4)	Maximum difference
$K_{0\max}$	0.924	0.932	0.933	0.926	1%
$K_{0\min}$	0.312	0.314	0.315	0.313	0.9%

$K_{0\max}$ and $K_{0\min}$ of P3. Using Equation (4) with predicted $K_{0\max}$ and $K_{0\min}$ of P3, the $K_0 - \sigma'_v$ fitting curve of P3 is obtained and plotted in Figure 7. It can be seen from Figure 7 that the predicted $K_0 - \sigma'_v$ curves have a good agreement with the corresponding test results. The difference between the K_0 value predicted by Equation (4) and the corresponding test result is less than 4.2%. This observation shows that based on the test data of test specimens with different d_M prepared by a given preparation technique, Equation (4) combined with Equations (5) and (6) can predict well the K_0 behavior of sandy gravels with another d_M prepared by the same preparation technique.

Therefore, based on the test data of test specimens prepared by a given preparation technique, $K_{0\max}$ and $K_{0\min}$ of sandy gravel in situ can be calculated using Equations (5) and (6), and then the K_0 behavior of sandy gravel in situ can be predicted using Equation (4) with corresponding $K_{0\max}$ and $K_{0\min}$ of sandy gravel in situ.

Based on the method discussed above, Equations (5) and (6) are used to fit the test data of test specimens prepared by three preparation technique, and the corresponding fitting parameters are obtained and given in Table 4. As shown in Table 4, the fitting parameters of test specimens prepared by three preparation techniques that are different, which indicates that parameters of Equations (5) and (6) can be only adopted for the same preparation technique.

Using Equation (4) with predicted $K_{0\max}$ and $K_{0\min}$ of sandy gravel in situ, $K_0 - \sigma'_v$ curves of sandy gravel in situ can be predicted as given in Figure 8. Figure 8 shows that the predicted K_0 behaviors of sandy gravel in situ for three preparation techniques are different; however, the maximum difference is below 8%, and thus, the difference may be almost ignored. Therefore, Equation (4) combined with Equations (5) and (6) can predict well the K_0 behavior of sandy gravel in situ.

As mentioned above, the approach to estimate the K_0 behavior of in situ sandy gravel can be summarized as (a) using the same preparation technique to reduce the original GSD of in situ sandy gravel to GSDs of test specimen with different d_M , (b) performing the laboratory K_0 test for those test specimens (c) using Equation (4) to fit the test data and obtain the $K_{0\max}$ and $K_{0\min}$ of test specimens, (d) using Equations (5) and (6) with $K_{0\max}$, $K_{0\min}$, and corresponding d_M of test specimens, $K_{0\max}$ and $K_{0\min}$ of sandy gravel in situ are calculated, and (5) using Equation (4) with $K_{0\max}$ and $K_{0\min}$ of sandy gravel in situ, the K_0 behavior of in situ sandy gravel can be predicted.

5. Conclusions

In this study, scalping technique, replacement technique, and parallel gradation technique are adopted to reduce the

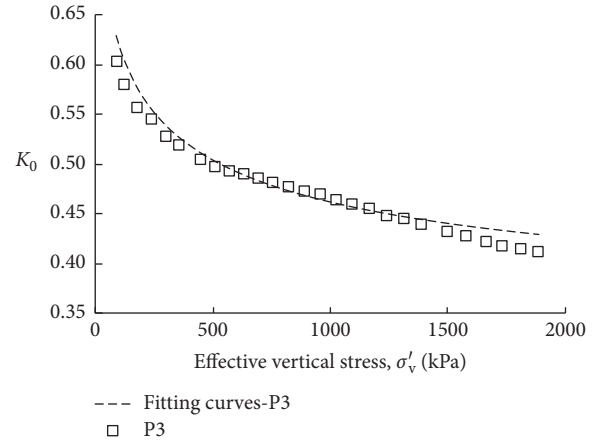
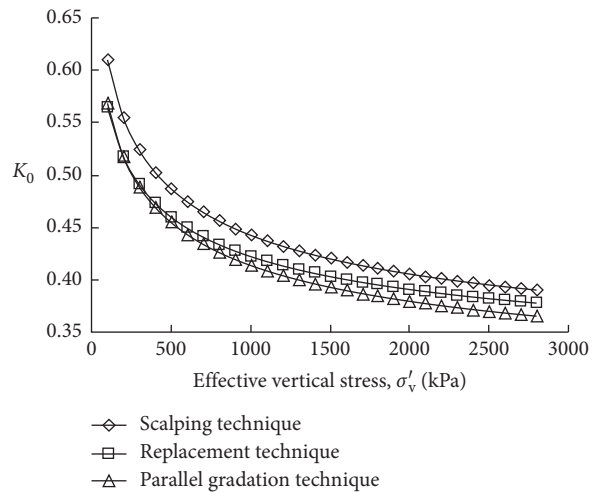
FIGURE 7: Testing and predicting $K_0 - \sigma'_v$ curves for P3.

TABLE 4: Fitting parameters of the tested specimen.

Preparation technique	c_0	c_1	c_2	c_3	$K_{0\max IS}$	$K_{0\min IS}$
Scalping technique	0.109	1.594	0.081	1.483	0.934	0.287
Replacement technique	0.075	1.588	0.144	1.622	0.868	0.27
Parallel gradation technique	0.142	1.546	0.111	1.593	0.84	0.29

FIGURE 8: Prediction of $K_0 - \sigma'_v$ curves under different preparation method.

GSD of in situ sandy gravel to GSDs of test specimen with different d_M , and the K_0 tests for the test specimens were performed using a large-size K_0 test apparatus. According to the test result, the conclusions are drawn as follows:

- (1) K_0 of sandy gravel tends to decrease with the increasing σ'_v , and therefore the influence of σ'_v should be taken into consideration when investigating K_0 behavior of sandy gravel.

- (2) d_M and preparation technique all have some influence on K_0 of test specimen, and different d_M or preparation techniques all induce the scale effect. Therefore, the scale effect should be taken into consideration when using K_0 test results to study the K_0 behavior of sandy gravel in situ.
- (3) Based on K_0 test results, an approach to predict the K_0 behavior of sandy gravel in situ is proposed and verified.

Data Availability

The data used to support the findings of this study are available from the corresponding author upon request.

Conflicts of Interest

The authors declare that there are no conflicts of interest regarding the publication of this paper.

Acknowledgments

The authors gratefully acknowledge the financial support from National Key R&D Program of China (2017YFC0404804), NSFC (Grants nos. 51479052 and 51579167), Postgraduate Research & Practice Innovation Program of Jiangsu Province (KYZZ16_0273), High Level Talents' Project of Lishui City (2015RC16), and Nanjing Hydraulic Research Institute (NHRI) (Grant No. Y316005).

References

- [1] J. Ji, C. Zhang, Y. Gao, and J. Kodikara, "Effect of 2D spatial variability on slope reliability: a simplified FORM analysis," *Geoscience Frontiers*, 2017, In press.
- [2] F. Zhang, Y. F. Gao, Y. X. Wu et al., "Upper-bound solutions for face stability of circular tunnels in undrained clays," *Géotechnique*, vol. 68, no. 1, pp. 1–10, 2017.
- [3] S. Zhu, Y.-M. Wang, and H.-Y. Weng, "Study of scale effect of density of coarse-grained dam materials," *Chinese Journal of Rock Mechanics and Engineering*, vol. 30, no. 2, pp. 348–357, 2011, in Chinese.
- [4] J. Zeller and R. Wullimann, "The shear strength of the shell materials for the Go-Schenenalp Dam, Switzerland," in *Proceedings of 4th Institutional Journal on Soil Mechanics and Foundation Engineering*, vol. 2, pp. 399–404, London, UK, 1957.
- [5] J. Lowe, "Shear strength of coarse embankment dam materials," in *Proceedings 8th International Congress on Large Dams*, pp. 745–761, Edinburgh, UK, May 1964.
- [6] R. J. Frost, *Some Testing Experiences and Characteristics of Boulder Gravel Fills in Earth Dams*, American Society for Testing and Materials, Special Technical Publication, West Conshohocken, PA, USA, 1973.
- [7] W. U. Li-Qiang, Z. Sheng, X. H. Zhang et al., "Analysis of scale effect of coarse-grained materials," *Rock & Soil Mechanics*, vol. 37, no. 8, pp. 2187–2197, 2016, in Chinese.
- [8] A. Bagherzadeh-Khalkhali and A. Asghar Mirghasemi, "Numerical and experimental direct shear tests for coarse-grained soils," *Particology*, vol. 7, no. 1, pp. 83–91, 2009.
- [9] J.-J. Wang, H.-P. Zhang, S.-C. Tang, and Y. Liang, "Effects of particle size distribution on shear strength of accumulation soil," *Journal of Geotechnical & Geoenvironmental Engineering*, vol. 139, no. 11, pp. 1994–1997, 2013.
- [10] D. Kim and S. Ha, "Effects of particle size on the shear behavior of coarse grained soils reinforced with geogrid," *Materials*, vol. 7, no. 2, pp. 963–979, 2014.
- [11] H. Louati, D. Oulahna, and A. D. Ryck, "Effect of the particle size and the liquid content on the shear behaviour of wet granular material," *Powder Technology*, vol. 315, pp. 398–409, 2017.
- [12] M. Abu-Farsakh and X. Yu, "Comparison of predicted embankment settlement from piezocone penetration test with field measurement and laboratory estimated," in *Geotechnical and Geophysical Site Characterization*, pp. 350–355, Taylor & Francis Group, London, UK, 2013.
- [13] K. M. Wei, S. H. Zhu, and X. H. Yu, "Influence of the scale effect on the mechanical parameters of coarse-grained soils," *Transactions of Civil Engineering*, vol. 38, no. 1, pp. 75–84, 2014.
- [14] J.-J. Wang, H.-P. Zhang, M.-W. Liu, and D.-P. Deng, "Compaction behaviour and particle crushing of a crushed sandstone particle mixture," *European Journal of Environmental and Civil Engineering*, vol. 18, no. 5, pp. 567–583, 2014.
- [15] J.-J. Wang, Y.-Z. Cheng, H.-P. Zhang, and D. P. Deng, "Effects of particle size on compaction behavior and particle crushing of crushed sandstone-mudstone particle mixture," *Environmental Earth Sciences*, vol. 73, no. 12, pp. 8053–8059, 2015.
- [16] C. S. Chang, Y.-B. Deng, and Z.-N. Yang, "Modeling of minimum void ratio for granular soil with effect of particle size distribution," *Journal of Engineering Mechanics*, vol. 143, no. 9, article 04017060, 2017.
- [17] Y.-M. Wang, S. Zhu, and J.-M. Ren, "Research on scale effect of coarse-grained materials," *Rock and Soil Mechanics*, vol. 34, no. 6, pp. 1799–1806, 2013, in Chinese.
- [18] J.-J. Wang, Y. Yang, J. Bai, J.-Y. Hao, and T.-L. Zhao, "Coefficient of earth pressure at rest of a saturated artificially mixed soil from oedometer tests," *KSCE Journal of Civil Engineering*, vol. 22, no. 5, pp. 1691–1699, 2017.
- [19] J.-G. Zhu, Y.-Y. Lu, M.-J. Jiang, and F.-Y. Chu, "Development and application of new-type apparatus for K_0 test," *Rock and Soil Mechanics*, no. 8, pp. 1–6, 2008, In press, in Chinese.
- [20] A. O. Landva, A. J. Valsangkar, and S. G. Pelkey, "Lateral earth pressure at rest and compressibility of municipal solid waste," *Canadian Geotechnical Journal*, vol. 37, no. 6, pp. 1157–1165, 2000.
- [21] L. David Suits, T. C. Sheahan, D. Wanatowski, and J. Chu, "Stress-strain behavior of a granular fill measured by a new plane-strain apparatus," *ASTM Geotechnical Testing Journal*, vol. 29, no. 2, pp. 149–157, 2006.
- [22] S. Lirer, A. Flora, and M. V. Nicotera, "Some remarks on the coefficient of earth pressure at rest in compacted sandy gravel," *Acta Geotechnica*, vol. 6, no. 1, pp. 1–12, 2011.
- [23] X. Gu, J. Hu, and M. Huang, " K_0 of granular soils: a particulate approach," *Granular Matter*, vol. 17, no. 6, pp. 703–715, 2015.
- [24] M. Mokhtari, N. Shariatmadari, A. H. R. Ali, and H. Salehzadeh, "Design and fabrication of a large-scale oedometer," *Journal of Central South University*, vol. 22, no. 3, pp. 931–936, 2015.
- [25] J. G. Zhu, M. J. Jiang, Y. Y. Lu, W.-L. Guo, and B. Zhang, "Experimental study on the K_0 coefficient of sandy gravel under different loading conditions," *Granular Matter*, vol. 20, no. 3, p. 40, 2018.
- [26] J. G. Zhu, L. W. Guo, Y. F. Wen, J.-H. Yin, and C. Zhou, "New gradation equation and applicability for particle-size

distributions of various soils," *International Journal of Geomechanics*, vol. 18, no. 2, article 04017155, 2018.

- [27] A. Varadarajan, K. G. Sharma, S. M. Abbas, and A. K. Dhawan, "Constitutive model for rockfill materials and determination of material constants," *International Journal of Geomechanics*, vol. 6, no. 4, pp. 226–237, 2006.
- [28] X.-G. Wang, "Discussion on some problems observed in high earth-rockfill dams," *Chinese Journal of Geotechnical Engineering*, vol. 40, no. 2, 2018, in Chinese.

Research Article

Experimental Studies on Drying-Wetting Cycle Characteristics of Expansive Soils Improved by Industrial Wastes

Hao Ye, Chengfu Chu , Long Xu, Kunlong Guo, and Dong Li

School of Resources and Environmental Engineering, Hefei University of Technology, Hefei 230009, China

Correspondence should be addressed to Chengfu Chu; chuchengfu@163.com

Received 5 June 2018; Revised 26 July 2018; Accepted 16 August 2018; Published 24 September 2018

Academic Editor: Dingwen Zhang

Copyright © 2018 Hao Ye et al. This is an open access article distributed under the Creative Commons Attribution License, which permits unrestricted use, distribution, and reproduction in any medium, provided the original work is properly cited.

The improved engineering properties of the expansive soil by mixing with various additives will be changed during the long-term variation of the meteorological and hydrological conditions. In the present work, a series of tests are performed to investigate the evolution of the unconfined compression strength and the Atterberg limits under drying-wetting cycling conditions for specimens treated by iron tailing sands and calcium carbide slag. Typical results of the unconfined compressive strength can be divided into three stages. The unconfined compressive strength increases initially and then decreases to reach a stable state with continuous drying-wetting process. The calcium carbide slag content (α_{CCS}) of 10% can be determined for the minimum effect of the drying-wetting cycle on the strength of the treated specimen. An exponential relationship is established to describe the evolution of the unconfined compressive strength with the drying-wetting cycle. The liquid limit and plastic index of the specimen increase initially followed by a decreasing trend, while a reverse trend was observed for that of the plastic limit during the drying-wetting process. The minimum effect of the drying-wetting cycle on the Atterberg limits can be presented for the specimen with α_{CCS} of 10% as well.

1. Introduction

Expansive soil is widely distributed in more than 40 countries around the world. Due to the highly contained hydrophilic clay minerals, such as montmorillonite and illite, significant swelling or shrinkage characteristics appear when the expansive soil gains or loses water, respectively. As a result, railway, highway, and buildings in the area of expansive soil severely suffer from ground deformation hazards, which are needed to be avoided in engineering practices [1, 2]. Based on the previous researches, industrial wastes were widely adopted to mix with the expansive soil for the improvement of the roadbed filler consisting of the expansive soil. Common conclusions had been reached that the volumetric deformation of the expansive soil could be effectively controlled by incorporation of the industrial wastes. However, in further period of operation, the meteorological and hydrological changes in the area of expansive soil induce drying-wetting cycling effects, which could result in secondary deterioration of the roadbed fillers

consisting of the treated expansive soils, i.e., significant swelling/shrinkage behavior and limited bearing capacity [3, 4]. Therefore, profound understanding of the engineering properties of the treated expansive soils under drying-wetting cycling conditions is of great significance to the engineering application.

In the previous researches, Gens and Alonso [5] and Alonso et al. [6] investigated the deformation properties of the expansive soil after drying-wetting cycles. Test results presented significant volumetric deformations of the specimens during the cycles. However, the magnitude of the deformation decreases with the increase in the drying-wetting cycle, failing to restore the initial state, which confirmed an irreversible influence of the drying-wetting cycle on the deformation properties of the soils. In further cyclic swell-shrink tests performed on reconstituted specimens, less expansion and shrinkage magnitude, decreased strength, and significant fatigue behavior of the specimen could also be observed during the drying and wetting cycling process, which were attributed to the rearrangement of the

soil particles and destruction of the microstructure [7–9]. Researches performed by Dong and wang [10], Kay and Dexter [11], and Yang and Xiao [12] reported that, with the continuous drying and wetting, the strength and compressibility of the specimen, respectively, decrease and increase in the initial cycles followed by stable trends in the later period. In further step, logarithmic and powder models were successfully adopted to describe the evolutions of strength and compressibility of the specimens with the number of cycles. The effects of the drying-wetting cycles on the shear strength of the specimens were also investigated by Malusis et al. [13], Zhang et al. [14], and Shi et al. [15]. Results showed that, in the early stage of drying-wetting, the number of macrocracks and microcracks in the specimen decreased and increased, respectively. As a result, the structure of the treated expansive soil would be destroyed due to the water infiltration, which would reduce the strength and increase the compressibility of the specimen. Explanations proposed by Wang and Wei [16] indicated that the effect of drying-wetting cycle on the engineering property of clay was attributed to the irreversible volume shrinkage, the increase of large pore volume, and the development of microfissure. The effects of the drying-wetting cycle on the Atterberg limits of specimens were tested and analyzed by Rao et al. [17] and Yang et al. [18]. Results reported that the liquid limit and plasticity index of the specimen increased in the initial period of the drying-wetting cycles followed by a stable state in the latter period. Explanation proposed by Mitchell [19] indicated that the Atterberg limits were related to the water adsorbed in the double electron layer on the surface of the soil particles, which was mainly affected by the size and specific surface area of the particles. The fine particle content in the specimen will increase with the continuous drying-wetting process, which contributed to the increase of liquid limit and plasticity index of the treated specimen.

As presented in previous researches, the engineering properties of the treated expansive soils under drying-wetting cycling conditions were mainly acquired on the basis of qualitative investigations. In the present work, the industrial wastes including iron tailing sands and calcium carbide slag are adopted to treat the expansive soils. After this, the evolution of the engineering properties of the treated soils under drying-wetting cycling conditions is experimentally and quantitatively investigated.

2. Materials and Testing Procedures

2.1. Materials. The soils adopted in the present work were sampled from a foundation pit in Hefei city, Anhui province, China (Figure 1). The basic physical properties of the soils are summarized in Table 1. As shown in Table 1, the free swelling ratio of the soil is in the range of 40%~60%, which could be classified as the weak expansive soils [20–22]. The maximum dry density of 1.83 g/cm^3 and the optimum water content of 16.5% are also determined by performing the compaction test as shown in Figure 2. The particle-size distribution of the tested soil is obtained by using the laser particle size analyzer (Figure 3), which shows the

nonuniform coefficient of 3.16 and curvature coefficient of 0.93.

The industrial wastes including iron tailing sand (ITS) and calcium carbide slag (CCS) were sampled in Anhui, China, which were adopted to treat the expansive soils in the present work (Figure 1). The corresponding chemical components were determined by the X-ray fluorescence (XRF) technique as shown in Table 2. The particle-size distribution of the iron tailing sand is shown in Table 3.

2.2. Testing Procedures. The specimens in the present work were prepared by mixing the expansive soils with the industrial wastes including iron tailing sand and calcium carbide slag. The content of iron tailing sand was fixed at 30% by mass, while the content of calcium carbide slag changing from 6% to 14% was designed in specimen preparation. Then, denotations of α_{CCS} (calcium carbide slag content) were created to represent the mass ratio of the calcium carbide slag to the mixtures.

During specimen preparation, the materials including the expansive soils and the industrial wastes were oven-dried at 100°C for 36 h, then grounded into powders, and sized through a 0.5 mm sieve. According to the optimum water contents determined by compaction tests performed on previously designed mixtures (Figure 4), a certain amount of water was homogeneously mixed with the powders of expansive soil, iron tailing sands, and calcium carbide slag which was cured in a period of 24 h. After this, a target amount of mixtures were statically compacted into a mould to obtain a target cylindrical specimen with a dimension of 50 mm in height, 50 mm in diameter, and the designed dry density equaled to 95% of the maximum dry density. Finally, the prepared specimens were maintained under standard curing conditions (temperature 20°C and relative humidity 95%) for 14 and 28 days, respectively.

When the curing was finished, the specimens were taken out to perform the drying-wetting cycling tests [23, 24]. In the drying process, each specimen was wrapped with plastic film and placed in an oven with temperature at $60 \pm 1^\circ\text{C}$ for 23 h. In the subsequent wetting process, the specimen was taken out from the oven and placed on a porous stone in an immersion chamber with temperature at $20 \pm 1^\circ\text{C}$ for 1 h (Figure 5). After this, distilled water was continuously added to immerse the porous stone and maintained for 23 h. Finally, the specimen was taken out of the chamber followed by 1 h equilibrium. Then the procedures mentioned above were repeated for 1, 3, 5, 7, 10, and 15 cycles.

After the designed drying-wetting cycles, the unconfined compressive strength tests were performed on the specimens following the *Standard Test Method for Unconfined Compressive Strength of Cohesive Soil (ASTM D2166-06)* [25]. The YHS-2[®] UCS testing apparatus with a vertical strain rate of 1%/min was adopted in the test, and three parallel specimens were tested in each test with the average value as the representative one. Tests for determination of the Atterberg limits were carried out according to the *Standard Test Methods for Liquid Limit, Plastic Limit, and Plasticity Index of Soils (ASTM D4318-17)* [26]. Two parallel specimens were

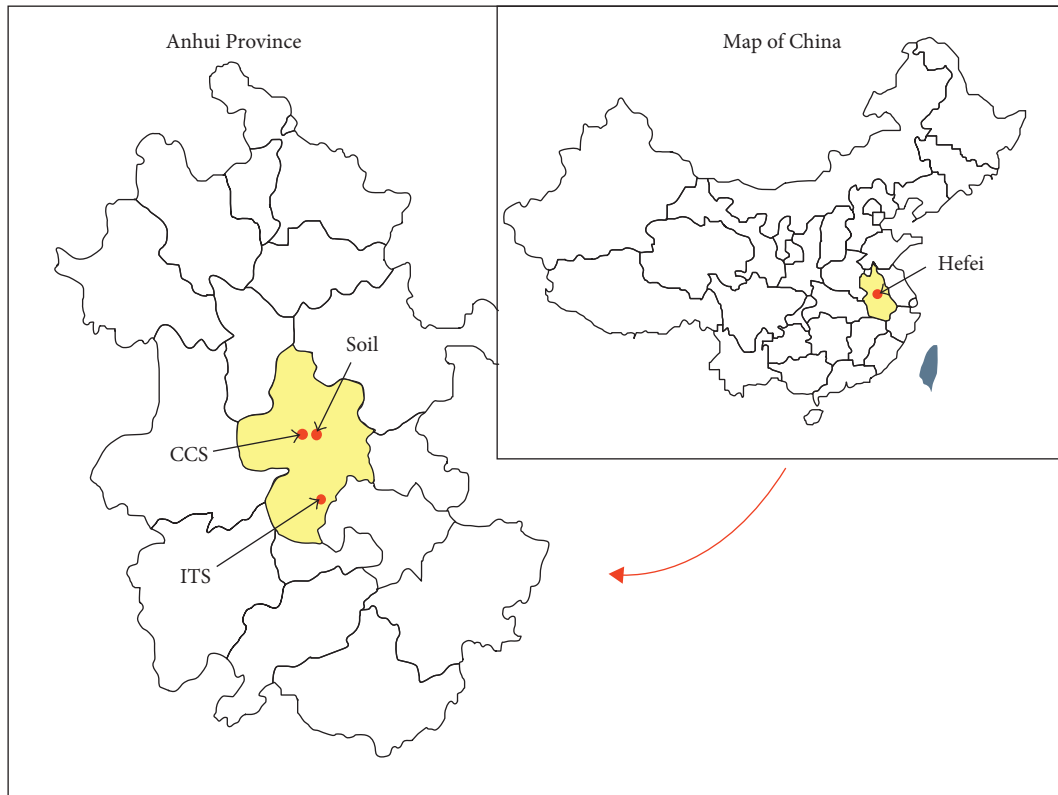


FIGURE 1: Sampling sites of the tested materials.

TABLE 1: Basic physical properties of the tested soils.

Density (g/cm)	Specific gravity	Void ratio	Liquid limit (%)	Plastic limit (%)	Plasticity index	Free swelling ratio (%)
1.92	2.72	0.76	46.6	22.1	24.5	53

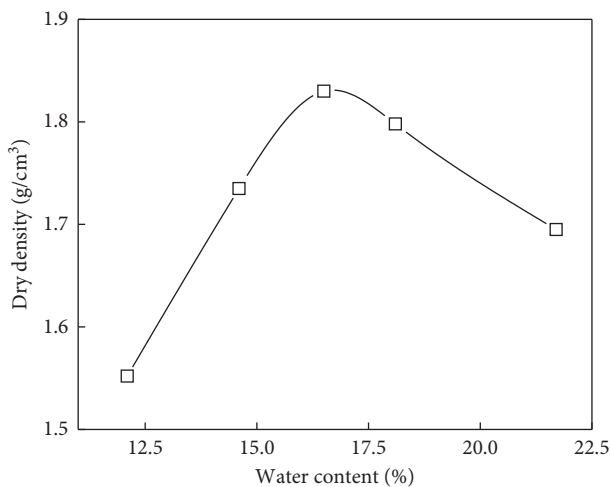


FIGURE 2: Compaction curve of the tested soils.

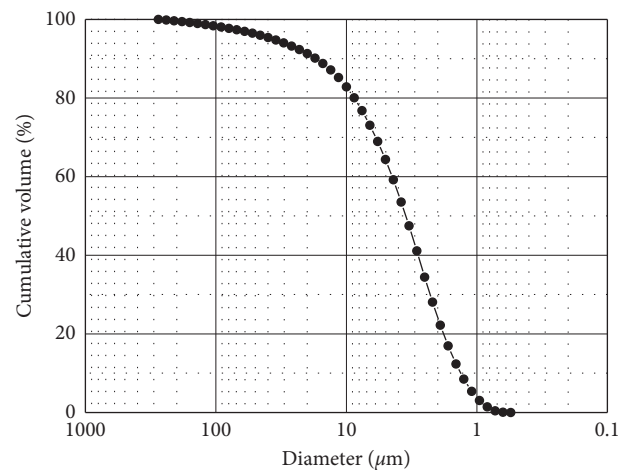


FIGURE 3: Particle-size distribution of the tested soil.

tested in each test with the average value as the representative one. In addition, the fine particle content (<0.002 mm) of the specimen after drying-wetting cycles was determined by performing particle-size analysis for mechanism research.

3. Test Results and Analysis

3.1. *Unconfined Compressive Strength.* Evolutions of the unconfined compressive strength with the number of drying-wetting cycles for specimens tested in the present work are shown in Figure 6.

TABLE 2: Chemical component of iron tailing sands and calcium carbide slag.

Components	SiO ₂	Al ₂ O ₃	Al ₂ O ₃	CaO	MgO	SO ₃
Contents (%) ITS	65.51	9.31	11.73	3.18	5.75	0.71
Contents (%) CCS	6.21	3.79	0.51	63.43	0.27	0.19

TABLE 3: Particle-size distribution of the iron tailing sands.

<2 mm	<1 mm	<0.5 mm	<0.25 mm	<0.075 mm
97.25	91.45	72.27	51.97	6.98

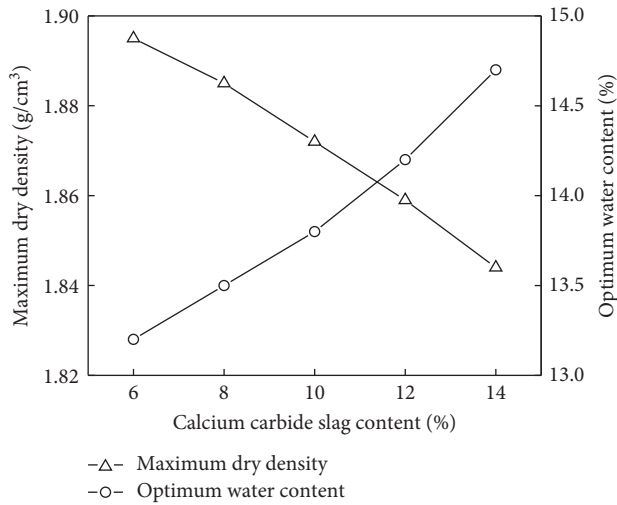


FIGURE 4: Compaction curves of the mixtures with different calcium carbide slag contents.



FIGURE 5: Drying-wetting cycling test in the present work.

As shown in Figure 6(a), for the specimens with a curing time of 14 d, the evolution of the unconfined compressive strength with the drying-wetting cycles can be divided into three stages. Initially, the unconfined compressive strength increases with the increase of the drying-wetting cycle, which could be attributed to the uncompleted physical and chemical reactions between the calcium carbide slag, the

expansive soil, and the existing water in the specimen. After the achievement of the peak value, the unconfined compressive strength starts to decrease and the decreasing rate reduces with the increase of the drying-wetting cycle. In this stage, the repeated drying-wetting process will induce the microcracks and destroy the integrity of the specimen followed by the infiltration of the water along the cracks, which results in the reduction of the unconfined compressive strength. Finally, after 10 cycles of drying-wetting, the unconfined compressive strength tends to be stable due to the limited variation of the microstructure of the specimen. As shown in Figure 6(b), a slight difference could be observed for the specimen with a curing time of 28 d, and only the latter two stages are presented in the strength evolution with the drying-wetting process, which is due to the completed physical and chemical reactions between the industrial wastes and the soils during the 28 d curing time.

The curves in Figure 6 also show significant effect of calcium carbide slag content (α_{CCS}) on the strength. In further analysis, the stable values of the unconfined compressive strengths after 15 drying-wetting cycles are extracted (Figure 7). As shown in Figure 7, the unconfined compressive strength increases initially and then decreases with α_{CCS} increasing. The maximum value of the strength is reached when α_{CCS} equals to 10%. It is clear that the initial increase of the calcium carbide slag content in the specimen will result in more intensive crystallization, pozzolanic, and carbonation reactions between the calcium carbide slag and the soils. Then the strength of the specimen increases with the formation of the hydrated calcium silicate, hydrated calcium aluminate, and CaCO₃ crystal. However, when a critical value of α_{CCS} is reached, the strength of the specimen will be controlled by the calcium carbide slag, which results in decreased strength of the specimen due to the lower strength of calcium carbide slag than that of the soil. According to the results presented in Figure 7, the critical α_{CCS} could be determined as 10%, which is the optimal value for improvement of the expansive soils by mixing with the industrial wastes.

In further step, since the uncompleted physical and chemical reactions between the calcium carbide slag, the expansive soil, and the existing water in the specimen, an exponential relationship is established to describe the evolution of the unconfined compressive strength with the drying-wetting cycles for the specimen with a curing time of 28 d, which is shown in Figure 8 and Equation (1), and the specific parameters for all tests are listed in Table 4:

$$q_u = A \cdot \exp(B \cdot N) + C, \quad (1)$$

where q_u is the unconfined compressive strength, MPa, and N is the number of drying-wetting cycles.

It is clearly shown in Table 4 that the parameters A and B are almost independent of the variation of α_{CCS} . Then, the average values of 2.0 and -0.20 can be adopted as the representative ones for A and B , respectively. The parameter C is strongly dependent on the variation of α_{CCS} . According to the researches performed by Dong and Wang [10], a linear

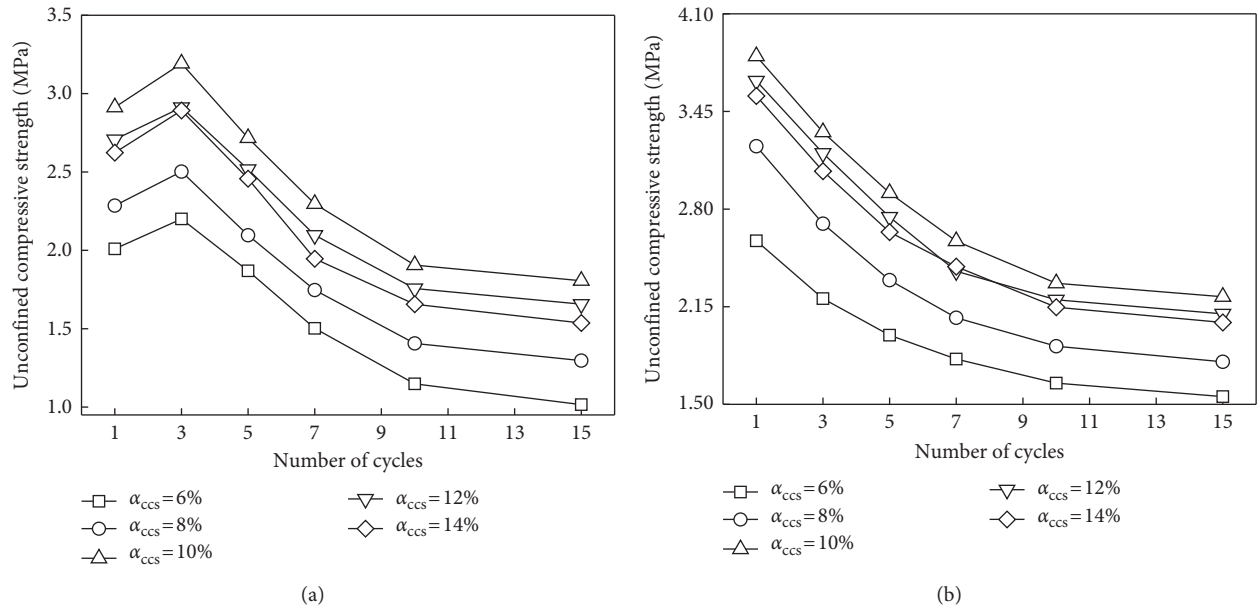


FIGURE 6: Evolutions of the unconfined compressive strength during the drying-wetting process. Curing time: (a) 14 d and (b) 28 d.

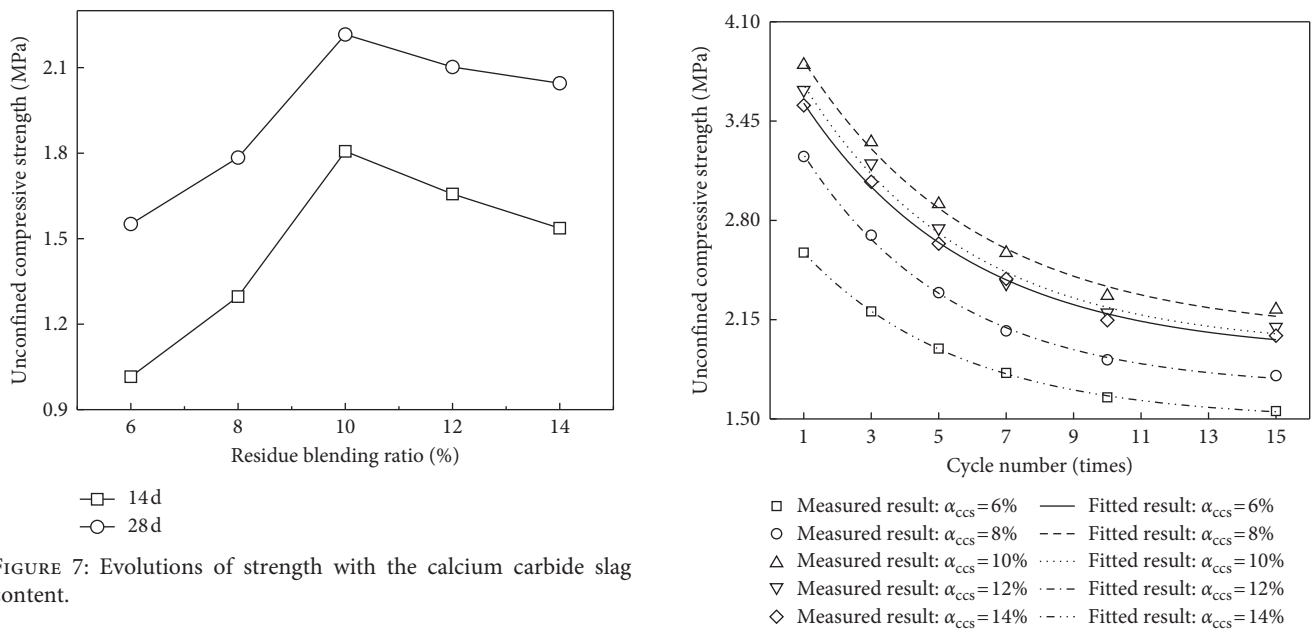


FIGURE 7: Evolutions of strength with the calcium carbide slag content.

relationship between the initial strength and the parameter C is established as presented in the following equation:

$$C = K \cdot q_{u0}, \quad (2)$$

where q_{u0} is the initial unconfined compressive strength of the specimen (MPa), which equals to 2.59 MPa, 3.19 MPa, 3.82 MPa, 3.65 MPa, and 3.55 MPa for the specimen with α_{CCS} of 6%, 8%, 10%, 12%, and 14%, respectively, and K is the linear coefficient that can be determined in the evolution of the parameter K with the calcium carbide slag content (Figure 9). It is evident that the variation of K is limited and average value of 0.54 can be used in the present work.

By submitting the values of parameters A , B , and K and Equation (2) into Equation (1), the empirical relation

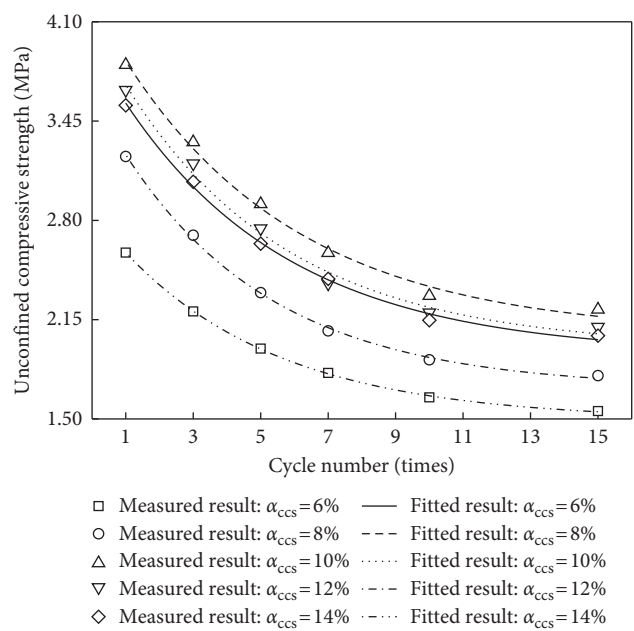


FIGURE 8: Relationships between the unconfined compressive strength and the number of drying-wetting cycles.

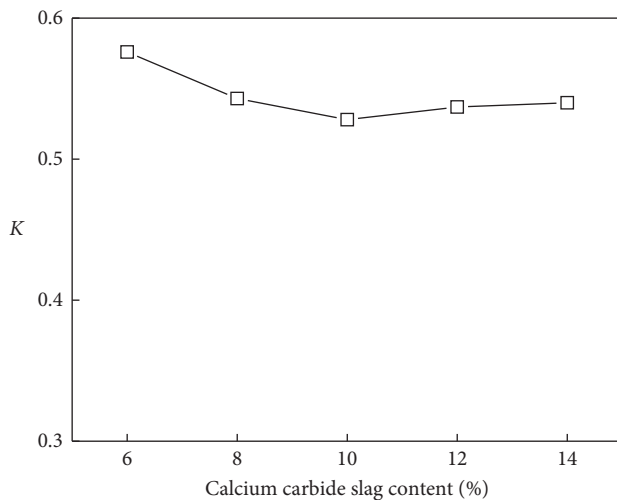
between the unconfined compressive strength and the drying-wetting cycle can be finally determined in the following equation:

$$q_u = 2 \cdot \exp(-0.20N) + 0.54q_{u0}, \quad R^2 = 0.992. \quad (3)$$

It is clearly shown in Equation (3) that the strength of the specimen under the drying-wetting cycling condition is only related to the cycle number and initial strength of the specimen, which is also reflected as the parallel curves in Figure 6. Therefore, the empirical relationship can be used to predict the unconfined compressive strength of the

TABLE 4: Parameters of the exponential relationship.

Calcium carbide slag content (%)	A	B	C	Goodness-of-fit (R^2)
6	1.85	-0.21	1.49	0.991
8	1.91	-0.22	1.70	0.997
10	2.17	-0.19	2.01	0.991
12	2.12	-0.20	1.96	0.985
14	2.01	-0.20	1.92	0.996

FIGURE 9: Evolutions of the parameter K with the calcium carbide slag content.

expansive soils treated with iron tailing sands and calcium carbide slag under drying-wetting cycling conditions.

3.2. Atterberg Limits. The evolutions of the liquid limit and the plastic limit with the drying-wetting cycle of the treated specimen are presented in Figure 10.

As shown in Figure 10, the liquid limit of the specimen increases initially followed by a decreasing trend, while a reverse trend can be observed for the evolution of the plastic limit during the drying-wetting process. This is because that the Atterberg limits are related to the water adsorbed in the double electron layer on the surface of the soil particles, which is mainly affected by the size and specific surface area of the particles. The microstructure of the specimen will be destroyed during continuous drying-wetting cycles resulting in the increase of the fine particle content (<0.002 mm) in the specimen as shown in Figure 11. As a result, the liquid limit of the specimen increases and the plastic limit decreases in the initial period [19]. However, after a certain number of drying-wetting cycles, the formation of microfissures leads to the fully developed water flow in the specimen, which will wash the fine particles away and result in the decrease of the liquid limit, as well as the increase of the plastic limit, of the specimen.

In order to investigate the effect of α_{CCS} on the Atterberg limits of the specimen, the maximum and minimum liquid limits and plastic limit of the specimen shown in Figure 10(a) are listed in Table 5. It is clear that the variations

of the Atterberg limits become limited when α_{CCS} is around 10%, which implies the minimum effect of the drying-wetting cycles on the microstructure of the specimen. Therefore, it could be concluded that the optimal α_{CCS} for improvement of the expansive soil is around 10%, which is consistent with the conclusion obtained from the unconfined compressive strength tests.

The plastic index of the specimens tested in the present work are calculated and presented in Figure 12. The curves in Figure 12 clearly showed that the plastic index of the specimen increases initially followed by a decreasing trend. This is because that the plastic index is related to the water adsorbed in the double electron layer on the surface of the soil particles, especially for the fine particles. During the continuous drying-wetting cycles, the microstructure of the specimen is destroyed and then it forms lots of fine particles in the specimen, which results in the increase of the plastic index. However, after a certain number of drying-wetting cycles, the formation of microfissures leads to the fully developed water flow in the specimen. The fine particles will be washed away along the microfissures, which results in the decrease of the plastic index.

4. Conclusions

In the present work, the unconfined compressive strength and the Atterberg limits of the industrial waste-treated expansive soils under the drying-wetting cycling conditions are investigated. Some main conclusions can be summarized as follows:

- (1) For specimens with a curing time of 14 d, the unconfined compressive strength initially increases with the increase of the drying-wetting cycle. After the achievement of the peak value, the unconfined compressive strength starts to decrease and the decreasing rate reduces with the increase of drying-wetting cycle. After 10 cycles of drying-wetting, the unconfined compressive strength tends to be stable. For the specimen with a curing time of 28 d, only the latter two stages could be observed in the strength evolution with the drying-wetting process.
- (2) An exponential relationship can be adopted to describe the evolution of the unconfined compressive strength with the drying-wetting cycles for expansive soils treated with iron tailing sands and calcium carbide slag.
- (3) During drying-wetting cycles, the liquid limit and the plastic index of the specimen increases initially

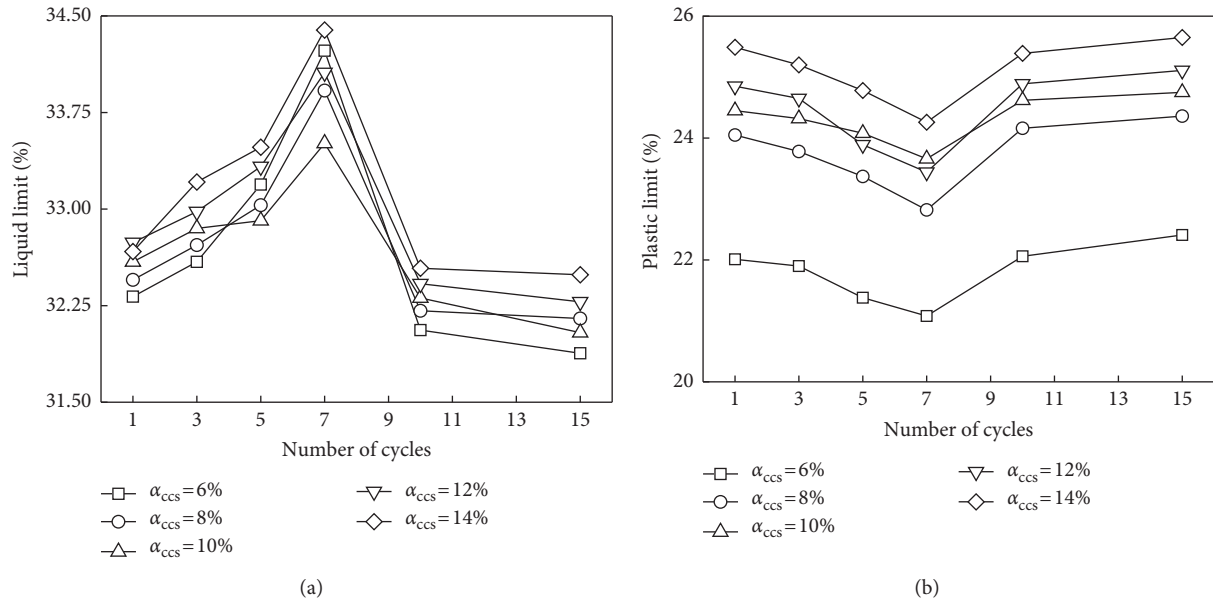


FIGURE 10: Evolutions of the Atterberg limits with the number of drying-wetting cycles: (a) liquid limit and (b) plastic limit.

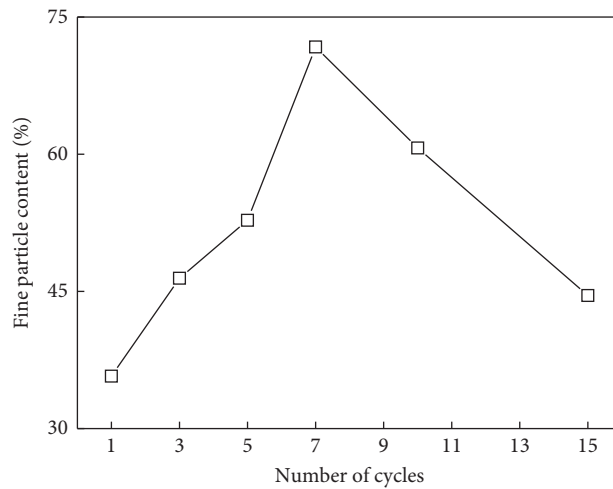


FIGURE 11: Relationships between of the fine particle content and the number of drying-wetting cycles.

TABLE 5: Atterberg limits of the tested specimen.

Calcium carbide slag content (%)	Maximum (%)				Minimum (%)				Variation magnitude (%)	
	Liquid limit	Number of cycles	Plastic limit	Number of cycles	Liquid limit	Number of cycles	Plastic limit	Number of cycles	Liquid limit	Plastic limit
6	34.23		22.06		31.88		21.08		7.37	4.65
8	33.92		24.36		32.15		22.82		5.50	6.75
10	33.51	7	24.75	10	32.02	10	23.66	7	4.59	4.60
12	34.06		25.11		32.28		23.44		5.55	7.12
14	34.39		25.65		32.49		24.26		5.58	5.73

followed by a decreasing trend, while a reverse trend can be observed for the evolution of the plastic limit.

(4) Investigations on the unconfined compressive strength and the Atterberg limits show that the critical α_{CCS} of 10% could be determined as the

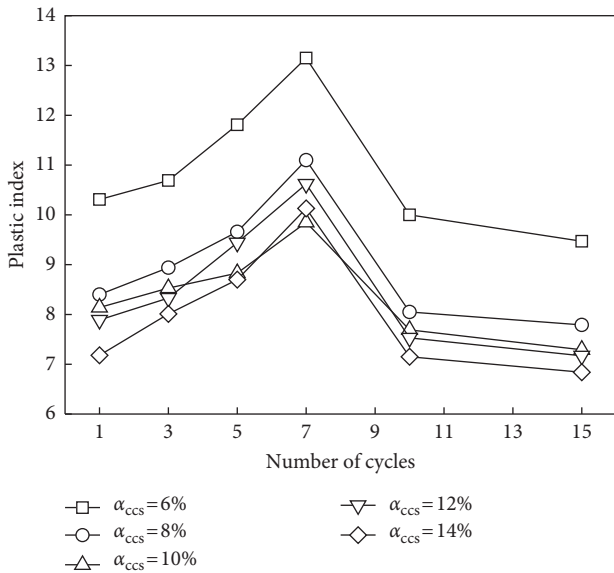


FIGURE 12: Evolutions of the plastic index with the number of drying-wetting cycles.

optimal value for improvement of the expansive soils by mixing with the industrial wastes, which implies the minimum effect of drying-wetting cycles on the properties of the specimen.

Data Availability

The data used to support the findings of this study are included within the article.

Conflicts of Interest

The authors declare that they have no conflicts of interest.

Acknowledgments

The authors are grateful to the financial support of Anhui Provincial National Science Foundation (Grant no. 1608085MD81), the National Science Foundation of China (Grant nos. 41572280 and 41672306), and China Scholarship Council (CSC) (Grant no. 201606695047).

References

- [1] B. R. Phani Kumar, R. S. Sharma, and M. ASCE, "Effect of fly ash on engineering properties of expansive soils," *Journal of Geotechnical and Geoenvironmental Engineering*, vol. 103, no. 7, pp. 764–767, 2004.
- [2] J. Yang, Z. Yang, G. D. Zhang, Y. W. Tang, and H. P. Chen, "Experimental research on the mixed sand ratio and initial dry density of weathered sand improved expansive soil free load swelling rate," *Engineering Science*, vol. 12, no. 3, pp. 77–83, 2014.
- [3] S. C. Qi and S. K. Vanapall, "Hydro-mechanical coupling effect on surficial layer stability of unsaturated expansive soil slopes," *Computers & Geotechnics*, vol. 70, pp. 68–82, 2015.
- [4] C. W. W. Ng, L. T. Zhan, C. G. Bao, D. G. Fredlund, and B. W. Gong, "Performance of an unsaturated expansive soil slope subjected to artificial rainfall infiltration," *Geotechnique*, vol. 53, no. 2, pp. 143–157, 2003.
- [5] A. Gens and E. E. Alonso, "A framework for the behaviour of unsaturated expansive clays," *Canadian Geotechnical Journal*, vol. 29, no. 6, pp. 1013–1032, 1992.
- [6] E. E. Alonso, A. Gens, and A. Josa, "A constitutive model for partially saturated soils," *Géotechnique*, vol. 40, no. 3, pp. 405–430, 1990.
- [7] P. C. Knodel, A. E. Dif, and W. F. Blumel, "Expansive soils under cyclic drying and wetting," *Geotechnical Test Journal*, vol. 14, no. 1, pp. 96–102, 1991.
- [8] A. A. Basma, A. S. Al-Hamoud, A. I. H. Malkawi, and M. A. AlBashabsheh, "Swelling-shrinkage behavior of natural expansive clays," *Applied Clay Science*, vol. 11, no. 1–4, pp. 211–227, 1996.
- [9] A. S. Al-Homoud, A. A. Basma, A. I. H. Malkawi, and M. A. A. Bashabsheh, "Cyclic swelling behavior of clays," *Journal of Geotechnical Engineering*, vol. 121, no. 7, pp. 562–565, 1995.
- [10] Y. Dong and B. T. Wang, "Test study on mechanical properties of the lime stabilized expansive soil under wet and dry cycle," *Applied Mechanics and Materials*, vol. 174–177, pp. 166–170, 2012.
- [11] B. D. Kay and A. R. Dexter, "The influence of dispersible clay and wetting-drying cycles on the tensile strength of a red-brown earth," *Australian Journal of Soil Research*, vol. 30, no. 3, pp. 297–310, 1992.
- [12] H. P. Yang and D. Xiao, "The influence of alternate dry-wet effect on the strength characteristic of expansive soils," *Journal of Hunan Light Industry College*, vol. 4, no. 4, pp. 1–5, 2005.
- [13] M. A. Malusis, S. Yeom, and J. C. Evavs, "Hydraulic conductivity of model soil-bentonite backfills subjected to wet-dry cycling," *Canadian Geotechnical Journal*, vol. 48, no. 8, pp. 1198–1211, 2011.
- [14] Z. J. Zhang, M. J. Tao, and M. Morvant, "Cohesive slope surface failure and evaluation," *Journal of Geotechnical and Geoenvironmental Engineering*, vol. 131, no. 7, pp. 898–906, 2005.
- [15] B. X. Shi, S. S. Chen, H. Q. Han, and C. F. Zheng, "Expansive soil crack depth under cumulative damage," *Scientific World Journal*, vol. 2014, Article ID 498437, 9 pages, 2014.
- [16] G. Wang and X. Wei, "Modeling swelling-shrinkage behavior of compacted expansive soils during wetting-drying cycles," *Canadian Geotechnical Journal*, vol. 1, no. 6, pp. 783–794, 2015.
- [17] S. M. Rao, B. V. V. Reddy, and M. Muttharam, "Effect of cyclic wetting and drying on the index properties of a lime-stabilised expansive soil," *Ground Improvement*, vol. 5, no. 3, pp. 107–110, 2001.
- [18] C. B. Yang, F. S. Zha, and K. R. Cui, "Effect of cyclic wetting and drying on the engineering properties of stabilized expansive soils," *Industrial Construction*, vol. 42, no. 1, pp. 98–102, 2012, in Chinese.
- [19] J. K. Mitchell, *Fundamentals of Soil Behavior*, Wiley & Sons, New York, NY, USA, 1993.
- [20] S. X. Chen, Y. Song, L. W. Kong, A. G. Guo, and G. S. Liu, "Study on approach to identification and classification of expansive soils," *Rock and Soil Mechanics*, vol. 26, no. 12, pp. 1895–1900, 2005, in Chinese.
- [21] H. Duan, S. X. Chen, F. Yu, and X. C. Xu, "Applicability of recommended classification in specification method for expansive soil in the middle area of Anhui province," *Chinese Journal of Rock Mechanics and Engineering*, vol. 25, no. 10, pp. 2121–2127, 2006, in Chinese.

- [22] Urban-Rural Development of the People's Republic of China, *Technical Code for Buildings in Expansive Soil Regions (GB50112-2013)*, China Architecture & Building Press, Beijing, China, 2012.
- [23] F. S. Zha, J. J. Liu, L. Xu, and K. R. Cui, "Cyclic wetting and drying tests on heavy metal contaminated soils solidified/stabilized by cement," *Journal of Geotechnical Engineering*, vol. 35, no. 7, pp. 1246–1252, 2013, in Chinese.
- [24] ASTM, "Standard test method for wetting and drying test of solid wastes," in *Annual Book of ASTM Standards D4843–88*, American Society of Testing and Materials (ASTM), West Conshohocken, PA, USA, 2016.
- [25] ASTM, "Standard test method for unconfined compressive strength of cohesive soil," *Annual Book of ASTM Standards D2166-06*, American Society of Testing and Materials (ASTM), West Conshohocken, PA, USA, 2006.
- [26] ASTM, "Standard test methods for liquid limit, plastic limit, and plasticity index of soil," *Annual Book of ASTM Standards D4318-17*, American Society of Testing and Materials (ASTM), West Conshohocken, PA, USA, 2010.

Research Article

Analysis of Large-Strain Consolidation Behavior of Soil with High Water Content in Consideration of Self-Weight

Yupeng Cao ¹, Jian Yang ¹, Guizhong Xu ², and Jianwen Xu ¹

¹College of Transportation, Shandong University of Science and Technology, No. 579, Qianwan'gang Road, Qingdao, Shandong 266590, China

²Geotechnical Research Institute, Yancheng Institute of Technology, No. 9, Xiwang Road, Yancheng, Jiangsu 224051, China

Correspondence should be addressed to Yupeng Cao; paradise456917@163.com

Received 20 April 2018; Revised 3 July 2018; Accepted 13 August 2018; Published 20 September 2018

Academic Editor: Xinbao Yu

Copyright © 2018 Yupeng Cao et al. This is an open access article distributed under the Creative Commons Attribution License, which permits unrestricted use, distribution, and reproduction in any medium, provided the original work is properly cited.

Based on the axisymmetric large-strain consolidation (ALSC) model with the void ratio as the variable under equal strain condition, difference schemes of model's equation, initial condition, and boundary condition were given. Taking phosphatic clay in Florida as a research object, the consolidation behaviors of soil with high water content by axisymmetric large-strain theory and one-dimensional large-strain theory were analyzed. The effect of different kinds of consolidation theories and self-weight stress on an average degree of consolidation was evaluated. The development of the void ratio and excess pore water pressure along the soil layer was clarified. The results show that the theoretical value of Terzaghi's consolidation degree is always less than that of ALSC (U_s , the average degree of consolidation defined by strain)-vertical drainage in the consolidation process. Terzaghi's solution overestimates the dissipation rate of excess pore water pressure during the earlier consolidation period but underestimates it during the later consolidation period. The degree of consolidation calculated by Hansbo develops faster than ALSC (U_p , the average degree of consolidation defined by stress)-radial drainage, but slower than ALSC (U_s)-radial drainage. In the ALSC model, U_s is always been faster than U_p . The effect of self-weight on the consolidation degree of axisymmetric large-strain consolidation theory is relatively small (maximum error is less than 16%), while it can accelerate the consolidation rate of soil in one-dimensional large-strain consolidation theory largely. When only the vertical drainage occurs, the consolidation rate in the middle of the soil is obviously lagging the upper and lower parts, while the radial drainage can reduce the void ratio and the excess pore water pressure along the soil layer uniformly and more rapidly.

1. Introduction

In dredging projects, such as port and dock construction projects, the treatment of large-area soft soils is often encountered. Due to the low permeability of soft soils, the consolidation rate under self-weight and applied loads is slow, and prefabricate vertical drains (such as plastic drainage boards) are often used in the site works to speed up the consolidation process of soil. Consolidation with the vertical drainage body in soft soil can be simplified as a single well consolidation problem. Axisymmetric consolidation theory proposed by Barron [1] is widely accepted, and the degree of soil's consolidation can be predicted by analytical or numerical methods. The consolidation properties of soil

can be revealed by this theory. Over the years, based on Barron's axial symmetry consolidation theory, the in-depth study of soil consolidation behavior was carried out from many aspects, such as well resistance and smearing [2–5], loading changes over time [6–10], nonlinear compression and penetration parameters [11, 12, 13], negative pressure loading [14, 15, 16, 17], and multi-layer [18, 19]. It provides theoretical support for design and calculation of the consolidation method with vertical drains in practical projects.

However, the accuracy of prediction and analysis of soil consolidation behavior is not only related to the parameters used in the model and calculation methods but also essentially related to the consolidation model itself. When using the above-mentioned theoretical models for

consolidation analysis of supersoft foundations, especially those with high water ocean soft soils or dredged soils that are in a flow state, there is a big difference between the theoretical and the field values [20]. This is mainly because these theoretical models are all based on the assumption of small strain, without considering the effect of large geometric strains.

Fox et al. [21] used a series of small-strain calculations to perform large-strain radial consolidation analysis by displacement-corrected coordinates. However, the variation of material nonlinearity with geometric large deformation was not considered. Indraratna et al. [22] analyzed the large-strain consolidation behavior considering radial nonlinear flow and non-Darcy's law under vacuum loading without considering vertical seepage. Jiang et al. [20] coupled geometric nonlinearity and material nonlinearity, considering vertical and radial simultaneous seepage, and expanded Gibson's one-dimensional large-strain consolidation theory to axisymmetric large-strain consolidation theory. More recently, Zhang et al. [23], Hu et al. [24], and Sun et al. [25] studied the sand-drained large-strain consolidation model with double-layer foundations, creep, and partially penetrated sand wells, respectively. Although the smearing effect controls the consolidation rate of soil [3], its effect on consolidation properties cannot be quantitatively described by these theories.

It should be pointed out that the above-mentioned theory of large-strain consolidation is under free-strain conditions (equal stress consolidation). Some scholars believe that under axisymmetric consolidation, the soil is closer to the state of free strain [7]. From the perspective of practical engineering, some scholars have pointed out that equal settlement is easier to achieve in the project because the horizontal spacing of vertical drainage bodies is the same [21]. The soil consolidation near the sand well is fast, which will cause the contact stress redistribution [26]. It is undeniable that results from the equal strain solutions and the free-strain solutions are very close [1, 3, 7, 27]. The theoretical solution based on the equal strain hypothesis is relatively simple. It can also easily reflect the effect of soil compression characteristics on consolidation in smeared and undisturbed zones. At present, researchers generally assume that the consolidation problem of sand wells is an equal vertical strain problem [26]. In order to facilitate the comparative analysis of large- and small-strain consolidation theories, Cao et al. [28, 29] established the axisymmetric large-strain consolidation model in positive loading pressure (named ALSC) and negative vacuum pressure (named NALSC) with the void ratio as the variable under equal strain condition and verified the validity of these models.

The axisymmetric large-strain consolidation theory breaks through the small-strain theoretical framework and can accurately analyze the settlement characteristics of soils. However, the focus of researchers is mainly on verifying the theory through numerical or analytical solutions or on the development of consolidation rate [20, 23, 24, 25, 28, 29]. Very few studies investigated the difference between axisymmetric large-strain and small-strain theories considering self-weight stress. Also, the effect of gravity stress and radial

drainage on the large-strain consolidation characteristics was not adequately investigated, especially for under-consolidated dredged soils with high water content.

In this study, based on the ALSC model, difference schemes of the consolidation equation, initial conditions, and boundary conditions were included. Taking the phosphatic clay in Florida as a research object [30], vertical drainage bodies were arranged based on scenario C (quiescent consolidation and surcharge loading of a pond having a uniform initial void ratio) to investigate the consolidation behavior of soils with high water content. The difference between the calculated values of large- and small-strain under axial symmetry and one-dimensional consolidation theory was analyzed. The influence of self-weight on the average degree of consolidation was considered. The variation of the void ratio and excess pore water pressure along soil height and consolidation time under different drainage modes was studied.

2. ALSC Model

Figure 1 shows the schematic representation of the case of a circular soil cylinder where a vertical drain is surrounded by a smeared zone and undisturbed soil. The soil has an initial layer thickness L , and it is freely draining at the top and impermeable at the bottom. The center of the cylinder contains a vertical drain well of radius r_w surrounded by a zone of remolded soil by radius r_s . The smear zone is surrounded by undisturbed soil with a radius of influence r_e . Let k_s and k_h represent the horizontal permeability of the smear zone and undisturbed zone, respectively, and k_v represent the vertical permeability of soil.

The convective coordinate ξ measured downwards in the direction of gravity is the same with one-dimensional large-strain consolidation. The Euler polar coordinates (r, θ) are used for radial flows, where r is measured away from the drain (Figure 2). Q_1 and Q_2 represent the vertical pore water inflow and outflow of the unit cell in the soil at a unit time, respectively. Q_3 and Q_4 represent the radial pore water inflow and outflow of the unit cell in the soil at a unit time, respectively.

Coupled flow equation, continuous equation of the saturated soil, stress balance equation, effective stress principle, etc. [28] established the ALSC model with the void ratio as variable under equal strain station. The model accounts for smear effect, soil self-weights, radial and vertical flows, and variable permeability and compressibility during the consolidation progress. Well resistance is not considered. The consolidation equation is expressed as shown in the following equation:

$$\begin{aligned} \frac{\partial e}{\partial t} - (G_s - 1) \frac{d}{de} \left(\frac{k_v}{1+e} \right) \frac{\partial e}{\partial z} + \frac{\partial}{\partial z} \left[\frac{k_v}{\gamma_w (1+e)} \frac{d\sigma'}{de} \frac{\partial e}{\partial z} \right] \\ = - \frac{8k_h (1+e)}{\gamma_w d_c^2 \mu} [(G_s - 1) \gamma_w z - \sigma' + q], \end{aligned} \quad (1)$$

where G_s is the specific gravity of the solid particles, γ_w is the unit weight of water, q is the loading pressure; n is the ratio

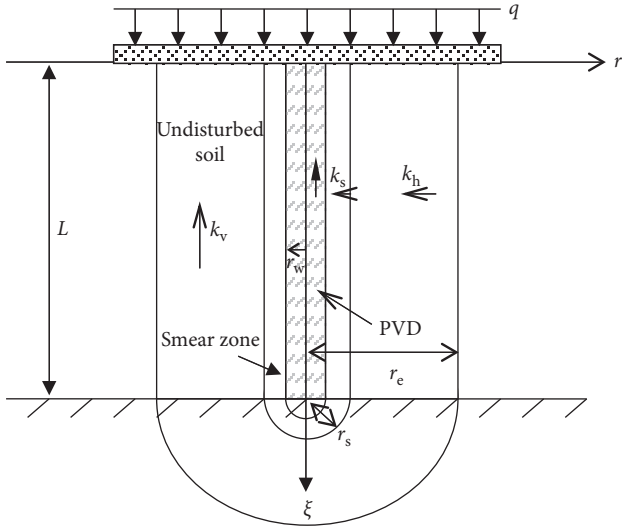


FIGURE 1: Schematic diagram of the typical cylindrical cell.

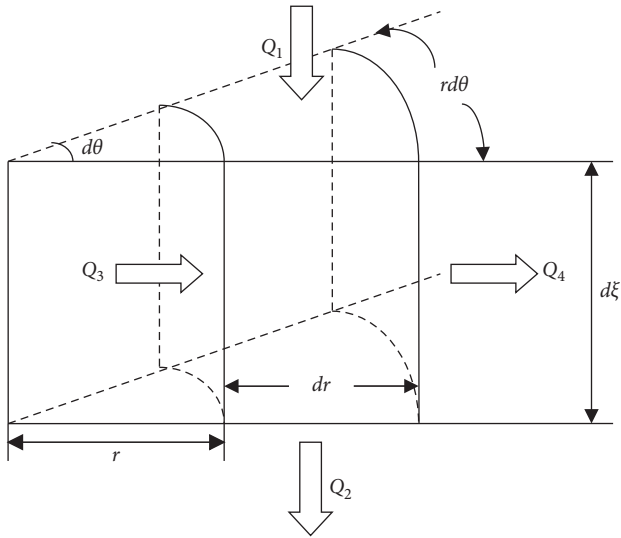


FIGURE 2: The diagram of coordinates systems.

r_e/r_w , s is the ratio r_s/r_w , σ' is the effective vertical stress, e is the void ratio, z is the spatial vertical coordinates in the Lagrange coordinate system, and d_e is the diameter of influence. μ is expressed as follows:

$$\mu = \frac{n^2}{(n^2-1)} \left(\ln \frac{n}{s} - \frac{3}{4} + \frac{k_h}{k_s} \ln s \right) + \frac{s^2}{n^2-1} \left(1 - \frac{s^2}{4n^2} \right) + \frac{k_h}{k_s} \frac{1}{n^2-1} \left(\frac{s^4-1}{4n^2} - s^2 + 1 \right). \quad (2)$$

Equation (1) is based on the following assumptions:

- (1) The soil is completely homogeneous and water-saturated.
- (2) Solid particles and water are incompressible, and the deformation of the soil is completely caused by the discharge of pore water.

- (3) The vertical and radial flows obey Darcy's law, and the coefficient of permeability changes with the void ratio during the consolidation.
- (4) All compressive strains within the soil occur in a vertical direction. The soil particles do not move along the radial and tangential directions, and no creep is considered.
- (5) Horizontal sections remain horizontal during the consolidation.
- (6) All vertical loads are applied instantaneously, and the load distribution is uniform over the whole cylindrical area.

The above assumptions remove the limits of small-strain hypothesis of soil. The vertical nonlinear compression characteristics, nonlinear permeability for radial and vertical flows, and skeleton deformation generated by vertical movement of soil particles are considered in model ALSM. Therefore, geometric nonlinearity and material nonlinearity are brought into equal strain consolidation for large-area loading condition, which agrees well with the settlement law with vertical drain in real engineering problems. Equation (1) can be rewritten into the one-dimensional large-strain consolidation equation as given by Gibson et al. [31, 32] by ignoring the horizontal radial flow (i.e., $k_h = 0$).

If the assumption of small strain is considered, and there is no vertical flow (i.e. $k_v = 0$), Equation (1) can be rewritten into the axisymmetric consolidation control equation as given by Hansbo [3].

3. Difference Schemes of the ALSM Model

As it can be seen, the theoretical model of formula (1) is a highly complex nonlinear equation, and it is difficult to solve it analytically. The finite difference method can be used for calculation and analysis. For convenience, Equation (1) can be written as

$$\frac{\partial e}{\partial t} = \frac{\partial}{\partial z} \left[g(z, t) \frac{\partial e}{\partial z} \right] + B(z, t) \frac{\partial e}{\partial z} - C(z, t) - D(z, t), \quad (3)$$

where,

$$g(z, t) = -\frac{k_v}{\gamma_w(1+e)} \frac{d\sigma'}{de}, \quad (4)$$

$$B(z, t) = (G_s - 1) \left[\frac{1}{1+e} \frac{dk_v}{de} - \frac{k_v}{(1+e)^2} \right], \quad (5)$$

$$C(z, t) = \frac{8k_h(1+e)}{\gamma_w d_e^2 \mu} (G_s - 1) \gamma_w z, \quad (6)$$

$$D(z, t) = \frac{8k_h(1+e)}{\gamma_w d_e^2 \mu} (-\sigma' + q). \quad (7)$$

Each of Equations (4)–(7) has its own unique parameters and perform different consolidation behavior. $B(z, t)$ and $C(z, t)$ constitute the gravity item, $D(z, t)$ is relevant to the radial drainage, and $g(z, t)$ represents the coefficient of one-dimensional large-strain consolidation.

Equation (3) is a variable coefficient convection-diffusion equation, $B(z, t)$, $C(z, t)$, $D(z, t)$, and $g(z, t)$ all have upper and lower limits, such as $0 < v \leq g(z, t) \leq f$, $0 \leq C(z, t) \leq f$, $0 \leq D(z, t) \leq f$, and $|B(z, t)| \leq f$.

Let Δz and Δt represent the space step and time step, respectively, $z_i = i\Delta z$, $i = 0, 1, 2, \dots, I$ and $t_j = j\Delta t$, $j = 0, 1, 2, \dots, J$. The difference scheme is like the convection-diffusion equation with constant coefficients. According to the upwind difference scheme, Equation (3) can be written in the following format, and the discrete schematic diagram of space and time is shown in Figure 3:

$$\begin{aligned} \frac{e_i^{j+1} - e_i^j}{\Delta t} = & \frac{1}{\Delta z^2} [g_{i+1/2}^j (e_{i+1}^j - e_i^j) - g_{i-1/2}^j (e_i^j - e_{i-1}^j)] \\ & + \frac{B_i^j + |B_i^j|}{2} \frac{e_{i+1}^j - e_i^j}{\Delta z} + \frac{B_i^j - |B_i^j|}{2} \frac{e_i^j - e_{i-1}^j}{\Delta z} - C_i^j - D_i^j, \end{aligned} \quad (8)$$

where

$$\begin{aligned} g_{i\pm 1/2}^j &= \frac{1}{2} (g_i^j + g_{i\pm 1}^j), \\ g_i^j &= -\frac{k_i^j}{\gamma_w (1 + e_i^j)} \left[\frac{d\sigma'}{de} \right]_i^j, \\ B_i^j &= (G_s - 1) \left\{ \frac{1}{1 + e_i^j} \left[\frac{dk_v}{de} \right]_i^j - \frac{k_{vi}^j}{(1 + e_i^j)^2} \right\}, \\ C_i^j &= \frac{8k_{hi}^j (1 + e_i^j)}{\gamma_w d_e^2 \mu} (G_s - 1) \gamma_w i \Delta z, \\ D_i^j &= \frac{8k_{hi}^j (1 + e_i^j)}{\gamma_w d_e^2 \mu} (-\sigma_i^j + q). \end{aligned} \quad (9)$$

Difference equations can better reflect the material nonlinear characteristics of soil, which is much closer to the actual situation than special assumptions of soil permeability and compressibility for obtaining analytical solutions easily. During the calculation, good results for any given form of $e - \sigma'$ and $e - k$ will be obtained by substituting k_{vi}^j , $[dk_v/de]_i^j$, $[d\sigma'/de]_i^j$, σ_i^j , k_{hi}^j into g_i^j , B_i^j , C_i^j , D_i^j .

4. Difference Schemes for Initial and Boundary Conditions

Assume that the initial thickness of the high water-saturated homogeneous soil is L (thickness H in the spatial vertical coordinates in the Lagrange coordinate system, $H = L/(1 + e_0)$). The initial void ratio e_0 at any position of soil for time zero is the same. Initial condition is described as

$$e(z, 0) = e_0 \quad (0 \leq z \leq H). \quad (10)$$

The difference scheme is given as

$$e_i^0 = e_0. \quad (11)$$

The average void ratio $e(z, t)$ can be obtained from the relationship of effective vertical stress with the void ratio.

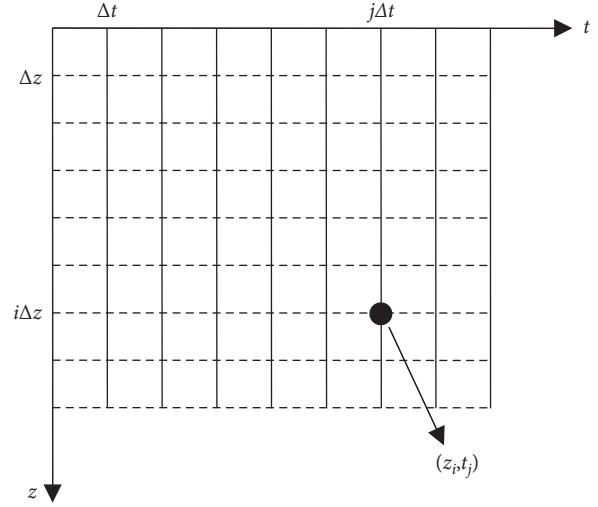


FIGURE 3: Discrete schematic diagram about the space and time.

The top of the soil is freely draining, and the excess pore water pressure dissipated instantaneously. According to the compression properties of soil, the final void ratio at the soil surface is given by

$$e(0, t) = e_f(0) \quad (t > 0). \quad (12)$$

The difference scheme for the upper boundary condition is given as

$$e_0^j = e_f(0) \quad (t > 0). \quad (13)$$

If the soil at the bottom is impermeable during the consolidation, the bottom boundary condition is determined as

$$\left. \frac{\partial e}{\partial z} \right|_{z=L} = (G_s - 1) \gamma_w \left. \frac{de}{d\sigma'} \right|_{z=H}. \quad (14)$$

The difference scheme for the bottom boundary condition is given as

$$\frac{e_{I+1}^j - e_I^j}{\Delta z} = (G_s - 1) \gamma_w \left[\frac{de}{d\sigma'} \right]_i^j \Big|_{z=H}. \quad (15)$$

5. Case Analysis

According to the ALSC model and the difference structure, the axisymmetric large-strain consolidation calculation program is compiled. Townsend and McVay [30] have described the predictions of ponds' (solids) elevation histories and one-year pore water pressure and void ratio profiles for four different wasted clay disposal scenarios (Scenario A: quiescent consolidation, uniform initial void ratio; Scenario B: stage filling, nonuniform initial void ratio; Scenario C: quiescent consolidation and surcharge loading of a pond having a uniform initial void ratio; and Scenario D: two-layer quiescent consolidation, sand/clay surcharge, and nonuniform initial void ratio). Station for Scenario C is closer to the assumptions (1) and (6) of the ALSC model, so Scenario C is selected for analysis. The nonlinear parameters,

i.e., Equations (16) and (17), are used for prediction by nine different large-strain consolidation models. However, the predictions are varying from program to program:

$$e = 7.72(\sigma')^{-0.22}, \quad (16)$$

$$k = 0.2532E - 6e^{4.65}. \quad (17)$$

Figure 4 shows the quiescent consolidation with the top freely draining and impermeable at the bottom. The sludge is water-saturated and homogeneous. A 7.2 m deep waste pond with a uniform initial void ratio of 14.8 is capped with a 9.48 kPa surcharge. The specific gravity of the solid particles is 2.82. To illustrate the difference between large- and small-strain consolidations with vertical drains, the PVD is quincunx arranged with the spacing of 1.0 m based on Scenario C. The width (w) * thickness (t) of the PVDs is 100 mm * 4 mm. So, the equivalent radius of the vertical drain (36.3 mm) can be calculated according to the formula $r_w = 2(w + t)/\pi$ proposed by Hansbo [33]. The radius of influence r_c is set to 525 mm. The large-strain material nonlinear parameters change with the void ratio seen in Equations (16) and (17), but the parameters of small-strain consolidation are the constant values. According to Equations (16) and (17), compressibility a_v shall be obtained at each level of the loading, and the vertical coefficient of consolidation C_v can be calculated from its definition. Assuming the soil is isotropy, we found the relationship $C_v = C_h$. The smearing is not considered during the simulation progress. The specific calculation parameters are shown in Table 1.

In the calculation program of the ALSC model, the soil is divided into 100 layers along the depth, and time step length is 0.1 day. Fifteen different kinds of simulations were performed, such as consolidation with or without self-weight, and only radial or vertical flows occurs. The whole computation time is 10000 days except for scenario “only vertical drainage without self-weight”, where the time is 30000 days. The calculation parameters were obtained from [30]. The unit conversion is as follows: 1 ft = 304.8 mm and 1 psf = 47.88 Pa.

In small-strain calculations, the time step is 1.0 day, the computation time of models “Hansbo” (which states that the axisymmetric small-strain consolidation theory of only radial flow is considered) and “Hansbo + Terzaghi” (which refers to that the vertical consolidation degree is calculated by Terzaghi’s theory, the radial consolidation degree is calculated by Hansbo’s theory, and then the average degree of consolidation is calculated according to Carrillo’s theorem) is 10000 days. However, the computation time of model “Terzaghi” (which means computing by the Terzaghi classical one-dimensional small-strain consolidation theory—vertical flows only) needs 70000 days to achieve stability.

6. Differences of Average Degree of Consolidation between Large-Strain and Small-Strain Theories

Figure 5 shows the average consolidation degree versus time for large- and small-strain consolidation theories.

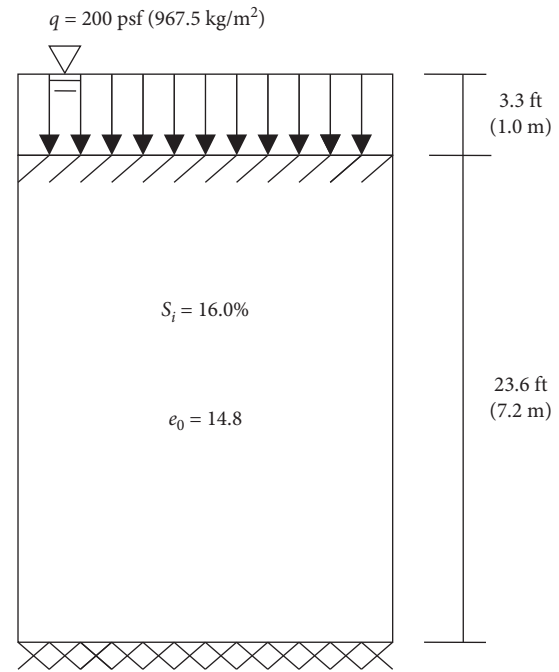


FIGURE 4: Scenario C.

“Double drainage” represents the simultaneous occurrence of vertical and radial flows, “radial drainage” indicates that only radial flow occurs ($k_v = 0$, when calculating), and “vertical drainage” means that only vertical flows occur ($k_h = 0$, when computing). In the calculation process, self-weight stress is considered, i.e., $G_s \neq 1$. At the same time, to reflect the difference between the settlement rate and the dissipating rate of excess pore water, the stress consolidation degree U_p (defined by stress) and the strain consolidation degree U_s (defined by strain) were calculated separately.

- (1) The difference between one-dimensional consolidations. During the early stage of consolidation (within 1000 days), the degree of consolidation for Terzaghi’s one-dimensional small-strain consolidation theory is faster than that for ALSC (U_p)-vertical drainage. This is because the consolidation coefficient remains unchanged in Terzaghi theory. After 1000 days, the development of the Terzaghi consolidation degree is obviously lagging and is always less than that of ALSC (U_s)-vertical drainage in the same consolidation time. This is because the large-strain theory considers the reduction in drainage distance during the consolidation process [34]. Terzaghi’s solution overestimates the dissipation rate of the excess pore water pressure in the early consolidation stage and underestimates it during the later period. We can see from the consolidation stability time, the Terzaghi solution clearly overestimates the settling time of the soil. Take the degree of consolidation of 80% as an example. Terzaghi’s theory needs 12853 days, while the time required for ALSC (U_s)-vertical drainage and ALSC (U_p)-vertical drainage are 876 days and 3247 days, and the

TABLE 1: Calculation parameters.

Surcharge (kPa)	Height (m)	G_s	Initial void ratio, e_0	$C_v/10^{-4} \text{ cm}^2 \text{ (s)}$	$C_h/10^{-4} \text{ cm}^2 \text{ (s)}$	$r_w \text{ (mm)}$	$r_e \text{ (mm)}$	s	k_h/k_s	n
9.48	7.2	2.82	14.8	2.65	2.65	36.3	525	1	1	14.46

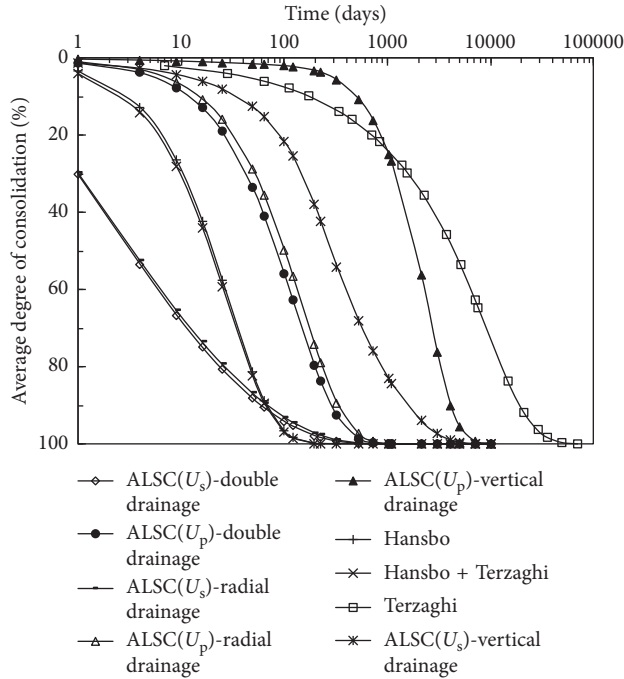


FIGURE 5: The average consolidation degree versus time for large-strain and small-strain consolidation theories.

consolidation time is 15 and 4 times those of the ALSC theory, respectively.

- (2) The difference of radial consolidation. The development of consolidation by Hansbo is always faster than ALSC (U_p)-radial drainage consolidation. This is because Hansbo's radial permeability coefficient is constant, while the ALSC (U_p)-radial permeability coefficient decreases with time. When the degree of consolidation is less than 90%, Hansbo's solution is smaller than ALSC (U_s)-radial drainage value; after 90% consolidation degree, the two are closer. This is mainly because ALSC (U_s) considers the vertical geometrical nonlinearities, and settlement changes faster before 90% consolidation. In the consolidation stability time, taking the degree of consolidation of 80% as an example, Hansbo's small-strain consolidation time requires 47 days, while the time required for U_s and U_p calculated by the ALSC model considering only radial flows are 27 days and 234 days, respectively. The large-strain consolidation time is 1/1.7 times and 5 times that of the small-strain theory, respectively.
- (3) The degree of consolidation for ALSC-double drainage in this case is like that for ALSC-radial drainage. However, the degree of consolidation for ALSC-vertical drainage is much smaller than that for

ALSC-radial drainage. It shows that when laying vertical drainage boards for working condition C, drainage path is shortened significantly, and radial soil consolidation (flows) occurs mainly in the soil. "Hansbo" solution is consistent with "Hansbo + Terzaghi" solution, and "Terzaghi" solution is much smaller than "Hansbo" solution, which also illustrates this point.

- (4) In small-strain consolidation theory, the degrees of consolidation defined by stress and by strain are the same due to the assumption of microdeformation. In the ALSC theory, material nonlinearity and geometric nonlinearity are considered. In the same consolidation time, development of U_s has always been faster than U_p [20]. Thus, the dissipation rate of excess pore water pressure always lags the settlement deformation rate. If the settlement is used as the guidance in the construction process, it will overestimate the shear strength of the soil.

7. Effect of Self-Weight on Large-Strain Consolidation Behavior under the ALSC Model

To discuss the effect of self-weight on large-strain consolidation behavior, let $G_s = 1$ (self-weight is not considered) and $G_s \neq 1$ (self-weight is considered). Figure 6 shows the effect of self-weight on the degree of consolidation of double drainage and radial flows only. It can be seen that, in the case of $G_s = 1$ and $G_s \neq 1$, development of the average consolidation degree with double drainage is basically similar to that with radial flows only. Therefore, the time-course curve of coupled radial and vertical flows is not drawn in Figure 7 in order to clearly reflect the effect of self-weight on the degree of consolidation.

Figure 7 shows that when only radial flows occur, compared with the consolidation rate when $G_s = 1$, the consolidation rate of U_s when $G_s \neq 1$ is faster. The error between the two is 16% on the first day and is less than 10% on the fourth day. The consolidation curve basically coincided after 100 days. The U_p curves, comparing the situation where self-weight is considered versus the situation where it is not, basically coincided.

For large-strain consolidation where only vertical flows occur, the degree of consolidation of U_s and U_p with considering self-weight is faster than those without considering it. Therefore, for this kind of unconsolidated soil with high water content, the self-weight stress has little effect on the radial consolidation degree. However, self-weight has some effects on the degree of vertical consolidation. If the self-weight of the soil is neglected, the settlement rate of the soil and the dissipation rate of excess pore water pressure are underestimated [35, 36].

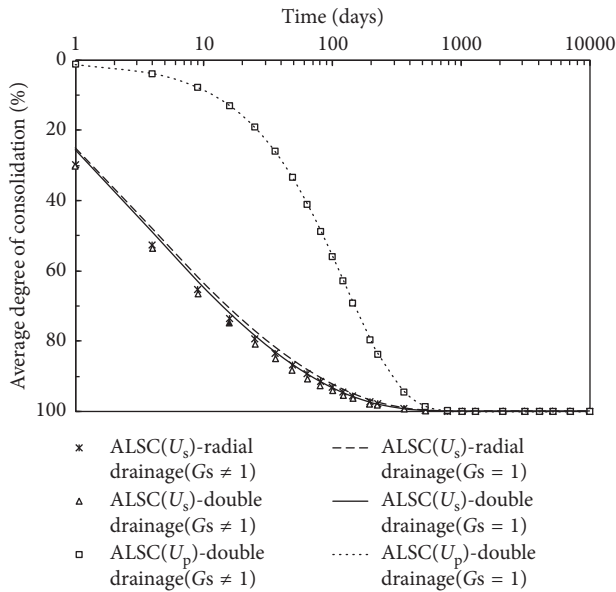


FIGURE 6: Effect of self-weight on the degree of consolidation of double drainage and radial flows only.

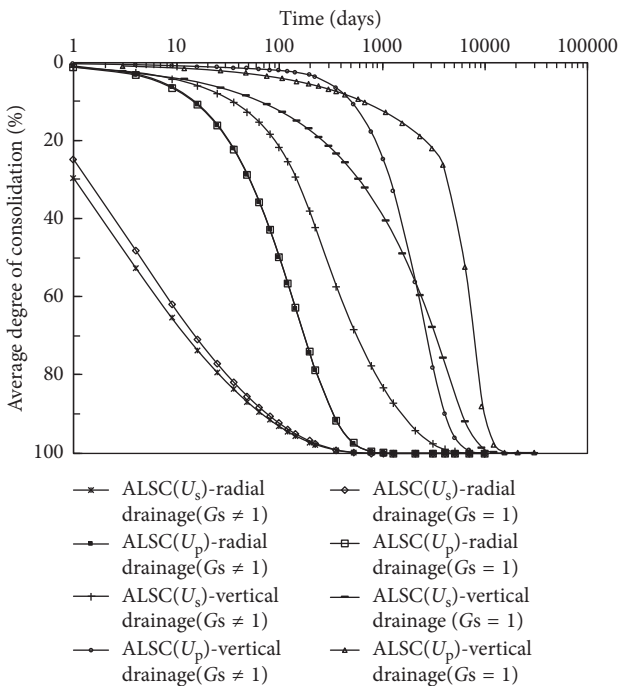


FIGURE 7: Effect of self-weight on the average degree of consolidation of radial flows only and vertical flows only.

8. Change Law of Void Ratio and Excess Pore Water Pressure with Soil Height and Consolidation Time

The variations of the void ratio and excess pore water pressure along the soil height are shown in Figures 8 and 9. As the consolidation time increases, the void ratio gradually decreases. When only vertical flows occur (Figure 8), the change rate of the void ratio varies greatly at different depths.

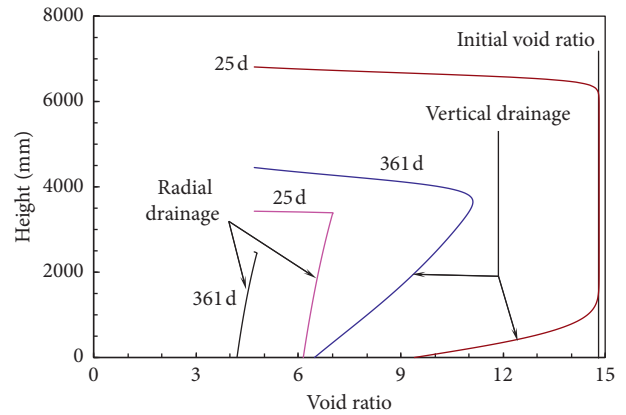


FIGURE 8: Curve of the void ratio along soil height under different consolidation time.

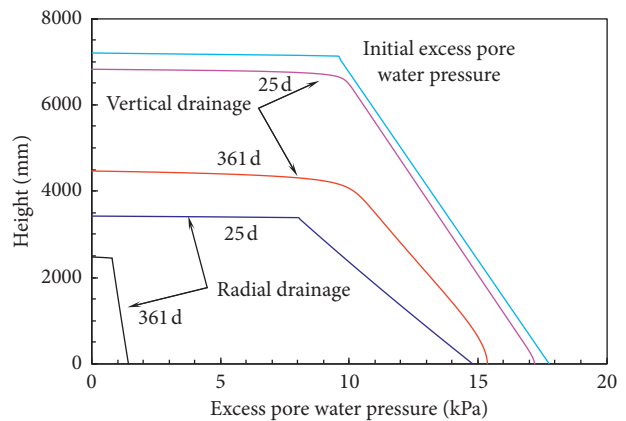


FIGURE 9: Curve of excess pore water pressure along soil height under different consolidation time.

Under the effect of external load and self-weight, the consolidation rate in the middle of the soil lags than that of the upper and lower parts [35]. When only radial flows occur, the void ratio is uniform along the height. In the same consolidation time, the reduction rate of the void ratio for radial flows only is faster than that of the vertical flows only, indicating that the arrangement of vertical drainage body can shorten the drainage path and accelerate soil consolidation rate.

From the change law of excess pore water pressure, it can be seen that, after the arrangement of the vertical drainage body, although the excess pore pressure of the soil at different depths is evenly dissipated, excess pore pressure along the depth is linearly increasing which is affected by the self-weight when only radial flows occur. However, distribution of the excess pore water pressure along the depth shows nonlinearity when only vertical flows occur. Like the change law of the void ratio, the dissipation rate of the excess pore pressure in the middle is slower than those in the upper and lower parts. From this point of view, radial flows significantly accelerate the dissipating rate of excess pore water pressure. For example, when the consolidation time is 361 days, the excess pore water pressure at the bottom of the soil when only radial flows occur is 1.5 kPa but when only

TABLE 2: Comparison of calculation results for consolidation of working condition C [30].

Predictor	Program	Number of layers	Final height (ft)	Time (days)	One-year profile		
					Height (ft)	Base, e	Base, u (psf)
B&CI	QSUS3, QSNS2	100	8.0	Infinite	17.0	6.49	324.5
B&CI	ULTDRAIN	—	—	—	—	—	—
N'Wstrn	—	—	8.8	2,460	18.5	—	—
UF	QSUS	50	17.8	Infinite	16.8	6.09	323.1
UF	QSUS	500	8.0	Infinite	14.7	6.44	322.9
UF	C. FORM	—	8.0	Infinite	—	—	—
WES	PCDDF	500	8.1	9,700	14.9	6.45	322.1
UCONN	—	20	8.2	5,206	15.6	6.47	323.1
A and assoc	SLUQUIS	100	8.0	1,642	14.7	6.44	323
McGill	—	10	8.6	3,650	14.9	6.40	326
UF	UF-McGS	20	8.1	6,476	14.8	6.44	325.3
TAGA	TAILS	40	8.6	5,174	14.3	6.60	323
ALSC of this paper	100	8.0/(2446 mm)	Infinite	14.7/(4468 mm)	6.47	321.2/(15.38 kPa)	—
Average	—	—	8.2	—	15.6	6.44	323.7

vertical flows occur is approximately 15 kPa (10 times larger than the values of the previous case).

Table 2 summarizes the pertinent data and statistics of nine research institutes [30] and model ALSC (vertical flows only) for Scenario C. The final average thickness of soil and other consolidation parameters after one year of nine research institutes are close to those of the model ALSC, which confirms that it is a reasonable model and good precision for soil or dredged sludge at high water content.

9. Conclusions

In this paper, based on the ALSC model under equal strain conditions (established by Cao et al. [28]), the consolidation behavior of soils with high water content considering self-weight was investigated, and the following conclusions are obtained:

- (1) The theoretical values obtained from Terzaghi's one-dimensional small-strain consolidation degree are always less than those obtained from ALSC (U_s)-vertical drainage. Terzaghi's solution overestimates the dissipation rate of excess pore water pressure in the earlier consolidation stage and underestimates it during the later consolidation stage. Terzaghi's solution overestimates the consolidation time of soil.
- (2) In the axisymmetric large-strain system and the small-strain theory system, the vertical drainage body can shorten the drainage path, and the consolidation of soils with high water content is dominated by radial flows. At the same consolidation time, the average degree of consolidation obtained from Hansbo's theory is smaller than the values of ALSC(U_s)-radial drainage, but it is higher than values obtained from ALSC(U_p)-radial drainage. In the ALSC model, development of U_s is always faster than U_p .
- (3) For the unconsolidated soil with high water content, the effect of self-weight stress on axisymmetric large-strain radial consolidation is small, but on one-dimensional large-strain vertical consolidation, it is large.

- (4) In one-dimensional large-strain consolidation, the consolidation rate in the middle of the soil lags than those in the upper and lower parts under the combined action of external load and self-weight. The vertical drainage body can evenly dissipate the excess pore water pressure and accelerate the consolidation rate. Affected by the self-weight, the void ratio and the excess pore water pressure are distributed linearly along the soil. The calculation results based on the ALSC model are close to the average statistics of the nine institutions, which verifies the accuracy and applicability of the ALSC model and the difference solution method.

Data Availability

The data used to support the findings of this study are available from the corresponding author upon request.

Conflicts of Interest

The authors declare that they have no conflicts of interest.

Acknowledgments

This research was supported by the Natural National Science Foundation of China (Grant no. 51608312) and Scientific Research Foundation of Shandong University of Science and Technology for Recruited Talents (Grant no. 2016RCJJ021).

References

- [1] R. A. Barron, "Consolidation of fine-grained soils by drain wells," *Transactions of American Society for Civil Engineers*, vol. 113, pp. 718–754, 1948.
- [2] Y. B. Deng, K. H. Xie, and M. M. Lu, "Consolidation by vertical drains when the discharge capacity varies with depth and time," *Computers and Geotechnics*, vol. 48, pp. 1–8, 2013.
- [3] S. Hansbo, "Consolidation of fine-grained soils by pre-fabricated drains," in *Proceedings of 10th International Conference on Soil Mechanics and Foundation Engineering*,

- vol. 3, pp. 677–682, Balkema, Rotterdam, Netherlands, June 1981.
- [4] C. Y. Ong, J. C. Chai, and T. Hino, “Degree of consolidation of clayey deposit with partially penetrating vertical drains,” *Geotextiles and Geomembranes*, vol. 34, pp. 19–27, 2012.
 - [5] H. Yoshikuni and H. Nakanodo, “Consolidation of soils by vertical drain wells with finite permeability,” *Soils and Foundations*, vol. 14, no. 2, pp. 35–46, 1974.
 - [6] B. Guo, Y. Han, X. N. Gong, and M. M. Lu, “Consolidation analysis with vertical drains and general time-dependent loading,” *Journal of Central South University (Science and Technology)*, vol. 43, no. 6, pp. 2369–2377, 2012, in Chinese.
 - [7] G. H. Lei, Q. Zheng, C. W. W. Ng et al., “An analytical solution for consolidation with vertical drains under multi-ramp loading,” *Geotechnique*, vol. 65, no. 7, pp. 531–547, 2017.
 - [8] C. J. Leo, “Equal strain consolidation by vertical drains,” *Journal of Geotechnical and Geoenvironmental Engineering*, vol. 130, no. 3, pp. 316–327, 2004.
 - [9] M. M. Lu, K. H. Xie, and S. Y. Wang, “Consolidation of vertical drain with depth-varying stress induced by multi-stage loading,” *Computers and Geotechnics*, vol. 38, pp. 1096–1101, 2011.
 - [10] G. F. Zhu and J. H. Yin, “Consolidation of soil with vertical and horizontal drainage under ramp load,” *Geotechnique*, vol. 51, no. 4, pp. 361–367, 2001.
 - [11] B. Indraratna, C. Rujikiatkamjorn, and I. Sathananthan, “Radial consolidation of clay using compressibility indices and varying horizontal permeability,” *Canadian Geotechnical Journal*, vol. 42, no. 5, pp. 1330–1341, 2005.
 - [12] M. M. Lu, S. Y. Wang, S. W. Sloan, D. C. Sheng, and K. H. Xie, “Nonlinear consolidation of vertical drains with coupled radial-vertical flow considering well resist,” *Geotextiles and Geomembranes*, vol. 43, no. 2, pp. 182–189, 2015.
 - [13] R. Walker, B. Indraratna, and C. Rujikiatkamjorn, “Vertical drain consolidation with non-Darcian flow and void ratio dependent compressibility and permeability,” *Geotechnique*, vol. 62, no. 11, pp. 985–997, 2012.
 - [14] X. Geng, B. Indraratna, and C. Rujikiatkamjorn, “Effectiveness of partially penetrating vertical drains under a combined surcharge and vacuum preloading,” *Canadian Geotechnical Journal*, vol. 48, no. 6, pp. 970–983, 2011.
 - [15] B. Indraratna, I. Sathananthan, C. Rujikiatkamjorn, and A. S. Balasubramaniam, “Analytical and numerical modeling of soft soil stabilized by prefabricated vertical drains incorporating vacuum preloading,” *International Journal of Geomechanics*, vol. 5, no. 2, pp. 114–124, 2005.
 - [16] B. Indraratna, M. E. Kan, D. Potts, C. Rujikiatkamjorn, and S. W. Sloan, “Analytical solution and numerical simulation of vacuum consolidation by vertical drains beneath circular embankments,” *Computers and Geotechnics*, vol. 80, pp. 83–96, 2016.
 - [17] W. H. Zhou, T. M. H. Lok, L. S. Zhao, G. X. Mei, and X. B. Li, “Analytical solutions to the axisymmetric consolidation of a multi-layer soil system under surcharge combined with vacuum preloading,” *Geotextiles and Geomembranes*, vol. 45, no. 5, pp. 487–498, 2017.
 - [18] X. W. Tang, B. Niu, G. C. Cheng, and H. Shen, “Closed-form solution for consolidation of three-layer soil with a vertical drain system,” *Geotextiles and Geomembranes*, vol. 36, pp. 81–91, 2013.
 - [19] J. C. Liu, G. H. Lei, and M. X. Zheng, “General solutions for consolidation of multilayered soil with a vertical drain system,” *Geotextiles and Geomembranes*, vol. 42, no. 3, pp. 267–276, 2014.
 - [20] H. H. Jiang, Y. P. Zhao, G. N. Liu, and W. B. Zhao, “Large strain consolidation of soft ground with vertical drains,” *Chinese Journal of Geotechnical Engineering*, vol. 33, no. 2, pp. 302–308, 2011, in Chinese.
 - [21] P. J. Fox, M. D. Nicola, and D. W. Quigley, “Piecewise-linear model for large strain radial consolidation,” *Journal of Geotechnical and Geoenvironmental Engineering*, vol. 129, no. 10, pp. 940–950, 2003.
 - [22] B. Indraratna, R. Zhong, P. J. Fox, and C. Rujikiatkamjorn, “Large-strain vacuum-assisted consolidation with non-darcian radial flow incorporating varying permeability and compressibility,” *Journal of Geotechnical and Geoenvironmental Engineering*, vol. 143, no. 1, article 04016088, 2017.
 - [23] M. Zhang, Y. M. Zhao, G. N. Liu, and R. H. Hu, “Finite difference solution to equation for large-strain consolidation of double-layered vertical drain ground,” *Chinese Journal of Geotechnical Engineering*, vol. 35, no. 9, pp. 1666–1674, 2013, in Chinese.
 - [24] Y. Y. Hu, W. H. Zhou, and Y. Q. Cai, “Large-strain elastic viscoplastic consolidation analysis of very soft clay layers with vertical drains under preloading,” *Canadian Geotechnical Journal*, vol. 51, no. 2, pp. 144–157, 2014.
 - [25] L. Q. Sun, T. Q. Jia, S. W. Yan, J. X. Lu, C. X. Yue, and Y. Y. Kang, “Study on consolidation theory of foundation with partially penetrated sand wells based on large strain,” *Chinese Journal of Rock Mechanics and Engineering*, vol. 36, no. 2, pp. 504–512, 2017, in Chinese.
 - [26] G. X. Li, *Advanced Soil Mechanics (Second Edition)*, Tsinghua University Press, Beijing, China, 2016, in Chinese.
 - [27] A. Onoue, “Consolidation by vertical drains taking well resistance and smear into consideration,” *Soils and Foundations*, vol. 28, no. 4, pp. 165–174, 1988.
 - [28] Y. P. Cao, Z. J. Sun, J. W. Ding, and F. Ji, “Axisymmetric large-strain consolidation model for dredged clay with high water content,” *Chinese Journal of Geotechnical Engineering*, vol. 38, no. 10, pp. 1904–1910, 2016, in Chinese.
 - [29] Y. P. Cao, J. W. Ding, Z. H. Ma, and Z. T. Zhang, “Axisymmetric large-strain consolidation model for dredged clay with high water content under vacuum preloading,” *Journal of Southeast University (Nature Science Edition)*, vol. 46, no. 4, pp. 860–865, 2016, in Chinese.
 - [30] F. C. Townsend and M. C. McVay, “SOA: Large strain consolidation predictions,” *Journal of Geotechnical Engineering*, vol. 116, no. 2, pp. 222–243, 1990.
 - [31] R. E. Gibson, G. L. England, and M. J. Hussey, “The theory of one-dimensional soil consolidation of saturated clays, I. Finite nonlinear consolidation of thin homogeneous layers,” *Geotechnique*, vol. 17, no. 3, pp. 261–273, 1967.
 - [32] R. E. Gibson, R. L. Schiffman, and K. W. Cargill, “The theory of one-dimensional soil consolidation of saturated clays, II. Finite nonlinear consolidation of thick homogeneous layers,” *Canadian Geotechnical Journal*, vol. 18, no. 3, pp. 280–293, 1981.
 - [33] S. Hansbo, “Consolidation of clay by band-shaped prefabricated drains,” *Ground Engineering*, vol. 12, no. 5, pp. 16–25, 1979.
 - [34] B. H. Li, H. W. Ying, K. H. Xie, and G. X. Zeng, “Analysis of 1-D large-strain consolidation considering the self-weight of soil,” *China Civil Engineering Journal*, vol. 33, no. 3, pp. 54–59, 2000, in Chinese.
 - [35] H. H. Jiang, G. N. Liu, and Y. M. Zhao, “A solution of Gibson’s governing equation of one-dimensional consolidation,”

Chinese Journal of Geotechnical Engineering, vol. 32, no. 5, pp. 745–750, 2010, in Chinese.

- [36] X. Y. Xie, J. Q. Huang, W. J. Wang, and J. Z. Li, “Influence of weight of soils on nonlinear finite strain consolidation for Ningbo soft clay,” *Journal of Zhenjiang University Engineering Science*, vol. 48, no. 5, pp. 827–834, 2014, in Chinese.

Research Article

Investigations on Engineering Properties of Solidified/Stabilized Pb-Contaminated Soil Based on Alkaline Residue

Fusheng Zha , Dongdong Pan, Long Xu, Bo Kang, Chengbin Yang , and Chengfu Chu

School of Resource and Environmental Engineering, Hefei University of Technology, Hefei 230009, China

Correspondence should be addressed to Chengbin Yang; yangchengbin@hfut.edu.cn

Received 18 April 2018; Accepted 6 June 2018; Published 19 September 2018

Academic Editor: Annan Zhou

Copyright © 2018 Fusheng Zha et al. This is an open access article distributed under the Creative Commons Attribution License, which permits unrestricted use, distribution, and reproduction in any medium, provided the original work is properly cited.

Solidification/stabilization (S/S) has been considered as one of the most effective techniques for remediation of the heavy metal-contaminated sites. Among various binders adopted in S/S, alkaline residue (AR) could be considered as a new binder to treat heavy metal-contaminated soil due to its strong adsorptive capacity for heavy metal ions. So in this paper, the strength, leaching, and microstructure characteristics of the solidified/stabilized Pb-contaminated soil by using alkaline residue are systematically investigated. Test results present that the unconfined compressive strength (UCS) of the treated soil will increase, while the leached Pb^{2+} concentration will decrease, with the increase of the alkaline residue content in the specimen. The UCS increases significantly with the curing time increasing during the initial 28 days, after which the UCS of the specimen becomes stable. The leached Pb^{2+} concentration decreases significantly at the initial 28 days followed by a stable trend with curing time increasing. The UCS decreases and the leached Pb^{2+} concentration increases with the increase of the initial Pb^{2+} concentration in the specimen. The microstructural analysis performed by scanning electron microscope (SEM) showed that the increase of the alkaline residue content and curing time will result in more hydration products and densified microstructure, which could effectively improve the engineering properties of the specimen.

1. Introduction

Widespread contamination of soil with heavy metal is one of the most severe environmental problems that can seriously deteriorate the environmental quality and human health. Remediation techniques are massively proposed for remediation of the heavy metal-contaminated site [1, 2], in which the stabilization/solidification (S/S) technique is intensively accepted for its efficiency, convenience, and cost-effectiveness. According to the remediation mechanism (including adsorption, encapsulation, precipitation, and complexation), selection of the binder for improvement of the strength and leaching characteristics is of great importance to the application of the stabilization/solidification technique [3–10].

Alkaline residue, the by-product generated from the manufacturing alkaline industry, attracts attentions in the S/S technique recently. The extremely fine particles consisted in alkaline residue would result in high specific surface area

and strong adsorptive capacity, which are beneficial for removal of heavy metal ions in the contaminated site. In addition, hydration products could be generated from the complicated interactions between the alkaline residue and soil, which will improve the leaching characteristics of the treated soils due to the adsorption and encapsulation mechanisms. Components like calcium oxide and aluminum oxide contained in AR can be the framework alongside with the hydration products generated from the hydration reaction, which will enhance the strength of the specimen. Based on the experimental investigations, Yan et al. [11] reported that the addition of alkaline residue in the contaminated soils could significantly reduce the leachability of Pb^{2+} to an acceptable level and the removal efficiency strongly depended on the pH value in the soils. The adsorption characteristics of the alkaline residue on heavy metal ions were also investigated by Cao et al. [12], in which the adsorption capacity of alkaline residue was confirmed to be susceptible to the pH, temperature, and the initial

concentration of heavy metal ions in the soils. Jin et al. [13] confirmed the remarkable adsorption characteristics of the alkaline residue and the important roles of the temperature and pH value played during the adsorption process. Additionally, Sun et al. [14] investigated the engineering properties of the expansive soil treated by using alkaline residue. Test results indicated remarkable improvement of the basic properties (including the relative density, liquid/plastic limit, and expansive potential) and strength characteristic of the treated soil, which was supported by the Wang et al. [15].

As mentioned above, alkaline residue is normally regarded as an effective binder because of its significant absorption characteristic in previous researches. Comprehensive investigations on the basis of engineering and environmental characteristics, as well as the microcosmic mechanism, are rarely reported. In the present work, the UCS and leaching characteristics, as well as the microstructure analysis of the alkaline residue-treated contaminated soil, are experimentally investigated to reveal the remediation efficiency and mechanism.

2. Testing Materials and Procedures

2.1. Testing Materials. The tested soil was excavated from a construction site at depth of 3.0–4.5 m in Wuhu City, Anhui province, which is in the eastern part of China. The basic physical properties and the major chemical components determined by the X-ray fluorescence (XRF) technique are listed in Tables 1 and 2, respectively. As can be seen, the tested soil is a kind of plastic clay with SiO_2 and Al_2O_3 contents more than 80%. The maximum dry density and the optimal water content are 1.81 g/cm^3 and 18.5%, respectively, according to the compaction test (Figure 1), which is conducted following the Test Methods of Soils for Highway Engineering (JTGE 40-2007) [16].

The alkaline residue adopted in the present work is collected from an ammonia alkali factory in Weifang, Shandong province, which is in the eastern part of China. The major chemical components determined by the XRF technique are presented in Table 3. It is clear that CaO takes dominant proportion in the alkaline residue, while MgO, SiO_2 , and Al_2O_3 also take a relatively large amount. As shown in Figure 2, the particle size of AR is mainly in the range of 1–10 μm , which confirms the large specific surface area and strong adsorptive capacity of the alkaline residue adopted in the present work.

In the present work, lead-contaminated soil is aimed for remediation due to its serious hazard and typical distribution in China. Analytical grade $\text{Pb}(\text{NO}_3)_2$ is selected as the heavy metal contaminants due to its high solubility, as well as the low interference of NO_3^- ions to the hydration process [17, 18].

2.2. Testing Procedures

2.2.1. Specimen Preparation. In specimen preparation, the Pb^{2+} concentrations (mg/kg) of 0.1%, 0.5%, 1%, 2%, and 3% and alkaline residue contents of 0%, 10%, 20%, 30%, 40%,

and 50% are designed in the present work. The contaminant concentrations of 0.1% indicates 1000 mg Pb^{2+} in the lead nitrate for 1 kg dry soil and is denoted as Pb0.1. The alkaline residue content of 10% is the mass ratio of alkaline residue to the dry soil and is denoted as AR10. After oven-drying at 105°C for 24 hours, the soil and alkaline residue were ground into powders and sized through 2 mm and 0.5 mm sieve, respectively. Then the soil and alkaline residue powders were mixed with the $\text{Pb}(\text{NO}_3)_2$ and deionized water at the designed proportions. After this, the mixtures were put into a compaction mould and statically compacted into targeted cylindrical specimens with a dimension of 100 mm in height, 50 mm in diameter, and a dry density of 1.72 mg/cm^3 , which equaled to the 95% of the maximum dry density. Finally, the prepared specimens were extruded from the mould and cured under standard curing conditions with temperature of $20 \pm 1^\circ\text{C}$ and relative humidity of 95% for 0 d, 1 d, 7 d, 14 d, 28 d, and 90 d.

2.2.2. Unconfined Compressive Strength (UCS) Test. After the completion of the curing, the unconfined compressive strength tests were performed on the specimens following the Standard Test Method for Unconfined Compressive Strength of Cohesive Soil (ASTM D2166-06) [19]. The YHS-2 UCS testing apparatus at a vertical strain rate of 1%/min was adopted in the test, and three parallel specimens were tested in each test with the average value as the representative one.

2.2.3. The Toxicity Characteristic Leaching Procedure (TCLP). The leachability of heavy metals from the stabilized soils was determined using the toxicity characteristic leaching procedure (TCLP) in accordance with the U.S EPA Method 1311 [20]. The prepared specimen was crushed into pieces with the size smaller than 9.5 mm. The leachant with pH value of 2.88 ± 0.05 was prepared by diluting 5.7 ml acetic acid (HAC) into 1 L deionized water. Then, 12.5 g crushed specimen and 250 ml leachant (solid-to-liquid ratio of 1 : 20) were mixed in a polythene bottle and vibrated at the rate of 180 rpm for 18 h. After this, the leachate was filtered through 0.45 μm filter membrane, and the pH value and Pb^{2+} concentration in the leachate were measured to analyze the leaching characteristic of the treated specimen.

2.2.4. Microstructural Test. The prepared specimen was cut into small pieces with sizes around 5 mm \times 5 mm \times 3 mm. Surface of the samples should be cleaned and polished carefully before freeze-drying in vacuum condition. Then, conductive coating was done to prepare the standard samples for the scanning electron microscope (SEM) test with the help from a professional institution.

3. Results and Discussion

3.1. Effects on the UCS of the Solidified/Stabilized Specimen. The UCS of the solidified/stabilized specimen is investigated with consideration of different influencing factors. The

TABLE 1: Basic physical properties of the tested soil.

Water content (%)	Specific gravity	Void ratio	Degree of saturation (%)	Liquid limit (%)	Plastic limit (%)	Plastic index	Cohesive strength (kPa)	Internal friction angle (°)
20.18	2.72	0.718	94	41.7	23.1	18.6	65	13.2

TABLE 2: Major chemical components of the tested soil.

Component	CaO	MgO	SiO ₂	Al ₂ O ₃	Fe ₂ O ₃	P ₂ O ₅	TiO ₂	Na ₂ O	K ₂ O	MnO
Content (%)	0.81	2.04	60.93	20.77	9.21	0.11	1.25	0.52	3.94	0.12

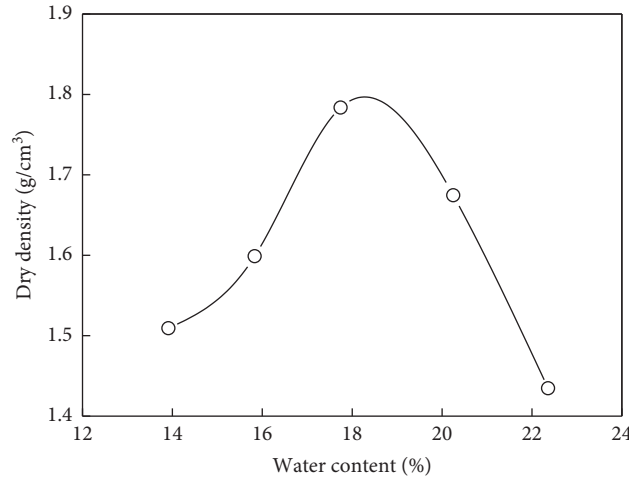


FIGURE 1: Compaction curve of the tested soil.

TABLE 3: Major chemical components of the alkaline residue.

Component	CaO	MgO	SiO ₂	Al ₂ O ₃	F	Fe ₂ O ₃	P ₂ O ₅	SO ₃	TiO ₂	Na ₂ O	K ₂ O	Cl
Content (%)	62.81	12.5	10.2	9.00	2.47	1.31	0.40	0.3	0.24	0.23	0.17	0.16

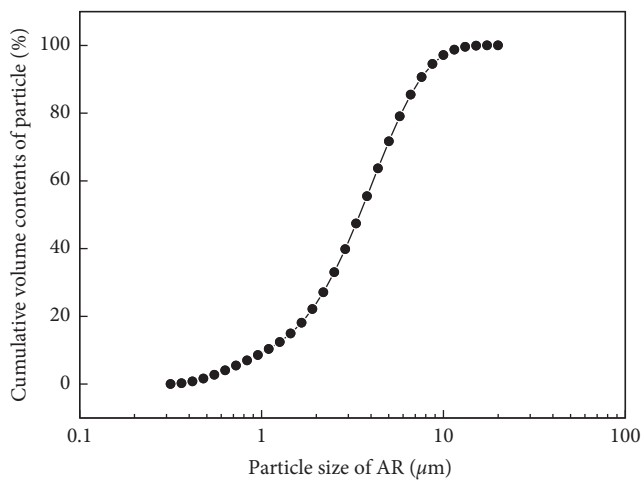


FIGURE 2: Curves of particle size analysis of AR.

evolutions of the UCS with the alkaline residue contents are typically shown in Figure 3.

Curves in Figure 3 showed significant increase of the UCS with incorporation of the alkaline residue into the

specimen. Such improvement of the strength characteristic by adding alkaline residue is attributed to the formation of hydration products like $\text{CaO} \cdot \text{SiO}_2 \cdot n\text{H}_2\text{O}$ (C-S-H) and $\text{CaSiO}_3 \cdot \text{CaCO}_3 \cdot \text{Ca}(\text{OH})_2 \cdot n\text{H}_2\text{O}$ arising from the reactions between the CaCO_3 , $\text{Ca}(\text{OH})_2$, and SiO_2 [14, 15]. Furthermore, the alkaline environment created by the alkaline residue could promote the hydration reaction and produce more hydration products. Existence of these hydration products decreases the porosity and increases the density and integrity of the specimen, which lead to the increase of the UCS. Additionally, calcium compounds like CaCO_3 contained in alkaline residue could form framework in the soil resulting in the improvement of the strength as well [14, 15].

As shown in Figure 3, the significant effect of the curing time on the UCS can be preliminarily observed after the comparison of diagrams (a) and (b). In further analysis, the evolutions of the UCS with the curing time are presented in Figure 4.

Results in Figure 4 show that the UCS of the solidified/stabilized specimen increases with the curing time increasing. A notable increasing magnitude of 38%–47% can be observed before 28-day curing. After this, the evolution of

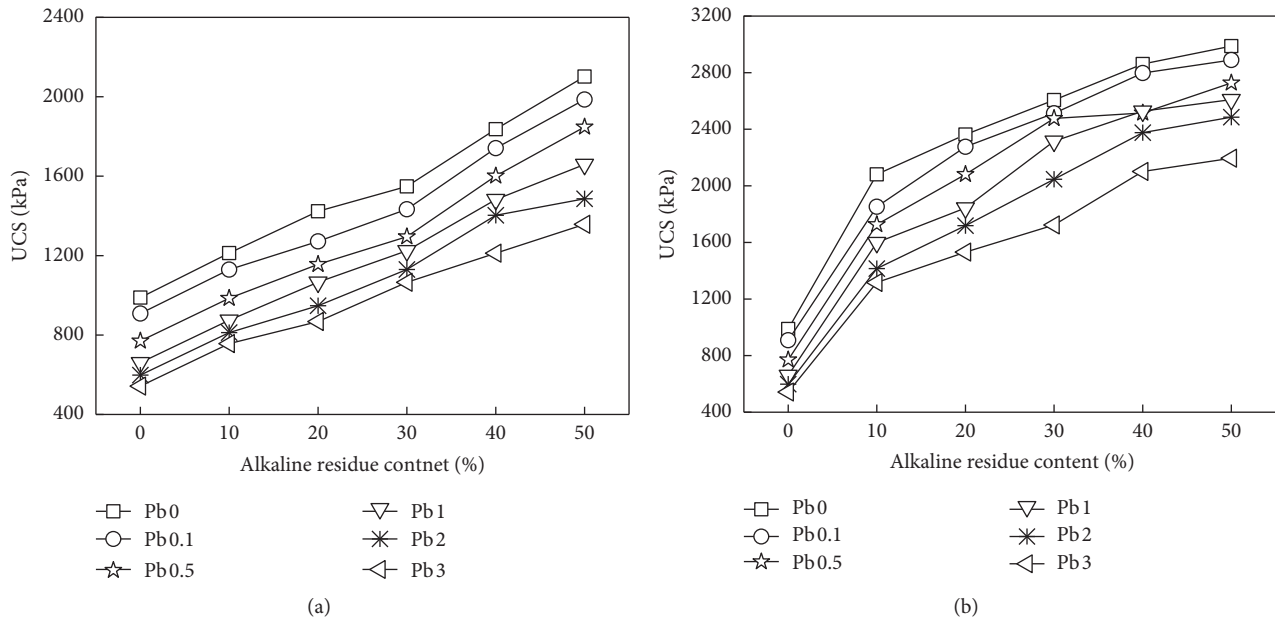


FIGURE 3: Evolutions of the UCS with the alkaline residue content of the specimen. Curing times of (a) 0 d and (b) 28 d.

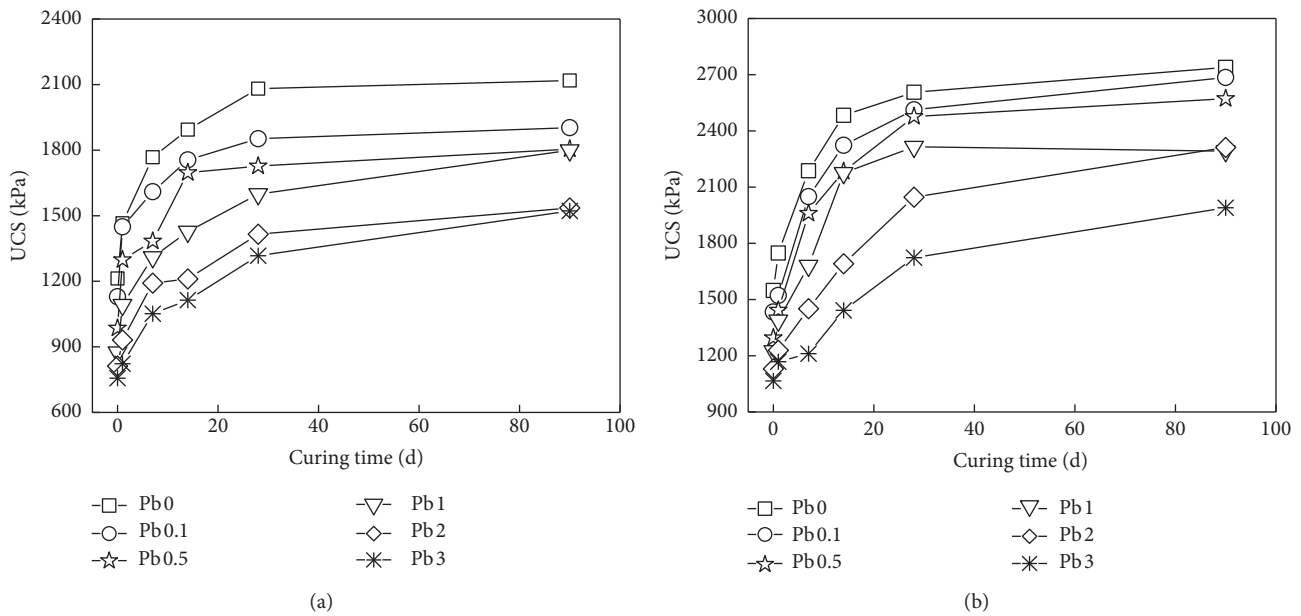


FIGURE 4: Evolutions of the UCS with the curing time of the specimen. Alkaline residue contents of (a) 10% and (b) 30%.

the UCS becomes stable with a slight increase in magnitude until 90-day curing is reached. As described in previous research, the improved strength of the specimen with curing time is attributed to the continuous formation of the hydration products during the hydration process. The pore space in the specimen can be filled, and the solid particles can be encapsulated by these hydration products, which contribute to the improvement of the strength. However, during the later period of the curing (after 28 days in the present work), hydration is fully developed and pores in the specimen are filled by the

hydration products at a large proportion. Then the microstructural variation of the specimen becomes limited resulting in relatively stable growth trend of the strength during this stage.

Results in Figure 4 also implied a significant effect of the initial Pb^{2+} concentration on the UCS of the specimen. For analysis in details, evolutions of the UCS with the initial Pb^{2+} concentration are depicted in Figure 5.

As shown in Figure 5, the increase of the initial Pb^{2+} concentration in the specimen leads to a notable decrease of the UCS. This is because the reactions between the

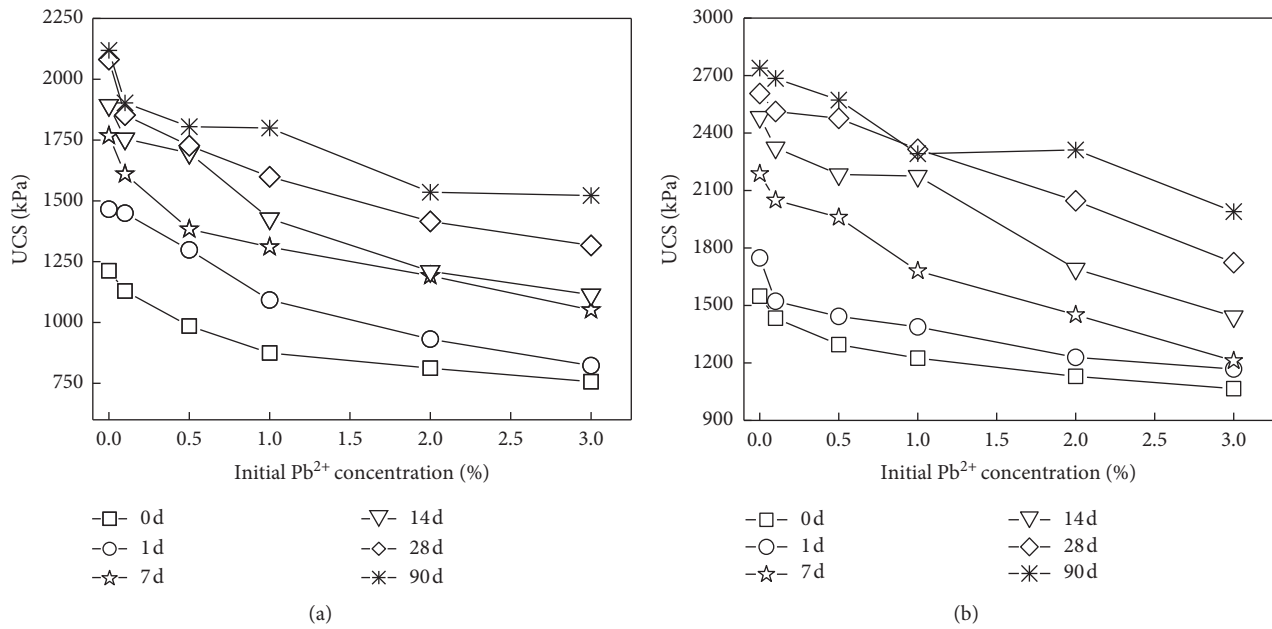


FIGURE 5: Evolutions of the UCS with the initial Pb²⁺ concentrations of the specimen. Alkaline residue contents of (a) 10% and (b) 30%.

alkaline residue and the soil particles can be retarded owing to the existence of Pb²⁺, and then the generation of the hydration products will be decelerated [9, 21–23]. Additionally, due to the alkaline environment created by the alkaline residue, Pb²⁺ will be involved in the hydration reactions resulting in generation of Pb complex and reduction of the hydration products. The Pb-precipitation will also form in this alkaline environment and encapsulate the alkaline residue and soil particles, which prevent the further hydration reaction [5, 23].

3.2. Effects on the Leaching Characteristic of the Solidified/Stabilized Specimen. The leaching characteristics of the solidified/stabilized specimen are investigated with consideration of different influencing factors. The effects of the alkaline residue content on the leaching characteristics are typically shown in Figure 6.

As shown in Figure 6, the leached Pb²⁺ concentrations are extremely high when alkaline residue contents are at low ranges and will decrease with the increase of the alkaline residue content. Notable decreasing magnitude of 94%–98% can be observed at the alkaline residue content of 30% and curing time of 28 d, which is of great importance to the engineering practice. This significant improvement of the leaching characteristic of the specimen is mainly attributed to the adsorption of Pb²⁺ by the generated hydration products [14]. Besides, Pb²⁺ could react with OH⁻ and CO₃²⁻ in such alkaline environment leading to the formation of precipitates with Pb²⁺ adsorbing on the particle surface. Moreover, Pb²⁺ can partially replace Ca²⁺ in CaO·SiO₂·nH₂O (C-S-H) and then be fixed in the reticular structure of silicate represented as C-Pb-S-H [21, 22, 24, 25].

The effects of the curing time on the leaching characteristics of the solidified/stabilized specimen are presented in Figure 7.

In Figure 7, the leached Pb²⁺ concentration decreases with the curing time increasing. Notable decreasing magnitude of 89%–98% can be observed before 28-day curing at the alkaline content of 30%. After this, the evolution of the leached Pb²⁺ concentration becomes stable until 90-day curing is reached. This is because the hydration process will be improved and fully developed with the curing time increasing. The hydration products like CSH will be generated and effectively immobile the Pb²⁺ in such high alkaline environment provided by alkaline residue, which contributes to the improvement of the leaching characteristics of the specimen. Based on this result, it can be concluded that the leaching characteristics of the specimen can be improved in a short time due to the existence of the alkaline residue.

One point should be paid attention in Figures 6 and 7 is that the leaching characteristics of the specimen are strongly dependent on the initial Pb²⁺ concentration in the specimen. For further analysis, the evolutions of the leached Pb²⁺ concentration with the initial Pb²⁺ concentration in the specimen are shown in Figure 8.

Results in Figure 8 suggest that the leached Pb²⁺ concentration is extremely high for the specimen with higher initial Pb²⁺ concentration and will increase with the increase of the initial Pb²⁺ concentration in the specimen, which is attributed to the retardation of the hydration process, as well as the limitation of the immobilized capacity, due to the existence of the Pb²⁺ in the specimen [24, 25].

3.3. Microstructure Analysis. For explanation of the strength and leaching characteristics of the solidified/stabilized

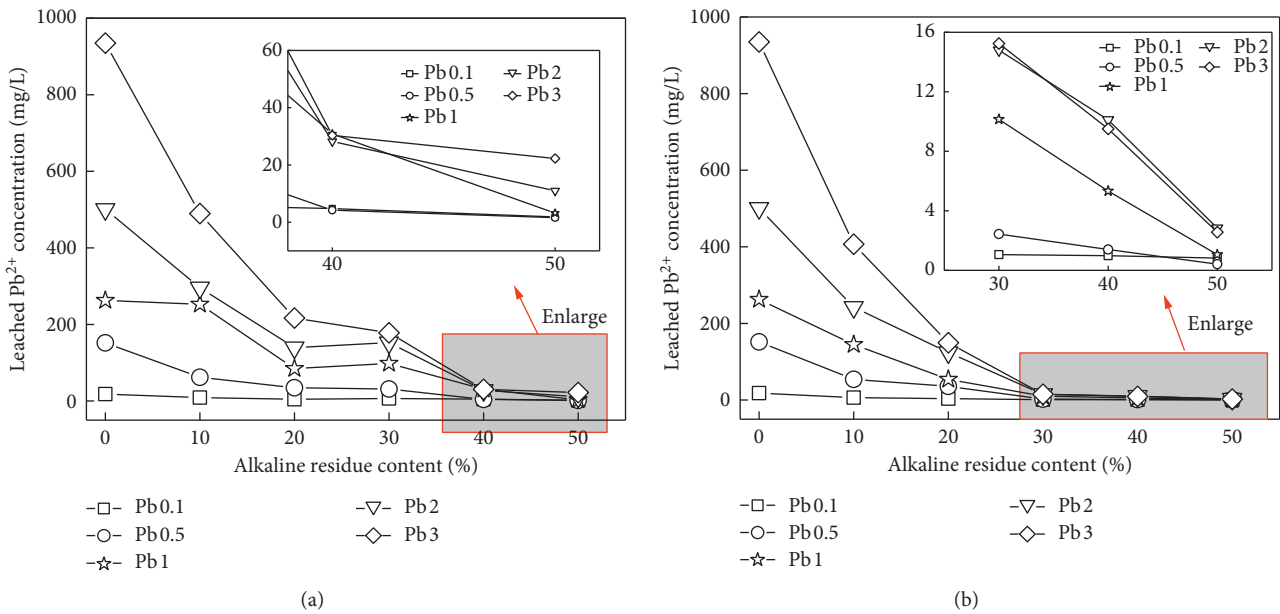


FIGURE 6: Evolutions of the leached Pb^{2+} concentration with the alkaline residue content of the specimen. Curing times of (a) 1 d and (b) 28 d.

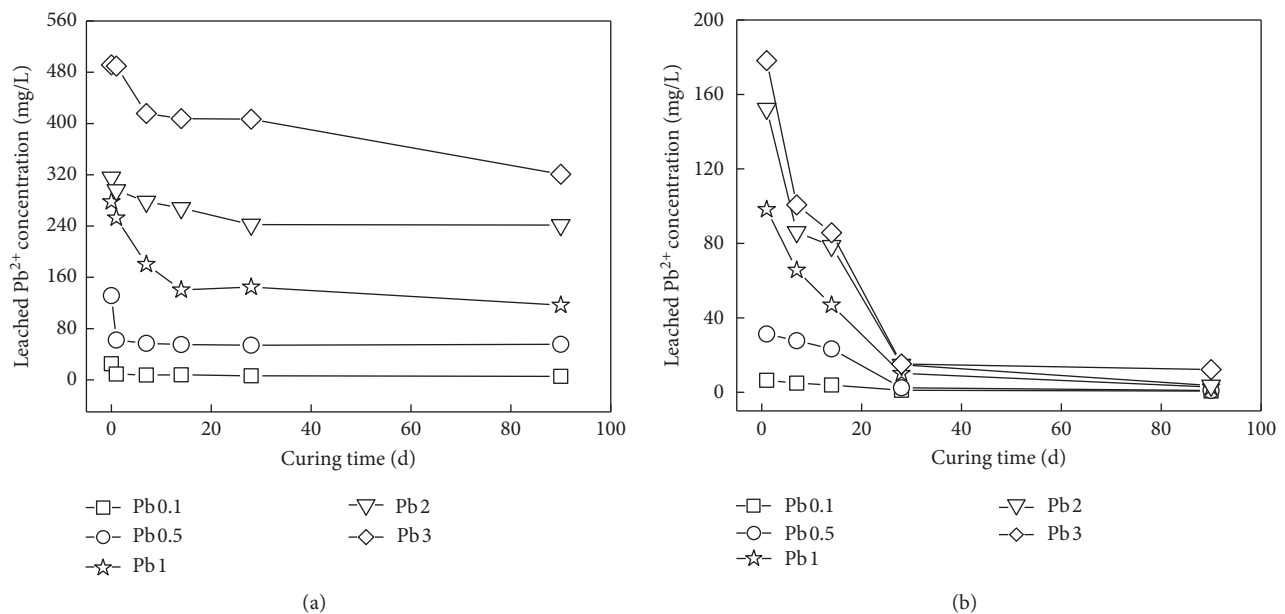


FIGURE 7: Evolutions of the leached Pb^{2+} concentration with the curing time of the specimen. Alkaline residue contents of (a) 10% and (b) 30%.

specimens under different conditions (alkaline residue content, curing time, and initial Pb^{2+} concentration), the SEM technique is adopted to perform the microstructural analysis as shown in Figure 9.

As shown in Figure 9, hydration products like cotton-like C-S-H, calcite drusy, and portlandite are presented in the solidified/stabilized specimen due to the physical-chemical reactions between the alkaline residue and soil [26]. Pb^{2+} will be immobilized in C-S-H through physical adsorption/encapsulation and chemical single

displacement reactions. Ca^{2+} contained in C-S-H will be substituted by Pb^{2+} resulting in the decrease of the strength and increase of the chemical connection between Pb^{2+} and hydration products. Pb-CSH gel could be observed on the surface of the soil particles, which implies the effective immobilization of Pb^{2+} in the specimen [27, 28]. Additionally, densification of the microstructure is clearly presented due to the massive formation of the hydration products. With the increase of alkaline residue content and curing time, the hydration process will be

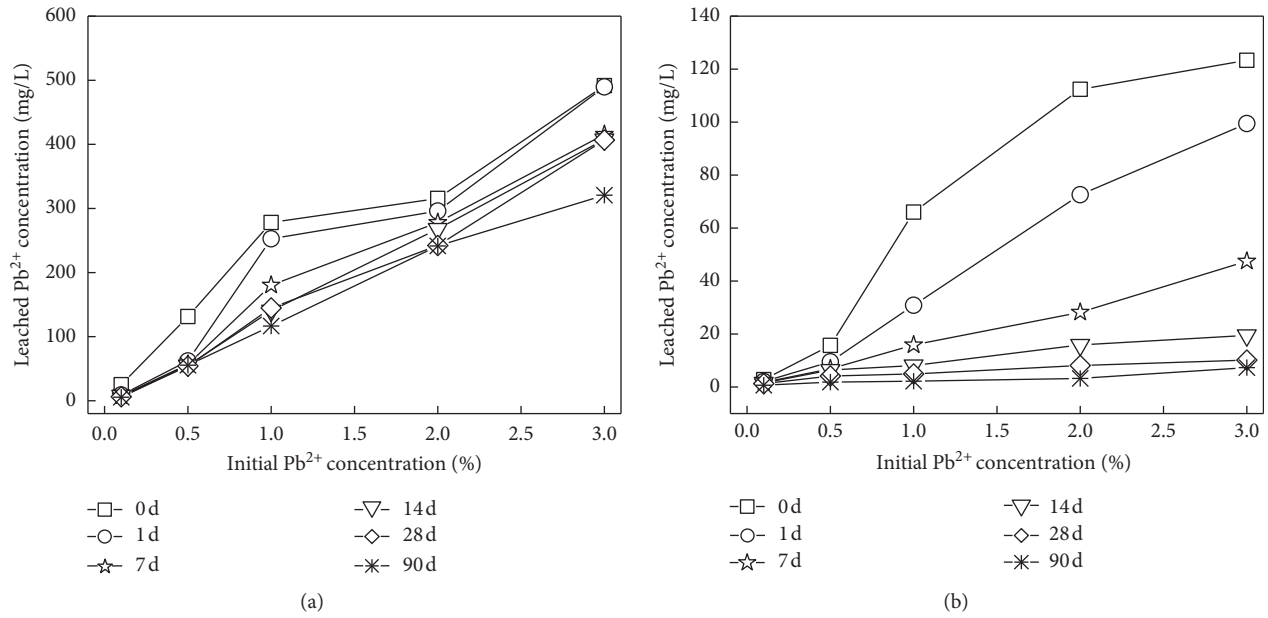


FIGURE 8: Evolutions of the leached Pb^{2+} concentration with the initial Pb^{2+} concentration of the specimen. Alkaline residue contents of (a) 10% and (b) 30%.

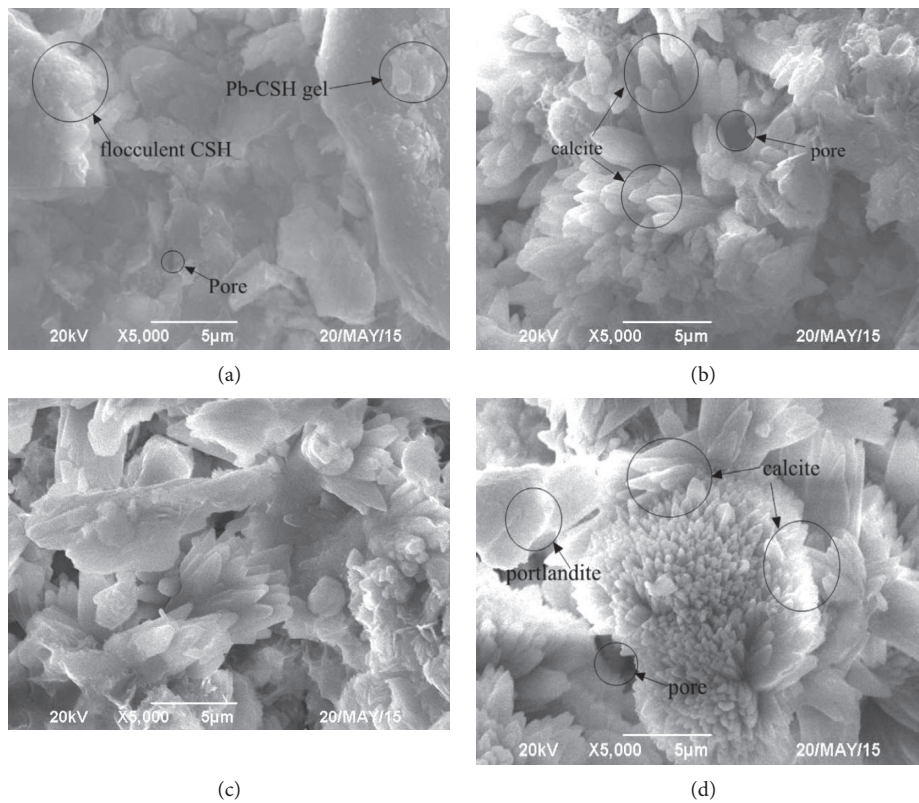


FIGURE 9: Microstructural characteristics of the specimens tested under different conditions. (a) AR10 + Pb1 (28 d). (b) AR30 + Pb1 (28 d). (c) AR30 + Pb3 (28 d). (d) AR30 + Pb1 (90 d).

promoted resulting in more hydration products. Based on these complicated physical-chemical reactions in the specimen, the strength and leaching characteristics will be effectively improved.

4. Conclusions

The strength and leaching characteristics, as well as the microstructural characteristic of the alkaline residue

solidified/stabilized Pb-contaminated soil, were experimentally investigated in the present work. Some main conclusions can be summarized as follows:

- (1) The UCS of the treated specimen increased with the increase of the alkaline residue content. The UCS of the treated specimen increased with the curing time increasing. Notable increasing magnitude was observed at the early period of curing followed by a slight increase in the long curing period. The increase of the initial Pb^{2+} concentration in the specimen resulted in a notable decrease of the UCS.
- (2) Leached Pb^{2+} concentration after the TCLP test decreased with the increase of the alkaline residue content and curing time, while increased with the increase of the initial Pb^{2+} concentration in the specimen. The higher initial Pb^{2+} concentration in the specimen will result in more notable increase of the leached Pb^{2+} concentration.
- (3) Microstructural analysis performed by the SEM technique confirmed the existence of CSH, calcite, portlandite, and other hydration products in the solidified/stabilized specimen. The amount of the hydration products, as well as the density and integrity of the specimen, increased with the increase of alkaline residue content and curing time.

Data Availability

The data used to support the findings of this study are available from the corresponding author upon request.

Conflicts of Interest

The authors declare that they have no conflicts of interest.

Acknowledgments

The authors are grateful to the National Natural Science Foundation of China (Project nos. 41672306 and 41372281).

References

- [1] B. M. Sunil, S. Shrihari, and S. Nayak, "Shear strength characteristics and chemical characteristics of leachate-contaminated lateritic soil," *Engineering Geology*, vol. 106, no. 1-2, pp. 20-25, 2009.
- [2] F. S. Zha, L. Xu, and K. R. Cui, "Strength characteristics of heavy metal contaminated soils stabilized/solidified by cement," *Rock and Soil Mechanics*, vol. 33, no. 3, pp. 652-656, 2012, in Chinese.
- [3] S. L. Lin, W. H. Cross, E. S. K. Chian, J. S. Lai, M. Giabbai, and C. H. Hung, "Stabilization and solidification of lead in contaminated soils," *Journal of Hazardous Materials*, vol. 48, no. 1-3, pp. 95-110, 1996.
- [4] M. A. Janusa, C. A. Champagne, J. C. Fanguy, G. E. Heard, P. L. Laine, and A. A. Landry, "Solidification/stabilization of lead with the aid of bagasse as an additive to Portland cement," *Microchemical Journal*, vol. 65, no. 3, pp. 255-259, 1998.
- [5] C. Y. Jing, X. G. Meng, and G. P. Korfiatis, "Lead leachability in stabilized/solidified soil samples evaluated with different leaching tests," *Journal of Hazardous Materials*, vol. 114, no. 1-3, pp. 101-110, 2004.
- [6] C.-Y. Yin, H. B. Mahmud, and M. G. Shaaban, "Stabilization/solidification of lead-contaminated soil using cement and rice husk ash," *Journal of Hazardous Materials*, vol. 137, no. 3, pp. 1758-1764, 2006.
- [7] X. D. Li, C. S. Poona, H. Sun, I. M. C. Lo, and D. W. Kirk, "Heavy metal speciation and leaching behaviors in cement based solidified/stabilized waste materials," *Journal of Hazardous Materials*, vol. 82, no. 3, pp. 215-230, 2001.
- [8] N. Bolan, A. Kunhikrishnan, R. Thangarajan et al., "Remediation of heavy metal(loid)s contaminated soils-to mobilize or to immobilize?," *Journal of Hazardous Materials*, vol. 266, pp. 141-166, 2014.
- [9] Y. J. Du, M. L. Wei, K. R. Reddy, Z. P. Liu, and F. Jin, "Effect of acid rain pH on leaching behavior of cement stabilized lead-contaminated soil," *Journal of Hazardous Materials*, vol. 271, pp. 131-140, 2014.
- [10] Q. Xue, P. Wang, J. S. Li, T. T. Zhang, and S. Y. Wang, "Investigation of the leaching behavior of lead in stabilized/solidified waste using a two-year semi-dynamic leaching test," *Chemosphere*, vol. 166, pp. 1-7, 2017.
- [11] Y. B. Yan, F. J. Qi, B. Seshadri et al., "Utilization of phosphorus loaded alkaline residue to immobilize lead in a shooting range soil," *Chemosphere*, vol. 162, pp. 315-323, 2016.
- [12] X. Cao, C. J. Jin, X. C. Liu, and G. Peng, "Adsorption characteristics of copper ions on alkaline sludge," *Environment Chemistry*, vol. 25, no. 4, pp. 414-419, 2006, in Chinese.
- [13] C. J. Jin, G. B. Tian, X. Cao, Z. L. She, and J. G. Zheng, "Adsorption characteristics of zinc ions on alkaline sludge," *Chinese Journal of Environmental Engineering*, vol. 9, no. 2, pp. 1218-1222, 2008, in Chinese.
- [14] S. L. Sun, Q. H. Zheng, J. Tang et al., "Experimental research on expansive soil improved by Alkaline residue," *Rock and Soil Mechanics*, vol. 33, no. 6, pp. 1608-1612, 2012, in Chinese.
- [15] F. Wang, Z. Q. Xu, L. X. Yan, and P. Cao, "Study on test methods and geotechnical properties of alkaline residue," *Chinese Journal of Geotechnical Engineering*, vol. 29, no. 8, pp. 1211-1214, 2007, in Chinese.
- [16] The Professional Standards Compilation Group of People's Republic of China, *JTGE 40-2007 Test Methods of Soils for Highway Engineering*, China Communications Press, Beijing, China, 2007.
- [17] S. K. Ouki and C. D. Hills, "Microstructure of Portland cement pastes containing metal nitrate salts," *Waste Management*, vol. 22, no. 2, pp. 147-151, 2002.
- [18] D. I. Boardman, *Lime stabilisation: clay-metal-lime interactions*, Ph.D. thesis, Loughborough University, Loughborough, UK, 1999.
- [19] ASTM, *Standard Test Method for Unconfined Compressive Strength of Cohesive Soil, Annual Book of ASTM Standards D2166-06*, American Society of Testing and Materials, West Conshohocken, PA, USA, 2000.
- [20] US EPA, *Toxicity Characteristic Leaching Procedure, Test Methods for Evaluating Solid Waste, Physical/Chemical Methods, SW-846*, US EPA, Washington, DC, USA, 3rd edition, 1992.
- [21] D. J. Lee, T. D. Waite, G. Swarbrick, and S. Lee, "Comparison of solidification/stabilization effects of calcite between Australian and South Korean cements," *Cement and Concrete Research*, vol. 35, no. 11, pp. 2143-2157, 2005.

- [22] D. J. Lee, "Formation of leadhillite and calcium lead silicate hydrate (C-Pb-S-H) in the solidification/stabilization of lead contaminants," *Chemosphere*, vol. 66, no. 9, pp. 1727–1733, 2007.
- [23] L. Chen, S. Y. Liu, Y. J. Du, and F. Jin, "Unconfined compressive strength properties of cement solidified/stabilized lead-contaminated soils," *Chinese Journal of Geotechnical Engineering*, vol. 32, no. 12, pp. 1898–1903, 2010, in Chinese.
- [24] M. S. Y. Bhatti, "Fixation of metallic ions in Portland cement," in *Proceedings of 4th National Conference on Hazardous Wastes and Hazardous Materials*, pp. 140–145, Washington, DC, USA, 1987.
- [25] D. L. Cocke and M. Y. A. Mollah, "The chemistry and leaching mechanisms of hazardous substances in cementitious solidification/stabilization systems," in *Chemistry of Microstructure Solidified Waste Forms*, Lewis, Ann Arbor, MI, USA, 1993.
- [26] J. Bensted and P. Barnes, *Structure and Performance of Cements*, Taylor & Francis, Didcot, UK, 2nd edition, 2002.
- [27] G. Thevenin and J. Pera, "Interactions between lead and different binders," *Cement and Concrete research*, vol. 29, no. 10, pp. 1605–1610, 1999.
- [28] N. Gineys, G. Aouad, and D. Damidot, "Managing trace elements in Portland cement-part I: interactions between cement paste and heavy metals added during mixing as soluble salts," *Cement and Concrete Composites*, vol. 32, no. 8, pp. 563–570, 2010.

Research Article

Quantification of the Transparency of the Transparent Soil in Geotechnical Modeling

Li-Da Yi,^{1,2} Hua-Bin Lv,¹ Tian Ye,¹ and Yi-Ping Zhang ¹

¹College of Civil Engineering and Architecture, Zhejiang University, 866 Yuhangtang Road, Hangzhou, Zhejiang, China

²Power China Huadong Engineering Co., Ltd, 201 Gaojiao Road, Hangzhou, Zhejiang, China

Correspondence should be addressed to Yi-Ping Zhang; zhangyiping@zju.edu.cn

Received 11 April 2018; Revised 2 July 2018; Accepted 15 July 2018; Published 9 September 2018

Academic Editor: Yonggui Chen

Copyright © 2018 Li-Da Yi et al. This is an open access article distributed under the Creative Commons Attribution License, which permits unrestricted use, distribution, and reproduction in any medium, provided the original work is properly cited.

An indispensable process of geotechnical modeling with transparent soils involves capturing and analyzing images, in which favorable transparency is required for optical measurements. This paper proposes an objective framework for quantification of transparency in transparent soil based on its transmittance. Specifically, transparent soil with fused quartz serves as the soil sample for the detection of transmittance, and transmittance's impact on imaging quality in geotechnical modeling with transparent soil is investigated through an evaluation function of image clarity. According to the results of research about transparent soil with fused quartz, viewing depth and refractive index matching are the dominant factors that affect variations in transmittance of transparent soil, and the variations of transmittance are subjected to exponential decay regarding viewing depth or refractive index matching based on the theoretical modeling's function of curve fitting. Moreover, experimental results indicate that imaging quality of geotechnical modeling with transparent soil is enhanced with increasing transmittance, and imaging quality shows a remarkable improvement when transmittance is greater than 90%.

1. Introduction

For geotechnical testing, transparent soil is perceived as a model to visualize the internal geotechnical properties, such as deformation, strain, and flow [1]. It is a porous medium, which consists of a transparent surrogate representing natural soil and fluids with a matched refractive index. Transparent soil provides approaches for geotechnical modeling of soil-structure interactions and multiphase flow in soils [2]. Pioneering researchers of transparent soil introduced precipitated silica to investigate non-Newtonian fluid flow [3] and conducted further research on the geotechnical properties of low-plasticity clay [4, 5]. Over time, other families of transparent soils have been developed for geotechnical testing, including silica gel [6], hydrogel [7], fused quartz [8], and laponite [9]. In addition to investigation of soil-structure interaction mechanisms and hydraulic behavior, notable work has recently extended geotechnical applications of transparent soils to centrifuge tests [10], soil mechanics lessons in

elementary schools [11], and research involving geoenvironmental models [12].

In addition to the ability of transparent soil to model natural soil, visualization of the transparent soil is of equal importance to application in geotechnical testing. An indispensable process of modeling with transparent soil involves capturing and analyzing images. By capturing continuous images in noninvasive measurements, including digital image correlation (DIC), transparent soil techniques rival apparatuses such as X-rays, computerized tomography (CT), and magnetic resonance imaging (MRI) [13]. DIC serves as a methodology of image analysis for measurement of kinematics within transparent soils [14], in which transparency is required.

To determine a favorable level of transparency for optical measurements, the transparency of transparent soil has been evaluated in recent studies. For example, grid lines were observed through some viewing depth of transparent soil to rank different levels of transparency for possible analysis [15]; an adapted Snellen chart was utilized in an "eye test"

calibration for viewing decreasing font-sized letters through transparent soils to estimate the transparency that is available for visualization [16]. However, the conventional methodology of the above assessments is subjective and nonquantitative and infers variable levels of acceptable transparency for visualization of transparent soils. Thus, a comprehensive, objective, quantitative, and robust framework of transparency assessment awaits development. Recently, the modulation transfer function (MTF) has been proposed for quantitative assessment and comparison of transparency [17].

However, MTF is determined according to the fidelity of transferred details from object to image, which involves an overall imaging capability of the whole optical system, which is characterized by not only transparency of transparent soil but also the photographic apparatus. Hence, in order to provide observations of how transparency affects the accuracy of imaging and measurement in transparent soil, the purpose of this research is to quantitatively evaluate the transparency of transparent soil itself. If such a framework of evaluation is developed for the optical characteristics of transparent soil, it shall provide guidance for modeling experiments of transparent soil to reduce limitations on geometry and refractive index matching.

Specifically, in this paper, an objective framework for quantification of transparency based on transmittance is established by combining geotechnical engineering and optics. First, the calculation method of transmittance and the experimental setup for detecting transmittance is proposed so that transmittance data of transparent soil are acquired. Second, it is suggested that variations of transmittance are subjected to exponential decay, which is well explained by the principle of the Christiansen effect. And such observation of transmittance shall provide approaches to improving transparency quality of transparent soil. Third, for experiments of detecting transmittance for different transparent soil samples, experimental results and digital images demonstrate the relationship between transmittance and imaging quality of visualization in transparent soil. The relationship between transmittance and imaging clarity is investigated using an evaluation function of the digital image.

2. Objective Framework for Quantification of Transparency in Transparent Soil Based on Transmittance

2.1. Transmittance. Transmittance defines the property that a substance permits transmitted light to pass through, while incident light is partially absorbed or scattered. It is the mathematical description of transparency. The theory of radiometry indicates that transmittance T is the luminous flux ratio of transmitted light φ_t to incident light φ_i [18], which is expressed as

$$T = \frac{\varphi_t}{\varphi_i} \quad (1)$$

The luminous flux refers to the power of electromagnetic radiation, which is modified due to varied sensitivity of the human eye to different wavelengths of light. It is calculated by a luminosity function regarding the issue. In the luminosity function, luminous efficacy is the weighting coefficient that represents the ratio of the luminous flux to the radiant flux. For a certain wavelength of light, the luminous flux φ is expressed as

$$\varphi = K_\lambda P, \quad (2)$$

where K_λ refers to the weighting coefficient at wavelength λ and P refers to the radiant flux. Based on (1) and (2), transmittance is denoted by the following equation:

$$T = \frac{P_t}{P_i}, \quad (3)$$

where P_t and P_i refer to the radiant flux of transmitted and incident light, respectively. Hence, the calculation method is capable of acquiring transmittance using optical measurements of a laser power meter in the experimental setup.

2.2. Measurement Method for Transmittance

2.2.1. Material. In the experimental setup, fused quartz, which is common in manufacturing, is applied as the solid particle of transparent soil. During the manufacturing process, fused quartz is highly purified by melting at approximately 2000°C and is formed by crystalline silica with a purity level of 99.9% to 99.95% [1]. Specifically, for the selected fused quartz in this research, it is shown in Figure 1 that the particle size ranges from 2.00 to 2.80 mm. At each wavelength of visible light, transmittance of fused quartz is well beyond 90%. The refractive index of fused quartz is reported as 1.4585 [19].

Fused quartz aggregate is matched with a blend of two oils, namely, 15# PURITY FG WO white mineral oil produced by Petro-Canada and EI solvent oil produced by TEACSOL. Both oils are transparent as well as colorless, with the physical properties that are listed in Table 1.

As listed in Table 1, higher flashing points of flammability indicate that the oils are safe to use under normal laboratory conditions at room temperature. Since the density of mineral oil is similar to that of EI oil, mixtures of such two oils are well blended. The refractive index of well-blended oils changes with the specific blending ratio to achieve different levels of refractive index matching. The refractive index is then measured by implementation of a 2WJ refractometer with a precision of 0.0002. However, there is considerable variation in the refractive index of matching liquids at different temperatures [20]. To investigate the variation of the refractive index due to changing temperature, configuration of the DK-S18 water bath and circulating pump is connected to the refractometer for maintaining a constant temperature of the matching liquid [8, 21]. On the basis of the Arago-Biot function [22], the relationship between the resulting refractive index and blending ratio is expressed by the following equation:



FIGURE 1: Selected particle of fused quartz.

TABLE 1: Physical properties of the pore fluid.

Matching liquid	Flashing point (°C)	Density (kg/L)	Refractive index (at 20°C)
15# white mineral oil	180	0.847	1.4662
EI solvent oil	83	0.796	1.4380

$$n_{12} = \lambda [\theta n_1 + (1 - \theta)n_2] + g, \quad (4)$$

where n_{12} , n_1 , and n_2 refer to the refractive index of blended liquids, the first matching liquid, and the second matching liquid, respectively; θ refers to the volume fraction of the first matching liquid; and λ or g refers to the coefficient determined by temperature. Specifically, n_{12} represents the refractive index of blended oils and θ represents the volume fraction of the 15# white mineral oil. For the following experiment, the room temperature is strictly maintained as 20°C using an air conditioner, whereas λ and g are experimentally determined as 1.0159 and -0.0232 based on the calculation of the blending ratio.

2.2.2. Experimental Apparatus. For optical measurements, the layout of the experimental setup is shown in Figure 2(a), which involves a laser transmitter that emits 532 nm laser light, a test chamber, a detector of light power, and a laser power meter for detecting transmitter light power. As also shown in Figures 2(b) and 2(c), the test chambers provide desirable ranges of viewing depth, and a cuvette or acrylic glass box serves as the test chamber, with identical wall thickness on each side. When a light beam from a laser transmitter passes through transparent soil in the test chamber, the radiant flux of transmitted light P_t is measured. Then, the radiant flux of incident light P_i is measured without transparent soil in the test chamber. P_t and P_i are measured from multiple incident positions of light at one side of the test chamber. The side of the test chamber for incident light was switched over for each measurement of the transparent soil sample. Specifically, the incident positions of light are located roughly equidistant. In this way, 16 pairs of P_t and P_i are acquired for each measurement. On the basis of the 16 pairs of experimental results, the average results of transmittance are calculated. Moreover, the confidence interval of the average transmittance is also denoted as the error bar in the figures.

2.3. Variation in Transmittance

2.3.1. Principle of the Christiansen Effect. To investigate the variation in transmittance of transparent soil and to analyze the qualitative relationship between the factors (that affect the variation in transmittance) and the transmittance, the principle of Christiansen effect is proposed for the curve fitting of experimental results of transmittance of transparent soil. Preparation of transparent soil should ensure that the transparent substance is immersed in the refractive index matching liquid, which is also involved in the process of producing transparent media in the experiment of the Christiansen effect [23]. Numerous solid-liquid interfaces exist within such transparent media. For incident light with a specific wavelength on the solid-liquid interface, the principle of the Christiansen effect indicates that when dispersion curves of solid and liquid coincide at specific wavelength, incident light in Christiansen experiment is mostly transmitted [24]. Either the optical interference or the scattering results in attenuation of transmitted light in the Christiansen effect. The theory of the Christiansen experiment is concluded from optical interference [24], and it states that the transmittance of transparent media undergoes exponential decay. Particularly within transparent soil, incident light is scattered and refracted consecutively on multiple solid-liquid interfaces while transmitted light is attenuated. Assuming that inhomogeneity of random packing in solid particles has a Gaussian distribution in the refractive index [25], a modified equation of the Raman Varshneya [26] method is derived as follows:

$$T = \exp \left\{ - \frac{k_1^2 \pi^2 [n_s - n_l]^2 + k_2 d}{\lambda_m^2} \right\}, \quad (5)$$

where n_s and n_l refer to the refractive index of the solid and liquid, respectively; k_1 refers to the coefficient that is modified by the size, shape, and distribution of the solid particle; k_2 refers to the coefficient that is modified by the shape and volume fraction of the solid particle; d refers to the transmitted thickness or viewing depth; and λ_m refers to the matching wavelength at which the solid and liquid refractive indexes are matched.

The principle of the Christiansen effect is the theoretical basis of this research that explains the factors that affect transmittance in optical measurements of transparent soil. With a consistent combination of grain size gradation and compactness within transparent soil, the subsequent impacts of size, shape, and distribution of solid particles are neglected in the following analysis. Besides, the modified equation of the Raman Varshneya method shall be utilized to provide observations into the function of curve fitting of the factors and to provide explanations on statistical parameter's physical meaning. Therefore, coefficients k_1 and k_2 remain constant for the same transparent soil sample. For the experimental setup in this study, the wavelength of transmitted light is maintained constant as 532 nm. Therefore, the viewing depth d and the refractive index matching ($n_s - n_l$) are the main factors that affect transmittance, and they are analyzed in following verification experiments. For transparent soil with

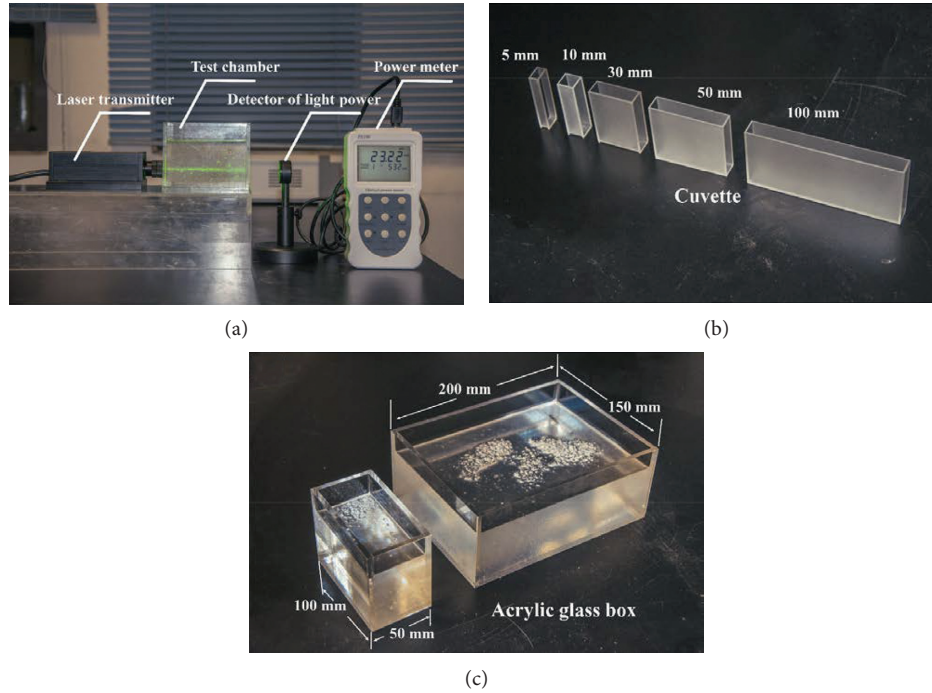


FIGURE 2: Layout of the experimental apparatus and test chambers.

fused quartz and mineral oil, the experiments are set up to validate that the transmittance of transparent soil is subjected to exponential decay due to viewing depth d and refractive index matching ($n_s - n_l$).

2.3.2. Impact of Viewing Depth. Assuming that viewing depth d is the single variable in (5), expression of transmittance T is simplified as

$$T = e^{-Kd}, \quad (6)$$

where K refers to the attenuation coefficient. In practice, (6) is also deduced from the Beer–Lambert law [27]. According to the Beer–Lambert law, the light that is absorbed by a substance is proportional to its transmitted thickness. In particular, transmitted thickness is identified as the viewing depth in this research. Figure 3 reveals the relationship between transmittance T and viewing depth d . For investigated transparent soil with fused quartz, the attenuation coefficient K is calculated to be 0.0021 mm^{-1} based on verification of experimental data. However, deviation ranges exist in the transmittance results, and the confidence interval of mean transmittance is denoted as the error bar in Figure 3.

2.3.3. Impact of Refractive Index Matching. A refractive index matching technique has been applied in various fields of study, including granular media and riverbeds [28]. Further research has also sought to establish a methodology of assessment for allowable refractive index mismatch [22]. In this analysis, to investigate the impact of refractive index matching on transmittance, the matching liquid is prepared with various oil mix ratios to achieve different levels of

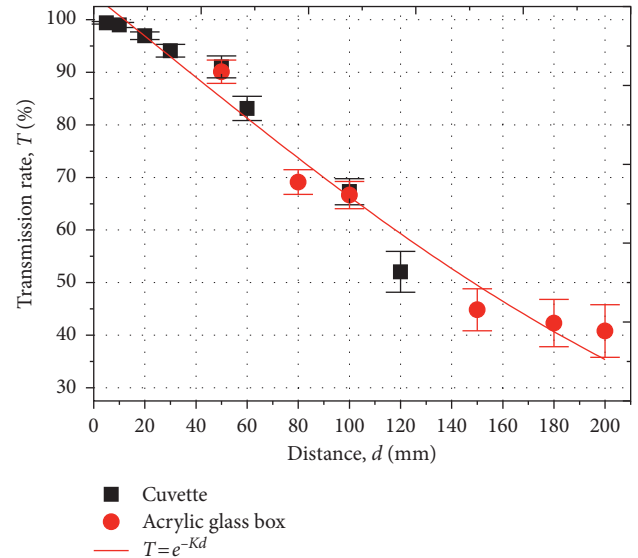


FIGURE 3: Relationship of transmittance T to viewing depth d .

refractive index matching ($n_s - n_l$). However, considering that a refractive index of fused quartz n_s remains consistent at room temperature of 20°C , changes in the resulting refractive index of matching liquid n_l represent refractive index matching. Assuming that the refractive index of matching liquid n_l is the single variable in (5), expression of transmittance T is simplified as

$$T = e^{K_1 n_l^2 + K_2 n_l + K_3}, \quad (7)$$

where K_1 , K_2 , and K_3 refer to the coefficients that are determined by the fitted curve. In Figure 4, the curve fitting

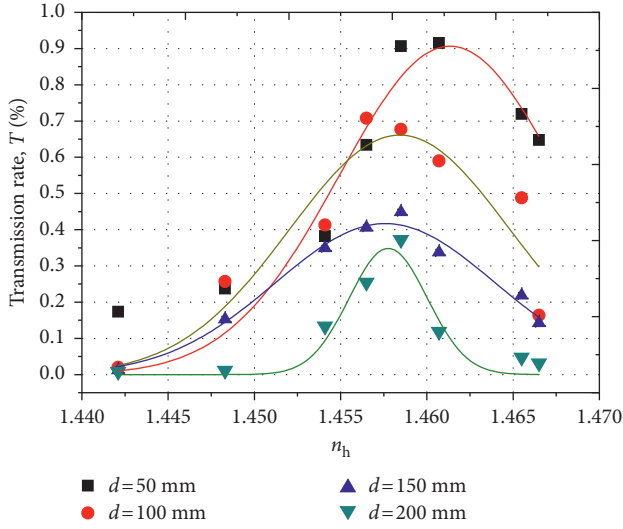


FIGURE 4: Relationship of transmittance T to refractive index matching.

results demonstrate that the transmittance reaches a peak value with the best match of the refractive index matching, whereas there are dips of transmittance as a result of the refractive index mismatch. In general, the impact of refractive index matching is well described by the exponential decay of principle of the Christiansen effect.

3. Relationship between Transmittance and Imaging Quality

3.1. Evaluation Function of Image Clarity. Transmittance describes transparency mathematically, and it is the fidelity in optical measurement of transparent soil that quantification of transparency counts for. Thus, it is necessary to establish the relationship between transmittance and evaluation function of image clarity. For digital image processing of transparent soil, image clarity is the primary concern of DIC precision [29] because captured images within transparent soil consist of different intensities at different pixel positions, which allow for identification. Improved image clarity of image texture is associated with a greater degree of variation in pixel intensity. For example, image intensity changes with the degree of saturation of transparent soil [30–32], with unsaturated transparent soil yielding degraded optical clarity.

Accordingly, the variation in pixel intensity is estimated by the intensity gradient in this research. The intensity gradient is calculated by the Sobel operator, which is prevalently adopted in the image processing technique of edge detection. It calculates the norm of the vector at each pixel of the digital image. By computing the approximated norm of the image gradient at the pixel position (x, y) in the horizontal and vertical directions, the Sobel operator is usually less computationally expensive with an isotropic 3×3 kernel. However, approximations of the derivatives can be defined at higher or lower degrees of accuracy by different kernels. In this paper, the experimental data demonstrate

that the approximated results of the isotropic 3×3 gradient Sobel operator are sufficient for distinguishing between different levels of the evaluation function, which corresponds to fidelity in the optical measurements.

As a gradient-based sharpness function in digital photography, the evaluation function E of image clarity of transparent soil is adapted from the Sobel operator. A digital image with $W \times H$ pixels is shown in Figure 5, and the pixel position (x, y) is determined in the following calculations.

Initially, the image intensity of pixel position (x, y) is denoted as $f(x, y)$. $A(x, y)$ is the 3×3 matrix that describes image intensity around pixel position (x, y) in a 3×3 pixel region. Then, 3×3 kernels are utilized in the Sobel operator to convolve with the image intensity $A(x, y)$. As a result, the image gradient vectors at pixel position (x, y) in the horizontal and vertical directions are acquired as $G_x(x, y)$ and $G_y(x, y)$ in (8) and (9), resp.:

$$G_x(x, y) = \begin{bmatrix} -1 & 0 & 1 \\ -2 & 0 & 2 \\ -1 & 0 & 1 \end{bmatrix} * A(x, y), \quad (8)$$

$$G_y(x, y) = \begin{bmatrix} -1 & -2 & -1 \\ 0 & 0 & 0 \\ 1 & 2 & 1 \end{bmatrix} * A(x, y), \quad (9)$$

where $*$ represents a 2-dimensional signal that computes convolution. In other words, $\nabla f(x, y)$ is calculated as

$$\nabla f(x, y) = (G_x(x, y), G_y(x, y)). \quad (10)$$

Meanwhile, $|\nabla f(x, y)|$ refers to an approximated modulus of the image gradient vector at pixel position (x, y) in a 3×3 pixel region. Thus, $|\nabla f(x, y)|$ is calculated by an image intensity vector from a convolution of the Sobel operator in both the horizontal and vertical directions as follows:

$$|\nabla f(x, y)| = \sqrt{G_x(x, y)^2 + G_y(x, y)^2}, \quad (11)$$

where $G_x(x, y)$ and $G_y(x, y)$ refer to the result of the discrete differentiation operator at pixel position (x, y) in the horizontal and vertical directions, respectively.

The approximated modulus of the image gradient $|\nabla A(x, y)|$ lays the foundation of evaluation function E . Evaluation function E is designated to establish different levels of image clarity. Considering that the mean intensity gradient is proposed to evaluate speckle pattern quality in DIC [33], the evaluation function E is defined as the mean square of the norm of the image gradient at all pixels in the captured image, denoted as follows:

$$E = \sum_{x=1}^W \sum_{y=1}^H \frac{|\nabla f(x, y)|^2}{N}, \quad (12)$$

where N refers to the sum of pixels in the digital image. In addition, it is noted that the evaluation function given in (12) is sensitive to changes of intensity. Consequently, for comparison between different levels of image clarity, the

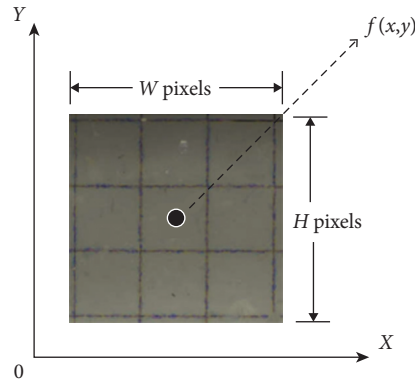


FIGURE 5: A digital image with $W \times H$ pixels ($x \in [1, W]$; $y \in [1, H]$).

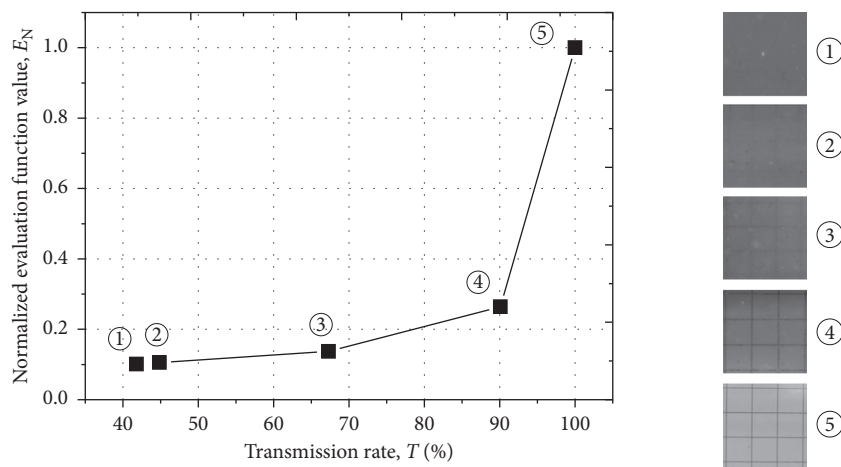


FIGURE 6: Relevance of transmittance T to the normalized evaluation function of image clarity E_N .

evaluation function E is normalized as E_N in unit-based normalization, expressed as follows:

$$E_N = \frac{E}{E_{\max}}, \quad (13)$$

where E_N refers to the normalized evaluation function and E_{\max} is determined by the evaluation function of image clarity with no degradation in transparent soil. Image clarity of transparent soil is quantitatively evaluated using the normalized evaluation function E_N .

3.2. Relevance of Transmittance to the Normalized Evaluation Function for Transparent Soil with Fused Quartz. As shown in Figure 6, the relevance of transmittance to image clarity is revealed by the relationship between transmittance T and the normalized evaluation function E_N . Such relevance is investigated for transparent soil with fused quartz. In detail, grid lines are uniformly printed on paper but are viewed through transparent soil with varied depth. Different sizes of the acrylic glass box are utilized for the test chamber containing the transparent soil to determine the viewing depth. For various viewing depths, images of grid lines are captured by a Nikon D7000 digital camera with a 50 mm $f/1.8$ D lens. Such photographic equipment produces images with

a resolution of 4928×3264 pixels by an aperture of $f/22$, an exposure time of 5 s, and ISO100. For digital image processing, the digital images are cut to the same size for calculation of the evaluation function E_N that defines the image clarity. To capture digital images ①~⑤ in Figure 6, configuration of the photographic equipment and alignment of the optical system are made consistent in each measurement, while transmittance of the transparent soil sample varies from case to case. Meanwhile, transmittance T of transparent soil is measured in each case. As a result, the correlation of transmittance to image clarity is revealed by the relevance of transmittance T to the evaluation function of E_N in Figure 6. Figure 6 includes representative results of transmittance for varied image clarity of transparent soil at the viewing depths of 50 mm (⑤), 100 mm (④), 150 mm (③), and 200 mm (②). In addition, when no transparent soil is in the test chamber, digital image ① is captured and the transmittance of the test chamber without transparent soil is detected.

For transparent soil with fused quartz and mineral oil, the experimental data show a significant increase in image clarity with transmittance higher than 90% (digital image ② with a transmittance of $90.09 \pm 2.22\%$). In addition, based on previous research of portraying the level of transparency [15], the viewing depth of transparent soil in the test was

typically 50 mm. Thus, the digital image ③ delivers a transmittance of $67.29 \pm 2.59\%$, which corresponds to a viewing depth of 50 mm. To draw a conclusion, for some categories of transparent soil such as the soil sample with fused quartz, there is a certain calibration curve as shown in Figure 6 that indicates the relationship between transmittance and imaging quality. And such relationship shall be of great value in further research into accuracy of digital image analysis.

4. Conclusions

The fundamental purpose of this paper is to propose an objective framework for quantification of transparency in transparent soil based on transmittance. In this framework, experimental apparatuses including laser transmitter and power meter are introduced in the measurement method for transmittance. Additionally, analysis of transparent soil property and the principle of the Christiansen effect are integrated in this paper. The principle of the Christiansen effect is proposed to govern the variation in transmittance and to investigate the impact factors that affect transmittance. Furthermore, the relationship between transmittance and imaging quality is also investigated.

On a basis of experimental results, exponential decay of transmittance is validated, and the dominant factors that affect variation in transmittance are viewing depth and refractive index matching. Besides, according to the relevance of transmittance to the evaluation function of the intensity variation, imaging quality of geotechnical modeling with transparent soil is enhanced with increasing transmittance, and imaging quality shows a remarkable improvement when transmittance is greater than 90%.

Above all, the principle of the Christiansen effect provides guidance for increasing the viewing depth of transparent soil and refining the refractive index matching technique to improve transparency in transparent soil in geotechnical modeling. Meanwhile, the relationship between transmittance and image clarity is established. Such relationship lays a foundation of further research regarding the accuracy of digital image analysis in transparent soil with different transmittance.

Conflicts of Interest

The authors declare that they have no conflicts of interest.

Acknowledgments

This work was supported by the National Natural Science Foundation of China (no. 51579219).

References

- [1] M. Iskander, *Modeling with Transparent Soils, Visualizing Soil Structure Interaction and Multi Phase Flow, Non-Intrusively*, Springer, New York, NY, USA, 2010.
- [2] P. Kelly, *Soil structure interaction and group mechanics of vibrated stone column foundations*, Ph.D. Thesis, University of Sheffield, Sheffield, UK, 2013.
- [3] R. Mannheimer, *Slurries You Can See Through, Technology Today*, Southwest Research Institute, San Antonio, TX, USA, 1990.
- [4] M. Iskander, J. Lai, C. Oswald, and R. Mannheimer, "Development of a transparent material to model the geotechnical properties of soil," *Geotechnical Testing Journal*, vol. 17, no. 4, pp. 425–433, 1994.
- [5] R. J. Mannheimer and C. J. Oswald, "Development of transparent porous media with permeabilities of soils and reservoir materials," *Ground Water*, vol. 31, no. 5, pp. 781–788, 1993.
- [6] M. Iskander, S. Sadek, and J. Liu, "Optical measurement of deformation using transparent silica gel to model sand," *International Journal of Physical Modelling in Geotechnics*, vol. 2, no. 4, pp. 13–26, 2003.
- [7] K. Tabe, "Transparent aquabeads to model LNAPL Ganglia migration through surfactant flushing," *Geotechnical Testing Journal*, vol. 38, no. 5, pp. 787–804, 2015.
- [8] F. M. Ezzein and R. J. Bathurst, "A transparent sand for geotechnical laboratory modeling," *Geotechnical Testing Journal*, vol. 34, no. 6, pp. 590–601, 2011.
- [9] J. Wallace and C. Rutherford, "Geotechnical properties of Laponite RD," *Geotechnical Testing Journal*, vol. 38, no. 5, pp. 574–587, 2015.
- [10] Z. Song, Y. Hu, C. O'Loughlin, and M. F. Randolph, "Loss in anchor embedment during plate anchor keying in clay," *Journal of Geotechnical & Geoenvironmental Engineering*, vol. 135, no. 10, pp. 1475–1485, 2009.
- [11] E. Suescun-Florez, M. Iskander, V. Kapila, and R. Cain, "Geotechnical engineering in US elementary schools," *European Journal of Engineering Education*, vol. 38, no. 3, pp. 300–315, 2013.
- [12] S. Kashuk, R. Mercurio, and M. Iskander, "Visualization of dyed NAPL concentration in transparent porous media using color space components," *Journal of Contaminant Hydrology*, vol. 162, pp. 1–16, 2014.
- [13] M. Iskander, R. Bathurst, and M. Omidvar, "Past, present, and future of transparent soils," *Geotechnical Testing Journal*, vol. 38, no. 5, pp. 557–573, 2015.
- [14] S. Sadek, M. Iskander, and J. Liu, "Accuracy of digital image correlation for measuring deformations in transparent media," *Journal of Computing in Civil Engineering*, vol. 17, no. 2, pp. 88–96, 2003.
- [15] J. Liu and M. G. Iskander, "Modelling capacity of transparent Soil," *Canadian Geotechnical Journal*, vol. 47, no. 4, pp. 451–460, 2010.
- [16] S. A. Stanier, *Modelling the behaviour of helical screw piles*, Ph. D. Thesis, University of Sheffield, Sheffield, UK, 2011.
- [17] J. A. Black and W. A. Take, "Quantification of optical clarity of transparent soil using the modulation transfer function," *Geotechnical Testing Journal*, vol. 38, no. 5, pp. 588–602, 2015.
- [18] J. M. Palmer and B. G. Grant, *The Art of Radiometry*, SPIE Press, Bellingham, WA, USA, 2010.
- [19] I. H. Malitson, "Interspecimen comparison of the refractive index of fused silica," *Journal of the Optical Society of America*, vol. 55, pp. 1205–1208, 1965.
- [20] I. Guzman, M. Iskander, E. Suescun, and M. Omidvar, "A transparent aqueous-saturated sand-surrogate for use in physical modeling," *Acta Geotechnica*, vol. 9, no. 2, pp. 187–206, 2014.
- [21] Y. P. Zhang, L. Li, and S. Z. Wang, "Experimental study on pore fluid for forming transparent soil," *Journal of Zhejiang University (Engineering Science)*, vol. 48, no. 10, pp. 1828–1834, 2014.

- [22] J. A. Dijkman, F. Rietz, K. A. Lorincz, M. Van Hecke, and W. Losert, "Refractive index matched scanning of dense granular materials," *Review of Scientific Instrument*, vol. 83, article 011301, 2012.
- [23] J. W. Gooch, *Encyclopedic Dictionary of Polymers*, Springer, New York, NY, USA, 2011.
- [24] C. V. Raman and K. S. Viswanathan, "A generalised theory of the Christiansen experiment," *Proceedings of the Indian Academy of Science*, vol. 41, no. 2, pp. 55–60, 1955.
- [25] S. Kang, D. E. Day, and J. O. Stoffer, "Measurement of the refractive index of glass fibers by the Christiansen-Shelyubskii method," *Journal of Non-Crystalline Solids*, vol. 220, no. 2, pp. 299–308, 1997.
- [26] A. K. Varshneya, M. C. Loo, and T. F. Soules, "Glass inhomogeneity measurement using the Shelyubskii method," *Journal of the American Ceramic Society*, vol. 68, no. 7, pp. 380–385, 2010.
- [27] A. Sassaroli and S. Fantini, "Comment on the modified Beer-Lambert law for scattering media," *Physics in Medicine and Biology*, vol. 49, no. 14, pp. 255–257, 2004.
- [28] A. E. Lobkovsky, A. V. Orpe, R. Molloy, A. Kudrolli, and D. H. Rothman, "Erosion of a granular bed driven by laminar fluid flow," *Journal of Fluid Mechanics*, vol. 605, pp. 47–58, 2008.
- [29] W. A. Take, "Thirty-Sixth Canadian Geotechnical Colloquium: advances in visualization of geotechnical processes through digital image correlation," *Canadian Geotechnical Journal*, vol. 52, no. 9, pp. 1199–1220, 2015.
- [30] S. B. Peters, G. A. Siemens, W. A. Take, and F. Ezzein, "A transparent medium to provide a visual interpretation of saturated/unsaturated hydraulic behavior," in *Proceedings of GeoHalifax*, pp. 59–66, Halifax, Nova Scotia, Canada, 2009.
- [31] G. A. Siemens, S. B. Peters, and W. A. Take, "Comparison of confined and unconfined infiltration in transparent porous media," *Water Resources Research*, vol. 49, no. 2, pp. 851–863, 2013.
- [32] G. A. Siemens, W. A. Take, and S. B. Peters, "Physical and numerical modeling of infiltration including consideration of the pore air phase," *Canadian Geotechnical Journal*, vol. 51, no. 12, pp. 1475–1487, 2014.
- [33] B. Pan, Z. Lu, and H. Xie, "Mean intensity gradient: an effective global parameter for quality assessment of the speckle patterns used in digital image correlation," *Optics & Lasers in Engineering*, vol. 48, no. 4, pp. 469–477, 2010.

Research Article

A Systematic Method to Evaluate the Shear Properties of Soil-Rock Mixture considering the Rock Size Effect

Minghui Ren ^{1,2}, Guangsi Zhao ^{1,2}, Xianhao Qiu,^{1,2} Qinghua Xue,^{1,2} and Meiting Chen^{1,2}

¹State Key Laboratory for Geomechanics and Deep Underground Engineering, China University of Mining & Technology, Xuzhou 221116, China

²School of Mechanics and Civil Engineering, China University of Mining & Technology, Xuzhou 221116, China

Correspondence should be addressed to Guangsi Zhao; zgscumt@126.com

Received 29 March 2018; Revised 23 June 2018; Accepted 2 August 2018; Published 5 September 2018

Academic Editor: Dingwen Zhang

Copyright © 2018 Minghui Ren et al. This is an open access article distributed under the Creative Commons Attribution License, which permits unrestricted use, distribution, and reproduction in any medium, provided the original work is properly cited.

The soil-rock mixture (S-RM) is widely applied in the geotechnical engineering due to its better mechanical properties. The shear strength, an essential aspect of S-RM which governs the stability and the deformation, is rather necessary to be revealed properly. The extraordinary issue of S-RM compared to fine-grained soils is the grain size effect on the strength analysis. This paper proposes a systematic method to obtain the realistic shear strength of S-RM by detecting the rock size effect. Firstly, based on fractal theory, the rock size was determined as 5 mm by the multifractal property of granular size distribution. Then, based on 2 selected specimen sizes combining the engineering dimension, shear gaps (T) effect and specimen size effect on the shear strength of S-RM have been investigated. It is shown that the gap of the direct shear test decides the physical mechanism of particles forming the shear resistance of S-RM based on the variation of apparent cohesion and mobilized internal friction angle. Specimen size effect is weakened by the gap effect considering the boundary effect. Realistic and stable shear strength parameters of S-RM have been researched by a reasonable gap ($0.2-0.4D$, where D is the largest particle size).

1. Introduction

Soil-rock mixture [1] (sand-gravel mixture [2], bimrocks [3, 4], and gravelly soil [5, 6]) is a kind of special geological material widely distributed in slopes and landslides and frequently exists in geotechnical engineering works such as embankment dam, foundations, and tunnel excavation. Due to the limited understanding of this special geomaterial, the prediction of landslides and engineering failure became an intractable issue recently, and branches of studies have been carried out. Different from the fine-grained soils, the oversized particles in the S-RM lead to complicated mechanical properties such as the size effect and the structural effect.

The S-RM is commonly regarded as a two-phase material by distinguishing the “soil” and “rock,” and the rock block content is regarded as the crucial input parameter to evaluate its mechanical properties [7–9]. It was found that the increase of rock block proportion can increase the strength of

S-RM [10, 11]. Accordingly, for the geomaterials with wide granular size distributions, the demarcation value between “soil” and “rock” is the essential physical quantity to understand the grading properties. However, the demarcation size of particles in related studies is differently arranged as 2 mm [2, 5], 4.75 mm [6], or undefined standard [12], which makes the related results difficult to be compared. Actually, with the increase of large particle size, the fixed “rock” size is not adaptive to calculate the rock proportion of S-RM. For this question, Medley [3] empirically found that bimrocks such as *mélanges* are scale independent in terms of engineering dimension—a fractal-like characteristic—and proposed that rock size in bimrocks is $0.05\sqrt{A}$, where A is the engineering dimension. It is assumed that the strength and deformation parameters determined for S-RM with a certain rock proportion can be applied for preliminary engineering design with similar rock proportion depending on the engineering dimension [13]. A series of empirical approaches of artificial S-RM based on the laboratory test have been

conducted [7–9], which consider the relative volumetric proportion determined by the characteristic dimension $0.05\sqrt{A}$. The rock size considering the researching dimension is more reasonable to evaluate the effect of rock blocks. Nevertheless, it still possesses the insufficiency which targets at the self-similar regularity of “rock” size, neglecting the description of overall particle size distribution. For instance, the number of blocks in engineering dimension may be different depending on the block size even if volumetric block proportions are the same [9]. In addition, for some coarse-grained soils naturally existed or artificially applied in engineering, the largest particle size is limited with engineering dimension. That is to say, an effective method to describe the granular size distribution is vital for the study of S-RM. Only if these questions have been demonstrated, the related research results can be well referred for engineering design effectively.

The shear strength parameters are valuable for design and failure prediction of engineering, and related laboratory investigations have been carried out to understand the shear behavior of S-RM. Based on the in situ shear test, Zhang et al. [14] found that the existence of rock blocks makes the deformation modulus and the internal friction angle of S-RM greater than that of the soil sample, while decreasing its cohesive force. The fracture plane in S-RM, often rounded rocks and formed in soil, is shown in an irregular shape because of the existence of rock blocks [15]. It was reported that the mechanical behavior of coarse-grained soils is influenced by the cemented properties [16]. The influence of particle size on the shear strength of coarse-grained soils, subjected to different gradation of the specimen, was investigated by numerical and experimental direct shear tests [17]. It is widely believed that the shear resistance of soil is affected by various factors, such as soil type, compactness, and grading properties. Most importantly, no matter what the kind of research purpose of S-RM is, the laboratory test method is definitely vital for acquiring the strength properties [18]. The direct shear test, adopted in this study due to simplicity and convenience, possesses some shortcomings such as the fixed failure plane and the nonuniform stress and deformation in the shear box. The shear resistance of gravelly soils basically originates from sliding of particles and particle rolling, so the formation of the shear band closely depends on specimen size and shear gap dimension which represents the opening between shear box halves. And it is reported that the formation of the shear band is the important cause of the scale effect [19].

However, according to the author’s knowledge, only few articles about shear gap effect on shear strength of coarse-grained materials have been published [20]. Shibuya et al. [21] pointed out that the space between the upper box and lower box should be maintained at a constant value slightly larger than the thickness of a free shear band (approximately 10–20 times D50 for the sands). If the opening between shear box halves is too small, a portion of rock particles within the specified shear band will have crush and fracture failures, which causes the overestimation of actual shear resistance of the coarse-grained soil, while a large opening causes stress reduction and material loss at the specimen edge. To this

end, this work attempts to acquire the reasonable shear gap of S-RM in the direct shear test, which is meaningful to obtain the more realistic strength.

2. The Fractal Structure of S-RM Gradation

The first aspect of size effect in S-RM is the particle size distributions (PSDs), which can be applied to predict its mechanical and physical properties. The existence of gravels decides the nonlinear characteristics in PSD of S-RM. Figure 1 presents the original size distribution of S-RM generated in the tunnel excavation in Xuzhou, China. The mixture contains the clayey matrix, gravel, and rock blocks, and the largest particle size of the samples is 60 mm by eliminating the oversize rock block. It can be analyzed that the traditional Talbot grading curve is not effective to depict the size grading properties because of the wide range of size distribution of S-RM.

The fractal theory was mainly used to explain the complex phenomenon in nature, which has also been applied in the geotechnical fields [22]. By using the cumulative solid mass distribution, the fractal representation of PSDs of soils was proposed [23], and the relation between fractal dimension and rock block size was discussed [24]. The fractal properties in two dimensions can be presented as follows [24]:

$$A(r > R) = C_a \left[1 - \left(\frac{R}{\lambda_a} \right)^{2-D} \right], \quad (1)$$

where R is the certain particle size, r is the granular size of S-RM, A is the cumulative area of particles whose sizes are over R , C_a is the shape factor, λ_a is the largest particle size, and D is the fractal dimension of granularity.

Taking the question into consideration,

$$V(r > R) = C_m \left[1 - \left(\frac{R}{\lambda_m} \right)^{3-D} \right], \quad (2)$$

where C_m is the shape factor, V is the cumulative granular volume of particles whose sizes are over R , and λ_m is the granular size. By multiplying the density ρ , the fractal characteristic based on the granular mass can be obtained as follows:

$$M(r > R) = \rho C_m \left[1 - \left(\frac{R}{\lambda_m} \right)^{3-D} \right]. \quad (3)$$

Meanwhile, the total mass of S-RM $M(r > 0)$ is presented as follows:

$$M(r > 0) = \rho C_m \left[1 - \left(\frac{0}{\lambda_m} \right)^{3-D} \right] = \rho C_m. \quad (4)$$

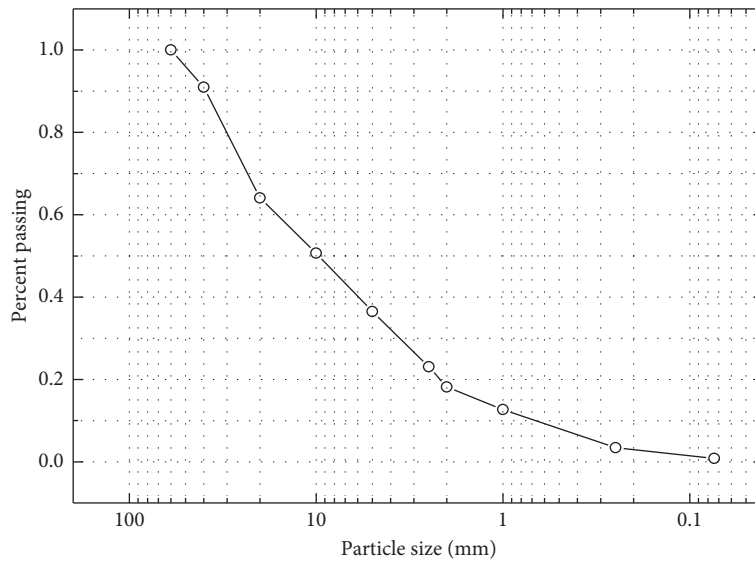
Consequently,

$$\frac{M(r > R)}{M(r > 0)} = 1 - \left(\frac{R}{\lambda_m} \right)^{3-D}. \quad (5)$$

Taking R as the largest particle size R_L in Equation (5), it is deduced that $\lambda_m = R_L$. The fractal presentation of S-RM can be obtained as follows [25]:



(a)



—○— Original size distribution

(b)

FIGURE 1: (a, b) Typical component and particle size distribution of S-RM.

$$\frac{M(r < R)}{M(r > 0)} = \left(\frac{R}{R_L}\right)^{3-D} \quad (6)$$

That is to say, the granular size properties can be characterized by the fractal exponent D if the plot $\lg(M(r < R)/M_T) - \lg R$ has the linear properties.

As soil is an open and self-organized system, and the quantity of fractal dimension, connected to evolutionary environment and mechanical properties, can effectively depict the gradation structure of S-RM. In order to obtain the fractal representation of S-RM, 3 series PSDs were calculated based on the Equation (6), and the average PSDs in Figure 2 is matched with the curves in Figure 1. The red solid line, fitted by the whole plot in Figure 2, indicates that the complexity of S-RM particle sizes can be well measured by a fractal exponent $D = 2.31$, which confirms the self-similar characteristic of S-RM. It is noted that the plots in Figure 2 do not strictly satisfy the strict linear relationship in the whole scale, which means the multifractal behavior in S-RM. Taking $R = 5$ mm as

the boundary, the granular sizes in the two domains have the more rigorous fractal features, which can be depicted by $D_1 = 2.10$ and $D_2 = 2.59$, respectively. By this way, it is proposed that the investigated S-RM has two self-similar size intervals, which reveal the different spatial structure of S-RM gradation corresponding to “soil” and “rock.” In this paper, $R = 5$ mm is regarded as the demarcation (rock size) which is not associated with the engineering dimension.

3. Experimental Procedure considering Size Effect

3.1. Determination of Specimen Size. In order to reveal the strength characteristic of S-RM further, the objective of this study is to attempt to investigate the proper relationship between rock block size and shear gap. Based on the size analysis in Figure 2, the largest particle size of the tested samples is selected as 10 mm, representing the “rock” (5–10 mm), and mass proportion is 28%. There has been some

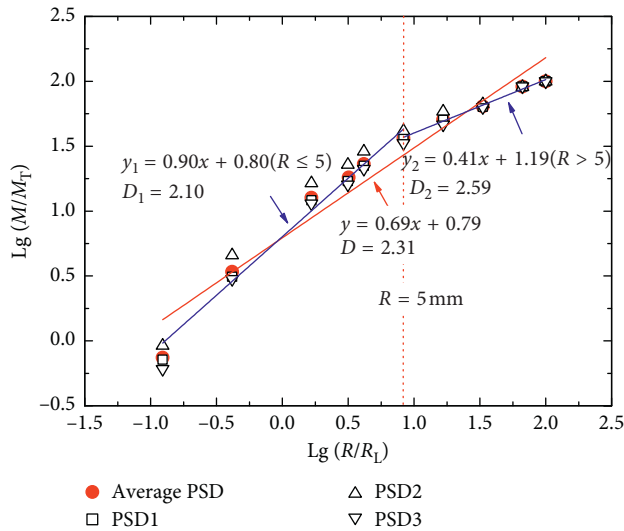


FIGURE 2: The multifractal properties of SRM.

controversy about the threshold ratio between specimen size and the characteristic particle size which bring out the size effect on the shear strength. In order to relatively avoid the specimen size effect on the testing results [26], the specimen sizes are determined as 300 mm (length, L) \times 300 mm (height, H) \times 300 mm (width, W) and 200 mm (radius, R) \times 300 mm (height, H). Essentially, the size of the largest particle is larger than $0.05L_c$ ($0.05H/2 = 7.5 \text{ mm}$), which can be regarded as the S-RM in engineering dimension [3]. The shear test was repeatedly performed based on the same specimen with little result departure existed in the same test condition. The residual strength is adopted to analyze the strength regularity with gaps as the abrasion and crushing of sample is little in the iterative test under low stress. In this case, the strength structural effect of large gravel acting on the specimen can be ignored and test duration can be reduced notably. It is noted that water effect was not taken into account to reveal the gap effect of S-RM in the present study. In order to avoid the cores in samples, the S-RM was made in the shear box compacted by 3 layers, respectively.

3.2. Testing Apparatus. The shear tests were carried out on the large-frame shear device ADS-500, as shown in Figure 3, with the corresponding standards in mind (ASTM, ISO, DIN 18137, part 3). The shear gap (T) can be adjusted according to the size of tested soils, and the sample surface can be selected as the effective surface area which produced the effective tangential stress of materials.

3.3. Arranging Shear Gaps and Related Parameters. As known, the failure surface of the soil specimen tested in the conventional direct shear test is along a straight plane without a certain thickness, which deviates from the real deformation and strength properties of the shear zone. On the one hand, the heterogeneity of stress and deformation is enhanced by the dislocation of the rock block in the shear process. Figure 4 presents the nonuniform deformation of



FIGURE 3: The large-frame shear device.



FIGURE 4: The nonuniform deformation of S-RM after the shear process without shear gap.

S-RM after the shear process without shear gap, which leads to the formation of the shear zone which is not a localized process. On the other hand, the shear strength of a single rock particle is much greater than that of a contact between particles in the shear zone.

The shearing process is achieved by moving the lower shear box above the guideway, and the upper shear box subjected to the vertical stress is fixed on the surrounding frame. In common conditions, the shear boxes are close to each other without space. In this study, by adding the prefabricated shim between the upper box and the surrounding frame, the upper box will be raised correspondingly after sample preparation. By this way, following the test procedure with a shear gap can be accomplished. The suggested shear gaps for the test of coarse-grained soils are not coherent [20, 21, 27], meaning that more work from an experimental or numerical aspect to discuss relation between grain size and gap effect is rather needed. In order to present the gap effect on the strength reduction properties of S-RM, the shear gaps were arranged from 0 mm to 8 mm with an increment amplitude of 2 mm in this work as the largest particle size is 10 mm. Then, the flat segment of shear strength varying with gaps and the regularity of strength parameters can be obtained, which indicates a suitable gap considering the rock size effect. The related information of direct shear tests of S-RM is presented in Table 1. Considering the excavated depth of samples, the vertical stresses are arranged at 100 kPa, 200 kPa, and 300 kPa, respectively,

TABLE 1: The related parameters of the direct shear test of S-RM considering the gap effect.

Largest particle size D_{\max} (mm)	Testing scale (mm)					Gap (mm)	Vertical stress (kPa)	Shear velocity (mm/min)	Water content (%)
	L	W	H	R	H				
10	300	300	300	200	300	0/2/4/6/8	100/200/300	1.4	0

and the shear velocity was set as 1.4 mm/min for a slow shearing process [28, 29].

4. Results and Discussion

The relationship between effective tangential stress and shear displacement with the shear box of $L=300$ mm, $W=300$ mm, and $H=300$ mm is presented in Figure 5. The curve of tangential stress can be approximately divided into 2 parts of an increased stage and a balanced stage. The increased part can be regarded as the elastic strain transfer of soils which is not a rigid material, and the balanced status means the formation of shear zone containing the plastic interaction of particles. With the increment of shear gap, the decline of shear stress can be easily observed. In the test of S-RM with lower shear gaps presented in Figures 5(a) and 5(b), the nonlinearity of shear stress curve is very conspicuous, and the variation of tangential stress with different vertical stress levels is not trenchant compared to Figures 5(c) and 5(d). By this, the systematic analysis needs to be performed to reasonably recognize the size effect induced by the rock size and thus to propose a suitable testing shear gap for evaluating the tangential properties of coarse-grained soils rigorously.

4.1. Gap Effect on the Shear Strength of S-RM. Taking the residual tangential stress at a shear displacement of $0.1L$ to be analyzed, it can be found that the relation between tangential stress and vertical stress with different gaps satisfies the Coulomb criterion as shown in Figure 6(a). At the lower vertical stress (100 kPa), the tangential stress without gaps is much larger than that with gaps. Although the dispersion of tangential stress reduces at higher vertical stress (200 kPa and 300 kPa), the results are overestimated at the smaller shear gap. It is noted that the tangential stresses with $T=2$ mm and $T=4$ mm are closely connected at different vertical stresses. The gap effect on tangential stress at the same vertical stress is presented in Figure 6(b). Peak tangential stress experiences a decline with the increment of shear gap from $T=0$ mm to $T=2$ mm and is kept at a stable status with the increment of shear gap changing to $T=4$ mm. Accordingly, the reasonable gap dimension can be ensured as $T=2-4$ mm. Meanwhile, in order to reveal the mechanism of granular interaction in the shearing process, the strength parameters, $\tan(\varphi)$, where φ is the internal friction angle, and cohesion, are obtained as shown in Figure 6(c). As believed, the internal friction angle is connected to the particle chain action, and the cohesion is mainly linked to particle occlusion and particle friction in coarse-grained soils. It is interesting that the relationship between cohesion and $\tan(\varphi)$ is in negative correlation with the increment of gaps, meaning the different particle interaction

mode which forms the shear resistance of S-RM. From $T=0$ mm to $T=2$ mm, the apparent cohesion has an obvious decrease because the behavior of rock block in the shear band is transforming from shearing to sliding and rolling. Apparent cohesion and internal friction are balanced with $T=2$ mm and $T=4$ mm, while the cohesion apparently decreased lower than 0 in the case of large shear gap with $T=6$ mm, which indicates the direct shear test loses the physical meaning as the specimen within the shear gap cannot form a normal shear zone. The $\tan(\varphi)$ increases obviously when $T=6$ mm; thus, it can be seen that the particle chain action provides the prominent sources of shear resistance of S-RM.

In the small gap, as shown in Figure 4, the location of the rock in the shear zone is constrained, and the granular dislocation leads to the nonuniform deformation and the intense friction formed by applied stress between particles. In the large gap, the shear resistance is mainly originated by the granular collusion within the shear band. However, as shown in Figure 5(d), the residual shear stress decreases with the increase of shear displacement because the effects of stress reduction during consolidation and shear would influence the results, which is probably caused by the collapse of the material at the edge and the structural failure of soils in the shear band rather. So a reasonable gap is suggested for testing the realistic strength parameters of S-RM.

The results derived from another shear box ($R=200$ mm and $H=300$ mm) are shown in Figure 7. As shown in Figure 7(a), the tangential strength at different vertical stress levels is sensitive to the gap T , and the tangential stresses at $T=2$ mm and $T=4$ mm are very adjacent. The relationship between residual tangential stress and gap T is presented in Figure 7(b). By comparison with Figure 6(b), the coherent conclusion can be drawn that the reasonable gap for obtaining appropriate tangential strength of S-RM is $T=2$ mm–4 mm. In addition, the relation between cohesion and $\tan(\varphi)$ is shown in Figure 7(c), which also indicates the different form of particle interaction to produce the shear resistance of S-RM with the variation of T . As shown, both the particle chain action and the particle occlusion have the significant contribution to shear resistance when $T=2$ mm and $T=4$ mm. In other cases, the particle behaviors in the shear zone are deviated from the real mechanism of the actual shear zone.

As presented in Figure 8, the failure plane is set in advance without gap, which restricts the development of the shear band. Under lower stress levels, as shown in Figure 4, the dislocation of particles is notable during the shearing process which leads to the inhomogeneous deformation of the specimen. Under higher vertical stress, abnormal crush and failure of the sheared rock block give the unreal strength parameters, while the contact between particles in a suitable gap, containing the particle rolling and particle sliding,

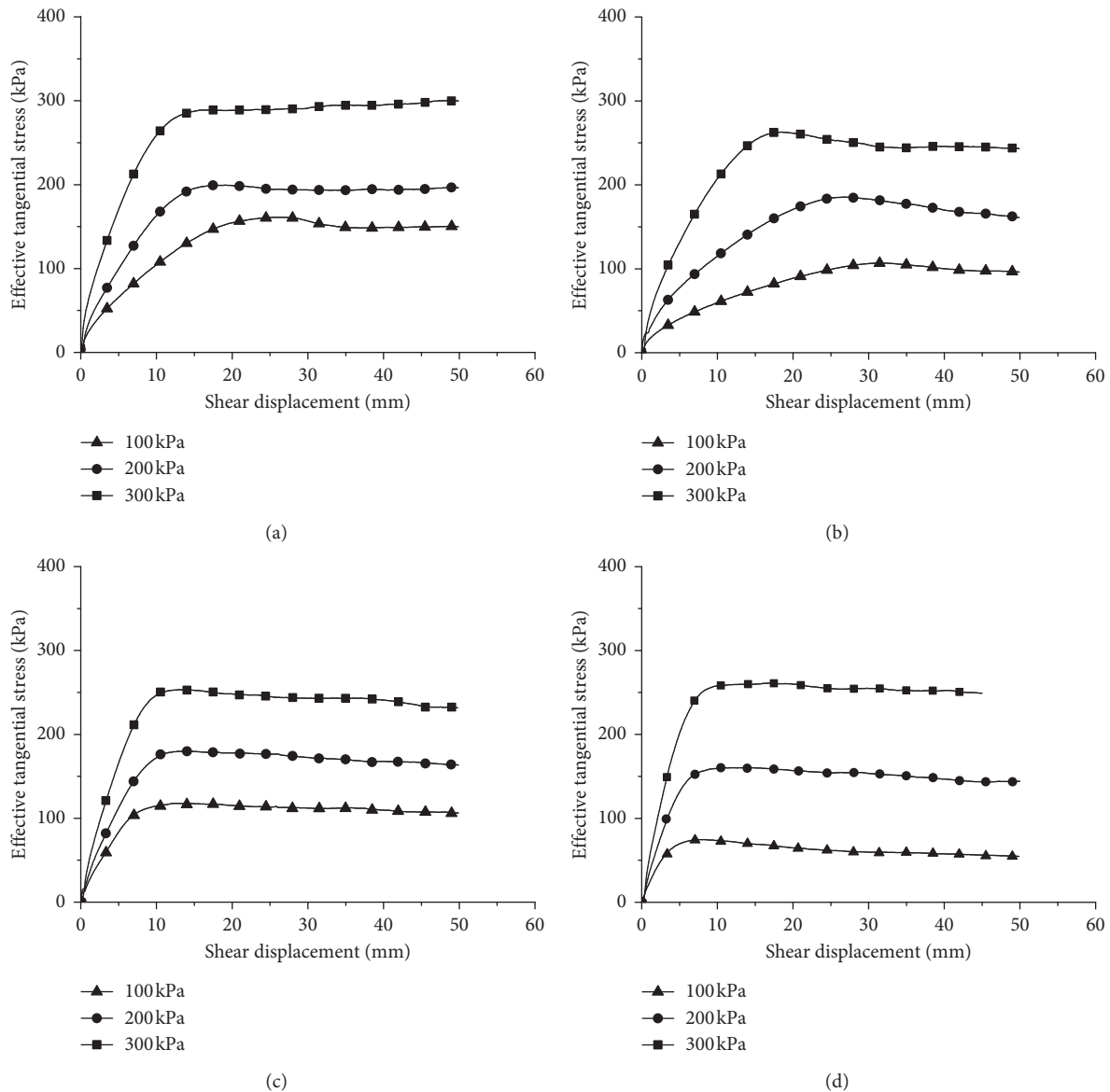


FIGURE 5: The relationship between tangential stress and shear displacement at $L = 300$ mm, $W = 300$ mm, and $H = 300$ mm: (a) $T = 0$ mm, (b) $T = 2$ mm, (c) $T = 4$ mm, and (d) $T = 6$ mm.

provides the stable resistance indicated by the flat segment in strength variation with T [20].

4.2. Specimen Size Effect on the Shear Strength of S-RM. In order to understand the specimen effect on the shear strength of S-RM, considering the gap effect, we choose the testing results at a vertical stress of 200 kPa for analysis. It is shown in Figure 9 that the shear strength reduces with the increase of specimen size, no matter whether there are gaps or not. By this, it can be found that the specimen effect with gap variation corresponds to the previous recognition without gap effect. Besides, increasing gap dimension can reduce the specimen size effect on S-RM shear strength caused by the boundary effect in different shear box sizes,

which can generate the realistic granular mechanism of shearing coarse-grained soils.

5. Conclusions

This paper proposes a systematic approach to evaluate the shear properties of S-RM. By considering the spatial distribution of particle size, the fractal theory is introduced to reveal the structural features existed in S-RM. Meanwhile, the realistic granular interaction in the shear band of S-RM and the gap effect on the shear strength have been discussed through experimental results. Based on the direct shear test considering the rock size effect, the main conclusions can be stated as follows:

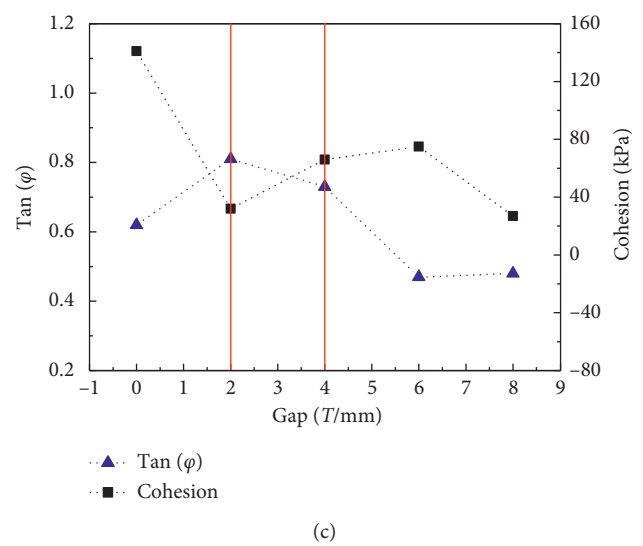
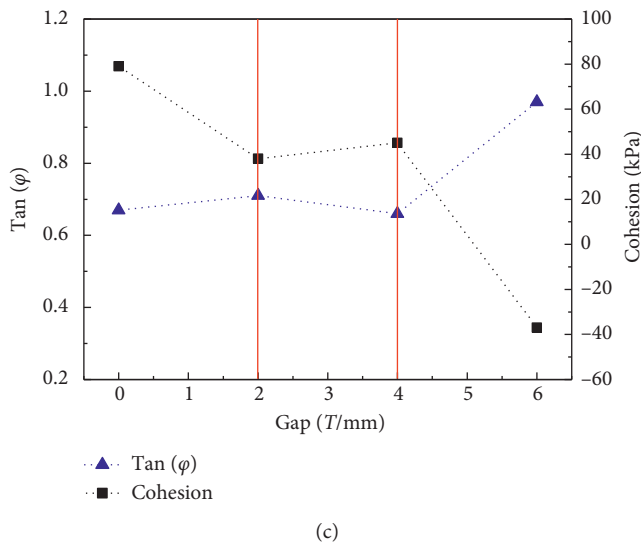
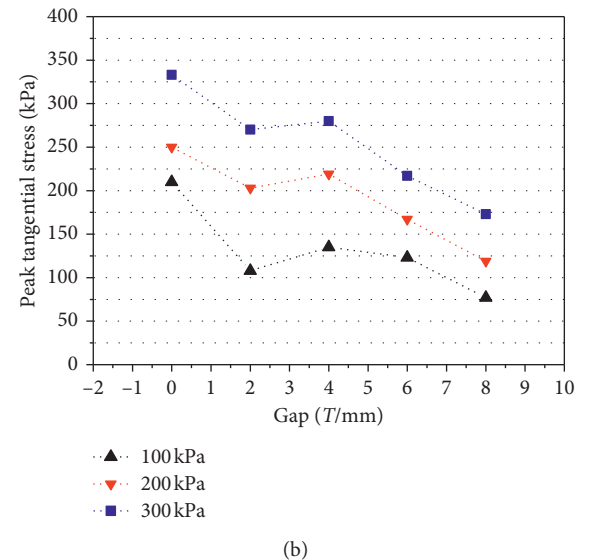
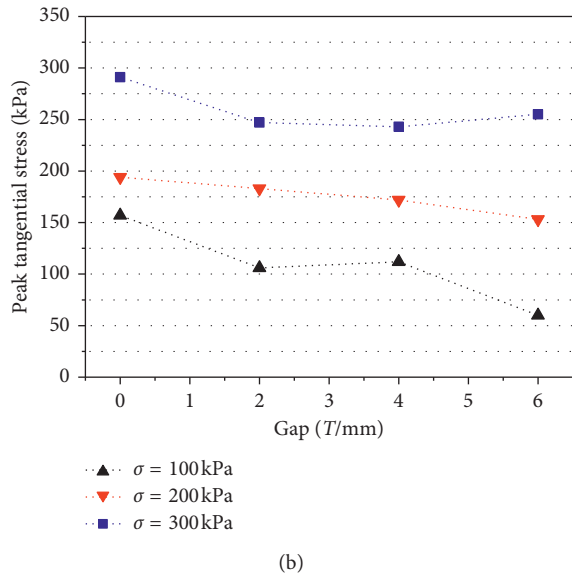
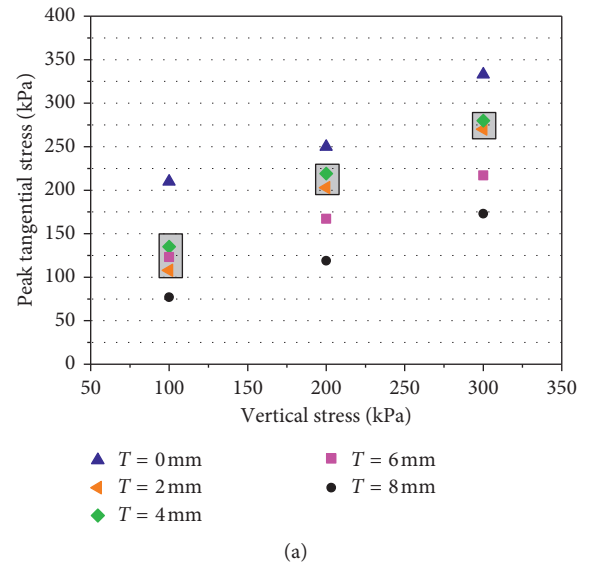
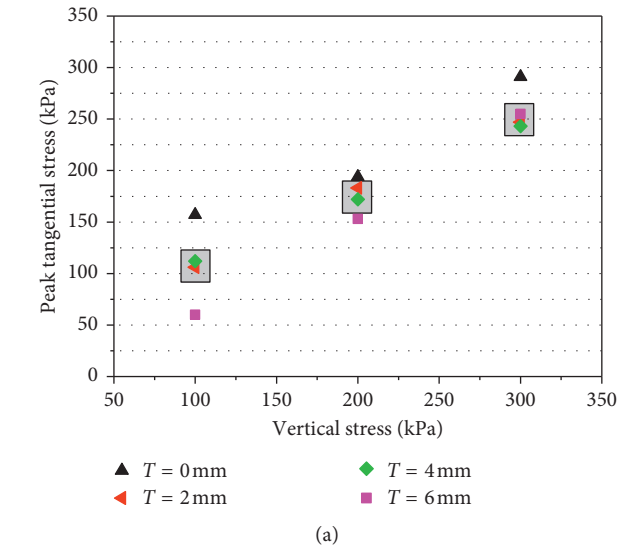


FIGURE 6: (a–c) The gap effect on the tangential properties of S-RM (shear box, $L = 300$ mm, $W = 300$ mm, and $H = 300$ mm).

FIGURE 7: (a–c) Gap effect on the tangential properties of S-RM (shear box, $R = 200$ mm and $H = 300$ mm).

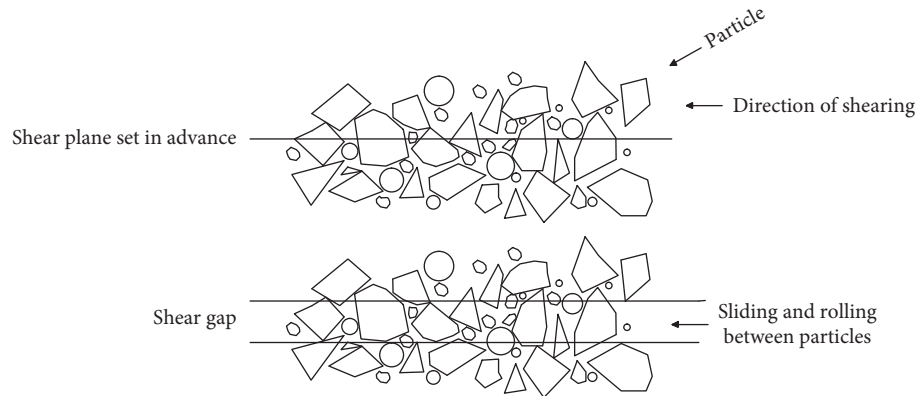


FIGURE 8: Illustration of the shear gap effect on the particle interaction behavior during shearing.

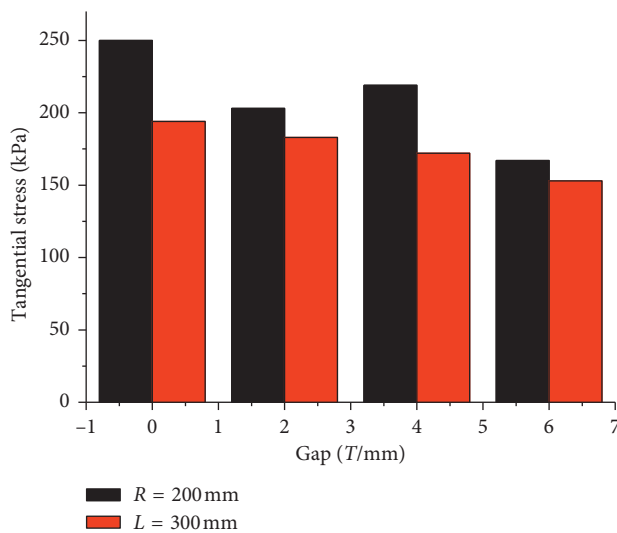


FIGURE 9: Comparison of tangential stress of different specimen sizes at a vertical stress of 200 kPa.

- The fractal presentation is a more effective method to evaluate the PSD of S-RM. These special soils with multifractal properties can be regarded as two-phase materials, and the distinguished size between “rock” and “soil” is the demarcation of scale-invariant interval.
- The shear behavior of S-RM is apparently controlled by the shear gap. With the gap increment, the relationship between internal friction angle and cohesion is in negative correlation. Stable and realistic shear strength of S-RM can be obtained in suitable gaps, and the specimen size effect also exists with the gap effect.
- The impact of the shear gap on shear strength has been analyzed from the granular interaction and the formation of the shear zone. Based on different sizes of the specimen, the reasonable shear gap of S-RM which considers rock size distribution with $D = 2.31$ is determined as $0.2D_{\max} - 0.4D_{\max}$.

Data Availability

The data used to support the findings of this study are available from the corresponding author upon request.

Conflicts of Interest

The authors declare that there are no conflicts of interest regarding the publication of this paper.

Acknowledgments

This study was supported by the Fundamental Research Funds for the Central Universities (no. 2014QNB38) and the National Natural Science Foundations of China (no. 41672343).

References

- W. J. Xu, Q. Xu, and R. L. Hu, “Study on the shear strength of soil–rock mixture by large scale direct shear test,” *International Journal of Rock Mechanics & Mining Sciences*, vol. 48, no. 8, pp. 1235–1247, 2011.
- A. Simoni and G. T. Houlsby, “The direct shear strength and dilatancy of sand–gravel mixtures,” *Geotechnical and Geological Engineering*, vol. 24, no. 3, pp. 523–549, 2006.
- E. W. Medley, “Orderly characterization of chaotic Franciscan melanges,” *Feldsbau Journal of Engineering Geology, Geomechanics and Tunnelling*, vol. 19, no. 4, pp. 20–33, 2001.
- E. W. Medley and P. F. Sanz Rehermann, “Characterization of bimrocks (rock/soil mixtures) with application to slope stability problems,” in *Proceedings of 53rd Geomech Colloquium, EUROCK 2004*, pp. 425–430, Salzburg, Austria, October 2004.
- K. Kuenza, I. Towhata, R. P. Orense, and T. H. Wassan, “Undrained torsional shear tests on gravelly soils,” *Landslides*, vol. 1, no. 3, pp. 185–194, 2004.
- W. J. Chang and T. Phantachang, “Effects of gravel content on shear resistance of gravelly soils,” *Engineering Geology*, vol. 207, pp. 78–90, 2016.
- W. J. Xu, Z. Q. Yue, and R. L. Hu, “Study on the mesostructure and mesomechanical characteristics of the soil–rock mixture using digital image processing based finite element method,” *International Journal of Rock Mechanics & Mining Sciences*, vol. 45, no. 5, pp. 749–762, 2008.
- M. L. Napoli, M. Barbero, E. Ravera, and C. Scavia, “A stochastic approach to slope stability analysis in bimrocks,” *International Journal of Rock Mechanics & Mining Sciences*, vol. 101, pp. 41–49, 2018.
- H. Sonmez, M. Ercanoglu, A. Kalender, G. Dagdelenler, and C. Tunusluoglu, “Predicting uniaxial compressive strength and deformation modulus of volcanic bimrock considering

- engineering dimension,” *International Journal of Rock Mechanics & Mining Sciences*, vol. 86, pp. 91–103, 2016.
- [10] A. T. Iannacchione, *Shear strength of saturated clays with floating rock particles*, Ph.D. dissertation, University of Pittsburgh, Pittsburgh, PA, USA, 1997.
- [11] T. Kokusho, T. Hara, and R. Hiraoka, “Undrained shear strength of granular soils with different particle gradations,” *Journal of Geotechnical & Geoenvironmental Engineering*, vol. 130, no. 6, pp. 621–629, 2004.
- [12] S. Yagiz, “Brief note on the influence of shape and percentage of gravel on the shear strength of sand and gravel mixtures,” *Bulletin of Engineering Geology & the Environment*, vol. 60, no. 4, pp. 321–323, 2001.
- [13] E. S. Lindquist, *The strength and deformation properties of melange*, Ph.D. thesis, University of California, Oakland, CA, USA, 1994.
- [14] Z. L. Zhang, W. J. Xu, W. Xia, and H. Y. Zhang, “Large-scale in-situ test for mechanical characterization of soil–rock mixture used in an embankment dam,” *International Journal of Rock Mechanics & Mining Sciences*, vol. 86, pp. 317–322, 2016.
- [15] X. Li, Q. L. Liao, and J. M. He, “In-situ tests and a stochastic structural model of rock and soil aggregate in the three gorges reservoir area, China,” *International Journal of Rock Mechanics & Mining Sciences*, vol. 41, no. 3, pp. 702–707, 2004.
- [16] Y. Amini and A. Hamidi, “Triaxial shear behavior of a cement-treated sand-gravel mixture,” *Journal of Rock Mechanics and Geotechnical Engineering*, vol. 6, no. 5, pp. 455–465, 2014.
- [17] A. Bagherzadeh-Khalkhali and A. A. Mirghasemi, “Numerical and experimental direct shear tests for coarse-grained soils,” *Particuology*, vol. 7, no. 1, pp. 83–91, 2009.
- [18] A. F. Cabalar, K. Dulundu, and K. Tuncay, “Strength of various sands in triaxial and cyclic direct shear tests,” *Engineering Geology*, vol. 156, no. 2, pp. 92–102, 2013.
- [19] Q. Zhou, H. H. Shen, B. T. Helenbrook, and H. Zhang, “Scale dependence of direct shear tests,” *Chinese Science Bulletin*, vol. 54, no. 23, pp. 4337–4348, 2009.
- [20] W. Fu, X. Zheng, X. Lei, and J. Deng, “Using a modified direct shear apparatus to explore gap and size effects on shear resistance of coarse-grained soil,” *Particuology*, vol. 23, no. 6, pp. 82–89, 2015.
- [21] S. Shibuya, T. Mitachi, and S. Tamate, “Interpretation of direct shear box testing of sands as quasi-simple shear,” *Geotechnique*, vol. 47, no. 4, pp. 769–790, 1997.
- [22] D. L. Turcotte, “Fractals and fragmentation,” *Journal of Geophysical Research*, vol. 91, no. B2, p. 1921, 1986.
- [23] S. W. Tyler and S. W. Wheatcraft, “Fractal scaling of soil particle-size distributions: analysis and limitations,” *Soil Science Society of America Journal*, vol. 56, no. 2, pp. 362–369, 1992.
- [24] X. Du, P. Zhang, and L. Jin, “A mesoscopic model of sand-gravel stratum in Beijing based on fractal theory,” *Chinese Journal of Rock Mechanics and Engineering*, vol. 36, no. 2, pp. 437–445, 2017, in Chinese.
- [25] B. B. Mandelbrot, *The Fractal Geometry of Nature*, W. H. Freeman, New York, NY, USA, 1983.
- [26] ASTM D3080/D3080M-11, *Standard Test Method for Direct Shear Test of Soils under Consolidated Drained Conditions*, ASTM International, West Conshohocken, PA, USA, 2012.
- [27] The Professional Standards Compilation Group of People’s Republic of China, DL/T5356-2006, *Code for Coarse-Grained Soil Tests for Hydropower and Water Conservancy Engineering*, China Electric Power Press, Beijing, China, 2006.
- [28] H. F. Deng, X. F. Yuan, and J. L. Li, “Research on failure characteristics and determination method for shear strength of earth-rock aggregate in direct shear tests,” *Chinese Journal of Rock Mechanics and Engineering*, vol. 32, no. s2, pp. 4065–4072, 2013, in Chinese.
- [29] G. J. Wang, C. H. Yang, and C. Zhang, “Experimental research on particle breakage and strength characteristics of rock and soil materials with different coarse-grain contents,” *Rock and Soil Mechanics*, vol. 30, no. 12, pp. 3649–3654, 2009, in Chinese.

Research Article

Thermal Conductivity of Compacted GO-GMZ Bentonite Used as Buffer Material for a High-Level Radioactive Waste Repository

Yong-Gui Chen ¹, Xue-Min Liu,¹ Xiang Mu,¹ Wei-Min Ye,¹ Yu-Jun Cui,² Bao Chen,¹ and Dong-Bei Wu³

¹Department of Geotechnical Engineering, Key Laboratory of Geotechnical and Underground Engineering of Ministry of Education, Tongji University, Shanghai 200092, China

²Laboratoire Navier/CERMES, Ecole des Ponts-ParisTech, 6-8 Av. Blaise Pascal, Cité Descartes, 77455 Marne-la-Vallée, France

³College of Chemistry and Chemical Engineering, Tongji University, Shanghai 200092, China

Correspondence should be addressed to Yong-Gui Chen; cyg@tongji.edu.cn

Received 19 May 2018; Revised 3 July 2018; Accepted 19 July 2018; Published 4 September 2018

Academic Editor: Filippo Ubertini

Copyright © 2018 Yong-Gui Chen et al. This is an open access article distributed under the Creative Commons Attribution License, which permits unrestricted use, distribution, and reproduction in any medium, provided the original work is properly cited.

In China, Gaomiaozi (GMZ) bentonite serves as a feasible buffer material in the high-level radioactive waste (HLW) repository, while its thermal conductivity is seen as a crucial parameter for the safety running of the HLW disposal. Due to the tremendous amount of heat released by such waste, the thermal conductivity of the buffer material is a crucial parameter for the safety running of the high-level radioactive waste disposal. For the purpose of improving its thermal conductivity, this research used the graphene oxide (GO) to modify the pure bentonite and then the nanocarbon-based bentonite (GO-GMZ) was obtained chemically. The thermal conductivity of this modified soil has been measured and investigated under various conditions in this study: the GO content, dry density, and water content. Researches confirm that the thermal conductivity of the modified bentonite is code-termined by the three conditions mentioned above, namely, the value of GO content, dry density, and water content. Besides, the study proposes an improved geometric mean model based on the special condition to predict the thermal conductivity of the compacted specimen; moreover, the calculated values are also compared with the experimental data.

1. Introduction

Burying the high-level radioactive waste (HLW) in a deep geological disposal (800 m–1500 m underground) has been widely accepted as an approach for the permanent disposal of such waste generated from a nuclear reactor. The HLW repositories generally consist of a multibarrier system, in which the natural geological barrier and an engineered barrier system are included. The buffer material, as a pivotal part of the engineered barrier, plays a crucial role in keeping the chronic safety of the HLW repository, from which enough strength for construction and effective intercept for the radionuclide can be drawn [1]. Compacted bentonite has been valued as the feasible buffer material for the HLW repository, due to its excellent properties of swelling and sealing, the low permeability, and high retention capability of radionuclides [2, 3]. In China, a local bentonite named Gaomiaozi (GMZ) has been selected for this aim [4, 5].

As in the deep geological disposal, the buffer material can diffuse decay heat generated from the HLW to the host rock. Literatures show that the ambient temperature could rise to a peak of 90°C [6] and the maximum temperature grades could reach 24°C over a buffer material whose thickness is 35 cm [7]. According to the design criterion [8–10], the highest temperature in the engineered barrier system ought not to exceed 100°C because the smectite may undergo a mineralogical alteration exposed to alkaline/salt pore fluids at high temperature [11–14]. Both compacted bentonite and the host rock will undergo a decrease in the hydraulic, mechanical, and chemical performances because of these kinds of transformation under the high temperature which could threaten the safety of the HLW disposal [13, 15]. Therefore, it is of essence to study the thermal conductivity of the buffer material and to comprehend how it behaves under the given conditions in the disposal.

Over the past few decades, previous researches have been conducted on the thermal conductivity of many kinds of soil, and calculation models were developed to predict its thermal conductivity under different conditions [16–18]. Thermal conductivity is the basic property of a material to conduct heat which depends mainly upon its composition, pore fluid, density, environment temperature, and texture [19]. Coulon et al. [20] have measured this property of 18 smectite clays from 14 deposits, and based on these measurement results, they claimed that the value of the thermal conductivity was jointly influenced by soil parameters such as the water content, the dry density, the microstructure of clay samples, and the mineral composition of the soil as well. A large volume of measured data has been found in the works of Zhu et al. [21] on GMZ bentonite, and the similar conclusion has been drawn. However, the thermal conductivity of bentonite fails to meet the expected value even at high density and water content [22–25]. To improve the thermal performance of bentonite as the buffer material, some admixtures were added physically to modify its property. Using sand as a modifier was first reported in Japan [26]. Moreover, results from further more investigations confirmed that the thermal conductivity of the bentonite-sand mixture will increase as the sand content increases [27–30]. Nevertheless, the increasing degree becomes constant or even decreases with more increasing sand content [25, 31]. Because of the high thermal conductivity of graphite, Pacovsky [32] added graphite to Czech RMN bentonite to increase its thermal conductivity. Michael and Gunter [33] compared the improvement effect of sand to graphite and found that using sand as the only admixture is not enough to achieve suitable thermal conductivity while the addition of 15% graphite can make the thermal conductivity of the barrier approximately equal to that of the clay host rock. Nanocarbon material possesses high specific surface and strong interface effect which exerts extraordinary mechanics and thermal property compared to the macro-material [34–36]; therefore, the graphene oxide was used as a proper modifier.

In China, a lot of studies about the basic physical and chemical properties, hydromechanical behaviour, and soil water retention characteristics (SWRC) of GMZ bentonite have been extensively researched during the past few years [37–44]. Studies on the thermal conductivity of pure bentonite and bentonite-sand mixture have also been carried out with varied sand content, dry density, and water content [45–47]. However, few researches consider graphite or other materials as a modifier to increase the thermal conductivity of bentonite [48].

In this study, graphene oxide (GO) was added to the GMZ bentonite, and the thermal conductivity of GO-GMZ bentonite was measured using the hot wire method. In this experiment, several factors including GO content, dry density, and water content of the modified soil were considered. At last, an empirical model was introduced to predict the thermal conductivity of compacted GO-GMZ bentonite in advance.

2. Materials and Method

2.1. Materials. The GMZ bentonite analysed with the X-ray diffraction in this test is sampled from Gaomiaozhi township in Northern China. This light-grey powder consists of several minerals including 75.4% of montmorillonite, 11.7% of quartz, 7.3% of cristobalite, 4.3% of feldspar, 0.5% of calcite, and 0.8% kaolinite [38]. The other basic properties are listed in Table 1 [49].

The graphene oxide (GO) used in the present work is produced by Suzhou Tanfeng Graphene Technology Co., Ltd (Jiangsu Province, China). It is a drab powder material whose monolayer ratio is more than 99%. The structure schematics of graphite and graphene oxide are pictured in Figure 1, and its basic properties are listed in Table 2. Graphene oxide is an important and promising ramification of graphite which is obtained by treating graphite with strong oxidizers and is produced based on the improved Hummers method [50]. It has been proved that graphene oxide is nontoxic and biodegradable among all nanocarbon materials [51].

2.2. Bentonite Modification. In order to obtain GO-GMZ bentonite, firstly the GMZ bentonite was grafted using 3-aminopropyltriethoxysilane (APTES); then, the graft bentonite was modified by using 1-ethyl-3-(dimethylamino) propylcarbodiimide (EDC) and *n*-hydroxysuccinimide (NHS) as an activator. The modification procedure is showed in Figure 2. Quantities of 2.5 g GMZ bentonite, 50 mL APTES, and 200 mL absolute ethanol (with a purity of 99.7%) were poured into a 500 mL round bottom flask with three necks. The mixture was heated in a water bath at 80°C for 2 h. To keep it uniform, the mixture was intensively stirred (400 rad/min) in the process. The product was washed with absolute ethanol for six times and then dried in a vacuum oven at 60°C. The dried mass was pulverized and sieved (200 mm sieve). Quantities of 2 g powder, 2.5 g NHS, 2.5 g EDC, and 20 ml GO solution (10 mg/mL) were poured into a 50 mL beaker and stirred uniformly for 12 h at room temperature. After standing, centrifugation, freeze-drying, and sieving in a 2 mm mesh, the GO-GMZ bentonite was ready to use.

2.3. Specimen Preparation. To obtain the compacted GO-GMZ bentonite at a certain dry density, its powder was compressed statically in a steel mould using a 300 kN electronic universal testing machine (Model CSS-44000, produced by Changchun Research Institute for Mechanical Science) at a steady displacement rate of 0.2 mm/min. Besides, in order to make the dry density of the specimen longitudinal uniformly, the compression process was divided into four steps: (1) 1/3 soil powder of the total mass was compacted to obtain a specimen whose height is 40 mm; (2) the upper surface of the compacted specimen was carefully scratched with a thin steel stick; (3) the next 1/3 soil powder of the total mass was poured and compacted to form another soil segment; and (4) repeat steps 2 and 3 until the height of the compacted soil rises up to its target height

TABLE 1: Basic properties of GMZ01 bentonite.

Chemical component	SiO ₂ , Al ₂ O ₃ , and H ₂ O
Specific gravity (mg/m ³)	2.66
Alkaline coefficient	1.14
pH value	8.68–9.86
Liquid limit (%)	276
Plastic limit (%)	37
Plastic index	239
Total specific surface area (m ² /g)	570
Cation exchange capacity (cmol/kg)	77.30
Main exchange cations (cmol/kg)	Na ⁺ (43.36); 1/2 Ca ²⁺ (14.57); 1/2 Mg ²⁺ (6.17); K ⁺ (2.51)

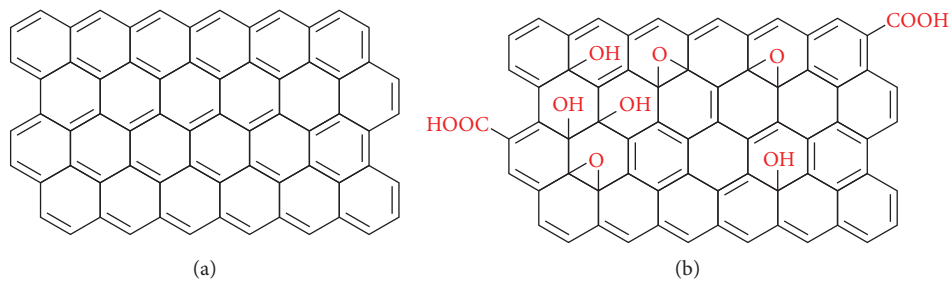


FIGURE 1: The structure schematic of (a) graphite and (b) graphene oxide.

TABLE 2: Basic properties of graphene oxide (GO).

Purity (wt.%)	>99
Thickness (nm)	0.6–1.0
Layers	1–2
Particle diameter (μm)	0.5–5
Specific surface area (m ² /g)	1000–1217

(i.e., 120 mm). Once the dry density of bentonite reached the desirable value (1.7 Mg/m³, 1.8 Mg/m³, and 1.9 Mg/m³), the press on bentonite will stop and be kept still for 1 hour to avoid resilience. The sample is 50 mm in diameter and 120 mm high.

2.4. Measurement Method

2.4.1. Apparatus and Test Principle. Usually, two main kinds of laboratory techniques, steady-state methods [52, 53] and unsteady methods [54, 55], are utilized to measure the thermal conductivity of many kinds of materials. In this study, the thermoprobe method, as one of the unsteady methods, is adopted to measure the thermal conductivity of compacted GO-GMZ bentonite using a Decagon Device KD2 PRO thermal analyser (Figure 3). It is composed of a thermal needle probe, a cable, and a controller. Through monitoring heat dissipation of linear heat resource under specific voltage, the thermal conductivity of materials can be calculated and displayed on the controller's screen (ASTM D 5334-00, 2000). After the insertion of the thermoprobe which is 1.28 mm in diameter and 120 mm long into the soil, the thermal conductivity can be obtained by heating the soil and monitoring temperature variation during the heat transfer.

2.4.2. Test Procedure. To ensure the smooth insertion of the thermoprobe, a hole sized 1.3 mm in diameter and 120 mm in depth is drilled into the middle of the specimen with a gimlet before testing. To avoid a small gap between the soil and thermoprobe which may influence the heat transfer, a thin layer of thermal grease was smeared on the surface of the thermoprobe. After that, it was inserted into the hole. Figure 3 shows the measuring operation and the KD2 analyser instrument. In the measurement, the controller was first balanced for 30 seconds, and the sample was then heated with the probe for another 30 seconds. The thermal conductivity was computed according to the cooling rate of the probe during the heat transmission. To ensure the accuracy of the experiment data, the testing values of repeated measurements were averaged as the final value.

3. Results and Discussion

3.1. Influence of GO Content on Thermal Conductivity. To figure out the enhancement of thermal conductivity of GO-GMZ bentonite, various GO contents (between 0 and 50% wt.) were used in the process of modification. The test results are illustrated in Figure 4, which shows a clear change of the thermal conductivity with different GO contents. According to the experimental data, the thermal conductivity shows apparent increases with greater dry density of GO content. Generally, the relation between the thermal conductivity and GO content can be formulated as a quadratic function with different dry densities: 1.7 Mg/m³, 1.8 Mg/m³, and 1.9 Mg/m³. As seen from the results, values of thermal conductivity range from 0.864 W/(mK) to 21.662 W/(mK) as GO content increases from 0% to 50% in given conditions. This attributes to the better heat

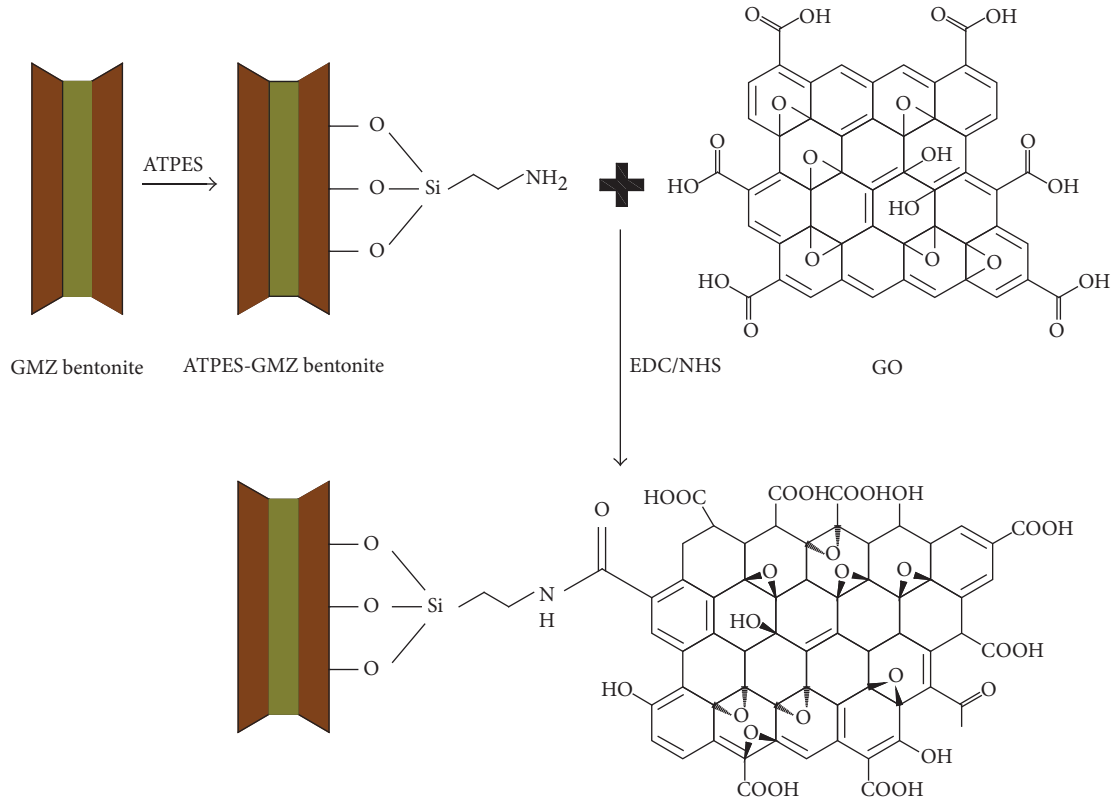


FIGURE 2: The schematic diagram of preparation of GO-GMZ bentonite.

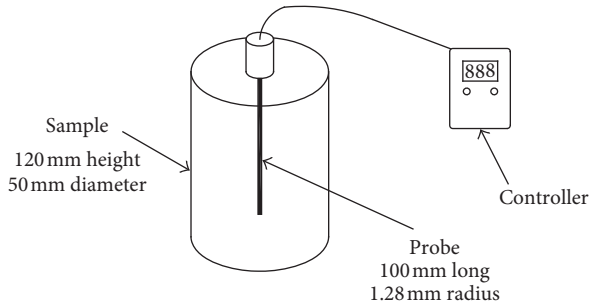


FIGURE 3: Measurement of thermal conductivity.

conduction behaviour of GO whose thermal conductivity is 129 W/(mK), much higher than that value of the pure bentonite. The thermal conductivity-GO content quadratic relationship at different dry densities can be expressed as follows:

$$\begin{aligned} \lambda &= 0.38E-3 \times \omega_{GO}^2 + 0.23 \times \omega_{GO} + 0.29 \quad \text{for} \\ &\quad \rho_d = 1.7 \text{ Mg/m}^3 (R^2 = 0.93), \\ \lambda &= 1.57E-3 \times \omega_{GO}^2 + 0.23 \times \omega_{GO} + 0.39 \quad \text{for} \\ &\quad \rho_d = 1.8 \text{ Mg/m}^3 (R^2 = 0.96), \\ \lambda &= 3.60E-3 \times \omega_{GO}^2 + 0.16 \times g + 1.42 \quad \text{for} \\ &\quad \rho_d = 1.9 \text{ Mg/m}^3 (R^2 = 0.97), \end{aligned} \quad (1)$$

where λ is the thermal conductivity (W/(mK)), ω_{GO} is the GO content of the specimens, ρ_d represents the dry density

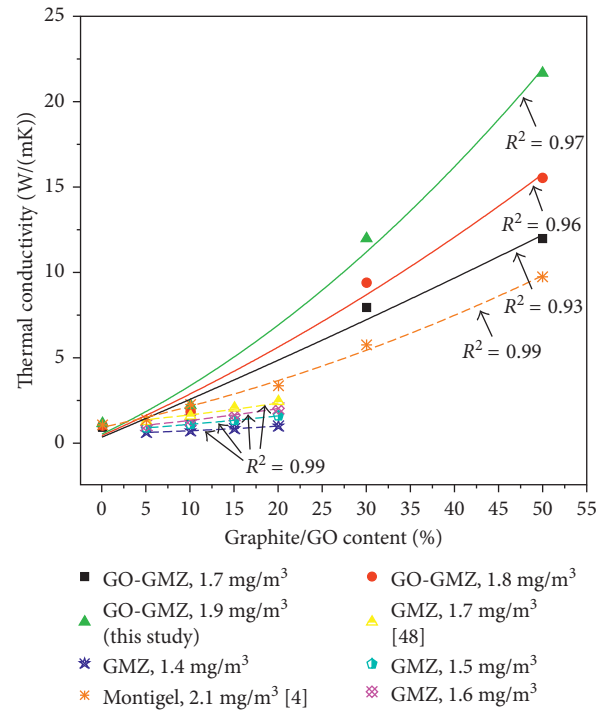


FIGURE 4: The thermal conductivity and graphite/GO content in the present study ($\omega = 10\%$) and available data in published literatures.

of compacted GO-GMZ bentonite (Mg/m^3), and R^2 is the correlation coefficient. As can be seen from the equations, the second-order coefficient for each equation increases with

the increase of dry density which maybe because of the increasing contact area between the bentonite and GO particles.

Though the measured data in this study are insufficient enough to draw a perfect relationship between several parameters, the work had been done in literatures and the good fitting result provides convincing evidence for the conclusion. Some researchers use graphite to improve the thermal conductivity of bentonite physically, and similar patterns can be found in Czech RMN bentonite [32], Montigel bentonite [33], and GMZ bentonite [48]. Numbers of experiment results of this study and other literatures have been illustrated in Figure 4. This figure shows the values of GO and graphite content range from 0% to 50%, while values of the dry density of different compacted bentonites range from 1.4 Mg/m^3 to 1.9 Mg/m^3 in different researches. After comparison, the thermal conductivity of bentonite-graphite mixture can range from 0.56 W/(mK) to 9.7 W/(mK) under different experiment conditions which is obviously lower than that of GO-GMZ bentonite. Probable reasons for this situation might be that (1) the thermal conductivity of GO nanoplatelets is higher than the bulk of graphite because of its single-layer structure [35, 56] and the increase in the interlayer coupling because of covalent interactions provided by the oxygen atoms and (2) the bentonite used in this study has been changed chemically with GO, leading to a better heat conduction behaviour. However, the relationship between the thermal conductivity of the mixture and the graphite content agrees with the modified bentonite: the higher the graphite content, the higher the value of thermal conductivity for the bentonite-graphite mixture. This maybe because the thermal conductivity of graphite is more than 10 times than that of pure bentonite [48]. Moreover, the thermal conductivity-graphite content shows similar quadratic trend for reported bentonite with GO-GMZ bentonite in this study for each dry density.

3.2. Influence of Dry Density on Thermal Conductivity. Measured values of thermal conductivity for highly compacted GO-GMZ bentonite with different dry densities (1.7 Mg/m^3 , 1.8 Mg/m^3 , and 1.9 Mg/m^3) are presented in Figure 5. As shown, the effect of dry density can be plotted as a linear function when the GO content equals to 0%, 10%, 30%, and 50%, respectively. For the specimen with GO content of 0% (i.e., pure GMZ bentonite), the value of thermal conductivity increases from 0.86 W/(mK) to 1.10 W/(mK) with the increase of dry density. While for the specimen whose GO content is 50%, its thermal conductivity increases from 11.94 W/(mK) to 21.66 W/(mK) when water content equals to 10%. This phenomenon can be explained as the increasing contact area between the same and different particles (i.e., GO-GMZ bentonite and water particles) with the increase of dry density, leading to a better performance of heat transmission, namely, the thermal conductivity. The specific linear fitting functions and the calculated correlation coefficients of thermal conductivity-dry density are as follows:

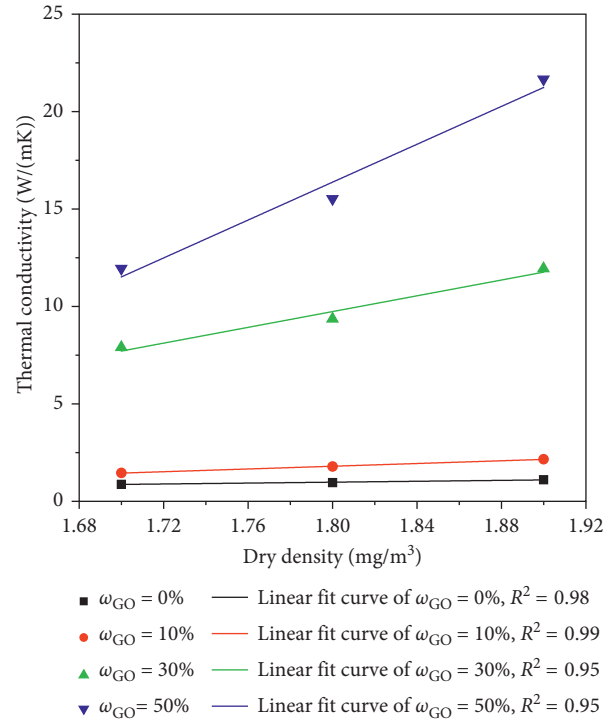


FIGURE 5: The thermal conductivity and dry density.

$$\begin{aligned}
 \lambda &= 1.16\rho_d - 1.11 \quad \text{for } \omega_{GO} = 0\% \quad (R^2 = 0.98), \\
 \lambda &= 3.52\rho_d - 4.5 \quad \text{for } \omega_{GO} = 10\% \quad (R^2 = 0.99), \\
 \lambda &= 20.24\rho_d - 26.70 \quad \text{for } \omega_{GO} = 30\% \quad (R^2 = 0.95), \\
 \lambda &= 48.61\rho_d - 71.12 \quad \text{for } \omega_{GO} = 50\% \quad (R^2 = 0.95),
 \end{aligned} \tag{2}$$

where the meaning of λ , ω_{GO} , and R^2 in this equation are the same with (1). According to the equations above, the thermal conductivity of GO-GMZ bentonite has a good linear relationship with its dry density when the water content keeps invariable. This is due to the increase of the contact area between the particles [57].

Figure 5 also shows that the slope coefficient has a greater value at higher GO content. This means that the influence degree of dry density is greater when GO content is higher. This probably attributes to much higher thermal conductivity of graphene oxide than pure bentonite. Previous studies have confirmed that, for various bentonites, a linearity exists in thermal conductivity-dry density relationship, which includes MX-80 [58, 59], Kunigel [60], FEBEX [61], GMZ [46] and Kyeongju bentonite [62]. This relationship has also been found in the bentonite-sand mixture [46, 47]. A comparison of this study with those of the results in literatures has been illustrated in Figure 6. As shown, the dry density for different bentonites and bentonite-sand mixtures ranged from 1.5 Mg/m^3 to 1.9 Mg/m^3 and the water content from 0% to 17.4%. At these experimental conditions, the thermal conductivity of various pure bentonites is in a range of 0.30 W/(mK) to 1.34 W/(mK) . In addition, its value for the bentonite-sand mixture ranges from 0.89 W/(mK) to 1.33 W/(mK) when the sand content ranges from 10% to

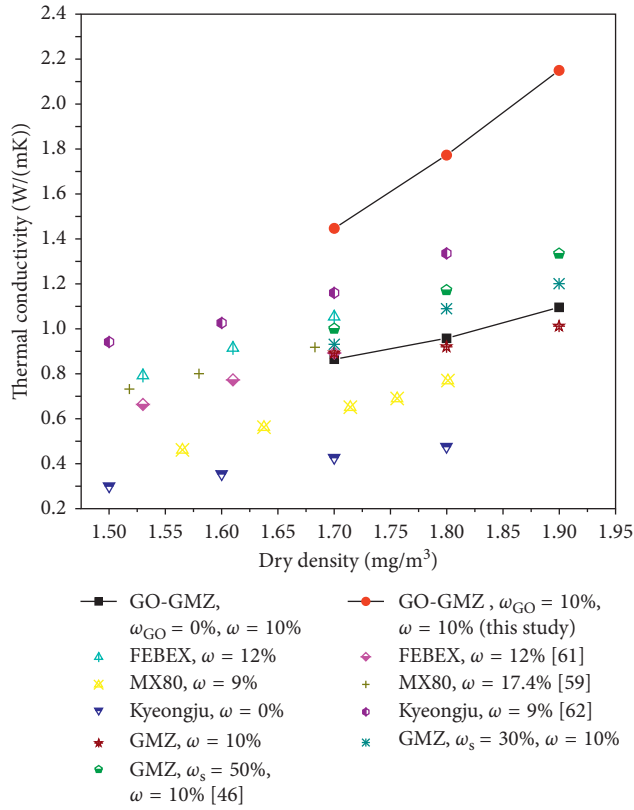


FIGURE 6: Comparison of the thermal conductivity and dry density in the present study with available data in published literatures.

50% and the dry density increases from 1.7 Mg/m^3 to 1.9 Mg/m^3 . This is because the thermal conductivity of sand is higher than that of bentonite. However, the maximum thermal conductivity of compacted GO-GMZ bentonite is 21.66 W/(mK) . Apparently, this value is much higher than that of bentonite-sand mixture. This maybe due to the better heat conduction behaviour of GO (129 W/(mK)) than quartz sand (7.7 W/(mK)) [63]. In general, the thermal conductivity-dry density relationship for various bentonites has a similar trend with GO bentonite. The denser the compacted soil specimen, the higher the thermal conductivity value of bentonites. This is due to the increase of the interacting area between bentonite particles with increase in dry density. Nevertheless, the increasing rates are somewhat different for different bentonites, and this probably attributes to the differences in their mineralogical composition, texture, and water content [62, 64].

3.3. Influence of Water Content on Thermal Conductivity.

The effect of water content on thermal conductivity is illustrated in Figure 7. As shown, the thermal conductivity and water content have a clear linear relationship with increasing water content when water content increases from 0% to 10% and GO content equals to 0%, 10%, 30%, and 50%, respectively. The minimum value of thermal conductivity is 0.37 W/(mK) , and the maximum value is 15.52 W/(mK) . This increase can be explained that the air in the void has been replaced by the water whose thermal

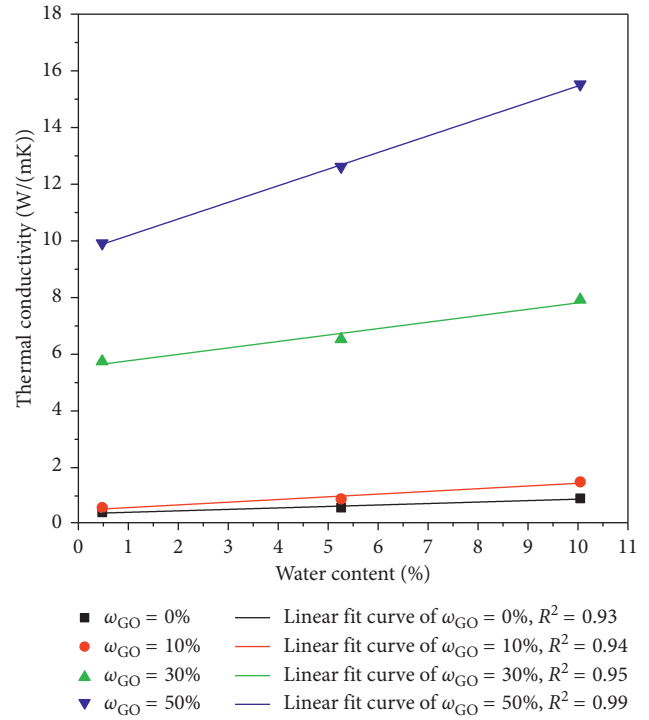


FIGURE 7: The thermal conductivity and water content.

conductivity is higher than air, leading to an additional increase of the thermal conductivity. The linear relationship can be expressed as follows:

$$\begin{aligned} \lambda &= 0.05\omega + 0.34 \quad \text{for } \omega_{GO} = 0\% \quad (R^2 = 0.93), \\ \lambda &= 0.09\omega + 0.48 \quad \text{for } \omega_{GO} = 10\% \quad (R^2 = 0.94), \\ \lambda &= 0.22\omega + 5.61 \quad \text{for } \omega_{GO} = 30\% \quad (R^2 = 0.95), \\ \lambda &= 0.56\omega + 9.85 \quad \text{for } \omega_{GO} = 50\% \quad (R^2 = 0.99), \end{aligned} \quad (3)$$

where ω is the water content. According to the equations above, the thermal conductivity of GO-GMZ bentonite has a good linear relationship with its water content. However, Lee et al. [62] reported that the thermal conductivity-water content relationship will become nonlinear when the water content is beyond 12%. Several studies used the sigmoidal-type equation to express this nonlinear relationship [61]:

$$\lambda = \frac{\lambda_0 - \lambda_s}{1 + \exp((S_r - S_a)/A)} + \lambda_s, \quad (4)$$

where λ_0 represents the value of λ when $S_r = 0$, λ_s represents that value when $S_r = 1$ (i.e., the specimen is saturated), S_a is the corresponding saturation degree when the thermal conductivity of the specimen equals to the average of the two extreme values, and while A functions as an empirical parameter, S_a is the corresponding saturation degree when the thermal conductivity of the specimen equals to the average of the two extreme value. In the equation above, the saturation degree (S_r) can be calculated by water content (ω), dry density (ρ_d), and water density (ρ_w) as follows:

$$S_r = \omega \cdot \frac{\rho_d}{\rho_w}. \quad (5)$$

Figure 8 plots the fitting curves of thermal conductivity and saturation degree. The parameter values are best fitted and listed in Table 3. Theoretically, the fitted values of λ_0 should be equal to the experimental values when saturation of the samples is 0. However, the fitted values are slightly higher when the GO content is equal or greater than 10%. This may be due to the inhomogeneous distribution of the material (i.e., GO-GMZ bentonite), leading to a decrease in its thermal conductivity [65].

3.4. Model of Thermal Conductivity for GO-GMZ Bentonite. In the HLW repository, the heat transfer behaviour of highly compacted bentonite can influence the process of decay heat from the high-level radioactive to the host rock greatly. Some additives will be added to improve its thermal property due to its low thermal conductivity. Because of the inflowing groundwater coming from the host rock, the buffer material will become saturated gradually. In addition, its dry density also will change when the confining pressure changes. These processes can change its thermal property which will influence the safety of HLW disposal. Therefore, the prediction of thermal conductivity of bentonite is an important part of study for the buffer material. Numerous predicting models of thermal conductivity have been proposed in the past several decades. Among them, empirical models [66–68] and geometric mean model are widely used [16, 62, 69]. Empirical models can be adopted to build up the relationship of the thermal conductivity between various types of soils and their dry density and water content. However, none of them take into account mass additives into the soil. The geometric mean model was firstly presented by Woodside and Messmer [69]. Then, it was improved and successfully used by Lee et al. [62]. Based on the volumetric composition of sample-forming minerals, the geometric mean model can be presented as follows:

$$\lambda = \prod_j^n \lambda_j^{\phi_j} \text{ with } \sum_j^n \phi_j = 1, \quad (6)$$

where \prod represents the product of $\lambda_j^{\phi_j}$. λ_j and ϕ_j are the thermal conductivity of each component and its volumetric proportion, respectively. Obviously, the sum of the volumetric proportion for each component equals to 1. j refers to the j th component, and there are n kinds of components in total.

According to the geometric mean model mentioned above, the present study proposes a new model to predict the thermal conductivity considering the influence of GO. The following prediction model is based on several assumptions: (1) bentonite is homogeneous; (2) GO disperses homogeneously in the soil; and (3) the voids in the compacted soil are full of air at first when the degree of saturation equals to 0, and it has been replaced by water with the increasing water content. To take all components into account, (6) can be rewritten as

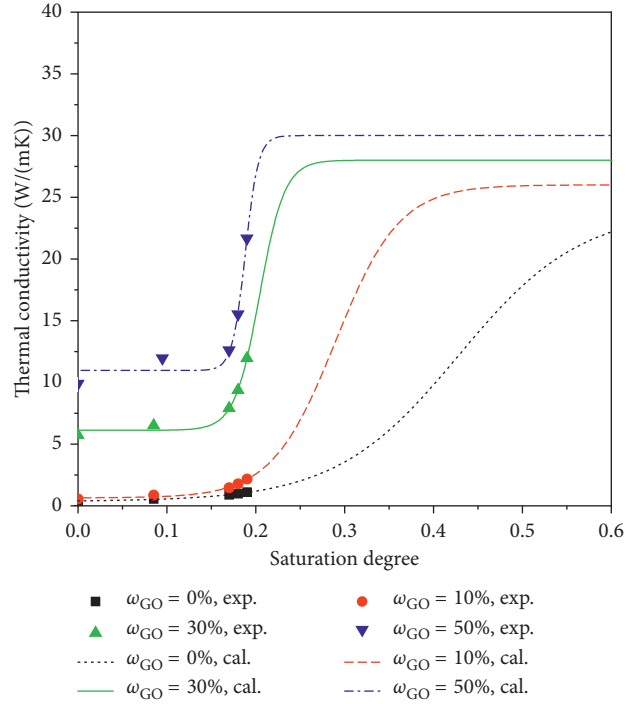


FIGURE 8: The thermal conductivity and the saturation degree.

TABLE 3: Fitting values of the parameters in (4).

GO content (%)	Coefficients of fitting				
	λ_0 (W/(mK))	λ_s (W/(mK))	S_a	A	R^2
0	0.034	24	0.428	0.069	0.97
10	0.627	26	0.290	0.036	0.93
30	6.106	28	0.204	0.014	0.95
50	10.954	30	0.188	0.007	0.90

$$\lambda = \lambda_b^{\phi_b} \lambda_{GO}^{\phi_{GO}} \lambda_w^{\phi_w} \lambda_a^{\phi_a} \text{ with } \lambda_b + \lambda_{GO} + \lambda_w + \lambda_a = 1,$$

$$\phi_b = \frac{\rho_d (1 - \omega_{GO})}{\rho_b},$$

$$\phi_{GO} = \omega_{GO} \left(\frac{\rho_d}{\rho_{GO}} \right), \quad (7)$$

$$\phi_w = (1 - \phi_b - \phi_{GO}) S_r,$$

$$\phi_a = (1 - \phi_b - \phi_{GO}) (1 - S_r),$$

where $\lambda_b, \lambda_{GO}, \lambda_w,$ and λ_a present the thermal conductivity of bentonite, GO, water, and air, respectively, while $\phi_b, \phi_{GO}, \phi_w,$ and ϕ_a are the volumetric proportions for bentonite, GO, water, and air, respectively; ρ_d is its dry density; ρ_b and ρ_{GO} are the particle densities of bentonite and graphene oxide, respectively; and S_r is the saturation degree of compacted specimens. Each component of the compacted material would not have homogeneous distribution and its influence on the thermal conductivity is different. In consideration of all these facts, (7) can be modified and expressed as follows:

$$\lambda = \lambda_b^{(n\rho_d(1-\omega_{GO})/\rho_b)} \lambda_{GO}^{(p\omega_{GO}\rho_d/\rho_{GO})} \cdot \left[\lambda_w^s \lambda_a^{(1-s_r)} \right]^q \left[1 - \left(\frac{\rho_d(1-\omega_{GO})}{\rho_b} - \frac{\omega_{GO}\rho_d}{\rho_{GO}} \right) \right] \quad (8)$$

where n , p , and q are the influence factors which take into account the different influence degrees for various components. The values of λ_{GO} , λ_w , and λ_a are 129 W/(mK), 0.059 W/(mK), and 0.024 W/(mK) at 20°C, respectively. However, the mineral composition of the compacted specimen may differ from each other because of uneven sampling, leading to a varying value of λ_b . Therefore, its value is determined with other parameters including n , p , and q with the multivariate regression analysis method. After regression, the modified model and the fitted values of parameters are presented as follows:

$$\lambda = 2.094^{(n\rho_d(1-\omega_{GO})/\rho_b)} 129^{(p\omega_{GO}\rho_d/\rho_{GO})} \cdot \left[0.59^s \cdot 0.024^{1-s_r} \right]^q \left[1 - \left(\frac{\rho_d(1-\omega_{GO})}{\rho_b} - \frac{\omega_{GO}\rho_d}{\rho_{GO}} \right) \right] \quad (9)$$

$$n = 1.195, p = 1.195, q = 0.663.$$

The correlation coefficient of (8) is 0.97. Values of n and p are higher than 1, respectively, while the value of q is lower than 1, which indicate that the bentonite and GO present stronger influence to the thermal conductivity than water and air does.

The comparison of measured values and calculated thermal conductivity using the proposed constitutive model above is plotted in Figure 9. As shown in the figure, when the GO content is higher than 10%, the calculated values are approximately equal to the experimental value. This means that this modified model is proper to predict the thermal conductivity of GO-GMZ bentonite when the GO content is higher than 10%. However, the calculated values are apparently higher than the measured values when the GO content is lower than 10%. Considering such fact, there may cause a misleading in the thermal conductivity prediction when the additive's content is low. Therefore, the practical application of the calculated thermal conductivity using the proposed constitutive model needs more consideration. In general, the modified geometric mean model proposed in this research can be adopted as a constitutive model to predict the thermal conductivity of the GO-GMZ bentonite, which has been considered as the feasible buffer material for an HLW repository in China.

Bentonite will undergo thermal, chemical, and mechanical effects when used in the HLW repository. Therefore, the durability of GO-GMZ bentonite is of concern. Generally, the structure of GO is stable chemically when there is no photocatalyst or peroxidase and its decomposition temperature is found to be above 100°C [70–72]. Some chemical bonds such as the amido bond form in this process, and they are stable thermally and chemically [73]. In addition, the size of the particles used and obtained in the modified process is too small (i.e., nanosized or even smaller) to be influenced by the mechanical pressure. Therefore, the structure of GO-GMZ will stay durable under swelling pressure or other mechanical forces.

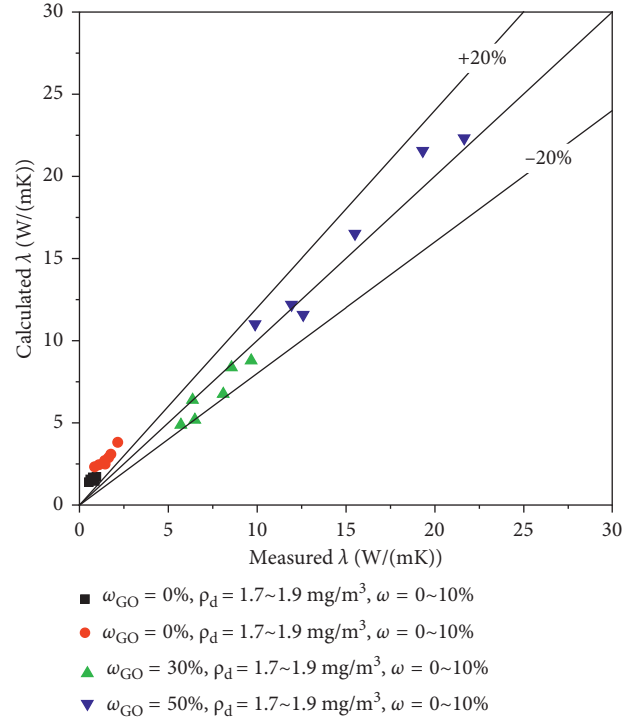


FIGURE 9: Comparison between the calculated values and experimental results of the thermal conductivity for GO-GMZ bentonite.

4. Conclusions

This research measures the thermal conductivity of highly compacted GO-GMZ bentonite under different conditions like graphene oxide content, dry density, and water content with the thermoprobe method. The thermal conductivity of GO-GMZ bentonite increases evidently as values of GO content, dry density, and water content are fortified. The functional relationship between the thermal conductivity and GO content is quadratic. However, thermal conductivity-dry density relationship or thermal conductivity-water content relationship is linear within a certain range. Moreover, a modified geometric mean model is also proposed in the present study to predict the thermal conductivity of GO-GMZ bentonite. The comparison between experimental data and calculated values implies that this model is appropriate for such buffer material when the GO content exceeds beyond a certain range. Therefore, this proposed model can be applied to predict the thermal conductivity of the GO-GMZ bentonite as a constitutive model for a HLW repository in China. In addition, hydraulic conductivity is another crucial parameter for its safe application which will be studied in the further work.

Data Availability

The data used to support the findings of this study are available from the corresponding author upon request.

Conflicts of Interest

The authors declare that they have no conflicts of interest.

Acknowledgments

The authors are grateful to the National Natural Science Foundation of China (41422207 and 41772279), China Atomic Energy Authority ([2011]1051), and Fundamental Research Funds for the Central Universities.

References

- [1] F. N. Hodges, J. H. Westsik, and L. A. Bray, "Development of a backfill for containment of high-level nuclear waste," *MRS Proceedings*, vol. 11, p. 641, 1981.
- [2] SNF Waste Management CO, "SKB91 final disposal of spent nuclear fuel: importance of the bedrock for safety," SKB Technical Report, pp. 92–120, SKB, Stockholm, Sweden, 1992.
- [3] JNC, "JNC supporting report 2: repository design and engineering technology," JNC TN 1400 99–012, Japan Nuclear Cycle Development Institute, Ibaraki, Japan, 1999.
- [4] G. Q. Xu, "Selection of buffer/backfill materials and their additives," *Cranium Geology*, vol. 12, no. 4, pp. 238–244, 1996.
- [5] J. Wang, R. Su, W. M. Chen, Y. H. Guo, Z. J. Wen, and Y. M. Liu, "Deep geological disposal of high-level radioactive wastes in China," *Chinese Journal of Rock Mechanics and Engineering*, vol. 25, no. 4, pp. 649–658, 2006.
- [6] B. Pastina and P. Hella, "Expected evolution of a spent nuclear fuel repository at Olkiluoto," POSIVA Report 2006-05, Posiva Oy, Olkiluoto, Finland, 2006.
- [7] H. Hökmark and B. Fälth, "Thermal dimensioning of the deep repository," Technical Report, TR-03–09, SvenskKärnbränslehantering, Stockholm, Sweden, 2003.
- [8] SKB, *Final Storage of Spent Nuclear Fuel-KBS-3*, Swedish Nuclear Fuel Supply Company, Stockholm, Sweden, 1983.
- [9] W. J. Cho, J. O. Lee, C. H. Kang, and K. S. Chun, "Basic physicochemical and mechanical properties of domestic bentonite for use as a buffer material in a high-level radioactive waste repository," *Journal of Korean Society*, vol. 31, pp. 39–50, 1999.
- [10] P. Wersin, L. H. Johnson, and I. G. McKinley, "Performance of the bentonite barrier at temperatures beyond 100°C: a critical review," *Physics and Chemistry of the Earth Parts A/B/C*, vol. 32, no. 8, pp. 780–788, 2007.
- [11] D. D. Eberl, "The reaction of montmorillonite to mixed-layer clay: the effect of interlayer alkali and alkaline-earth cations," *Geochimica et Cosmochimica Acta*, vol. 42, pp. 1–7, 1978.
- [12] T. Sato, M. Kuroda, S. Yokoyama et al., "Dissolution kinetics of smectite under alkaline conditions," in *Proceedings of International Meeting on Clays in Natural and Engineering Barriers for Nuclear Waste Confinement*, Tours, France, 2005.
- [13] J. O. Lee, I. M. Kang, and W. J. Cho, "Smectite alteration and its influence on the barrier properties of smectite clay for a repository," *Applied Clay Science*, vol. 47, no. 1, pp. 99–104, 2010.
- [14] W. M. Ye, Y. He, Y. G. Chen, B. Chen, and Y. J. Cui, "Thermochemical effects on the smectite alteration of GMZ bentonite for deep geological repository," *Environmental Earth Sciences*, vol. 75, no. 10, p. 906, 2016.
- [15] A. Inoue, M. Utada, H. Nagata, and T. Watanabe, "Chemical and morphological evidence for the conversion of smectite to illite," *Clay and Clay Minerals*, vol. 35, no. 2, pp. 111–120, 1987.
- [16] J. Cote and J. Konrad, "Generalized thermal conductivity model for soils and construction materials," *Canadian Geotechnical Journal*, vol. 42, no. 2, pp. 443–458, 2005.
- [17] N. H. Abu-Hamdeh and R. C. Reeder, "Soil thermal conductivity: effects of density, moisture, salt concentration, and organic matter," *Soil Science Society of America Journal*, vol. 64, no. 4, pp. 1285–1290, 2000.
- [18] B. Usowicz, J. Lipiec, and A. Ferrero, "A prediction of soil thermal conductivity based on penetration resistance and water content or air-filled porosity," *International Journal of Heat Mass Transfer*, vol. 49, no. 25–26, pp. 5010–5017, 2006.
- [19] Aurangzeb, L. A. Khan, and A. Maqsood, "Prediction of effective thermal conductivity of porous consolidated media as a function of temperature: a test example of limestones," *Journal of Physics D: Applied Physics*, vol. 40, no. 16, pp. 4953–4958, 2007.
- [20] H. Coulon, A. Lajudie, P. Debrabant et al., "Choice of French clays as engineered barrier components for waste disposal," *Materials Research Society Symposium Proceedings*, vol. 84, pp. 813–824, 1987.
- [21] G. P. Zhu, Y. M. Liu, and T. A. Luo, "Study on heat conductivity of Gaomiaozi bentonite," *Resources Environment and Engineering*, vol. 19, no. 3, pp. 220–222, 2005.
- [22] Y. J. Cui, N. Sultan, and P. Delage, "A thermomechanical model for saturated clays," *Canadian Geotechnical Journal*, vol. 37, no. 3, pp. 607–620, 2000.
- [23] E. E. Alonso, J. Alcoverro, F. Coste et al., "The FEBEX benchmark test: case definition and comparison of modelling approaches," *International Journal of Rock Mechanics and Mining Sciences*, vol. 42, no. 5–6, pp. 611–638, 2005.
- [24] X. Pintado and A. Lloret, "Thermohydraulic test on bentonite," *Journal of Thermal Analysis and Calorimetry*, vol. 84, no. 2, pp. 325–330, 2006.
- [25] L. Xu, W. M. Ye, B. Chen, Y. G. Chen, and Y. J. Cui, "Experimental investigations on thermo-hydro-mechanical properties of compacted GMZ01 bentonite-sand mixture using as buffer materials," *Engineering Geology*, vol. 213, pp. 46–54, 2016.
- [26] JNC, "H12 project to establish the scientific and technical basis for HLW disposal in Japan, supporting report 2: repository design and engineering technology," JNC-TN1410 2000-003, Japan Nuclear Cycle Development Institute, Ibaraki, Japan, 2000.
- [27] D. A. Sun, H. B. Cu, and W. J. Sun, "Swelling of compacted sand-bentonite mixtures," *Applied Clay Science*, vol. 43, no. 3–4, pp. 485–492, 2009.
- [28] D. A. Sun, W. J. Sun, and L. Fang, "Swelling characteristics of Gaomiaozi bentonite and its prediction," *Journal of Rock Mechanics and Geotechnical Engineering*, vol. 6, no. 2, pp. 113–118, 2014.
- [29] S. L. Cui, H. Y. Zhang, and M. Zhang, "Swelling characteristics of compacted GMZ bentonite-sand mixtures as a buffer/backfill material in China," *Engineering Geology*, vol. 141–142, no. 3, pp. 65–73, 2012.
- [30] M. Zhang, H. Y. Zhang, S. Y. Cui, L. Y. Jia, L. Zhou, and H. Chen, "Engineering properties of GMZ bentonite-sand as buffer/backfilling material for high-level waste disposal," *European Journal of Environmental and Civil Engineering*, vol. 16, no. 10, pp. 1216–1237, 2012.
- [31] Y. C. Zhuang, K. H. Xie, and Y. H. Sun, "Experimental study on thermal conductivity of mixed materials of sand and bentonite," *Rock and Soil Mechanics*, vol. 26, no. 2, pp. 261–269, 2005, in Chinese.
- [32] J. Pacovsky, "Selected results from geotechnical research on bentonite," in *Proceedings of the 8th International Conference on Radioactive Waste Management and Environmental Remediation*, Bruges, Belgium, 2001.

- [33] J. Michael and B. Gunter, "Influence of graphite and quartz addition on the thermo-physical properties of bentonite for sealing heat-generating radioactive waste," *Applied Clay Science*, vol. 44, no. 3-4, pp. 206-210, 2009.
- [34] C. Lee, X. Wei, J. W. Kysar, and J. Hone, "Measurement of the elastic properties and intrinsic strength of monolayer graphitic," *Science*, vol. 321, no. 5887, pp. 385-388, 2008.
- [35] A. A. Balandin, S. Ghosh, W. Bao et al., "Superior thermal conductivity of single-layer graphene," *Nano Letters*, vol. 8, no. 3, pp. 902-907, 2008.
- [36] M. D. Stoller, S. Park, Y. Zhu, J. An, and R. S. Ruoff, "Graphitic-based ultracapacitors," *Nano Letters*, vol. 8, no. 10, p. 3498, 2008.
- [37] Y. M. Liu and Z. R. Chen, "Bentonite from Gaomiaozhi, inner Mongolia as an ideal buffer/backfilling material in handling highly radioactive wastes-a feasibility study," *Acta Mineralogica Sinica*, vol. 21, no. 3, pp. 541-543, 2001.
- [38] Z. J. Wen, "Physical property of China's buffer material for high-level radioactive waste repositories," *Chinese Journal of Rock Mechanics and Engineering*, vol. 25, no. 4, pp. 794-800, 2006.
- [39] W. M. Ye, X. L. Lai, Y. Liu, Y. G. Chen, and Y. J. Cui, "Ageing effects on swelling behaviour of compacted GMZ01 bentonite," *Nuclear Engineering and Design*, vol. 265, pp. 262-268, 2013.
- [40] W. M. Ye, Z. J. Zheng, B. Chen, Y. G. Chen, Y. J. Cui, and J. Wang, "Effects of pH and temperature on the swelling pressure and hydraulic conductivity of compacted GMZ01 bentonite," *Applied Clay Science*, vol. 101, pp. 192-198, 2014.
- [41] D. A. Sun, J. Y. Zhang, J. R. Zhang, and L. Zhang, "Swelling characteristics of GMZ bentonite and its mixtures with sand," *Applied Clay Science*, vol. 83-84, pp. 224-230, 2013.
- [42] C. M. Zhu, W. M. Ye, Y. G. Chen, B. Chen, and Y. J. Cui, "Influence of salt solutions on the swelling pressure and hydraulic conductivity of compacted GMZ01 bentonite," *Engineering Geology*, vol. 166, pp. 74-80, 2013.
- [43] M. Wan, W. M. Ye, Y. G. Chen, Y. J. Cui, and J. Wang, "Influence of temperature on water retention properties of compacted GMZ01 bentonite," *Environmental Earth Science*, vol. 73, no. 8, pp. 4053-4061, 2014.
- [44] Y. G. Chen, C. M. Zhu, W. M. Ye, Y. J. Cui, and Q. Wang, "Swelling pressure and hydraulic conductivity of compacted GMZ01 bentonite under salinization-desalinization cycle conditions," *Applied Clay Science*, vol. 114, pp. 454-460, 2015.
- [45] Y. M. Liu, M. F. Cai, and J. Wang, "Thermal properties of buffer material for high-level radioactive waste disposal," *Chinese Journal of Rock Mechanics and Engineering*, vol. 26, pp. 3891-3896, 2007.
- [46] W. M. Ye, Q. Wang, H. Pan, and B. Chen, "The thermal conductivity of high compacted GMZ01 bentonite," *Chinese Journal of Geotechnical Engineering*, vol. 32, no. 6, pp. 821-826, 2010.
- [47] J. L. Xie, Y. M. Liu, and H. W. Zhou, "Measurement of thermal conductivity of sand-bentoinite mixtures," in *The 3rd Proceedings of Waste Underground Disposal*, pp. 439-444, Beijing, China, 2010, in Chinese.
- [48] C. Ma, "Study on the thermal conductivity of crushed granite and bentonite mixture," Master thesis, China University of Geosciences, Beijing, China, 2014.
- [49] L. X. Qian, *A fundamental study of GMZ bentonite as buffer material in deep geological disposal for high-level radioactive waste*, Ph.D. thesis, Tongji University, Shanghai, China, 2007.
- [50] M. Hirata, T. Gotou, S. Horiuchi, M. Fujiwara, and M. Ohba, "Thin-film particles of graphite oxide 1: high-yield synthesis and flexibility of the particles," *Carbon*, vol. 42, no. 14, pp. 2929-2937, 2004.
- [51] X. Zhang, J. Yin, C. Peng et al., "Distribution and biocompatibility studies of graphitic oxide in mice after intravenous administration," *Carbon*, vol. 49, no. 3, pp. 986-995, 2011.
- [52] L. Kubicar, V. Vretenar, V. Stofanik, and V. Bohac, "Hot-ball method for measuring thermal conductivity," *International Journal of Thermophysics*, vol. 31, pp. 1904-1918, 2010.
- [53] D. Kraemer and G. Chen, "A simple differential steady-state method to measure the thermal conductivity of solid bulk materials with high accuracy," *Review of Scientific Instruments*, vol. 85, no. 2, pp. 1-7, 2014.
- [54] N. H. Abu-Hamdeh, I. Khedair, and R. C. Reeder, "A comparison of two methods used to evaluate thermal conductivity for some soils," *International Journal of Heat Mass Transfer*, vol. 44, no. 5, pp. 1073-1078, 2001.
- [55] O. K. Nusier and N. H. Abu-Hamdeh, "Laboratory techniques to evaluate thermal conductivity for some soils," *Heat and Mass Transfer*, vol. 39, no. 2, pp. 119-123, 2003.
- [56] R. Prasher, "Graphene spreads the heat," *Science*, vol. 328, no. 5975, pp. 185-186, 2010.
- [57] P. N. Mishra, S. Surendran, V. K. Gadi, R. A. Joseph, and D. N. Arnepalli, "Generalized approach for determination of thermal conductivity of buffer materials," *Journal of Hazardous Toxic and Radioactive Waste*, vol. 21, no. 4, pp. 172-178, 2017.
- [58] G. Kahr and M. Muellervonmoos, *Warmeleitfähigkeit War-meleitfähigkeit von Bentonit MX80 und von Montigel nach der Heizdrahtmethode*, NAGRA, Cheseaux-sur-Lausanne, Switzerland, 1982.
- [59] A. M. Tang and Y. J. Cui, "Effects of mineralogy on thermo-hydro-mechanical parameters of MX80 bentonite," *Journal of Rock Mechanics and Geotechnical Engineering*, vol. 2, no. 1, pp. 91-96, 2010.
- [60] H. Suzuki, M. Shibata, J. Yamagata, I. Hirose, and K. Terakado, "Physical and mechanical properties of bentonite (I)," PNC TN1410 92-52, 1992, in Japanese.
- [61] M. V. Villar, *Thermo-Hydro-Mechanical Characterization of a Bentonite From Cabo de Gata*, ENRESA Publication Tecnica, Barcelona, Spain, 2002.
- [62] J. O. Lee, H. Choi, and J. Y. Lee, "Thermal conductivity of compacted bentonite as a buffer material for a high-level radioactive waste repository," *Annals of Nuclear Energy*, vol. 94, pp. 848-855, 2016.
- [63] O. Johansen, "Thermal conductivity of soils," Ph.D. thesis, Trondheim University, Trondheim, Norway, 1975.
- [64] I. Kukkonen and I. Suppala, "Measurement of thermal conductivity and diffusivity in situ: literature survey and theoretical modelling of measurements," *Journal of Molecular Structure*, vol. 857, pp. 447-455, 1999.
- [65] P. G. Klemens, "Thermal conductivity of inhomogeneous materials," *International Journal of Thermophysics*, vol. 10, no. 6, pp. 1213-1219, 1989.
- [66] M. S. Kersten, "Laboratory research for the determination of the thermal properties of soils," *ACFEL Technical Report*, vol. 23, pp. 153-182, 1949.
- [67] H. Kiyohashi and K. Banno, "Effective thermal conductivity of compact bentonite as a buffer material for high level radioactive waste," *High Temperatures-High Pressures*, vol. 27-28, no. 6, pp. 653-663, 1995.
- [68] W. J. Cho, J. O. Lee, and S. Kwon, "An empirical model for the thermal conductivity of compacted bentonite and a bentonite-sand mixture," *International Journal of Heat and Mass Transfer*, vol. 47, no. 11, pp. 1385-1393, 2011.

- [69] W. H. Woodside and J. H. Messmer, "Thermal conductivity of porous media I: unconsolidated sands & II: consolidated sands," *Journal of Applied Physics*, vol. 32, no. 9, pp. 1688–1699, 1961.
- [70] G. Williams, B. Seger, and P. V. Kamat, "TiO₂-graphene nanocomposites. UV-assisted photocatalytic reduction of graphene oxide," *ACS Nano*, vol. 2, no. 7, pp. 1487–1491, 2008.
- [71] F. Yin, D. Z. Chen, J. J. Liu, Q. Chen, H. X. Kong, and C. J. Wu, "Preparation technology and thermostability of graphite oxide," *Journal of Materials Science and Engineering*, vol. 31, no. 3, pp. 328–335, 2013, in Chinese.
- [72] E. Siegfried, G. Stefan, and H. Andreas, "Investigation of the thermal stability of the carbon framework of graphene oxide," *Chemistry-A European Journal*, vol. 20, no. 4, pp. 984–989, 2014.
- [73] W. Liao, F. Wei, D. Liu, M. X. Qian, G. Yuan, and X. S. Zhao, "FTIR-ATR detection of proteins and small molecules through DNA conjugation," *Sensors and Actuators B: Chemical*, vol. 114, no. 1, pp. 445–450, 2006.

Research Article

Geotechnical Properties and Microstructure of Lime-Fly Ash-Phosphogypsum-Stabilized Soil

Tebogo Pilgrene Mashifana ^{1,2}, Felix Ndubisi Okonta,² and Freeman Ntuli¹

¹Department of Chemical Engineering, University of Johannesburg, P.O. Box 17011, Doornfontein 2088, South Africa

²Department of Civil Engineering Sciences, University of Johannesburg, P.O. Box 524, Auckland Park 2000, South Africa

Correspondence should be addressed to Tebogo Pilgrene Mashifana; tmashifana@uj.ac.za

Received 1 May 2018; Revised 16 July 2018; Accepted 31 July 2018; Published 2 September 2018

Academic Editor: Yonggui Chen

Copyright © 2018 Tebogo Pilgrene Mashifana et al. This is an open access article distributed under the Creative Commons Attribution License, which permits unrestricted use, distribution, and reproduction in any medium, provided the original work is properly cited.

The use of industrial waste as a potential stabilizer of marginal construction materials is cost effective. Phosphogypsum and fly ash are industrial wastes generated in very large quantities and readily available in South Africa. In order to explore the potential stabilization of vastly abundant expansive soil using larger quantity phosphogypsum waste as a potential modifier, composites with a mixture of lime-fly ash-phosphogypsum-basic oxygen furnace slag were developed. However because of the presence of radionuclide, it was necessary to treat the phosphogypsum waste with mild citric acid. The effect of the acid treatment on the geotechnical properties and microstructure of expansive soil stabilized with phosphogypsum-lime-fly ash-basic oxygen furnace slag (PG-LFA-BOF) paste was evaluated, in comparison with the untreated phosphogypsum. Expansive soil stabilized with acid-treated PG-LFA-BOF paste exhibited better geotechnical properties; in particular, the high strength mobilized was associated primarily with the formation of various calcium magnesium silicide and coating by calcium silicate hydrate and calcium aluminate hydrate. The soil microstructure was improved due to the formation of hydration products. The stabilized expansive soil met the specification for road subgrades and subbase. Stabilization of expansive soils with phosphogypsum, fly ash, and basic oxygen fly ash does not only improve engineering properties of soil but also provides a solution in relation to disposal and environmental pollution challenges.

1. Introduction

Expansive soils are widely distributed throughout the world [1, 2] and tend to change greatly in volume with variation in water content. Expansive soils are extremely problematic and form a wide range of problems related to geotechnical engineering [3]. The greatest challenge is the high montmorillonite mineral content in the soil. Due to this problem, expansive soils need to be modified or stabilized in order to render it suitable for construction applications [3].

This soil type is abundant in arid zones with conditions suitable for the formation of clayey minerals of mainly the smectite group such as montmorillonite or illites [2, 4, 5]. Large specific area and high cation exchange capacity (CEC) are the characteristics associated with the expansive soils [5, 6]. These soils are extremely difficult to handle during

construction and have very poor strength and low bearing capacity [3]. Three factors readily contribute to the swelling of these soils, namely, local environmental conditions, the engineering factors of the soil, and geology. Geology primarily determines the presence of expansive clay minerals. Among the engineering factors included are the soil moisture content, plasticity, and dry density. The most important local environmental conditions to consider are the amount of the clay fraction in the soil, its initial moisture conditions, and confining pressure [2]. The great volume changes associated of these types of soil are amongst the major causes of disasters worldwide due to the extensive damages caused to the structures and infrastructure [7–11], when built on top of the expansive soil. Chen et al. refer to these types of soils as “calamitous soils” [9], which is the soil with special characteristics in relation to shrinking, swelling,

fissures, and strength reduction. Expansive soils are also associated with swelling when they absorb water and shrink upon evaporation of water [12]. Stabilized expansive soil can be used as a backfill material; in 2015, Sun et al. utilized bentonite as a potential buffer/backfill material for deeply buried geological disposal system to isolate high-level radioactive waste [13].

Phosphogypsum and fly ash are normally discharged to the environment without any treatment leading to environmental contamination, occupation of considerable land, and pollution of soil and water [14]. These two industrial wastes, fly ash and phosphogypsum are produced by thermal power plants and phosphoric acid production companies, respectively [15]. An estimated 100–280 million tons of PG was generated worldwide per annum [16], and although excess of 35 million tons of fly ash is produced in South Africa, only 3 million tons were utilized. Currently only a relatively little amount of PG is utilized for building and civil engineering applications due to the presence of radionuclides [17–21]. Waste PG was treated with citric acid to reduce its radionuclides and render the material applicable for civil engineering works. To enhance the geotechnical properties of PG, both the raw and treated PG were then stabilized with fly ash, lime, and basic oxygen furnace slag before they were used further. The composites developed from different proportions of raw and acid-treated phosphogypsum, fly ash, lime, and basic oxygen furnace slag were then investigated as potential stabilizers for bentonite-rich reconstituted soils (expansive soil). The main objective of this study was to stabilize expansive soil by enhancing its geotechnical properties, using voluminous phosphogypsum waste and other wastes such as fly ash and basic oxygen furnace slag.

2. Materials and Methods

2.1. Materials. The raw phosphogypsum was obtained from a phosphoric acid manufacturing plant in South Africa. The treated phosphogypsum was produced by treating the raw phosphogypsum with mild citric acid to reduce its radioactivity. The effect of stirring speed on the leaching of raw PG with citric acid was studied by investigating the speed of 200, 400, and 600 rpm. For the leaching reagent concentration, citric acid was varied from 0.25 M, 0.5 M, to 0.75 M. The effect of temperature was also studied and temperature was set at 25°C, 30°C, and 40°C. The optimum operating conditions were the concentration of 0.5 M, stirring speed of 200 rpm, and temperature of 25°C. The major contributor to the radioactivity of phosphogypsum was ²³²thorium with a concentration of 290 Bq/kg, which resulted into the following activity indexes: $I_1 = 1.405$, $I_2 = 0.505$, and $I_3 = 0.217$. Thorium radioactivity was reduced to 121 Bq/kg after treatment. Acid-treated phosphogypsum yielded the following activity indexes: $I_1 = 1.386$, $I_2 = 0.136$, and $I_3 = 0.055$, removing any limitation for the material to be used in building, construction of street or playground, and for landfilling. I_1 , I_2 , and I_3 are the activity indexes for materials intended for use in building construction, material used in road, street, playgrounds, and related construction work, and material used for landfilling,

respectively. Expansive soil was reconstituted in the laboratory by blending sand, kaolin, bentonite, and gravel.

2.2. Samples Preparation. The expansive soil utilized consists of 40% bentonite, 35% sand, 20% kaolin, and 5% gravel. The raw PG and the treated PG were stabilized with LFA and BOF slag. The developed binders with the PG proportion of 50% for both raw and treated PG were prepared separately with a mix design containing the following composition: PG 50%, FA 30%, and L 20% for raw PG and PG 50%, FA 10%, L 10%, and BOF slag 30% for treated PG. Stabilized raw PG mobilized unconfined compressive strength of 4.8 MPa, and stabilized acid-treated composites mobilized strength of 1.5 MPa (without BOF slag), both at 50% PG content. To further stabilize the treated PG, basic oxygen furnace slag was added in order to improve the strength. The application of the raw and treated PG composites separately as stabilizer using different proportions was investigated to the ratio of the expansive soil: 1 : 9, 2 : 8, 3 : 7, 4 : 6, and 5 : 5. Ratios from 10% to 50% stabilizers were investigated. The maximum dry density (MDD) and optimum moisture content (OMC) at different stabilizers to expansive soil were determined. The specimens were then cast in a 100 × 100 × 100 mm³ moulds.

To ensure that the composites developed are environmentally friendly and will not leach back to the environment, they were subjected to the toxicity characteristic leaching procedure (TCLP). The composites for the raw and treated PG were milled after determining UCS and leached with an extraction buffer of acetic acid and sodium hydroxide (pH 4.93 ± 0.05) at a liquid/solid ratio of 20 : 1. A thermostatic shaker was used for the extraction, and the cured composites were subjected to 24 hours shaking at 25 ± 2°C. After 24 hours, three samples were taken per test conducted and filtered. The leachate was analysed using the inductively coupled plasma-optical emission spectrometer (ICP-OES) to determine the concentration of leached heavy metals. The results obtained showed the concentration of the heavy metals in the leachate ranging between 0.01 and 6.59 ppm, indicating a lower leachability of the composites and that they are environmentally friendly and have no potential contaminating the environment.

2.3. Curing, Determination of Unconfined Compressive Strength, Atterberg Limit Tests, and Microstructure. The specimens were cured for 7 days in a chamber at the temperature of 40°C. After the curing process, the UCS of the specimens was determined in accordance with ASTM method D698 [22]. The liquid limit and plastic limit tests were performed on the expansive soil and the stabilized soil, following the ASTM D4318 method [23]. The expansive soil and stabilized soils were characterized using XRF, XRD, and SEM to study the chemical composition, mineralogy, and the morphology of the microstructures, respectively.

2.4. Properties of Expansive Soil. Tables 1 and 2 present the results for the raw and treated PG chemical composition and the properties of expansive soil, respectively.

TABLE 1: Chemical composition of raw PG, lime, fly ash, treated PG, and BOF.

Component (%)	F	Al ₂ O ₃	SiO	P ₂ O	SO ₃	CaO	TiO	Fe ₂ O ₃	MgO	MnO	CrO ₃	Radionuclides
Raw PG	1.06	0.23	1.37	1.28	51	44		0.121				0.62
L		0.28	0.5	0.03	0.2	73		0.225				
FA		28	48	0.73	0.6	5.1	2.47	4.83				
Treated PG		0.09	0.86	0.72	54	43		0.05				0.41
BOF slag		4.67	14.1	1.21		44	0.27	28.47	3.53	2.84	0.05	

TABLE 2: Properties of expansive soil.

	Sand (%)	Bentonite (%)	Gravel (%)	Kaolin (%)	pH	Density (g/cm ³)	Plastic limit (%)	Liquid limit (%)	Plastic index (%)	UCS (MPa)
Expansive soil	35	20	5	40	10.3	2.55	74.5	94.9	20.40	0.15

The raw phosphogypsum was mainly laden with calcium oxide and sulphur trioxide, and the semiquantitative results using XRD indicated traces of radionuclides. The actual radioactivity showing the concentration of radionuclides was measured by a gamma ray spectrometer. Treating PG with citric acid resulted into a reduction of contaminants such as flourides, phosphorus, and radionuclides, which has a potential to hinder strength development of the material. Calcium oxide was predominant in the hydrated lime utilized. Fly ash consisted of constituent such as silica, calcium oxide, ferrous iron, and titanium oxide [24]. The high wt.% of sulphate measured in both the raw and treated materials may have a detrimental effect on the strength development of the material. Although sulphate slightly increased after the treatment of PG, it was drastically reduced after curing. The relative proportion of sulphate was reduced from 51 wt.% to 35.21 wt.%, 32.88 wt.%, 26.15 wt.%, and 20.82 wt.%, for raw PG 30, 40, 50, and 60, respectively, and from 54 wt.% to 20.19 wt.%, 24.67 wt.%, 28.23 wt.%, and 30.42 wt.% for treated PG 30, 40, 50, and 60 composites, respectively.

The expansive soil had the UCS of 0.15 MPa, and it is a basic material with a pH of 10.32. The properties of soil also show a clay mineral with high plastic and liquid limits indicating the high water adsorption capability of the soil. The specific density of the expansive soil was measured to be 2.55 g/cm³.

The respective MDD and OMC results with the increment in content of raw and treated PG stabilizers are presented in Table 3.

An increment in the stabilizers content for both raw and treated PG resulted in the decrease in MDD. The expansive soil had a MDD of 1765 kg/m³, and raw and treated PG had MDDs of 1204 kg/m³ and 1100 kg/m³, respectively, leading to an overall reduction in density when the expansive soil was stabilized. The lower expansive soil dry density may have less swelling potential when compared to expansive soil with a higher dry density. The OMC however increased with increasing stabilizers content, and this may be due to the mineralogical composition especially the presence and specific surface of the montmorillonite and calcium-silica reactions [25]. The increase in OMC indicates an increased demand for water for curing and strength development.

TABLE 3: MDD and OMC with raw and treated PG stabilizers.

Stabilizer (%)	0	10	20	30	40	50
MDD (kg/m ³), raw PG	1765	1702	1683	1674	1663	1618
OMC (%)	13	18	21	24	28	30
MDD (kg/m ³), treated PG	1765	1647	1619	1501	1404	1314
OMC (%)	11	15	17	22	25	28

Particle agglomeration together with voids left by water is also responsible for the decrease in MDD [26].

2.5. Relative Density and pH of Expansive Soil. The relative density and pH of expansive soil before and after stabilization are shown in Table 4.

An increment in both the raw and treated PG stabilizer contents resulted in the increase in pH. The soil stabilized with treated PG possesses higher pH as compared to that with raw PG, and this is attributed to the availability of hydrogen ions in the lime which interact with alkalinity hence increasing the pH. The pH proves to have played a role on the higher strengths developed with treated PG as a stabilizer as the pozzolanic reactions are triggered at a higher pH of 12.

The relative density results for stabilized soil with raw PG show an increasing trend with the increase in the stabilizer content. The stabilized soil densities obtained with treated PG are higher than those of the raw PG. The treated PG contains slag, and the specific gravity of steel slags depends on their chemical composition, mineralogy, and particle structure. The presence of high iron oxide contents in the slags makes them to have specific gravity values larger than those of natural soils/aggregates [27]. Pozzolanic reactions are hastened by the presence of PG [28–30]. Pozzolanic reactions require a high pH environment [31] which in the present case is enabled by the presence of lime and calcium from slag for the treated PG stabilizer.

3. Results and Discussion

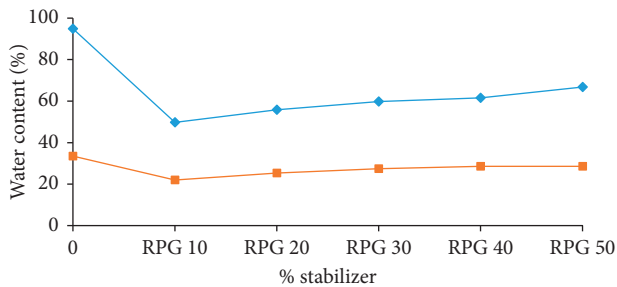
3.1. Atterberg Limits of Stabilized Soil by Raw PG-LFA and Treated PG-LFA. Figures 1(a) and 1(b) depict the liquid

TABLE 4: pH and specific density of expansive soil (raw PG and treated PG).

Stabilizer (%)	pH		Specific density (g/cm ³)	
	Raw PG	Treated PG	Raw PG	Treated PG
0	10.32	10.32	2.652	2.652
10	10.52	11.55	2.666	2.669
20	10.37	11.63	2.673	2.678
30	10.73	11.91	2.678	2.688
40	11.01	12.23	2.681	2.697
50	11.53	12.57	2.685	2.698

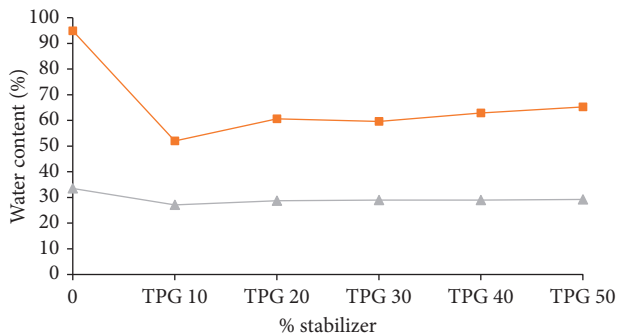
TABLE 5: PI of stabilized soil.

% stabilized	PI-raw PG	PI-treated PG
0	61.4	61.4
10	27.27	24.9
20	30.50	31.86
30	32.29	30.60
40	33.06	33.93
50	38.18	36.06



— Liquid limit: raw PG as a stabilizer
 — Plastic limit: raw PG as a stabilizer

(a)



— Liquid limit: treated PG as a stabilizer
 — Plastic limit: treated PG as a stabilizer

(b)

FIGURE 1: Liquid limit and plastic limits of soil samples that were stabilized by (a) raw PG-LFA and (b) treated PG-LFA-BOF.

limit and plastic limit of the soil stabilized with raw and treated PG.

The expansive soil initially had a liquid limit of 94.90%, and a 42% reduction in the liquid limit is observed at the highest PG content of 50%. The plastic limit decreased from 33.50% to 28.59%. A significant decrease in the liquid limit from 94.90% to 65.26% was achieved. Plastic limit decreased steadily by 25.45% with the increment in PG content to 50%, when comparing the expansive and stabilized soil. It is also evident that the effect of treated PG stabilizer on plasticity is through the liquid limit modification. In 2014, Kumar et al. studied the engineering properties of soil stabilized with lime and phosphogypsum and reported that increment of PG content increased both the liquid and plastic limits [19].

The increment in the stabilizer content from 10 to 50% resulted in the increase in both liquid and plastic limits. The effect herein is directly reflected on the plasticity of the stabilized soil as evident from the similarity in the gradually increasing plasticity. The overall plastic index of stabilized soil has decreased by 61% and 70% for maximum content of the raw and treated PG stabilizers, respectively. The reduction in plasticity is greater with the treated PG stabilizer; this is attributed to the lime content available sources used. The overall liquid limit, plastic limit, and plasticity index of the stabilized soil are less than those of the expansive soil. The reduction in the liquid limit is due to replacement of sodium ions with calcium ions, reduction in diffused double layer, and increase in electrolyte concentration of pore fluid. Phosphogypsum which is chemically calcium sulphate also acts as a source of calcium ions, thus contributing to similar effects on the expansive soil [32]. When the amount of phosphogypsum in mixture increases, the plastic limit value gradually rises. With the focus of utilizing voluminous waste PG for the stabilization of expansive soils, the higher quantity of PG can be used, even though the trends reveal that 10% stabilization in the optimum and shows a gradual increment in PL and LL thereafter. In the study conducted by James et al., in investigating the strength and index properties of phosphogypsum stabilized expansive soil, they found that addition of up to 50% PG has resulted in an increase in the plastic limit from 25.16% to 28.19% only, a mere 3.03% upon 50% addition of PG [33].

The PI of the unstabilized and stabilized soil with raw and treated PG is reported in Table 5.

The PIs of the stabilized soil using the raw PG and treated PG contents that yielded highest strength show a PI reduction of 90% and 70%, respectively. Ji-ru and Xing found that a change of expansive soil texture takes place when lime and fly ash are mixed with expansive soil [34]. The plastic limit increases by mixing lime, and liquid limit decreases by mixing fly ash, which decreases the plasticity index.

The plasticity chart showing the classification of the expansive and stabilized soil is presented in Figure 2. The figure shows that there is a change in the classification of the stabilized soil when comparing with the unstabilized soil. The expansive soil was initially classified as CE material exhibiting an extremely high plasticity material with high liquid limit and high plastic index. The raw and treated PG stabilized soils with a stabilizer content of 10–50% fall mainly under CL-CH region, displaying a medium to high plasticity behaviour. Both the stabilizers utilized in the study greatly improved the expansive soil properties. There is

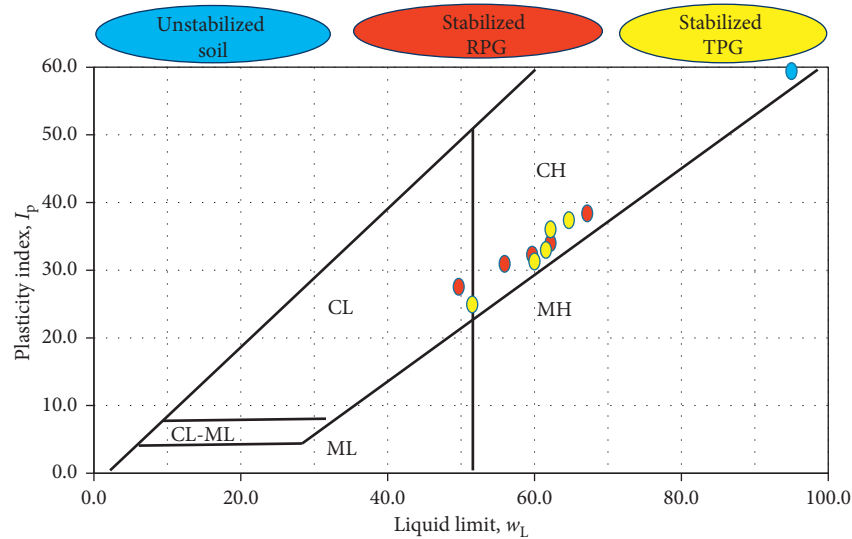


FIGURE 2: Plasticity chart for the stabilized soil.

a significant and distinct improvement in the soil properties which has resulted in a change in soil classification from clay of high plasticity to low plasticity, and similar results were obtained by James and Pandian [35]. CL is of low plasticity. They are used as subgrade pavement materials because of their low swelling and shrinkage potential. The addition of PG-LFA and PG-LFA-BOF effectively converts the soil from an expansive clay to a clay of low expansivity. The local TRH4 specification recommends low plasticity clayey soils (CLs) as good candidate materials for modified pavement subgrade.

3.2. Unconfined Compressive Strength (UCS)-Stabilization of Expansive Soil with the Raw and Treated PG. The results for the unconfined compressive strength of the expansive soil stabilized with the raw and treated PG are presented in Figures 3(a) and 3(b).

The expansive soil initially had the UCS of 0.15 MPa, and stabilization with 10–50% raw PG improved the strength. The optimum strength is observed at the stabilizer content of 30%, and an increment in the stabilization material above to 40% and 50% resulted into strength reduction by 13% and 43%, respectively. James et al. also found that, in the stabilization of expansive soil, the optimum PG content that yielded the highest strength of 250 kN/m² was 40%; thereafter, there was a reduction in the strength with increment of PG content [33]. Lime in excess can remain unreacted and act as weak filler in the compacted lime-fly ash-phosphogypsum composites, resulting in reduction of strength [36]. Also, insufficient lime to raise the pH and stabilize soils contributes greatly to strength reduction. The strength development for lime-fly ash-phosphogypsum specimen depends on a number of factors and lime-fly ash ratio being one of the most important factors affecting strength. Both the raw and treated PG stabilizers prepared at the PG content of 50%. The lime to fly ash ratio was 0.6 for the raw PG and 1 for the treated PG specimen. Lime

and fly ash in the treated PG were partially replaced by BOF which played a significant role in maintaining an improving strength. In the study conducted by Sivapullaiah and Jha on the induced strength behaviour of fly ash-lime-stabilized expansive soil, the change in strength behaviour was studied at different curing periods [32]. The researchers found that the variations in the strength of soil with curing period were due to cation exchange and flocculation initially, and binding of particles with cementitious compounds formed after curing. Early strength development was initially observed; thereafter, there was a decrease in strength due to annoyance of clay matrix with the increase in size of ettringite needle. The decrease in UCS after stabilization with 30% raw PG is attributed to excess lime content in the stabilizer. Therefore, raw PG stabilized with lime and fly ash can improve the geotechnical properties of expansive soil by increasing the unconfined compressive strengths of the soil, when added up to 30%.

In the unconfined compressive strength of the stabilized composite developed from treated PG-lime-fly ash-basic oxygen furnace slag, a significant improvement on the strength of expansive soil with increase in binder content was evident. The maximum UCS of 1.65 MPa was mobilized by composite with 50% binder. Basic oxygen furnace slag as a well-known aggregate in civil engineering for building and road construction has existing free lime, coming from the raw material and precipitated lime from molten slag [37]. The lime to fly ash ratio was higher in the treated PG content, but there is evidence of lime consumption during the curing process. In this case due to the lime consumption, the access lime in the slag played a significant role in the improvement of the strength by maintaining the lime-fly ash ratio. The XRD results showed that the BOF slag constitute of magnesium ferrite (MgFe₂O₄) and larnite (Ca₂SiO₄). Larnite has silica and calcium which plays a significant role in the strength development, and it had the higher intensity. The calcium and silica in the slag supplemented quartz and lime and promoted higher strengths in the treated PG. The results

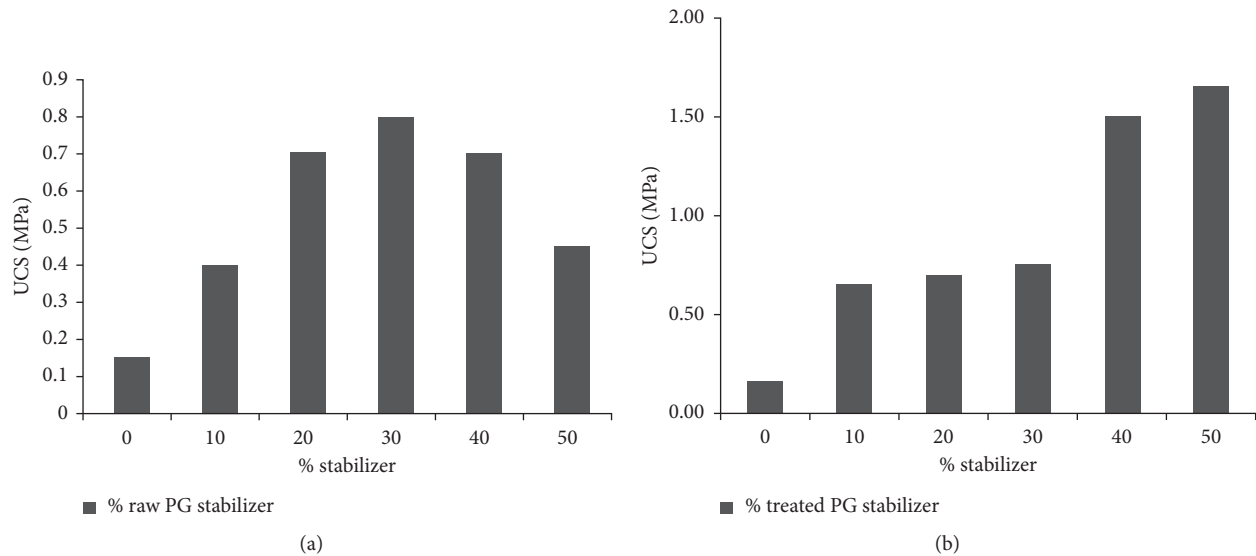


FIGURE 3: Stabilization of expansive soil with (a) raw PG and (b) treated PG.

obtained agree with the results reported by Tossavainen et al., who have reported the same predominant phases on BOF slag [38].

Comparing the two composites developed, it is evident that the treated PG composites perform better than the raw PG. The UCS of the raw PG composite increased by up to 30%, while continuous improvement in UCS was evident from acid-treated PG composite. According to the results, using treated PG for the development of a potential binder results in voluminous usage of the PG. Thus, the reactivity of treated PG composite in expansive soil stabilization was highly relative to raw PG binder and allowed for utilization of greater percentage of PG for pozzolanic reaction. The rearrangement of clay matrix and suppression of sulphate effects with formation of cementitious compounds are observed and found to be the main responsible factors for strength recovered [32].

3.3. XRD Analysis of Soil with Raw and Treated PG Stabilizers. The mineralogy of the expansive and stabilized soils with raw and treated PG determined by XRD is presented in Figures 4(a) and 4(b).

The predominant phases in the expansive soil (unstabilized) are those of montmorillonite $8(KAl_4(SiAl)O_{10}(OH)_4)$, bentonite $(Ca_{0.06}Na_{0.21}K_{0.27})(Al_{11.64})$, kaolinite $(Al_2(Si_2O_5)(OH)_4)$, and quartz (SiO_2) . The presence of montmorillonite mineral in the soil is responsible for the expansive characteristics of the soil [28]. Stabilization of expansive soil with raw PG and curing for 7 days formed new hydration products of feldspar $(Al_2Si_2O_8)$. The strength gain in the raw PG stabilized soil was due to the new hydration product formed.

New products of calcium magnesium silicide $(CaMgSi)$, sillimanite $(Al_2(SiO_4)O)$, kaolinite $(Al_2(Si_2O_5)(OH)_4)$, feldspar $(Al_2Si_2O_8)$, and trikalsilite $((KNa)AlSiO_4)$ were formed. The higher strength gain of treated PG stabilized

soil was primarily caused by the formation of various calcium magnesium silicide phases. The exact products formed, however, depend on the type of soil mineralogy and the reaction conditions including temperature, moisture, and curing conditions [39]. The highly alkaline stabilized soil with treated PG 50 at the pH of 12.57 stimulated the dissolution of siliceous and aluminous compounds from the soil mineral lattice. The compounds dissolved from the clay mineral lattice reacted with calcium ions in the pore water to form calcium silicate hydrate and calcium aluminate hydrate which coat the soil particles and subsequently crystallize to bond them [40], and hence, the significant strength is improved.

3.4. SEM Micrograph Analysis of Soil with Raw and Treated PG Stabilizers. The SEM results are presented in Figure 5.

The expansive soil structure shows a discontinuous structure, where the voids are more visible because of the absence of hydration products. The stabilized soil by raw PG 50 reveals that needle-like shape and euhedral to subhedral crystals were formed after curing. The EDS results showed the majority of silicon (Si) and aluminium (Al) minerals and trace amounts of potassium (K) and sodium (Na) minerals in the stabilized soil. The orientation of the soil particles in the soil mass and the spacing between particles will influence the manner in which the particles interact [41]. SEM results show a formation of more larger particles in the stabilized soil by treated PG. The hydration products in this case are not empty but intermixed and occupied by hardened epoxy structure. The micrographs also demonstrate the evidence of development of a more compact structure after curing time. The EDS analysis showed the presence of Ca and Si in the stabilized soil with treated PG, indicating presence of C-S-H, the main cementing product responsible for strength gain [42, 43]. Also peaks of Al, Fe, and Mg are

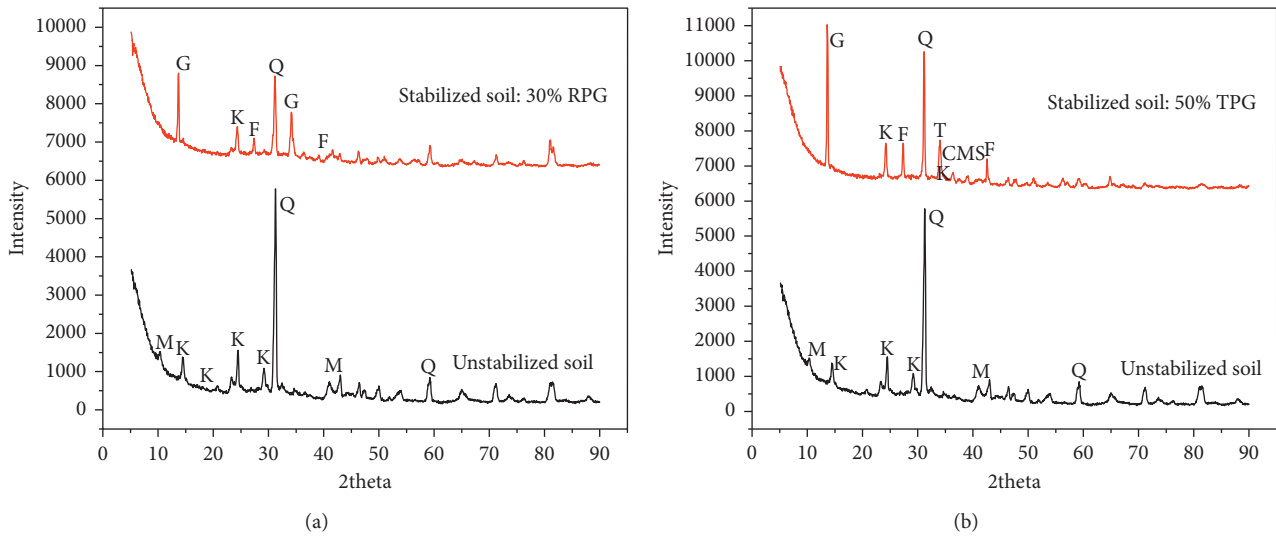


FIGURE 4: Mineralogy of expansive soil and stabilized soil by (a) raw PG (M: montmorillonite; B: bentonite; Q: quartz; G: gypsum; K: kaolinite; F: feldspar) and (b) treated PG (M: montmorillonite; B: bentonite; Q: quartz; G: gypsum; K: kaolinite; F: feldspar; TK: trikaolite; CMS: calcium magnesium silicide; S: sillimanite).

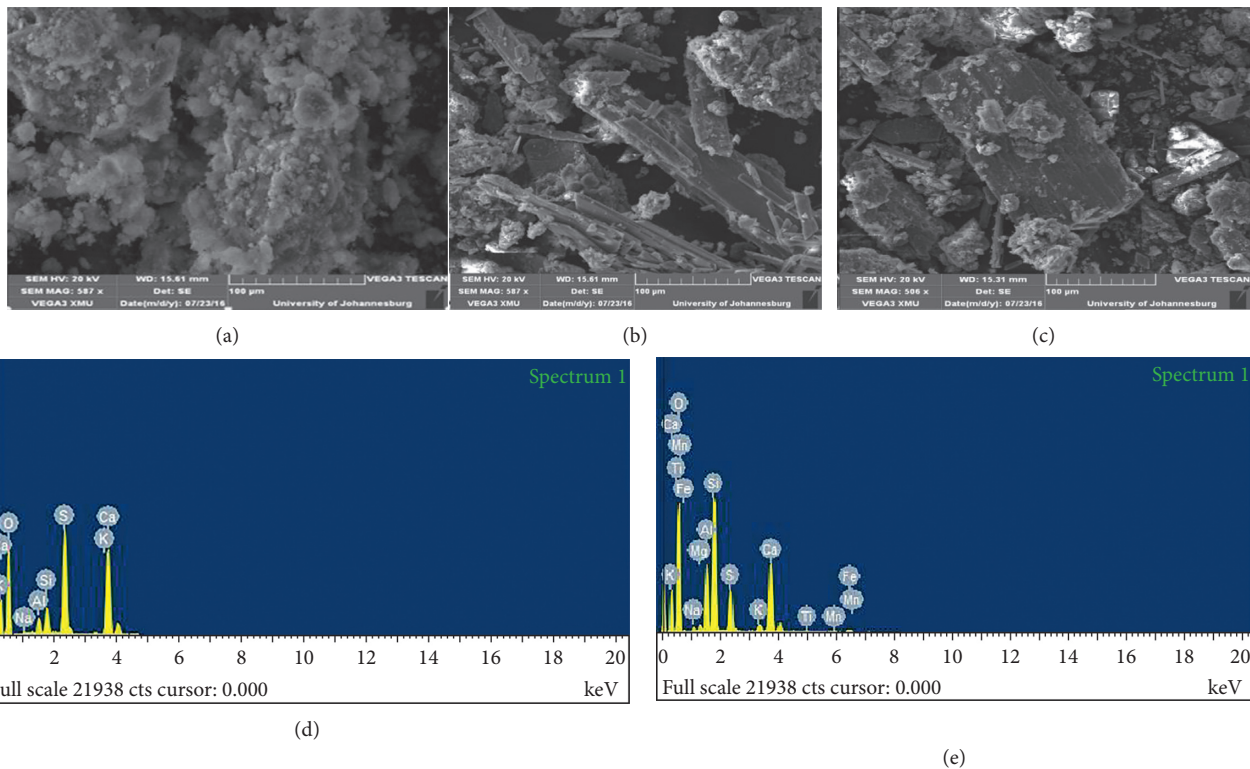


FIGURE 5: SEM micrograph and EDS of (a) expansive soil, (b) stabilized soil by raw PG, and (c) stabilized soil by treated PG. EDS of (d) stabilized soil by raw PG and (e) stabilized soil by treated PG.

visible in the material, constituents initially available in slag. The scanning electron microscope image of treated PG stabilized soil also shows that due to BOF slag, the material mainly consists of larger subrounded to angular particles with the surface having a rough surface texture.

BOF slag larger particles increased the contact between the particles cementing the particles together and increasing the UCS. The EDS shows that the elements detected were in accordance with the XRF results presented in Table 1.

4. Conclusion

Bentonite-rich soils can be simultaneously modified by mechanical and chemical stabilization. Residual industrial waste PG was treated with mild citric acid to reduce the radionuclides and then progressively modified with LFA-BOF. Expansive soil was then stabilized with the raw and treated PG binders. Both the raw and acid-treated stabilizers improved the geotechnical properties of the expansive soil by improving its liquid limit, plastic limit, and unconfined compressive strength. When treated PG-LFA was added to the expansive soil, the predominant hydration products formed contributed significantly to strength improvements. Curing resulted in the formation of harder and larger particles which also contributed to the strengths of the soils, and the hydration reaction products formed are responsible for the change in microstructure and improvement in physical and mechanical properties. The liquid limit and plastic limit of the expansive soil were reduced by both the raw and treated PG stabilizers, which implies improved plasticity characteristics of the soil. According to ASTM D4609 [44], an increase in the UCS of 345 kPa or more is considered an effective soil stabilization. In this study, the improvements of 650 kPa to 1500 kPa were achieved with LFA-modified raw and LFA-BOF-treated PG, respectively. The stabilized composite with UCS >750 kPa is suitable for the development of road subgrades and subbase in accordance with South African Roads TRH4 specifications. Fly ash-lime-basic oxygen slag stabilized PG can be used in larger quantities, up to 50% PG as a stabilizer for stabilizing expansive soils and enhancing the properties of soil. The analysis of the environmental impacts of the products produced shows an extremely low contaminants leachability back to the environment; thus the products will not contaminate the environment should leaching occur. The concentrations for all the measured elements are within the stipulated standards by the South African Department of Water and Sanitation [45].

Data Availability

The data used to support the findings of this study are included within the article.

Conflicts of Interest

The authors declare that they have no conflicts of interest.

Acknowledgments

The authors would like to thank the University of Johannesburg, the National Research Foundation (Grant no. 99826) of South Africa for the financial support, and iThemba laboratory for GRS.

References

- [1] R. Huang and L. Wu, "Stability analysis of unsaturated expansive soil slope," *Earth Science Frontiers*, vol. 14, no. 16, pp. 129–133, 2007.

- [2] A. Sabtan, "Geotechnical properties of expansive clay shale in Tabuk, Saudi Arabia," *Journal of Asian Earth Sciences*, vol. 25, no. 5, pp. 747–757, 2005.
- [3] J. James and P. K. Pandian, "Plasticity, swell-shrink, and microstructure of phosphogypsum admixed lime stabilized expansive soil," *Advances in Civil Engineering*, vol. 2016, pp. 1–10, 2016.
- [4] H. Nowamooz and F. Masrouri, "Hydromechanical behaviour of an expansive bentonite/silt mixture in cyclic suction-controlled drying and wetting tests," *Engineering Geology*, vol. 101, no. 3–4, pp. 154–164, 2008.
- [5] S. Fityus and O. Buzzi, "The place of expansive clays in the framework of unsaturated soil mechanics," *Applied Clay Science*, vol. 43, no. 2, pp. 150–155, 2009.
- [6] Z. Nalbantoğlu, "Effectiveness of class C fly ash as an expansive soil stabilizer," *Construction and Building Materials*, vol. 18, no. 6, pp. 377–381, 2004.
- [7] E. Avsar, R. Ulusay, and H. Sonmez, "Assessments of swelling anisotropy of Ankara clay," *Engineering Geology*, vol. 105, no. 1–2, pp. 24–31, 2009.
- [8] A. Assadi and S. Shahabuddin, "A micro-mechanical approach to swelling behavior of unsaturated expansive clays under controlled drainage conditions," *Applied Clay Science*, vol. 45, no. 1–2, pp. 8–19, 2009.
- [9] L. Chen, Z. Yin, and P. Zhang, "Relationship of resistivity with water content and fissures of unsaturated expansive soils," *Journal of China University of Mining and Technology*, vol. 17, no. 4, pp. 537–540, 2007.
- [10] V. Ferber, J. C. Auriol, Y. J. Cui, and J. P. Magnan, "On the swelling potential of compacted high plasticity clays," *Engineering Geology*, vol. 104, no. 3–4, pp. 200–210, 2009.
- [11] L. D. Jones and I. Jefferson, *Expansive Soils*, ICE Publishing, London, UK, 2012.
- [12] X. S. Cao, *Anti-Slide Piles Reinforcement of Expansive Soil Landslides*, Pan-M CGS conference, Toronto, Canada, 2011.
- [13] D. A. Sun, L. Zhang, J. Li, and B. Zhang, "Evaluation and prediction of the swelling pressures of GMZ bentonites saturated with saline solution," *Applied Clay Science*, vol. 105–106, pp. 207–216, 2015.
- [14] P. Bhawan and E. A. Nagar, "Guidelines for management and handling of phosphogypsum generated from phosphoric acid plants (final draft)," *Hazard Waste Manage*, 2012.
- [15] N. Degirmenci, A. Okucu, and A. Turabi, "Application of phosphogypsum in soil stabilization," *Building and Environment*, vol. 42, no. 9, pp. 3393–3398, 2007.
- [16] H. Tayibi, A. López-Delgado, M. Choura, F. J. Alguacil, and A. López-Delgado, "Environmental impact and management of phosphogypsum," *Journal of Environmental Management*, vol. 90, no. 8, pp. 2377–2386, 2009.
- [17] M. Singh, "Influence of blended gypsum on the properties of Portland cement and Portland slag cement," *Cement and Concrete Research*, vol. 30, no. 8, pp. 1185–1188, 2000.
- [18] I. A. Altun and Y. Sert, "Utilization of weathered phosphogypsum as set retarder in Portland cement," *Cement and Concrete Research*, vol. 34, no. 4, pp. 677–680, 2004.
- [19] S. Kumar, R. K. Dutta, and B. Mohanty, "Engineering properties of bentonite stabilized with lime and phosphogypsum," *Slovak Journal of Civil Engineering*, vol. 22, no. 4, pp. 35–44, 2014.
- [20] M. Singh and M. Garg, "Cementitious binder from fly ash and other industrial wastes," *Cement and Concrete Research*, vol. 29, no. 3, pp. 309–314, 1999.
- [21] C. J. R. Verbeek and B. J. G. W. du Plessis, "Density and flexural strength of phosphogypsum-polymer composites,"

- Construction and Building Materials*, vol. 19, no. 4, pp. 265–274, 2005.
- [22] ASTM D698, *Standard Test Methods for Laboratory Compaction Characteristics of Soil Using Standard Effort*, Annual Book of ASTM Standards, West Conshohocken, PA, USA, 2012.
- [23] ASTM D4318, *Standard Test Methods for Liquid Limit, Plastic Limit, and Plasticity Index of Soils*, Annual Book of ASTM Standards, West Conshohocken, PA, USA, 2010.
- [24] T. P. Mashifana, F. N. Okonta, and F. Ntuli, “Geotechnical properties and application of lime modified phosphogypsum waste,” *Materials Science (MEDŽIAGOTYRA)*, 2018, In press.
- [25] A Kézdi, “Soil physics selected topics developments in geotechnical engineering 25,” *International Journal of Rock Mechanics and Mining Sciences and Geomechanics Abstracts*, vol. 17, no. 2, p. 21, 1979.
- [26] B. V. V. Reddy and K. S. Jagadish, “The static compaction of soils,” *Géotechnique*, vol. 43, no. 2, pp. 337–341, 1993.
- [27] D. W. Lewis, *Resource Conservation by Use of Iron and Steel Slags*, National Institute for Transport and Road Research, Pretoria, South Africa, 1982.
- [28] W. Shen, M. Zhou, and Q. Zhao, “Study on lime–fly ash–phosphogypsum binder,” *Construction and Building Materials*, vol. 21, no. 7, pp. 1480–1485, 2007.
- [29] W. Shen, M. Zhou, W. Ma, J. Hu, and Z. Chai, “Investigation on the application of steel slag–fly ash–phosphogypsum solidified material as road base material,” *Journal of Hazardous Materials*, vol. 164, no. 1, pp. 99–104, 2009.
- [30] Y. Min, Q. Jueshi, and P. Ying, “Activation of fly ash–lime systems using calcined phosphogypsum,” *Construction and Building Materials*, vol. 22, no. 5, pp. 1004–1008, 2008.
- [31] G. Rajasekaran, “Sulphate attack and ettringite formation in the lime and cement stabilized marine clays,” *Ocean Engineering*, vol. 32, no. 8-9, pp. 1133–1159, 2005.
- [32] P. V. Sivapullaiah and A. K. Jha, “Gypsum induced strength behaviour of fly ash–lime stabilized expansive soil,” *Geotechnical and Geological Engineering*, vol. 32, no. 5, pp. 1261–1273, 2014.
- [33] J. James, S. V. Lakshmi, and P. K. Pandian, “Strength and index properties of phosphogypsum stabilized expansive soil,” *International Journal of Applied Environmental Sciences*, vol. 9, no. 5, pp. 2721–2731, 2014.
- [34] Z. Ji-ru and C. Xing, “Stabilization of expansive soil by lime and fly ash,” *Journal of Wuhan University of Technology*, vol. 17, no. 4, pp. 73–77, 2002.
- [35] J. James and P. K. Pandian, “Soil stabilization as an avenue for reuse of solid wastes: a review,” *Acta Technica Napocensis: Civil Engineering and Architecture*, vol. 58, no. 1, pp. 50–76, 2015.
- [36] B. V. Reddy and K. Gourav, “Strength of lime–fly ash compacts using different curing techniques and gypsum additive,” *Materials and Structures*, vol. 44, no. 10, pp. 1793–1808, 2011.
- [37] P. H. Shih, Z. Z. Wu, and H. L. Chiang, “Characteristics of bricks made from waste steel slag,” *Waste Management*, vol. 24, no. 10, pp. 1043–1047, 2004.
- [38] M. Tossavainen, F. Engstrom, Q. Yang, N. Menad, M. L. Larsson, and B. Bjorkman, “Characteristics of steel slag under different cooling conditions,” *Waste Manage*, vol. 27, no. 10, pp. 1335–1344, 2007.
- [39] P. G. Nicholson and V. Kashyap, “Fly ash stabilization of tropical Hawaiian soil,” *Science, Engineering and Medicine*, no. 36, 1993.
- [40] S. M. Rao and P. Shivananda, “Role of curing temperature in progress of lime–soil reactions,” *Geotechnical and Geological Engineering*, vol. 23, no. 1, pp. 79–85, 2005.
- [41] J. D. Nelson, K. C. Chao, D. D. Overton, and E. J. Nelson, *Foundation Engineering for Expansive Soil*, John Wiley & Sons, Hoboken, NJ, USA, 2015.
- [42] M. Choquett and M. A. Bérubé, “Mineralogical and micro-textural changes associated with lime stabilization of marine clays from eastern Canada,” *Applied Clay Science*, vol. 2, no. 3, pp. 215–232, 2000.
- [43] A. H. Lav and M. A. Lav, “Microstructural development of stabilized fly ash as pavement base material,” *Journal of Materials in Civil Engineering*, vol. 12, no. 2, pp. 157–163, 2000.
- [44] ASTM D4609, *Standard Guide for Evaluating Effectiveness of Admixtures for Soil Stabilization*, Annual Book of ASTM Standards, West Conshohocken, PA, USA, 2008.
- [45] Government Gazette, “Requirements for the purification of wastewater or effluent,” 1984. Regulation 991.

Research Article

Experimental Study on Electrical Resistivity of Cement-Stabilized Lead-Contaminated Soils

Zhiguo Cao , Lian Xiang, Erxing Peng, and Kai Li

Institute of Geotechnical Engineering, School of Transportation, Southeast University, Nanjing 210096, China

Correspondence should be addressed to Zhiguo Cao; 230159208@seu.edu.cn

Received 12 June 2018; Accepted 29 July 2018; Published 27 August 2018

Academic Editor: Yonggui Chen

Copyright © 2018 Zhiguo Cao et al. This is an open access article distributed under the Creative Commons Attribution License, which permits unrestricted use, distribution, and reproduction in any medium, provided the original work is properly cited.

Geotechnical applications based on soil resistivity measurement are becoming more popular in recent years. In order to explore the potential application of the electrical resistivity method in stabilization/solidification of contaminated soils, two kinds of lead-contaminated soils stabilized with cement were prepared, and the electrical resistivity and unconfined compressive strength of specimens after curing for various periods were measured. The test results show that a high lead content leads to a low value of electrical resistivity of cement-stabilized soils, and increasing cement content and curing time result in a significant increase in electrical resistivity. The reduction in porosity and degree of saturation, as a result of the cement hydration process, leads to an increase in electrical resistivity. The ratio of porosity-lead content/cement content-curing time, combining together the effect of lead content, cement content, curing time, and porosity on electrical resistivity of stabilized soils, can be used as a fundamental parameter to assess electrical resistivity of cement-stabilized lead-contaminated soils. Archie's law can be extended to apply to cement-stabilized lead-contaminated soils by using this ratio, replacing the porosity. The new resistivity formula obtained in this paper is just empirical. There is a power function correlation between unconfined compressive strength and electrical resistivity of lead-contaminated soils stabilized with cement. Electrical resistivity measurement can be used as an economical and time-effective method to assess the quality of cement-stabilized lead-contaminated soils in practice.

1. Introduction

Cement stabilization/solidification (s/s) technology is a widely used method for the remediation of heavy metal-contaminated sites. In the s/s process, contaminated soils are mixed with a binder agent to lower the release of heavy metals and enhance soil strength through precipitation, chemisorption, ion exchange, and physical encapsulation [1, 2]. Many researchers have performed experimental studies on the leaching behavior, strength, and compressibility of cement-stabilized heavy metal-contaminated soils [3–6]. Heavy metals, such as lead or zinc, can suppress or delay the cement or lime hydration process [7, 8]. However, very few studies have been conducted to assess the electrical resistivity of treated contaminated soils.

The electrical resistivity measurement has increasing applications in geotechnical and geoenvironmental practices owing to its economical, time-effective, and nondestructive advantages [9–12]. Soil resistivity is a material inherent

property, and the main factors influencing resistivity are water content, porosity, degree of saturation, and ion concentration of pore solution [13, 14]. Previous studies have shown that the electrical resistivity method can be used to investigate engineering properties of soils and rocks [15–22], to monitor contaminants and delineate contaminant transport in soils [10, 23–25], and to detect defects and heterogeneity in the landfill cover material [26].

For cement-based materials, Taylor and Arulanadan [27], Tashiro et al. [28], and McCarter et al. [29] reported the electrical response of the cementitious system. Li et al. [30, 31] and Xiao and Li [32] presented a new understanding of the cement hydration mechanism by using a noncontact electrical resistivity measurement method and established the relationship between resistivity and concrete setting time. Liu et al. [11] analyzed the variation of resistivity of cement-treated soils and found that there was a good correlation between resistivity and unconfined compressive strength. Zhang et al. [33] evaluated the effect of salt

concentration on resistivity of cement-treated soft clays. Cardoso [12] analyzed the influence of porosity and tortuosity on electrical resistivity of artificially cemented sand. The electrical resistivity method can also be used to detect and locate crack and spalling in concrete [34–36]. It is feasible and meaningful to introduce the electrical resistivity method into the mechanism revelation and quality assessment of *s/s*. However, very few researchers have addressed the effect of heavy metals on electrical resistivity of cement-stabilized soils.

This study begins with a brief review of soil resistivity models. Experimental studies were performed on two kinds of artificial lead-contaminated soils stabilized with cement to investigate the effect of lead content, cement content, and curing time on electrical resistivity of stabilized soils. A resistivity empirical formula of cement-stabilized lead-contaminated soils was proposed based on Archie's law [15]. The relationship between electrical resistivity and unconfined compressive strength was also explored. This study can provide a theoretical basis for the application of the electrical resistivity method in *s/s*.

2. Soil Resistivity Model

The electrical resistivity of any material is defined as the resistance between opposite faces of a unit cube of that material. In previous studies, soil resistivity is modeled as an integration of resistivity of solid, liquid, and air by a parallel connection, a series connection, or a compound model of these two connections [9, 37, 38]. Archie [15] developed an empirical law to correlate electrical resistivity of saturated sand (ρ) to electrical resistivity of pore fluid (ρ_f) and porosity (n). The general Archie's law can be written as follows:

$$\rho = a \cdot \rho_f \cdot n^{-m}, \quad (1)$$

where a is the fitting parameter and m is the cementation exponent. The value of m mainly depends on the interconnectivity of the pore network and tortuosity, and the full connectivity of pore fluid is achieved for $m = 1$. Archie [15] reported that the value of m ranged from 1.8 to 2.0 for consolidated sand and was tested as 1.3 for loose sand. Friedman and Seaton [39] suggested a value of $m = 1.38$ – 2.3 for saturated sand with a porosity of 0.3–0.49. Friedman [40] summarized the research on the value of m and found that it varied from 1.2 to 4.4 for saturated geomaterials depending on the porosity, grain size distribution, particle shape, and consolidation condition.

For unsaturated soil, soil resistivity is also related to degree of saturation. Keller and Frischknecht [41] reported that electrical resistivity of unsaturated soil (ρ) was correlated with electrical resistivity of saturated soil (ρ_{sat}) by the following equation:

$$\frac{\rho}{\rho_{sat}} = S_r^{-b}, \quad (2)$$

where S_r is the degree of saturation and b is the empirical factor.

In order to better understand the resistivity behavior of cement-stabilized heavy metal-contaminated soils, it is

necessary to establish a corresponding resistivity formula. However, the influence of the cement hydration process on soil resistivity cannot be reflected in Equations (1) and (2). Cardoso [12] pointed out that Archie's law may not be valid for cement-treated materials. Therefore, in this paper, we just present an empirical resistivity formula that can take account of the influence factors of electrical resistivity of cement-stabilized soils, based on the parameter porosity in Archie's law.

3. Materials and Methods

3.1. Materials. Two soils (S1 and S2) were used in this study. Soil S1 was obtained by mixing 15% kaolin and 85% sand by oven-dried weight. Soil S2 was collected from the Jiulonghu campus of Southeast University in Nanjing City, China. Physical parameters of kaolin and S2 are shown in Table 1, and grain size distribution curves of kaolin, sand, and S2 are shown in Figure 1. According to the Unified Soil Classification System [42], soil S1 is classified as clayey sand and soil S2 is classified as lean clay. The optimum moisture content and maximum dry density are 10.0% and 1.96 g/cm³ for soil S1 and are 12.4% and 1.91 g/cm³ for soil S2, with the standard Proctor compaction test [43].

Lead was selected as the target heavy metal since it is commonly encountered in contaminated sites worldwide, especially in China [8]. Lead nitrate was selected as the lead pollutant resource because it has a high solubility and nitrate ion has a low impact on the cement hydration process [7]. Ordinary Portland cement type I was used as the binder. The main chemical compositions of cement are 65.0% calcium oxide, 19.0% silicon dioxide, and 6.5% aluminum oxide.

3.2. Sample Preparation. In order to obtain a homogeneous mixture, air-dried soil was passed through a 2 mm sieve and admixed with cement powder for about 10 min, and then it was mixed with a certain volume of prepared lead nitrate solution with the desired lead content for another 10 min. The mixture was then compacted into a cylindrical mold having a 5 cm inner diameter and a 10 cm height with the optimum water content (10.0%) and maximum dry density (1.96 g/cm³) for the specimen of soil S1 and with a water content of 18.0% and 95% maximum dry density for the specimen of soil S2. After standing without disturbance in the mold for 3 h, the specimens were demolded, sealed in polyethylene bags, and cured at a constant temperature of 20 ± 2°C and a relative humidity of 95%. The electrical resistivity measurement and unconfined compressive test were conducted when the specimens were cured to a predetermined period.

The experimental scheme is presented in Table 2. According to the monitoring results of foundation soil of a chemical plant in Nanjing City, China, lead contents (termed as w_{pb}) were selected as 0.1%, 1%, and 3% (i.e., 1000 mg/kg, 10000 mg/kg, and 30000 mg/kg dry soil) for the specimen of soil S1 and as 0.1%, 0.5%, and 2.5% (i.e., 1000 mg/kg, 5000 mg/kg, and 25000 mg/kg dry soil) for the specimen of soil S2, typically. For comparison, controlled specimens without lead (i.e., 0 mg/kg) were also prepared. Cement

TABLE 1: Physical parameters of kaolin and soil S2 used in this study.

Soil type	Liquid limit (%)	Plastic limit (%)	Specific gravity	Sand (%) (>0.075 mm)	Silt (%) (0.075–0.002 mm)	Clay (%) (<0.002 mm)
Kaolin	68.0	32.0	2.72	0.0	80.0	20.0
S2	44.0	16.9	2.71	11.0	74.8	14.2

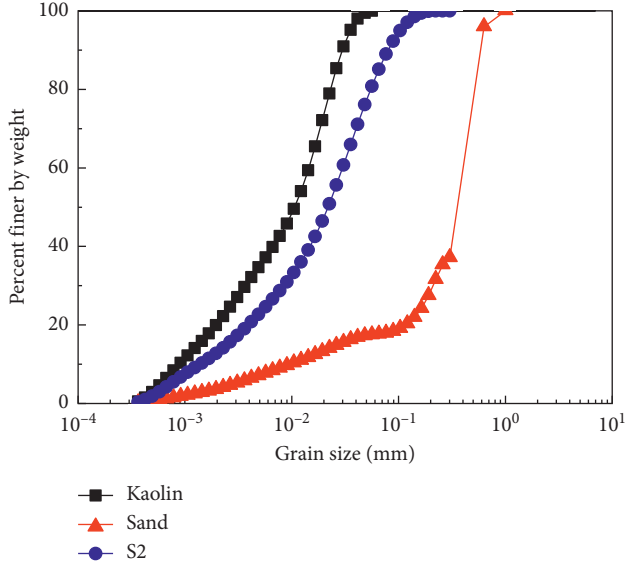


FIGURE 1: Grain size distribution curves of soils used in this study.

TABLE 2: The lead content, cement content, and curing time for electrical resistivity measurement.

Soil type	Lead content (w_{pb} , %)	Cement content (a_w , %)	Curing time (T , d)
S1	0, 0.1, 1, 3	5, 7.5, 10	7, 14, 28, 56, 90
S2	0, 0.1, 0.5, 2.5	9, 12, 15	7, 14, 28

contents (termed as a_w) were set as 5%, 7.5%, and 10% (on the dry soil weight basis) for the specimen of soil S1 and as 9%, 12%, and 15% (on the dry soil weight basis) for the specimen of soil S2, as recommended by Kogbara and Al-Tabbaa [44].

3.3. Test Methods. Before electrical resistivity measurement, the volume and mass were measured to calculate the density of specimens. The electrical resistivity of each specimen was measured using a GW Instek LCR-817 apparatus with a plate two-electrode method. Two copper electrodes, with a thickness of 2 mm and a diameter of 50 mm, were placed on the top and at the bottom of the specimens during electrical resistivity measurement. A vertical pressure of 5 kPa was applied on the copper electrodes to make the specimen and copper electrode in a good contact. This pressure was found to have a negligible effect on the electrical resistivity and strength of the specimen. In order to avoid the influence of the electrode polarization effect and double-layer relaxation effect [15, 33], the frequency used to measure electrical resistivity was selected as 2 kHz. Electrical resistivity tests were carried out at a constant temperature of $20 \pm 2^\circ\text{C}$. The schematic diagram of a specimen resistivity test is shown in Figure 2.

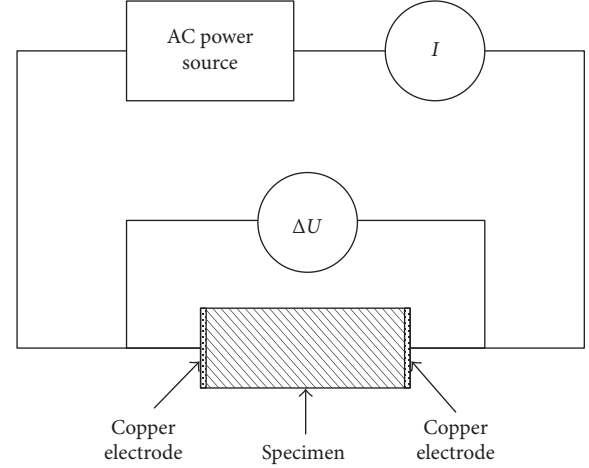


FIGURE 2: Schematic diagram of the electrical resistivity test.

The electrical resistivity of the specimen can be determined by the following equation:

$$\rho = \frac{\Delta U}{I} \cdot \frac{S}{L} \quad (3)$$

where ρ is the electrical resistivity of the specimen ($\Omega \cdot \text{m}$), ΔU is the electrical voltage applied to the specimen (V), I is the electrical current (A), S is the cross-sectional area through which electrical current conducts (m^2), and L is the length of the specimen parallel to electrical current (m).

After electrical resistivity measurement, the unconfined compressive test was performed following the method of ASTM D2166/D2166M-16 at a strain rate of 1%/min [45]. The water content of the specimen was also measured after the unconfined compressive test.

Triplicate specimens were tested for electrical resistivity measurement and unconfined compressive test, and the average values of test results were presented, analyzed, and discussed in this study.

3.4. Data Analysis Methods. In order to assess the effectiveness of Archie's law in the application of cement-stabilized lead-contaminated soils, the porosity of the specimen at various curing times (n_t) was determined by the void ratio at various curing times (e_t) using Equation (4). The void ratio was calculated by using the solid-liquid-air phase concept:

$$n_t = \frac{e_t}{1 + e_t} \quad (4)$$

$$e_t = \frac{(1 + \omega_t)G_s \gamma_w}{\gamma_t} - 1 \quad (5)$$

where ω_t is the water content at various curing times, which was measured after the unconfined compressive test; γ_t is the

unit weight of stabilized soils (kN/m^3), which was determined based on the calculation results of density; γ_w is the unit weight of water (kN/m^3); and G_s is the composite specific gravity of stabilized soils [33], which was derived as the mass-weighted mean of each solid ingredient, including soil, cement, and lead nitrate. The values of specific gravity of kaolin, sand, soil S2, cement, and lead nitrate are 2.72, 2.68, 2.71, 3.10, and 4.53, respectively. Degree of saturation of samples was also calculated by using the solid-liquid-air phase concept, based on the test results of water content (ω_t) and the calculation results of specific gravity (G_s) and void ratio (e_t) of stabilized soils.

4. Results, Analysis, and Discussion

4.1. Effect of Lead Content, Cement Content, and Curing Time on Electrical Resistivity. For specimens of soil S1, the variations of electrical resistivity with lead content, cement content, and curing time are shown in Figure 3. The lead content plays a key role in electrical resistivity of stabilized soils. As shown in Figure 3, the electrical resistivity decreases with the increase of lead content. The electrical resistivity of specimens with 0.1% lead content is slightly lower than that of specimens without lead (controlled specimens); for specimens with 1% and 3% lead content, the electrical resistivity is significantly lower than that of controlled specimens. The effect of lead content on resistivity of cement-stabilized soils can be found in two aspects: firstly, the addition of lead nitrate induces an increasing trend in the ion concentration of pore solution, and the presence of ions enhances the electrical current flow [13, 14]. As a result, the electrical resistivity of pore solution decreases with the increase of lead content. Secondly, the high lead content in soils greatly suppresses or delays the cement hydration process [7]. The generation of cement hydration products is suppressed, which consequently leads to a low value of electrical resistivity.

Figure 3 also shows that electrical resistivity of cement-stabilized soils increases with the increase of cement content. This can be interpreted by the cement hydration process. Higher cement content leads to a greater amount of hydration products, such as calcium hydroxide and calcium silicate hydrate. These products fill in the pore spaces and intersect each other, resulting in a denser structure in soils. Moreover, the consumption of free water, as a result of hydration reaction, further increases the pore tortuosity for electric current. Consequently, soil resistivity increases obviously with the increase of cement content. However, owing to cement hydration, the mobile ions in cement, such as calcium (Ca^{2+}), ferric (Fe^{3+}), and magnesium (Mg^{2+}), dissolve into the pore water. The presence of these ions leads to a decrease in electrical resistivity of pore solution. The increase of electrical resistivity with the increase in cement content marks a competition process between the ion dissolving process and the solid phase nucleation in the cement hydration process.

In addition, increasing curing time results in a significant increase in electrical resistivity, as shown in Figure 3. Longer curing time leads to a greater amount of hydration products,

and the formation of hydration products is the main reason for the increase in electrical resistivity [11]. With the development of hydration reaction, a certain amount of ions, such as Ca^{2+} , are involved with the formation of hydration products. As a result, the pore solution concentration decreases and the electrical resistivity of pore solution increases. For specimens without lead or with 0.1% lead content, the electrical resistivity increases distinctly before curing for 28 days and then tends to be steady. However, the variations of electrical resistivity with curing time are different at various cement contents, for specimens with 1% or 3% lead content. These phenomena are attributed to the cement hydration rate depending on lead content and cement content [7, 46].

Figure 4 shows the electrical resistivity of specimens of soil S2. The variations of electrical resistivity with lead content, cement content, and curing time are consistent with those of specimens of soil S1.

4.2. Electrical Resistivity with Porosity. As mentioned by Archie [15], soil resistivity mainly depends on the porosity. Figure 5 shows the relationship between electrical resistivity and porosity. When lead content is certain, an increase in electrical resistivity is observed with the decrease in porosity. For cement-stabilized soils, hydration products fill in the pore spaces, leading to a decrease in porosity and an increase in pore tortuosity. As a result, electrical resistivity increases with the reduction of porosity. The test results from specimens of soils S1 and S2 all show similar trends with Archie's law. However, it can be seen that there is a large scatter of data of specimens of both soil S1 and soil S2. Archie's law is based on saturated sand without cement hydration process; the porosity parameter cannot fully reflect the effect of the hydration process and pozzolanic reaction on electrical resistivity in cement-stabilized soils.

It should be noted that Archie's law is a generalized law for pure sandy samples. The clay content in particular makes ineffective such a kind of relationship between electrical resistivity and porosity, owing to the effect of the electric double layer of the clay particle [14]. Some researchers have reported the limitation of Archie's law in case of no pure sandy samples [14, 47, 48]. The soils used in this study, S1 and S2, have clay contents. But for stabilized soils, cement can reduce the thickness of the electric double layer of the clay particle [49]. As a result, the effect of clay contents on electrical resistivity is weakened and even can be ignored.

4.3. Electrical Resistivity with Degree of Saturation. Degree of saturation is also one of the key factors influencing soil resistivity [13, 41]. Figure 6 shows the relationship between electrical resistivity and degree of saturation of cement-stabilized soils. The consumption of pore water, owing to hydration reaction, leads to a reduction in degree of saturation and a decrease in connectivity of pore solution. Therefore, electrical resistivity increases with the reduction in degree of saturation at a given lead content, as shown in Figure 6. For both specimens of soils S1 and S2, the variations of measured electrical resistivity with degree of

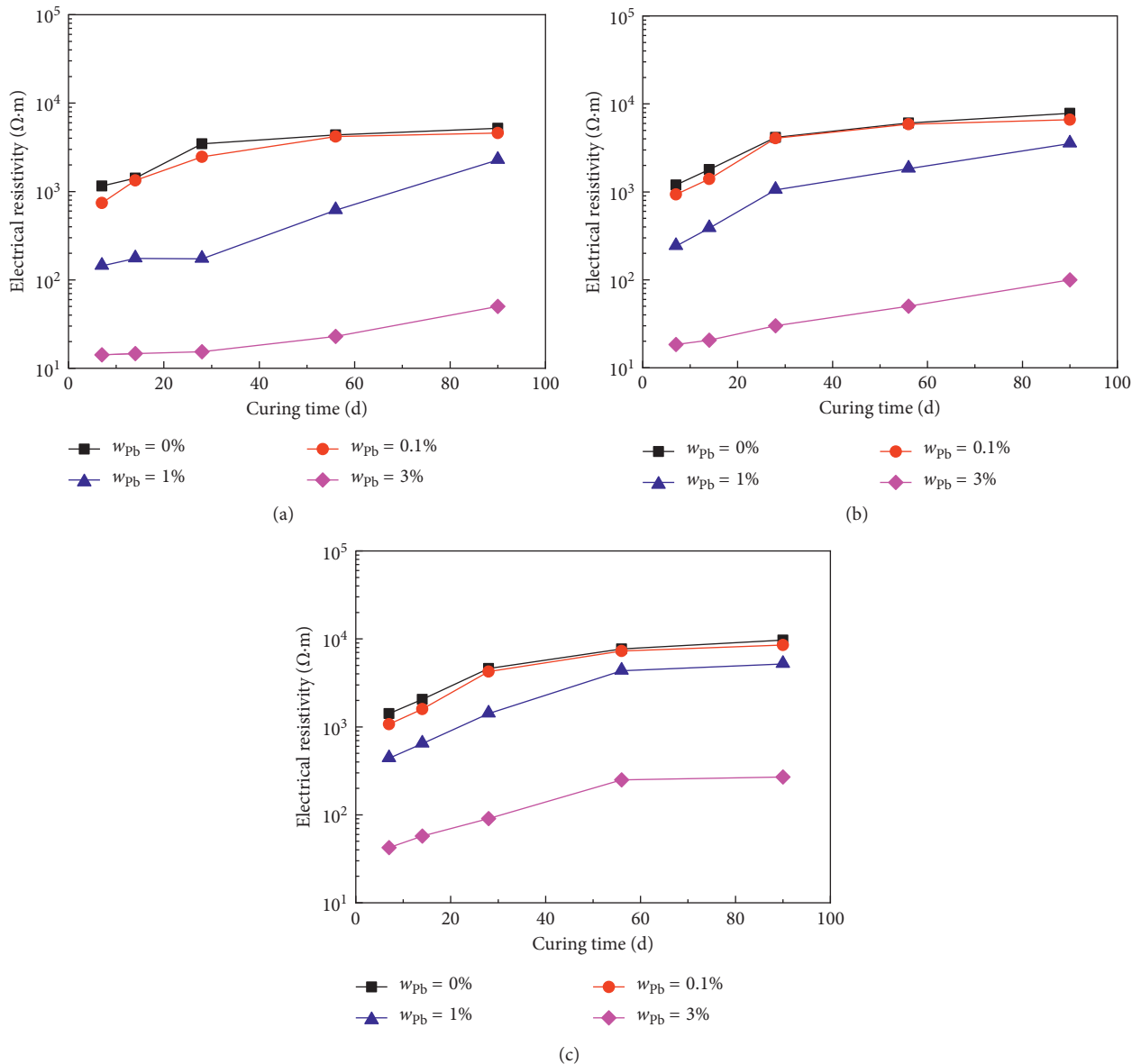


FIGURE 3: Variation of electrical resistivity with curing time of specimens of soil S1: (a) $a_w = 5\%$; (b) $a_w = 7.5\%$; (c) $a_w = 10\%$.

saturation are consistent with the experimental results obtained by Kibria and Hossain [13]. However, the dispersion of data is also obvious. The effect of the cement hydration process and pozzolanic reaction on electrical resistivity cannot also be effectively reflected by degree of saturation.

4.4. Resistivity Empirical Formula of Cement-Stabilized Lead-Contaminated Soils. As mentioned earlier, porosity or degree of saturation cannot be used alone as a key parameter controlling electrical resistivity of cement-stabilized lead-contaminated soils. The electrical resistivity is also dependent on lead content, cement content, and curing time. It is logical to utilize a synthetic parameter combining together the effect of these factors. Zhang et al. [33] proposed a parameter, termed as the “porosity/cement content-curing

time ratio,” $n_t / (a_w \cdot T^{0.5})$, which can reflect the effect of the cement hydration process and soil compactness on electrical resistivity of cement-treated soils without lead. The variation of measured electrical resistivity in this study with the ratio of porosity/cement content-curing time is shown in Figure 7. For specimens of soil S1 or S2, there is a good correlation between this ratio and electrical resistivity at a given lead content. The effect of lead content on electrical resistivity cannot be reflected by this ratio. By means of regression analysis of the test data, a new parameter, termed as the “porosity-lead content/cement content-curing time ratio,” $(n_t \cdot \alpha^{100w_{pb}}) / a_w \cdot T^{0.5}$, is proposed. It is worth pointing out that α is a fitting parameter, which is related to the influence level of lead on electrical resistivity of cement-stabilized soils. In this study, the value of α is 2 for specimens of soils S1 and S2. It may be a different value for other kinds of heavy metals.

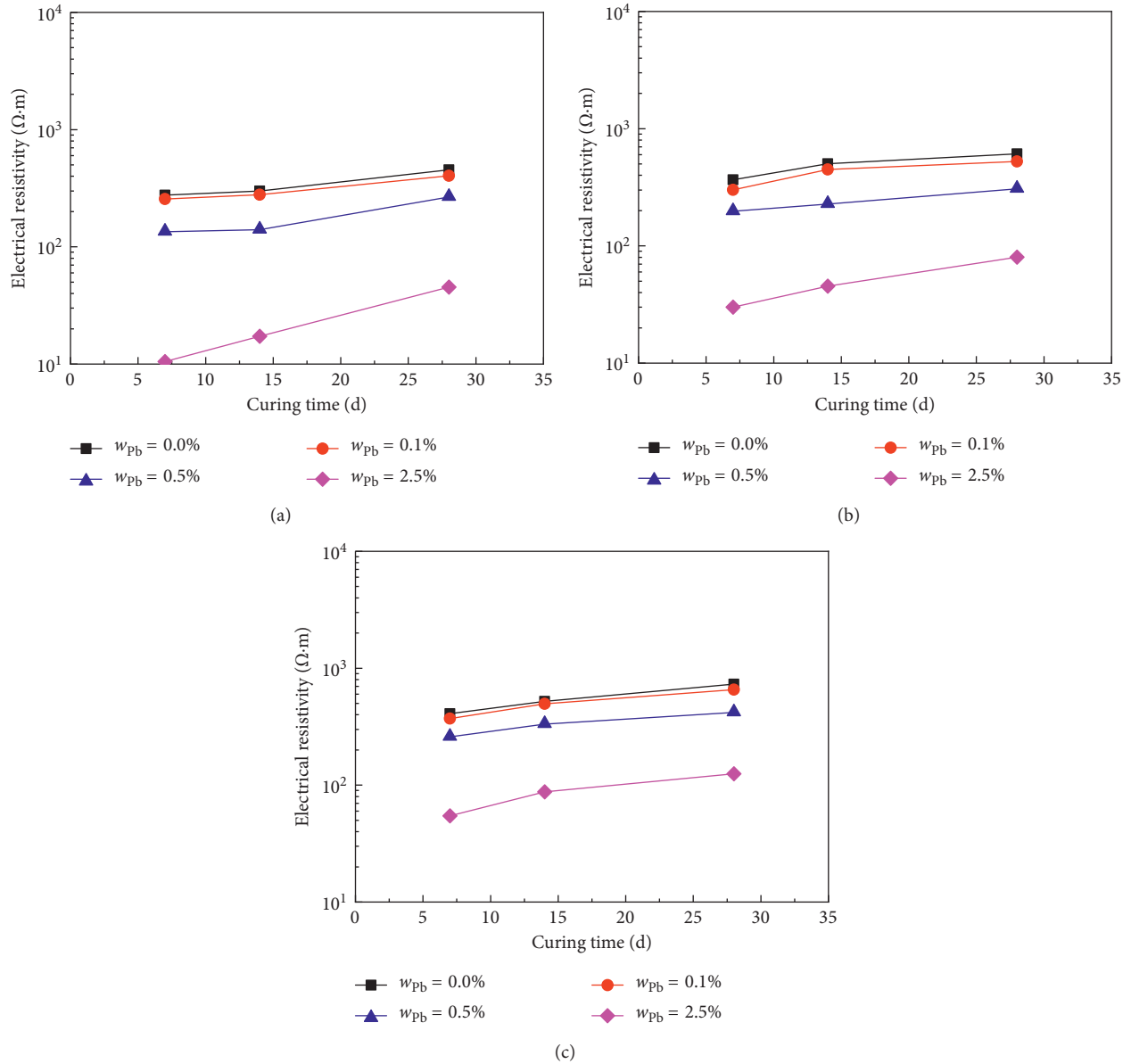


FIGURE 4: Variation of electrical resistivity with curing time of specimens of soil S2: (a) $a_w = 9\%$; (b) $a_w = 12\%$; (c) $a_w = 15\%$.

Figure 8 shows a good correlation between electrical resistivity and the ratio of porosity-lead content/cement content-curing time. The coefficients of determination (R^2) are all 0.94 for specimens of soils S1 and S2. It is indicated that the new ratio can combine together the effect of these factors, including lead content, cement content, curing time, and porosity, on electrical resistivity of stabilized soils. The resistivity empirical formula of cement-stabilized lead-contaminated soils can be expressed as follows:

$$\rho = A \left[\frac{(n_t \cdot \alpha^{100w_{pb}})}{(a_w \cdot T^{0.5})} \right]^{-B}, \quad (6)$$

where $\alpha = 2$ and A and B are empirical constants. The parameter A is mainly dependent on the type of soil and water content; the value of B , similar to the cementation exponent

in Archie's law [15], mainly depends on the pore connectivity and soil compactness. In this study, the values of A and B are 1982 and 1.87 for specimens of soil S1 and are 335 and 1.25 for specimens of soil S2.

Comparing Equations (1) and (6), it is interesting to find that the resistivity formula proposed in this study is similar to Archie's law. That is to say, Archie's law can be extended to apply to cement-stabilized heavy metal-contaminated soils by using a synthetic parameter, termed as the "porosity-lead content/cement content-curing time ratio," $(n_t \cdot \alpha^{100w_{pb}}) / (a_w \cdot T^{0.5})$. When lead content is 0%, this formula can be returned to the resistivity formula of cement-treated soils without lead developed by Zhang et al. [33]. It should be noted that this synthetic parameter has no specific physical meaning, and Equation (6) is an empirical resistivity formula.

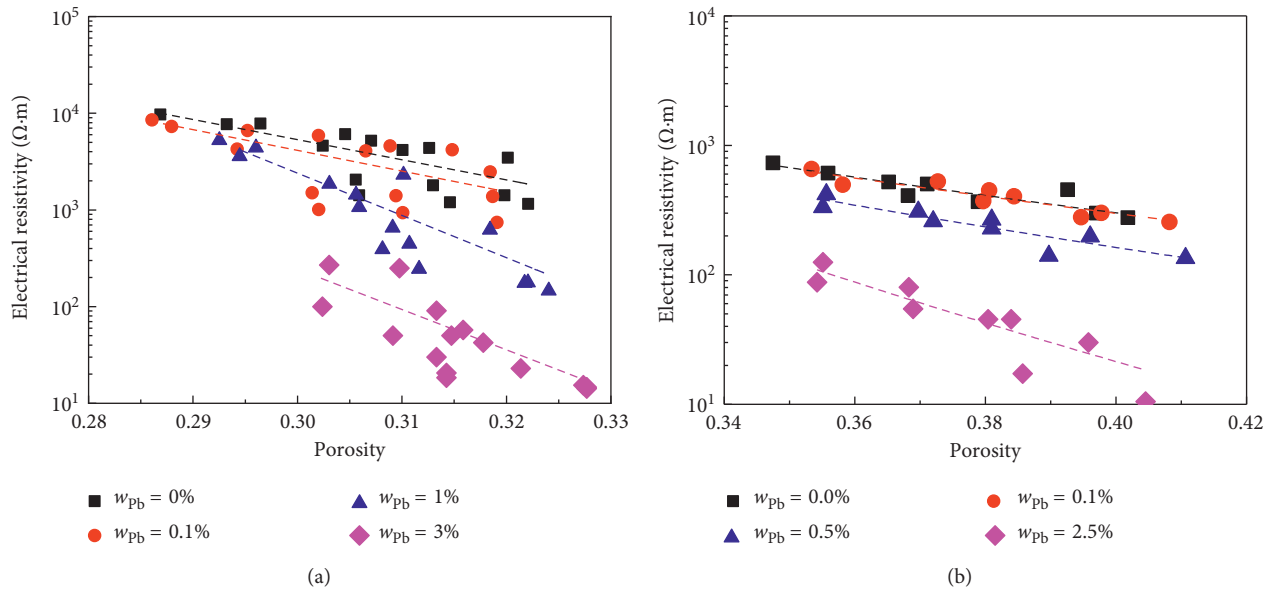


FIGURE 5: Variation of electrical resistivity with porosity: (a) specimens of soil S1; (b) specimens of soil S2.

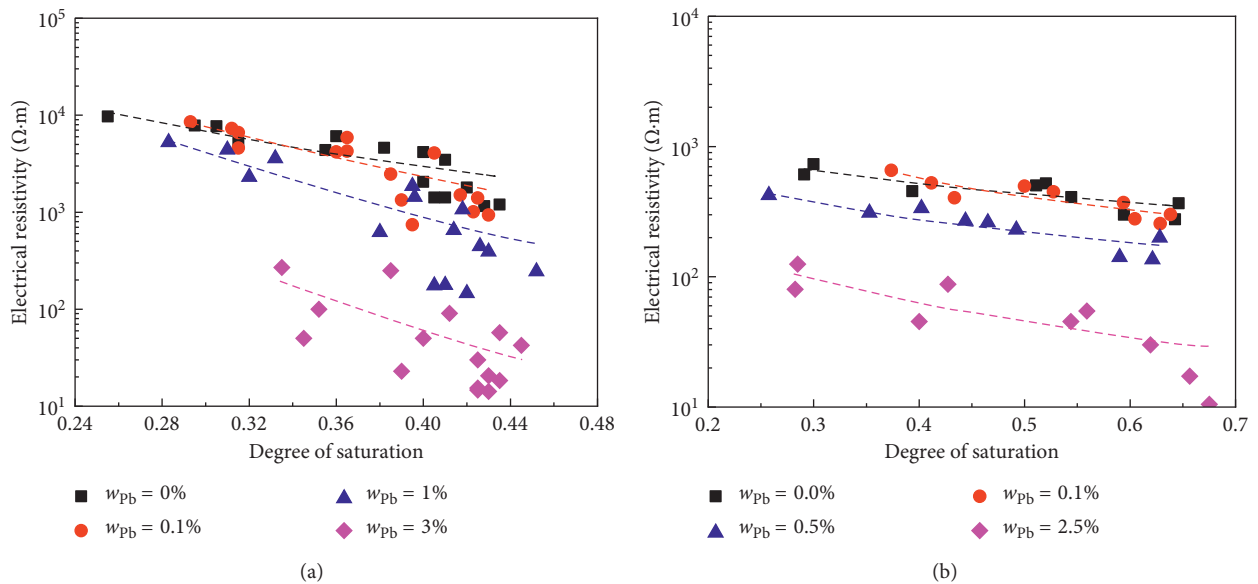


FIGURE 6: Variation of electrical resistivity with degree of saturation: (a) specimens of soil S1; (b) specimens of soil S2.

In addition, the degree of saturation of samples is not considered in this synthetic parameter. This may indicate that the effect of degree of saturation on electrical resistivity of stabilized soils is lower than that of lead content, cement content, and curing time. The good correlation between electrical resistivity and the ratio of porosity-lead content/cement content-curing time is sufficient for engineering applications. It may not be necessary to introduce degree of saturation into this ratio. However, for unsaturated soils without cement hydration process, degree of saturation is very important and cannot be ignored [13].

The resistivity empirical formula reveals the influence factors of electrical resistivity. The result shows that a unique

power function adapts well electrical resistivity with the ratio of porosity-lead content/cement content-curing time. Therefore, this ratio can be used as a fundamental parameter sufficient to characterize electrical resistivity of cement-stabilized lead-contaminated soils. The ratio can also be used to monitor and control the quality of s/s.

4.5. Relationship between Electrical Resistivity and Unconfined Compressive Strength. Unconfined compressive strength is an important parameter for evaluating the effectiveness of s/s [50]. Figure 9 presents the relationship between measured strength and electrical resistivity. The strength of

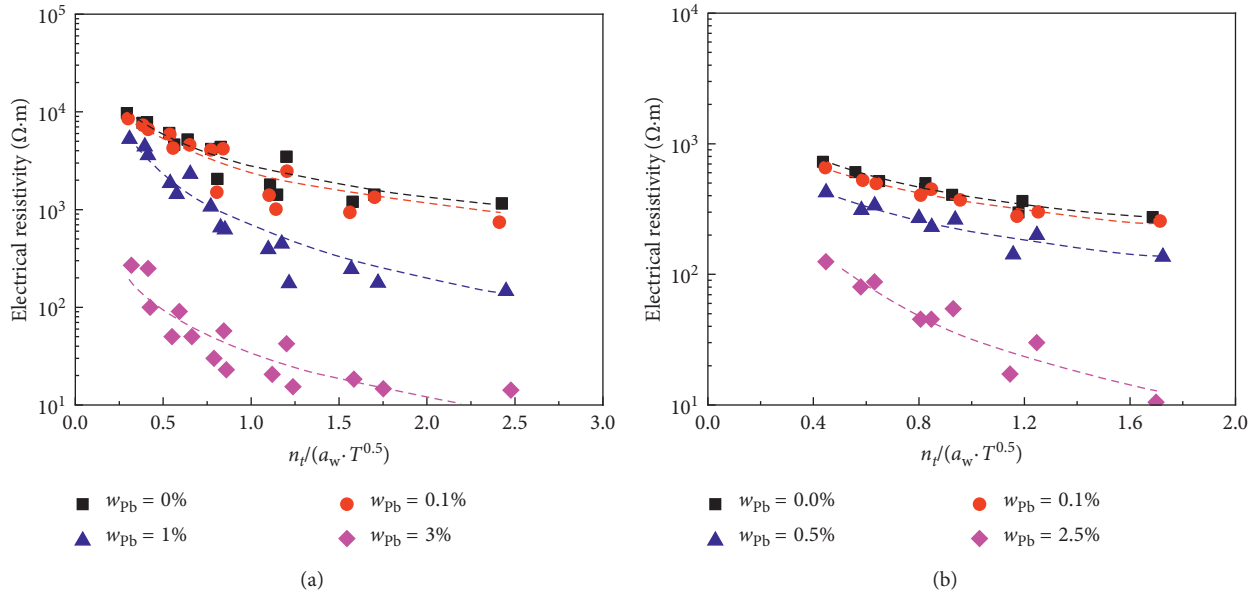


FIGURE 7: Relationship between electrical resistivity and $n_t/a_w \cdot T^{0.5}$: (a) specimens of soil S1; (b) specimens of soil S2.

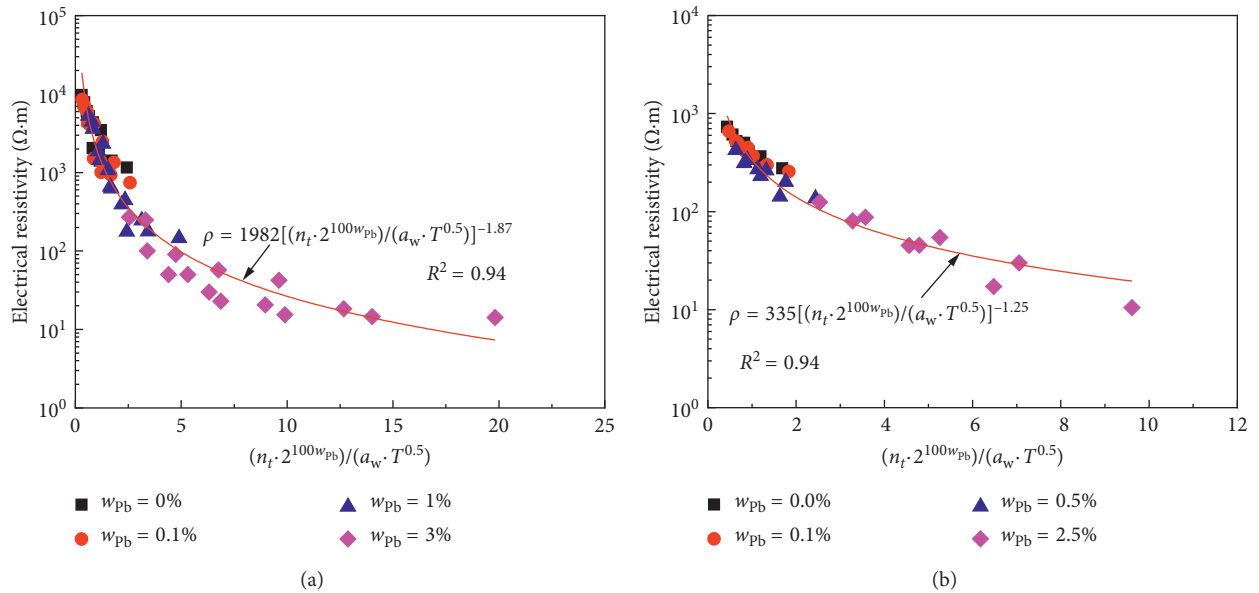


FIGURE 8: Relationship between electrical resistivity and $(n_t \cdot 2^{100w_{pb}})/a_w \cdot T^{0.5}$: (a) specimens of soil S1; (b) specimens of soil S2.

stabilized soils primarily depends on cement hydration products and pore structure of soil, which are also the main factors affecting electrical resistivity. Therefore, unconfined compressive strength can be related to the electrical resistivity of cement-stabilized soils, as shown in Figure 9. The result shows that the relationship between strength and electrical resistivity is not unique and depends on lead content. The presence of lead not only hinders the cement hydration process but also changes the ion concentration of pore solution. The former can delay the development of strength and electrical resistivity, and the latter mainly

affects the resistivity of stabilized soils. The influence mechanisms of lead on strength and electrical resistivity of stabilized soils are not exactly the same, resulting in different relationships at different lead contents.

As shown in Figure 9, there is a power function correlation between unconfined compressive strength and electrical resistivity at a given lead content, expressed as follows:

$$q_u = C \cdot \rho^D, \tag{7}$$

where q_u is the unconfined compressive strength and C and D are empirical constants, which depend on lead content

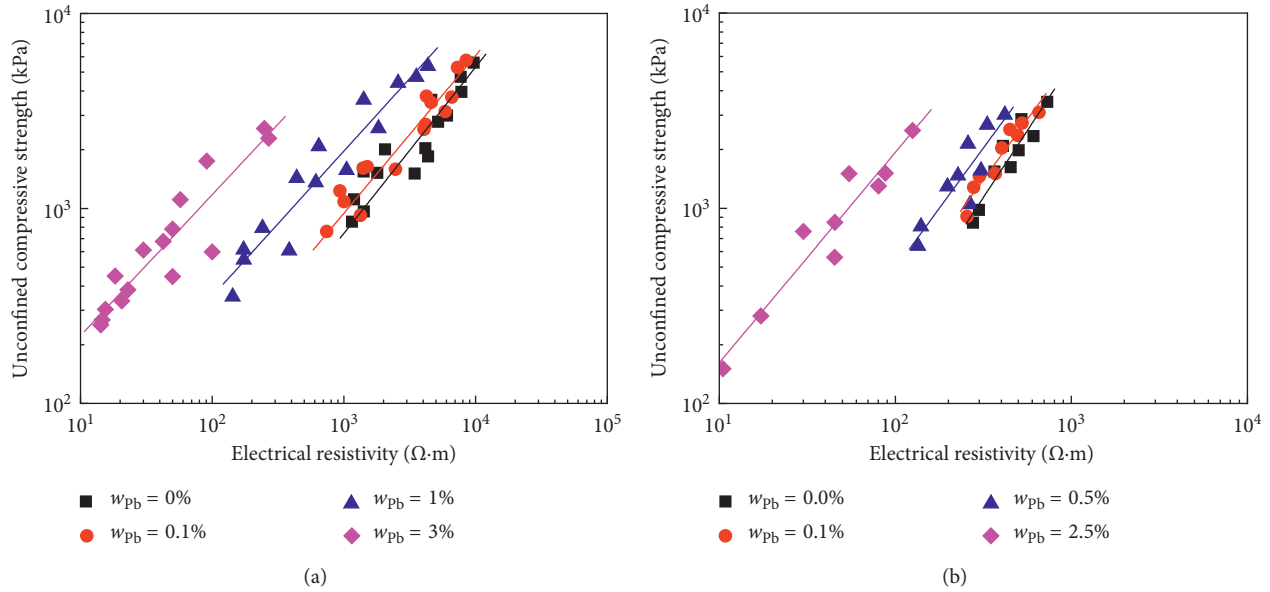


FIGURE 9: Relationship between unconfined compressive strength and electrical resistivity: (a) specimens of soil S1; (b) specimens of soil S2.

TABLE 3: Empirical constants between unconfined compressive strength and electrical resistivity.

Soil type	Lead content (%)	C	D	R^2
S1	0	2.0	0.85	0.86
	0.1	3.5	0.81	0.90
	1	11.5	0.75	0.94
	3	42.1	0.72	0.85
S2	0.0	0.4	1.37	0.82
	0.1	1.1	1.24	0.89
	0.5	1.7	1.23	0.76
	2.5	13.5	1.08	0.88

and are listed in Table 3. The value of C increases significantly with the increase in lead content and is also related to soil type. The value of D , ranging from 0.72 to 0.85 for specimens of soil S1 and from 1.08 to 1.37 for specimens of soil S2, is also related to soil properties. When $D=1$, Equation (7) presents a linear relationship between strength and electrical resistivity, which is similar to the results reported by Liu et al. [11] and Zhang et al. [33].

As shown in Table 3, the correlation coefficient (R^2) of Equation (7) is higher than 0.85 for specimens of soil S1 and is higher than 0.76 for specimens of soil S2. It is indicated that unconfined compressive strength can be correlated with electrical resistivity of cement-stabilized soils. Therefore, the electrical resistivity method can be used as a time-effective and economical technology to quantify the mechanical behavior of cement-stabilized heavy metal-contaminated soils in the field. Combining the resistivity formula developed in this study, engineers can choose a proper amount of cement to meet the strength requirement of the actual project, taking into account the effect of lead.

5. Conclusions

This study investigated the effect of lead content, cement content, and curing time on electrical resistivity of stabilized soils, proposed a resistivity empirical formula of cement-stabilized lead-contaminated soils based on Archie's law, and explored the relationship between unconfined compressive strength and electrical resistivity. Based on the experimental results, analysis, and discussion reported, the specific conclusions can be drawn as follows:

- (i) The electrical resistivity of lead-contaminated soils stabilized with cement decreases with the increase in lead content and increases with the increase of cement content and curing time. The reduction in porosity and degree of saturation, as a result of the cement hydration process, leads to an increase in electrical resistivity of stabilized soils.
- (ii) A unique power function well adapts electrical resistivity with the ratio of porosity-lead content/cement content-curing time, $(n_t \cdot \alpha^{100w_{pb}}) / a_w \cdot T^{0.5}$. This ratio can be used as a fundamental parameter to assess electrical resistivity of cement-stabilized lead-contaminated soils.
- (iii) Archie's law can be extended to apply to cement-stabilized lead-contaminated soils by using the ratio of porosity-lead content/cement content-curing time, replacing the porosity. It should be noted that this ratio has no specific physical meaning, and Equation (6) is just an empirical resistivity formula.
- (iv) There is a power function correlation between unconfined compressive strength and electrical resistivity of cement-stabilized lead-contaminated soils.

Electrical resistivity measurement can be used as an economical and time-effective method to assess the quality of cement-stabilized lead-contaminated soils in practice.

Data Availability

The data used to support the findings of this study are included within the article.

Conflicts of Interest

The authors declare that they have no conflicts of interest.

Acknowledgments

This study was supported by the National Natural Science Foundation of China (Grant no. 51578148) and the Research Innovation Program for College Graduates of Jiangsu Province (no. KYLX16_0241).

References

- [1] R. Malviya and R. Chaudhary, "Leaching behavior and immobilization of heavy metals in solidified/stabilized products," *Journal of Hazardous Materials*, vol. 137, no. 1, pp. 207–217, 2006.
- [2] Q. Y. Chen, M. Tyrer, C. D. Hills, X. M. Yang, and P. Carey, "Immobilisation of heavy metal in cement-based solidification/stabilization: a review," *Waste Management*, vol. 29, no. 1, pp. 390–403, 2009.
- [3] A. Al-Tabbaa and C. W. Evans, "Pilot in situ auger mixing treatment of a contaminated site: part 1. Treatability study," *Proceedings of the Institution of Civil Engineers-Geotechnical Engineering*, vol. 131, no. 1, pp. 52–59, 1998.
- [4] D. H. Moon and D. Dermatas, "An evaluation of lead leachability from stabilized/solidified soils under modified semi-dynamic leaching conditions," *Engineering Geology*, vol. 85, no. 1-2, pp. 67–74, 2006.
- [5] B. Pandey, S. D. Kinrade, and L. J. J. Catalan, "Effects of carbonation on the leachability and compressive strength of cement-solidified and geopolymer-solidified synthetic metal wastes," *Journal of Environmental Management*, vol. 101, pp. 59–67, 2012.
- [6] N. J. Jiang, Y. J. Du, S. Y. Liu, and J. J. Zhu, "Experimental investigation of the compressibility behavior of cement-solidified/stabilised zinc-contaminated kaolin clay," *Géotechnique Letters*, vol. 4, no. 1, pp. 27–32, 2014.
- [7] D. J. Boardman, "Lime stabilization: clay-metal-lime interactions," Ph.D. thesis, Civil and Building Engineering, Loughborough University, Loughborough, UK, 1999.
- [8] Y. J. Du, M. L. Wei, K. R. Reddy, F. Jin, H. L. Wu, and Z. B. Liu, "New phosphate-based binder for stabilization of soils contaminated with heavy metals: leaching, strength and microstructure characterization," *Journal of Environmental Management*, vol. 146, pp. 179–188, 2014.
- [9] M. Fukue, T. Minati, H. Horibe, and N. Taya, "The microstructures of clay given by resistivity measurements," *Engineering Geology*, vol. 54, no. 1-2, pp. 43–53, 1999.
- [10] V. Damasceno and D. Fratta, "Monitoring chemical diffusion in a porous media using electrical resistivity tomography," in *Proceedings of Site and Geomaterial Characterization*, vol. 149, pp. 174–181, Shanghai, China, May 2006.
- [11] S. Y. Liu, Y. J. Du, L. H. Han, and M. F. Gu, "Experimental study on the electrical resistivity of soil-cement admixtures," *Environmental Geology*, vol. 54, no. 6, pp. 1227–1233, 2008.
- [12] R. Cardoso, "Porosity and tortuosity influence on geophysical properties of an artificially cemented sand," *Engineering Geology*, vol. 211, pp. 198–207, 2016.
- [13] G. Kibria and M. S. Hossain, "Investigation of geotechnical parameters affecting electrical resistivity of compacted clays," *Journal of Geotechnical and Geoenvironmental Engineering*, vol. 138, no. 12, pp. 1520–1529, 2012.
- [14] T. Oh, G. Cho, and C. Lee, "Effect of soil mineralogy and pore-water chemistry on the electrical resistivity of saturated soils," *Journal of Geotechnical and Geoenvironmental Engineering*, vol. 140, no. 11, article 06014012, 2014.
- [15] G. E. Archie, "The electrical resistivity log as an aid in determining some reservoir characteristics," *Transactions of the AIME*, vol. 146, no. 1, pp. 54–62, 1942.
- [16] Z. S. Abu-Hassanein, C. H. Benson, and L. R. Blotz, "Electrical resistivity of compacted clays," *Journal of Geotechnical Engineering*, vol. 122, no. 5, pp. 397–406, 1996.
- [17] P. H. Giao, S. G. Chung, D. Y. Kim, and H. Tanaka, "Electric imaging and laboratory resistivity testing for geotechnical investigation of Pusan clay deposits," *Journal of Applied Geophysics*, vol. 52, no. 4, pp. 157–175, 2003.
- [18] J. Abedi-Koupai and H. Mehdizadeh, "Estimation of osmotic suction from electrical conductivity and water content measurements in unsaturated soils," *Geotechnical Testing Journal*, vol. 31, no. 2, article 100322, 2008.
- [19] L. S. Bryson and A. Bathe, "Determination of selected geotechnical properties of soil using electrical conductivity testing," *Geotechnical Testing Journal*, vol. 32, no. 3, article 101632, 2009.
- [20] S. Seladji, P. Cosenza, A. Tabbagh, J. Ranger, and G. Richard, "The effect of compaction on soil electrical resistivity: a laboratory investigation," *European Journal of Soil Science*, vol. 61, no. 6, pp. 1043–1055, 2010.
- [21] H. H. Ryu, T. M. Oh, G. C. Cho, K. Y. Kim, K. R. Lee, and D. S. Lee, "Probabilistic relationship between Q-value and electrical resistivity," *KSCE Journal of Civil Engineering*, vol. 18, no. 3, pp. 780–786, 2014.
- [22] T. M. Oh, G. C. Cho, T. A. Son, H. H. Ryu, and C. Lee, "Experimental approach to evaluate weathering condition of granite using electrical resistivity," *Geomechanics and Engineering*, vol. 8, no. 5, pp. 675–685, 2015.
- [23] B. Andrew, H. P. Sionhan, and S. Ben, "Examination of solute transport in an undisturbed soil column using electrical resistance tomography," *Water Resources Research*, vol. 32, no. 4, pp. 763–769, 1996.
- [24] G. L. Yoon and J. B. Park, "Sensitivity of leachate and fine contents on electrical resistivity variations of sandy soils," *Journal of Hazardous Materials*, vol. 84, no. 2-3, pp. 147–161, 2001.
- [25] S. Grellier, K. R. Reddy, J. Gangathulasi, R. Adib, and C. C. Peters, "Correlation between electrical resistivity and moisture content of municipal solid waste in bioreactor landfill," in *Proceedings of ASCE Geoenvironmental Engineering*, vol. 163, pp. 1–14, Denver, CO, USA, February 2007.
- [26] F. Genelle, C. Sirieix, J. Riss, and V. Naudet, "Monitoring landfill cover by electrical resistivity tomography on an experimental site," *Engineering Geology*, vol. 145–146, pp. 18–29, 2012.
- [27] M. A. Taylor and K. Arulanadan, "Relationships between electrical and physical properties of cement pastes," *Cement and Concrete Research*, vol. 4, no. 6, pp. 881–897, 1974.

- [28] C. Tashiro, K. Ikeda, and Y. Inome, "Evaluation of pozzolanic activity by the electric resistance measurement method," *Cement and Concrete Research*, vol. 24, no. 6, pp. 1133–1139, 1994.
- [29] W. J. McCarter, T. M. Chrisp, G. Starrs, and J. Blewett, "Characterization and monitoring of cement-based systems using intrinsic electrical property measurements," *Cement and Concrete Research*, vol. 33, no. 2, pp. 197–206, 2003.
- [30] Z. J. Li, X. S. Wei, and W. Li, "Preliminary interpretation of Portland cement hydration process using resistivity measurements," *ACI Materials Journal*, vol. 100, no. 3, pp. 253–257, 2003.
- [31] Z. J. Li, L. Z. Xiao, and X. S. Wei, "Determination of concrete setting time using electrical resistivity measurement," *Journal of Materials in Civil Engineering*, vol. 19, no. 5, pp. 423–427, 2007.
- [32] L. Z. Xiao and Z. J. Li, "New understanding of cement hydration mechanism through electrical resistivity measurement and microstructure investigations," *Journal of Materials in Civil Engineering*, vol. 21, no. 8, pp. 368–373, 2009.
- [33] D. W. Zhang, Z. G. Cao, L. B. Fan, S. Y. Liu, and W. Z. Liu, "Evaluation of the influence of salt concentration on cement stabilized clay by electrical resistivity measurement method," *Engineering Geology*, vol. 170, pp. 80–88, 2014.
- [34] C. Sirieix, J. F. Lataste, D. Breyse, and M. Frappa, "Electrical measurement to characterize concrete damage," *Materials and Structures*, vol. 35, no. 4, pp. 204–210, 2002.
- [35] J. F. Lataste, C. Sirieix, D. Breyse, and M. Frappa, "Electrical resistivity measurement applied to cracking assessment on reinforced concrete structures in civil engineering," *NDT & E International*, vol. 36, no. 6, pp. 383–394, 2003.
- [36] K. Karhunen, A. Seppanen, A. Lehtikoinen, P. J. Monteiro, and J. P. Kaipio, "Electrical resistance tomography imaging of concrete," *Cement and Concrete Research*, vol. 40, no. 1, pp. 137–145, 2010.
- [37] J. K. Mitchell, "Conduction phenomena: from theory to geotechnical practice," *Geotechnique*, vol. 41, no. 3, pp. 299–340, 1991.
- [38] W. J. McCarter and P. Desmazes, "Soil characterization using electrical measurements," *Geotechnique*, vol. 47, no. 1, pp. 179–183, 1997.
- [39] S. P. Friedman and N. A. Seaton, "Critical path analysis of the relationship between permeability and electrical conductivity of three-dimensional pore networks," *Water Resources Research*, vol. 34, no. 7, pp. 1703–1710, 1998.
- [40] S. P. Friedman, "Soil properties influencing apparent electrical conductivity: a review," *Computers and Electronics in Agriculture*, vol. 46, no. 1–3, pp. 45–70, 2005.
- [41] G. V. Keller and F. C. Frischknecht, *Electrical Methods in Geophysical Prospecting*, Pergamon Press, Oxford, UK, 1966.
- [42] ASTM, *Standard Practice for Classification of Soils for Engineering Purposes (Unified Soil Classification System)*, D2487-11, ASTM, West Conshohocken, PA, USA, 2011.
- [43] ASTM, *Standard Test Method for Laboratory Compaction Characteristics of Soil using Standard Effort (12400 ft-lbf/ft³ (600 kN-m/m³))*, D698-12e2, ASTM, West Conshohocken, PA, USA, 2012.
- [44] R. B. Kogbara and A. Al-Tabbaa, "Mechanical and leaching behavior of slag-cement and lime-activated slag stabilised/solidified contaminated soil," *Science of the Total Environment*, vol. 409, no. 11, pp. 2325–2335, 2011.
- [45] ASTM, *Standard Test Method for Unconfined Compressive Strength of Cohesive Soil*, D2166/D2166M-16, ASTM, West Conshohocken, PA, USA, 2016.
- [46] D. Lee, T. D. Waite, G. Swarbrick, and S. Lee, "Comparison of solidification/stabilization effects of calcite between Australian and South Korean cements," *Cement and Concrete Research*, vol. 35, no. 11, pp. 2143–2157, 2005.
- [47] P. W. Glover, M. J. Hole, and J. Pous, "A modified Archie's law for two conducting phases," *Earth and Planetary Science Letters*, vol. 180, no. 3-4, pp. 369–383, 2000.
- [48] P. W. Glover, "Archie's law—a reappraisal," *Solid Earth*, vol. 7, no. 4, pp. 1157–1169, 2016.
- [49] N. D. Quang and J. C. Chai, "Permeability of lime- and cement-treated clayey soils," *Canadian Geotechnical Journal*, vol. 52, no. 9, pp. 1221–1227, 2015.
- [50] USEPA, *Solidification/Stabilization Use at Superfund Sites*, EPA 542-R-00-010, Office of Solid Waste and Emergency Response, Washington, DC, USA, 2000.

Research Article

Estimation of Influence Scope of Lateral Displacement of Soft Ground under Vacuum Pressure with PVD

Jingyun Liu,¹ Hongtao Fu,¹ Jun Wang ,² Yuanqiang Cai,³ and Xiuqing Hu⁴

¹College of Architecture and Civil Engineering, Wenzhou University, Wenzhou 325035, China

²The Key Laboratory of Engineering and Technology for Soft Soil Foundation and Tideland Reclamation of Zhejiang Province, Wenzhou University, Wenzhou 325035, China

³Zhejiang University of Technology, Hangzhou 310014, China

⁴Innovation Centre of Tideland Reclamation and Ecological Protection, Wenzhou University, Wenzhou 325035, China

Correspondence should be addressed to Jun Wang; sunnystar1980@163.com

Received 8 June 2018; Accepted 26 July 2018; Published 19 August 2018

Academic Editor: Yongfeng Deng

Copyright © 2018 Jingyun Liu et al. This is an open access article distributed under the Creative Commons Attribution License, which permits unrestricted use, distribution, and reproduction in any medium, provided the original work is properly cited.

The application of vacuum pressure to a treated area not only induces vertical settlement and inward lateral displacement but also causes the formation of tension cracks near the ground surface. In general, the strain method is applied to calculate the lateral displacement at the boundary of a treated area; however, the influence scope of lateral displacement has not yet been presented. Based on the *in situ* data of soft clayey soil foundation treated by vacuum consolidation, lateral displacement was estimated in the influence scope in this study. To calculate the influence scope of lateral displacement induced by vacuum pressure, the ratio of the lateral displacement within the influence scope to the ground surface settlement under the centre of the treated area is defined as the maximum value of the lateral displacement (ELD) within the influence scope. This paper proposes a direct relationship between ELD and the distance from the treated area boundary (L_x), considering the length of the prefabricated vertical drain. In addition, the FEA (finite-element analysis) is used to simulate the process of vacuum preloading to reinforce soft soil foundation. The influence scope simulated is almost close to the calculated value L_x . Accordingly, the safety distance between the boundary of the treated area and the surrounding building can be estimated when the soft soil foundation is consolidated by using a vacuum preloading method.

1. Introduction

The preloading of a soft clayey deposit through vacuum or embankment loading is commonly used as a soft ground improvement method. With several advantages over embankment loading, vacuum pressure applied to the processing of soft clay has a higher practicability, such as no fill material, shorter construction periods, and nonrequirement for heavy machinery. In addition, the vacuum preloading method does not add any chemical admixtures into the ground and is consequently an environmental-friendly ground improvement method [1, 2]. However, owing to the principle effect of the vacuum preloading method, the treated area will not only induce vertical settlement and inward (toward the centre of the loading area) lateral

displacement of the ground but also cause crack adjacent to the treated area. Especially, lateral displacement of soil at reclaimed coastal regions is more obvious because of the poor engineering properties of soft soil, as shown in Figure 1. In most preloading projects, the prediction of the consolidation settlement and lateral displacement of the ground is an essential design requirement. In particular, the prediction of ground lateral displacement induced by geotechnical engineering activities in an urban environment may sometimes be a crucial design consideration [3].

The current methods for calculating lateral displacement of soil consist of the strain method (the horizontal displacement at the boundary is calculated based on the strain of the soil in the treated area) [1] and the method of determining the ratio of the settlement and lateral displacement [4]. It is



FIGURE 1: Deformation of the soil under vacuum consolidation.

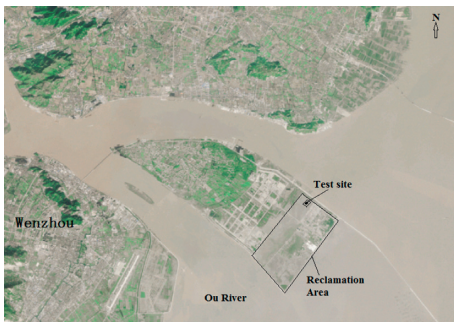


FIGURE 2: Location of the test.

noteworthy that the above methods are not used to solve the deformation of the soil influenced by the different lengths of a prefabricated vertical drain (PVD). Generally, the aforementioned methods can be used to calculate or analyse the lateral deformation of soil at the boundary of the treated area. As shown in Figure 1, in spite of the lateral displacement, soil crevices at the affected area are often induced by vacuum pressure. Till now, there is no practical, easy-to-use method to evaluate the effect of the scope induced by vacuum pressure to adjacent engineering structures.

In this study, according to a practical application of the vacuum preloading method to engineering practice, the strain method was generalised to calculate the lateral displacement of soil at the affected area. Furthermore, based on the observed results of the case history and the strain method, an empirical equation is proposed for calculating the influence scope of vacuum preloading method, considering the different lengths of PVD. Finally, the FEA was applied to compare the simulated range of influence with the calculated value L_x to evaluate the feasibility of the empirical equation.

2. Site and Soil Conditions

Wenzhou Vocational Secondary School is located in the new district of Oujiang estuary, China. The site of this project is shown in Figure 2. The treated area covers approximately $157,820 \text{ m}^2$.

The field is located in a reclamation area with different thicknesses of dredger fill at the ground surface. For the convenience of construction, the test site should be reinforced using the vacuum preloading method for preliminary shallow layer treatment. During this process, the strengthened depth is

approximately 3–5 m. Figure 3 shows the physical properties of the soil after shallow treatment, where the moisture content is still greater than 62%, and the compression index is approximately 1.1. These characteristics cause the soil to produce a large postconstruction settlement [5, 6], which can only satisfy the bearing capacity for the smooth functioning of the light-weight machine but cannot meet the requirements of the foundation treatment. Thus, the test site should be further reinforced using a vacuum preloading method again because of the poor engineering properties of soft soil.

3. In Situ Instrumentation

According to different reinforcement requirements, two PVD lengths (0.1 m wide and 4.0 mm thick) were applied to this project. To prevent the pile of buildings from sloping into the construction, a 6 m PVD was adopted at Section 1. Similarly, a 15 m PVD was adopted at Section 2 to prevent the cracking of the pavement and playground in use. Both the PVDs were arranged in a winter sweet shape with a spacing of 0.8 m.

Vacuum pressure was applied using the air-sealing sheet method [7], and the sheet used for this project was a 0.5 mm thick polyvinyl chloride (PVC) membrane. Before placing the sealing membrane, three layers of geotextiles were laid down, and a sealing membrane was placed around in the sealing groove. In addition, the groundwater level at the site was approximately 0.48 m from the ground surface. To avoid air leakage through the top unsaturated zone, the edges of the sealing sheet were embedded in a 1.5 m deep trench.

After installing the PVDs, 13 surface settlement plates, 53 multilevel settlement gauges, and 11 inclinometers were installed to monitor the performance of the treated ground. Figures 4(a) and 4(b) present the general plan views of the test sites, and Table 1 tabulates the installed depths of the layered settlement gauges.

The measured vacuum pressure applied under the air-sealing sheet was over 80 kPa. At the time of stopping the vacuum pump, the measured ground surface average settlement from Sections 1 and 2 was approximately 908 and 1197 mm, respectively. The curve of the settlement over time in each treated area is shown in Figures 5(a) and 5(b).

4. Lateral Displacement

4.1. At the Boundary of Treated Area. For the soft soil foundation, the soil can be considered in the K_0 consolidation state. If only the vacuum pressure is larger than the lateral stress required for a no horizontal strain condition, an inward lateral displacement is observed. Based on a series of test results, Chai et al. [1] reported an approximate method for calculating the ground lateral displacement induced by vacuum pressure. Their method was used in the current study to calculate the lateral displacement of soil at boundary of the treated area. The dimensions of Sections 1 and 2 were $230 \text{ m} \times 101 \text{ m}$ and $185 \text{ m} \times 140 \text{ m}$ (length \times width), respectively. Table 2 lists the information needed to calculate the lateral displacement induced by vacuum consolidation by using the approximate method.

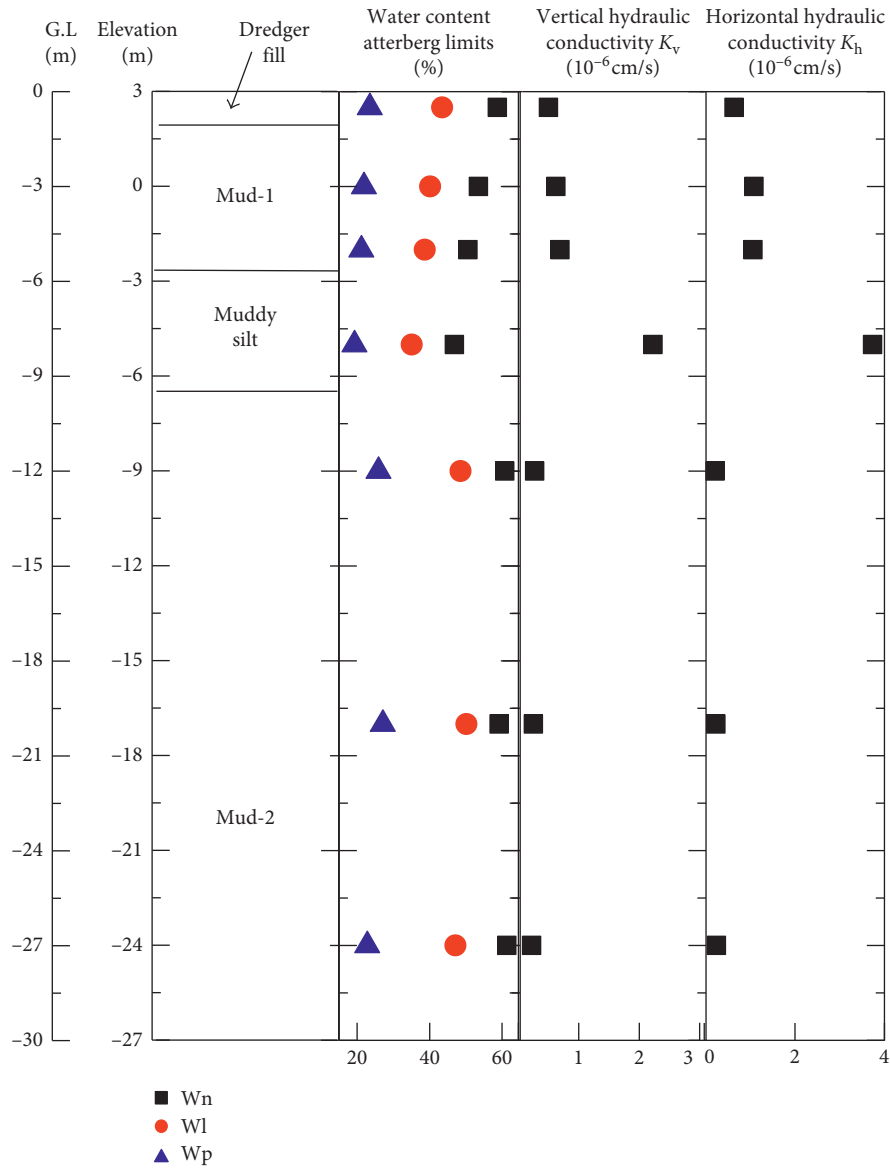


FIGURE 3: Soil profile and some physical properties at the test site.

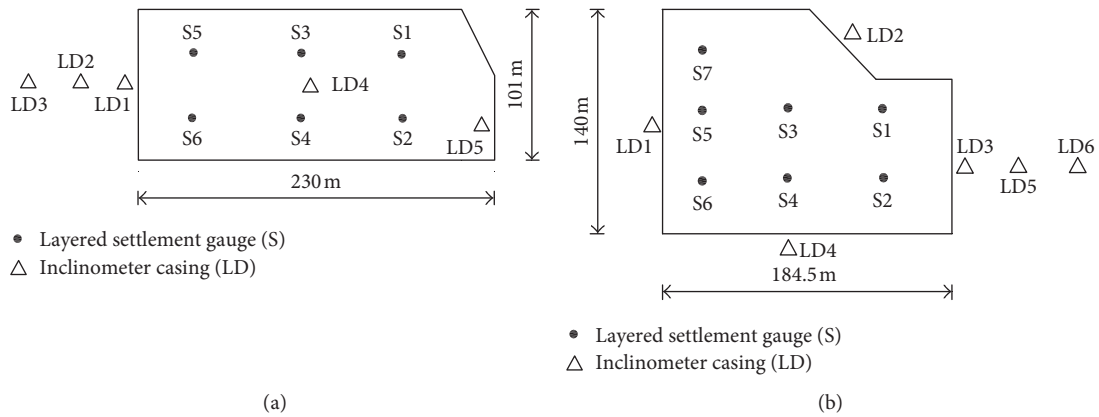
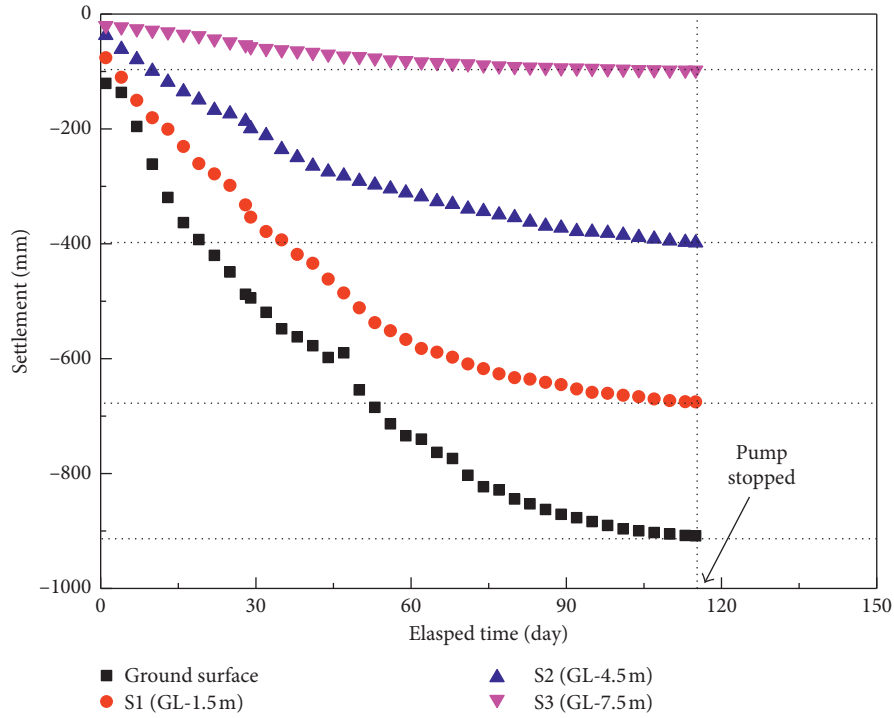


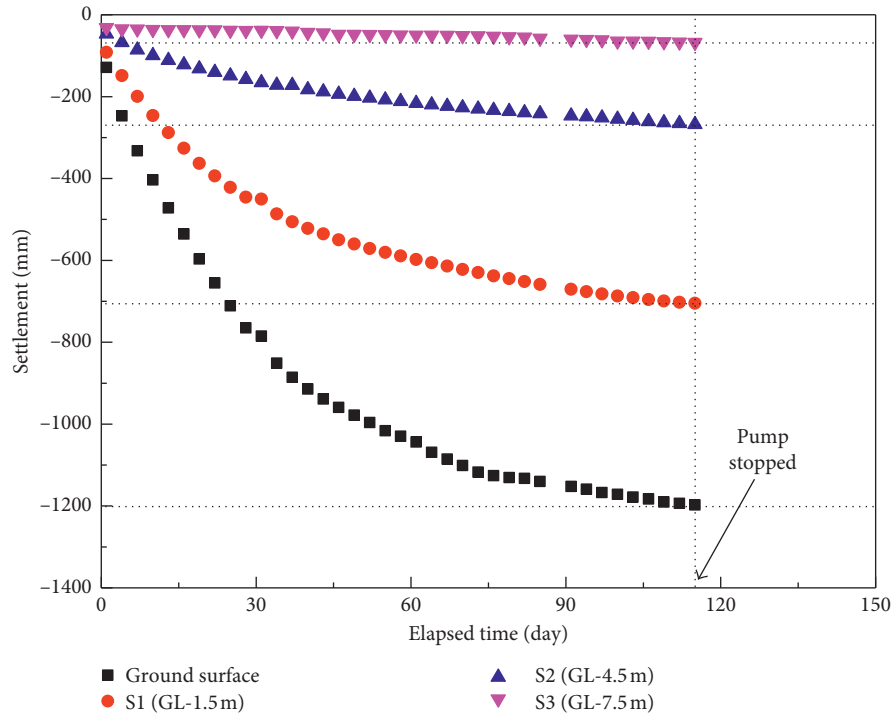
FIGURE 4: Plan layout of instrumentation points. (a) Section 1 and (b) Section 2.

TABLE 1: Installed depth of layered settlement gauges.

	Monitoring points	Installed depth (m)
Section 1	S1, S2, S3, S4, S5, S6	1.5, 4.5, 7.5
Section 2	S1, S2, S3, S4, S5, S6, S7	1.5, 4.5, 7.5, 10.5, 15.0



(a)



(b)

FIGURE 5: Settlement versus elapsed time curve. (a) Section 1 and (b) Section 2.

TABLE 2: Parameters for the soil at Wenzhou Vocational Secondary School Foundation.

	K_0	K_a	c' (kPa)	γ_t (kN/m ³)	λ	e	E_s (MPa)	ϕ' (°)
Dredger fill	0.8246	0.7016	8.3	16	-0.1717	1.639	1.98	10.1
Mud 1	0.8958	0.6747	7.9	16.5	-0.1659	1.516	1.34	11.2
Muddy silt clay	0.6596	0.4921	7.4	17	-0.2645	1.267	2.31	15.4
Mud 2	0.847	0.7346	10.3	15.8	-0.1063	1.718	1.67	24.5
Silty clay	0.7802	0.6396	14.5	16.8	-0.2362	1.312	2.48	8.8

Note. K_a is the active earth pressure coefficient; $K_a = \tan^2(45 - (\phi'/2))$.

The method proposed by Chai et al. [1] for calculating lateral displacement of the soil at the treated area boundary as a result of the vacuum-drain consolidation can be summarized as follows:

- (1) horizontal earth pressure coefficient calculation:

$$K_{a0} = \beta K_a + (1 - \beta)K_0, \quad (1)$$

where K_a is the active earth pressure coefficient, K_0 is the at-rest earth pressure, and β is an empirical factor. It is suggested that β should normally be assigned a value in the range from 0.67 to 1.

- (2) The maximum depth (z_1) calculation of soil with lateral displacement is as follows:

$$Z_c = \frac{2c'}{\gamma_t \sqrt{K_a}}, \quad \text{for } z_c < z_w, \quad (2a)$$

$$Z_c = \frac{1}{\gamma_t - \gamma_w} \left(\frac{2c'}{\sqrt{K_a}} - \gamma_w z_w \right), \quad \text{for } z_c > z_w, \quad (2b)$$

$$\sigma'_{av} = \begin{cases} 0, & \text{for } z < z_c, \\ K_{a0} z' \gamma', & \text{for } z_1 > z > z_c, \end{cases} \quad (3)$$

$$\Delta\sigma_{vac} = \frac{K_0 \cdot \sigma'_{v0} - \sigma'_{av}}{1 - K_0}, \quad (4)$$

where γ_t is total unit weight of soil, γ_w is the unit weight of pore water, c' is the effective stress cohesion, z_c is the depth of cracking, z_w is the groundwater level, and the depth below which no lateral displacement occurs in the soil is given as $z_1 = z_c + z'$.

- (3) The variation of the model parameter (α) with depth is given as

$$\alpha = \alpha_{\min} + \frac{1 - \alpha_{\min}}{\Delta\sigma_{vac}} \left(\frac{K_0 \sigma'_{v0} - \sigma'_{av}}{1 - K_0} \right), \quad \text{for } z_c \geq z \geq z_1. \quad (5)$$

- (4) The calculations for volumetric and horizontal strains are given as

$$\varepsilon_{vol} = \frac{\lambda}{1 + e} \ln \left(1 + \frac{\Delta\sigma_{vac}}{\sigma'_{v0}} \right), \quad (6a)$$

$$\varepsilon_h = \frac{1}{2} (1 - \alpha) \frac{\lambda}{1 + e} \ln \left(1 + \frac{\Delta\sigma_{vac}}{\sigma'_{v0}} \right), \quad (6b)$$

where λ is the virgin compression index in an $e - \ln p'$ plot, e is the voids ratio, $\Delta\sigma_{vac}$ is the

incremental vacuum pressure of the treated area, σ'_{a0} is the *in situ* vertical effective stress in the treated area, and σ'_{av} is the horizontal effective stress. Parameters ε_h and ε_{vol} are the horizontal and volumetric strains under vacuum consolidation, respectively.

- (5) Lateral displacement of the soil at the treated area boundary is given as

$$\delta_h = \varepsilon_h B, \quad (7)$$

where B is the half width of the treated area.

It is suggested that for triaxial stress conditions, the model parameter $\alpha_{\min} = 0.8$, where α has the minimum value (α_{\min}) at the ground surface. Moreover, the parameter reaches a unit value when $z > z_1$. In this case, the initial effective stress applied to the field is zero or at least close to zero. The lateral displacements of the boundaries of two treatment sections are shown in Figures 6(a) and 6(b).

According to the calculation results, the value of β mainly influences the lateral displacement at deeper locations and the calculated depth at which the lateral displacement becomes insignificant. The smaller the β value is, the larger the calculated lateral displacement is and the larger the z_1 value (below which no lateral displacement occurs in the soil) is. In Section 1, when $\beta = 0.67$, $z_1 \cong 21$ m; $\beta = 0.84$, $z_1 \cong 16.5$ m; and $\beta = 1$, $z_1 \cong 14$ m. In contrast, in Section 2, when $\beta = 0.67$, $z_1 \cong 26$ m; $\beta = 0.84$, $z_1 \cong 20$ m; and $\beta = 1$, $z_1 \cong 17$ m. The comparison of the calculation results shows that the z_1 value is not related to the depth of the PVD. In addition, the overall value of $\beta = 1.0$ seems to provide a better simulation of the *in situ* data. Of course, $\beta = 1.0$ corresponds to the active earth pressure state and will obviously underestimate the earth pressure for soil at depths near z_1 . The figure shows that the longer the length of the PVD is, the greater the depth of the reinforcement is and the greater the maximum horizontal displacement is.

4.2. In the Affected Area. Although the mechanism of vacuum preloading method is researched relatively perfectly, the influence of vacuum pressure on the consolidation and deformation of soil adjacent to the treated area is not very clear. According to the actual situation of engineering applications, in this study, the formula used to calculate the lateral deformation of the soil of the treated area boundary is generalised to calculate lateral deformation of the affected area.

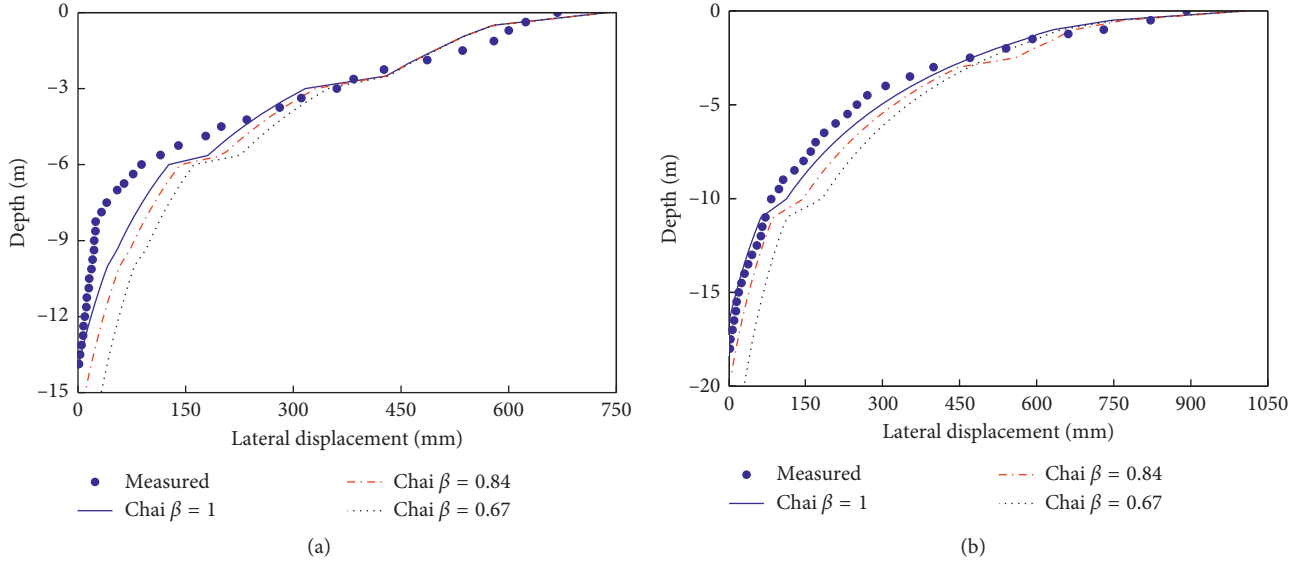


FIGURE 6: Lateral displacement of soil at treated area. (a) Section 1 and (b) Section 2.

The following changes have been adapted in the process of calculating the lateral displacement for the expansion of the strain method:

- (1) According to a series of laboratory tests, Robinson [8] proposed that lateral stresses should be considered when estimating the vertical strains of the soil in the affected area. The magnitude of vertical and lateral strains also depends on the magnitude of horizontal stress. When the horizontal stress from the affected area is equivalent to the active pressure, a more vertical settlement is observed compared to when the horizontal stress is equivalent to the earth pressure at rest. Similarly, the lateral strain is greater when the horizontal stress from the affected area is at rest. Assuming that the volumetric strain varies with the magnitude of the vacuum pressure in the affected area, the effective volumetric strain of the soil in the affected area can be calculated according to (6a) as follows:

$$\varepsilon_{\text{vol}-e} = \eta \times \varepsilon_{\text{vol}}, \quad (8)$$

where η is the attenuation coefficient of the volumetric strain.

Kondner [9] proposed a hyperbolic function to describe the stress-strain relationship of clay soil consolidation drainage tests.

$$\frac{\varepsilon_{\text{vol}-e}}{\sigma_1 - \sigma_3} = a + b\varepsilon_{\text{vol}-e}, \quad (9)$$

where σ_1 and σ_3 are the maximum and minimum principal stresses, respectively. According to the stress-strain normalization characteristics of cohesive soil [10], a and b can be calculated from the stress-strain values of the treated area. When $K_0 = 0.65$, $a = 0.0002$ and $b = 0.0342$, and when

$K_0 = 0.89$, $a = 0.0007$ and $b = 0.1089$. According to (9) and (10), the calculated value of η is given in Table 3.

- (2) Under plane strain conditions, the lateral strain factor (LF), which is the ratio of lateral strain ($\varepsilon_{\text{h}-e}$) to volumetric strain ($\varepsilon_{\text{vol}-e}$), can be determined by the method of Poulos and Davis [11] as

$$\text{LF} = \frac{\varepsilon_{\text{h}-e}}{\varepsilon_{\text{vol}-e}} = \frac{\chi(1-\nu) - \nu}{(1+\chi)(1-2\nu)}, \quad (10)$$

where $\chi = \Delta\sigma_{\text{vac,h}} / (\Delta\sigma_{\text{vac,v}} + \sigma'_{\text{vo}})$, σ'_{vo} is the *in situ* vertical effective stress in the affected area, and ν is Poisson's ratio. Under k_0 condition ($\chi = k_0$), there is no lateral deformation, such that

$$\nu = \frac{K_0}{1 + K_0}. \quad (11)$$

- (3) The lateral displacement at distance L_x from the boundary of the affected area can be calculated by

$$\delta_{\text{h}-e} = \varepsilon_{\text{h}-e} \times L_x, \quad (12)$$

where $\varepsilon_{\text{h}-e}$ is the horizontal strain of the soil in the affected area and L_x is the distance from the treated area boundary (m).

Figure 7 plots the variations in the LF, where the $\text{LF} = 0$ when $\chi = K_0$. A stress ratio (k) [1] was defined as

$$k = \frac{\Delta\sigma_{\text{vac}}}{\Delta\sigma_{\text{vac}} + \sigma'_{\text{vo}}}. \quad (13)$$

They postulated that if $k \leq K_0$, there will be no lateral displacement and vice versa. The lateral deformations of the different distances of the treated area boundary are shown in Figures 8–11. Despite the affected area being

TABLE 3: Calculation results of the η value.

Section 1				Section 2			
$K_0 = 0.65$		$K_0 = 0.89$		$K_0 = 0.65$		$K_0 = 0.89$	
$L_x = 10$	$L_x = 20$						
0.1160	0.0502	0.1274	0.0552	0.1151	0.0500	0.1268	0.0551

Note. K_0 is the at-rest earth pressure; L_x is the distance from the treated area boundary (m).

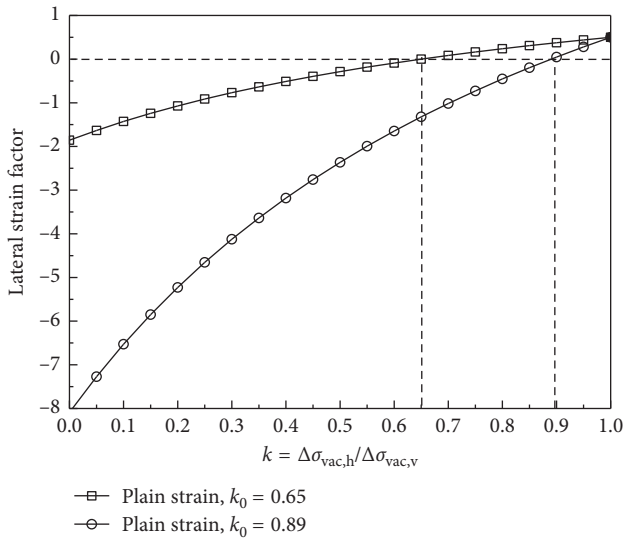


FIGURE 7: Lateral strain factor variations.

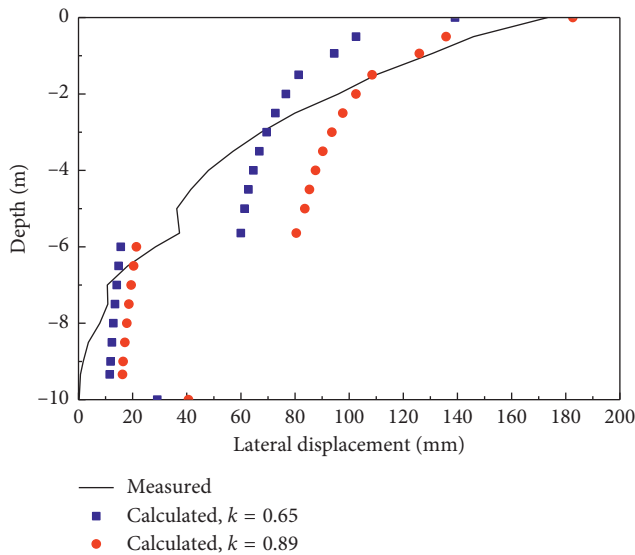


FIGURE 8: Lateral displacement at a distance of 10 m from Section 1 boundary.

without air-sealing sheet, the surface or subsurface soil layer acts as an equivalent air-sealing sheet for sealing the upper soil layer. This method was proposed by Chai et al. [12].

As the vacuum in the affected area is less than that in the treated area, the farther it is away from the boundary of the treated area, the smaller the degree of the vacuum

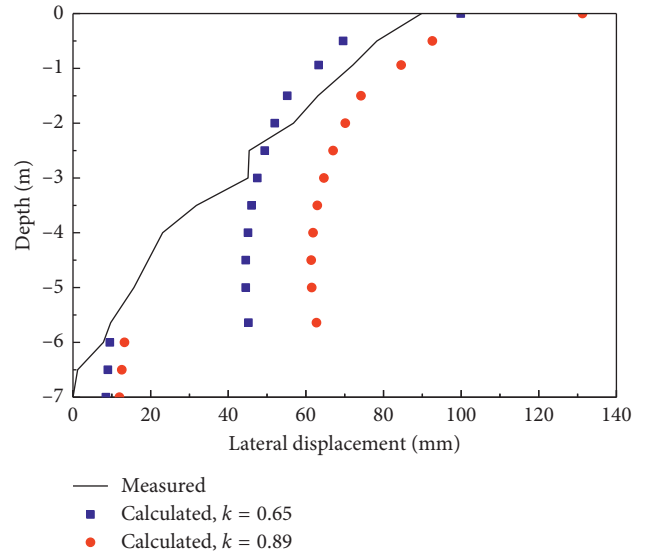


FIGURE 9: Lateral displacement at a distance of 20 m from Section 1 boundary.

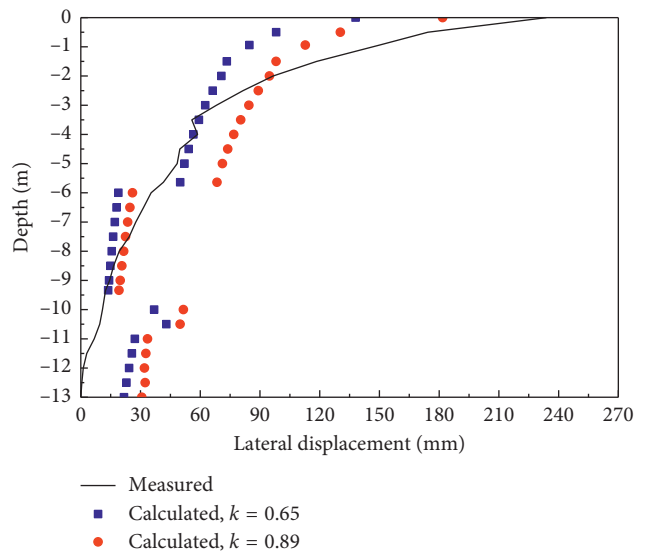


FIGURE 10: Lateral displacement at a distance of 10 m from Section 2 boundary.

is. Assuming that the attenuation rate of vacuum pressure is 2 kPa/m in the horizontal direction, the vacuum pressures at 10 and 20 m distance from the treated area boundary are 60 and 40 kPa, respectively; it was observed that it mainly depended on the vacuum pressure at the

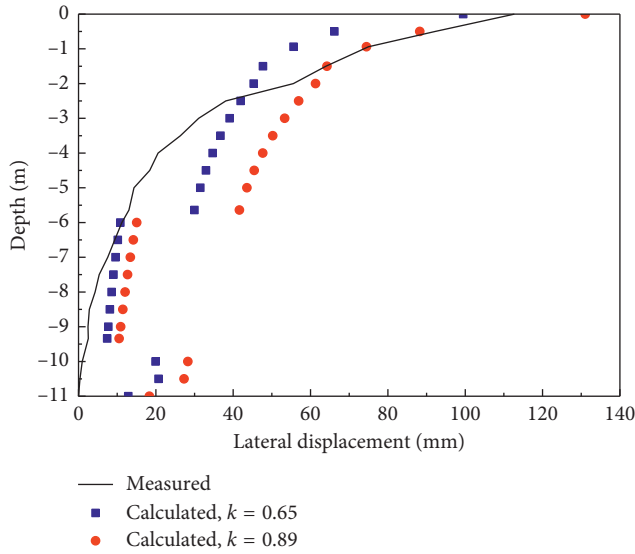


FIGURE 11: Lateral displacement at a distance of 20 m from Section 2 boundary.

ground surface. These assumptions are attributed to the following factors:

- Owing to the surface or subsurface soil layer being the sealing layer, the soil of the affected area could be maintained under the influence of vacuum pressure.
- In the range of natural sludge, the attenuation rate of vacuum pressure in horizontal direction is 6 kPa/m in the vertical direction [13].
- The attenuation of the vacuum is responsible for the permeability coefficient of the soil; the greater the permeability coefficient is, the slower the attenuation rate is [14]. In this case, the horizontal permeability coefficient of the soil is approximately three times of the vertical permeability coefficient.

At the affected area, the vacuum pressure can be considered to vary linearly from the ground surface to z_1 (below which no lateral displacement occurs in the soil) [1]. In the affected area, the coefficients of lateral earth pressure were assumed to vary linearly from k_0 at the bottom of the drain to k_a at the surface [8]. The calculated inward lateral earth pressures with $k = 0.65$ and 0.89 under plane strain conditions are plotted in Figures 8–11. The figures show that at shallow depths, $\chi = 0.89$ can predict the lateral displacement very well, whereas the measured values approach the predicted values when $k = 0.65$ (at-rest condition). It is noted that the sudden change of k at the boundary of the soil layer was attributed to a change in the parameters of soil between each layer.

5. Scope of Influence under Vacuum Pressure

Under vacuum consolidation, the settlement and lateral displacement induced by the vacuum pressure were determined. The effective stress increased in the treated area, which will cause soil reinforcement outside of the treated area in some

way and induced the lateral displacement. Through research, many domestic scholars believe that the range of influence under the vacuum pressure is approximately 22–42 m [15]. Although the vacuum preloading method has been widely used, at present there has been no practical, easy-to-use method for predicting the scope. Based on the observed results of case histories, an empirical equation was proposed in the present study for estimating the maximum value of the scope.

The maximum value of the effected lateral displacement (ELD), which is a dimensionless parameter, can be expressed as

$$\text{ELD} = \frac{\delta_{h-e}}{s}, \quad (14)$$

where S is the ground surface settlement under the centre of the treated area. The values of S and δ_{h-e} at the end of vacuum consolidation are desirable for substitution in this equation.

As the shallow soil is subjected to vacuum pressure to produce tension cracks, the soil can be considered to be close to the isotropic consolidation. However, no tensile cracks were observed in the lower soil, and the soil is considered to be close to a one-dimensional consolidation. According to the settlement calculation formula proposed by Liu et al. [16], S can be calculated as

$$S = \sum_1^n \alpha_i \cdot \frac{\Delta\sigma_{\text{vac}} - 20\% \times \Delta\sigma_{\text{vac}} \cdot (h_i/Z_i)}{E_i} \cdot h_i, \quad \text{for } 0 < h_i \leq Z_i, \quad (15)$$

where E_i is the compression modulus of each soil layer and h_i is the thickness of each soil layer. The calculated settlement values in Sections 1 and 2 are 821.4 and 1105.3 mm, respectively. It is obvious that the calculated value is less than that obtained in the *in situ* observations. The defined errors for Sections 1 and 2 are 9.5% and 7.7%, respectively, and meet the engineering requirements.

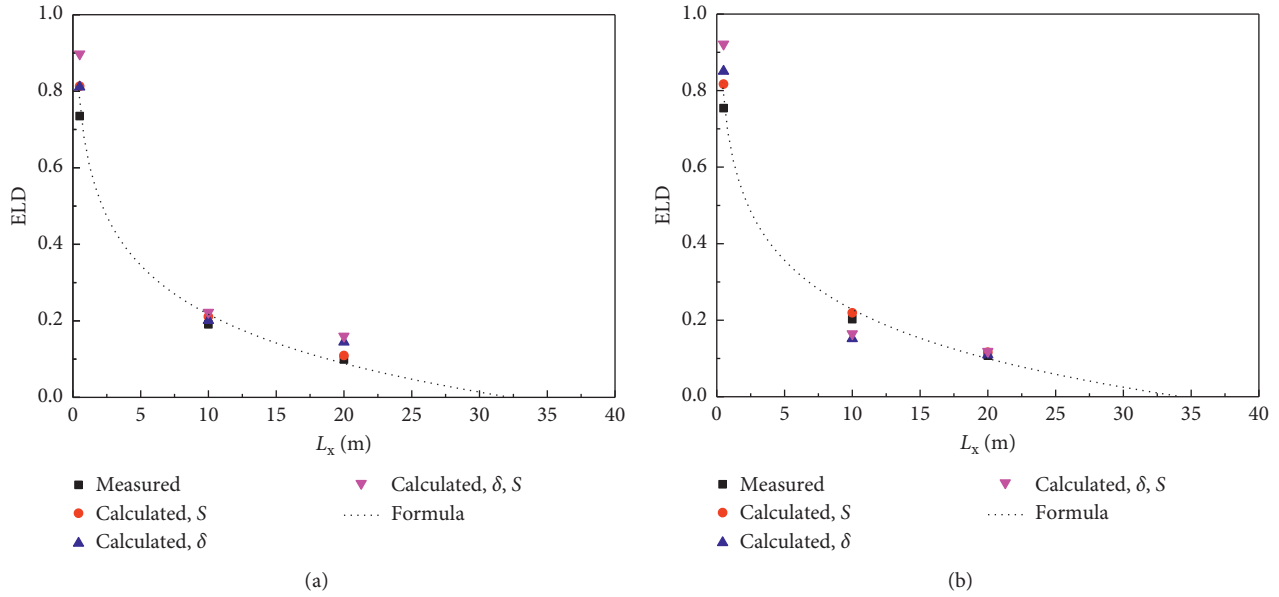
According to the monitoring data analysis, the relationship between ELD and L_x (the distance from the treated area boundary) can be expressed as follows:

$$\text{ELD} = a \ln(L_x) + b, \quad (16)$$

where L_x is the value of distance from the treated area boundary (m). When the length of PVD is 6 m, $a = -0.185$ and $b = 0.643$. When the length of PVD is 15 m, $a = -0.185$ and $b = 0.6541$. For a 6 m PVD length, when $\delta_{h-e} = 0$ and 30 mm as the boundary, $L_x = 32.32$ and 26.53 m, respectively. For a 15 m PVD length, when $\delta_{h-e} = 0$ and 30 mm as the boundary, $L_x = 34.32$ and 29.63 m, respectively. The relationship between the values of L_x and ELD analysed from the measured results of the field cases and calculation is plotted in Figures 12(a) and 12(b).

6. Numerical Simulation

The present authors considered a PVD-induced horizontal radial consolidation and simulated through FEA (finite-element analysis) and analysed. The FEA is performed by the use of Plaxis 2D (version 2017.01). And the soft soil model (SSM) was


 FIGURE 12: Relationship between the values of L_x and ELD. (a) Section 1 and (b) Section 2.

adopted. The model used in the FEA is shown in Figure 13. Meshing is divided finely. In Section 1 case, there are 3882 elements and 31789 nodes, and there are 5326 elements and 43241 nodes in Section 2 case. $X_{\min}=0\text{ m}$, $X_{\max}=345\text{ m}$ and $Y_{\min}=-40\text{ m}$, $Y_{\max}=0\text{ m}$ for case 1, and $X_{\min}=0\text{ m}$, $X_{\max}=276\text{ m}$ and $Y_{\min}=-40\text{ m}$, $Y_{\max}=0\text{ m}$ for case 2.

The values of the model parameters are listed in Table 2 and Figure 3. Two ideal cases without the effect of smear and well resistance were considered for the PVD-induced consolidation.

It was assumed that the model ground was weightless with an initial vertical effective stress of K_0 consolidation condition, and an incremental load of vacuum pressure was then applied at the top boundary. The Taylor [17] equation was used to consider the permeability variation with the void ratio reduction:

$$k = k_0 \times 10^{-((e_0 - e)/c_k)}, \quad (17)$$

where e_0 and e are the initial and current void ratios, k_0 and k are the permeability corresponding to void ratios e_0 and e , respectively, and c_k is a constant. The coefficient of consolidation, c , can be calculated as

$$c = \frac{(1 + e)k \cdot p'}{\lambda \cdot \gamma_w}, \quad (18)$$

where p' is the consolidation stress, λ is the slope of the virgin compression curve in the $e - \ln p'$ plot, and γ_w is the unit weight of water. The duration of vacuum consolidation maintained for 113 days in Section 1 and 103 days in Section 2. After the vacuum was completed, the horizontal displacement of the soil in each section case was shown in Figures 14 and 15.

It can be seen from Figures 14 and 15 in the process of the vacuuming, the soft soil in the affected area continuously moves towards the centre of the treated area under the influence of

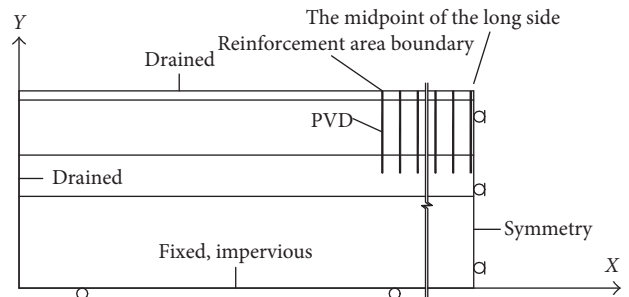


FIGURE 13: Model for FEA.

vacuum, and the maximum lateral displacement occurs at the boundary of the treated area. The result of this deformation has agreement with *in situ* data measured. The surface lateral displacement development of the two affected areas is summarized in Figure 16. The surface lateral displacement within the range of 0–15 m outside the treated area greatly developed, while the lateral displacement in the 15–25 m range developed slowly, specially, the surface lateral displacement is smaller at the 25 m away from the treated area. Meanwhile, it can be considered that $L_{x \max}$ is equal to 34 m in Section 1 and $L_{x \max}$ is equal to 37 m in Section 2. This is basically close to the result of calculation. According to the calculation results of (14)–(16), $L_{x \max}$ of Sections 1 and 2 are equal to 32.32 and 34.32, respectively.

To confirm the safe distance between the boundary of treated area and structure, a series of factors must be considered carefully, which consist of the ability to resist structural deformation, type of structural infrastructure, and soil properties inside and outside the treated area. According to the calculation results from (14) to (16) and simulation, it is feasible for engineering practice that the safe distances away from the treated area can be determined to 32.32 and 34.32 m.

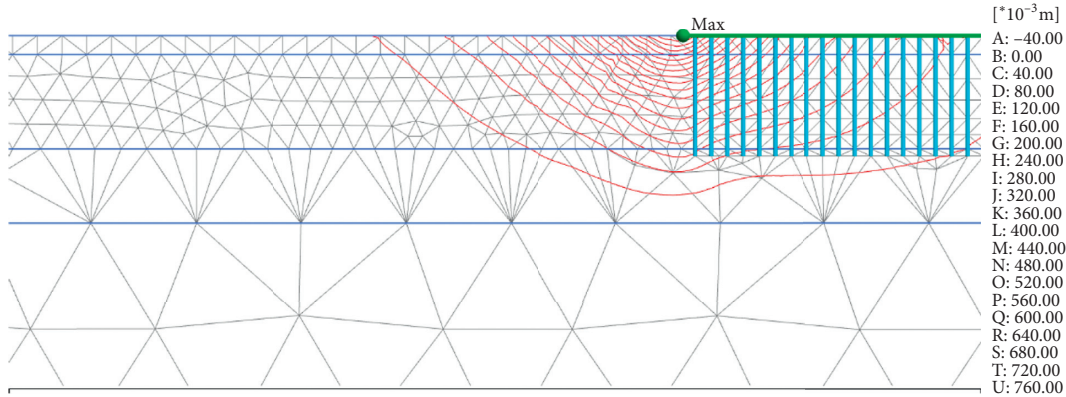


FIGURE 14: Lateral displacement of the soil outside Section 1.

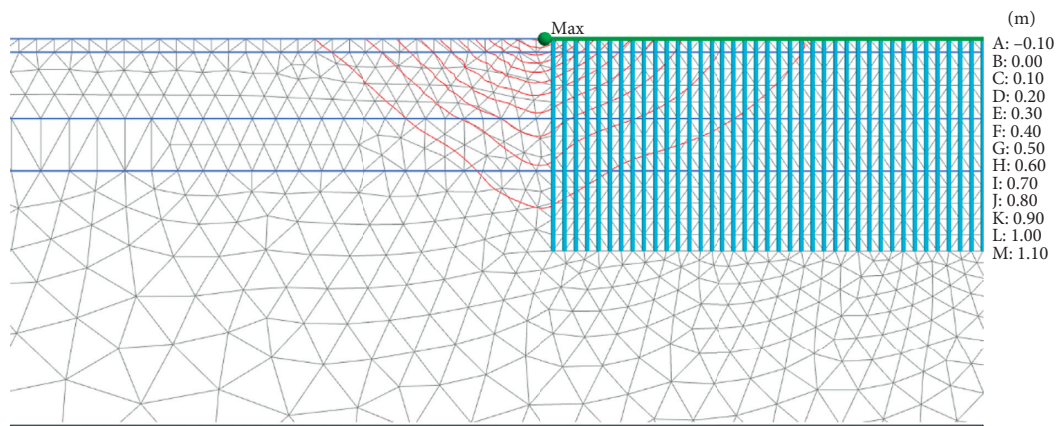


FIGURE 15: Lateral displacement of the soil outside Section 2.

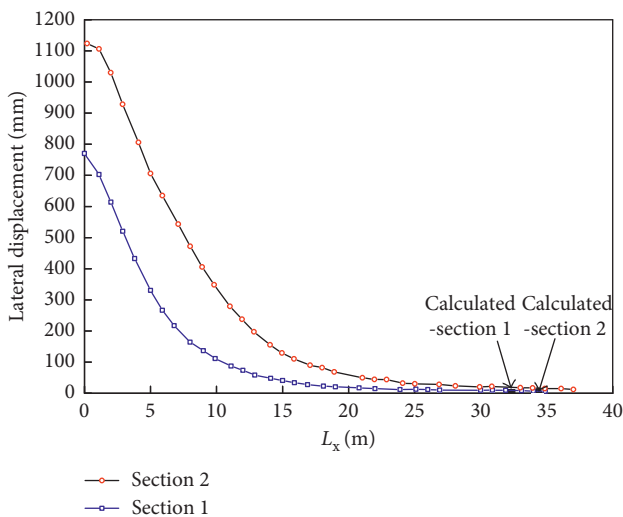


FIGURE 16: Variation of surface lateral displacement in the affected area.

7. Conclusions

The performance of vacuum preloading with PVDs was used to reinforce soft soils at the Oujiang, Wenzhou reclamation project. Based on the *in situ* measurements and subsequent

analyses, an empirical formula is proposed to calculate the influence scope of the vacuum preloading method. At the same time, the field case was simulated by the finite-element method. The safe distance away from the treated area is in agreement with simulated results. According to the work done in this paper, we can get the following conclusions:

- (1) When the soft soil foundation is consolidated using the vacuum preloading method, a generalisation formula of lateral deformation is proposed to calculate the lateral deformation of the soil at the affected area provided the soil properties of the affected area are known.
- (2) Based on the observed results of the case history, an empirical equation is proposed for calculating the influence scope of the vacuum preloading method.
- (3) According to the deformation analysis of the soil at the affected area, the safety distance between the reinforcement area boundary and the surrounding building should be determined to 34.32 m or more when the soft soil foundation is strengthened through vacuum preloading.

Data Availability

The authors worked with a reputable foundation treatment company and thus were accessible to the data. In the agreement

of their collaboration, any kinds of data including testing and records were owned by the company and thus are confidential to anybody else.

Conflicts of Interest

The authors declare that they have no conflicts of interest.

Acknowledgments

The presented work was supported by the National Key Research and Development Program of China (Grant no. 2016YFC0800203), Program of the International Science and Technology Cooperation (Grant no. 2015DFA71550), Programs of National Natural Science Foundation of China (Grant nos. 51778500, 51778501, 51622810, 51620105008, and 51478364), Key Research and Development Programs of Zhejiang Province (Grant no. 2018C03038), Natural Science Foundation Programs of Zhejiang Province (Grant nos. LR18E080001 and LY17E080010), and Programs of Science and Technology of Wenzhou (Grant nos. S20150015 and S20150030). These financial supports were gratefully acknowledged.

References

- [1] J. C. Chai, J. P. Carter, and S. Hayashi, "Ground deformation induced by vacuum consolidation," *Journal of Geotechnical and Geoenvironmental Engineering*, vol. 131, no. 12, pp. 1552–1561, 2005.
- [2] J. Wang, J. F. Ni, and Y. Q. Cai, "Combination of vacuum preloading and lime treatment for improvement of dredged fill," *Engineering Geology*, vol. 227, pp. 149–158, 2017.
- [3] C. Y. Ong and J. C. Chai, "Lateral displacement of soft ground under vacuum pressure and surcharge load," *Frontiers of Architecture and Civil Engineering in China*, vol. 5, no. 2, pp. 239–248, 2011.
- [4] G. Mesri and A. Q. Khan, "Ground improvement using vacuum loading together with vertical drains," *Journal of Geotechnical and Geoenvironmental Engineering*, vol. 138, no. 6, pp. 680–689, 2012.
- [5] Z. G. Jiang and Z. A. Yao, "Deformation and consolidation effect of soft soils treated by vacuum preloading method," *Geotechnical Engineering Technique*, vol. 1, pp. 36–38, 2005.
- [6] B. Indraratna, C. Rujikiatkamjorn, J. Ameratunga et al., "Performance and prediction of vacuum combined surcharge consolidation at port of brisbane," *Journal of Geotechnical and Geoenvironmental Engineering*, vol. 137, no. 11, pp. 1009–1018, 2011.
- [7] J. Wang, Y. Q. Cai, J. J. Ma, and J. Chu, "Improved vacuum preloading method for consolidation of dredged clay-slurry fill," *Journal of Geotechnical and Geoenvironmental Engineering*, vol. 142, no. 11, article 06016012, 2016.
- [8] G. Robinsonretnamony, I. Buddhima, and R. Cholachat, "Final state of soils under vacuum preloading," *Canadian Geotechnical Journal*, vol. 49, no. 6, pp. 729–739, 2012.
- [9] R. L. Kondner, "Hyperbolic stress-strain response: cohesive soils," *Journal of the Soil Mechanics & Foundations Division*, vol. 89, no. 1, pp. 115–143, 1963.
- [10] S. X. Chen, P. P. Ling, and S. Xiu, "Experimental study on deformation behavior of silty clay under unloading," *Rock & Soil Mechanics*, vol. 213, no. 4, pp. 548–566, 2007.
- [11] H. G. Poulos and E. H. Davis, *Elastic Solutions for Soil and Rock Mechanics*, John Wiley & Sons, New York, NY, USA, 1974.
- [12] J. C. Chai, N. Miura, and D. T. Bergado, "Preloading clayey deposit by vacuum pressure with cap-drain: analyses versus performance," *Geotextiles and Geomembranes*, vol. 26, no. 3, pp. 220–230, 2008.
- [13] Q. F. Zhu, C. S. Gao, and S. H. Yang, "Transfer properties of vacuum degree in treatment of super-soft muck foundation," *Chinese Journal of Geotechnical Engineering*, vol. 9, pp. 1429–1433, 2010.
- [14] Y. D. Wu, H. S. Wu, R. P. Luo, and C. C. Zeng, "Analytical solutions for vacuum preloading consolidation considering vacuum degree attenuation and change of permeability coefficient in smear zones," *Journal of Hehai University (Natural Sciences)*, vol. 2, pp. 122–128, 2016.
- [15] H. L. Li and W. Li, "Research on influence range of vacuum preloading for horizontal displacement of dredger-filled silt foundation," *Port Engineering Technology*, vol. 6, pp. 85–91, 2016.
- [16] Z. Z. Liu, J. W. Ding, and G. Wang, "Calculation method for vacuum preloading induced settlement considering vacuum degree attenuation," *Journal of Southeast University (Natural Science Edition)*, vol. 46, pp. 191–195, 2016.
- [17] D. W. Taylor, *Fundamentals of Soil Mechanics*, John Wiley & Sons Inc., New York, NY, USA, 1948.

Research Article

Calculation of Capillary Rise Height of Soils by SWCC Model

Yuhan Li ^{1,2,3}, Chen Zhang,¹ Chenghao Chen ¹ and Hao Chen ¹

¹Geotechnical Engineering Department, Nanjing Hydraulic Research Institute, Nanjing 210029, China

²Key Laboratory of Ministry of Education for Geomechanics and Embankment Engineering, Hohai University, Nanjing, China

³Jiangsu Research Center for Geotechnical Engineering Technology, Hohai University, Nanjing 210089, China

Correspondence should be addressed to Yuhan Li; 229197814@qq.com

Received 21 March 2018; Accepted 11 June 2018; Published 15 August 2018

Academic Editor: Annan Zhou

Copyright © 2018 Yuhan Li et al. This is an open access article distributed under the Creative Commons Attribution License, which permits unrestricted use, distribution, and reproduction in any medium, provided the original work is properly cited.

The maximum capillary rise height of soil is a complex system which is mainly determined by the distribution characteristics of soil pores. The tests of the rising height of capillary water on 8 kinds of soils by the method of vertical tube are widely conducted to measure the maximum capillary rise height. Based on the BCC model and principles of thermodynamics, the soil-water characteristic curve test is designed for the purpose of calculating the pore distribution of soil samples. A new method for calculating the maximum capillary rise height of soil is proposed by the author by using the distribution function of the soil pore. The coefficient β which reflects the relationship between the maximum capillary rise and the average pore radius of soils is utilized during the calculation process, and then the reference range of β for different soils is obtained according to series of experiments corresponding. The proposed calculation method offers an effective way to calculate the maximum capillary rise height, which can be applied to analyze the capillary effect area of relevant engineering problems.

1. Introduction

Capillary-driven liquid flow is the main transport mechanism in the soil system of which the water erodes continuously by capillary rise from a lower elevation to higher elevation. Such capillary rise phenomena lead to an increase of the saturation of the soil, which will not only decrease the strength of the soil but also alter the elastic modulus of substructure soils, thereby leading to the corresponding changes in stress and strain response under the external load, for example, the traffic load. Therefore, the defect of the roadbed is closely related to capillary rise erosion. Seasonally frozen ground has always been an important problem in highway construction and channel slope at high latitudes. In the research of frost heaving zone, it is inevitable to determine the height of capillary rise of the substructure. For channel slope and embankment close to the riverside, capillary action path is shortened as well as the effect of capillary action on the supply of water is accelerated. As a result, these infrastructures are more prone to defect and frost heave in such particular areas because of capillary rise. To sum up, study of capillary rise, particularly the maximum

capillary rise height, is of great significance to the design of the substructure and channel because the maximum capillary rise height is tightly connected to the strength reduction region and frost area.

A series of studies have been carried out on the capillary rise; LU offered a complete analytical solution for the relationship between the rate and time of capillary rise in soils [1]. However, in the equation, the maximum height of capillary rise h_c is a known soil parameter. In other words, the accurate determination of the maximum height of capillary rise is the prerequisite to calculate the rate of capillary rise. The maximum height of capillary rise has an important influence on the overall engineering behavior of unsaturated soils and is a highly complex system of both the soil and pore water properties. It is extremely difficult to calculate the maximum capillary height accurately in real soils. In order to overcome this, scholars have done a lot of studies and have put forward some empirical formulas which established the correlation between the maximum capillary height and certain measured soil parameters. The earliest formula was proposed by Lane and Washburn [2, 3], after conducting the capillary rising test for 8 kinds of

different soils, and the result shows that the maximum capillary height is linear with $\ln D_{10}$:

$$h_c = -990(\ln D_{10}) - 1540. \quad (1)$$

On the basis of (1), Peak and Hansen put forward another empirical formula [4]:

$$h_c = \frac{C}{eD_{10}}. \quad (2)$$

In this formula, 10% particle size d_{10} , void ratio e , and the coefficient C ($C = 3 \times 10^{-5} \text{ m}^2 \sim 8 \times 10^{-5} \text{ m}^2$) are used to calculate the maximum capillary rise height. However, the coefficient C is difficult to choose because the range of C is relatively large, and the value of C depends hugely on the real condition of soil. Kumar and Malik by carrying out indoor tests summarized as follows [5]:

$$h_c = h_a + 134.84 - 5.16\sqrt{r}, \quad (3)$$

where h_a is the height corresponding to air-entry pressure value of soils and r is the equivalent of capillary radius of soils. In this formula, the unit of r is μm , so it has little influence on the result of the calculation. Therefore, h_a is the only key computational parameter which can be determined by the soil-water characteristic curve. However, it requires an instrument to control the matric suction very precisely especially when the suction is less than 1 kPa [6].

We summarized that according to previous research results, using the micropore distribution of soils and using the pore radius parameter instead of the gradation parameter and void ratio are effective methods to accurately calculate the maximum capillary rise height. In this paper, a new method is proposed to calculate the maximum capillary rising height by using the radius of microscopic pore distribution. A large number of capillary rise tests as well as soil-water characteristic (SWCC) tests have been done for different kinds of soils, from which the parameters of different soils required for the calculation are obtained, and the feasibility of this method will be verified.

2. Theoretical Framework

2.1. Capillary Rise Equilibrium Equation in Soil System. In a single capillary when water column reaches the maximum height, the gravity of the water column is balanced by the surface tension along water-solid interface, as shown in Figure 1. The balance equation is as follows:

$$h_c \rho_w g \pi r^2 = T_s \pi d \cos \alpha, \quad (4)$$

where α is the liquid-solid contact angle; ρ_w is the density of water; r is the radius of the capillary channel ($r = d/2$); and T_s is the surface tension of water.

For soils, we regard it as homogenous porous media, which means the pores inside are similar in diameter and the dispersion is small. In the interior of soils, tiny pores which are connected with each other fulfill the precondition of capillary rise [7, 8]. The total capillary gas-liquid area A in each cross section can be expressed as follows:

$$A = \phi_A \pi \left(\int_0^\infty r f(r) dr \right)^2, \quad (5)$$

where ϕ_A is the number of gas-liquid interfaces in total capillary gas-liquid area A of each cross section and $f(r)$ is pore size distribution (PSD) function in the porous system of soils [9, 10]. When we established the gravity-tension balance equations assuming that soil pores are interconnected with each other, the capillary migration path of water is not like a single capillary tube, meaning that channel interleaving was bent and most of the gas-liquid interfaces on the same section are connected. As a simplified model, we argue that the total capillary route is equal to the maximum capillary rise height h_c multiplied by a path retardation coefficient β ; thereafter, the capillary equilibrium equation for any gas-liquid interface can be modified from (4) to

$$h_c \rho_w g \pi \left[\int_0^\infty r f(r) dr \right]^2 \beta = 2T_s \pi \int_0^\infty r f(r) dr, \quad (6)$$

$$h_c = \frac{2T_s \cos \alpha}{\rho_w g \beta \int_0^\infty r f(r) dr}. \quad (7)$$

When $\rho_w = 1 \text{ g/cm}^3$, $g = 980 \text{ cm/m}^2$, $T_s = 72 \text{ mN/m}$, and $\alpha = 0^\circ$ (dehydration process), (7) can be simplified as follows:

$$h_c = \frac{0.15}{\beta \int_0^\infty r f(r) dr}. \quad (8)$$

2.2. Testing Method of PSD $f(r)$. One effective way to study the pore characteristics of homogenous porous media is to establish the microscopic pore structure model. Many conventional models for pore characteristics, liquid distribution, flow, and transport in porous media are based on representing pore space geometry as a bundle of cylindrical capillaries (BCC model) [11, 12]. In the literature, there have been some standardized experimental methods for directly measuring pore size distribution (MIP, mercury intrusion porosimetry; BM, bubble method), and these methods are based on the basic theory of the BCC model. In BCC model, according to the Young-Laplace equation, the relationship between the pore radius r and the suction S (or capillary pressure) is represented as follows:

$$S = 2T_s \cos \frac{\alpha}{r}. \quad (9)$$

Based on the assumption of pore local equilibrium, the balance of soil is achieved in a given suction S^* inside the pore while one part of the pore with the pore radius greater than r^* ($r^* = 2T_s \cos \alpha / S^*$) is filled with air and the other one with pore radius less than r^* is filled with water. By defining $g(r)$ as pore size distribution function, $g(r) dr$ represents the percentage of void volume with pore radius ranging from r to $r + dr$ under the unit soil volume. When the suction of the soil reaches S , the maximum pore radius which is filled with water becomes C/S ($C = 2T_s \cos \alpha$). Therefore, the relationship between soil volumetric water content and pore distribution can be expressed as follows:

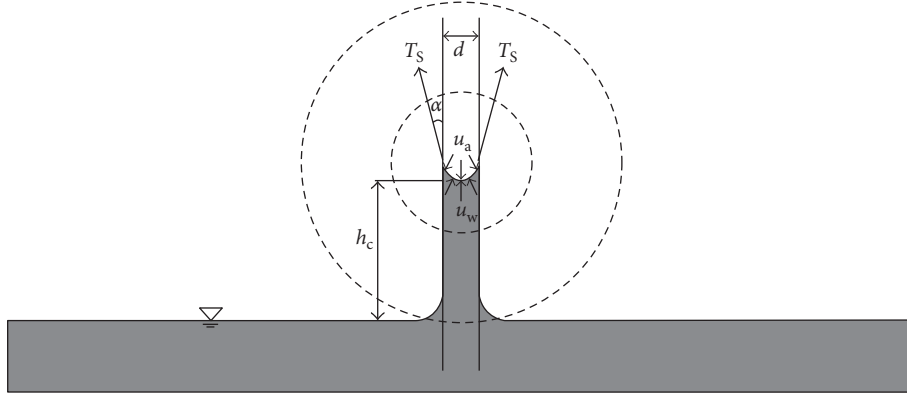


FIGURE 1: Mechanical equilibrium of capillary rise in the small diameter tube.

$$d\theta = g(r) dr. \quad (10)$$

In this formula, θ indicates the volumetric water content of soil when soil suction equals S and $d\theta$ represents the ratio of pore water volume with soil particle radius between r and $r + dr$ to the total pore water volume under a well-saturated condition. In fact, in this formula, the volume of water being evacuated is used as an alternative to that of void in the soil. When the calculated radius is in the range of the whole pore medium, $g(r)$ can be equal to $f(r)$.

In this paper, the pore size distribution of soil was measured, and the methods mentioned above have some limitations when being applied. Taking MIP as an example, sample preparation for MIP is difficult, and under high pressure, liquid mercury will jeopardize soil particles, resulting in the deformation of soil skeleton and pore during the test. Another important reason which restricts the widespread use of conventional methods is the low popularity of test instruments as well as high test costs, which forced us to look for other convenient testing methods. In this case, mercury is replaced by water, and the soil-water characteristic curve is utilized instead of the mercury injection curve. Pores among soil particles rather than the internal pore of the particle are mainly considered with regard to the soil capillary phenomenon and the pore water flow problem. When the soil-water characteristic curve is used, the pressure can be increased to 2 MPa, which means the pore radius can be attached to 1000 Å correspondingly. In other words, it can obtain the exact pore distribution of the above 1000 Å, allowing us to have enough pore radius distribution data to analyze soil capillary phenomenon.

2.3. Basic Theories and Calculation Method. The pore of soil can be regarded as a capillary in the Kelvin formula without violating original characteristics of soil system. Radius, contact angle between soil particles and pore water, and surface tension are denoted by r , α , and T_S , respectively. When using measurable physical quantities, Kelvin formula is expressed as

$$\frac{2T_S v_w \cos \alpha}{r} = -RT \ln \frac{u_{v1}}{u_{v0}} = \mu_1 - \mu_0, \quad (11)$$

where form of matric suction is described as

$$r = \frac{2T_S \cos \alpha}{u_a - u_w}, \quad (12)$$

where $R = 8.314 \text{ J}/(\text{mol} \cdot \text{K})$ is the universal gas constant; $T = 298 \text{ K}$ is the thermodynamic temperature; μ_{v0} (kPa) is the free water saturated vapor pressure in equilibrium state under the condition of temperature T . μ_{v1} (kPa) is the vapor pressure value of solution at the state of balance; $v_m = 18 \times 10^{-6} \text{ m}^3/\text{mol}$ is the partial molar volume of water vapor. $u_a - u_w$ is the matric suction, u_{v1}/u_{v0} is defined as relative humidity (RH) and can be obtained from (13) which is another expression of (11):

$$RH = \exp\left(-\frac{(u_a - u_w)v_w}{RT}\right). \quad (13)$$

When the relative humidity or matric suction is in the increment of Step i , the volume change of the pore volume of soil mass which is replaced by the gas can be calculated as

$$\nabla v_p^i = \frac{\nabla w^i}{\rho_w}. \quad (14)$$

Kelvin radius can be estimated by (12), while the actual pore radius is expressed as

$$r_p^i = r_k^i + t^i, \quad (15)$$

where the thickness of adsorbed water film t^i corresponding to RH or matric suction at Step i can be expressed by Halsey equation as [13]

$$t^i = \tau \left[-\frac{5}{\ln(RH^i)} \right]^{1/3}, \quad (16)$$

where τ is the effective diameter of adsorbed water molecules. Assuming that the cross-sectional area occupied by the water molecules is approximately 10.8 Å and the Avogadro constant N_A is $6.02 \times 10^{23}/\text{mol}$, the value of τ can be calculated as

$$\tau = \frac{v_w}{AN_A} = 2.77 \text{ \AA}. \quad (17)$$

TABLE 1: Main physical indexes of fine-grained soils.

Soil samples	$\gamma_{d(\max)}$	ω_p	ω_L	I_p	Particle size (mm) and content (%)				
					≥ 0.5 mm	0.25~0.05 mm	0.05~0.01 mm	0.01~0.002 mm	≤ 0.002 mm
CL	1.88	22.4	41.8	19.4	0.8%	13.4%	21.7%	34.5%	29.6%
CH	1.84	27.9	55.6	27.7	0.3%	9.5%	17.5%	37.1%	35.6%
ML	1.93	18.2	28.3	8.1	3.9%	29.6%	31.3%	25.4%	7.8%
CHE	1.83	28.3	65.2	36.9	0.2%	7.3%	16.5%	34.8%	41.2%

After terminating the calculation of pore radius which corresponds to different suctions, points can be selected in the SWCC to calculate the pore size distribution curve. Considering the nonuniform pore size and inhomogeneous pore distribution as well as the data of pore distribution curve obtained by point-selecting method, r_0 as average pore radius of soil by using weighted average of the statistical theory is defined as

$$r_0 = \frac{\sum v_p r_p^i}{\sum r_p^i} \quad (18)$$

Similar to the parameters of d_{10} , d_{60} , and C_u found in the particle size distribution curve, the average capillary pore radius can be obtained by pore size distribution curve. According to the definition, r_0 represents the average radius within the calculating range. For example, if suction value ranges from 1 kPa to 10000 kPa, then the r_0 is the average radius of the pore which falls into the corresponding range.

When the calculated aperture range relates to the whole soil (suction value ranges from the air-entry pressure value S_s to the residual suction S_r), we can approximate r_0 as $r_0 = \sum_{i=1}^n r_i/n$, by $\sum_{i=1}^n r_i \approx nE(r)$ where

$$E(r) = \int_0^\infty r f(r) dr. \quad (19)$$

We can easily argue that

$$\int_0^\infty r f(r) dr \approx r_0. \quad (20)$$

By conducting substitution of (20) to (8), (8) can be simplified as follows:

$$h_c = \frac{0.15}{\beta r_0}. \quad (21)$$

As a parameter, average pore radius r_0 characterizing the pore state can be obtained by SWCC, and path retardation coefficient β as an empirical parameter will be measured by the following tests.

3. Materials and Methods

3.1. Test Materials. The test soils are distinguished as two different kinds of soils: fine-grained soils and coarse-grained soils. Fine-grained soils include low liquid limit clay (CL), high liquid limit clay (CH), low liquid limit silt (ML), and high liquid limit expansive clay (CHE), while coarse-grained soils include silt sand (SS), fine sand (FS), medium sand (MS), and coarse sand (CS). The parameters of the soil

samples are obtained by the conventional tests and are shown in Tables 1 and 2.

3.2. Capillary Rise Test. The method of vertical tube (a transparent plexiglass tube with diameter of 4.5 cm and height of 500 cm) is applied when performing soil capillary rise test. 20 capillary plexiglass tubes with 8 kinds of soil samples are tested and the compaction degree of soils is controlled by the total density of soils during the sample loading process. The test results of the steady rising height of capillary water in different soil samples are shown in Table 3.

3.3. SWCC Test. SWCC is mainly determined by pressure plate method, in which four samples of each kinds of soil and the as-fabricated samples were placed in a vacuum saturator for 48 h to ensure the full saturation. PF moisture characteristic curve instrument (DIK-4303) is used for measuring soil-water characteristic curve. First of all, samples are weighted by using electronic balance to ensure that the mass is recorded. And then, samples are put into a determinator (4 samples at a time) which connects a water channel between the instrument and the ceramic plate. The upper cover should be well tightened in case of air leakage. The maximum pressure is set to 1200 kPa, which is controlled by the increment of each step of the 100 kPa, and before applying the pressure, each sample's gravimetric mass is recorded. The suction balance will be achieved if no water flows out from the pipe within 48 hours.

4. Analysis and Calculation

The results of the SWCC test are shown in Figures 2 and 3, but due to the design restriction in pressure plate method which means that a pressure over 1200 kPa cannot be exerted and maintained in the experiment, points exceeding 1200 kPa in SWCC are obtained by fitting with VG model [14]. To be precise, the datum acquired from the test is injected into Van-Genuchten model in ORIGIN to obtain soil-water characteristic curve in a wider range of suction. The fitting equation is

$$\theta = (\theta_s - \theta_r) \left[\frac{1}{1 + a^n (u_a - u_w)^n} \right]^m + \theta_r, \quad (22)$$

where θ is the volumetric water content; θ_s is the saturated volumetric water content; θ_r is the residual volumetric water content; and a , m , and n are independent coefficients (satisfy the condition $m = 1 - 1/n$ as much as possible). The fitting results from (22) for the soil samples are shown in Table 4.

TABLE 2: Main physical indexes of coarse-grained soils.

Soil samples	$\gamma_{d(max)}$	Particle size (mm) and content (%)							
		≥ 5 mm	5~2 mm	2~0.5 mm	0.5~0.25 mm	0.2~0.075 mm	0.07~0.01 mm	0.0~0.005 mm	≤ 0.005 mm
SS	2.08	0%	0.3%	1.2%	26.5%	41.8%	27.8%	2.1%	0.3%
FS	1.91	0%	1.6%	8.7%	34.4%	39.8%	13.8%	1.5%	0.2%
MS	1.84	1.9%	7.6%	17.5%	48.1%	19.9%	4.6%	0.3%	0.1%
CS	1.78	2.1%	11.6%	48.3%	32.7%	2.1%	1.2%	0.1%	0.1%

TABLE 3: The test results of the steady rising height of capillary water.

Sample	Compaction degree	Maximum height (cm)
CL	0.9	331
	0.85	317
	0.8	301
CH	0.9	355
	0.85	334
	0.8	315
ML	0.9	293
	0.85	267
	0.8	239
CHE	0.9	391
	0.85	358
	0.8	339
SS	0.9	194
	0.85	181
	0.8	159
FS	0.85	140
	0.8	121
MS	0.85	91
	0.8	81
CS	0.85	73

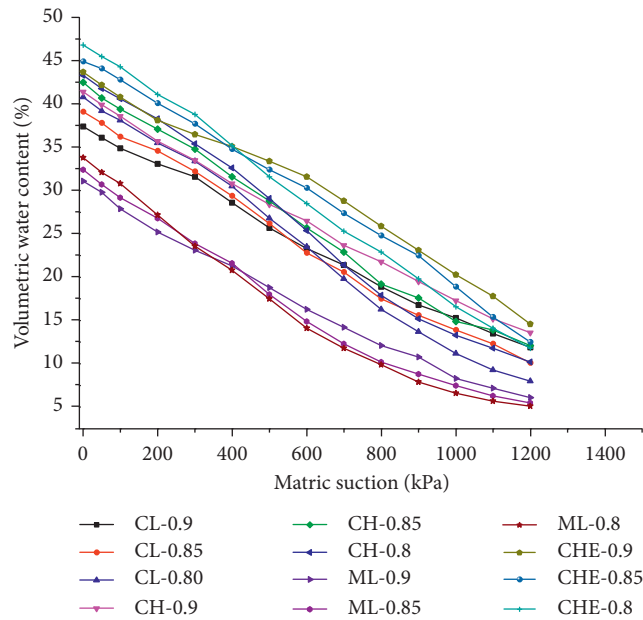


FIGURE 2: Soil-water characteristic curve test result for fine-grained soils.

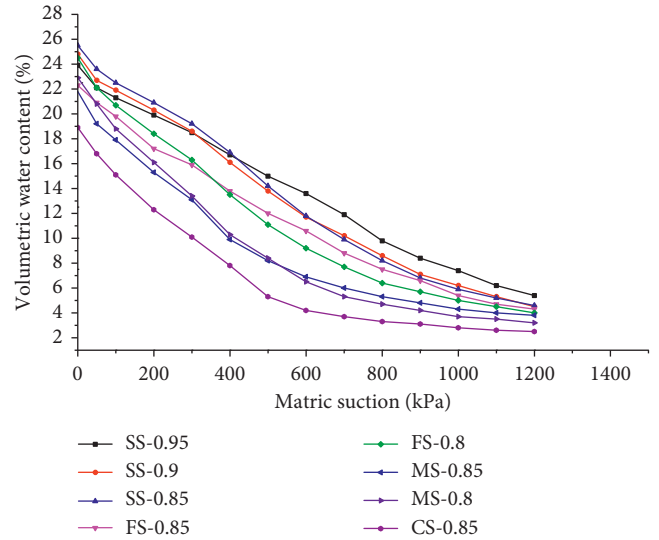


FIGURE 3: Soil-water characteristic curve test result for coarse-grained soils.

When selecting suction calculation range, the value range should be considered to represent the entity of soil as well as the measurement range of suction. After many attempts, we propose that fine-grained soils matric suction range be controlled at 200 kPa~10000 kPa and that the range of coarse-grained soils be controlled at 50 kPa~4000 kPa. (The external values of the test range are calculated by fitting the results of VG model.)

According to the theory introduced above, soil-water characteristic curve is used to calculate the radius r_0 . Calculation results of soil sample of CL with compaction degree 0.9 are listed in Table 5 as an example while the numerical integration calculation steps are as follows:

- (1) Get the SWCC of the soil and select the data of 200 kPa~20000 kPa (the data outside the range of test are obtained by fitting with VG model).
- (2) Calculate RH (relative humidity) of matrix suction according to (13).
- (3) Translate mass water content into per unit mass of soil-water filled pore volume (volumetric water content).
- (4) Use (12) to calculate the Kelvin radius r_k^i under the suction of different substrates with which the contact angle α is 0 (soil in dehydration process).

TABLE 4: Fitting results of SWCC parameters for soil samples.

Samples	rd	θ_s (%)	θ_r (%)	a	n	m
CL	0.9	38.2163	1.7842	0.0012	1.7798	0.6021
	0.85	39.9741	2.0259	0.0013	1.9266	0.5988
	0.8	40.5377	1.9624	0.0014	2.3215	0.5002
CH	0.9	41.3376	1.0621	0.0012	1.6198	0.5549
	0.85	42.2937	1.2063	0.0013	1.8688	0.4889
	0.8	43.2986	1.4079	0.0014	2.1398	0.4766
ML	0.9	30.6177	0.8823	0.0016	1.8423	0.4501
	0.85	31.7787	0.7213	0.0018	1.9932	0.4821
	0.8	33.1944	0.5056	0.0020	1.9161	0.4533
CHE	0.9	43.6997	2.2268	0.0010	2.0968	0.5001
	0.85	44.4501	0.9385	0.0012	2.0152	0.4896
	0.8	46.7998	1.3176	0.0013	1.9668	0.5102
SS	0.9	23.2396	0.7603	0.0014	1.9339	0.5983
	0.85	23.9630	0.5382	0.0017	1.9117	0.6021
	0.8	24.8004	0.6886	0.0017	2.0129	0.5891
FS	0.85	21.7180	0.2819	0.0018	1.6740	0.6213
	0.8	23.9116	0.5884	0.0022	1.6523	0.6011
MS	0.85	21.4904	0.3096	0.0026	1.3913	0.6542
	0.8	22.2219	0.2342	0.0027	1.5630	0.7311
CS	0.85	18.5616	0.1443	0.0033	1.5067	0.7001

TABLE 5: Equivalent radius calculated form of soil sample of CL with compaction degree 0.9.

$u_a - u_w$ (kPa)	W (g/g)	RH (%)	V_p (cm ³ /g)	r_k (Å)	t (Å)	r_p (Å)	Δv_p (cm ³ /g)	$(r_p)_{avg}$ (Å)	$\sum (V_p)$ (cm ³ /g)
200	0.176	99.85	0.176	7200	41.827	7241.8	—	—	—
300	0.168	99.78	0.168	4800	36.539	4836.5	0.008	6039.2	0.008
400	0.152	99.71	0.152	3600	33.198	3633.2	0.016	4234.9	0.024
500	0.137	99.64	0.137	2880	30.818	2910.8	0.015	3272.0	0.039
600	0.124	99.57	0.124	2400	29.001	2429.0	0.013	2669.9	0.052
700	0.114	99.49	0.114	2057	27.549	2084.7	0.010	2256.8	0.062
800	0.101	99.42	0.101	1800	26.349	1826.3	0.013	1955.5	0.076
900	0.089	99.35	0.089	1600	25.335	1625.3	0.011	1725.8	0.087
1000	0.081	99.28	0.081	1440	24.461	1464.5	0.008	1544.9	0.095
1100	0.072	99.20	0.072	1309	23.696	1332.8	0.010	1398.6	0.104
1200	0.063	99.13	0.063	1200	23.018	1223.0	0.009	1277.9	0.113
2000	0.054	98.56	0.054	720	19.414	739.4	0.009	981.2	0.122
4000	0.048	97.14	0.048	360	15.409	375.4	0.006	557.4	0.128
6000	0.036	95.74	0.036	240	13.461	253.5	0.012	314.4	0.140
10000	0.025	93.00	0.025	144	11.354	155.4	0.011	204.4	0.150
20000	0.018	86.48	0.018	72	9.011	81.011	0.007	118.2	0.158

- (5) Calculate the thickness of the water film t^i under the suction of different substrates by (16).
- (6) Calculate actual pore radius r_p^i by results (4) and (5) applying (15).
- (7) Calculate the reduction of pore volume water Δv_p in per unit mass of soil when the matrix suction is changed form one substrate to another. (Here, Δv_p is the pore volume corresponding to the water that is discharged.)
- (8) Calculate the average pore radius $(r_p)_{avg}$ in the process of evacuation of pore water by averaging the result of (6) for per step. (Here $(r_p)_{avg}$ is the average pore radius corresponding to the pore volume v_p .)
- (9) Add the pore volume to calculate the cumulative pore volume $\sum (V_p)$ of per unit mass, and draw

relationship diagram between the pore volume Δv_p and the average pore radius $(r_p)_{avg}$.

- (10) Calculate the r_0 by (18).

The average pore radius r_0 of soil sample is calculated by the method above. After determining the radius r_0 , the retardation coefficient β of different soil samples will be obtained. And the results of coefficient β are shown in Table 6.

As clearly observed from the above chart, the coefficient of the fine-grained soils was about 21 cm⁻² while the range barely fluctuates with value relatively fixed. But for coarse-grained soils, β changes from 23 cm⁻² to 26 cm⁻². One main reason we argue for coarse-grained soils is that the proportion of large pore size increased significantly, contributing greatly to a maximum capillary rise. As a result, for

TABLE 6: Calculation result of coefficient β for soil samples.

Sample	Compaction degree	Maximum height (cm)	Capillary radius (Å)	Coefficient β
CL	0.9	331	2128	21.3
	0.85	317	2212	21.4
	0.8	301	2336	21.3
CH	0.9	355	2014	21.0
	0.85	334	2107	21.3
	0.8	314	2234	21.4
ML	0.9	293	2359	21.7
	0.85	267	2650	21.2
	0.8	239	2881	21.8
CHE	0.9	391	1811	21.2
	0.85	358	1989	21.1
	0.8	339	2090	21.2
SS	0.9	194	3305	23.4
	0.85	181	3399	24.4
	0.8	159	3841	24.6
FS	0.85	140	4499	23.8
	0.8	121	4950	25.0
MS	0.85	91	6374	25.9
	0.8	81	7116	26.0
CS	0.85	73	7854	26.2

TABLE 7: Test and calculation results of maximum capillary rise height for 44 kinds of soils.

Test number	Soil sample	Void ratio e	d_{10} (cm)	Coefficient β (cm ⁻²)	h_a (cm)	Capillary radius (Å)	Measured height (cm)	Results by formula (e/er)/cm	Results by (1) (e/er)/cm	Results by (2) (e/er)/cm	Results by (3) (e/er)/cm
1	CL	0.89	0.001	21	178	2253	309	317 (8/2.5%)	530 (221/72%)	281 (-28/9.1%)	312 (3/1.0%)
2	CL	0.92	0.001	21	202	2158	325	331 (6/1.8%)	530 (205/63%)	271 (-54/17%)	336 (11/3.4%)
3	CL	1.05	0.0008	21	194	2070	324	345 (21/6.5%)	552 (228/70%)	297 (-27/8.3%)	328 (4/1.2%)
4	CL	0.88	0.0007	21	184	2268	319	315 (-4/1.3%)	565 (246/77%)	404 (85/27%)	318 (-1/0.3%)
5	CL	0.88	0.0009	21	192	2001	341	357 (16/4.7%)	540 (199/58%)	317 (-24/7.0%)	326 (-15/4.4%)
6	CL	0.81	0.001	21	199	2171	322	329 (7/2.2%)	530 (208/65%)	309 (-13/4.0%)	333 (11/3.4%)
7	CL	0.98	0.0011	21	195	2089	318	340 (22/6.9%)	520 (202/64%)	231 (-87/27%)	329 (11/3.5%)
8	CL	1.01	0.0007	21	180	2035	344	351 (7/2.0%)	565 (221/64%)	350 (6/1.7%)	314 (-30/8.7%)
9	CH	0.96	0.0008	21	214	2312	317	309 (-8/2.5%)	552 (235/74%)	327 (10/3.2%)	348 (31/9.8%)
10	CH	0.84	0.0006	21	231	2158	328	331 (3/0.9%)	580 (252/77%)	494 (166/51%)	365 (37/11%)
11	CH	0.73	0.0007	21	209	2165	343	330 (-13/3.8%)	565 (222/65%)	492 (149/43%)	343 (0/0%)
12	CH	0.96	0.0006	21	218	2232	329	320 (-9/2.7%)	580 (251/76%)	433 (104/32%)	352 (23/7.0%)
13	CH	1.01	0.0007	21	199	2158	315	331 (16/5.1%)	565 (250/79%)	355 (40/13%)	333 (18/5.7%)
14	CH	0.89	0.0009	21	233	2191	347	326 (-21/6.1%)	540 (193/56%)	310 (-37/11%)	367 (20/5.8%)
15	ML	0.74	0.0018	21	145	2421	288	295 (7/2.4%)	472 (184/64%)	186 (-102/35%)	279 (-9/3.1%)
16	ML	0.90	0.0025	21	165	2524	276	283 (7/2.5%)	439 (163/59%)	110 (-166/60%)	299 (23/8.3%)

TABLE 7: Continued.

Test number	Soil sample	Void ratio e	d_{10} (cm)	Coefficient β (cm ⁻²)	h_a (cm)	Capillary radius (Å)	Measured height (cm)	Results by formula (e/er)/cm	Results by (1) (e/er)/cm	Results by (2) (e/er)/cm	Results by (3) (e/er)/cm
17	ML	0.86	0.0029	21	137	2655	259	269 (10/3.9%)	424 (165/64%)	100 (-159/61%)	271 (12/4.6%)
18	ML	0.78	0.0031	21	131	2716	247	263 (16/6.5%)	418 (171/69%)	104 (-143/58%)	265 (18/7.3%)
19	ML	0.74	0.0043	21	158	2636	260	271 (11/4.2%)	385 (125/48%)	78 (-182/70%)	292 (32/12%)
20	ML	0.82	0.0019	21	122	2758	248	259 (11/4.4%)	466 (218/88%)	161 (-87/35%)	256 (8/3.2%)
22	MH	0.72	0.003	21	101	2892	236	247 (11/4.7%)	421 (185/78%)	116 (-120/51%)	235 (-1/0.4%)
23	MH	0.78	0.0022	21	95	2869	257	249 (-8/3.1%)	452 (195/76%)	146 (-111/43%)	229 (-28/11%)
24	MH	0.69	0.0037	21	88	3161	221	226 (5/2.3%)	400 (179/81%)	97 (-124/56%)	222 (1/0.5%)
25	MH	0.81	0.0042	21	94	2737	259	261 (2/0.8%)	388 (129/50%)	73 (-186/72%)	228 (-31/12%)
26	MH	0.72	0.0035	21	88	3079	240	232 (-8/3.3%)	406 (166/69%)	99 (-141/59%)	222 (-18/7.5%)
27	SM	0.62	0.009	25	78	4167	199	180 (-19/9.5%)	312 (113/57%)	40 (-159/72%)	211 (12/6.0%)
29	SM	0.60	0.0085	25	83	4121	204	182 (-22/10.8%)	318 (114/56%)	49 (-155/59%)	216 (12/5.9%)
30	SM	0.62	0.0081	25	80	4190	185	179 (-6/3.2%)	323 (138/75%)	50 (-135/80%)	213 (28/15%)
34	SS	0.42	0.019	25	58	4098	197	183 (-14/7.1%)	238 (41/21%)	31 (-166/84%)	191 (-6/3.0%)
35	SS	0.53	0.012	25	71	4167	184	180 (-4/2.2%)	284 (100/54%)	39 (-145/79%)	204 (20/10%)
36	SS	0.46	0.021	25	61	4491	178	167 (-11/6.2%)	228 (50/28%)	26 (-152/85%)	194 (16/9.0%)
37	SS	0.43	0.015	25	58	4190	180	179 (-1/0.6%)	262 (82/46%)	39 (-141/78%)	191 (11/6.1%)
38	FS	0.52	0.031	25	43	5474	139	137 (-2/1.4%)	190 (51/37%)	16 (-123/88%)	176 (37/27%)
39	FS	0.42	0.052	25	41	6356	110	118 (8/7.3%)	139 (29/26%)	11 (-99/90%)	174 (64/58%)
40	FS	0.49	0.047	25	39	6466	118	116 (-2/1.4%)	149 (31/26%)	11 (-107/91%)	172 (54/46%)
41	FS	0.42	0.055	25	42	7353	98	102 (4/4.1%)	133 (35/36%)	11 (-87/89%)	175 (77/79%)
42	MS	0.38	0.092	25	34	7732	86	97 (11/12.8%)	82 (-4/5%)	7 (-79/92%)	167 (81/94%)
43	MS	0.33	0.1	25	30	8152	83	92 (9/10.8%)	74 (-9/11%)	8 (-75/90%)	163 (80/96%)
44	MS	0.41	0.0864	25	29	8523	79	88 (9/11.4%)	88 (9/11%)	7 (-72/91%)	162 (83/105%)

(21) the numerical value of the coefficient β is considered to be 21 cm⁻² and 25 cm⁻² for fine-grained soils and coarse-grained soils, respectively.

5. Verification and Discussion

In this study, in order to verify the accuracy of the maximum capillary rise height formula proposed by the author, capillary rise tests are carried out on 44 kinds of soil samples, and thereafter, a comparison is made between the capillary

rise estimated from our equation (21) and the estimations from (1)–(3). Here, the coefficient C for (2) takes 5×10^{-5} m²

The test results and calculation results of the maximum capillary rise height for 44 kinds of soil samples are shown in Table 7.

It can be seen from the table that the estimating error of the maximum height from the formula proposed by the author is always less than 10% and the maximum error is 22 cm (204 cm), indicating its relatively higher accuracy compared with other formulas mentioned in this paper. This

also means that the results coincide better with the actual situation and have higher practical value.

Accurately determining the maximum capillary rise height of the soils is a complicated issue. In this paper, we calculated the average pore radius by method of SWCC and then determined the maximum capillary rise height using the pore radius. Obtaining the pore distribution data from the SWCC data is the core of the calculation method. We can easily get the pore distribution curve through the soil-water characteristic curve. However, similar to the particle size curve, we need to find a set of parameters to evaluate this curve as well as calculate the maximum capillary rise height. At first, we tried to use r_{50} as the evaluation parameter but later found when fine-soil samples are at different degrees of compaction, the r_{50} values are very close. According to the definition, as long as the soils have the same matrix suction at the saturation of 50%, the values of r_{50} still remain the same. It is difficult to use a specific pore radius to represent the equivalent capillary radius in the calculation of the maximum capillary rise height of the soil; therefore, we chose the weighted average of the pore radius r_0 as the calculation parameter. Whether there is a better way to evaluate the distribution of soil pore and to analyze the behavior of soils is a project that we still need to explore.

Another important parameter is β which is an empirical one obtained from the test. We use r_0 to distinguish different soil samples, so we hope different soil samples would obtain the same values of β as much as possible. Test results show that β of fine-grained soil is very close and can be directly taken to 21, but β also has the tendency to augment with the increase of average pore radius r_0 and this trend is particularly evident in coarse-grained soils. Therefore, there is an issue about how to pick the value of β in the actual calculation process and we argue that β of fine-grained soils can be fixed to 21, but for coarse-grained soil the value of β is not a settled figure, ranging from 24 to 26. Moreover, the value rises with the increase of the content of the coarse particles. Here the author suggests taking an average of 25.

6. Conclusion

After theoretical calculation and large numbers of indoor experiments, the following conclusions can be summarized as follows:

- (1) The average pore radius formula is deduced on summary of experiments and statistical theory, and the calculation theory can be used to distinguish the pore distribution characteristics of different compaction degree of soil samples with different particle size distribution. Therefore, it can offer references for similar research and also can be used for estimating the maximum height of capillary. In particular, for fine-grained soils the calculation results for the maximum capillary height are relatively accurate.
- (2) Using the soil pore radius to calculate the maximum capillary rise height is an accurate and feasible approach. During the calculation process, the coefficient β of the fine-grained soil was about 21 to 22,

while β of the coarse-grained soil was about 24 to 26. The greater the number of coarse particles is, the greater the retardation coefficient β is.

- (3) The maximum capillary rise height of the soil is mainly determined by the distribution of the large size pore, and meanwhile, the effect of the small size pore is quite insignificant.

Notations

h_c :	Maximum capillary rise height of soils
D_{10} :	Particle size d_{10} of soils
d_{10} :	Fine-grain diameter of ten percent of total soil mass
e :	Void ratio of soils
h_a :	Height corresponding to air-entry pressure value of soils
α :	Liquid-solid contact angle
r :	Radius of capillary channel
ρ_w :	Density of water
T_S :	Surface tension of water
A :	Total capillary gas-liquid area in each cross section
ϕ_A :	Number of gas-liquid interface in total capillary gas-liquid area A
$f(r)$:	Pore size distribution (PSD) function of soil
β :	Path retardation coefficient
S :	Matric suction
R :	Universal gas constant
T :	Thermodynamic temperature
μ_{v0} :	Free water saturated vapor pressure in equilibrium state under the condition of temperature T
μ_{v1} :	Vapor pressure value of solution at the state of balance
v_m :	Partial molar volume of water vapor
u_a :	Pore air pressure
u_w :	Pore water pressure
RH:	Relative humidity
v_p :	Pore volume of soil
r_k :	Kelvin pore radius
r_p :	Actual pore radius
t :	Thickness of adsorbed water film
τ :	Effective diameter of adsorbed water molecules
N_A :	Avogadro constant $6.02 \times 10^{23}/\text{mol}$
d_{60} :	Fine-grain diameter of 60 percent of total soil mass
C_u :	Nonuniform coefficient of soil
r_0 :	Average pore radius
θ :	Volumetric water content
θ_S :	Saturated volumetric water content
θ_r :	Residual volumetric water content
a, m, n :	Independent coefficients of VG model.

Data Availability

The data used to support the findings of this study are available from the corresponding author upon request.

Conflicts of Interest

The authors declare that they have no conflicts of interest.

Acknowledgments

This study was supported by the National Natural Science Foundation of China (Grant no. 51709185). Interactions with research engineers at State Key Laboratory of Hydrology-Water Resources and Hydraulic Engineering, Nanjing Hydraulic Research Institute, People Republic of China, were very helpful in this work.

References

- [1] N. Lu and W. J. Likos, "Rate of capillary rise in soil," *Journal of Geotechnical and Geoenvironmental Engineering*, vol. 130, no. 6, pp. 646–650, 2004.
- [2] K. S. Lane and D. E. Washburn, "Capillary tests by capillary meters and by soil filled tubes," *Proceedings of Highway Research Board*, vol. 26, no. 9, pp. 460–473, 1946.
- [3] L. L. Handy, "Determination of effective capillary pressures for porous media from imbibition data," *Transactions of the Metallurgical Society of AIME*, vol. 219, pp. 75–80, 1960.
- [4] R. B. Peck and W. E. Hansen, *Foundation Engineering*, Wiley, New York, NY, USA, 2nd edition, 1994.
- [5] S. Kumar and R. S. Malik, "Verification of quick capillary rise approach for determining pore geometrical characteristics in soils of varying texture," *Soil Science*, vol. 150, no. 6, pp. 883–888, 1990.
- [6] D. G. Fredlund and H. Rahardio, *Soil Mechanics for Unsaturated Soils*, Wiley & Sons Inc., New York, NY, USA, 1993.
- [7] N. Fries and M. Dreyer, "Dimensionless scaling methods for capillary rise," *Journal of Colloid and Interface Science*, vol. 338, no. 2, pp. 514–518, 2007.
- [8] B. A. Faybishenko, "Hydraulic behavior of quasi-saturated soils in the presence of entrapped air: laboratory experiments," *Water Resources Research*, vol. 31, no. 10, pp. 2421–2435, 2009.
- [9] D. Geng, Y. Wang, and Y. Li, "Study on the pore radius of unsaturated soil," *Geo-China (ASCE)*, vol. 265, pp. 102–111, 2016.
- [10] F. J. Griffiths and R. C. Goshi, "Changes in pore size distribution due to consolidation of clays," *Geotechnique*, vol. 39, no. 1, pp. 159–167, 1999.
- [11] S. Sasanian and T. A. Newson, "Use of mercury intrusion porosimetry for microstructural investigation of reconstituted clays at high water contents," *Engineering Geology*, vol. 158, no. 8, pp. 15–22, 2013.
- [12] L. M. WillArya and J. F. Paris, "A physic-empirical model to predict the soil moisture characteristic from particle-size distribution and bulk density data," *Soil Science Society of America Journal*, vol. 45, no. 6, pp. 1023–1030, 1981.
- [13] G. D. Halsey, "Physical adsorption on non-uniform surfaces," *Journal of Chemical Physics*, vol. 16, no. 10, pp. 931–937, 1948.
- [14] M. T. van Genuchten, "A closed form equation for predicting the hydraulic conductivity of unsaturated soils 1," *Soil Science Society of America Journal*, vol. 44, no. 5, pp. 892–899, 1980.

Research Article

Microstudy of the Anisotropy of Sandy Material

Kunyong Zhang ^{1,2}, Zhenjun Zang ^{1,2}, Leslie Okine,^{1,2} and Jose Luis Chavez Torres ^{1,2}

¹Key Laboratory of Ministry of Education for Geomechanics and Embankment Engineering, Hohai University, Nanjing 210098, China

²Institute of Geotechnical Engineering, Hohai University, Nanjing 210098, China

Correspondence should be addressed to Kunyong Zhang; ky_zhang@hhu.edu.cn

Received 21 May 2018; Accepted 9 July 2018; Published 14 August 2018

Academic Editor: Xinbao Yu

Copyright © 2018 Kunyong Zhang et al. This is an open access article distributed under the Creative Commons Attribution License, which permits unrestricted use, distribution, and reproduction in any medium, provided the original work is properly cited.

Through numerical simulation based on the particle flow method, DEM numerical test samples were generated with the results of laboratory tests on standard sand. The method consists of the use of gravity deposition and radius expansion modeling of irregular sand particles, where samples of the biaxial test are assembled by generated long particle units. Different steps of deposition or initial stresses were applied during the sample generation process in order to simulate different sample states. The loads from the horizontal and vertical directions are, respectively, applied to samples, and then the stress-strain curve and macroscopic mechanical parameters are acquired. The numerical experiment results show that the gravitational deposits have significant impact on the major axis orientation arrangement of particles and on the average coordination number, as well as the initial stress has a significant effect on it. There is a remarkable effect on the stress-strain curve and on the acquired mechanical parameters as a result of the application of load to samples from the horizontal and vertical directions. The sand samples show an obvious property of inherent anisotropy and stress-induced anisotropy.

1. Introduction

Sand is composed of discrete particles. The gradation, shape, size, and physical properties of particles determine the macromechanical properties of sand under different stress conditions. Anisotropy is a typical characteristic of sand.

There are two types of sand anisotropy: inherent anisotropy and stress-induced anisotropy. Inherent anisotropy means that irregular particles show a tendency of directional arrangement because its particle structure is influenced by external factors like gravity and water in the deposition process. This directional arrangement has an effect on the microstructure of the sand and also shows the anisotropy in the macroscopic mechanical properties [1–3]. Stress-induced anisotropy means that the change of the stress state leads to the change of the mechanical properties and parameters of the sand when complex load is applied in different directions [4, 5]. Considering the microscopic mechanism of anisotropy, both the inherent anisotropy and stress-induced anisotropy can be attributed to the structural

properties of the material itself. As sand particles have a nonspherical structure, this makes the particle arrangement, contact, and microstructure change under the action of the external load, which results in a macroscopic anisotropy.

From the macroscopic view, the main reason for the inherent anisotropy of sand is that the particles are arranged along the principal stress direction during the gravitational deposition process, and finally, the difference between the vertical and horizontal mechanical properties is formed on the macroscopic scale. The inherent anisotropy can be described by the elastic theory: vertical elastic modulus E_v and Poisson's ratio ν_v , horizontal elastic modulus E_h and Poisson's ratio ν_h , and shear strength G . In addition to the above, the vertical modulus E_v is greater than the horizontal modulus E_h . In terms of stress-induced anisotropy, Zhang and Yin [6] found that the stress-strain relationship of the soil under the complex stress state shows significant stress anisotropy, based on the true triaxial test. The internal mechanism of the inherent anisotropy and the stress-induced anisotropy is that

the external conditions (gravity, load, water, etc.) change the microstructure of the soil, and thus, the soil shows different stress and deformation characteristics macroscopically. Based on the true triaxial test, Hoque and Tatsuoka [7] also concluded that the elastic modulus in the horizontal and vertical directions of the soil showed significant anisotropy under nonisotropic loading.

PFC2D (particle flow code in 2 dimensions) [8] is the general-purpose code based on discrete element method (DEM) put forward by Cundall [9], which simulates movement and interaction of granular media, confirming particle's location and velocity in every moment according to the motion equation of translator motion and rotation. In this paper, PFC2D was used to establish several sets of irregular sand particles, to reveal the formation and development mechanism of soil anisotropy, by simulating the biaxial compression numerical test of standard sand, and loading from the horizontal and vertical directions, respectively. Then, the stress-strain curve and the mechanical parameters were obtained in different directions, and the microscopic mechanism of two anisotropic conditions is explained by the micromechanic parameters such as the average coordination number and the normal contact force of the particles.

2. Introduction of the PFC2D and the Numerical Specimen

2.1. DEM and PFC2D. Most of the former laboratory experiments and theoretical studies on soil anisotropy have assumed that the soil is a continuous and isotropic medium. Limited to the theoretical basis and experimental conditions, microanalysis of the structural causes of soil anisotropy cannot be carried out. DEM and PFC provide the conditions for microanalysis on the basis of traditional continuous medium research [10, 11].

The macroscopic mechanical behavior of the material analyzed in PFC was conducted by studying the microscopic parameters of the particles and obtaining the relationship between the microstructure and the macroscopic mechanical behavior. Chi [12] used PFC to simulate the formation and development of sand shear zone, and the principle governing sand was obtained under different confining stress. Jiang et al. [13] studied the formation mechanism of the soil shear zone by discrete element simulation of the plane strain biaxial test. Tong et al. [14] used the DEM to analyze the microstructures of anisotropic particles from the orientation of the major axis and void ratio of the particles. These studies have analyzed the effect of the change of microstructure on the macroscopic mechanical behavior of soil, which proved that PFC is an effective and powerful tool. In this paper, PFC2D is also used to study the anisotropic behaviors of sands under complicated stress states.

2.2. Method for Numerical Sample Preparation

2.2.1. The Calibration of Numerical Sample Parameters

(1) The Results of Fujian Standard Sand in Laboratory Tests. This paper is based on the laboratory triaxial test of Fujian

sand [15] to calibrate the parameters. Fujian standard sand is a kind of well-graded medium sand. The macroscopic parameters obtained in triaxial tests are shown in Table 1.

In Table 1, E_{50} is the secant deformation modulus, corresponding to the slope of the stress-strain curve at half the peak intensity. ν_{50} is the secant Poisson's ratio, which is on the lateral strain-loading direction strain curve, corresponding to half of the peak intensity cut line ratio, and φ is the internal friction angle calculated from the peak intensity of the stress-strain curve. They are calculated using following equations:

$$\begin{aligned} E_{50} &= \left(\frac{\Delta\sigma_1}{\Delta\varepsilon_1} \right)_{50}, \\ \nu_{50} &= \frac{1}{2} \left[1 - \left(\frac{\Delta\varepsilon_v}{\Delta\varepsilon_1} \right)_{50} \right], \\ \varphi &= \arcsin \left(\frac{\sigma_{1f} - \sigma_{3f}}{\sigma_{1f} + \sigma_{3f}} \right), \end{aligned} \quad (1)$$

where $\Delta\sigma_1$ is the major principal stress increment, $\Delta\varepsilon_1$ is the strain increment in the direction of the major principal stress, $\Delta\varepsilon_v$ is the volumetric strain increment, and σ_{1f} and σ_{3f} are the major principal stress and the minor principal stress at the peak intensity, respectively.

(2) Numerical Test Environment. The calibration of the microscopic parameters is determined by comparing the numerical results with the laboratory test results. The results of the laboratory test in this paper are the results of the triaxial test of Fujian standard sand described above. The numerical sample is a two-dimensional specimen, and PFC2D was used to simulate the biaxial test. The model for the numerical sample is shown in Figure 1.

h and w represent the height and width of the numerical sample, respectively.

(3) The Generation and Loading of Numerical Samples. Original PFC2D particles are standard discs, which differ greatly from the irregular shape of the actual sand particles. In order to simulate the irregular structure of the actual sand particles, several disc particles were assembled into a complex shape block, and relative deformation and displacement between the disc particles were limited. Only the contact between the blocks was taken into account without regarding the contact and force transfer between the disc particles constituting the block. The soil particles used in this paper are composed of three discs, and the comparison with the standard sand is shown in Figure 2. The center of the three disc particles is on the same line, and the angle θ is the major axis orientation angle of the irregular element (the angle between the horizontal axis and that through the center line of the irregular element).

The numerical sample is formed by the radius expansion method as described by the following steps:

(1) Two-dimensional space was generated having a width and height of 50 mm and 105 mm,

TABLE 1: Macroscopic parameters of Fujian sand in laboratory tests.

E_{50} (MPa)	ν_{50}	φ (°)
44.3	0.3	41.2

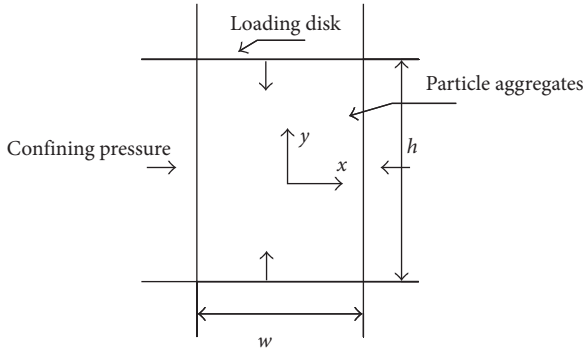


FIGURE 1: Model for the numerical sample.

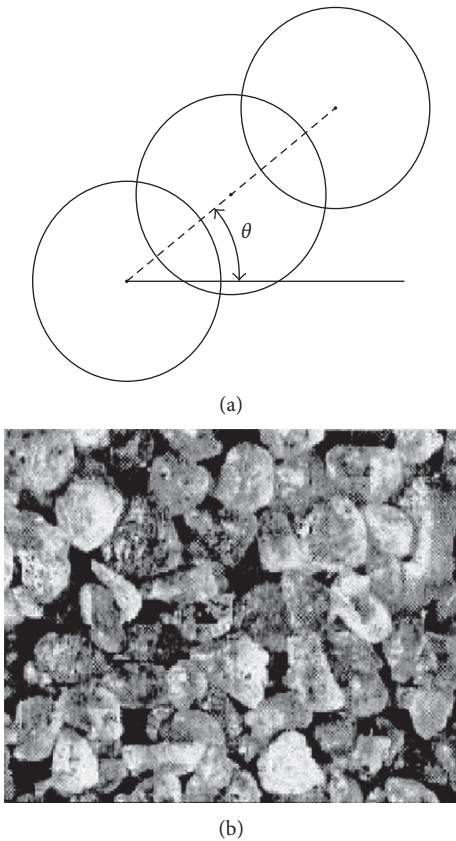


FIGURE 2: Comparison between irregular element and Fujian sand.

respectively, as shown in Figure 3(a), and the radius expansion method was used to generate disc particles with parameters, as shown in Table 2. The disc particles were evenly distributed, as shown in Figure 3(b). In order to reduce the effect of particle size, the ratio of the size of the biaxial specimen to the particle size satisfies $L/R > 30$, so the minimum and maximum particle sizes of the particles were kept as 0.6 mm and

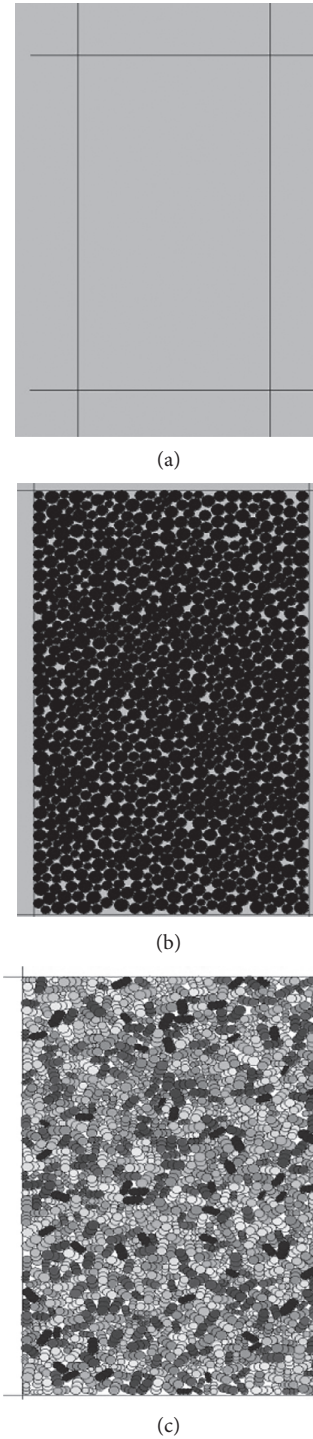


FIGURE 3: Process of generating numerical samples: (a) generating wall; (b) generating disc unit samples; (c) generating long unit samples.

1.2 mm. The porosity area was 0.15, and its macroscopic mechanical properties were close to the dense sand.

- (2) A program was coded using the FISH language in PFC to record the center position and radius of the two-dimensional disc particles, and then the disc

TABLE 2: Microscopic parameters of samples at the initial state.

k_n (Pa)	k_n/k_s	f	R_{max} (mm)	R_{min} (mm)	n
$2e8$	2	0.5	1.2	0.6	0.18

Note: k_n is the normal stiffness of the particles, k_s is the tangent stiffness of the particles, k_n/k_s is the tangential stiffness ratio, f is the coefficient of friction, R_{max} is the maximum radius of the particles, R_{min} is the minimum radius of the particles, and n is the porosity (area porosity).

particles were removed. In the same position, the irregular elements were generated according to the principle of "Area and mass equivalent." The major axis orientation of the irregular elements was 0° to 180° randomly distributed, as shown in Figure 3(c).

After the test was completed, the confining pressure and the load were applied and subjected to a biaxial test. By adjusting the initial sample parameters in Table 2, the macroscopic mechanical properties exhibited by the sample were consistent with the laboratory triaxial test results.

2.2.2. Parameter Calibration Results. The initial microscopic parameters were adjusted until the macroscopic parameters of the model were similar to the macroscopic parameters obtained by the ordinary triaxial test. The final microscopic parameters of the standard sand in Fujian are shown in Table 3.

The macroscopic mechanical parameters, axial stress, and axial strain curves obtained from numerical experiments and the comparison with laboratory test results are shown in Table 4 and Figure 4.

From Table 4 and Figure 4, the parameter calibration of the irregular unit is basically the same as that of Shi [15] and the laboratory test results. However, from Figure 4, the numerical model results of this paper are closer to the laboratory test results. This also shows that the irregular particle unit is more suitable to simulate the real structure of the sand, and the numerical simulation of Fujian standard sand with the irregular particle unit is more realistic, and therefore, the numerical test of the wider stress path can be carried out on the basis of this sample.

3. Standard Sand Numerical Test Process and Results

3.1. Sample Preparation. In order to find out the difference and relationship between the inherent anisotropy and stress-induced anisotropy of the sand, the same method and test environment and parameters were used for the anisotropic numerical samples.

(1) Test Environment and Parameters. The biaxial test is carried out with the experimental environment shown in Figure 2, and the expected size of the specimen was $60\text{ mm} \times 60\text{ mm}$. The particle unit of the biaxial specimen was the irregular unit, and the microscopic parameter of the sample particle was calibrated with the parameter, as shown in Table 3.

TABLE 3: Microscopic parameters of samples at the final state.

k_n (Pa)	k_n/k_s	f	R_{max} (mm)	R_{min} (mm)	n
$1.3e8$	3	0.5	1.2	0.6	0.15

TABLE 4: Parameters of numerical simulation and laboratory test.

Fujian standard sand	Initial modulus (MPa)	Poisson's ratio	Internal friction angle ($^\circ$)
Laboratory test	44.3	0.30	41.2
Shi [15]	48.4	0.34	41.0
This article	43.3	0.27	40.8

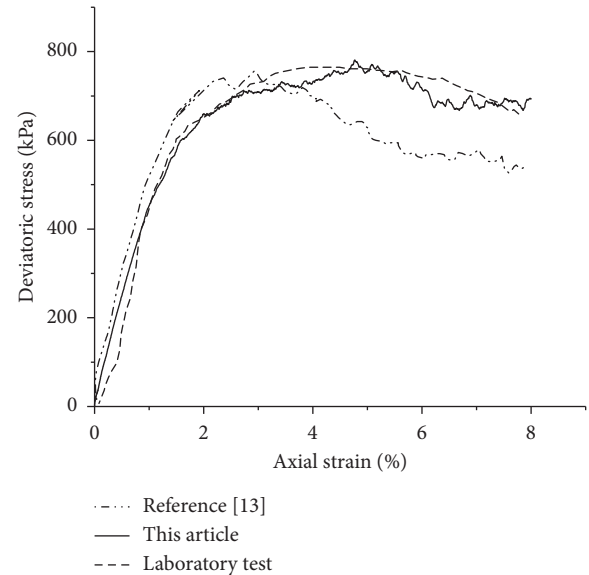


FIGURE 4: Curves of numerical simulation and laboratory test.

(2) Sample Generation. The two-axis numerical sample generation steps are as follows: firstly, a two-dimensional space of 100 mm and a width of 60 mm were generated, and then microscopic parameters were generated in the space. The particle gradation follows a uniformly distributed disc particle, and irregular units were generated by using the program coded in the FISH language in PFC. The initial major axis of the regular element was randomly distributed. The original top wall was deleted, and a new top wall was regenerated at a height of 60 mm . Finally, the particles above the new wall were removed, and the numerical sample was generated.

3.2. Sample Loading and Control

3.2.1. The Stress Path of the Inherent Anisotropy. The basic unit used in this test is an irregular unit which is under the action of gravity deposition, and the major axis orientation of particles was arranged in a specific direction. In order to simulate the effect of soil deposition on the microstructure and macroscopic mechanical properties of soil particles, the gravity was applied to the irregular unit, and the sedimentation occurred under the action of gravity. Three sets of

samples were generated according to the number of gravity deposition sample steps, and then the gravity load was removed. The confining pressure of 100 kPa was applied to make the sample reach the initial equilibrium state. Sample number, the number of deposition steps, and the subsequent loading direction are shown in Table 5.

In Table 5, each set of samples which has the same letter used the same number of gravity deposition steps. A slight initial stress was imposed in the horizontal and vertical directions to keep the sample stable. The stress increment was applied firstly in the horizontal direction and then the vertical direction to compare the macroscopic mechanical properties in the horizontal and vertical directions with the same initial sample. The number of deposition steps in Table 5 refers to the time step in order to make the numerical calculation stable and select the time less than a critical time step, which is related to the frequency of each particle unit.

The numerical test stress path is shown in Figure 5.

3.2.2. The Stress Path of the Stress-Induced Anisotropy.

In this experiment, six samples were divided into three sets according to the initial stress state (Table 6). The initial stress state of the two samples in each set was the same, and then three groups of samples were loaded from the horizontal and vertical directions, respectively. The stress-strain curves and macroscopic mechanical parameters of the samples in different directions were obtained. The stress path of the numerical test is shown in Figure 6.

3.3. Test Results. The stress-strain curves obtained from the horizontal and vertical loading are shown in Figure 7, and the relative mechanical parameters are shown in Table 7. The initial modulus refers to the stress and strain ratio when the strain of the load direction reaches 1%.

From Figures 7(a)–7(c), it can be seen that the stress-strain curves of the three groups show a common principle: the stress peak and the initial modulus at the time of loading in the vertical direction (deposition direction) are larger than those in the horizontal direction. Since the two samples in each set of tests experienced the same number of gravitational steps, they had the same porosity, cell size and sample size, and the initial state. The only difference between the two samples is that the load increment was applied in the horizontal direction for one and the other was loaded from the vertical direction. The macroscopic mechanical response in different directions shows obvious anisotropy. From the stress and strain curves of different deposition steps, it can be noticed that the larger the number of deposition steps, the greater the peak stress.

From Figures 7(d)–7(f), the stress-strain curves obtained from the minimum principal stress direction (horizontal direction) of the three sets are higher than those obtained by loading from the maximum principal stress direction. The initial elastic modulus and the stress peak are larger than those obtained from the maximum principal stress direction. With the increase of the initial stress difference in the horizontal and vertical directions, the difference of the

TABLE 5: List of samples and test parameters.

Sample number	Gravity deposition steps	Loading direction
A1	90000	Horizontal
A2		Vertical
B1	120000	Horizontal
B2		Vertical
C1	150000	Horizontal
C2		Vertical

relevant mechanical parameters is also more obvious. It shows that the specimen exhibits obvious anisotropy after being subjected to unequal stress.

In the inherent anisotropic soil, the major axis orientation arrangement of the soil particles forms a macroscopic anisotropic layered foundation, making the elastic modulus of the deposition direction (i.e., vertical direction) larger than that of the horizontal direction.

But for the stress-induced anisotropy, the gravitational loading step is not applied, the sample is initially isotropic, and the particle arrangement does not have a major axis oriented arrangement. Because of the initial stress of the primary isotropic specimen, the initial stresses in the direction of maximum principal stress and minimum principal stress are different, resulting in different strain increments when stress increases are applied from different directions, so that the elastic modulus of the maximum principal direction is smaller than that of the direction of minimum principal stress. The difference in the principle of macroscopic stress and deformation is entirely due to the additional stress increment, which is a typical stress-induced anisotropy.

4. Anisotropic Microscopic Mechanism Analysis

4.1. Analysis of Microcosmic Mechanism of the Inherent Anisotropy. From the macroscopic mechanical parameters and the stress-strain curves of the numerical experiments, it shows that there is obvious inherent anisotropy in different directions due to gravity deposition. In this paper, by analyzing the change of the major axis orientation and the change of the coordination number of the internal particles in the sample during the loading process, the occurrence and development of the inherent anisotropy were found from the perspective of the microstructure parameters.

4.1.1. The Effect of Major Axis Orientation on the Particles.

In order to analyze the specific principles of the microstructures in the gravitational deposition process, a program coded with the FISH language was used to track the changes of the major axis orientation of the particle units before and after gravity deposition. Prior to gravitational deposition, the major axes of the irregularly shaped units are randomly distributed and are approximately equal in each interval. Figures 8(a)–8(c) show the major axis distribution of the particles in the three sets of samples. In the figure, the abscissa is the angle between the center line axis of the

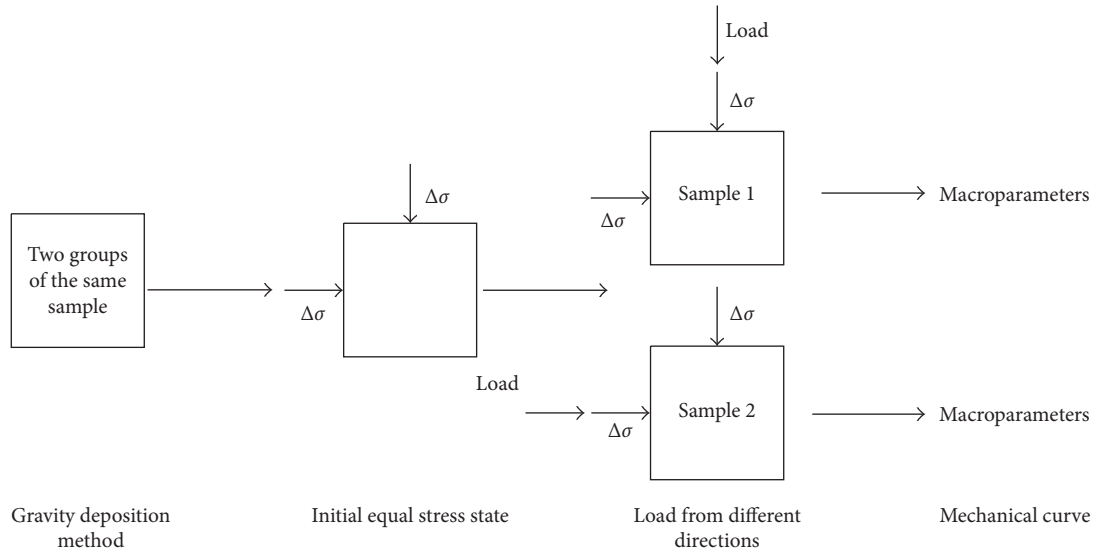


FIGURE 5: Stress paths of inherent anisotropy.

TABLE 6: Sample number and load condition.

Sample number	Initial stress	Stress increment direction
D1	$\sigma_{10} = 200 \text{ kPa}$	Horizontal
D2	$\sigma_{30} = 150 \text{ kPa}$	Vertical
E1	$\sigma_{10} = 250 \text{ kPa}$	Horizontal
E2	$\sigma_{30} = 150 \text{ kPa}$	Vertical
F1	$\sigma_{10} = 300 \text{ kPa}$	Horizontal
F2	$\sigma_{30} = 150 \text{ kPa}$	Vertical

particle and the horizontal direction, and the ordinate is the proportion of the total particles in a certain range of angles.

Figures 8(a)–8(c) show the distribution of the major axis orientation of the particles after different deposition processes. With the development of gravity deposition, the major axis orientation of the irregular unit changes obviously. In the angle range of $(-90, -60)$ and $(60, 90)$, particle major axis orientation was significantly reduced, and there was a decrease in the range of $(-60, -30)$, but in the angle range of $(30, 60)$ and $(-30, 0)$, the particle major axis orientation was significantly increased. It is shown that the microstructure of the specimen changes under the action of gravity deposition, so that the arrangement of the particles in the sample is different in the horizontal direction and the vertical direction because the long-axis orientation distribution of the irregularly shaped granular unit is closer to the horizontal direction and make the contact of the particles in the direction of gravitational deposition tighter. This leads to the stress peak of the specimen in the vertical deposition direction, and the initial elastic modulus is larger than the horizontal direction, which is consistent with the principle of the inherent anisotropy.

4.1.2. The Effect of the Average Coordination Number. Figures 9(a)–9(c) show the curves of the average coordination number in the sample during the loading process when the strain is less than 1%.

The average coordination number in PFC refers to the average number of particles in contact with the surroundings in a measurement circle. It is used to describe the stability of particle samples which states that the greater the coordination number, the closer the contact between particles, and the more difficult the compression of the particle becomes. Thus, the sample is kept more stable in this direction. It can be seen from Figure 9 that when the load is applied from the horizontal and vertical directions, the change of the average coordination number of the particles is not the same. When the load is applied from the vertical direction (gravity deposition direction), the average coordination number of the particles at the same strain is higher than the average of it obtained from the horizontal direction. The greater the number of particles in contact with each other in a measurement circle, the more stable the sample becomes, so when it is loaded from the vertical direction, the sample stability in the vertical direction is higher, and therefore, the sample has a smaller compression capacity in the vertical direction. At the same time, the initial elastic modulus and the stress peak in the vertical direction of Figures 7(a)–7(c) are larger than those in the horizontal direction.

Figures 9(a)–9(c) show that with the increase of the number of gravity deposition steps, the contact coordination number increases too, indicating that the greater the number of gravity deposition steps, the particle contact becomes closer, and therefore, the compression of the initial modulus and the stress peak will be greater too.

4.2. Analysis of Microcosmic Mechanism of the Stress-Induced Anisotropy. Stress-induced anisotropy is observed in specimens after being subjected to unequal initial stress states, and the anisotropy showed that the elastic modulus and stress peak in the direction of minimum principal stress were larger than those of the maximum principal stress. This is significantly different from the inherent anisotropy.

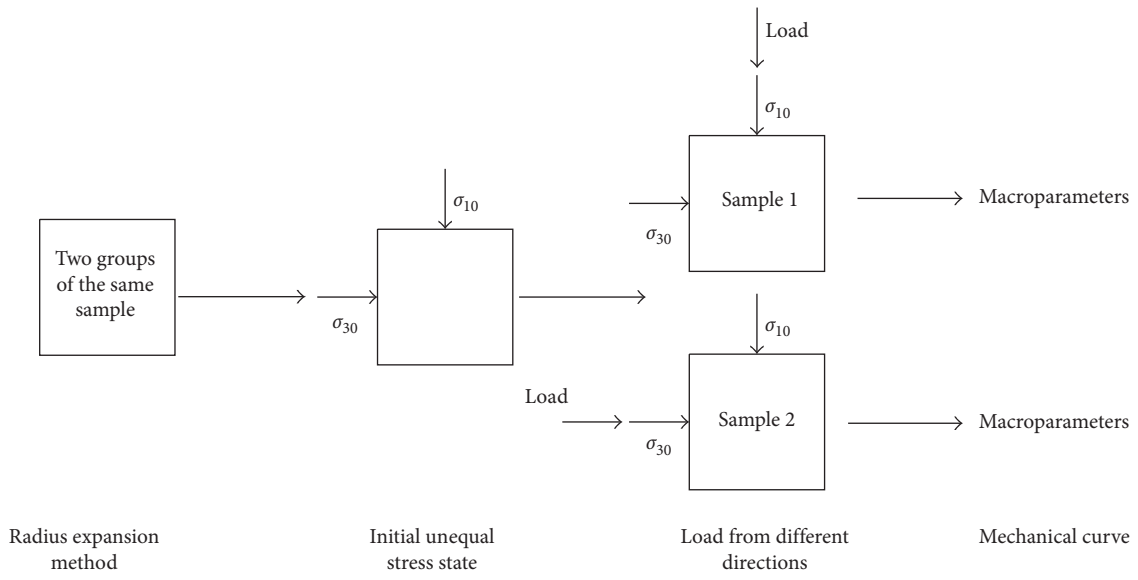


FIGURE 6: Stress path of induced anisotropy.

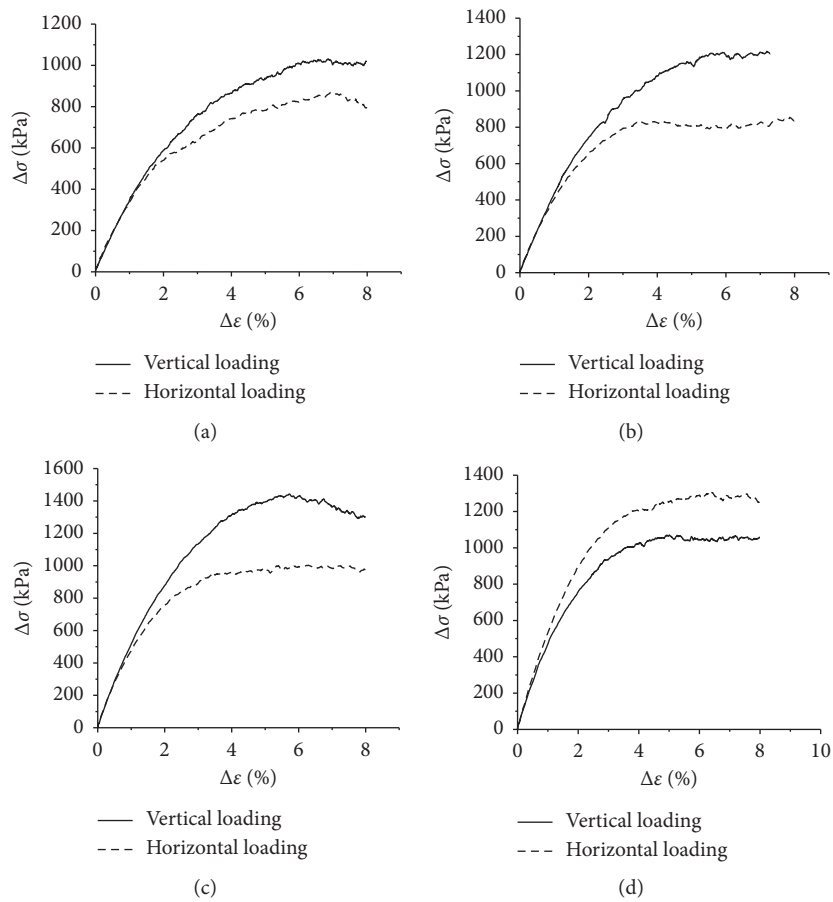


FIGURE 7: Continued.

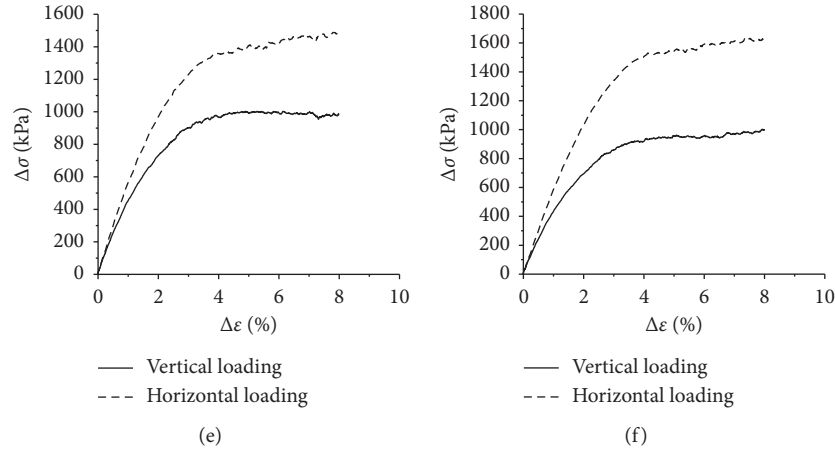


FIGURE 7: Curves of stress-strain relationship of three samples: (a) samples A1 and A2; (b) samples B1 and B2; (c) samples C1 and C2; (d) samples D1 and D2; (e) samples E1 and E2; (f) samples F1 and F2.

TABLE 7: Macromechanical parameters of samples.

Sample number	Initial modulus (MPa)	Stress peak (kPa)
A1	33.8	873
A2	34.8	1030
B1	40.7	856
B2	43.8	1250
C1	47.5	1001
C2	51.7	1443
D1	50.3	1303
D2	43.9	1070
E1	53.9	1490
E2	41.8	1003
F1	56.1	1636
F2	39.6	1002

4.2.1. The Effect of Major Axis Orientation on the Particles.

In the study of above inherent anisotropy, the particles were arranged along the particle center line axis before deposition occurred under the action of gravity. In the stress-induced anisotropy test, there is no gravity deposition step. The following is an example of the F1 and F2 samples to analyze the variation of the center line axis orientation of the particles in the stress-induced anisotropy test, as shown in Figure 10.

Figure 10 shows the change of the major axis orientation of the particles with the load increment in the horizontal direction (minimum principal stress direction) or the vertical direction (maximum principal stress direction), and the particles do not produce obvious layer arrangement. This indicates that, for the stress-induced anisotropy of the specimen, the long-axis orientation of the irregular element particles is not the main cause of the sample's anisotropy in the horizontal and vertical directions. For stress-induced anisotropy, before the application of unequal stress, the sample had formed a certain degree of density, the particle unit contact was close, and the friction was relatively larger. The force is applied through the plate or test instrument at the end rather than applying directly to each particle above, so the particles will have a greater rotation and larger

frictional resistance. For the inherent anisotropy, the major axis orientation of the particle unit changes obviously after the sample is completely formed. However, for the stress-induced anisotropy, due to the large frictional and rotational torque, the energy of the particle itself is small and the center line axis orientation of the particle unit is difficult to change, so the change of the center line axis orientation of the particle contributes little to the stress-induced anisotropy.

4.2.2. The Effect of the Average Coordination Number.

In Figure 11, the curves of the average coordination number are presented. The specimens are in the same initial stress state, since the initial stress is not equal in the horizontal and vertical directions, and the average coordination number of particles varies with the strain increment when they are loaded from the horizontal and vertical directions. When the load is applied from the horizontal direction (minimum principal stress direction), the average coordination number of the same strain particles is higher than the average number of particles in the vertical direction (maximum principal stress direction). The larger average coordination number stabilizes the sample more; so when it is loaded from the minimum principal stress direction due to the maximum principal stress constraints, the sample stability is higher. Hence, there will be an initial modulus and stress peak of the minimum principal stress direction which is higher than those of the maximum principal stress direction. In addition, as shown in Figures 11(a)–11(c), the difference between the initial stress in the horizontal and vertical directions is large. The greater the coordination number obtained in the horizontal direction is, the smaller the coordination number obtained in the vertical direction becomes. It is more difficult to compress the sample from the horizontal direction, but from the vertical direction, the opposite is observed. Therefore, the sample will show macroscopically that, with the increase of the initial anisotropy stress, the difference between the initial elastic modulus and the stress peak in the horizontal direction and the vertical direction is larger, as shown in Figures 7(d)–7(f).

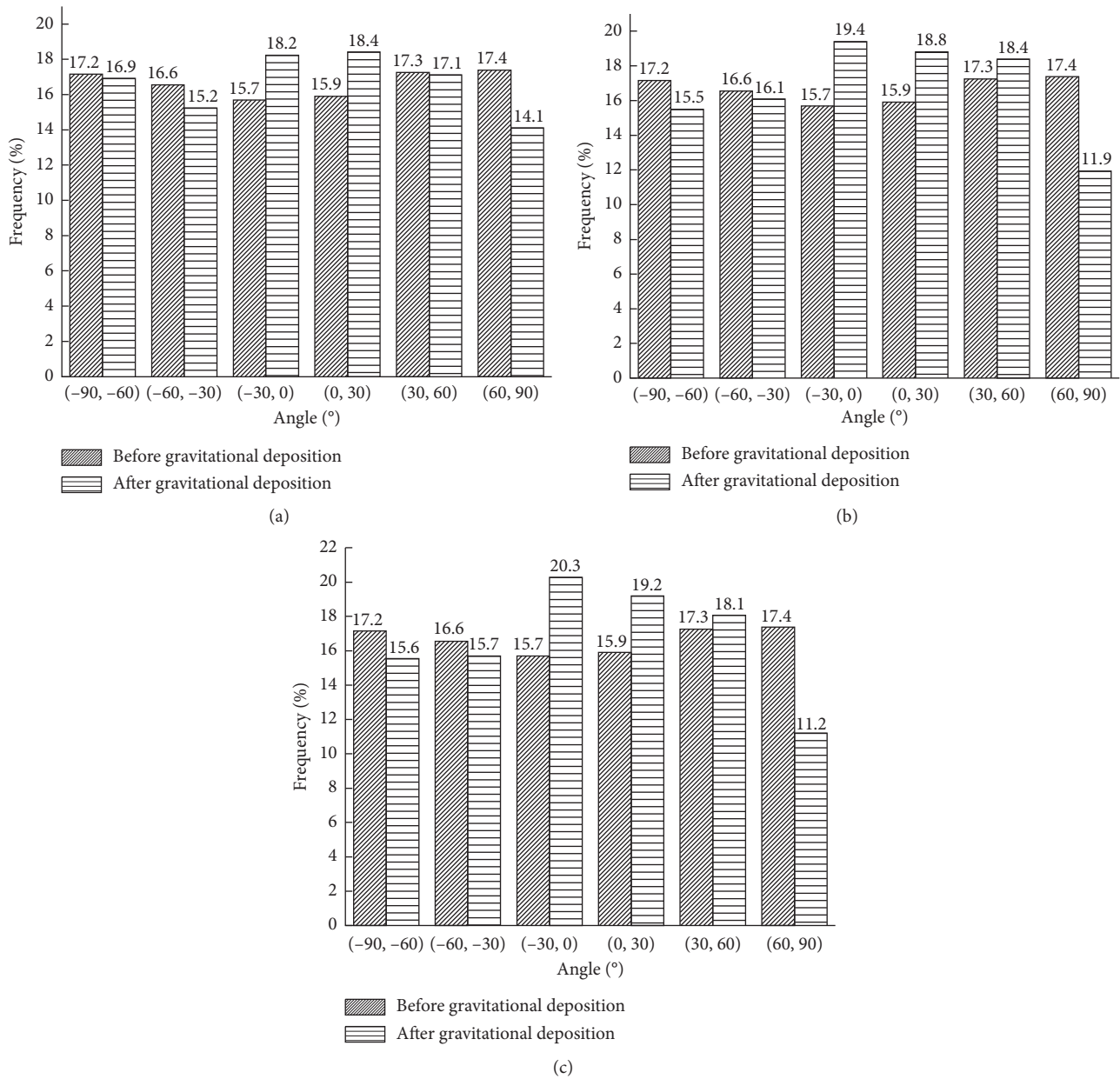


FIGURE 8: Distribution of the major axis orientation of particles: (a) 9,000 deposition steps; (b) 12,000 deposition steps; (c) 15,000 deposition steps.

4.2.3. The Effect of the Contact Force between the Particles.

The microscopic mechanism of stress-induced anisotropy in soil is also reflected in the contact force distribution. During the loading process, the contact force variation between the particles in the sample is different when the samples are loaded from the horizontal direction and the vertical direction. Figures 12 and 13 show the distribution of particle normal contact force and direction during the process of loading from horizontal and vertical directions when the samples F1 and F2 are in the initial stress state of 300 kPa and 150 kPa. Each dot in the graph represents contact force between two particles, and the distance from the origin of the coordinates represents the magnitude of the contact force. The different quadrants and dots of different positions also

represent the direction of the contact force. The more the dots are in the vertical direction, the more inclined this distribution is. In addition, the figure also gives the horizontal and vertical contact force of the average. When the strain is 0 (before loading), the horizontal and vertical directions of the normal distribution are oval, and the major axis is in the vertical direction. This shows that the distribution of the particle normal contact force and direction are the same before the loading of the two groups, as shown in Figures 12(a) and 13(a). But when the two groups of samples were loaded from the horizontal and vertical directions, the distribution of the particle normal contact force and direction was significantly different with the strain increment. When the load is applied in the horizontal direction

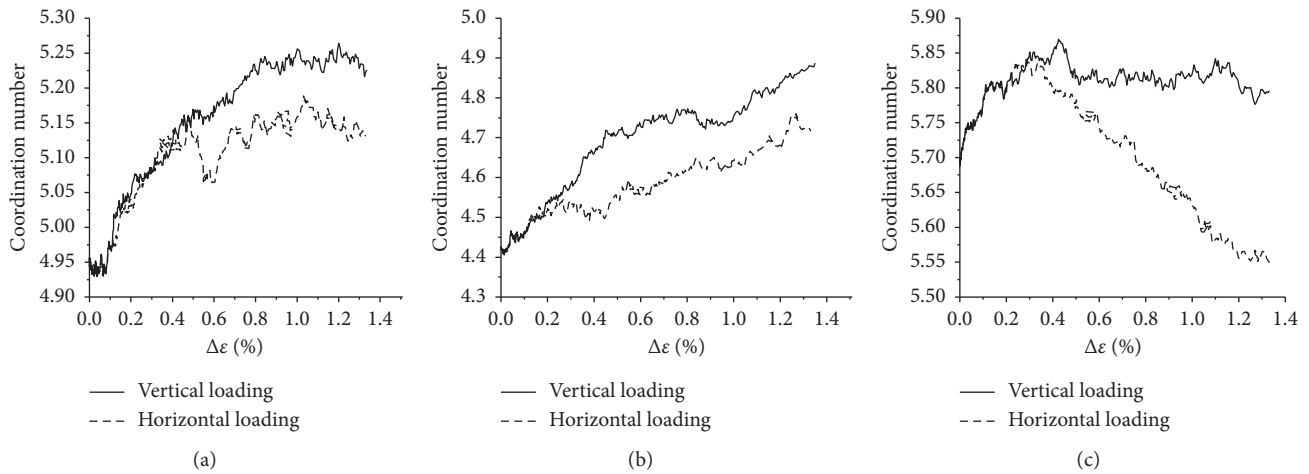


FIGURE 9: Curves of coordination numbers: (a) sample group A; (b) sample group B; (c) sample group C.

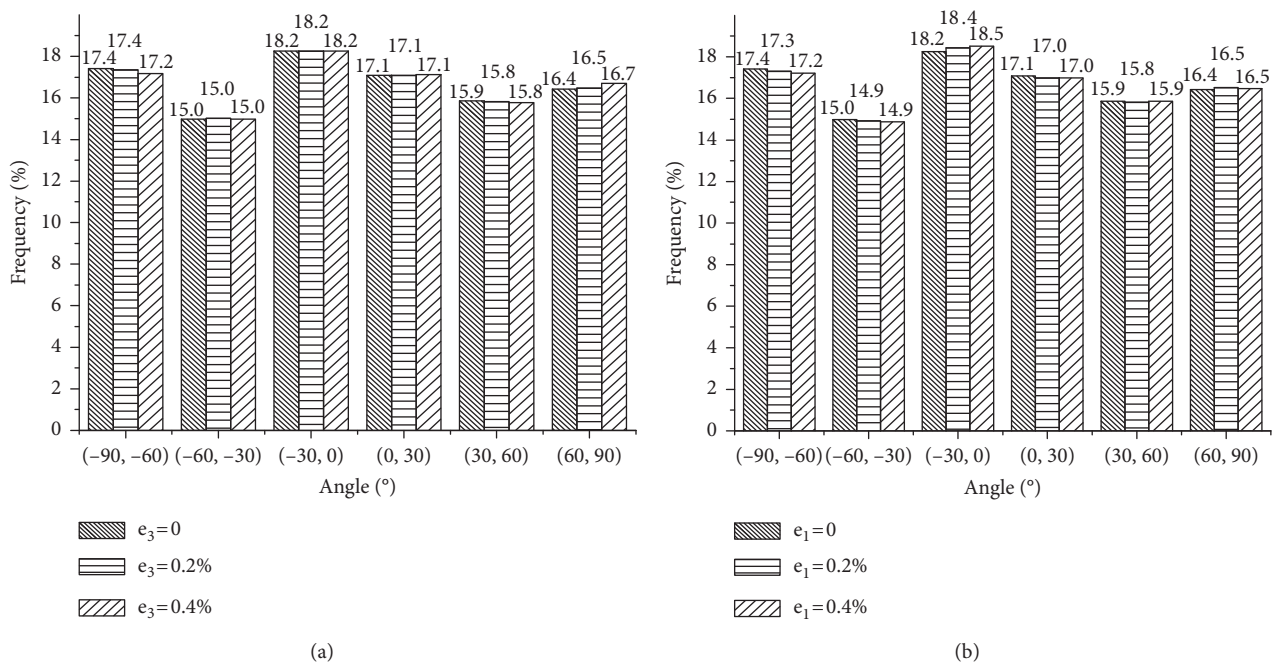


FIGURE 10: Distribution of major axis orientation of particles: (a) F1 sample long axis orientation change; (b) F2 sample long axis orientation change.

(minimum principal stress direction), the normal contact force in the horizontal direction increases rapidly with the increase of the strain, and the vertical direction (the direction of the maximum principal stress) changes slightly. The distribution of the contact force gradually changes from elliptical to circular. This means that the advantage of the distribution of the contact force in the vertical direction tends to reduce as the loading progresses. As the strain increment continues to increase, the contact force in the horizontal direction starts to exceed the contact force in the vertical direction. The particle movement is difficult in a relatively stable state, so the elastic modulus and peak stress are larger when loading from the horizontal direction. When the load is applied in the vertical

direction, the distribution of particle normal contact force gradually increases, the difference in the contact force between the vertical and horizontal directions of the particles increases from the beginning, and the movement of the particles is easy. When it is loaded from the vertical direction, the specimen's modulus and stress peaks will be lower than the relevant parameters obtained from the horizontal direction.

4.3. *The Differences and Relations between the Two Kinds of Anisotropy.* Analyses are conducted on the two kinds of anisotropy of soil in detail, and there are some relations and differences between them. The microscopic mechanism of

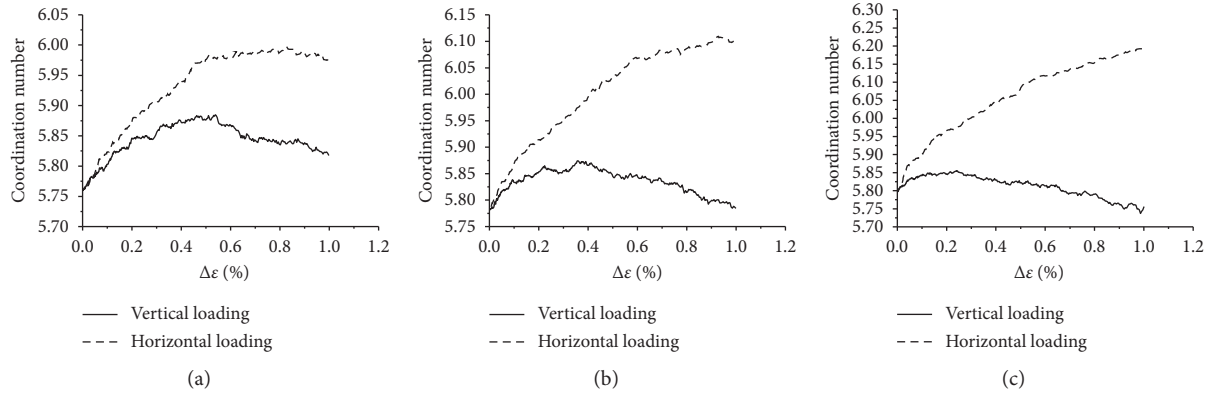


FIGURE 11: Curves of the average coordination number: (a) sample group A; (b) sample group B; (c) sample group C.

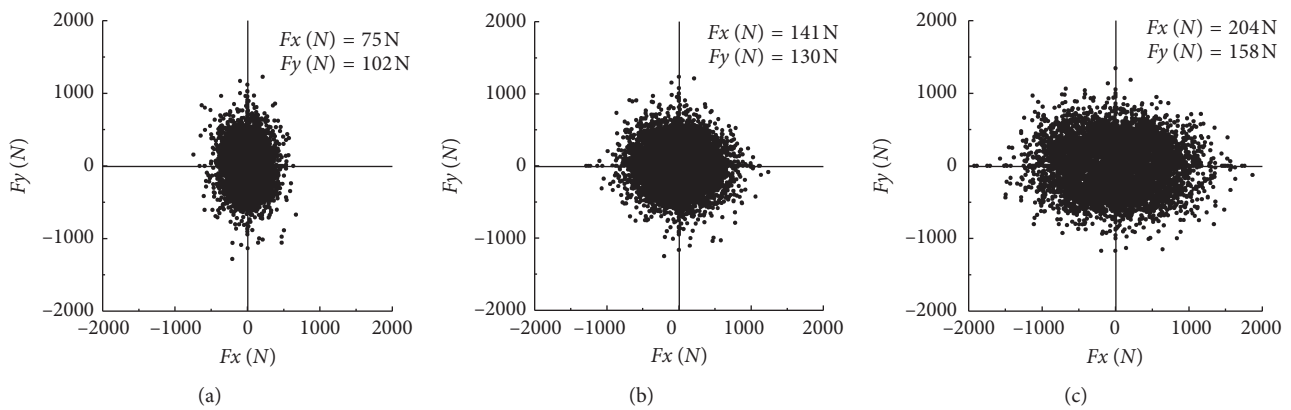


FIGURE 12: Distribution of the particle normal contact force and direction during the process of sample F1 loading: (a) $\epsilon_3 = 0$; (b) $\epsilon_3 = 0.4\%$; (c) $\epsilon_3 = 0.8\%$.

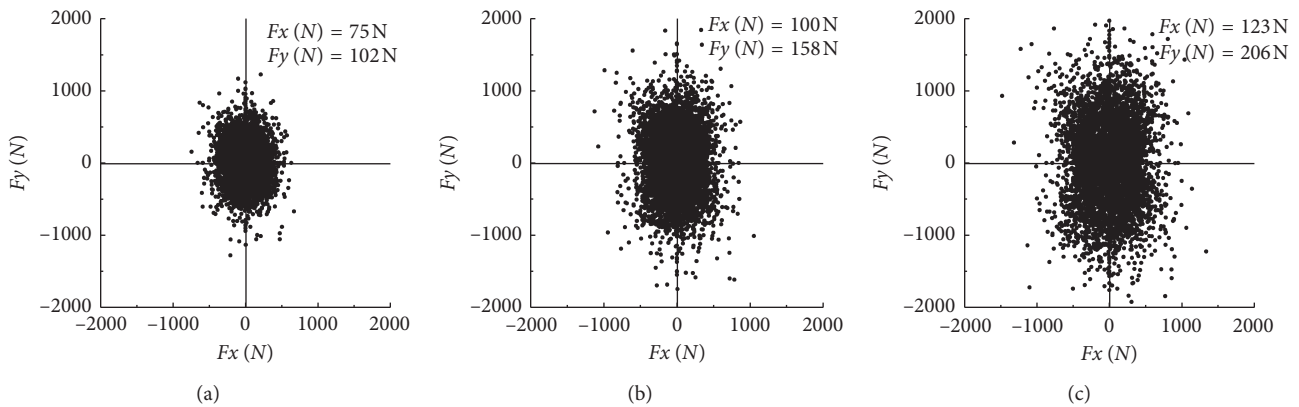


FIGURE 13: Distribution of the particle normal contact force and direction during the process of sample F2 loading: (a) $\epsilon_1 = 0$; (b) $\epsilon_1 = 0.4\%$; (c) $\epsilon_1 = 0.8\%$.

the two kinds of anisotropy is uniform. Both the inherent anisotropy and the stress-induced anisotropy are mainly caused by the different distribution and arrangement in different directions in soil microstructure, such as directional distribution of major axis of the particle unit, the arrangement of particles in space pore distribution, and the average coordination number of particles.

However, there are some differences between the forms of expression of the anisotropy. In the course of deposition, the particles easily rotate and loose contact between each other. When the particles are subjected to gravity, the layers are arranged in the horizontal direction, resulting in tight contact in the vertical direction and difficulty in compression. The stress peak and the elastic modulus in the vertical

direction are larger than those in the horizontal direction, which are called inherent anisotropy. The contact between particles is not lost as the before gravity deposition condition, and there is a strong force between particles and hence it is not easy to rotate; this is called the stress-induced anisotropy. The soil sample is subjected to an unequal initial stress state, resulting in differences in the horizontal and vertical distributions of the contact force and the coordination number. In the late loading process in the vertical direction (maximum principal stress direction), the shear trend increases from the commencement of loading. In the horizontal direction (minimum principal stress direction), the shear trend of sample decreases first and thereafter increases. The sample undergoes a gradual compression and stability process. Therefore, the stress peak and elastic modulus in the final horizontal direction are larger than those in the vertical direction.

5. Conclusion and Discussion

As a discontinuous discrete material, the mechanical properties and research methods of sandy materials are quite different from those of continuous materials. Because of the discreteness of the particle structure the sandy materials show an obvious anisotropy on the macroscopic scale under the action of gravity or under the condition of unequal stress. The generation of this anisotropy is also closely related to the microstructural properties of the bulk material. In view of the limitations of the research methods of discontinuous discrete materials and the complexity of laboratory tests, the numerical simulation software of particle flow (PFC2D) was adopted in this paper. A group of plane biaxial specimens was established by gravity deposition and radius expansion method. Stress and strain curves and macromechanical parameters in different directions under different conditions were obtained by loading in horizontal and vertical directions. The macroscopic anisotropy was analyzed and explained from the microscopic point of view, using the parameters of particle orientation, and coordination number, and the magnitude of the particle indirect contact force as an index. The conclusions are as follows:

- (1) In this paper, numerical results of an irregular element are closer to the results of the triaxial test of the standard sand sample. The proposed irregular unit is more suitable for the shape characteristics of soil particles than the original disk unit in PFC. Based on this numerical specimen, a numerical test of a more extensive stress path can be carried out.
- (2) In the process of gravity deposition, the particle units are obviously arranged in layers. This arrangement gives the soil more contact and compression in one direction than in the other. In the later loading process, the soil shows obvious anisotropic mechanical characteristics.
- (3) The stress-induced anisotropy of soil is produced by the interaction of the irregular internal structure and external unequal stress. The change of the internal structure of the soil is concomitant with the change of the external stress state. The fundamental reason for the anisotropy is that the microstructure of the material has undergone uneven changes, but the reason for this change is the role of external load.
- (4) The reasons for the two kinds of anisotropy can be attributed to the inhomogeneous changes of microstructure and to the micromechanical mechanism, but there are differences in their forms of expression.
- (5) In this paper, the PFC simulation of sand inherent and stress-induced anisotropy is carried out. It is suggested that a scale numerical test tool will be established by numerical simulation of the completed macrounit tests. The reliability of the discrete element numerical tools is preliminarily verified by comparing with the results of unit tests. The numerical experiments under more extensive stress path can be carried out, and the stress and strain of granular materials under complex stress conditions are obtained. It provides a reference for the macroscopic mechanism of the macroscopic mechanical behavior of granular materials and for establishing the macroscopic constitutive model of rock.

Data Availability

The data that support the findings of this study are available from the corresponding author upon reasonable request.

Conflicts of Interest

The authors declare that they have no conflicts of interest.

Acknowledgments

The work was supported by the project of National Natural Science Foundation of China (nos. 41530637 and 51578214).

References

- [1] A. V. Abelev and P. V. Lade, "Effects of cross anisotropy on three-dimensional behavior of sand I: stress-strain behavior and shear banding," *Journal of Engineering Mechanics*, vol. 29, no. 2, pp. 160–166, 2003.
- [2] J. R. F. Arthur and B. K. Menzies, "Inherent anisotropy in a sand," *Geotechnique*, vol. 22, no. 1, pp. 115–128, 1972.
- [3] K. Y. Zhang, *Study and Application on Soil's Constitutive Model with the Consideration of Stress-Induced Anisotropy*, Hohai University, Nanjing, China, 2004, in Chinese.
- [4] J. R. F. Arthur, K. S. Chua, and T. Dunstan, "Induced anisotropy in a sand," *Geotechnique*, vol. 27, no. 1, pp. 13–30, 1977.
- [5] K. Y. Zhang and F. N. Charkley, "An anisotropic constitutive model of geomaterials based on true triaxial testing and its application," *Journal of Central South University*, vol. 24, no. 6, pp. 1430–1442, 2017.
- [6] K. Y. Zhang and Z. Z. Yin, "Discussion on soil's anisotropy under complicated stress state and the study method," *Rock and Soil Mechanics*, vol. 28, pp. 149–154, 2007.

- [7] E. Hoque and F. Tatsuoka, "Anisotropy in elastic deformation of granular materials," *Soils and Foundations*, vol. 38, no. 1, pp. 163–179, 1998.
- [8] Itasca Consulting Group, Inc., *PFC2D Particle Flow Code in 2 Dimensions Version 5.0*, Itasca Consulting Group, Inc., Minneapolis, MN, USA, 2014.
- [9] P. A. Cundall, "A computer model for simulating progressive large-scale movement in blocky rock systems," in *Proceedings of Symposium of the International Society of Rock Mechanics*, vol. 1, Nancy, France, 1971.
- [10] A. T. Procopio and A. Zavaliangos, "Simulation of multi-axial compaction of granular media from loose to high relative densities," *Journal of the Mechanics and Physics of Solids*, vol. 53, no. 7, pp. 1523–1551, 2005.
- [11] P. A. Cundall, "A discontinuous future for numerical modelling in geomechanics," in *Proceedings of the Institution of Civil Engineers-Geotechnical Engineering*, vol. 149, London, 2001.
- [12] Y. Chi, *A Study of the Mechanical Properties of the Soil-A Simulation of the Particle Flow in the Shear Zone of the Stress-Strain Relationship*, Tongji University, Shanghai, China, 2002.
- [13] M. J. Jiang, D. Peng, Z. F. Shen et al., "DEM analysis on formation of shear band of methane hydrate bearing soils," *Journal of Geotechnical and Geoenvironmental Engineering*, vol. 36, no. 9, pp. 1624–1630, 2014.
- [14] C. X. Tong, M. Zhou, L. W. Zhang et al., "Numerical modelling of biaxial compression tests for granular materials with inherent anisotropy using DEM," *Chinese Journal of Rock Mechanics and Engineering*, vol. 33, no. 2, pp. 4227–4232, 2014, in Chinese.
- [15] D. D. Shi, *Micromechanical Simulations of Sand Behavior under Monotonic and Cyclic Loading*, Tongji University, Shanghai, China, 2007.

Research Article

Influences of Drying and Wetting Cycles and Compaction Degree on Strength of Yudong Silt for Subgrade and Its Prediction

Junran Zhang ¹, Tong Jiang ¹, Xingcui Wang,¹ Chong Liu,² and Zhiquan Huang¹

¹Henan Province Key Laboratory of Geomechanics and Structural Engineering, North China University of Water Resources and Electric Power, Zhengzhou, Henan 450045, China

²College of Civil Engineering and Architecture, Guangxi University, No. 100 of University East Road, Nanning, Guangxi 530004, China

Correspondence should be addressed to Tong Jiang; jiangtong@ncwu.edu.cn

Received 5 February 2018; Revised 7 April 2018; Accepted 6 May 2018; Published 22 July 2018

Academic Editor: Yonggui Chen

Copyright © 2018 Junran Zhang et al. This is an open access article distributed under the Creative Commons Attribution License, which permits unrestricted use, distribution, and reproduction in any medium, provided the original work is properly cited.

In order to investigate the influences of drying and wetting cycles, initial degree of compaction, and water content on shear strength of the Yudong subgrade silt, a series of direct shear tests were performed at saturated and unsaturated states. The test results show that effects of the drying and wetting cycles, water content, and compaction degree on cohesion are more evident than those on the internal friction angle. According to the test data, a formula for the cohesion was proposed, which accounts for the drying and wetting cycles, water content, and degree of compaction. Because Bishop's strength formula for unsaturated soils could not be applied to Yudong silt, a formula is given based on Fredlund's formula for predicting the shear strength of unsaturated Yudong silt from the soil-water characteristic curve.

1. Introduction

The silt distributes widely on the Yellow River alluvial plain in the eastern Henan province (referred to as Yudong) and thus is often used as a road subgrade or fill material. Yudong silt has a high content of silt-size particles, and the silt-size particles do not bond very well in drying state and are easily crushed. However, it is sensitive to water and easily becomes liquefaction alike, which means that it has poor engineering stability as a road building material. The soils in nature are subjected to climate change and undergo periodical drying and wetting cycles. The drying and wetting cycles can significantly alter the hydromechanical behavior of soil and damage earth structures [1]. In the natural environment, there are changes in groundwater level and seasonal drying and wetting by evaporation and infiltration of precipitation, respectively, and thus, subgrade soils are subjected to multiple drying and wetting cycles, resulting in deformation and uneven settlement of the subgrade layer, surface crack, and other failures. Because of their importance in engineering

applications, the effect of drying and wetting cycles and water content on the shear strength of silt needs to be considered.

In recent years, there have been many studies on the effect of drying and wetting cycles on soil strength. A literature review on hydraulic cycles shows that several drying-wetting cycles [2–4] produce an equilibrium state after which the soil exhibits elastic behavior. Moreover, the irreversible volumetric deformation during the drying and wetting cycles was found to be the function of compaction conditions and the subsequent variation of stress/hydration paths [5, 6]. Goh et al. [7] showed that the shear strength characteristics of soils under the drying and wetting cycles are different. Zhang et al. [8] and Sun et al. [9] showed that even if the same path of net stress and suction was followed during triaxial shearing, the stress-strain and strength behavior are different between specimens experiencing different suction histories. After experiencing a larger suction, the void ratio decreases significantly, and thus, the specimen exhibits the deformation characteristics similar to the overconsolidated clay during shearing [10]. The effect of

3. Experimental Methods

3.1. Soil-Water Characteristic Curve. The GCTS unsaturated soil consolidation apparatus [31] was used to test the soil-water characteristic curve of the silt that had not experienced wetting or drying cycle under a net stress of 0, a degree of compaction of 96%. Matric suction imposed on the specimens was applied by using the axis translation technology [32].

The specific suction path is shown in Table 2. The suction equilibrium was determined from the amount of water drainage, by measuring the amount of water pumped in and out through the burette. The variation in the water content was based on the difference between the suction equilibrium points measured for the specimens. During the test process, the bottom pipes below the ceramic plate were flushed out at regular intervals so that there was more free drainage, thereby shortening the time to achieve equilibrium. The suction equilibrium of each level was achieved in between 2 and 3 days during the test conditions. The tests for measuring the soil-water characteristic curves in drying and wetting cycles were carried out over a period of about 1.5 months.

3.2. Effect of Water Content on Strength of Unsaturated Yudong Silt. After passing through a 2 mm sieve, soil samples were placed in an oven and were dried at 110°C for 24 h. They were then cooled in a dryer and divided into 9 portions with 8 different water contents and one with the optimum water content. The amount of water was calculated according to the targeted water content and the quality of the dry soil, and then, the water was added to the dry soil to reach the targeted water content. The soils were mixed with the water, and the mixtures were then placed into double-layer storage bags and were allowed them to be sealed for 24 hours. The actual initial water content of the soil samples was measured from part of the soil samples oven-dried.

To study the effect of water content on the strength of Yudong silt, a series of direct shear tests were performed on 24 unsaturated specimens of Yudong silt. The test specimens with the same initial degree of compaction of 96% have the initial water contents of 6.9%, 10.4%, 12.3%, 15.8%, 18.2%, 20.5%, 22.1%, and 23.9%. The specimens were subjected to vertical stresses of 100, 200, and 400 kPa, respectively. To ensure that the pore water pressure is completely dissipated during shearing, the shear method was adopted slowly, and the shear rate is 0.02 mm/min. The specific details of the tests are listed in Table 3.

3.3. Effects of Drying and Wetting Cycle and Degree of Compaction on Shear Strength of Saturated Yudong Silt. To obtain better and more realistic simulations of the true environmental conditions in eastern Henan, the testing conditions reported in this study were based on the regional annual average precipitation. The maximum and minimum water contents during drying and wetting cycles were estimated from the amount of evaporation from samples, that is, $w_{\max} = w_s$ and $w_{\min} = 10\%$ [27]. The laboratory temperature was controlled between 17°C and 18°C. Specific details of the test conditions are as follows:

TABLE 2: Suction paths.

Path type	Suction path
Drying	1 kPa → 10 kPa → 20 kPa → 40 kPa → 80 kPa → 160 kPa → 320 kPa → 480 kPa
Wetting	480 kPa → 320 kPa → 160 kPa → 80 kPa → 40 kPa → 20 kPa → 10 kPa → 1 kPa

TABLE 3: Direct shear test program for unsaturated Yudong silt.

Compaction degree, d (%)	Initial water content, w_0 (%)	Normal stress, σ_v (kPa)
96	6.9	100, 200, 400
	10.4	
	12.3	
	15.8	
	18.2	
	20.5	
	22.1	
	23.9	

Note. w_s is saturated water content in % and $w_s = 23.9\%$.

TABLE 4: Testing conditions for direct shear tests on saturated Yudong silt.

Compaction degree, d (%)	Number of drying and wetting cycles, n (times)	Normal stress, σ_v (kPa)
94, 96, 98	0	100, 200, 300, 400
	1	
	3	
	5	
	5	

- (1) During the drying process, the prepared saturated specimens were wind-dried indoor. The specimens were weighed, and the water content was calculated every 2 hours until it reached the minimum water content w_{\min} . The drying process was stopped, and the specimens were allowed to stand for 24 hours.
- (2) During the wetting process, the air-dried specimens were saturated with a vacuum pump to achieve a water content of w_s . The vacuum pump was stopped, and the specimens were allowed to stand for 24 hours.
- (3) Steps 1 and 2 were repeated to replicate multiple drying and wetting cycles.

The initial degrees of compaction of the specimens were controlled at 94%, 96%, and 98%. The specimens were subjected to 0, 1, 3, and 5 drying and wetting cycles, and vertical stresses of 100, 200, 300, and 400 kPa were applied. The 48 direct shear tests were performed, using the slow-velocity shear method at the shear rate of 0.02 mm/min. Details of the test setup are provided in Table 4.

4. Results and Discussion

4.1. Soil-Water Characteristic Curve. The soil-water characteristic curves for the saturated Yudong silt specimen experiencing drying and wetting cycles with a compaction degree of 96% and under a net stress of 0 kPa are shown in Figure 3. The results show that the water content and saturation degree

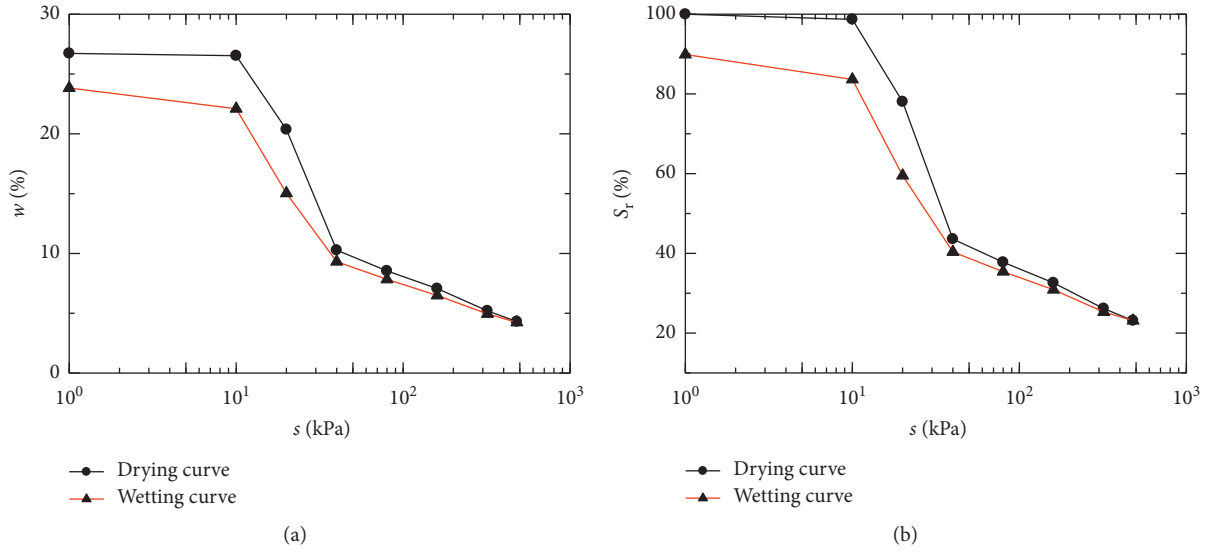


FIGURE 3: SWCCs of Yudong silt: (a) w - s curve; (b) s - s_r curve.

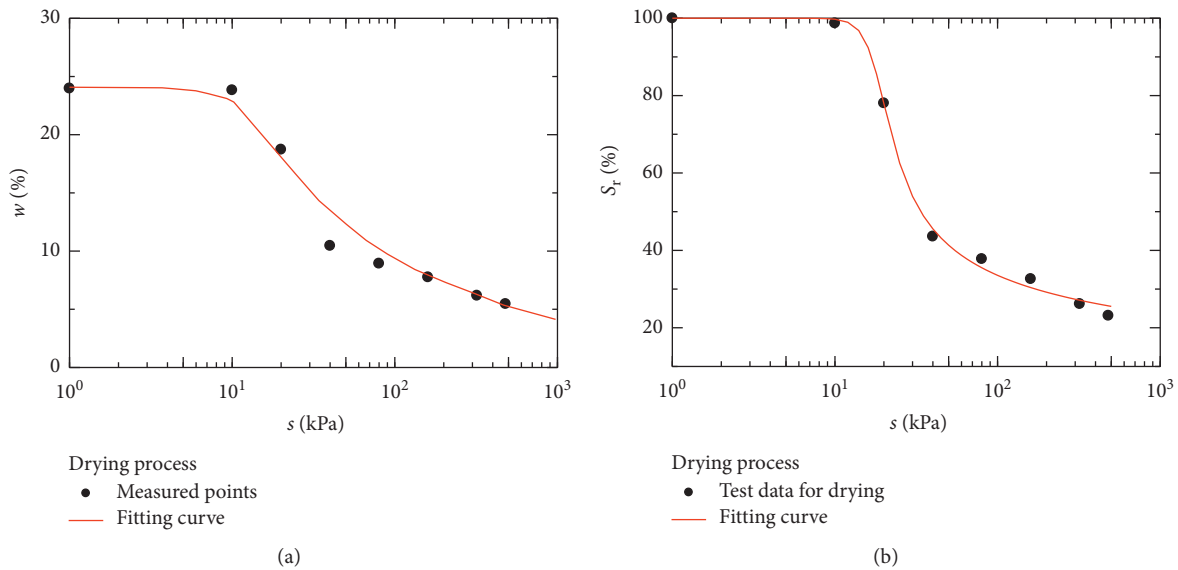


FIGURE 4: Fitting of the drying curve: (a) w - s curve; (b) s - s_r curve.

of the specimen decrease as the suction increases and increase as the suction decreases. Because of the bottle ink effect, there was hysteresis in the drying and wetting curves and consistent with the results from other studies [9, 33]; that is, the drying curve was always higher than the wetting curve. When the suction was less than 100 kPa, there was significant hysteresis in the drying and wetting soil-water characteristic curves, but there was no hysteresis when the suction was greater than 100 kPa.

The measured drying curve can be fitted using the Van Genuchten model [34] as follows:

$$w = \frac{w_s}{[1 + (\psi/a)^n]^m}, \quad (1)$$

where ψ denotes the suction; w denotes the water content corresponding to the suction; w_s is the saturated water

content; and a , n , and m are the fitting parameters. $w_s = 23.9$, $a = 8.95$, $n = 40.02$, and $m = 0.01$ were used for fitting the SWCC in Figure 4(a).

The renowned mathematical equation developed by Fredlund and Xing [35] was adopted to fit the drying SWCC measured by the pressure plate method, as shown in Figure 4(b). The SWCC equation proposed by Fredlund and Xing [35] can be expressed as

$$S_r = \frac{C(s)}{\{\ln[2.71828 + (s/a)^n]\}^m},$$

where $C(s)$ is defined as $C(s) = 1 - \frac{\ln(1 + (s/s_{re}))}{\ln(1 + (10^6/s_{re}))}$, s_{re} is the residual suction, and m is a fitting parameter.

$$C(s) = 1 - \frac{\ln(1 + (s/s_{re}))}{\ln(1 + (10^6/s_{re}))},$$

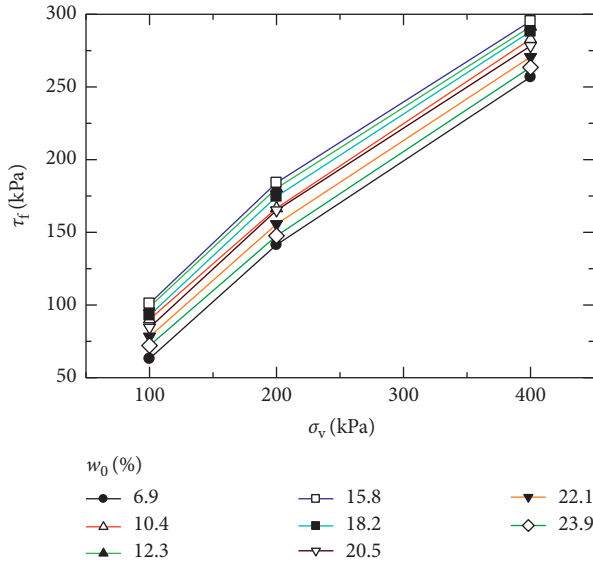


FIGURE 5: Relationship between shear strength and normal stress at different water contents.

where s_{re} is the residual suction and a , n , and m are three fitting parameters. The fitting parameters of the SWCC in Figure 4(b) are as follows: $s_{re} = 100000$ kPa, $a = 17.02$, $n = 7.60$, and $m = 0.42$.

4.2. Effect of Water Content on Strength of Unsaturated Yudong Silt. The relationships between the shear strength and normal stress for unsaturated silt specimens with different initial water contents are shown in Figure 5. The shear strength line of Yudong silt increases first and then decreases as the initial water content increases.

The strength indexes were determined by fitting the test data using the least squares method under different test conditions, as shown in Table 5. The cohesion increases first and then decreases as the initial water content increases, as shown in Figure 6. However, the initial water content has little influence on the internal friction angle, which changes only between 29° and 31°, as shown in Figure 7; the result is consistent with the results of Vanapalli et al. [36].

The pore water in an unsaturated soil can be divided into two categories: capillary water and adsorbed water. Only the capillary water contributes to the shear strength [37, 38]. The water content is an important influential factor on the cohesion except for the soil strength caused by the friction. The changes in cohesion mentioned above are related to the mode of connection between soil particles. For example, when the soil is dry, the bound water decreases, the weakly-bound water in the diffusion layer becomes thinner, and the concentrations of the dissolved liquid electrolyte increase, resulting in dry coagulation. The clay content of silt is low, so the cohesion is very weak during drying, and the particles are mainly connected with the capillary water. When the water content is low, silt is held together very loosely and can be broken easily. When the water content is very high, the connection force of soil particles from the capillary water becomes weak, resulting in reduced cohesion. Therefore, the

TABLE 5: Initial state and strength parameters of unsaturated Yudong silt.

w_0 (%)	c (kPa)	φ (°)
6.9	33.53	30.00
10.4	57.02	29.91
12.3	67.56	29.78
15.8	69.53	29.91
18.2	61.52	30.09
20.5	53.57	29.96
22.1	47.05	29.87
23.9	41.44	30.34

Note. w_0 is initial water content in %; w_s is saturated water content in %; $w_s = 23.9\%$.

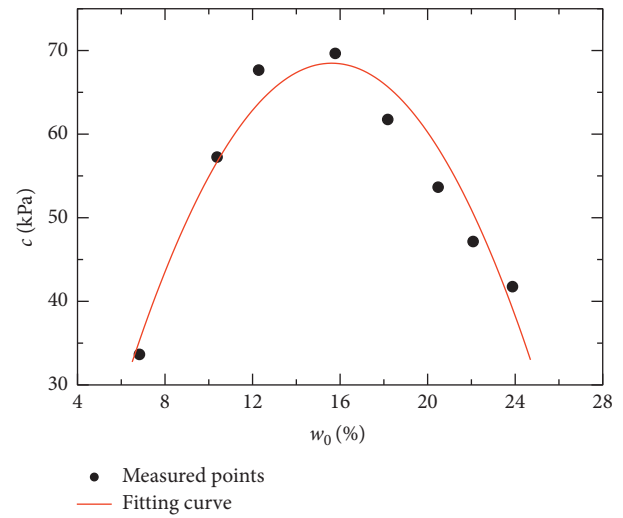


FIGURE 6: Relationship between initial water content and cohesion.

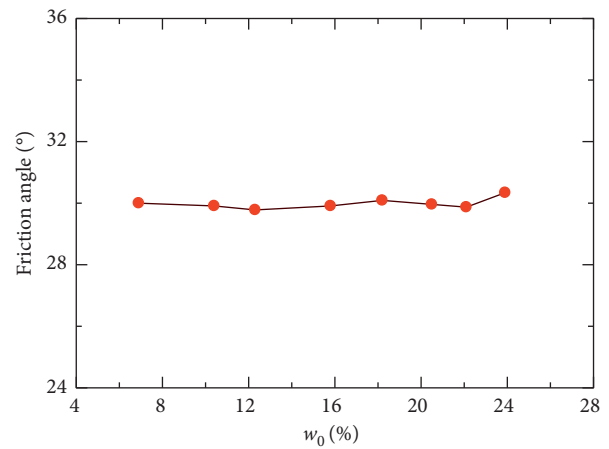


FIGURE 7: Relationship between initial water content and friction angle.

cohesion of silt first increases and then decreases as the initial water content increases.

As silt particles are generally within a relatively narrow range of particle size, the effect of water on the lubrication between the particles is limited, and thus, the impact on the frictional strength is limited. Therefore, the internal friction angle changes little during the change of water content.

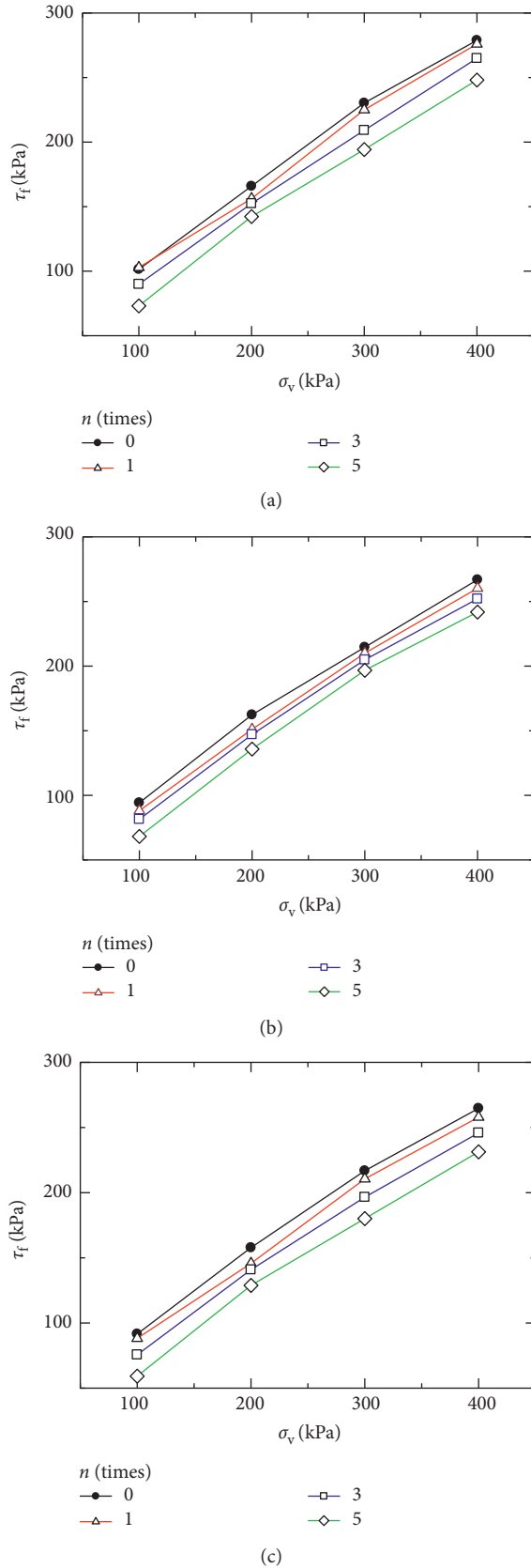


FIGURE 8: Relationships between shear strength and normal stress at different compaction degrees and drying-wetting cycles. Compaction degree: (a) 98%; (b) 96%; (c) 94%.

TABLE 6: Initial state and strength parameters of saturated Yudong silt.

d (%)	n (times)	c (kPa)	φ ($^{\circ}$)
94	0	37.76	30.04
	1	31.31	29.83
	3	22.1	29.65
	5	8.29	29.48
96	0	41.44	30.34
	1	35.91	30.09
	3	27.63	30.04
	5	14.73	29.78
98	0	44.92	30.77
	1	42.36	30.56
	3	33.15	30.21
	5	20.26	29.96

As shown in Figure 6, the relationship between the initial water content and cohesion for Yudong silt can be fitted by a parabolic curve. The mathematical expression for the relationship is as follows:

$$c = -0.43w_0^2 + 13.43w_0 - 36.38, \quad (3)$$

where c is the cohesion in kPa and w_0 is the initial water content in %.

4.3. Effects of Drying and Wetting Cycles and Degree of Compaction on Shear Strength of Saturated Yudong Silt. The relationship between the shear strength and normal stress for saturated silt specimens under different degrees of compaction and different numbers of wetting and drying cycles is shown in Figure 8. The shear strength line of Yudong silt moves down as the number of drying and wetting cycles increases when the initial degrees of compaction are the same. The shear strength line of Yudong silt moves up with increasing the initial degree of compaction when the number of drying and wetting cycles was the same.

The strength indexes were determined by fitting test data using the least squares method under different testing conditions. As shown in Table 6, the cohesion decreases obviously as the number of drying and wetting cycles increases, while the cohesion increases as the initial degree of compaction increases, as shown in Figure 9. The wetting and drying cycles and the initial degree of compaction have little effect on the internal friction angle, which changes only between 29° and 31° , as shown in Figure 10.

The drying and wetting cycles have a significant effect on the cohesion of Yudong silt. During the drying and wetting process, the soil microstructure changes and the intergranular joints are weakened by small fissure channels or salt solute, resulting in a lower cohesion. The cohesion of silt is also influenced by the degree of compaction because the cohesion is mainly a function of electrostatic attraction and the adhesion between soil particles. When the degree of compaction increases, the distance between the soil particles decreases, the interaction between the particles becomes stronger, and the cohesion increases [39]. The internal friction angle is caused by the friction, including occlusal

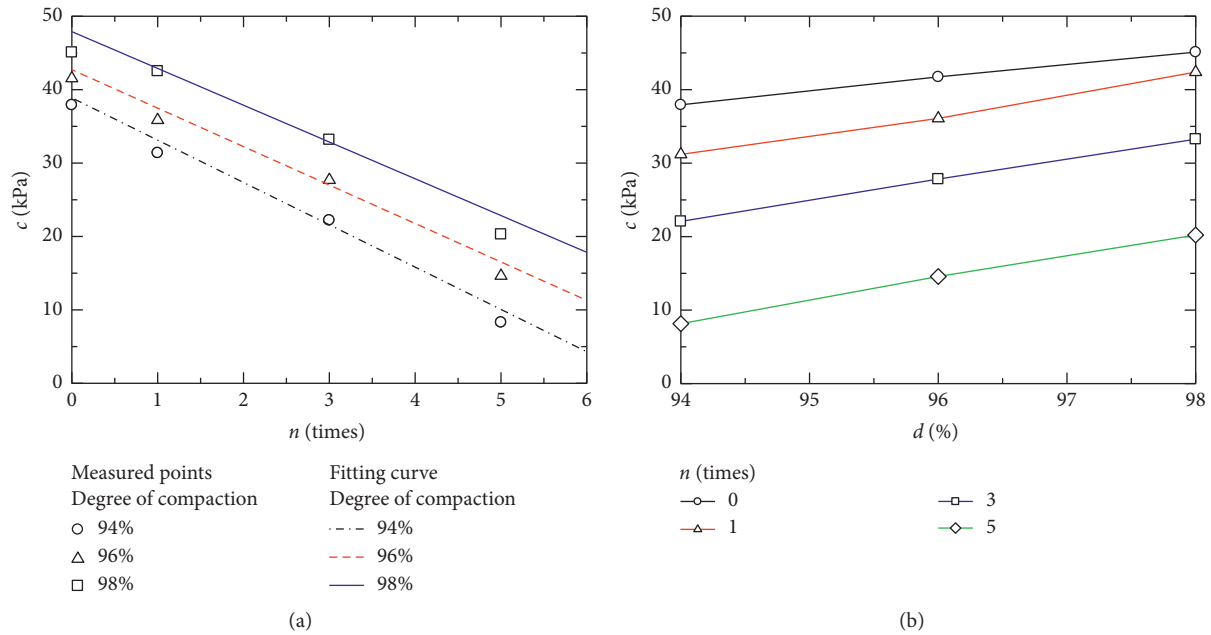


FIGURE 9: Effects of drying and wetting cycles and compaction degree on cohesion. Relationship between (a) cohesion and number of drying and wetting cycles; (b) cohesion and degree of compaction.

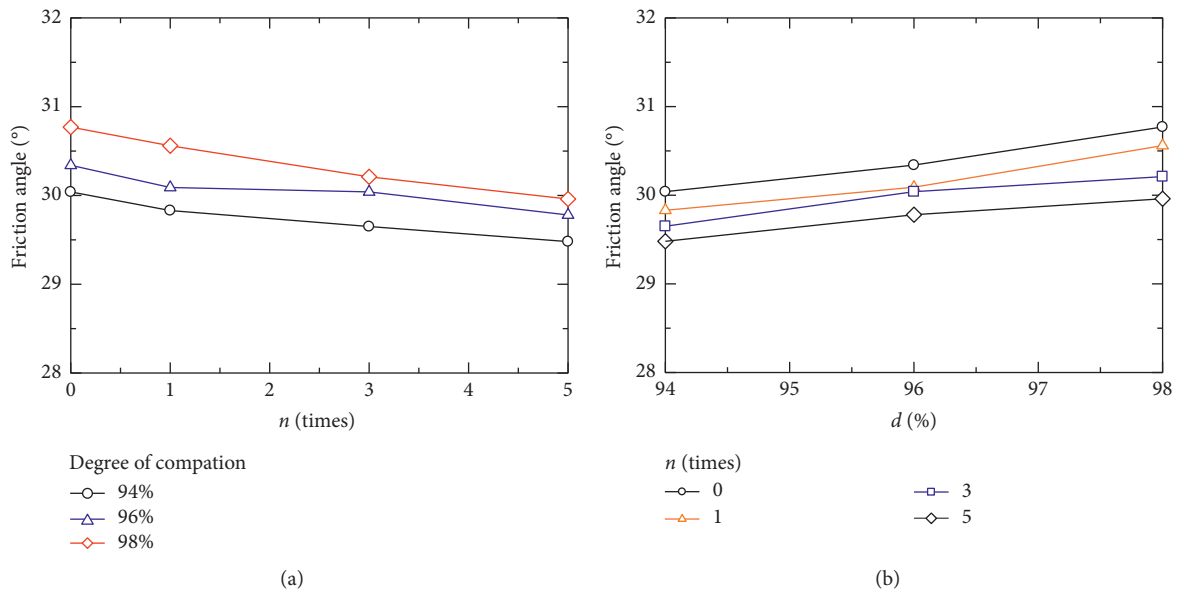


FIGURE 10: Effects of drying and wetting cycle and compaction degree on friction angle. Relationship between (a) friction angle and number of drying and wetting cycles; (b) friction angle and degree of compaction.

friction and sliding friction, between the particles; the size of which depends on the particle morphology, pore pressure, and the soil structure and other factors. The drying and wetting cycles cause irreversible damage to the connection between the particles, and subtle cracks appear that reduce the integrity of the sample. Silt has a uniform particle size, and the clay content is very low, which means that the changes in the soil structure after the drying and wetting cycles are limited, and so, while the friction angle has decreases, the decrease is not obvious. The uniform particle size

of silt is uniform, which means that it is dense and difficult to shape. As the degree of compaction increases, the pores of the silt are not really filled but are shaped into a type of building block framework, so any increases in the internal friction angle are not obvious.

Cohesion of Yudong silt is plotted against the number of drying and wetting cycles and degree of compaction in Figures 9(a) and 9(b), respectively. There were clear linear relationships between the cohesion and the number of drying and wetting cycles and the degree of compaction. The

TABLE 7: Fitting parameters a and b for different degrees of compaction.

Compaction degree, d (%)	Fitting parameter		
	a	b	Fitting degree
94	37.79	-5.74	0.99
96	41.66	-5.21	0.98
98	46.38	-4.98	0.97

linear relationship between the degree of cohesion and the number of drying and wetting cycles in Figure 9(a), can be expressed as:

$$c = a + bn, \quad (4)$$

where c is the cohesion, n is the number of drying and wetting cycles, a is the intercept, and b is the slope. The fitting parameters a and b for different initial compaction conditions are listed in Table 7.

There is a linear relationship between the parameter a and the degree of compaction, as shown in Table 6, while there is a reciprocal-type function between the parameter b and the degree of compaction, which are expressed as follows:

$$a = 214.8d - 164.2, \quad (5)$$

$$b = \frac{1}{0.47 - 0.69d} \quad (6)$$

Substituting (5) and (6) into (4) results in the following equation:

$$c = 214.8d - 164.2 + \frac{n}{0.47 - 0.69d} \quad (7)$$

The cohesion of saturated Yudong silt for any degree of compaction and any number of drying and wetting cycles can be predicted by (7).

According to the program of the direct shear tests on saturated and unsaturated silt specimens, the tests are orthogonal to the group saturated specimen with the compaction degree of 96% and the drying and wetting cycles of 0. The cohesion of specimens of this group obtained by the direct shear tests is 41.44 kPa. (3) is divided by 41.44 kPa and then is multiplied by (7) as follows:

$$c(w_0, d, n) = \frac{c(w_0)}{41.44} \times c(d, n). \quad (8)$$

Substituting (3) into (8) results in the following equation:

$$c = (-0.43w_0^2 + 13.43w_0 - 36.38) \times \left[5.18d - 3.96 + \frac{n}{19.48 - 28.59d} \right]. \quad (9)$$

With (9), the cohesion can be predicted for Yudong silt with different initial water contents and for different degrees of compaction and different numbers of drying and wetting cycles in the range of test conditions.

4.4. Predicting Strength of Yudong Silt Using SWCC. The strength theories for unsaturated soils are mostly based on

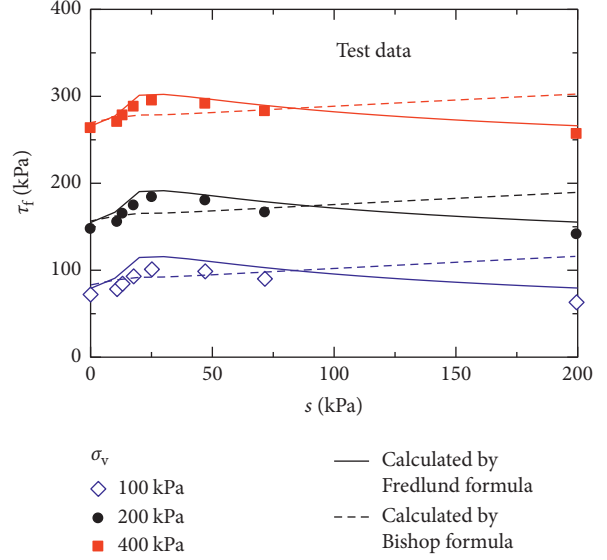


FIGURE 11: Measured and predicted shear strength versus suction under different vertical stresses.

the Mohr–Coulomb criterion. Numerous formulae for the strength of unsaturated soils are recognized by geotechnical community, including the strength formulae proposed by Bishop [40] and Fredlund and Morgenstern [41].

Bishop [40] proposed a univariate effective stress formula, which can be written as

$$\tau_f = c' + [\sigma - u_a + \chi(u_a - u_w)] \tan \phi'. \quad (10)$$

Fredlund and Morgenstern [41] proposed a bivariate formula, which can be written as

$$\tau_f = c' + (\sigma - u_a) \tan \phi' + (u_a - u_w) \tan \phi^b. \quad (11)$$

From the corresponding values of suction obtained under different initial water contents from the drying curve (Figure 4(a)), the relationships between the shear strength and suction for net normal stresses of 100, 200, and 400 kPa can be calculated with (10). The relationship between χ and the saturation degree of noncohesive silt was determined by Bishop and Donald [42], and the value of χ is approximately equal to the value of the saturation degree (Figure 4(b)). The data were input into (11), and the relationships between the shear strength and suction for net normal stresses of 100, 200, and 400 kPa were also obtained. The measured net normal stresses in the tests were 100, 200, and 400 kPa, and the relationship between the shear strength and the suction of the Yudong silt is shown in Figure 11.

There were very large deviations between the shear strength calculated by (10) and the measured values, as shown in Figure 11. The shear strength calculated by the Bishop formula did not decrease but always increases with increasing the suction when the suction value is greater than 30 kPa. Therefore, there are still certain limitations associated with applying the shear strength formula for unsaturated soils proposed by Bishop [40] to the Yudong silt. There were small deviations between the shear strength calculated by (11) and the measured values, as shown in Figure 11.

The measured shear strength versus suction shows that when the water content is close to the optimum water content, the suction is 30 kPa, and the peak shear strength also occurred at the water content. The soil used in this study has a uniform particle size distribution and has many pores. When the suction decreases from 30 kPa, the silt specimen tends to be saturated rapidly. Part of water weakens the interactions between the soil particles and reduces the bonding between the particles, resulting in a decrease in shear strength [41]. When the suction exceeds 30 kPa, the silt is relatively dry with little capillary water, and then, some small cracks exist in the silt specimens, which have small shear strength.

From the above discussions, (1), (9), and (11) can quickly provide the technical parameters for the design and construction of the road subgrade or fill materials.

5. Conclusions

- (1) The cohesion of saturated Yudong silt decreases with increasing the number of drying and wetting cycles, increases with increasing the degree of compaction, and increases first and then decreases as the initial water content increases. An empirical formula was given according to the experimental data. The formula can predict the cohesion of the saturated Yudong silt under different degrees of compaction or different numbers of drying-wetting cycles in the range of test conditions.
- (2) The internal friction angle of Yudong silt, which changes between 29° and 31°, was only slightly influenced by the number of drying and wetting cycles, the initial compaction degree, and the initial water content.
- (3) According to results of the direct shear tests and the soil-water characteristic curve of Yudong silt, the shear strength formula proposed by Bishop is not applicable, while an alternative method based on the Fredlund formula is appropriate.

Data Availability

The data used to support the findings of this study are available from the corresponding author upon request.

Conflicts of Interest

The authors declare that they have no conflicts of interest.

Acknowledgments

The authors express their gratitude for the grant provided by the National Natural Science Foundation of China (nos. 41602295 and U1704243). The work was partially supported by the High-level Talents Foundation of the North China University of Water Conservancy and Electric Power (201501001).

References

- [1] D. Y. Wang, C. S. Tang, Y. J. Cui, B. Shi, and J. Li, "Effects of wetting-drying cycles on soil strength profile of a silty clay in micro-penetrometer tests," *Engineering Geology*, vol. 206, pp. 60–70, 2016.
- [2] E. E. Alonso, E. R. C. Hoffmann, and E. Garcia-Escudero, "Expansive bentonite-sand mixtures in cyclic controlled-suction drying and wetting," *Engineering Geology*, vol. 81, no. 3, pp. 213–226, 2005.
- [3] H. Nowamooz and F. Masroui, "Mechanical behaviour of expansive soils after several drying and wetting cycles," *Geomechanics and Geoengineering*, vol. 5, no. 4, pp. 213–221, 2010.
- [4] H. Nowamooz, E. Jahangir, and F. Masroui, "Volume change behaviour of a swelling soil compacted at different initial states," *Engineering Geology*, vol. 153, pp. 25–34, 2013.
- [5] Y. J. Cui, M. Yahia-Aissa, and P. Delage, "A model for the volume change behavior of heavily compacted swelling clays," *Engineering Geology*, vol. 64, pp. 232–250, 2002.
- [6] H. Nowamooz and F. Masroui, "Shrinkage-swelling of compacted clayey dense and loose soils," *Comptes Rendus Mécanique*, vol. 337, no. 11, pp. 781–790, 2009.
- [7] S. G. Goh, H. Rahardjo, and E. C. Leong, "Shear strength of unsaturated soils under multiple drying-wetting cycles," *Journal of Geotechnical and Geoenvironmental Engineering*, vol. 140, no. 2, article 06013001, 2014.
- [8] J. R. Zhang, D. A. Sun, A. N. Zhou, and T. Jiang, "Hydro-mechanical behavior of expansive soils with different suctions and suction histories," *Canadian Geotechnical Journal*, vol. 53, no. 1, pp. 1–13, 2015.
- [9] D. A. Sun, J. R. Zhang, Y. Gao, and D. C. Sheng, "Influence of suction history on hydraulic and stress-strain behavior of unsaturated soils," *International Journal of Geomechanics*, vol. 16, no. 6, article 04015001, 2016.
- [10] Y. P. Yao, W. Hou, and A. N. Zhou, "UH model: three-dimensional unified hardening model for overconsolidated clays," *Geotechnique*, vol. 59, pp. 451–469, 2009.
- [11] C. F. Chiu, X. W. Ni, and L. S. Zhang, "Effect of hydraulic hysteresis on shear strength of unsaturated clay," *Engineering Geology*, vol. 173, pp. 66–73, 2014.
- [12] H. Nowamooz, E. Jahangir, F. Masroui, and J. P. Tisot, "Effective stress in swelling soils during wetting drying cycles," *Engineering Geology*, vol. 210, pp. 33–44, 2016.
- [13] A. Bouazza, S. Jefferis, and T. Vangpaisal, "Investigation of the effects and degree of calcium exchange on the Atterberg limits and swelling of geosynthetic clay liners when subjected to wet-dry cycles," *Geotextiles and Geomembranes*, vol. 25, no. 3, pp. 170–185, 2007.
- [14] H. Komine, K. Yasuhara, and S. Murakami, "Swelling characteristics of bentonites in artificial seawater," *Canadian Geotechnical Journal*, vol. 46, no. 2, pp. 177–189, 2009.
- [15] C. S. Tang, B. Shi, C. Liu, W. B. Suo, and L. Gao, "Experimental characterization of shrinkage and desiccation cracking in thin clay layer," *Applied Clay Science*, vol. 52, no. 2, pp. 69–77, 2011.
- [16] A. Hoor and R. K. Rowe, "Potential for desiccation of geosynthetic clay liners used in barrier systems," *Journal of Geotechnical and Geoenvironmental Engineering*, vol. 139, no. 10, pp. 1648–1664, 2013.
- [17] T. Mukunoki, T. Nakano, J. Otani, and J. P. Gourc, "Study of cracking process of clay cap barrier in landfill using X-ray CT," *Applied Clay Science*, vol. 101, no. 10, pp. 558–566, 2014.
- [18] F. Zangl and W. Likos, "Alternative methods for wet-dry cycling of geosynthetic clay liners," *Journal of Geotechnical*

- and *Geoenvironmental Engineering*, vol. 142, no. 11, article 04016063, 2016.
- [19] D. A. Sun, H. B. Cui, H. Matsuoka, and D. C. Sheng, "A three-dimensional elastoplastic model for unsaturated compacted soils with hydraulic hysteresis," *Soils and Foundations*, vol. 47, no. 2, pp. 253–264, 2007.
- [20] D. A. Sun, D. C. Sheng, H. B. Cui, and S. W. Sloan, "A density-dependent elastoplastic hydro-mechanical model for unsaturated compacted soils," *International Journal for Numerical and Analytical Methods in Geomechanics*, vol. 31, no. 11, pp. 1257–1279, 2007.
- [21] D. A. Sun, D. C. Sheng, and S. W. Sloan, "Elastoplastic modelling of hydraulic and stress-strain behavior of unsaturated soils," *Mechanics of Materials*, vol. 39, no. 3, pp. 212–221, 2007.
- [22] D. A. Sun, D. C. Sheng, and Y. F. Xu, "Collapse behavior of unsaturated compacted soil with different initial densities," *Canadian Geotechnical Journal*, vol. 44, no. 6, pp. 673–686, 2007.
- [23] C. P. K. Gallage and T. Uchimura, "Effects on dry density and grain size distribution on the soil-water characteristic curves of sandy soils," *Soil and Foundations*, vol. 50, no. 1, pp. 161–172, 2010.
- [24] Y. Gao and D. A. Sun, "Soil-water retention behavior of compacted soil with different densities over a wide suction range and its prediction," *Computers and Geotechnics*, vol. 91, pp. 17–26, 2017.
- [25] A. N. Zhou and D. C. Sheng, "An advanced hydro-mechanical constitutive model for unsaturated soils with different initial densities," *Computers and Geotechnics*, vol. 63, pp. 46–66, 2015.
- [26] K. M. Y. Ho, J. M. K. Tse, and C. W. W. Ng, "Influence of drying and wetting history and particle size on state-dependent soil water characteristic curves (SDSWCCs)," in *Proceedings of the 3rd Asian Conference on Unsaturated Soils*, pp. 213–218, Nanjing, China, 2007.
- [27] L. W. Kong, H. Md Sayem, and H. H. Tian, "Influence of drying-wetting cycles on soil-water characteristic curve of undisturbed granite residual soils and microstructure mechanism by nuclear magnetic resonance (NMR) spin-spin relaxation time (T₂) relaxometry," *Canadian Geotechnical Journal*, vol. 55, no. 2, pp. 208–216, 2018.
- [28] A. N. Zhou, "A contact angle-dependent hysteresis model for soil-water retention behaviour," *Computers and Geotechnics*, vol. 49, pp. 36–42, 2013.
- [29] Ministry of Communications Highway Science Research Institute, *JTG/E40-2007 Test Methods of Soils for Highway Engineering*, People's Communications Press, Beijing, China, 2007, in Chinese.
- [30] China Railway Survey and Design Institute, *JTG/D30-2004 Specifications for Design of Highway Subgrades*, People's Communications Press, Beijing, China, 2004, in Chinese.
- [31] N. Perez-Garcia, S. L. Houston, W. N. Houston, and J. M. Padilla, "An oedometer-type pressure plate SWCC apparatus," *Geotechnical Testing Journal*, vol. 31, no. 2, pp. 115–123, 2008.
- [32] J. W. Hilf, *An Investigation of Pore-Water Pressure in Compacted Cohesive Soils*, U.S. Department of the Interior, Bureau of Reclamation, Design and Construction Division, Technical Memorandum, No. 654, Denver, CO, USA, 1956.
- [33] J. R. Zhang, Q. Xu, and D. A. Sun, "Simulation of soil-water characteristic curves during drying and wetting cycles," *Rock and Soil Mechanics*, vol. 35, no. 3, pp. 689–695, 2014, in Chinese.
- [34] M. T. Van Genuchten, "A closed form equation for predicting the hydraulic conductivity of unsaturated soils," *Soil Science Society of America Journal*, vol. 44, no. 5, pp. 892–898, 1980.
- [35] D. G. Fredlund and A. Xing, "Equations for soil-water characteristic curve," *Canadian Geotechnical Journal*, vol. 31, no. 4, pp. 521–532, 1994.
- [36] S. K. Vanapalli, D. G. Fredlund, D. E. Pufahl, and A. W. Clifton, "Model for the prediction of shear strength with respect to soil suction," *Canadian Geotechnical Journal*, vol. 33, pp. 379–392, 1996.
- [37] R. Baker and S. Frydman, "Unsaturated soil mechanics: critical review of physical foundations," *Engineering Geology*, vol. 106, no. 1-2, pp. 26–39, 2009.
- [38] J. M. Konrad and M. Lebeau, "Capillary-based effective stress formulation for predicting shear strength of unsaturated soils," *Canadian Geotechnical Journal*, vol. 52, no. 12, pp. 2067–2076, 2015.
- [39] L. Y. Peng, J. K. Liu, J. H. Xiao, and L. H. Chen, "Mechanical properties of compacted silt on Beijing-Kowloon Railway," *Journal of Beijing Jiaotong University*, vol. 31, no. 4, pp. 56–60, 2007, in Chinese.
- [40] A. W. Bishop, "The principal of effective stress," *Teknisk Ukeblad*, no. 39, pp. 859–863, 1959.
- [41] D. G. Fredlund and N. R. Morgenstern, "Stress state variable for unsaturated soils," *Journal of Geotechnical Engineering*, vol. 103, no. 5, pp. 447–466, 1977.
- [42] A. W. Bishop and I. B. Donald, "The experimental study of partly saturated soil in triaxial apparatus," in *Proceedings of the 15th International Conference on Soil Mechanics and Foundation Engineering*, vol. 1, pp. 13–21, Boulder, CO, USA, July 1961.

Research Article

Test on the Stabilization of Oil-Contaminated Wenzhou Clay by Cement

Chuang Yu, Raoping Liao, Chaopeng Zhu, Xiaoqing Cai, and Jianjun Ma 

College of Architecture and Civil Engineering, Wenzhou University, Wenzhou 325035, China

Correspondence should be addressed to Jianjun Ma; jianjun_ma@wzu.edu.cn

Received 9 May 2018; Accepted 21 June 2018; Published 12 July 2018

Academic Editor: Yonggui Chen

Copyright © 2018 Chuang Yu et al. This is an open access article distributed under the Creative Commons Attribution License, which permits unrestricted use, distribution, and reproduction in any medium, provided the original work is properly cited.

Oil-contaminated soils have been paid much attention due to the reclamation of industrial lands in coastal cities of China. As known, oil-contaminated soils are inapplicable for construction due to their weak engineering properties, thus leading to the requirement of remediation and reclamation for oil-contaminated sites. This study presents an experimental investigation on the stabilization of contaminated soils with Portland cement. Investigations including the Atterberg limits, unconfined compressive strength, direct shear strength, and microstructure of cement-stabilized soils have been carried out, verifying the suitability of applying cement to improve engineering properties. Experimental results show that the geotechnical properties of contaminated soil are very poor. With the application of cement, the liquid limit and plasticity index of contaminated soil samples decrease dramatically, and the strength of treated soils has been improved. Experimental results from scanning electron microscope (SEM) indicate that cement-stabilized oil-contaminated soil is featured with a stable supporting microstructure, owing to the cementation between soil particles. This also confirms the applicability of cement to be served as an additive to treat oil-contaminated soils.

1. Introduction

Remediation and reclamation of oil-contaminated sites has been paid increasing attentions in recent decades. This is mainly due to the fast development of industry all over the world and its impact on global environment [1, 2]. As known, oil spills during transportation, leakage from storage tanks, discharge of industrial waste liquid with oil, and so on would result in serious contamination to soils. For example, leather industry is popular and advanced in Wenzhou, China, which is regarded as one of the most important economic pillars for the local government. However, due to the loose regulation and lagging industry in the past few decades, liquid industrial waste was dumped without proper treatment in this region [2]. Contaminated soils normally contain toxic heavy metals and chloride salt, which have been suggested to be stabilized using cement [3–6]. However, the stabilization for contaminated soils induced by oil pollution becomes much more complicated and difficult.

Investigations on engineering properties of oil-contaminated geomaterials have been carried out since 1990s. For instance,

Alsanad et al. [7, 8] carried out a laboratory test to investigate the effects of oil contamination on strength parameters, compressibility, permeability, and compaction characteristics of the Kuwaiti sand. Later on, Khamchian et al. [9] carried out series of tests to study the effects of oil contamination on geotechnical properties of clays, and they found that increasing oil content for soil samples would decrease its strength, permeability, maximum dry density, optimal water content, and Atterberg limits. However, they did not provide specific measures to solve this problem. With the booming population in coastal cities around the world, oil-terminated soils have been employed for construction after proper stabilization. Thus, a few measures have been reported in literature for oil-contaminated soils, including the replacement of oily soil with uncontaminated soil, incineration, absorption, biodegradation, and so on, which are time-consuming and expensive [2, 10]. Therefore, some scholars recently commented that soil improvement with cement is attractive for its mature technology and economy [1, 10, 11]. As known, cement reacts with water and binds loose particle materials in a short time, which



FIGURE 1: The location of borrow pit.

would produce strength and durability for soils [12]. For example, Akinwumi [11] applied Portland cement to treat oil-contaminated soil in his/her study. Other study on the stabilization/solidification of contaminated soils [1, 3, 13–17, 26–29] also suggested that cement-stabilized soils have been improved sufficiently and are capable to support a structural foundation or road pavements.

Despite this, the solidifying effect of cement on oil-contaminated soils remains to be studied. First and most importantly, the extent of contamination depends on the chemical composition of the contaminant and the properties of soils [22]. Also, in connection with repair works, geotechnical properties and mechanical behaviors should be investigated for any potential applications of oil-contaminated soils. In addition, mechanism of cement-stabilized oil-contaminated soil is also required through microscale investigation. However, there are limited studies on geotechnical properties of contaminated soils in literature.

Based on the discussion aforementioned, a laboratory testing program was carried out to investigate the effects of improvement on Wenzhou clay with different doses of oil and various contents of cement. The testing included basic soil properties, Atterberg limits, direct shear strength, unconfined compressive strength, and microstructure characteristics of cement solidified natural and contaminated soils.

2. Material and Methods

2.1. Materials. Soil samples used in this study were obtained from a borrow pit at Wenzhou (latitude $27^{\circ}51'N$ and longitude $121^{\circ}08'E$; Figure 1 shows the location), China. The marine clay sludge in coastal area is also named as Wenzhou Clay, with typical characteristics being high moisture content, high compressibility, and low strength [10, 23]. Samples were collected from the sidewall of the soil profile at around 10 m depth. They were stored in labeled and sealed sacks and transferred to Geotechnical Laboratory (Wenzhou University), field subsamples were also taken to determine their natural moisture contents.

Plant oil (peanut and soybean reconciled oil) was applied in this study, for the consideration that its physic-chemical characteristics are similar to that of the petroleum oil (i.e., nontoxic, nonvolatile, etc.). The main components of plant oil (obtained through the product description) are unsaturated fatty acid (around 80%, including 41.2% oleic

acid and 37.6% linoleic acid) and saturated fatty acid (around 20%, including palmitic acid, stearic acid, and arachidic acid). While, the main components of petroleum oil are low levels of heavy metals and total petroleum hydrocarbons (TPH), as reported in literature [13, 14]. Both plant oil and petroleum oil would impose lubrication effects on soil particles, thus leading to lower geotechnical properties of contaminated sites. As known, the main mechanisms involved in the stabilization/solidification of oil-contaminated soils are chemical fixation and physical encapsulation or adsorption [13, 24]. Based on the concept of process of envelopes [13–17], contaminants generated by similar process are characterized by similar physical properties and composition; thus, the treatment method applied to plant oil-contaminated soil also can be applied to other waste of the same type. This explanation may justify the adoption of plant oil to replace petroleum oil in this study. Another consideration is that it is difficult to obtain crude oil nearby; commercial petro oil has been purified and is featured with volatile organic compounds, imposing difficulties on the control of waste dosage with room temperature.

2.2. Experimental Program. Soil samples were oven-dried at $105^{\circ}C$ for 24 hours, then the soil particles were crushed and passed through $75\ \mu m$ sieve. Hereafter, both cement and dry soil sample were mixed by a mixing drum. The dry cement-soil mixture was then sprayed by oil-water mixture, the volume of which was calculated according to the optimal compaction moisture content (OMC) and maximum dry density (OMD) [25, 26]. Finally, the contaminated soil was stored in an airtight plastic container for a period of time and allowed to equilibrate prior to commencement of laboratory tests [27].

Specific gravity, Atterberg limits, compaction, unconfined compressive strength (UCS), and scanning electron microscopy (SEM) tests were conducted on both natural soils, contaminated soils (0%, 0.1%, 1%, and 3% oil contents, by dry weight of soil), and cement-stabilized contaminated soil samples with various proportions of Portland cement (4%, 8%, and 12%, by weight of the soil). These tests were performed for the purpose of studying the effects of cement on the improvement of geotechnical properties of oil-contaminated soils.

The soil plasticity index was determined from liquid and plastic limits tests, with the help of a combined liquid plastic apparatus. The UCS tests were conducted based on the method suggested by ASTM D2166 [28]. Specimens (30 mm diameter \times 80 mm height) were prepared at the optimal moisture content and tested after 0, 7, 14, and 28 days of curing coated with preservative film under controlled temperature ($20 \pm 3^{\circ}C$) and relative humidity (95%). The direct shear test was conducted following a standard approach [29]. Samples were prepared at their optimal moisture contents and tested after 0, 7, 14, and 28 days of curing.

3. Results and Discussion

3.1. Materials Characterization. The chemical compositions of Wenzhou clay were expressed in terms of oxides and

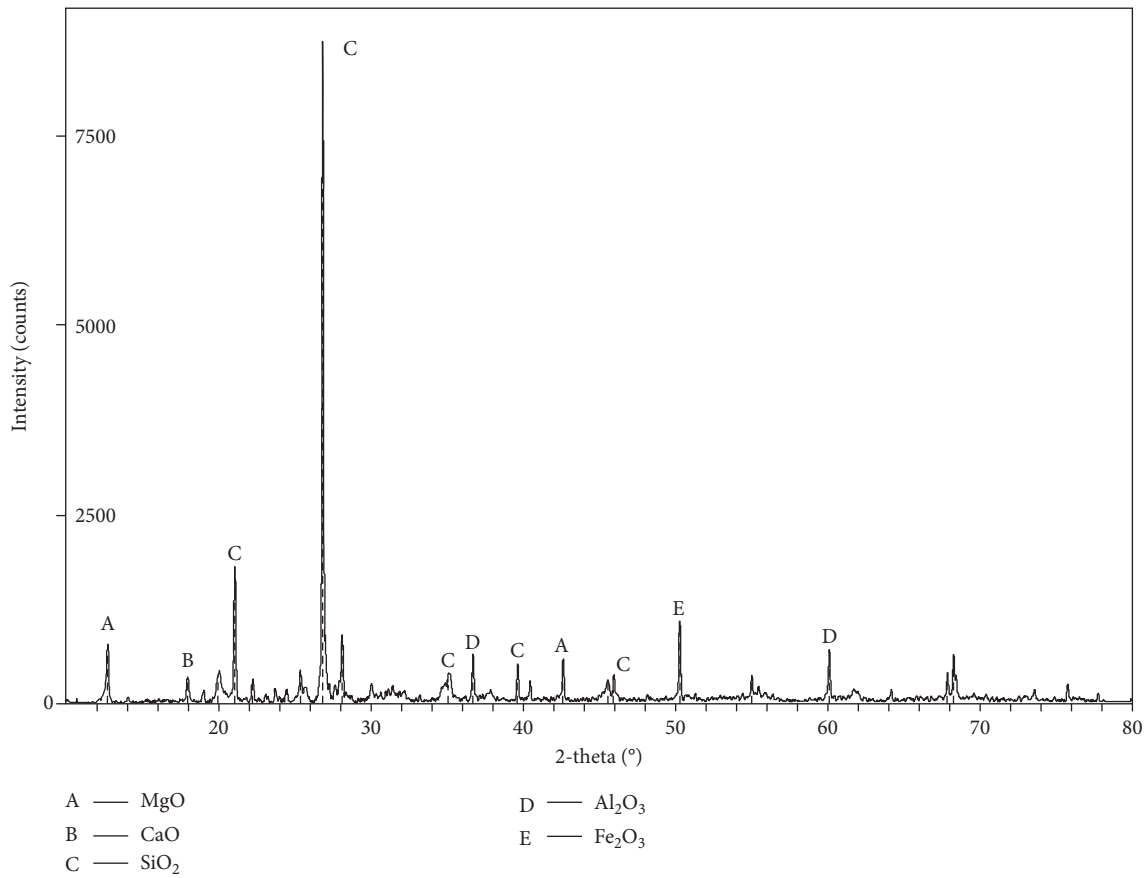


FIGURE 2: X-ray diffractograms (XRD) of uncontaminated clay.

TABLE 1: Chemical compositions of uncontaminated Wenzhou clay (XRD results).

Compounds	Percentage (%)
Silicon dioxide (SiO ₂)	48.6
Magnesium oxide (MgO)	10.9
Aluminum oxide (Al ₂ O ₃)	7.8
Ferric oxide (Fe ₂ O ₃)	5.2
Calcium oxide (CaO)	2.5
Others	24.7

calculated from elemental analysis determined by XRD, as shown in Figure 2, and the main components are listed in Table 1. And the components of cement used in the test are shown in Table 2, which can be obtained directly from the “Production Description” printed on the cement package. It is apparent that the major components of natural Wenzhou clay is silicon dioxide (SiO₂), taking up around 50%, then other oxides; the main content of Portland cement is calcium oxide (CaO), taking up about 60%, followed by silicon dioxide (SiO₂), with a portion of around 24%.

3.2. Geotechnical Properties of the Uncontaminated Soil and the Plant Oil-Contaminated Soil. Basic soil properties, including liquid limit, plastic limit, OMC, specific gravity, maximum dry density (MDD), moisture content, and density of the uncontaminated clay, are presented in Table 3.

TABLE 2: Chemical composition of cement (product description).

Compounds	Percentage (%)
Silicon dioxide (SiO ₂)	23.67
Calcium oxide (CaO)	59.98
Ferric oxide (Fe ₂ O ₃)	3.07
Aluminum oxide (Al ₂ O ₃)	7.21
Magnesium oxide (MgO)	2.07
Potassium oxide (K ₂ O)	0.68
Sodium oxide (Na ₂ O)	0.17
Sulfur trioxide (SO ₃)	2.14
Loss	1.01

This further confirms that Wenzhou clay is characterized by higher water content and high liquid limit.

Figure 3 shows the plots of liquid limit, plastic limit, and plasticity index of oil-contaminated clay samples with different doses of oil. As can be seen, the liquid limit and plasticity index of the contaminated soil samples decrease with the increasing oil content, while the change in plastic limit is not apparent. This can be explained by noting that clay minerals exhibit surface charge imbalance and the negative charged surface turns to be balanced by hydrated cations, thereby forming a thin layer of water (diffuse double layer) bonded to its surface [5, 10, 22]. The attractable hydrated cations provided by the clay minerals have been increased due to the oil contamination, and this consequently increases the thickness of the

TABLE 3: Basic soil properties for uncontaminated Wenzhou clay.

Natural moisture content (%)	Density (g/cm ³)	Specific gravity	Liquid limit (%)	Plastic limit (%)	OMC	MDD
66.0	1.58	2.68	58.0	26.1	30.0	1.45

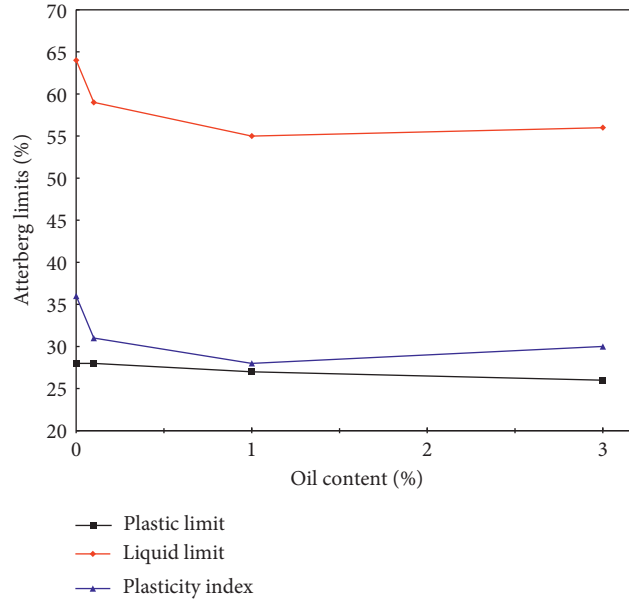


FIGURE 3: Influence of oil content on Atterberg limits of contaminated clay.

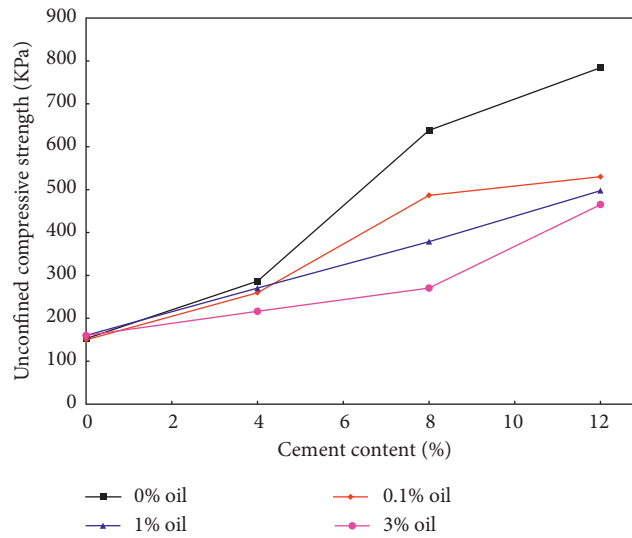


FIGURE 4: UCS of the cement-stabilized oil-contaminated soils with different oil contents.

diffuse double layer. In addition, lubricating characteristics of oil itself also seem to be another reason to explain the decrement of both liquid limit and plasticity limit in oil-contaminated soils.

3.3. *Unconfined Compressive Strength.* Figure 4 plots the variation of UCS of cement-stabilized oil-contaminated soils. It shows the strength of oil-contaminated soils (contaminated by different oil contents) stabilized by an addition

of 12% cement after curing 28 days. UCS of all oil-contaminated soil samples increases with the increasing cement, which indicates that cement can be served as an effective additive to solidify oil-contaminated soils. While, the stabilization effect in soils with lower oil contents is better than that in their counterparts with higher oil contents. The stabilization induced by cement lies on the exchange between monovalent (hydrated) cations in contaminated soils and divalent cations (such as Ca^{2+} and Mg^{2+}) provided by cement [30, 31]. Inspection of Figure 4 also shows that, the strength of soil would

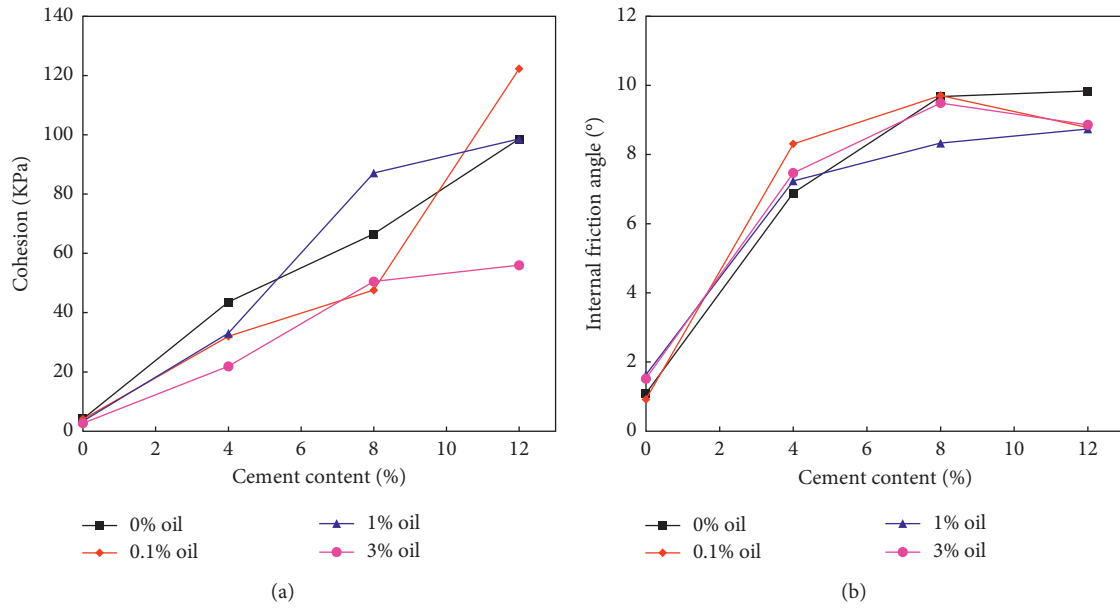


FIGURE 5: Influence of cement contents on shear strength parameters of contaminated soils.

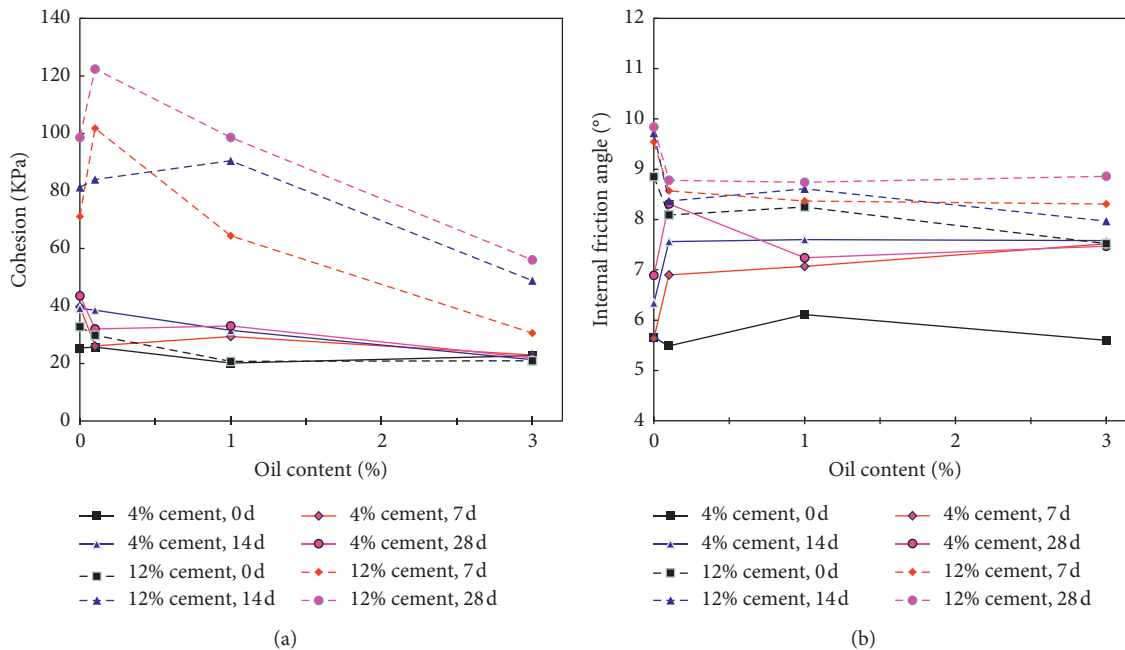


FIGURE 6: Influence of oil content on shear strength parameters of soil samples.

decrease significantly along with increment of oil contents. The presence of oil appears to act as a hydration retarder and decreases the strength of soils. As stated in Section 3.2, the size of diffuse double layer on the surface of clay minerals decreases with increasing cement contents, thus in turn reducing the barriers between soil particles and getting soil clumps together.

3.4. Direct Shear Test. A graphical illustration of changes in cohesion strength (c) and friction angle (ϕ) for the oil-contaminated soil with different doses of cement is

presented in Figure 5. These samples were cured for 28 days before carrying out direct shear test. Obviously, with the increasing cement being added in contaminated soil samples, both cohesion strength and friction angle increase dramatically. This tendency is similar to that of UCS discussed in Section 3.3, particularly for the case of cohesion (Figure 5(a)). While, the friction angle turns to be stable when the dose of cement approaches a certain level (Figure 5(b)). This is because the friction angle mainly depends on the size of soil particles, which may change slowly for cases with higher cement contents [5, 22].

Effects of oil content on the improvement of contaminated soils are demonstrated in Figure 6. It presents a negative correlation between oil content and shear strength parameters (cohesion (c), internal friction angle (ϕ)). There exists a remarkable decrement in cohesion (c) along with increasing oil contents, as shown in Figure 6(a). However, from the plots of soil specimen with 12% of cement (cured for 28 days), one can find that the cohesion value of uncontaminated soil specimen is equal to that of contaminated soils with 1% of oil. This attributes to two main reasons: on one hand, cohesion and internal friction angle can be improved by cement; on the other hand, they get deteriorated by the presence of oil. The competitive results of two contradict mechanisms also can be seen in Figure 6(b) for internal friction angle, which depends on relative amounts of both cement and oil.

4. Scanning Electron Microscopy Analysis

SEM was applied to capture the morphological changes in both natural soils and cement-stabilized oil-contaminated soils. The standard procedure for SEM is as follows:

Step 1: *Specimen preparation*: Soil samples were oven-dried firstly, then they were cut into small thin pieces; hereafter, these thin soil samples were mounted onto a sample holder, the surface of which was covered by fulmargin (Figure 7). Later on, thin soil samples were loaded into an airlock chamber; after the chamber being vacuumed, metal spraying was employed to treat them.

Step 2: *SEM scanning*: Soil samples were mounted into the sample chamber, and then scan parameters were adjusted, and an optimal point for observation was figured out. Thereafter, the magnification was increased to zoom in on details of soil samples, and photos were finally taken (Figure 8).

Figure 9 compares the SEM photomicrograph of cement-stabilized contaminated soils (0% and 3% oil content) with various doses of cement (4%, 8%, and 12%). The curing age of cement solidification soil was 28 days, and the scanning electron microscope (SEM) image magnification was 10000 times.

From the comparative analysis of Figures 9(a), 9(c), and 9(e), it is known that natural soils stabilized by cement are characterized by flocculations, which become denser with the increasing cement. Obviously, the existence of flocculations produced by cement would result in a more stable soil structure with dense particles and thus enhancing its strength. Figures 9(b), 9(d), and 9(f) show the microscopic diagram of cement-stabilized soil contaminated by 3% oil. Similarly, with the increasing dose of cement, the amount of flocculations increased dramatically, indicating an enhanced strength for contaminated soils. This can be explained by noting that flocculations are the product of cement hydration during the curing period, and a larger amount of cement would result in stronger hydration, products of which in the soil particles are the cementation of loose soil particles in the form of flocculations, thereby forming solid aggregates and improving the soil strength [1, 5, 10, 22].

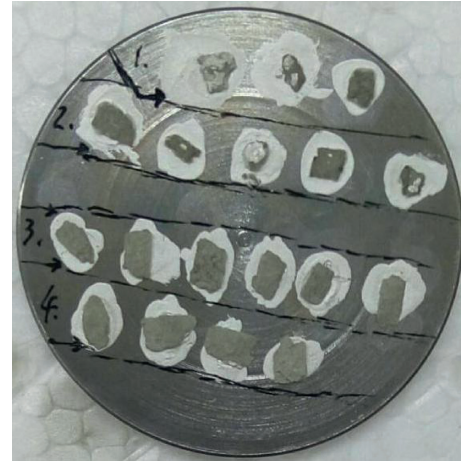


FIGURE 7: Soil samples placed on a sample holder.



FIGURE 8: SEM scanning.

Comparison between Figures 9(a) and 9(b) indicates that with the incorporation of 3% oil, the cement-stabilized contaminated soils were characterized by thin and loose structure. This difference becomes more apparent comparing Figures 9(d) and 9(f) with Figures 9(c) and 9(e), suggesting that flocculations of cement-stabilized contaminated soil formed loose and sliding structures and the cementation effect was weaker in oil-contaminated soil samples. This may be explained as that the addition of additive agents (cement in this study) would produce noncrystalline chemical compounds, which coats over soil particles and bridges them. Coating over solid grains thus in turn enhances the bridging action between soil particles and further results in the development of a strong cellular and nodular mass [32].

5. Conclusions

In this paper, laboratory tests on cement-stabilized oil-contaminated soils were carried out, and the improvement on Atterberg limit, unconfined compressive strength, shear strength, and microstructure were studied. The following conclusions can be obtained based on this study:

- (1) The liquid limit and plasticity limit of contaminated soil decreased significantly compared with that of natural soils, with slight influence on plastic index being observed.
- (2) With increasing oil content, the unconfined compressive strength of cement-stabilized soil decreased

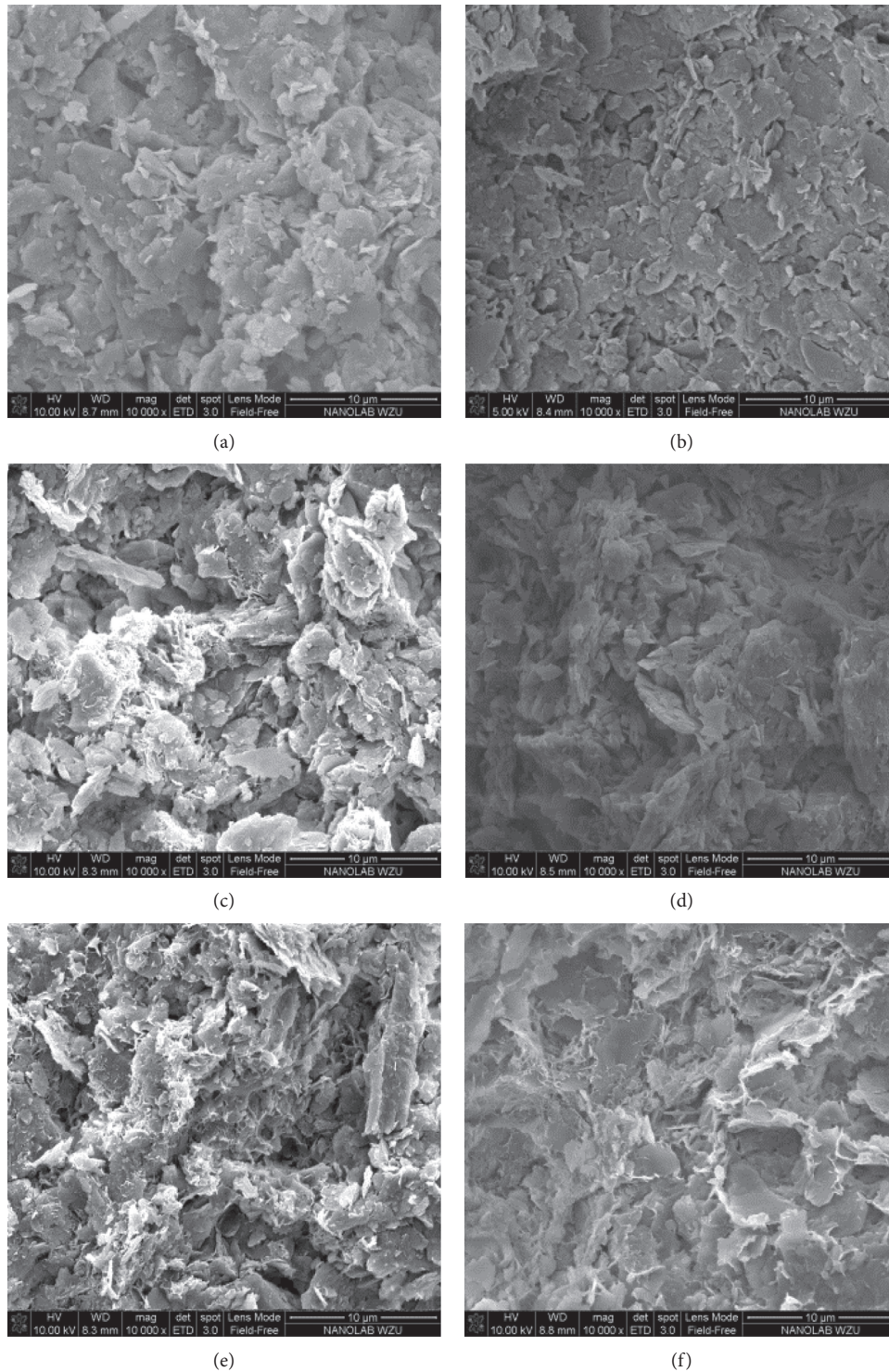


FIGURE 9: SEM photomicrograph of oil-contaminated soils stabilized by cement. (a) 0% oil; 4% cement, (b) 3% oil; 4% cement, (c) 0% oil; 8% cement, (d) 3% oil; 8% cement, (e) 0% oil; 12% cement, (f) 3% oil; 12% cement.

dramatically; by contrast, with the increase in cement content and curing age, the unconfined compressive strength had been enhanced remarkably; this confirms that cement can be served as an additive agent to solidify oil-contaminated soils.

(3) Direct shear strength tests show that with the increase of oil content, both cohesion and internal friction angle of solidified soil turned to decrease, while, with increasing the curing age and cement content, both properties had been improved gradually.

- (4) The results of SEM show that the hydration products of cement stabilized oil-contaminated soil decreased with the increment in oil content, and its microstructure got deteriorated. However, with the increasing dose of cement, the hydration products increased and the soil structure had been enhanced significantly.

Data Availability

The experimental data presented in this study can be referred to the corresponding author (Jianjun Ma), who would share these data once required.

Conflicts of Interest

The authors declare that they have no conflicts of interest.

Acknowledgments

This work was supported by the National Natural Science Foundation of China (nos. 51508418, 51578427, and 51508416), Plan Project of Science and Technology of Zhejiang Province (nos. 2014C33015, 2015C33220, and 2017C33220), and the Plan Project of Science and Technology of Wenzhou (nos. ZS2017002 and S20170001).

References

- [1] Y. G. Chen, L. Y. Jia, W. M. Ye, B. Chen, and Y. J. Cui, "Advances on experimental investigation on hydraulic fracturing behavior of bentonite-based materials used for HLW disposal," *Environmental Earth Sciences*, vol. 75, no. 9, pp. 787–800, 2016.
- [2] C. Yu, J. Liu, J. Ma, and X. Yu, "Study on transport and transformation of contaminant through layered soil with large deformation," *Environmental Science and Pollution Research*, vol. 25, no. 13, pp. 12764–12779, 2018.
- [3] Y. G. Chen, L. Y. Jia, Q. Li, W. M. Ye, Y. J. Cui, and B. Chen, "Swelling deformation of compacted GMZ bentonite experiencing chemical cycles of sodium-calcium exchange and salinization-desalinization effect," *Applied Clay Science*, vol. 141, pp. 55–63, 2017.
- [4] D. Dermatas and X. Meng, "Utilization of fly ash for stabilization/solidification of heavy metal contaminated soils," *Engineering Geology*, vol. 70, no. 3-4, pp. 377–394, 2003.
- [5] D. H. Moon, D. G. Grubb, and T. L. Reilly, "Stabilization/solidification of selenium-impacted soils using Portland cement and cement kiln dust," *Journal of Hazardous Materials*, vol. 168, no. 2-3, pp. 944–951, 2009.
- [6] M. Lei, D. Lin, J. Liu et al., "Modified chloride diffusion model for concrete under the coupling effect of mechanical load and chloride salt environment," *AIP Advances*, vol. 8, no. 3, article 035029, 2018.
- [7] H. A. Alsanad, W. K. Eid, and N. F. Ismael, "Geotechnical properties of oil contaminated Kuwaiti sand," *Journal of Geotechnical Engineering*, vol. 121, no. 5, pp. 407–412, 1995.
- [8] H. A. Alsanad and N. F. Ismael, "Aging effects on oil-contaminated Kuwaiti sand," *Journal of Geotechnical and Geoenvironmental Engineering*, vol. 123, no. 3, pp. 290–293, 1997.
- [9] M. Khamehchiyan, A. Hossein Charkhabi, and M. Tajik, "Effects of crude oil contamination on geotechnical properties of clayey and sandy soils," *Engineering Geology*, vol. 89, no. 3-4, pp. 220–229, 2007.
- [10] Y. F. Deng, X. B. Yue, S. Y. Liu, Y. G. Chen, and D. W. Zhang, "Hydraulic conductivity of cement-stabilized marine clay with metakaolin and its correlation with pore size distribution," *Engineering Geology*, vol. 193, pp. 146–152, 2015.
- [11] I. I. Akinwumi, C. A. Booth, D. Diwa, and P. Mills, "Cement stabilisation of crude-oil-contaminated soil," *Proceedings of the Institution of Civil Engineers-Geotechnical Engineering*, vol. 169, no. 4, pp. 336–345, 2016.
- [12] C. W. Jones, "Stabilization of expansive clay with hydrated lime and with Portland cement," *BMC Neuroscience*, vol. 13, no. 1, pp. 1–2, 1958.
- [13] R. B. Kogbara, Y. Yi, and A. Al-Tabbaa, "Process envelopes for stabilization/solidification of contaminated soil using lime-slag blend," *Environmental Science and Pollution Research*, vol. 18, no. 8, pp. 1286–1296, 2011.
- [14] R. B. Kogbara, A. Al-Tabbaa, Y. Yi, and J. A. Stegemann, "pH-dependent leaching behaviour and other performance properties of cement-treated mixed contaminated soil," *Journal of Environmental Sciences*, vol. 24, no. 9, pp. 1630–1638, 2012.
- [15] R. B. Kogbara, A. Al-Tabbaa, Y. Yi, and J. A. Stegemann, "Cement-fly ash stabilization/solidification of contaminated soil: performance properties and initiation of operating envelopes," *Applied Geochemistry*, vol. 33, pp. 64–76, 2013.
- [16] C. Shi and R. Spence, "Designing of cement-based formula for solidification/stabilisation of hazardous, radioactive, and mixed wastes," *Critical Review of Environmental Science Technology*, vol. 34, no. 4, pp. 391–417, 2004.
- [17] J. A. Stegemann and Q. Zhou, "Development of process envelopes for cement-based stabilisation/solidification of metal treatment filtercakes," in *Waste Management and the Environment IV, WIT Transactions on Ecology and the Environment*, M. Zamorano, V. Popov, A. G. Kungolos, C. A. Brebbia, and H. Itoh, Eds., vol. 109, pp. 21–30, WIT, Southampton, UK, 2008.
- [18] A. Al-Rawas, H. F. Hassan, R. Taha, A. Hago, B. Al-Shandoudi, and Y. Al-Suleimani, "Stabilization of oil-contaminated soils using cement and cement by-pass dust," *Management of Environmental Quality: An International Journal*, vol. 16, no. 6, pp. 670–680, 2005.
- [19] M. Kermani and T. Ebadi, "The effect of oil contamination on the geotechnical properties of fine-grained soils," *Soil and Sediment Contamination: An International Journal*, vol. 21, no. 5, pp. 655–671, 2012.
- [20] A. M. A. Nasr, "Utilisation of oil-contaminated sand stabilised with cement kiln dust in the construction of rural roads," *International Journal of Pavement Engineering*, vol. 15, no. 10, pp. 889–905, 2014.
- [21] S. J. Shah, A. V. Shroff, J. V. Patel, K. C. Tiwari, and D. Ramakrishnan, "Stabilization of fuel oil contaminated soil—a case study," *Geotechnical and Geological Engineering*, vol. 21, no. 4, pp. 415–427, 2003.
- [22] P. Fine, E. R. Graber, and B. Yaron, "Soil interactions with petroleum hydrocarbons: abiotic processes," *Soil Technology*, vol. 10, no. 2, pp. 133–153, 1997.
- [23] J. Ma, M. Qian, C. Yu, and X. Yu, "Compressibility evaluation of reconstituted clays with various initial water contents," *ASCE's Journal of Performance of Constructed Facilities*, 2018.
- [24] J. R. Conner, *Chemical Fixation and Solidification of Hazardous Wastes*, Van Nostrand Reinhold, New York, NY, USA, 1990.
- [25] ASTM D698, *Standard Test Method for Laboratory Compaction Characteristics of Soil Using Standard Effort (12,400 ft*

- lb/ft³ (600 kN-m/m³)), ASTM, West Conshohocken, PA, USA, 2012.*
- [26] ASTM D1557, *Test Method for Laboratory Compaction Characteristics of Soil Using Standard Effort (56,000 ft-lb/ft³ (2,700 kN-m/m³))*, ASTM, West Conshohocken, PA, USA, 2000.
- [27] M. Khamehchiyan, A. H. Charkhabi, and M. Tajik, "Effects of crude oil contamination on geotechnical properties of clayey and sandy soils," *Engineering Geology*, vol. 89, no. 3-4, pp. 220–229, 2007.
- [28] ASTM International, *Standard Test Method for Unconfined Compressive Strength of Cohesive Soil*, ASTM International, West Conshohocken, PA, USA, 1998d.
- [29] ASTM International, *Standard Test Method for Direct Shear Test of Soils under Consolidated Drained Conditions, ASTM D3080-98*, ASTM International, West Conshohocken, PA, USA, 1998a.
- [30] P. Beetham, T. Dijkstra, N. Dixon, P. Fleming, R. Hutchison, and J. Bateman, "Lime stabilisation for earthworks: a UK perspective," *Proceedings of the Institution of Civil Engineers-Ground Improvement*, vol. 168, no. 2, pp. 81–95, 2014.
- [31] H. L. Bohn, *Soil Chemistry*, Wiley, New York, NY, USA, 2002.
- [32] S. Kalra, N. R. Cashman, Z. Caramanos, A. Genge, and D. L. Arnold, "Gabapentin therapy for amyotrophic lateral sclerosis: lack of improvement in neuronal integrity shown by MR spectroscopy," *American Journal of Neuroradiology*, vol. 24, no. 3, pp. 476–480, 2003.

Research Article

A Simplified Nonlinear Method for a Laterally Loaded Pile in Sloping Ground

Pingbao Yin ¹, Wei He ¹ and Zhaohui Joey Yang ²

¹School of Civil Engineering, Changsha University of Science and Technology, Changsha 410114, China

²Department of Civil Engineering, University of Alaska Anchorage, Anchorage, AK 99508, USA

Correspondence should be addressed to Wei He; wadeho@csust.edu.cn

Received 24 January 2018; Accepted 31 May 2018; Published 10 July 2018

Academic Editor: Xinbao Yu

Copyright © 2018 Pingbao Yin et al. This is an open access article distributed under the Creative Commons Attribution License, which permits unrestricted use, distribution, and reproduction in any medium, provided the original work is properly cited.

A simplified nonlinear method was proposed to evaluate lateral behavior of a pile located in or nearby a slope, based on the traditional p - y method. This method was validated with field test results of a steel pipe pile in clay and model tests of piles in sand slopes. The comparison indicated that the calculated horizontal displacement and bending moment of piles agree well with experimental results. Then, parametric studies were performed, and it shows that horizontal displacement, rotation, bending moment, and shear force increase along with increasing slope angles; the depth of maximum moment locates at about $1.6D$ below ground surface for horizontal ground, while this value turns to be about $3.6D$ and $5.6D$ for sloping ground of 30° and 60° , respectively. The study clearly shows that slope angle has a significant effect on the deflection and lateral capacity of piles.

1. Introduction

The urban infrastructure development in China increases the possibility to construct piles in or nearby slopes, to support bridges, high-rise buildings, transmission towers, off-shore structures, retaining walls, etc. [1–5]. The lateral bearing behavior of these piles is extremely complicated due to sloping ground [6–8]. Compared to conventional piles, they may undergo severe reduction in horizontal bearing behavior. Although conventional laterally loaded piles have been studied by many researchers [9–15], limited literature can be found for piles in sloping ground [16–23]. In the past, the lateral behavior of piles could be evaluated with assumed earth pressure distribution, which can also be determined from field or model tests. This method usually assumes linearly increasing subgrade reaction modulus and cannot account for the influence of sloping ground. Thus, further studies have to be carried out to fill this gap.

This paper presented a simplified p - y method of laterally loaded piles located in or nearby slopes. A field test result of a steel pipe pile in clay and small-scale pile tests in sand slopes were employed to verify the proposed method and to

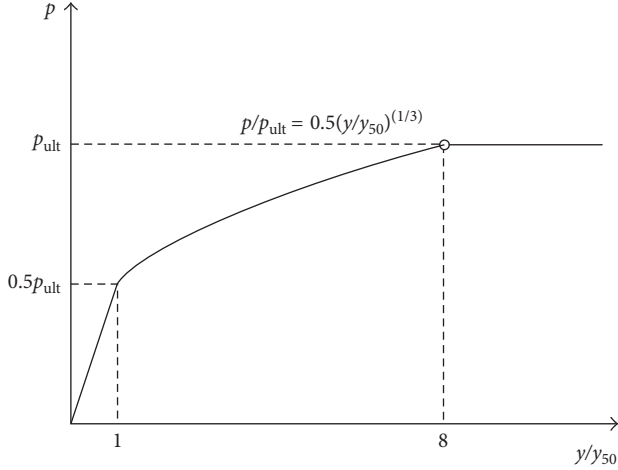
assess the influence of slope angles on the maximum deflection and required length of a pile.

2. The p - y Analysis for Sloping Ground

For a laterally loaded pile, the p - y method is a simple and practical way to account for the relationship between soil reaction p and pile deflection y along pile shaft. The p - y curve can be measured in field, by loading cells installed on pile-soil interface, or stress meters installed on steel cages as proposed by McClelland and Focht [24].

2.1. The p - y Curve of Clay Slopes. According to field test results, a p - y curve of Houston soft clay was proposed by Matlock, as shown in Figure 1, and has been adopted by the American Petroleum Institute (API). It can be expressed as follows [9, 10, 25]:

$$\frac{p}{P_{ult}} = \begin{cases} 0.5 \left(\frac{y}{y_{50}} \right)^{1/3}, & (y \leq 8y_{50}) \\ 1, & (y > 8y_{50}), \end{cases} \quad (1)$$

FIGURE 1: The p - y curve proposed by Matlock [9].

where p is the soil reaction; y is the pile deflection; p_{ult} is the ultimate soil resistance; p/p_{ult} is the ratio of soil resistance; y/y_{50} is the ratio of pile deflection; and y_{50} is the pile deflection when soil resistance reaches 50% of its ultimate value, and it can be evaluated by the following equation:

$$y_{50} = 2.5\varepsilon_{50}d, \quad (2)$$

where ε_{50} is the strain when the soil resistance reaches a half of its ultimate value and d is the pile diameter.

When a laterally loaded pile locates in a clay slope of a slope angle θ , the ultimate soil resistance in front of a pile can be computed by the following equation [24, 26]:

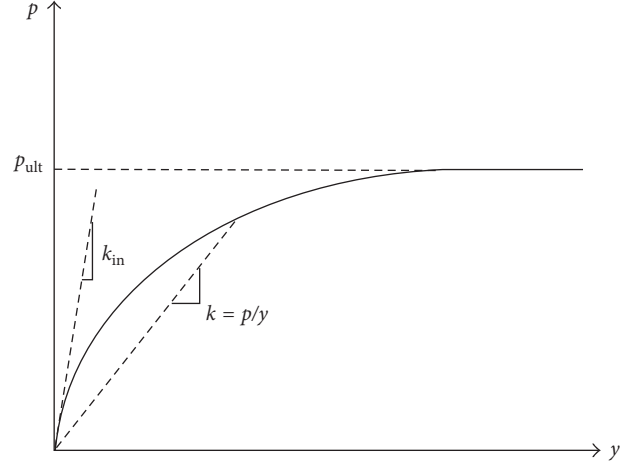
$$p_{ult} = \begin{cases} (2c_u d + \gamma dz + 2.83c_u z) \frac{1}{1 + \tan \theta}, & z < z_r \\ 9dc_u, & z \geq z_r, \end{cases} \quad (3)$$

where c_u is the average undrained shear strength; γ is the average unit weight of soil; z is the depth from ground surface to a studied point on the pile; θ is the slope angle; and z_r can be computed by the following equation:

$$z_r = \frac{(7 + 9 \tan \theta)c_u d}{\gamma d + 2.83c_u}. \quad (4)$$

2.2. The p - y Curve of Sand Slopes. A hyperbolic model was proposed to best-fit normalized p - y curves for laterally loaded piles in sand ground, as shown in Figure 2. This p - y curve is featured with an initial stiffness k_{in} and the relevant equation is as follows [27–32]:

$$p = \frac{y}{(1/k_{in}) + (y/p_{ult})}, \quad (5)$$

FIGURE 2: Hyperbolic p - y model.

where k_{in} is the initial stiffness, which depends on the soil stiffness, the pile stiffness, and the pile diameter. The initial stiffness, k_{in} , can be assumed to increase linearly with depth in sands as [33–35]:

$$k_{in} = n_h z, \quad (6)$$

where n_h is the coefficient of horizontal subgrade reaction, which is related to the internal friction angle, the relative density, etc. n_h can be determined according to internal angle and relative density of sands [26].

The ultimate soil resistance in front of a pile located in sand slope can be described by the following equation [24, 26]:

$$p_{fult} = \gamma z \left[\frac{K_0 z \tan \phi \sin \beta}{\tan(\beta - \phi) \cos \alpha} (4D_1^3 - 3D_1^2 + 1) \right] + \gamma z \left[\frac{\tan \beta (dD_2 + z \tan \beta \tan \alpha D_2^2)}{\tan(\beta - \phi)} \right] + \gamma z [K_0 z \tan \beta (\tan \phi \sin \beta - \tan \alpha) (4D_1^3 - 3D_1^2 + 1) - K_a d], \quad (7)$$

where

$$D_1 = \frac{\tan \beta \tan \theta}{\tan \beta \tan \theta + 1},$$

$$D_2 = 1 - D_1 = 1 - \frac{\tan \beta \tan \theta}{\tan \beta \tan \theta + 1}, \quad (8)$$

$$K_a = \cos \theta \frac{\cos \theta - \sqrt{\cos^2 \theta - \cos^2 \phi}}{\cos \theta + \sqrt{\cos^2 \theta - \cos^2 \phi}}$$

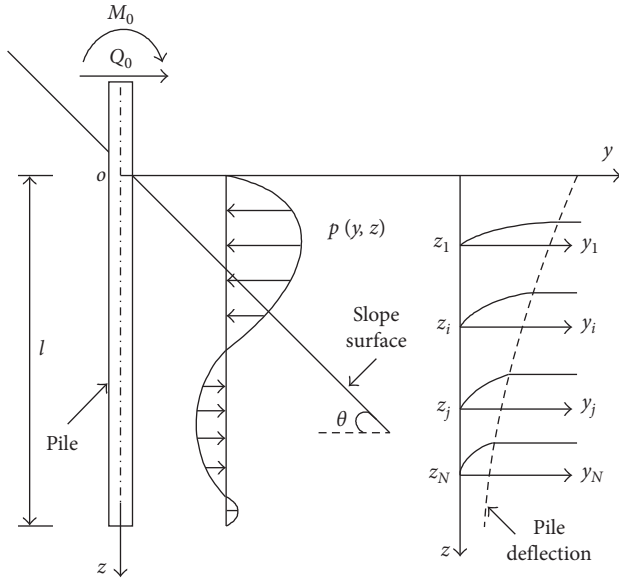


FIGURE 3: Simplified p - y model of laterally loaded piles in sloping ground.

where K_0 is the coefficient of static earth pressure; ϕ is the internal friction angle; $\beta = 45^\circ + (\phi/2)$; and α is the angle of the wedge. Bowman [36] suggested that $\alpha = \phi/3 \sim \phi/2$ for loose sand and $\phi/2 \sim \phi$ for dense sand; K_a is the coefficient of active earth pressure.

3. Simplified p - y Method of Laterally Loaded Pile in Sloping Ground

3.1. Basic Equations. Assuming that the slope is stable and ignoring friction on the pile, a simplified method for laterally loaded piles in sloping ground can be established as shown in Figure 3. This yields to the differential equation as follows [20, 26]:

$$EI \frac{d^4 y}{dz^4} + dp_i(y, z) = 0, \quad (9)$$

where EI is the flexural stiffness of a pile and $p_i(y, z)$ is the soil resistance of sloping ground.

3.2. Boundary Conditions. The boundary condition at pile top can be free, hinged, and partially or fully fixed, while that at pile toe can be fixed or hinged [20, 26]. In this paper, a bending moment M_0 and a shear force Q_0 are considered as external load on the pile head, and the pile toe is fixed, which yields to the following boundary conditions:

Free pile top:

$$\begin{aligned} EIY''|_{z=0} &= M_0, \\ EIY'''|_{z=0} &= Q_0. \end{aligned} \quad (10)$$

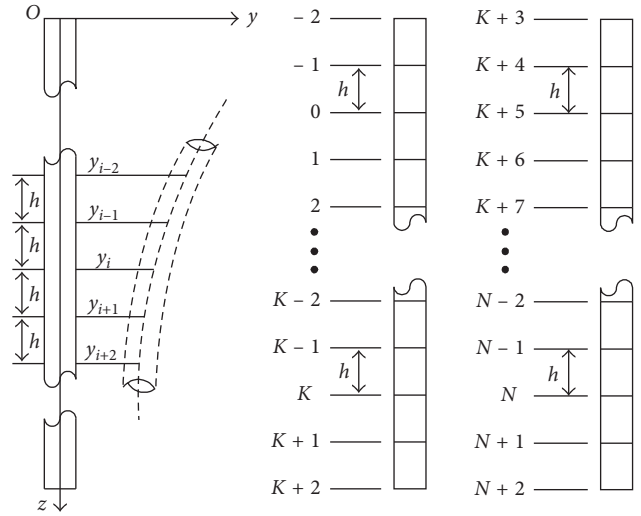


FIGURE 4: Deflection and differential points of the pile.

Fixed pile toe:

$$\begin{aligned} y|_{z=l} &= 0, \\ y'|_{z=l} &= 0. \end{aligned} \quad (11)$$

3.3. Finite Difference Solution. Subdividing the pile into N sections, the length of each section is $h = l/N$, as shown in Figure 4. According to the principle of the central difference method, two virtual nodes are added at the pile head and toe, respectively. Thus, there are $N + 1$ nodes on the pile shaft (node number: from 0 to N), 2 virtual nodes at the top (node number: -2 and -1), and another 2 virtual nodes at the toe (node number: $N + 1$ and $N + 2$).

Let the horizontal displacement at each node be y_i (where $i = 0 \sim n$), then (9) can be rewritten as

$$y_{i-2} - 4y_{i-1} + 6y_i - 4y_{i+1} + y_{i+2} + \frac{h^4 dp_i(y, z)}{EI} = 0. \quad (12)$$

The slope, φ_i , the moment, M_i , and the shear force, Q_i , along the pile shaft can be obtained by using the difference method:

$$\begin{aligned} \varphi_i &= \frac{(y_{i+1} - y_{i-1})}{2h}, \\ M_i &= \frac{(y_{i-1} - 2y_i + y_{i+1})EI}{h^2}, \\ Q_i &= \frac{(-y_{i-2} + 2y_{i-1} - 2y_{i+1} + y_{i+2})EI}{2h^3}. \end{aligned} \quad (13)$$

The boundary conditions of the pile, namely, (10) and (11), can also be rewritten as follows:

$$\begin{aligned} y_1 - 2y_0 + y_{-1} &= \frac{M_0 h^2}{EI}, \\ y_2 - 2y_1 + 2y_{-1} - y_{-2} &= \frac{2Q_0 h^3}{EI}, \end{aligned} \quad (14)$$

$$\begin{aligned} y_n &= 0, \\ y_{N+1} - y_{N-1} &= 0. \end{aligned} \quad (15)$$

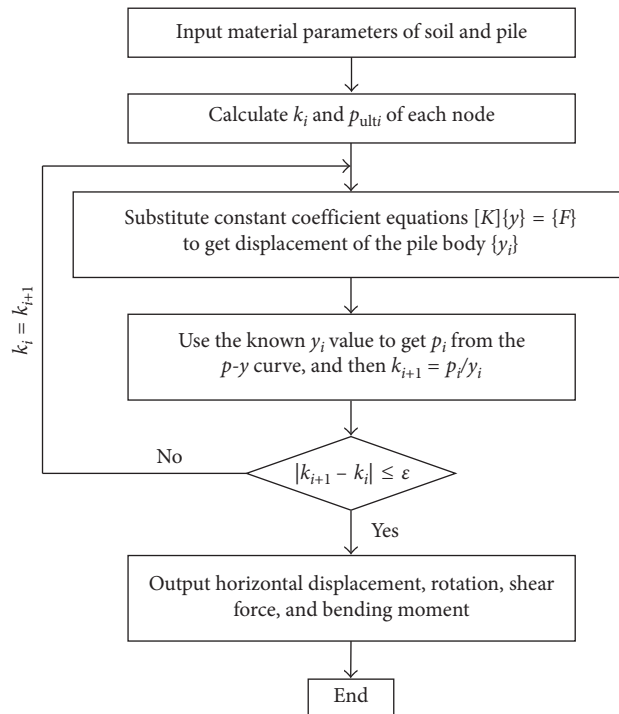


FIGURE 5: Iteration flowchart.

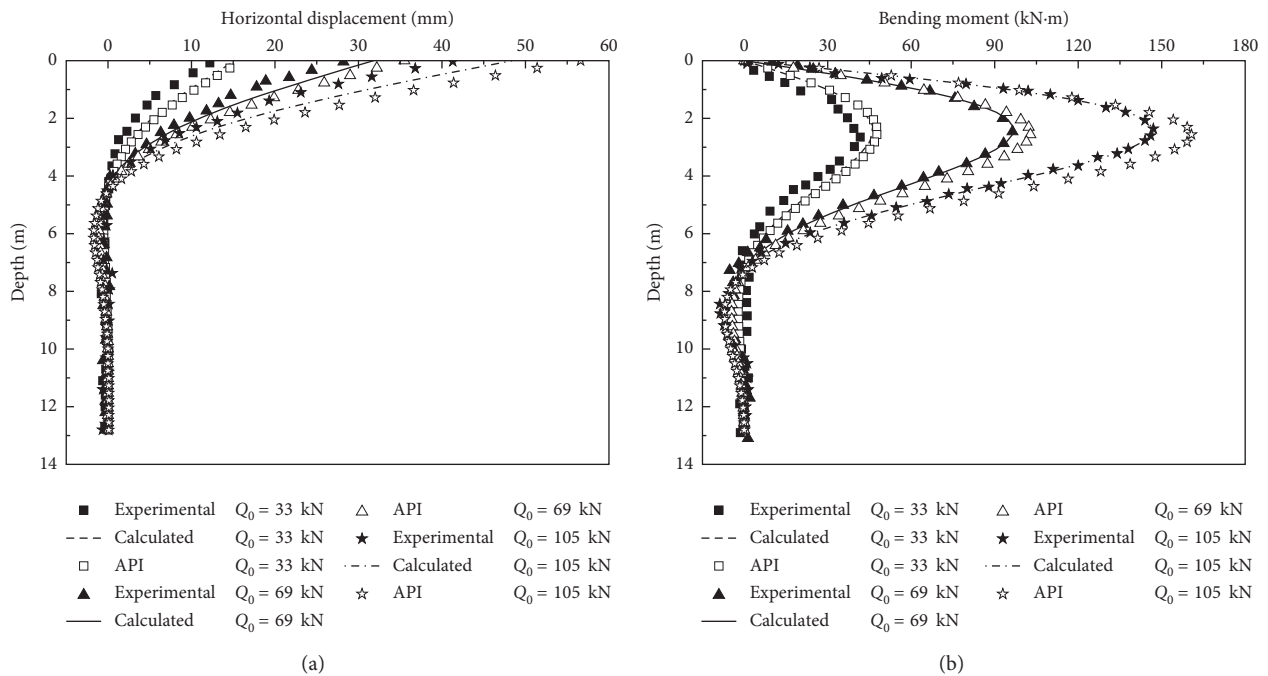


FIGURE 6: The comparison of the horizontal displacement (a) and bending moment (b).

$\gamma = 18 \text{ kN/m}^3$; the undrained strength of soils, $c_u = 39.1 \text{ kPa}$; $\epsilon_{50} = 0.012$; and the slope angle, $\theta = 0^\circ$. The comparison between the calculated and measured pile deflection and the bending moment is plotted in Figure 6.

It is clear in Figure 6 that the calculated horizontal displacement and bending moment agree well with the measured and API method.

4.2. Model Tests of Piles in Sand Slopes. The objective of the model tests is to verify the proposed method. The model piles were made by the PPR (polypropylene random) pipe, which is of 63 mm in outside diameter, 58 mm in inner diameter, and 1680 MPa in elastic modulus. The total length of piles is 1200 mm, and the embedded depth is 900 mm, as shown in Figure 7. The model slope was filled by sand using

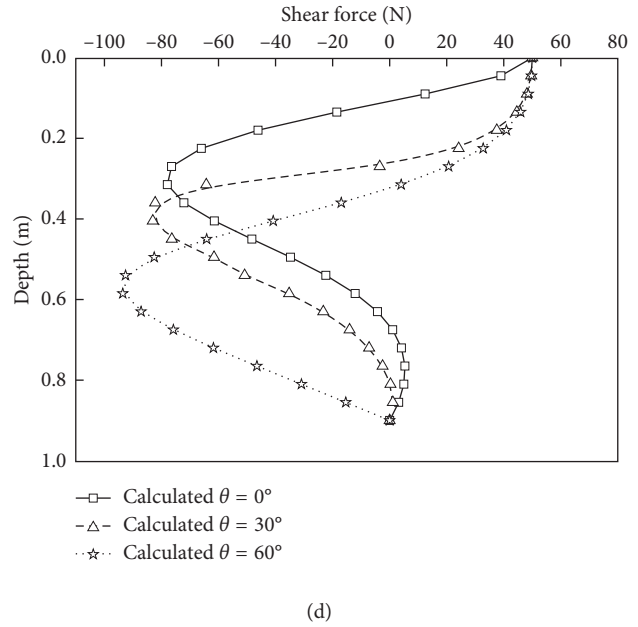
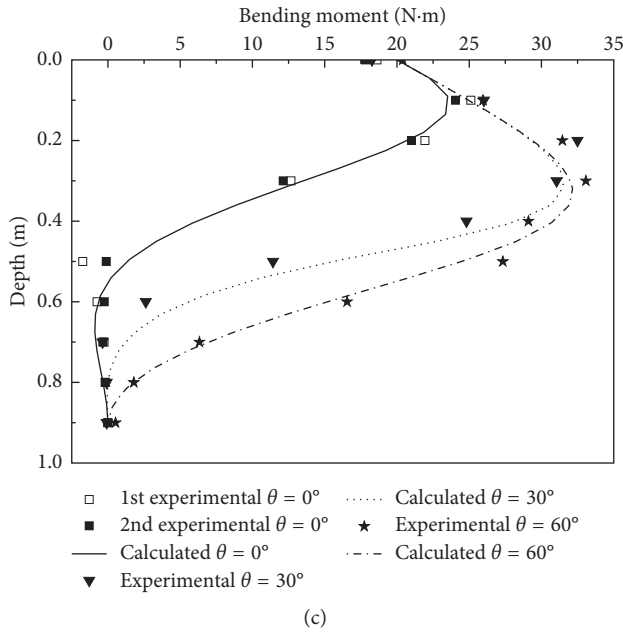


FIGURE 8: Pile behavior under the horizontal load, $Q_0 = 50$ N: (a) horizontal displacement; (b) rotation; (c) bending moment; (d) shear force.

TABLE 1: Comparison of pile behavior between the proposed method and the model tests.

Method	Horizontal displacement			Maximum bending moment		
	y_0 (mm)			M_{max} (N·m)		
Slope angle θ (°)	0	30	60	0	30	60
Experimental	3.2	7.6	18.2	24.1	32.5	33.1
Calculated	3.3	7.5	15.3	23.5	31.6	32.2
Absolute error (%)	3.1	1.3	15.9	2.5	2.7	2.7

the rainfall method. The physical and mechanical properties of the sand were tested in laboratory, including the moisture content, $w = 2.43\%$; the internal friction angle, $\phi = 39^\circ$; the unit weight of sand, $\gamma = 15.65$ kN/m³; the relative density, $D_r = 0.81$; and the coefficient of horizontal subgrade reaction, $n_h = 70$ MN/m³. The laboratory test carried out and the details of the model test preparation have been presented in the reference [37]. The predicted horizontal displacement and bending moment of piles are compared to the measured in Figure 8 and Table 1.

We can learn from Figure 8 and Table 1 that the pile head deflection and bending moment predicted by the proposed method agree well with the measured in the model tests, and the discrepancy is 2.7% for bending moment and 15.9% for pile head deflection.

As we can learn from Figure 8, the depth of the maximum moment increases from about 10 cm ($1.6D$, D is the pile diameter) below ground level in even ground ($\theta = 0^\circ$) to 22.5 cm ($3.6D$) and 36 cm ($5.6D$) below ground level in sloping ground of 30° and 60° in slope angle, respectively.

The results also show that the pile head deflection on slope surface rises from 3.3 mm in even ground ($\theta = 0^\circ$) to 7.5 mm (127%) and 15.3 mm (364%) in sloping ground of 30°

and 60° in angle, respectively; the rotation at the top of the pile rises from -1.15° in even ground ($\theta = 0^\circ$) to -1.84° ($\theta = 30^\circ$) and -2.74° ($\theta = 60^\circ$) in sloping ground; the maximum bending moment increases from 23.5 N·m in even ground ($\theta = 0^\circ$) to 31.6 N·m ($\theta = 30^\circ$) and 32.2 N·m ($\theta = 60^\circ$) in sloping ground, which are 34% and 37% increase, respectively; the maximum shear force increases from -78 N in even ground to -83 N ($\theta = 30^\circ$) and -93 N ($\theta = 60^\circ$) in sloping ground.

5. Conclusion

A simplified p - y method of piles located in slopes was proposed and solved using difference method in this paper. The proposed method was verified by the field tests of a steel pipe pile in clay and the model tests of piles in sand slopes. The main influence factor, namely, the slope angle, was discussed by parametric study. The results indicate that the horizontal displacement, rotation, bending moment, and shear force increase with increasing slope angle; the depth of maximum moment is about $1.6D$ below ground level for even ground and about $3.6D$ and $5.6D$ for sloping ground of 30° and 60° , respectively. It is suggested that steep slope should be avoided when designing a laterally loaded pile in sloping ground.

Data Availability

The data used to support the findings of this study are available from the corresponding author upon request.

Conflicts of Interest

The authors declare that they have no conflicts of interest.

Acknowledgments

The research described in this paper was financially supported by the National Natural Science Foundation of China (Grant nos. 51478051 and 51408066) and Postdoctoral Science Foundation of China (Grant no. 2017M612544).

References

- [1] W. He, "Application of the meshfree method for evaluating the bearing capacity and response behavior of foundation piles," *International Journal of Geomechanics*, vol. 12, no. 2, pp. 98–104, 2011.
- [2] R.-p. Chen, Y.-x. Sun, B. Zhu, and W. D. Guo, "Lateral cyclic pile-soil interaction studies on a rigid model monopile," *Proceedings of the Institution of Civil Engineers: Geotechnical Engineering*, vol. 168, no. 2, pp. 120–130, 2015.
- [3] M. Hajjalilue-Bonab, Y. Sojoudi, and A. J. Puppala, "Study of strain wedge parameters for laterally loaded piles," *International Journal of Geomechanics*, vol. 13, no. 2, pp. 143–152, 2011.
- [4] M. E. Sawwaf, "Lateral resistance of single pile located near geosynthetic reinforced slope," *Journal of Geotechnical and Geoenvironmental Engineering*, vol. 132, no. 10, pp. 1336–1345, 2006.
- [5] K. S. Chae, K. Ugai, and A. Wakai, "Lateral resistance of short single piles and pile groups located near slopes," *International Journal of Geomechanics*, vol. 4, no. 2, pp. 93–103, 2004.
- [6] H. Zhao, P. Yin, and X. Li, "Mechanical response of bridge piles in high-steep slopes and sensitivity study," *Journal of Central South University*, vol. 22, no. 10, pp. 4043–4048, 2015.
- [7] P. Yin, M. Zhao, C. Yang et al., "Experimental study on bearing capacity of bridge piles in cross slopes under complex loads," *China Civil Engineering Journal*, vol. 47, no. 5, pp. 110–117, 2014.
- [8] M. Zhao, C. Yang, M. Yang et al., "Mechanical analysis of bridge pile foundation in high and steep slopes based on finite bar element method," *China Journal of Highway and Transport*, vol. 27, no. 6, pp. 51–58, 2014.
- [9] H. Matlock, "Correlations for Design of Laterally Loaded Piles in Soft Clay," in *Offshore Technology in Civil Engineering's Hall of Fame Papers from the Early Years*, pp. 77–94, American Society of Civil Engineers, Reston, VA, USA, 1970.
- [10] L. C. Reese, W. R. Cox, and F. D. Koop, "Analysis of laterally loaded piles in sand," in *Offshore Technology in Civil Engineering Hall of Fame Papers from the Early Years*, pp. 95–105, American Society of Civil Engineers, Reston, VA, USA, 1974.
- [11] M. F. Randolph, "The response of flexible piles to lateral loading," *Geotechnique*, vol. 31, no. 2, pp. 247–259, 1981.
- [12] Z. Yang and B. Jeremic, "Numerical analysis of pile behaviour under lateral loads in layered elastic-plastic soils," *International Journal for Numerical and Analytical Methods in Geomechanics*, vol. 26, no. 14, pp. 1385–1406, 2002.
- [13] Y. Hsiung, "Theoretical elastic-plastic solution for laterally loaded piles," *Journal of Geotechnical and Geoenvironmental Engineering*, vol. 129, no. 5, pp. 475–480, 2003.
- [14] W. Higgins, C. Vasquez, D. Basu et al., "Elastic solutions for laterally loaded piles," *Journal of Geotechnical and Geoenvironmental Engineering*, vol. 139, no. 7, pp. 1096–1103, 2012.
- [15] Z. Yang, Q. Li, J. Horazdovsky et al., "Performance and design of laterally loaded piles in frozen ground," *Journal of Geotechnical and Geoenvironmental Engineering*, vol. 143, no. 5, article 06016031, 2016.
- [16] S. Mezazigh and D. Levacher, "Laterally loaded piles in sand: slope effect on p-y reaction curves," *Canadian Geotechnical Journal*, vol. 35, no. 3, pp. 433–441, 1998.
- [17] C. W. W. Ng and L. M. Zhang, "Three-dimensional analysis of performance of laterally loaded sleeved piles in sloping ground," *Journal of Geotechnical and Geoenvironmental Engineering*, vol. 127, no. 6, pp. 499–509, 2001.
- [18] L. M. Zhang, C. W. W. Ng, and C. J. Lee, "Effects of slope and sleeving on the behavior of laterally loaded piles," *Soils and Foundations*, vol. 44, no. 4, pp. 99–108, 2004.
- [19] K. Muthukkumaran, R. Sundaravadivelu, and S. R. Gandhi, "Effect of slope on py curves due to surcharge load," *Soils and Foundations*, vol. 48, no. 3, pp. 353–361, 2008.
- [20] M.-h. Zhao, J.-h. Liu, D.-q. Liu, and Y. Wang, "Force analysis of pile foundation in rock slope based on upper-bound theorem of limit," *Journal of Central South University of Technology*, vol. 15, no. 3, pp. 404–410, 2008.
- [21] K. Muthukkumaran, "Effect of slope and loading direction on laterally loaded piles in cohesionless soil," *International Journal of Geomechanics*, vol. 14, no. 1, pp. 1–7, 2013.
- [22] V. A. Sawant and S. K. Shukla, "Effect of edge distance from the slope crest on the response of a laterally loaded pile in sloping ground," *Geotechnical and Geological Engineering*, vol. 32, no. 1, pp. 197–204, 2014.
- [23] R. Deendayal, K. Muthukkumaran, and T. G. Sitharam, "Response of laterally loaded pile in soft clay on sloping ground," *International Journal of Geotechnical Engineering*, vol. 10, no. 1, pp. 10–22, 2016.
- [24] B. McClelland and J. A. Focht, "Soil modulus for laterally loaded piles," *Transactions of the American Society of Civil Engineers*, vol. 123, no. 1, pp. 1049–1063, 1958.
- [25] American Petroleum Institute, (RP2A-WSD) *Recommended Practice for Planning, Designing, and Constructing Fixed Offshore Platforms-working Stress Design*, American Petroleum Institute, Washington, DC, USA, 2000.
- [26] L. C. Reese and W. F. Van Impe, *Single Piles and Pile Groups under Lateral Loading*, August Aimé Balkema, Rotterdam, Netherlands, 2010.
- [27] M. Georgiadis, C. Anagnostopoulos, and S. Saflekou, "Cyclic lateral loading of piles in soft clay," *Geotechnical Engineering*, vol. 23, no. 1, pp. 47–60, 1992.
- [28] S. S. Rajashree and T. G. Sitharam, "Nonlinear finite-element modeling of batter piles under lateral load," *Journal of Geotechnical and Geoenvironmental Engineering*, vol. 127, no. 7, pp. 604–612, 2001.
- [29] B. T. Kim, N. K. Kim, W. J. Lee et al., "Experimental load-transfer curves of laterally loaded piles in Nak-Dong River sand," *Journal of Geotechnical and Geoenvironmental Engineering*, vol. 130, no. 4, pp. 416–425, 2004.
- [30] R. Liang, K. Yang, and J. Nusairat, "p-y criterion for rock mass," *Journal of Geotechnical and Geoenvironmental Engineering*, vol. 135, no. 1, pp. 26–36, 2009.
- [31] K. Georgiadis and M. Georgiadis, "Undrained lateral pile response in sloping ground," *Journal of Geotechnical and Geoenvironmental Engineering*, vol. 136, no. 11, pp. 1489–1500, 2010.
- [32] G. Wang and M. Yang, "Nonlinear analysis of laterally loaded piles in sand," *Rock and Soil Mechanics*, vol. 32, no. S2, pp. 261–267, 2011.
- [33] M. T. Davisson, "Behavior of flexible vertical piles subjected to moment, shear, and axial load," Ph.D. dissertation, University of Illinois, Urbana, IL, USA, 1960.
- [34] L. C. Reese and H. Matlock, *Non-Dimensional Solutions for Laterally-Loaded Piles with Soil Modulus Assumed*

- Proportional to Depth*, Association of Drilled Shaft Contractors, Dallas, TX, USA, 1956.
- [35] S. Prakash and S. Kumar, "Nonlinear lateral pile deflection prediction in sands," *Journal of Geotechnical Engineering*, vol. 122, no. 2, pp. 130–138, 1996.
- [36] E. R. Bowman, "Investigation of the lateral resistance to movement of a plate in cohesionless soil," Ph.D. dissertation, University of Texas, Austin, TX, USA, 1958.
- [37] Y. Pingbao, H. Wei, Z. Jianren et al., "Study on spatial effect of slope and horizontal bearing behavior of piles in sloping ground," *China Civil Engineering Journal*, vol. 51, no. 4, pp. 94–101, 2018.

Research Article

Study on the Fractal Characteristics of Fracture Network Evolution Induced by Mining

Tao Liang,¹ Xiaoli Liu ,¹ Sijing Wang,^{1,2} Enzhi Wang,¹ and Quansheng Li³

¹State Key Laboratory of Hydro-Science and Engineering, Tsinghua University, Beijing 100084, China

²Institute of Geology and Geophysics of the Chinese Academy of Sciences, Beijing 100029, China

³State Key Laboratory of Water Resources Protection and Utilization in Coal Mining, Shenhua Group Co., Ltd., Beijing 100011, China

Correspondence should be addressed to Xiaoli Liu; xiaoli.liu@tsinghua.edu.cn

Received 16 January 2018; Revised 8 April 2018; Accepted 30 April 2018; Published 20 June 2018

Academic Editor: Dingwen Zhang

Copyright © 2018 Tao Liang et al. This is an open access article distributed under the Creative Commons Attribution License, which permits unrestricted use, distribution, and reproduction in any medium, provided the original work is properly cited.

The evolution and distribution of fracture network induced by mining is essential to determine the mechanical properties and permeability of disturbed rock mass. In this paper, the similar material model tests are employed to simulate the stress variation, cyclic breaking, and fracture formation and distribution status of the overlying strata with different loading conditions, rock properties, and mining process. The fractal dimension of mining-induced fracture network varied with mining advancing, and the evolution laws of fracture network with mining advancing and different mining advancing footage are concerned and obtained. By establishing the relationship between the fractal dimension and the mining length in different horizontal and vertical zones, it demonstrates that the fractal dimensions in horizontal and vertical zones have a self-similar characteristic, and the distribution of the fractal dimension of the mining-induced fractures shows generally the “W”-type trend.

1. Introduction

The original equilibrium state of the underground rock is disturbed by mining, and the fracture network in the overlying rock mass gradually forms and evolves with the rock stress redistribution. The mechanism of the fracturing and evolution of mining-induced cracks plays a great important role on the permeability assessment, overburden strata subsidence prediction, and the security and stability evaluation of mining rock mass [1–6]. According to Yu et al. [2], it is probably one of the most important issues in mining science to recognize and describe quantitatively the evolution of fracture network resulting from mining processes, on which many researchers have carried out fruitful research in recently years. Qian and Xu [7] proposed the two-stage development law of mining-induced cracks and revealed the “O”-shape distribution characteristics in a long-wall face of a coal mine. Li et al. [8] discussed the effect of key strata on the distribution of fractures and concluded that an elliptic paraboloid zone would be formed in the overlying strata due

to the connection of the rock mass breaking induced fractures and the strata layers separation induced fractures in mining process. Li et al. [9] described the distribution characteristics of roof separation fractures in the process of fully mechanized top coal caving and derived the equivalent areas of bed-separated cracks before and after the key strata breaking and the permeability coefficients in different crack districts.

The fractal geometry proposed by Mandelbrot [10] is a powerful tool to quantitatively describe complex objects and phenomenon of irregular. In recent years, increasing attention has been focused on the combined application of fractal theory and physical models, by which considerable progress has been made in quantitative description of the evolution law of mining-induced fractures [11–20].

In the process of coal mining, the authors put forward underground reservoirs construction technology in mined out area, which is a new idea on coal-water coordinate mining, for comprehensive utilization of underground water

TABLE 1: Site stratigraphy and physical properties.

Strata number	Lithology	Strata thickness (m)	Initial permeability coefficient (m/d)	In situ vertical stress (MPa)	Strata density (kg/m ³)
1	Aeolian sand and loess	30	0.5–5.0		2000
2	Mudstone	15	0.0002	34.86	2304
3	Medium coarse-grained sandstone	5	0.02	50.00	2550
4	Mudstone	20	0.0002	25.22	2204
5	Fine sandstone-siltstone	10	0.004	5.26	2133
6	Mudstone	15	0.0002	25.22	2204
7	Number 2 coal seam	5	0.0001	14.49	1306
8	Mudstone	15	0.0002	34.86	2304
9	Fine sandstone-siltstone	20	0.004	5.26	2133
10	Mudstone	15	0.0002	34.86	2304
11	Medium coarse-grained sandstone	20	0.02	50.00	2550
12	Mudstone	20	0.0002	25.22	2204
13	Fine sandstone-siltstone	10	0.004	5.26	2133
14	Mudstone	10	0.0002	25.22	2204
15	Medium coarse-grained sandstone	20	0.02	50.00	2550
16	Mudstone	20	0.0002	25.22	2204
17	Medium coarse-grained sandstone	20	0.004	5.26	2133
18	Number 5 coal seam	5	0.0001	19.54	1295
19	Mudstone	15	0.0002	34.86	2304
20	Medium coarse-grained sandstone	15	0.02	50.00	2550
21	Mudstone	10	0.009	34.86	2304
22	Medium coarse-grained sandstone	10	0.02	50.00	2550

resources, protection of aquifer, safe production of coal mines, and underground water reuse. This technology is meaningful for sustainable development of underground resources, including coal mine resources, especially in arid and semiarid areas, where the water resources are very short. The distribution and evolution of mining-induced fractures in the overlying and floor rock mass play an important role in determining the location and capacity of the underground reservoir and in groundwater operation and purification as well. In this study, the Daliuta coal mine in the Ordos Basin of northeastern China, where underground reservoirs were constructed, is taken as the engineering background. Fracture network evolution and distribution induced by mining is essential to determine the mechanical properties and permeability of disturbed rock mass. In this paper, the physical similarity model was made and by which the deformation and collapse of the overlying rock mass were well observed and recorded under different conditions. By analyzing the fractal dimension variation of fracture networks of different working conditions and different zones with the mining face advancing, the distribution and evolvement laws of fracture network with mining speed and in different horizontal and vertical zones are concerned, which provides a basis for studying the relationship between cracks evolution and corresponding permeability change of mining rock mass.

2. Experimental Procedure

2.1. Geological Conditions. According to the geological investigation, the representative stratigraphic distribution in the Daliuta mine field and the physical properties are presented in Table 1.

TABLE 2: Similarity ratios.

Similarity coefficient	Similarity ratio
C_{ω_a}	1/10
$C_\gamma, C_\mu, C_\epsilon, C_\varphi, C_R$	1
C_k, C_t	10
$C_L, C_\delta, C_c, C_\sigma, C_{\sigma_t}, C_{\sigma_c}, C_E$	100

γ : bulk density; L : length; δ : displacement; e : strain; E : elastic modulus; σ : stress; σ_t : tensile strength; σ_c : compressive strength; c : cohesion; φ : internal friction angle; μ : Poisson's ratio; k : permeability coefficient; R : softening coefficient; ω_a : water absorption; t : time duration.

2.2. Similarity Theory and Similar Materials. Similar simulation study is an important means for scientific research, during which a model with artificial materials is made in the laboratory according to the similar principles and with a certain scale. With the aid of test instruments, the physical and mechanical parameters and distribution rules in the model are observed and obtained, from which the mechanical phenomenon and law of rock-pressure distribution of the prototype are inferred, and hereby to solve the practical problems in rock engineering.

Similar material and prototype used in the fluid-solid coupling model test should satisfy (1) and (2) simultaneously [21, 22]:

$$K_x \frac{\partial^2 p}{\partial x^2} + K_y \frac{\partial^2 p}{\partial y^2} + K_z \frac{\partial^2 p}{\partial z^2} = S \frac{\partial p}{\partial t} + \frac{\partial e}{\partial t} + W, \quad (1)$$

where K_x , K_y , and K_z are the permeability coefficients in x , y , and z directions, respectively; p is the water pressure; S is the water storage coefficient; e is the volumetric strain; and W is the source and sink.

TABLE 3: Physical and mechanical parameters of the prototype and the model.

Number	Parameters	Prototype	Model
1	Bulk density (kN/m^3)	21.0~25.5	21.0~25.5
2	Compressive strength (MPa)	5~50	0.05~0.5
3	Permeability coefficient (cm/s)	$1 \times 10^{-4} \sim 1 \times 10^{-3}$	$1 \times 10^{-5} \sim 1 \times 10^{-4}$
4	Softening coefficient	Greater than 0.75	Greater than 0.75
5	Water absorption	0.2%~0.5%	2%~5%

TABLE 4: Similar material parameters.

Number	Simulated rock stratum	Bulk density (kg/m^3)	Compressive strength (MPa)	Permeability coefficient (cm/s)	Softening coefficient	Water absorption
1	Mudstone	2300	0.35	$7.2E-5$	0.88	0.02
2	Medium coarse-grained sandstone	2550	0.50	$9.0E-5$	0.81	0.03
3	Mudstone	2200	0.25	$1.0E-4$	0.78	0.03
4	Fine sandstone-siltstone	2100	0.05	$9.0E-5$	0.75	0.03

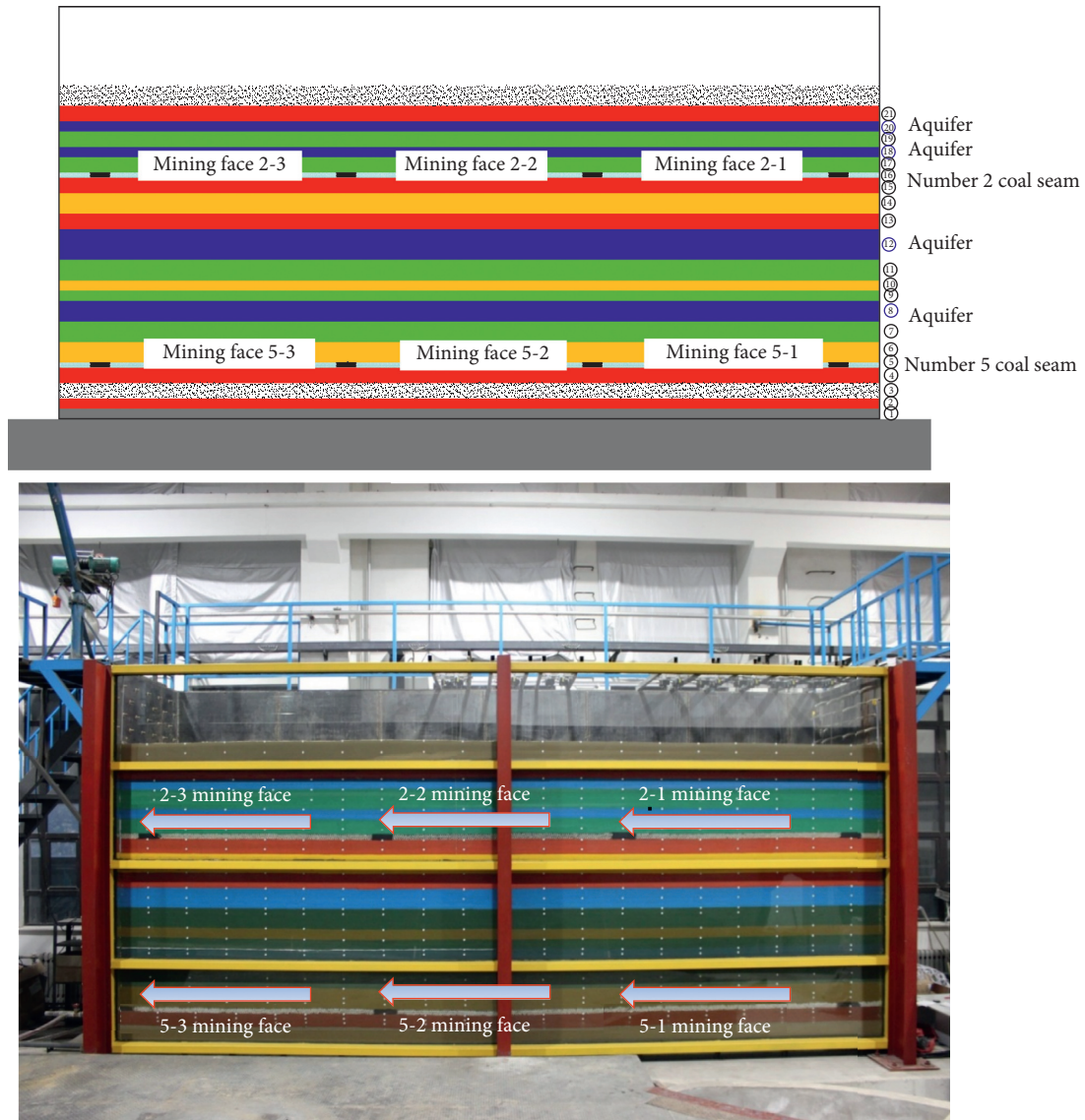
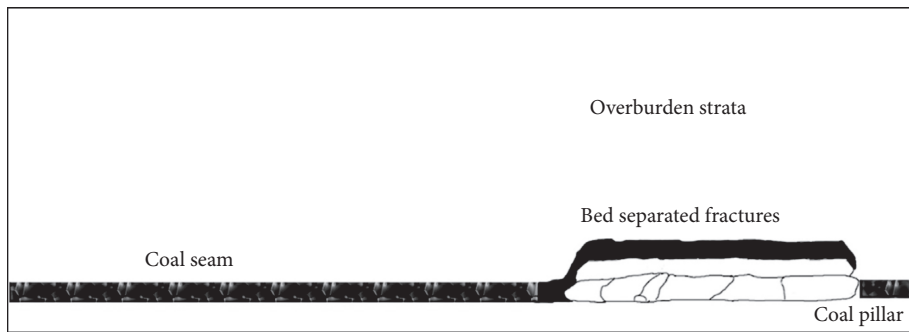


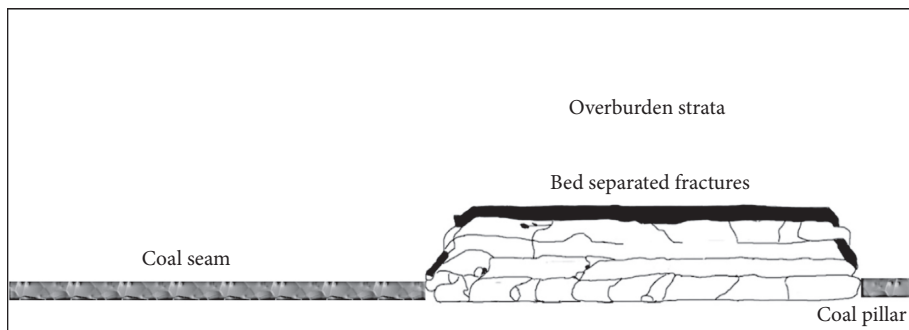
FIGURE 1: Cross section of the physical simulation model.

TABLE 5: Description of the mining process (mining face 5-3).

Mining length (mm)	Caving height (mm)	Caving length (mm)	Caving description
300	50	300	Immediate roof falls
500	50	200	Immediate roof falls
600	50	100	Immediate roof falls
700	50	100	Immediate roof falls
800	50	100	Immediate roof fall
850	100	800	Main roof collapses (integral)
900	50	100	Immediate roof falls
950	50	50	Immediate roof falls
1100	100	300	Main roof collapses (partial)
1150	50	50	Immediate roof falls
1200	200	1200	Main roof collapses (integral)
1250	50	50	Immediate roof falls
1350	100	100	Immediate roof falls
1400	50	50	Immediate roof falls
1450	200	250	Main roof collapses (partial)
1500	300	500	Main roof collapses (partial)
1550	50	100	Immediate roof falls
1650	100	200	Main roof collapses (partial)
1750	50	100	Immediate roof falls
1800	600	1800	Main roof collapses (integral)
1850	50	50	Immediate roof falls
1900	50	50	Immediate roof falls
1950	50	50	Immediate roof falls
2100	50	150	Immediate roof falls



(a)



(b)

FIGURE 2: Continued.

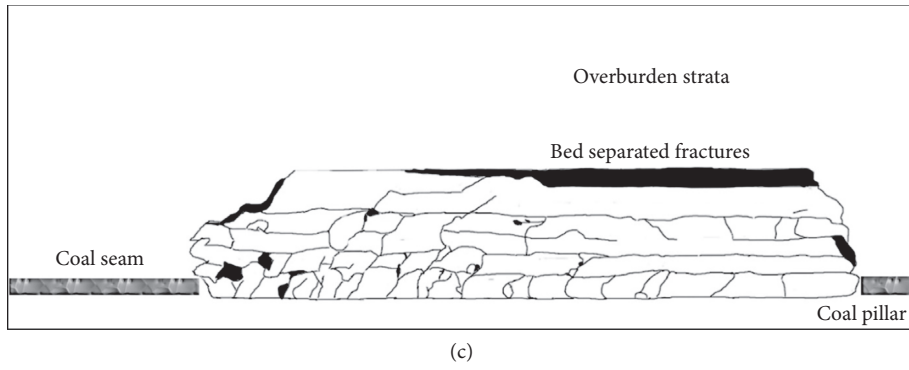


FIGURE 2: Fracture network diagrams (mining face 5-3). Mining length: (a)850 mm; (b)1200 mm; (c)1800 mm.

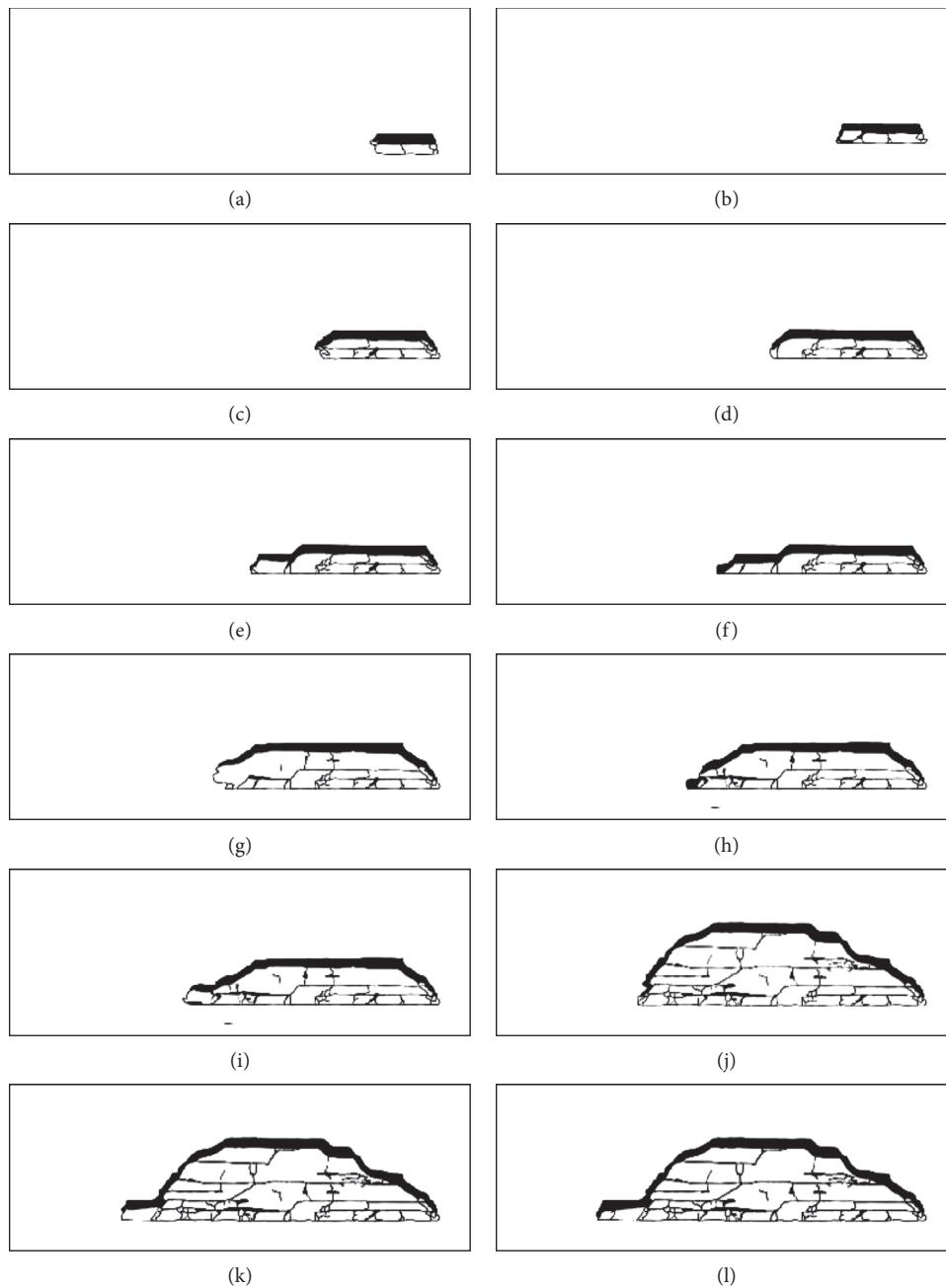


FIGURE 3: Continued.

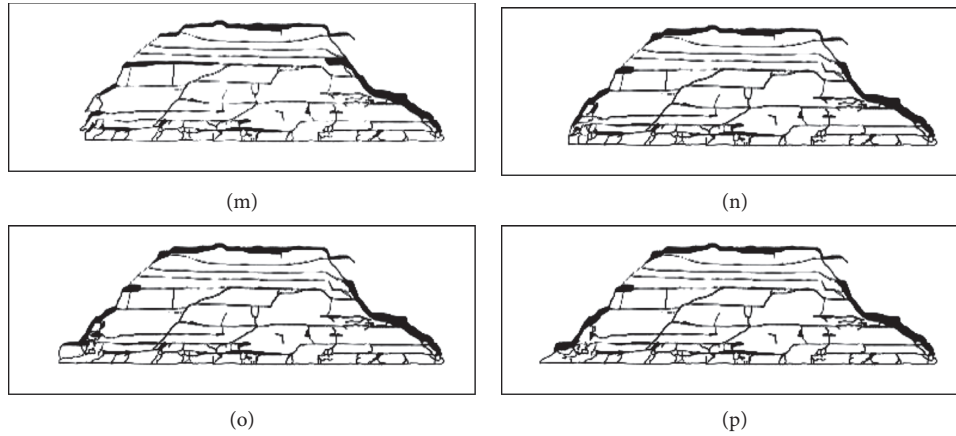


FIGURE 3: Fracture network evolution (mining face 5-1). Mining length: (a) 300 mm; (b) 450 mm; (c) 600 mm; (d) 800 mm; (e) 1000 mm; (f) 1100 mm; (g) 1200 mm; (h) 1250 mm; (i) 1350 mm; (j) 1500 mm; (k) 1700 mm; (l) 1800 mm; (m) 1900 mm; (n) 1950 mm; (o) 2050 mm; (p) 2100 mm.

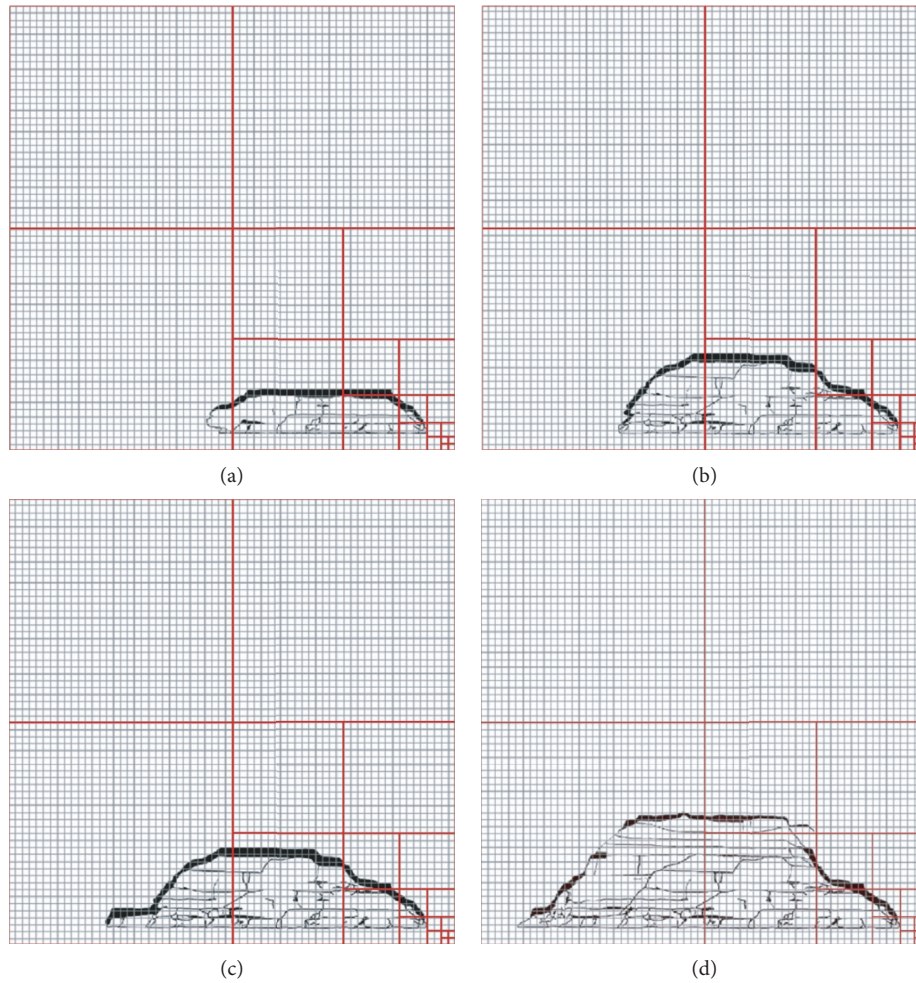


FIGURE 4: Schematic diagram for the "counting the boxes" method. Mining face 5-1 at a mining length of (a) 1200 mm; (b) 1500 mm; (c) 1800 mm; (d) 2100 mm.

TABLE 6: List for calculating D_f (mining face 5-1 at a mining length of 1200 mm).

r	1	2	4	8	16	32	64	128
N	24509	7071	2130	711	249	92	34	14
$\ln(1/r)$	0	-0.69	-1.39	-2.08	-2.77	-3.47	-4.16	-4.85
$\ln N$	10.11	8.86	7.66	6.57	5.52	4.52	3.53	2.64

TABLE 7: List for calculating D_f (mining face 5-1 at a mining length of 1500 mm).

r	1	2	4	8	16	32	64	128
N	38677	11458	3750	1350	510	180	63	21
$\ln(1/r)$	0	-0.69	-1.39	-2.08	-2.77	-3.47	-4.16	-4.85
$\ln N$	10.56	9.35	8.23	7.21	6.23	5.19	4.14	3.04

TABLE 8: List for calculating D_f (mining face 5-1 at a mining length of 1800 mm).

r	1	2	4	8	16	32	64	128
N	49959	14383	4579	1599	578	190	66	22
$\ln(1/r)$	0	-0.69	-1.39	-2.08	-2.77	-3.47	-4.16	-4.85
$\ln N$	10.82	9.57	8.43	7.38	6.36	5.25	4.19	3.09

TABLE 9: List for calculating D_f (mining face 5-1 at a mining length of 2100 mm).

r	1	2	4	8	16	32	64	128
N	59485	18261	6243	2320	910	316	104	34
$\ln(1/r)$	0	-0.69	-1.39	-2.08	-2.77	-3.47	-4.16	-4.85
$\ln N$	10.99	9.81	8.74	7.75	6.81	5.76	4.64	3.53

$$\begin{aligned}
G\nabla^2 u + (\lambda + G) \frac{\partial e}{\partial x} + X + p \frac{\partial \alpha}{\partial x} + \alpha \frac{\partial p}{\partial x} &= \rho \frac{\partial^2 u}{\partial t^2}, \\
G\nabla^2 v + (\lambda + G) \frac{\partial e}{\partial y} + Y + p \frac{\partial \alpha}{\partial y} + \alpha \frac{\partial p}{\partial y} &= \rho \frac{\partial^2 v}{\partial t^2}, \\
G\nabla^2 \omega + (\lambda + G) \frac{\partial e}{\partial z} + Z + p \frac{\partial \alpha}{\partial z} + \alpha \frac{\partial p}{\partial z} &= \rho \frac{\partial^2 \omega}{\partial t^2},
\end{aligned} \quad (2)$$

where $\nabla^2 = (\partial^2/\partial x^2) + (\partial^2/\partial y^2) + (\partial^2/\partial z^2)$ is the Laplace operator; $G = (E/2(1 + \mu))$ is the shear modulus; $\lambda = (\mu E / ((1 + \mu)(1 - 2\mu)))$ is the lame constant; $e = (\partial u/\partial x) + (\partial v/\partial y) + (\partial \omega/\partial z)$ is the volume strain; E is the modulus of elasticity; μ is Poisson's ratio; u , v , and ω are the displacements in the directions x , y , and z , respectively; X , Y , and Z are the volume forces in the directions x , y , and z , respectively; α is the effective stress coefficient; ρ is the density; p is the water pressure.

Equations (1) and (2) are the basic equations of the fluid-solid coupling theory. The archetype and the model need to satisfy the above equations. Based on the similarity theory [23], the similarity coefficients of the similar model tests are derived to satisfy the following equations:

$$C_G \frac{C_u}{C_l^2} = C_\lambda \frac{C_e}{C_l} = C_G \frac{C_e}{C_l} = C_\gamma = C_p \frac{C_\alpha}{C_l} = C_\alpha \frac{C_p}{C_l} = C_\rho \frac{C_u}{C_t^2}, \quad (3)$$

$$C_k \frac{C_p}{C_l^2} = C_s \frac{C_p}{C_t} = \frac{C_e}{C_t} = C_w, \quad (4)$$

where C is the similarity coefficient. $C_G = G'/G''$, $C_\rho = \rho'/\rho''$, and so on, where the lower foot mark represents the physical variables or parameters that it represents, ' represents the prototype, and '' represents the model.

The model test should be based on the similarity principles, the hydrologic and geological conditions of the prototype, and the specific requirements of the research problems. At the same time, the similarity index and similarity ratio should be determined according to the conditions mentioned above as well as the field conditions of the model test. The similar materials were tested by adjusting the composition and proportion of similar materials and then determined through experimental verification. The main concerns of this model test are the deformation, failure, and permeability change of the overlying rock, so the main parameters of the similar model test are the bulk density, compressive strength (or tensile strength), and permeability coefficient. At the same time, because of the effect of groundwater, the softening coefficient and water absorption also need to satisfy a certain similarity with the prototype.

According to the principles of the similarity model test, the geometrical size, boundary condition, load and movement conditions of the model, and physical and mechanical parameters (e.g. bulk density, strength, deformation characteristics, and water characteristics) of the similar materials are similar to that of the prototype. Based on the elastic mechanics, the dimensional analysis method combined with the fluid-solid coupling theory; the values of the similar parameters are detailed in Table 2.

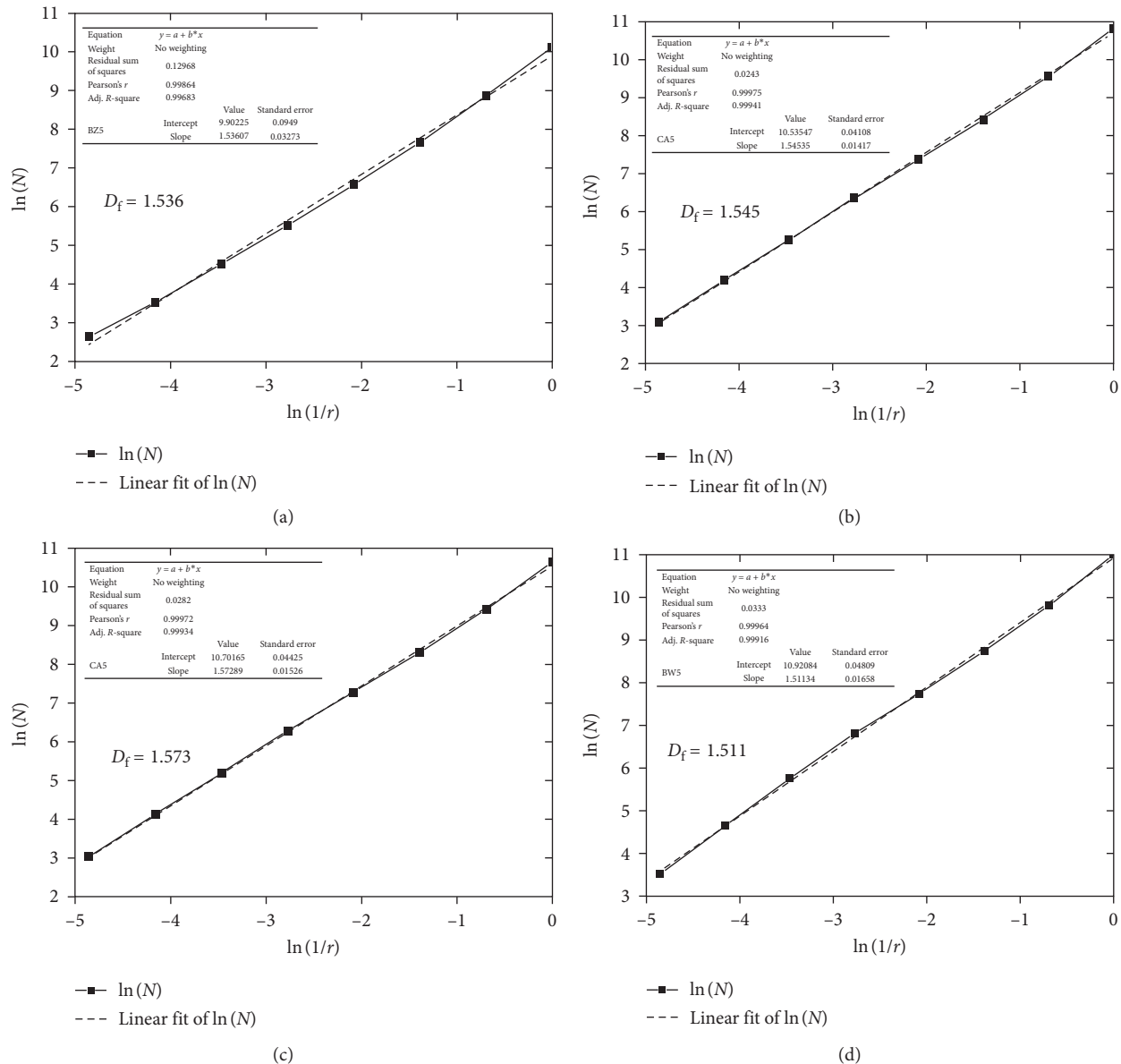


FIGURE 5: Schematic diagram for calculating D_f . Mining face 5-1 at a mining length of (a) 1200 mm; (b) 1500 mm; (c) 1800 mm; (d) 2100 mm.

The range of the physical and mechanical parameters of the similar materials in the model test is described in Table 3.

Based on the materials developed in [24], after many times of proportioning tests, similar materials meeting the test requirements are made, and the similar material parameters are listed in detail in Table 4.

2.3. Similarity Physical Model. The experiment is carried out in a large-scale model test bed designed by the authors, which is 8000 mm long, 1800 mm wide, and 4000 mm high, with the outer frame composed of I steel and channel steel and positive for toughened glass. There are open channels with the sealing cover on the elevation of coal seams on the back plate, used to simulate coal seam excavation, and inlet and outlet holes and flow control table on both sides of the test bed.

As shown in Figure 1, there are 21 similar material layers in the test bed from the bottom to the top, with a total height of 3000 mm, including the number 2 and number 5 similar coal seams with 50 mm thickness located on the elevation of 2250 mm and 500 mm, respectively. The similar pillar is 300 mm wide, by which each similar coal seam is separated in 3 mining faces with a length of 2100 mm. With different mining speeds, the coal seam in a different mining face is mined and the overburden strata movement, and the spatial distribution and evolution process of mining-induced fractures are observed and studied.

A real-time in situ monitoring program was carried out during and after the mining process. The items of monitoring include the stress in overburden strata and coal pillar, the displacement of overburden strata, and the water pressure in aquifer. A total of 160 sensors (e.g., displacement

meter, rock-pressure gauge, and water-pressure gauge) are arranged in the model, from which the data acquisition processing system feedback to the control terminal and the real-time curve will be obtained. Meanwhile, with the aid of total station instrument, 3D laser scanner, and high-speed digital camera, the displacement of 486 monitoring points distributed on the surface of the model is obtained as well.

3. Evolution of Mining-Induced Fracture Network

3.1. Simulation of the Mining Process. With the aid of the physical similarity model, the deformation and collapse of the overlying rock mass can be observed directly during the mining process. Taking the mining face 5-3, for example, the immediate roof falls with a width of 300 mm and height of 50 mm at the mining length of 300 mm. From 300 mm to 800 mm of the mining length, the immediate roof falls four times at an average width of 100 mm and height of 50 mm. Then, the main roof collapses with a height of 100 mm when the mining face advances 850 mm. During the next mining process, the integral caving of the main roof occurs at the mining length of 1200 mm and 1800 mm, accompanying periodical fall of the immediate roof at an average length of 50 mm to 150 mm and several partial collapses of the main roof. With the advancement in mining process, the fractures generate and propagate in the overlying rock strata. At the end of the mining process, the fracture network evolves within the whole mined out area with a caving height of 600 mm. The description of the mining process in detail is presented in Table 5, and representative fracture network diagrams are shown in Figure 2.

3.2. Calculation of Fractal Dimension. In order to quantitatively analyse the expansion of fractures in mining rock masses, real-time video recording is performed in the process of the model test. Through the observation section in front of the physical model, the whole process of fracture generation, expansion, evolution, and strata failure during mining is well recorded. With the help of digital processing technology, the fracture network diagrams at different mining lengths are digitized (as shown in Figure 3). In this study, the calculation of fractal dimension is done by the method of “counting the boxes.” Each diagram is extended to a square area with a length of integer power times of 2. The fracture network with a unit length size of box is covered, and the number of boxes needed to cover the network is counted. The size of the box is enlarged by 2 times, the calculation of the number of boxes required to cover the fracture network is repeated, and so on (as shown in Figure 4). For each fracture network, a set of data corresponding to box length r and the number of boxes N is obtained in this way. If the fracture network has a fractal character, the size of the box r and the number of boxes $N(r)$ will follow the relationship as shown in the following equation:

$$N(r) = r^{-D_f}, \quad (5)$$

where D_f is the fractal dimension. By drawing the relationship between $N(r)$ and $1/r$ in the double logarithmic

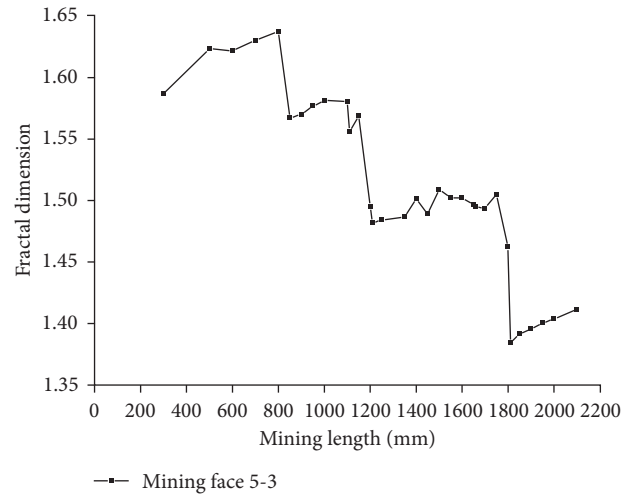


FIGURE 6: Evolution of the fractal dimension of fracture network with mining length.

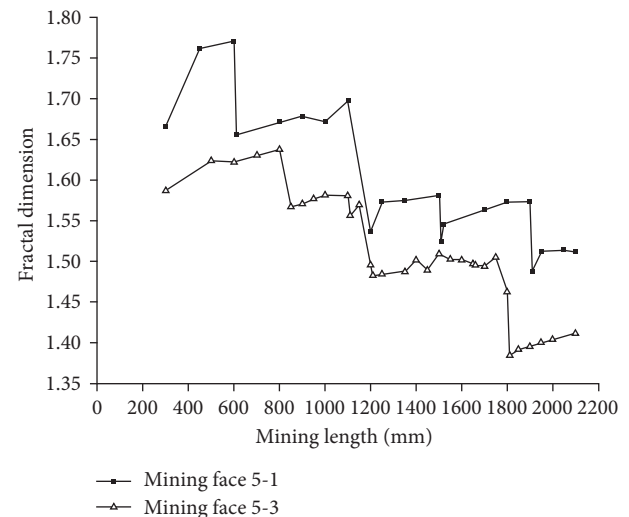


FIGURE 7: Relationship between the fractal dimension and mining length with different mining footage.

coordinates, a straight line will be obtained, of which the slope is equal to D_f . Taking the mining face 5-1 at the mining lengths of 1200 mm, 1500 mm, 1800 mm, and 2100 mm, for example, N and r of the covering boxes for calculating the fractal dimension are listed in Tables 6–9. By drawing the relationship between $N(r)$ and $1/r$ in the double logarithmic coordinates, the slope of the straight line equal to D_f is obtained (as shown in Figure 5).

From (5) and the fractal dimension calculation process, we can see that for each fracture network, the fractal dimension reflects the density of fractures in the unit area, and the increase in the fractal dimension indicates the expanding of fractures and the increasing of the fractures density. By analyzing the fractal dimension variation of fracture diagrams of different working conditions and different zones at different mining lengths, we can quantitatively analyse the fracture expansion and evolution laws.

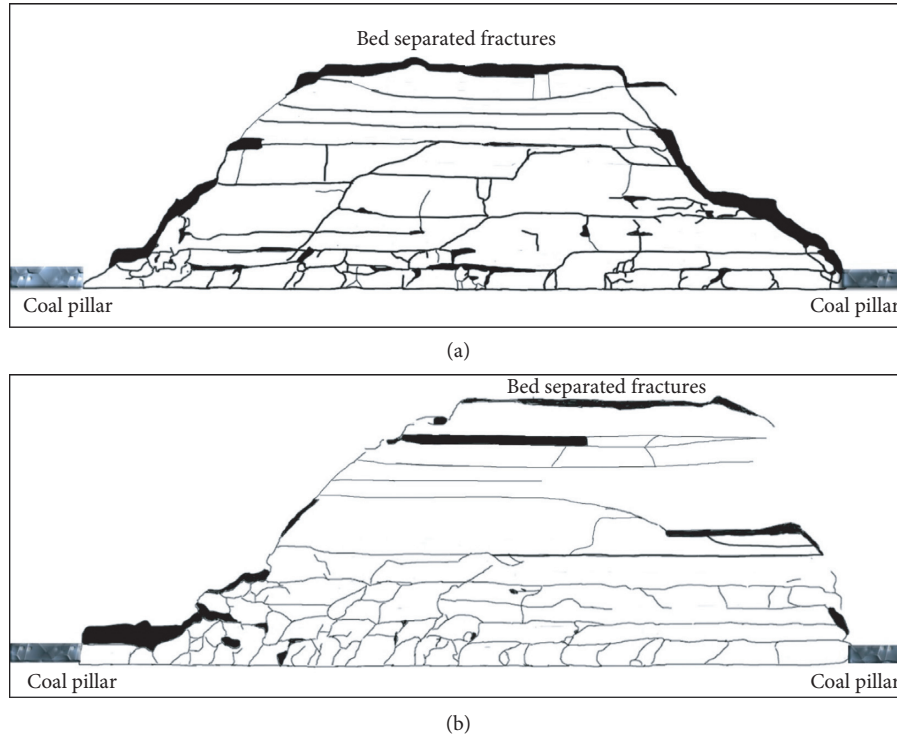


FIGURE 8: Fracture networks at the end of the mining process. Mining face: (a) 5-1; (b) 5-3.

TABLE 10: Horizontal zone description.

Zone number	H1	H2	H3	H4	H5	H6	H7
Mining length(mm)	0–300	300–600	600–900	900–1200	1200–1500	1500–1800	1800–2100

3.3. *Fractal Dimension Evolution of Fracture Networks with Mining Process.* The evolution of the fractal dimension of fracture networks with mining length is shown in Figure 6, by which the following features can be obtained:

- (1) The curve can be separated in several stage-type folding lines, containing increasing segment and descending segment.
- (2) The descending point corresponds exactly to the mining length, at which the main roof collapses (as shown in Table 5).
- (3) Every point in the linear increasing segment corresponds to the mining length, at which the immediate roof falls (as shown in Table 5).
- (4) The increasing segment can be fitted to a straight line, which means the regression relation between the fractal dimension D and the mining length L can be given by the following equation:

$$D = a * L + b, \quad (6)$$

where a and b are the parameters determined by the hydrogeological conditions, rock mechanical parameters, mining method, and so on.

TABLE 11: Vertical zone description.

Zone number	Zone height(mm)
V1	0–100
V2	100–200
V3	200–300
V4	300–400
V5	400–500
V6	500–600

3.4. *Evolution of Fractal Dimension with Different Mining Footage.* In order to analyse the influence of mining speed on the damage of overlying strata and the evolution of fracture propagation, mining faces 5-1 and 5-3 are mined with different mining advance footage. The relationship between the fractal dimension and mining length with different mining footage is shown in Figure 7, by which we can see that the mining face 5-1 (with a faster mining speed) has a larger fractal dimension than the mining face 5-3. Both the mining faces have the similar stage-type of the fractal dimension curve. Nevertheless, the 5-3 mining face has more points in increasing segment of the fractal dimension curve, which means having the shorter weighting interval in the immediate roof and a more developed fracture network in the caving zone, which can also be concluded from the

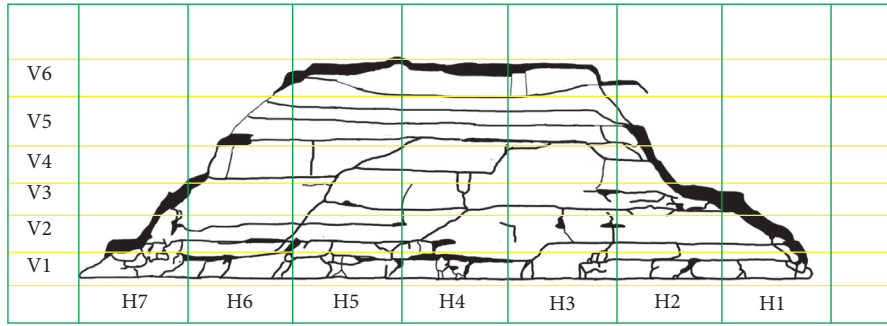


FIGURE 9: Schematic diagram for the fracture zones.

fracture network at the end of the mining process (as shown in Figure 8).

3.5. Evolution of Fractal Dimension in Different Caving Zones. With the advancing of mining face, how the fractures generate and develop in different horizontal and vertical zones is an aspect deserving to pay more attention on in this study. Based on this concern, 7 horizontal zones and 6 vertical zones are separated in mining face 5-1 (as shown in Tables 10 and 11 and Figure 9); the fractal dimension is calculated, respectively, and the fractal dimension curves are shown in Figures 10–13. The key findings are as follows:

- (1) Figure 10 describes the evolution of the fractal dimension in horizontal zones with the mining face advancing. The evolution curves indicate that the fractal dimension in horizontal zones has a similar trend with the fractal dimension on the whole, that is, gradually increasing in general and reduces when the main roof collapses. The main reason may be that the collapse of the main roof gives rise to the closure of fractures in the caving zone.
- (2) Figures 10 and 11 show that the fractal dimension at different mining progresses (such as 90 m, 120 m, 150 m, and 190 m) decreases with the increase of mining footage. On the whole, at the end of the mining process, the horizontal zone H3 and zone H6 have a relatively low fractal dimension, and the zones H1, H4, and H7, on the contrary, have a relatively high fractal dimension. The distribution of the fractal dimension of the fractures shows generally the “W”-type trend.
- (3) Through the analysis of the fractal characteristics of the fracture networks of the working face and combining the district partition of the fractured rock mass after mining [15], it is found that the fractal dimension of the fractured rock mass near the cutting area decreases gradually with the increase of mining footage, which indicates that the fractures in the area are gradually compressed and closed, which is called the re-compressed area. The fractal dimension of fractured rock mass near the mining face area increases, which indicates that the fractures are gradually developed and expanded with the increase of mining footage, which is called the separation zone. With the increase of mining footage, the

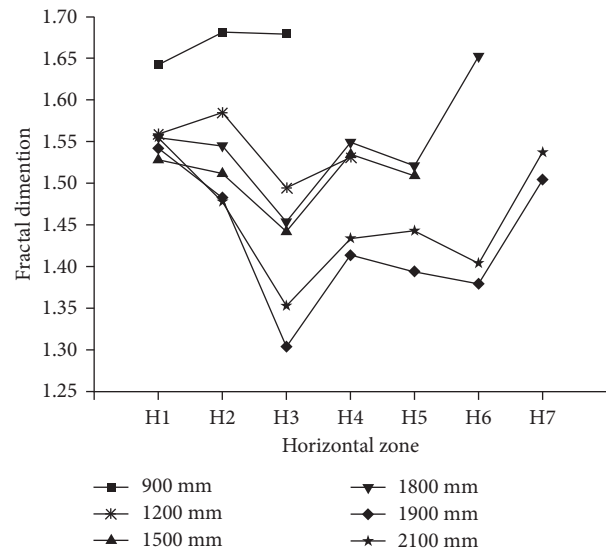


FIGURE 10: Evolution of the fractal dimension of crack network in different horizontal zones.

separation area away from the mining face is gradually transformed into a re-compressed area and the re-compressed area is gradually transformed into a stable area so that the fractal dimension of the horizontal zones of the fractured rock mass in the goaf is in dynamic changing.

- (4) Figure 12 shows the similar developing pattern of fractal dimension in vertical zones with that in horizontal zones. At the same time, it may be concluded by Figure 13 that, in general, the fractal dimensions reduce with the increase of the caving height; that is, the caving zone has a more developed fracture network than the fractured zone. Meanwhile, however, it should be pointed out that there is an exception sometimes in the transition zone between the fractured zone and sinking zone, due to the formation of the strata-separated fractures, which contribute much to the increase of the fractal dimension.

4. Conclusions

The fractal dimension is a very good tool to describe the evolution of mining-induced fractures network and its

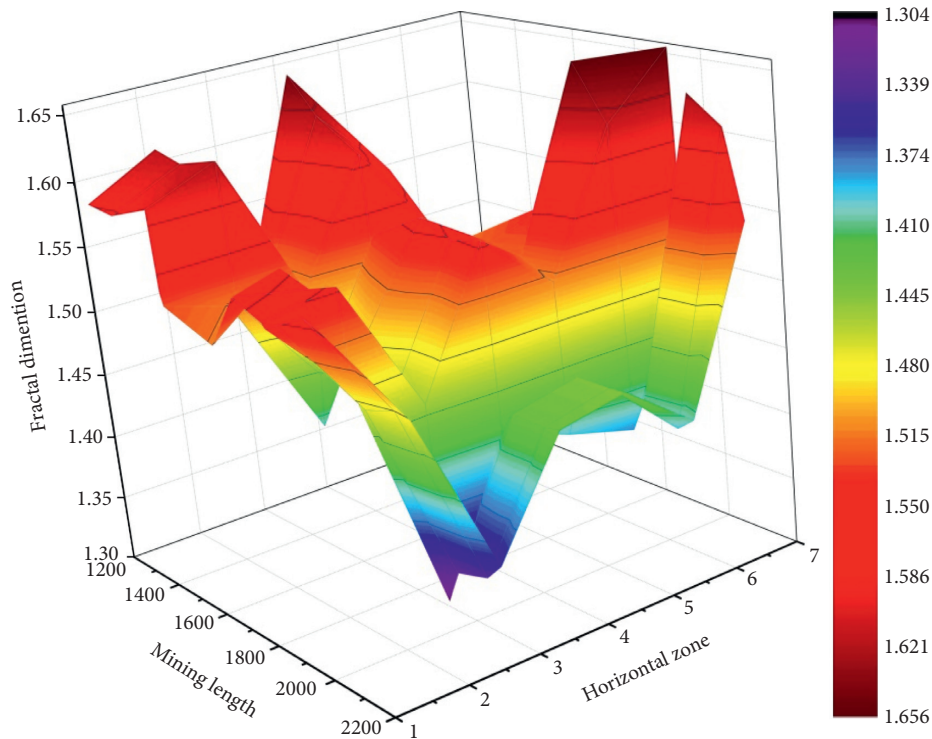


FIGURE 11: 3D colour map surface of evolution of the fractal dimension of crack network with mining length in different horizontal zones.

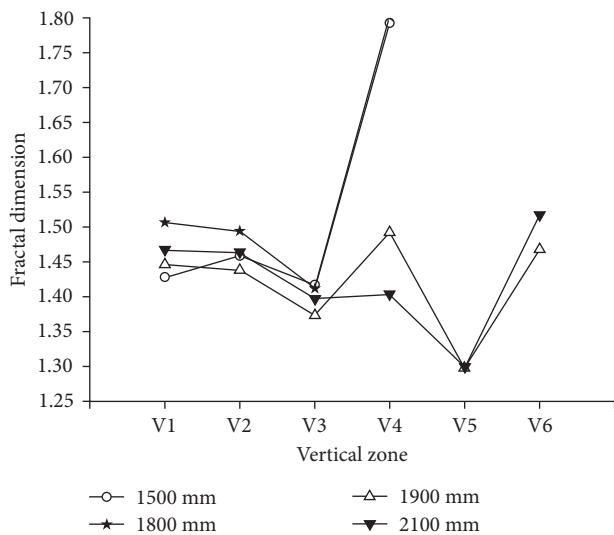


FIGURE 12: Evolution of the fractal dimension of crack network in different vertical zones.

evolution. In this paper, the fractal characteristics of fractures network induced by mining are studied in detail, and the following conclusions can be drawn:

- (1) The evolution curves of the fractal dimension with mining length can be separated into several stage-type folding lines, containing increasing segment and descending segment. The descending point corresponds exactly to the mining length, at which the main roof collapses. The increasing segment can be described by linear relationship.

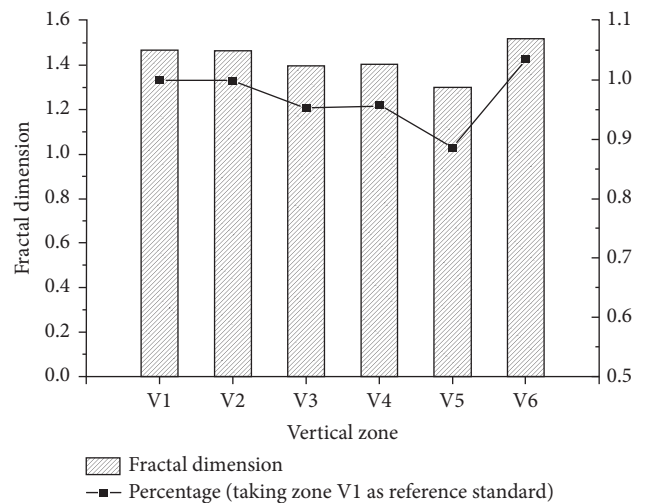


FIGURE 13: Ratio of the fractal dimension of crack network in different vertical zones.

- (2) The mining face with a faster mining speed has a larger fractal dimension. Nevertheless, the opposite of that has a shorter weighting interval in immediate roof and a more developed fracture networks in the caving zone.
- (3) The fractal dimensions in horizontal and vertical zones have a self-similar characteristic, that is, gradually increasing in general and reduces when the main roof collapses, similar to the features on the whole.
- (4) At the end of the mining process, the spatial distribution of mining-induced cracks may be saddle shaped.

- (5) Generally, the fractal dimension reduces with the increase of the caving height, while in the transition zone between the fractured zone and sinking zone, on the contrary, the fractal dimensions increase because of the separation of strata layers.

Data Availability

The data used to support the findings of this study are available from the corresponding author upon request.

Conflicts of Interest

The authors declare that they have no conflicts of interest.

Acknowledgments

The authors would like to acknowledge the support by the National Natural Science Foundation-Outstanding Youth Foundation (Grant no. 51522903), the National Key Research and Development Plan (Grant no. 2016YFC0501104), the National Natural Science Foundation of China (Grant nos. 51479094 and 41772246), and the Open Research Fund Program of the State Key Laboratory of Hydrosience and Engineering (Grant nos. 2016-KY-02 and 2016-KY-05).

References

- [1] T. Q. Liu, "Influence of mining activities on mine rock mass and control engineering," *Journal of China Coal Society*, vol. 20, pp. 1-5, 1995.
- [2] G. M. Yu, H. P. Xie, H. W. Zhou, Y. Z. Zhang, and L. Yang, "Distribution law of cracks in structured rock mass and its experimental investigation," *Journal of Experimental Mechanics*, vol. 13, pp. 145-154, 1998.
- [3] H. P. Xie, G. M. Yu, L. Yang, and Y. Z. Zhang, "Research on the fractal effects of crack network in overburden rock stratum," *Chinese Journal of Rock Mechanics and Engineering*, vol. 18, no. 2, pp. 147-151, 1999.
- [4] O. Bour, P. Davy, C. Darcel et al., "A statistical scaling model for fracture network geometry, with validation on a multiscale mapping of a joint network (Hornelen Basin, Norway)," *Journal of Geophysical Research: Solid Earth*, vol. 107, no. B6, pp. 347-383, 2002.
- [5] J. Weiss, "Scaling of fracture and faulting of ice on earth," *Surveys in Geophysics*, vol. 24, no. 2, pp. 185-227, 2003.
- [6] P. A. Dowd, C. Xu, K. V. Mardia, and R. J. Fowell, "A comparison of methods for the stochastic simulation of rock fractures," *Mathematical Geology*, vol. 39, no. 7, pp. 697-714, 2007.
- [7] M. G. Qian and J. L. Xu, "Study on the 'O-shape' circle distribution characteristics of mining-induced fractures in the overlying strata," *Journal of China Coal Society*, vol. 23, no. 5, pp. 466-469, 1998.
- [8] S. G. Li, M. G. Qian, and P. W. Shi, "Study on the dynamic distribution characteristic of fissures elliptic paraboloid zone in the mining overlying strata," *Mine Pressure and Roof Management*, no. 3-4, pp. 44-46, 1999.
- [9] S. G. Li, M. G. Qian, and P. W. Shi, "Study on bed-separated fissures of overlying stratum and interstice permeability in fully-mechanized top coal caving," *Chinese Journal of Rock Mechanics and Engineering*, vol. 19, no. 5, pp. 604-607, 2000.
- [10] B. B. Mandelbrot, *The Fractal Geometry of Nature*, W. H. Freeman, San Francisco, CA, USA, 1982.
- [11] T. Hirata, "Fractal dimension of fault systems in Japan: fractal structure in rock fracture geometry at various scales," *Pure and Applied Geophysics*, vol. 131, no. 1-2, pp. 157-170, 1989.
- [12] T. Villemin, J. Angelier, and C. Sunwoo, "Fractal distribution of fault length and offsets: implications of brittle deformation evaluation—The Lorraine Coal Basin," in *Fractals in the Earth Sciences*, C. C. Barton and P. R. La Pointe, Eds., Springer, Boston, MA, USA, 1995.
- [13] G. M. Yu, H. P. Xie, J. F. Zhao, and L. Yang, "Fractal evolution of a crack network in overburden rock strata," *Discrete Dynamics in Nature and Society*, vol. 5, pp. 47-52, 1999.
- [14] F. J. Molz, H. Rajaram, and S. Lu, "Stochastic fractal-based models of heterogeneity in subsurface hydrology: origins, applications, limitations, and future research questions," *Reviews of Geophysics*, vol. 42, no. 1, 2004.
- [15] M. Qian and X. Miu, "Theoretical analysis on the structural form and stability of overlying strata in longwall mining," *Chinese Journal of Rock Mechanics and Engineering*, vol. 14, no. 2, pp. 97-106, 1995.
- [16] Z. G. Wang, H. W. Zhou, and H. P. Xie, "Research on fractal characterization of mined crack network evolution in overburden rock stratum under deep mining," *Rock and Soil Mechanics*, vol. 30, pp. 2403-2408, 2009.
- [17] A. Jafari and T. Babadagli, "Estimation of equivalent fracture network permeability using fractal and statistical network properties," *Journal of Petroleum Science and Engineering*, vol. 92, pp. 110-123, 2012.
- [18] X. J. Wei, M. Z. Gao, Y. C. Lv, X. C. Shi, H. L. Gao, and H. W. Zhou, "Evolution of a mining induced fracture network in the overburden strata of an inclined coal seam," *International Journal of Mining Science and Technology*, vol. 22, no. 6, pp. 779-783, 2012.
- [19] A. Jafari and T. Babadagli, "Relationship between percolation-fractal properties and permeability of 2-D fracture networks," *International Journal of Rock Mechanics and Mining Sciences*, vol. 60, pp. 353-362, 2013.
- [20] H. Y. Li, W. H. Wang, Q. X. Qi, and L. Zhang, "Study on fissure development rule of overlying strata influenced by mining based on fractal theory," *Journal of China Coal Society*, vol. 39, pp. 1023-1030, 2014.
- [21] H. U. Yaoqing, Y. Zhao, and D. Yang, "Simulation theory and method of 3D solid-liquid coupling," *Journal of Liaoning Technical University*, vol. 26, no. 2, pp. 204-206, 2007.
- [22] Y. Zhao, *Multi Field Coupling of Porous Media and its Engineering Response*, Science Press, Beijing, China, 2010.
- [23] X. Li, Y. Lu, Y. Kang, and B. Rao, *Experimental Simulation Technology of Rock Mechanics*, Science Press, Beijing, China, 2007.
- [24] S. Li, Y. Zhou, L. Li, and Q. Zhang, "Development and application of a new similar material for underground engineering fluid-solid coupling model test," *Chinese Journal of Rock Mechanics and Engineering*, vol. 37, no. 6, pp. 1128-1137, 2012.

Research Article

Effects of Spatially Varying Seismic Ground Motions and Incident Angles on Behavior of Long Tunnels

Yundong Zhou, Yongxin Wu , Ziheng Shangguan, and Zhanbin Wang

Key Laboratory of Ministry of Education for Geomechanics and Embankment Engineering, Hohai University, Nanjing 210098, China

Correspondence should be addressed to Yongxin Wu; yxwuhhu@163.com

Received 14 March 2018; Accepted 7 May 2018; Published 11 June 2018

Academic Editor: Yongfeng Deng

Copyright © 2018 Yundong Zhou et al. This is an open access article distributed under the Creative Commons Attribution License, which permits unrestricted use, distribution, and reproduction in any medium, provided the original work is properly cited.

Seismic behavior of long circle tunnels is significantly influenced by the nature of input motion. This study, based on the 3D finite-element method (FEM), evaluates the effects of spatially varying seismic ground motions and uniform input seismic ground motions and their incident angles on the diameter strain rate and tensile/compressive principal stresses under different strata. It is found that (1) the spatially varying seismic ground motions induced larger diameter strain rate (radially deformation) than the uniform input seismic motion, (2) the spatially varying seismic ground motions had an asymmetric effect on the radial strain rate distributions, and (3) the rising incident angles changed the pure shear stress state into a complex stress state for tunnels under specified input motion.

1. Introduction

Tunnels, as an integral part of the infrastructure of modern society, would suffer damages when subjected to dynamic loadings during earthquake activity, for example, in Kobe earthquake (1995) [1], Chi-Chi earthquake (1999) [2], Duzce earthquake (1999) [3], Mid-Niigata Prefecture earthquake (2004) [4], Wenchuan earthquake (2008) [5], and Tohoku earthquake (2011) [6]. Nevertheless, the number of large tunnels and underground structures had grown significantly in recent decades. Therefore, seismic evaluation of tunnels in seismically active areas is critical during engineering design.

Seismic behavior of tunnels has been widely studied by many researchers [7–11], and these researches have concentrated mostly on 2D analysis. For the analysis of axial and bending deformations of tunnels, it is most appropriate to utilize 3D models.

However, for the 3D analysis of seismic behavior of tunnel, soil-tunnel analyses in the past were typically limited to relatively small regions, which made it difficult to fully consider the complex spatial features involved in such large structures [12]. Tunnels often had significant length and could be built on different strata foundations, which made the seismic analysis of tunnels a complex problem and was

usually evaluated under idealized conditions by using numerical methods, such as the finite-element method (FEM).

For the seismic analysis of complex stress distribution and deformation of long-distance tunnels, it is often more reliable to adopt three-dimensional (3D) methods. With the rapid development of science and technology, it is now possible to use high-performance computers to conduct large-scale 3D FEM seismic analysis for tunnels. There are three kinds of deformation, such as axial compression/extension, longitudinal bending, and ovaling/racking, occurring in tunnels during earthquake [10]. Particularly, the cross-sectional distortion of the tunnel can be related to seismic waves propagating along the tunnel.

Yu et al. [13, 14] presented a multiscale 3D FEM analysis of long tunnels under seismic loads where the mechanical characteristics of the tunnel segments and joints under artificial or recorded earthquake loads were evaluated in detail. The model in this paper would take into account not only the motion distribution with time but also the spatial variability (incoherency effect), the wave-passage effect, and the site-response effect.

This paper, based on an earlier report by the authors [15], attempts to develop a new model for seismic analysis of long tunnels with multisupport excitations, which properly accounts for the spatial variability. The main focus of this paper

is to assess the influence of multisupport input earthquake waves and uniform input earthquake waves as well as their incident angles on the diameter strain rate and tensile/compressive principal stresses under different strata. A full-scale 3D finite-element model is built comprising geological data, tunnel geometry, and so on to farthest simulate actual situation.

2. Simulation of Seismic Ground Motions

2.1. Simulation of Uniform Seismic Ground Motion. Consider a zero mean Gaussian stationary seismic ground motion with a target autospectral density $S(\omega)$. The seismic ground motions can be generated through the following expression:

$$x(t) = 2 \sum_{l=1}^N \sqrt{S(\omega_l) \Delta\omega} \cos(\omega_l t + \varphi_l), \quad (1)$$

where N is the number of frequency intervals, $\Delta\omega = \omega_u/N$ is frequency increment with ω_u as the cutoff frequency, $\omega_l = l\Delta\omega$, and the φ_l 's are statistically independent random phase angles uniformly distributed between $(0, 2\pi]$. Equation (1) is valid if there is an upper cutoff frequency ω_u above which the contribution of the power spectral density (PSD) to the simulations is negligible for practical purposes.

2.2. Simulation of Spatially Varying Seismic Ground Motions. The variations in ground motion are caused by the following four sources: (1) the ‘‘incoherence effect,’’ (2) the ‘‘wave-passage effect,’’ (3) the ‘‘site-response effect,’’ and (4) the ‘‘attenuation effect.’’ The spectral representation method is one of the most widely used methods in simulating the spatially varying seismic ground motions.

In practical application, spatially correlated ground motions can be considered as a one-dimensional, n -variety (1D- n V) stochastic vector process $X(t)$ with components $x_j(t)$ ($j = 1, 2, \dots, n$). Based on the spectral representation method, the j th component of the ground motions can be generated by [13]

$$x_j(t) = 2 \sum_{k=1}^n \sum_{l=1}^N |H_{jk}(\omega_l)| \sqrt{\Delta\omega} \cos[\omega_l t - \phi_{jk}(\omega_l) + \varphi_{kl}],$$

$$\omega_l = l\Delta\omega \quad (l = 0, 1, K, \dots, N-1),$$

$$\Delta\omega = \frac{\omega_u}{N}, \quad (2)$$

where ω_u is the upper cutoff frequency beyond which elements of the power spectral can be assumed to be zero for either mathematical or physical reasons and φ_{jk} are independent random phase angles uniformly distributed over $(0, 2\pi]$. $|H_{jk}(\omega)|$ and $\phi_{jk}(\omega)$ are the modulus and phase parts of $H_{jk}(\omega)$, respectively, which can be obtained by the root decomposition of power spectral density matrix as follows:

$$\mathbf{S}(\omega) = \mathbf{H}(\omega)\mathbf{H}^T(\omega), \quad (3)$$

where the superscript T denotes conjugate transpose.

The power spectral density matrix is given as

$$\mathbf{S}(\omega) = \begin{bmatrix} S_{11}(\omega) & S_{12}(\omega) & \cdots & S_{1m}(\omega) \\ S_{21}(\omega) & S_{22}(\omega) & \cdots & S_{2m}(\omega) \\ \vdots & \vdots & \ddots & \vdots \\ S_{m1}(\omega) & S_{m2}(\omega) & \cdots & S_{mm}(\omega) \end{bmatrix}, \quad (4)$$

where $S_{jj}(\omega)$ is the autopower spectral density function and $S_{jk}(\omega, t)$ is the cross-power spectral density function, which can be expressed as

$$S_{jk}(\omega, t) = |\gamma_{jk}(\omega)| \sqrt{S_{jj}(\omega)S_{kk}(\omega)} e^{i\theta_{jk}(\omega)}, \quad (5)$$

where $|\gamma_{jk}(\omega)|$ is the lagged coherence function representing ‘‘incoherence’’ effect and $\theta_{jk}(\omega)$ is composed of wave passage.

However, the ground motions simulated by the above method are stationary, while the actual seismic records are nonstationary. Therefore, to obtain nonstationary seismic ground motion, the way of multiplying an envelope function is applied. The envelope function is as follows:

$$f(t) = \begin{cases} (t/t_1)^2, & t < t_1 \\ 1, & t_1 \leq t < t_2, \\ e^{-c(t-t_2)}, & t \geq t_2 \end{cases}, \quad (6)$$

where t_1 , t_2 , and c are three parameters describing the shape of the envelope function. In this study, they are set to be $t_1 = 6$, $t_2 = 10$, and $c = 0.5$, respectively.

3. FE Model

The tunnel model adopted in this paper was built with circular appearance, whose outside diameter is 10 m, inside diameter is 9 m, and length is 1000 m. It had a buried depth of 30 m from the tunnel center to soil surface. The simulation setup is shown in Figure 1. It consists of a $1000 \times 300 \times 100$ m box with the 1000 m length circular tunnel. The space coordinates were built by taking the length direction as the Z -axis, the width direction as the X -axis, and the height direction as the Y -direction. The soil profile was modeled as four layers of Mohr–Coulomb materials and tunnel as the elastic material. All the property parameters used can be found in Tables 1 and 2. An infinite domain by using the artificial boundary was adopted [12], where both borders of the tunnel were fixed in the Z -direction.

In this work, the constitutive model of the tunnel is an elastic model, which is given as follows:

$$\boldsymbol{\sigma} = \lambda I_1 \boldsymbol{\delta} + 2G\boldsymbol{\varepsilon}, \quad (7)$$

in which $\boldsymbol{\sigma}$ is the stress tensor, $\boldsymbol{\varepsilon}$ is the strain tensor, I_1 is the first strain invariant, λ is the Lamé constant, and G is the shear modulus.

The Mohr–Coulomb yield criterion for soil is expressed as follows:

$$\frac{m+1}{2} \max\left(|\sigma_1 - \sigma_2| + K(\sigma_1 + \sigma_2), |\sigma_1 - \sigma_3| + K(\sigma_1 + \sigma_3), |\sigma_2 - \sigma_3| + K(\sigma_2 + \sigma_3)\right) = S_{yc}, \quad (8)$$

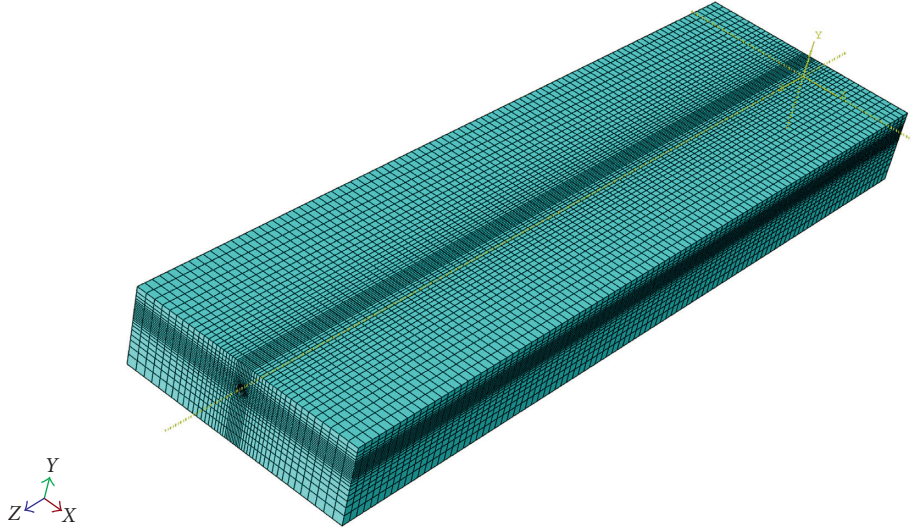


FIGURE 1: Finite-element mesh model adopted in the 3D FE analyses for soil with long tunnels.

TABLE 1: Properties of different soil layers.

Layer number	Young's modulus (MPa)	Poisson's ratio	Density (kg/m ³)	Cohesion (kPa)	Internal friction angle (°)	Thickness (m)
1	3.029	0.45	1760	10.8	14.2	20.6
2	6.135	0.36	1810	17.7	18.9	23.9
3	6.319	0.47	1870	22	22.9	24.2
4	6.251	0.36	1950	24.9	18.2	31.5

TABLE 2: Properties of the tunnel.

Elastic modulus (kg/m ³)	Poisson's ratio	Unit weight (kN/m ³)
3.6e7	0.2	25.7

where

$$m = \frac{S_{yc}}{S_{yt}}, \quad (9)$$

$$K = \frac{m-1}{m+1},$$

and the parameters S_{yc} and S_{yt} are the yield stresses of the material in uniaxial compression and tension, respectively.

On the interface, the deformation of the tunnel and soil is in concert and harmony.

4. Computation and Analysis

In computation, a regular 3D finite-element model was built based on geotechnical data, tunnel geometry, and so on. The traveling waves velocity motivated from bedrock surface was 500 m/s in the 3D spatially varying seismic ground motion field. The schematic diagram of different incident angles used is shown in Figure 2. The simulated spatially varying ground motions are plotted in Figure 3.

4.1. Effect on Radial Deformations. The diameter strain rate Δd is defined as

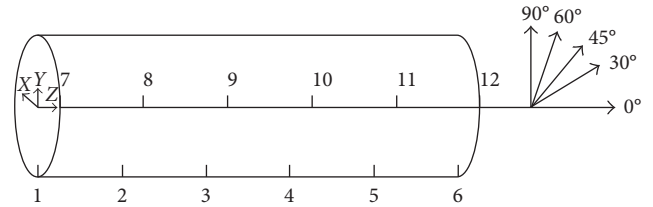


FIGURE 2: The schematic diagram at different incident angles.

$$\Delta d = \frac{d' - d}{d}, \quad (10)$$

where d and d' are the tunnel diameters before and after deformation.

The positive rate value denotes that the tunnel cross section undergoes tensile deformation in radial direction, and the negative value corresponds to compressive deformation. In this section, d_{\max} is defined as the maximum of Δd in the earthquake time process. d_{\max} in the vertical direction is calculated from displacement time processes at the vertex and nadir of tunnel in the Y-axis direction while the one in the lateral direction is obtained from processes at the right and left sides of the tunnel in the X-axis direction. It was found from the simulation that lateral Δd and vertical Δd were equal and opposite in the direction at any arbitrary time, videlicet, the primary deformation of tunnel under seismic waves was ovaling. In addition, the partial feature results under uniform and spatially varying seismic ground motions, that is, the lateral d_{\max} at $Z = 100$ m, 300 m, 500 m, 700 m, and

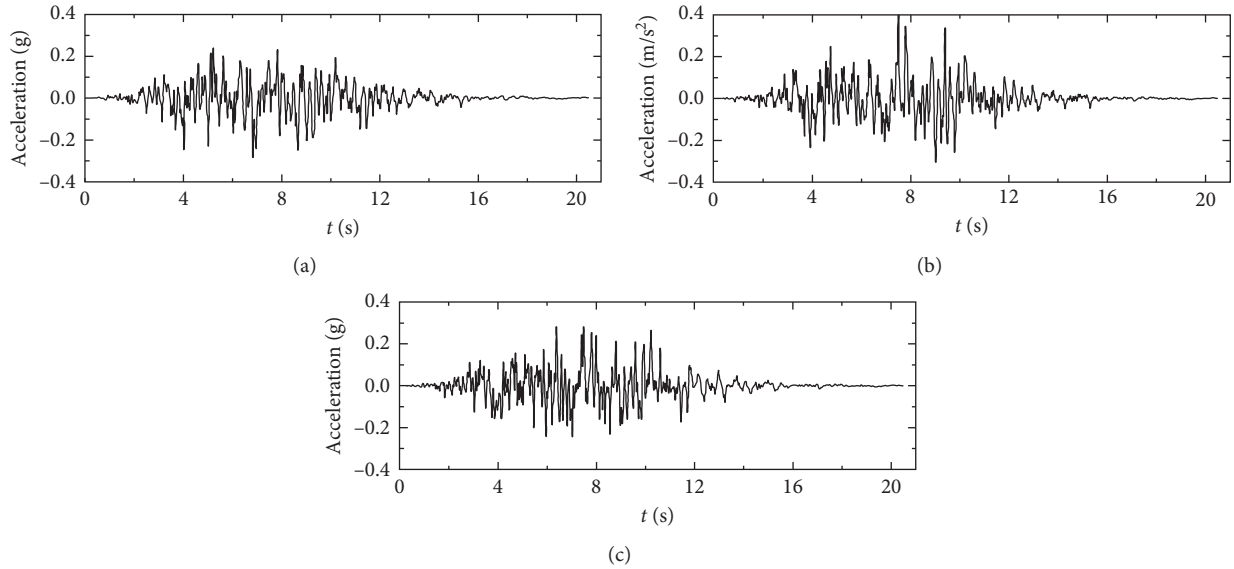


FIGURE 3: The simulated spatially varying seismic ground motions: (a) $x=0$ m, (b) $x=500$ m, and (c) $x=1000$ m.

TABLE 3: Lateral maximum diameter strain rate of tunnel under uniform seismic motion.

Incident angle	Z = 100 m	Z = 300 m	Z = 500 m	Z = 700 m	Z = 900 m
0°	-0.036%	-0.004%	0	-0.004%	-0.036%
30°	0.087%	0.113%	0.118%	0.113%	0.087%
45°	0.130%	0.158%	0.165%	0.158%	0.130%
60°	0.171%	0.196%	0.204%	0.196%	0.171%
90°	0.214%	0.226%	0.236%	0.226%	0.214%

900 m with incident angles of 0°, 30°, 45°, 60°, and 90° can be found in Tables 3 and 4.

It could be observed that the lateral d_{\max} increases with increasing incident angles for both seismic input forms, but the maximum positions differ from each other. For uniform seismic input simulations, the lateral d_{\max} position is at the middle point ($Z=500$ m) of the tunnel and the diameter strain rates are symmetrically distributed on the left and right sides of the tunnel. This can be attributed to the balanced boundary conditions and uniform seismic waves. For spatially varying seismic ground motions, the lateral d_{\max} is located between $Z=700$ m and $Z=900$ m and exhibits asymmetric features due to the nonuniform waves. The table also implies that the lateral d_{\max} for the whole tunnel under spatially varying seismic ground motions is greater than that under uniform input ground motions.

4.2. Effect on Stress Distributions. The maximum principal shear ($\sigma_{t\max}$) and compressive ($\sigma_{c\max}$) stresses are commonly used to analyze the effect of seismic input ground motions on tunnels. The peak stresses under different incident angles are illustrated in Table 5.

It is indicated that the maximum tensile stress is identical to the maximum compressive stress while the incident angle is 0° for uniform seismic input tunnels. This is owing to the

TABLE 4: Lateral maximum diameter strain rate of tunnel under multisupport seismic motion.

Incident angle	Z = 100 m	Z = 300 m	Z = 500 m	Z = 700 m	Z = 900 m
0°	0.022%	-0.045%	0.033%	0.035%	0.039%
30°	0.075%	-0.125%	-0.169%	-0.169%	-0.098%
45°	0.111%	-0.163%	-0.225%	-0.225%	-0.123%
60°	0.141%	-0.193%	-0.269%	-0.269%	-0.143%
90°	0.170%	-0.208%	-0.293	-0.293%	-0.155%

TABLE 5: Maximum stresses of tunnel body at different incident angles.

Motion form	Principal stress	0°	30°	45°	60°	90°
Uniform	$\sigma_{t\max}$	11.60	10.85	9.24	7.18	7.45
	$\sigma_{c\max}$	-11.60	-10.58	-10.02	-8.99	-6.81
Multisupport	$\sigma_{t\max}$	17.74	13.92	11.29	8.94	6.66
	$\sigma_{c\max}$	-18.84	-15.68	-13.37	-11.16	-8.49

tunnel and soil profile placed in pure shear stress state. When incident angles are equal to 30°, 45°, 60°, and 90°, the values of maximum tensile and compressive stresses are different because of the complex shear and normal stress states induced by seismic load. It can be thus concluded that the earthquake acceleration in the vertical direction changes not only the maximum stress but also the stress characteristics. In addition, the spatially varying seismic ground motion is another factor influencing the stress state according to the different values between the maximum tensile stress and maximum compressive stress at an incident angle of 0° under spatially varying seismic ground motions. Meanwhile, the value of maximum tensile/compressive stresses decreases with the increasing incident angles. The maximum tensile stress nephogram at an incident angle of 0° for both uniform and spatially varying seismic ground motions is, respectively, shown in Figures 4 and 5.

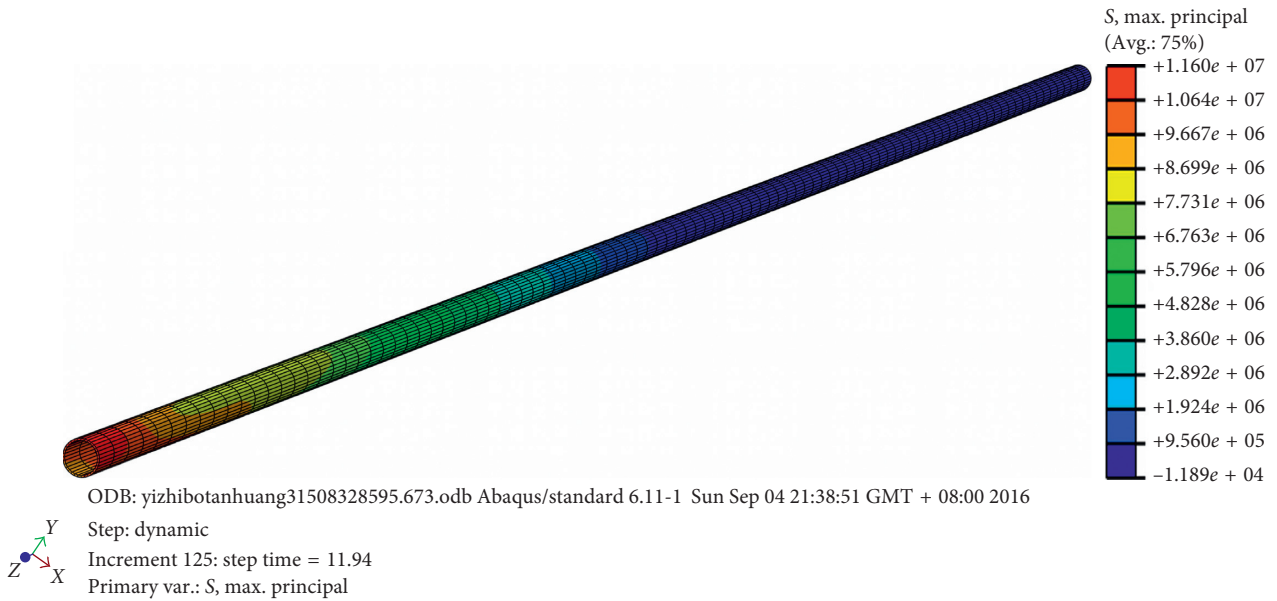


FIGURE 4: The maximum tensile stress nephogram at an incident angle of 0° under uniform seismic input motion.

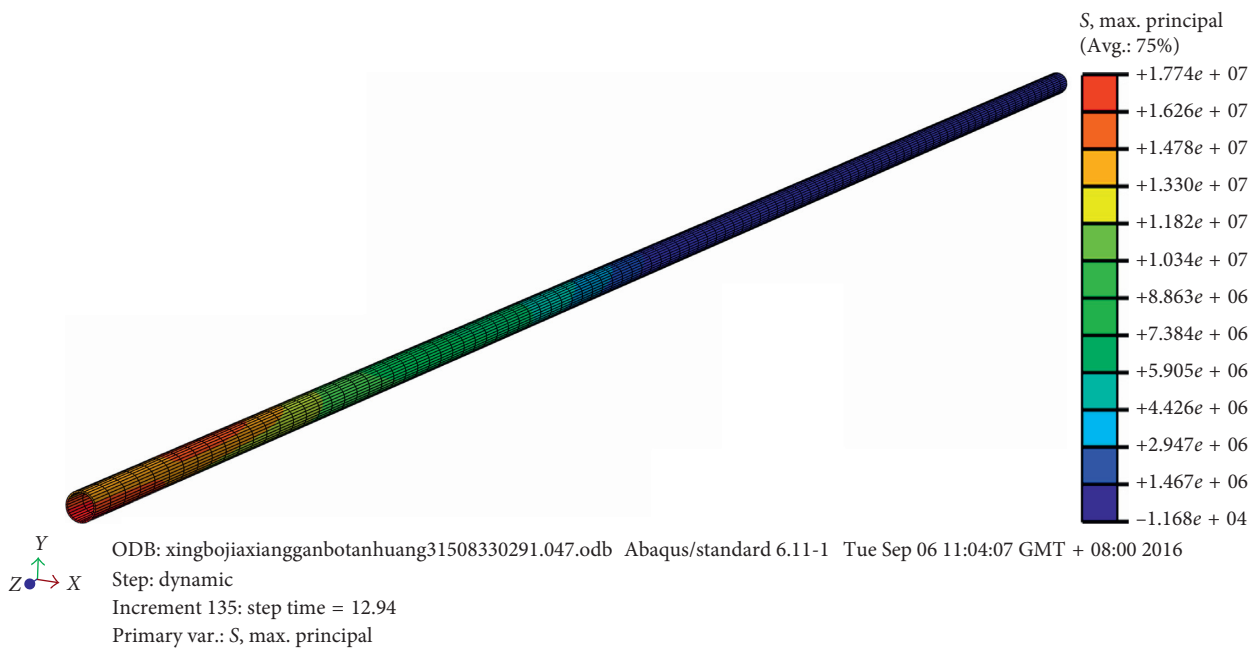


FIGURE 5: The maximum tensile stress nephogram at an incident angle of 0° under multisupport seismic input motion.

The red upper portion of the tunnel end ($Z=1000\text{ m}$) in Figure 4 is the maximum tensile stress, responding to the red lower portion near the tunnel end. It is suggested that the spatially varying seismic ground motion affects the stress distribution.

5. Conclusions

Numerical simulation was an effective method for studying the tunnel responses under seismic event. In this paper, a novel large-scale analytical method was established for estimating the seismic response of long tunnels within soil foundations. Based on the 3D FEM platform, this method could offer a reliable way for investigating the nonlinear

seismic behavior of long tunnels. Main findings are summarized as follows:

- (1) The spatially varying seismic ground motions induced larger diameter strain rates (radial deformation) than the uniform input seismic motion. The maximum radial strain rate increased with the increasing incident angles for both seismic input forms.
- (2) For uniform seismic input simulations, the maximum radial strain rate occurred at the middle point of the tunnel and the radial strain rates were symmetrically distributed on the left and right sides of the tunnel. Moreover, the spatially varying seismic

ground motions had an asymmetric effect on the radial strain rate distributions.

- (3) The rising incident angles changed the pure shear stress state into a complex stress state for tunnels under specified input motion. The spatially varying seismic ground motions also influenced the stress state relative to the uniform seismic input. Meanwhile, the values of maximum tensile/compressive stresses decreased with the increasing incident angles.

Data Availability

All the data supporting the conclusions of this study are presented in the tables of the article. The code and details of the FEM for the analysis are available upon request from the corresponding author.

Conflicts of Interest

The authors declare that they have no conflicts of interest.

Acknowledgments

The supports by the National Natural Science Foundation of China (Grant no. 41630638), the National Key Basic Research Program of China (Grant no. 2015CB057901), and the Fundamental Research Funds for the Central Universities (Grant no. 2018B13914) are greatly acknowledged.

References

- [1] H. Iida, T. Hiroto, N. Yoshida et al., "Damage to Daikai subway station," *Soils and Foundations*, vol. 36, pp. 283–300, 1996.
- [2] W. L. Wang, T. T. Wang, J. J. Su et al., "Assessment of damage in mountain tunnels due to the Taiwan Chi-Chi earthquake," *Tunnelling and Underground Space Technology*, vol. 16, no. 3, pp. 133–150, 2001.
- [3] C. Menkiti, R. Mair, and R. Miles, "Highway tunnel performance during the 1999 Duzce earthquake," in *Proceedings of the Fifteenth International Conference on Soil Mechanics and Geotechnical Engineering*, Istanbul, Turkey, August 2001.
- [4] T. Tobita, S. Iai, M. G. Wang et al., "Preliminary report of the Mid Niigata Prefecture, Japan, earthquake in 2004," *Journal of Japan Society for Natural Disaster Science*, vol. 23, no. 4, pp. 595–602, 2005, in Japanese.
- [5] Z. Cao, L.-Q. Hou, X. Yuan et al., "Characteristics of liquefaction-induced damages during Wenchuan Ms 8.0 earthquake," *Rock and Soil Mechanics*, vol. 31, no. 11, pp. 3549–3555, 2010, in Chinese.
- [6] S. A. Ashford, R. W. Boulanger, J. L. Donahue et al., *Geotechnical Quick Report on the Kanto Plain Region during the March 11, 2011, Off Pacific Coast of Tohoku Earthquake, Japan*, GEER Association Report No. GEER, Geotechnical Extreme Events Reconnaissance (GEER), Tokyo, Japan, 2011.
- [7] A. Bobet, "Effect of pore water pressure on tunnel support during static and seismic loading," *Tunnelling and Underground Space Technology*, vol. 18, no. 4, pp. 377–393, 2003.
- [8] S. E. Kattis, D. E. Beskos, and A. H. D. Cheng, "2D dynamic response of unlined and lined tunnels in poroelastic soil to harmonic body waves," *Earthquake Engineering & Structural Dynamics*, vol. 32, no. 1, pp. 97–110, 2003.
- [9] S. A. S. Youakim, S. E. E. El-Metewally, and W. F. Chen, "Nonlinear analysis of tunnels in clayey/sandy soil with a concrete lining," *Engineering Structures*, vol. 22, no. 2, pp. 707–722, 2000.
- [10] A. Amorosi and D. Boldini, "Numerical modeling of the transverse dynamic behavior of circular tunnels in clayey soils," *Soil Dynamics and Earthquake Engineering*, vol. 29, no. 6, pp. 1059–1072, 2009.
- [11] S. B. Kojic and M. Trifunac, "Transient pressures in hydro-technical tunnels during earthquakes," *Earthquake Engineering and Structural Dynamics*, vol. 16, no. 4, pp. 523–539, 1988.
- [12] H. Dobashi, E. Ochiai, T. Ichimura et al., "3D FE analysis of seismic response of complicated large-scale ramp tunnel structure," in *Proceedings of the ECCOMAS Thematic Conference on Computational Methods in Structural Dynamics and Earthquake Engineering*, pp. 13–16, Rethymno, Crete, Greece, 2007.
- [13] H. Yu, Y. Yuan, and A. Bobet, "Multiscale method for long tunnels subjected to seismic loading," *International Journal for Numerical and Analytical Methods in Geomechanics*, vol. 37, no. 4, pp. 374–398, 2013.
- [14] H. Yu, Y. Yuan, Z. Qiao et al., "Seismic analysis of a long tunnel based on multi-scale method," *Engineering Structures*, vol. 49, no. 2, pp. 572–587, 2013.
- [15] W. U. Yongxin, Y. Gao, and D. Li, "Simulation of spatially correlated earthquake ground motions for engineering purposes," *Earthquake Engineering and Engineering Vibration*, vol. 10, no. 2, pp. 163–173, 2011.

Research Article

Experimental and Theoretical Studies on the Creep Behavior of Bayer Red Mud

Baoyun Zhao ^{1,2}, Wei Huang,^{1,2} Zhile Shu,³ Mengmeng Han,⁴ and Yanbo Feng⁵

¹School of Civil Engineering and Architecture, Chongqing University of Science and Technology, Chongqing 401331, China

²Chongqing Key Laboratory of Energy Engineering Mechanics and Disaster Prevention and Mitigation, Chongqing 401331, China

³School of Civil and Environmental Engineering, Xihua University, Chengdu 610039, China

⁴Chongqing Test Center of Geology and Minerals, Chongqing 400042, China

⁵School of Civil Engineering and Architecture, Chongqing University of Arts and Sciences, Chongqing 402160, China

Correspondence should be addressed to Baoyun Zhao; baoyun666@163.com

Received 11 January 2018; Accepted 29 March 2018; Published 2 May 2018

Academic Editor: Annan Zhou

Copyright © 2018 Baoyun Zhao et al. This is an open access article distributed under the Creative Commons Attribution License, which permits unrestricted use, distribution, and reproduction in any medium, provided the original work is properly cited.

Long-term stability and safety of the Bayer red mud (BRM) disposal field is very important for the local residents' life, which necessitates the knowledge of its creep behavior. In order to investigate the creep behavior of BRM, a series of triaxial drained creep tests were conducted by using an improved triaxial creep apparatus. The results indicate that the creep behavior of BRM is significant with confining and deviatoric stresses being critical factors. The creep strain is in a nonlinear relationship with stress and time, and a larger deviator stress will lead to a larger creep strain. The main failure mechanism of BRM is plastic shear, accompanied by a significant compression and ductile dilatancy. Based on the test results, two well-established creep models, the Burgers creep model and Singh–Mitchell creep model, were used to comparatively analyze the creep behavior of the Bayer red mud under a certain stress level. Then, an improved Burgers creep damage constitutive model with the addition of a damage variable was proposed, whose parameters were also analyzed in detail. The comparison of the calculated values of the creep model and the experimental values shows that the proposed creep damage model can better describe the instant elastic deformation, attenuation creep, steady-state creep, and accelerated creep stages of the Bayer red mud.

1. Introduction

The Bayer red mud (BRM), also called as bauxite residue, is a hazardous solid waste generated during the Bayer alumina extraction from bauxite ore [1, 2]. It generally exists as a highly alkaline slurry (Ph 10–12.5) that is appropriately regarded as a hazardous material [3]. As there is a great deal of industrial alkali, fluoride, heavy metals, and other potential pollutants in red mud, long-term stockpiling would not only occupy scarce land resources but also easily lead to serious pollution of the surrounding soil, air, and groundwater [4]. In the past 50 years, the wet process was used to stockpile the Bayer red mud in Guizhou Aluminum Factory red mud disposal field, which led to much unconsolidated BRM in the disposal field. At present, the production technique has been upgraded to the sintering method, more

and more dried red mud was stockpiled on the unconsolidated ones directly, which much exceed the original design storage capacity. Therefore, to make disposal field stable when renewing the dry red mud, we must evaluate the long-term stability of the original Bayer red mud.

Good mechanical performance and especially creep behavior of the BRM is essential for safe and stable operation of such disposal field. Many laboratory studies investigated the creep behavior of various soils [5–7]. Yu et al. [8] performed several creep tests (lasting more than one year) to study the delayed mechanical behavior of Boom clay under the hydromechanical coupling effect. Wen and Jiang [9] discussed creep behavior of natural clayey soil with gravel at the residual state through a series of creep shear tests. Liao et al. [10] conducted a series of triaxial creep on warm frozen silts extracted from Qinghai–Tibet Plateau at a temperature

TABLE 1: Basic physical properties of the Bayer process red mud.

Wet density ($\text{g}\cdot\text{cm}^{-3}$)	Water content (%)	Specific gravity	Liquid limit (%)	Plastic limit (%)	Plastic index	Compressibility (MPa^{-1})
1.75	44.00	2.72	48.89	35.77	13.12	0.20

of -1.5°C under the confining pressures of 0.5, 1.0, and 2.0 MPa, respectively. Karimpour and Lade [5] performed triaxial compression tests on dense specimens of Virginia Beach sand at low and high confining pressures to study time effects that relate to grain crushing due to static fatigue or delayed fracture. The abovementioned experimental studies mostly investigated clay, sand, and frozen silts. However, concerning the study of creep mechanical behavior of the Bayer red mud, little experimental data have been reported. Therefore, studies focusing on the Bayer red mud are needed to further our understanding of its creep mechanical behavior.

Based on experimental investigations, various viscoelastic-plastic models [11, 12] taking into account soil and rock microstructure and damage have been proposed. These models can be classified into three categories: empirical models, rheological models, general stress-strain-time models [7, 13], and damage-involved models [14, 15]. The empirical models are mainly obtained by fitting the experimental results from creep tests; due to its relatively simple mathematical formulation and few parameters, the empirical models [16–18] are widely used to simulate the creep behavior of various soils. Rheological models usually use differential representation, visualizing the material by the elementary mechanical models composed of elastic springs, plastic sliders, and viscous dashpots [13, 19, 20]. The general stress-strain-time models are often in the incremental form and usually implemented in numerical software [21], such as the overstress model proposed by Karstunen and Yin [22] and the further extended overstress model by Yin et al. [23]. Due to its clear physical meaning and numerical convenience in programming, the general stress-strain-time model is recommended for engineering practice [21].

To clarify the creep behavior of the Bayer red mud, a series of triaxial compression creep tests were conducted on the Bayer red mud samples under different confining pressures. Based on the results, two well-established creep models, the Burgers creep model and the Singh–Mitchell equation, were used to describe the creep behavior of the Bayer red mud under a certain stress level. And then, an improved Burgers creep damage model is built to describe the creep mechanical behavior and damage evolution process of the Bayer red mud under compression. The validity of the improved model is tested by comparing the numerical simulations and test results.

2. Test Conditions and Results

2.1. Materials and Sample Preparation. The Bayer red mud materials were obtained from the disposal field of Guizhou aluminum factory in southwest of China. Natural Bayer red mud is a bauxite residue generated from the Bayer process (a wet process) for alumina production, which presents the

color of reddish brown. X-ray diffraction was used to determine the clay minerals [24]. According to the X-ray diffraction, the Bayer red mud is comprised of cancrinite, hydrogrossular, tilleyite, calcite, and xonotlite; the main chemical constituent was SiO_2 (accounting for 22.35%), followed by 20.80% of Al_2O_3 , 18.51% of CaO , 8.83% of Na_2O , 7.73% of Fe_2O_3 , and a small amount of mixture of K_2O , MgO , TiO_2 , and SO_3 .

To avoid the nonuniformity of the undisturbed specimens, the remolded specimens were used in this study; that is, the specimens were formed into cylindrical shape, which has a height of 80 mm and diameter of 39.1 mm. The average values of the index properties along with the main characteristics of the tested material are mentioned in Table 1. The Bayer red mud can be classified, according to the Unified Soil Classification System [25], as high-plasticity clays (CH).

2.2. Experimental Apparatus and Procedures. An improved strain control triaxial apparatus of TSZ-6A was used to test the creep behavior of the samples (Figure 1). The improved apparatus changes the former axial strain-controlled loading system into a weight-controlled stress loading system [26]. It also retains the confining/back pressure, pore pressure, volume change, and displacement measurement systems of the former triaxial apparatus.

After the sample was saturated under both 140 kPa confining pressure and 110 kPa back pressure for at least 24 hours, the triaxial creep tests were performed at an ambient temperatures of $(20 \pm 2)^{\circ}\text{C}$. Based on the measured triaxial short-term compression strength, the axial deviatoric stress levels of multistep creep tests of the Bayer red mud samples were determined (Table 2), which are 16.67%, 33.33%, 50.00%, 66.67%, 83.33%, and 100% of the maximum short-term deviatoric stress value. Each deviatoric stress level was maintained for no less than 4500 minutes before the final failure.

2.3. Test Results and Discussions. To show the creep behavior that took place under each stress level clearly, the axial strain-time curve obtained for each stress level is plotted separately in Figure 2 (due to the limitation of the device, the volumetric creep responses of the BRM was not discussed). It is found that, under the low deviatoric stress level (less than maximum short-term deviatoric stress value), the creep curve of the Bayer red mud is composed of instant elastic deformation, attenuation creep, and steady-state creep stages. As shown in Figures 2(a)–2(c), when the deviatoric stresses are less than 591 kPa, 684 kPa, and 849 kPa, respectively, only attenuation and steady creep appears in the test, while the creep phenomenon of the samples becomes significant with the increase of the deviatoric stress. It also can be obtained from Figure 2 that attenuation creep

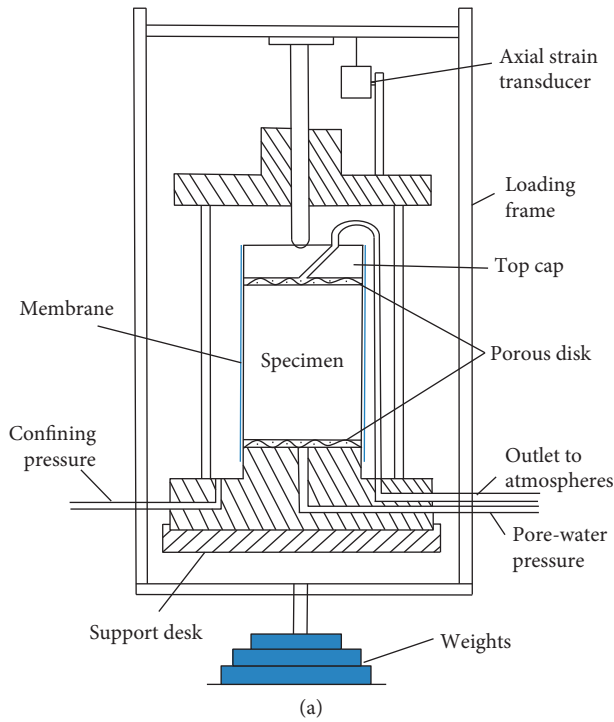


FIGURE 1: The weight-controlled stress loading system. (a) A schematic diagram. (b) Real picture of the apparatus.

TABLE 2: Experimental deviatoric stress levels at different confining pressures (unit: kPa).

Confining pressure	Axial deviatoric stress levels					
100	98.5	197.0	295.5	394.0	492.5	591.0
150	114.1	228.0	342.0	456.0	570.0	684.0
200	141.5	283.0	424.5	566.0	707.5	849.0

occurred for a very short time and was not obvious, indicating that internal damage could not continue to occur over time under a stable lower loading level.

When the deviatoric stress reaches a certain level (100% of the maximum short-term deviatoric stress value), the creep strain is much greater than that at previous stress levels; the accelerated creep stage appears, while instant elastic deformation and attenuation creep strain are unnoticeable. As shown in Figures 3 and 4, when the deviatoric stresses are 591 kPa, 684 kPa, and 849 kPa, respectively, the original structure of the soil sample begins to destruct while

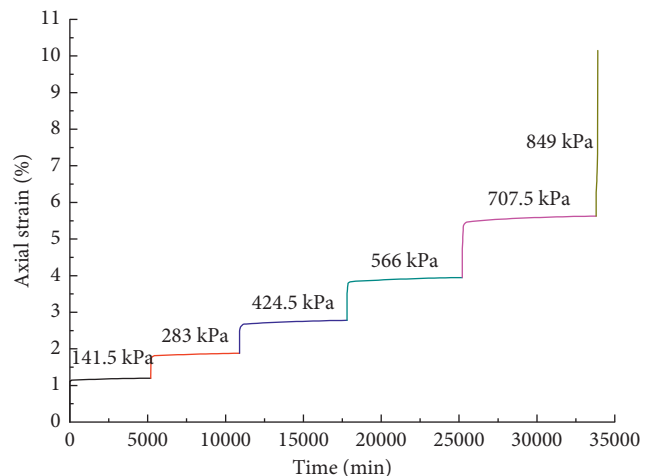
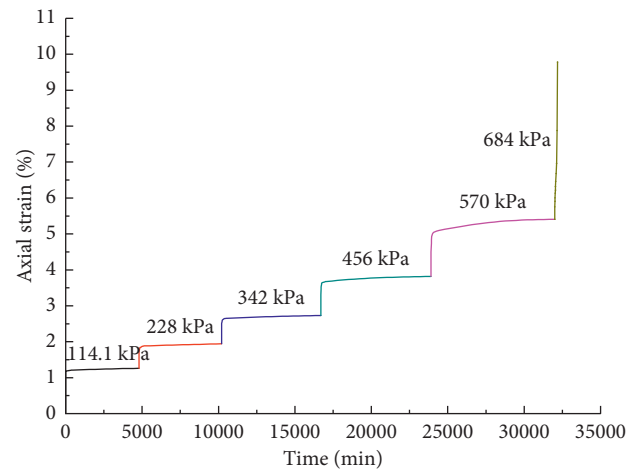
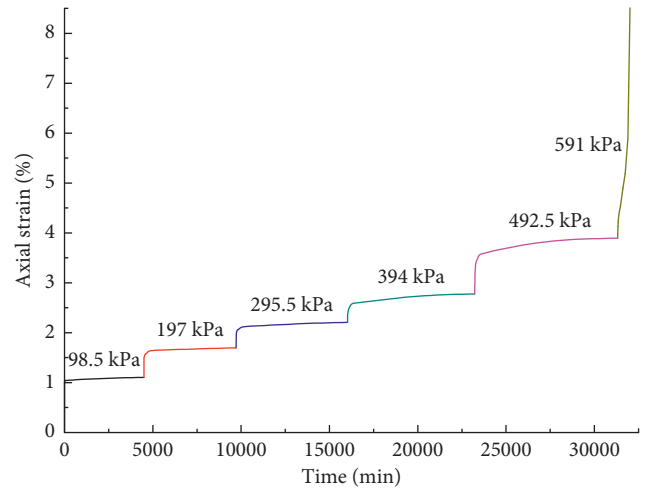


FIGURE 2: Relation between creep strain and time under different confining pressures: (a) 100 kPa, (b) 150 kPa, and (c) 200 kPa.

the displacement of the soil grains is produced that causes the creep strain of the samples to increase rapidly and fail eventually. Under the maximum deviatoric stress level, the

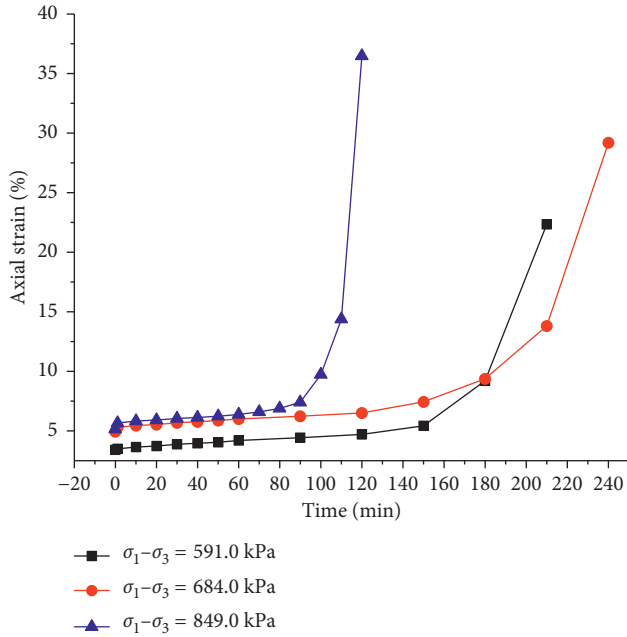


FIGURE 3: Relation between creep strain and time under different confining pressures.

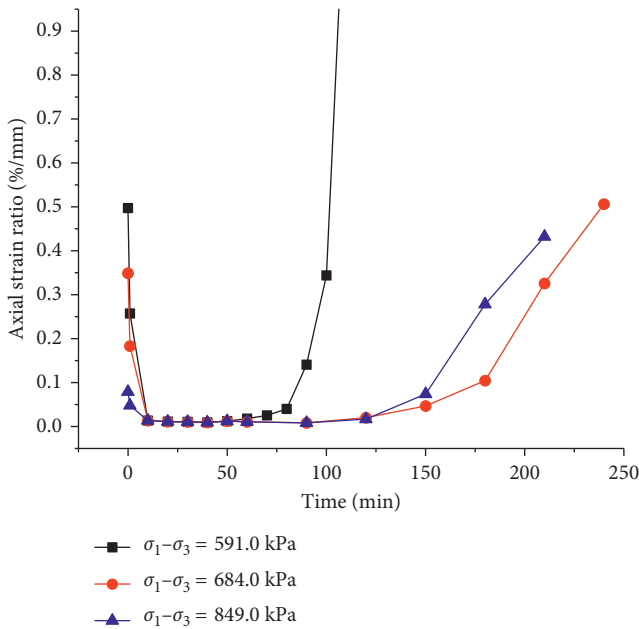


FIGURE 4: Relation between the creep strain ratio and time under different confining pressures.

process for each stress level lasts only for 110, 210, and 210 minutes. Figure 5 shows a schematic view of the red mud sample after failure under the deviatoric stress of 591 kPa and the confining pressure of 100 kPa; the main feature associated with the failure is the high axial plastic strain due to the accumulation of the former deviatoric stress level’s damage effects, and no brittle damage is observed in the samples. These results indicated that damage had begun to occur in weak local areas of the soil sample, causing increasing



FIGURE 5: Failure mode of the specimen tested under the deviatoric stress of 590 kPa and the confining pressure of 100 kPa.

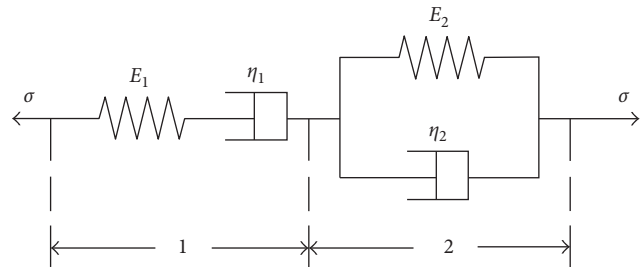


FIGURE 6: The Burgers creep model.

damage and time required for internal stress nonlinear adjustment to an equilibrium state with increased load.

3. Comparative Analysis of Two Creep Constitutive Models

The creep curves in Figure 2 show that the Bayer red mud sample experiences an attenuation creep stage and a steady creep stage when the stress level was less than a certain threshold and no obvious damage occurred over time.

According to the behavior shown by these curves, two well-established creep models, the Burgers creep model and the Singh–Mitchell equation, were used to describe the creep behavior of the Bayer red mud.

The Burgers creep model [27, 28] is made up of the Kelvin and Maxwell models in series as shown in Figure 6.

The creep equation of the Burgers creep model is

$$\varepsilon = \frac{\sigma}{E_1} + \frac{\sigma}{\eta_1} t + \frac{\sigma}{E_2} \left(1 - e^{-(E_2/\eta_2)t} \right), \quad (1)$$

where σ is the deviatoric stress; E_1 and η_1 are the elastic modulus and viscosity coefficient of the Maxwell body; and E_2 and η_2 are the elastic modulus and viscosity coefficient of the Kelvin body, respectively.

The Singh–Mitchell model is an empirical equation with three parameters [16]. The creep equation of the Singh–Mitchell model is given as [27]

$$\varepsilon = B_1 e^{\beta D} \left(\frac{t}{t_1} \right)^\lambda,$$

$$B_1 = \frac{A_1 t_1}{1 - m}, \quad (2)$$

$$\beta = \alpha,$$

$$\lambda = 1 - m,$$

where λ is the slope of $\ln \varepsilon$ against $\ln t$ at any fixed value of D , β is the slope of $\ln t$ against D , at any fixed time, and B_1 is the intercept of $\ln \varepsilon$ against D at $t = t_1$.

The data measured under multistep loading in the test are processed using the Boltzmann superposition [29]. Based on the quasi-Newton search method [30] by the software of Origin 8.5, the Burgers model and the Singh–Mitchell model are used to fit the creep data to obtain the creep parameters. The comparison among the Burgers model’s predictions of creep curves, the Singh–Mitchell model’s predictions of creep curves, and the experimental creep results under different confining pressures is shown in Figure 7. The relevant parameters of the Burgers creep model and the Singh–Mitchell model identified from the data processing are shown in Tables 3 and 4. It is observed that both the models can capture the creep behavior of the Bayer red mud, but the Burgers model results are consistent with the experimental data, and the model can better describe the typical creep behavior under the stress less than a certain threshold.

4. Damage Evolution Equation and Improved Burgers Creep Damage Model

4.1. Damage Evolution. According to the former test results, it can be obtained that if the applied load is much higher, the structure of the soil sample begins to destruct and the creep strain of the samples increases rapidly in the accelerated creep stage and fails eventually. Kachanov [31] suggested that this increase in the strain rate can be described by the introduction of a damage variable into the constitutive equation. The concept of an effective stress proposed by Kachanov [32] has been used to formulate constitutive equations for damaged materials [33]. From the test results, we assume that the damage evolution begins at the steady creep stage. So, the evolution equation of the damage variable can be expressed as [10]

$$D = 1 - \exp\left(-\frac{\varepsilon - \varepsilon_0}{\varepsilon_0}\right), \quad (3)$$

where ε and D are creep strain and damage factor, respectively; while ε_0 is the damage initial strain, which can be obtained at the starting point of the steady creep stage.

According to the whole creep curves (Figure 3), an exponential equation (4) was used to describe the strain of $\varepsilon - \varepsilon_0$. The fitting test results are shown in Figure 8 when ε_0 are 4.13%, 5.91%, and 6.28%, respectively. And the squares of

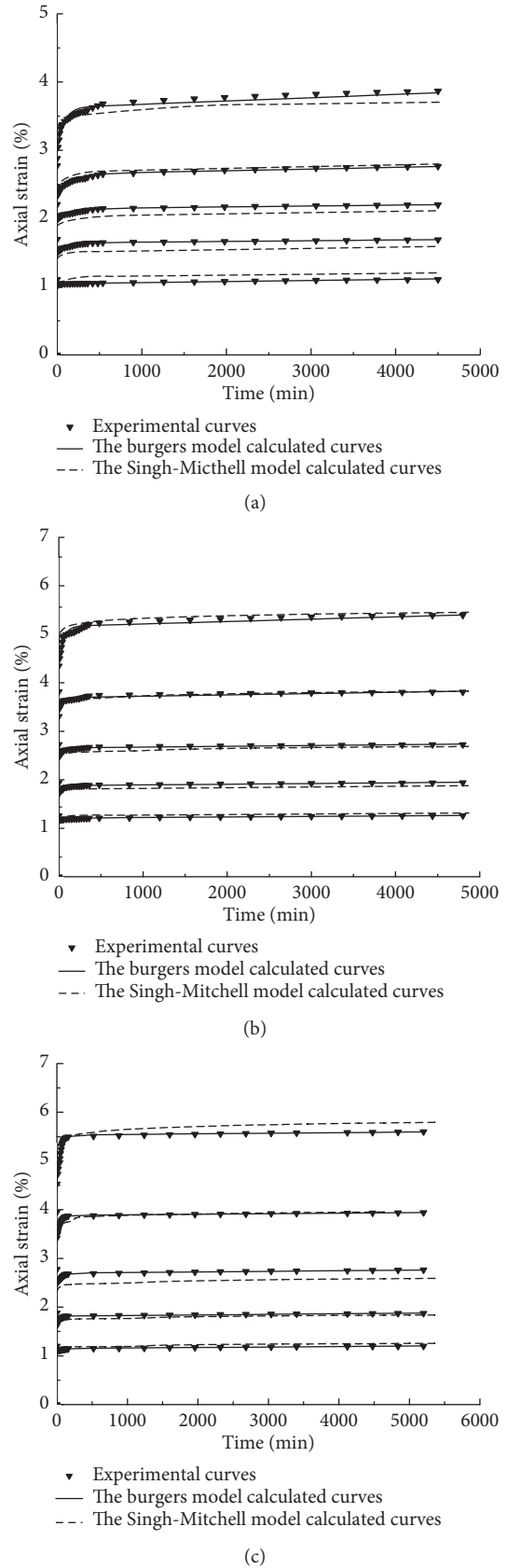


FIGURE 7: Comparison between the Burgers mode predicted creep curves and the experimental curves. Confining pressure: (a) 100 kPa, (b) 150 kPa, and (c) 200 kPa.

TABLE 3: Burgers model creep parameters of the BRM under different confining pressures.

Confining pressure (kPa)	Deviatoric stress (kPa)	Burgers model parameters				R^2
		E_1 (kPa)	η_1 (kPa-min)	E_2 (kPa)	η_2 (kPa-min)	
100	98.5	128.17	13966524.90	3020.84	13966524.9	1.000
	197	173.71	24214292.80	1509.58	52422.20	0.995
	295.5	171.01	33992245.50	1973.32	140306.04	0.991
	394	166.11	50861180.30	1191.11	54682.70	0.991
	492.5	157.47	57960664.70	680.23	31802.25	0.962
150	114.1	96.86	10789254.90	3369.48	872176.59	0.993
	228	132.50	15930262.60	1432.39	77164.05	0.992
	342	138.43	20909142.90	1830.65	3036.11	0.982
	456	136.74	16576719.60	1263.86	40147.25	0.951
	570	130.22	11547983.90	724.10	38893.11	0.967
200	141.5	128.17	13966524.90	3020.84	234325.89	0.995
	283	173.71	24214292.80	1509.58	52422.20	0.992
	424.5	171.01	33992245.50	1973.32	140306.04	0.993
	566	166.11	50861180.30	1191.11	54682.70	0.999
	707.5	157.47	57960664.70	680.23	31802.25	0.996

TABLE 4: Singh–Mitchell model parameters of the BRM under different confining pressures.

Confining pressure (kPa)	Deviatoric Stress (kPa)	Singh–Mitchell model parameters			
		D	β	B_1	Average λ
100	98.500	0.166	1.690	0.840	0.0191
	197.000	0.332			
	295.500	0.497			
	394.000	0.663			
	492.500	0.829			
150	114.100	0.166	2.121	0.873	0.014
	228.000	0.334			
	342.000	0.501			
	456.000	0.667			
	570.000	0.834			
200	141.500	0.167	2.286	0.803	0.015
	283.000	0.334			
	424.500	0.501			
	566.000	0.668			
	707.500	0.835			

the fitting correlation coefficient (R^2) are 0.995, 0.983, and 0.946, respectively, indicating that the exponential equation (4) can well describe the steady creep and accelerated stages of the Bayer red mud samples.

$$\varepsilon - \varepsilon_0 = At^\beta. \quad (4)$$

By substituting (4) into (3), we can construct the soil damage evolution constitutive model:

$$D = 1 - \exp\left(-\alpha \frac{t^\beta}{t_0^\beta}\right), \quad (5)$$

where α and β are the parameters controlling the damage evolution with time, which are related to the stress levels. t is the creep time and t_0 is the unit time, which value is 1. The relationship between the damage evolution and creep time, obtained by fitting the test results, is shown in Figure 9; the parameters of the damage constitutive model are listed in Table 5.

4.2. Improved Burgers Creep Damage Model. The viscous coefficient will increase with the effect of low stress and decrease when the stress that exceeds the long-term ultimate strength [34]. According to the above test results, a new nonlinear viscoplasticity model was presented based on the creep damage model represented by (5). Also, in series with the Burgers creep model, a new improved Burgers creep damage model (Figure 10) was proposed, which can accurately describe the properties of the BRM during the instantaneous creep, decay creep, steady creep, and accelerating creep stages, to explain the evolution law of the damage characteristics over time.

If a series connection is made for each creep body in Figure 10, then

$$\varepsilon = \varepsilon_1 + \varepsilon_2 + \varepsilon_3. \quad (6)$$

Based on (1–6), the creep equation of the improved Burgers damage model I under the effect of constant compression stress is

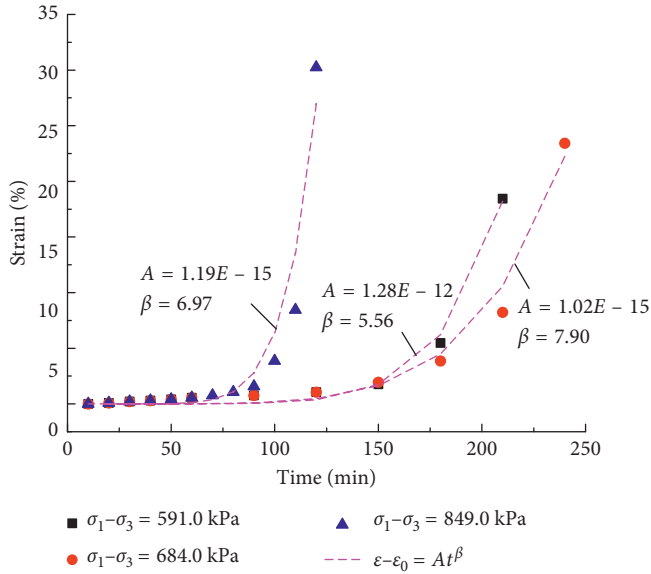


FIGURE 8: Relationship between the exponential equation fitting curves and test curves.

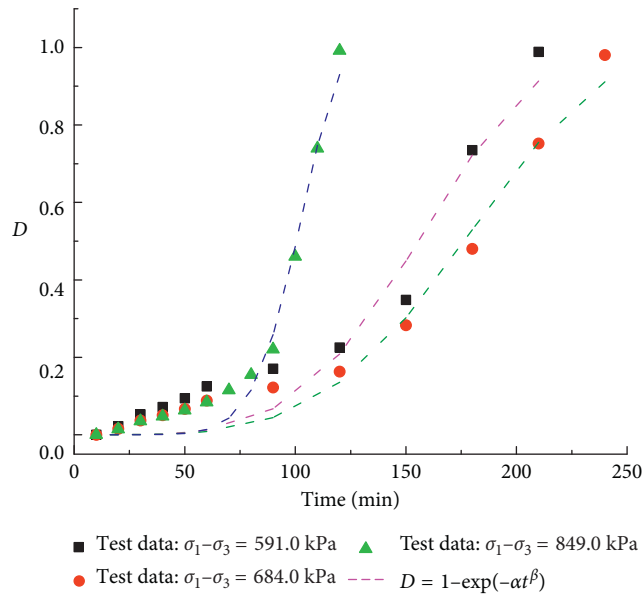


FIGURE 9: Damage evolution under different stress levels.

TABLE 5: The parameters of the damage constitutive model.

Confining pressure (kPa)	Deviatoric stress (kPa)	α	β	R^2
100	591	$4.43E-10$	4.19	0.97
150	684	$5.35E-10$	4.06	0.98
200	849	$4.16E-16$	7.60	0.99

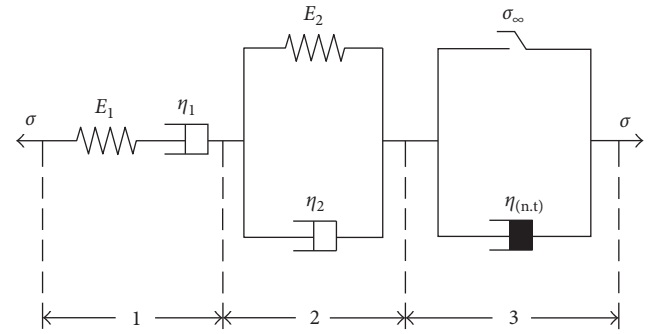


FIGURE 10: Illustration of the improved Burgers damage model.

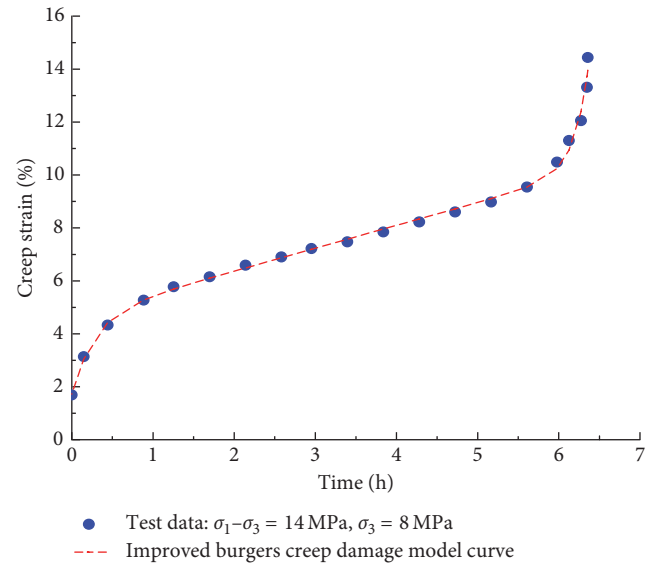


FIGURE 11: Comparison between the improved Burgers creep damage model curve with the test result from Li et al. [35].

$$\varepsilon = \frac{\sigma_0}{E_1} + \frac{\sigma_0}{\eta_1} t + \frac{\sigma_0}{E_2} \left(1 - \exp\left(-\frac{E_2}{\eta_2} t\right) \right) \quad (\sigma < \sigma_\infty)$$

$$\varepsilon = \frac{\sigma_0}{E_1} + \frac{\sigma_0}{\eta_1} t + \frac{\sigma_0}{E_2} \left(1 - \exp\left(-\frac{E_2}{\eta_2} t\right) \right) + \frac{\sigma_0 - \sigma_\infty}{\eta_3 (1 - D)} t \quad (\sigma \geq \sigma_\infty), \quad (7)$$

where σ_∞ is the long-term strength which is the threshold of the damage and η_3 is the original viscosity coefficient.

Test data of artificially frozen soil that is reproduced from [35] was used to validate and analyze the applicability of the improved Burgers damage model, as shown in

Figure 11. The creep parameters of this soil are shown in Table 6. It can be seen clearly that the creep experimental results of the Bayer red mud agree very well with the numerical prediction using the improved Burgers creep damage model, and square of the correlation coefficient (R^2)

TABLE 6: Improved Burgers damage creep model parameters of artificially frozen soil [35].

E_1 (kPa)	η_1 (kPa·min)	E_2 (kPa)	η_2 (kPa·min)	η_3 (kPa·min)	α	β	R^2
376.26	752.45	205.89	57.49	$3.27E+11$	0.63	1.86	0.996

TABLE 7: Improved Burgers damage creep model parameters under different confining pressures.

E_1 (kPa)	η_1 (kPa·min)	E_2 (kPa)	η_2 (kPa·min)	η_3 (kPa·min)	α	β	R^2
15168.31	$7.33E+11$	135781.55	0.74	$1.30E+11$	0.76	0.52	0.995
12649.08	$6.27E+06$	187336.83	2.97	$1.03E+15$	2.47	0.39	0.996
15089.88	$1.58E+21$	81472.33	0.22	$3.06E+14$	1.01	0.63	0.996

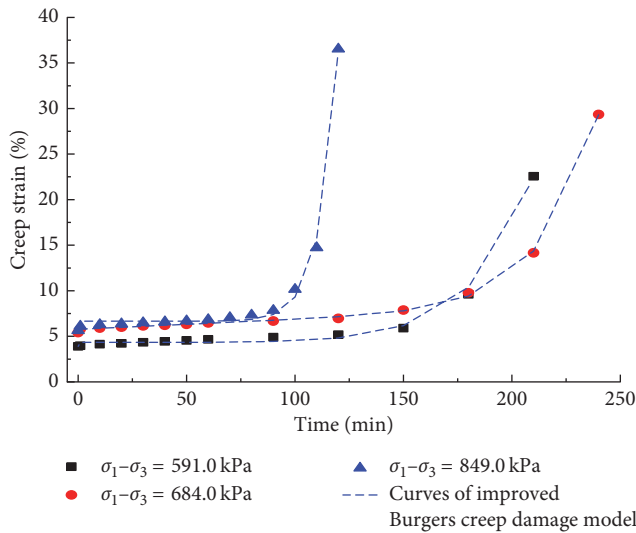


FIGURE 12: Comparison between the improved Burgers creep model's prediction of creep curves and the tested results.

is 0.996, indicating that the improved Burgers creep damage model has good applicability.

4.3. Parameter Identification of Improved Burgers Creep Model. In order to determine creep mechanical parameters of the improved Burgers creep model at different deviatoric stresses, an iteration procedure was used based on the quasi-Newton search method [30]. The relevant parameters of the improved Burgers creep damage model were identified from data processing, as shown in Table 7, and the calculated results of the creep curves and the tested ones are shown in Figure 12. From Figure 12, it is found that the calculated results of the proposed model are in good agreement with the tested results under these three deviatoric stress (591 kPa, 684 kPa, and 849 kPa). The correlation coefficient squares (R^2) of the three curves are 0.995, 0.996, and 0.996, respectively, indicating that the prediction precision of the proposed model here is high in the simulating properties of the Bayer red mud.

5. Conclusions

The aim of this research is to lay a foundation for the evaluation and design processes in the Bayer red mud in the Guizhou Aluminum Factory red mud disposal field. A series

of triaxial drained creep tests were conducted under different confining and deviatoric stresses. The test results indicate that the Bayer red mud has two creep stages under lower deviatoric stresses, namely, the attenuation creep stage and the steady creep stage; while in high deviatoric stress level, the accelerated creep stage with less instant elastic deformation and attenuation creep strain appears. The main failure mechanism of the Bayer red mud is plastic shear, accompanied by a significant compression and ductile dilatancy.

Based on the tested results, the creep parameters of the Burgers creep model and Singh–Mitchell creep model were determined through the curve fitting of the measured data. The results demonstrate a high precision of the Burgers creep model in prediction of the creep curve under certain deviatoric stress level, compared with the Singh–Mitchell creep model.

A new damage evolution constitutive equation of the Bayer red mud was constructed according to the creep strain of steady creep and accelerating creep stages and combined with the Burgers creep model, and a new improved Burgers creep damage model was proposed, which parameters were also analyzed in detail. The improved Burgers creep damage model which has been verified by the conformity of the result of the experiment illustrates that the model can accurately describe the properties of the BRM during the instant elastic strain, attenuation creep, steady creep, and accelerating creep stages.

Conflicts of Interest

The authors declare that there are no conflicts of interest regarding the publication of this paper.

Acknowledgments

This study was partially supported by the National Natural Science Foundation of China (Grant no. 41302223), Science and Technology Plan Projects of Chongqing Administration of Land, Resources and Housing (KJ-2015047), Chongqing No. 3 Colleges and Universities Youth Backbone Teachers Funding Plans and Chongqing Research Program of Basic Research and Frontier Technology (cstc2016jcyjA0074, cstc2016jcyjA0933, and cstc2015jcyjA90012), and Scientific and Technological Research Program of Chongqing Municipal Education Commission (KJ1713327 and KJ1600532). The authors also thank Professor Yang Mijia, Department of

Civil and Environmental Engineering, North Dakota State University, for his valuable suggestions and English improvement of this manuscript.

References

- [1] A. R. Hind, S. K. Bhargava, and S. C. Grocott, "The surface chemistry of Bayer process solids: a reviews," *Colloids and Surfaces A: Physicochemical and Engineering Aspects*, vol. 146, no. 1–3, pp. 359–374, 1999.
- [2] Y. F. Huang, G. H. Han, J. T. Liu, and W. J. Wang, "A facile disposal of Bayer red mud based on selective flocculation desliming with organic humics," *Journal of Hazardous Materials*, vol. 301, pp. 46–55, 2016.
- [3] X. F. Zhu, T. A. Zhang, Y. X. Wang, G. Z. Lü, and W. G. Zhang, "Recovery of alkali and alumina from Bayer red mud by the calcification-carbonation method," *International Journal of Minerals, Metallurgy and Materials*, vol. 23, no. 3, pp. 257–268, 2016.
- [4] P. Wang and D. Y. Liu, "Physical and chemical properties of sintering red mud and Bayer red mud and the implications for beneficial utilization," *Materials*, vol. 5, no. 10, pp. 1800–1810, 2012.
- [5] H. Karimpour and P. V. Lade, "Creep behavior in Virginia Beach sand," *Canadian Geotechnical Journal*, vol. 50, no. 11, pp. 1159–1178, 2013.
- [6] Y. B. Zhu and H. M. Yu, "Unsaturated creep behaviors of weak intercalated soils in soft rock of Badong formation," *Journal of Mountain Science*, vol. 12, no. 6, pp. 1460–1470, 2015.
- [7] X. L. Lai, S. M. Wang, W. M. Ye, and Y. J. Cui, "Experimental investigation on the creep behavior of an unsaturated clay," *Canadian Geotechnical Journal*, vol. 51, no. 6, pp. 621–628, 2014.
- [8] H. D. Yu, W. Z. Chen, Z. Gong et al., "Creep behavior of boom clay," *International Journal of Rock Mechanics and Mining Sciences*, vol. 76, pp. 256–264, 2015.
- [9] B. P. Wen and X. Z. Jiang, "Effect of gravel content on creep behavior of clayey soil at residual state: implication for its role in slow-moving landslides," *Landslides*, vol. 14, no. 2, pp. 559–576, 2017.
- [10] M. K. Liao, Y. M. Lai, E. L. Liu, and X. S. Wan, "A fractional order creep constitutive model of warm frozen silt," *Acta Geotechnica*, vol. 12, no. 2, pp. 377–389, 2017.
- [11] H. Zhou, Y. Jia, and J. Shao, "A unified elastic–plastic and viscoplastic damage model for quasi-brittle rocks," *International Journal of Rock Mechanics and Mining Sciences*, vol. 45, no. 8, pp. 1237–1251, 2008.
- [12] T. Bui, H. Wong, F. Deleruyelle, and A. Zhou, "Constitutive modelling of the time-dependent behaviour of partially saturated rocks," *Computers and Geotechnics*, vol. 78, pp. 123–133, 2016.
- [13] D. K. Kim, "Comparisons of overstress theory with an empirical model in creep prediction for cohesive soils," *KSCSE Journal of Civil Engineering*, vol. 9, no. 6, pp. 489–494, 2005.
- [14] V. De Gennaro and J. A. Pereira, "Viscoplastic constitutive model for unsaturated geomaterials," *Computers and Geotechnics*, vol. 54, pp. 143–151, 2013.
- [15] T. A. Bui, H. Wong, F. Deleruyelle, L. Z. Xie, and D. T. Tran, "A thermodynamically consistent model accounting for viscoplastic creep and anisotropic damage in unsaturated rocks," *International Journal of Solids and Structures*, vol. 117, pp. 26–38, 2017.
- [16] A. Singh and J. K. Mitchell, "General stress-strain-time function for soils," *Journal of Soil Mechanics and Found Engineering Division*, vol. 94, no. 1, pp. 21–46, 1968.
- [17] G. Mesri, E. Rebres-Cordero, D. R. Shields, and A. Castro, "Shear stress strain-time behavior of clays," *Géotechnique*, vol. 31, no. 4, pp. 537–552, 1981.
- [18] J. H. Yin, "Non-linear creep of soils in oedometer tests," *Geotechnique*, vol. 49, no. 5, pp. 699–707, 1999.
- [19] J. K. Mitchell, *Fundamentals of Soil Behavior*, Wiley, New York, NY, USA, 2nd edition, 1993.
- [20] H. M. Gao, Y. M. Chen, H. L. Liu, J. Y. Liu, and J. Chu, "Creep behavior of EPS composite soil," *Science China Technological Sciences*, vol. 55, no. 11, pp. 3070–3080, 2012.
- [21] S. H. Wang, J. L. Qi, Z. Y. Yin, J. M. Zhang, and W. Ma, "A simple rheological element based creep model for frozen soils," *Cold Regions Science and Technology*, vol. 106–107, pp. 47–54, 2014.
- [22] M. Karstunen and Z. Y. Yin, "Modelling time-dependent behaviour of Murro test embankment," *Geotechnique*, vol. 60, no. 10, pp. 735–749, 2010.
- [23] Z. Y. Yin, M. Karstunen, C. S. Chang, M. Koskinen, and M. Lojander, "Modeling time-dependent behavior of soft sensitive clay," *Journal of Geotechnical and Geoenvironmental Engineering*, vol. 137, no. 11, pp. 103–1113, 2011.
- [24] M. M. Han, *Study on Creep Characteristics of Red Mud from Bayer Process*, M.S. thesis, Chongqing University, Chongqing, China, 2015.
- [25] ASTM, *Standard Practice for Classification of Soils for Engineering Purpose. Annual Book of ASTM Standards*, ASTM International D4767-11, West Conshohocken, PA, USA, 2011.
- [26] W. Huang, D. Y. Liu, B. Y. Zhao, Y. B. Feng, and Y. C. Xia, "Study on the rheological properties and constitutive model of Shenzhen mucky soft soil," *Journal of Engineering Science and Technology*, vol. 7, pp. 55–61, 2014.
- [27] M. J. Sun, H. M. Tang, M. Y. Wang, Z. G. Shan, and X. L. Hu, "Creep behavior of slip zone soil of the Majiagou landslide in the Three Gorges area," *Environmental Earth Sciences*, vol. 75, no. 16, p. 1199, 2016.
- [28] W. B. Ma, Q. H. Rao, P. Li, S. C. Guo, and K. Feng, "Shear creep parameters of simulative soil for deep-sea sediment," *Journal of Central South University*, vol. 21, no. 12, pp. 4682–4689, 2014.
- [29] T. K. Tan, Z. O. Shi, Z. H. Yu, and W. X. Yang, "Dilatancy, creep and relaxation of brittle rocks measured with the 8000 kN multipurpose triaxial apparatus," *Physics of the Earth and Planetary Interiors*, vol. 55, no. 3–4, pp. 335–352, 1989.
- [30] Y. Zhang, W. Y. Xu, J. F. Shao, H. B. Zhao, and W. Wang, "Experimental investigation of creep behavior of clastic rock in Xiangjiaba Hydropower Project," *Water Science and Engineering*, vol. 8, no. 1, pp. 55–62, 2015.
- [31] L. M. Kachanov, *The Theory of Creep: Part I*, National Lending Library for Science and Technology, Boston, MA, USA, 1967.
- [32] L. M. Kachanov, "Rupture time under creep conditions," *International Journal of Fracture*, vol. 97, pp. 11–18, 1999.
- [33] J. Lemaitre and J. L. Chaboche, *Mechanics of Solid Materials*, Cambridge University Press, New York, NY, USA, 1990.
- [34] P. Cao, Y. D. Wen, Y. X. Wang, H. P. Yuan, and B. X. Yuan, "Study on nonlinear damage creep constitutive model for high-stress soft rock," *Environmental Earth Sciences*, vol. 75, no. 10, p. 900, 2016.
- [35] D. W. Li, J. H. Fan, and R. H. Wang, "Research on visco-elastic-plastic creep model of artificially frozen soil under high confining pressures," *Cold Regions Science and Technology*, vol. 65, no. 2, pp. 219–225, 2011.